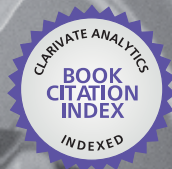




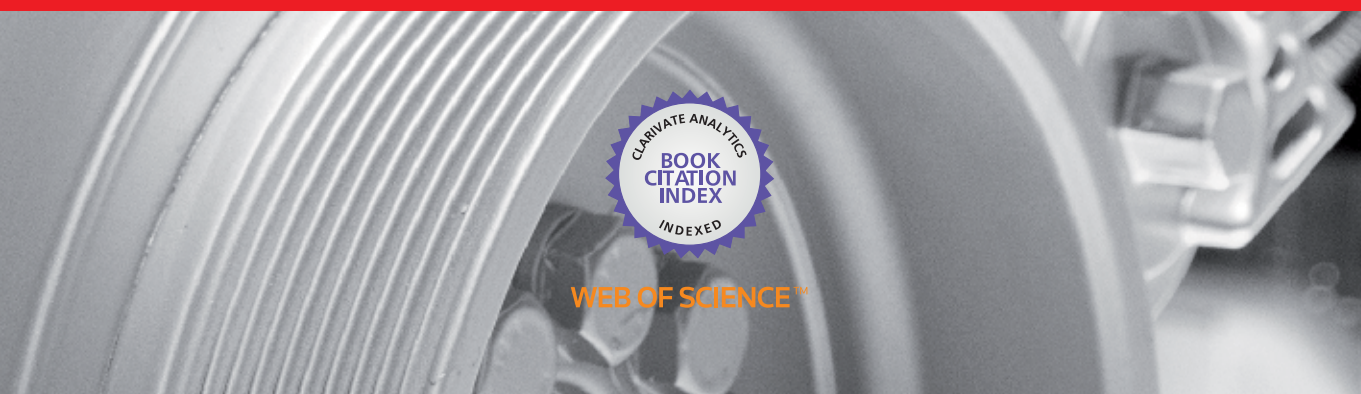
IntechOpen

New Trends and Developments in Automotive System Engineering

Edited by Marcello Chiaberge



WEB OF SCIENCE™



NEW TRENDS AND DEVELOPMENTS IN AUTOMOTIVE SYSTEM ENGINEERING

Edited by **Marcello Chiaberge**

New Trends and Developments in Automotive System Engineering

<http://dx.doi.org/10.5772/552>

Edited by Marcello Chiaberge

Contributors

Abdullah Al-Shabibi, Ciaran Hughes, Ronan O'Malley, Diarmaid O'Cualain, Martin Glavin, Edward Jones, Mathias Johanson, Aidy Ali, Yann Guezennec, Ahmed Al-Durra, Stephen Yurkovich, Paolo Mercorelli, Marcello Chiaberge, Gianluca Botto, Mirko De Giuseppe, Roman Jobava, David Karkashadze, Faik Bogdanov, Paata Tsereteli, Anna Gheonjian, Ekaterina Yavolovskaya, Christoph Ullrich, Hicham Tazi, Detlef Schleicher, Jonas Gruber, Adriano R. V. Benvenho, Rosamaria W. C. Li, Renata Lippi, Ryuichiro Ebara, Tom P. Kohler, Rainer Gehring, Joachim Froeschl, Dominik Buecherl, Hans-Georg Herzog, Guillaume Andrieu, Francisco J. Sánchez-Alejo, Miguel A. Alvarez, Francisco Aparicio, José M^a Lopez, Francisco Ebeling, Mariana Iootty, Helder Queiroz Pinto, Jr., Mariagrazia Graziano, Massimo Ruo Roch, Berenika Hausnerova, Brendan David Pell, Wayne Rowe, Edin sulic, Kamran Ghorbani, Sabu John, N. A. Kadhim, Shahrum Abdullah, A.K. Ariffin, Philippe Colomban, Andrea Festini, Enrico Zenerino, Andrea Tonoli, Helfried Steiner, Günter Brenn, Franz Ramstorfer, Bernd Breitschädel, Niels Koch, Gereon Weiss, Marc Zeller, Dirk Eilers, Faisal Mufti, Robert Mahony, Jochen Heinzmann, Fan Zeng, Beshah Ayalew, Julio Viana, Carlos Ribeiro, Omar Maluf, Jéferson Aparecido Moreto, Marco Antônio Colósio, José Carlos Santos, Waldek Wladimir Bose Filho, Dirceu Spinelli, Mauricio Angeloni, Md Abul Kalam, Bruno Charles De Cooman, Masaki Takahashi, Takashi Kumamaru, Kazuo Yoshida, Preeti Bajaj, Dinesh Padole

© The Editor(s) and the Author(s) 2011

The moral rights of the and the author(s) have been asserted.

All rights to the book as a whole are reserved by INTECH. The book as a whole (compilation) cannot be reproduced, distributed or used for commercial or non-commercial purposes without INTECH's written permission.

Enquiries concerning the use of the book should be directed to INTECH rights and permissions department (permissions@intechopen.com).

Violations are liable to prosecution under the governing Copyright Law.



Individual chapters of this publication are distributed under the terms of the Creative Commons Attribution 3.0 Unported License which permits commercial use, distribution and reproduction of the individual chapters, provided the original author(s) and source publication are appropriately acknowledged. If so indicated, certain images may not be included under the Creative Commons license. In such cases users will need to obtain permission from the license holder to reproduce the material. More details and guidelines concerning content reuse and adaptation can be found at <http://www.intechopen.com/copyright-policy.html>.

Notice

Statements and opinions expressed in the chapters are these of the individual contributors and not necessarily those of the editors or publisher. No responsibility is accepted for the accuracy of information contained in the published chapters. The publisher assumes no responsibility for any damage or injury to persons or property arising out of the use of any materials, instructions, methods or ideas contained in the book.

First published in Croatia, 2011 by INTECH d.o.o.

eBook (PDF) Published by IN TECH d.o.o.

Place and year of publication of eBook (PDF): Rijeka, 2019. IntechOpen is the global imprint of IN TECH d.o.o.

Printed in Croatia

Legal deposit, Croatia: National and University Library in Zagreb

Additional hard and PDF copies can be obtained from orders@intechopen.com

New Trends and Developments in Automotive System Engineering

Edited by Marcello Chiaberge

p. cm.

ISBN 978-953-307-517-4

eBook (PDF) ISBN 978-953-51-4536-3

We are IntechOpen, the world's leading publisher of Open Access books Built by scientists, for scientists

3,550+

Open access books available

112,000+

International authors and editors

115M+

Downloads

151

Countries delivered to

Our authors are among the
Top 1%

most cited scientists

12.2%

Contributors from top 500 universities



WEB OF SCIENCE™

Selection of our books indexed in the Book Citation Index
in Web of Science™ Core Collection (BKCI)

Interested in publishing with us?
Contact book.department@intechopen.com

Numbers displayed above are based on latest data collected.
For more information visit www.intechopen.com



Meet the editor



Marcello Chiaberge is assistant professor at Electronic Department of Politecnico di Torino and vice-director of Centro per i Servizi di Prototipazione of Politecnico di Torino, where he is also responsible and coordinator of the Electronic Group at Mechatronics Laboratory (LIM) of Politecnico di Torino. His research interests are: hardware implementation of neural networks and fuzzy systems, design and implementation of reconfigurable computing architectures for hard-real-time control systems, design and implementation of hybrid control systems based on programmable state-of-the-art devices (DSP, FPGA and FPAA), implementation of fault-tolerance communication networks based on plastic optical fibers (POF). Another research field is the design and implementation of non-conventional power driver systems for special actuation systems in the automotive, industrial and space fields of application. He is also involved in the design and control of small rovers for space exploration, archeological prospecting and humanitarian/anti-terrorism application in collaboration with Piedmont Region, Thales Alenia Space and Italian Space Agency (ASI). Chiaberge is an IEEE member, the author of more than 60 articles accepted in international conferences and reviews and a co-author of 7 international patents.

Contents

Preface XIII

Part 1 Fuel Efficiency and ESU Improvements 1

Chapter 1 **Experimental Test of a Diesel Engine using Envo-Diesel as an Alternative Fuel 3**
M.A.Kalam and H.H. Masjuki

Chapter 2 **Analytical Methods for Determining Automotive Fuel Composition 13**
Jonas Gruber, Renata Lippi,
Rosamaria W. C. Li and Adriano R. V. Benvenho

Chapter 3 **Automotive Fuel Consumption in Brazil: Applying Static and Dynamic Systems of Demand Equations 29**
Mariana Iooty, Helder Pinto Jr. and Francisco Ebeling

Part 2 Material Characterization and Improvements 45

Chapter 4 **Fatigue and Fracture Behavior of Forging Die Steels 47**
Ryuichiro Ebara

Chapter 5 **Optimization of Injection Moulded Polymer Automotive Components 65**
Ribeiro, C.J. and Viana, J.C.

Chapter 6 **High Mn TWIP Steels for Automotive Applications 101**
B. C. De Cooman, Kwang-geun Chin and Jinkyung Kim

Chapter 7 **Powder Injection Moulding – An Alternative Processing Method for Automotive Items 129**
Berenika Hausnerova

- Chapter 8 **Thermomechanical and Isothermal Fatigue Behavior of Gray Cast Iron for Automotive Brake Discs 147**
Omar Maluf, Jéferson Aparecido Moreto, Maurício Angeloni, Marco Antônio Colósio, José Carlos Santos, Waldek Wladimir Bose Filho and Dirceu Spinelli
- Chapter 9 **Advanced Robotic Radiative Process Control for Automotive Coatings 167**
Fan Zeng and Beshah Ayalew
- Part 3 New Components and Related Technologies 187**
- Chapter 10 **DC/DC Step-Up Converters for Automotive Applications: a FPGA Based Approach 189**
M. Chiaberge, G. Botto and M. De Giuseppe
- Chapter 11 **The Thermo-mechanical Behavior in Automotive Brake and Clutch Systems 207**
Abdullah M. Al-Shabibi
- Chapter 12 **Dynamic Analysis of an Automobile Lower Suspension Arm Using Experiment and Numerical Technique 231**
S. Abdullah, N.A. Kadhim, A.K. Ariffin and M. Hosseini
- Chapter 13 **Increased Cooling Power with Nucleate Boiling Flow in Automotive Engine Applications 249**
Helfried Steiner, Günter Brenn, Franz Ramstorfer and Bernd Breitschädel
- Chapter 14 **The “Equivalent Cable Bundle Method”: an Efficient Multiconductor Reduction Technique to Model Automotive Cable Networks 273**
Guillaume Andrieu, Xavier Bunlon, Lamine Koné, Jean-Philippe Parmantier, Bernard Démoulin and Alain Reineixl
- Chapter 15 **Fatigue Characteristic of Automotive Jounce Bumper 297**
Aidy Ali, R.S. Sidhu and M.S.A. Samad
- Part 4 Control Systems and Algorithms 307**
- Chapter 16 **On the Control of Automotive Traction PEM Fuel Cell Systems 309**
Ahmed Al-Durra, Stephen Yurkovich and Yann Guezennec
- Chapter 17 **An Adaptive Two-Stage Observer in the Control of a New Electromagnetic Valve Actuator for Camless Internal Combustion Engines 343**
Paolo Mercorelli

- Chapter 18 **Integrated Controller Design for Automotive Semi-Active Suspension Considering Vehicle Behavior with Steering Input 369**
Masaki Takahashi, Takashi Kumamaru and Kazuo Yoshida
- Chapter 19 **Design of an Embedded Controller for Some Applications of an Automotives 383**
Preeti Bajaj and Dinesh Padole
- Chapter 20 **Arbitration Schemes for Multiprocessor Shared Bus 395**
Preeti Bajaj and Dinesh Padole
- Chapter 21 **Towards Automotive Embedded Systems with Self-X Properties 411**
Gereon Weiss, Marc Zeller and Dirk Eilers
- Chapter 22 **4D Ground Plane Estimation Algorithm for Advanced Driver Assistance Systems 433**
Faisal Mufti, Robert Mahony and Jochen Heinzmann
- Part 5 Infotainment and Navigation Systems 449**
- Chapter 23 **The Car Entertainment System 451**
Niels Koch
- Chapter 24 **Information and Communication Support for Automotive Testing and Validation 473**
Mathias Johanson
- Chapter 25 **Trends towards Automotive Electronic Vision Systems for Mitigation of Accidents in Safety Critical Situations 493**
Ciarán Hughes, Ronan O'Malley, Diarmaid O' Cualain, Martin Glavin and Edward Jones
- Chapter 26 **Advancements in Automotive Antennas 513**
Brendan D. Pell, Edin Sulic, Wayne S. T. Rowe, Kamran Ghorbani and Sabu John
- Part 6 Development Tools 539**
- Chapter 27 **Automotive VHDL-AMS Electro-mechanics Simulations 541**
Mariagrazia Graziano and Massimo Ruo Roch
- Chapter 28 **Potential and Drawbacks of Raman (Micro)Spectrometry for the Understanding of Iron and Steel Corrosion 567**
Philippe Colombar

- Chapter 29 **Computational Techniques
for Automotive Antenna Simulations 585**
Faik Bogdanov, Roman Jobava, David Karkashadze,
Paata Tsereteli, Anna Gheonjian, Ekaterina Yavolovskaya,
Detlef Schleicher, Christoph Ullrich and Hicham Tazi
- Chapter 30 **Voltage Stability Analysis of Automotive Power Nets
Based on Modeling and Experimental Results 611**
Tom P. Kohler, Rainer Gehring, Joachim Froeschl,
Dominik Buecherl and Hans-Georg Herzog
- Part 7 Vehicle Design 631**
- Chapter 31 **Urban and Extra Urban Vehicles:
Re-Thinking the Vehicle Design 633**
Andrea Festini, Andrea Tonoli and Enrico Zenerino
- Chapter 32 **Analysis Approach of How University Automotive
Competitions Help Students to Accelerate
Their Automotive Engineer Profile 649**
Francisco J. Sánchez-Alejo, Miguel A. Álvarez,
Francisco Aparicio and José M. López

Preface

In the last few years the automobile design process is asked to become more responsible and responsibly related to environmental needs.

Basing the automotive design not only on the appearance, the visual appearance of the vehicle needs to be thought together and deeply integrated with the “power” developed by the engine.

So, vehicle design is becoming more and more differentiated and the vehicle behavior does not actually meet one single standard but is following the market trends. The vehicles are being designed according to detailed specifications and the product is characterized by specific customer’s profile looking for specific solutions to their own problems, which may be different for different customer’s profile.

In this complex scenario the definition of niche product is becoming obsolete and the automobile market is becoming a sum of many and very different vehicle categories: micro car, city car, minivan, SUV, roadster.

Also technological needs are changing, and the race to luxury and big comfortable, high powered sedan is now leaving place to “smart” vehicles designed to look for an intelligent solution to different mobility problems.

Or at least this is how it should be.

The vehicle of the future, and the vehicle that customers are looking for nowadays, is designed upon the basic needs, starting the vehicle and subsystems design according to the main mission of the vehicle itself: carrying people and goods.

Many aspects are “fighting” each other in the “design process”, spanning from economic/strategic needs (maintenance costs, taxes used to depend on engine displacement and/or insurance on power, parking areas, driving licenses, etc.) to emerging standards (The Corporate Average Fuel Economy CAFÉ, new rating method NCAP, EUROxx regulations, etc.) ending with more technological mission/comfort needs:

- Ergonomic needs
- Small vehicles for urban environment, to reduce traffic jams
- Fuel efficiency and pollution reduction
 - o Lightweight

- o Alternative fuels
- o Vehicle usage optimization
- o Engine Downsizing
- Safety
- Performance
- Offering to the customer the capability of changing the vehicle configuration (seats, luggage)

The need of reducing pollution and fuel consumption then indicates technologies like Stop & start – Micro & mild hybrids, as suitable powertrain layouts, dramatically reducing pollution while in traffic jams, or allowing the downsizing of the thermal engine, while keeping the performance at an acceptable level.

All these considerations lead to the conclusion that the optimization of the vehicle can be done only by optimizing the entire system, not looking for the optimum solution in each single subsystem.

The purpose of this book is therefore to try to present the new technologies development scenario, and not to give any indication about the direction that should be given to the research in this complex and multi-disciplinary challenging field.

Marcello Chiaberge
Mechatronics Laboratory – Politecnico di Torino
Italy

Part 1

Fuel Efficiency and ESU Improvements

Experimental Test of a Diesel Engine using Envo-Diesel as an Alternative Fuel

M.A.Kalam and H.H. Masjuki

*Department of Mechanical Engineering, University of Malaya
50603 Kuala Lumpur,
Malaysia*

1. Introduction

Recently, the use of diesel engines has increased rapidly because of their low fuel consumption and high efficiencies. Nowadays, diesel engines are used in transportation, power plant generation equipment, construction and industrial activities. These wide fields of the usage lead to increase the demand for petroleum fuel. The world is presently confronted with crises of fossil fuel depletion and environmental degradation.

The present energy scenario has stimulated active research interest in non-petroleum, renewable, and non-polluting fuels. The world reserves of primary energy and raw materials are, obviously, limited. According to an estimate, the reserves will last for 218 years for coal, 41 years for oil, and 63 years for natural gas, under a business-as-usual scenario (Agarwal 2007).

The depletion of world petroleum reserves and increasing of demand also causes rise in fuel prices. The prices of crude oil keep rising and fluctuating on a daily basis which are at near record levels and are stabilizing at about US\$140 per barrel now at Malaysia. This necessitates developing and commercializing unconventional fuel from natural sources. This may well be the main reason behind the growing interest for unconventional bio-energy sources and fuels around the world especially developing countries, which are striving hard to offset the oil monopoly.

This study concentrates on assessing the viability of using alternative fuels in the existing internal combustion engines. In Malaysia, many researches are carried out on palm oil to produce biofuel or biodiesel as an alternative fuel. Malaysia has become the biggest palm oil producer country in the world followed by Indonesia. Recently, Malaysian Palm Oil Board (MPOB) has been produces the P5 palm oil-based biofuel called "Envo Diesel" for local use. After palm oil, coconut oil is the next potential oil that can be produced as biofuel because of its high amount of oxygen contents that enhance the combustion process. The objective of this study is to carry out an experimental investigation of the performance and the exhaust emission characteristics of a diesel engine fueled with Envo Diesel and coconut oil blends and compared them with ordinary diesel fuel.

2. Experimental setup and procedures

The schematic of the experimental setup for used engine test bed can be seen in Fig.1. A commercial diesel (2L series) was selected for this investigation. The engine is type 2L, 53.6

kW capacities, fixed speed (4000 rpm). It is water-cooled, indirect diesel injection engine. The specifications of engine are shown in Table 1.

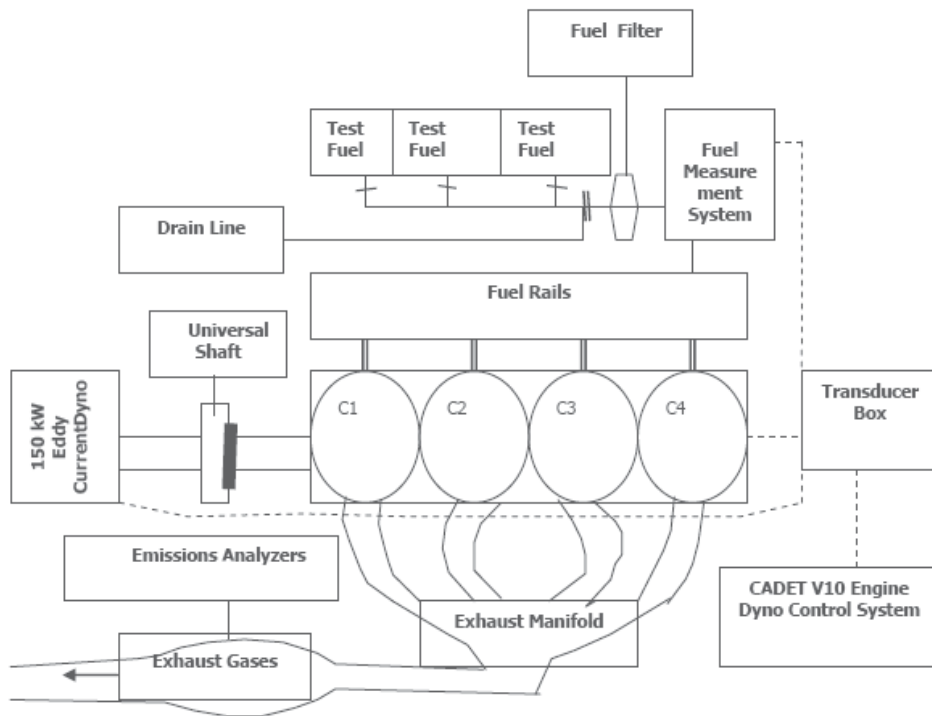


Fig. 1. Schematic Diagram of Engine Test Bed.

Engine	Diesel cycle
Model	2L
Type	Four strokes, water-cooled
Combustion	IDI, naturally aspirated
Number of cylinder	4
Bore x Stroke	92 x 92mm
Displacement	2.4 L (2446 cc)
Compression ratio	22.3 :1
Combustion chamber	Swirl chamber
Nozzle type	Throttle
Cooling system	Pressurized circulation
Continuous power output	53.6 kW at 4000 rpm
Torque	155.9 Nm at 2200 RPM

Table 1. Specification of used diesel Engine

2.1 Exhaust gas analyzer

Horiba exhaust gas analyzer was used to measure HC, CO, CO₂ and NO_x emissions. The analyzer was interfaced with engine controlled software so that all the data from emission analyzer and engine are logged at same time. The Hartridge smoke meter was used to measure smoke emission.

2.2 Test fuel

The analysis and the preparation of test fuels were conducted at the Engine Tribology Laboratory, Department of Mechanical Engineering, University of Malaya. A total of three test fuels were selected for this investigation. The test fuels chosen are (1) 100% conventional diesel fuel (B0) supplied by Malaysian petroleum company (Petronas), (2) P5 as 5% palm olein and 95% B0. It can be mentioned that fuel P5 is known as "Envo diesel" in Malaysia. (3) C5 as 5% coconut oil and 95% B0. The fuel C5 is being selected to be compared with Envo diesel. Details about Envo diesel can be seen in below-

2.3 Envo Diesel (Direct blending)

Envo Diesel consists of 5 percent processed palm oil commonly known as cooking oil and 95 percent conventional diesel fuel. The Malaysian Government has decided on the Envo Diesel for the local market because production cost of palm olein is RM1 per litre cheaper than ethyl ester. The Envo Diesel will be implemented in stages starting with vehicles of selected governmental agencies and then moving on the public use. The Malaysian palm oil board (MPOB) is using the blends of processed palm oil with petroleum diesel to produce Envo Diesel. The advantages of envo diesel are:

- a. No engine modification is required.
- b. Results in terms of engine performance, fuel consumption, exhaust emissions, repair and maintenance are acceptable.

2.4 Fuel properties test

The main properties of fuel tested such as calorific value, viscosity, specific density and flash point have been tested through standard method. The ordinary diesel fuel properties are compared with blended fuels.

Heat calorific value: Oxygen Bomb Calorimeter was used to obtain the heating value of each fuel. The sample was ignited and burned in the combustion chamber in the presence of 20 bar of oxygen, and the energy released is transferred to the surrounding water. The energy contain in the fuel was calculated on the basis of the conservation of energy principle by measuring the temperature rise of the water. $\text{Mass of fluid} \times \text{Caloric value} = (\text{Mass of water} + \text{water equivalent of bomb}) \times \text{Corrected temperature rise} \times \text{specific heat capacity of water}$.

Viscosity: Automatic viscometer was used for determining the kinematic viscosity of fuels. It provides a measure of the time required for a volume of fuels to flow under gravity through a calibrated glass capillary tube.

Specific gravity: Model DMA 4500/5000 specific gravity concentration meter was used to obtain the specific density value of tested fuels. The fuels density is measure at 15°C in g/cm³.

Flash point: Flash Point Tester HFP 380 Pensky Martens was used to measure the flash point value of each tested fuels. The flash point is determined by heating the fuel in a small

enclosed chamber until the vapors ignite when a small flame is passed over the surface of the fuel. The temperature of the fuel at this point is the flash point.

The test fuel physicochemical properties and compositions can be seen in Table 2 and Table 3 respectively.

Country			Germany	USA	Malaysia			
Properties/Fuels			Rape seed methyl ester	Soy bean methyl ester	Palm oil methyl ester	Envo diesel (P5)	C5	B0
1.	Density 15°C	g cm ⁻³	0.875-0.90	0.80-0.90	0.8783	0.827	0.827	0.82
2.	Viscosity 40°C	mm ² s ⁻¹	3.5-5.0	1.9-6.0	4.415	4.15	3.90	3.55
3.	Distillation 95%	°C	-	≤ 360	-	-		
4.	Flash point	°C	>100	>130	182	>140	>140	98
5.	High calorific value	MJ/kg	-	-	39.21	42.5	42.6	43

Table 2. Physicochemical properties of fuels

Fuel	Compositions
B0	100% diesel fuel
P5 (Envo diesel)	5% palm olein and 95% B0.
C5	5% coconut oil and 95% B0.

Table 3. Test Fuel Compositions

3. Results and discussion

From physicochemical test results, it is found that, the C5 has better heating value than P5. The higher heating value contributes more power output after burning the fuel in the engine cylinder. The heating values of both the P5 and C5 are slightly lower as compared to B0. From viscosity test result, it is found that the C5 fuel has lower viscosity than P5. Lower viscosity of a fuel contributes better atomization. However, the viscosity of both P5 and C5 are slightly higher than B0. Similar differences of all other properties along with biodiesel properties from other countries can be seen in Table 3.

Engine brake power versus speed at constant 85% throttle setting can be seen in Fig.2. It can be seen that brake power increases with increasing engine speed until 3000 rpm and then power starts to drop due to the effect of higher frictional force. The maximum brake power obtained by B0, C5 and P5 are 36.7 kW, 36.10 kW and 36.20 kW respectively at 3000 rpm. The lower brake power by C5 and P5 as compared to B0 is mainly due to their respective lower heating values. The average brake power all over the speed range is found as 28.28 kW, 28.08 kW and 27.94 kW by B0, C5 and P5 respectively.

The variation of exhaust gas temperatures of all the fuels are shown in Fig. 3. Exhaust gas temperatures of the blended fuels are lower than those of the diesel fuel due to the lower

heating value. However, their differences are small such as an average of all over the speed range 0.77% and 0.8% lower by C5 and P5 respectively.

The highest temperatures are found at 3000 rpm for all the fuels such as 735 °C, 732.5 °C and 733.6 °C by B0, C5 and P5 respectively.

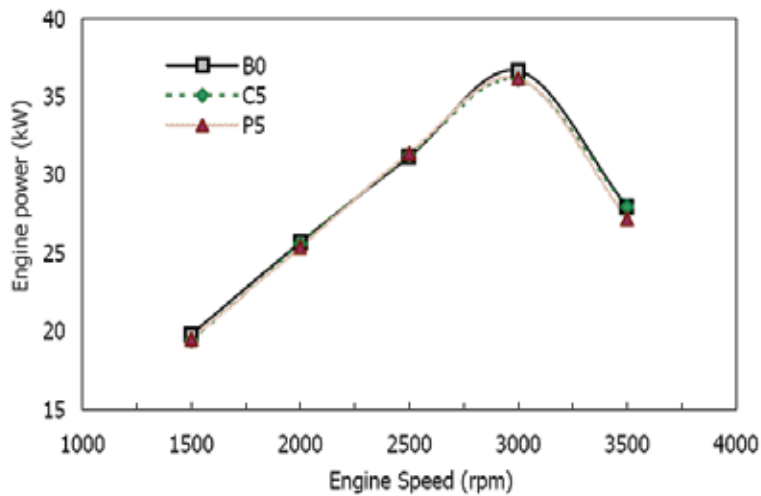


Fig. 2. Engine Brake Power Vs Speed At 85% Throttle.

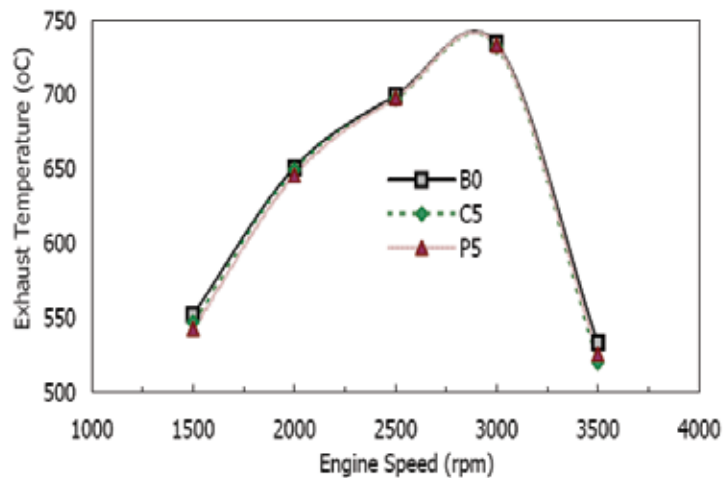


Fig. 3. Exhaust Temperature Vs Speed At 85% Throttle.

As diesel engine operates with an overall lean mixture, their CO emissions are normally lower than gasoline engines. Carbon monoxide (CO) is a toxic gas formed by the results from incomplete combustion. Emissions of CO are greatly dependent on the air-fuel ratio relative to the stoichiometric proportions. The CO emission depends on many parameters such as air-fuel ratio and fuel combustion performance into the engine cylinder. The CO emission versus engine speed is shown in Fig.4. The maximum value of CO emission is found at 3000 rpm such as 1.54%, 1.44% and 1.21% for B0, C5 and P5 respectively. The lowest CO emission is found from enviro diesel P5, followed by C5 and B0. On average all over the speed range, C5 and P5 reduce CO emission by 7.3% and 21% respectively.

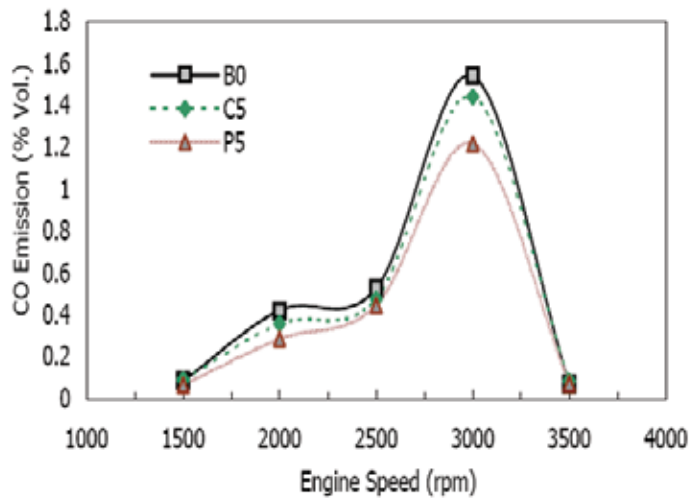


Fig. 4. CO Emissions Vs Engine Speed At 85% Throttle.

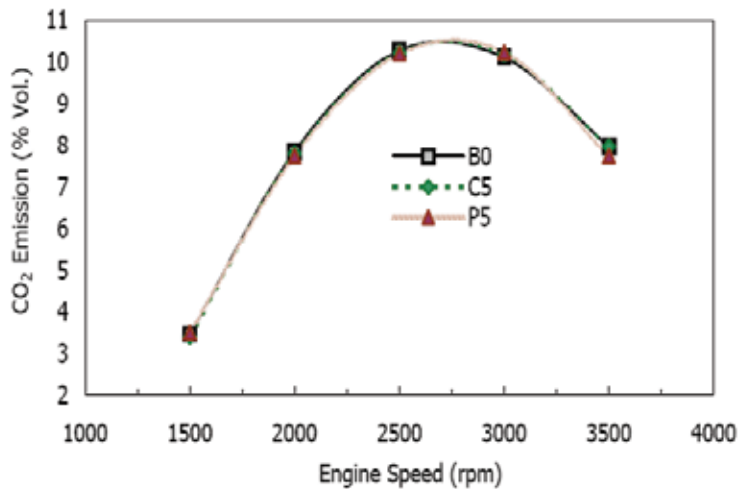


Fig. 5. CO₂ Emissions Vs Engine Speed At 85% Throttle.

The CO₂ emissions of different fuels are shown in Fig.5. Increasing CO₂ emission means better combustion phenomena. The maximum CO₂ are found between 2500 rpm to 3000 rpm due to better combustion at the current throttle-speed position. The maximum CO₂ emission is found at 3000 rpm for all the fuels as shows 10.12%, 10.19% and 10.25% by B0, C5 and P5 respectively. The envo diesel produces more CO₂ than C5 and B0 fuels which means better combustion and it is proven since P5 produces lowest CO emission (Fig.4.)

Unburned hydrocarbons (HC) are the results of fuel incomplete combustion. Similar to carbon monoxide, unburned hydrocarbons result from flame quenching in crevice regions and at cylinder walls. Other causes of unburned hydrocarbons are running engine on too rich fuel air ratio with insufficient oxygen and the incomplete combustion of lube oil. Another cause is the oil film around the cylinder absorbs hydrocarbons, preventing them from burning, and then releases them into the exhaust gas. Also misfire admits hydrocarbons into the exhaust. It can be seen (in Fig. 6) that the lowest level of HC is produced by Envo diesel P5 followed by C5 and B0. The maximum difference is found at 3000 rpm such as 21.8 ppm, 19.8 ppm and 14.9 ppm by B0, C5 and P5 respectively. However, all over the test cycle, it is found that C5 and P5 reduce HC emission by 5.5% and 18% respectively as compared to B0 fuel. Now, based on CO, CO₂ and HC emissions, it can be confirmed that envo diesel P5 produce better combustion than C5 and B0 fuels.

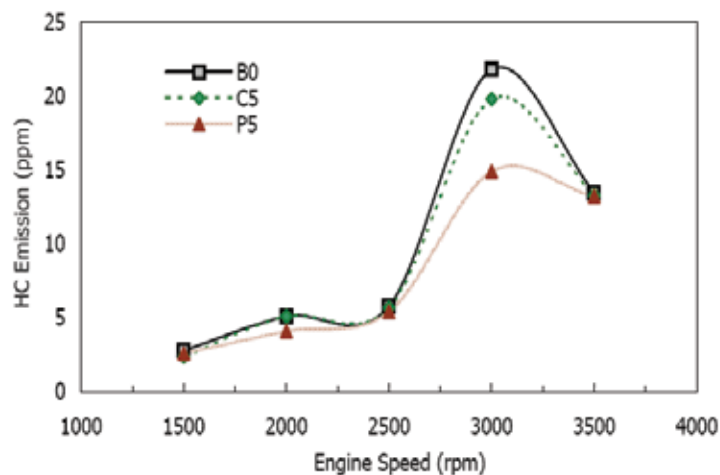


Fig. 6. HC Emission Vs Engine Speed At 85% Throttle.

Oxides of nitrogen (NO_x) emission is shown in Fig. 7. The NO_x emission is strongly related to lean fuel with high cylinder temperature or high peak combustion temperature. A fuel with high heat release rate at premix or rapid combustion phase and lower heat release rate at mixing – controlled combustion phase (Masjuki et al. 2000) will produce NO_x emission.

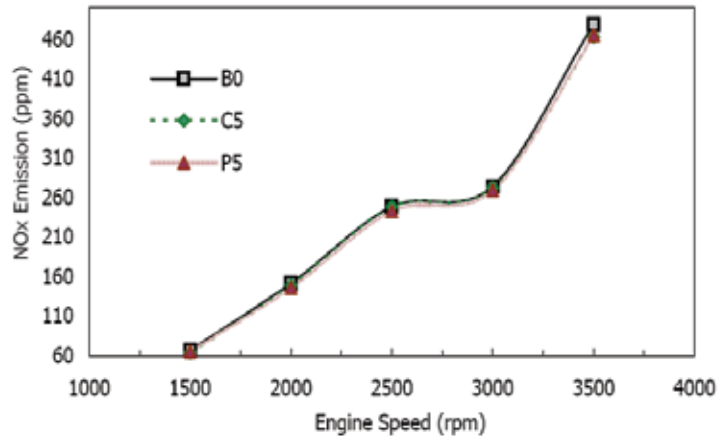


Fig. 7. Nox Emission Vs Engine Speed At 85% Throttle.

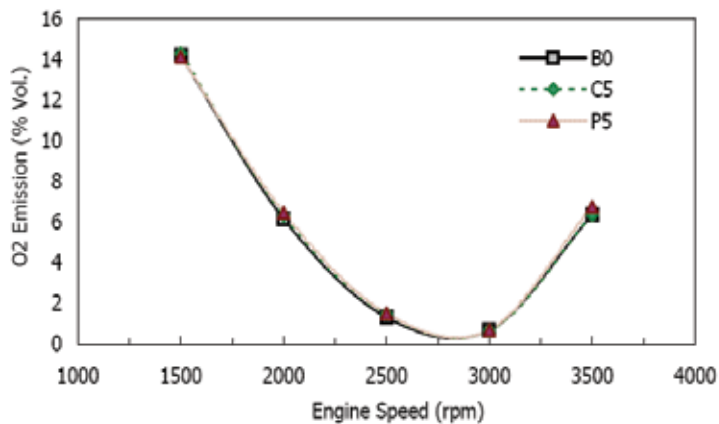


Fig. 8. O₂ Concentration Vs Engine Speed At 85% Throttle.

It can be seen that NO_x increases with increasing engine speed due to increasing combustion temperature into engine cylinder. The maximum NO_x is found at 3500 rpm such as 478.7 ppm, 462.7 ppm and 465 ppm by B0, C5 and P5 respectively. However, on average all over the speed range, C5 and P5 reduce NO_x emission by 2% and 2.50% respectively as compared to B0 fuel.

The O₂ emissions of different fuels from the engine are shown in Fig.8. Increasing engine speed decreases O₂ concentration due to better combustion. At 3000 rpm, the O₂ concentration was lower as 0.7%, 0.68% and 0.71% for B0,C5 and P5 respectively. Fuels C5 and P5 show higher O₂ due to contain O₂ in pure coconut oil and palm oil as compared to B0. On average, all over the speed range, C5 and P5 produce 1.30% and 2.90% higher O₂ as compared to B0 fuel.

Smoke is a suspension in air (aerosol) of small particles resulting from incomplete combustion of a fuel. It is commonly an unwanted by-product of fuel combustion. Smoke produces from incomplete combustion of fuel resulting from fuel cooling effect or fuel air mixing problem etc. The relative smoke emission is shown in Fig.9. It is found that the lowest smoke produces by P5 fuel followed by C5 and B0 fuels. This proves that fuel envo diesel or P5 produces complete combustion as compared to C5 and B0 fuels. On average all over the speed range, the C5 and P5 fuels show 1.75% and 3.30% lower smoke opacity than B0 fuel.

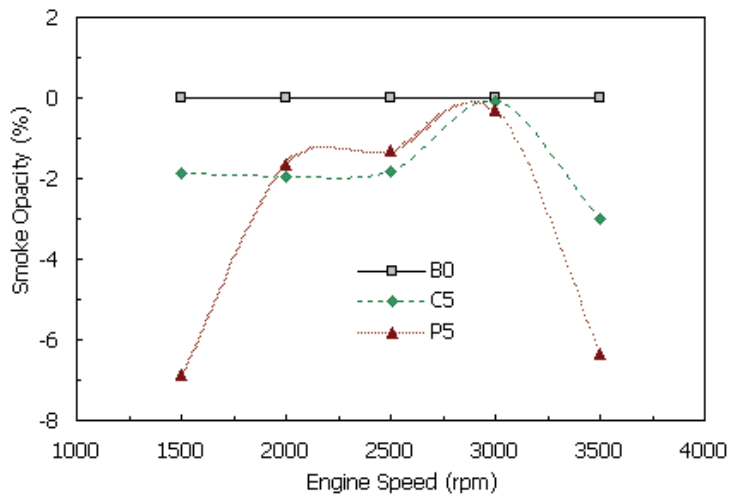


Fig. 9. Smoke Emission Vs Engine speed At 85% Throttle.

5. Conclusions

The following conclusions may be drawn from present investigation such as –

1. Envo diesel (P5) produces 1.2% lower brake power as compared to diesel fuel B0.
2. Envo diesel (P5) shows better emission results such as lower CO, HC, NO_x and smoke emissions as compared to C5 and B0 fuels.

6. Acknowledgement

The author would like to thank Sulaiman Bin Arifin for providing technical assistance and University of Malaya who made this study possible through research grant RG 040/09AET.

7. References

- Agarwal, A. K., (2007). Biofuels (alcohols and biodiesel) applications as fuels for Internal Combustion Engines, *Procd of Energy Combustion Sci* , 33(3),pp.223-330.
- Masjuki, H. H., Kalam, M. A., Maleque, M. A. (2000). Combustion characteristics of biological fuel in diesel engine. SAE 2000 World Congress, Detroit, Michigan, Paper No. 2000-01-0689.

Analytical Methods for Determining Automotive Fuel Composition

Jonas Gruber¹, Renata Lippi¹, Rosamaria W. C. Li¹
and Adriano R. V. Benvenho²

¹*Instituto de Química da Universidade de São Paulo São Paulo-SP*

²*Centro de Ciências Naturais e Humanas da Universidade
Federal do ABC, Santo André-SP
Brazil*

1. Introduction

Gasoline, a sub-product from the fractional distillation of petroleum, is a mixture of several hundred organic volatile compounds, mainly hydrocarbons, ranged from four to twelve carbon atoms with boiling points in the range of 30 – 225 °C (Fialkov et al., 2008). The physico-chemical properties depend on the origin and method used to obtain the gasoline (Barbeira et al., 2007).

It has been used as fuel for internal combustion engine vehicles for over a century, albeit the possibility of producing alternative sustainable fuels was considered long time ago, as can be learnt from Henry Ford's statement to the New York Times in 1925 (French & Malone, 2005): "There is fuel in every bit of vegetable matter that can be fermented. There's enough alcohol in one year's yield of an acre of potatoes to drive the machinery necessary to cultivate the fields for a 100 years."

In the last decades, there has been a growing concern with regard to some important environmental aspects as, for instance, the vehicle-generated greenhouse gas emissions leading to air pollution and the need for renewable fuels due to energy shortage. Ethanol has been considered as an attractive alternative fuel, because it can be obtained from domestic crops, such as sugar cane, corn, sorghum, wheat and potatoes and presents higher octane number and faster combustion speed than gasoline (Yao et al., 2009). Interestingly, ethanol, as automotive fuel, started to be used in Brazil as early as the 1930s (Szklo et al., 2007), but it was only after the two major oil shocks of the 1970s that its consumption became significant either as a gasoline additive or as a gasoline substitute. Currently, several other countries such as the USA, Thailand, China and Sweden are using blends of gasoline and ethanol, to fuel vehicles.

Gasohol is gasoline blended with anhydrous ethanol at different percentages expressed by an E-number, which corresponds to the percentage in volume of alcohol present in the fuel (Muncharoen et al., 2009). For instance, E20 contains ethanol at 20% and gasoline at 80%, by volume.

In the last decade, flexible-fuel vehicles (FFV), that can use gasoline, gasohol, hydrated ethanol or any mixture of them, became very popular. Currently, in Brazil, more FFV

vehicles are sold than those powered by gasohol. Since the composition of the fuel in the tank may fluctuate widely depending on the type of fuel a driver decides to buy, and since the optimal air:fuel ratio in the combustion chambers is a function of this composition and is crucial for the smooth operation of the engine, the need for sensors capable to directly or indirectly measure the alcohol:gasoline ratio became very important. Currently, most vehicles are equipped with lambda sensors or universal exhaust gas oxygen (UEGO) sensors (Regitz & Collings, 2008) which do not determine the real fuel composition, but the amount of oxygen present in the exhaust gases. Besides, they are exposed to high temperatures (up to 1000 °C) and high vibrations (up to 50 g), which may lead to fast degradation of the sensor (Hanrieder et al., 1992).

1.1 Environmental aspects

Transport facilities belong to one of the most important sources of air pollutants (Sobanski et al., 2006). One of the crucial parameters that influence the formation of pollutant gases in internal combustion engines is the nature of the fuel and its additives. A recent study comparing the emissions of several pollutants and greenhouse gases when gasoline and gasohol are used as fuels (Zhai et al., 2009) has shown that although the latter may reduce products of incomplete combustion, such as CO (-35–60%), the emission rates of methane are increased (+30–40%), as well as of NO_x and especially of acetaldehyde (+60% and +200%, respectively, as the ethanol content was increased to 40%). Besides, gasohol has a higher vapour pressure than gasoline, thus raising concerns about evaporative emissions (Pumhrey et al., 2000).

Anti-knock additives such as tetraethyl lead (TEL), which contributed to increase atmospheric pollution and octane enhancers such as methyl *tert*-butyl ether (MTBE), which caused contamination of underground waters are no longer required when using gasohol, since ethanol has anti-knock properties and enhances the octane number. On the other hand, its content must be monitored to keep the octane number aligned with the standard (Muncharoen, et al., 2009).

The emission of volatile organic compounds (VOCs) to ambient air is of increasing concern also because of the role of these compounds in the formation of photochemical smog and the toxicity of some individual compounds such as benzene (Winebrake and Deaton, 1999; Leong et al., 2002).

The comprehensive approach to reduce pollution requires the control of automotive fuel composition, which is currently performed by accredited laboratories being costly and time consuming. Hence, inexpensive analytical methods to certify the quality of fuels are important to be developed (Pereira et al., 2006).

1.2 Fuel adulteration

The standards for fuels are usually regulated by governmental agencies. Unfortunately, in many countries, people intentionally add cheaper organic substances in an attempt to raise profit margins. This illicit practice is called adulteration. It affects public coffers through tax embezzlement, since solvents such as mineral spirits, kerosene, rubber solvents, naphta, and thinner are levied at different rates (Pereira et al., 2006). It may also severely damage the engines and produce emissions that increase environmental pollution.

In Greece, for example, three types of diesel fuel are commercialized: automotive, domestic heating and marine diesel fuel. Marine and domestic are cheaper than automotive diesel fuel, and are therefore used to adulterate the latter (Kalligeros et al., 2001).

In the United States of America biodiesel blends are adulterated with soy oil (Mahamuni & Adewuyi, 2009). In Southeast Asia diesel is adulterated with kerosene, cyclohexane, crude hexane and turpentine oil (Bahari et al., 1990; Roy 1999; Patra & Mishara, 2002).

Since 1979 the Brazilian gasoline labelled 'gasolina C' or gasohol has been combined with ethanol in different proportions from 19-27% (v/v) that are specified by the Brazilian governmental body 'Agência Nacional do Petróleo' (ANP) (De Oliveira et al., 2004). The proportion depends on the national production of ethanol from sugar cane, and is currently 25% (Aleme et al., 2009). The end of the fuel distribution monopoly, opened the road to the criminal practice of adulteration of gasohol (Pereira et al., 2006), which mainly consists increasing the fraction of ethanol outside the range specified by ANP and/or the addition of organic solvents (Ré-Poppi et al., 2009). Since 1975 anhydrous ethanol has been used in Brazil and has been adulterated with methanol and even water (Carneiro et al., 2008; Xiong & Sisler, 2010). Methanol is cheaper and quite similar to ethanol in many physico-chemical properties, but presents high toxicity and may cause temporary or permanent corneal, pancreatic and liver damage or even death by inhalation or skin absorption. (Carneiro et al., 2008; Costa et al., 2005; Treichel, et al., 2003).

Some years ago, ANP began to introduce tracers in all solvents commercialized in Brazil, which can be detected by specific analytical techniques. Although efficient, this measure is quite expensive (Pereira et al., 2006).

For the purpose of overcoming fuel adulteration practices, it is necessary to develop novel, *in situ*, low-cost and reliable methods to monitor the fuel composition.

2. Analytical methods

The most traditional methods to qualitatively and quantitatively estimate fuel composition are gas chromatography (GC) (Pedroso et al., 2008) and high-performance liquid chromatography HPLC (Zinbo, 1984). These techniques involve the separation of mixtures of compounds by differential rates of elution by passing through a chromatographic column, governed by their distribution between a mobile and a stationary phase.

Infrared spectroscopy has been reported for quantitative analysis of ethanol and methanol in fuels by using attenuated total reflectance (ATR) (Battiste, 1981) and Fourier transform near infrared (FT-NIR) (Fernandes et al, 2008).

^{17}O nuclear magnetic resonance spectroscopy (^{17}O NMR) was used for the quantification of oxygenated additives in gasoline (Lonnon & Hook, 2003).

Although these methods are reliable they need trained professionals and costly equipments and cannot be performed *in loco*. This chapter will focus on modern analytical methods that can be incorporated into vehicles at a reasonable cost.

2.1 Fuel analysis based on electrical conductivity change

There are several types of gas sensors based on the change in electrical dc resistance (or ac impedance) upon exposure to volatile compounds. They are known as chemoresistive sensors and are usually made from metal oxide semiconductors (MOS), MOS field-effect-transistors (MOSFET) or, more recently, from conducting polymers (CP). The oldest and most commonly used chemoresistive sensor is the so-called Taguchi sensor, which consists of ceramic devices made by sintering powdered *n*-type or *p*-type MOS. Such sensors have been widely used to detect reducing and oxidizing gases as, for instance, petrol vapours in filling stations, ethanol in exhaled air etc. (Gründler, 2007). These sensors present as

drawbacks the high working temperature (200 to 600 °C) and the slow change in their performance characteristics over time.

CP based sensors have attracted much interest, specially for electronic noses, which are analytical instruments developed to mimic the human nose, and are basically formed by an array of dissimilar gas sensors, that generate different response patterns for different types of smells, attached to a pattern recognition system (Gardner & Bartlett, 1999). The reasons for using CPs for this purpose are that a huge number of different CPs can be synthesized, they respond to a wide range of volatile compounds and they operate at room temperature, which implies in low power consumption and, hence, portability. The most common CPs used for gas-sensing purposes are polypyrrole (De Melo et al., 2005), polythiophene (Chang et al., 2006), polyaniline (Anitha & Subramanian, 2003) and more recently also poly(*p*-phenylenevinylene) derivatives (Benvenho et al., 2009) and poly-*p*-xylylenes (Li et al., 2008; Li et al., 2009). Their chemical structures are shown in Figure 1. Interestingly, although poly-*p*-xilylene is known for its excellent insulating property, aryl-substituted derivatives become conducting upon doping and are highly stable to air and humidity, being very convenient for gas sensors (Li et al., 2008).

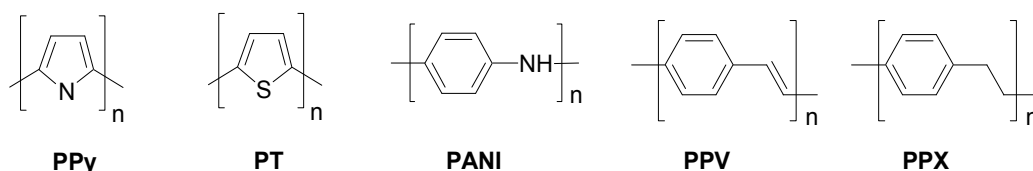


Fig. 1. Chemical structures of polypyrrole (PPy), polythiophene (PT), polyaniline (PANI), poly(*p*-phenylenevinylene) (PPV) and poly-*p*-xylylene (PPX).

The sensors usually consist of thin (1 – 50 μm) doped polymer films deposited by spin-coating, drop-casting or other technique onto interdigitated electrodes. These, depending on the desired distance between digits can be obtained by several methods as, for instance, circuit printing (Li et al., 2008) and graphite line patterning (Venancio et al., 2008) (for distances > 200 μm) or lift-off and conventional lithography (for distances between 1 μm and 200 μm).

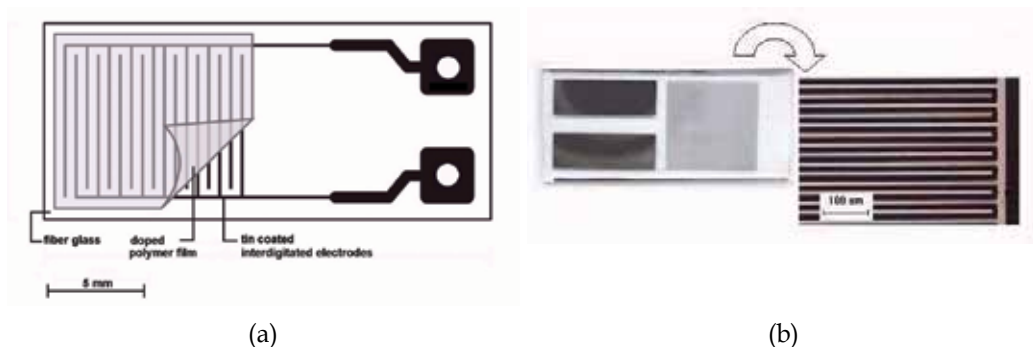


Fig. 2. (a) Polymeric gas sensor using a printed circuit interdigitated electrode and (b) interdigitated electrode obtained by conventional lithography.

Reversible changes in the electrical conductance of the CP films, upon exposure to volatile compounds, can be measured using a conductivity meter. The reasons for these changes remain not fully understood but may involve swelling of the polymer and also charge-

transfer interactions caused by the penetrating vapours (Meruvia et al., 2007; Slater et al., 1992). A typical measuring system using a single sensor is shown in Figure 3.



Fig. 3. Block diagram of the measuring system using one gas sensor.

The above-mentioned system was used to detect and discriminate many different types of volatile organic compounds. For instance, Figure 4 shows the response pattern of three similar sensors (differing only in the CP film thickness) when exposed sequentially to air saturated with five different carbonyl compounds, often present in polluted indoor air (Li et al., 2009). As can be seen, the pattern (amplitude, positive or negative response and shape) is different for each volatile compound.

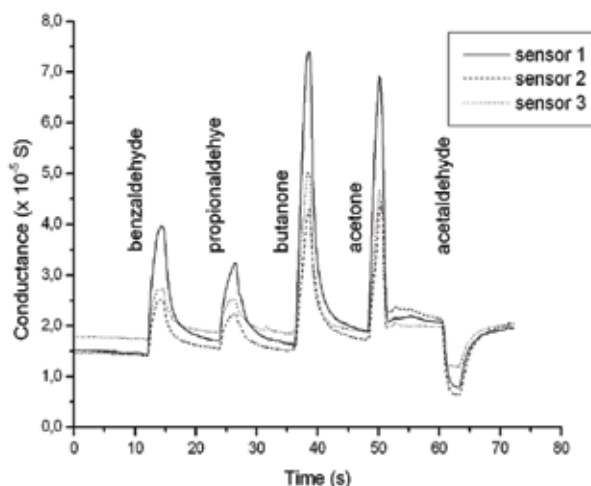


Fig. 4. Response of three CP based gas sensors to five volatile carbonyl compounds. Polymer film thickness (μm): 30 (sensor 1), 15 (sensor 2) and 10 (sensor 3). (Reproduced from Li et al., 2009, with permission of Elsevier ©)

In order to analyse data generated by several sensors (three, in this particular case) three parameters were defined, the relative response (R_a), the half-response time (T_1) and the half-recovery time (T_2), as follows:

$$R_a = (G_2 - G_1) / G_1 \quad (1)$$

$$T_1 = T_{(G_1 + G_2)/2} - T_{G_1} \quad (2)$$

$$T_2 = T_{(G_2 + G_3)/2} - T_{G_2} \quad (3)$$

Where G_1 is the conductance immediately before exposure to a particular vapour, G_2 is the conductance at the end of the exposure period and G_3 is the conductance after the recovery period. Figure 5 represents these parameters.

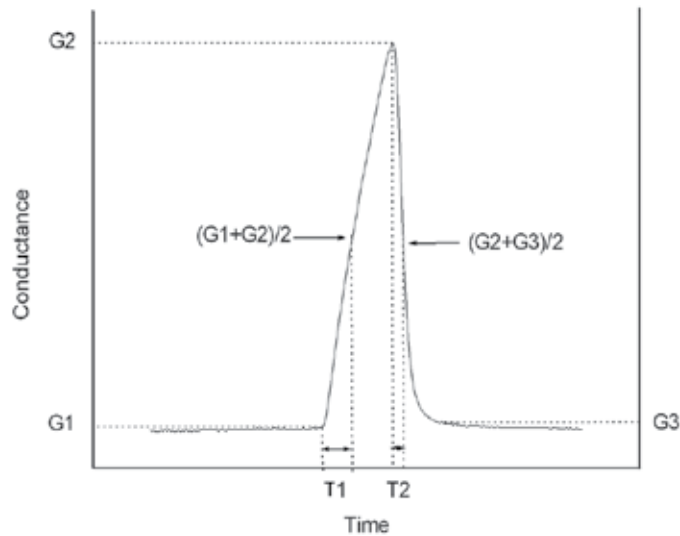


Fig. 5. Parameters used for calculating $T1$ and $T2$. (Reproduced from Li et al., 2009, with permission of Elsevier ©)

A plot of $Ra \times T1 \times T2$ (Figure 6) reveals the discrimination power of these sensors. There are five separate clusters of data points corresponding each one to a particular organic compound, i.e. benzaldehyde, propionaldehyde, butanone, acetone and acetaldehyde. It is worth mentioning that the cost of each sensor is less than US\$ 1 and it lasts for at least one year. Besides, they are easy to fabricate, operate at room temperature, have extremely low power consumption (< 1 mW) and are insensitive to humidity.

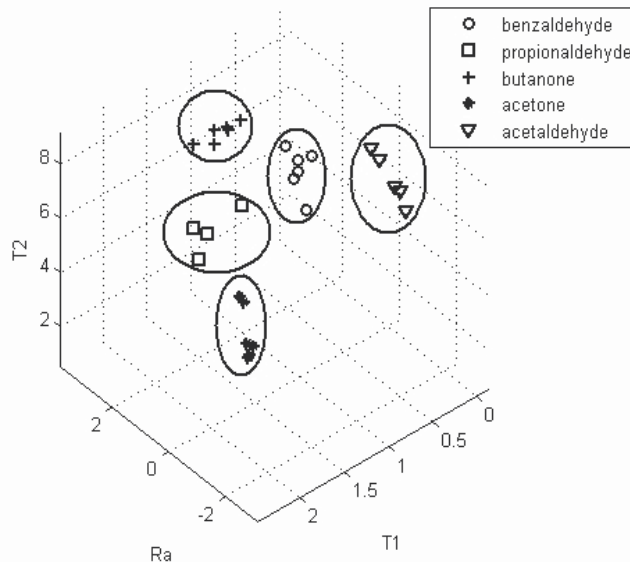


Fig. 6. Three-dimensional plot of $Ra \times T1 \times T2$. (Adapted from Li et al., 2009, with permission of Elsevier ©)

The results above are qualitative, i.e. the sensorial system identifies de volatile compound but does not indicate its concentration. For fuel analysis, this kind of information is important but quantification is crucial. Thinking of flex-fuel vehicles, in which the alcohol-gasoline composition may vary widely, a sensor was developed that is insensitive to hydrocarbons (gasoline) but quite sensitive to ethanol (Benvenho et al., 2009). The sensor was made of a thin (30 μm) film of poly(2-bromo-5-hexyloxy-1,4-phenylenevinylene)-co-(1,4-phenylenevinylene) (BHPPV-co-PPV), doped with dodecylbenzenesulfonic acid (17 % w/w), drop-casted onto an interdigitated electrode having a gap of 0.2 mm between digits and active area of 1 cm^2 . Several sensors were fabricated and tested of over one year. Some of them were kept in closed vessels containing ethanol, gasoline and a 1:1 mixture of both. Figure 7 shows a linear relative response (Ra) of these sensors towards gasohols ranging from E5 to E100.

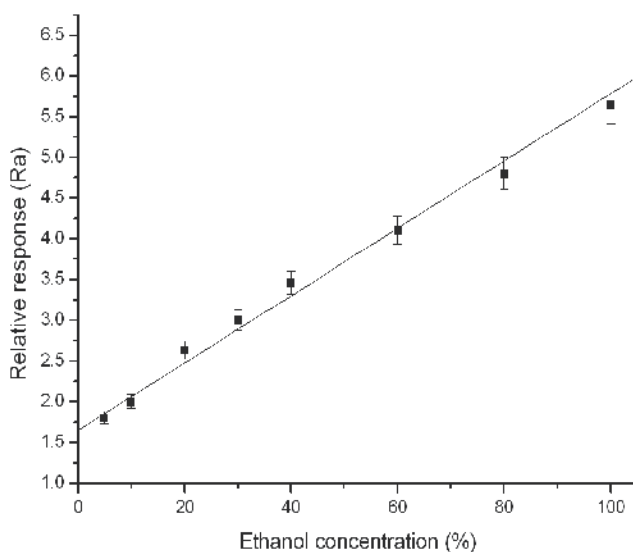


Fig. 7. Relative response (Ra) of the sensor in function of the concentration of ethanol in gasoline. (Reproduced from Benvenho et al., 2009, with permission of Elsevier ©)

2.2 Fuel analysis based on capacitance change

Gas sensors based on capacitive properties or chemocapacitors (CAP) have been used in the study of organic volatile substances. The CAPs have been constructed in different geometries. The most common structure is planar with interdigitated electrodes having as sensitive layer conducting oxides (Ponce et al., 2009), porous silicon (Tutov et al., 2000) and polymers (Josse et al., 1996; Meruvia et al., 2007), for example.

The chemocapacitor is based on the change of capacitance caused by a change of dielectric constant, due the modifications in polarization properties of molecules and/or atoms inside the active layer by external perturbations, such as the interaction with volatile organic compounds (VOC). These layers are permeable for permitting the interaction between the analytes and the sensors (Pearce et al., 2003). For generation of an electrical signal, the method uses alternate current (AC) in the frequency range from a few kHz up to 500 kHz (Pearce et al., 2003).

Matter consists of positive and negative charges that are not completely separated inside a neutral molecule resulting in molecular dipoles or molecule dipole moments that depend on the structure of atoms or molecules and that can be externally perturbed by electrical fields. The molecule polarization is given by.

$$P = \epsilon_0 \chi E \quad (1)$$

where ϵ_0 is the vacuum permittivity, χ is the susceptibility and E is the electric field.

The study of the physical characteristics by static methods is not very meaningful. More relevant, both experimentally and technologically, are time or frequency dependent methods (Jonscher, 1983).

In the case of gas sensors based on change of dielectric constant, the usual method is the frequency-dependence domain. This method is very useful in systems with a non-linear process.

The frequency method implies the need of a mathematical transformation from time-domain to frequency-domain, which is achieved by a Fourier transform (FT). The frequency dependent polarization is thus given by (Jonscher, 1983):

$$P(\omega) = \epsilon_0 \chi(\omega) E(\omega) \quad (2)$$

where the electric field is frequency dependent and susceptibility is a complex function

$$\chi(\omega) = \chi'(\omega) - i\chi''(\omega) \quad (3)$$

in which $\chi'(\omega)$ gives the amplitude in phase with the harmonic driving field and $\chi''(\omega)$ gives the component of quadrature with field.

The changes of susceptibility can be modelled as changes of dielectric responses that thus can be written in a complex form as

$$\epsilon(\omega) = \epsilon'(\omega) - i\epsilon''(\omega) \quad (4)$$

The first term is the contribution of the material susceptibility and the second term is due to dielectric loss.

The geometrical capacitance can be defined by

$$C = \epsilon A / d \quad (5)$$

where A is the electrode area, d is the distance between the electrodes and ϵ is the relative permittivity.

The capacitance which is the scaled device equivalent of the material parameter ϵ becomes

$$C(\omega) = C'(\omega) - iC''(\omega) \quad (6)$$

where $C'(\omega)$ corresponds to the ordinary capacitance and $C''(\omega)$ represents the dielectric loss component.

The experimental method used to measure the properties as a function of frequency is called immittance and can be a measure for admittance (Y) and impedance (Z). The detailed explanation of these methods can be found in (Jonscher, 1983; Barsoukov, 2006).

In the case of gas sensors the capacitance depends on the relation between the electrical permittivity of the sensor sensitive layer and the analyte; if the permittivity of the analyte is greater than the permittivity of the sensitive layer the capacitance increases, if opposite the capacitance decreases (Pearce et al., 2003).

This method has been used to study the composition of fuels (Kim et al., 2000). Using porous silicon as active layer they studied the dielectric response for methanol-water and ethanol-water. In both systems, increasing the alcohol concentration led to the elevation of the capacitance.

Li et al. (Li et al., 2007) using as active layer nanoporous silicon between interdigitated electrodes observed a non-linear increase of the capacitance when the concentration of ethanol in air was increased. This interesting result is shown in Fig. 8. Other important features mentioned in this work are long-term stability, high sensitivity and fast response time.

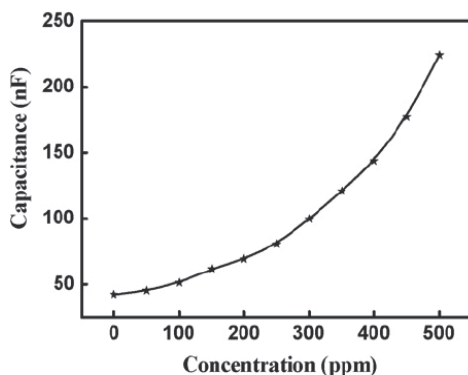


Fig. 8. Change of capacitance with the concentration of ethanol at 200 Hz signal frequency (Reproduced from Li et al., 2007, with permission of Elsevier ©)

Wiziack et al. (Wiziack et al., 2009) used an array of eight capacitive polymeric sensors to discriminate gasoline, diesel, ethanol and some common fuel adulterants as toluene, hexane and water. These results depend on the polymeric material used as active layer and their interaction with organic volatile compounds. Since it is not possible to represent all the experimental data generated by eight sensors in a two dimensional plot, the authors used principal component analysis (PCA) projecting the original data in two main dimensions as represented in Fig. 9.

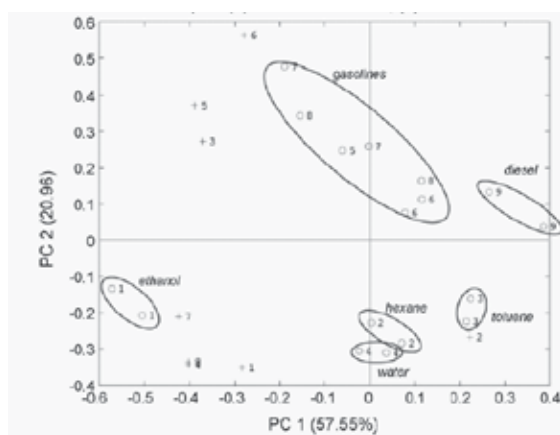


Fig. 9. Biplot of principal components obtained from capacitance measurements (Reproduced from Wiziack et al., 2007, with permission of Elsevier ©)

As can be seen, this multi sensor system can discriminate efficiently different fuel adulterants. The capacitive sensors presented good reliability for the measurements of fuel components. A drawback is that the equipment setup is expensive.

2.3 Fuel sensors based on refractive index measurements

Among the different existing gas sensors, optical sensors based on the change in the refractive index are important in the study of different analytes, such as arterial blood (Soller, 1994; Leiner, 1995), organic solvents (Abdelghani et al., 1997; Albert et al., 2001), combustion gas (Brown et al., 2008) and fuel (Falate et al., 2005).

Sensors based on refractive index are usually constituted of optical fibers (OFs) coated with sensing materials such as polymers, porous silica, and fluorescent indicators. In the experimental setup other components as, for instance, light sources and detectors are also necessary. The operation principle is based on the optical changes exhibited in response to the exposure to different volatile chemical compounds.

Optical fibers began to be used in commercial communication systems in the 1970s and the transmission is based on a dielectric optical waveguide. The light is confined to the core of the waveguide by total reflection inside the structure. Thus, OFs need a high refractive index material in the core (n_0) compared to that of the cladding layer (n_1) and it is possible to define a critical angle (θ_c) (Bass et al., 1995; Yin, Ruffin & Yu, 2008) as:

$$\Theta_c = \arcsin(n_0/n_1) \quad (7)$$

For the total reflection to occur it is necessary that the light that enters the fiber forms an angle greater than the critical angle.

The transmission in these OF sensors is based on different physical processes such as fluorescence, chemiluminescence, bioluminescence, surface plasmon resonance (SPR) and absorption, being the latter the most useful for fuel analysis. In such experiments the light energy is absorbed by atoms and molecules of the sensitive layer (cladding) or the core, and is described mathematically by the Lambert-Beer law:

$$I=I_0 \exp(-\alpha C\Delta x) \quad (10)$$

Where I_0 is the intensity of the incident light, α is the absorption coefficient of the absorbing agent, C is the concentration of the analyte and Δx is the thickness of the sensitive layer.

Another method to determine the intercation of volatile substances is the study of the reflectivity of the active sensitive layer to the analyte which depends on the difference between the refractive index of the analyte and that of the sensitive layer. The reflectivity (R) is given by:

$$R=\{ (n_A-n_F)/(n_A+n_F)\}^2 \quad (11)$$

in which n_A the refractive index of the analyte and n_F of the sensitive layer.

Using the methodology described above, sensors based on refractive index have been studied by several research groups in different countries for the determination of fuel composition. For instance, in India where adulteration of fuel is a major problem, Roy (Roy, 1999) studied the adulteration of diesel and petrol by addition of kerosene. The increase of kerosene concentration in the mixture diesel-kerosene decreases the refractive index. On the other hand, it increases as the kerosene concentration becomes higher in petrol-kerosene blends. These results are shown in Fig. 10.

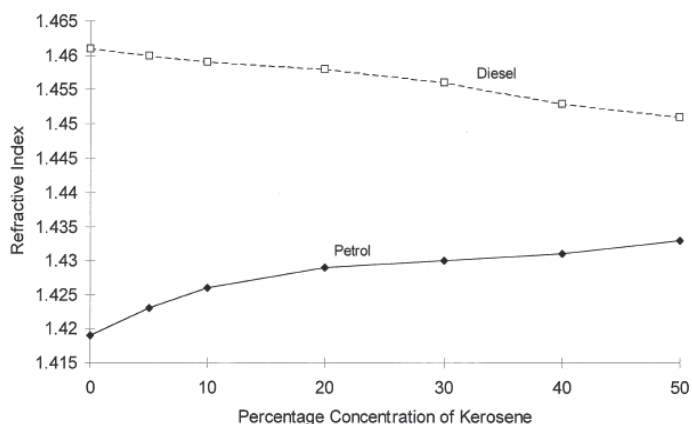


Fig. 10. Change of refractive index of the optical fiber in mixtures diesel-kerosene and petrol kerosene (Reproduced from Roy et al., 1999; with permission of Elsevier ©)

As described in section 1.2, Brazil also suffers from fuel adulteration practice and studies focused on determining fuel composition by refractive index changes in optical fibers have been published. Thus, Falate et al. (Falate et al., 2005) studied the vapour of hydrocarbons and possible adulterants in gasoline. In their work they used fiber optics connected to long-period gratings (LPG) to measure changes in attenuation peak wavelength for ethanol-gasoline mixtures in different proportions, and adulteration by addition of other solvents such as naphtha, turpentine and paint thinner in Brazilian commercial gasoline. It was possible to observe changes in the position of the maximum peak in the electromagnetic spectra and consequently also in the refractive index values (Fig. 11).

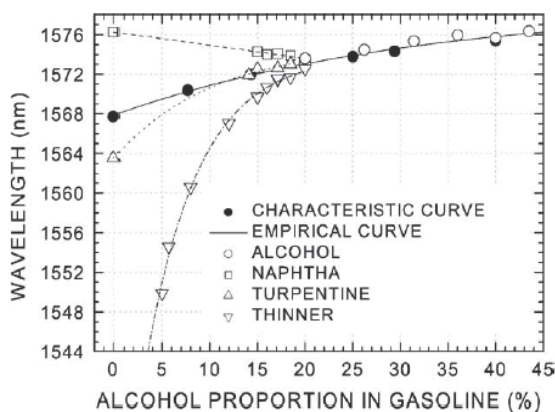


Fig. 11. Curves of attenuation peak as a function of alcohol proportion in gasoline and other mixtures with different solvents. (Reproduced from Falate et al., 2005; with permission of Elsevier ©)

3. Summary and perspectives

In view of (a) the growing concerns in developing alternative fuels such as alcohols (mainly ethanol and methanol) for use in flexible fueled vehicles capable of operating on gasoline,

alcohol or mixtures of both of any composition (gasohol), (b) the increasingly strict laws for emissions of pollutants from motor vehicles and (c) illegal practices as, for instance, mislabeling or physical adulteration of fuels by adding lower-price components, with no regard for health and safety considerations; the need for novel *in situ*, low-cost and reliable sensors for monitoring fuel composition and, hence, its quality has become a high priority. Recent progress achieved in the field of chemoresistive, chemocapacitive and chemooptical sensors, briefly described in this chapter, will certainly play an important role to accomplish these tasks.

4. Acknowledgements

The authors are grateful to Conselho Nacional de Desenvolvimento Científico e Tecnológico (CNPq) and to Fundação de Amparo à Pesquisa do Estado de São Paulo (FAPESP) for their financial support.

5. References

- Abdelghani, A.; Chovelon, J.M.; Jaffrezic-Renault, N.; Lacroix, M.; Gagnaire, H.; Veillas, C.; Berkova, B.; Chomat, M. & Matejec, V. (1997). Optical fiber sensor coated with porous silica layers for gas and chemical vapour detection. *Sensors and Actuators B: Chemical*, Vol.44, No. 1-3, October 1997, pp.495-498, ISSN 0925-4005.
- Albert, K.J.; Walt, D.R.; Gill, D. & Pearce, T.C. (2001). Optical multibead arrays for simple and complex odour discrimination. *Analytical Chemistry*, Vol.73, No.11, June 2001, pp. 2501-2508, ISSN 0003-2700.
- Aleme, H.G; Costa L. M. & Barbeira, P. J. S. (2009). Determination of ethanol and specific gravity in gasoline by distillation curve and multivariate analysis. *Talanta*, Vol. 78, No. 4-5, June 2009, pp. 1422-1428, ISSN 0039-9140.
- Anitha, G. & Subramanian, E. (2003). Dopant induced specificity in sensor behaviour of conducting polyaniline materials with organic solvents. *Sensors and Actuators B*, Vol. 92, No. 1-2, July 2003, pp. 49-59, ISSN 0925-4005.
- Bahari, M.S.; Cridlle, W. J. & Thomas, J. D. R. (1990). Determination of the adulteration of petrol with kerosene using a rapid phase-titration procedure. *Analyst*, Vol. 115, No. 4, April 1990, pp. 417-419, ISSN 0003-2654.
- Barbeira, P. J. S.; Pereira, R. C. C. & Corgozinho, C. N. C. (2007). Identification of gasoline origin by physical chemical properties and multivariate analysis. *Energy & Fuels*, Vol. 21, No. 4, July 2007, pp. 2212-2215, ISSN 0887-0624.
- Barsoukov, E. & Macdonald, J.R. (2005). *Impedance spectroscopy – Theory, experimental, and applications*, John Wiley & Sons, ISBN 0-471-64749-7.
- Bass, M.; Van Stryland, E.W.;Williams, D. R. & Wolfe W.L. (1995). *Handbook of optics – devices, measurements & properties*, Vol. II, McGraw-Hill, ISBN 0-07-047974-7, USA.
- Battiste, D. R.; Fry, S. E. White, F. T.; Scoggins, M. W. & McWilliams, T. B. (1981). Determination of ethanol in gasohol by infrared spectrometry. *Analytical Chemistry*, Vol. 53, No. 7, June 1981, pp. 1096-1099, ISSN 0003-2700.
- Benvenho, A. R. V.; Li, R. W. C. & Gruber, J. (2009). Polymeric electronic gas sensor for determining alcohol content in automotive fuels. *Sensors and Actuators B*, Vol.136, No.1, February 2009, pp.173-176, ISSN 0925-4005.

- Brown, D.M.; Sandvik, P.M.; Fedison, J.B.; Hibshman, J. & Matocha K. S. (2008). Determination of lean burn combustion temperature using ultraviolet emission. *IEEE Sensors Journal*, Vol.8, No.3-4, March-April 2008, pp. 255-260, ISSN 1530-437X.
- Carneiro, H. S. P.; Medeiros, A. R. B.; Oliveira, F. C. C.; Aguiar, G. H. M.; Rubim, J. C.; Suarez, P. A. Z. (2008). Determination of ethanol fuel adulteration by methanol using partial least-squares models based on Fourier transform techniques. *Energy & Fuels*, Vol. 22, No. 4, July 2008, pp. 2767-2770, ISSN 0887-0624.
- Chang, J. B.; Liu, V.; Subramanian, V.; Sivula, K.; Luscombe, C.; Murphy, A.; Liu, J. & Fréchet, J. M. J. (2006). *Journal of Applied Physics*, Vol.100, No.1, July 2006, pp. 014506-1-014506-7, ISSN 0021-8979.
- Costa, L.G.; Guizetti, M. & Vitalone, A. (2005). Diet-brain connections: role of neurotoxicants. *Environmental Toxicology and Pharmacology*, Vol. 19, No.3, May 2005, pp. 395-400, ISSN 1382-6689.
- De Melo, C. P.; Neto, B. B.; de Lima, E. G.; de Lira, L. F. B. & de Souza, J. E. G. (2005). *Sensors and Actuators B*, Vol. 109, No. 2, September 2005, pp. 348-354, ISSN 0925-4005.
- De Oliveira, F. S.; Teixeira, L. S. G.; Araujo, M. C. U. & Korn, M. (2004). Screening analysis to detect adulterations in Brazilian gasoline samples using distillation curves. *Fuel*, Vol. 83, No. 7-8, May 2004, pp. 917-923, ISSN 0016-231.
- Falate, R.; Kamikawachi, R.C.; Müller, M.; Kalinowski, H.J. & Fabris, J.L. (2005). Fiber optics for hydrocarbon detection. *Sensors and Actuators B*, Vol.105, No. 2, March 2005, pp.430-436, ISSN 0925-4005.
- Fernandes, H. L.; Raimundo Jr., I. M.; Pasquini, C. & Rohwedder, J. J. R. (2008). Simultaneous determination of methanol and ethanol in gasoline using NIR spectroscopy: effect of gasoline composition. *Talanta*, Vol. 75, No. 4, May 2008, pp. 804-810, ISSN 0039-9140.
- Fialkov, A. B.; Gordin A. & Amirav A. (2008). Hydrocarbons and fuel analyses with the supersonic gas chromatography mass spectrometry - the novel concept of isomer abundance analysis. *Journal of Chromatography A*, Vol. 1195, No. 1-2, June 2008, pp. 127-135, ISSN 0021-9673.
- French, R. & Malone, P. (2005). Phase equilibria of ethanol fuel blends. *Fluid Phase Equilibria*, Vol. 228-229, February 2005, pp.27-40, ISSN 0378-3812.
- Gardner, J. W.; Bartlett, P. N. (1999). *Electronic Noses. Principles and Applications*. Oxford University Press, Oxford - ISBN 0198559550.
- Gründler P. (2007). *Chemical Sensors. An Introduction for Scientists and Engineers*. Springer-Verlag, Berlin - ISBN 978-3-540-45742-8.
- Hanrieder, W.; Kornely, S.; Lampe, U. & Meixner, H. (1992). Causes of fast degradation of thin-film lambda probes in motor vehicle exhaust and initial measures to improve long-term stability, *Sensors and Actuators B: Chemical*, Vol. 7, No. 1-3, March 1992, pp.792-798, ISSN 0925-4005.
- Jonscher, A. K. (1983). *Dielectric relaxation in solids*. Chelsea Dielectric Press, London - ISBN 0950871109.
- Josse, F.; Lukas, R.; Zhou, R.; Schneider, S. & Everhart, D. (1996). AC-impedance-based chemical sensors for organic solvent vapours. *Sensors and Actuators B*, Vol.36, No. 1-3, October 1996, pp.363-369, ISSN 0925-4005.

- Kalligeros, S.; Zannikos, F.; Stournas S.; Lois, S. & Anastopoulos, G. (2001). A survey of the automotive diesel quality in Athens area. *International Journal of Energy Research*, Vol. 25, No. 15, December 2001, pp. 1381-1390, ISSN 0363-970X.
- Kim, S.J.; Jeon, B.H.; Choi, K.S. & Min, N.K. (2000). Capacitive porous silicon sensors for measurement of low alcohol gas concentration at room temperature. *Journal of Solid State Electrochemistry*, Vol.4, No. 6, July 2000, pp.363-369 ISSN 1432-8488.
- Leiner, M.J.P. (1995). Optical sensors for in vitro blood gas analysis. *Sensors and Actuators B: Chemistry*, Vol.29, No.1-3, October 1995, pp.169-173, ISSN 0925-4005.
- Leong, S.T.; Muttamara, S. & Laortanakul, P. (2002). Applicability of gasoline containing ethanol as Thailand's alternative fuel to curb toxic VOC pollutants from automobile emission. *Atmospheric Environment*, Vol. 39, No. 21, July 2002, pp.3495-3503 ISSN 1352-2310.
- Li, R. W. C.; Ventura, L.; Gruber, J.; Kawano, Y. & Carvalho, L. R. F. (2008). A selective conductive polymer-based sensor for volatile halogenated organic compounds (VHOC). *Sensors and Actuators B: Chemical*, Vol.131, No.2, May 2008, pp.646-651, ISSN 0925-4005.
- Li, R. W. C.; Carvalho, L. R. F.; Ventura, L. & Gruber, J. (2009). Low cost selective sensor for carbonyl compounds in air based on a novel conductive poly(p-xylylene) derivative. *Materials Science and Engineering C*, Vol.29, No.2, March 2009, pp.426-429, ISSN 0928-4931.
- Li, X.J., Chen, S.J. & Feng, C. Y. (2007). Characterization of silicon nanoporous pillar array as room-temperature capacitive ethanol gas sensor. *Sensors and Actuators B: Chemical*, Vol.123, No.1, April 2007, pp.461-465, ISSN 0925-4005.
- Lonnon, D. G. & Hook, J. M. (2003). ¹⁷O quantitative nuclear magnetic resonance spectroscopy of gasoline and oxygenated additives. *Analytical Chemistry*, Vol. 75, No. 17, September 2003, pp. 4659-4666, ISSN 0003-2700.
- Mahamuni, N. N. & Adewuyi (2009). Fourier transform infrared spectroscopy (FTIR) method to monitor soy biodiesel and soybean oil in transesterification reactions, petrodiesel – biodiesel blends, and blend adulteration with soy oil. *Energy & Fuels*, Vol. 23, No. 7, July 2009, pp.3773-3782, ISSN 0887-0624.
- Meruvia, M. S.; Hümmelgen, I. A. Gonçalves, C. S.; Benvenho, A. R. V. & Gruber, J. (2007). Ferrocene-based copolymer for the sensing and discrimination of low-molecular-weight alcohols. *Sensor Letters*, Vol. 5, No. 3/4, September/December 2007, pp.625-628, ISSN 1546-198X.
- Muncharoen, S.; Sitanurak, J.; Tiyaopongpattana, W.; Choengchan, N.; Ratanawimarnwong, N.; Motomizu, S.; Wilairat, P. & Nacapricha, D. (2009). Quality control of gasohol using a micro-unit for membraneless gas dissolution. *Microchimica Acta*, Vol. 164, No. 1-2, January 2009, pp.203-210, ISSN 0026-3672.
- Patra, D. & Mishara, A. K. (2002). Study of diesel contamination by excitation emission matrix spectral subtraction fluorescence. *Analytica Chimica Acta*, Vol. 454, No. 2, March 2002, pp. 209-215, ISSN 003-2670.
- Pearce, T.C.; Schiffman, S.S.; Nagle, H.T. & Gardner, J.W. (2003). *Handbook of machine olfaction – electronic nose technology*, Wiley-VCH, ISBN 3-527-30358-8, Germany.
- Pedroso, M. B.; de Godoy, L. A. F.; Ferreira, E. C.; Poppi, R. J. & Augusto, F. (2008). Identification of gasoline adulteration using comprehensive two-dimensional gas

- chromatography combined to multivariate data processing. *Journal of Chromatography A*, Vol. 1201, No. 2, August 2008, pp. 176-182, ISSN 0021-9673.
- Pereira, R. C. C.; Skrobot, V. L.; Castro, E. V. R.; Fortes, I. C. P. & Pasa, V. M. D. (2006). Determination of gasoline adulteration by principal component analysis-linear discriminant analysis applied to FTIR spectra. *Energy & Fuels*, Vol. 20, No. 3, May 2006, pp. 1097-1102, ISSN 0887-0624.
- Ponce, M.A.; Parra, R.; Savu, R.; Joanni, E.; Bueno, P.R.; Cilense, M.; Varela, J. A. & Castro, M.S. (2009). Impedance spectroscopy analysis of TiO₂ thin film gas sensors obtained from based anatase colloids. *Sensors and Actuators B:Chemical*, Vol. 139, No. 2, June 2009, pp.447-452, ISSN 0925-4005
- Pumphrey, J. A.; Brand, J. I. & Scheller, W. A. (2000). Vapour pressure measurements and predictions for alcohol-gasoline blends. *Fuel*, Vol. 79, No. 11, September 2000, pp.1405-1411, ISSN 0016-231.
- Regitz, S. & Collings, N. (2008). Fast response air-to fuel ratio measurements using a novel device based on a wide band lambda sensor. *Measurement Science and Technology*, Vol. 19, No. 7, July 2008, pp. 075201-1-075201-10, ISSN 0957-0233.
- Ré-Poppi, N.; Almeida, F. F. P.; Cardoso, C. A. L.; Raposo Jr., J. L.; Viana, L. H.; Silva, T. Q.; Souza, J. L. C. & Ferreira, V. S. (2009). Screening analysis of type C gasoline by gas chromatography - flame ionisation detector. *Fuel*, Vol. 88, No. 3, March 2009, pp. 418-423, ISSN 0016-231.
- Roy, S. (1999). Fiber optic sensor for determining adulteration of petrol and diesel by kerosene. *Sensors and Actuators B: Chemical*, Vol.55, No.2-3, May 1999, pp.212-216, ISSN 0925-4005.
- Slater, J. M.; Watt, E. J.; Freeman, N. J.; May, I. P. & Weir, D. J. (1992). Gas and vapor detection with poly(pyrrole) gas sensors. *Analyst*, Vol. 117, No. 8 August 1992, pp.1265-1270, ISSN 0003-2654.
- Sobanski, T.; Szczurek, A.; Nitsch, K.; Licznarski, L. & Radwan, W. (2006). Electronic nose applied to automotive fuel qualification. *Sensors and Actuators B: Chemical*, Vol. 116, No. 1-2, July 2006, pp.207-212, ISSN 0925-4005.
- Soller, B. R. (1994). Design of intravascular fiber optic blood-gas sensors. *IEEE Engineering in Medicine and Biology Magazine*, Vol.13, No.3, June-July 1994 , pp.327-335, ISSN 0739-5171.
- Szklo, A.; Schaeffer, R. & Delgado, F. (2007). Can one say ethanol is a real threat to gasoline? *Energy Policy*, Vol. 35, No.11, November 2007, pp.5411-5421, ISSN 0301-4215.
- Treichel, J.L.; Henry, M.M.; Skumatz, C.M.B.; Eells, J.T. & Burke J.M. (2003). Formate, the toxic metabolite of methanol, in cultured ocular cells. *NeuroToxicology*, Vol. 24, No. 2, pp. 825-834, ISSN 0161-813X
- Tutov, E. A.; Andrinov, A.Y. & Ryabtsev, S.V. (2000). Nonequilibrium process in capacitive sensors based on porous silicon. *Technical Physics Letters*, Vol. 26, No. 9, September 2009, pp. 53-58 ISSN 1063-7850.
- Venancio, E. C.; Mattoso, L. H. C.; Hermann Jr., P. S. P. & MacDiarmid, A. G. (2008). Line patterning of graphite and the fabrication of cheap, inexpensive, "throw-away" sensors. *Sensors and Actuators B*, Vol.130, No.2, March 2008, pp.723-729, ISSN 0925-4005.
- Winebrake, J. J. & Deaton, M. L. (1999). Hazardous air pollution from mobile sources: a comparison of alternative fuel and reformulated gasoline vehicles. *Journal of the Air*

- & Waste Management Association, Vol. 49, No.5, May 1999, pp.576-581, ISSN 1047-3289.
- Wiziack, N. K. L.; Catini, A.; Santonico, M.; D'Amico, A.; Paolesse R.; Paterno, L. G.; Fonseca, F. J. & Di Natale. A sensor array based on mass and capacitance transducers for the detection of adulterated gasolines. *Sensors and Actuators B: Chemical*, Vol. 140, No.2, July 2009, pp.508-513, ISSN 0925-4005.
- Xiong, F. B. & Sisler, D. (2010). Determination of low-level water content in ethanol by fiber-optic evanescent absorption sensor. *Optics Communications*, Vol. 283, No. 7, April 2010, pp.1326-1330, ISSN 0030-4018.
- Yao, C.; Yang, X.; Raine, R. R.; Cheng, C.; Tian, Z. & Li, Y. (2009). The effects of MTBE/ethanol additives on toxic species concentration in gasoline flame. *Energy & Fuels*, Vol. 23, No. 7, July 2009, pp.3543-3548, ISSN 0887-0624.
- Yin, S; Ruffin, P.B. & Yu, F.T.S. (2008). *Fiber optic sensors*, CRC Press, ISBN 978-1-4200-5365-4, USA.
- Zhai, H.; Frey, H. C.; Roupail, N. M.; Gonçalves, G. A. & Farias, T. L. (2009). Comparison of flexible fuel vehicle and life-cycle fuel consumption and emissions of selected pollutants and greenhouse gases for ethanol 85 versus gasoline. *Journal of the Air & Waste Management Association*, Vol. 59, No. 8, August 2009, pp.912-924, ISSN 1047-3289.
- Zinbo, M. (1984). Determination of one-carbon to three-carbon alcohols and water in gasoline/alcohol blends by liquid chromatography. *Analytical Chemistry*, Vol. 56, No. 2, February 1984, pp. 244-247, ISSN 0003-2700.

Automotive Fuel Consumption in Brazil: Applying Static and Dynamic Systems of Demand Equations

Mariana Iootty^{1,2}, Helder Pinto Jr.¹ and Francisco Ebeling³

¹*Institute of Economics- Federal University of Rio de Janeiro*

²*Federal Rural University of Rio de Janeiro*

³*Brazilian Petroleum Institute
Brazil*

1. Introduction

The demand of automotive fuel is an important topic in energy policy since the demand sensibility to income and price changes can give great insights for policy makers relating, for instance, to climate change, optimal taxation and national security. The study of the automotive fuels demand in Brazil is especially relevant since in the last decades its automotive fuel market has witnessed relevant changes in the consumption structure, which used to be dominated by traditional fuels, like gasoline and diesel.

In this changing context two periods can be identified. First, from 1970 to 1990, in a context of two oil crises, the consumption grew 4.5% per year, and ethanol combustible has emerged, in 1973, as a part of a government program to reduce the oil dependency. Compressed natural gas (CNG) has also been brought on as another innovation, in the end of the 1980's, although its consumption has only begun to grow at the middle 1990's due to the government policy of fixing a substantial price differential in favor of CNG. So far, the Brazilian automobile industry fell short to produce CNG vehicles¹; CNG consumers still have to install a kit which allows them to convert the vehicle between CNG as well as the original engine fuel. Most of CNG consumption in Brazil is related to light-duty trucks – such as taxi cabs, especially in the states of Rio de Janeiro and Sao Paulo, where the CNG stations network is relevant.

In the second period, from 1991 to 2005, overall combustible consumption has grown at a faster rate, of 2.8% per year. Another innovation was brought in, the flex fuel vehicles which are specially designed to run on gasoline and ethanol. In 2003, the production of flex fuel cars accounted for only 2.6% of the total auto production; three years later, this number was 75%.

The essential point to grasp here is that the introduction of flex fuel (gasoline-ethanol) vehicles and the raise of CNG have enlarged the options available to consumers to choose their automotive fuel, therefore altering, in some extent, the demand for captive fuels as gasoline. In this context, and given the assumption that demand elasticity is a useful tool to

¹ One notable exception is Fiat, who has started to produce CNG, Gasoline and Ethanol compatible engines.

summarize the consumers behavior, this work tries to shed light on the performance of the Brazilian demand for automotive fuels.

While the price and income elasticities of automotive fuels demand (specially gasoline) around the world have been extensively studied; see Basso and Oum (2006) for recent exercises, Goodwin, Dargay and Hanly (2004) for a recent survey and Dahl and Sterner (1991) for thorough review. However, there are very few published papers on the estimation of demand elasticities for the Brazilian automotive fuels market. Alves and Bueno (2003) constitute a single work on this regard. Through a co-integration method they estimated the cross-price elasticity between gasoline and alcohol, and find alcohol as an imperfect substitute for gasoline even in the long-run. Even though relevant, this work has focused on the gasoline market therefore not shedding light on the demand for other automotive fuels in Brazil, as diesel, ethanol and CNG.

In this turn, this work goes one step further as it estimates the matrix of price and income elasticities - in relation to gasoline, ethanol, CNG and diesel. Two related estimation approaches are employed. First it uses the traditional linear approximation of the Almost Ideal Demand System (AIDS), originally developed by Deaton and Muellbauer (1980). This is a structural and static model which fulfills the desired theoretical properties of demand (homogeneity and symmetry restrictions) while also being parsimonious in terms of number of parameters to be estimated. In order to also analyze the dynamic aspect of the long run demand, this work adopts a second approach of AIDS model using cointegration techniques based on Johansen (1988) procedures. The use of this second approach is especially relevant since the variables can be non-stationary, which could change the estimates of elasticities.

The chapter is organized as follows; section two describes the evolution of automotive fuels consumption profile in Brazil since the 1970's. Section three presents the data used. The following section describes the linear approximation of the static AIDS model and presents the first results. The fifth section develops the dynamic analysis using cointegration techniques and displays the results. The sixth, and last section, presents in a nutshell the main conclusions.

2. The evolution of automotive fuel matrix in Brazil

Table 1 presents the yearly consumption evolution in tones oil equivalent (toe) in the automotive vehicles fuel matrix since 1979. Two analytical periods must be highlighted. In the first one, between 1979-1990, the total fuel consumption presented a 2.2% growth per year, while the GNP grown at a yearly medium rate of 2.05%.

In the period between 1979 and 1990, when one considers the individual performance of each series, the ethanol is highlighted as the fuel with the highest yearly growth rate, of 71.3% per year. Indeed, the consumption level rose from eight thousand tonnes of oil equivalent, in 1979, to 5.205 thousand in 1990, causing an expressive accumulated growth. This significant expansion rhythm reflects the "Programa Nacional do Álcool" (National Ethanol Program), launched in 1973, whose the second phase was named "Proálcool", started in December 1978, when the government decided to stimulate the production of ethanol vehicles. In the first analytical period, it is also remarkable the reduction in the gasoline consumption, with an accumulated fall of 28.5% between 1979 and 1990.

	<i>CNG</i>	<i>Diesel</i>	<i>Gasoline</i>	<i>Ethanol</i>	<i>TOTAL</i>
1979	0	10.902	10.397	8	22.491
1980	0	11.401	8.788	219	21.611
1981	0	11.280	8.413	709	21.014
1982	0	11.515	8.014	853	21.460
1983	0	11.025	6.847	1.504	20.549
1984	0	11.486	6.140	2.332	21.070
1985	0	11.846	6.043	3.103	22.124
1986	0	13.948	6.808	4.280	26.340
1987	0	14.689	5.931	4.546	26.306
1988	3	14.981	5.809	4.974	26.817
1989	2	15.868	6.527	5.641	28.905
1990	2	15.983	7.436	5.205	29.276
Average yearly annual growth (1979-1990)*	-13,9%	3,2%	-2,8%	71,3%	2,2%
Accumulated growth rate (1979-1990)	-36,1%	46,6%	-28,5%	63725,0%	30,2%
1991	2	16.587	8.059	5.225	30.751
1992	0	16.882	8.023	4.784	30.878
1993	22	17.325	8.436	4.931	32.012
1994	40	18.106	9.235	4.974	34.025
1995	43	19.280	11.057	5.069	37.250
1996	32	20.165	12.946	4.987	40.295
1997	41	21.422	14.156	4.233	42.530
1998	116	22.453	14.772	3.933	44.124
1999	140	22.704	13.770	3.594	43.412
2000	275	23.410	13.261	2.774	42.766
2001	503	24.071	12.995	2.170	42.946
2002	862	25.086	12.426	2.214	44.459
2003	1.169	24.252	13.115	1.919	44.329
2004	1.390	25.939	13.560	2.466	47.334
2005	1.711	25.804	13.595	2.885	48.073
Average yearly annual growth (1991-2005)	58,2%	3,0%	3,5%	-3,9%	3,0%
Accumulated growth rate (1991-2005)	97171%	56%	69%	-45%	56%

* The annual growth rate of CNG was based on the period 1988/1990

Source: own elaboration based on data from MME (2005)

Table 1. Annual Fuel Consumption of Automotive Vehicles (10^3 toe): 1979-2005

In the second analytical period, between 1991-2005, the total automotive fuel consumption presented a pace higher than the period before, having reached the expansion rate of 3% per year, while the GNP grown at 2.4% per year. In this period, the negative point is the ethanol, with yearly fall of 3.9% per year. On the other hand, gasoline presented a growth rate of 3.5% per year, which reinforces the negative (substitution) relationship between the

dynamics of consumption of gasoline and ethanol. impressive remarkable aspect of this period was the CNG fuel expansion, with yearly growth rate of 58%, having increased from 2 thousands toe in 1991 to 1.171 thousands toe in 2005 (see Table 1).

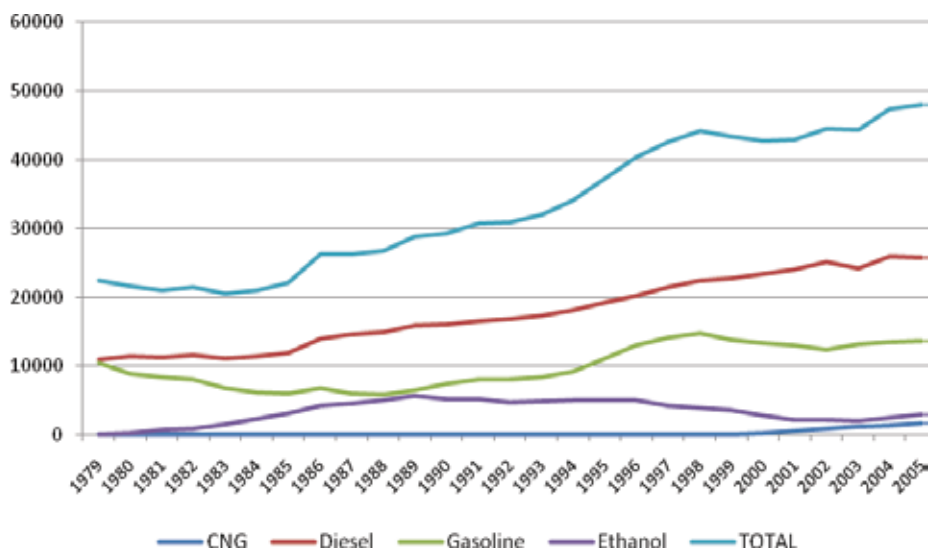


Fig. 1. Evolution of Fuel Consumption of Automotive Vehicles (10^3 toe): 1979-2005

Regarding diesel fuel, it is worth emphasizing its almost constant expansion rate; while in the first period, between 1979 and 1990, the growth was of 3.2% per year, in the period after 1991 the growth rate was of yearly 3.0%.

Considering the same analytical periods, but focusing on the consumption share of each fuel and not on their individual series performance, it is possible to identify aspects that are as relevant.

Diesel performs as the main automotive fuel used in two periods. Between 1979 and 1990 its average share was of 53.7%; in the following period, from 1991 to 2005, the average share was of 53.4%. The diesel share in the vehicle fuel matrix has thus kept almost constant in the last three decades. Some possible explanations for this picture is the high dependency of the road transport modal, and the fact that 100% of the production and sales of buses and trucks - which are the most used in long distance transport, use diesel engines. It is worth noting that ever since 1979 there have not been effective replacements of diesel in the consumption structure, in spite of the relevant imports pressures of the fuel to Brazil.

As expected, gasoline evolves as the second fuel with the highest relative share in the vehicle fuel matrix in the two periods; with average share of 31% in the first period and 29.4%, in the second. It is important to mention, however, that in spite of the fact that this average share has kept steady in the periods considered, there were distinct movements in the demand behavior of gasoline in the two periods. While between 1979-1990 the gasoline share fell from 46.2% in 1979 to 25.4% in 1990; in the second analytical period, the share rose from 26.2% to 28.3% in 2005.

The role played by the ethanol is worth to mention. The average share has kept almost steady in the analyzed periods: 10.8% between 1979-1990 and 9.8% between 1991- 2005. However, there had been different trends during this period. In the first period the share rose significantly, going from 0% in 1979 to 17.8% in 1990, as a consequence of the programs focused on the ethanol diffusion. In the second period, there was a fall from 17%, in 1991, to

6.0% in 2005. Finally, it is important to stress the CNG role, of little relevance, having reached the average share of 0.9% between 1991 and 2005.

In the analysis of the performance of all these fuel consumptions a relevant aspect to be highlighted is the demand sensibility to price and income variations, which is captured by the price- and income elasticities, respectively. Detecting a high or reduced sensibility of demand to price and income parameters can give interesting insights to the policy planning about what is the goal of the vehicle fuel matrix in Brazil.

3. The data

Time-series data for the consumption of automotive fuels in Brazil are not in abundant supply. The Brazillian Ministry of Mines and Energy (MME) has historically collected annual data for prices and consumption of automotive fuels since 1970 (see MME(2006)). More recently, (June, 2001), the National Petroleum Agency (ANP) has also taken this role and started to collect monthly data on price and consumption of fuels². This work has used the annual data collected by MME, since it is better suited to identify the long term consumption profile. A companion paper uses the monthly data for a shorter period of time to implement a similar exercise to also analyze the elasticity, and is available upon request to the authors. Table 2 shows the main descriptive statistics of the main series used in this analysis, namely, the natural log of the prices and the consumption-share of diesel, gasoline, CNG and ethanol drawn from "Balanço Energético Anual"(MME, 2006).

Variable	N	Mean	SD	Min	Max
Year	36	1988	-	1970	2005
Natural log of the price - Gasoline ¹	33	4.551	0.387	3.17	5.142
Natural log of the price - Ethanol ¹	27	4.714	0.264	4.235	5.204
Natural log of the price - CNG ¹	29	3.165	0.339	2.329	3.877
Natural log of the price - Diesel ¹	33	3.883	0.392	2.854	4.758
Expenditure-share Gasoline ²	33	49.065	14.489	31.529	77.234
Expenditure-share Ethanol ²	27	16.095	9.705	0.043	31.807
Expenditure-share CNG ²	18	0.212	0.308	0	0.943
Expenditure-share Diesel ²	33	37.651	7.462	22.766	51.594

Source: own elaboration based on data from MME⁽²⁰⁰⁵⁾. ¹prices are in 2005 US\$/boe (US\$ per barrel of equivalent oil); ²Expenditure share of each fuel means the expenditure (price x quantity) with this fuel in terms of total expenditure with the four fuels.

Table 2. Summary Statistics of Main Variables of Interest

4. The static approach: measuring elasticities through a Linear Approximation of an Almost Ideal Demand System (LA-AIDS)

The elasticities of energy consumption in automotive segment in Brazil, in the 1970-2005 period, are initially estimated through a linear approximation of the Almost Ideal Demand System (hereby called LA-AIDS).

² Actually, ANP collects monthly data on price of CNG, diesel gas, and ethanol. Regarding consumption, it gives monthly data on gasoline, ethanol and diesel (including that for industrial use), but not on CNG.

The traditional LA-AIDS model, developed by Deaton and Muellbauer(1980), departs from a specific cost function and gives the share equations in a n-good system as:

$$w_i = \alpha_i + \sum_{j=1}^n \gamma_{ij} \ln p_j + \beta_i \ln \left(\frac{X}{P} \right) \quad (1)$$

where w_i is the budget-share associated with the i^{th} good, α_i is the constant coefficient in the i^{th} share equation, γ_{ij} is the slope coefficient associated with the j^{th} good in the i^{th} share equation, total expenditure X is given by $X = \sum_{i=1}^n p_i q_i$ in which q_i is the quantity demanded for the i^{th} good, p_j is the price on the j^{th} good and P is a linear price index defined as $\sum_{i=1}^n w_i \ln p_i$.

The conditions required to make the model consistent with the theory of demand are:

$$\text{Adding-up: } \sum_{i=1}^n \alpha_i = 1, \sum_{i=1}^n \gamma_{ji} = \sum_{i=1}^n \beta_i = 0 \quad (2)$$

$$\text{Homogeneity: } \sum_{j=1}^n \gamma_{ji} = 0 \quad (3)$$

$$\text{Symmetry: } \gamma_{ij} = \gamma_{ji} \quad (4)$$

The conditions (2) and (3) are linear restrictions which may be tested by standard techniques, whereas condition (4) is imposed by the model and so is not testable. Once these restrictions are observed, system (1) characterizes a demand function system of which the sum equals total expenditure, is homogeneous of 0 degree in prices and expenditure, and satisfies the Slutsky symmetry propriety. Relative price variations affect demand through the parameters γ_{ij} - a percentual variation of the j^{th} good affects the expenditure share of i^{th} good, holding real expenditure X/P constant - and variations on real expenditure affect demand through parameters β_i .

Based on these especifications, a LA-AIDS model of the Brazilian automotive fuel demand of four categories of fuel (gas, ethanol, CNG and diesel) can then be written as:

$$w_{it} = \alpha_i + \sum_j \gamma_{ij} \ln p_{jt} + \beta_i \ln \left(\frac{X_t}{P_t} \right) + \mu_{it} \quad (5)$$

where:

w_{it} = consumption share of fuel i in period t , defining $w_{GAS}, w_{ETH}, w_{CNG}, w_{DIE}$;

p_{it} = price of the i^{th} good in period t , defining $p_{GAS}, p_{ETH}, p_{CNG}, p_{DIE}$;

X_t = total expenditure in all fuels in period t ;

P_t = geometric price index in period t ; and

μ_{it} = error term

From the estimation of system (5), Marshallian³ price (ε_{ij}) and expenditure (η_{ij}) elasticities can be calculated as:

³ Marshallian elasticities (also refereed as uncompensated elasticities) are derived from the Marshallian demand equation and are specifically obtained from maximizing utility subject to the budget constraint.

$$\varepsilon_{ij} = \frac{\lambda_{ij}}{w_i} - \beta_i \left(\frac{w_j}{w_i} \right) \quad (6)$$

$$\varepsilon_{ii} = -1 + \frac{\lambda_{ij}}{w_i} - \beta_i \quad (7)$$

$$\eta_i = \frac{\beta_i}{w_i} + 1 \quad (8)$$

Since the expenditure shares, w_i , add up to 1, the variance-covariance matrix is singular, and so the estimation requires omitting one of the share equations; after the estimation of the remaining share equations, the parameters of the omitted equation are obtained via the adding up restrictions. The technique in LA-AIDS model estimation is Zellner's Generalised Least Square method for seemingly unrelated regression (SUR).

4.1 Parameter estimates

	Coef.	Std. Err.	z	P>z	95% Conf. Interval	
qDemand1						
$\ln P_{GAS}$	-0.013	0.058	-0.230	0.821	-0.127	0.100
$\ln P_{ETH}$	0.161	0.051	3.130	0.002	0.060	0.262
$\ln P_{CNG}$	-0.005	0.002	-3.170	0.002	-0.008	-0.002
$\ln P_{DIE}$	-0.143	0.022	-6.470	0.000	-0.187	-0.100
$\ln X / P$	-0.201	0.065	-3.090	0.002	-0.328	-0.073
cons	4.714	1.369	3.440	0.001	2.031	7.397
qDemand2						
$\ln P_{GAS}$	0.161	0.051	3.130	0.002	0.060	0.262
$\ln P_{ETH}$	-0.019	0.050	-0.380	0.704	-0.117	0.079
$\ln P_{CNG}$	-0.002	0.001	-1.640	0.101	-0.004	0.000
$\ln P_{DIE}$	-0.141	0.011	-12.480	0.000	-0.163	-0.119
$\ln X / P$	0.133	0.063	2.130	0.033	0.011	0.256
cons	-2.684	1.323	-2.030	0.042	-5.277	-0.091
qDemand3						
$\ln P_{GAS}$	-0.005	0.002	-3.170	0.002	-0.008	-0.002
$\ln P_{ETH}$	-0.002	0.001	-1.640	0.101	-0.004	0.000
$\ln P_{CNG}$	0.001	0.001	0.870	0.382	-0.001	0.002
$\ln P_{DIE}$	0.006	0.001	4.150	0.000	0.003	0.009
$\ln X / P$	0.005	0.001	3.620	0.000	0.002	0.007
cons	-0.096	0.027	-3.570	0.000	-0.148	-0.043

Source: own elaboration

Table 3. The Restricted SUR Estimation of the Demand System Equation Using Static LA-AIDS Model

Table 3 presents the seemingly unrelated regression (SUR) estimation results of the LA-AIDS model – as defined in (5) – with homogeneity and symmetry restrictions imposed.

Tables 4 and 5 present price and income elasticities calculated at the mean values of the budget shares (\bar{w}_i). All own-price elasticities ($\varepsilon_{11}, \varepsilon_{22}, \varepsilon_{33}$) are negative and inelastic. Concerning the cross price elasticities, some inconsistencies are depicted since $\varepsilon_{13}, \varepsilon_{31}, \varepsilon_{14}, \varepsilon_{41}, \varepsilon_{23}, \varepsilon_{32}, \varepsilon_{24}$ and ε_{42} are negative, thus indicating, for instance, a surprisingly complementarity between gasoline and CNG and between gasoline and diesel.

		Gasoline (P ₁)	Ethanol (P ₂)	CNG(P ₃)	Diesel(P ₄)
ε_{1j}	Gasoline	-0.826	0.395	-0.009	-0.138
ε_{2j}	Ethanol	0.595	-1.263	-0.012	-1.186
ε_{3j}	CNG	-3.180	-1.815	-0.753	1.881
ε_{4j}	Diesel	-0.462	-0.400	0.015	-0.324

Table 4. The Marshallian Uncompensated Price Elasticities of the Demand System Equation using Static LA-AIDS Model

η_1	Gasoline	0.591
η_2	Ethanol	2.013
η_3	CNG	4.983
η_4	Diesel	1.166

Source: own elaboration

Table 5. The Expenditures Elasticities of the Demand System Equation using Static LA-AIDS Model

Before trying to explore these surprising outcomes, it is necessary to check if they satisfy the economic properties defined in restrictions (2) and (3). The Wald test presents a test statistic of $\chi^2(6) = 13.71$, above the critical value at the 5 per cent level of significance, 12.59), therefore indicating a strongly rejection of symmetry and homogeneity restrictions. Furthermore, the residual analysis of the model showed being non White Noise with serial correlation (see Table 6).

qDemand1	Portmanteau (Q) statistics	48.6008
	Prob > chi2(14)	0.000
qDemand2	Portmanteau (Q) statistics	58.296
	Prob > chi2(14)	0.000
qDemand3	Portmanteau (Q) statistics	47.0503
	Prob > chi2(14)	0.000

Source: own elaboration

Table 6. Portmanteau Test for White Noise

5. The dynamic approach: estimating a cointegrated LA-AIDS model

The economic inconsistency of the results presented above clearly underscores the necessity to consider in more depth the dynamic aspect of consumer choice. The point is that the rejection of homogeneity and symmetry restrictions is probably a consequence of dynamic mis-specification of the model. In order to overcome this aspect and to better explain the consumer behavior in the long run, this work employs now a dynamic approach with non-stationarity and cointegration of the time-series.

This second approach here applied follows the idea that there may exist a long run equilibrium cointegrating demand system which can be identified and estimated for it would provide a basis to test the effects of price and income on the demand for automotive fuels. The short run adjustments towards the long run equilibrium are also considered. The process of correction may not be completed in one period – probably because of consumer habits, imperfect information and adjustment costs – and so the short run responses to price and income changes guide to the long run effects towards the equilibrium. In this turn, the restrictions of symmetry and homogeneity may not be accepted in the short run, but can be satisfied in the long run, that is why it is important to consider the long run equilibrium. This work then incorporates this dynamic aspect of consumer choice following the cointegration theory for it is possible to meet the requirements of identification/estimation of: long run preference parameters; separation of short run from long run effects; and LA-AIDS system.

In order to describe the dynamic model of LA-AIDS, the system in (5) can be rewritten as a vector error correction model (VECM) as follows:

$$\Delta Y_t = \mu D_t + \Gamma_1 \Delta Y_{t-1} + \dots + \Gamma_{q-1} \Delta Y_{t-q+1} + \Pi Y_{t-1} + e_t \quad (9)$$

where $Y_t = (w_{GAS}, w_{ETH}, w_{CNG}, w_{DIE}, \ln P_{GAS}, \ln P_{ETH}, \ln P_{CNG}, \ln P_{DIE}, \ln(X/P))'$ - in other words, a 8×1 column vector of budget shares (9 less one variables, which is arbitrarily deleted in order to overcome the singularity of the system), prices and real expenditure - D_t is a vector of deterministic variables (intercept, trends...); μ is the matrix of parameters associated with D_t , Γ_i are 8×8 matrices of short run parameters ($i=1, \dots, q-1$), where q is the number of lags; Π is a 8×8 matrix of long run LA-AIDS parameters; and e_t is the vector of disturbances following identical and independent normal distributions with zero mean and $E(e_t e_t') = \Sigma$.

Once the series in Y_t are integrated of order one, the balance between left and right hand side of model (13) will be achieved only if the series are cointegrated. The number of cointegrating vectors is defined by the rank of the matrix Π ; if $\text{rank}(\Pi) = r$, then Π can be written as a product of $(8 \times r)$ matrices α and β , as follows $\Pi = \alpha \beta'$. Matrix β has the long run parameters, such that $\beta' Y_{t-1}$ represents the r long run steady-state equilibriums. Matrix α is called the loading matrix, and their parameters represent the speed of adjustment to disequilibrium after a shock in the long run relationships. The matrices α and β are not unique, and thus there are many possible α and β matrices containing the cointegrating relations (or linear transformations of them). In those cases, cointegrating relations with economic content cannot be extracted purely from observed time series (Krätzig and Lütkepohl 2004). Therefore, the economic interpretation of the cointegrating vectors as structural long run relationships requires the imposition of at least r^2 restrictions (r of which

are related to normalization conditions) on cointegrating space. In this work, in order for the cointegrating vectors to correspond to consumer demands based on a LA-AIDS model, symmetry and homogeneity restrictions were imposed.

It is worth emphasizing how the error correction model (9) depicts the consumption behavior. When consumers reach their long run optimizing allocation of expenditure across products they define a baseline plan. This baseline expenditure pattern can be modified for two reasons. First, through new information (on prices and real income) available since previous period, and whose impact in the baseline budget-shares is captured through the terms $\Gamma_j s = (1, \dots, q-1)$, the short term parameters and second, through the natural changes of budget shares in the current period, even without new information of last period. This is captured by the term $(\alpha\beta'Y_{t-1})$; which is the error correction term and where α denotes the speed of adjustment towards the long run equilibrium $(\beta'Y_{t-1})$.

5.1 Parameter estimates

Before the estimation of VECM model it is common practice to test for stationarity and orders of integrations in time series data. This is done here through the Augmented Dickey Fuller test (see Table 7). Results indicate that it is not possible to reject the hypothesis that all variables are I(1) using 1% and 5% levels of significance

Variable	Lags	Model ^a	t-statistic
w_{GAS}	1	τ	-1.623
Δw_{GAS}	0	τ	-3.325***
w_{ETH}	7	τ_μ	-2.804
Δw_{ETH}	3	τ	-2.039**
w_{CNG}	9	τ	5.996
Δw_{CNG}	0	τ	-3.508***
$\ln P_{GAS}$	8	τ_τ	-2.712
$\Delta \ln P_{GAS}$	0	τ	-6.972***
$\ln P_{ETH}$	1	τ	-2.183
$\Delta \ln P_{ETH}$	0	τ	-8.151***
$\ln P_{CNG}$	10	τ_τ	-3.292
$\Delta \ln P_{CNG}$	0	τ	-5.407***
$\ln P_{DIE}$	0	τ_τ	-3.322
$\Delta \ln P_{DIE}$	0	τ	-6.273***
$\ln X / P$	0	τ	2.522
$\Delta \ln X / P$	0	τ	-4.026***

a: Model τ indicates that Dickey Fuller does not contain any deterministic component; τ_μ indicates that only a constant is considered; and τ_τ indicates the inclusion of an intercept and a trend

***(**) Denotes the rejection of the null hypothesis at the 1%(5%) level of significance

Source: own elaboration

Table 7. Unit roots tests

Once identified the non stationarity of the variables, a VECM is specified with eight variables (w_{DIE} is excluded to avoid singular matrix). This model becomes operational once defined the lag order (q), the deterministic component to be considered, and the cointegration rank(r). Due to the almost heavily parameterized nature of the system and the modest sample size ($t=33$), the decision was taken to obtain the most parsimonious system as possible. The estimation was then carried out with just one lag ($q=1$)⁴. Relating to the cointegration rank, it is normally assumed that among $(2n+1)$ variables (n budget shares, n prices and real expenditure) there are $n-1$ cointegrating vectors. In this work, with 9 variables, it is thus expected to have 3 cointegrating equations. Table 8 presents the Johansen trace statistic, which confirms the presence of three cointegrating relationships⁵.

Maximum rank	Trace statistic	5% critical value
0	174.74	124.24
1	103.83	94.15
2	70.08	68.52
3	44.24*	47.21
4	22.15	29.68
5	8.34	15.41
6	0.44	3.76
7		

Source: own elaboration

Table 8. Results from Johansen Cointegration Rank Test

As mentioned previously, the economic interpretation of the cointegrating vectors as structural long run relationships requires the imposition of at least r^2 restrictions. In this work, it should be at least 9 restrictions. Therefore, besides the three normalization restrictions, it was also imposed three homogeneity and three symmetry constraints in order to be consistent with economic theory. Table 9 reports the estimated α and β matrices with the standard errors of the parameters⁶.

The diagnosis statistics of the results are clearly satisfactory. The jointly hypothesis testing of the symmetry and homogeneity restrictions points out their empirical support; the likelihood ratio statistic of over-identifying constraints was 10.18, which is under the

⁴ This is a reasonable premise since relatively low order vector auto regressive models generally suffice in cointegration analysis. Concerning the deterministic term, the model was specified with the constant terms restricted to cointegration space.

⁵ Due to the small sample used, it could be argued that this result is not valid. It was used then the Juselius (1999) approach, in which the significance of the adjustment coefficients of 3rd cointegrating vector is tested. According to this proposal, if all α_{i3} are non-significant, the cointegration rank should be reduced to 2. In the present case, all of the estimated adjustment coefficients for the third cointegration vector were significant, indicating that the model does have exactly the same number of cointegrating vectors and equations estimated (see Table 9 for loading coefficients from VECM estimation).

⁶ A first check on the model statistical adequacy is made through some misspecification tests, like Doornik and Hansen normality test and Breusch-Godfrey autocorrelation test. The results approve the one lag specification; the test statistic of normality test was 18.86, with p-value of 0.275, while the Breusch-Godfrey test statistic was 11.20, p-value of 0.190.

critical value of at the 5 per cent level of significance ($\chi^2(6)=12.59$). Overall, considering both the residual analysis and the hypothesis test of symmetry and homogeneity restrictions, it seems reasonable to indicate that dynamic model is more appropriate than the static model to describe the expenditure allocation process of Brazilian demand of automotive fuels

Tables 10 and 11 finally present the elasticities calculated. Before discussing the elasticities estimated, it must be emphasized that they are functions of price and expenditure shares and therefore vary over the data set. Following Balcombe and Davis(1996), the elasticities are here calculated at the last point in the data set, and not at the mean values, due to the fact that elasticities are themselves non-stationary random variables, given the nonstationarity of the data used (see Table 7).

	w_{GAS}	w_{ETH}	w_{CNG}	$\ln P_{GAS}$	$\ln P_{ETH}$	$\ln P_{CNG}$	$\ln P_{DIE}$	$\ln X / P$	Constant
$\hat{\beta}'_1$	1	0	0	1.237 (0.125)	-1.061 (0.099)	-0.034 (0.006)	-0.142 (0.037)	-0.749 (0.134)	15.354 (2.819)
$\hat{\beta}'_2$	0	1	0	-1.061 (0.099)	0.680 (0.082)	0.039 (0.004)	0.342 (0.022)	0.724 (0.110)	-15.489 (2.320)
$\hat{\beta}'_3$	0	0	1	-0.034 (0.006)	0.039 (0.004)	-0.001 (0.002)	-0.004 (0.005)	0.010 (0.005)	-0.198 (0.097)
	α coefficients			t-values for α					
Δw_{GAS}	0.216	0.325	0.814		0.187	0.196	1.126		
Δw_{ETH}	-0.501	-0.567	-2.928		0.131	0.137	0.791		
Δw_{CNG}	-0.002	-0.002	0.000		0.007	0.008	0.044		
$\Delta \ln P_{GAS}$	0.982	0.950	13.233		1.498	1.566	9.018		
$\Delta \ln P_{ETH}$	1.790	1.887	8.792		1.812	1.895	10.909		
$\Delta \ln P_{CNG}$	1.535	1.498	7.137		2.270	2.374	13.666		
$\Delta \ln P_{DIE}$	0.674	0.520	9.757		1.465	1.532	8.819		
$\Delta \ln X / P$	-1.040	-1.087	-4.611		0.380	0.397	2.287		

* Standard error under parenthesis

Source: own elaboration

Table 9. Estimated β^* and α matrices under long run structural identification

As already shown the model has been approved by statistical tests, but if this is to be presented as a reasonable picture of Brazilian automotive fuels consumption, the implied behavioral measures must be in conformity to the theory of demand. From this point of view the results are also satisfactory. As required the own-price elasticities has negative signs. Ethanol and gasoline are, by far, the most sensitive fuels with quite elastic reactions to

their own price changes. Focusing on the cross price elasticities, the positive signs for $(\epsilon_{12}, \epsilon_{21})$ and $(\epsilon_{13}, \epsilon_{31})$ indicates a substitution relation between gasoline and ethanol, and between gasoline and CNG. This can, a priori, indicates that the flex fuel technology (gasoline and ethanol) and the CNG conversion technology have preserved the substitutability among the fuels. These results are then consistent with microeconomic predicitions sincethese technologies tend to reinforce the substitution relation between the referred fuels as it allows the individual consumer to consider two fuels options in the same utility function, in which he will choose the cheaper option, holding fixed the energetic equivalence ratio of substitution between them.

Also relevant are the estimated sizes of $\epsilon_{11}, \epsilon_{21}, \epsilon_{31}$ and ϵ_{41} being - 3.84, 8.09, 0.54 and 0.27; these numbers show that when gasoline price increases by 1 per cent, for example, consumers reduce the gasoline consumption by 3.84%, while compensating for the ethanol (8.09%) CNG (0.54%) and diesel (0.27%). This can so be regarded as evidence of a high substitutability, first, between gasoline and ethanol and, second, between gasoline and CNG. Concerning the superiority of the substitutability level of gasoline/ ethanol in relation to the level of gasoline/CNG, what can be argued is that the choice between the gasoline and ethanol seems to be more attractive for the consumers, since they don't have to pay any extra cost besides the cost related of the vehicle acquisition. In this regard, this trend will be certainly reinforced as long as the production of original flex fuel vehicles increases. On the other hand, the choice between CNG and gasoline is more restricted since the consumer has to face two distinct costs, the cost of buying a vehicle and the cost of installing the conversion kit of CNG.

		Gasoline (P1)	Ethanol (P2)	CNG(P3)	Diesel(P4)
ϵ_{1j}	Gasoline	-3.848	1.503	0.007	0.258
ϵ_{2j}	Ethanol	8.097	-3.583	-0.044	-3.881
ϵ_{3j}	CNG	0.540	-0.620	-0.780	1.374
ϵ_{4j}	Diesel	0.269	-0.668	0.269	-0.627

Source: own elaboration

Table 10. Marshallian Uncompensated Price Elasticities of the Demand System Equation using Dynamic LA-AIDS Model

η_1	Gasoline	1.188
η_2	Ethanol	0.077
η_3	CNG	-0.523
η_4	Diesel	1.014

Source: own elaboration

Table 11. Expenditures Elasticities of the Demand System Equation using Dynamic LA-AIDS Model

With respect to the depicted substitutability between gasoline and diesel, some comments have to be made. The result seems reasonable only because the model uses aggregated data. On the other hand, from a microeconomic perspective this result does not make sense, since

these fuels do not represent real substitution options. First, because of the absence of a technology, which could allow this substitution and second, because diesel and gasoline are used by different profiles of automobiles; those devoted to long distance freight transport or land carriage typically use diesel, since it is cheaper than gasoline. In this sense, it is worth stressing that the model neglects the control for the fact that choice possibilities are different among different kinds of automobiles. This lack of control can also justify other inconsistent result here produced, the negative cross price elasticities of $(\varepsilon_{23}, \varepsilon_{32}, \varepsilon_{24}, \varepsilon_{42})$, which could evidence a surprisingly complementarity between ethanol and diesel, and between ethanol and natural gasoline.

As regards the expenditure elasticities, Table 11 shows that gasoline, ethanol and diesel are normal goods, and with the exception of ethanol, they are expenditure elastic. An interesting result concerns the CNG. Its elasticity is negative and is thus estimated to be an inferior good.

This result is possibly related to the motivation and income profile of current CNG consumers. The Brazilian production of new cars originally designed to run on CNG is almost irrelevant. The great majority of CNG consumers install the conversion kit expecting substantial fuel expenditure savings, in particular for those that drive long distance on a regular basis, as light duty passenger vehicles (essentially taxi drivers). In this sense, the CNG consumption profile in Brazil is not devoted to the large scale public transport system, as in Bangladesh, Pakistan or India. It is then important to note that the investment on conversion kit to CNG act as a fixed cost that only consumers who really want to save expenditure are inclined to pay. Hence, CNG consumers are definitely motivated by the cost saving purposes, especially due to the government policy of fixing relative prices favoring the fuel as a way to promote the expansion of natural gas consumption in the country⁷. The Brazilian demand of CNG is then still related to small scale transport, for which income is a great restriction.

What seems clear is that the choice of CNG fuel is thus driven mainly by the price aspect and less by the non pecuniary factors, as its energetic efficiency. Hence, it is reasonable to outline that as income increases the saving purposes tend to be less relevant and even if there are more consumers who are able to pay the fixed cost of the conversion kit, there would also be an increasing number of consumers – at least among those not interested in commercial purposes as taxi drivers are – who could begin to consider the low efficiency of the fuel⁸ as reasonable criteria of choice, and so CNG could be less preferred.

This result is reinforced by the signals estimated of real expenditure $(\ln(X/P))$ parameters of $-\beta_1, \beta_2$ and β_3 in model (13). Once the symmetry and homogeneity restrictions are valid, as it is the case, demand theory predicts that positive β 's means "luxury good", and a negative sign means "necessary good" (Deaton and Muellbauer 1980) (Deaton and Muellbauer 1980). The real expenditure parameter of CNG share equation (β_3) is negative, while β_1 and β_2 have positive signs (see Table 9). CNG is so estimated as a "necessary good", and gasoline and ethanol are considered "luxury goods", in the sense that as the consumer gets more income he demands proportionally more gasoline and ethanol, and less CNG.

Overall, even though the estimations from cointegrated LA-AIDS are statistically (and economically) better interpreted than those from the static model, it is necessary to put forward that they still have to be cautiously evaluated. First, due to the limited span of

⁷ This pricing policy was stated by the government in order to diffuse the natural gas consumption in Brazil when the natural gas imports from Bolivia begun.

⁸ At least in the way the CNG is currently used by engines not originally designed to run on it

observations over time, resulting in only 33 points in time for each variable⁹. For instance, the absence of longer data series makes difficult a bootstrapping analysis to estimate standard errors of the elasticities. Second, because the model uses aggregated data and not micro level records for households; and even with aggregated data it does not consider vehicle characteristics factors – as fleet composition by fuel, which could be a significant parameter in explaining the expenditure allocation process.

6. Conclusions

This work aimed at estimating the price and income elasticities of automotive fuels demand in Brazil. The analysis of the expenditure allocation process among the gasoline, ethanol CNG and diesel was carried out through the estimation of a linear approximation of an AIDS model. This model is very convenient due to its ability to fulfill much of the desired theoretical properties of demand, being at the same time parsimonious regarding the number of parameters. Furthermore, the equations to be estimated derived from LA-AIDS are linear in parameter which allows the use of econometric methods widely available in terms of testing and estimating procedures. Two estimation methods were tried: a static and a dynamic (cointegrated). Specification tests seem to support the use of the dynamic model. Based on the favorable diagnostic on the second set of estimations it is important to point out some of their relevant results.

First, it is worth to remark the high substitutability between gasoline and ethanol, and also the fact that this substitution relation is larger than the one observed between gasoline and CNG. Some comments concerning this result are thus in order. This finding seems to confirm the rationale that flexible technologies tend to reinforce the substitution relation between the fuels. This is particularly true for the gasoline and ethanol because the consumers don't have to pay an extra cost besides those related with the vehicle buying to access the possibility of choosing between the refereed fuels. On the other hand, the option between CNG and gasoline is more restricted since the consumers have to pay not only for a vehicle but also to install the conversion kit of CNG. There is then a transaction cost which is not irrelevant. This difference in favor of the substitutability between gasoline and ethanol seem to increase as the production of original flex fuel vehicles increase.

Second, the estimations here produced suggest that gasoline, ethanol and diesel are normal goods, and except for ethanol, they are expenditure elastic. An interesting result concerns the CNG which is estimated as an inferior good. A possible explanation for this outcome could be the motivation and income profile of current CNG consumers. These consumers are mainly interested in saving purposes, since CNG is favored by a specific government policy of price differential with liquid fuels. For this reason, the choice of CNG fuel is driven mainly by the price aspect and less by the non pecuniary factors, as its low energetic efficiency. As income increases, the saving purposes tend to be less relevant and even though there are more consumers who are able to pay the cost to install the CNG kit, there would also be an increasing number of consumers who would consider the low efficiency performance of the fuel as a reasonable choice criteria, and so CNG could be less preferred.

⁹ By the time this work was reviewed the Brazillian Ministry of Mines and Energy has launched the Balanco Energetico Nacional from 2009 which contains annual data on fuel price and consumption until 2008. Therefore, even if the work has considered this last annual data collection it would have resulted in only three more annual observations for each variable. That being the case, it is reasonable to assume that the results here produced would not present significant changes if the data was extended.

Overall this work tried to improve the understanding of the consumer's behavior and their possibilities and criteria to choose automotive fuel in Brazil. Two important policy implications can be derived from this analysis. First, there are implications on tax revenues from gasoline sales. Based on the result of a high substitutability between ethanol and gasoline and considering that the production of flex fuel vehicles has been augmenting in an expressive rate since its launching in 2003, the future gasoline consumption is likely to be more dependent on ethanol prices. For this reason, the tax revenue from gasoline can be affected by the supply of ethanol which as an agricultural commodity has intrinsic seasonalities and can be subject to potential supply disruptions. Considering that the share of tax on final price of gasoline is quite relevant in most state governments in Brazil, governments may have to redesign their fiscal policy regarding this fuel in order to smooth its tax revenue. Second, there are implications on the government strategy to promote the use of natural gas. Considering that the pace of GNC expansion has presented an impressive level (see Table 1) and assuming the fact here assessed that the fuel is an inferior good, the government may have to readequate its fuel pricing policy in order to direct the consumption of natural gas to other worthier uses than for small scale transportation.

A possible extension to this work is to examine some specific states from Brazil, for which is possible to use monthly data (at least from 2001 onwards), to explicitly consider the taxes charged on the fuels (which assume different levels among the states), and to include further controls through aggregated data on stock of vehicles by fuel (which is available only at the states level). Through this measures it will be possible improve the estimation of the parameters of interest.

7. References

- Alves, D. and Bueno R. (2003). "Short-run, long-run and cross elasticities of gasoline demand in Brazil". *Energy Economics*, Vol. 25, No. 2: 191-199.
- Balcombe, K. G. and J. R. Davis (1996). "An application of cointegration theory in the estimation of the Almost Ideal Demand system for food consumption in Bulgaria." *Agricultural Economics* 15: 47-60.
- Dahl, C. and Sterner, T (1991) "Analysing gasoline demand elasticities: a survey" *Energy Economics*, 13, 203-210
- Deaton, A. S. and J. Muellbauer (1980). "An Almost Ideal Demand System." *American Economic Review* 70(3): 312-26.
- Flood, L., Islam N. and Sterner, T (2008) "Are demand elasticity affected by politically determined tax levels? Simultaneous estimates of gasoline demand and price" *Applied Economic Letters*, 1-4
- Goodwin, P. Dargay, J. and Hanly, M. (2004) "Elasticities of Road Traffic and Fuel Consumption With Respect to Price and Income: A Review" *Transport Reviews*, 24,3,275-292
- Johansen, S. (1988). "Statistical analysis of cointegration vectors." *Journal of Economic Dynamics and Control* 12: 231-254.
- Juselius, K. (1999). "Models and relations in economics and econometrics." *Journal of Economic Methodology* 6(2): 259-290.
- Krätzig, M. and H. Lütkepohl (2004). *Applied time series econometrics*. Cambridge, Cambridge University Press.
- Lewis, W. A. (1954). "Economic Development with Unlimited Supplies of Labour." *Manchester School*: 139-191.
- Ministério das Minas e Energias (2006). *Balanco Energético Anual*. Brasília.

Part 2

Material Characterization and Improvements

Fatigue and Fracture Behavior of Forging Die Steels

Ryuichiro Ebara
*Hiroshima Institute of Technology,
Japan*

1. Introduction

Forging die failures for automotive components are caused by inadequacy of variables such as die materials, die design, die manufacturing and forging operations [1].

The forging die frequently fails from the corner where stress concentrate. Fig.1 shows a typical failure of hot forging die for a knuckle. From the macroscopic fracture surface observation it looks to be easily judged that a brittle failure initiated from the corner. These fractures are frequently observed on hot forging dies for knuckle, connecting rod, crank shaft and flange yoke for automotive components. However it can be clearly identified by low magnification observation that the most of the brittle fractures initiated from short cracks initiated from the corner due to fatigue and thermal fatigue. Fig. 2 shows the fracture surface of a flange yoke die made in SKT4 steel after 2000 forging operations [2]. It is clear that the brittle crack initiated at 3.5mm from the surface where nonmetallic inclusion MnS located. The stretched zone is most frequently observed at the transition zone from fatigue to impact fracture. In this case a stretched zone with 8 to 10 μ m width was observed between fatigue and impact fracture surface as shown in Fig. 3 [2]. The reason of this failure was determined to be an insufficient preheating temperature for the hot forging die by use of the relationship among dynamic fracture toughness, temperature and stretched zone width. The stretched zone can also be observed in failed cold forging die [3].It is possible to evaluate the fracture toughness of the failed cold forging die for automotive component by measuring the stretched zone width.

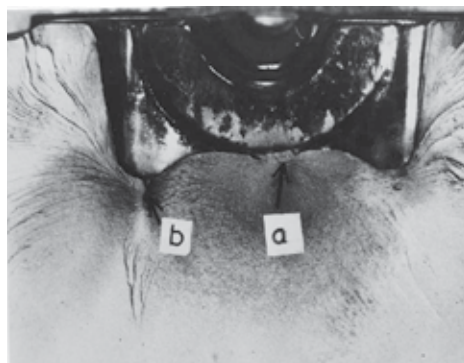


Fig. 1. Macroscopic fracture surface of a knuckle forging die for a motor vehicle [1]. Arrow a and b shows crack initiation area respectively. Forging die steel: SKD62

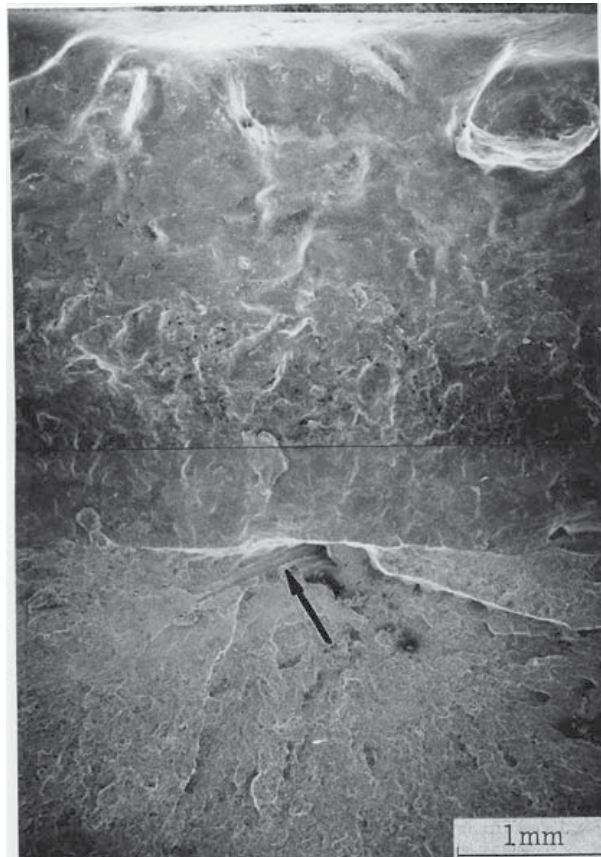


Fig. 2. Fracture surface of a flange yolk forging die [2]. Arrow shows MnS where impact failure initiated

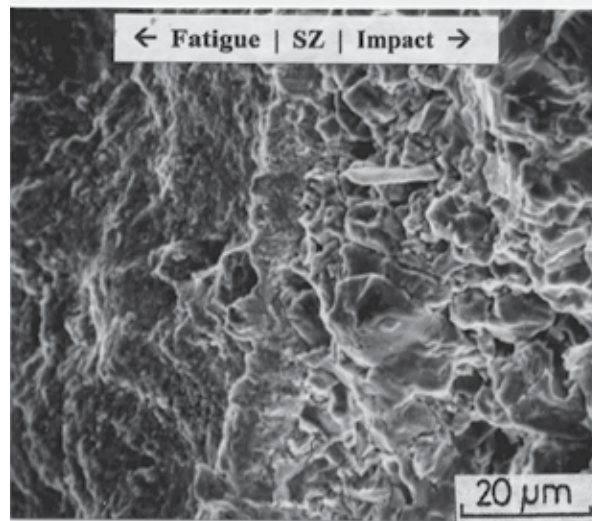


Fig. 3. Stretched zone between fatigue and impact fracture surface [2]. Flange yolk forging die

Thus it is indispensable to evaluate fatigue and fracture behavior of forging die steels in order to prevent forging die failure and to improve die life. It can also be mentioned that the role of microfractography in failure analysis of forging dies for automotive component is very important.

2. Fracture behavior of forging die steels

2.1 Hot forging die steels

Instrumented impact tests were conducted for fatigue crack introduced 2 mm U notched Charpy impact specimens. Fig.4 shows dynamic impact fracture toughness K_{1d} as a function of testing temperature for SKD 61 steel. Maximum K_{1d} is attained at 573K. The ductile-brittle transition temperature is observed at around 423K.

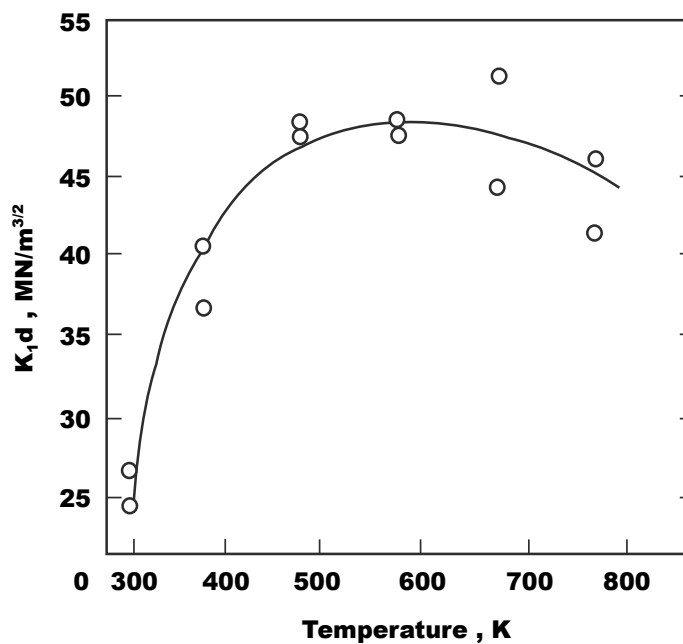


Fig. 4. Dynamic fracture toughness, K_{1d} as a function of tested temperature [4].

Fig. 5 shows impact fracture surfaces of SKD62 steel. Cleavage fracture is observed at room temperature (Fig. 5 a)), while dimple is observed at 673K (Fig. 5 b)). In general ductile-brittle transition temperature is in the range of 373K to 423K for hot forging die steel. Mixed mode of cleavage and intercrystalline fracture is predominant at temperature lower than ductile-brittle transition temperature, while dimple is predominant at temperature higher than ductile-brittle transition temperature. Thus impact fracture whether ductile or brittle can be qualitatively identified by use of microfractography of these impact fracture surface characteristics. Fig. 6 shows stretched zone observed between fatigue and impact fracture surface of hot forging die steel SKD62. The higher the testing temperature the wider the stretched zone width is. Fig. 7 shows K_{1d} as a function of stretched zone width. As aforementioned the failed temperature of hot forging die failure can be quantitatively determined by measuring stretched zone width on fracture surface.

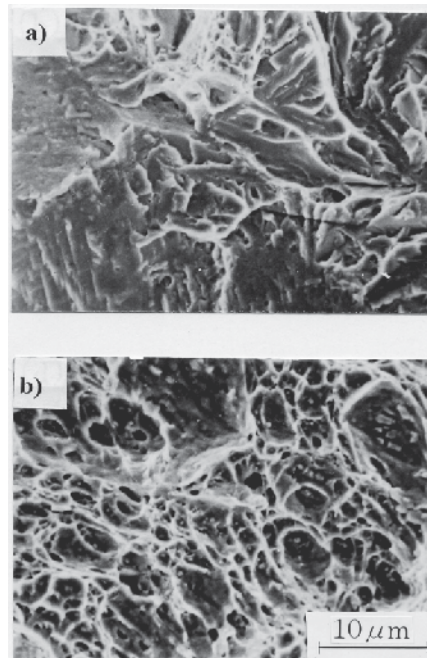


Fig. 5. Impact fracture surface, SKD62[4]. a) RT b) 673K

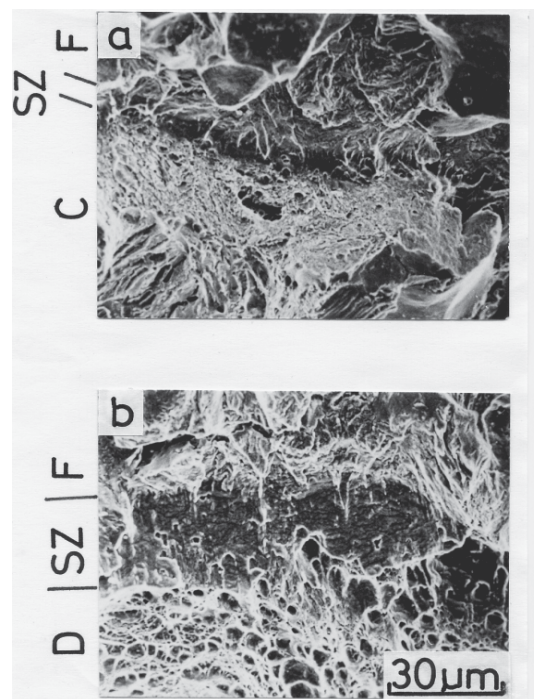


Fig. 6. Stretched zone, SKD62[4]. a) RT b) 673K, SZ: stretched zone, F: fatigue, C: cleavage, D: dimple

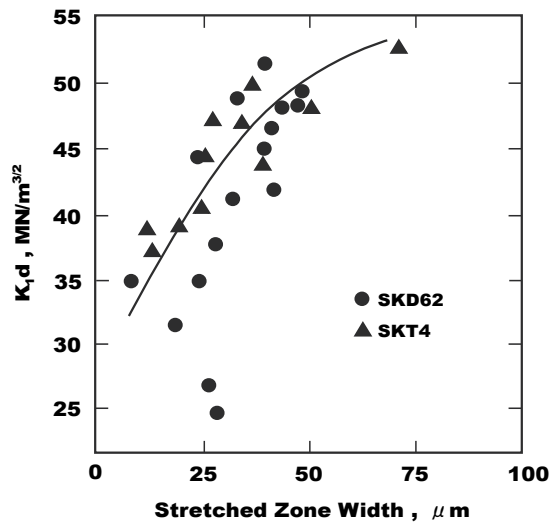


Fig. 7. Dynamic fracture toughness K_{1d} as a function of stretched zone width[4].

2.2 Cold forging die steels

Fig. 8 shows the Charpy Impact test results investigated for specimens with 5mm U notch, 2.5 mm saw cut and 2.5mm saw cut with fatigue crack (1.64-2.25mm)[3]. The commercial cold forging die steels such as tool steels of SKD61, SKD11 and QCM8, high speed steels of YXM1,YXM4,YXR3,YXR33 and YXR3,powdered high speed steel of HAP72 and cemented carbide GM60 were used. These steels were quenched and tempered and the Rockwell C scale hardness numbers are 52 to 67 [5].

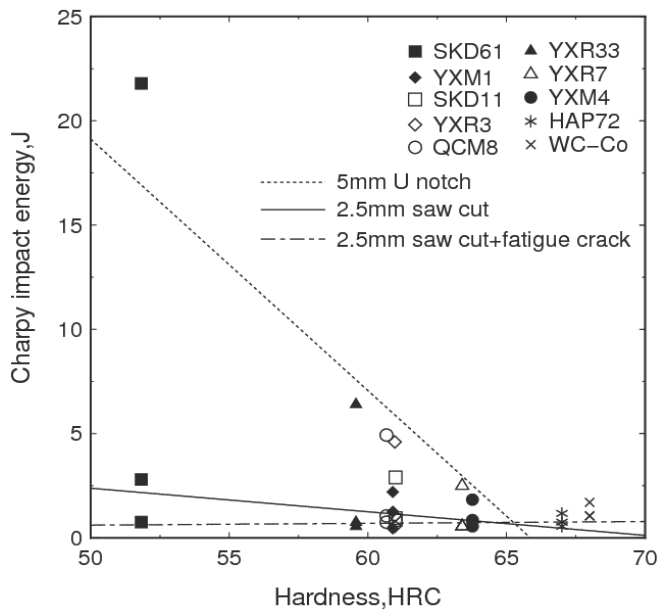


Fig. 8. Charpy impact energy of cold forging die steels with different notch figure [3].

The Charpy impact energy of cold forging die steels is very sensitive to the notch figure. The most prominent notch effect can be observed in SKD61. The larger the hardness the smaller the Charpy impact energy is. The Charpy impact energy of cold forging die steels was low as compared with those of other ductile structural steels. Macroscopic fracture surfaces of 5mm U notched specimens were brittle with radial zone. The shear lips were observed on SKD61 with relatively smaller hardness. Macroscopic fracture surfaces of 2.5mm saw cut and 2.5mm saw cut with fatigue crack were more brittle.

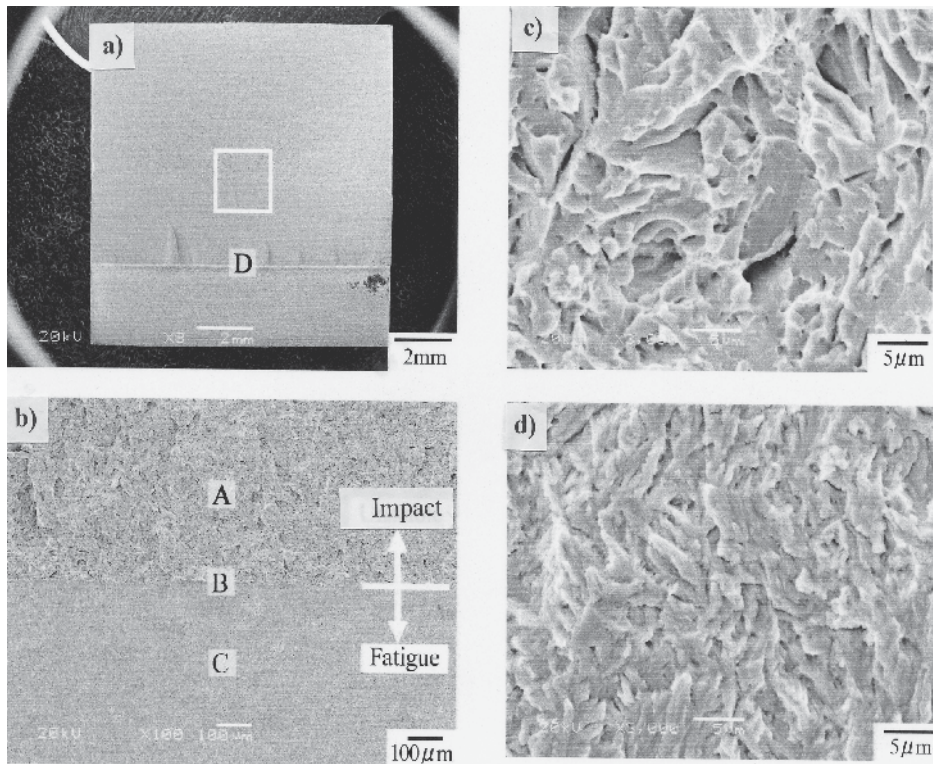


Fig. 9. Impact fracture surface. SKD61, HRC 52, 2.5mm saw cut with fatigue crack[3]. a) Macroscopic fracture surface, b) Enlargement of the window area in a), c) Impact fracture surface (A in c)), Fatigue fracture surface(C in c))

Cleavage fracture surfaces are predominantly observed on fracture surfaces of all tested steels except WC-Co. The fracture surface of WC-Co was intergranular. Fig. 9 shows fracture surface of 2.5mm saw cut with fatigue crack in SKD61. It can be easily discriminate fatigue fracture surface from impact fracture surface even in macroscopic fracture surface (Fig. 9a)). The discrimination is much more easily in low magnified fracture surface for the window area in Fig. 9a) (Fig. 9b)). The discrimination is not easy for the steel such as HAP72 with higher hardness of HTC67. The fatigue fracture surface was transgranular (Fig. 9d)) and impact fracture surface was cleavage (Fig. 9c)) for tool steels and high speed steels. However intergranular fracture is predominant for WC-Co. The stretched zone was clearly observed between fatigue fracture surface and impact fracture surface for tool steels and high speed steels. The stretched zone width is wider in the steel with lower hardness. For hard steels

the stretched zone can be identified for powdered steel HAP72 (Fig. 11d)), while it can not be easily identified for sintered steel WC-Co.

The three point bending fracture toughness tests were conducted in accordance with ASTM Standard E399-90 by use of the specimen with 55mm long, 10mm wide and 10mm thick. Fatigue crack with length of 1.64 to 2.25mm was introduced ahead of saw cut notch with 2.5 mm long[3]. Fig.10 shows the relation between fracture toughness and hardness of cold forging die steels. The higher the hardness the lower the fracture toughness was. The relation between hardness and fracture toughness can be expressed as follows.

$$\text{Fracture toughness (MPa}\sqrt{m}) = -1.445 \times \text{HRC} + 110.37$$

Fracture surface morphology of three point bending fracture surfaces are basically same as that of the Charpy impact fracture surfaces with 2.5mm saw cut with fatigue crack. The morphology of the fatigue and unstable fracture surface of the three point bending fracture surface was same as that of the impact fracture. The stretched zone is clearly observed on fracture surface between fatigue and unstable fracture.

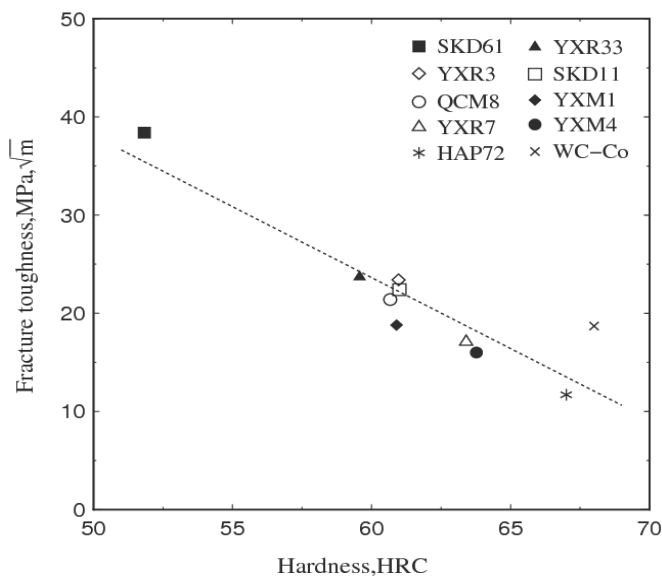


Fig. 10. Relation between fracture toughness and hardness of cold forging die steels[3].

Fig. 11. shows three point bending fracture surfaces of SKD62 and HAP72. It is easily discriminate between fatigue and unstable fracture surface from macroscopic fracture surfaces [Fig. 11a), c)]. The stretched zone can be clearly identified between fatigue and unstable fracture surface [Fig.11b), d)]. It was reported by Bates and Clark that the stretched zone width can be well correlated to fracture toughness [7]. The K_c/σ_y can be depicted for various kinds of structural materials including cold forging die steels as shown in Fig. 12. The relation between SZW (μm) and $K_c/\sigma_y(\sqrt{\text{mm}})$ can be expressed as shown below.

$$\text{SZW}(\mu\text{m}) = 3.28(K_c/\sigma_y)^{1.24}$$

This relation shows that the quantitative analysis is possible by measuring the stretched zone width on fracture surface in the failure analysis of cold forging dies.

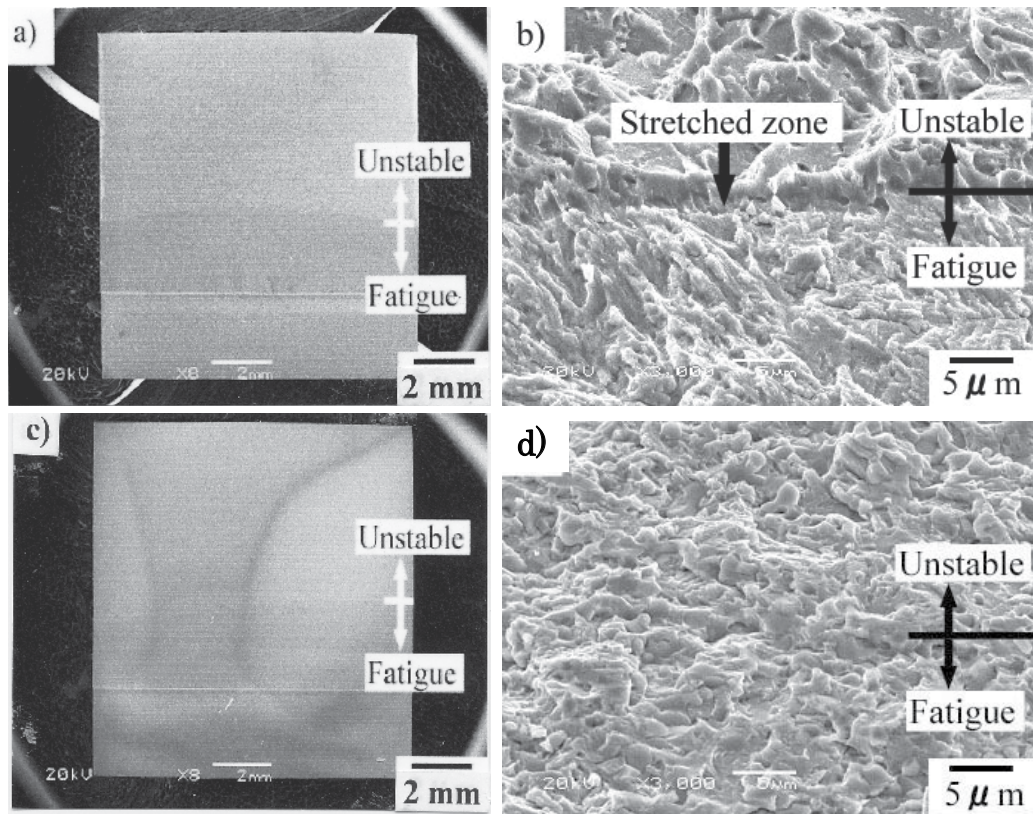


Fig. 11. Stretched zone on three point bending fracture surface[3]. a), b) SKD61 c), d) HAP72

3. Fatigue behavior of forging die steels

3.1 Hot forging die steels

Effect of testing temperature, steel hardness, stress concentration factor of specimen and surface treatments effect on low cycle fatigue strength of hot forging die steels are mainly evaluated. Load controlled low cycle fatigue tests were conducted at 473K and 673K by use of an axial fatigue testing machine (98kN). Round notched bar specimen with minimum diameter of 8mm was used. The stress concentration factor was 1.31. Testing frequency was 0.083Hz and R value (minimum to maximum stress in the loading cycle) was 0.05.

Fig. 13 shows low cycle fatigue strength of hot forging die steels with different hardness under various temperatures. The low cycle fatigue strength at RT was almost same as that at 473K and 14% higher than that at 723K. It was also obtained that the low cycle fatigue strength of the notched specimen with stress concentration factor of 2.3 for SKD62 with HRC43.5 at 573K was almost same as that at RT as shown in Fig. 14. [4]. Therefore it can be mentioned that temperature effect on the low cycle fatigue strength of SKD62 appears in a temperature range over than 573K. The fatigue strength of SKD46 at 10^4 cycles was 25, 10 and 13% higher than that of SKD62 with HRC43.5 at tested temperatures of RT, 573K and 723K. The major reason for the fatigue strength increase in SKD62 with higher hardness is attributed to the delay of fatigue crack initiation due to the higher ultimate tensile strength.

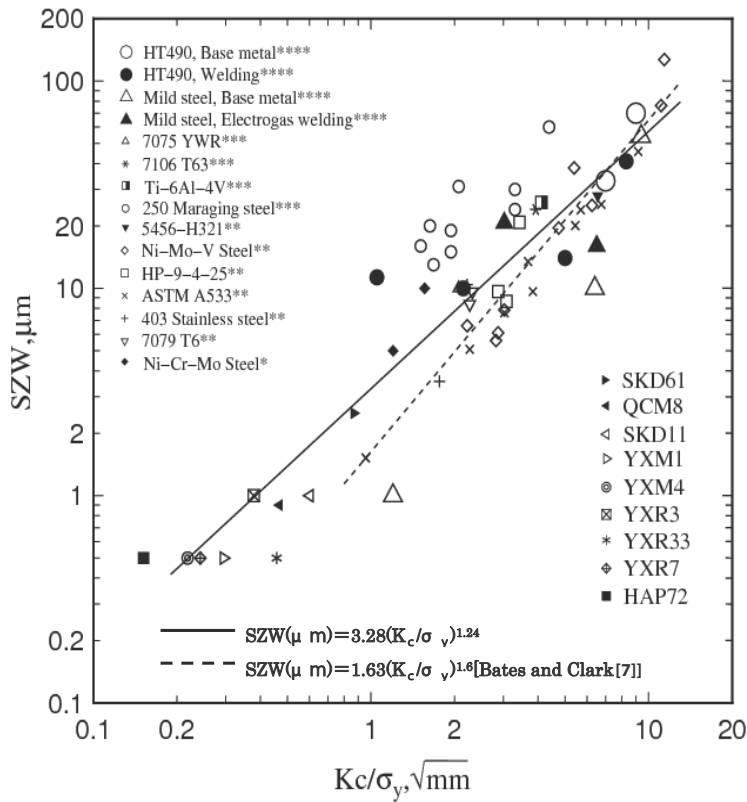


Fig. 12. Stretched zone width as a function of K_c/σ_y [3]. *Spitzig[6], **BatesandClark [7], ***Brothers [8], ****Ebara et al. [9]

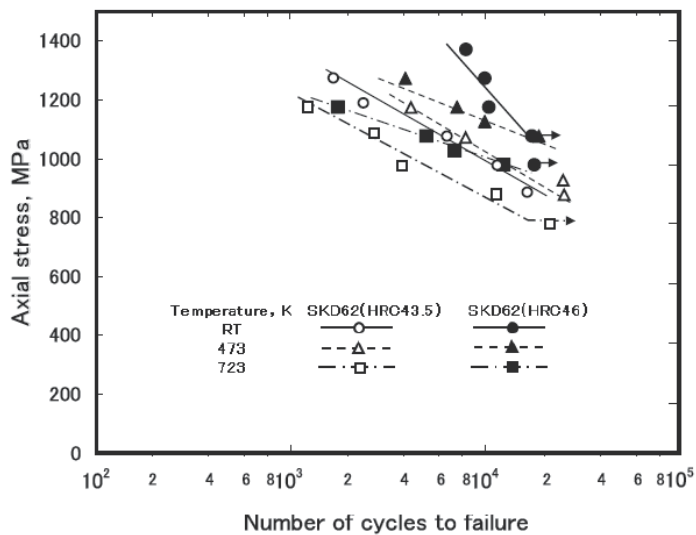


Fig. 13. S-N diagrams of SKD62(HRC43.5) and SKD62(HRC46)[10].

Fig. 14 shows conventional S-N diagrams of base metal, ion nitrided (773Kx30hr) specimen, ion nitrided (723Kx30hr)specimen and tufftrided(843Kx12hr)specimen for SKD62 [4]. The effect of surface treatment such as tufftride and ion nitride cannot be expected at high stress amplitude. Repeated axial stress and number of cycles expected for fatigue strength improvement are summarized in Table 1 [4].

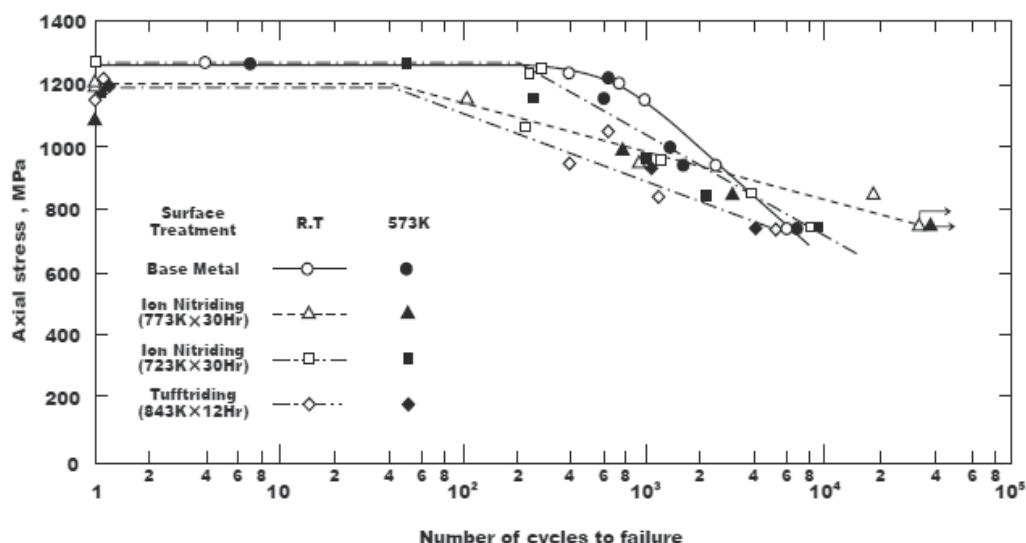


Fig. 14. Influence of surface treatments on low cycle fatigue strength of SKD62[4]

Surface treatment	σ_c / σ_B	N_c , cycles
Ionnitride(773Kx30h)	0.79	3×10^3
Ion nitride(723Kx30h)	0.73	5×10^3
Tufftride(823Kx12h)	0.63	7×10^3

σ_c : Stress expected for surface hardening

N_c : Number of cycles expected for surface hardening effect

Table 1. Surface hardening effect on low cycle fatigue strength of SKD62[4].

The strong reason of ineffective ion nitride effect at the higher stress amplitude can be explained by earlier fatigue crack initiation at brittle nitride compounds formed on the ion nitrided surface [11]. While ion nitride effect at lower stress amplitude can be expected by delayed fatigue crack initiation at ion nitride layer. The different effect of ion nitride effect on fatigue strength depend on surface hardness, hardened depth, properties of hardened layer and residual stress of ion nitride layer [12]. The surface treatment effect on fatigue strength of hot forging die steel is different in fatigue loading manner. The improvement effect could not be observed in reversed axial loading with mean stress [13].

Fig. 15 shows representative fracture surface morphology of SKD62 in low cycle fatigue range at 573K. Crack initiated from the notched surface (Fig. 15a, c)) and propagated with transgranular mode. Striation was identified at failed number of cycles over than 10^2 (Fig. 15d)) and was predominantly observed on low cycle fatigue fracture surfaces at

RT, 473K and 723K. Dimple was observed at crack initiation area at failed number of cycles lower than 10 (Fig. 4b)) [4].

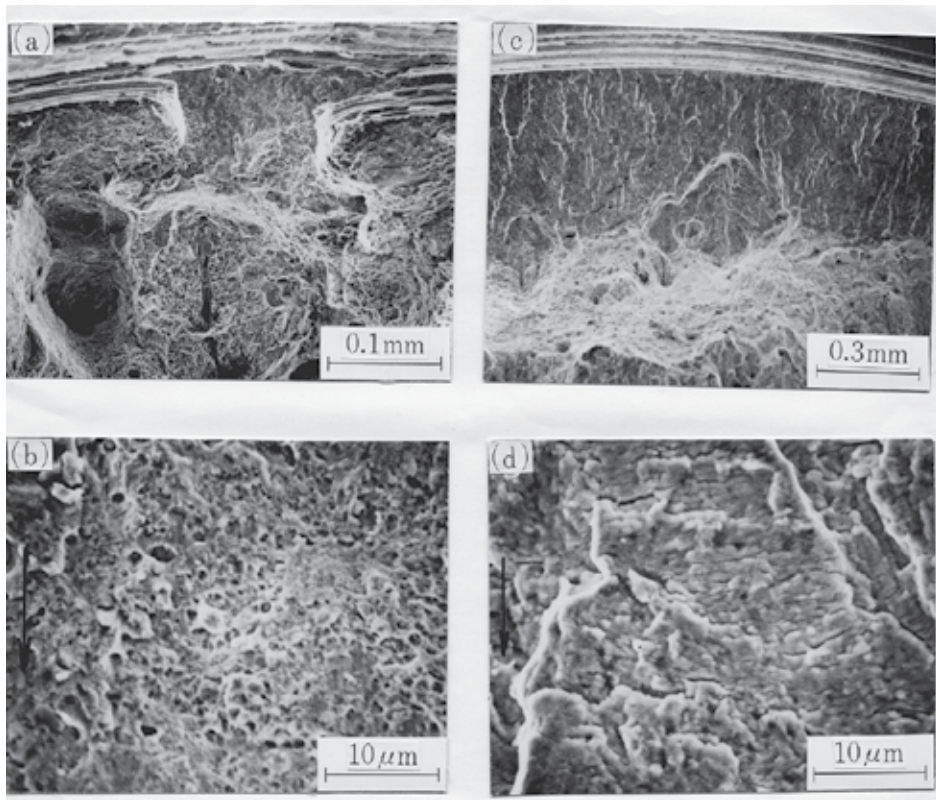


Fig. 15. Low cycle fatigue fracture surface[4]. a), b) Axial stress 1274.9 MPa, Number of cycles 7 c),d) Axial stress 1029.7 MPa, Number of cycles 1.4×10^3 b), d) are enlargement of a),c), respectively. Arrow shows crack propagation direction.

Fatigue crack propagation tests were conducted for SKD62 steels with different hardness by use of an axial fatigue testing machine (98kN). Plate specimens of 5mm thickness with a semi circular single edge notch were used. Frequency was 0.083Hz and R value was 0.05. Fig. 16 shows the crack propagation curves for SKD62 with HRC46 at [10]. The da/dN at 723K was faster than that at RT in the ΔK from 40 to 150 $\text{MPa}\sqrt{\text{m}}^{1/2}$. However, the da/dN at 473K was slower than that at RT. Further investigation on the role of oxide during crack closure may be needed to clarify this phenomenon.

Crack propagated with transgranular mode and striation was predominantly observed at crack propagation area for all tested temperatures.

Thermal fatigue tests were conducted at 473K, 673K, 873K, 1073K and 1273K by use of the laboratory made thermal fatigue testing apparatus[10]. Plate specimens of 25mm thick with an electric discharge cut of 1.52 to 4.22mm deep and 0.37 to 0.41 mm wide were used for thermal fatigue crack initiation test. Plate specimens with a fatigue pre-crack cut from CT specimens with 25mm thick after introducing fatigue crack were used for thermal fatigue crack propagation tests.

The number of cycles for thermal fatigue crack initiation at 673K, 873K, 1073K and 1273K was 61, 36, 22, and 1. The lower the heating temperature, the shorter the number of cycles for thermal fatigue crack initiation and thermal fatigue crack lengths were. Thermal fatigue crack initiation was not depended on the notch ratio with length to width of the specimen.

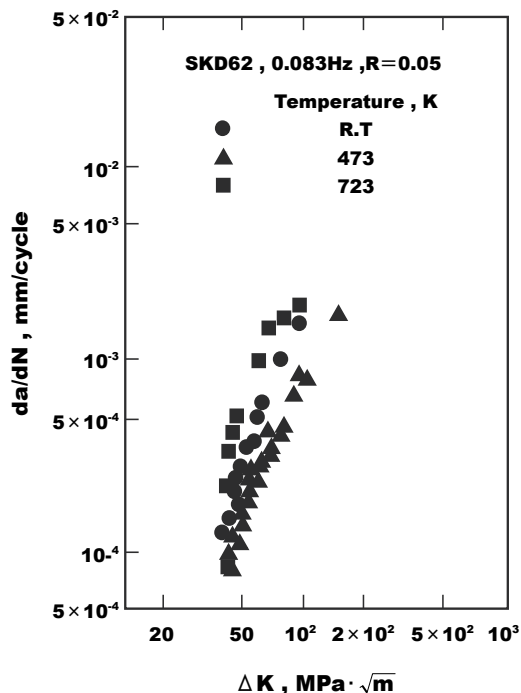


Fig. 16. Crack propagation curves of SKD62[10].

The ion nitride effect was also examined on thermal fatigue crack initiation. Thermal fatigue crack initiation was not observed up to 100 cycles at 673K. However the number of cycles for thermal fatigue crack initiation was half and the length of thermal fatigue crack was twice as compared with those of base metal at 873K. The ion nitride effect on thermal fatigue crack initiation depends on the testing temperature. Therefore in order to improve thermal fatigue life in actual hot forging dies by surface treatments the careful temperature control of hot forging dies is necessary during hot forging operation.

Thermal fatigue crack propagation tests were conducted to the number of cycles up to 100. Fig. 17 shows thermal fatigue crack propagation curves [10]. Thermal fatigue crack propagation was not observed up to 100 cycles at 473K. Thermal fatigue crack propagated up to 50 cycles, then arrested up to 100 cycles at 673K. The crack arresting phenomenon was also observed at 873K and 1073K. The cause of these phenomena is deeply related to the behavior of the oxide produced in the crack surface during thermal fatigue process. The thermal fatigue crack propagated with transgranular mode and striation like pattern were predominantly observed on thermal fatigue fracture surfaces. The typical thermal fatigue fracture surface at 873K is shown in Fig. 18. The morphology of the fracture surface and striation like pattern was very similar to the fracture surface of an actual reverse gear forging die failed after one thousand forging operations [10].

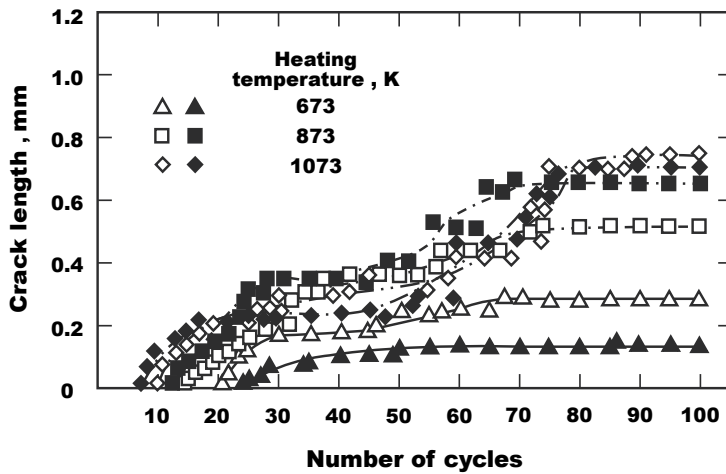


Fig. 17. Thermal fatigue crack propagation curves[10].

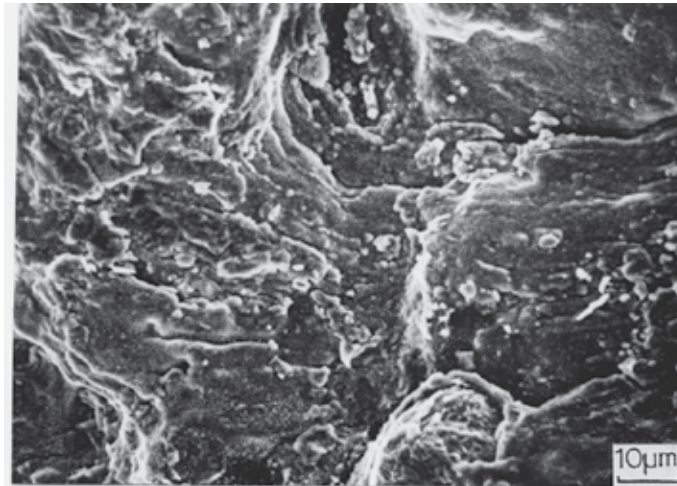


Fig. 18. Thermal fatigue fracture surface of the specimen[10]. SKD62, Heating temperature: 873K, Number of cycles: 100

3.2 Cold forging die steels

Load controlled low cycle fatigue tests were conducted for representative cold forging die steels of SKH51 and YXR3 (0.65mass% C high speed steel). Ultimate tensile strength and Rockwell C scale hardness number (HRC) of SKH51 and YXR3 steel are 2550MPa,66.0 and 2240MPa,61.5,respectively. The round bar specimens with 6.5 mm at minimum diameter was used. Frequency was 20Hz and R value was 0.05.Fig.19 shows S-N curves of the lapped plane bar specimens of YXR3 and SKH51 heat-treated in vacuum [14]. Fatigue strength of SKH51 steel is higher than that of YXR3.

This is because of the higher ultimate tensile strength of SKH51 than that of YXR3 steel. Fig. 20 shows S-N diagrams of SKH51 heat treated in vacuum and salt bath. The effect of surface roughness on low cycle fatigue strength can be observed for specimen heat treated in

vacuum. However the fatigue strength of the lapped plane bar specimen was just a little lower than that in YXR3 steel [14]. The effect of surface roughness on fatigue strength is prominent at low stress amplitude in rotating bending fatigue [15]. It can be concluded that the steel with smoother surface has higher fatigue strength for SKH51 as a result of a delay in fatigue crack initiation from the surface [16].

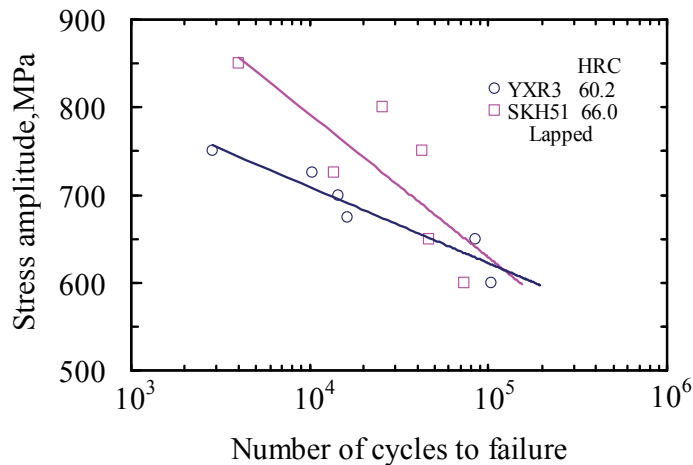


Fig. 19. S-N diagrams of the lapped plane bar specimen of SKH51 and YXR3 steel heat treated in vacuum [14].

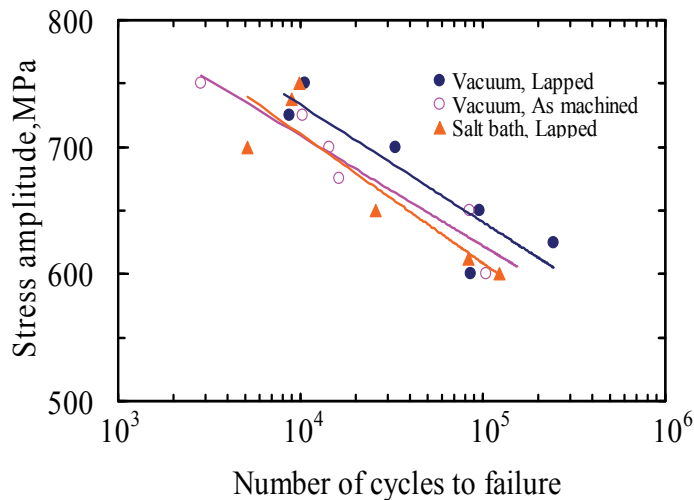


Fig. 20. S-N diagrams of SKH51 heat treated in vacuum and in salt bath[14].

Fig. 21 shows S-N diagrams of YXR notched specimens with stress concentration factor 1.5 to 2.5. Fatigue life of the notched specimen with larger stress concentration factor is shorter than that with smaller stress concentration factor. It is also apparent that fatigue life is influenced by angle of notch with same stress concentration factor. Thus low cycle fatigue strength of cold forging die steel is very sensitive to notch [14].

Ion nitride effect on fatigue strength could not be observed at number of cycles at 1.5×10^4 cycles for YXR3 steel. In YXR3 steel with higher hardness, stress expected for ion nitride effect decreased as compared with those in SKD61 steel. Higher the Vickers hardness numbers of forging die steel the lower the stress expected for ion nitride effect as observed in hot forging die steels. The strong reason of ineffective ion nitride effect can be explained by fatigue crack initiation at brittle nitride compounds formed on the surface [17].

SEM fracture surface observation for plane bar specimens revealed that subsurface crack initiation was observed at failed number of cycles over than 8×10^4 cycles for YXR3 steel and 4.5×10^4 cycles for SKH51 steel. Transgranular fracture surfaces were predominant in crack propagation area for both steels. The typical subsurface fracture surface initiation and the transgranular fracture surface of plane bar specimen in YXR3 steel are shown in Fig. 22a) and Fig. 22b), respectively. Macroscopic fracture surface observation on notched specimens of YXR3 steel revealed that the smaller the stress concentration factor and the larger the stress amplitude the smoother fatigue fracture surface was observed [14]. Crack initiation occurred from the surface in notched specimens of cold forging die steel. Thus the crack initiation mode in notched specimens is completely different from that in plane bar specimens.

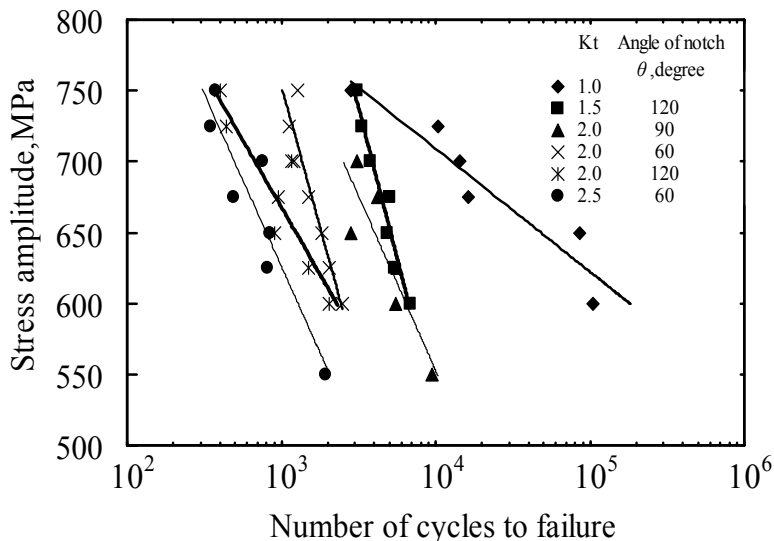


Fig. 21. S-N diagrams of YXR3 steel notched specimens with various stress concentration factor [14].

High cycle fatigue tests were conducted for quenched and tempered YXR3, 0.65 mass % carbon matrix high speed steel. Ultimate tensile strength and Rockwell C scale hardness number of this YXR3 steel was 2192MPa and 60.0, respectively. Plane bar specimen with 6.5mm at minimum diameter and notched round bar specimens with stress concentration factor with 1.5, 2.0 and 2.5 were used. A hydraulic fatigue testing machine (Instron Fast track 8801, 98kN) was used. Frequency was 20Hz and R value was 0.05.

Fig. 23 shows S-N diagrams of YXR3 steel in high cycle regime [18]. In considering about the higher ultimate tensile strength of this steel, fatigue limit of 400MPa at 10^7 cycles is low. This is because of the mean stress effect on fatigue strength of the high speed steel. The similar phenomenon was reported on low cycle fatigue strength of high speed steel, SKH51. The

low cycle fatigue data shown in Fig.21 are again plotted in Fig.23. It is apparent that the same behaviour can be observed both in low cycle and high cycle regime for plane and notched bar specimens of YXR3 steel.

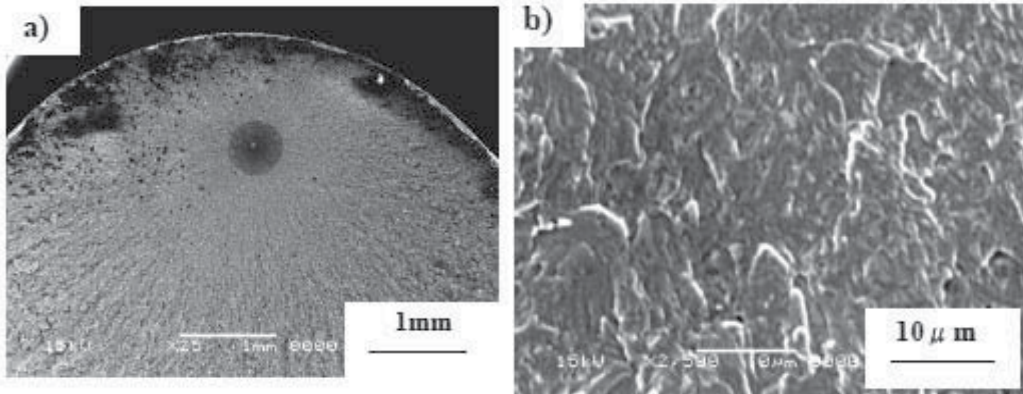


Fig. 22. Fatigue fracture surface of the lapped plane bar specimen heat treated in vacuum[14]. YXR3 steel, 600MPa, 1×10^5 cycles a) initiation area b) propagation area

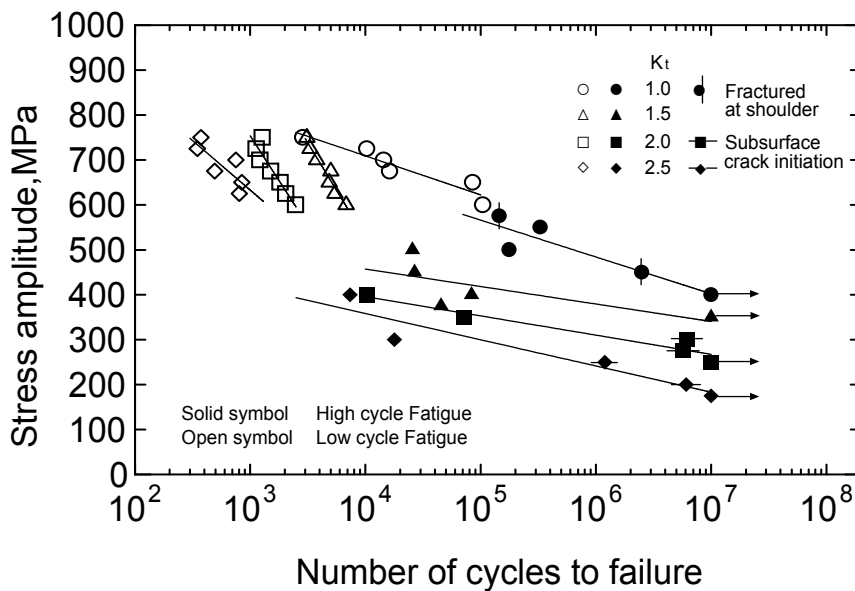


Fig. 23. S-N diagrams of notched specimens, YXR3 steel [18].

In high cycle fatigue for plane bar specimen crack initiated at subsurface as observed on low cycle fatigue fracture surfaces [18]. On the contrary crack initiation site was changed from notched surface to subsurface at failed number of cycles over than 10^6 for all notched specimens with stress concentration factor K_t of 2.0 and 2.5. Fig. 24 a),b) shows the difference of crack initiation site in notched bar specimen with stress concentration factor of 2.0. The emphasis is focused upon the change of crack initiation site in high cycle range over

than 10^6 cycles for the notched specimen in YXR3 steel with high ultimate tensile strength of 2192 MPa. The reason of this phenomenon may be deeply related to the notch sensitivity and fracture toughness of YXR3 steel. Transgranular fracture surfaces were predominant (Fig. 24c, d)) and well defined striation were not observed in crack propagation area for all tested specimens.

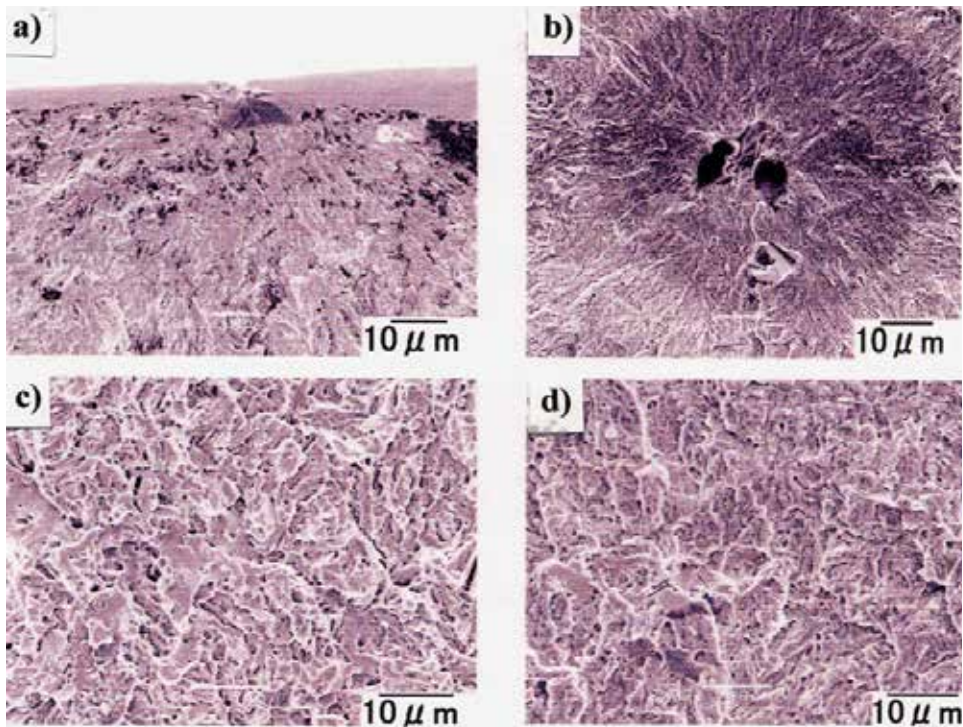


Fig. 24. Fatigue fracture surface of YXR3 steel with $K_t=2.0$ [18]. a),b) crack initiation area,c)0.8mm from initiation,d)0.6mm from initiation a), c) 400MPa, 1×10^4 cycles, b), d) 300MPa, 6.2×10^6 cycles

4. Concluding remarks

In this chapter fatigue and fracture behavior of representative hot and cold forging die steels are summarized. However the information is still limited in materials, design, manufacturing and operations of hot and cold forging dies. In particular the fatigue crack initiation behavior of SKD62 steel is recommended to investigate. Thermal fatigue crack propagation rate is also recommended to obtain in low cycle regime. The fatigue data for other hot forging die steels except SKD62 are fundamentally needed in design of hot forging dies. For quantitative analysis of fatigue fracture surfaces of hot forging dies more information on fracture surface morphologies is absolutely needed in failure analysis. Because of the high hardness the information on fatigue strength and fatigue crack propagation is very limited on cold forging die steels. The low cycle fatigue characteristics of cold forging die steels except SKH51 and YXR3 are recommended to investigate. Fatigue crack propagation rate and fracture surface characteristics of cold forging die steels are recommended to obtain for

failure analysis of cold forging dies. In particular crack initiation mechanism for notched specimens must be clarified. Recent progress of die steel, surface treatment and stress analysis enabled to develop general failure analysis method. Besides cracking problems due to poor wear resistance must be evaluated[19]. Scientific analysis of fracture behavior of forging die steels must be usefully linked to modern technology enabled to prevent hot and cold forging die failure and to extend die life.

5. References

- [1] R. Ebara and K. Kubota, *Journal of the Japan Society for Technology of Plasticity*, 23 (1982), 977-983.
- [2] R. Ebara, *Macro and Microscopic Approach to Fracture*, S. -I. Nishida Ed. WIT Press, 2003, 243-253.
- [3] R. Ebara, K. Takeda, Y. Ishibashi, A. Ogura, Y. Kondo and S. Hamaya, *Engineering Failure Analysis*, 16 (2009), 1968-1976.
- [4] R. Ebara, K. Inoue and K. Kubota, *Journal of the Soc. of Materials Science, Japan*, 29(1980) 599-604.
- [5] R. Ebara, K. Takeda, Y. Ishibashi, A. Ogura, Y. Kondo and S. Hamaya, *Proc. of the ECF17*, 2369-2376, 2008.
- [6] W. G. Spitzig, *Trans. of the ASM*, Vol.61(1961)344-348.
- [7] R. C. Bates and W. G. Clark, *Trans. of the ASM*, Vol. 62(1969)380-388.
- [8] A. J. Brothers et al. *ASTM STP493*, 3-19, 1971.
- [9] R. Ebara, T. Yamane, Y. Yamamoto, H. Yajima, A. Otsuka and S. Nishimura, *Mitsubishi Juko Giho*(in Japanese), Vol. 17 (1980) 344-349.
- [10] R. Ebara, Y. Yamada, T. Yamada and K. Kubota, *Journal of Materials Science, Japan*, 36(1987) 513-19.
- [11] R. Ebara, *International Journal of Fatigue*, 32(2010)830-840.
- [12] H. Nakamura T, Horikawa, *Fatigue strength of metal and application to fatigue strength design*, 2008, Corona publishing Co.
- [13] K. Fujitani S, Okazaki T, Sakai and T. Tanaka, *J Soc Mater Sci. Jpn.*, 30 (1981) 123-127.
- [14] R. Ebara, J. Katayama, S. Yamamoto, R. Ueji, K. Kawamura, A. Ogura, Y. Kondo and S. Hamaya, *Fatigue and Plasticity: From Mechanisms to Design*, Proc. of the 12 th International Spring Meeting; 257-264, 2008, SF2M.
- [15] M. Shinohara et al., *J. Japan Soc for Tech of Plasticity*, 22(1981).159-165.
- [16] H. Kobayash, R. Ebara, A. Ogura, Y. Kondo and S. Hamaya, *Proc. of the fourth Intern. Conf. on Very High Cycle Fatigue*, Allison J. E., J. Jones W, Larsen J. M. and R.O.Ritchie R O, Ed., 319-324, 2007, TMS.
- [17] T. Yamashita, T. Bito, R. Ebara and K. Kubota, *Proc. of the International Conference on Advanced Technology in Experimental Mechanics*, 2007, CDROM, JSME.
- [18] R. Ebara, R. Nohara, R. Ueji, A. Ogura Y. Ishihara and S. Hamaya, *Key Engineering Materials*, 417-418(2010)225-228.
- [19] R. Ebara and K. Kubota, *Engineering Failure Analysis*, 15 (2008)881-893.

Optimization of Injection Moulded Polymer Automotive Components

Ribeiro, C.J.¹ and Viana, J.C.²

¹PIEP – Innovation in Polymer Engineering

²IPC – Institute for Polymers and Composites

Department of Polymer Engineering, University of Minho, Guimarães,
Portugal

1. Introduction

The use of polymer materials in automotive applications is growing steadily in the last decades. Their use present several advantages such as reduced weight, high design flexibility and styling capabilities, good balance of properties (ductility, insulation, no corrosion), superior level of integration of functionalities, low processing costs.

Automotive components (e.g., car interior, exterior and under-the-bonnet applications) are most often being manufactured in thermoplastic polymers by high-throughput processes, like injection moulding. The optimization of injection moulded polymer automotive components is a crucial design task for obtaining high quality, enhanced mechanical response and low cost components. This can be achieved by proper mould design, adequate material processing and by the knowledge of the relationships between the thermo-mechanical environment resulting from processing, the developed material morphology and the moulded component properties. In these activities, the availability of accurate process and in-service behaviour simulations and efficient optimization methods is of paramount importance.

This chapter addresses the application of the engineering design optimization methods and tools to the design of automotive polymer components. It will present several case studies where the optimization of injection moulded polymer automotive components is achieved following different routes and methodologies. Namely:

- a. *Mould cooling system layout optimization* – a proper design of the mould cooling system is crucial for process productivity and part quality improvements.
- b. *Optimization of automotive pillar geometry* – the design of an automotive car pillar is done, optimizing its geometry for maximizing passenger safety (specifically, the minimization of the Head Injury Criteria, HIC).
- c. *Relationships between processing and moulding mechanical properties* – the establishment of these relationships allows the setting of processing conditions for a given property enhancement.
- d. *Design with injection moulded fibre reinforced polymers, FRP* – the design of injection moulded FRP components is a challenging engineering task, where processing effects must be taken into account effectively, either at in terms of using reliable experimental mechanical data and of selecting a pertinent constitutive model.

- e. *Impact behaviour of injection moulded long fibre reinforced thermoplastic, LFT* - the establishment of the relationships between processing and the impact properties of LFT allows the enhancement of the mechanical response of structural automotive applications of these advanced polymers.
- f. *Multi-objective optimization of the mechanical behaviour of injection moulded components* - the simultaneous enhancement of the mechanical response (e.g., stiffness, strength, toughness) of injection moulded components requires a judicious setting of the processing conditions.

In these case studies are proposed several design methodologies for the optimization of injection moulded polymer automotive components, making extensive use and integration of advanced design tools, such as, design of experiments, analysis of variance (ANOVA), injection moulding process simulations, structural simulations and optimization methods.

2. State-of-the-art

Automotive polymer components can be complex products. This high product complexity level leads to high levels of design and manufacturing process complexities. The implementation of advanced approaches to product development procedures in the automotive industry is critical and has been persuaded increasingly driven by the high needs for innovate and optimised products. The design of automotive polymer components and their behaviour optimization are still nowadays plain of complexities and engineering challenges. In this context, the use of computational simulations tools and optimization procedures is becoming of paramount importance on the optimization process of injection moulded polymer automotive components.

In the following are described, for each particular case study, their specific objectives and main relevant works on the topic. All presented case studies aim at the optimization of the mechanical response of injection moulded polymer components based on the intensive use of computational tools.

2.1 Mould cooling system layout optimization

Efficient injection mould design, mainly of the cooling system, is required for improved productivity and manufacturing of high quality polymer products. The cooling phase represents generally more than $\frac{3}{4}$ of the total cycle time. An efficient cooling system design can therefore reduce considerably the cooling time, with significant increments upon the process productivity. The proper design of the cooling system is also crucial in the heat transfer process, with a strong influence on the part properties and quality:

- the cooling process influences markedly the morphology development and the mechanical properties of the moulded articles;
- the cooling process determines the material shrinkage and the development of thermal stresses in the final moulded product;
- a non-uniform cooling process results in part warpage;
- the cooling process affects part aesthetics (e.g., gloss) and the appearance of defects such as sink marks and voids.

The optimised design of the cooling systems of injection moulds has been performed over the last decades. Park and Know (Park, 1998) developed an algorithm to improve the performance of a cooling system by solving the thermal problem by the boundary element

method. They proposed that the optimization with respect to all the design variables (mould cooling system and processing conditions) at the same type is the most appropriate strategy. Process simulation tools are available for simulating all injection moulding cycle (filling, packing and cooling phases). Several cooling systems architectures can therefore be easily explored through simulations. Processing conditions can be optimised. The optimization of the mould cooling system is based normally in two main design objective functions (Park, 1998): a) minimization of the cooling time; and b) temperature uniformity over the part surface. The design variables include: inlet coolant temperature; inlet coolant flow rate; cooling channel diameter; and cooling channel location. Liang (Liang, 2002) uses a one-dimensional cooling analysis combined with the maximization of the heat absorption rate by the coolant per unit area in order to optimise the cooling channel diameter, ϕ , the distance between cooling channels, a , and the distance between the cooling channel and the cavity wall, b . The numerical optimisation method has based on an alternate constraint coordinate method. The optimal performance of the mould cooling system is achieved for $a = b = 2\phi$. Li et al (Li, 2005) proposed the automation of the mould cooling system layout design by formulating a heuristic search process based on fuzzy evaluation of the cooling performance and of the manufacturability of candidate designs. A cooling performance index was defined to estimate of the effectiveness of the cooling circuit in carrying away the heat from the mould. Tang et al (Tang, 2007) used a design of experiments approach, based on the Taguchi method, to assess the effect of processing conditions (melt temperature, filling time, packing pressure and packing time) on the part warpage. Melt temperature is identified as the most effective parameter that should be kept at a low level. Lam et al (Lam, 2004) optimized both cooling system design and process condition simultaneously through an evolutionary algorithm. A genetic algorithm and process simulation code are integrated. The objective was to achieve a uniform cavity surface temperature distribution. Hassan et al (Hassan, 2009) adopted a cyclic transient cooling analysis using a finite volume method to analyse a T-shape polymer part. They investigated the effect of the cooling channels cross-section geometry and their location on the temperature profile along the cavity wall and on the polymer solidification degree, but no optimization routine was adopted. The results show that the cooling rate is improved as the cooling channels take the form of the product. Furthermore, they argued that the cooling system layout that minimise the cooling time does not necessary lead to an optimum temperature distribution on the product.

Recent technological developments proposed conformal cooling as an alternative method for a highly efficient cooling system. In this concept, the cooling channels conforms to the shape of the cavity and core of the mould, providing a better heat transfer and resulting in a lower cycle time and a more uniform cooling (Xu, 2001). The dynamic control of the mould wall temperature has been also proposed as method to improve the process performance by potential increments upon productivity and part quality (Kazmer, 2000).

In this chapter is presented a case study where injection mould filling simulations, design of experiments and ANOVA techniques are integrated to optimise the cooling system of injected mouldings.

2.2 Optimization of automotive pillar geometry

Occupant safety is of paramount importance in the automotive industry due to the increasing of legal requirements and customer demands. (Lin, 2004). Recent standards (e.g., FMVSS-201) impose specific requirements to plastic components used in automotive

interiors, which have to afford impact protection for occupants, namely against head impact (e.g., pillars). The head injury criterion (HIC) is an analytical tool that is currently recognized to determine if the blow to the head exceeds a maximum tolerable threshold that causes severe injury. HIC is an acceleration-profile-based criterion that requires the knowledge of the time history of the magnitude of the linear deceleration of the centre of gravity of the head during impact. HIC defines the severity of impact to the head, being given by:

$$HIC = \sup_{t_1, t_2} \left\{ \left[\frac{1}{t_2 - t_1} \int_{t_1}^{t_2} a(t) dt \right]^{2.5} \times (t_2 - t_1) \right\} \quad (1)$$

where $a(t)$ is the resultant acceleration of the centre of gravity of the head and $(t_2 - t_1)$ is the time interval during the crash where the HIC value is maximised. Its value is determined between two-time points where the acceleration curve gives the maximum value of HIC. The corresponding time interval is considered as unlimited, (HIC), or equivalent to maxima of 36 ms (HIC36) or 15 ms (HIC15). In order to consider only the free motion head-form (FMH) during the simulation process, the HIC value needs to be converted to a dummy equivalent value HIC(d), expressed as:

$$HIC(d) = 166.4 + 0.75466 \times HIC \quad (2)$$

The National High Traffic Systems Authority, NHTSA, specifies that, in automotive interiors, the HIC(d) of the FMH should not exceed 1000, to be recognized as providing head impact protection under FMVSS-201. (FMVSS-201, 2007) (Gholami, 2002). The design criteria requires further a deceleration lower than 180 g's ($1 \text{ g} = 9.81 \text{ m.s}^{-2}$) in order to avoid severe occupant head injuries. The plastic components are therefore required to act as passive safety components. (FMVSS-201, 1997).

The design of polymeric parts against impact loadings is determined mainly by the high interactions between the polymer behaviour and the component geometry (Viana, 2006). T. Gholami et al. investigated the response of energy absorbing polymeric egg-box like structures under an impact loading by conducting head impact simulations (Gholami, 2002). The behaviour of these structures under a range of conditions was also analysed and compared with other commonly available solutions for energy absorption by M. Ashmead et al. (Ashmead, 1998). M. Zerull et al. designed interior ribbed plastic components in order to meet FMVSS-201 standard requirements (Zerrul, 2000).

In this work, the impact of an anthropomorphic mass in a polymeric pillar is simulated in a finite element code (ABAQUS) (Ribeiro, 2006). Several pillar geometries and material parameters are tested using numerical simulations in order to meet the standards' requirements.

2.3 Relationships between processing and moulding mechanical properties

The mechanical properties of moulded polymers are extremely dependent upon the processing method and conditions used to produce them. The processing thermomechanical conditions imposed to the melt governs the morphology development that affects the mechanical response of the moulded product. An injection moulded semicrystalline polymeric component shows a laminated morphology, featuring a very oriented skin layer and a highly crystalline core. A thicker skin layer results in a high stiffness, strength and

enhanced impact response (Viana, 1999; Cunha, 1995). A high degree of crystallinity results in a higher stiffness, but it is generally detrimental for the capability of the material to absorb energy in very short time intervals (van der Wal, 1998). A high level of molecular orientation is also beneficial in terms of impact strength, but it reduces the deformation capabilities of the mouldings (Viana, 1999; Cunha, 1995).

The prediction of the morphology development of injection moulding has been revealed as an extremely hard task, mainly for semi-crystalline polymers. The current commercially available software codes do not compute polymer morphology, and therefore do not estimate the mechanical response of the moulded product. Methodologies to link process to mechanical simulations in the design workflow of automotive components are still under development (Wust, 2009).

In order to be able of predicting the mechanical properties of injection moulded components a methodology based on thermomechanical indices has been proposed. These thermomechanical indices relate to main physical phenomena involved and aim at evaluating the morphology development (Cunha, 2000; Viana 2002):

- the cooling index, Y , characterises the thermal level of the moulding, being related to the degree of crystallinity of the mouldings. It is defined as the ratio between the superheating degree and the cooling difference:

$$Y = \frac{T_b - T_c}{T_b - T_i} \quad (3)$$

where T_b is the bulk temperature (the local average temperature through the moulding thickness), T_c the crystallization temperature, and T_i is the mould/polymer interface temperature.

- the thermo-stress index, τ_Y , is the ratio between the level of molecular orientation imposed during mould filling (indirectly assessed by the shear stress at the solid/liquid polymer interface, τ_w) and the level of molecular relaxation occurring during cooling (assumed proportional to Y), being defined as:

$$\tau_Y = \frac{\tau_w}{Y} \quad (4)$$

Thermomechanical indices are easily computed by mould filling simulations over the entire spatial domain of the component. They have been proposed as a promising route to establishing the relationships between processing and the moulding mechanical properties, supporting engineering design methodologies with polymers. In this chapter are established the relationships between the thermomechanical indices and the impact properties for an injection moulded disc geometry.

2.4 Design with injection moulded fibre reinforced polymers, FRP

The demand from industry for injection moulded polymeric parts is increasing due to the capability of high-volume production, suitable material properties, high geometrical freedom of design and function integration, and reduced costs. The mechanical and physical properties of these moulded parts can be improved by the use of short fibre reinforced polymers, SFRP (Luts et al, 2009). Polymeric structural components can be produced with

SFRP. The design with these polymers is an intricate task because the polymer mechanical behaviour is difficult to characterise (e.g., impact) or to simulate (e.g., constitutive model). Furthermore, the effects of processing conditions (e.g., fibre orientation profiles) on the mechanical response need to be considered. As mechanical properties of SRFP injected parts depend upon fibre orientation, there is a big interest in validating and improving models which link the fibre orientations to mechanical properties (Vincent et al, 2005).

In order to better design with FRP, this work shows a comparison between several constitutive models (linear, non-linear, isotropic, non-isotropic) in the structural simulations of an injection moulded FRP component. The computed behaviour was compared against experimental one. Different gating options were considered.

2.5 Impact behaviour of injection moulded long fibre reinforced thermoplastic, LFT

Long fibre thermoplastics, LFT, are increasingly been used in load-bearing polymeric components due to their excellent properties (e.g., specific mechanical properties, impact resistance, corrosion resistance and design flexibility) and easy of process (e.g., complex shapes, function integration) (Jacobs, 2002). The mechanical properties of LFT are highly dependent upon the fibre content, the fibre orientation and length, the fibre-matrix interface and matrix morphology. The most influencing variable is much determined by the fibre content level: for high amount of fibres (typically of more that 10-15% of incorporation) the fibre orientation and length are the most relevant variables for the mechanical response; for low levels of incorporation (less than 10-15%) the matrix morphology becomes also a relevant variable. All the abovementioned variables are determined by the processing thermo-mechanical history (Krasteva, 2006).

The complex relationships between the processing conditions and the mechanical properties complicate the control of final composite part properties: accuracy, point-to-point variations, high levels of anisotropy, etc. (Constable, 2002; Schijve, 2002). The prediction of the mechanical properties of moulded LFTs is an intricate task. Currently, computer simulations of the injection moulding process are able of computing the mechanical properties of fibre reinforced polymers. The calculations are based on the prediction of fibre orientation and on a micromechanical constitutive model. Elastic modulus and coefficient of thermal expansion are locally computed through the moulding thickness and over its spatial domain. However, and mainly for LFTs, the effect of fibre attrition during processing becomes an important factor. Currently, commercial processing simulations codes are not able of predicting fibre breakage during injection moulding.

In this chapter are established the relationships between the thermomechanical indices and the mechanical properties of an injection moulded LFTs. This methodology is revealed as a very interesting engineering approach to assess the mechanical properties of injection moulded LFTs.

2.6 Multi-objective optimization of the mechanical behaviour of injection moulded components

At present, the maximization of the mechanical properties of injection moulded components is done by tentative trial-and-errors or by the adoption of structured statistical techniques procedures (e.g., structured design of experiments) (Yang, 2007; Chen, 2009). The processing conditions are varied in order to achieve the best mechanical performance. However, different envisaged mechanical responses (e.g., stiffness and toughness) may require distinct

sets of processing conditions (Viana, 1999). Using similar methodologies, the maximization of the mechanical properties of injection moulded components can be performed also by computer simulations. The simulations allow the computation of the thermal and mechanical fields imposed to the polymer during processing, letting the calculation of thermomechanical indices that can be used to estimate the mechanical properties of the moulded component (Viana, 1999; Viana, 2002). These latter can be maximized by variation of the processing conditions, changes upon the part geometry, exploitation of different gating and cooling system options. Nevertheless, the absence of a global computer optimization methodology for maximization of the mechanical properties of injection moulded parts is evident. In fact, from an engineering design point of view, there still exists a hiatus between process simulation/optimization and mechanical simulation/optimization (Wust, 2009) that needs to be fulfilled.

Several works of process optimization using different optimization strategies, such as, Artificial Neural Networks (ANN) and Genetic Algorithms (GA) have been reported. Lotti and Bretas (Lotti, 2003; Lotti, 2007) applied ANN to predict the morphology and the mechanical properties of an injection moulded part of different polymer systems as a function of the processing conditions (mould and melt temperatures and flow rate). Castro et al (Castro, 2003; Castro, 2007) combined process simulations, statistical testing, artificial neural networks (ANNs) and data envelopment analysis (DEA) to find the optimal compromises between multiple objectives on the settings of the injection moulding processing conditions.

Turng and Peic (Turng, 2003) developed an integrated computer tool that couples a process simulation code with optimization algorithms to determine the optimal process variables for injection moulding. Latter, Zhou and Turng (Zhou, 2007) proposed novel optimization procedure based on a Gaussian process surrogate modelling approach and design of experiments applied to computer simulation for the optimization of the injection moulding process. The global optimal solutions were found based on a hybrid genetic algorithm. In both cases, only warpage and shrinkage of moulded components was minimised. Gaspar-Cunha and Viana (Gaspar-Cunha, 2005) coupled an optimization method based on evolutionary algorithms with process simulation code to set the processing conditions that maximise the mechanical properties of injection moulded components, More recently Fernandes et al. (Fernandes, 2010) used a similar approach to adjust the processing conditions in order to meet multiple process criteria (temperature difference on the moulding at the end of filling, the maximum cavity pressure, the pressure work, the volumetric shrinkage and the cycle time).

In this chapter an automatic optimization methodology based on Multi-Objective Evolutionary Algorithms, MOEA, is used to optimize the mechanical behaviour of injection moulded components (Gaspar-Cunha, 2005). The thermomechanical indices are computed from mould filling simulations and related to the mechanical properties, the processing conditions being optimized in order to reach the best mechanical performance.

3. Presentation of case studies

3.1 Mould Cooling System Layout Optimization

A computer simulation study was performed adopting a design of experiments approach based on the Taguchi method for the analyses of the influence of the mould cooling system design variables on the uniformity of moulding surface temperatures and on the shrinkage and warpage of the moulding (Viana, 2008).

The moulded part is a centred gated rectangular box with 150 mm of length, 72 mm wide, 16 mm of lateral height and 1.5 mm of thickness. The injection moulding simulations were performed in Moldflow software using cooling-warping analysis. The polymer is a polypropylene, PP, Appryl 3120 MU5 from ATOFINA (with properties from Moldflow database). The geometrical cooling system design factors selected were (Fig. 1): cooling channel diameter, ϕ [8, 12 mm]; distance between cooling channels centres, a [10, 14 mm]; distance between the cooling channels and mould cavity surface, b [20, 25 mm]; orientation of the cooling channels [horizontal (X-direction), vertical (Y-direction)]; symmetry of cooling channels [sym., non-sym.]; cooling channels length, L [10, 20 mm]; number of cooling channels [4, 6]. All these factors were varied in two levels according to the DOE orthogonal matrix (L8 Taguchi array) presented in Figure 1.

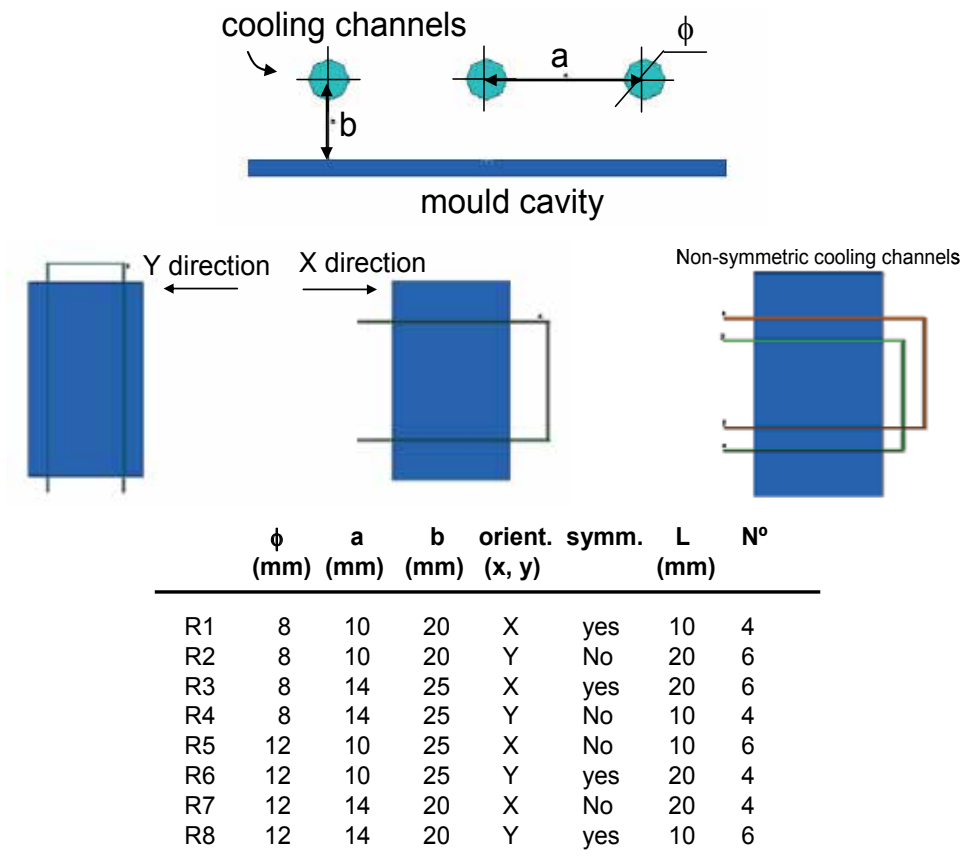


Fig. 1. Cooling system design parameters.

The other processing parameters were kept constant (melt temperature of 240 °C, mould temperature of 50 °C, injection flow rate of 43 cm³/s corresponding to an injection time of 0.64 s). Figure 2 shows the eight simulation models built, and respective changed design parameters. The results envisaged were: a) the maximum and minimum temperature in the part, T_{max} and T_{min} , respectively; b) the difference between these temperatures, $\Delta T = T_{max} -$

T_{min} ; c) the volumetric shrinkage (average of the values measured at the four box corners), S ; and d) the local deflection at the box corners (average of the four corners), δ . This case study identifies the most relevant cooling system design factors, their percentage of contribution, the set of factors minimising the selected responses, and highlights the importance and potential of mould filling simulations on the optimization of the injection moulding process.



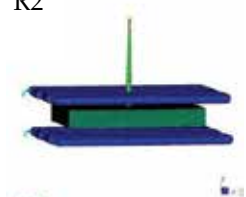
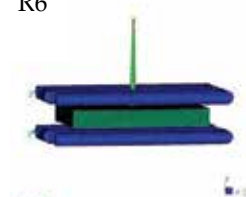


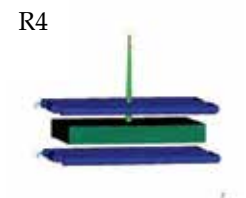
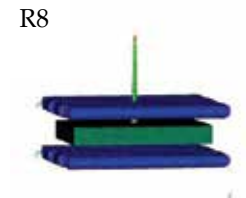
Moldflow model	Design parameters	Moldflow model	Design parameters
R1 	$\phi = 8$ mm $a = 10$ mm $b = 20$ mm orientation = X dir. symmetric channels $L = 10$ mm no. channels = 4	R5 	$\phi = 12$ mm $a = 10$ mm $b = 25$ mm orientation = X dir. non-sym. channels $L = 10$ mm no. channels = 6
R2 	$\phi = 8$ mm $a = 10$ mm $b = 20$ mm orientation = Y dir. non-sym. channels $L = 20$ mm no. channels = 6	R6 	$\phi = 12$ mm $a = 10$ mm $b = 25$ mm orientation = Y dir. symmetric channels $L = 20$ mm no. channels = 4
R3 	$\phi = 8$ mm $a = 14$ mm $b = 25$ mm orientation = X dir. symmetric channels $L = 20$ mm no. channels = 6	R7 	$\phi = 12$ mm $a = 14$ mm $b = 20$ mm orientation = X dir. non-sym. channels $L = 20$ mm no. channels = 4
R4 	$\phi = 8$ mm $a = 14$ mm $b = 25$ mm orientation = Y dir. non-sym. channels $L = 10$ mm no. channels = 4	R8 	$\phi = 12$ mm $a = 14$ mm $b = 20$ mm orientation = Y dir. symmetric channels $L = 10$ mm no. channels = 6

Fig. 2. Simulations with different cooling system design parameters.

3.2 Impact behaviour of injection moulded automotive components

In this work, the impact of an anthropomorphic mass with a given mass and velocity in a plastic pillar cover (Figure 3) is simulated by a finite element code ABAQUS/Explicit. The objective was to achieve optimized pillar geometry meeting the requirements of FMVSS-201 standards. The meshes of the pillar and chassis were generated with the ABAQUS mesh module being comprised of 3D linear tetrahedric elements (C3D4 elements). A mesh size of

1 mm was used. The impactor was modelled as a non-deformable rigid part (with no material data associated) having a diameter of 165 mm and a mass of 4.54 kg, according to the FMVSS-201 standard. An initial velocity of 6 m.s⁻¹ was imposed to the impactor that moves normal to the pillar surface (Ribeiro, 2005).

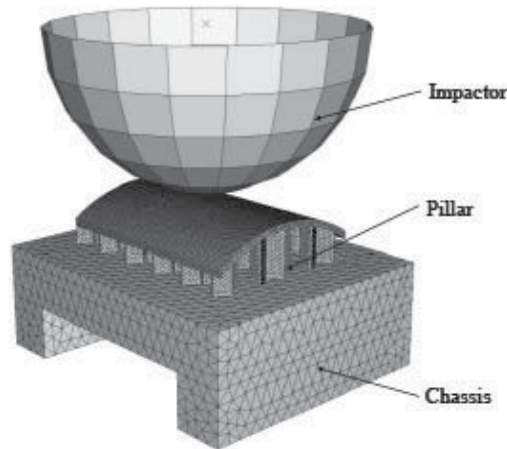


Fig. 3. Finite element model for pillar-A impact simulation.

The contact between the three bodies was considered in the simulations. In a contact problem multiple structural bodies interact. These interactions result in stiffness variations and, hence, the problem changes continuously throughout the simulation, and an iterative approach is required for converge to the final solution. The contact behaviour between the impactor and the pillar and between the pillar and the chassis was defined to be rough (perfect adhesion). Later, a Coulomb contact was assumed.

The polymer properties were obtained at high strain-rates, being listed in Table 1 (Viana, 1999). An elasto-plastic constitutive model was used to model polymer mechanical behaviour and a linear-elastic model to model the steel chassis.

Property	Pillar polymer	Chassis steel
Elastic modulus, E (GPa)	2 GPa	200 GPa
Yield stress, σ_Y (MPa)	55 MPa	-
Poisson coefficient, ν	0.35	0.32
Density, ρ (kg.m ⁻³)	908	7280

Table 1. Material properties for polymer and steel materials.

Several pillar geometries (e.g., ribs geometry and height) and materials parameters (e.g., Young modulus, yield stress, stress at break and strain at break) were evaluated using numerical simulations.

- **Effect of ribs geometry**

Three different geometries of the ribbed pillar were tested as shown in Fig. 4. In the ROD geometry (Fig. 4.1) the ribs have a cylindrical shape, being inter-connected. Fig. 4.2 shows the HEX geometry where the ribs have a hexagonal form. Finally, a special geometry was developed: the GAV geometry (Fig. 4.3) that is composed of three interconnected rectangular ribs in a common centre at an angle of 120° (triplet rib).

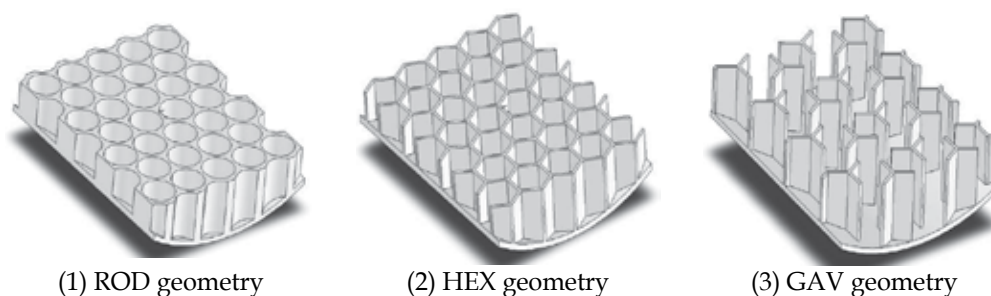


Fig. 4. Geometries for testing the pillar geometry effect.

- **Effect of Ribs Height**

The rib height is an important geometric parameter of the pillar, as it limits the deceleration distance controlling therefore the impact time. Different rib heights were used in simulations: 17.5, 22 and 25 mm. The simulations were performed with an optimised GAV geometry (Fig. 5) and an impactor mass of 6.4 kg (as enforced by the more recent FMVSS-201 standard requirements).

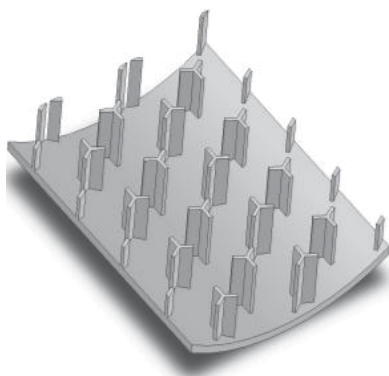


Fig. 5. Geometry (optimised GAV) used to test the ribs height influence.

- **Effect of Materials Properties**

The geometry for this study was similar to the presented in Figure 5. The definition of this optimised GAV geometry was based in previous work performed (Ribeiro, 2006) (and it was patented EP1 712 428A1). This geometry (ribs shape, ribs height and thickness, the space between ribs and ribs fillet radius) was optimized making extensive use of FEM simulations and a design of experiments (DOE) approach. In this case a complete pillar was considered, as show in Fig. 6.

The pillar, chassis and impactor meshes were generated in ABAQUS. Details are shown in Table 2.

	Element type	Element shape	Geometric order	Mesh size	N°. elements
Pillar	C3D4	Tetrahedral	Linear	1 mm	193376
Chassis	C3D8R	Brick	Linear	10 mm	1200
Impactor	R3D4	Rigid quadrilateral	Linear	-	536

Table 2. Mesh details for pillar, chassis and impactor.

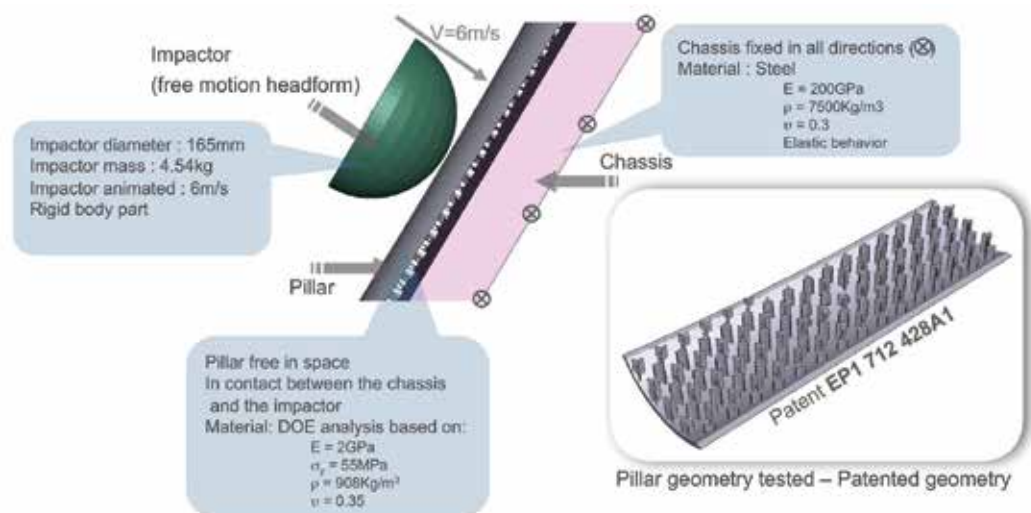


Fig. 6. Model used to verify the materials properties influence.

The impactor has a diameter of 165 mm, a mass of 4.54 kg and is animated with a velocity of 6 m.s⁻¹, as imposed by FMVSS-201 standard. The impactor moves restrained in the vertical in the pillar direction (Ribeiro, 2007).

The large strain and non-linear behaviour of the material was described by an isotropic elasto-plastic model, whose parameters were obtained elsewhere (Viana, 1999). This model considers an initial linear-elastic response characterised by two materials parameters (the Young's modulus, E , and the Poisson's ratio, ν). The non-linear part of the stress-strain curve is attributed to plastic deformation and occurs at a stress level regarded as the first yield stress (Fremgen, 2005). The reference properties of the polypropylene copolymer used are listed in Table 1.

The materials properties were modified in order to verify their effects on the pillar impact performance, according to a DOE based in a Taguchi orthogonal array (Table 3). Each material parameter was varied in two levels (maximum and minimum values).

	E_1 (MPa)	σ_y (MPa)	σ_b (MPa)	ϵ_b (mm/mm)
V1	1000 (1)	27.5 (1)	55 (1)	0.5 (1)
V2	1000 (1)	27.5 (1)	55 (1)	1 (2)
V3	1000 (1)	55 (2)	75 (2)	0.5 (1)
V4	1000 (1)	55 (2)	75 (2)	1 (2)
V5	2000 (2)	27.5 (1)	75 (2)	0.5 (1)
V6	2000 (2)	27.5 (1)	75 (2)	1 (2)
V7	2000 (2)	55 (2)	55 (1)	0.5 (1)
V8	2000 (2)	55 (2)	55 (1)	1 (2)

Table 3. Design of Experiments (L8 table Taguchi) for investigating the effect of materials properties on the impact response of the pillar (coded values between parentheses).

The results envisaged from the simulations were the computed force-displacement curves. From these, the maximum acceleration and HIC(d) values were calculated and served as outputs for the ANOVA of the data.

3.3 Relationships between processing and moulding mechanical properties

This case study investigates the relationships between the processing thermomechanical environment, the developed morphology upon processing and the impact properties of injection moulded parts (Viana, 2009). This is done by the establishment of the relationships between two thermomechanical indices and the impact properties.

The specimen is a lateral gated disc of 150 mm of diameter and 1.5 mm of thickness, injection moulded in PP copolymer. Several discs were injection moulded with variations of the injection flow rate, Q_{inj} , the melt temperature, T_{inj} , and the mould temperature, T_w , in a total of 15 different processing conditions. The thermomechanical indices, Y and τ_Y , were computed at the end of the filling phase using C-Mold software. The impact properties were assessed in an instrumented multiaxial plate deflection test, at 1 m/s and 23 °C. The discs are clamped around a perimeter of 40 mm. The non-lubricated 25 kg striker has a hemispherical tip with a diameter of 10 mm. The envisaged impact properties are the peak force and energy, F_p and U_p , respectively, that were measured from the recorded force-deflection curves.

3.4 Mechanical behaviour of injection moulded FRP

Figure 7 depicts the geometry of this case study: an airbag housing. The simulations were performed with an implicit FEM code. A vertical displacement was imposed to the jig at 500 mm/min. The upwards movement of the jig promotes a tensile load in the polymeric part, whereas the downwards motion applies a compressive loading. Experimental tests of the two setups were performed and compared with the simulation results.

The finite element mesh of the part was created based on tetraedrical elements, with quadratic formulation (10 nodes per element). The number of elements was, approximately, 50.000 for the total model. The jig was screwed on the airbag housing. The polymeric material for the airbag housing was a polyamide with 40% glass fibre (PA GF40).

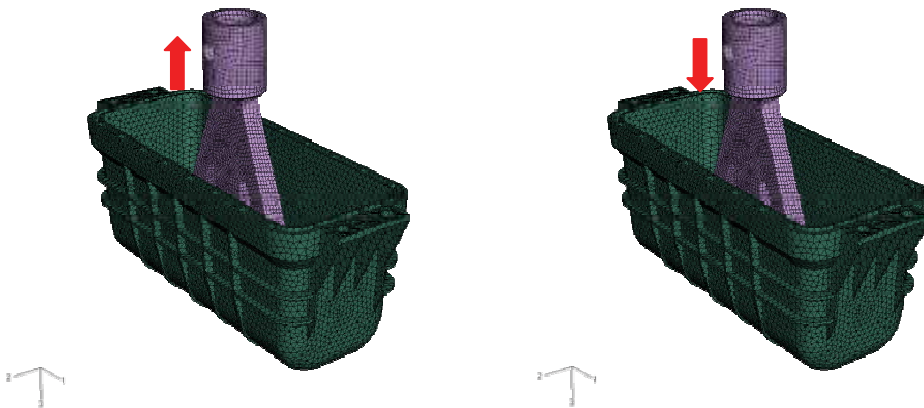


Fig. 7. Tensile (left) and compression (right) loads.

The influence of fibre orientation on the mechanical response of the PA GF49 was considered on the constitutive law using the results from Moldflow simulations. Figure 8 shows a typical profile of fibre orientation through the moulding thickness. A skin-core structure can be assumed, where the skin features a high level of fibre orientation in the flow direction, FD, and the core shows mostly fibre orientation transverse to FD. Based on the data of Fig. 8, it was assumed that the skin has a thickness of 70% (percentage of material

with a high fibre orientation in FD) of the overall thickness, and the core the remained 30% (percentage of material with a fibre orientation transverse to FD). These percentages were later used to weight the through-the-thickness distribution of fibre orientation on the mechanical response of the moulded component.

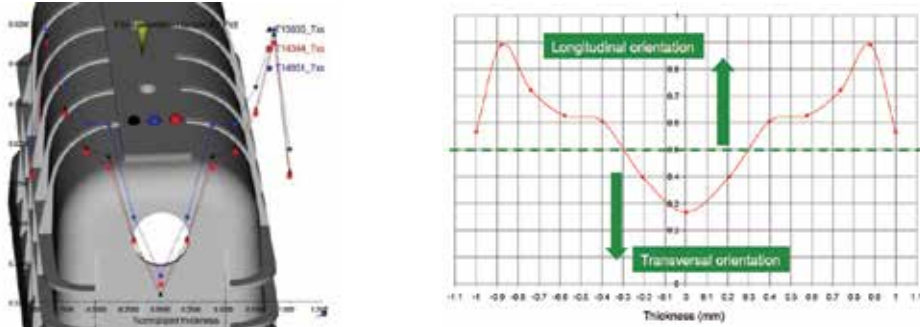


Fig. 8. Distribution of fibre orientation through the thickness on the injection moulded component: (left) profiles at three different location in the component (in different colours); and (right) typical profile showing the assumed skin-core structure.

The mechanical behaviour of the PA GF40 was assumed as anisotropic. Fig. 9 presents the mechanical response in the longitudinal (fibre direction) and transverse directions, given by material supplier. It was assumed that for fibre orientation values higher than 0.5 (see Fig. 8-right), the mechanical behaviour is represented by the longitudinal curve (Fig. 9) and for values lower than 0.5, the mechanical response is defined by the transversal curve. The respective influence of the skin-core structure on the global mechanical response of the material was assumed to be according to the abovementioned percentage weights, i.e., the contribution of the longitudinal curve was 70% (skin) and of the transversal curve of 30% (core). The red line on Fig. 9 represents the considered mechanical behaviour of PA GF40, assuming the skin-core effect.

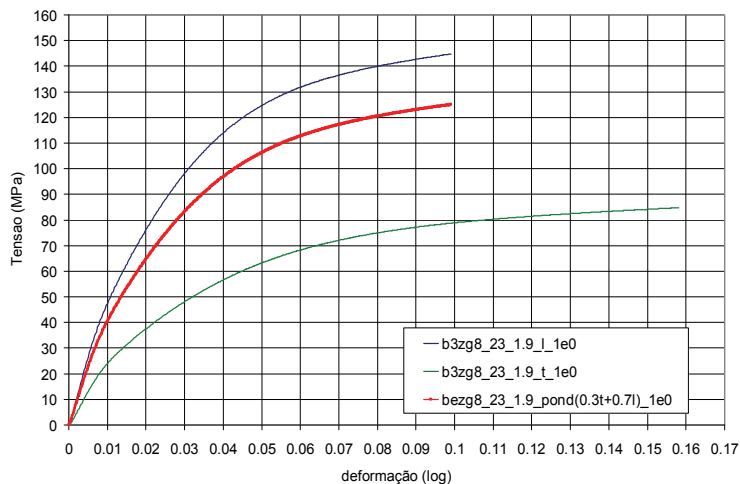


Fig. 9. Stress-strain curves of PA GF40 in the fibre (blue) and transverse (green) directions; and respective skin-core weighted curve (in red).

Several constitutive laws were used to characterize the material behaviour in the computational simulations. Namely:

- **Isotropic non-linear with longitudinal curve - tangent elastic modulus at 1% elongation**

Young modulus = 4700 MPa

Poisson coefficient = 0.4

Yield stress (MPa)	Strain (mm/mm)
62	0
115	0.019
145	0.072

- **Isotropic non-linear with Moldflow results - tangent elastic modulus at 1% elongation**

Young modulus = 4000 MPa

Poisson coefficient = 0.4

Yield stress (MPa)	Strain (mm/mm)
53	0
98	0.019
125	0.072

- **Orthotropic linear (using three different Young modulus to define the material behaviour in each orientation direction)**

E1 = 4700 MPa; E2 = 2387 MPa; E3 = 2387 MPa

Nu12 = 0.403; Nu13=Nu23 = 0.459

G12=G13=G23 = 2841 MPa

- **Orthotropic non-linear (the nonlinearity is given by the Hill's Potential).**

A 3-D plastic potential function was used to describe the nonlinear behaviour of anisotropic fibre composites, following classical plasticity theory.

$$f(\sigma) = \sqrt{F(\sigma_{22} - \sigma_{33})^2 + G(\sigma_{33} - \sigma_{11})^2 + H(\sigma_{11} - \sigma_{22})^2 + 2L(\sigma_{23})^2 + 2M(\sigma_{31})^2 + 2N(\sigma_{12})^2} \quad (5)$$

where F, G, H, L, M, N are constants that have to be determined experimentally and σ_{ij} are the stresses. The quadratic Hill yield criterion depends only on the deviatoric stresses and it is pressure independent. It predicts the same yield stress in tension and in compression:

$$\begin{aligned} F &= \frac{(\sigma^0)^2}{2} \left(\frac{1}{\sigma_{22}^2} + \frac{1}{\sigma_{33}^2} - \frac{1}{\sigma_{11}^2} \right) = \frac{1}{2} \left(\frac{1}{R_{22}^2} + \frac{1}{R_{33}^2} - \frac{1}{R_{11}^2} \right) \\ G &= \frac{(\sigma^0)^2}{2} \left(\frac{1}{\sigma_{33}^2} + \frac{1}{\sigma_{11}^2} - \frac{1}{\sigma_{22}^2} \right) = \frac{1}{2} \left(\frac{1}{R_{33}^2} + \frac{1}{R_{11}^2} - \frac{1}{R_{22}^2} \right) \\ H &= \frac{(\sigma^0)^2}{2} \left(\frac{1}{\sigma_{11}^2} + \frac{1}{\sigma_{22}^2} - \frac{1}{\sigma_{33}^2} \right) = \frac{1}{2} \left(\frac{1}{R_{11}^2} + \frac{1}{R_{22}^2} - \frac{1}{R_{33}^2} \right) \\ L &= \frac{3}{2} \left(\frac{\tau^0}{\sigma_{23}} \right)^2 = \frac{3}{2R_{23}^2} \\ M &= \frac{3}{2} \left(\frac{\tau^0}{\sigma_{13}} \right)^2 = \frac{3}{2R_{13}^2} \\ N &= \frac{3}{2} \left(\frac{\tau^0}{\sigma_{12}} \right)^2 = \frac{3}{2R_{12}^2} \end{aligned} \quad (6)$$

where each $\bar{\sigma}_{ij}$ is the measured yield stress values when σ_{ij} is applied as the only nonzero stress component; σ^0 is the user-defined reference yield stress; R_{11} , R_{22} , R_{33} , R_{12} , R_{13} , and R_{23} are anisotropic yield stress ratios; and $\tau^0 = \sigma^0 / \sqrt{3}$. The six yield stress ratios are defined as follows:

$$R_{11} = \frac{\bar{\sigma}_{11}}{\sigma^0}; R_{22} = \frac{\bar{\sigma}_{22}}{\sigma^0}; R_{33} = \frac{\bar{\sigma}_{33}}{\sigma^0}; R_{12} = \frac{\bar{\sigma}_{12}}{\tau^0}; R_{13} = \frac{\bar{\sigma}_{13}}{\tau^0}; R_{23} = \frac{\bar{\sigma}_{23}}{\tau^0} \quad (7)$$

The values for the non-linear orthotropic constitutive model were:

$E1 = 4700 \text{ MPa}$; $E2 = 2387 \text{ MPa}$; $E3 = 2387 \text{ MPa}$

$\text{Nu}12 = 0.403$; $\text{Nu}13 = \text{Nu}23 = 0.459$

$G12 = G13 = G23 = 2841 \text{ MPa}$

$R11 = 1$; $R22 = 0.546$; $R33 = 0.546$; $R12 = 1.73$; $R13 = 0.946$; $R23 = 0.946$

The main goal of this study was to select the best constitutive model describing the (anisotropic) mechanical behaviour of injection moulded components.

3.5 Impact behaviour of injection moulded LFT

This case study aims at relating the thermomechanical indices with the impact performance of injection moulded LFTs. For this purpose, rectangular plates have been injection moulded (fixed moulding conditions) and mechanically characterised at different locations. The impact properties were then related with the local thermomechanical indices computed from process simulations (van Hattum, 2004). The material used is a PP reinforced with 30 wt% of long glass fibres, with nominal initial fibre length of 12 mm. The material was processed by injection moulding in rectangular plates with dimension of 200x100x3 mm. These plates were gated centrally. The processing conditions were kept constant during processing: melt temperature of 250 °C; mould temperature of 50 °C; injection flow rate of 8.5 cm³/s; material packing pressure of 650 MPa; cooling time of 30 s; and zero back-pressure (to reduce fibre breakage). From these plates, un-notched impact bars were cut at different locations in the plate and in orthogonal directions, as shown in Fig. 10. The process

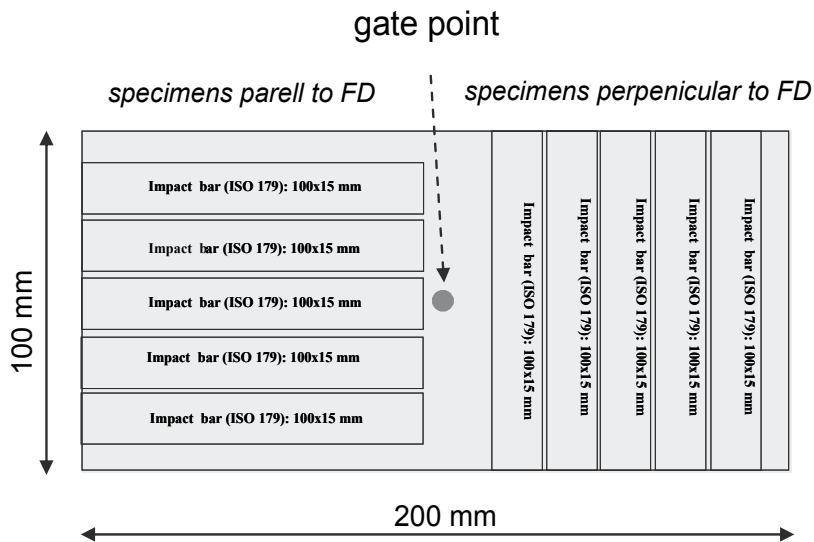


Fig. 10. Moulded plate and specimen location.

simulations were performed using CMOLD software, allowing the computation at the end of filling stage of the cooling index, the wall shear stress, τ_w , and frozen layer ratio, S_a . These variables were calculated at the locations where the impact tests were performed (middle of the impact bar).

The un-notched impact bars of 15x100 mm were tested in an instrumented falling weight impact test machine, Rosand IFWIM type 5, at controlled room temperature (23 °C), according to ISO179 standard. The support span was of 40 mm and the test velocity of 2 m/s. The line striker was lubricated with oil. From the recorded, Force-displacement, F-d, curve, the following values were measured: peak force, and energy, F_p and U_p , and total energy, U_t .

3.6 Multi-objective optimization of the mechanical behaviour of injection moulded components

This case study proposes an automatic optimization methodology based on Multi-Objective Evolutionary Algorithms to optimize the mechanical behaviour of injection moulded components (Gaspar-Cunha, 2005). The moulded part is an axi-symmetric (circular cross-section) tensile specimen moulding of 1.5 mm diameter and 20 mm and 60 mm of reference (circular cross-section) and total length, respectively (Fig. 11). The polymer is a propylene copolymer (APPRYL3120MR5). Tensile specimens were injection moulded with different processing conditions, consisting in variations of Q_{inj} , T_{inj} and T_w . The thermomechanical indices were computed at the end of the filling phase using C-Mold software. The tensile-impact mechanical properties were assessed at a velocity of 3 m/s (corresponding to a nominal strain-rate of $1.50 \times 10^2 \text{ s}^{-1}$).

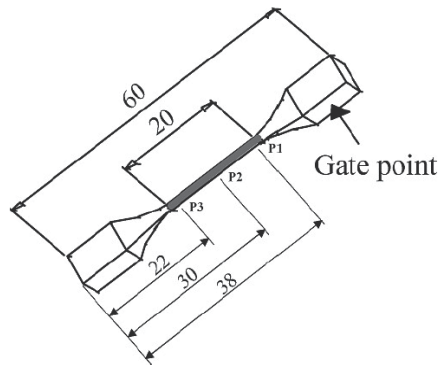


Fig. 11. Geometry of the moulded part.

The relationships between the thermomechanical indices and the mechanical properties were fitted by polynomial approximations, namely (Viana, 1997):

$$\begin{aligned}
 E &= 2.914 - 0.053 ((1-S_a).Y)^{-1} + 6.334 (S_a.\tau_Y) && \text{(in GPa)} \\
 \sigma_y &= 44.34 - 1.41 ((1-S_a).Y)^{-1} + 60.29 (S_a.\tau_Y)^{0.5} && \text{(in MPa)} \\
 \varepsilon_b &= -0.097 - 0.065 \ln ((1-S_a).Y) - 0.109 \ln (S_a.\tau_Y) && \text{(in mm/mm)}
 \end{aligned} \tag{3}$$

The methodology for the optimization of operating conditions of the injection moulding process is presented in Fig. 12. The operating conditions to be optimized and the corresponding range of variation are defined. The MOEA defines the solutions to be

evaluated and passes this information to the simulation routine that evaluates these solutions in terms of the considered criteria and delivers this information to the MOEA. This process is repeated until a stop criterion is reached. At the end the optimal results are shown through a Pareto frontier. Details on MOEA can be found elsewhere (Gaspar-Cunha, 2005; Fernandes, 2010). Several optimization runs were carried out, aiming at optimizing the thermomechanical indices and the mechanical properties. Here, only the optimization of the high strain-rate properties will be considered (using equations 3): the initial modulus, E_2 , the yield stress, σ_{y2} , and the strain at break, ϵ_{b2} , were optimized simultaneously.

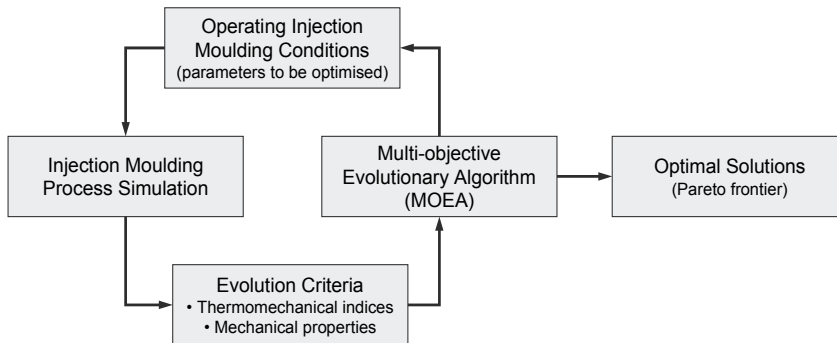


Fig. 12. Operating conditions optimization methodology.

4. Results

4.1 Mould cooling system layout optimization

Previous results shown that, for this moulding geometry and polymer, the selected design factors have a small contribution on the variations of the part cooling time, which varied only 4.3 % (Viana, 2008). Their effect on the volumetric shrinkage, S , and maximum deflection at the box lateral edges, δ , is also small (Table 4). However, they have a stronger effect on the maximum and minimum temperatures on part surface, T_{\max} and T_{\min} respectively, and in their difference, $\Delta T = T_{\max} - T_{\min}$, and may affect the warpage of the moulded part (which investigation is out of the scope of the present work). These results are presented in Table 4 (see Fig. 1 and 2 for identification of runs).

Run	T_{\max} (°C)	T_{\min} (°C)	ΔT (°C)	S (%)	δ (mm)
R1	47.4	32.9	14.4	6.04	0.697
R2	40.9	31.1	9.8	6.10	0.677
R3	43.0	32.5	10.5	6.20	0.684
R4	43.0	32.6	10.4	6.16	0.683
R5	41.3	30.2	11.1	6.15	0.679
R6	40.5	30.5	10.1	6.09	0.677
R7	46.6	31.8	14.8	6.06	0.693
R8	41.5	31.4	10.1	6.10	0.678
var (%)	16.9	9.0	50.7	3.6	3.0

Table 4. Results of the flow-cooling analysis simulations.

The maximum temperature in the part changes almost 17% and the minimum temperature by 9% due to variations on the cooling system design factors. The difference between both these temperatures has the highest variation with an effect of almost 51%. Fig. 13 shows the contour plots of temperature distribution in the part for runs 2 and 7, corresponding to the maximum and minimum values of T_{\max} , T_{\min} and ΔT .

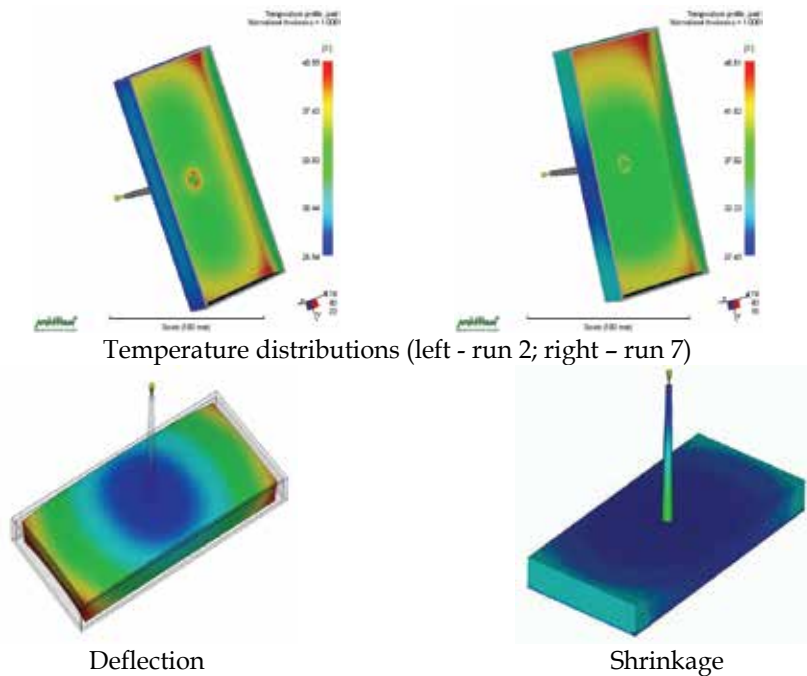


Fig. 13. Temperature distribution on the centre gated box moulding for runs 2 and 7, and deflection and shrinkage profiles (run 2 only).

Higher temperatures are found at the corners of the box moulding. Both runs show similar temperature distribution profiles and minimum values of T_{\min} (at the lateral walls of the box), but run 7 showing higher values of T_{\max} . The deflection and shrinkage profiles are also similar for all the runs, only with slight variations on S and δ (Table 4). The highest δ values are found at the top (free edge) of the middle of the smallest lateral wall, whilst the major S values are found at the bottom (base edge) of the smallest lateral wall, as would be expected. The deflection profile is qualitatively in good agreement with experimental results.

Fig. 14 shows the percentage of contribution of the varied factors (Figure 1) for the envisaged results (ΔT , S and δ). Each factor has a different percentage of contribution depending upon the selected output. ΔT is mainly determined by the orientation of the cooling channels (47%), followed by the number of cooling lines (29%) and the distance between them (22%). These variables should have the highest influence upon the distribution of heat transfer rates in the part surface. S is mainly influenced by the distance between cooling channels (56%), and in a less degree by the number of cooling lines (25%), the distance of the cooling channel to the cavity surface (12%) and the cooling channel diameter (6%). These variables should have the highest influence on the amount of heat exchanged by the cooling system. The most contributing factors for δ are the same as for ΔT .

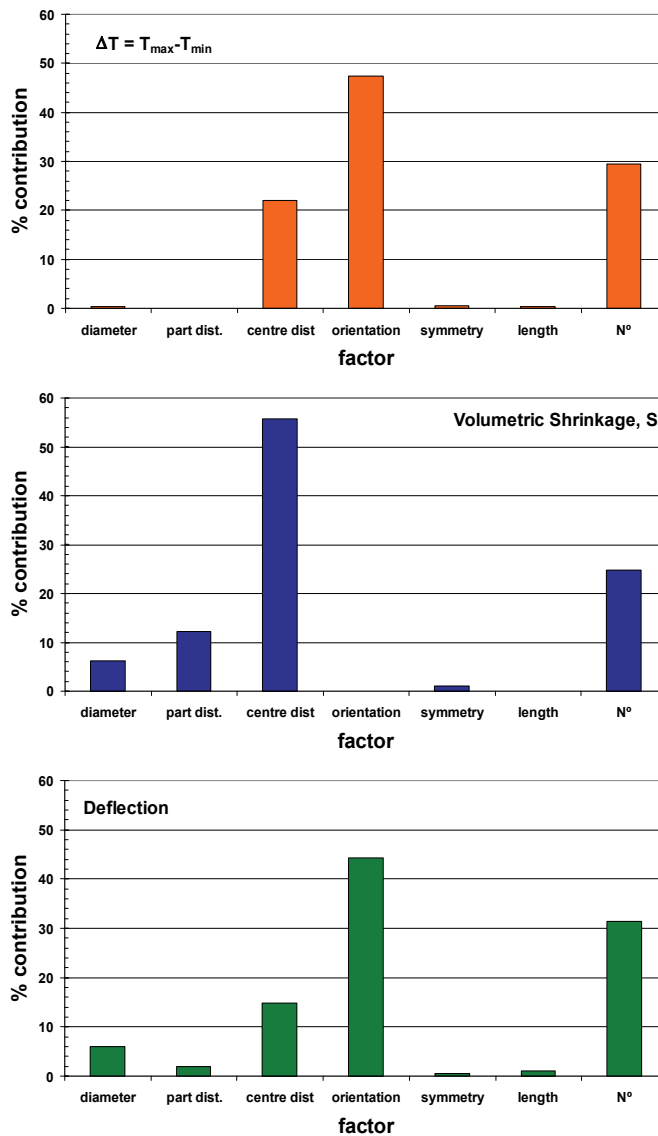


Fig. 14. Percentage of contribution of the design variable for the performance of the cooling system evaluated by the temperature difference, ΔT , shrinkage, S , and the maximum deflection.

Fig. 15 presents the variations of the assessed results as function of the more contributing design variables. ΔT and δ are minimized by the setting of the design variables at their highest values: $a = 14$ mm, Y orientation of cooling channels and n° of channels = 6. S values are minimized by the following set: the highest channel diameter, $\phi = 12$ mm, and the lowest distance from the cooling channel to the cavity wall, $b = 20$ mm, the smallest distance between cooling channels centres, $a = 10$ mm, and the least n° of cooling channels, $N^{\circ} = 4$. The simultaneous reduction of the shrinkage and of the deflection is not possible by only variation of the selected design variables.

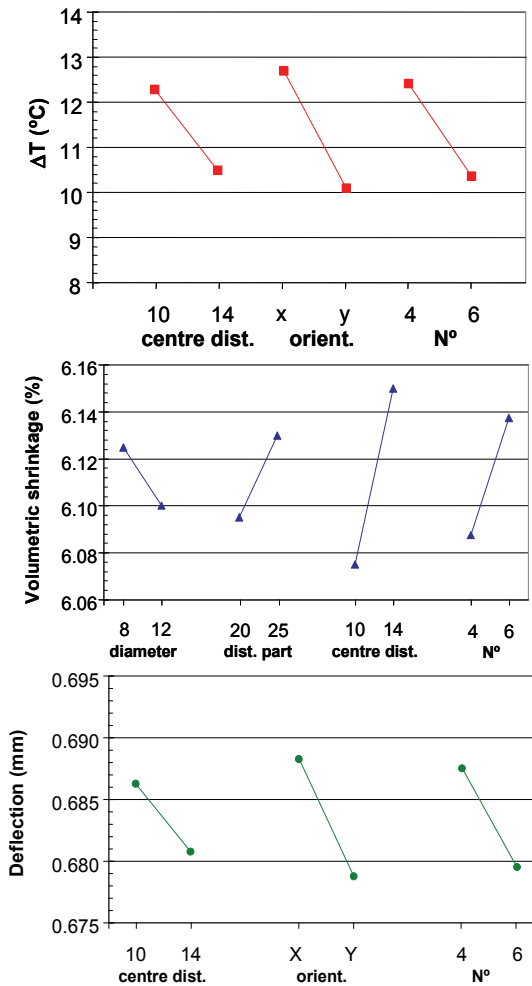


Fig. 15. Effects of the design variables upon the selected performance metrics.

For the studied case, the design factors of the cooling system must be set up as follows in order to minimize ΔT , S and δ :

- Diameter → Maximum
- Part distance → Minimum
- Centre distance → Minimum to minimise S
→ Maximum to minimise ΔT and δ
- Channels orientation → Y (cooling fluid flowing in the melt flow direction)
- Channels symmetry → not relevant
- Channels length → not relevant
- N° channels → Maximise to minimise ΔT and δ
→ Minimize to minimize S

Due to the high number of cooling system parameters its design is a complex task. The process simulators can be therefore integrated with optimization methods (e.g., evolutionary algorithms) and several design strategies can be investigated (Lam, 2004;

Michelitsch, 2004; Pirc, 2009). Experience shows that savings potential of 10-40% can be attained in the injection moulding process through optimized mould cooling.

4.2 Impact behaviour of injection moulded automotive components

The impact response of a ribbed plastic pillar when struck by a free motion head form (FMH) according to the FMVSS-201 standard was simulated in ABAQUS explicit code.

- **Effect of ribs geometry**

Fig. 16 shows the deceleration-time curves for the three considered geometries of the ribbed pillars: ROD, HEX and GAV geometries.

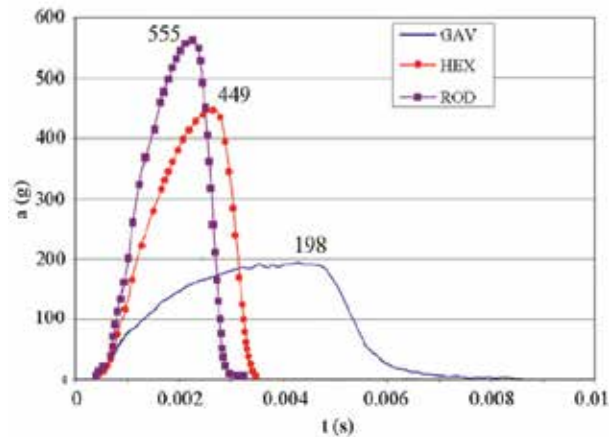


Fig. 16. Comparison of deceleration, a , vs. time, t , curves for GAV, HEX and ROD geometries.

The ROD geometry gives the highest deceleration and HIC(d) values (Table 5). For this rib geometry, the ribs are thicker and their deformation ability is reduced, not being able of decelerating the impactor (lower energy dissipation). The best performance is obtained by the GAV geometry, with a maximum deceleration of 198 g 's and a HIC(d) = 1187.

Geometry	a_{\max} (g)	HIC(d)
ROD	555	4339.3
HEX	449	3234.5
GAV	198	1186.5

Table 5. Deceleration and HIC(d) results for the three geometries tested.

The rib geometry has a strong effect on the deceleration-time curve. As the ribs deform, the impact energy is dissipated. A very constrained rib geometry (such as the circular, ROD, and hexagonal, HEX, one studied in this work) leads to a peak on the deceleration-time curve, resulting in a high maximum deceleration and maximum HIC(d) values. A more deformable rib structure (such as the GAV geometry) provides better energy dissipation, and the result is a smooth deceleration curve along the time with lower maximum deceleration and HIC(d) values.

Effect of Ribs Height

The effect of the rib height on the deceleration-time curves is shown in Fig. 17 and on the maximum deceleration and HIC(d) values are presented in Fig. 18.

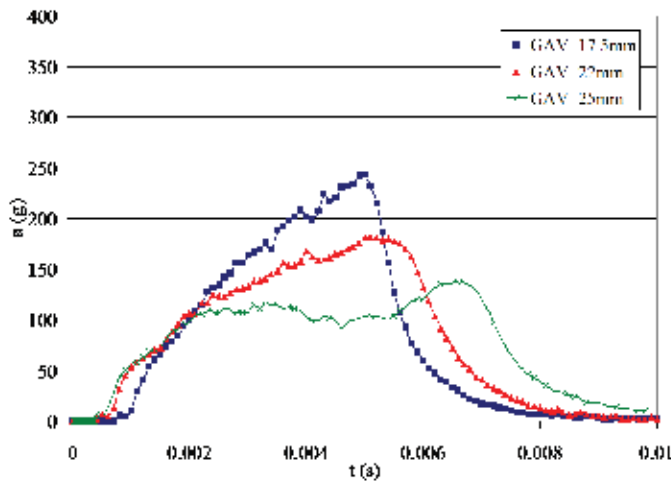


Fig. 17. Results from the different ribs height in GAV geometry.

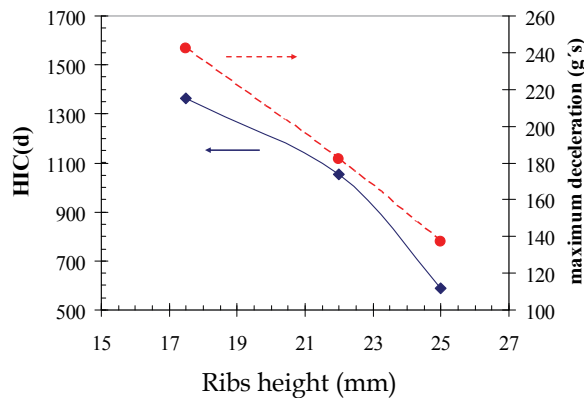


Fig. 18. Variations of the maximum deceleration and HIC(d) with rib height.

The increment of the rib height leads to a decrease of the HIC(d). Concomitantly, the maximum deceleration decreases linearly. The GAV geometry with a rib height of 25 mm has a maximum deceleration value of 137 g/s and a HIC(d) of 590.44, fully meeting the FMVSS-201 standard requirements.

Effect of material parameters

In Fig. 19 are presented the eight simulated deceleration vs. time curves with variation of the material parameters according to the Taguchi orthogonal matrix (Table 3). The profiles of some curves are identical, but curves referenced as V1 and V5 show a high deceleration peak. In Fig. 19 are also presented the deformation profiles of the pillar maximum deceleration.

The values of maximum deceleration and the calculated HIC(d) values are shown in Table 6. The maximum value of deceleration is obtained for condition V1, reaching the highest limit of 1223.7 g/s. The minimum value of a_{max} was presented by V7 with 190.9 g/s. The HIC(d)

registries also have the same trends: simulation V1 showing a maximum value of 11296 and the lowest HIC(d) value evidenced by condition V7 with 1100. These results are already anticipated from the curves of Fig. 19.

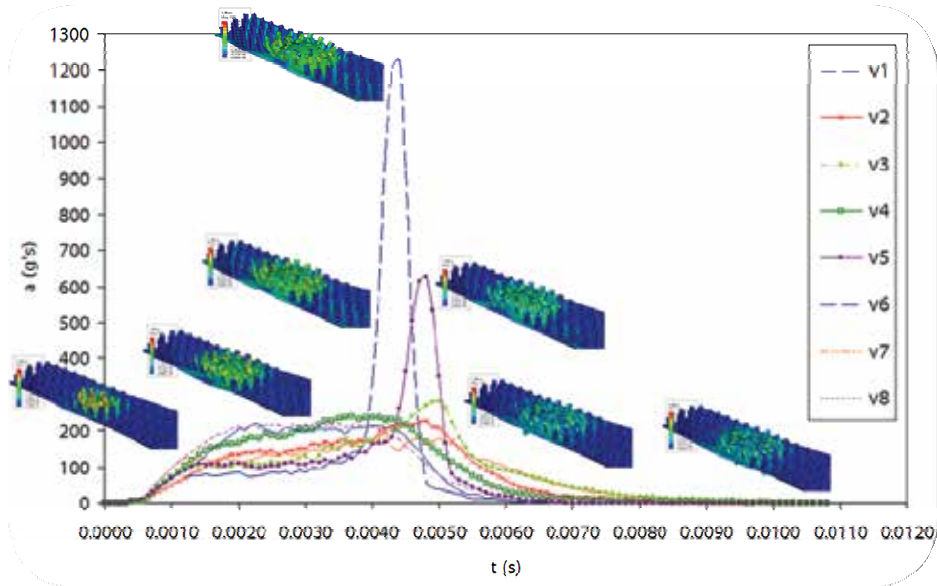


Fig. 19. Deceleration vs. time curves for the DOE plan varying the material parameters.

	E_1	σ_y	σ_r	ϵ_b	a_{\max}	HIC(d)
V1	1	1	1	1	1223.7	11296
V2	1	1	1	2	227.7	1243
V3	1	2	2	1	283.2	1214
V4	1	2	2	2	238.5	1678
V5	2	1	2	1	627.9	2609
V6	2	1	2	2	217.4	1491
V7	2	2	1	1	190.9	1100
V8	2	2	1	2	218.2	1623

Table 6. Results of DOE plan for assessment of the effect of material mechanical parameters on the impact deceleration-time curve.

Fig. 20 shows the contribution of each selected factor for the variations of HIC(d) and a_{\max} . Varying the material properties, the maximum deceleration and HIC(d) values can be adjusted and optimised. σ_r doesn't have a great influence on the maximum deceleration value (3 %) and it contributes 10% for variation of HIC(d). The most significant material parameters affecting a_{\max} are the yield stress, the strain at break and their interaction (with c.a. 26-28%). In the case of HIC(d), the interaction between the yield stress and the strain at break has the most significant effect (c.a. 22%), followed by the yield stress and the strain at break, and with less contribution of the others.

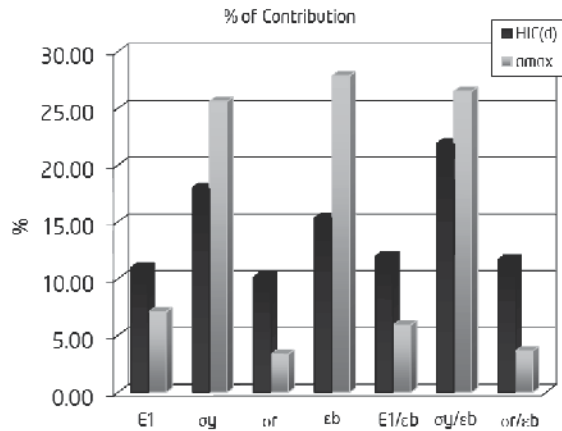


Fig. 20. Percentage of contribution of the material properties for HIC(d) and a_{max}.

Fig. 21 shows the influence of significant material properties on a_{max} and HIC(d) values. Both are determined by similar settings of the material mechanical parameter, although with different significance. Both HIC(d) and a_{max} decrease with the increment of the material parameters. From Figure 21, the best configuration of material parameters (for the selected pillar geometry) that minimise both HIC(d) and a_{max} is the one with the maximal E, σ_y and ε_b, as would be expected as this set of material properties maximizes the toughness of the material.

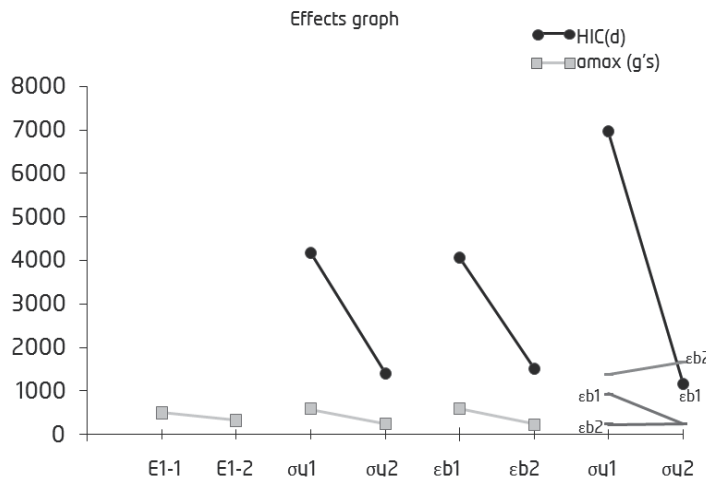


Fig. 21. Effect graphs showing the variations of HIC(d) and a_{max} with the material parameters.

The combination of geometry and material properties plays an important role on the crashworthiness response of polymeric components. This means that the simultaneous consideration of both geometry and material properties must be taken into account in the design phase. The procedure proposed in this work (extensive used of computer simulations and of design of experiments) is therefore of paramount relevance when design with polymers against impact (Ribeiro, 2005; Ribeiro, 2006; Ribeiro 2007)

4.3 Relationships between processing and mechanical properties of injection mouldings

Fig. 22 shows the variations of the impact properties (peak force and energy, F_p and U_p , respectively, normalised with respect to the specimen thickness) of an injection moulded propylene copolymer lateral gated discs (divergent/convergent flow type) with the weighted thermomechanical indices (these indices are weighted by the skin ratio, Sa (Viana, 1999)). F_p/h increases with the skin ratio weighted thermo-stress index (level and amount of molecular orientation) and decreases with the weighted cooling index (degree of crystallinity). The peak force is mainly determined by the cooling index. U_p/h is reduced for high values of both weighted thermo-stress and cooling indices. The peak energy is influenced almost equally by both thermomechanical indices.

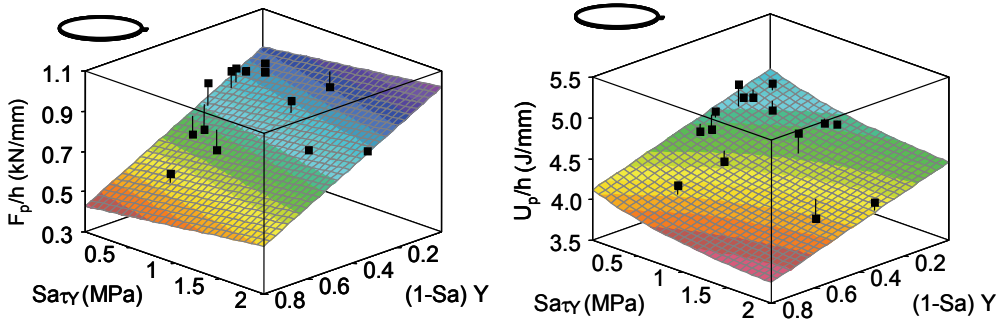


Fig. 22. Variations of the peak force, F_p , and energy, U_p (both normalised to the specimen thickness, h) with the weighted thermomechanical indices for a lateral gated disc (divergent/convergent flow type).

However, these variations are dependent upon the moulding geometry and gating options/flow type). Fig. 23 shows the relationships between the impact properties and the thermomechanical indices for a box like moulding (radial flow type). The effect of processing conditions is different for this moulding as compared with the lateral gated discs (Fig. 22). For the box like moulding (Fig. 23), F_p/h increases with both weighted thermo-stress and cooling indices. The peak force is mainly determined by the cooling index, but also slightly by the thermo-stress index. U_p/h is only dependent upon the weighted thermo-stress index, increasing with it. The main difference between the box and disc mouldings is the distinct (opposed) effect of the weighted cooling index on impact properties.

Comparing both mouldings, the discs present higher variations of the cooling index: the highest values are similar for both moulding, but the lowest values are much lower. Furthermore, the discs show higher thermo-stress indices.

The thermomechanical environment imposed during injection moulding of different components geometries can be compared by dimensionless analysis. The relative importance of the principal physical phenomena that take place and their degree of interaction can be quantified by dimensionless numbers, most commonly used being (Cunha, 2000; Viana 2004):

- the Cameron number, Ca - is the ratio between the heat conduction in the thickness direction to the heat convection in the longitudinal one;
- Brinkman number, Br - is the ratio between the heat generated by viscous dissipation and the heat exchanged by conduction through the moulding boundaries.

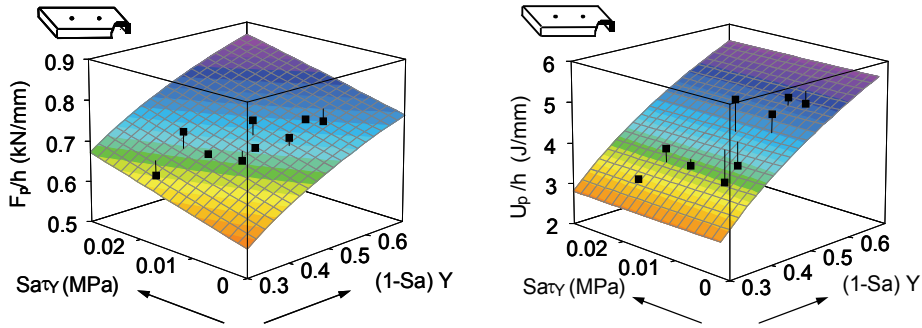


Fig. 23. Variations of the peak force, F_p , and energy, U_p (both normalised to the specimen thickness, h) with the weighted thermomechanical indices for a box moulding (radial flow).

Comparing both mouldings, the discs show the highest Ca as a result of the highest heat losses by conduction through the mould walls; the disc mouldings present also lower values of Br than the box mouldings (Viana, 2004). Although, resulting in similar values of the cooling index, the morphology development in both mouldings is different as a result of the different flow type and cooling conditions. Figure 24 illustrates the effect of distinct thermal levels upon the microstructure of the discs and boxes mouldings, as revealed by polarised light optical microscopy.

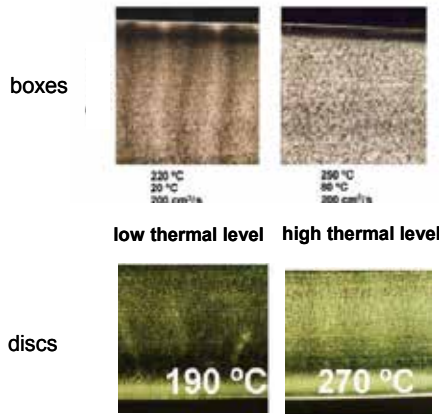


Fig. 24. Typical microstructures of the disc and box mouldings at a low and high thermal levels.

Box mouldings feature smaller skin layer thickness and a coarser spherulitic structure due to the less aggressive cooling conditions. The development of different residual stresses values for both types of mouldings may also affect the morphology-impact properties relationships. The establishment of quantitative relationship between the morphology and the impact properties of injection mouldings is still rather difficult. This is partly due to the lack of knowledge of the significant morphological parameters controlling the mechanical response at high strain-rates on polymeric material systems.

4.4 Mechanical behaviour of injection moulded FRP

Fig. 25 and 26 compare the experimental and simulated curves of the airbag housing for both loading modes. Different constitutive models are considered and evaluated.

Compression load

Figure 25 shows the force vs. displacement curves for compression load mode for each material constitutive model considered. The experimental result is also shown.

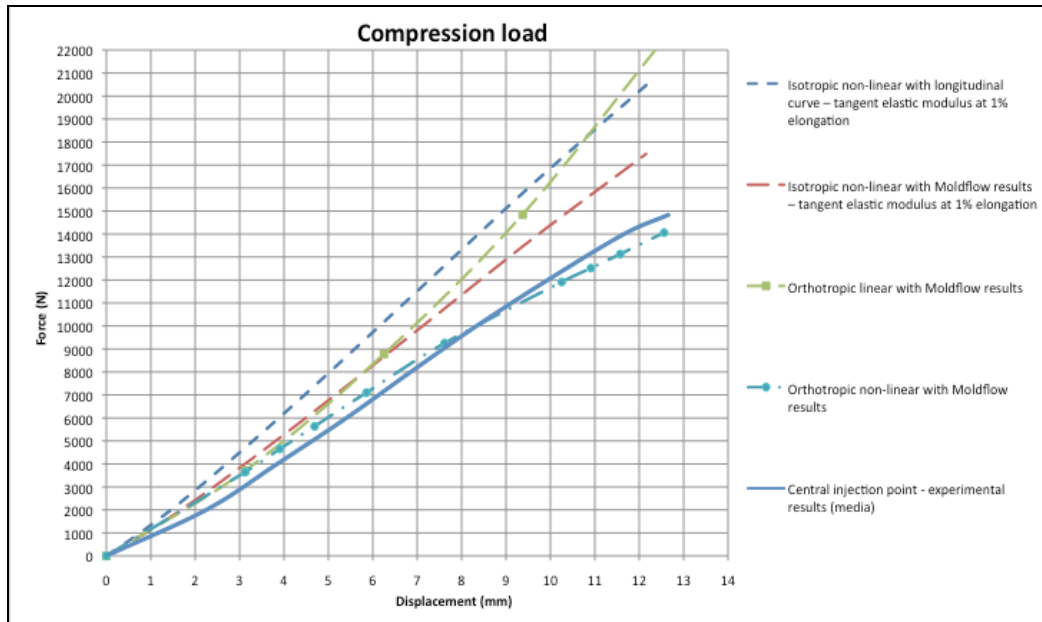


Fig. 25. Force vs. displacement curves for different constitutive model in compression load of housing airbag.

The orthotropic non-linear model presents the best results, with a good approximation to the experimental results (deviation of 5% in force and 1% in deformation). The results of the isotropic non-linear and the orthotropic linear behaviour are outside an acceptable deviation.

Tensile load

Fig. 26 shows the force vs. displacement curves for tensile load mode for each material constitutive model considered. The experimental result is also shown.

All the constitutive models tested had a force vs. displacement curve above the experimental one. The orthotropic non-linear model was the one with best results, with a good approximation of experimental results (deviation of 7% in force and 6% in deformation). The results show that all models, except the orthotropic non-linear model, have a high error and can't be considered for the structural analysis of fibre reinforced polymeric components.

Analysing the results, some conclusions can be withdrawn:

- The constitutive models based on the isotropic non-linear behaviour showed bad results, when compared with experimental results. These constitutive models should not be used on the design of fibre reinforced polymeric injection moulded components.
- The non-linear orthotropic model provides a good agreement with experimental data, in all load situations tested. The deviations obtained are minimal, not exceeding 7%.

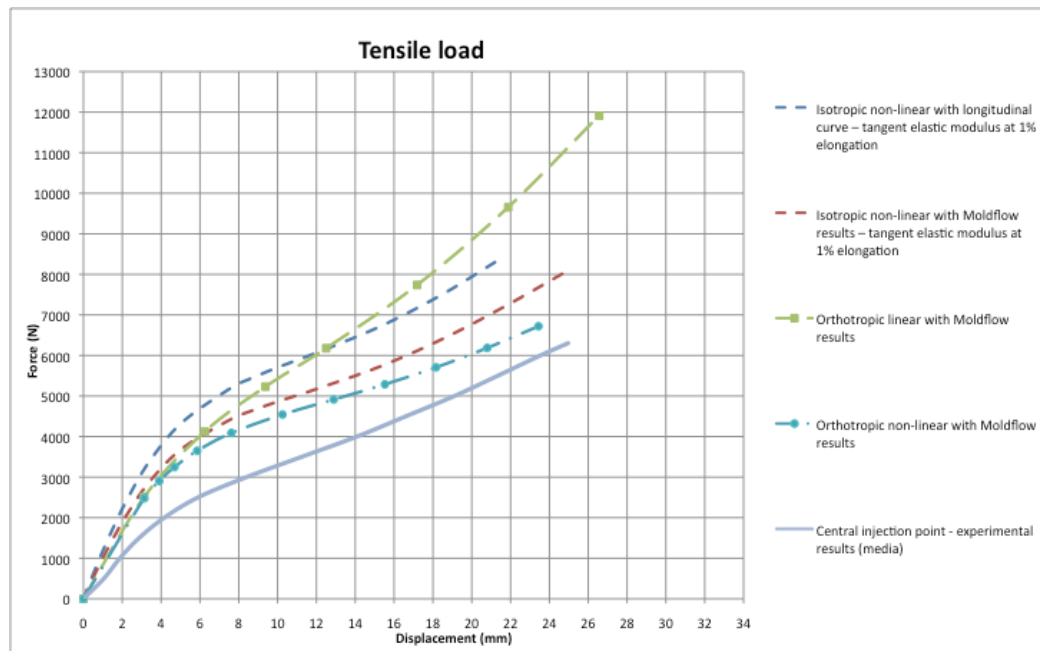


Fig. 26. Force vs. displacement curves for different constitutive model in tensile load of housing airbag.

- The approach adopted to take into account the typical skin-core structure of injection moulded FRP was able of giving reasonable results. But the results are not very different from those obtained with the use of longitudinal curve for the material behaviour. This approach must be considered conservative.

4.5 Impact behaviour of injection moulded LFT

The impact test results on the injection moulded plate are show in Fig. 27, in terms of peak force and energy. The specimens cut parallel to the flow direction (FD) allow the assessment of the impact properties in the transverse direction (TD); conversely specimens cut perpendicular to FD allow the assessment of the impact properties in FD. This is illustrated in Fig. 27 by the inset figures on the plate surface. Two general conclusions can be withdrawn from these results: the variations are higher along the flow path, but in this direction the values of the impact properties are smaller. This is expected taking into account the direction that the specimens were cut with respect to the FD (also, the direction of the fibre orientation), as depicted by the inset graphs on Fig. 27. In TD the impact properties are almost constant. Both F_p and U_p tend to decrease along the flow path. The level of anisotropy (defined as by the quotient of the longitudinal (L) and transversal (T) specimen properties at location L/T50) is 1.5 and 1.6, respectively for F_p and U_p .

The gating option (central gate) of the moulding imposes a radial flow of the polymer. This imposes expectantly a radial fibre orientation (in the skin layer). The specimens cut in the longitudinal direction present therefore different fibre orientation relatively to the loading direction. This was taken into account by a new thermomechanical variable defined as:

$$\tau_w^0 = \tau_w \cos(\theta) \quad (4)$$

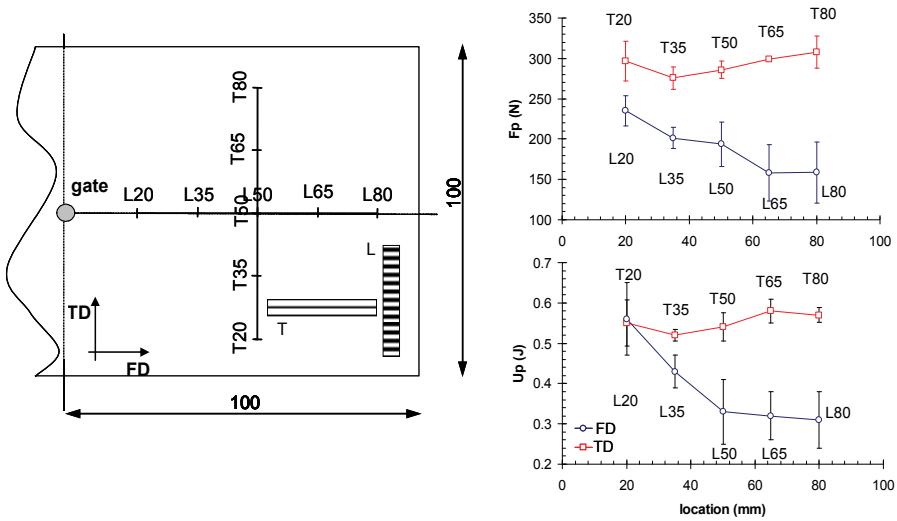


Fig. 27. Variations of the impact peak force, F_p , and energy, U_p , along the longitudinal (L) and transverse (T) directions of the plate.

Where, θ is the angle between the fibre orientation and the loading direction. This implies that for the specimens cut perpendicularly to FD, along the flow path (referenced as L in Fig. 27) $[Sa.\tau_w^0] = 0$, and their mechanical properties are mainly dependent upon the thermal level that is $[(1-Sa).Y]$. These assumptions allow us to relate globally the mechanical properties of the specimens cut in different locations and with distinct fibre orientations with the local thermomechanical indices.

Fig. 28 shows the variations F_p and U_p with $[(1-Sa).Y]$ and $[Sa.\tau_w^0]$. Both properties increase with the reduction of $[(1-Sa).Y]$ and the increment of $[Sa.\tau_w^0]$. In general, the flexural impact properties are enhanced for a reduced thermal level (low degree of crystallinity), thicker skin layers and higher levels of fibre orientation.

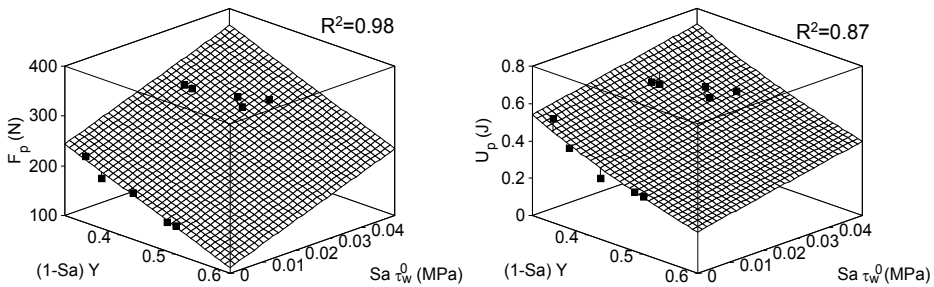


Fig. 28. Variation of the impact properties (at 2 m/s) with the weighted thermomechanical indices (F_p – peak force; U_p – peak energy).

4.6 Multi-objective optimization of the mechanical behaviour of injection moulded components

The tensile properties at high strain-rate (3 m/s) of an injection moulded tensile specimen were optimised through an automatic optimization methodology based on Multi-Objective

Evolutionary Algorithms (Gaspar-Cunha, 2005). The initial modulus, E_2 , yield stress, σ_{y2} , and strain at break, ϵ_{b2} , were optimized simultaneously, with the aim of establishing the set of thermomechanical indices (or processing conditions) that maximise, at the same time, the stiffness, the strength and toughness of the moulding. Fig. 29 shows the relationships between pairs of properties, for a better visualization. A high scatter on the data was found, as compared to the same relationships obtained at low velocity testing (2 mm/min), although with the same dependences (Gaspar-Cunha, 2005): E_2 increase with σ_{y2} ; σ_{y2} decreases with ϵ_{b2} ; ϵ_{b2} decreases with E_2 . The set of simultaneously optimised mechanical properties at high strain-rates can be found: $E_2 = 5.8$ GPa; $\sigma_{y2} = 66$ MPa; and $\epsilon_{b2} = 0.15$ mm/mm. Any other solution will decrease one of the properties.

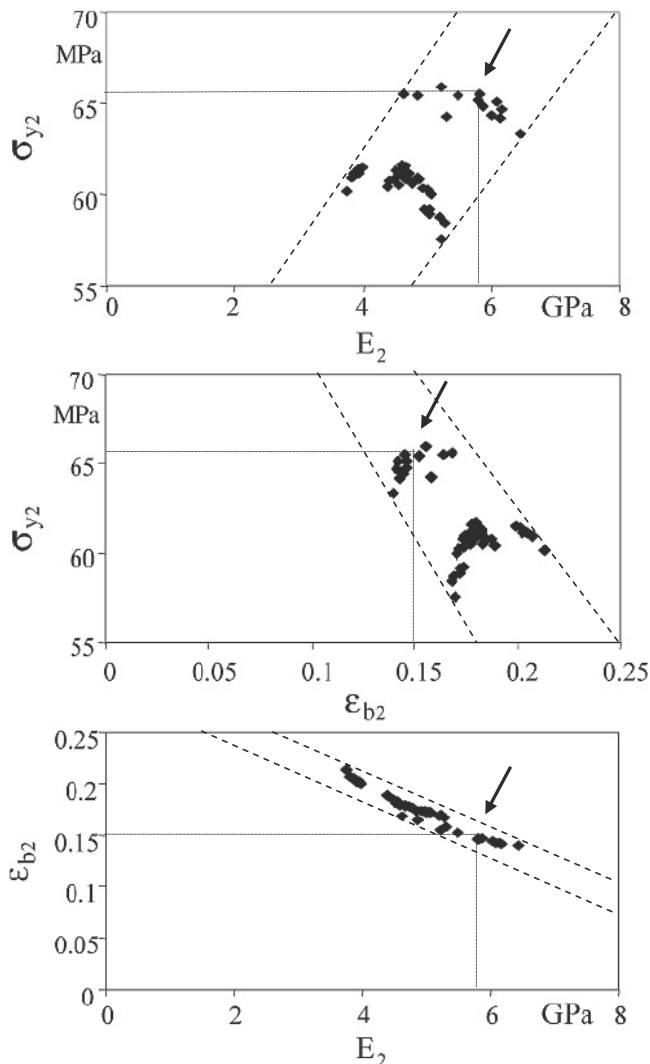


Fig. 29. Optimization of the mechanical properties at high strain rates: E_2 – initial modulus, ρ_{y2} – yield stress; ϵ_{b2} – strain at break.

Table 7 compares the setting of processing conditions and correspondent thermomechanical indices at high testing velocities that maximise each mechanical property individually. Both E_2 and σ_{Y2} are maximized for a low setting of the injection and mould temperatures and injection flow rate (or higher injection times); but ϵ_{b2} for the opposed adjustment. This is also reflected on the morphological state of the mouldings, as evaluated by the thermomechanical indices: a more oriented (higher τ_Y) and thicker skin layer and a less crystalline (low Y) core material shows high E_2 and σ_{Y2} ; but a less oriented, thinner skin layer and higher crystalline core material will present a high ϵ_{b2} . The optimised set of the mechanical properties at high strain-rates ($E_2 = 5.8$ GPa, $\sigma_{Y2} = 66$ MPa, and $\epsilon_{b2} = 0.15$ mm/mm) is obtained for the following adjustment of the processing conditions: $T_{inj} = 201$ °C, $T_w = 9$ °C and $t_{inj} = 4.7$ s.

	Criteria (high vel.)		
	E_2	σ_{Y2}	ϵ_{b2}
T_{inj} (°C)	200	206	255
T_w (°C)	6	18	41
t_{inj} (s)	4.96	4.47	2.40
Y	0.263	0.306	0.520
τ_Y (MPa)	0.687	0.383	0.251
Sa	0.61	0.53	0.28

Table 7. Settings of the processing conditions (and respective thermomechanical indices) leading to the maximization of the mechanical properties at high strain-rates.

It is interesting to note that the simultaneous maximization of both low and high strain rate tensile properties results in different values for the optimised mechanical properties, which also corresponds to a different adjustment of the processing conditions (Gaspar-Cunha-2005) when compared with the individual maximization of the mechanical response at each test velocity.

The proposed methodology based on the use of a Multi-Objective Evolutionary Algorithm, MOEA, coupled with a process simulation tool appears as a relevant design tool for the maximization of the desired mechanical response of injection moulded components and the appropriate setting of the processing conditions. Furthermore, the exploitation of thermomechanical indices allows the interpretation of the results based on the expected morphological development occurring during processing.

5. Final remarks

The use of thermoplastic polymers in automotive components is growing steadily in the last years and they are the future obvious material solutions for new mobility concepts where lightweight and eco-sustainability are imperative requirements. These polymeric components are being mostly manufactured by high-throughput and low cost processes, like injection moulding. The optimization of injection moulded polymer automotive components is a crucial design task for obtaining high quality, enhanced mechanical

response and low cost components. Two main optimization routes are normally addressed, most of the time separately: the optimization of the injection moulding process and the optimization of the properties of the injection moulded components. Nevertheless, the adoption of a holistic approach, optimising simultaneously the manufacturing process (e.g., mould design, reduction of defective parts), and the component specifications (e.g., mechanical properties) is required. In this approach the knowledge of the relationships between the processing thermo-mechanical environment, the polymer morphology and the moulding properties is essential at the component design stage. Nowadays, the automotive component design makes intensive use of computer simulations (e.g., process, functional, structural). Improved part quality and reduced cost requirements demand the integration of advanced simulation resources, of accurate process-properties relationships and of optimization tools.

This chapter addressed the application of the engineering design optimization methods and tools to the design of polymeric automotive polymer components moulded by the injection moulding process. Different routes and methodologies were presented based on process (injection moulding) and structural (mechanical response) simulations, on the processing-properties relationships for unreinforced and reinforced polymer systems, on diverse optimization methods (combined DOE/ANOVA statistical tools and multi-objective evolutionary algorithms). Currently, there is a panoply of advanced tools available to the automotive component designers that need to be intelligently combined in order to efficiently design with polymeric materials. Besides part quality and cost reductions, next engineering challenges will address eco-design concerns.

6. References

- Ashmead, M., et al (1998) Advanced Materials for Enhanced Automotive Safety, Cellbond Composites Ltd, Huntingdon, Cambridgeshire, *SAE Techn. Papers*, pp. 23-32
- Castro, C.E., Cabrera-Rios, M., Lilly, B., Castro, J.M., Mount-Campbell (2003), Identifying The Best Compromises Between Multiple Performance Measures In Injection Molding (IM) Using Data Envelopment Analysis (DEA), *J Integrated Design & Process Science Archive*, 7(1) pp. 77-86
- Castro, C.E., Cabrera-Rios M, Castro JM, Lilly B (2007) Multiple Criteria Optimization With Variability Considerations in Injection Molding, *Polym Eng. Sci.*, 47(4), pp. 400-409
- Chen C-P, Chuang M-T, Hsiao Y.H, Yang Y-K, Tsai C-H (2009) Simulation and experimental study in determining injection molding process parameters for thin-shell plastic parts via design of experiments analysis, *Expert Systems with Applications*, 36(7), pp. 10752-10759
- Constable, RC, Kattas, LN (2002), Long glass fiber composites: rapid growth and change, *Proc. ANTEC'02*, S. Francisco, USA
- Cunha AM, Pouzada AS (1995) in *Impact and dynamic fracture of polymers and composites*, ESIS19, ed. J.G. Williams and A. Pavan, Mech. Eng. Public., London, p. 315-325
- Cunha AM, Godinho JS, Viana JC (2000) in *Structure Development during polymer processing*, NATO-ASI series, v. 370, eds Cunha, A.M. and Fakirov S., Kluwer Acad. Pub., p. 255-277

- Fernandes C, Pontes AJ, Viana JC, Gaspar-Cunha A (2010) Using Multiobjective Evolutionary Algorithms in the Optimization of Operating Conditions of Polymer Injection Molding, *Polym Eng. Sci.*, 50(8), pp. 1667-1678
- FMVSS-201 (1997) Code of Federal Regulations – *Transportation FMVSS-201. Standard N° 201: Occupant protection in interior impact.*
- Fremgen C, Mkrtchyan L, Hubera U, Maier M (2005), *Sci. Techn. Adv. Mat.*, 6
- Gaspar-Cunha A., Viana JC (2005) Using Multiobjective Evolutionary Algorithms to Optimize Mechanical Properties of Injection Molded Parts, *Intern. Polym. Proc.*, XX, 3, pp. 274-285
- Gholami, T., et al (2002) Finite Element Analysis of Head Impact According to Extended FMVSS-201, *ABAQUS Users Conference*, 23.-24. September, Wiesbaden, Germany
- Hassan H, Regnier N, Lebot C, Pujos C, Defaye G (2009) Effect of cooling system on the polymer temperature and solidification during injection molding, *Applied Thermal Eng.*, 29, pp. 1786–1791
- Jacobs, A (2002) Car makers increase their use of composites, *Reinf. Plastics*, 48(2), p. 26-32
- Kazmer DO (2000) Axiomatic design of the injection molding process, Proc. ICAD2000, 1st Intern. Conf. Axiomatic Design, Cambridge, June 21-23, pp.123-129
- Krasteva D, Hattum FWJ, Viana JC, Impact properties of injection moulded long fibre reinforced polypropylene composites, *Proc. 10th Portuguese conference on fracture*, 22-24 Feb., Guimaraes, Portugal
- Lam, YC, Zhai LY, Tai K, Fok SC (2004) An evolutionary approach for cooling system optimization in plastic injection moulding, *Intern. J. Prod. Research*, 42(10), pp. 2047-2061
- Li, CL, Li GC, Mok ACK (2005) Automatic layout design of plastic injection mould cooling system, *Computer-Aided Design*, 37 (7) pp. 645-662
- Liang J-Z (2002) An optimal design of cooling system for injection mold, *Polymer-Plastics Techn. Eng.*, 41(2), pp. 261-271
- Lin, JZ, Pitrof, SM (2004) Analytical design of cockpit modules for safety and comfort, *SAE World Congress*, Detroit, Michigan
- Lotti C, Bretas, RES (2006) Correlations between Injection Molding Parameters, Morphology and Mechanical Properties of PPS Using Artificial Neural Networks, *Intern Polym Proc*, 2, pp. 104-115
- Lotti C, Bretas RES (2007) Correlation between Injection Molding Parameters, Morphology and Mechanical Properties of PPS/SEBS Blend Using Artificial Neural Networks, *Intern. Polymer Proc.*, 1, pp. 105-116
- Luts W, Herrmann J, Kockelmann M, Hosseini HS, Jackel A, Schmauder S, Predak S, Busse G (2009) Damage development in short-fiber reinforced injection molded composites, *Computational Materials Sci.*, 45(3), pp. 698-708
- Michelitsch T, Mehnen J (2004) Evolutionary Optimization of Cooling Circuit Layouts Based on the Electrolytic Tank Method. *Proc. 4th CIRP Intern. Seminar on Intelligent Computation Manuf. Eng. CIRP ICME '04*, pp. 199-206 R. Teti (Ed.), Sorrento
- Park SJ, Won TH (1998) Optimal Cooling System Design for the Injection Molding Process, *Polym. Eng. Sci.*, 28 (9)

- Pirc N, Schmidt FM, Mongeau M, Bugarin F (2006) BEM-based cooling optimization for 3D injection molding, *Intern. J. Mechanical Sci., Proc. ASMDO'07*, 48 (4), pp. 430-439
- Ribeiro, CJ, Viana, JC, Vilaça, F, Azenha, J (2005) Design and simulation of automotive pillars for occupant protection, *AUTOPOLYMERS 2005, USA-Portuguese Workshop*, Charleston - USA: October 27-31
- Ribeiro CJ, Viana JC, Vilaça F, Azenha J (2006) Design and simulation of automotive plastic pillars for occupant protection, *Plastic, Rubber Comp.*, 35(6)
- Ribeiro, CJ, Viana, JC, Vilaça, F, Azenha, J (2007) Development of automotive plastic pillars for preventing occupant injuries by finite element simulations: The role of material properties, *Proc. MATERIAIS 2007, IV Intern. Mat. Symp.*, Porto, PORTUGAL: April 1-4
- Schijve, W (2002) Properties of long glass fibre polypropylene composites with length distributions, *Proc. ECCM-10*, Brugge, Belgium
- Tang SH, Tan YJ, Sapuan SM, Sulaiman S, Ismail N, Samin R (2007) The use of Taguchi method in the design of plastic injection mould for reducing warpage, *J. Mat. Proc. Techn.*, 182, pp. 418-426
- Turng LS, Peic M (2002) Computer-aided Process and Design Optimization for Injection Molding, *J Eng Manufacture, Proc. Institution Mech Eng Part B*, 216(B12), pp. 1523-1532
- van der Wal A, Mulder JJ, Gaymans RJ (1998), *Polymer*, 39, p. 5477-548
- van Hattum FWJ, Viana JC (2004) Optimising the mechanical performance of long fibre thermoplastic composites through process modelling, *9th Portuguese Conf. Fracture*, Setúbal, Portugal
- Viana, JC, Cunha, AM, Billon, N (1997) *Polym. Intern.* 43, p. 159
- Viana JC, Cunha AM, Billon N (1999) *Polym. Eng. Sci.*, 39, pp. 1463-1472
- Viana JC, Cunha AM, Billon N (2002) The thermomechanical environment and the microstructure of an injection moulded polypropylene copolymer, *Polymer*, 43, pp. 4185-4196
- Viana JC (2004), Development of the skin layer in injection moulding: phenomenological model, *Polymer*, 45, pp. 993-1005
- Viana JC (2006) Polymeric materials for impact and energy dissipation, *J. Plastics, Rubber Comp*, 35 (6/7) 260-267
- Viana JC, (2008) Reduction of cycle time in injection moulding, *Revista O Molde*, CEFAMOL July 2008 (in Portuguese and English)
- Vincent M, Giroud T, Clarke T, Eberhardt C (2005) Description and modelling of fiber orientation in injection molding of fiber reinforced thermoplastics, *Polymer*, 46(17) pp. 6719-6725.
- Wust A, Hensel T, Jansen D (2009), Integrative optimization of injection-moulded parts, *7th European LS-Dyna Conf*, May, Salzburg, Austria
- Xu X, Sach E, Allen S (2001), The Design of Conformal Cooling Channels in Injection Moulding Tooling, *Polym Eng Sci*, 4(1), pp. 1269-1272
- Yang Y-K (2007) Optimization of Injection-Molding Process of Short Glass Fiber and Polytetrafluoroethylene Reinforced Polycarbonate Composites via Design of Experiments Method: A Case Study, *Mat. Manuf. Proc.*, 21 (8), pp. 915-921

- Zerull, M., et al (2000) Using Suitable Plastic Components to Improve Vehicle Interior Safety to Comply with FMVSS-201, *SAE Techn. Papers*, pp. 209-231.
- Zhou J, Turng LS (2007) Process Optimization of Injection Molding Using an Adaptive Surrogate Model With Gaussian Process Approach, *Polym Eng Sci*, 47(5), pp. 684-694

High Mn TWIP Steels for Automotive Applications

B. C. De Cooman¹, Kwang-geun Chin² and Jinkyung Kim¹

¹*Graduate Institute of Ferrous Technology*

Pohang University of Science and Technology, Pohang

²*POSCO Technical Research Laboratories, Gwangyang
South Korea*

1. Introduction

Modern car design puts an increasing emphasis on the notion that a material used in building the body-in-white (BIW) should be selected on the basis of how well it helps achieving specific engineering targets such as low vehicle weight, high passive safety, stability, stiffness, comfort, acoustics, corrosion, and recycling. Steel is at present still the material of choice for car bodies, with 99% of the passenger cars having a steel body, and 60-70% of the car weight consisting of steel or steel-based parts. The automotive industry is however continuously making excursions in the area of light materials applications. At present, most car makers are routinely testing multi-materials concepts, which are not limited to the obvious use of light materials for closures, e.g. the use of Al for the front lid or thermosetting resins for trunk lids. The steel industry has made a sustained effort to innovate and create advanced steels and original steel-based solutions and methods in close collaboration with the manufacturers by an early involvement in automotive projects, but also by involving automakers in their own developments. Carmakers have increasingly built passenger cars with body designs which emphasize passenger safety in the event of a collision, and most passenger cars currently achieve high ratings in standardized crash simulations such as the EURO NCAP or the North American NHST tests. The safety issue directly related to the BIW materials is passive safety. High impact energy absorption is required for frontal crash and rear collision, and anti-intrusion properties are required in situations when passenger injury must be avoided, i.e. during a side impact and in case of a roll over, with its associated roof crush. Increased consumer expectations have resulted in cars which have steadily gained in weight as illustrated in figure 1. This weight spiral is a direct result of improvements in vehicle safety, increased space, performance, reliability, passenger comfort and overall vehicle quality. This trend has actually resulted in an increased use of steel in car body manufacturing in absolute terms, and this increase may in certain cases be as high as 25%. The weight issue is therefore high on the agenda of BIW design, as it is directly related to environmental concerns, i.e. emissions of CO₂, and the economics of the gas mileage. Reports on weight saving resulting from the use of Advanced High Strength Steels (AHSS) are difficult to evaluate as these tend to focus on the use of advanced steels and improved designs for a single part, rather than the entire car body. The use of Dual Phase (DP) and Transformation-Induced Plasticity (TRIP) steels has been

reported to result in a weight saving in the range of 10-25%. Similar weight reductions of about 25% are reported for the use of stainless steels. The potential for weight reductions become very important when very high strength steels are considered.

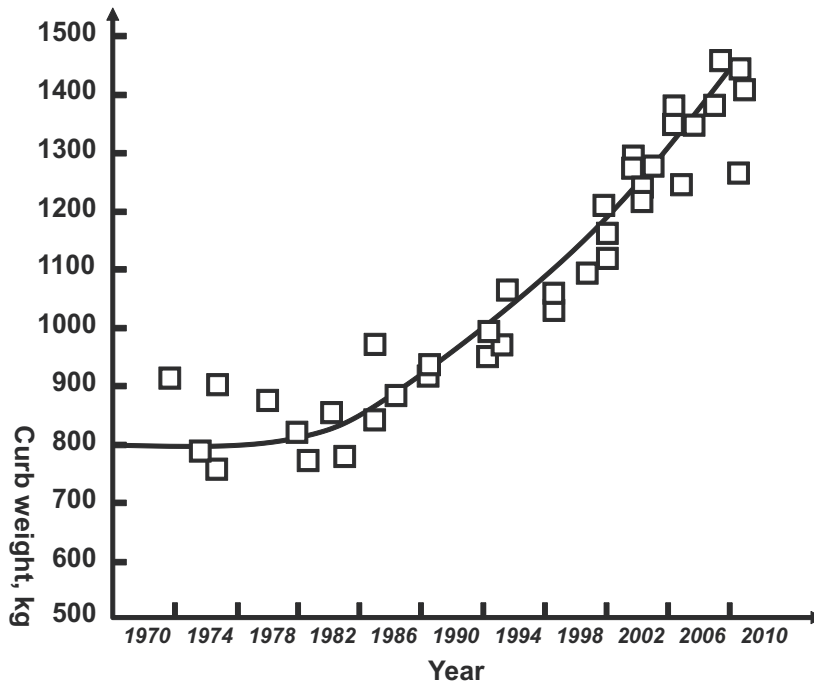


Fig. 1. Midsize passenger car weight increase in the EU. The weight increase is close to 90% for the period of 1970 to 2010.

Weight reductions of about 30-40% are typically reported for 1300-1500MPa steels. A 36% weight reduction can be expected when a body part used as anti-intrusion barrier is made of press hardening 22Mn5B steel. Most industry experts agree that, as illustrated in figure 2, steel based parts designs using advanced high strength steels offer both the potential for vehicle mass containment and lower production cost. Hence, when material-specific properties are considered, there is an increasingly important interest in very high strength materials. This has been the driving force behind most of the current automotive steel research efforts. This is obvious when one considers the need for the increased strength for parts related to passenger safety, such as the B-pillar, an essential element for passenger protection in side impact collisions.

DP and TRIP steels are now well established as AHSS, with major applications in BIW parts related to crash energy management. In addition to a high strength, a high stiffness and only very low levels of deformations, typically less than 5%, may be allowed for these parts. Strength levels as high as 1800MPa have been mentioned as future requirements for anti-intrusion parts. Whereas press-formable CMnB grades are receiving attention for the B-pillar and front-rear reinforcements, there is still considerable interest in TRIP and DP steels. In the case of DP grades the emphasis is on front end applications and exterior panels. Having said this, standard high strength micro-alloyed steels continue to be still being widely used. Two decades ago most BIW designs were based on steels with Ultimate Tensile

Strength (UTS) values in the 200-300MPa range. Recent BIW designs tend to use much more high strength steels. Whereas less low strength steels ($YS < 180\text{MPa}$) are being used, mainly for outer body parts, there is a pronounced increase in the use of High Strength Steels (HSS), with a yield strength ($YS > 300\text{MPa}$), Very High Strength Steels (VHSS) with a $YS > 500\text{MPa}$, and Ultra High Strength Steels (UHSS) with UTS values up to 1500MPa . This increased use of high strength steel grades has resulted in a moderate relative decrease of steel mass per car body.

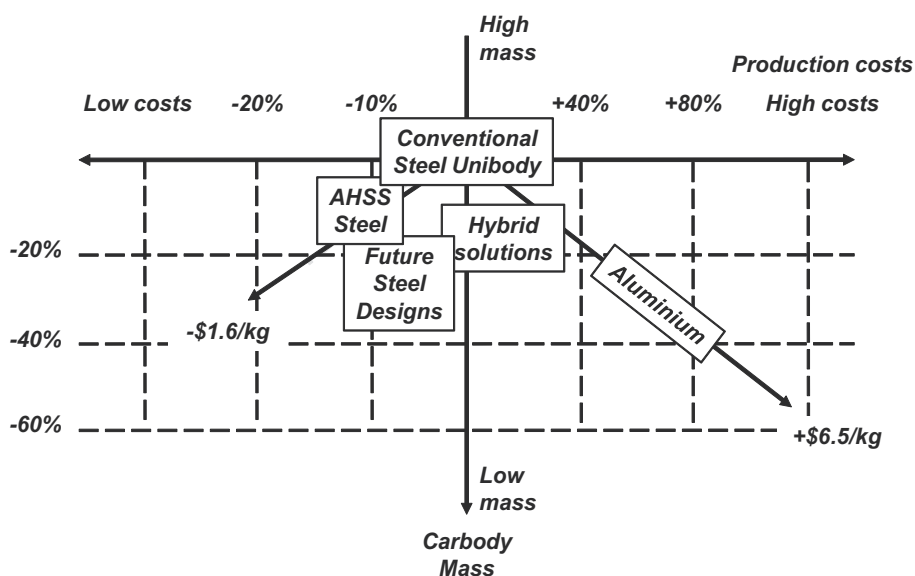


Fig. 2. Comparison of the production cost and vehicle mass containment for designs based on different material selections.

The present contribution reviews the important development of ultra-ductile TWIP steel for BIW applications. FeMn TWIP is a high-strength steel concept with superior formability, which may be close to being produced industrially. High manganese TWIP steels are highly ductile, high strength Mn austenitic steels characterized by a high rate of work hardening resulting from the generation of deformation-nucleated twins (Grassel et al., 1997; Grassel et al., 2000; Frommeyer, 2003; Prakash et al., 2008). Their Mn content is in the range of 15-30 mass%. Alloying additions of C, Si and/or Al are needed to obtain the high strength and the large uniform elongation associated with strain-induced twinning. Depending on the alloy system, the carbon content is either low, i.e. less than 0.05 mass-%, or high, typically in the range of 0.5-1.0 mass-%. Si and Al may be added to achieve a stable fully austenitic microstructure with low stacking fault energy in the range of 15-30mJ/m². High Mn alloys characterized by strength ductility products 40.000-60.000MPa% have reached the stage of large scale industrial testing and the industrial focus is mainly on TWIP steels with the following compositional ranges: 15-25 mass-%Mn, with 0-3%Si, 0-3% Al and 200-6000ppm C. The dominant deformation mode in TWIP steel is dislocation glide, and the deformation-induced twins gradually reduce the effective glide distance of dislocations which results in the "Dynamical Hall-Petch effect" illustrated in the schematic of figure 3.

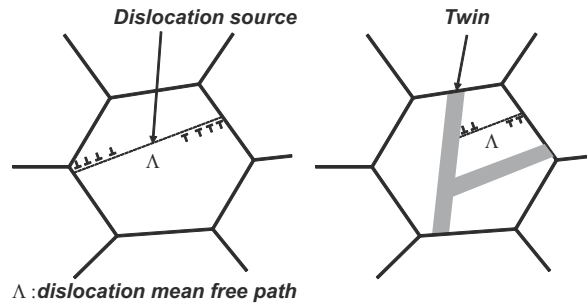


Fig. 3. Illustration of the dynamical Hall-Petch effect. Mechanical twins are formed due to the low stacking fault energy. They gradually reduce the effective glide distance of dislocations, resulting in the very high strain hardening observed in TWIP steel.

The mechanical properties of typical TWIP steels are reviewed in figure 4. These steels have received attention only recently, and the early work on high Mn ferrous alloys by Schuman (Schuman, 1971) in Germany, Remy and Pineau (Remy & Pineau, 1977) in France and Kim (Kim, 1993; Kim et al., 1993) in South Korea did not receive much attention originally. The work of Frommeyer (Grassel et al., 1997; Grassel et al., 2000; Frommeyer, 2003) at the Max Planck Institute in Dusseldorf, Germany, and the interest in advanced high strength steels from the automotive industry renewed the interest in the properties of high Mn TWIP steels and mainly three types of TWIP steel compositions have been extensively investigated: Fe-22%Mn-0.6%C (Allain, 2004), Fe-18%Mn-0.6%C, Fe-18%Mn-0.6%C-1.5%Al (Kim et al., 2006) and the low carbon Fe-25%-30%Mn-3%Si-%Al (Grassel et al., 2000). The high rate of strain hardening associated with the deformation twinning phenomenon allows for the combination of higher strengths and higher uniform elongations, as illustrated in figure 5 which compares the properties of conventional multi-phase TRIP steel with those of TWIP steel.

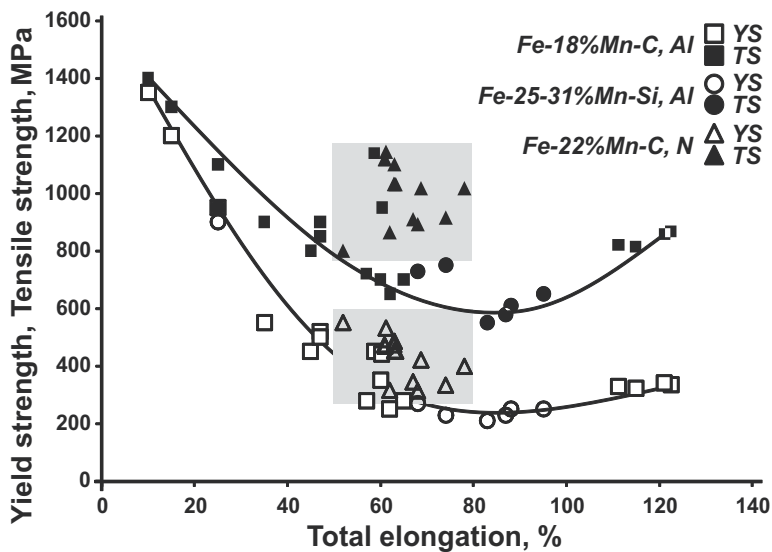


Fig. 4. Typical ranges for the mechanical properties of TWIP steel.

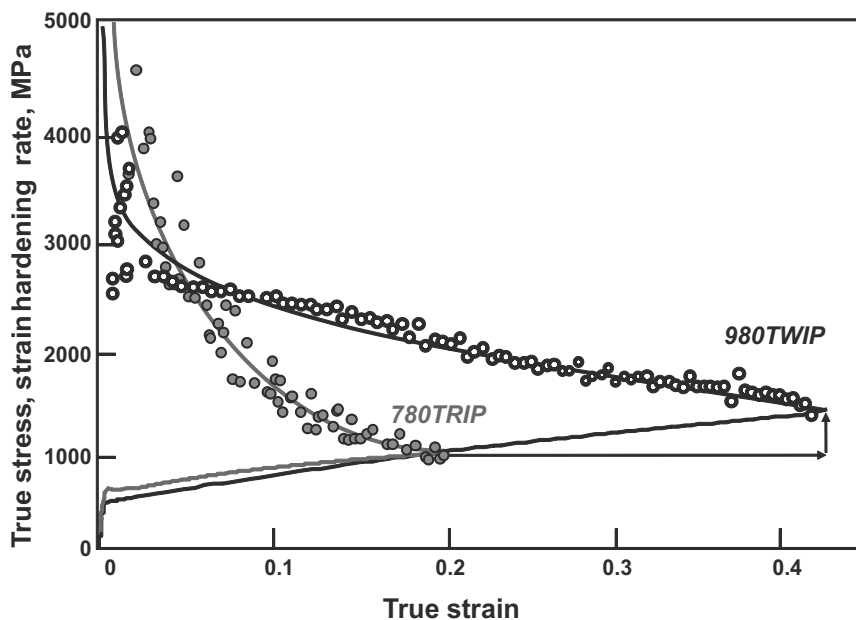


Fig. 5. Comparison of the stress-strain curves and the strain hardening rate for TRIP and TWIP steel. TWIP steel has a uniform elongation twice that of TRIP steel and a considerably higher ultimate strength.

2. Thermodynamic properties of TWIP steel

The Fe-Mn equilibrium phase diagram has recently been revised (Witusiewicz et al., 2004). On the Fe rich side of the diagram, the binary system would appear to be relatively simple with an open γ -loop. The meta-stable Fe-Mn diagram (figure 6) however reveals much more of the information which is required to understand the microstructures observed in practical non-equilibrium conditions. Between 5 mass-% and 25 mass-% of Mn, the room temperature multi-phase microstructure of Fe-Mn alloys is dominated by the presence of α' martensite, at low Mn contents, and ϵ -martensite, at higher Mn content.

Small Mn additions have a pronounced hardenability effect, resulting in the formation of cubic α' martensite. At higher Mn contents h.c.p. ϵ -martensite is formed. Both types of martensite are also generated by stress and strain-induced transformations of the retained austenite phase. Stabilizing the austenite at room temperature requires Mn contents in excess of 27 mass-% in the binary Fe-Mn alloy system. In order to obtain a stable room temperature austenite phase in alloys with less than 25 mass-% of Mn, the formation of α' and ϵ martensite must be suppressed. This can be done by carbon additions. Carbon additions of approximately 0.6 mass-% make it possible to obtain uniform, carbide-free, austenitic microstructures and avoid the formation of ϵ -martensite (Schumann, 1971). Higher carbon additions result in M_3C carbide formation.

Figure 7 illustrates the microstructure of a Fe-18%Mn-0.6%C TWIP steel. The structure is single phase austenitic, with relatively coarse grains, which may contain wide recrystallization twins. The XRD results also illustrate the fact that this TWIP steel does not transform to martensite during straining.

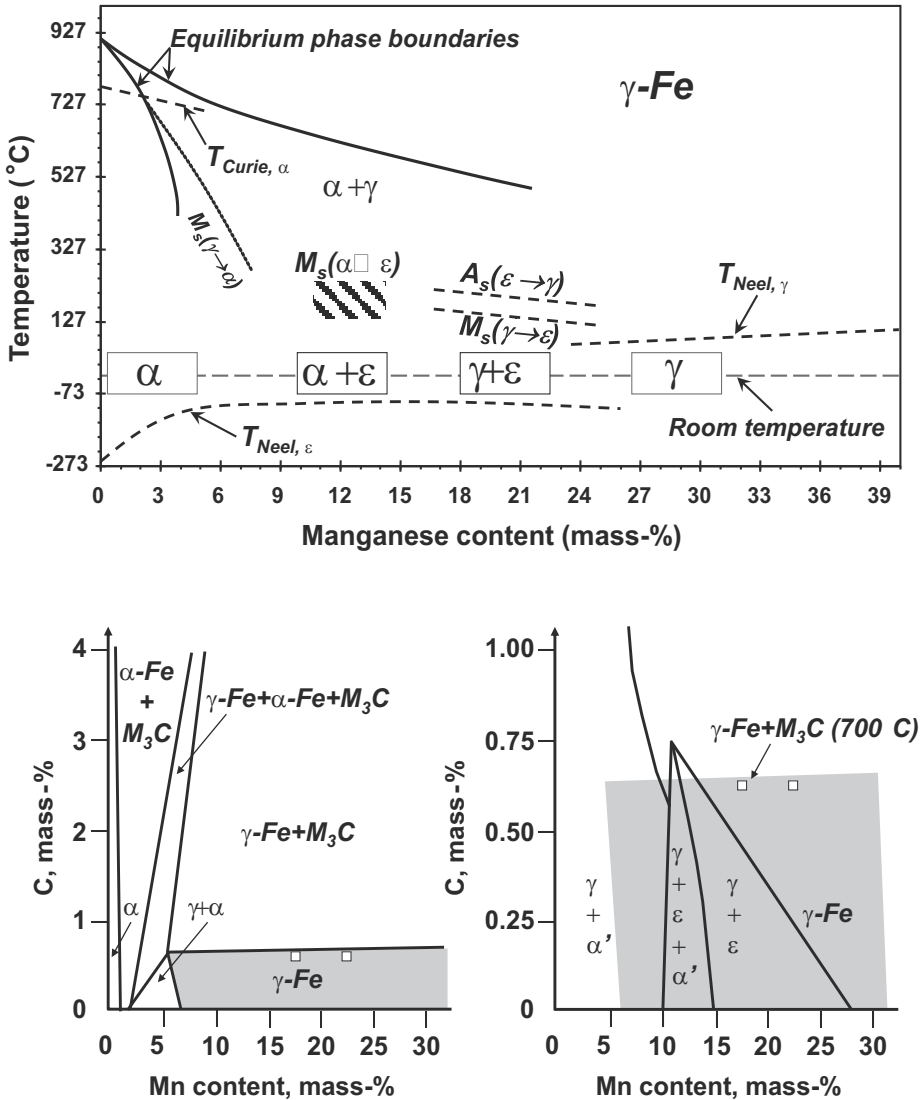


Fig. 6. (Top) Meta-stable Fe-Mn Phase diagram. (Below, left) Fe-rich corner of the Fe-Mn-C equilibrium phase diagram at 700°C showing the austenite stability range in grey. (Below, right) Superposition of the 700°C austenite stability range and the microstructure observed after quenching to room temperature from 950°C.

An alternative approach to obtain TWIP steel with uniform, carbide-free, austenitic microstructures is to use a high Mn content and avoid carbon additions. This TWIP steel composition concept typically requires Si and Al additions to control the stacking fault energy. The importance of the Al additions cannot be underestimated and needs further attention as it results in much improved TWIP properties. It has been shown by Jung *et al.* (2008) that even small additions of Al facilitated the TWIP effect and they reported that the suppression of ϵ -martensite was achieved after addition of 1.5 mass-% Al to a Fe-15%Mn-0.6%C steel.

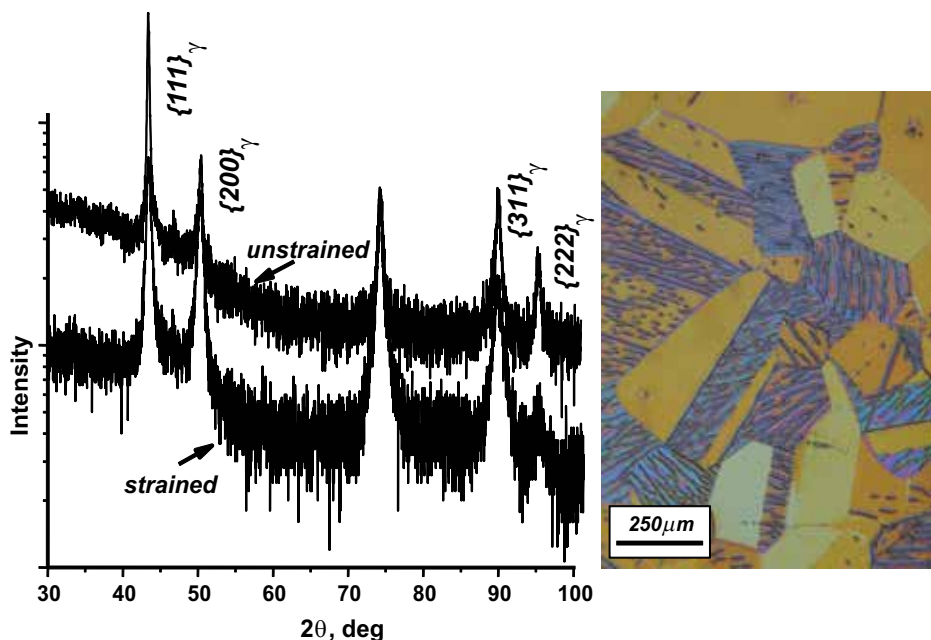


Fig. 7. XRD data for unstrained and strained Fe-18%Mn-0.6%C TWIP steel (left). The log scale was used for the intensity to emphasize the possible presence of small α' and ϵ diffraction peaks, which are clearly absent. Corresponding optical micrograph (right) obtained by color etching.

3. Mechanical properties of TWIP steel

TWIP steel research currently focuses on the influence of the alloy composition on the microstructure evolution during deformation and the resulting mechanical properties. In TWIP steel deformation is achieved by dislocation motion and twinning. The TWIP-effect is believed to be due mainly to a dynamic Hall-Petch effect. As the formation of mechanical twins involve the creation of new crystal orientations, the twins progressively reduce the effective mean free path of dislocations and increase the flow stress, resulting in a high strain hardening behavior. The best way to gain insight into the deformation behavior of TWIP steels is by TEM studies, as the twinning microstructure is very fine. Typical TEM observations are illustrated in figure 8. The dislocations are clearly widely dissociated. In addition, wide stacking faults are often found to be emitted by grain boundaries. At low strains, the dislocation density increases and the grain boundaries seem to be particularly effective source of isolated stacking faults. Therefore, the deformation mechanism of TWIP steel at low strains is considered to be planar slip and the formation of wide stacking faults. The onset of twinning requires multiple slip within deformed grains. At 20% strain, the higher dislocation density between the deformation twins clearly shows that twin boundaries act as effective barriers for dislocation movement. Frequently one twinning system is activated, together with dislocation glide. These high aspect ratio twins cross the entire grain. In addition, the twins are internally faulted. High resolution TEM clearly reveals their very narrow width. The twins are very thin and there seems to be a continuous nucleation of new deformation twins of increasingly smaller size. Consequently, the twin

volume fraction does not represent a large portion of the total volume. This observation seems to be in agreement with recent constitutive models of TWIP steels. The SFE plays an essential role in the occurrence of the TWIP effect. Although the role of deformation-induced twins will be mainly be discussed in the following paragraphs, it must not be forgotten that the rate of dislocation accumulation will automatically increase when an alloy has a low SFE, independently of twin formation, as the larger dissociation width will more effectively reduce the cross-slip and result in a higher rate of dislocation accumulation. As shown in figure 9, it is essential for the occurrence of the strain-induced twinning that the SFE be within a very specific range to observe mechanical twin formation. A very low SFE results in the strain-induced transformation to either α' or ε martensite. A low SFE, i.e. less than $<20\text{mJ}/\text{m}^2$, favors the $\gamma \rightarrow \varepsilon$ transformation. As the SFE is an essential parameter, there has been a considerable interest in determining its value for TWIP steels. There is still considerable uncertainty about the exact value of the SFE in Mn alloys, and whereas the theoretical evaluations agree on the range there is still considerable scatter in the reported SFE values. There are currently no experimental SFE available for most TWIP alloy systems, but a considerable number of theoretical calculations are available in the literature. From a theoretical point of view, the SFE is proportional to the f.c.c. and h.c.p. free energies difference, $\Delta G^{\gamma-\varepsilon}$. Interfacial energy, $\Delta G_{\text{surface}}^{\gamma-\varepsilon}$, and magnetic energy contribution, $\Delta G_{\text{magnetic}}^{\gamma-\varepsilon}$, to the stacking fault energy need to be taken into account as they may have a significant influence:

$$\gamma = \frac{1}{8 \cdot \sqrt{2/3}} \cdot (\Delta G_{\text{bulk}}^{\gamma-\varepsilon} + \Delta G_{\text{surface}}^{\gamma-\varepsilon} + \Delta G_{\text{magnetic}}^{\gamma-\varepsilon})$$

The interfacial energy can be taken as the coherent twin boundary energy and the energy of the twinning dislocations. The high value of the stacking fault energy at the f.c.c./h.c.p. transition temperature in austenitic stainless steels has been explained by consideration of magnetic effects.

Most authors report that stable, fully austenitic microstructures with TWIP properties have a SFE in the range of $20\text{mJ}/\text{m}^2$ to $30\text{mJ}/\text{m}^2$ (Schuman, 1971; Adler et al., 1986; Miodownik, 1998; Yakubtsov et al., 1999; Allain et al., 2004). Carbon additions are required to obtain a low SFE, but the addition of carbon is limited by the formation of M_3C carbide.

Some data on the effect of the carbon content in Fe-22%Mn-C alloys has been reported by Yakubtsov *et al.* (1999). They report that the SFE of a Fe-22%Mn alloy is approximately $30\text{mJ}/\text{m}^2$. Carbon additions less than 1 mass-% reduce the SFE to approximately $22\text{mJ}/\text{m}^2$. At higher carbon contents the SFE is reported to increase.

The critical stacking fault region to achieve twinning-induced plasticity is still unclear. Frommeyer *et al.* [3] indicate that whereas a SFE larger than about $25\text{mJ}/\text{m}^2$ will results in the twinning effect in a stable γ phase, a SFE smaller than about $16\text{mJ}/\text{m}^2$, results in ε phase formation. Allain *et al.* (2004) give a much narrower range. According to them the SFE should be at least $19\text{mJ}/\text{m}^2$ to obtain mechanical twinning. They mention that a SFE less than $10\text{mJ}/\text{m}^2$ results in ε phase formation. Dumay *et al.* (2008) mention that below a SFE of $18\text{mJ}/\text{m}^2$ twinning tends to disappear and is replaced by ε -platelets. They mention that a SFE of about $20\text{mJ}/\text{m}^2$ is needed for the best hardening rate. Jin *et al.* (2009) mention that a SFE value of $33\text{mJ}/\text{m}^2$ is required to obtain twinning in Fe-18%Mn-0.6%C-1.5%Al. Recently, Kim *et al.* (2010) measured that the SFE of Fe-18%Mn-0.6%C-1.5%Al TWIP steel was $30 \pm 10\text{mJ}/\text{m}^2$ (figure 10).

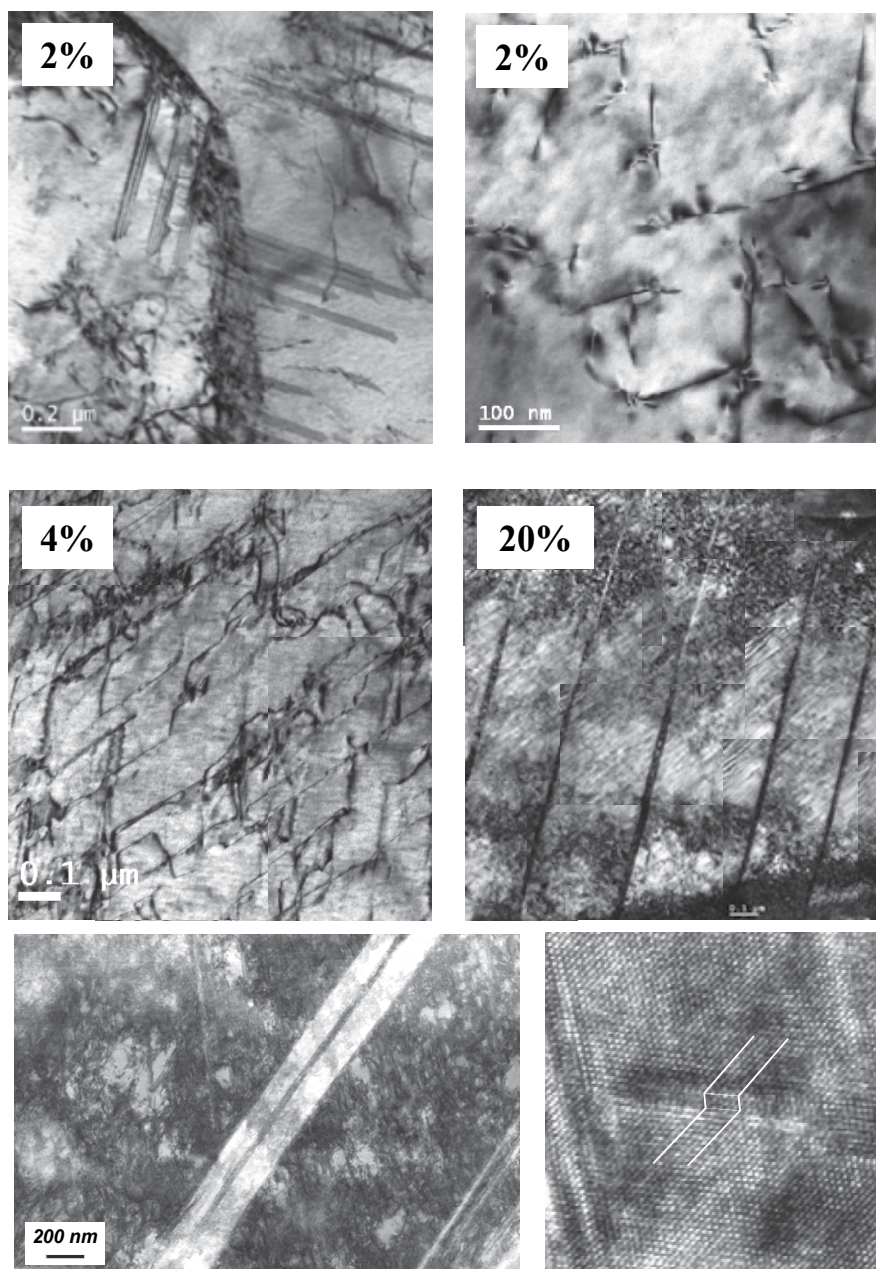


Fig. 8. (Top) TEM micrographs of TWIP steel after 2%, 4% and 20% of pre-straining showing that in the initial stages of deformation, the dislocation density increases and there is no formation of twins. In addition, some grain boundaries emit bundles of stacking faults. At higher strains, the early twins cross the entire grain. The twins often have an internal dislocation sub-structure. (Below, left) TEM micrograph of a TWIP steel deformed at high strains close to fracture. (Below, right) High resolution lattice image of a short secondary twin impinging on a larger primary twin located on the left hand side of the micrograph.

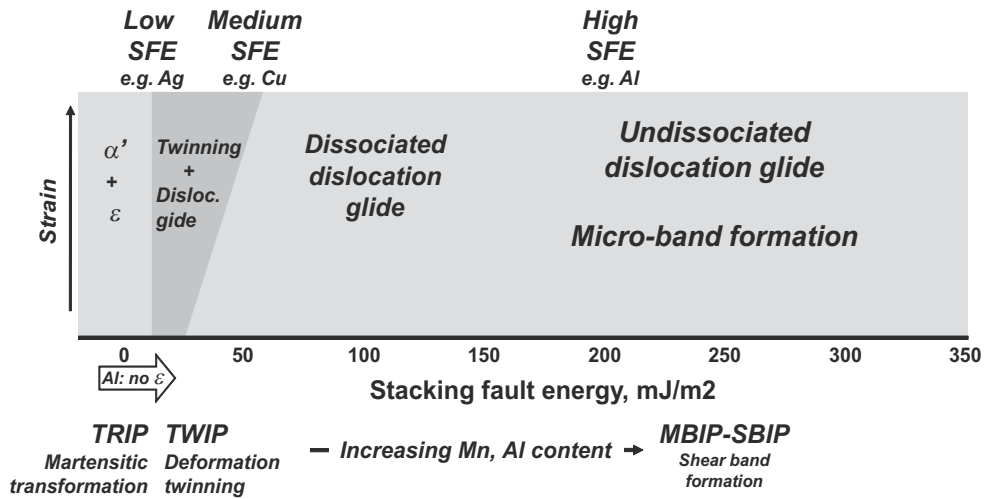


Fig. 9. Schematic showing the relation between SFE and the operating deformation mechanism in f.c.c. metals and alloys.

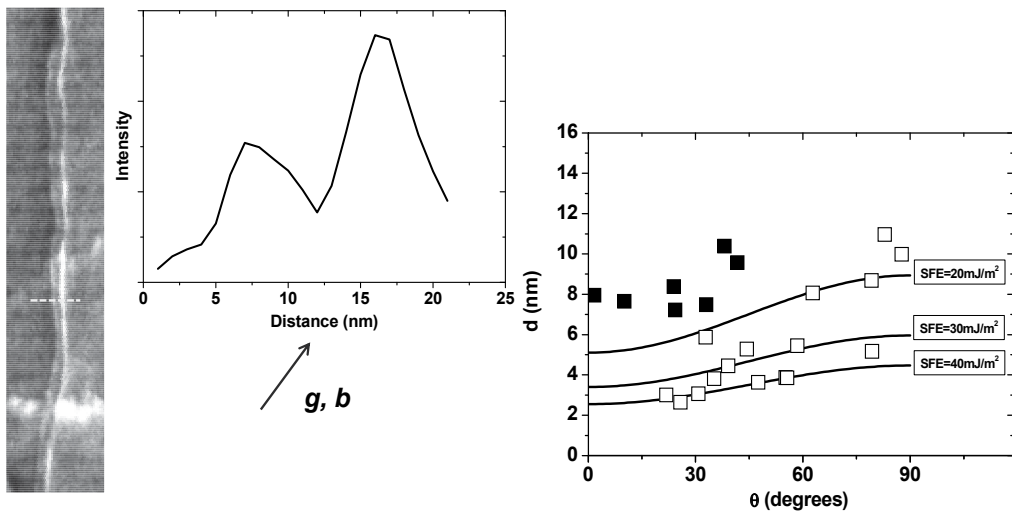


Fig. 10. (Left) Weak-beam dark field image of a dissociated dislocation on its glide plane. The SFE of this dislocation was 23.5mJ/m² based on four measurements of the partial dislocation separation on this micrograph. (Right) Partial dislocation separation is a function of the angle between the Burgers vector of the perfect dislocation and the dislocation line. The experimental points are consistent with a SFE of 30±10 mJ/m².

The effect of Al addition to TWIP steel has received much attention as it has resulted in TWIP steels with improved properties and a lower sensitivity to delayed fracture. Al increases the SFE, it also lowers the strain hardening resulting in TWIP steels with slightly lower tensile strengths. Al also very effectively suppresses the $\gamma \rightarrow \epsilon$ transformation. Instead, similar observations have been made for N. Both Al and N reduced the stacking fault formation probability. The SFE for Fe-Mn-Si-Al TWIP steel has been studied by Huang et al.

(2008). They have also studied the effect of 0.011-0.052% nitrogen on the SFE of Fe-20.24-22.57%Mn-2-3%Si-0.69-2.46%Al containing 100ppm carbon, by means of X ray diffraction. Although they do not report actual SFE values, their results indicate that both Al and N are favorable for the formation of twins as they increase the SFE and decrease the stacking fault formation probability. Similarly Dumay et al. (2008) calculate that Al increases the SFE by about +5 mJ/m² per added mass-% of Al, whereas Si is also found to increase the SFE by about +1 mJ/m² per mass-% of Si. Their results are not confirmed by the experimental measurements of Tian et al. (2008) who measured the SFE measured for Fe-25%Mn-0.7%C-Al steel with 1.16% to 9.77% of Al. They report a much smaller effect of Al on the increase of the SFE, about +1.4 mJ/m² per added mass-% of Al.

Although there is a general consensus that the stacking fault energy is an essential parameter, it is by no means proven that it is the single most important parameter controlling the TWIP mechanism. In fact, Wang et al. (2008) have remarked that it is rather surprising that only a very small difference in SFE of the order of 5-10 mJ/m² seemed to cause an apparently very sharp transition from strain-induced ϵ -martensite formation to strain-induced twinning. Recent experimental measurements on the nature of the stacking faults have resulted in the suggestions that ϵ -martensite formation and mechanical twinning is mediated by ESF and ISF respectively. Idrissi et al. (2009) studied the deformation mechanism of a two phase $\alpha+\gamma$ Fe-19.7%Mn-3.1%Al-2.9%Si steel. Deformation at 86°C and 160°C resulted in ϵ -martensite and twinning at low temperature, and exclusively mechanical twinning at the high temperature. At room temperature only ϵ -martensite was observed. They argue that this was due to the presence of extrinsic SFs at lower temperatures acting as precursors to ϵ -martensite formation and ISF at higher temperatures acting as twin precursors.

4. Strain-induced twinning

Figure 11 compares the structure and the energy of the various planar faults which can occur in f.c.c. metals and alloys. It illustrates the relation between the h.c.p. structure and the extrinsic stacking faults and the relation between the coherent twin and the intrinsic stacking fault.

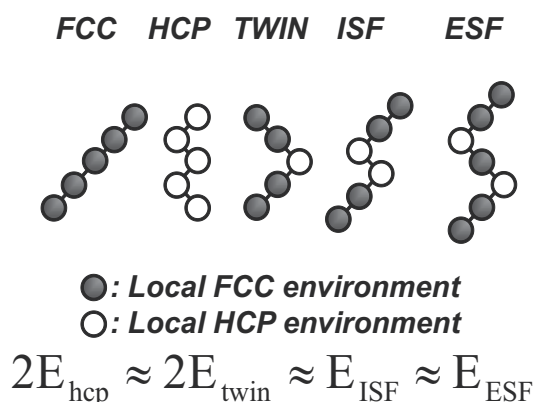


Fig. 11. Comparison of the structure and energy of the planar faults in f.c.c. metals and alloys.

The nucleation of twins in TWIP steel does not seem to be a homogeneous process. Instead, the nucleation stage in deformation twinning is closely related to prior dislocation activity, as the process always occurs after some amount of prior dislocation generation and dislocation-dislocation interactions on different slip systems. Twins are initiated in special dislocation configurations created by these interactions generally resulting in multi-layer stacking faults which can act as twin nuclei.

The effect of the deformation twinning process is twofold: the twinning shear makes a relatively small contribution to the deformation and the twin boundaries, which act as barriers to dislocation motion, reduce the dislocation mean free path (Meyers et al., 2001).

The most likely mechanism for strain-induced twinning (figure 12) has been proposed by Venables (Venables, 1961; Venables, 1964; Venables, 1974). In a first stage a jog is created on a dislocation by dislocation intersection. This jog dissociates in a sessile Frank partial dislocation and a Shockley partial dislocation. When the partial dislocation moves under the influence of an externally applied force, it trails an intrinsic stacking fault and it rotates repeatedly around the pole dislocations, generating a twin in the process.

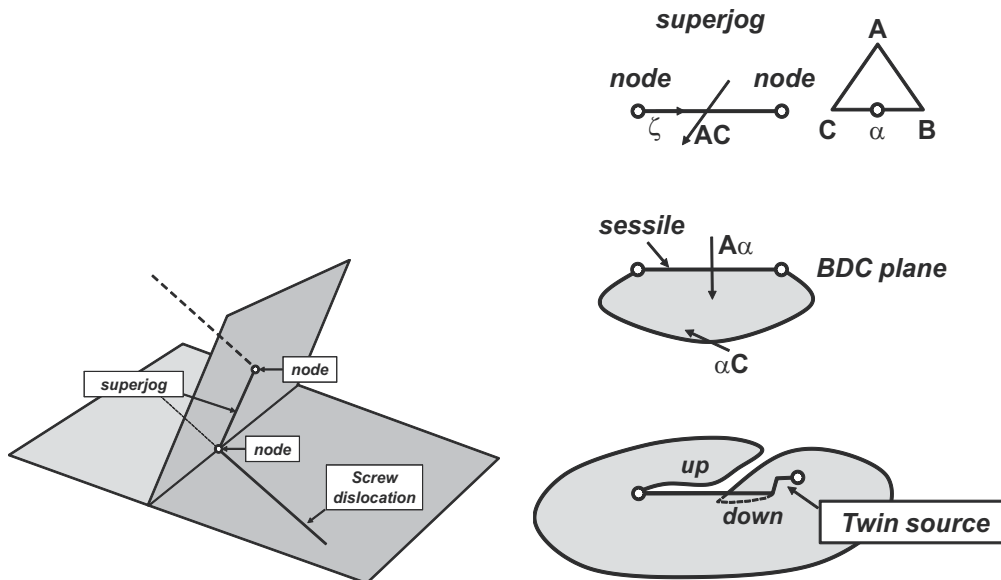


Fig. 12. Schematic showing the different stages in the Venables pole mechanism for strain-induced twinning.

As the stress increases, the volume fraction of twins increase steadily, continuously dividing grains into smaller units. It can be considered a dynamic Hall-Petch effect as the effective grain size is continuously being decreased.

Glide type deformation-induced twinning mechanisms have also been proposed. In glide mechanisms it is assumed that the passage of identical $a/6\langle 112 \rangle$ type partials on successive $\{111\}$ planes. This process requires very high stresses with specific orientations. Glide sources are therefore less probable source of twins, but Bracke et al. (2009), who studied twinning in Fe-22%Mn-0.5%C TWIP steel by means of TEM, support a model for the creation of a three layer stacking fault acting as a twin nucleus. They report a critical shear stress for twinning to be 89MPa.

In the absence of preferred crystallographic orientations and assuming the orientation factors for twinning and slip are equal, the transition from slip only deformation to slip and twinning deformation occurs when the slip stress reaches the twinning stress. As there is no agreed model for twin formation, the stress required to nucleate a twin is difficult to compute without making some essential simplifications. In practice, the growth of a twin requires a much lower stresses than what is usually computed by models. Hence nucleating stresses must be due to local stress concentration, as externally applied tensile stresses result in homogeneous stresses too low to nucleate twins. The twinning stress increases with increasing SFE, and the stress required to nucleate a twin is related to the intrinsic stacking fault energy in a quadratic or linear manner (Muir et al., 1968). Byun (2003) derived the following equation for the twinning stress, assuming that partial dislocation breakaway was the mechanism for the initiation of deformation twinning:

$$\tau_T = 6.14 \cdot \frac{\gamma_{ISF}}{|b_p|}$$

The equation is illustrated in figure 13 for SFE = 20mJ/m².

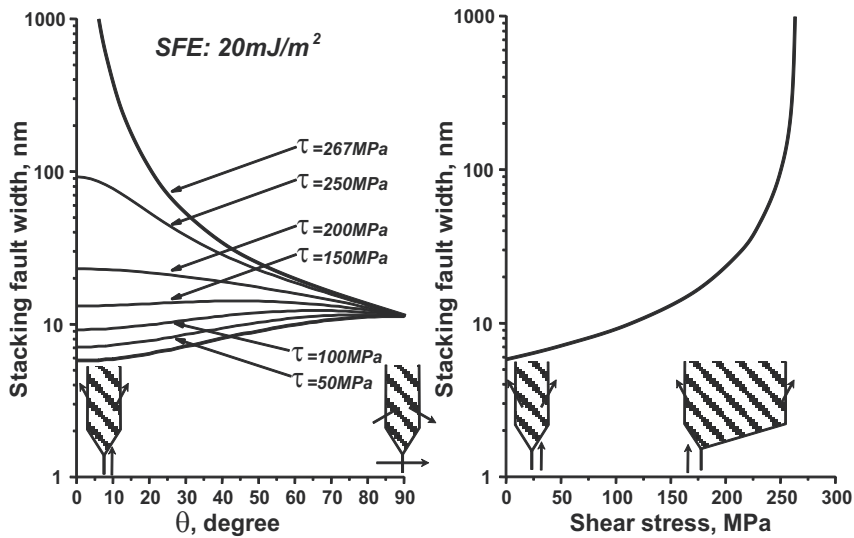


Fig. 13. Illustration of the Byun “infinite separation” approach for the determination of the twinning stress. This approach assumes that for dislocations close to the screw orientation, partial dislocation break-away is possible and that this process initiates deformation-induced twinning. For a SFE of 20mJ/m² a tensile stress of approximately 820MPa is required. This is achieved at 20-25% of strain, i.e. a much higher stress than is needed to experimentally observe twinning.

Meyers et al., (2001) proposed a model where twins are formed at grain boundaries and he reports the following equation for the twinning stress:

$$\sigma_T = M \cdot \left(\frac{n \cdot l \cdot E}{M \cdot A_0} \right)^{\frac{1}{1+m}} \cdot \dot{\epsilon}^{\frac{1}{1+m}} \cdot e^{\frac{Q}{(m+1) \cdot R \cdot T}}$$

The parameter m relates the dislocation velocity to the applied shear stress. n is the number of dislocations in the grain boundary pile up causing a local stress increase. The parameter l is the distance between the dislocation source and the grain boundary. E is Young's modulus. Q is the activation energy for dislocation motion. M is an orientation factor.

The grain size D may play a role in the value of the twinning stress and larger grains tend to expand the twinning domain:

$$\sigma_T = \sigma_{T0} + \frac{k_T}{\sqrt{D}}$$

The k_T value is usually much larger than the k_y value for dislocation slip in the standard Hall-Petch relation.

Sevillano (2009) has recently proposed a strain-hardening model for TWIP steels by considering that its behavior is similar to that of a plastically heterogeneous composite. He argues that the observation of an important Bauschinger effect, the back stress contributing as much as half of the total stress, by Bouaziz et al. (2008) is due to the fact that the simultaneous deformation of the grains and their twinned parts requires the presence of a forward internal stress operating on the twin and a backward internal stress operating on the untwinned matrix. This is due to the fact that the twins must share similar strain components with their matrix. The twins must however have an important contribution to the strength, which can only be based on their small nanometer thickness. Bouaziz *et al.* (2008) however link the back-stress to dislocations of a given slip system being stopped at grain and twin boundaries and developing a stress which prevents similar dislocations from moving ahead.

Jin et al. (2009) have studied the strain hardening of Fe-18%Mn-0.6%C-1.5%Al in detail and report that at large strains the deformation twinning rate greatly decreases deformation twins with different growth directions and that the amount of twinned volume is controlled not by the lateral growth of the deformation twins, but by the increase in the number of new deformation twins.

Various models have been proposed to model the TWIP-effect in high Mn steel in order to understand the parameters controlling their pronounced work-hardening. Bouaziz et al. (2001) and Allain et al. (2004) were probably the first to attempt to model the effect of the strain-induced twinning on the work-hardening of TWIP steel on a physical basis using the Kocks-Mecking (Kocks & Meckings, 1981) approach. In their description the twins act as impenetrable obstacles. The model computes uniaxial tensile stress-strain curves on the basis of the evolution of the dislocation density and the twin volume fraction. Their description of the evolution of the dislocation density is given by:

$$\frac{d\rho}{d\gamma} = \frac{1}{b} \cdot \left(\frac{1}{d} + \frac{1}{t} + k \cdot \sqrt{\rho} \right) - f \cdot \rho$$

$$t = 2 \cdot e \cdot \frac{1-F}{F}$$

The twin volume fraction is given by:

$$F = 1 - e^{-m \cdot \varepsilon}$$

The SFE enters indirectly in the Bouaziz-Allain model through the value of the m -parameter. Applying their model to Fe-22%Mn-0.6%C TWIP steel, they found the following

values for the main parameters: $k=0.011$, $f=3$ and $m=1.95$. Interestingly, k and f are exactly the same as for AISI 409 and 304L grades. The same authors described an extension to their original model using a visco-plastic description and a homogenization law to deal with a randomly oriented polycrystal. These results support the fact that the total volume fraction of the twins is very low and that plastic deformation is mainly achieved by dislocation glide. In contrast to recrystallization twins, deformation twins tend to be very thin. The twins are estimated to be 15nm thick. Allain et al. (2004) also proposed a mechanism for the twinning behavior of the deformation-induced twins whereby in a first stage a few tens of nanometer thick twin will move until it reaches a strong boundary, a grain boundary or a twin boundary. In the second stage the twins thicken. They also notice that two twinning systems are sequentially activated in most grains. The first twins develop across the entire grain. The twins of second system develop between the primary twins and are much shorter and thinner.

Shiekhelsouk et al. (2009) developed a very detailed physically-based, micro-mechanical model incorporating elasto-visco-plasticity, to obtain a constitutive model for Fe-22%Mn-0.6%C TWIP steel using a randomly oriented representative volume element of 800 grains. They report that the twinned volume fraction is dependent on the grain orientation, and is less than 0.08 for a macroscopic strain of 0.4.

Kim *et al.* (2010) used the Kubin-Estrin model (1986) to compute the strain hardening from the evolution of the coupled densities of the mobile dislocations, ρ_m , and immobile forest dislocations, ρ_f . In this model the two dislocation densities saturate at large strains and two dislocation densities are coupled via terms which simultaneously appear as annihilation terms in the evolution equation for ρ_m and as production terms in the evolution equation for ρ_f . The following set of differential equations was used:

$$\frac{d\rho_m}{d\varepsilon_g} = M \left[\frac{C_1}{b^2} \left(\frac{\rho_f}{\rho_m} \right) - C_2 \rho_m - \frac{C_3}{b} \rho_f^{1/2} \right]$$

$$\frac{d\rho_f}{d\varepsilon_g} = M \left[C_2 \rho_m + \frac{C_3}{b} \rho_f^{1/2} - C_4 \rho_f \right]$$

In these equations C_1 is a production term, with forest obstacles acting as pinning points for fixed dislocation sources. C_2 takes into account the mobile density decrease by interactions between mobile dislocations. C_3 describes the immobilization of mobile dislocations with a mean free path proportional to $\rho_f^{1/2}$, assuming a spatially organized forest structure. C_4 is associated with the rearrangement and annihilation of forest dislocations by climb or cross-slip.

The Bouaziz et al. (2001) expression for the twin spacing was modified to take into account the fact that as a set of parallel planar twins of identical thickness cross a grain, the areal fraction and the volume fraction of twins are the same means and the factor of 2 should not be considered, hence:

$$t = e \frac{1-F}{F}$$

where t is the average twin spacing, e is the average twin thickness which is independent of strain, and F is the twin volume fraction.

Combining the three previous equations, the dislocation density evolution was expressed as follows:

$$\frac{d\rho}{d\varepsilon_g} = M\left[\frac{1}{b}\left(\frac{1}{d} + \frac{1}{t} + k\sqrt{\rho}\right) - k_2\rho\right] = M\left[\frac{1}{b}\left(\frac{1}{d} + \frac{1}{e} \cdot \frac{F}{1-F} + k\sqrt{\rho}\right) - k_2\rho\right]$$

The twinning-related term is expected to result in a remarkable increase of the strain hardening behavior compared to the classical strain hardening behavior. A modification to these equations taking into account dynamic strain aging (DSA) was also included. The result for a Fe-18%Mn-0.6%C-1.5%Al TWIP steel is shown in figure 14. The model correctly predicts that the strain hardening $d\sigma/d\varepsilon$ has a more or less flat behavior in the intermediate strain levels, rather than continuously decreasing as it occurs in the case of high SFE metals. This sustained strain hardening level is due to the gradual decrease in the dislocation mean free path.

Dini et al. (2010) analyzed the dislocation density evolution in Fe-31%Mn-3%Al-3%Si TWIP steel during straining by means of XRD. They calculate a large twin volume fraction of 0.56 at a strain of 0.4. They report a value of 18nm for the twin lamella thickness.

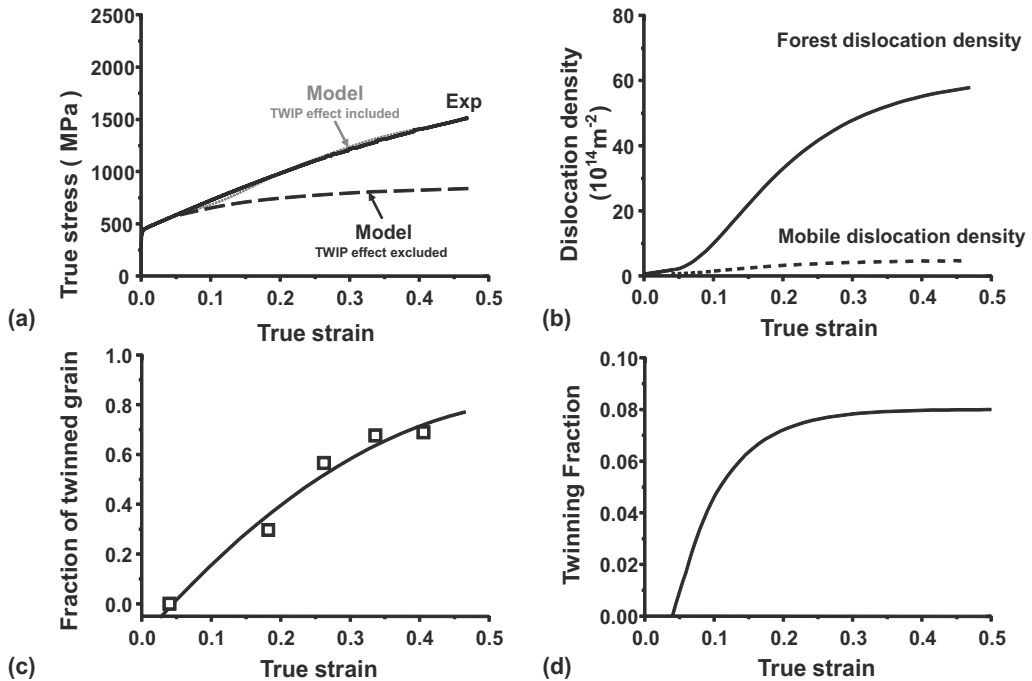


Fig. 14. (a) Comparison of the experimental true stress-true strain curves and the model calculation. (b) Mobile and forest dislocation density for twinned grains as a function of true strain. (c) The average volume fraction of twins inside a twinned grain as a function of true strain. (d) Fraction of twinned grain as a function of true strain.

5. Forming properties

The normal anisotropy and the strain hardening are usually considered the most important sheet forming properties. The normal anisotropy of Fe-18%Mn-0.6%C-1.5%Al TWIP steel, as measured in the RD, TD and at 45° to RD is illustrated in figure 15. The normal anisotropy

value is relatively low, but this is expected to have a relatively low impact on the forming performance because of the high strain hardening coefficient, as illustrated in figure 16. The strain hardening can be seen to increase steadily up to a strain of approximately 0.25. At that stage the strain hardening assumes a constant value of about 0.5. Comparison of the data in figure 16 and the results of the model calculations shown figure 14(d) reveal that the strain hardening is closely related to the formation of strain-induced twins. It can also be seen that the strain hardening reaches a constant value at a strain of approximately 0.25, which coincide with the saturation of the twin volume fraction.

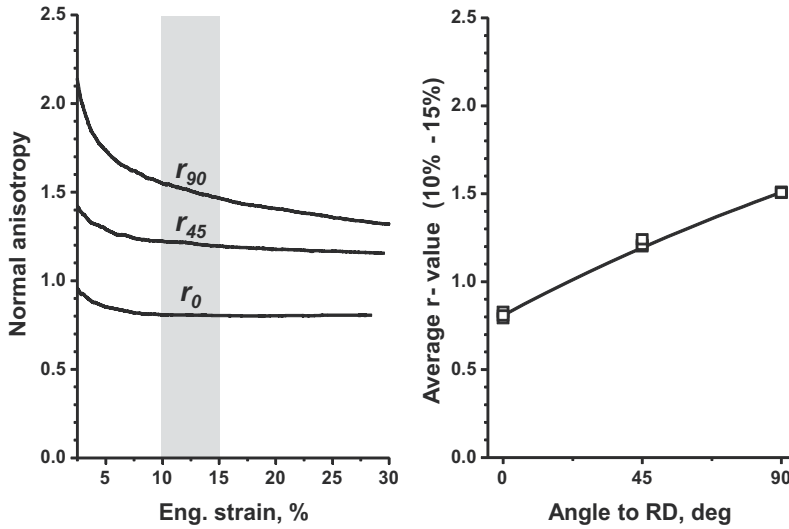


Fig. 15. Strain dependence of the normal anisotropy for tensile samples taken at 0°, 45° and 90° to the rolling direction (left). Planar anisotropy in the 10%-15% strain range (right).

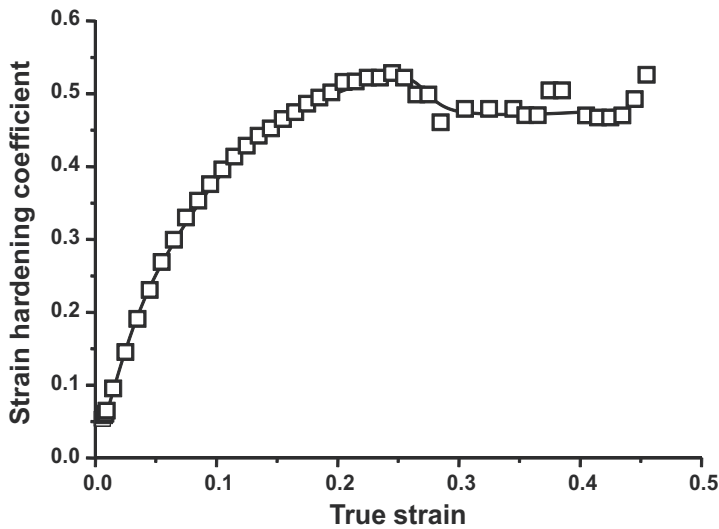


Fig. 16. Strain hardening of Fe-18%Mn-0.6%C-1.5%Al TWIP steel.

The stretch forming properties of TWIP steel are considerably better than those of the other AHSS of similar strength level. The low r -value and the negative strain rate sensitivity results in low values when the starting hole is made using a method that leads to considerable deformation of the hole edge, such as hole punching. This is illustrated in figure 17.

Having said this, the actual forming performance of TWIP steel has proven to be excellent in practice. This is illustrated by the example of the shock absorber housing in figure 18.

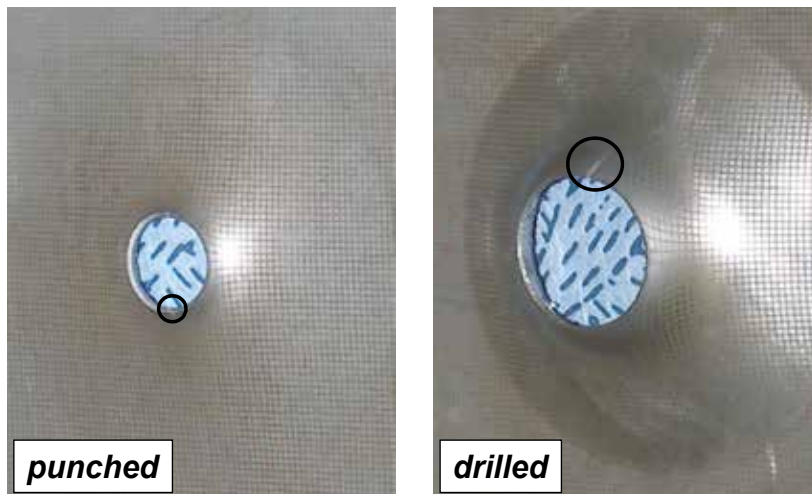
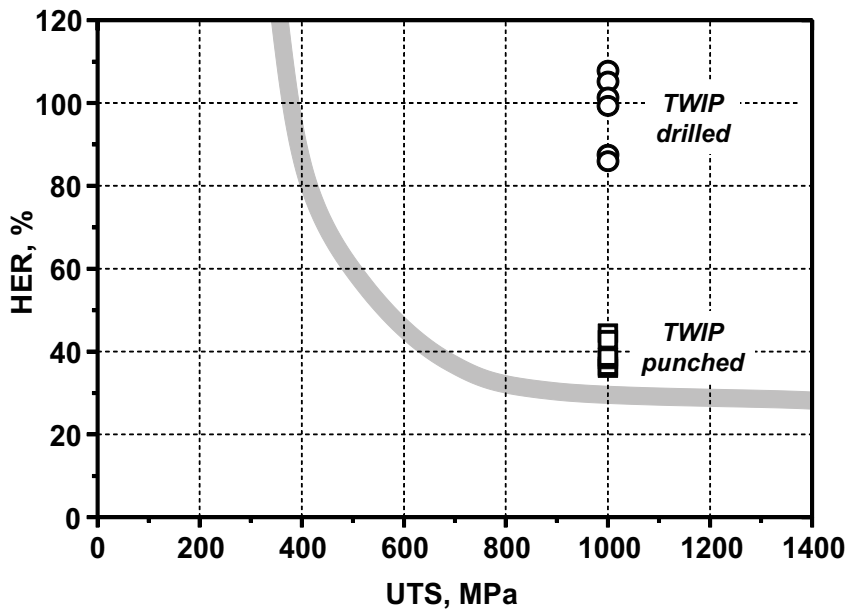


Fig. 17. HER for TWIP steel compared to the HER-UTS relation observed for a large number of automotive materials indicated by the gray band (top). Illustration of the difference in TWIP steel hole expansion performance for a low quality punched hole (below, left) and a high quality drilled hole (below, right).

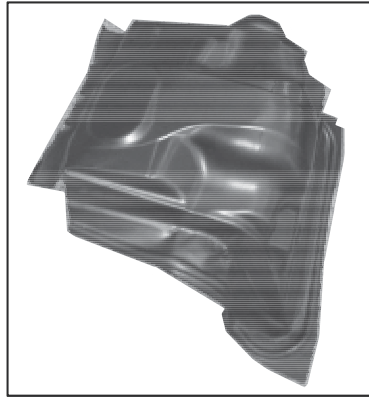


Fig. 18. Example illustrating the use of TWIP steel for the press forming of an automotive shock absorber housing.

6. High strain rate properties

Figure 19 compares the dynamic energy absorption of different types of automotive steels when tested at a strain rate of 10^3s^{-1} . High strain rate properties of TWIP steels have been reported by Frommeyer et al. (2003) for a Fe-25%Mn-3%Si-3%Al-0.03%C TWIP steel where the formation of α' and ϵ is fully suppressed, even after straining. This TWIP steel has a moderate strain hardening (Yield strength: 280MPa; Tensile Strength: 650MPa) and dislocation glide has been reported as the main deformation mechanism. At lower temperatures the amount of twinning increases. Extensive twin formation occurs during high strain rate deformation, and no brittle fracture is observed even at a temperature as low as -200°C .

Ueji et al. (2007) studied the high strain rate deformation of Fe-31%Mn-3%Si-3%Al TWIP steel for a grain size in the range of $1.1\mu\text{m}$ - $35.5\mu\text{m}$. In contrast to the observation made for ferritic steels there is still a large elongation at small grain sizes. They explain their observations by the limited dynamic recovery in TWIP steels due to a low SFE. The elongation is only slightly smaller at higher strain rates 10^{-3} to 10^{+3}s^{-1} .

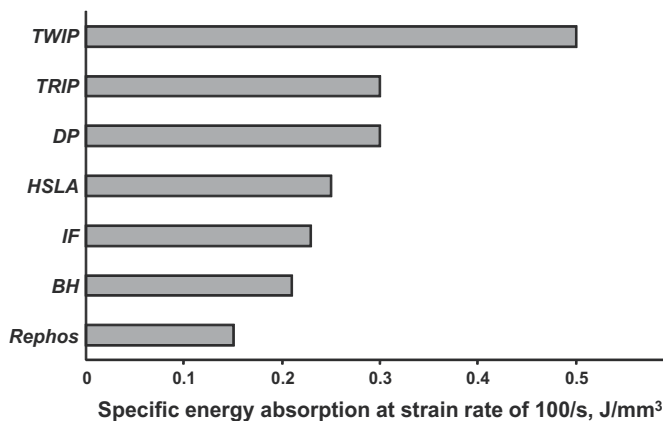


Fig. 19. Comparison of the energy absorption, in J/mm^3 , for common types of automotive steels during high strain deformation (Strain rate: 10^3s^{-1}).

Sahu et al. (2010) have studied the mechanical behavior of two Fe-24%Mn-0.5%Si-(0.11-0.14)%C TWIP steels with 0.91% and 3.5% Al additions in the strain rate range of 10^{-4} -4000 s^{-1} . The transformation of austenite to martensite is reported to take place up to a strain rate of $10^3 s^{-1}$. The TWIP steel alloyed with 3.5% Al had a higher stability, and the transformation of this TWIP steel was limited to the strain rate range of $10^{-3} s^{-1}$ to 720 s^{-1} . Irrespective of the Al content, the transformation of the austenite phase is suppressed during high strain rate deformations due to the adiabatic heating of the sample. Based on the observation of serrated grain boundaries, they also argue that dynamic recrystallization may be taking place during the high strain rate tests.

7. Strain localization

Room temperature dynamic strain aging (DSA) occurs in the most commonly studied carbon-alloyed TWIP steels Fe-22%Mn-0.6%C and Fe-18%Mn-0.6%C. DSA-related type A serrations are shown in figure 20. It is very likely due to the presence of C-Mn complexes, which re-orient in the presence of dislocations via a single hop diffusion mechanism. This mechanism is similar to a model recently developed by Curtin et al. (2006). This re-orientation does not require long range diffusion, only a single diffusional hop of the interstitial carbon in the C-Mn complex to achieve a suitable orientation with respect to the strain field of the partial dislocation. The fast dislocation core diffusion has been proposed as an alternative, to explain this widely observed room temperature DSA (Chen et al., 2007).

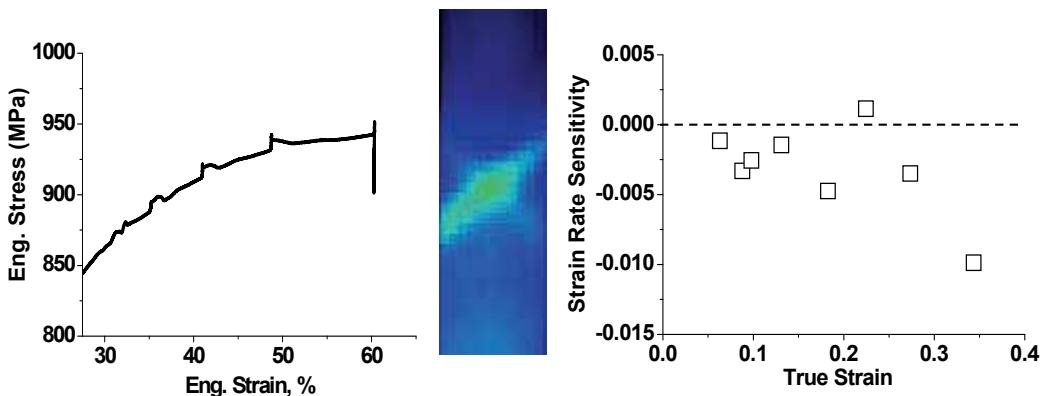


Fig. 20. Direct evidence for DSA in TWIP steel: type A serrations due to the passage of individual PLC bands (left), IR thermography of an isolated PLC band (middle), strain rate sensitivity measurement showing negative values (right).

Detailed DSA studies have been carried out by Chen et al. (2007), Kim et al. (2009) and Zavattieri et al. (2009) for Fe-17-18Mn-0.6%C-1-1.5%Al have analyzed the PLC band properties. They report that the band velocity decreases with strain and that the band strain rate is 15-100 times the applied value. Localization may in principle result in press forming difficulties, but the occurrence of PLC bands in uni-axial tensile testing has not been reported to lead to the poor press forming performance for Fe-22Mn-0.6C TWIP steel (Allain, 2008). This is very likely related to the fact that the occurrence of DSA-related surface defects are stress state and strain rate dependent. Based on data for the critical strain of Bracke (2006) the schematic in figure 21 is proposed.

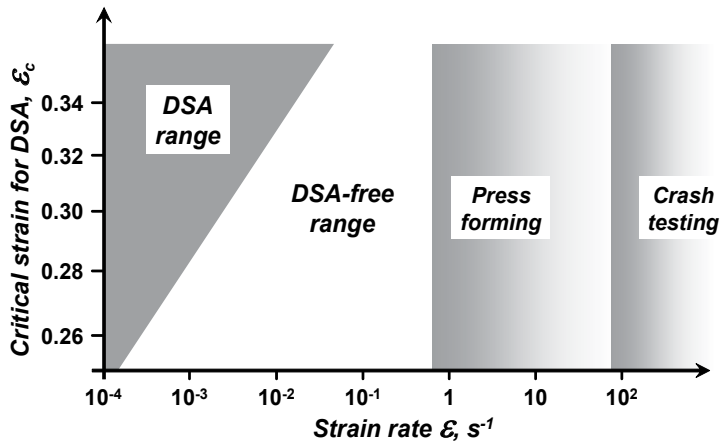


Fig. 21. Schematic showing the approximate strain rate and critical strain region for DSA.

The other aspects of DSA should however not be overlooked, as DSA is related to a negative strain rate sensitivity and hence a very limited post-uniform elongation, as illustrated in figure 22.

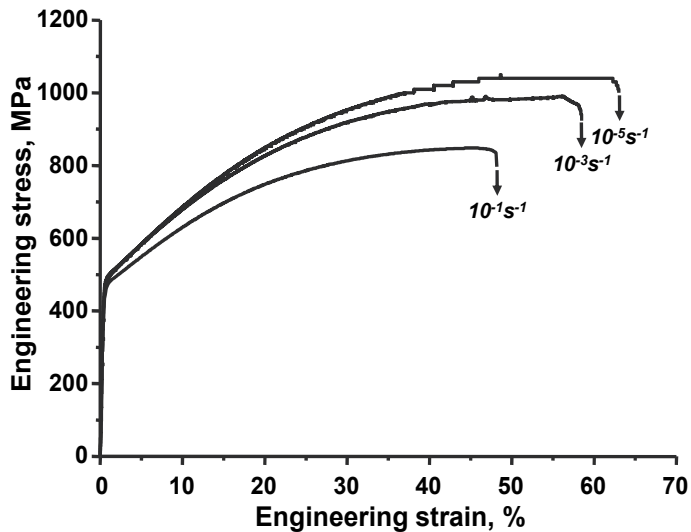


Fig. 22. Stress-strain curves for Fe-18%Mn-0.6%C-1.5%Al TWIP steel clearly showing the negative strain rate sensitivity of this material: the flow stress decreases with increasing strain rate. Note the suppression of the serrations when the material is tested at higher strain rates.

In carbon-alloyed f.c.c. alloys the room temperature DSA cannot be explained by long range diffusion of carbon. Instead it results from the presence of point defect complexes which can re-orient themselves in the stress field of dislocations or in the stacking faults. Possible defect complexes in high Mn TWIP steels are the following: carbon-vacancy complex, carbon-carbon complex, and carbon-Mn complex. The two first complexes are unlikely due to the very low vacancy concentration and the strong repulsive carbon-carbon interaction.

The carbon-Mn complexes are very likely due to the strong attractive interaction between interstitial carbon and the substitutional Mn. The most likely carbon-Mn complex in Fe-Mn-C TWIP steel has one carbon atom and one Mn atom (figure 23).

Serrated stress-strain curves can be avoided by increasing the Al content as illustrated in figure 24. As Al additions are known to increase the stacking fault energy, this data seems to suggest that the main interaction giving rise to the flow localization is the interaction between the C-Mn point defect complexes and the stacking faults. A similar

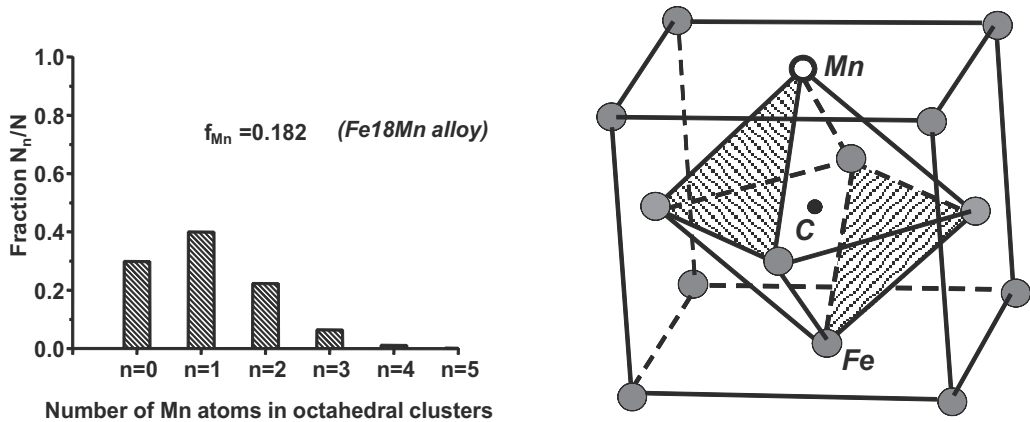


Fig. 23. Distribution of the various types of C-Mn complexes in a Fe-18%Mn-0.6%C TWIP steel (left). The most likely complex is a octahedral cluster containing one carbon atom and one Mn atom (right).

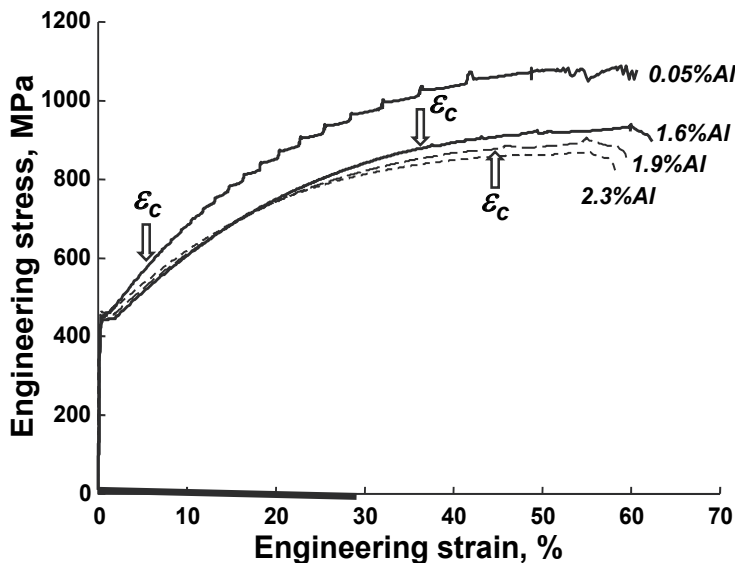


Fig. 24. Stress-strain curves Fe-18%Mn-0.6%C TWIP steel with increasing Al alloying additions. The additions delay the onset of the serrations, and at 2.3% Al no serrations are observed.

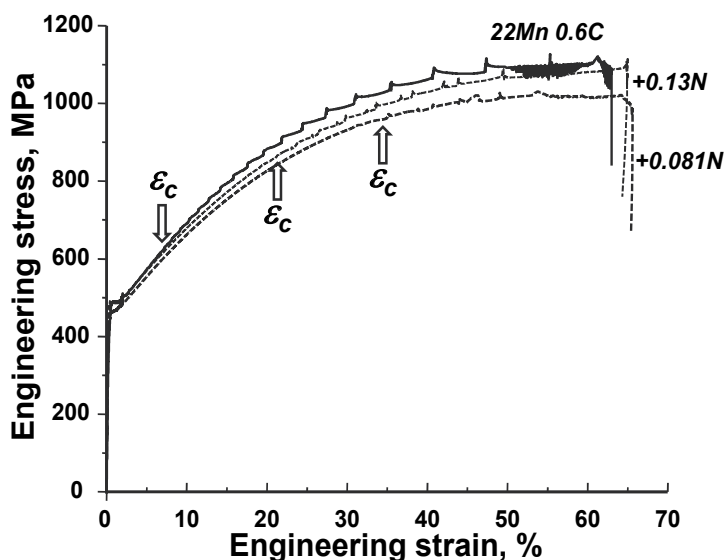


Fig. 25. Influence of N alloying additions on the stress-strain curve of Fe-22%Mn-0.6%C TWIP steel.

effect is expected from nitrogen additions. At nitrogen contents lower than 0.3 mass-%, the SFE increases. The effect of nitrogen additions on the suppression of the serrations is illustrated in figure 25.

8. Delayed fracture

The need to study delayed fracture remains important. The phenomenon is very likely related to hydrogen induced cracking and it will require further fundamental analysis as delayed fracture has been identified as the major problem for Fe-22%Mn-0.6%C TWIP steel. The effect appears readily in deep drawn cup as deep edge cracks a certain time after the cup has been drawn. The edge of a fully drawn cup is subjected to residual tensile hoop stresses. The exact mechanism for delayed fracture has not yet been identified, but Kim et al. (2008) have suggested that it is related to martensitic transformation in the presence of residual stresses and possibly hydrogen. They investigated the influence of the $\gamma \rightarrow \alpha'$ and $\gamma \rightarrow \varepsilon$ martensitic transformations formed during the tensile testing in Fe-18%Mn-0.6%C and Fe-18%Mn-0.6%C-1.5%Al TWIP steel. The Al-alloyed TWIP steel remained free of martensite. Both TWIP steel contained martensite after cup drawing however, but the amount of martensite was slightly less for the Al alloyed TWIP steel. The suppression of delayed fracture by Al-additions is illustrated in figure 26. This may be due to the fact that, as martensitic transformations require the ease of formation of planar faults, an increase of the SFE resulting from Al-additions will limit the nucleation of a martensite phase which may be embrittled by the presence of small amount of solute hydrogen.

Jung et al. (2008) compared the hydrogen embrittlement of TRIP and TWIP steel after cathodic hydrogen charging. They report that Fe-15%Mn-0.45%C-1%Al and Fe-18%Mn-0.6%C TWIP steels, with and without Al-additions, contained less hydrogen and were much more resistant to embrittlement than TRIP steel after U-bend and cup drawing tests.

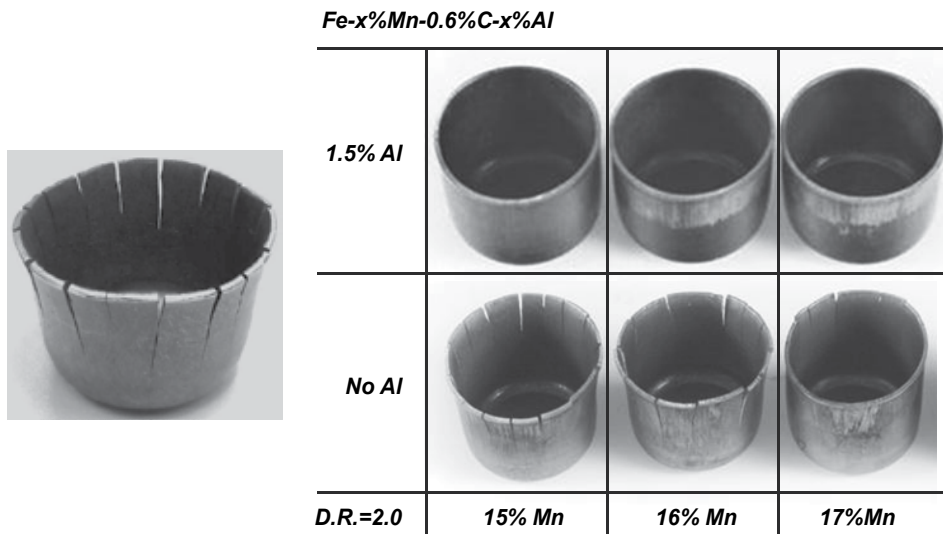


Fig. 26. Example of delayed fracture deep drawn Fe-22%Mn-0.6%C TWIP steel (Left). Suppression of delayed fracture in deep drawn Fe-(15-17)%Mn-0.6%C TWIP steel by alloying additions of 1.5% Al (Right).

9. Fatigue properties

The performance of a 1160MPa tensile strength Fe-22%Mn-0.52%C TWIP steel during cyclic loading has been reported to be influenced by the pre-straining (Niendorf et al., 2009). A significant longer fatigue life was achieved when the TWIP steel is pre-deformed. This is explained by the formation of new twins during the pre-deformation and their evolution hindering the dislocation motion. This leads to a stable deformation response in cyclic loading and a longer fatigue life. When tested in the as-received state, the dislocation density decreases and the existing twins widen, leading to a cyclic softening due to a lack of dislocation-twin interaction, and a lack of nucleation of new twins. Hamada et al. (2009) have studied the high cycle fatigue behavior of Fe-22.3%Mn-0.6%C (SFE: 26 mJ/m²), Fe-17.8%Mn-0.6%C with a 200ppm Nb addition (SFE: 23 mJ/m²) and Fe-16.4%Mn-0.29%C-1.54%Al (SFE: 19 mJ/m²) TWIP steels were studied in flexural bending fatigue using a zero mean stress. They report that the three steels had the same 2x10⁶ cycles fatigue stress limit of 400MPa, i.e. well above the yield stress of the steels. The ratio of fatigue limit to tensile strength was in the range of 0.42-0.48, i.e. common to austenitic steels. No twins or ϵ -martensite were formed during the fatigue test, but fatigue cracks nucleated at intersections of slip band and grain boundaries and annealing twin boundaries.

10. Ultra-fine grained TWIP steel

Ultra-fine grained (UFG) ferritic steels are characterized by a combination of ultra-high strength and limited elongation. This does not seem to be the case for UFG austenitic TWIP steel. Ueki et al. (2007) have reported that UFG Fe-31%Mn-3%Al-3%Si TWIP steel retained a considerable ductility in contrast to UFG Al or IF steel. Bouaziz et al. (2009) have studied the properties of nano-structured Fe-22%Mn-0.6%C TWIP steel obtained by a combination of

cold deformation and recovery-annealing. The process decreases the dislocation density and retains the very dense nano-scale twin microstructure, leading to very high yield stresses and adequate elongations.

11. TWIP steel industrialization

The considerable interest in high Mn TWIP steels is due to their superior mechanical properties. Compared to standard low carbon steels, high Mn TWIP steels have high carbon and Mn contents. When Al is added the content also tends to be high. It is clear that the cost issue will be important in addition to remaining technical problems. Ferro-Manganese is reportedly rich in P which will require more attention during steelmaking. Whereas TWIP steels have demonstrated their formability for complex automotive parts despite their high strength, their behavior in stretch forming, in particular during hole expansion, is not as good as one may have expected, when compared e.g. to that of IF steel. This is mainly due to the absence of post-uniform strain, which is a direct consequence of the low strain rate sensitivity. The application of Zn and Zn alloy coatings by hot dip galvanizing requires special care as there are clear indications that a MnO surface layer is formed during continuous annealing and processing in a hot dip galvanizing line. This MnO surface layer will very likely influence coating adhesion, and electrolytic Zn deposition will very likely be the preferred route for coating TWIP steels. Both HDG and electrolytic coating of TWIP steel have been attempted and examples of defect-free Zn coatings are shown in figure 27.

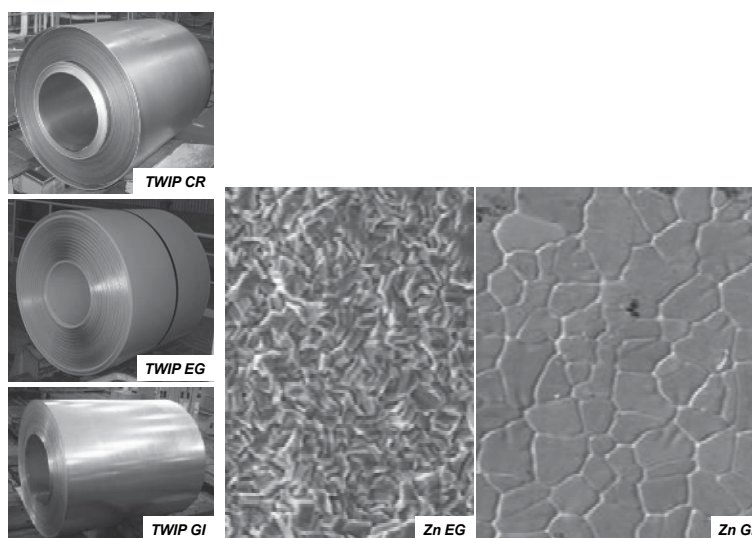


Fig. 27. Examples of cold rolled TWIP steel coils. Electrodeposited and hot dip pure Zn coating quality on TWIP steel showing the absence of bare spots.

12. Conclusion

The present review of the properties of high Mn Twinning-Induced Plasticity (TWIP) steels clearly shows that the Fe-(15-30)%Mn alloy system with additions of C, Al and/or Si to fully

stabilize the f.c.c. phase and control the SFE within the narrow range of 15-30 mJ/m², results in steels with very wide range of mechanical properties, making this relatively new class of steels of interest for many automotive applications. The physical metallurgy of TWIP steels is still relatively limited and the following aspects need to receive an in depth analysis: the twinning mechanism, texture evolution, and delayed fracture. The determination of the twinned volume fraction remains a challenge and is needed to evaluate the different models proposed to explain the mechanical behavior of TWIP steels. The distribution of the twinning as it related to the formation of texture components must also be given a clear analysis. The mechanism of delayed fracture is still not known. In particular the complex interaction of factors related to transformation, residual stresses, and the influence of hydrogen has made the issue particularly difficult to address. Having said this it is clear that Al-added TWIP steels may be considered immune to the problem.

13. References

- Grässel O., Frommeyer G., Derder C., Hofman H. (1997), *J. Phys. IV France*, vol.60, 383
- Grässel O., Kruger L., Frommeyer G., Meyer L. (2000), *International Journal of Plasticity*, 16, 1391
- Frommeyer G., Brux U., Neumann P. (2003), *ISIJ International*, vol. 43, No. 3, 438-446
- Prakash A., Hochrainer T., Reisacher E., Riedel H. (2008), *Steel Research International*, 79, No.8, 645
- Schuman H. (1971), *Neue Hutte* 17, 605-609
- Remy L., Pineau A. (1977), *Mat. Sci. Eng.*, 28, 99
- Kim T.W., (1993), *Mat. Sci. Eng. A*, 160, 13
- Kim Y.G., Kim T. W., Hong S. B. (1993), *Proceedings of the ISATA*, Aachen, Germany, 1993, 269
- Allain S. (2004), Ph.D. INPL, Nancy, France
- Kim S.K., Choi J., Kang S. C., Shon I. R., Chin K. G. (2006), *POSCO Technical Report*, vol. 10, No.1, 106-114
- Witusiewicz V.T., Sommer F., Mittemeijer E.J. (2004), *J. Phase Equilib. Diff.*, 25(4), 346-354
- Jung J.K., Lee O. Y., Park Y.K., Kim D.E., Jin K. G., Kim S.K., Song K.H. (2008), *J. Korean Inst. Met. & Mater.*, vol. 46, No.10, 627-633
- Miodownik A.P. (1998), *Z. Metallkunde* 89, 840-846
- Adler P.H., Olson G.B., Owen W.S. (1986), *Metallurgical Transactions A*, vol. 17, 1725
- Alain S., Chateau J.-P., Bouaziz O., Migot S., Guelton N. (2004), *Materials Science and Engineering A* 387-389, 158-162
- Yakubtsov I.A., Airapour A., Perovic D.D. (1999), *Acta Materialia*, Vol. 47, No. 4, 1271-1279
- A.Dumay, J.-P. Chateau, S. Allain, S. Migot, O. Bouaziz (2008), *Materials Science and Engineering A*, 483-484, 2008, 184-187
- Jin Jae-Eun, Lee Young-Kook (2009), *Materials Science and Engineering A*, 527, 157-161
- Kim Jinkyung, De Cooman B.C., Unpublished results
- Huang B.X., Wang X.D., Wang L., Rong Y.H. (2008), *Metallurgical and Materials Transactions A*, vol. 39A, 717
- Tian X., Li H., Zhang Y. (2008), *J. Mater. Sci.*, 43, 6214-6222

- Wang X.D., Huang B.X., Rong Y.H. (2008), *Philosophical Magazine Letters*, vol. 88, no.11, 845-851
- Idrissi H., Ryelandt L., Veron M., Schryvers D., Jacques P.J. (2009), *Scripta Materialia*, 60, 941-944
- Meyers M.A., Vohringer O., Lubarda V.A. (2001), *Acta Mater.* 49, 4025
- Venables J.A. (1961), *Phil. Mag.*, 6, 379-396
- Venables J.A. (1964), *J. Phys. Chem. Solids*, vol. 25, 693-700
- Venables J.A. (1974), *Phil. Mag.* 30:5, 1165-1169
- Bracke L., Kestens L., Penning J. (2009), *Acta Materialia*, 57, 1512-1524
- Muira S., Takamura J.I., Narita N. (1968), *Trans. J. Inst. Met. Suppl.*, 9, S555
- Byun T.S. (2003), *Acta Materialia*, Volume 51, Issue 11, Pages 3063-3071
- Sevillano J.G. (2009), *Scripta Materialia*, 60, 336-339
- Bouaziz O., Geulton N., Scott C. (2008), *Scripta Materialia*, 58, 484-487
- Bouaziz O., Geulton N. (2001), *Materials Science and Engineering*, A319-321, 246-249
- Allain S., Chateau J.-P., Bouaziz O. (2004), *Materials Science and Engineering A* 387-389, 143-147
- Kocks U.F., Mecking H. (1981), *Acta Metallurgica*, 32, 1865
- Allain S., Chateau J.-P., Dahmoun D., Bouaziz O. (2004), *Materials Science and Engineering A* 387-389, 272-276
- Shiekhelsouk M.N., Favier V., Inal K., Cherkaoui M. (2009), *International Journal of Plasticity* 25, 105-133
- Kim Jinkyung, Graduate Institute of Ferrous Technology, POSTECH, Unpublished results
- Estrin Y., Kubin L.P. (1986), *Acta Metallurgica*, Vol. 34, No. 12, pp. 2455-2464
- Dini G., Ueji R., Najafizadeh A., Monir-Vaghefi S.M. (2010), *Materials Science and Engineering A* 527, 2759-2763
- Rintao Ueji, Kenji Harada, Noriyuki Tsuchida, Kazutoshi Kunishige (2007), *Materials Science Forum*, vol. 561-565, 107-110
- Sahu P., Curtze S., Das A., Mahato B., Kuokkala V.-T., Gosh Chowdhury S. (2010), *Scripta Materialia*, 62, 5-8
- Curtin W.A., Olmsted D. L., Hector, Jr L. G. (2006), *Nature Materials*, Vol. 5, 875
- Allain S., Cygy P., Scott C., Chateau J.-P., Rusinek A., Deschamps A. (2008), *Int. J. Mat. Res.*, 99, 7, 734
- Chen L., Kim H.-S., Kim S.-K., De Cooman B.C. (2007), *ISIJ International*, vol. 47 (12), 1804-12
- Kim J.-K., Chen L., Kim H.-S., Kim S.-K., Estrin Y., De Cooman B.C. (2009), *Metallurgical and Materials Transactions A*, vol. 40, no. 13, 3147-3158
- Zavattieri P.D., Savic V., Hector Jr L.G., Fekete J.R., Tong W., Xuan Y. (2009), *International Journal of Plasticity*, 25, 2298
- Bracke L. (2006), Ph.D. Thesis, Ghent University, Ghent, Belgium
- Kim Y., Kang N., Park Y., Kim G., Kim S., Cho K. (2008), *J. Korean Inst. Met. & Mater.*, Vol. 46, No. 12, 780-787
- Jung J.K., Lee O.Y., Park Y. K., Kim D.E., Jin K.G. (2008), *Korean J. Mater. Res.*, vol. 18, no. 7, 394-399

- Niendorf T., Lotze C., Canadinc D., Frehn A., Maier H.J. (2009), *Materials Science and Engineering A*, 499, 518-524
- Hamada A.S., Karjalainen L. P., Puustinen J. (2009), *Materials Science and Engineering A*, 517, 68-77
- Ueki R., Tsuchida N., Fujii H., Kondo A., Kunishige K. (2007), *J. Japan Inst. Metals*, vol. 71, No. 9, 815-821
- Bouaziz O., Scott C.P., Petitgrand G. (2009), *Scripta Materialia*, 69, 714-716

Powder Injection Moulding – An Alternative Processing Method for Automotive Items

Berenika Hausnerova
*Polymer Centre, Tomas Bata University in Zlin
Czech Republic*

1. Introduction

Powder injection moulding (PIM) technology represents a challenging production method for automotive items, alternative to machining and investment casting. The European automotive industry utilizes PIM applications over 50% of the time (Kearns, 2009). In Germany the first Schunk penetrations into the automotive industry were lock caps and lock shafts, followed by cable seals used to fix the cable to car sunroofs, soft magnetic sensor housing parts, cams for electrical adjustment mechanism of car seats, bonnet lock fixing bearings, or rocker arms for VVT engines used by BMW, produced now at an annual rate of 4.5 million pieces. Nowadays, even more stringent parts such as turbocharger vanes, rollers and adjustment rings are produced there (Schlieper, 2007). Concerning ceramics, good application examples are the 8-inch-diameter turbine wheels produced by General Motors for a turbine engine and large static components for automotive gas turbine programs (Moritz & Lenk, 2009).

Recently, a *HYDRO-PIM* project in Austria was aimed at developing potential applications for PIM stainless steel for use in extreme low temperatures for BMW Hydrogen 7 (anonym, 2007). Another European project, *CarCIM*, was initiated in 2006 to develop ceramic components for automotive and railway applications – glow plug, gear wheel, a valve set and braking pads using two-component PIM (Moritz, 2008). Fraunhofer IFAM has coordinated a European project dealing with new material laws for PIM feedstocks called *MATLAW* to improve feedstock's characteristics and mould filling simulation approaches (Williams, 2009).

Although PIM technology was first commercialized in North America, nowadays Asia is the largest market. The automotive sector remains the largest (19.9 %) user of PIM parts in Japan (anonym, 2010). The earliest application of PIM in China was an alumina spark plug body for automobile engines in the 1960s (Li, 2007).

During the PIM process, a powder must be at first compounded with a suitable polymer *binder* to obtain a highly (typically around 60 vol. %) concentrated compound, which is then processed in injection moulding machines utilized in the plastics industry. In the next step, a binder is chemically or thermally withdrawn from the moulded (*green*) part, and the remaining purely metal or ceramic (*brown*) part is sintered to its final dimensions and density.

PIM is clearly an interdisciplinary technique combining metallurgy with the processing of plastics. Therefore, products made with PIM technology take advantage of the material

flexibility of powder metallurgy and the design flexibility of plastics moulding. PIM technology has several advantages in comparison to traditional metalworking as it is a no scrap technique, suitable for designs difficult to machine. German (2007) presented a survey of over 200 PIM components already in production around the world in order to analyze their geometrical attributes and special features such as length, mass, slenderness, wall thickness, number of holes, slots, undercuts, surface texture, e.t.c. and proposed an "ideal" PIM part design (Fig. 1). A great potential of PIM technology is its ability to combine multiple parts into a single item, as for example a drive wheel for a bonnet lock mechanism (Fig. 2), where eight individual parts were combined into one (Schlieper, 2007).



Fig. 1. Design of a PIM part (Schlieper, 2007; courtesy of *PIM International*).

Further, PIM, as an injection moulding technique, can be adopted to combine different materials via two-component PIM (2C-PIM), production of very small parts via micro PIM (μ PIM) or using the advantages of gas assisted PIM (GA-PIM). On the other hand, there are several factors still limiting the mass expansion of PIM technology, and tooling and set-up expenses are difficult to justify for low production quantities. According to German (2008), PIM is usually attractive for an annual production of more than 200,000 parts.

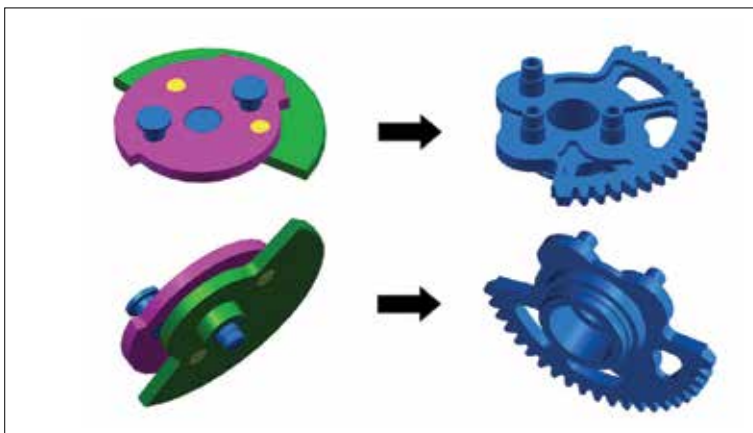


Fig. 2. Demonstration of multiple parts combination into a single PIM item (Schlieper, 2007; courtesy of *PIM International*).

The fundamentals of PIM technology have been described in several books (especially German, 1990; German & Bose, 1997). Within the following text, particular stages of the PIM process - mixing, injection moulding, debinding and sintering - will be briefly introduced, describing the current state-of-the-art and providing some practical information for the producers considering PIM as an alternative route for automotive items. The main focus of this work, however, consists of discussing rheological approaches to control and optimize the mixing and injection moulding steps of the process, because the majority of PIM companies originate from a metallurgical background and not a polymer processing background. Some of the quality issues arising from the moulding step, especially phase separation of powder and binder during mould filling, might cause visual defects, porosity, warpage or even cracks in the final products. Therefore, such quality influencing factor for PIM technology is considered as well, interpreting the latest results of both theoretical and experimental studies.

2. Description of the process

The first task to be considered when planning PIM production is to select material – powder and binder. The availability and cost of PIM quality powders are still major limiting factors affecting decision making. Nevertheless, any metal (except for pure aluminium, due to an oxide film on the surface inhibiting sintering) or ceramic powder can be utilized in both PIM divisions (MIM – Metal Injection Moulding and CIM – Ceramic Injection Moulding) if it is prepared in the suitable form. Important powder characteristics such as particle size, particle size distribution and shape of particles are governed by the way of their preparation. New technologies in powder production have been implemented to extend the range of fine metal and ceramic powders for PIM producers (German & Bose, 1997). An increasing demand motivates powder manufacturers to meet the special requirements of PIM. The ISO TC119 SC5 committee is responsible for MIM materials specifications. A final release of approved specifications is projected for 2011.

The powders used for automotive PIM applications include plain and low alloy steels, high speed steels, stainless steels, super alloys, magnetic alloys and hard metals, and aluminium or zirconium oxides for ceramics. The majority of PIM automotive items, however, are produced from 17-4PH stainless steel. Also, an increased potential has been recently recognized for high Ni content MIM alloys (MECO 26 or 28), which are hot gas corrosion resistant and have better microstructure and mechanical properties than parts made by centrifugal casting (Langer, 2007). MIM316L steel, showing an almost threefold increase in tensile strength and only modest decay in ductility at -253 °C compared with room temperature properties, proved to be an excellent candidate for the BMW Hydrogen 7 car (anonym, 2007). GKN Sinter Metal (Germany) produces several hundred tons of MIM parts per year, mainly for automotive industry from Fe-Ni alloys, 42CrMo4, 17-4PH and superalloys for high temperature applications (Schlieper, 2010).

Material component, allowing for the shaping of metal/ceramic powders via injection moulding, is a binder. A typical binder consists of three components: main body, backbone (non-reactive during debinding process, keeping the shape of the part prior to sintering) and additive (German, 1990). Waxes (paraffin, carnauba, microcrystalline, beeswax) in the main body are often combined with the thermoplastic backbone (PE, PP, PS, PA, PMMA, EVA) and stearic or oleic acid. Block copolymers (EVA, EBA, EAA), as they are made of polymer blocks soluble in the dispersion medium and blocks with high affinity to powder, provide

suitable interactions with powder, imparting steric stabilization of a compound, and thus prevent separation from the powder during the flow. Currently, water-soluble binders based on polyethylene oxide (PEO) are increasingly being employed. Using cemented carbides and a three-component binder (PEO, PMMA, stearic acid) Chuankrerkkul et al. (2008) investigated the effect of the molecular weight of PEO on compound viscosity and discovered that lowering the molecular weight of the PEO did not affect the flow behaviour of the feedstock.

Injection moulding of metal and ceramic powders requires preparing a feedstock, where individual powder particles are fully covered (lubricated) with the smallest effective amount of a binder, Fig. 3. The adjustment of optimum powder/binder ratio within a feedstock is one of the critical tasks during PIM processing and will be discussed in detail in Chapter 3.2.

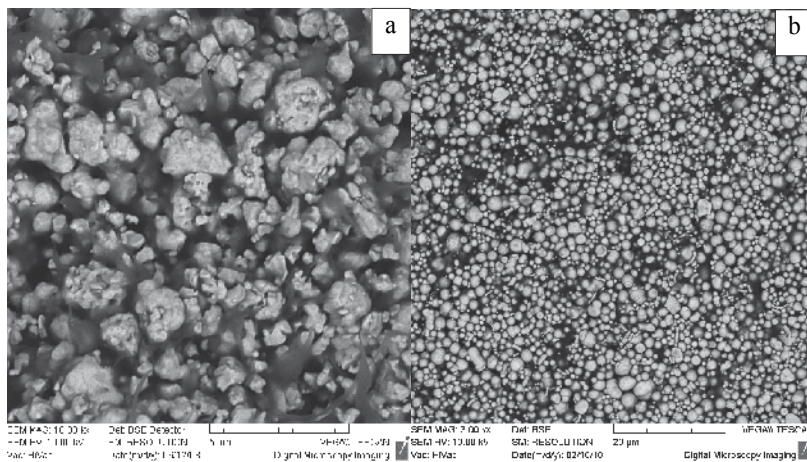


Fig. 3. SEM micrographs of alumina (a) and stainless steel (b) feedstocks.

To ensure precise homogenization, sufficient shear stress is necessary, since PIM powders are rather fine (from 0.1 to 20 μm) with an enhanced tendency towards agglomeration. In this respect, a batch mixing in planetary or Z-blade mixers would be preferred, although usually taking a couple of hours. In a high volume production, twin screw extruders or shear rolls are employed for the feedstock preparation. Nevertheless, a current trend is to buy ready to use (commercial) feedstocks based on a patented binder system mixed with different powders. Perhaps the most widely used is the polyacetal binder Catamold® (BASF), which provides good processability and excellent shape retention. However, its removal is carried out in a highly concentrated nitric acid, and thus its utilization brings enhanced concerns for health and safety regulations. Such an issue can be overcome with water-soluble binders based on polyethylene oxide or polyvinyl alcohol offered by several producers (e.g. Polymer-Chemie, eMBe).

The step during which the feedstock is formed into the desired shape is injection moulding, a technique well known in the automotive industry. Although there is no fundamental difference between injection moulding of PIM compounds and plastics, machines are usually optimized for the processing of powdery materials with a wear-resistant cylinder and screw, and a screw geometry adopted to lower compression rate and extended compression zone compared to standard screws for thermoplastics (Williams, 2008).

The injection moulding process naturally creates undesirable features such as gate marks, ejector pin marks, or parting lines which must be located in noncritical positions or suppressed after fabrication. Design restrictions include uniform or gradual section thickness changes, minimized wall thickness (reducing not only material consumption and moulding cycle time, but considerably also debinding and sintering), round corners to reduce stress concentrations and risk of fracture, and minimum undercuts on internal bores (Kazmer, 2007; German 2008). Contrary to conventional injection moulding, for PIM it is important (whenever possible) to design items with one flat surface, which allows standard support trays during sintering.

After injection moulding the binder is removed from a green part via chemical, thermal or combined chemical/thermal processes (German, 1990). The choice of debinding method corresponds to the selected binder system. During solvent debinding an immersion of the binder is performed by placing the parts into a solvent (water, ethylene dichloride, n-heptane or trichlorethane, e.t.c.) for several hours; alternatively, a solvent vapour, initiating condensation, and subsequently liquid extraction of the binder components is used. If thermal debinding is utilized, the binder is removed through an applied heat. It is carried out, depending on the selected powder, under air, hydrogen, nitrogen or argon atmospheres at various temperatures. Slight and uniform heating (lasting hours, even days) is required in order to withdraw a binder by evaporation or liquid extraction using a wicking material (porous substrate) without disruption of a part.

After the binder removal, the strength of a brown part is to a large extent reduced. Thus, it has to be sintered to the final density, which generally reaches more than 97% of theoretical (German & Bose, 1997). Sintering is a technique widely employed in the powder metallurgy. It is carried out at temperatures below the melting point of a powder (usually between 0.6 and 0.9 of the melting temperature) in a sintering furnace in a protective or vacuum atmosphere for metals and an air atmosphere for ceramics. Since an isotropic and uniform sintering shrinkage is required, fine powders, sintering more readily with improved surface finish than coarser powders, are preferred (German & Bose, 1997). As demonstrated in Fig. 4, defects arising from inhomogeneous mixing evidence themselves on the final sintered parts.

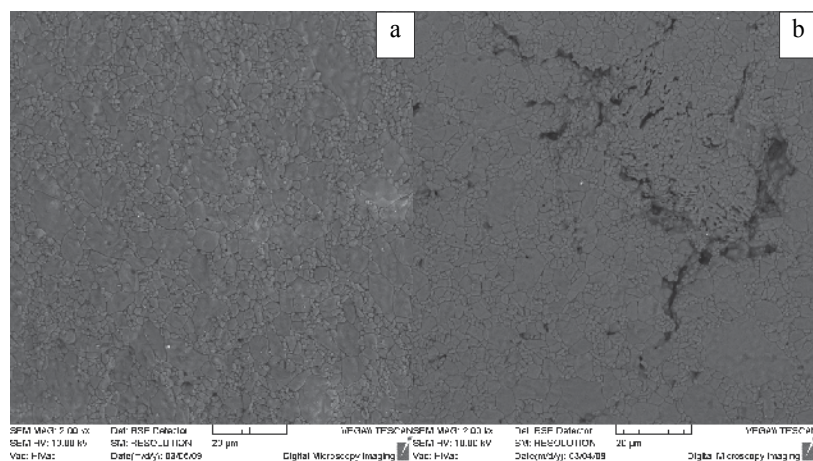


Fig. 4. SEM micrographs of the sintered surface resulting from homogenous (a) and inhomogeneous (b) mixing.

An important advantage of PIM technology is a possibility of integration of various effects without additional operations. As an example, OBE (Germany) produces watchcases for the Mercedes-Benz AMG from 316L stainless steel with the brushed effect on the surface incorporated in the injection moulding tool, thus, without any finishing (anonym, 2008). Further, as already mentioned in the introduction, PIM allows a combining of metals with ceramics via 2C-PIM, resulting in electric or thermal conductive/insulating, magnetic/non-magnetic, or ductile/hard items. A crucial aspect of 2C-PIM is the sintering rate control – both components must sinter at similar shrinkage, rates and temperatures (Moritz & Lenk, 2009).

Currently, applications are highly focused to microPIM items having a weight as little as 0.0004 g, thin walls (20 μm), aspect ratios up to 20, structural details in the range of 20-50 μm , and surface roughness less than 0.05 μm . With microPIM additional demands are the size of powders (the grain size of the sintered part must be at least one order of magnitude smaller than the minimum internal dimension of the item) and homogeneity (Moritz & Lenk, 2009). Finally, a close variant to PIM is powder extrusion moulding used for example in the production of yttrium stabilized zirconia thin walled tubular electrolytes for fuel cells (Jardiel et al., 2009).

3. Rheological approaches to optimize the process

3.1 Binder composition

Rheology, as a scientific discipline studying material flow properties, represents a powerful tool in the sophisticated treatment of several quality determining factors of the PIM process. For a successful mixing of PIM compounds, the rheological properties of a binder are important when seeking a tailored binder formulation or selecting a proper additive (e.g. Hens et al., 1991; Edirisinghe, 1991; Karatas et al., 2004). As the majority of researchers have concentrated on the effect of binder composition on the rheological properties of feedstocks, the roles of particular binder components and their interrelationships remain unclear. Hsu et al. (1994) compared four kinds of wax - paraffin, polyethylene wax, carnauba and acrawax, serving together with LDPE as a binder for 304L stainless steel. They demonstrated that the latter two waxes exhibited higher viscosity and more suitable pseudoplastic flow, arising from their polar characters (carnauba is alkyl acid ester and acrawax is a secondary amide) forming hydrogen bonds with a metal powder. Hausnerova et al. (2000) studied three types of polymer binders differing in block copolymer used (ethylene-butyl acrylate, ethylene-vinyl acetate, ethylene-acrylic acid). In doing so, they noticed that as the volume concentration of a solid component increased to 30 vol. %, the influence of the particular binder composition on flow properties decreased. Furthermore, Hsu and Lo (1996) employed the McLean-Anderson statistic method (Murray, 1984) to study the fluidity (inverse of viscosity) and pseudoplasticity (in terms of the power-law index) of 15 binder formulations. Their systematic investigation resulted in contour maps demonstrating how fluidity and pseudoplasticity vary with binder components.

Viscosity of a binder should be less than 0.1 Pa.s in order to provide PIM feedstocks with viscosity below 10^3 Pa.s (German, 1990). Thus, researchers must properly select a testing set-up for rheological measurements. A capillary rheometry is currently recognized as the best approach to predict the flow behaviour of PIM compounds. This approach, however, is complicated by several factors such as flow restrictions caused by instabilities (Hausnerova et al., 2000) or the so-called Serge-Silberberg effect, i.e. movement of particles from the

capillary wall to the centre during flow, which achieves a great magnitude, and thus leads to an axial solids concentration gradient (Kubat & Szalanczi, 1974). In the case of binders, however, a capillary rheometry is difficult to realize due to inherently low viscosity; instead, rotational rheometers of cocylindrical geometry are preferred.

If a steady-state mode of rotational rheometers is employed for concentrated compounds, the material trapped between the plates or cone and plate tends to hang out during measurements (Shenoy, 1999). Further, as reviewed in Hausnerova (2010), the accuracy of using cone and plate rheometers for the measurement of materials prone to wall-slip, secondary flows and temperature changes due to dissipation energy from shear heating should be thoroughly analysed similarly to Kurzbeck et al. (1996). In their work, wall slip was discerned using two geometries according to the Mooney method, secondary flows were accounted for via estimation approaches, where relative torque (ratio of measured torque influenced by secondary flow to a theoretical one under laminar flow) is related to Reynold's number. In the case of the compounds employed in Kurzbeck et al. (1996), the maximum increase of torque due to secondary flows was 0.2%, and an increase of temperature due to dissipation was calculated under adiabatic condition to be 40 K, but the measured values reached less than 1 K.

As pointed out in Hausnerova (2010), interpretations of rheological data of PIM systems often lack the relevant application of corrections necessary to compensate for non-newtonian flow character. Failure to recognize this fact can lead to errors both in the reporting of reliable data and the comparison of various rheological approaches.

3.2 Determination of optimal powder/binder ratio

Optimum powder loading within a feedstock refers to a powder concentration for which a compound exhibits good flow properties (viscosity less than 10^3 Pa.s) as well as homogeneity and stability in the shear rate range of $10^2 - 10^5$ s⁻¹; it should be set 6-14% lower than a value of maximum powder loading attainable for a given system (Dihoru et al., 2000). There are generally three approaches to determine the maximum powder loading: density measurement, mixing torque evaluation, and rheological tests. Barreiros & Vieira (2006) proposed an interesting combination of the last two methods employing torque rheometry to determine optimum compositions of PIM feedstocks. The optimum particle loading was determined to be the highest value resulting from the intersections of the adjustment of linear functions of the mixing torque as a function of powder loading plots. Dihoru et al. (2000) demonstrated the possibility of determining optimal solid loading through the aid of neutral network modelling.

Nevertheless, rheological investigation of capillary flow data still represents the most sophisticated evaluation of optimum loading, bearing the relative viscosity (ratio of a feedstock viscosity to the viscosity of a binder) as a variable to obtain maximum packing fraction for a particular powder-binder compound. As a powder concentration reaches the maximum, all of the binder is confined among powder particles, i.e. the flow of the feedstock is restrained, resulting in a sharp increase in relative viscosity.

Clearly, the value of the maximum loading level of a feedstock is influenced by the characteristics of a powder as well as packing procedure. In this respect an ideal PIM powder (German, 1990) should combine large and small particles in a tailored particle size distribution, which provides high packing values. Spherical or rounded shaped powders are preferred due to their easily predictable flow behaviour during mixing with a binder and consequent injection moulding of a feedstock, but the risk of poor shape retention is enhanced.

According to German (1990) more than a hundred empirical and theoretical relations have been proposed in order to obtain the value of maximum packing fraction from the relative viscosity data. Often a simple empirical Maron-Pierce relation (Maron & Pierce, 1956) is employed to calculate maximum loading levels for PIM compounds. In cases where the Maron-Pierce model departs from experimental data, its modification, as proposed by German & Bose (1997), might offer good results, predicting the maximum loading value with high accuracy.

A set of most often recommended relations in the literature (Metzner, 1985; German, 1990) was tested (Honek et al., 2005) on capillary flow data of PIM compounds based on a multi-component polymer binder (polyethylene, paraffin, ethylene-based copolymers and polyethylene glycol) and three various hard-metal carbide powders. The powders were prepared by milling all components in an inert liquid in a ball mill. The first two powders (UNI 1, UNI 2) had unimodal particle size distribution, while the third powder (BI) had a bimodal one. The shape of the particles was irregular; UNI 1 powder had a smaller aspect ratio of the particles than the two remaining materials.

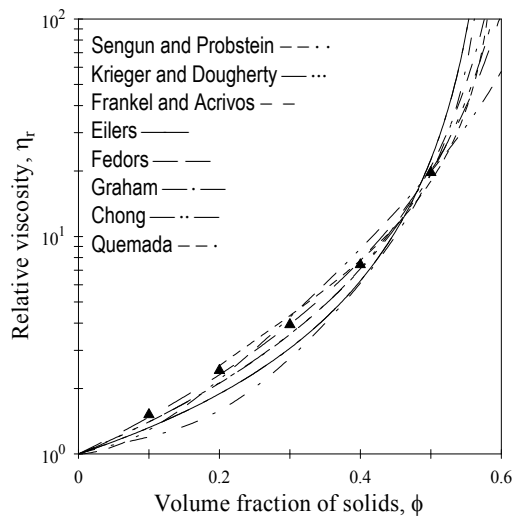


Fig. 5. Relative viscosity data as a function of volume fraction of solids for UNI 1 hard-metal carbide powder; the lines represent mathematical models (Honek et al., 2005).

The fitting of the flow data of the UNI 1 based compounds is depicted in Fig. 5, showing that the fitting curves of the majority of the models lie slightly below the experimental values of relative viscosity. For the UNI 2 compounds the results are even more inconclusive. The irregular shape of particles together with their smaller sizes most probably led to high attractive forces and the formation of a three dimensional network within the compound, and hence to rather enhanced relative viscosities. Thus, the models underestimate the experimental data. The bimodal particle size distribution of BI powder caused a marked decrease of the compound's relative viscosity as compared to UNI 2 data; the Graham model provides the best fit for the experimental data. An agreement between experimental and predicted data in the region of a higher (40 vol.% and more) volume fraction of particles might be caused by a closer proximity of the particles, and thus enhanced attractive forces between particles, which lead to a faster build up of the relative viscosity within a higher concentration range.

Table 1 (Honek et al., 2005) demonstrates on a UNI 1 compound that the predicted values of the maximum volume fraction of the same powder vary with the models applied. Nevertheless, the maximum loading levels determined using relevant models coincide well with the powder characteristics: the highest value of maximum loading (0.69 derived from a linearized Mooney model) corresponded to the powder with the broadest distribution of particle sizes (BI), while the lowest value (0.53 from the Frankel-Acrivios model) was attained for powder with a high portion of small particles (UNI 2). This was further supported by rheological measurements (Hausnerova et al., 1999), where compounds containing particles having unimodal particle size distribution showed higher viscosity values at the corresponding shear rates than the bimodal powder (as an example, the flow curve of 40 vol. % UNI compounds coincides with that of 50 vol. % BI material). It supports the findings of Chang and Powell (1994) and Metzner (1985), which verified that viscosity can be significantly reduced for powders with large differences in size by adding smaller particles, which fill the inter-particle voids, thereby releasing previously immobilised fluid.

Model	Maximum packing (-)
Eilers	0.60
Chong	0.60
Fedors	0.68
Frankel-Acrivios	0.60
Quemada	0.64
Graham	0.58
Krieger - Dougherty	0.66
Sengun - Probstein	0.71

Table 1. Maximum packing values for UNI 1 compounds; bold values correspond to the models fitting well with the experimental data (Honek et al., 2005).

3.3 Flow data relevant for process simulations

The flow of a feedstock into a mould cavity during injection moulding should be simulated prior to mould construction since some defects such as air traps, dead zones, or weld lines created during moulding cannot be reduced or eliminated during the following debinding and sintering steps. Simulation approaches currently available, built on rheological models describing pseudoplastic flow of polymer melts, might be successfully used for uncomplicated PIM items, providing information e.g. about the stress concentrations' zones as demonstrated on Fig. 6, on which basis the part design can be optimized.

Nevertheless, in order to embody more stringent flow situations, the software should be adopted to the rheological specifics of PIM compounds to produce non-defect parts. This implies that at first, the rheological parameters of PIM feedstocks have to be known with sufficient accuracy, and second, that the rheological model has to be developed to describe the specific flow features as those reported e.g. for a very fine aluminium oxide powder mixed with commercially available binder (Hausnerova et al., 2010a). The viscosity of this feedstock (60 vol. %) decreased with increasing shear rate only up to 500 s⁻¹, suggesting particle or binder molecule orientation and ordering with flow. As the shear rate was further

increased, shear thinning turned into a dilatant flow, indicating that particles could not form layers and slide over each other (flow cause firstly reported by Hoffman (1972). In addition, for the alumina feedstock investigated (Hausnerova et al., 2010a) such structure restructuralization appeared repeatedly, i.e. the flow changed from pseudoplastic to dilatant and back to pseudoplastic, implying a failure of the rheological models currently available.

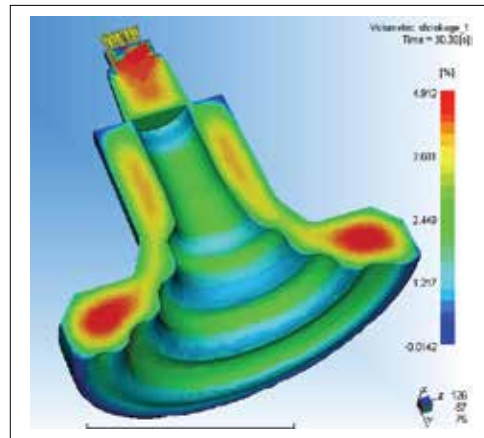


Fig. 6. A MoldFlow simulation of the PIM mould filling.

Rheological data of PIM compounds should be studied not only as a function of shear rate (stress), but also as a variable of processing conditions - temperature and pressure. Temperature sensitivity of PIM compounds can be accounted for via activation energy of shear flow. German (1990) suggests an increase of activation energy with increasing filler content. His idea is based on the explanation that the relative rate of viscosity decrease is typically faster in the loaded system due to the superimposed change in a volume fraction of powder associated with a difference in thermal expansion coefficients of powder and binder. On the other hand, Shenoy (1999) proposes an opposite dependence of activation energy on powder content; the viscosity of a compound is less temperature sensitive as compared to a binder viscosity, because powder provides very little free volume change with temperature in relation to a binder.

To confirm one of the two mechanisms presented, temperature effect on the flow properties of PIM materials on compounds based on a hard-metal carbide powder in a thermoplastic binder (polyethylene, ethylene butyl acrylate block copolymer and paraffin) in a broad temperature range (140 - 200 °C) on a capillary rheometer have been investigated (Honek et al., 2002). Activation energy was calculated using the Arrhenius relation, which was found to be valid for PIM compounds only in the stable flow region (without evidence of pressure oscillations). It should be mentioned that the temperature effect reported (Honek et al., 2002) was studied with specific regard to the flow instabilities accompanying the flow of PIM compounds, which has apparently not been reported heretofore.

The activation energy of carbide compounds decreased with powder content, indicating a decay of the sensitivity of a compound to temperature changes. Hausnerova et al. (2009), employed another approach to determine temperature sensitivity of PIM compounds and reached the same conclusion. Very recently, Contreras et al. (2010) broaden this finding for a set of three bronze and four Inconel 718 powders. According to their observation, activation

energy diminishes with increasing powder content up to the optimum powder loading of the particular compound, while for feedstocks exceeding optimum loading, the activation energy becomes enhanced. Thus, the evaluation of activation energy might serve as a simple method to determine an optimum loading level of powder of a PIM feedstock as discussed in Chapter 3.2.

In spite of the fact that pressure might alter the viscosity of many materials significantly, it is a parameter disregarded in simulation approaches, mainly due to the lack of reliable data caused by ambiguous definitions of pressure sensitivity coefficients, various evaluation techniques and test artefacts connected. It is only accounted for through pressure-volume-temperature (PVT) characteristics employed to predict a holding pressure during moulding (Greene & Heaney, 2007) or shrinkage of final parts (Laddha et al., 2009). PVT data measurements of PIM materials are reported scarcely (Wie et al., 2000; Greene & Heaney, 2007; Laddha et al., 2009; Persson et al., 2009).

The evaluation methods of a viscosity's sensitivity to pressure are direct -experimental, and indirect - analysis and/or correlation to other properties (described in detail in Hausnerova et al., 2006). The first group concerns double piston rheometers, or single piston rheometers modified by a secondary chamber located downstream of a capillary. An indirect evaluation is based mainly on calculations from Bagley plots (Duvdevani & Klein, 1967) intercepting non-linearities in the pressure profiles (capillary and slit) or from the relationship between viscosity and free volume (Utracki, 1985; Sedlacek et al., 2005). Goubert et al. (2001) compared Utracki's approach, calculations from Bagley plots and measurements on a modified single piston rheometer, and proved the reliability of the last mentioned method.

In a series of papers (Hausnerova et al., 2006; 2009; 2010b) the direct measurement of the pressure influence on the flow properties using this technique was applied on cemented carbide compounds. A single piston rheometer was modified (Polymer Centre, TBU in Zlin) with an additional device generating backpressure, thus enhancing pressure actuating on a tested melt (Sedlacek et al., 2004). It consists of a chamber with a restricting needle valve moving horizontally by means of a screw thread in order to set the level of pressurization applied on the material during its flow through the die. The Carreau-Yasuda model (Yasuda, 1981) was employed to fit the experimental data of temperature and pressure dependent shear viscosity.

German (1990) stated that sensitivity to pressure should decrease with a loading level of powder in a PIM compound. This was confirmed for the low to moderate (up to 30 vol. %) powder concentrations in Hausnerova et al. (2006). However, at higher loading levels (50 vol. %), the sensitivity to pressure seems to be enhanced in comparison to a pure polymer binder (Hausnerova et al., 2009). It can be speculated that the compressibility of a structure formed within interacting particles becomes important at a high loading level, while for low to moderate concentrations the pressure sensitivity is governed predominantly by a polymer binder. The mechanism of viscosity dependency pressure is not yet clarified, although for PIM compounds it is supposed to vary with the characteristic (particle size and particle size distribution) of powder used.

In Hausnerova et al. (2010b), three types of PIM compounds, differing in their particle size distributions and mean diameters of particles, have been considered with the conclusions supporting the idea of altering a compound's pressure sensitivity via the tailoring of powder characteristics. The highest pressure sensitivity coefficient (32.9 GPa⁻¹) was found for a feedstock containing broad particle size distributed powder having a perceptible portion of small particles. It implies the coexistence of the two mechanisms. First, at low to

moderate loading levels the pressure sensitivity of the compounds is governed by the sensitivity of a binder component, which is connected to the free volume changes as recently shown by Sedlacek et al. (2005), and diminishes as powder concentration increases. Second, at high powder loading the driving factor is the compressibility of the powder itself related to the (re)organization of the particles within the melt during pressurization.

Finally, it should be noted that the temperature sensitivity of a carbide compound does not vary significantly with pressure (revealing the value $(18.4 \pm 0.7) 10^{-3} \text{ } ^\circ\text{C}^{-1}$ for pressures up to 50 MPa), in contrast to the pure binder, the temperature sensitivity coefficient of which is a linear increasing (from $18.8 10^{-3} \text{ } ^\circ\text{C}^{-1}$ at ambient pressure to $59.4 10^{-3} \text{ } ^\circ\text{C}^{-1}$ at 50 MPa) function of pressure.

3.4 Quantifying quality issues through rheological approaches

A portion of sintered parts, which do not reach the quality requirements, might in some instances achieve up to 25 % (Williams, 2009). If a major quality influencing issue appearing during injection moulding - a separation of binder from the feedstock, could be recognized prior to debinding and sintering steps, material, energy and time would be saved. The mechanism of a phase separation is still not fully understood much like its onset and extent is not quantified.

Recently, Thornagel (2009) demonstrated that local shear rate gradients force powder particles to leave areas of high gradients, thus making them the trigger for phase separation. Assuming no slip condition, i.e. good adhesion of the feedstock to the wall of the channel, a significant shear rate peak occurs close to the wall, while the middle of the flow domain is characterised with a plateau at a much lower shear rate level.

Particles flowing in the peak area close to the wall then experience a non-uniform shear rate leading to rotation, which increases in severity as the shear stress gradients increase. Rotating particles naturally move away from areas of high shear gradients (Fig. 7). As a result, the area of the highest shear rate is characterized by high binder content, while the plateau of the lower shear rate accommodates a powder rich material. To predict the situation in which a separation pattern changes continuously during moulding would require a multi-phase simulation, taking into account the particular feedstock components.

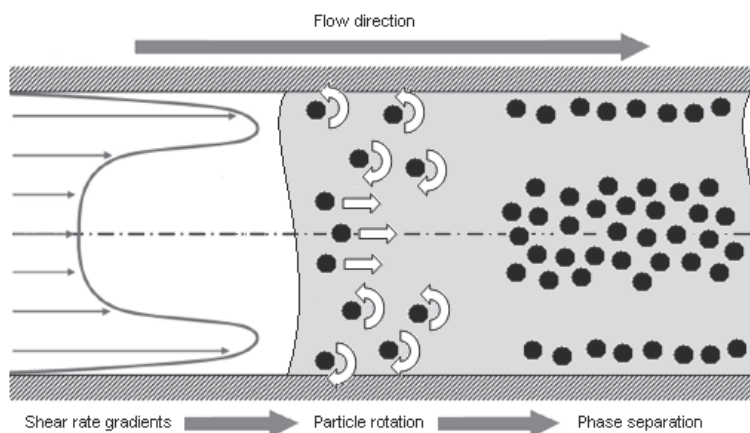


Fig. 7. Flow pattern of PIM feedstock across the channel causing powder - binder separation as proposed by Thornagel (2009).

Instead, Thornagel (2009) proposes a simplified simulation, modelling the feedstock as a bulk and extending the currently popular 3D Navier Stokes equations in a way that powder and binder concentrations and their variations can be predicted depending on shear rate history. If validated, such an approach might be a breakthrough in PIM computer aided support.

In another approach Jenni et al. (2008; 2009) used a software simulation based on the balance model of the flow of rigid, spherical particles in a Newtonian fluid to compare the influence of injection moulding parameters on separation appearance. A differential scanning calorimeter (DSC) was selected to quantify the local powder content. To compare different materials and processing parameters used for injection moulding, three testing moulds were used, as schematically demonstrated in Fig. 8.

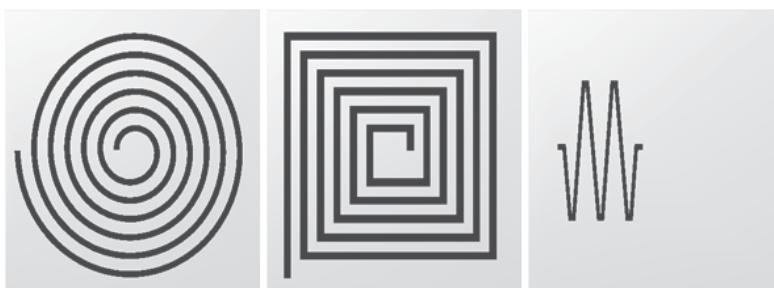


Fig. 8. Spiral, square spiral and zig-zag designs of a testing mould.

The experiments incorporated dependent parameters for mouldability - flow length and input variables (nozzle and mould temperatures and injection speed). In cavity geometry, it has been demonstrated that powder content decreases to some extent as the number of corners increases.

To quantify the separation, the results from the software simulation using the balance model were compared with experimental findings obtained using radiography, computer tomography and DSC. The authors (Jenni et al., 2008) demonstrated that the balance model clearly portrays the migration of particles for simple geometries, but irregularities in the feedstock flow, such as slip effects at the wall and the fountain flow, are not taken into account by this model.

The testing moulds depicted in Fig. 8 only partly fulfill the purpose of forcing phase separation during mould filling. Thus, a mould (developed in cooperation between TBU in Zlin and IFAM, Bremen) including inner and outer corners, radical thickness changes, weldlines and a thin film part was recently constructed in order to investigate the separation development during mould filling, Fig. 9.

SEM analysis of the particular cross sections derived from this testing mould (Fig.10), combined with EDX analysis of the distribution of the elements typical for powder and binder, then provides a quantitative evaluation of the powder-binder separation (Hausnerova et al., 2010c).

The next step is a rheological/simulation approach directly linking the factors responsible for powder-binder separation during injection moulding to the quantified defects appearing on final sintered products. In this respect, a wall slip phenomenon could be considered as a qualitative parameter indicating powder-binder separation absence/occurrence, because it represents an often used practical approach to avoid powder-binder separation by setting up conditions under which a compound flows as a plug, i.e. slips at the wall.

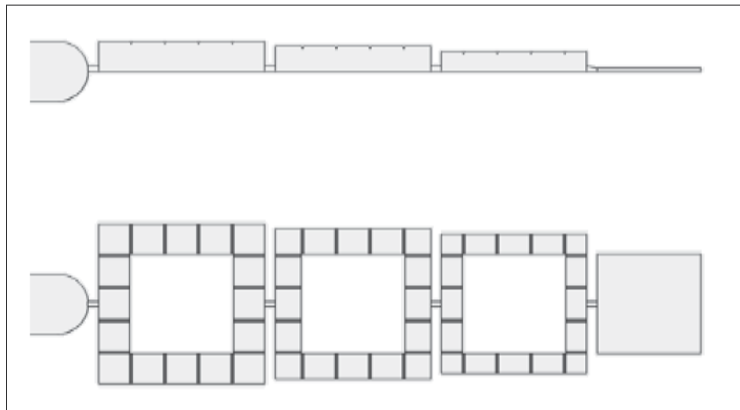


Fig. 9. Design of a mould testing powder-binder separation (Community Design 001704974, Tomas Bata University in Zlin)

The conditions at which a material slips at the wall depend on material characteristics such as the type of powder and polymer binder, the size and particle size distribution of the powder, the concentration of the powder and its surface treatment as well as on processing parameters such as temperature, pressure, and shear rate, and most important, on the microscopic nature of the channel wall. The last mentioned parameter is, however, different during processing and rheo-testing. Thus, a rheometer should be modified accordingly. It is believed that implementing recently acquired knowledge into existing simulation software will lead to the production of defect-free items.

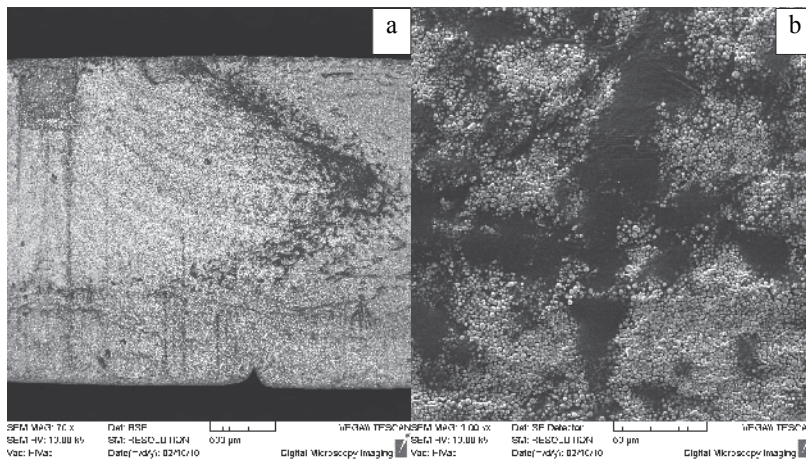


Fig. 10. Flow pattern of powder-binder separation (a) and detail of separated binder area (b).

4. Conclusion

Still widely considered a new technology, PIM constitutes an ongoing topic of both commercial and scientific interest. As an effective processing route (high added value), it represents an interesting production method for automotive items, especially in an economic downturn periods.

As a developing technology, PIM has many quality determining issues to be dealt with. The quality of PIM products is usually tested after the final, sintering step, however, the defects might arise during previous stages – mixing, moulding, and debinding.

Rheology could play a role of considerable importance in controlling and optimizing the PIM process and eliminating some critical quality concerns. At present, the potential of rheological models available to describe the peculiarities of the flow behaviour of PIM compounds is rather limited as these models are not established for multiphase systems containing several binder components and powders of irregular shape, broad distribution of particle sizes and sizes with enhanced tendency to form agglomerates. Therefore, the challenging task for the current research is to design a model validated on reliable flow data conducted considering the structural changes of PIM compounds upon shearing, and its implementation into the approaches simulating the flow of the PIM feedstocks.

5. Acknowledgments

This work has been financially supported by the Ministry of Education, Youth and Sports of the Czech Republic (Project No. MSM 7088352101). Lukáš Jiránek (Tomas Bata University in Zlín) is gratefully acknowledged for creating the schematic figures.

6. References

- anonym (2007). MIM 316L stainless seeks applications in BMW Hydrogen 7 car. *PIM International*, 1, 4, 5, ISSN 1753-1497
- anonym (2008). Clock casing for luxury automotive applications. *PIM International*, 2, 4, 29, ISSN 1753-1497
- anonym (2010). MIM sales set to rebound in Japan after falls in 2008 and 2009. *PIM International*, 4, 1, 10, ISSN 1753-1497
- Barreiros, F. M. & Vieira, M. T. (2006). PIM of non-conventional particles. *Ceramics International*, 32, 3, 297-302, ISSN 0272-8842
- Contreras, J. M.; Jimenez-Morales, A. & Torralba, J. M. (2010). Experimental and theoretical methods for optimal solids loading calculation in MIM feedstocks fabricated from powders with different particle characteristics. *Powder Metallurgy*, 53, 1, 34-40, ISSN 0032-5899
- Chang, C. & Powell, R.L. (1994). Effect of particle size distributions on the rheology of concentrated bimodal suspensions. *Journal of Rheology*, 38, 1, 85-98, ISSN 0148-6055
- Chuankrerkkul, N.; Messer, P. F. & Davies, H. A. (2008). Flow and void formation in powder injection moulding feedstocks made with PEG/PMMA binders. Part 1 - Experimental observations. *Powder Metallurgy*, 51, 1, 66-71, ISSN 0032-5899
- Dihoru, L. V.; Smith, L. N. & German R. M. (2000). Experimental analysis and neural network modeling of the rheological behaviour of powder injection moulding feedstocks formed with bimodal powder mixtures. *Powder Metallurgy*, 43, 1, 31-36, ISSN 0032-5899
- Duvdevani, J. & Klein, I. (1967). Analysis of polymer melt flow in capillaries including pressure effects. *SPE Journal*, 23, 41-45, ISSN 1086-055X
- Edirisinghe, M. J. (1991). The effect of processing additives on the properties of a ceramic-polymer formulation. *Ceramics International*, 17, 2, 89-96, ISSN 0272-8842

- Goubert, A.; Vermant, J.; Moldenaers, P.; Göttfert, A. & Ernst, B. (2001). Comparison of measurement techniques for evaluating the pressure dependence of the viscosity. *Applied Rheology*, 11, 1, 26-37, ISSN 1430-6395
- German, R. M. (1990). *Powder Injection Moulding*. Metal Powder Industries Federation, ISBN 978-0918404954, Princeton
- German, R. M. & Bose, A. (1997). *Injection Moulding of Metals and Ceramics*. Metal Powder Industries Federation, ISBN 978-1878954619, Princeton
- German, R.M. (2007). Inverse approach to optimizing MIM shape/size. *PIM International*, 1, 4, 37-38, ISSN 1753-1497
- German, R. M. (2008). Designing for metal injection moulding: a guide for designers and end-users. *PIM International*, 2, 4, 17-25, ISSN 1753-1497
- Greene, C. D. & Heaney, D.F. (2007). The PVT effect on the final sintered dimensions of powder injection molded components. *Materials & Design*, 28, 1, 95-100, ISSN 0261-3069
- Hausnerova, B.; Saha P. & Kubat, J. (1999). Capillary flow of hard-metal carbide powder compounds, *International Polymer Processing*, 14, 3, 254-260, ISSN 0930-777X
- Hausnerova, B.; Saha, P.; Kubat, J.; Kitano, T. & Becker, J. (2000). Rheological behaviour of hard-metal carbide powder suspensions at high shear rates. *Journal of Polymer Engineering*, 20, 4, 237-265, ISSN 0250-8079
- Hausnerova, B.; Sedlacek, T.; Slezak, R. & Saha, P. (2006). Pressure-dependent viscosity of powder injection moulding compounds, *Rheologica Acta*, 45, 3, 290-296, ISSN 0035-4511
- Hausnerova, B.; Sedlacek, T. & Vltavska, P. (2009). Pressure-affected flow properties of powder injection moulding compounds. *Powder Technology*, 194, 3, 192-196, ISSN 0032-5910
- Hausnerova, B. (2010). Rheological characterization of powder injection moulding compounds. *Polimery*, 55, 1, 3-11, ISSN 0032-2725
- Hausnerova, B.; Marcanikova, L.; Filip, P. & Saha, P. (2010a). Optimization of powder injection molding of feedstock based on aluminium oxide and multicomponent water-soluble polymer binder. *Polymer Engineering and Science*, submitted
- Hausnerova, B.; Sedláček, T.; Filip, P. & Saha, P. (2010b). Rheological properties of powder injection moulding compounds at elevated pressures. *Powder Technology*, submitted
- Hausnerova, B.; Marcanikova, L.; Filip, P. & Saha P. (2010c). Wall-slip velocity as a quantitative measure of powder-binder separation during powder injection moulding, *Proceeding of PM2010*, Firenze, October 2010, accepted
- Hens, J.; Lee, D. & German R. M. (1991). Integrity of complex shape products by powder injection molding, *Powder Metallurgy*, 23, 1, 15-21, ISSN 0032-5899
- Hoffman, R. L. (1972). Discontinuous and dilatant viscosity behavior in concentrated suspensions. I. Observation of a flow instability. *Transactions of the Society of Rheology*, 16, 1, 155-173, ISSN 0038-0032
- Honek, T.; Hausnerova, B. & Saha, P. (2002). Temperature dependent flow instabilities of highly filled polymer compounds. *Applied Rheology*, 12, 2, 72-80, ISSN 1430-6395
- Honek, T.; Hausnerova, B. & Saha, P. (2005). Relative viscosity models and their application to capillary flow data of highly filled hard-metal carbide powder compounds. *Polymer Composites*, 26, 1, 29-36, ISSN 0272-8397

- Hsu, K. C.; Lin, C. C. & Lo, G. M. (1994). Effect of wax composition on injection moulding of 304L stainless steel powder. *Powder Metallurgy*, 37, 4, 272-276, ISSN 0032-5899
- Hsu, K. C. & Lo, G. M. (1996). Effect of binder composition on rheology of iron powder injection moulding feedstocks: experimental design. *Powder Metallurgy*, 39, 4, 286-289, ISSN 0032-5899
- Jardiel, T.; Levenfeld, B.; Jimenez, R. & Varez, A. (2009). Fabrication of 8-YSZ thin-wall tubes by powder extrusion moulding for SOFC electrolytes. *Ceramics International*, 35, 6, 2329-2335, ISSN 0272-8842
- Jenni, M.; Schimmer, L.; Zauner, R.; Stampfl, J. & Morris, J. (2008). Quantitative study of powder binder of feedstocks. *PIM International*, 2, 4, 50-55, ISSN 1753-1497
- Jenni, M.; Zauner, R. & Stampfl, J. (2009). Measurement methods for powder binder separation in PIM components. *Proceedings of EURO PM 2009*, 2, 141-146, ISBN 978-1899072071, Copenhagen, October 2009, European Powder Metallurgy Association
- Karatas, C.; Kocer, A.; Ünal, H. I. & Saritas, S. (2004). Rheological properties of feedstock prepared with steatite powder and polyethylene-based thermoplastic binders. *Journal of Materials Processing Technology*, 152, 77-83, ISSN 0924-0136
- Kazmer, D. O. (2007). *Injection Mould Design Engineering*, Hanser Gardner Publications, ISBN 978-1569904170, Cincinnati
- Kearns, M. (2009). European MIM status. *Proceedings of PIM 2009 International Conference on Powder Injection Molding*, Orlando, March 2009, Metal Powder Industries Federation
- Kubat, J. & Szalanczi, A. (1974). Polymer-glass separation in the spiral mold test. *Polymer Engineering and Science*, 14, 12, 873-877, ISSN 0032-3888
- Kurzbeck, S.; Kaschta, J. & Münstedt, H. (1996). Rheological behaviour of a filled wax system. *Rheologica Acta*, 35, 5, 446-457, ISSN 0035-4511
- Laddha, S.; Wu, C.; Vallury, S.; Lingam, G.; Lee, S.; Simmons, K.; Thomas, P.; Levenfeld, B.; Varez, A.; Park, S.J.; Ahn, S.; German, R.M. & Atre, S.V. (2009). Characterisation of alumina feedstock with polyacetal and wax-polymer binder systems for micro powder injection moulding (μ PIM). *PIM International*, 3, 3, 64-70, ISSN 1753-1497
- Langer I. (2007). Schunk builds on designing successful automotive MIM parts. *PIM International*, 1, 4, 39, ISSN 1753-1497
- Li Y. (2007). Demand for precision components set to drive Chinese PIM manufacturing into the mainstream. *PIM International*, 1, 4, 17-25, ISSN 1753-1497
- Maron, S. H. & Pierce, P. E. (1956). Application of Ree-Eyring generalized from theory to suspensions of spherical particles. *Journal of Colloid Science*, 11, 80-95, ISSN 0095-8522
- Metzner A. B. (1985). Rheology of suspensions in polymeric liquids. *Journal of Rheology*, 29, 6, 739-775, ISSN 0148-6055
- Moritz, T. (2008). Two-component CIM parts for the automotive and railway sectors. *PIM International*, 2, 4, 38-39, ISSN 1753-1497
- Moritz, T. & Lenk, R. (2009). Ceramic injection moulding: a review of developments in production technology, materials and applications. *PIM International*, 3, 3, 23-34, ISSN 1753-1497
- Murray, J.S. Jr. (1984). *X-Stat statistical experiment design/data analysis/nonlinear optimization*, John Wiley & Sons, ISBN 978-0471524441, New York

- Persson, H.; Hausnerova, B.; Nyborg, L. & Rigdahl, M. (2009). Rheological and thermal properties of a model system for PIM. *International Polymer Processing*, 24, 2, 206-212, ISSN 0930-777X
- Schlieper, G. (2007). Leading German manufacturer works to develop the market for MIM in automotive sector. *PIM International*, 1, 3, 37-41, ISSN 1753-1497
- Schlieper, G. (2010). Global PM leader GKN Sinter Metals optimistic as MIM gains acceptance with end-users. *PIM International*, 1, 4, 44-46, ISSN 1753-1497
- Sedlacek, T.; Zatloukal, M.; Filip, P.; Saha, P. & Boldizar, A. (2004). On the effect of pressure on the shear and elongational viscosities of polymer melts. *Polymer Engineering and Science*, 44, 7, 1328-1337, ISSN 0032-3888
- Sedlacek, T.; Cermak, R.; Hausnerova, B.; Zatloukal, M.; Boldizar, A. & Saha, P. (2005). On pvt and rheological measurements of polymer melts: correction of the hole fraction-viscosity relationship. *International Polymer Processing*, 20, 3, 286-295, ISSN 0930-777X
- Shenoy, A.V. (1999). *Rheology of Filled Polymer Systems*, Kluwer Academic Publishers, ISBN 0-412-83100-7, Dordrecht
- Thornagel, M. (2009). MIM-simulation: A virtual study on phase separation, *Proceedings of EURO PM 2009*, 2, 135-140, ISBN 978-1899072071, Copenhagen, October 2009, European Powder Metallurgy Association
- Utracki, L.A. (1985). A method of computation of the pressure effect on melt viscosity. *Polymer Engineering and Science*, 25, 655-668, ISSN 0032-3888
- Wie, W.C.J.; Wu, R.Y. & Ho, S.J. (2000). Effects of pressure parameters on alumina made by powder injection moulding. *Journal of the European Ceramic Society*, 20, 9, 1301-1310, ISSN 0955-2219
- Williams, N. (2008). Arburg sets the pace in the production of moulding machines for PIM. *PIM International*, 2, 3, 49-52, ISSN 1753-1497
- Williams, N. (2009). Fraunhofer IFAM: A commitment to industry oriented research helps drive MIM product development. *PIM International*, 3, 3, 51-56, ISSN 1753-1497
- Yasuda, K.; Armstrong, R.C. & Cohen, R.E. (1981). Shear flow properties of concentrated solutions of linear and star branched polystyrenes, *Rheologica Acta*, 20, 2, 163-178, ISSN 0035-4511

Thermomechanical and Isothermal Fatigue Behavior of Gray Cast Iron for Automotive Brake Discs

Omar Maluf, Jéferson Aparecido Moreto, Maurício Angeloni,
Marco Antônio Colósio, José Carlos Santos,
Waldek Wladimir Bose Filho and Dirceu Spinelli.

*Department of Materials, Aeronautic and Automotive Engineering, University of São Paulo
Brazil*

1. Introduction

At the end of the 19th century, in the wake of railway transportation and the beginning of automotive vehicle production, new technology-based materials became necessary for the manufacture of brake systems to provide safer and more effective braking of vehicles transporting heavy loads at higher speeds. These devices serve to decelerate vehicles by friction, transforming most of the kinetic energy into thermal energy, which is dissipated by the brake system during the braking process [IOMBRILLER, 2002].

Many parts contribute actively or passively to a vehicle's satisfactory performance, but safety is closely linked to the efficiency of the brake system, which is subjected to relatively high thermal and mechanical stresses during regular braking action. Therefore, a crucial factor is the precision of the analysis and development of brake systems taking into account all the aspects involved in their thermal and dynamic behavior [MAZUR et al., 2005].

During severe deceleration by braking, the temperature of the brake system may reach up to 650°C and overheating of the brake discs may lead to serious consequences that reduce the vehicle's safety [IOMBRILLER, 2002]. This temperature variation causes thermal shock and localized overheating points, changing the behavior of the metal involved due to metallurgical transformations, as well as crack nucleation in the disc in response to plastic flow of the surface metal and inducing stresses after cooling [MAZUR et al., 2005].

Even disregarding the presence of thermal shock, a few braking cycles with abrupt deceleration still suffice to produce small cracks in the usable part of brake discs. The study of the mechanical behavior and fracture mechanisms of these materials is essential to allow for the design and rational use of these components. **Figure 1** illustrates the failure in front brake rotor in a disc submitted to penetrating liquid inspection to reveal cracks.

The cyclic stresses resulting from the continuous use of vehicles can cause fatigue, propagate cracks and fracture of the brake component [IOMBRILLER, 2002]. This mechanism may cause crack nucleation and growth in the material when subjected to cyclic strain. As cyclic loading conditions in brake discs are induced mainly by temperature gradients, thus essentially strain-controlled tests were planned for this study. In this way, it

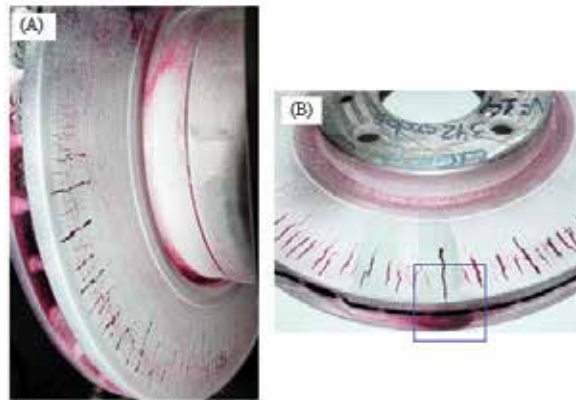


Fig. 1. (A) After 160 cycles, and (B) after 320 cycles. Note the macroscopic cracks propagating on the friction surface along the radial direction, extending from the inner to the outer radius of the disc [Maluf, 2007].

is clear that cracking in brake discs should be seen as an isothermal and thermomechanical problem. Isothermal Fatigue (IF) consists in the application of a variable mechanical strain at a constant temperature. The main advantages of this test are its simplicity and lower cost than that of anisothermal tests (thermomechanical).

Until recently, the fatigue strength of materials at high temperatures was estimated based on IF tests at the maximum temperature expected in the Thermal Fatigue (TF) cycle. However, this procedure proved to be insufficient because the strength of materials in TMF is significantly lower than that expected for the IF-based estimate. This is due to mechanisms possibly activated during the thermal cycling of TMF, which does not occur in IF, where the temperature is kept constant.

There are two main types of brake systems: drum and disc. The use of disc in place of drum brakes in heavy vehicles has become increasingly common in recent years.

This is due mainly to the search for greater braking efficiency, since disc brakes withstand higher temperatures than drum brakes [BOIOCCHI, 1999]. However, simply changing the drum shoe for the disc pad system does not suffice, making it necessary to analyze the brake system as a whole, as well as its influence on the vehicle's performance and safety.

In many high responsibility applications – as in the case of brake discs, knowing the results of tensile, impact and hardness testing is not enough to characterize the materials used in components, because these results cannot provide the information needed to reliably predict the behavior of these parts in real working conditions. Ideally, the materials used in brake systems should possess several properties such as good thermal conductivity, good corrosion resistance, good durability, stable friction, low wear rate and good cost-benefit [WEINTRAUB, 1998].

1.1 Thermomechanical Fatigue – TMF

Several components are subject to a variety of thermomechanical and isothermal loading due to temperature variations during a vehicle's operation. The cyclic loading conditions induced by temperature gradients are essentially loads limited by strain. Therefore, laboratory studies of Isothermal Fatigue, IF, are usually limited by strain control in low cycle fatigue tests [HETNARSKI, 1991].

Thermomechanical fatigue, TMF, describes fatigue under simultaneous variation of temperature and mechanical strain. Mechanical strain, which is determined by subtracting the thermal strain from the total strain, should be uniform in every specimen and originates from external restrictions or loads applied externally, e.g., if a specimen is held between two rigid walls and subjected to thermal cycling (without allowing expansion), it will undergo external compressive mechanical strain. Examples of TMF can be found in pressure vessels and pipes in the electric power industry, where structures undergo pressure loads and thermal transients with temperature gradients in the thickness direction, and in the aeronautical industry, where turbine blades and discs undergo temperature gradients superimposed to rotation-related stresses.

According to Sehitoglu [SEHITOGLU, 1996] TMF may involve several mechanisms in addition to fatigue damage, including creep at high temperatures and oxidation, which contribute directly to damage. These mechanisms differ depending on the history of strain and temperature. They are different from those foreseen by the phenomenon of creep tests (non-reverse) and by oxidation tests in the absence of stresses (or of constant stresses).

Microstructural degradation may occur under TMF in the form of:

1. Overaging, such as the coalescence of precipitates and formation of lamellae;
2. Strain aging, in the case of solid solution hardening systems;
3. Precipitation of secondary phase particles; and
4. Phase transformation within the cycle's ultimate temperature.

Variations in the mechanical properties or in the coefficient of thermal expansion in the matrix and precipitates, which are present in many alloys, also result in local stresses and cracks. These mechanisms influence the material's strain characteristics, which are associated with damage processes.

1.2 Isothermal Fatigue – IF

IF test consists of imposing variable mechanical strains while maintaining the temperature constant. This type of test has been widely employed since the 1970s, with the advent of test machines operating in closed cycle. The main advantages of this test are its simplicity and low cost when compared to anisothermal tests, and results for a variety of materials are available in the literature [COFFIN Jr, 1954].

Observations by researchers have shown that service life under IF is longer than that found in anisothermal fatigue [HETNARSKI, 1951; SHI et al., 1998]. This was reported by Shi *et al.* [SHI et al., 1998] in a study of a molybdenum alloy containing 0.5% of Ti, 0.08% of Zr and C in the range of 0.01 to 0.04%, **see Figure 2**.

The lives obtained in IF tests at two temperature levels studied, 350°C and 500°C, were higher, in both cases, than those found in TMF in phase for temperatures from 350°C to 500°C, demonstrating that temperature variations cause extensive damage of the material. However, no obvious difference was found between the two isothermal tests analyzed regarding the number of cycles to failure of the specimens, confirming that in this temperature range the material maintains a good cyclic resistance. Hence, designs based solely on the isothermal fatigue of components that work at high temperatures are not reliable, thus requiring a more in-depth study of the behavior of the materials subjected to this phenomenon, including tests at different temperature intervals (anisothermal fatigue) and in a variable range of stresses and strains.

Figure 3 indicates that the longest IF life of specimens occurs within an intermediary range of the applied temperature. In this range, the shortest life found for 316L (N) austenitic

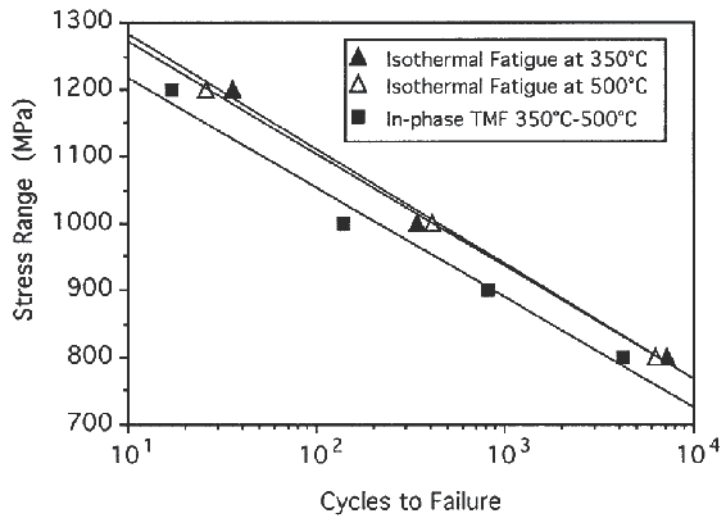


Fig. 2. IF and TMF curves [SHI et al., 1998].

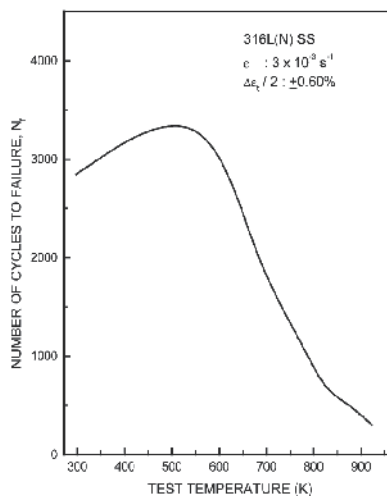


Fig. 3. Influence of temperature on the fatigue life [SRINIVASAN et al., 2003]

stainless steel was found at ambient temperature at which the strain induced the formation of martensite phase.

The microstructural recovery of the material, which was responsible for the increased life, occurred at the temperature of 573 K (300°C). The reduction of life with continuous increases in temperature is attributed to several effects of dynamic strain, such as the concentration of stresses produced in sites of stacking unconformities when the maximum stress of the cycle is reached, causing an increase in crack growth rate.

This is clearly evident at temperatures above 873 K (600°C), at which the lifetime was significantly reduced by oxidation [SRINIVASAN et al., 2003].

Another aspect to be observed under in IF with controlled strain is the behavior of cyclic stress as a function of life. The behavior of the 316L (N) austenitic stainless steel was monitored during four stages, as illustrated in **Figure 4** [SRINIVASAN et al., 2003].

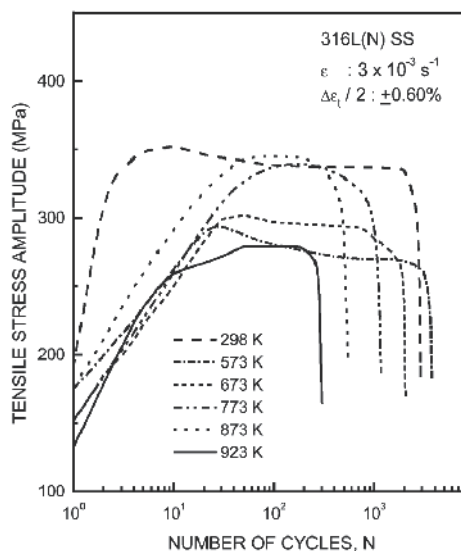


Fig. 4. Cyclic stress response as a function of temperature [SRINIVASAN et al., 2003].

The alloy exhibited a brief period of cyclic hardening, reaching its maximum stress in the early stage of life, followed by cyclic softening before attaining the stable regime. In the period prior to fracture, the stress amplitude decreased rapidly, indicating crack nucleation and propagation.

This figure also shows that the amplitude of the peak stress increased with rising temperature from 573 to 873 K, and also that some factors contribute to the drop in the material's strength with the increase in temperature. These factors are an abnormal cyclic hardening rate and reduction of the amplitude of plastic strain in the lifetime intermediary to fracture, and an increase in the maximum stress rate in the initial cycles in response to increased temperature, which develop due to the inductive interaction between diffusion solutes and mobility of the unconformities during strain. All these phenomena are considered manifestation processes of the period of dynamic strain.

2. Materials and methods

Table 1 lists the chemical composition of the four gray cast iron alloys that are used in the production of automotive brake discs and that were the object of this study.

After selecting these four alloys, isothermal and thermomechanical fatigue tests were performed on specimens in conditions of strain, in-phase and out-of-phase. The failure criterion adopted was a 50% decrease of the maximum load reached during the test.

Figure 5 (a) shows a Y-shaped block, according to the ASTM A476/476M standard, indicating regions A and B from which the test specimens were removed. **Figure 5 (b)** shows the dimensions and geometry of the test specimens used in the IF and TMF tests.

Samples were removed from regions A and B of the Y-shaped blocks to machine fabricate the specimens for the TMF and IF tests, as indicated in **Figure 5b**.

TMF and IF tests were performed in the Laboratory of Mechanical Properties of the Department of Materials, Aeronautics and Automotive Engineering at the Engineering School of São Carlos, University of São Paulo. All tests were conducted in a 250 kN capacity

Elements	Alloys			
	A	B	C	D
%C	3.36	3.45	3.71	3.49
%Si	2.07	2.11	2.0	1.87
%Mn	0.63	0.71	0.69	0.53
%P	0.03	0.068	0.059	0.03
%S	0.06	0.05	0.052	0.11
%Cr	0.16	0.30	0.19	0.29
%Mo	0.06	0.41	0.42	-
%Cu	0.08	0.10	0.40	0.52

Table 1. Cast iron alloys chemical composition (weight %)

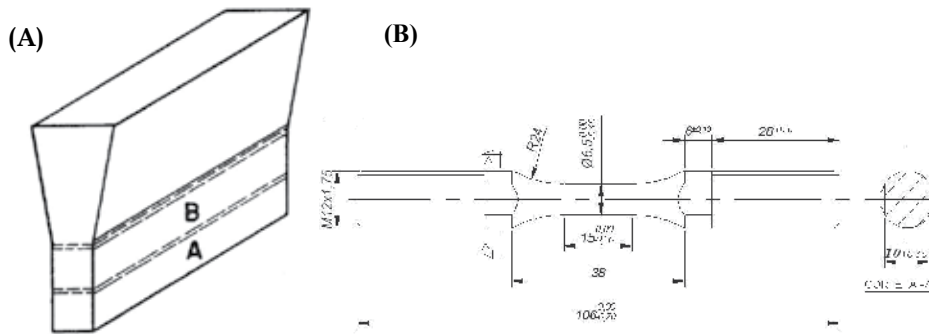


Fig. 5. (A) Y-shaped block according to the ASTM A476/476M standard, showing regions A and B from which the specimens were removed, and (B) geometry and dimensions of specimen used in the TMF and IF tests, dimensions in mm.

MTS 810 servo-hydraulic testing system, equipped with an MTS Micro Console 458.20 controller, Figure 6 and specially adapted to for TMF tests under total strain control. A high temperature axial strain gauge, MTS model 632.54F-14, was used to control the amplitude of total strain. The hydraulic grip system was an MTS model 680.01B, which is suitable for mechanical tests at high temperatures.

The test specimens were heated in a 75 kW inductive heating system operating at a frequency of 200 kHz. The temperature was measured using an optical pyrometer equipped with a laser target focused midway along the length of the specimen, providing the input for the temperature controller, which received the command signal from a microcomputer. The temperature gradient along the specimen length was minimized using an induction coil with optimized geometric dimensions. The auxiliary cooling system of the clamps grips for the thermomechanical fatigue tests consisted of two spiral copper tubes for circulating cold water and two compressed air pipes attached at to the upper and lower ends of the clamps grips. Figure 7 shows a localized detailed view of the region where the test specimen was fixed in the MTS 810 machine.



Fig. 6. Overall view of the testing apparatus, showing the induction furnace and the MTS 810 servo-hydraulic testing system.

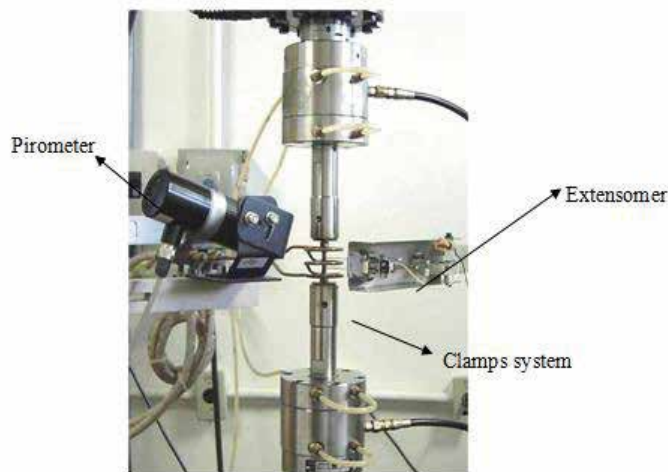
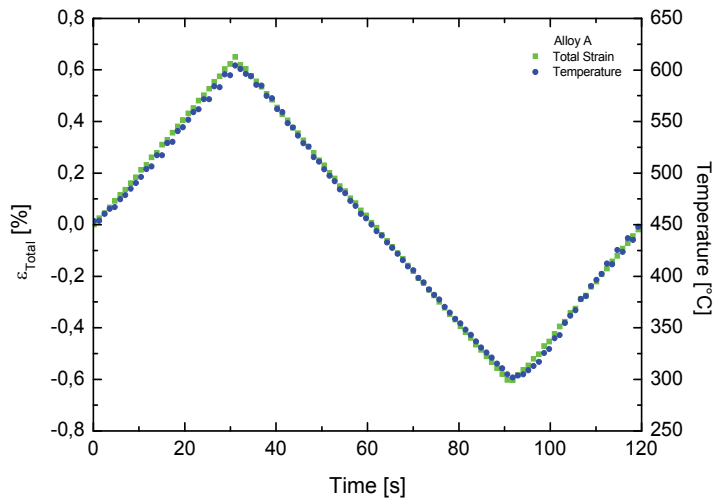


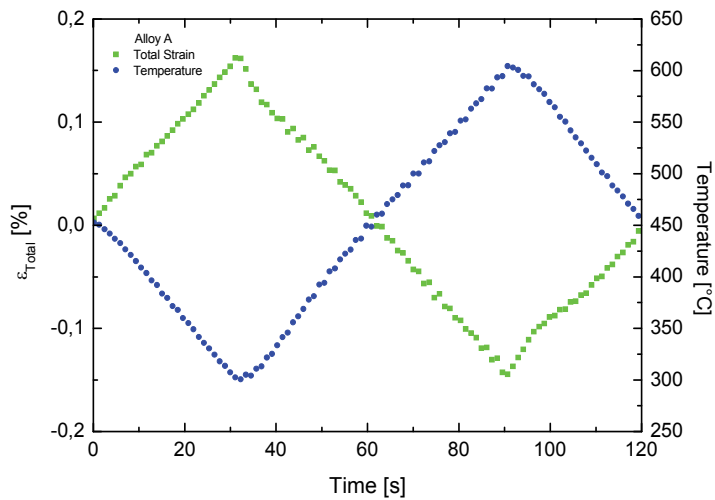
Fig. 7. Detail of the specimen, induction coil, auxiliary cooling system of the grips, and the strain gauge with ceramic rods used in the tests.

The TMF tests were performed in thermal cycles of 120s, the minimum time required to allow for stable cooling of the gray cast iron specimen and to maintain synchronism between the thermal and mechanical cycles, load ratio, $R = -1$, as illustrated in Figures 8 (a) and (b).

In-phase and out-of-phase TMF tests were carried out in the temperatures from 300 to 600°C. For in-phase TMF, positive strain corresponds to the maximum temperature of the cycle, negative strain corresponds to the minimum temperature of the cycle, and strain is equals zero at the temperature of 450°C, as illustrated in **Figure 9**.



(A)



(B)

Fig. 8. Variation of total strain as a function of time and temperature, in initial cycles of TMF tests on alloy A, under controlled mechanical strain (0.4%): (A) in-phase, and (B) out-of-phase.

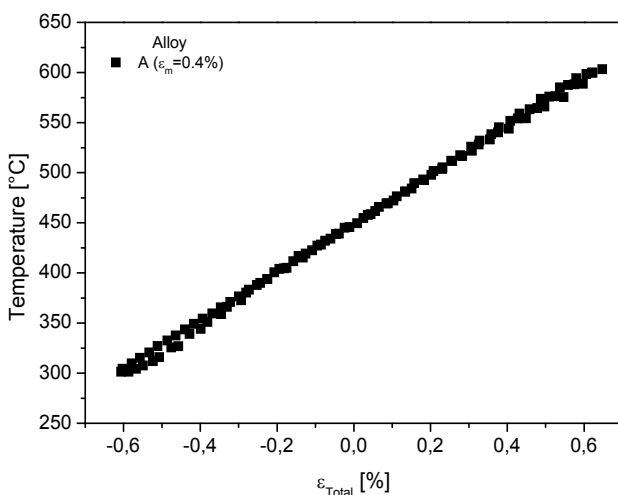


Fig. 9. Temperature hysteresis loop as a function of total strain in an in-phase TMF test. Hysteresis loop for alloy A.

In out-of-phase TMF tests, the positive strain corresponds to the lower cycle temperature, negative strain to the higher cycle temperature, and strain is zero at 450°C, as indicated in Figure 10.

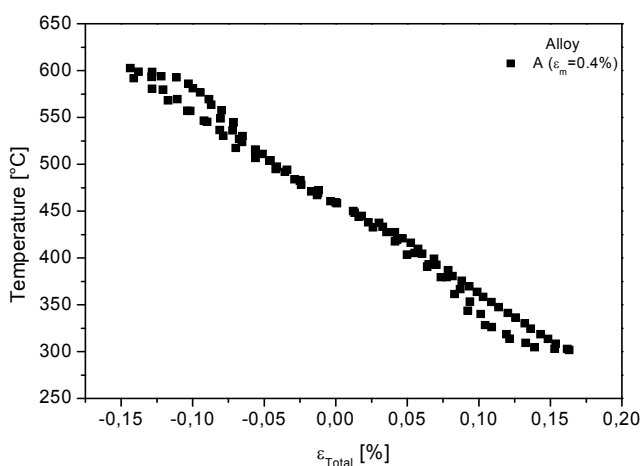


Fig. 10. Temperature hysteresis loop as a function of total strain in an out-of-phase TMF test.

3. Results and discussion

The behavior of total strain amplitude ($\Delta\epsilon_m/2$) as a function of the number of cycles to failure was obtained in alloys A, B, C and D for several levels of strain in the thermal cycle from 300 and 600°C. It was found that the higher the total strain applied the shorter the lifetime of the material, which is due to the increase in stress required to reach higher strains.

Figure 11 presents the curve of total strain amplitude, $\Delta\epsilon_t/2$, vs. the number of reversals to failure ($2N_f$), indicating the behavior of the four alloys tested in-phase. As can be seen, at mechanical strain amplitude of 0.10% in the in-phase test condition, the alloys exhibited an anomalous behavior, i.e., they presented premature fatigue life values than those obtained in the tests at higher amplitudes of mechanical strain. This was very likely due to the occurrence of the phase transformation known as graphite expansion caused by decomposition of the cementite phase in the perlite microconstituent, which transforms into ferrite and vein graphite [ASM International handbook, 1999].

This microstructural transformation leads to a significant decrease in the alloy's mechanical strain amplitude values, producing a rapid drop in the applied tensile load as a function of the number of reversals to failure. This demonstrates the non-validation of the fatigue life criterion adopted in the condition of 50% decrease of the ultimate load, to study the mechanical behavior of gray cast iron loaded under thermomechanical fatigue at very low levels of mechanical strain amplitude.

Thus, since the results for the strain amplitude of 0.1% are not valid, they were disregarded in the construction of the tendency lines in **Figure 11**.

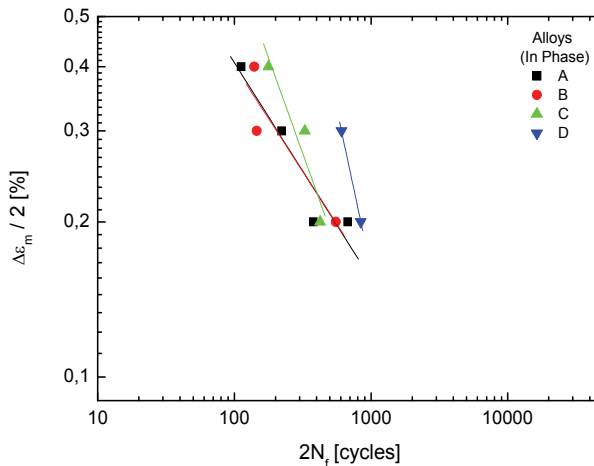


Fig. 11. Comparative plot of the mechanical strain amplitude of the four alloys as a function of the number of reversals to failure in the TMS in-phase condition.

The results obtained in the in-phase loading condition indicate that the behavior of the gray cast iron alloys A, B, and C in in-phase TMF were very similar or superior in terms of the number of reversals to failure at mechanical strain amplitudes of 0.2%, 0.3% and 0.4%. In other words, the three alloys presented practically the same in-phase life at values of mechanical strain amplitude equal to or higher than 0.2%.

As the graph in **Figure 11** indicates, alloy D presented the best performance in in-phase TMF at all of the applied strain amplitudes. It was thus demonstrated that, among the four gray cast iron under study, the alloy with the best performance was the one with relatively low equivalent carbon content and containing the alloying elements chromium and copper. These conclusions were based on the results of in-phase TMF, where alloy A, albeit devoid of any special alloying element, presented a behavior similar to that of both alloys C and B, which are the most alloyed.

Figure 12 depicts the behavior of the four alloys in thermomechanical out-of-phase fatigue. Note that in this loading condition, the alloying elements as well as the equivalent carbon content exerted little or no influence on the low-cycle fatigue strength of the alloys.

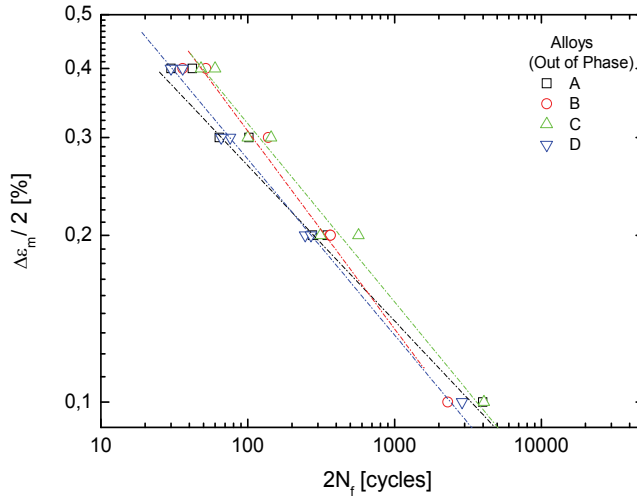


Fig. 12. Comparative plot of the mechanical strain amplitude *vs.* number of reversals to failure of the four alloys, in TMF out-of-phase.

To facilitate a comparison of the results of the alloys' behavior in both TMF conditions, they were plotted in the same figure, but without taking into account the mechanical strain amplitudes less than 0.2%. This artifice allowed for a clearer view of the performance of the alloys (**Figure 13**).

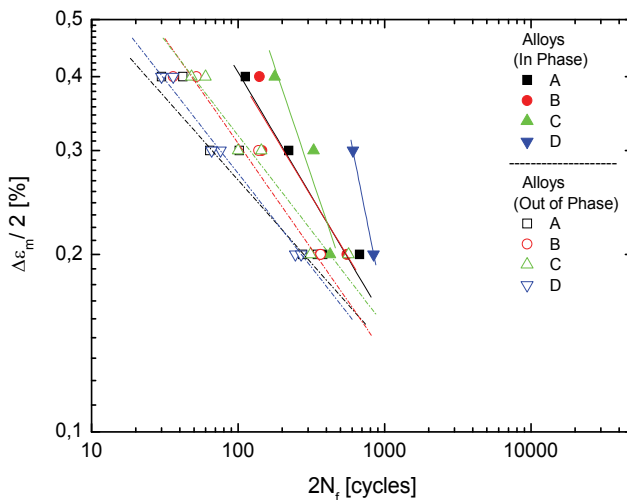


Fig. 13. Comparative plot of the mechanical strain amplitude *vs.* number of reversals to failure of the four alloys, in-phase and out-of-phase, neglecting amplitudes lower than 0.2%.

Based on the curves in **Figure 13**, it can be stated that among the low-cycle TMF tests carried out on specimens of four gray cast iron alloys, the ones performed in the out-of-phase condition were the most critical, since they led to failure in a lower number of reversals. This greater severity of the out-of-phase tests is justified by the fact that the tensile stresses in this test condition are applied at the lowest temperatures of the cycle, in which the material presents low ductility, thus requiring the application of higher stresses to become strained than those that would be required to strain it at higher temperatures. The same reasoning with respect to temperature can be employed to study the behavior of compressive stresses. The effect of the test condition on the application of stresses is easily observed from the behavior of the mean stress curves in the low-cycle thermomechanical fatigue tests. These curves were negative in the in-phase and positive in the out-of-phase condition, as displayed in **Figure 14**.

The total strain amplitude that occurs in a TMF test is the sum of the mechanical strain amplitude, which is predetermined, and the amplitude of thermal strain, which is a function of the coefficient of thermal expansion of the material and the variation in temperature.

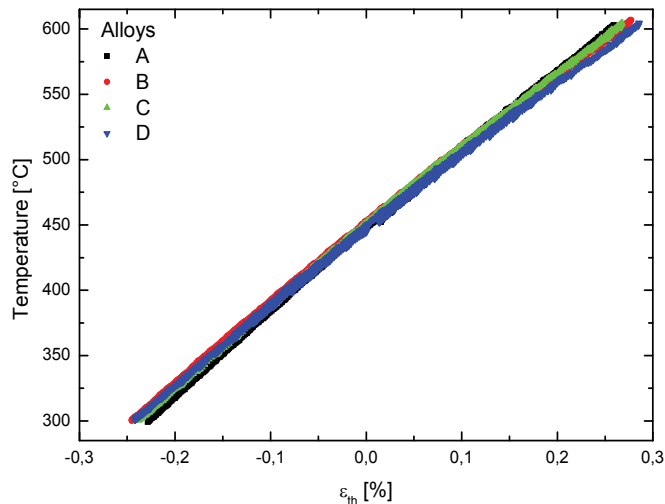


Fig. 14. Thermal strain presented by alloys A, B, C and D in response to temperature increase.

Therefore, the value of the percent amplitude of thermal strain employed to obtain the percent of mechanical strain amplitude for the four alloys of this study in the thermomechanical fatigue tests was 0.3%.

In order to ascertain whether the IF tests could be adopted, as is normally done, to predict the alloys' behavior in TMF, the IF and TMF curves of the four alloys of this study were plotted on the same graphs of % of total strain amplitude as a function of the number of reversals. As can be seen in the plots in **Figures 15, 16, 17 and 18**, when subjected to IF at any of the temperatures of 25°C, 300°C and 600°C, alloys **A, B, C and D** presented longer lifetimes than in out-of-phase TMF, indicating an increase in the severity of the test when temperature variations occur during cyclic loading.

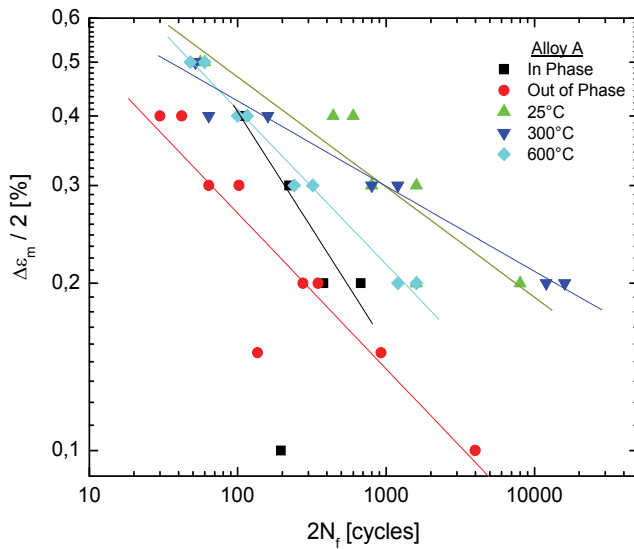


Fig. 15. Mechanical strain amplitude as a function of number of reversals to failure for alloy A. Comparison of in-phase and out-of-phase TMF, and IF at 25°C, 300°C and 600°C.

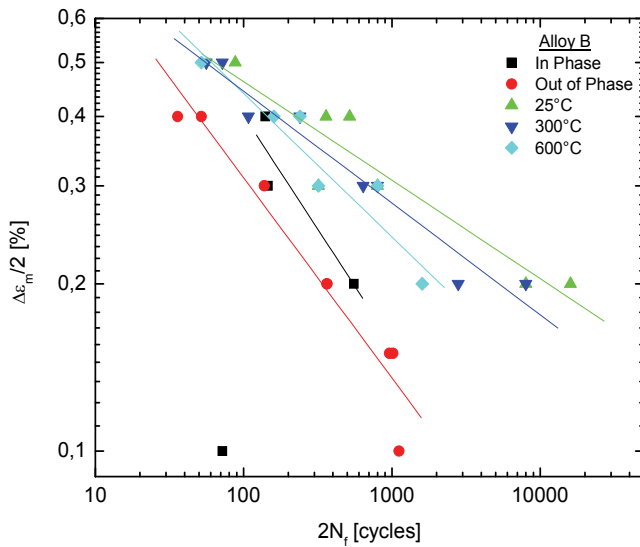


Fig. 16. Mechanical strain amplitude as a function of number of reversals to failure for alloy B. Comparison of in-phase and out-of-phase TMF, and IF at 25°C, 300°C and 600°C

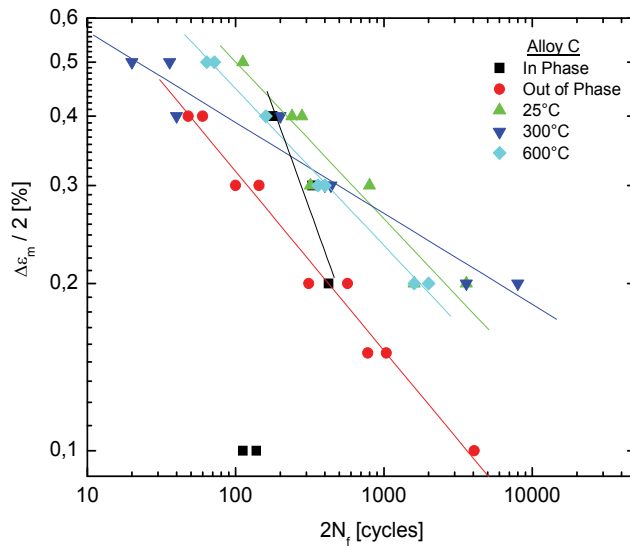


Fig. 17. Mechanical strain amplitude as a function of number of reversals to failure for alloy C. Comparison of in-phase and out-of-phase TMF, and IF at 25°C, 300°C and 600°C.

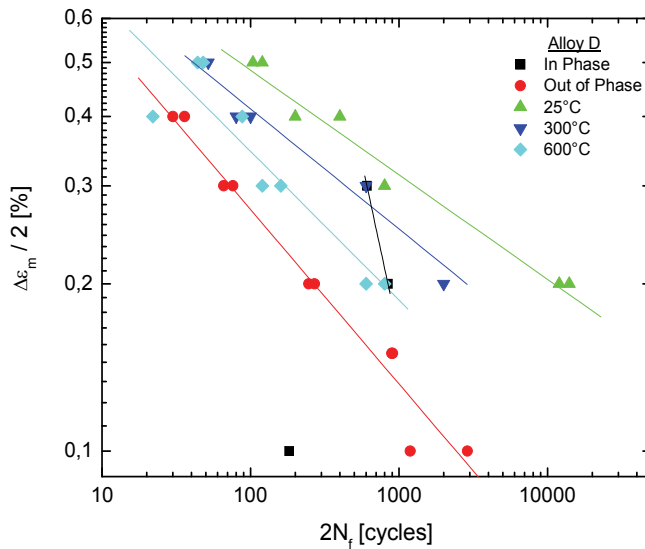


Fig. 18. Mechanical strain amplitude as a function of number of reversals to failure for alloy D. Comparison of in-phase and out-of-phase TMF, and IF at 25°C, 300°C and 600°C.

As can be seen from the curves, the severity of the tests increases, and hence, the lifetime decreases in the following sequence: IF at 25°C, IF at 300°C, IF at 600°C and out-of-phase TMF. This clearly indicates that IF tests are unsuitable to predict thermomechanical fatigue behavior, at least in the case of the materials of this study.

The precision of the direction to be considered for the in-phase TMF curves, particularly for alloy **D**, was impaired because the results of the mechanical strain amplitude of 0.1%, due to the anomalous results, were not considered. Thus, they were not analyzed from the standpoint of severity. In general, and apart from anomalies, the smaller the preestablished mechanical strain the longer the duration of thermomechanical fatigue tests; hence, phenomena such as creep and oxidation have an opportunity to act, reducing the material's lifetime.

The gray cast iron alloys that are used in the production of automotive brake discs were subjected to IF tests because vein graphite behaves like microcracks. Therefore, the conventional method of calculating the plastic and elastic components of strain cannot be used because it would yield incorrect values since, depending on the hysteresis, the tensile unloading tangent could find negative values of plastic strain. Therefore, the extent of hysteresis at half-life was determined by the mean stress, as shown in **Figure 19** [KANDIL, 1999].

Note that the distance **db** corresponds to the plastic strain amplitude, the horizontal distance **ac** corresponds to the total strain amplitude, and the vertical distance **ac** corresponds to the stress amplitude; E_1 is the modulus of elasticity in tensile unloading, and E_2 is the modulus of elasticity in compressive unloading.

The plots of strain amplitude *versus* number of reversals ($\Delta\epsilon_t \times 2N_f$) (**Figures 20 to 25**) indicate that the lives of the alloys under study showed significant differences at 25°C, 300°C and 600°C. This occurred at all the levels of strain analyzed, i.e., 0.2%, 0.3%, 0.4% and 0.5%, due to the low ductility of the alloys in question. In these cases, the equivalent carbon (CE) does not seem to exert any influence on fatigue life at any of the test temperatures. However, it was found that the life of alloy **B** increased along with increasing temperature, which is due to the presence of alloying elements such as molybdenum and chromium, indicating that these elements increase the materials' hot mechanical strength.

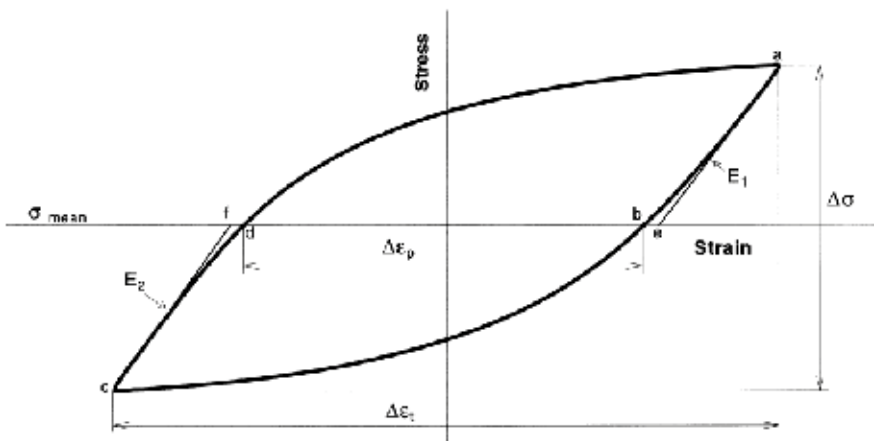


Fig. 19. Hysteresis curve [KANDIL, 1999].

The alloys with high mechanical strength require greater stresses to become strained. Therefore, an analysis of the behavior of the alloys of this study based on the plots of stress

amplitude vs. number of reversals ($\sigma \times 2N_f$) at the temperatures of 25°C and 300°C (Figures 20 to 25) indicates that there was no significant decrease in the stress amplitude of the four alloys. However, when the temperature reaches about 600°C (Figure 25), there is a more pronounced decline in the stress amplitude of the alloys containing little or no molybdenum, clearly evidencing its relationship with the increase in resistance at high temperatures. This therefore clearly shows that the alloys most resistant to a decrease in their mechanical properties in response to temperature, i.e., alloys B, A and D, present a better performance in terms of the IF lifetime.

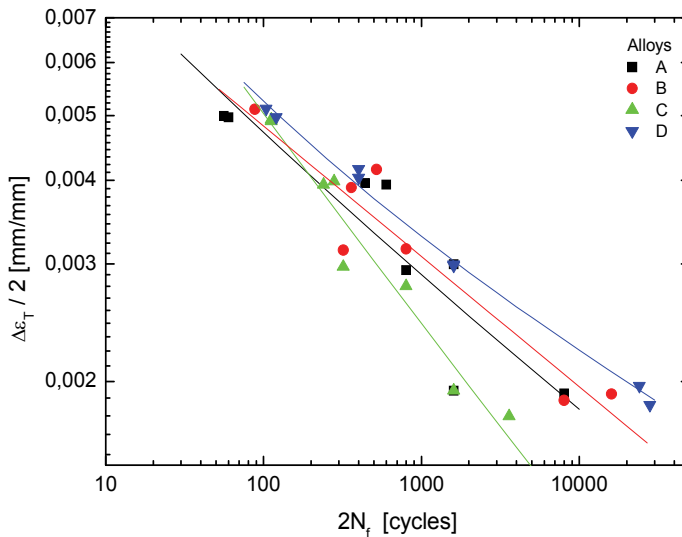


Fig. 20. IF: Comparative plot of total strain amplitude vs. number of reversals at 25°C.

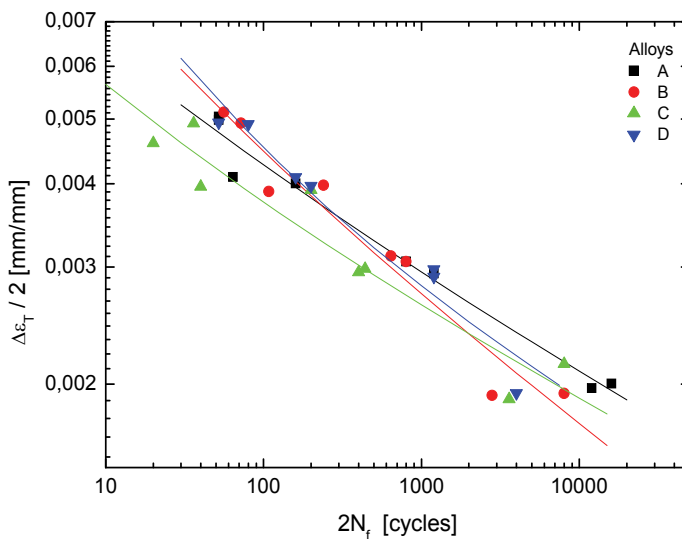


Fig. 21. IF: Comparative plot of total strain amplitude vs. number of reversals at 300°C.

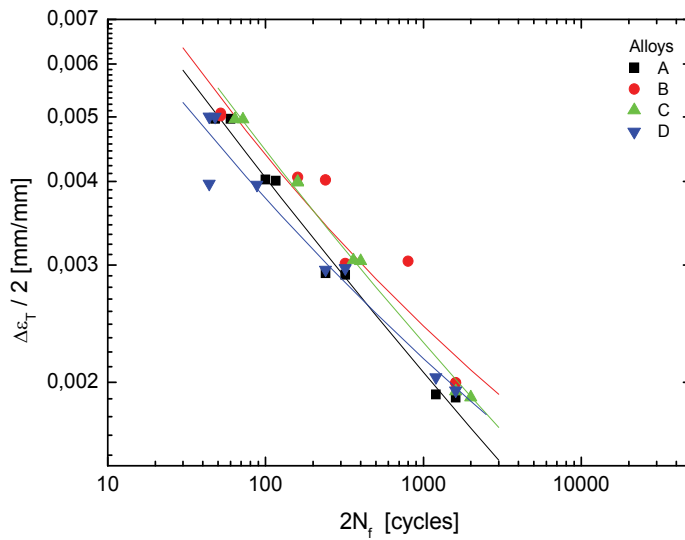


Fig. 22. IF: Comparative plot of total strain amplitude vs. number of reversals at 600°C.

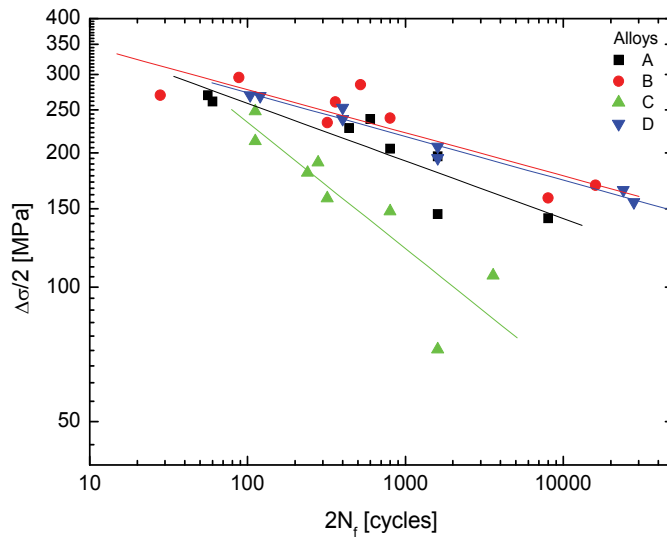


Fig. 23. IF: Comparative plot of stress amplitude vs. number of cycles at 25°C.

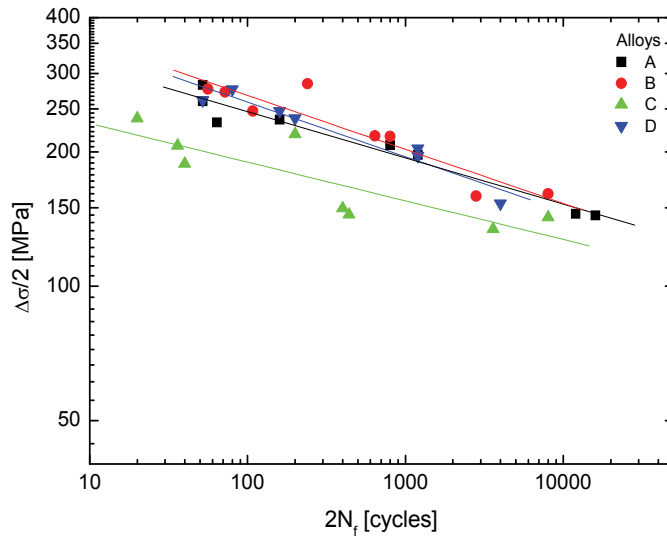


Fig. 24. IF: Comparative plot of stress amplitude vs. number of cycles at 300°C.

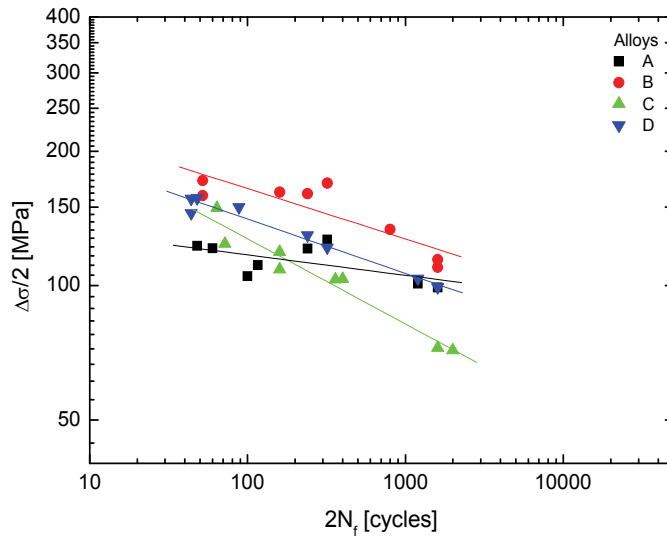


Fig. 25. IF: Comparative plot of stress amplitude vs. number of cycles at 600°C.

4. Conclusions

- At in-phase TMF mechanical strain amplitudes of 0.10% the value of fatigue life showed an anomalous behavior in all the analyzed alloys, which failed prematurely according to the adopted criterion of a 50% decrease in maximum tensile stress. In other words, their $2N_f$ was lower than that of the highest amplitudes of mechanical strain.
- The in-phase TMF curves indicated that the behavior of the gray cast iron alloys A, B and C were very similar in terms of $2N_f$ at mechanical strain amplitudes of 0.2%, 0.3% and 0.4%. In other words, the three alloys presented practically the same in-phase TMF life at mechanical strains equal to or higher than 0.2%.
- The out-of-phase TMF tests were the most critical, leading specimens to failure in a smaller number of reversals. This greater severity of the out-of-phase tests is explained by the maximum tensile stresses at the lower temperatures of the cycle.
- The best TMF performance was exhibited by the alloys with relatively low equivalent carbon content and containing the alloying elements Cr and Cu.
- As for the IF properties, the alloys under study did not show a significant difference at temperatures of 25°C, 300°C and 600°C, as indicated by the $\epsilon - N$ curves. The CE, was apparently uncorrelated with the fatigue life.
- Based on the $\sigma - N$ curves one can see that, even at ambient temperature, there is a difference among the alloys. With the increase in temperature there is a decline in the stress amplitude, which is more pronounced in the alloys containing little or no Cr and Mo. Thus, the alloys with higher mechanical strength require a higher stress to become strained.
- When subjected to IF at any of the temperatures, 25°C, 300°C and 600°C, the alloys presented longer lives and in out-of-phase TMF, revealed an increase in the severity of the test with the variation in temperature.
- The IF tests were less critical than the out-of-phase TMF tests.

5. References

- [1] IOMBRILLER, S. F. "Análise térmica e dinâmica do Sistema de Freio a Disco de Veículos Comerciais Pesados". Dissertation (doctorate in Mechanical Engineering), São Carlos: USP - Universidade de São Paulo, p. 177, 2002.
- [2] MAZUR, Z., LUNA-RAMÍZES, A., JUÁREZ-ISLAS, J. A., CAMPOS-AMEZCUA, A. "Failure Analysis of a Gas Turbine Blade made of Inconel 738 LC Alloy", *Engineering Failures Analysis*, Elsevier, V. 12, p. 474 - 486, 2005.
- [3] Maluf, O. "Fadiga Termomecânica em ligas de ferro fundido cinzento para discos de freios automotivos". PhD. Thesis (doctorate in Science and Materials Engineering), São Carlos: USP - Universidade de São Paulo, p. 47-130, 2007).
- [4] BOIOCCHI, T., "Technological Differences between Tractors, Trailers and Impact in the Safety and Drivability", in *Colloquium Internacional de Freios*, 4, Caxias do Sul, p. 23 - 28, 1999.
- [5] WEINTRAUB, M., "Brake additives consultant", *Private Communication*, 1998.
- [6] HETNARSKI, R. B. "Mechanics and Mathematical Methods - Thermal Stress II", *North-Holland, Oxford*, 2nd Series, V. 2, 1991.
- [7] SEHITOGLU, H. "Thermal and thermomechanical fatigue of structural alloys". In: *ASM HANDBOOK - Fatigue and Fracture*. Ohio, V.9, 1996.

-
- [8] COFFIN Jr., L.F., *A study of the effects of cyclic thermal stresses on a ductile metal*, Transactions of the ASME, n° 53-A76, 1954, p. 931-949.
- [9] HETNARSKI, R. B. *“Mechanics and Mathematical Methods – Thermal Stress II”*, North-Holland, Oxford, 2nd Series, V. 2, 1991.
- [10] SHI, H-J., KORN, C., PLUVINAGE, G., *“High Temperature Isothermal and Thermomechanical Fatigue on a Molybdenum-Based Alloy”*, *Materials Science and Engineering*, A247, p. 180 – 186, 1998.
- [11] SRINIVASAN, V.S., VALSAN, M., RAO, B. S., MANNAN, S.L., RAJ, B. *“Low Cycle Fatigue and Creep-Fatigue Interaction Behavior of 316L(N) Stainless and Life Prediction by Artificial Neural Network Approach”*, *International Journal of Fatigue*, V. 25, p. 1327 – 1338, 2003.
- [12] ASM International handbook. Heat Resistant Materials, pp. 183-186, 1999.
- [13] KANDIL, F.A. *Cycle Potential ambiguity in the determination of the plastic strain range component in LCF testing*. *International Journal of Fatigue*, 21 (1999), 1013-1018.

Advanced Robotic Radiative Process Control for Automotive Coatings

Fan Zeng and Beshah Ayalew

*Clemson University - International Center for Automotive Research
United States of America*

1. Introduction

In modern automotive manufacturing, coating, drying and curing processes provide essential protection for car bodies besides decorative functions. However, current coating and curing processes largely involve the use of convection bake-ovens and contribute immensely to the energy consumption and greenhouse gas emissions. For example, according to a recent study (Siewert, 2008), the total energy consumption per car manufactured averages about 3 MW-hr, of which 1.0-1.4 MW-hr (33-46%) happens in the painting/coating booth. Likewise, of the nearly 1.1 tons of CO₂ emissions per car manufactured, 0.4 tons (37%) of CO₂ emissions arise in the painting booths (Prendi et al., 2008). Assuming even the lowest industrial energy costs and considering the total annual global sales of nearly 70 million cars, estimated energy costs of painting booth operations alone run into trillions of dollars, not to mention the emission of tens of millions of tons of CO₂ into the atmosphere.

The energy and environmental issues involved in current automotive coating/paint curing processes may be alleviated by recent radiation-based methods which use either ultraviolet (UV) or infrared (IR) radiation to activate/initiate the curing or drying processes (Hagood et al., 2008) (Vgot, 2007). Compared to convection bake-ovens (Fig. 1a), these radiation-based methods use less energy, give improved productivity, and produce less air pollutions, such as CO₂, volatile organic compounds (VOCs), etc. As an example, a case study reported in (U.S. Department of Energy, 2003) showed that the replacement of the convection oven by a new IR oven allowed a metal finishing plant to increase its production by 50% and reduce natural gas consumption by 25% annually. Another study showed that the implementation

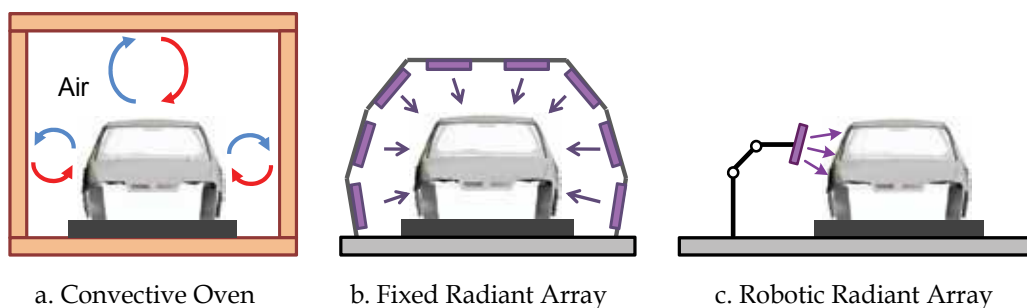


Fig. 1. Alternative automotive paint curing processes

of UV-curable coatings for aluminum can production may save as much as 55% in capital and installation costs over thermal curing and reduce 47,000 tons / year of CO₂ emission if implemented industry-wide (U.S. Department of Energy, 1999).

Early applications of radiation-based methods (e.g. UV) in the automotive industry can be found in curing coated components, such as headlamp lenses, reflectors, instrument panels, and so on (Starzmann, 2001). The application of UV curing to whole car bodies (clearcoat) was reported in (Mills, 2001) and (Fey, 2003), in which the coated car bodies were enclosed and cured by a set of fixed UV lamps with predesigned positions and orientations (Fig. 1b). Industrial robotic manipulators have also been used in curing automotive parts and whole car bodies for further improvements in process quality and energy efficiency (Raith et al., 2001) (Mills, 2005). In these applications, the robotic manipulator is used to move the UV radiative device (e.g. UV lamp or LED panel attached to the end effector of the robot) around the target object in a pre-designed path (Fig. 1c). To ensure the curing quality, both off-line simulations (for process analysis and path design) and online trial tests (for irradiance measurement and parameter tuning) should be done before the curing system is implemented in actual production lines (Raith et al., 2001) (Mills, 2005).

However, the open-loop control structure of current robotic UV curing applications, including the off-line simulations and online trial tests described above, has difficulties in maintaining the desired quality during actual processes due to the presence of various disturbances. These include unevenness in UV absorption, geometrical variations, changes in convective environment etc. In addition, for these open-loop methods, the change in product shapes and materials not only requires the redesign of the path of the robot manipulator, but it also causes the repetitive and time-consuming trial tests for calibrating the curing process.

Compared to typical trial-and-error methods (open-loop), closed-loop control of robotic actuated processes have been widely used in various industrial applications, such as welding (Hardt, 1993) (Huissoon et al., 1994) (Moore et al., 1997), painting (Seelinger et al., 1997) (Omar et al., 2006), spray forming (Jones et al., 2003), and so on. For the robotic UV curing of automotive coatings discussed in this chapter, the authors have developed some closed-loop methods, including 1) feedback control through thermal imaging (Zeng & Ayalew, 2009), 2) online process state and parameter estimation (Zeng & Ayalew, 2010-a), and 3) multi-variable coordination and optimization (Zeng & Ayalew, 2010-b), in order to improve the process quality and energy efficiency. These closed-loop control and estimation methods will be detailed in this chapter.

The rest of the chapter is organized as follows. The second section describes the fundamental modelling and feedback control design for the robotic UV curing process. The third section details the design of a state/parameter estimator for online monitoring of the curing process. This is followed by a section which discusses two fundamental approaches to achieve optimization of the curing process, and a section that describes a prototype robotic UV curing system developed for experimental implementation. Finally, the last section gives the summary and points out future research directions.

2. Process modelling and feedback control design

This section describes the modelling of the robotic UV paint curing process and the design of a set of closed-loop control strategies through cure-status feedback. Despite the complex geometries of automotive parts or whole car bodies, the UV lamp/LED moving with the

robotic end effector only illuminates a small region of the whole target at a certain time and the dominant radiation usually occurs in the normal direction of that region. Therefore, for the currently illuminated region, the 3D curing process can be reduced to a 2D problem as illustrated in Fig. 2. The following subsections detail the modelling of the curing process and the feedback control design based on this 2D description.

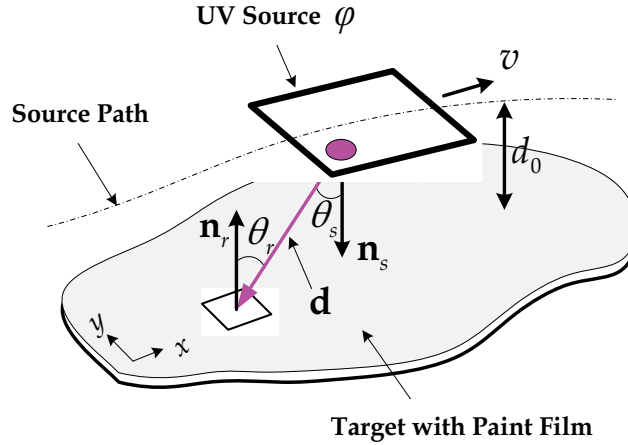


Fig. 2. The reduced schematic of a robotic UV curing process for a 2D target

2.1 Modeling the robotic UV curing process

In general, the UV curing mechanism can be broken into three coupled physical processes: irradiation, photo-initiated polymerization, and thermal evolution. Given the 2D schematic shown in Fig. 2, the mathematical description of the three fundamental processes is detailed as follows.

2.1.1 Irradiation

The major energy of the UV source is delivered to the target through radiation. The irradiance (power density) received by the target is strongly determined by the power level of the UV source and the relative distance and orientation between the source and the target. In this work, an LED type UV source is selected for its high efficiency and fast on-off response. As shown in Fig. 2, the LED UV source is composed of a set of small units and each unit can be modeled as a monochromatic Lambertian point source (Ashdown, 1994). Since the LED is an incoherent light source, the total irradiance arriving at the target surface can be obtained by superposition. Given the notations used in Fig. 2, the irradiance distribution on the target surface is represented by (Modest, 1993):

$$I(x, y, t) = \sum_{i=1}^N k(x, y) \frac{\varphi(t) \cos \theta_s^i(x, y, t) \cos \theta_r^i(x, y, t)}{N \pi |d_i(x, y, t)|^2} \quad (1)$$

where, the spatial coordinates for an arbitrary point on the target surface and the time are denoted by (x, y) and t , respectively. The irradiance distribution on the target surface is represented by $I(x, y, t)$. The number of the LED units and the index of each unit are denoted by N and i , respectively. The relative distance and orientation between each LED

unit and the target surface are characterized by d_i (position vector), θ_s^i (emission angle), and θ_r^i (incidence angle). The total power level of the UV LED is represented by the radiant flux $\varphi(t)$. The coefficient $k(x, y)$ is used to model the varying UV absorption throughout the target surface. It can be observed from equation (1) that the irradiance received by the target varies with both time and coordinate. This characteristic will also strongly influence the photo-initiated polymerization and thermal evolution processes to be described later.

2.1.2 Photo-initiated polymerization

Most curing processes involve the polymerization of various monomers. In the UV curing process, the polymerization is initiated by the UV radiation instead of high temperature. A typical photo-initiated polymerization is composed of three fundamental phases: initiation, propagation, and termination. In initiation, the photo-initiators (mixed with the paint) absorb the UV radiation and create free radicals which initiate the growth of polymer chain. Propagation follows cross-linking more polymer chains. Termination occurs when growing chains come together and react to form the dead polymer. Detailed description of the photo-initiated polymerization can be found in (Hong, 2004) (Goodner, 2002). A simplified kinetic model is used here to characterize the three fundamental phases of the photo-initiated polymerization (Hong, 2004).

$$\frac{d[PI](x, y, t)}{dt} = -\phi\varepsilon[PI](x, y, t)I(x, y, t) \quad (2)$$

$$\begin{aligned} & \frac{d[M](x, y, t)}{dt} \\ &= -\frac{k_p}{k_t^{0.5}}(\phi\varepsilon)^{0.5}[M](x, y, t)\{[PI](x, y, t)\}^{0.5}\{I(x, y, t)\}^{0.5} \end{aligned} \quad (3)$$

where, the concentrations of photo-initiator and monomer are denoted by $[PI]$ and $[M]$. ϕ and ε represent the quantum of yield for initiation and molar absorptivity, respectively. The propagation and termination rate constants are denoted by k_p and k_t . It can be seen from equations (2) and (3) that the spatial distributions of both the photo-initiator and monomer concentrations are highly influenced by the distribution the UV irradiance.

2.1.3 Thermal evolution

The thermal evolution in the curing process is characterized by the following energy balance equation:

$$\begin{aligned} & \rho c \frac{dT(x, y, t)}{dt} \\ &= \nabla\{\lambda\nabla T(x, y, t)\} - \Delta H \frac{d[M](x, y, t)}{dt} - h\{T(x, y, t) - T_\infty\} \end{aligned} \quad (4)$$

In equation (4), the internal energy accumulation (described by the intensity ρ , specific heat capacity c , and the change of temperature T) is determined by the heat conduction throughout the target (λ and ∇ denote the thermal conductivity and the gradient operator, respectively), the heat generation in the photo-initiated polymerization phase (ΔH is the

polymerization enthalpy), and heat convection between the target and the environment (h and T_∞ denote the convective heat transfer coefficient and the ambient temperature, respectively). All radiative heat transfer terms are ignored in this energy balance equation as they are assumed to be comparatively smaller than the retained terms.

2.2 Feedback control design

Given the system dynamics modeled in subsection 2.1, the objective of the feedback control design is to take some of those measurable process outputs as feedback and manipulate the radiant source (either in motion or power) so that the desired process quality set-point can be achieved. In the present case, since the cure-conversion level (normalized monomer concentration) is usually difficult to measure directly, the temperature, which is highly correlated to the cure-conversion, can be used to provide on-going curing status information for the controller. The temperature can be measured through one or more infrared (IR) cameras. The following paragraphs will detail the use of temperature feedback and the corresponding feedback control design.

2.2.1 Temperature feedback through infrared (IR) cameras

The principle of temperature measurement through IR cameras is a form of thermal imaging, in which the IR camera captures the images of the target in the infrared frequency domain and correlates them to the temperature distribution of the target based on fundamental radiative heat transfer theory. Three possible configurations (as shown in Fig.3) can be used to implement online temperature measurement through IR cameras for the purpose of robotic process control.

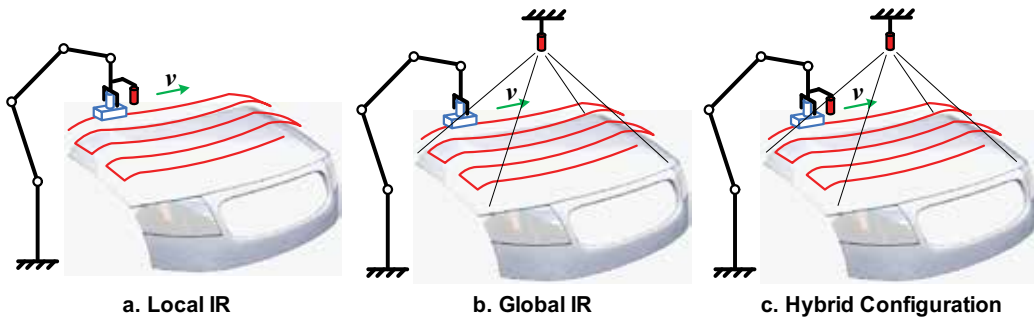


Fig. 3. Alternative temperature measurement configurations through IR cameras

In the local IR configuration (Fig. 3a), the IR camera is co-located with the moving radiant source, so it mainly focuses on the area which is currently being cured. This configuration is simple and effective for local temperature measurement. In the global IR configuration, the IR camera is fixed to the global coordinate system (e.g. test bench) so that it can have a full view of the target. With this configuration, the controller can receive more information from the IR camera (e.g. the complete temperature map of the target), but it also increases the image processing complexity. The hybrid configuration combines both the advantages of both the local and global ones, and it can help achieve better control performance with moderate cost compromise. The authors have developed different feedback control strategies for these alternative temperature measurement configurations, and the following subsection will give an overview of these strategies.

2.2.2 Control of the motion or power of the radiant source

With the temperature feedback obtained via the IR camera(s), some closed-loop control strategies are developed to improve the disturbance rejection capability of the system. In these closed-loop control strategies, only one of the two major manipulated variables (motion and power) of the radiant source is regulated online and the other is calibrated off-line or kept constant during the process. The general structure for these control strategies is illustrated in Fig. 4.

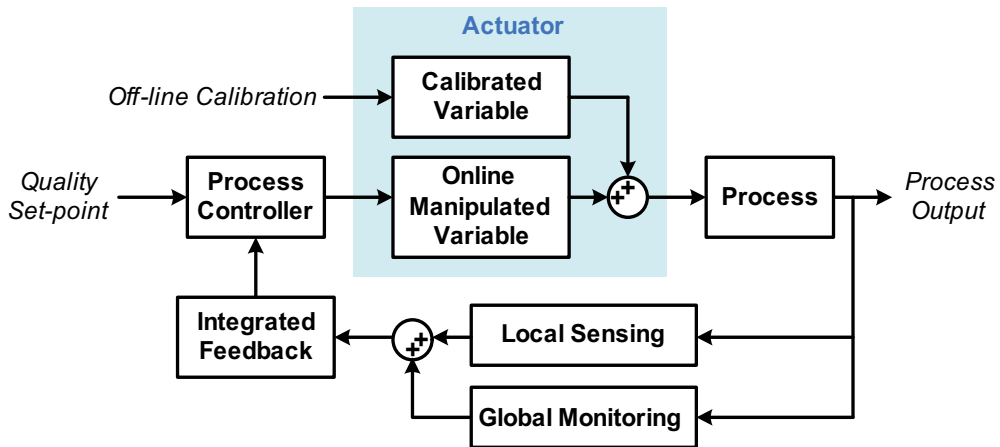


Fig. 4. The general output (temperature) feedback control structure

The control structure in Fig. 4 provides the framework for designing feedback control strategies based on different temperature measurement configurations depicted in Fig. 3. For the local IR configuration, a sequential curing style is selected, in which the radiant source stays at each segment of the target for a while and moves to the next one after the current segment has been cured. In this case, the power of the UV source is kept constant, while the motion of the robot is adjusted online (the controller determines the curing time for each segment based on the corresponding temperature level of the same segment, and commands the robot when it should move to the next one). For the global IR configuration, the radiant source is moved by the robot in a continuous manner, but the complete curing process is divided into several runs. The IR camera captures the temperature map of the target at the end of each run, and the controller decides if it is necessary to adjust the trajectory of the robot based on the global temperature feedback. The power of the UV source is still kept constant during the process for this configuration. For the hybrid configuration, the local and global temperature measurements are integrated into a real-time control structure, in which either the motion or the power of the radiant source can be adjusted continuously at any time of the process based on the integrated temperature feedback.

In these strategies above, the controller uses online temperature measurements directly to determine the appropriate motion or power applied to the radiant source. This can improve the process quality to some extent. However, the correlation between the temperature (process output, measured by IR cameras) and the cure-conversion level (controlled variable, difficult to be measured online) still needs to be calibrated through experiments. In the next section, an online estimator is developed to obtain such information by using a process model and the Kalman filtering method.

3. Online process state/parameter estimation

State/parameter estimation has been widely used for various industrial process control applications. For the automotive robotic UV curing, the development of a process estimator faces two major challenges. First, the target state (cure-conversion level) of the process is a spatially distributed variable and requires a large dimensional estimator. This may increase the computational cost. Second, the spatial movement of the radiant source can change the observability of the system. This has a significant influence on the estimation performance and it has to be carefully considered when designing the process estimator. This section details the development of a process state/parameter estimation scheme and discusses proposed solutions to the two major issues (large dimension and changing observability) described above.

3.1 Model reduction and simplification

To illustrate the development of the process estimator, the authors consider using a one-dimensional (1D) description (as shown in Fig. 5) to further simplify the robotic UV paint curing process depicted in Fig. 2.

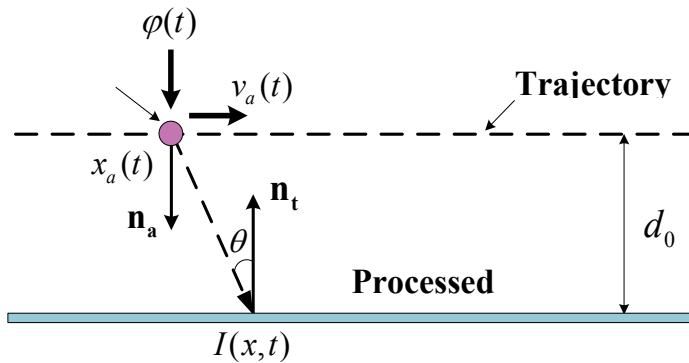


Fig. 5. The 1D description of the robotic UV paint curing process

In this 1D description, the actual UV radiant device is simplified as a point source. The variation along the cross-section direction is also ignored at this time. In addition, only a small segment of the processed target is considered here, so the 2D processed target has been reduced to a 1D strip. Then the corresponding process model can be reduced and simplified. For example, the simplified irradiation phase can be written as follows:

$$I(x, t) = k(x) \frac{\varphi(t) d_0^2}{\pi \{ [x_a(t) - x]^2 + d_0^2 \}^2} \quad (5)$$

Similar reduction and simplification can be applied to the photo-initiated polymerization and the thermal evolution phases. The detailed equations can be found in (Zeng & Ayalew, 2010-a).

3.2 Development of the state/parameter estimation scheme

This subsection describes the development of the state/parameter estimation scheme by using the dual extended Kalman filtering (DEKF) method. The main advantage of this method is that

it can help improve estimation accuracy by estimating some unknown process parameters, and subsequently correcting the process model that is used for estimation. Considering the two issues (large dimension and changing observability) mentioned at the beginning of this section, the authors develop the state/parameter estimation scheme keeping in mind the spatially distributed nature of the robotic radiative curing process.

3.2.1 Design of the dual extended Kalman filter (DEKF)

The dual extended Kalman filter (Wan and Nelson, 1997) is one of several variants of the original Kalman filter (Kalman, 1960), which provides combined state and parameter estimation through the use of two extended Kalman filters (EKFs) in parallel. Both EKFs follow the standard two-step (prediction and correction) estimation procedure. For the robotic UV curing process, the target state to be estimated is the monomer concentration, and the unknown process parameters considered here include the UV absorption coefficient and the convective heat transfer coefficient of the target. The basic structure of the DEKF adopted for this work is illustrated in Fig. 6.

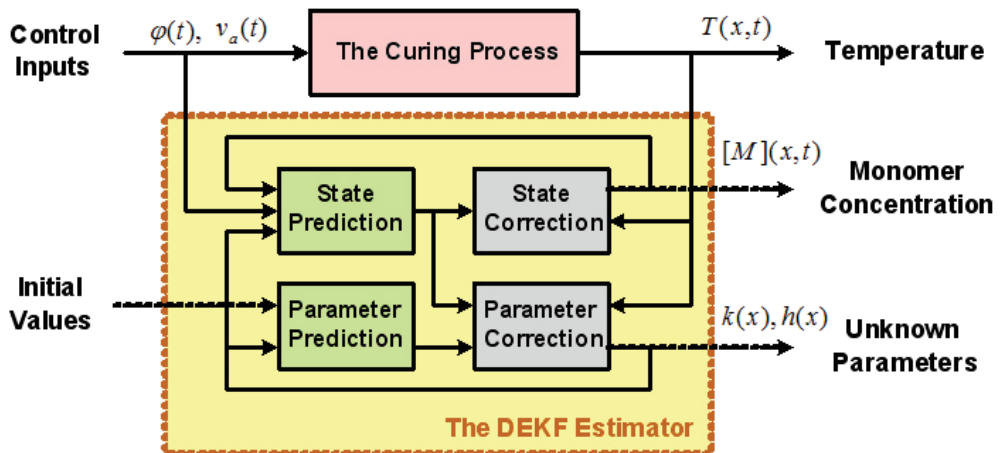


Fig. 6. The structure of the DEKF estimator

In Fig. 6, the two major inputs (power and motion) of the system are denoted by $\varphi(t)$ and $v_a(t)$. The output of the system is the temperature ($T(x,t)$), which can be measured online through IR cameras. The objective is to estimate the target state $[M](x,t)$ from the known inputs and the measured output. Parameter estimation is also applied to unknown process parameters ($k(x), h(x)$) to improve the accuracy of the process model and further improve the state estimation performance.

The following formulation outlines the two-step (prediction and correction) estimation procedure adopted for this application. More details about the standard procedure for Kalman filter can be found in (Kalman, 1960) (Haykin, 2001).

$$\text{Parameter Prediction:} \quad \hat{p}^-(j) = \hat{p}(j-1) \quad (6)$$

$$\text{State Prediction:} \quad \hat{x}^-(j) = F[\hat{x}(j-1), u(j-1), \hat{p}(j-1)] \quad (7)$$

State Correction:
$$\hat{x}(j) = \hat{x}^-(j) + K_s [y(j) - C\hat{x}^-(j)] \tag{8}$$

Parameter Correction:
$$\hat{p}(j) = \hat{p}^-(j) + K_p [y(j) - C\hat{x}^-(j)] \tag{9}$$

where, the discrete time index is denoted by j . The state and parameter vectors to be estimated are represented by x and p , respectively. The input vector is denoted by u , and the measured output is represented by y . At the first step, only the state vector is updated by using the process model, which is described by a nonlinear function ($F(\cdot)$) of the state, input, and parameter vectors at the previous time $j-1$. At the second step, the state and parameter vectors obtained at the prediction step will be further corrected based on current process output measurements. Two Kalman gain matrices (K_s and K_p , corresponding to state and parameter, respectively) are used here to weigh the prediction and correction parts, and give the final estimates at time j . The two gain matrices are also updated with time by following the standard procedure.

3.2.2 Implementation of the DEKF estimation scheme

Two major issues should be considered when implementing the DEKF estimation scheme to the robotic UV curing process: the large dimension of the estimator and the changing observability of the system caused by the moving radiant source. The detailed derivation and discussion on the changing observability can be found in the authors' previous work in (Zeng and Ayalew, 2010-a). To resolve the two issues, a distributed estimation structure with a moving activation policy (depicted in Fig. 7) can be developed and applied to the robotic UV curing process.

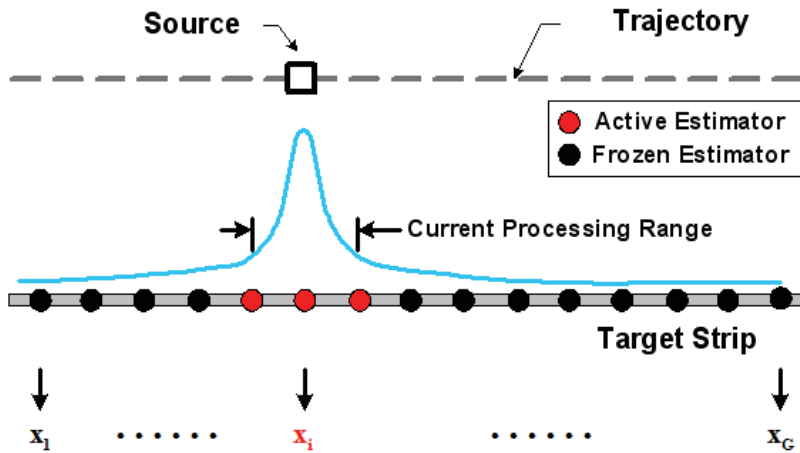


Fig. 7. The distributed estimation structure and the moving activation policy

In the distributed estimation structure shown in Fig. 7, the original process state vector x (describing the monomer concentration distribution along the whole target strip) is divided into a set of low-order subsystems which are denoted by $x_1, \dots, x_i, \dots, x_G$ (each of these subsystems only describes the local monomer concentration distribution around its own location), respectively. In these subsystems, only those that are located within the current processing range of the radiant source will be activated for the DEKF estimation, and the others are kept frozen at this time. As the radiant source moves through the target strip,

each subsystem will be activated sequentially to provide state and parameter estimation for the current processing range during the whole process. The distributed estimation structure described above can help reduce the computational cost thanks to the reduction of the dimension of the DEKF estimator. Meanwhile, since the moving activating policy ensures that the state/parameter estimation is only applied to the current processing range (subsystems within this range have better observability than other areas of the target strip), it can help compensate for the changing observability caused by the movement of the radiant source. The next subsection will give an example to demonstrate the DEKF estimation scheme developed for the robotic UV curing application.

3.3 Estimation results

In this subsection, simulation results are presented to illustrate the implementation of the DEKF estimation scheme to a 1D robotic UV curing example. In this example, the state to be estimated is the monomer concentration distribution (further normalized to the cure-conversion level) along the 1D target strip. Two unknown process parameters are considered here: UV absorption coefficient k and convective heat transfer coefficient h (the two parameters are estimated simultaneously). The assumed spatial distributions of the two parameters along the target strip are illustrated in Fig. 8.

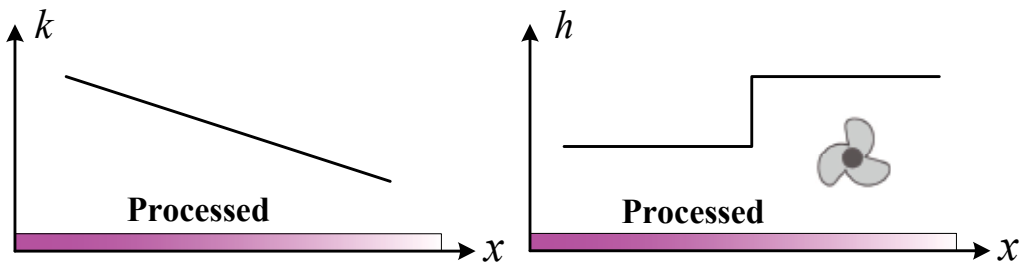


Fig. 8. Assumed distribution of the UV absorption coefficient and convective heat transfer coefficient along the 1D target strip

As shown in Fig. 8, the UV absorption coefficient is assumed to decrease in a linear manner from the left end to the right end of the target strip. For the convective heat transfer coefficient, a cooling fan is assumed to operate on the right-half part of the target strip, and a step function is used to describe the corresponding distribution of the convective heat transfer coefficient. Since this example is only used to demonstrate the estimation scheme (not the control strategy), the inputs of the system (motion and power of the radiant source) are kept constant during the whole process. Other process parameters used in this example are obtained from (Hong, 2004). The corresponding results are presented in Fig. 9 ~ Fig. 11. The solid ball shown in Fig. 9 ~ Fig. 11 denotes the UV radiant source which moves through the target strip (from left to right). The state estimation result is given in Fig. 9 in both the spatial (a) and temporal (b) domains. The shaded area in Fig. 9(a) represents the current processing (activating) window in which the corresponding local low-order estimators are activated for estimating the states and parameters. The time index t_L and t_R in Fig. 9(b) define the time when the estimation is activated and when it is frozen again for the selected position ($x=0.9$). t_M represents the time when the radiant source is exactly crossing the position ($x=0.9$). The spatial and temporal results in Fig. 9 show that the estimated state (cure-conversion level) has a good match to the actual state.

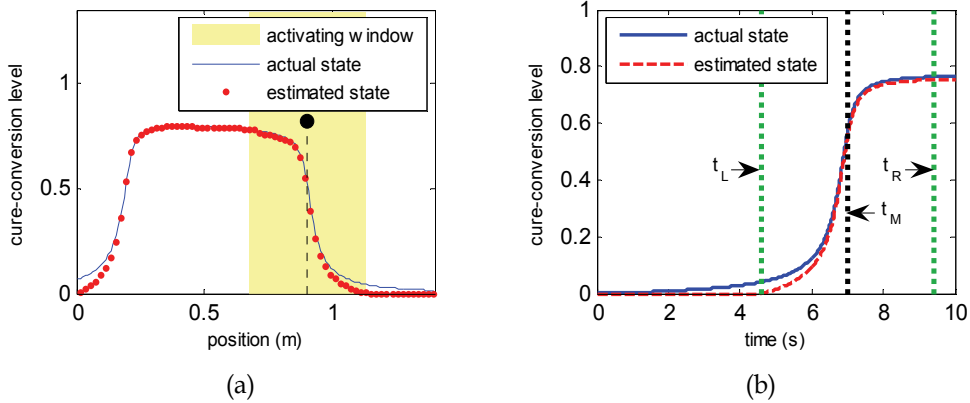


Fig. 9. (a) The distribution of the cure-conversion level along the target strip when the source is crossing the position ($x=0.9m$) (b) The time history of the cure-conversion level for the position ($x=0.9m$)

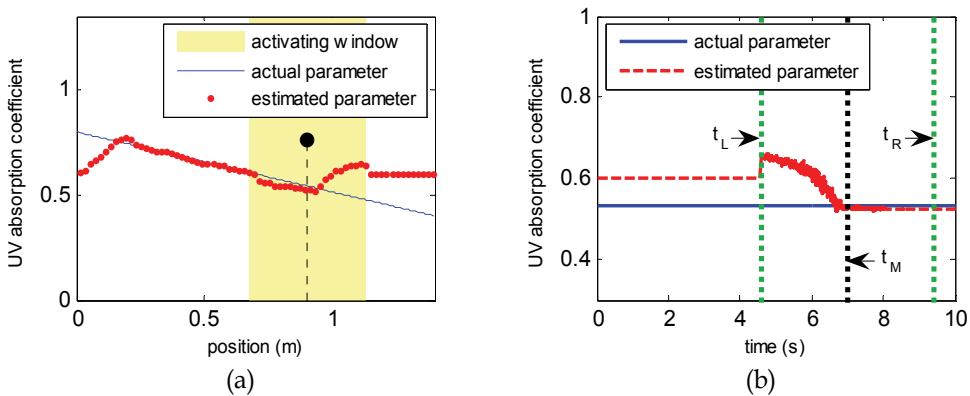


Fig. 10. (a) The distribution of the UV absorption coefficient along the target strip when the source is crossing the position ($x=0.9m$) (b) The time history of the UV absorption coefficient for the position ($x=0.9m$)

The estimation results for the UV absorption coefficient are given in Fig. 10. First, Fig. 10 (a) shows the spatial distributions of the estimated and actual UV absorption coefficient. It can be observed that the estimation performance for the cured area (on the left-hand side of the source) is better than that of the uncured areas (on the right-hand side of the source). This is because the estimation for the uncured areas hasn't been activated or it is currently being activated. Similar observations can be found in the temporal result depicted in Fig. 10 (b).

Fig. 11 presents the estimation results for the convective heat transfer coefficient. Again, for those areas in which the estimation has been activated, the estimated convective heat transfer coefficient matches the actual value well. On the other hand, for those areas covered by frozen estimators or the ones that are being activated, the estimation performance is not good at the beginning but is improved after the estimators have been completely activated.

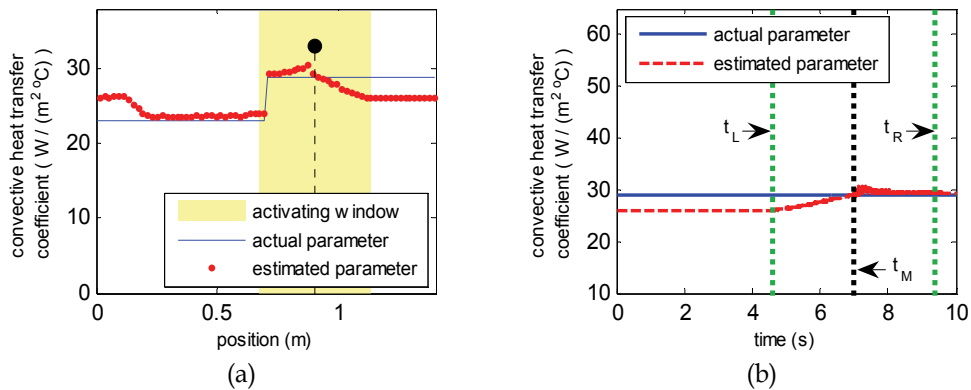


Fig. 11. (a) The distribution of the convective heat transfer coefficient along the target strip when the source is crossing the position ($x=0.9\text{m}$) (b) The time history of the convective heat transfer coefficient for the position ($x=0.9\text{m}$)

4. Process optimization and predictive control

To further improve quality and energy efficiency, optimization of multiple control inputs should be incorporated into the closed-loop control of the robotic UV curing process. This section presents two fundamental approaches to achieve the process optimization through either a rule-based control method or a model predictive control (MPC) strategy. A general discussion about the two approaches is given at first. Then the authors propose a framework for guiding the design of the predictive control strategy. Finally, a demonstrative example is provided to illustrate and compare the two process optimization approaches.

4.1 Off-line and online process optimization

The robotic UV curing process involves two major control inputs: the power and motion of the radiant source. The control of a single manipulated variable (either the power or the motion) based on temperature feedback has been discussed in Section 2. To achieve improved quality level and energy efficiency, the two control inputs should be manipulated in a coordinated and optimal manner. Two approaches are considered for achieving such process optimization: a rule-based control method (off-line optimization) and a model predictive control strategy. Both of the two approaches use essential process feedback provided by the state/parameter estimator.

4.1.1 Rule-based control

The rule-based control method is still a closed-loop control approach that uses some off-line process optimization results. The first step is to calculate the optimal trajectories of the two control inputs in an open-loop manner. For example, for curing a 1D target strip, the optimal trajectories of the two control inputs could be two constant values of the power and the speed (motion) which can minimize the pre-defined objective function (e.g. minimal curing level non-uniformity with minimal energy use). However, these off-line optimal control trajectories cannot be directly applied to the process due to the presence of disturbances during the actual process. Therefore, the next step is to close the loop by incorporating online process estimates and coordinating the control inputs based on some

designed rules. Although this method is not necessary optimal once the loop has been closed (the control inputs will be adjusted around the off-line optimal results), it can help achieve an acceptable compromise between process optimization and disturbance rejection.

4.1.2 Model predictive control

The other approach is to use model predictive control (MPC) to achieve online process optimization. Compared to the rule-based control method, the MPC approach calculates the optimal control inputs in a frequent manner by using online process estimates and a process model. The process model is used to predict future process states from the current state estimates. At each calculation cycle, the MPC controller determines the control inputs in an optimal way that can minimize the deviation of future process states from the set-point and the corresponding control costs. This calculation is repeated to generate new optimal control signals once the new state estimates are available, so the controller can detect the changes of the process (e.g. influence of disturbances) online and make necessary adjustment to compensate for these changes. The two process optimization approaches discussed above are illustrated in Fig. 12.

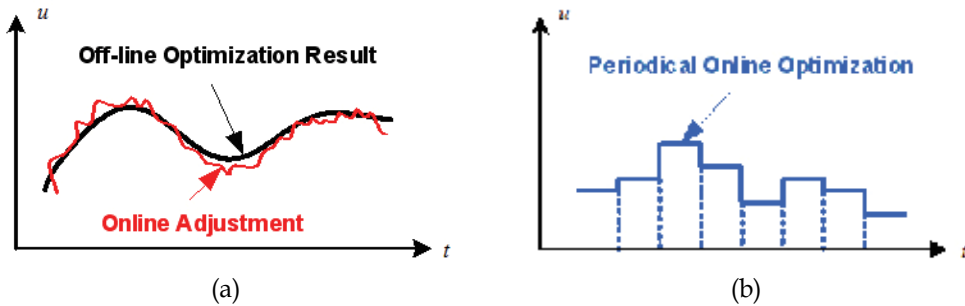


Fig. 12. (a) The rule-based control method (b) The predictive control strategy

4.2 Predictive control strategy

This subsection presents a framework for developing the predictive control strategy for the robotic UV curing process. This framework outlines the fundamental procedures in the control design process, including model linearization and simplification, control problem formulation, solution, and implementation, etc. The basic structure of this framework is depicted in Fig. 13.

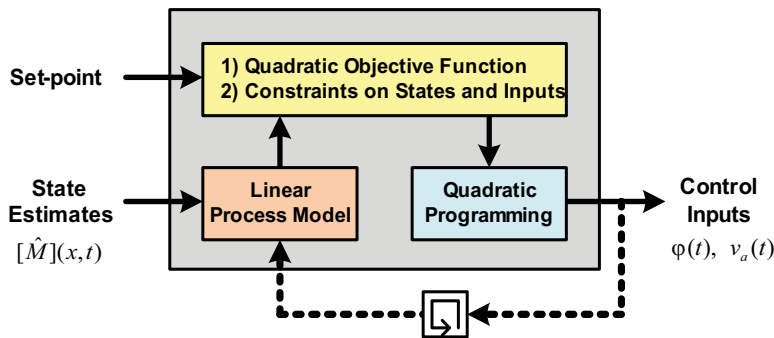


Fig. 13. The structure of the model predictive control framework for robotic UV curing

The steps involved in the predictive control strategy are described as follows:

1. Acquire new state estimates (monomer concentration) from the DEKF estimator discussed in Section 3.
2. Linearize the process model around the current state estimates and the previous control inputs.
3. Calculate future process states along the prediction horizon by using the linear model
4. Update the objective function and constraints on both states and inputs.
5. Solve the constrained optimization problem to find the optimal sequence of control inputs along the control horizon.
6. Apply the first part of the optimal sequence as the current control inputs to the process.

The above calculation will be repeated when the new state estimates are available. The detailed mathematical derivation and formulation of the predictive control strategy can be found in the authors' previous work in (Zeng & Ayalew, 2010-b).

4.3 A demonstrative example

This subsection provides a 1D curing example to demonstrate the rule-based control method and the predictive control strategy as used for process optimization. Two simulation scenarios (named as S1 and S2) are given in this example, regarding different disturbances in the UV absorption coefficient distribution along the target strip. For the first scenario (S1), the UV absorption coefficient has the same distribution as what is shown in Fig. 8. For the second scenario (S2), the distribution of the UV absorption coefficient is described by a step function. The simulation results for S1 are presented in Fig. 14 and Fig. 15.

As shown in Fig. 14, both the rule-based and predictive control methods successfully maintain the uniformity of the cure-conversion level along the target strip, although the UV absorption coefficient has a descending distribution. The open-loop method fails to maintain the uniformity due to the lack of essential process feedback. Fig. 15 gives the time history of the two major control inputs: power and motion. It can be observed that for both the rule-based and predictive control methods, the power of the radiant source is increased while the speed of the source is reduced during the process. This explains why the two closed-loop methods can compensate for the disturbance in the UV absorption coefficient.

The simulation results for S2 are presented in Fig. 16 and Fig. 17.

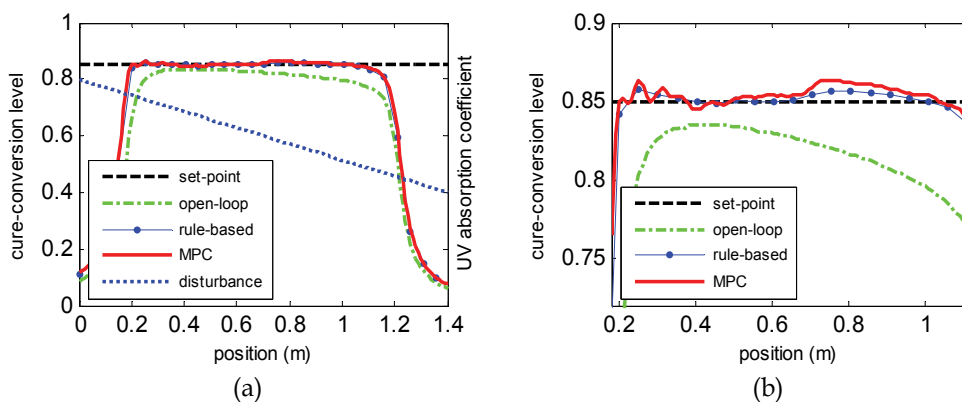


Fig. 14. The distribution of the cure-conversion level along the target strip (S1): (a) Full-range view (b) Zoomed view around the set-point

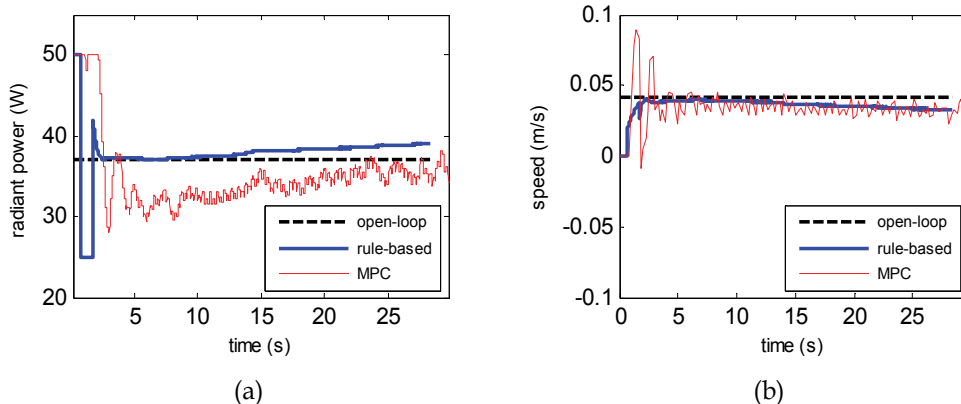


Fig. 15. The time history of the control inputs (S1): (a) radiant power (b) speed

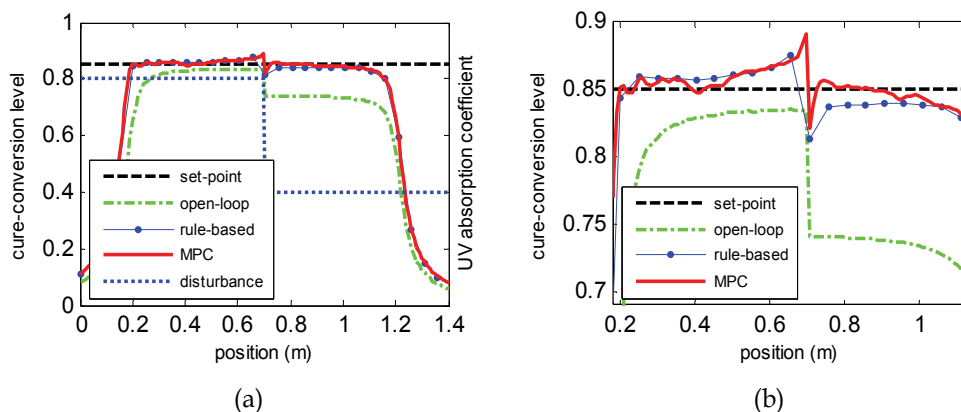


Fig. 16. The distribution of the cure-conversion level along the target strip (S2): (a) Full-range view (b) Zoomed view around the set-point

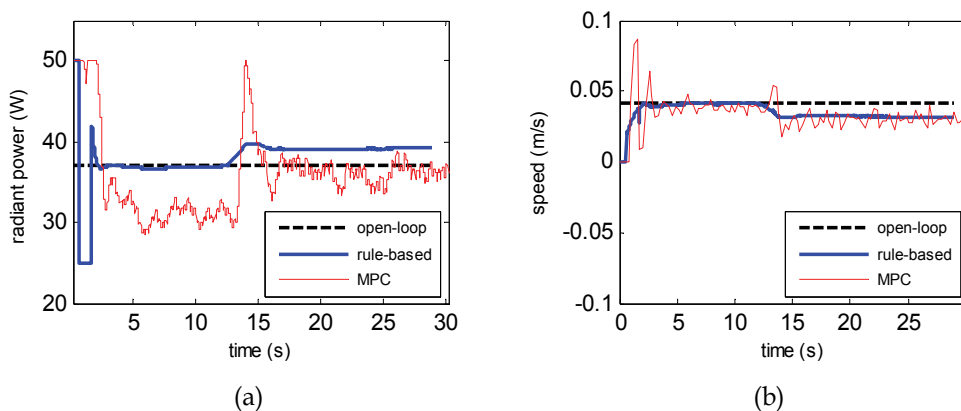


Fig. 17. The time history of the control inputs (S2): (a) radiant power (b) speed

In this scenario, a step change is introduced to the distribution of the UV absorption coefficient along the target strip (as shown in Fig. 16). Similarly, the rule-based and the predictive control methods successfully compensate for this step change and give acceptable process uniformity, compared to the uneven curing in the open-loop method. The time history of the control inputs given in Fig. 17 shows that the power and the speed of the radiant source are also manipulated in a step manner during the process (for both the rule-based and the predictive control methods). It can be observed that the predictive control method increases the radiant power more drastically than the rule-based method does when the radiant source crosses the step point. This is because the predictive control strategy can detect the step change in advance and make corresponding adjustment in time. Another observation is that the predictive strategy uses lower radiant power than the rule-based method at most time of the curing process. This explains the major difference between the two process optimization approaches. Since the predictive control strategy performs the optimization online, it can give better energy efficiency (minimize power level) than the rule-based method which only uses off-line optimization results to determine nominal values of the control inputs.

5. A prototype robotic UV curing system

A prototype robotic UV curing system has been developed to implement the closed-loop control methods in experiment and investigate their potential applications in automotive manufacturing plants. The hardware structure of the prototype robotic UV curing system is illustrated in Fig. 18.

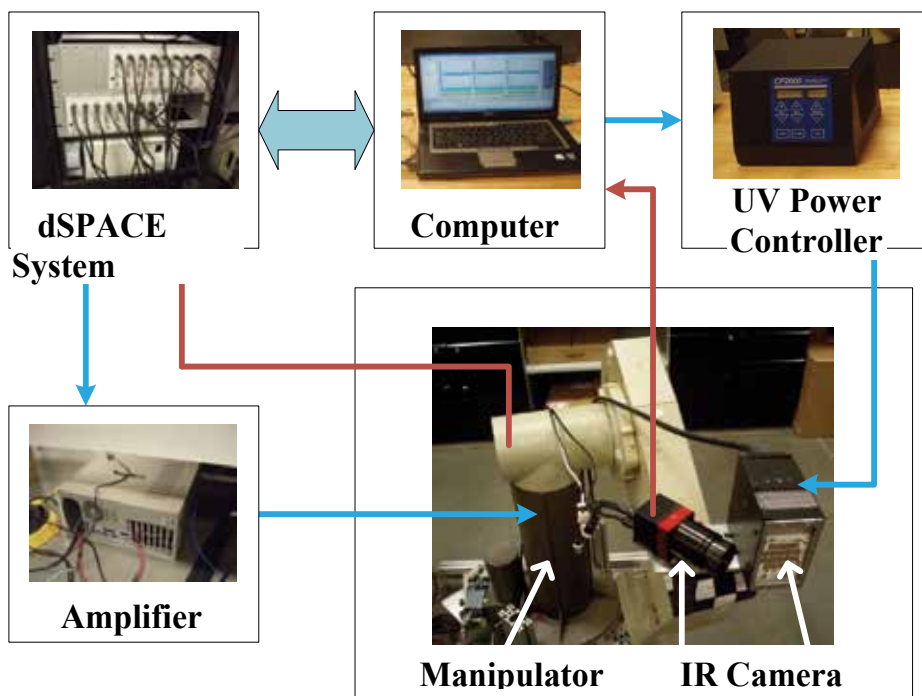


Fig. 18. The hardware structure of the prototype robotic UV curing system

As shown in Fig. 18, the prototype system is composed of four basic parts: a robotic manipulator, a UV LED panel with power controller, a thermal vision system, and a dSPACE rapid control prototyping system. A six degree-of-freedom (DOF) PUMA560 manipulator is used here to carry the UV LED panel and the IR camera. This manipulator is driven by six new pulse-width modulation (PWM) amplifiers. The UV LED panel includes 42 cells which can send out UV radiation with a wavelength concentrated around 365 nm. The UV LED is connected with its own power controller (named CF2000). This controller can be treated as an instrument terminal of a personal computer (PC) through a USB interface. The IR camera used in the prototype system has a 640×320 pixel array and can measure the temperature from 20 to 150 °C. The IR camera is connected with the computer through a USB interface and it can send out digital thermal image data at a frame rate of 30Hz. The dSPACE system includes an embedded processor and necessary A/D and D/A converters. The dSPACE system is used to achieve rapid control prototyping by converting MATLAB/Simulink control models into real-time codes that can be implemented in hardware to control the whole system.

Fig. 19 shows two test configurations with the prototype robotic UV curing system.

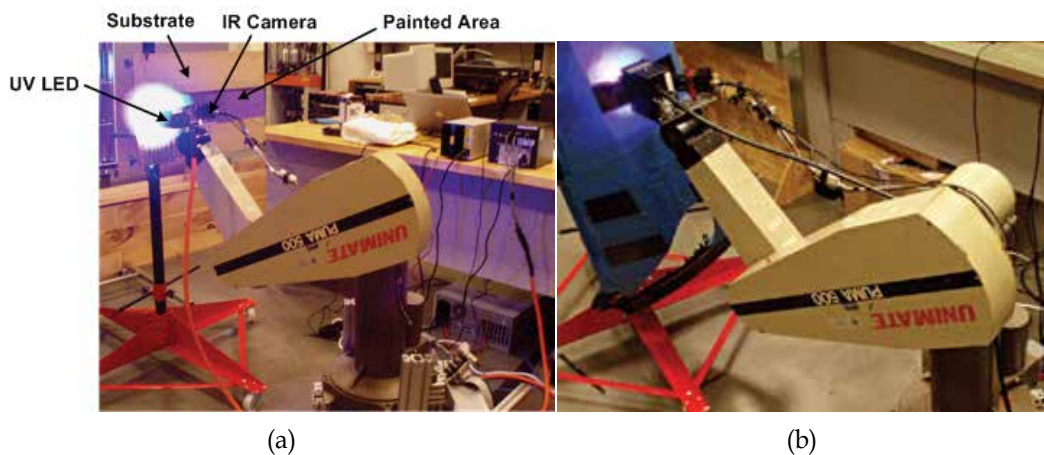


Fig. 19. Test configurations with the prototype robotic UV curing system: (a) 2D plane-type target (b) Actual automotive body part (a front fender)

At first, the prototype system is used to cure a 2D plane-type target (with thin-film clearcoat) for validating the temperature feedback control strategy discussed in Section 2. It can also be used to cure some real automotive body parts, such as a front fender, as shown in Fig. 19(b). In this case, the trajectory of the robot is typically designed offline to make the UV LED panel have different distances matched to the profile of the fender as it moves through different locations. With the closed-loop structure, the controller can determine how long the UV LED panel should stay at each patch of the fender based on the temperature level of that patch as measured by the IR camera.

6. Summary and future directions

This chapter presented a framework for advanced robotic radiative process control in automotive coating, drying and curing applications. This framework provides potential solutions to the closed-loop control problems, particularly to those involved in the robotic UV curing processes. These solutions include, 1) online process monitoring through IR camera(s) and direct temperature feedback control, 2) online process state/parameter estimation by using temperature measurements and the dual extended Kalman filtering, and 3) process optimization through rule-based and predictive control methods. Simulation studies have been conducted to demonstrate the major approaches discussed in this chapter. The results show that the proposed framework (control, estimation, and optimization) provides improved process quality and energy efficiency by adaptively compensating for disturbances and optimally coordinating multiple control inputs (power and motion). A prototype system has also been established for further investigations and implementations on robotic UV curing for automotive applications.

Future research work will include implementing the state/parameter estimation schemes and the predictive control strategy in hardware, conducting investigations on advanced UV radiant sources for more control options, and pursuing the cooperation with manufacturers for further on-site tests and applications.

7. References

- Ashdown, I. (1994). *Radiosity: A Programmer's Perspective*, John Wiley and Sons, New York, NY.
- Fey, T. and Muhle, J. (2003). UV-dualcure systems for automotive applications. RadTech, 2003, Berlin, Germany.
- Goodner, M.D. and Bowman, C.N. (2002). Development of a comprehensive free radical photopolymerization model incorporating heat and mass transfer effects in thick films. *Chemical Engineering Science*, Vol. 57, No. 5, pp. 887-900.
- Hagood, D., Kelly, M. (2008). Extolling the advantages of UV-Curing processes. *Metal Finishing*, Vol. 106, No. 4, pp. 71-74.
- Hardt, D.E. (1993). Modeling and control of manufacturing processes: Getting more involved. *Transactions of the ASME. Journal of Dynamic Systems, Measurement and Control*, Vol. 115, No. 2B, pp. 291-300.
- Haykin, S.S. (2001). *Kalman filtering and neural networks*, John Wiley and Sons, New York, NY.
- Hong, W., Lee, Y.T., and Gong, H. (2004). Thermal analysis of layer formation in a stepless rapid prototyping process. *Applied Thermal Engineering*, Vol. 24, No. 2-3, pp. 255-268.
- Huissoon, J.P., Strauss, D.L., Rempel, J.N., Bedi, S., and Kerr, H.W. (1994). Multi-variable control of robotic gas metal arc welding. *Journal of Materials Processing Technology*, Vol. 43, No. 1, pp. 1-12.
- Jones, P.D.A., Duncan, S.R., Rayment, T., and Grant, P.S. (2003). Control of temperature profile for a spray deposition process. *IEEE Transactions on Control Systems Technology*, Vol. 11, No. 5, pp. 656-667.

- Kalman, R.E. (1960). A new approach to linear filtering and prediction problems. *Transactions of the ASME-Journal of Basic Engineering*, Series D, Vol. 82, pp. 35-45.
- Mills, P. (2001). Team UV: Leading edge technology for the automotive industry. RadTech, 2001, Basel, Switzerland.
- Mills, P. (2005). Robotic UV curing for automotive exterior applications: A cost-effective and technically viable alternative for UV curing. North American Automotive UV Consortium Report, Stongsville, OH.
- Modest, M.F. (1993). *Radiative Heat Transfer*, McGraw Hill, New York, NY.
- Moore, K.L., Naidu, D.S., Yender, R., and Tyler, J. (1997). Gas metal arc welding control: Part I : Modeling and analysis. *Nonlinear Analysis, Theory, Methods and Applications*, Vol. 30, No. 5, pp. 3101-3111.
- Omar, M. A., Viti, V., Saito, K., and Liu, J. (2006). Self-adjusting robotic painting system. *Industrial Robot: An International Journal*, Vol. 33, No. 1, pp. 50-55.
- Prendi, L. and Tam, Edwin K.L. (2008). Life cycle inventory of the automotive paint process. *Journal of Coatings Technology*.
- Seelinger, M.J., Robinson, M., Dieck, Z., and Skaar, S.B. (1997). A vision-guided, semi-autonomous system applied to a robotic coating application. in *Proceedings of the SPIE - The International Society for Optical Engineering*, Vol. 3209, pp. 133-144.
- Siewert, U. (2008). Solutions for energy and environmental issues in automobile manufacturing, in *Durr Investor's Day*, 2008, Darmstadt, Germany.
- Starzmann, O. (2001). UV-light curing in the automotive industry. RadTech, 2001, Basel, Switzerland.
- Raith, T., Bischof, M., Deger, M., Gemmler, E. (2001). 3-D UV technology for OEM coatings. RadTech, 2001, Basel, Switzerland.
- U.S. Department of Energy, Office of Industrial Technologies, Energy Efficiency and Renewable Energy (2003). Progressive powder coating: New infrared curing oven at metal finishing plant increases production by 50% (BestPractices Case Study).
- U.S. Department of Energy, Office of Industrial Technologies, Energy Efficiency and Renewable Energy (1999). UV-Curable coatings for aluminum can production (Chemicals Project Fact Sheet).
- Vogt, M. (2007). Infrared drying lowers energy costs and drying times. *Plastics, Additives and Compounding*, Vol. 9, No. 5, pp. 58-61.
- Wan, E.A. and Nelson, A.T. (1997). Neural dual extended Kalman filtering: applications in speech enhancement and monaural blind signal separation. Neural Networks for Signal Processing VII., in *Proceedings of the 1997 IEEE Signal Processing Society Workshop*, pp. 466-475.
- Zeng, F., Ayalew, B., and Omar, M. A. (2009). Robotic automotive paint curing using thermal signature feedback. *Industrial Robot: An International Journal*, Vol. 36, No. 4, pp. 389-395.
- Zeng, F. and Ayalew, B. (2010-a). Estimation and coordinated control for distributed-parameter processes with a moving radiant actuator. *Journal of Process Control*, Vol. 20, No. 6, pp. 743-753.

Zeng, F. and Ayalew, B. (2010-b). Model predictive control of a distributed parameter process employing a moving radiant actuator. ASME Dynamic Systems and Control Conference, Cambridge, MA, USA, September 13-15, 2010 (accepted).

Part 3

New Components and Related Technologies

DC/DC Step-Up Converters for Automotive Applications: a FPGA Based Approach

M. Chiaberge, G. Botto and M. De Giuseppe
*Mechatronics Laboratory – Politecnico di Torino
Italy*

1. Introduction

One emerging application of power electronics is the driving of piezoelectric actuators. These actuators can be used for different kinds of application. They are employed for micro and nano positioning tasks as well as hydraulic or pneumatic valves, where they replace magnetic control elements. Piezoelectric actuators have some specific advantages such as high resolution of the displacement, excellent dynamic properties and energy consumption near to zero for static or quasi static operations.

So, high performances, low emissions and less fuel consumption bring car designers to adopt new technologies in automotive systems. The use of piezoelectric actuators (used as injectors) allows less response time with respect to traditional magnetic actuators but requires high driving voltages in order to be driven in a smaller time. This is a big concern in automotive environment, where the battery voltage is still the main power source available.

A switching amplifier for reactive loads generally consists of two components. A unidirectional DC/DC converter with a small input power loads and large buffer capacitor and, a second bidirectional DC/DC converter that controls the energy exchanged between the buffer capacitor and the reactive load.

The requirements on the unidirectional DC/DC converter are few. It only needs to compensate the power losses of the two stages plus the energy dissipated in the actuator and the connected mechanical system. Second stage presents more problems, because it must be designed for full system power.

Conventional DC/DC boost converter is not the best solution in piezoelectric based applications where high step-up ratio and high efficiency power conversion is required.

The coupled inductor boost converter meets the demanding requirements of these applications, including high reliability, relative low cost, safe operation, minimal board space and high performance, therefore an excellent choice for interfacing the battery with the high voltage DC_{BUS} used for piezoelectric actuator system. An FPGA based controller allows interleaving two phases reducing both peak primary current and output current ripple. Moreover, a quasi constant frequency hysteretic current control technique reduces EMI interferences and ensures control loop stability. A soft start sequence permits to limit average input current and guarantees start-up phase in a short time.

In this chapter an FPGA based interleaved coupled inductor boost converter is presented for high step-up automotive applications.

Design and analysis of the proposed converter are reported. Finally experimental results are provided for verification of the proposed converter.

2. System specification and topology

Nowadays piezoelectric actuator allows less response time with respect to traditional magnetic actuator but requires high driving voltages.

In a traditional magnetic actuator the voltage applied is less than 100V, so a standard DC/DC Boost topology can be used to step up the 12V battery input voltage. Piezoelectric actuator require a high DCbus voltage to obtain high performances so high voltage step-up DC/DC converters are necessary to provide the interface between the standard energy storage component (battery) and the high voltage DCbus of the bidirectional converter used to drive the reactive load.

Fig.1 shows the typical power train of automotive piezoelectric actuator system.

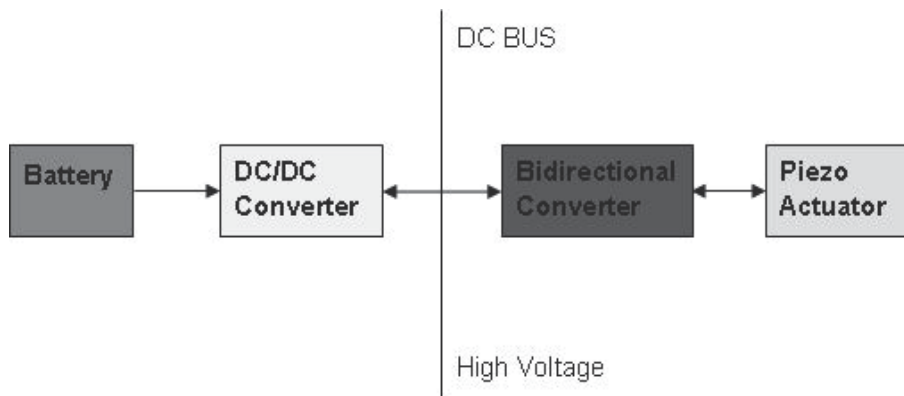


Fig. 1. Power solution for automotive piezoelectric actuators

So, the boost converter must be able to generate the a voltage up to 350V starting from a standard 9V-18V automotive range. If the input voltage is lower than this range, the system works in safe mode. Limit start up-time to reach the maximum output voltage is limited to 150ms and the maximum output power is 100W. The efficiency of the converter must be at least 85% under standard operating conditions.

In a conventional DC/DC Boost converter the duty ratio increases as the output to input voltage ratio increases. This class of DC/DC converter is not the best solution in piezoelectric based applications where a high step-up ratio (more than 20) and high efficiency power conversion is required.

Fig.2 shows a coupled inductor DC/DC boost converter topology: this converter is a good solution to the above problems since it reduces the required duty ratio for a given output to input voltage ratio in conjunction with a small voltage across the switch S (reducing switching losses).

The duty ratio and the switch voltage stress can be controlled by the N_2/N_1 turns ratio of the primary and secondary inductors (L1 and L2). Therefore, for high voltage step-up

applications, the coupled inductor boost converter can be more efficient than the conventional boost converter.

Moreover, for high power requirements and redundancy purposes, the coupled inductor boost converter can be easily interleaved to achieve high power, high reliability and efficient operation with reduced inductor and capacitor sizes. Various advantages of interleaving are well reported in the literature (Zhao & Lee, 2003).

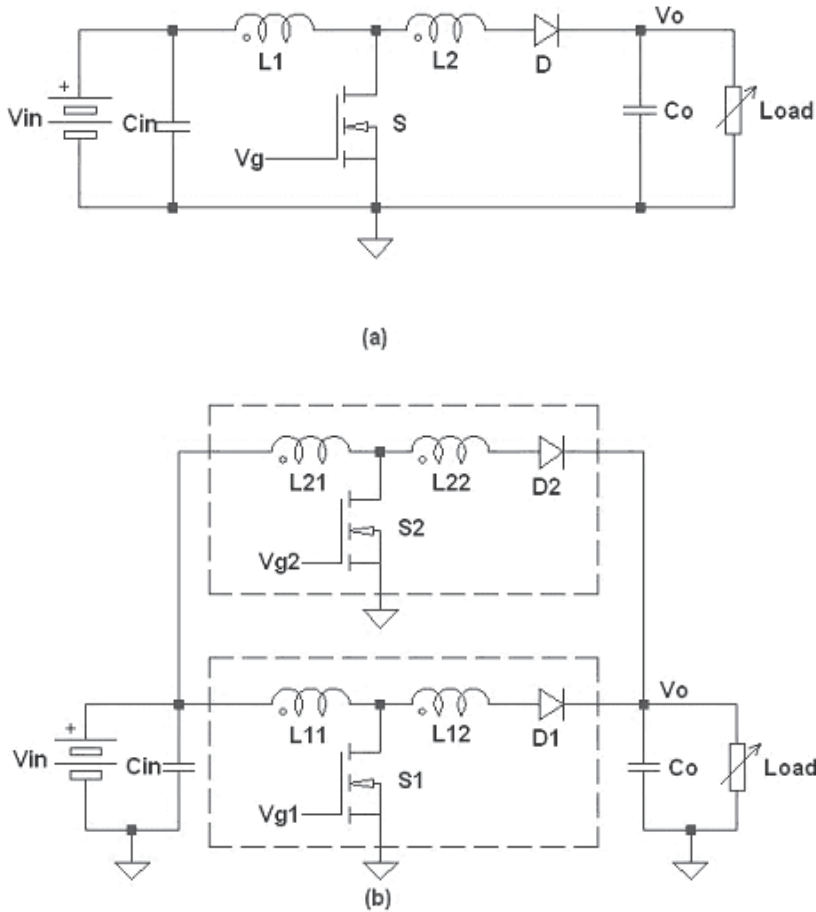


Fig. 2. (a) coupled inductor and (b) two phases interleaved coupled inductor boost converters

3. Design

Assuming the coupled inductor boost converter is in a continuous conduction mode (CCM) the steady state output voltage to input voltage ratio for an ideal converter can be obtained as:

$$\frac{V_o}{V_i} = \frac{(1+kD)}{1-D} \quad (1)$$

where V_i is the input voltage, V_o is the output voltage, D is the duty cycle of the converter and k is the secondary to primary inductor turns ratio. It can be seen from eq.1 that, for the same voltage gain, the duty cycle can be reduced by increasing turn ratio.

For high current or high power applications interleaving boost converter are well suited (Dwari & Parsa , 2007). In this approach a single coupled inductor boost converter cell (fig.2a) is treated as a phase of 'n' parallel connected phases (fig.2b). In order to operate at the same duty ratio a phase shift but of $2\pi/n$ radiant electrical angle must be considered. Under normal of full load condition each phase equally shares the total output load.

3.1 Switching frequency

In an interleaved system the number of cell (n) mainly depends on the step up voltage ratio and the maximum power demand of the load. In this work the nominal input voltage is taken as 12V and the range is the automotive standard 9V-18V.

With an output DCbus voltage of 350V, the voltage ratio is greater than 29. Referring to fig.3, using a secondary to primary inductor turn ratio (k) of 10 and incorporating the switch voltage and diode forward drop in the converter in equation 1, the duty cycle D is 0.72.

The expression of boundary inductance depends by load condition (eq.2) so, assuming minimum output power of 50W (half of total output power) the product Lf_{sw} must be greater than 0.767V/A.

$$Lf_{sw} = \frac{R_L D(1-D)^2}{2(1+k)(1+kD)} \quad (2)$$

Assuming a $5\mu\text{H}$ of primary inductance, the minimum switching frequency in order to satisfy the CCM condition is 153kHz, a quite high control frequency that requires a parallel implementation on a FPGA device with some control tricks to guarantee the control loop strategy.

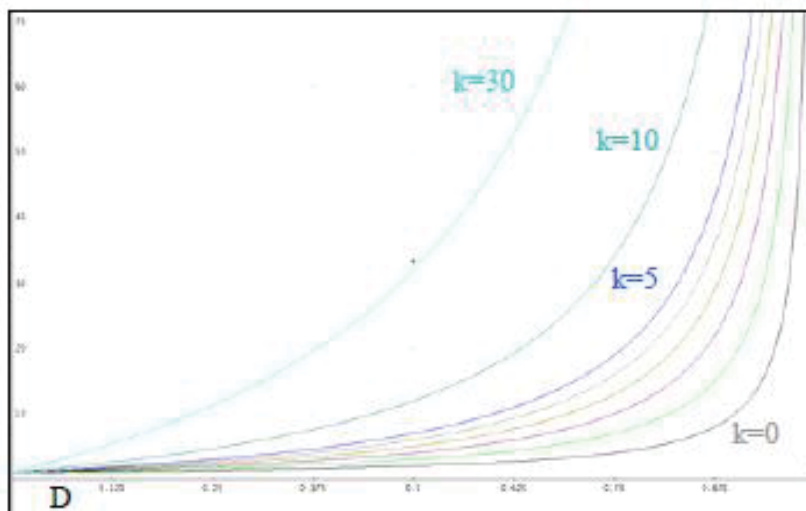


Fig. 3. Comparison among V_o/V_i as k fuction

3.2 Selection of power switch and freewheeling diode

The power switch is a high speed MOSFET in order to have fast rise and fall time and relatively low R_{DSon} that ensure less switching and conduction losses.

One of the main advantages of this topology respect to traditional Boost converter is that the maximum voltage on the MOSFET drain is limited by the turns ratio between primary and secondary inductors:

$$V_{Dmax} = \frac{V_o - V_i}{1 + N} = \frac{350V - 6V}{1 + 10} = 30.7V \quad (3)$$

where V_i is the input voltage, V_o is the output voltage and N is the inductors turns ratio.

The value in eq.3 is obtained considering the worst case, that is when the minimum input voltage occurs. To avoid over voltage MOSFET damaging the drain source voltage is chosen at least 1.5 times the V_{Dmax} .

The primary peak current value is determined by the duty cycle and the T_{on} period:

$$I_{pk1} = \frac{V_i D}{L_p f_{SW}} = \frac{6V \cdot 0.84}{5\mu H \cdot 200kHz} = 5A \quad (4)$$

The free-wheeling diode in Boost circuit plays a central role. When the switching transistor turns on, the diode should turn off immediately because otherwise the transistor will switch on into a full short circuit to the boosted output voltage close to 350V causing extreme over current and high dissipation.

Three different technologies could be used:

1. PiN
2. SiC Schottky Barrier Diodes
3. Fast Recovery Epitaxial Diode (FRED)

While Schottky and PiN diodes offer similar circuit functionality, their behavior is determined fundamentally different physical mechanisms. These differences directly impact the power dissipation associated with these devices.

Schottky Barrier Diodes (SBDs) offer a low junction voltage, low switching loss and high speed, but suffer from high on resistance.

When operated at high current density, PiN diodes offer significantly reduced on-resistance due to conductivity modulation, but suffer from high junction voltage and high switching loss.

The FRED diodes could be a good compromise between forward voltage, low peak reverse recovery currents with soft recovery. These diodes are characterized by a soft recovery behavior, showing even at very high di/dt ($>800A/\mu s$) no tendency to "snap-off", but present higher leakage current than other diode. However the power loss caused by the leakage current is small compared to forward current and reverse recovery losses.

In this converter, the output diode should be able to support high voltage (higher than 350V) but a quite low average current (this is the average output current and so it is less than 0.3A).

3.3 Input filter capacitor

The input filter capacitor limits the supply ripple voltage. The less ripple voltage desired, the larger the capacitor, and the larger the surge current during the power up period. There are three major considerations when selecting a capacitor for this function:

- Capacitance value
- Voltage rating
- Ripple current rating

The value of the bulk capacitor can be found by:

$$C_{IN} \cong \frac{2P_{OUT}}{f_{SW}V_{RIPPLEpp}} = \frac{200W}{200kHz \cdot 3V} = 330\mu F \tag{4}$$

We have placed three 100μF electrolytic capacitors and four 10μF ceramic in parallel.

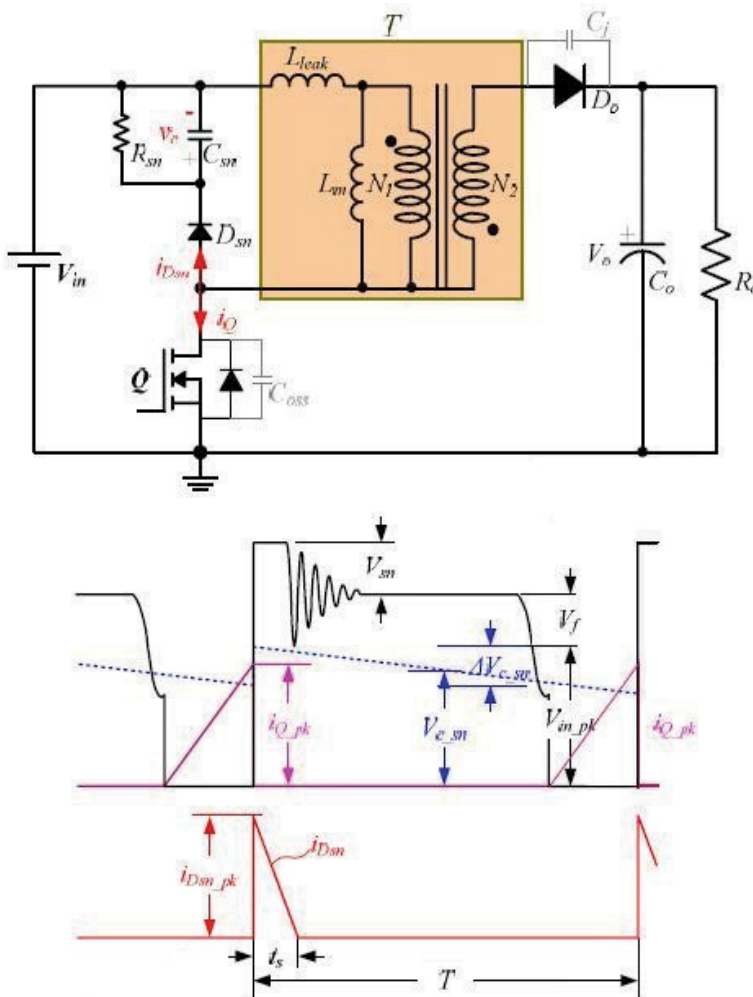


Fig. 4. Snubber Circuit

3.4 Current sense

High side current sense amplifier has been used to monitor the primary input current across a shunt resistor. The sense voltage is amplified and shifted from the analog power supply to

a ground referred output. Considering 300 μ F as output capacitance, start up time is less than 150ms and low input voltage, the average input current in this phase is:

$$I_{INstart-up} = \frac{V_{OUT}}{V_{IN}} C_{OUT} \frac{V_{OUT}}{\delta t} = \frac{350V}{9V} 300\mu F \frac{350V}{150ms} = 27.2A \quad (5)$$

Assuming a peak current about 30A, to limit the voltage drop below 5% of nominal input voltage and therefore the power losses, the shunt resistor must have a value lower than 20m Ω . A four wire Kelvin terminals resistance is used to limit the parasitic resistance as well as series inductance. A high side, unipolar current shunt monitor IC has been mounted in order to correctly acquire and convert the shunt voltage with the analog voltage range of digital platform.

3.5 Snubber circuit design

In this type of converter, the resonance between L_{leak} and C_{oss} causes an excessively high voltage surge, that cause damage to the MOSFET during turn-off. This voltage surge must be suppressed and snubber circuit is therefore necessary to prevent MOSFET failures as shown in fig.4.

The clamping voltage by snubber is:

$$V_{sn} = V_f + L_{leak} \frac{\Delta i}{\Delta t} = V_f + L_{leak} \frac{I_{Dsnpk}}{t_s} \quad (6)$$

Therefore:

$$t_s = \frac{L_{leak} I_{Dsnpk}}{V_{sn} - V_f} = \frac{L_{leak} I_{Dsnpk}}{1.5V_f} \quad (7)$$

The maximum power dissipation of the snubber circuit is determined by:

$$P_{sn} = \frac{1}{T} \int_0^{t_s} V_{sn} I_{Dsn}(t) dt = \frac{1}{2} L_{leak} I_{Dsnpk}^2 f_{SW} \quad (8)$$

The maximum power dissipation is:

$$P_{sn(max)} = \frac{1}{2} L_{leak} I_{Dsnpk}^2 f_{SW} = \frac{V_c^2}{R_{sn}} \quad (9)$$

Where:

$$V_c = V_{sn} = V_f + V_{Lr-} \quad (10)$$

Therefore, the resistance R_{sn} , is determined by:

$$R_{sn} = \frac{2V_c^2}{L_{leak} I_{Dsnpk}^2 f_{SW}} \quad (11)$$

The maximum ripple voltage of the snubber circuit is obtained by:

$$\Delta V_c = \frac{V_c}{C_{sn} R_{sn} f_{SW}} \quad (12)$$

The larger snubber capacitor results, the lower voltage ripple, but the power dissipation increases. Consequently, selecting the proper value is important. In general, it is reasonable to determine that the surge voltage of snubber circuit is 1.5 times of V_f and the ripple voltage is 25V. Thus, the snubber resistor and capacitor are determined by the following equations:

$$I_{D_{snpk}} = \frac{V_i D}{L_p f_{SW}} = 5A \quad (13)$$

$$V_{sur} = 1.5V_f = 1.5 \frac{V_o - V_i}{1 + N} = 45V \quad (14)$$

$$t_s = \frac{L_{leak} I_{D_{snpk}}}{1.5V_f} = \frac{0.1\mu H 5A}{45V} = 11ns \quad (15)$$

$$R_{sn} = \frac{2V_c^2}{L_{leak} I_{D_{snpk}}^2 f_{SW}} = \frac{2(45V^2)}{0.1\mu H (5A^2) 150kHz} = 10.8k\Omega \quad (16)$$

$$C_{sn} = \frac{V_{sn}}{\Delta V_c R_{sn} f_{SW}} = \frac{30V + 45V}{25V 10.8k\Omega 150kHz} = 1.85nF \quad (17)$$

4. Control

The proposed DC/DC converter is controlled using a quasi constant frequency hysteretic current mode technique with current sharing and interleaving phases as inner loop in order to have symmetrical current partition between the switching phases. The outer control loop is based on a digital PI control law in order to stabilize the DC/DC output voltage.

Fig. 5 shows the schematic diagram of the proposed control technique.

The PWM signal obtained by feedback loop (from the hysteretic comparator) is acquired by the FPGA and processed to correctly control the two phases of the tapped boost.

To avoid sub-harmonic instability a variable frequency control is needed and to stabilize the switching frequency it is necessary to introduce a high speed period feedback loop. This is performed by an integral control law which, starting from the outer loop command, generates the variable hysteresis for the comparator.

Fig.6 shows a block diagram of a hysteretic control with frequency control loop.

There are several challenges to efficiently implement the proposed control technique with analog and discrete components. These challenges along with the FPGA implementation are related to:

- Current/voltage sharing and control
- Frequency feedback

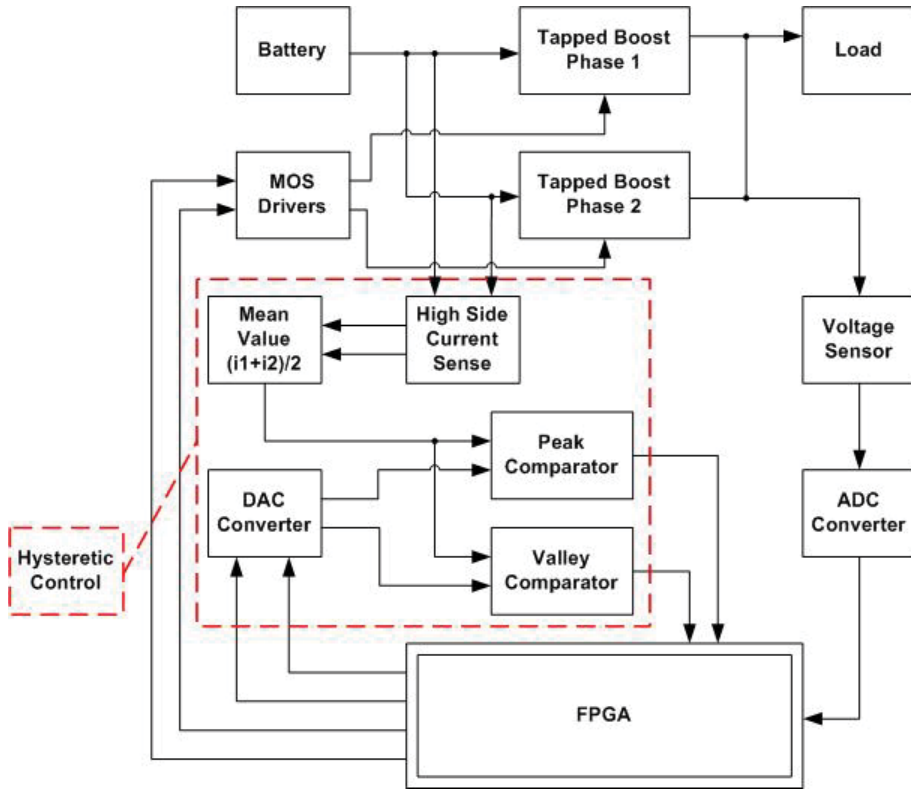


Fig. 5. Schematic diagram of coupled inductor control technique

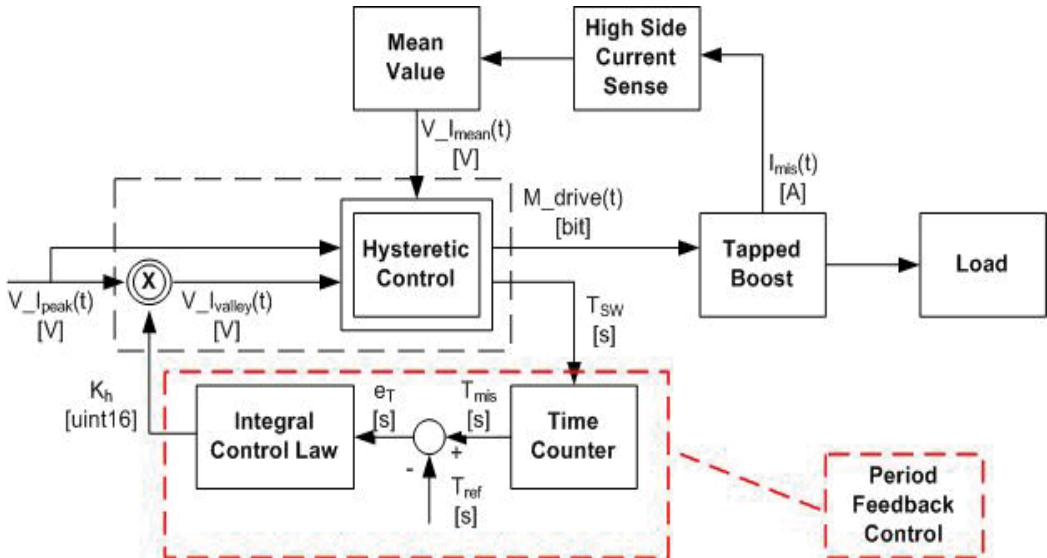


Fig. 6. Diagram of a quasi constant frequency hysteretic current control with a period feedback loop

4.1 Current sharing

It is really important to obtain an almost equally distributed current between the interleaved phases.

Unfortunately, components tolerances, connections differences from phase to phase, load conditions and other non idealities may cause the current distribution (sharing) to be unequal especially during large load transients.

Current sharing between the interleaved converters can be achieved by averaging current of each converter phase and compare the obtained value with command derived by the outer loop. Each phase is then turned on using two control strategies:

1. Sequence toggle mode where the ON signal is present only for one phase per cycle
2. Phase shift control technique where the two phases are shifted of half period

Current sharing functionality can be easily implemented using a fast FPGA.

In the first one the two control pulses (C_{m1} and C_{m2}) are generated interleaved starting from the C_m PWM signal coming from hysteretic comparator (Fig 7a).

In the second control technique C_{m1} and C_{m2} are shifted half period starting from the main control signal generated by the hysteretic comparator (Fig. 7b).

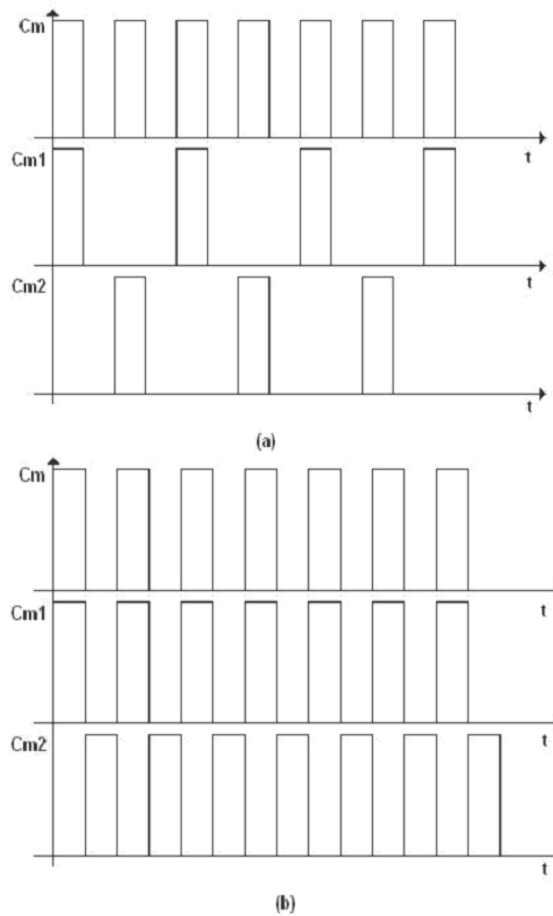


Fig. 7. Different control techniques: (a) toggle with the two phases (b) half period phase shift

The phase shift control technique has been implemented and tested but it presents some problems due to the inner frequency control.

4.2 Hysteretic current control circuit

Input current of each phase is sensed using a high side current sense amplifier with a very low shunt resistor value in order to reduce power losses. Sensed currents are decoupled, averaged, merged and included in the hysteretic current control.

Peak and valley current commands come from the digital outer voltage loop: peak value is the output of a PI control law while the valley one is obtained multiplying the command with a corrective factor derived by the frequency feedback loop.

Peak and valley comparator outputs are directly connected to the FPGA and are used to generate the two control signal applied to the switches.

4.3 Frequency feedback loop

The frequency feedback loop is implemented on FPGA in order to:

- Speed-up the computation of the control law
- Guarantee the modularity of the control law
- Generate a variable hysteretic width based on frequency measure (or period)

To minimize the number of analytical operations and to simplify the IP design on FPGA, we have implemented a switching period feedback loop.

This technique is based on switching period measured using a counter and comparator with a reference previously set (this is a variable of the proposed control). The difference is used as input of a regulator which generates a corrective factor on the nominal hysteretic width in order to stabilize the switching frequency.

The relation of corrective factor at the next step is:

$$k_h(i) = K_h(i - 1) + K_i(T_{mis}(i) - T_{ref}) \quad (18)$$

Where k_h is the corrective factor, K_i is the integral gain, i is the digital sampling period, T_{ref} and T_{mis} are the nominal switching period and the measured one.

The generated hysteretic width acts on the value of valley current, leaving the peak current unchanged.

4.4 Frequency feedback loop

Outer loop is a classic digital PI control law with anti-wind up algorithm. The output voltage is sensed and converted using a 12 bit resolution ADC and compared to the reference value on an FPGA IP. The error obtained is then transferred to a PI block that generates the command for the inner current control.

The right half plane zero (RHP) is present and its frequency depends of duty cycle, inductor value (smaller is better) and the load resistance, so at heavy loads its frequency is the lowest and the phase delay is the greatest; at light loads instead the RHP zero frequency is higher, and the converter is easier to control. The RPH zero frequency is obtained using:

$$\omega_{zero} = \frac{\frac{V_{OUT}^2}{P_{OUT}}(1-D)^2}{L_p(1+N)(1+ND)} \quad (18)$$

Common choice is to limit the bandwidth of the control feedback loop at about $1/5^{\text{th}}$ of the RHP zero frequency, which considering the worst case (100W at 350V with 12V as input voltage) is about 17kHz. The cross-over frequency is designed in order to stay under 3kHz.

5. Implementation

As previously explained, the control architecture is based on an inner loop that control and limit the average current of the two primary inductor currents, starting from a current reference obtained by an outer loop that maintains stable the DC bus voltage.

Control loops of Boost converter are illustrated in the following technological scheme (fig.8). All the feedback loops are implemented as IP on FPGA operated at a 100MHz clock, mounted on a prototype board (EKU) completely designed by the Mechatronic Laboratory.

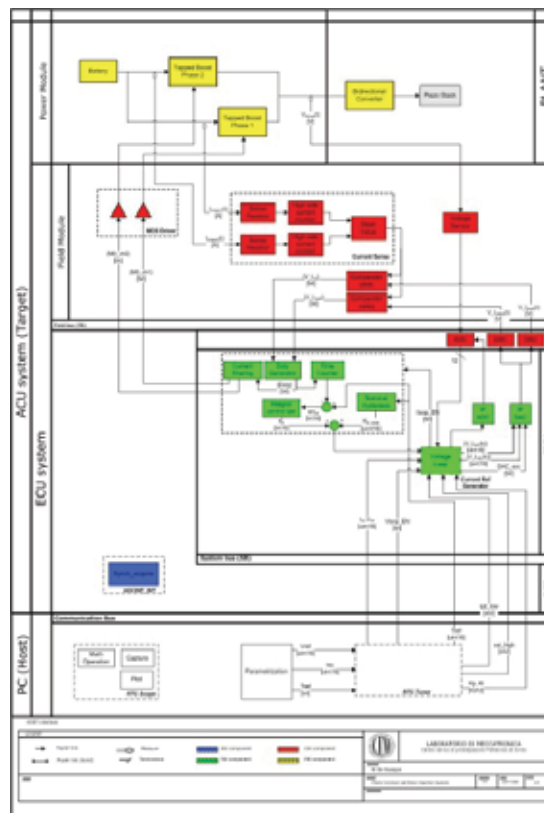


Fig. 8. Technological scheme of the Boost converter implemented

5.1 Current loop

The inner loop of the Boost section controls and limits the input current of each phase monitoring the voltage across the sense resistor connected in high side configuration using a current shunt monitor. The two amplifier's outputs are filtered and averaged in order to obtain a signal that drives the two comparators (peak and valley). With this control strategy the inductor currents ramp alternately between an upper limit and a lower limit.

Digital current control is based on two main blocks that are implemented as IP-core on FPGA:

- Duty Cycle Generator
- Current Sharing Algorithm

The Duty Cycle Generator, starting from peak and valley comparator outputs, controls the intrinsic behavior of an SR flip-flop, which turns the transistor of and on (considering one phase). A current sharing algorithm is added to equally subdivide the input current between the two phases: our strategy called sequence toggle mode, generates commands where only one phase is active at switching cycle; phase shift technique is also implemented but presents instability due to the inherent variable frequency during start up.

Peak and valley references are generated by DAC converters that are directly interfaced with the FPGA using a dedicated IP.

The hysteretic control maintains a controlled difference between the comparator's input and therefore variable frequency current loop. The introduction of a frequency feedback loop in this control leads to have variable hysteresis band but with the advantage of stabilizing the switching period.

5.2 Voltage loop

The outer loop maintains the output voltage stable around a reference value sent by engine control unit as a word parameter via CAN. Output voltage are sensed with a voltage monitor, converted by ADC and compared with digital reference in order to obtain an input to apply to the voltage loop block.

The tapped inductor open loop transfer function is:

$$\frac{V_o(s)}{d(s)} = \frac{V_o(k+1) \left(\frac{sL_p(1+k)(1+kD)}{R_L(1-D)^2} - 1 \right)}{(D-1)(1+kD) \left(\frac{s^2L_pC(1+k)^2}{(D-1)^2} + \frac{s^2L_pC(1+k)^2}{R_L(D-1)^2} + 1 \right)} \quad (19)$$

It is characterized by two poles, associated to LC output filter components, and one zero, determined by the ESR of output capacitor that for simplicity is neglected.

The two complex poles are placed at a lower frequency:

$$\omega_{poles} = \frac{(1-D)}{(1+k)\sqrt{L_pC}} \quad (20)$$

Additionally it presents a RHP zero. This is characteristic of boost and boost derived converters.

RHP zero determines a phase lag in loop gain of the voltage mode controlled boost converter forcing the maximum cross over frequency to be at most 1/5 RHP frequency. For this reason, a current mode is preferred, as the effect of RHP zero is mitigated.

RHP is a function of the duty cycle, load and inductance and causes an increase in loop gain while reducing the loop phase margin.

A common practice is to determine the worst case RHPZ frequency and set the loop unity gain frequency below one-third of the RHPZ.

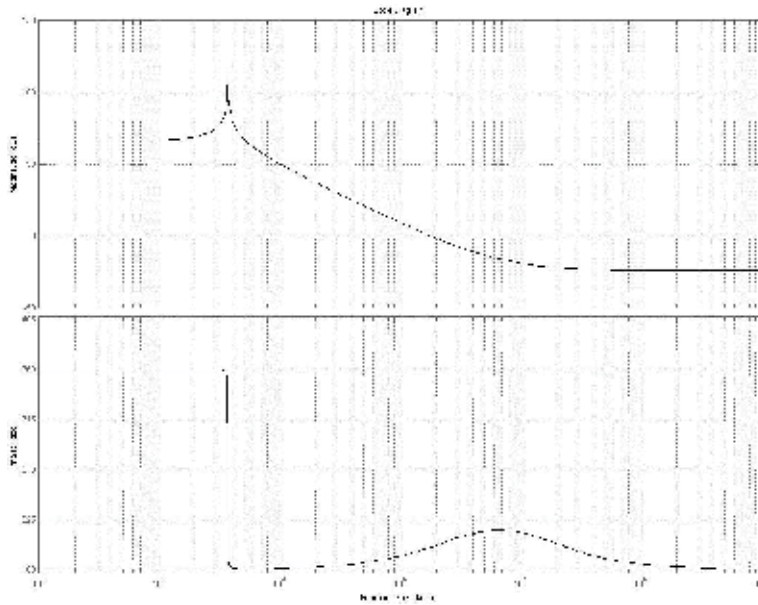


Fig. 9. Bode plot of Power Stage

Reducing the primary inductance increase the RHP zero location, therefore it may be possible to increase the close loop cross over frequency.

The Bode plot (Fig. 9) shows the frequency response of the power stage from the error amplifier output through to power stage output voltage. These approximated plots can be used to understand how to design the control/compensation circuitry.

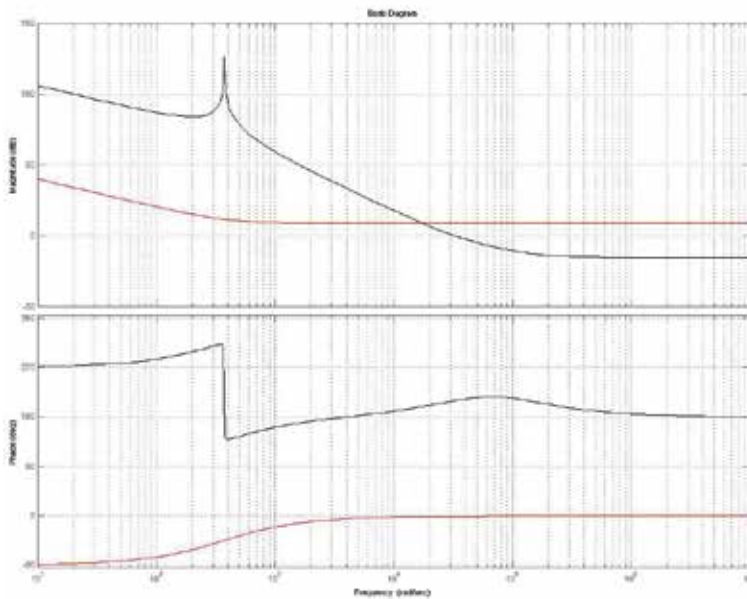


Fig. 10. Bode plot of Type I compensation network and the open loop TF

Type I compensation network is added to the control output TF in order to meet the static and dynamic performance requirements while maintaining stability.

This control gives one pole in the origin and one zero. The pole in the origin increase the DC gain to reduce the DC error in steady state. The zero is added at low frequency to obtain a at gain at mid frequency. Bode plot shows the effect of type I compensation. Fig. 10 shows the gain and phase of the overall system (power stage plus compensation). A cross-over frequency of 5kHz is achieved with a theoretical phase margin of 30°.

7. Experimental results

A 100W, 12V-to-350V step-up converter was completely designed and tested and the resulting power circuit components used are:

- Inductor: Coilcraft Flyback Transformer GA3459-BL with 5uH as primary inductance and 1:10 turns ratio
- Input capacitors: two 4.7uF ceramic and one 100uF electrolytic for high RMS current ripple
- Output capacitors: two 1uF plastic film and 150uF electrolytic
- MOSFETs: IRF1018 with 60V VDSS and 7.1mΩ of $R_{\text{DS(on)}}$
- Switching frequency: 200KHz

Operating duty cycle of the interleaved converter is 0.72. Figure 11 shows the prototype of the converter with the FPGA programmable device mounted on the above control board (a FPGA based ECU system developed at CSPP-LIM for fast prototyping applications).



Fig. 11. The experimental set-up of the proposed FPGA controlled DC/DC step-up converter

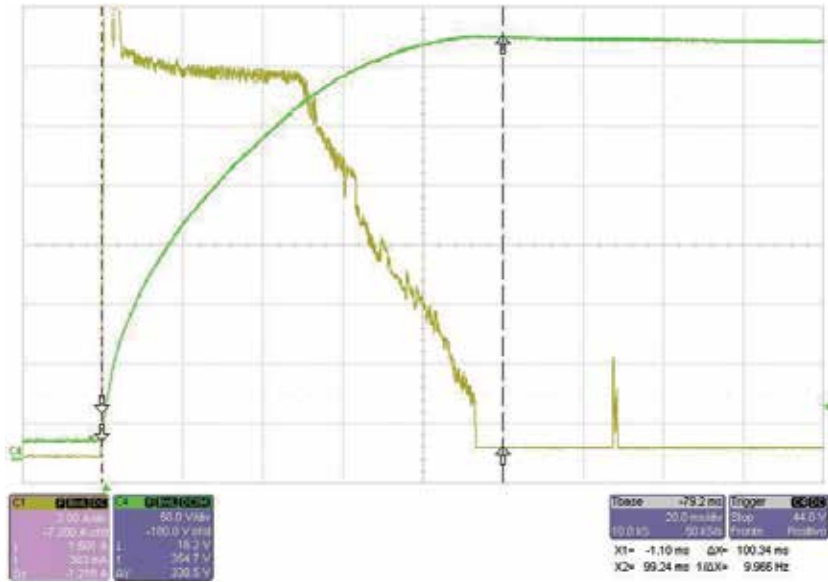


Fig. 12. DC/DC converter behavior during start-up sequence

Fig. 12 shows the output voltage (green) and output current (yellow) of the converter during start up sequence. During this time high primary inductor current in each phase is present as can be seen from the oscilloscope picture. The system goes in stable conditions in less than 100ms.

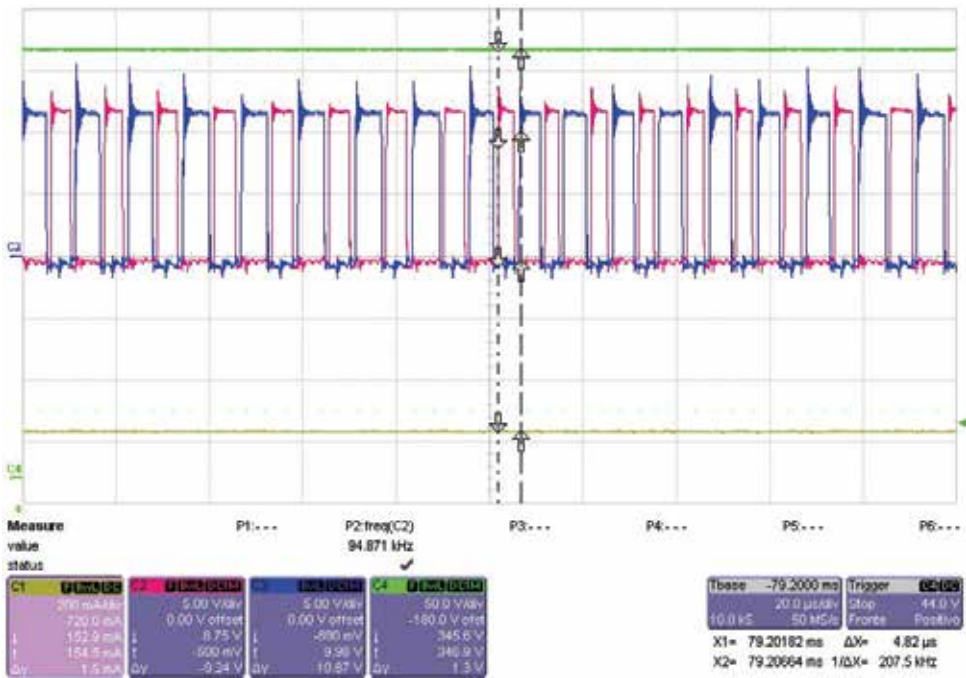


Fig. 13. Converter steady-state conditions

Fig. 13 shows the converter output voltage (green), output current (yellow) and $Cm1/Cm2$ signals (blue/red) in steady-state conditions. It can be seen that the switching frequency is stabilized around 200kHz that represent the reference current period of frequency loop.

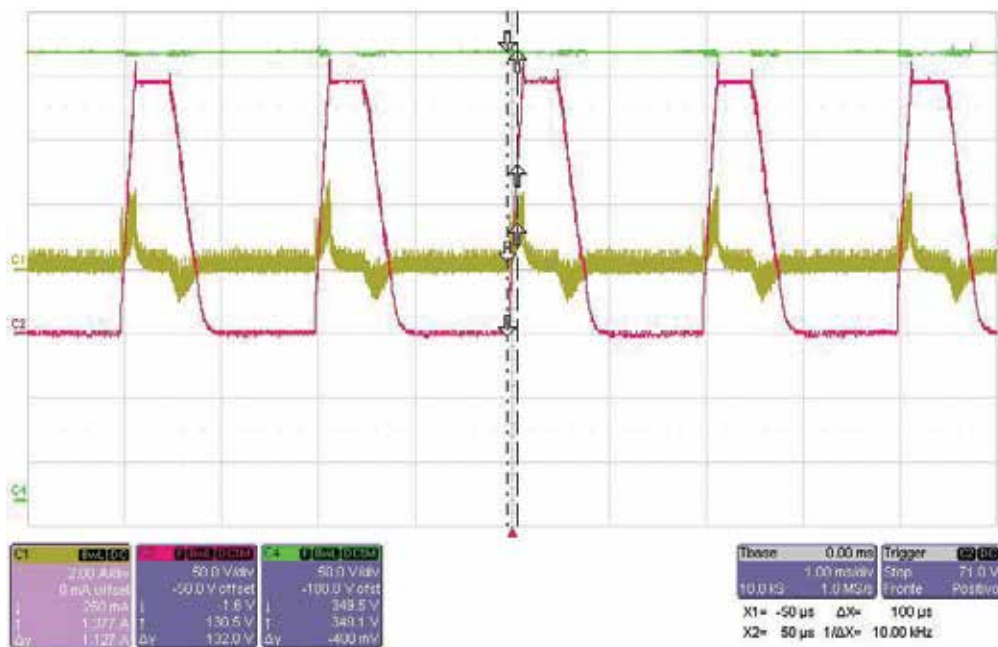


Fig. 14. Converter response under impulsive load test (10uF / 1.8Ω series RC load)

Fig. 14 shows converter output voltage (green), converter output current (yellow) and load voltage (red) during a impulsive load test (500Hz charge/discharge of a series 10uF / 1.8Ω RC load). It can be seen that the converter output voltage is very stable with a ripple less than 5V during 2A load driving transients.

7. Conclusion

In this chapter a new concept of FPGA controlled coupled inductor boost converter is presented as a good option to solve high boosting requirements in automotive applications. High power efficient converters with reduced size output filter can be obtained by interleaving and control these type of converters.

Using a quasi-constant frequency hysteretic current control it is possible to join the advantages of fixed and variable frequency control introducing a frequency feedback loop in a classic hysteretic CM control. Moreover, the FPGA implementation ensures good dynamic performances, reliability and high computational performances resulting in high efficiency overall characteristics.

The switching frequency is stabilized around 10% of nominal reference frequency: this allows the designer to easily estimate the switching losses and efficiently design the output EMI filter.

8. References

- Chang, C. & Knights, Mike A. (1995). Interleaving technique in distributed power conversion systems. *IEEE Transactions on Circuits and Systems I: Fundamental Theory and Applications*, vol. 42, (May 1995) pp. 245 – 25.
- Dixon, L. H. (1990). Average Current Mode Control of Switching Power Supplies, *Unitrode Power Supply Design Seminar SEM-700*, vol. 5, pp. 1-14.
- Dwari, S. & Parsa, L. (2007). A Novel High Efficiency High Power Interleaved Coupled-Inductor Boost DC-DC Converter for Hybrid and Fuel Cell Electric Vehicle. *VPPC 2007*, pp. 399-404
- Levin, G. & O'Malley, K. (1996). Designing with hysteretic current-mode control. , *EDN Magazine*, vol.41, pp 5
- Sokal, N. & Redl, R. (1985). Current-mode control, five different types used with three basic classes of power converters. *PESC 1985*, pp. 771-785.
- Yang, X. & Wang, Z. A. (2003). A Novel Quasi-Constant Frequency Hysteretic Current Mode Control Approach. *PESC 2003*, vol. 3, pp. 1147-1150.
- Zhao, Q. & Lee, F. C. (2003). High-Efficiency, High Step-Up DC-DC Converters. *IEEE Transaction on Power Electronics*, vol. 18, (Jan 2003) pp. 65- 73.

The Thermo-mechanical Behavior in Automotive Brake and Clutch Systems

Abdullah M. Al-Shabibi
Sultan Qaboos University
Oman

1. Introduction

Automotive brakes and clutches involve bodies that are in contact and move relative to each other. Typically in the clutch, the contacting bodies take the shape of an axisymmetric disk. As similar as the contacting parts may be from system to system, their functions often vary. While they are used to decelerate or stop the motion of a rotating disk in the automotive brake, in the clutch system they are a mean of transmitting motion between two rotating parts. In the brake system the contact usually takes place between a rotating disk and a stationary friction pad. In the clutch system, however, the contacting disks are rotating at relative speeds and the contact results in a sliding motion over a short period of time till the two bodies are at the same speed. The length of the sliding motion depends on the amount of contact pressure applied, as well as the friction coefficient. The contact engagement in these systems takes place between the friction material of the friction disk and a steel surface.

The main problem associated with these types of systems is the variation of contact pressure distribution during engagement, which leads to areas of high-pressure concentration. As a result of sliding motion and friction, areas of high heat generation or hot spots may result which can in turn damage the contact surfaces. The damage can take different forms such as variation in the contacting disk thickness and surface cracks. The variation in disk thickness is expressed as disturbance to the applied load resulting in a low frequency vibration. Overheating of materials at the contact points, on the other hand, can lead to material degradation, which effectively reduces the lifetime of the effected system. Fig. 1 shows an example of hot spots patterns found in a clutch disk. The problem of hot spots has imposed design constraints to the brake and clutch systems in the past. Recently, it has become crucial to investigate the problem of hot spots promoted by the use of new materials and design improvements. The main objective of these investigations are to, if at all possible, completely eradicate the hot spots. This requires identification and examination of the parameters responsible for hot spots and simulation of the engagement process.

The sliding motion from the contact lasts for a short period of time that might not exceed half of a second, as is the case in the clutch system. Considering the short time of engagement the transient solution is indeed the key to understanding the process of hot spot formation. This will help to recognize how the problem fields, such as the temperature and the contact pressure evolve with time, in addition, to determine the possibility of material yielding through the computation of thermal stresses. Furthermore, design sensitivity analysis can be carried out with the availability of a transient solution.

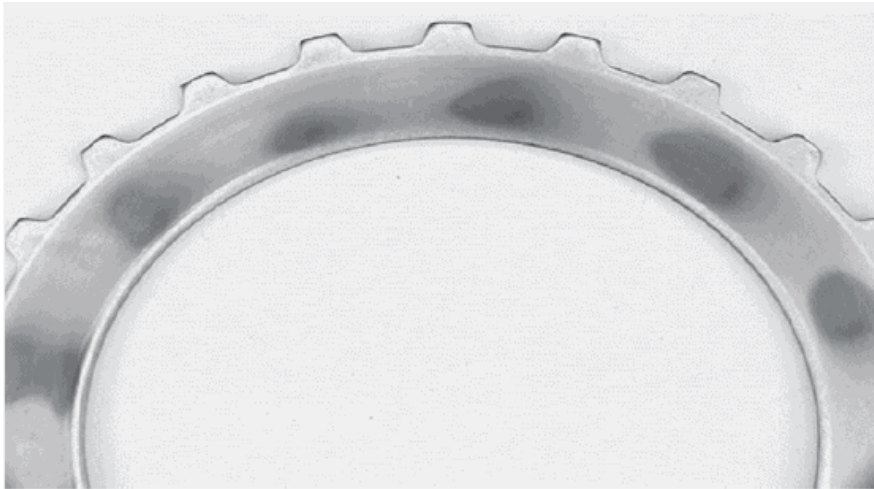


Fig. 1. Hot spot as it appears on a clutch desk.

1.1 Automotive brake and clutch system

There are two types of automotive clutch systems: wet and dry clutches. Dry clutch is typically used in a car with a manual transmission and its function is to connect the engine to the transmission. There are three main parts that make up the dry clutch: a flywheel, and clutch and pressure plates. The flywheel is connected to the engine whereas the clutch plate is connected to the transmission through a shaft. The flywheel and the clutch plate are engaged by pushing the pressure plate against the clutch disk, which in turn is pressed against the flywheel. This locks the engine to the transmission input's shaft, causing them to rotate at the same speed. The wet clutches, on the other hand, are used with the automatic transmission and they involve fluid flow across the contacting surfaces. They are used to engage different gears to the shaft transmitting the engine's rotation. The wet clutch consists of a pressure plate, pack of discs and an endplate. The disc pack is mounted between the pressure and end plates and consists of friction and steel disks. There are two types of friction disks that are commonly used in manufacturing the wet clutch system: single and double-sided friction disks. In the first, the friction material is applied to one side of a steel core, whereas, in the second, the friction material is layered on both sides of the steel core. For the case where double-sided friction disks are used, disc pack consists of alternating layers of friction and steel plates. Friction plates are splined on the inside, where they are locked to one of the gears. The steel plates, on the other hand, are splined on the outside, where they are locked to the clutch housing that transmits the engine's rotation. Grooves are also found on the surface of the friction disk that provides passages for the coolant fluids. The coolant fluid is used to cool down the contact interface, which also helps stabilizing the friction coefficient.

Similarly, there are two kinds of automotive brake systems that are commonly used in the automotive industry: disk and drum brakes. Most of the cars have disk brake on their front wheels and it composes of two friction pads, a steel disk mounted to the wheel hub and a caliper, which contains a piston. Disk brake operates through engaging the two pads in contact with the rotating steel disk. The steel disk contains a set of vanes that provide cooling to the brake system. The drum brake, on the other hand, consists of a steel drum,

hydraulic actuators and two brake shoes lined with a friction material. The hydraulic actuators are used to push the brake shoes against the brake drum.

1.2 Frictionally excited thermoelastic instability (TEI)

When two bodies are in contact and sliding relatively, frictional heat generation causes thermoelastic distortion that, in turn, modifies the initial contact pressure distribution. This feedback process is found to be unstable when the sliding speed exceeds a certain critical value. This phenomenon was first identified and explained by Barber (1967,1969) and was called "frictionally excited thermoelastic instability" or TEI. A microscopic disturbance in the contact pressure can grow resulting in areas of high-pressure concentrations and subsequently creating areas of high heat generations or 'hot spots'. Hot spots have been reported in a number of mechanical systems such as mechanical seals, aircraft brakes, railways and automotive clutch and brake systems. This phenomenon has been investigated both theoretically and experimentally over the last four decades. An overview of these investigations is presented in the following two sections to provide a better understanding of the TEI problem.

1.3 Field observations and experimental works

Parker and Marshall (1948) were the first to report evidence of TEI in railway brakes. Barber (1968,1969) carried a theoretical and experimental investigation and provided an explanation for the TEI phenomenon. He noted that a thermoelastic deformation causes a widely spread contacting asperities to concentrate at one or more discrete contact areas which are smaller than the nominal area. When the effect of thermoelastic distortion exceeds that of wear, the contact area changes can become unstable. Regions of high contact subsequently become regions of high heat flux that penetrate into sliding bodies causing thermal damages such as thermal cracks. Sehitoglu (1983) provided an explanation for the development of surface cracking, in which he noted that constraint on free thermal expansion of the hot spot by relatively cooler surrounding material is responsible for the formation of thermal fatigue cracks. Evidence of thermal cracks has been observed in railway brakes (Dow (1980), Fec and Sehitoglu (1985)), mechanical seals (Netzel (1980), Kennedy and Karpe (1982)) and automotive brakes (Anderson and Knapp (1989)). High temperatures are another consequence of the high local heat flux, which also has been reported in the railway brake (Van Swaay (1969), Ho et al. (1974), Wentenkamp and Kipp (1976), Van Swaay (1979), Hewitt and Musial (1979)).

Investigations have been carried out to improve the performance of the brake system primarily through lowering the surface temperatures. Ho et al. (1974) conducted an investigation concerning aircraft brake in an attempt to develop improved brake materials. They suggested a criterion for determining the number and thickness of brake disks, where the thermal diffusivity and the length of the braking cycle play a very important role. Lower surface temperatures can be achieved by using materials of high specific heat and density, and by maximizing the contact area. Santini and Kennedy (1975) monitored the surface temperature in an aircraft disk brake during a drag test, during which the sliding speed drops to zero from some initial value within a certain period of time. They noticed the development of non-uniform contact areas that are constantly shifting.

Evidences of thermoelastic instability were also observed in automotive brake and clutch systems over the past three decades. High local temperatures are found responsible for thermal cracking in automotive brakes (Anderson and Knapp (1989)), resulting in brake

fade (Lee and Barber (1993)). Furthermore, heat flux fluctuation can lead to thermoelastic distortion in the form surface waviness, which is expressed as disturbance to the applied load resulting in a low frequency or sometimes known as *brake judder* (Kreitlow et al. (1985), Thomas (1988)). Lee and Barber (1993) conducted an experimental investigation to better understand the TEI mechanism in the brake system and to validate the theoretical approximation as far as the onset of instability is concerned. They observed non-uniformities in the temperature, which is a clear evidence of thermoelastic instability in the brake system. They also reported changes in the form of the dominant perturbation as temperature is increased. Zagrodzki (1990, 1991) reported thermoelastic instability in a multi-disk clutch that resulted in permanent distortion such as coning. Lee and Dinwiddie (1998) investigated the effect of various contact conditions on the heating patterns and judder characteristics of a disk brake using infrared camera technology and vibration measurements. They showed that modified brake materials based on the theory of thermoelastic instability, in which the critical speed is increased to achieve a more stable brake system, can lead to a better judder performance. A similar investigation was also conducted by Edward Little *et al.* (1998), in which they demonstrated that increasing thermal disk thickness variation is accompanied by increasing brake torque variation. Yi *et al.* (2001) conducted a series of drag tests to investigate the phenomenon of TEI in an automotive disc brake. They used Fast Fourier Transform method to determine the exponential growth rate for various hot spot numbers and critical speed. Their results for critical speed and number of hot spots showed good agreement with the numerical prediction.

1.4 Theoretical investigations

The study of the thermoelastic process over the last four decades has followed mainly three branches; the study of stability analysis or critical speed, steady state solution and transient behavior.

Stability analysis

Stability analysis is mainly about the determination of the critical speed. Dow and Burton (1972) were the first in this field and they examined the stability of a sinusoidal perturbation that can grow exponentially in time for a semi-infinite plane sliding on a rigid surface. Their study reveals that the perturbation is unstable above a certain value of a sliding speed and this speed is different for different wave numbers. The critical speed for the system is then determined by the speed at which the first perturbation grows unstable.

Later, Burton *et al.* (1973) investigated the problem of two straight Blades contacting along a straight common interface which has been developed geometrically from a two cylindrical tubes pressed against each other by a uniform pressure. They found that for materials contacting their own kind, instability would be seen only at high values of friction coefficient. On the other hand, if one cylinder is changed to an insulator and one to a conductor, the disturbance will almost be stationary relative to the conductor and almost all of the heat will go into it. The stability in this case has a strong dependence on the sliding speed and the critical speed is low.

These findings, however, are not consistent with experimental observations in which evidence of instability was reported for contacting materials of similar properties. Berry (1984) has noted instabilities over a wide range of speeds and loads with various material combinations including cases of similar materials. Burton (1973) later offered an explanation

for this in which he explained that surface films such as natural oxidation products would act as thermal insulator. These thin films can change the stability behavior leading to instability. If the perturbation has a high velocity with respect to the body containing the film, the thermal penetration is small and the film properties may dominate the system.

Heckmann and Burton (1977) have also studied the effect of frictional shear traction on the stability boundary that has previously been neglected. They applied this study to the case where one body is considered a nonconductor and concluded that the introduction of shear has little effect on the predicted critical speed. Later, Lee and Barber (1993) studied the effect of shear traction when both materials are deformable and thermal conductors. They have shown that there is a significant change in the predicted critical speed when both materials have thermal properties of the same order of magnitude. Whereas stable behavior is predicted for two materials of similar thermal properties when shear effect is neglected, the presence of shear effect is shown to lead to bounded values of critical speed.

In studies so far, the model of two semi-infinite layers have been adopted where critical speed predicted by this model is more conservative when compared to that observed experimentally for automotive brake systems (Kreitlow et al. (1985), Anderson and Knapp (1989)). Lee and Barber (1993) extended Burton's model to include the dimension effect by studying the stability of a finite thickness layer that slides between two half-planes. This geometry is typical in the disk brake system where a finite thickness disk slides against two pads. They concluded that there is a preferred wavelength for instability whereas in two half planes model the critical speed decreases monotonically with wavelength. The threshold of instability is characterized by an antisymmetric perturbation leading to hot spots at alternating positions on the two sides of the disk. Their results of critical speed are of the order of those observed experimentally. Later, Lee (2000) developed a one sided heating model for automotive drum brakes and found the stability behavior of this model is similar to that of antisymmetric model of two sided heating with a higher critical speed. He also concluded that thermal expansion and friction coefficients are the most influential properties. Hartsock and Fash (2000) have also considered the effect of the friction pads' thickness on the stability behavior of the two-sided heating model. They incorporated the thickness of the pads by appropriately modifying their elastic modulus. They showed that the critical speed for thick friction pads is close to Lee's prediction but fell below it for thin pads.

Lee's model gives a better representation for the critical speed yet the computational complexity precludes extending it for a more realistic geometry. This complexity has been overcome by Du (1997) through the use of the finite element method to discretize the problem in space and formulate a discrete eigenvalue problem for the TEI. He examined his approach by solving a simple problem of half-plane sliding against rigid, non-conductive surface. Later Yi (2001) extended the finite element approach to solve the problem of two sliding bodies of a finite thickness including the three-dimensional disk problem.

Steady state problem

Stability analysis can determine the critical speed and shape of the unstable mode, however, it falls short to determine the amplitude of the contact pressure and the temperature field. Steady state solution, on the other hand, can show the value of the maximum thermal stresses and temperature encountered by the TEI system. This part of the TEI problem has been the focus of a number of studies in the past. Burton et al. (1973) has obtained the steady state solution for a conductive body sliding on a rigid nonconductive body. They assumed a

configuration of contacting spots separated by regions where the surfaces are parted and used power series to determine the contact pressure distribution for such a spot. They concluded that the distribution of pressure in the contact zone is approximately given by a parabolic relationship and the magnitude of the maximum pressure is dependent upon contact loading and the ratio of the operating velocity to the critical velocity. Burton and Nerliker (1975) obtained the solution for two conducting semi-infinite plates using the same technique of power series representation for the contact pressure in the contact region. They found two configurations that satisfy the boundary conditions, one of which is unstable. Latter Barber (1976) solved the problem of axisymmetric geometry using harmonic potential function and found that his solution is converging much faster than that of Burton using power series.

Transient problem

Although the steady state solution can predict the maximum pressure encountered by the TEI systems, typically, the engagement in the automotive brake and clutch systems take place over a very short period of time that is not enough for the system to reach the steady state. The best presentation is then acquired by solving for the transient behavior. The presence of the time variable in the governing equations makes it harder to obtain the transient solution, compared to the effort acquired by the other two solutions.

The transient solution has been the focus of some studies in the past. Barber (1980) presented a solution for the transient thermoelastic contact of a sphere sliding on a rigid non-conducting plane, subject to a Hertzian approximation to the contact pressure distribution. The aim of this study was to describe the transient process where an initially small pressure disturbance develops into a condition of patch like contact. They concluded if the ratio between the initial contact radius and the radius achieved in the steady state is large enough, the initial reduction in radius is linear with time depending only upon the initial contact radius and thermal diffusivity. Later, Barber et al. (1985) used the same model to evaluate the effect of design and operating conditions on the maximum temperature reached in brake and showed that in the case of uniform deceleration, the duration of the stop is significant. If the stop is sufficiently small for hot spots to develop, the temperature is high. High temperature is also reached if the stop is sufficiently fast because of the high rate of heat generation. There exists an optimum between these two extremes.

Azarkhin and Barber (1985) presented a transient solution for an elastic conducting cylinder sliding against a rigid non conducting half plane. They used Green's function developed by Barber and Martin-Moran (1982), in which the solution of a thermoelastic contact problem can be expressed as a double integral of the surface heat input or temperature in time and space. Their method allowed them to follow the transient behavior of the system until it approaches the steady state for some values of the initial contact width. They also showed if the width of the initial contact is sufficiently large, bifurcation will occur and their method is not suited to pursue this phase of the process because of computational time and accuracy considerations. They have been able to overcome these difficulties by using a volume rather than the surface representation of the variables. Their solution has proven to be more accurate in comparison to that given by the Hertzian approximation and also enables them to follow the process through bifurcation.

The analytical solution of the transient thermoelastic contact problems such as those mentioned above are limited to a number of ideal problems which involve approximate geometry developed from a practical application. They also involve an extensive

computational time to reach convergence in the solution. Finite element method is an attractive alternative in which the domain of the problem is divided into sub-domains resulting in a system of linear first order differential equations. These equations are then solved utilizing time integration. A number of researchers have adopted this approach to study the transient thermoelastic contact problems, investigating the effect of different boundary condition configurations on the solution. Optimal design is also sought in those solutions in which geometrical dimensions and material properties played a very important role.

Kinney and Ling (1974) used finite element method to simulate the thermoelastic instabilities in the high-energy disk brakes. They investigated the effect of different material parameters on the temperature distribution in an attempt to determine the most important parameters for safe and reliable brake performance. Axisymmetric models were developed for a single-pad and annular disk brakes and the effect of wear was incorporated in these models by proposing a criterion followed from experimental observations. They concluded that lower temperature in the disk brake assembly could be achieved by increasing the conductivity, the volume and the heat capacity of the heat sink component. Day (1984, 1988) presented a finite element analysis for drum brakes to investigate the role that interface pressure and thermal effects play in brake performance. They indicated the interdependence of interface pressure, temperature and wear over the friction material rubbing surface. Day and Tirovie (1991) has also described how the pressure at the friction interface of a drum and disc brake varies due geometry and deformation of the brake components, predicting interface pressure distribution and surface temperatures. Other finite element simulation involves investigating the transient thermoelastic behavior in composite brake disks (Sonn et al. 1995, 1996). Composite disks have demonstrated a lower temperature and pressure distribution along the friction surfaces.

Finite element analysis has also been used to investigate the transient process in the clutch system. Zagrodzki (1990, 1991) presented the axisymmetric solution of the transient problem for a multi-disk clutch, showing the effect of the TEI on the thermal stresses. He concluded that the thermomechanical phenomena occurring on any friction surface strongly effect the other friction surfaces and the Young's modulus of the friction material is very important. By reducing the modulus, the undesirable thermomechanical effects can be reduced.

1.5 Geometric modeling developments of TEI system

Because of the complexity of the TEI problem, early investigation of the TEI relied on an approximate two-dimensional model. Presuming an axisymmetric shape for the contacting bodies, Fourier series decomposition can be used along the circumferential direction. This allows the treatment of each Fourier mode separately and simplifies the mathematical formulations of the problem, providing no intermittent contact is experienced along the circumferential direction. Furthermore, plane strain or stress approximation can be adopted for the variation along the radial direction, where for small wave numbers plane strain is used and vice versa. The first two-dimensional model was used by Burton (1973) to study the stability of two sliding half-planes developed geometrically from a mechanical seal consisting of two cylindrical tubes. The same model has been used to predict the onset of instability for automotive brake system. Lee and Barber (1993) introduced a more representative two-dimensional model, in which they include finite thickness effect of the steel disk found in the disk brake system. Due to the geometric complexity involves in this class of problem, finite element approach is a more appropriate tool to treat a more realistic

geometry. Principally, finite element method can be used to model any TEI problem regardless of its geometric complexity.

The two-dimensional model has proven to be effective in determining the onset of instability in the brake system. Yi and Barber (1999) showed that except for a relatively small number of spots, the two-dimensional model give a very good prediction for the critical speed and the dominant wave length. The two-dimensional model, however, accounts only for instability along the sliding direction. Evidence of instability has also been observed across the sliding direction. Furthermore, the dominant thermal effect is found to be independent of the circumferential direction in some cases, in which axisymmetric solution can be adopted. This model has been used to model the variation of the problem fields along the radial direction for the brake (Kennedy and Ling (1974) and clutch (Zagrodzki (1990, 1991)) problems. For a non-axisymmetric solutions a complete three-dimensional model is needed.

1.6 Finite element simulation of transient behavior

A clutch or a brake engagement can be simulated through a direct computer simulation. A schematic diagram representing the finite element simulation is shown in Fig. 2, which involves solving two coupled problems at the same time. This is achieved by constructing two different models, the first of which is used to solve the thermoelastic problem to yield displacement field and contact pressure distribution. The other model is used to solve the

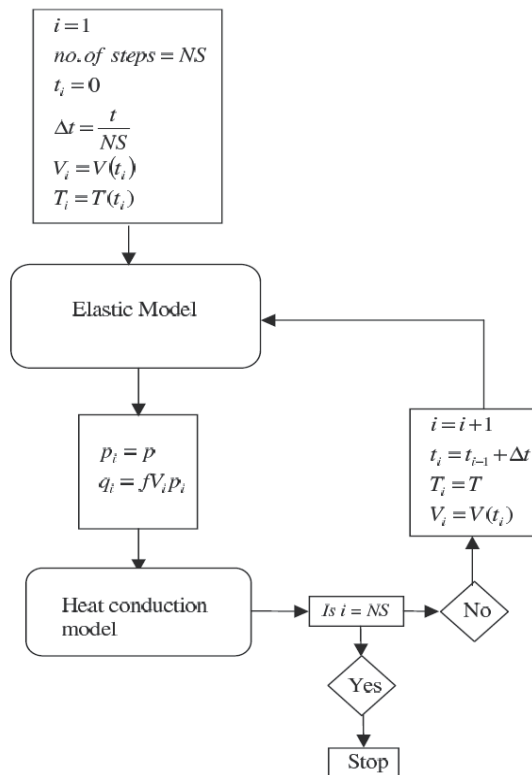


Fig. 2. Schematic diagram of FE simulation

transient heat conduction problem to account for the change in the temperature field during the simulated time step. The two models are coupled through the fact that the contact pressure from the first model is necessary in the second one to define the frictional heat flux. Moreover, the temperature field from the heat conduction model is needed for the computation of the contact pressure. This requires defining small time steps during which the contact pressures and sliding speed are assumed to remain constant. To acquire more accurate solutions, fine finite element mesh should be used which in turn requires the use of even smaller time steps to preserve numerical stability. This yields an extensive computational time, and although this is manageable for a two-dimensional problem it becomes extremely hard for a more realistic three-dimensional geometry.

2. Thermoelastic instability of half-plane sliding against rigid body

The aim of this section is to show how to analytically investigate the thermoelastic instability of sliding objects. A simple problem of a half-plane sliding against a rigid body is considered. Burton's method of investigating TEI is to identify solutions of the perturbation problem of the exponential form

$$T(x, y, z, t) = e^{b_i t} \theta(x, y, z), \quad (1)$$

where T is the temperature field in Cartesian coordinates x , y , z and t is time. Substitution of equation (1) into equations of heat conduction and thermoelasticity and the boundary conditions leads to an eigenvalue problem for the exponential growth rate b_i and the associated eigenfunction θ_i .

A general solution for the transient evolution of a perturbation at constant sliding speed can be written as an eigenfunction series

$$T(x, y, z, t) = \sum_{i=1}^{\infty} C_i e^{b_i t} \theta_i(x, y, z), \quad (2)$$

where C_i is a set of arbitrary constants determined from the initial condition $T(x, y, z, 0)$. It follows from equation (2) that if at least one eigenvalue is positive or complex with positive real part, the perturbation will grow without bounds and the system is unstable in the linear regime.

Fig. 3 shows the thermoelastic half plane $y > 0$ sliding against a rigid non-conducting body at speed V , which may be a function of time. The two bodies are infinite in extent in the x -direction and are pressed together by a uniform pressure p_0 applied at the extremities distant from the interface. Sliding friction occurs at the interface $y = 0$ with coefficient f , leading to the generation of frictional heat

$$q(x, t) = fVp(x, t), \quad (3)$$

where $p(x, t)$ is the contact pressure. Since the lower body is non-conducting, all of this heat must flow into the thermoelastic half plane, resulting in the thermomechanically coupled boundary condition

$$q_y(x, 0, t) = -K \frac{\partial T}{\partial y}(x, 0, t) = fVp(x, t), \quad (4)$$

where K is the thermal conductivity of the half plane.

This transient thermomechanical contact problem has a simple one-dimensional solution in which the contact pressure and the temperature field are independent of the x -coordinate. However, Burton *et al.* have shown that if the sliding speed is sufficiently high, this solution may be unstable, leading to the exponential growth of sinusoidal perturbations in temperature and pressure. For example, the contact pressure will then take the form

$$p(x, t) = p_0(t) + p_1 e^{bt} \cos(mx). \quad (5)$$

Eventually these perturbations will grow sufficiently large for separation to occur, after which the assumption of linearity will cease to apply

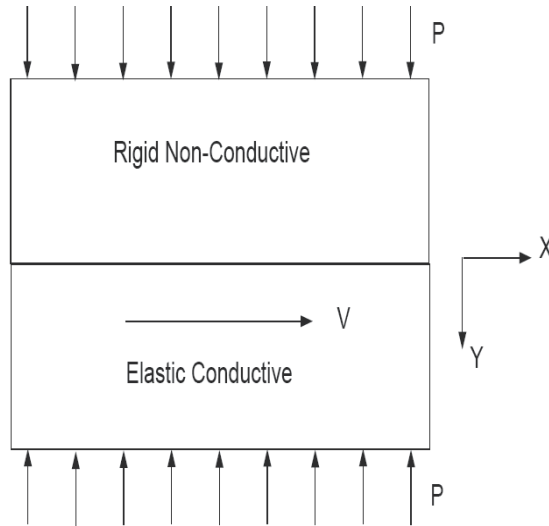


Fig. 3. Sliding contact of an elastic half-plane against a rigid plane surface

Solving for the exponential growth rate b proceeds in three steps. First, the transient heat equation (6) is solved for the temperature field that satisfies the thermal boundary conditions (4)

$$\frac{\partial^2 T}{\partial x^2} + \frac{\partial^2 T}{\partial y^2} = \frac{1}{k} \frac{\partial T}{\partial t}, \quad (6)$$

where

$$k = \frac{K}{\rho c_p}$$

is the thermal diffusivity and K , ρ , C_p are the thermal conductivity, density, and specific heat respectively. The second step involves solving the thermoelastic problem for the displacement and stress components induced by the temperature field and satisfies the mechanical boundary conditions. Finally, the coupling term presented in the frictional heat flux is introduced to the two solutions.

Following Burton *et al.*, we consider cases in which the perturbation in the temperature field takes the sinusoidal form

$$T(x, y, t) = \theta(y)e^{bt} \cos(mx). \quad (7)$$

Substitution in the transient heat conduction equation (6) yields the ordinary differential equation

$$\frac{d^2\theta}{dy^2} - \lambda^2\theta = 0 \quad (8)$$

for $\theta(y)$, where

$$\lambda = \sqrt{m^2 + \frac{b}{k}} \quad (9)$$

Notice that λ is real for $b > -km^2$, which includes all cases of unstable perturbation ($b > 0$). Equation (8) has the two solutions $\theta = \exp(\pm\lambda y)$, but we restrict attention to the negative exponent, since the perturbed temperature field is assumed to decay as $y \rightarrow \infty$. We therefore obtain

$$T(x, y, t) = T_0 e^{-\lambda y + bt} \cos(mx), \quad (10)$$

where T_0 is an arbitrary constant.

The thermoelastic problem is solved for the displacements and stresses induced by the temperature field T as well as the mechanical boundary conditions. The particular solution corresponding to the temperature field is obtained by solving for the strain potential ψ through the following relation (Barber, 1993).

$$2\mu \underline{u} = \nabla \psi \quad (11)$$

where

$$\nabla^2 \psi = \frac{2\mu\alpha(1+\nu)}{1-\nu} T \quad (12)$$

and \underline{u} , μ , α , ν are the displacement vector, shear modulus, coefficient of thermal expansion and Poisson's ratio respectively. Substituting for T into the relations above, we obtain

$$\psi = \frac{2\mu\alpha(1+\nu)}{(1-\nu)(\lambda^2 - m^2)} T \quad (13)$$

The corresponding normal displacement and stress components are defined as followed

$$u_y = \frac{1}{2\mu} \frac{\partial \psi}{\partial y} \quad (14a)$$

$$\sigma_{yy} = -\frac{\partial^2 \psi}{\partial x^2} \quad (14b)$$

$$\sigma_{xy} = -\frac{\partial^2 \psi}{\partial x \partial y} \quad (14c)$$

The particular solution presented above satisfies the field equation and it does not account for the mechanical boundary conditions of the problem where the stress components are required to decay to zeros away from the contact interface.

$$\sigma_{xx}, \sigma_{yy}, \sigma_{xy} \rightarrow 0 \quad \text{as } y \rightarrow 0 \quad (15)$$

These boundary conditions are also found at interface or $y = 0$

$$u_y = 0 \quad (16a)$$

$$\sigma_{yy} = -p(x, t) \quad (16b)$$

$$\sigma_{xy} = 0 \quad (16c)$$

To satisfy the mechanical boundary conditions, the isothermal solutions A and D of Green and Zerna (1954) is superimposed to the particular solution. The corresponding normal displacement and stresses for the isothermal solutions are

$$u_y = \frac{1}{2\mu} \left\{ \frac{\partial \varphi}{\partial y} + y \frac{\partial \omega}{\partial y} - (3 - 4\nu)\omega \right\} \quad (17a)$$

$$\sigma_{yy} = -\frac{\partial^2 \varphi}{\partial x^2} + y \frac{\partial^2 \omega}{\partial y^2} - 2(1 - \nu) \frac{\partial \omega}{\partial y} \quad (17b)$$

$$\sigma_{xy} = -\frac{\partial^2 \varphi}{\partial x \partial y} + y \frac{\partial^2 \omega}{\partial x \partial y} - (1 - 2\nu) \frac{\partial \omega}{\partial x} \quad (17c)$$

where

$$\nabla^2 \varphi = 0 \quad (18)$$

$$\nabla^2 \omega = 0$$

φ and ω are chosen to satisfy the boundary conditions in (16)

$$\varphi = Ae^{-my} \cos mx \quad (19)$$

$$\omega = Be^{-my} \cos mx$$

Substituting (13) into (14 a-c) and (19) into (17 a-c) and superimposing the two solutions yields,

$$u_y = \left\{ \frac{\alpha(1+\nu)\lambda}{(1-\nu)(\lambda^2 - m^2)} T_0 e^{-\lambda y + bt} \cos mx \right\} + \frac{1}{2\mu} m A e^{-my} \cos mx \quad (20a)$$

$$+ \frac{1}{2\mu} \{my + (3 - 4\nu)\} m B e^{-my} \cos mx$$

$$\sigma_{yy} = \frac{2\mu\alpha(1+\nu)m^2}{(1-\nu)(\lambda^2-m^2)} T_0 e^{-\alpha y+bt} \cos mx + m^2 A e^{-my} \cos mx + \{my + 2(1-\nu)\} m B e^{-my} \cos mx \quad (20b)$$

$$\sigma_{xy} = \frac{2\mu\alpha(1+\nu)m^2}{(1-\nu)(\lambda^2-m^2)} T_0 e^{-\alpha y+bt} \sin mx + m^2 A e^{-my} \sin mx + \{my + (1-2\nu)\} m B e^{-my} \sin mx \quad (20c)$$

The conditions (16a and 16c) are now used to define the constants A and B

$$A(t) = \frac{1}{m} \left\{ \frac{2\mu\alpha(1+\nu)T_0}{(1-\nu)(\lambda^2-m^2)} [2\nu(\lambda-m) + (m-2\lambda)] \right\} e^{bt} + \frac{1}{m} \left\{ (1-2\nu) \frac{p_0}{m} \right\} e^{bt} \quad (21a)$$

$$B(t) = \left\{ \frac{2\mu\alpha(1+\nu)T_0}{(1-\nu)(\lambda+m)} + \frac{p_0}{m} \right\} e^{bt} \quad (21b)$$

The condition (16b) is used to obtain the relationship between p_0 and T_0

$$p_0 = \frac{2\mu\alpha(1+\nu)m}{(\lambda+m)} T_0 \quad (21)$$

Finally, the coupling term of the frictional heat flux (4) is introduced which yielded the growth rate b as a function of the sliding speed V .

$$b(V) = k \left(\frac{mf\beta V}{K} - \frac{m^2}{2} - m \sqrt{\left(\frac{m}{2}\right)^2 + \frac{mf\beta V}{K}} \right) \quad (22)$$

where

$$\beta \equiv \frac{2\mu\alpha(1+\nu)}{1-\nu}$$

Fig. 4 shows the plot of the growth rate b as a function of the sliding speed V for two different wave numbers m . A critical speed exists for each wave number above which the sinusoidal perturbation will grow. Furthermore, different perturbation wave number holds different critical speed.

3. Finite element solution

In the previous section, the dominating eigenfunction has been identified. For a sliding speed above the critical value, the dominating eigenfunction is unstable and tends to

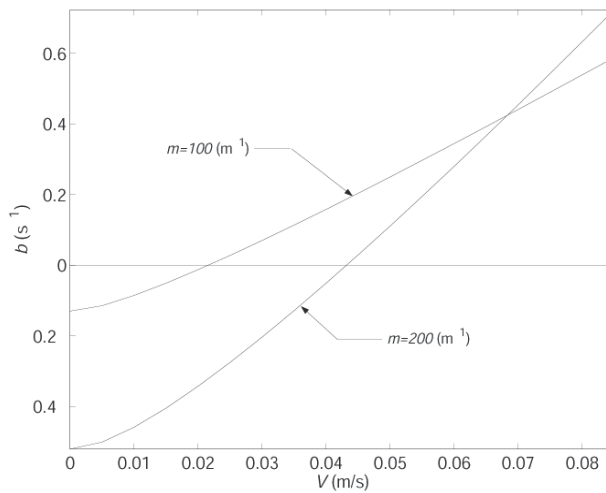


Fig. 4. The exponential growth rate b as a function of speed for two different wave numbers dominate the solution. However, as the speed drops below the critical value, which is the case for a varying sliding speed, more eigenfunctions are needed in the expansion to maintain a reasonable amount of error in the solution. Obtaining the whole set of the eigenfunctions is a difficult task even for a simple geometry such as that considered in the previous section. This is mainly because of the coupling presented in the thermoelastic contact problem, which also involves solving two systems at the same time. Furthermore, treating a more realistic geometry add more complexity to the problem. Finite element method is a good alternative in which the problem is discretized in space. This will allow obtaining a set of eigenfunctions equivalent to the system's degrees of freedom. A more realistic geometry with practical material properties, similar to that found in the clutch problem can easily be incorporated in the finite element solution.

In this section, we should explore the method of governing a discrete eigenvalue problem considering a three dimensional model of two thermoelastic layers sliding relative to each other. This will involve solving for the exponential growth rate and the associated eigenfunction.

Fig. 5 shows two thermoelastic bodies Ω_1 and Ω_2 with surface boundaries Γ_1 and Γ_2 , respectively, sliding at speed $V_1(t)$ and $V_2(t)$, which may be a function of time. The two bodies are infinite in extend in the x -direction and have a common contact interface $\Gamma_c = \Gamma_1 \cap \Gamma_2$ which is time independent.

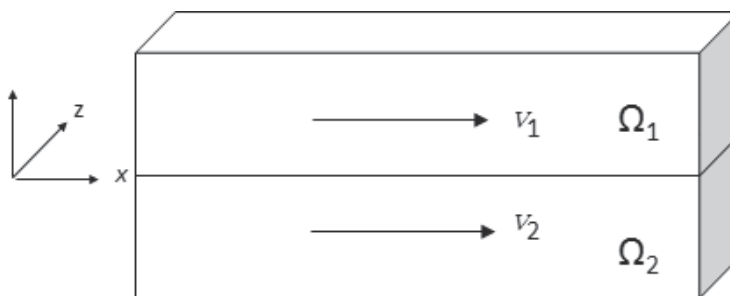


Fig. 5. Sliding contact of two elastic bodies.

Sliding friction occurs at the interface $y = 0$ with coefficient f , leading to the generation of frictional heat

$$q(x, z, t) = fVp(x, z, t), \quad (23)$$

where $p(x, z, t)$ is the contact pressure. The heat flow into the two bodies at the interface results in the thermomechanically boundary condition

$$q_y(x, 0, z, t) = -\left(K^1 \frac{\partial T^1}{\partial y}(x, 0, z, t) + K^2 \frac{\partial T^1}{\partial y}(x, 0, z, t)\right) = fVp(x, z, t), \quad (24)$$

where K^1 and K^2 are thermal conductivity of Ω_1 and Ω_2 respectively. Furthermore, temperature continuity requires the temperature of the two bodies at the interface to be equal

$$T^1(x, 0, t) = T^2(x, 0, t). \quad (25)$$

Thermal insulation can be assumed for the surface boundary $\Gamma_1 \cup \Gamma_2 - \Gamma_c$

$$\frac{\partial T}{\partial n}(x, y, z, t) = 0, \quad (x, y, z \in \Gamma_1 \cup \Gamma_2 - \Gamma_c), \quad (26)$$

where n is the outward normal to the surface. This boundary condition is appropriate since $\Gamma_1 \cup \Gamma_2 - \Gamma_c$ are usually in contact with the atmospheric air and they hardly effect the transient solution.

Surface continuity requires the displacement field normal to the contact interface to be equal for the two bodies

$$u^1(x, 0, t) = u^2(x, 0, t). \quad (27)$$

3.1 Growth of a sinusoidal perturbation

Transient heat equation

Following Burton *et al.* (1973), we consider cases in which the perturbation in the temperature field takes the sinusoidal form and grows exponentially in time

$$T(x, y, z, t) = \Re\left\{\theta(y, z)e^{bt+jmx}\right\}. \quad (28)$$

This perturbation is then substituted in the transient heat conduction equation for body β ($\beta = 1, 2$) relative to frame of reference

$$\frac{\partial}{\partial x}\left(K^\beta \frac{\partial T^\beta}{\partial x}\right) + \frac{\partial}{\partial y}\left(K^\beta \frac{\partial T^\beta}{\partial y}\right) + \frac{\partial}{\partial z}\left(K^\beta \frac{\partial T^\beta}{\partial z}\right) = \rho^\beta c_p^\beta \left(\frac{\partial T^\beta}{\partial t} + V^\beta \frac{\partial T^\beta}{\partial x}\right), \quad (29)$$

to yield the ordinary differential equations

$$\frac{\partial}{\partial y}\left(K^\beta \frac{\partial \theta^\beta}{\partial y}\right) + \frac{\partial}{\partial z}\left(K^\beta \frac{\partial \theta^\beta}{\partial z}\right) - \left[K^\beta m^2 \theta^\beta + \rho^\beta c_p^\beta (jmV^\beta + b)\right] \theta^\beta = 0 \quad (30)$$

for $\theta(y, z)$, where ρ^β and c_p^β are the density and specific heat of the material β . If the geometry is discretized by the finite element method, the instantaneous temperature field for each body can be characterized by a finite set of n^β nodal temperatures and it follows that there will be $n = n^1 + n^2$ terms in the eigenfunction series (2). To develop the eigenvalue problem, we first approximate the temperature function $\theta^\beta(y, z)$ of equation (28) in the form

$$\theta^\beta(y, z) = \sum_{i=1}^{n^\beta} N_i(y, z) \Theta_i^\beta, \quad (31)$$

where Θ_i^β are nodal temperatures in body β and $N_i(y, z)$ are a set of n^β shape functions. Applying the weighted residual method to equation (30), we obtain the set of equations

$$\int_{\Omega^\beta} W_j \left(\frac{\partial}{\partial y} \left(K^\beta \frac{\partial \theta^\beta}{\partial y} \right) + \frac{\partial}{\partial z} \left(K^\beta \frac{\partial \theta^\beta}{\partial z} \right) - \left[K^\beta m^2 \theta^\beta + \rho^\beta c_p^\beta (jmV^\beta + b) \right] \theta^\beta \right) d\Omega^\beta = 0, \quad (32)$$

where W_j is a set of linearly independent weighting functions. The second derivative in equation (32) is replaced with first derivative through integration by parts

$$\begin{aligned} & - \int_{\Omega^\beta} \left(K^\beta \frac{\partial W_j}{\partial y} \frac{\partial \theta^\beta}{\partial y} + K^\beta \frac{\partial W_j}{\partial z} \frac{\partial \theta^\beta}{\partial z} - \left[K^\beta m^2 \theta^\beta + \rho^\beta c_p^\beta (jmV^\beta + b) \right] W_j \theta^\beta \right) d\Omega^\beta \\ & + \int_{\Omega^\beta} \left(K^\beta \frac{\partial}{\partial y} \left(W_j \frac{\partial \theta^\beta}{\partial y} \right) + K^\beta \frac{\partial}{\partial z} \left(W_j \frac{\partial \theta^\beta}{\partial z} \right) \right) d\Omega^\beta = 0 \end{aligned} \quad (33)$$

The second integral in (33) can then be replaced by a surface integral using Gauss' theorem to yield after considering the boundary condition (26)

$$\begin{aligned} & - \int_{\Omega^\beta} \left(K^\beta \frac{\partial W_j}{\partial y} \frac{\partial \theta^\beta}{\partial y} + K^\beta \frac{\partial W_j}{\partial z} \frac{\partial \theta^\beta}{\partial z} - \left[K^\beta m^2 + \rho^\beta c_p^\beta (jmV^\beta + b) \right] W_j \theta^\beta \right) d\Omega^\beta \\ & + \int_{\Gamma_c} (W_j q^\beta) d\Gamma_c \end{aligned} \quad (34)$$

where

$$q^\beta = -K^\beta \frac{\partial \theta^\beta(y, z)}{\partial n}, \quad (y, z \in \Gamma_c) \quad (35)$$

Substituting (31) into (34) and using the same functions N_i as both shape and weighting functions, we obtain the matrix equation

$$\left(\mathbf{C}^\beta - m^2 \mathbf{H}^\beta + jmV^\beta \mathbf{M}^\beta \right) \mathbf{\Theta}^\beta + \mathbf{q}^\beta = b \mathbf{M}^\beta \mathbf{\Theta}^\beta, \quad (36)$$

where

$$C_{ji}^\beta = \int_{\Omega^\beta} \left(K^\beta \frac{\partial W_j}{\partial x} \frac{\partial W_i}{\partial x} + K^\beta \frac{\partial W_j}{\partial y} \frac{\partial W_i}{\partial y} \right) d\Omega^\beta,$$

$$M_{ji}^{\beta} = \int_{\Omega^{\beta}} \left(\rho^{\beta} c_p^{\beta} W_j W_i \right) d\Omega^{\beta},$$

$$H_{ji}^{\beta} = \int_{\Omega^{\beta}} \left(K^{\beta} W_j W_i \right) d\Omega^{\beta},$$

and

$$q_j^{\beta} = \begin{cases} \int_{\Gamma_c} \left(W_j q^{\beta} \right) d\Gamma_c, & j \in \Gamma_c \\ 0 & j \notin \Gamma_c \end{cases},$$

Adding the matrix equations for the two bodies yields an assembled matrix equations for the whole system

$$\left(\mathbf{C} - m^2 \mathbf{H} + jm \mathbf{VM} \right) \Theta + \mathbf{q} = b \mathbf{M} \Theta, \quad (37)$$

It might be more convenient to express (37) in the form

$$\left(\mathbf{C} - m^2 \mathbf{H} + jm \mathbf{VM} \right) \Theta + \mathbf{A} \mathbf{q} = b \mathbf{M} \Theta \quad (38)$$

where

$$\mathbf{A} = \begin{bmatrix} \mathbf{I}_c \\ \mathbf{0} \end{bmatrix} \quad (39)$$

and \mathbf{I}_c is the identity matrix of order $n_c \times n_c$ and n_c is the number of the contact nodes.

The thermoelastic problem

A second equation linking the contact pressure to the temperature distribution can be obtained from the finite element solution of the thermoelastic contact problem. We define a quasi-static displacement field in the form

$$u_x^{\beta}(x, y, z) = u^{\beta}(y, z) \sin(mx), \quad (40a)$$

$$u_y^{\beta}(x, y, z) = v^{\beta}(y, z) \cos(mx), \quad (40b)$$

$$u_z^{\beta}(x, y, z) = w^{\beta}(y, z) \cos(mx). \quad (40c)$$

Time variable has been eliminated from the displacement field since the thermoelastic governing equations is time-independent. The displacement functions u, v and w are written in the discrete form

$$u^{\beta}(y, z) = \sum_{i=1}^{n^{\beta}} N_i(y, z) U_i^{\beta}, \quad (41a)$$

$$v^\beta(y, z) = \sum_{i=1}^{n^\beta} N_i(y, z) V_i^\beta, \quad (41b)$$

$$w^\beta(y, z) = \sum_{i=1}^{n^\beta} N_i(y, z) W_i^\beta, \quad (41c)$$

where U_i^β , V_i^β and W_i^β are the components of the nodal displacement vector \mathbf{U}^β . The potential energy for the body β can then be written

$$\Pi^\beta = \frac{1}{2} \int_{\Omega^\beta} (\boldsymbol{\varepsilon}^{\beta T} \boldsymbol{\sigma}^\beta - \boldsymbol{\varepsilon}_0^{\beta T} \boldsymbol{\sigma}^\beta) d\Omega^\beta - \int_{\Gamma_c} u_y^\beta p^\beta d\Gamma_c \quad (42)$$

where

$$\boldsymbol{\sigma} = \{\sigma_x, \sigma_y, \sigma_z, \tau_{xy}, \tau_{xz}, \tau_{yz}\},$$

$$\boldsymbol{\varepsilon} = \{\varepsilon_x, \varepsilon_y, \varepsilon_z, \gamma_{xy}, \gamma_{xz}, \gamma_{yz}\},$$

$$\boldsymbol{\varepsilon}_0 = \alpha T(x, y, z) \{1, 1, 1, 0, 0, 0\},$$

are, respectively, the stress, strain and thermal strain vectors. The stress and strain are related by

$$\boldsymbol{\sigma}^\beta = \mathbf{D}^\beta (\boldsymbol{\varepsilon}^\beta - \boldsymbol{\varepsilon}_0^\beta) \quad (43)$$

Where

$$\mathbf{D} = \frac{E}{(1+\nu)(1-2\nu)} \begin{bmatrix} 1-\nu & \nu & \nu & 0 & 0 & 0 \\ \nu & 1-\nu & \nu & 0 & 0 & 0 \\ \nu & \nu & 1-\nu & 0 & 0 & 0 \\ 0 & 0 & 0 & (1-2\nu)/2 & 0 & 0 \\ 0 & 0 & 0 & 0 & (1-2\nu)/2 & 0 \\ 0 & 0 & 0 & 0 & 0 & (1-2\nu)/2 \end{bmatrix}.$$

Substituting (41a-c) into the strain-displacement relations, we obtain the discrete form of the strains as

$$\boldsymbol{\varepsilon}^\beta = \sum_{i=1}^n \mathbf{B}_i \mathbf{U}_i^\beta, \quad (44)$$

$$\boldsymbol{\varepsilon}_0^\beta = \sum_{i=1}^n N_i \Theta_i^\beta \{1, 1, 1, 0, 0, 0\}, \quad (45)$$

where

$$\mathbf{B}_i = \begin{bmatrix} mN_i \cos(mx) & 0 & 0 \\ 0 & \frac{\partial N_i}{\partial y} \cos(mx) & 0 \\ 0 & 0 & \frac{\partial N_i}{\partial z} \cos(mx) \\ \frac{\partial N_i}{\partial y} \sin(mx) & -mN_i \sin(mx) & 0 \\ \frac{\partial N_i}{\partial z} \sin(mx) & 0 & -mN_i \sin(mx) \\ 0 & \frac{\partial N_i}{\partial z} \cos(mx) & \frac{\partial N_i}{\partial y} \cos(mx) \end{bmatrix} \quad (46)$$

We then substitute (43-45) into (42) and perform the integrations. Minimizing the resulting expressions with respect to the nodal displacements \mathbf{U} then yields the system of equations

$$\mathbf{K}^\beta \mathbf{U}^\beta = \mathbf{G}^\beta \mathbf{\Theta}^\beta + \mathbf{P}^\beta, \quad (47)$$

where

$$\mathbf{K}^\beta = \int_{\Omega^\beta} \tilde{\mathbf{B}}^T \mathbf{D}^\beta \tilde{\mathbf{B}} d\Omega^\beta; \mathbf{G}^\beta = \int_{\Omega^\beta} \tilde{\mathbf{B}}^T \mathbf{D} \tilde{\mathbf{C}} d\Omega^\beta; \mathbf{P}^\beta = \int_{\Gamma_c} \mathbf{N} p d\Gamma_c \quad (48)$$

and

$$\mathbf{B} = [\tilde{B}_1 \quad \tilde{B}_2 \quad \dots \quad \tilde{B}_{n^\beta}]; \mathbf{C} = [C_1 \quad C_2 \quad \dots \quad C_n]; \mathbf{N} = [N_1 \quad N_2 \quad \dots \quad N_{n^\beta}] \quad (49)$$

with

$$\tilde{\mathbf{B}}_i = \begin{bmatrix} mN_i & 0 & 0 \\ 0 & \frac{\partial N_i}{\partial y} & 0 \\ 0 & 0 & \frac{\partial N_i}{\partial z} \\ \frac{\partial N_i}{\partial y} & -mN_i & 0 \\ \frac{\partial N_i}{\partial z} & 0 & -mN_i \\ 0 & \frac{\partial N_i}{\partial z} & \frac{\partial N_i}{\partial y} \end{bmatrix}; \tilde{\mathbf{C}}_i = N_i \begin{Bmatrix} 1 \\ 1 \\ 1 \\ 0 \\ 0 \\ 0 \end{Bmatrix} \quad (50)$$

Adding the matrix equations for the two bodies yield an assembled matrix equations for the whole system

$$\mathbf{K}\mathbf{U} = \mathbf{G}\mathbf{\Theta} + \mathbf{P}, \quad (51)$$

The unknown nodal displacements can be eliminated from the linear algebraic equations (51) to yield a system of equations for \mathbf{P}_c in terms of $\tilde{\mathbf{\Theta}}$ which can be written in the symbolic form

$$\mathbf{P}_c = \mathbf{L}\Theta \quad (52)$$

The frictional heating relation $\mathbf{q}_c = fV\mathbf{p}_c$ and equations (38, 52) can then be used to eliminate \mathbf{p}_c , \mathbf{q}_c , leading to the generalized linear eigenvalue equation

$$\left(fV\mathbf{A}\mathbf{L} - \mathbf{C} - m^2\mathbf{H} + jm\mathbf{V}\mathbf{M} \right) \Theta = b\mathbf{M}\Theta. \quad (53)$$

If the eigenvalues and eigenfunctions of this equation are denoted by b_k , $\hat{\Theta}_i^k$ respectively, a general solution for the evolution of the nodal temperatures $\Theta_i(t)$ at constant speed can be written as

$$\Theta_i(t) = \sum_{k=1}^n C_k \hat{\Theta}_i^k e^{b_k t}, \quad (54)$$

where the constants C_k are to be determined from the initial conditions.

4. Results for axisymmetric geometry

Critical speed corresponds to the sliding speed at which the exponential growth rate b is equal to zero. In the two-dimensional model of half plane sliding on a rigid surface, there exists one eigenmode that has the potential of becoming unstable beyond a certain value of the sliding speed. In the three-dimensional model of two axisymmetric disks, however, the growth rate is a complex number except for the axisymmetric or banding mode corresponding to $m = 0$.

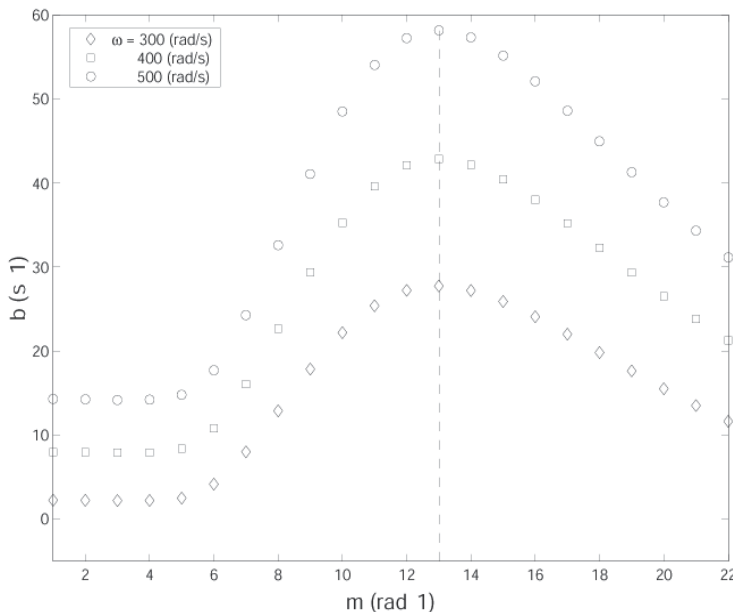


Fig. 6. Exponential growth rate of the dominating eigenmode as a function of wave number m for different operating speeds

Figure 6 shows the exponential growth rate of the dominating mode for each Fourier wave number and it can be seen that, $m=13$ will grow faster than the other modes and it is therefore

anticipated the transient behavior of the system will be dominated by this Fourier mode. This is especially true for the case where the sliding speed is constant. The stability of the system is determined by the wave number with the lowest critical speed. Unlike equation (22) where the critical speed increases monotonically with the wave number, there is a preferred wave number for the critical speed. Furthermore, there are more than one eigenmode that has the potential of becoming unstable depending on the value of the operating speed. The critical speed for each wave number m is determined by the speed at which the first eigenmode becomes unstable.

For each wave number m , there are n numbers of eigenmodes corresponding to the number of nodes used in the finite element model. Depending on the sliding speed, some of these eigenfunctions can be unstable. It is anticipated that the eigenfunction with the highest growth rate to dominate the transient process and the final solution is expected to take the shape of this eigenfunction. The dominating eigenmode for temperature in the contact surface is shown in Fig. 7 for $m=13$.

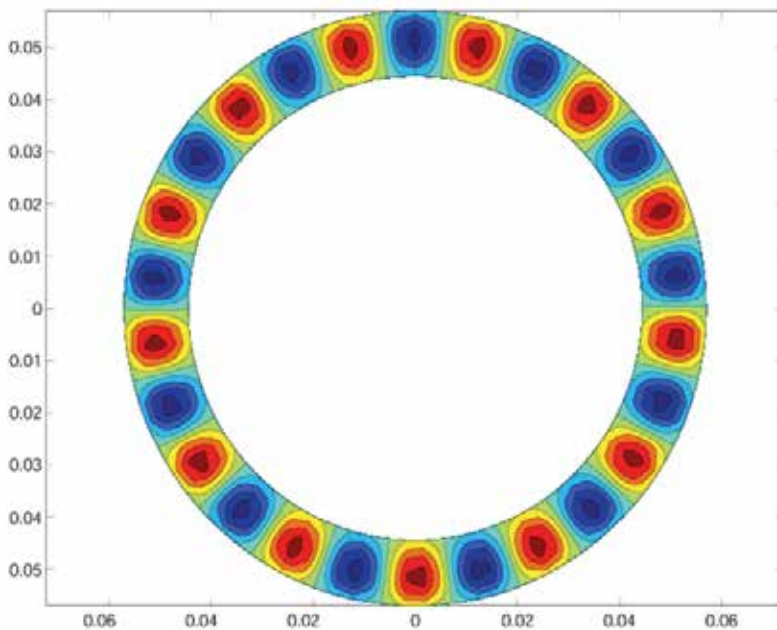


Fig. 7. Dominant eigenmode for the temperature in the contact surface for $m = 13$

5. Conclusion

This chapter sheds some light on the thermomechanical behavior of automotive brake and clutch systems. The coupling between the thermoelastic problem and the thermal heat equation was found to result in the so called thermoelastic instability when the sliding speed is high enough. The first part of this chapter gave a historical literature review on the advancements that have been made in the area of thermoelastic instability. The research on this regard has mainly followed three streams, the stability analysis, the transient behavior and the steady state solution. Two approaches of investigating the thermoelastic instability

have been presented, the analytical approach which is only possible for simplified geometries such as half-plane sliding against rigid body and the finite element approach which can accommodate a more complex geometries like those found in real brake and clutch systems.

6. References

- Anderson, A.E. & Knapp, R.A. (1989), Hot spotting in automotive friction systems, Int. Conf. On wear of materials, Vol., 2, pp. 673-680
- Azarkhin, A. & Barber, J.R. (1985), Transient thermoelastic contact problem of two sliding half-planes, Wear, Vol., 102, pp. 1-13
- Barber, J.R. (1967), The influence of thermal expansion on the friction and wear process, Wear, Vol., 10, pp. 155-159
- Barber, J.R. (1969), Thermoelastic instabilities in the sliding of conforming solids, Proc. Roy. Soc., Vol., A312, pp. 381-394
- Barber, J.R. (1976), Some thermoelastic contact problems involving frictional heating, Q. J. Mech. Appl Math, Vol., 29, pp.1-13
- Barber, J.R. (1980), The transient thermoelastic contact of a sphere sliding on a plane, Wear, Vol., 59, pp. 21-29
- Barber, J.R. & Martin-Moran, C.J. (1982), Green's functions for transient thermoelastic contact problems for the half-plane, Wear, Vol., 79, pp. 11-19
- Barber, J.R.; Beamon, T.W.; Waring, J.R. & Pritchard, C. (1985), Implications of thermoelastic instability for the design of brakes, J. Tribology, Vol., 107, pp. 206-210
- Barber, J.R. (1992), Elasticity, Kluwer Academic Publisher
- Berry, G.A. & Barber, J.R. (1984), The division of frictional heat – A guide to the nature of sliding contact, ASME J. Tribology, Vol., 106, pp. 405-415
- Burton, R.A.; Nerlikar, V. & Kilaparti, S.R. (1973), Thermoelastic instability in a seal-like configuration, Wear, Vol., 24, pp. 177-188
- Burton, R.A. (1973), The role of insulating surface films in frictionally excited thermoelastic instabilities, Wear, Vol., 24, pp. 189-198
- Burton, R.A.; Kilaparti, S.R. & Nerlikar, V. (1973), A limiting stationary configuration with partial contacting surfaces, Wear, Vol., 24, pp. 199-206
- Carslaw, H.S. & Jaeger, J.C. (1959), Conduction of Heat in Solids, Oxford: Clarendon
- Day, A.J.; Harding, P.R.J. & Newcomb, T.P. (1984), Combined thermal and mechanical analysis of drum brakes, Proc. Instn. Mech. Engrs., 198D(15), pp. 287-294
- Day, A.J. (1988), An analysis of speed, temperature, and performance characteristics of automotive drum brakes, Trans. ASME, J. Tribology, Vol., 110, pp. 298-305
- Day, A.J.; Tirovic, M. & Newcomb, T.P. (1991), Thermal effects and pressure distributions in brakes, Proc. Instn. Mech. Engrs, Vol., 205, pp. 199-205
- Dow, T.A. & Burton, R.A. (1972), Thermoelastic instability of sliding contact in the absence of wear, Wear, Vol., 19, pp. 315-328
- Dow, T.A. (1980), Thermoelastic effects in brakes, Wear, Vol., 59, pp. 213-221
- Du, S.; Zagrodzki, P.; Barber, J.R. & Hulbert, G.M. (1997), Finite element analysis of frictionally-excited thermoelastic instability, J. Thermal stresses, Vol., 20, pp. 185-201
- Fec, M.C. & Sehitoglu, H. (1985), Thermal-mechanical damage in railroad wheels due to hot spotting, Vol., 20, pp. 31-42

- Green, A.E. & Zerna, W. (1954), *Theoretical Elasticity*, Clarendon Press, Oxford
- Hartsock, D.L. & Fash, J.W. (2000), Effect of pad/caliper stiffness, pad thickness and pad length on thermoelastic instability in disk brakes, *ASME J. Tribology*
- Heckmann, S.R. & Burton, R.A. (1977), Effects of shear and wear on instabilities caused by frictional heating in a seal-like configuration, *ASLE Trans.*, Vol. 20, pp. 71-78
- Hewitt, G.G. & Musial, C. (1979), The search for improved wheel materials, *Inst. Mech. Eng., Int. Conf. on Railway Braking*, York, p. 101
- Ho, T.L.; Peterson, M.B. & Ling, F.F. (1974), Effect of frictional heating on braking materials, *Wear*, Vol. 26, pp. 73-91
- Kennedy Jr., F.E. & Ling, F.F. (1974), A thermal, thermoelastic and wear simulation of a high energy sliding contact problem, *J. Lub. Tech.*, Vol. 96, pp. 497-507
- Kennedy Jr., F.E. & Karpe, S.A. (1982), Thermocracking of a mechanical face seal, *Wear*, Vol. 79, pp. 21-36
- Kreitlow, W.; Schrodter, F. & Matthai, H. (1985), Vibration and hum of disc brakes under load, SAE 850079
- Lee, Kwangjin & Barber, J.R. (1993), The effect of shear tractions on frictionally-excited Thermoelastic instability, *Wear*, Vol. 160, pp. 237-242
- Lee, Kwangjin & Barber, J.R. (1993), Frictionally-excited Thermoelastic instability in automotive disk brakes, *ASME Journal of Tribology*, Vol. 115, pp. 607-614
- Lee, Kwangjin & Dinwiddie, R.B. (1998), Conditions of frictional contact in disk brakes and their effects on brake judder, SAE 980598
- Lee, K. (2000), Frictionally excited thermoelastic instability in automotive drum brakes, *ASME J. Tribology*, Vol. 122, 849-855
- Netzel, J.P. (1980), Observations of thermoelastic instability in mechanical face seals, *Wear*, Vol. 59, pp. 135-148
- Parker, R.C. & Marshall, P.R. (1984), The measurement of the temperature of sliding surfaces with particular reference to railway blocks, *Proc. Inst. Mech. Eng.*, Vol. 158, pp. 209-229
- Santini, J.J. & Kennedy, F.E. (1975), An experimental investigation of surface temperatures and wear in disk brakes, *Lub. Eng.*, pp. 402-417
- Sonn, H.W.; Kim, G.G.; Hong, C.S. & Yoon, B.I. (1995), Transient thermoelastic analysis of composite brake disks, *Journal of Reinforced Plastics and Composites*, Vol. 14, pp. 1337-1361
- Sonn, H.W.; Kim, G.C.; Hong, C.S. & Yoon, B.I. (1996), Axisymmetric analysis of transient thermoelastic behaviors in composite brake disks, *Journal of Thermophysics and Heat Transfer*, Vol. 10, pp. 69-75
- Thoms, E. (1988), Disc brakes for heavy vehicles, *Inst. Mech. Eng., Int. Conf. on Disc Brakes for Commercial Vehicles*, C464/88, pp. 133-137
- Van Swaay, J.L. (1979), Thermal damage to railway wheels, *Inst. Mech. Eng., Int. Conf. on Railway Braking*, York, p. 95
- Wentenkamp, H.R. & Kipp, R.M. (1976), Hot spot heating by composite shoes, *J. Eng. Ind.*, pp. 453-458
- Yi, Y.; Barber, J.R. & Fash, J.W. (1999), Effect of geometry on thermoelastic instability in disk brakes and clutches, *ASME J. Tribology*, Vol. 121, pp. 661-666

- Yi, Y.; Barber, J.R. & Zagrodzki, P. (2000), Eigenvalue solution of thermoelastic instability problems using Fourier reduction, *Roy. Soc.*, Vol. A456, pp. 2799-2821
- Zagrodzki, P. (1990), Analysis of thermomechanical phenomena in multidisc clutches and brakes, *Wear*, Vol. 140, pp. 291-308
- Zagrodzki, P. (1991), Influence of design and material factors on thermal stresses in multiple disk wet clutches and brakes, SAE 911883

Dynamic Analysis of an Automobile Lower Suspension Arm Using Experiment and Numerical Technique

S. Abdullah¹, N.A. Kadhim¹, A.K. Ariffin¹ and M. Hosseini²

¹*Universiti Kebangsaan Malaysia*

²*Taylor's University College
Malaysia*

1. Introduction

All machines, vehicles and buildings are subjected to dynamic forces that cause vibration. Most practical noise and vibration problems are related to resonance phenomena where the operational forces excite one or more modes of vibration. Modes of vibration that lie within the frequency range of the operational dynamic forces always represent potential problems. Mode shapes are the dominant motion of a structure at each of its natural or resonant frequencies. Modes are an inherent property of a structure and do not depend on the forces acting on it. On the other hand, operational deflection shapes do show the effects of forces or loads, and may contain contributions due to several modes of vibration.

Modal analysis is an efficient tool for describing, understanding, and modelling structural dynamics (Sitton, 1997). The dynamic behaviour of a structure in a given frequency range can be modelled as a set of individual modes of vibration. The modal parameters that describe each mode are: natural frequency or resonance frequency, (modal) damping, and mode shape. The modal parameters of all the modes, within the frequency range of interest, represent a complete dynamic description of the structure. By using the modal parameters for the component, the model can subsequently be used to come up with possible solutions to individual problems (Agneni & Coppotelli, 2004).

Published studies have demonstrated the different purposes from performing modal analysis. Initially, Wamsler & Rose (2004) found the mode shapes and study the dynamic behavior of structure in automotive applications. Gibson (2003), presented a comparison of actual dynamic modal test data to the analytically predicted mode shapes and natural frequencies for a missile and its launcher structure that was created in MSC.Patran/MSC.Nastran. Then Guan et al. (2005) evaluated the modal parameters of a dynamic tire then carried out the dynamic responses of tire running over cleats with different speeds. In other study, Leclere et al. (2005) performed modal analysis on a finite element (FE) model of engine block and validated the experimental results. Hosseini et al. (2007) performed experimental modal analysis of crankshaft to validate the numerical results.

In particular, studies using a computational model to estimate component fatigue have been actively developed because of the low cost and time savings associated with the estimation (Yim & Lee, 1996; Lee et al., 2000; Kim et al., 2002; Jung et al., 2005). Recently, Choi et al.

(2007) used the damage index method to localize and estimate the severity of damage within a structure using a limited number of modal parameters for steel plate girder and other highway bridges. This article reports on experimental investigation on timber beams using experimental modal analysis to extract the required modal parameters. The results are then used to compute the damage index, and hence to detect the damage. By a studying the response of modal parameters, Damir (2007), investigated the capability of experimental modal analysis to characterize and quantify fatigue behaviour of materials. While, Jun et al. (2008) predicted the fatigue life at the design stage of the suspension system module for a truck and a flexible body dynamics analysis is used to evaluate the reliability of the suspension frame. Dynamic Stress Time History has been calculated using a flexible body dynamics analysis and the Modal Stress Recovery method through generating a FE model. Finally, Hosseini et al. (2009), utilized the frequency response analysis to obtain the transfer functions of a crankshaft. These transfer functions were used later to estimate the combustion forces of the engine.

In order to calculate the vibration fatigue damage from Power Spectral Density's (PSD's) of input loading and stress response, frequency response analysis was required. To perform this kind of analysis, an eigenvalue analysis was required to determine the frequencies to use as dynamic excitation. This can be accomplished automatically in a modal frequency or manually with a modal analysis. Once confidence was established in the frequency domain procedures, the global fatigue analysis could proceed. Numerical and experimental dynamic behaviour have been viewed as a result from FEA and test respectively. This was to identify the component resonance frequencies and to extract the damping ratios from experimental modal test which used in the numerical modal analysis for the FEA accuracy purposes. An experimental modal test is initiated and it has been compared with analytical simulation result for the purpose of validation. Initial static FEA has been performed as another kind of validation to get the model stress or strain distribution. Another purpose is to classify the suitable location for choosing the position of fixing the strain gauge in the experimental strain road data collection from the automobile lower suspension arm. The FEA and measured strain values have been compared. The FEA strain results showed acceptable agreement with the experimental strain road data collection.

2. Quasi-static stress analysis

The quasi-static analysis method is a linear elastic analysis that is associated with external load variations. The idea of this method is that each external load history acting on the component or structure is replaced by static unit load acting at the same location in the same direction as the history. A static stress analysis is then performed for each individual unit load. Dynamic stresses produced by each individual load history can be evaluated by multiplying that history by the static stress influence coefficients that result from the corresponding unit load. The principle of superposition is then used to calculate the total dynamic stress histories within the component. Eq. (1) represents the mathematical form of this method at a specific finite element node assuming plane stress considerations and linear elastic (Kuo & Kelkar, 1995).

$$\sigma_x(t) = \sum_{i=1}^n \sigma_{xi} P_i(t); \quad \sigma_y(t) = \sum_{i=1}^n \sigma_{yi} P_i(t); \quad \tau_{xy}(t) = \sum_{i=1}^n \tau_{xyi} P_i(t) \quad (1)$$

where n is the number of applied load histories and $\sigma_{xi}(t)$, $\sigma_{yi}(t)$, $\tau_{xyi}(t)$ are the stress influence coefficients. A stress influence coefficient is defined as the stress field due to a unit load applied to the component at the identical location and in the same direction as the load history, $P_i(t)$.

The quasi-static method has routinely been used in the vehicle industry to ascertain stresses and fatigue life (Sanders & Tesar, 1978). They showed that the quasi-static stress-strain evaluation is a valid form of approximation for most industrial mechanisms that are stiff and operate subsequently below their natural frequencies. However, this is not true when the dynamics of the structure have significant influence on the fatigue life of the component. An overall system design is formulated by considering the dynamic environment. The natural frequencies and mode shapes of a structure provide enough information to make design decisions.

The Lanczos method (Lanczos, 1950), overcomes the limitation and combines the best features of the other methods. It requires that the mass matrix be positive semi-definite and the stiffness be symmetric. It does not miss roots of characteristic equation, but has the efficiency of the tracking methods; due to it only makes the calculations necessary to find the roots. This method computes accurate eigenvalues and eigenvectors. This method is the preferred method for most medium-to large-sized problems, since it has a performance advantage over the other methods. The basic Lanczos recurrence is a transformation process to tridiagonal form. However, the Lanczos algorithm truncates the tridiagonalization process and provides approximations to the eigenpairs (eigenvalues and eigenvectors) of the original matrix. The block representation increases performance in general and reliability on problems with multiple roots. The matrices used in the Lanczos method are specially selected to allow the best possible formulation of the Lanczos iteration.

3. Modal frequency response analysis

The frequency response analysis is used to calculate the response of a structure about steady state oscillatory excitation. The oscillatory loading is sinusoidal in nature. In its simplest case, the load is defined as having amplitude at a specific frequency. The steady-state oscillatory response occurs at the same frequency as the loading. The response can have time shift due to damping in the system. This shift in response is called a phase shift due to the peak loading and peak response no longer occurs at the same time Phase Shift, which is shown in Fig. 1.

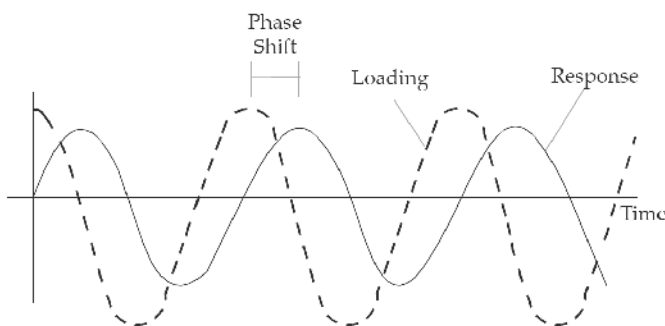


Fig. 1. Phase shift between loading and response amplitude

Modal frequency response analysis is an alternative approach to determining the frequency response of a structure. Modal frequency response analysis uses the mode shapes of the structure to reduce the size, uncouple the equation of motion (when modal or no damping is used), and make the numerical solution more efficient. Due to the mode shapes are typically computed as part of characterization of the structure, modal frequency response analysis is a natural extension of a normal mode analysis.

At the first step in the formulation, transform the variables from physical coordinates $\{u(\omega)\}$ to modal coordinates $\{\xi(\omega)\}$ by assuming

$$\{x\} = [\phi] \{\xi(\omega)\} e^{i\omega t} \quad (2)$$

The mode shapes $[\phi]$ are used to transform the problem in terms of the behaviour of the modes as opposed to the behaviour of the grid points. The Eq. (2) represents equality if all modes are used. However, due to all modes are rarely used, the equation usually represents an approximation.

Once, if all damping are ignored, the undamped equation for harmonic motion at forcing frequency ω is obtained in the form of the following equation:

$$-\omega^2 [M] \{x\} + [K] \{x\} = \{P(\omega)\} \quad (3)$$

Substituting the modal coordinate in Equation (2) for the physical coordinates in Eq. (3) and simplify, then the following is obtained:

$$-\omega^2 [M][\phi] \{\xi(\omega)\} + [K][\phi] \{\xi(\omega)\} = \{P(\omega)\} \quad (4)$$

The equation of motion using modal coordinates is finally obtained, but, the equation is still in the state of coupling. To uncouple the equation, pre-multiply both side of equation by $[\phi]^T$. Then, the new expression is presented in Eq. (5) as:

$$-\omega^2 [\phi]^T [M][\phi] \{\xi(\omega)\} + [\phi]^T [K][\phi] \{\xi(\omega)\} = [\phi]^T \{P(\omega)\} \quad (5)$$

where $[\phi]^T [M][\phi]$ is the generalized modal mass matrix, $[\phi]^T [K][\phi]$ is the generalized modal stiffness matrix, and $[\phi]^T \{P\}$ is the modal force vector.

The final step uses the orthogonal of the mode shapes to formulate the equation of motion in terms of the generalized mass and stiffness matrices, which are diagonal matrices. These diagonal matrices do not have the off-diagonal terms that couple the equation of motion. Therefore, in this form the modal equation of motion are uncoupled. In this uncoupled form, the equation of motion can be written as a set of uncoupled single degree-of-freedom systems as presented in Eq. (6), i.e.

$$-\omega^2 m_i \xi_i(\omega) + k_i \xi_i(\omega) = p_i(\omega) \quad (6)$$

where m_i is the i -th modal mass, k_i is the i -th modal stiffness, and p_i is the i -th modal force. If there is no damping has been included, the modal form of the frequency response equation of motion can be solved faster than the direct method, which it is due to an uncoupled single degree-of freedom system.

Vibration analysis (Crandell & Mark, 1973; Newland, 1993; Wirsching et al. 1995) is usually carried out to ensure that potentially catastrophic structural natural frequencies or resonance modes are not excited by the frequencies present in the applied load. Sometimes this is not possible and designers then have to estimate the maximum response at resonance caused by the loading.

4. Methodology

In order to achieve the objectives of the research, several steps in the flowchart, as presented in Fig. 2, should be implemented. In this flowchart, the three blocks; geometry, material, and loads and boundary conditions (loads and BCs) represent the input for the static and then modal frequency response finite element analysis, while only geometry and material represent the input for the numerical modal analysis. A comparison has been performed between the static analysis and road data strain results. If the strain result was almost the same in the critical area, then it can be considered as validation for the finite element analysis part. Then the model can be used in modal frequency response analysis. From another side, to identify the component resonance frequency and to extract damping ratios, which will be used later in the numerical modal analysis, experimental modal test has been performed. After that, another comparison has been performed between the experimental and numerical modal analysis, which can be considered as another validation for the finite element analysis part. The out put from the Modal frequency response analysis represents the most critical case result in a certain frequency which cause higher damage for the component if in reality it is work in this frequency. In a future work, this case result will be used as input for the fatigue analysis.

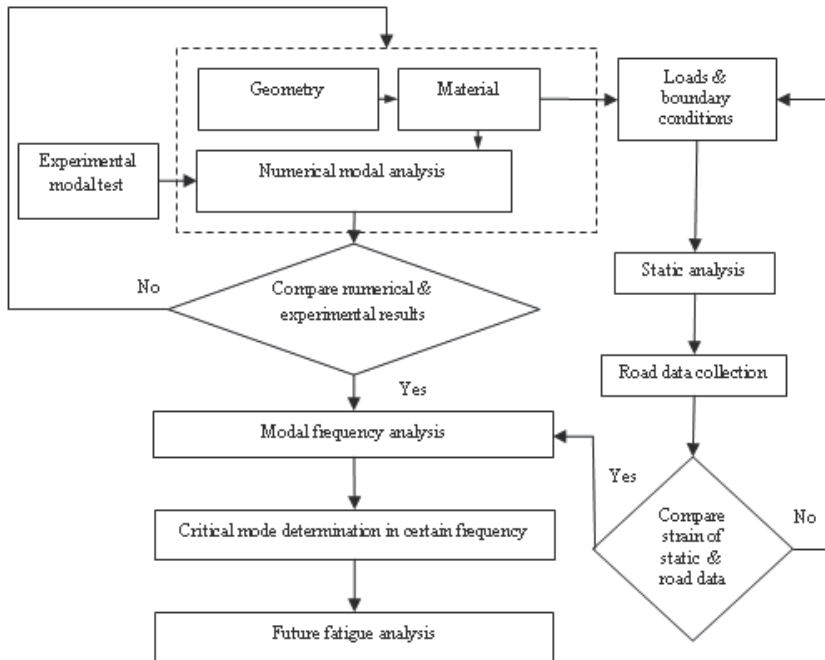


Fig. 2. Schematic diagram of research effort.

4.1 Geometry

A geometric model for an automobile lower suspension arm is considered in this study, and this component is presented in Fig. 3.



Fig. 3. A geometric model of an automobile lower suspension arm.

Three-dimensional lower suspension arm model geometry was drawn using the CATIA software, as shown in Fig. 4. The auto tetrahedral meshing approach is a highly automated technique for meshing solid regions of the geometry (MSC. Patran guide, 2002; Kadhim et al., 2010). It creates a mesh of tetrahedral elements for any closed solid including boundary representation solid. The tetrahedral meshing technique produces high quality meshing for boundary representation solids model imported from the most CAD systems. The specific mesh can give more accurate solution and the 10 nodes tetrahedral (TET10) element was used for the analysis with the adoption of a quadratic order interpolation function. A FE model of the lower suspension arm was implemented to find the modal parameters. According to 20 mm global edge element length, total of 25517 elements and 41031 nodes were generated for the model.



Fig. 4. An automobile lower suspension arm model.

4.2 Material

The purpose of analysing the chemical composition of a steel sample is to enable material classification. Based on Table 1, the steel sample can be classified as alloy steel since a carbon content range 0.27-0.33%, a manganese content range 1.4-2%, sulfur ≤ 0.04 , silicon range 0.15-0.35% and phosphorous $\leq 0.035\%$ (ASM specialty handbook, 1996). This represents the fabricated material for the 2000 cc Sedan lower suspension arm and was the material used in simulations. One sample was cut from the lower suspension arm using a cutter. The sample was subsequently ground with successive SiC papers (grit 200-1200) and then polished with polishing cloth and Alumina solution of grain size $6\mu\text{m}$, and finally $1\mu\text{m}$.

Element	C	Mn	Si	V	Cr	Ni	Pb	Fe
Measured value wt%	0.30	1.43	0.21	0.07	0.02	0.06	0.52	Balance

Table 1. Chemical composition of the steel

4.3 Normal modes analysis

Modal analysis is the process of determining modal parameters that are useful to understand the dynamic behaviour of the component. It may be accomplished either through analytical or experimental techniques (Hosseini et al., 2007), which are presented in the following parts.

4.3.1 Experimental

A schematic diagram of performing the experimental modal test is presented in Fig. 5. Measurements and recording of excitation and response signals were carried out over an automobile lower suspension arm.

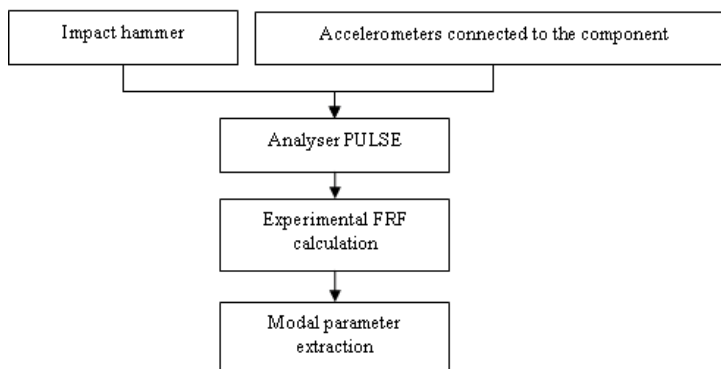


Fig. 5. Schematic diagram of experimental modal test

The component was impacted with a hammer along the x-axis as shown in Fig. 6, then another two measurements in y and z-axis separately. It was a SIMO system and the system response model can be written as follows:

$$\begin{bmatrix} y_1 \\ \cdot \\ \cdot \\ \cdot \\ y_n \end{bmatrix}_{n \times 1} = \begin{bmatrix} H_1 \\ \cdot \\ \cdot \\ \cdot \\ H_n \end{bmatrix}_{n \times 1} [F]_{1 \times 1} \quad (7)$$

where n is the number of response channels along the object. Bruel & Kjaer portable and multi-channel analyzer PULSE type 3560D with ENDEVCO Isotron accelerometers type 751-100 and impact hammer type 2302-10 were utilized in the measurement devices. The Bruel & Kjaer Pulse LabShop was the measurements software and the B & K calibration exciter



Fig. 6. The set up of data acquisition Portable Analyser Pulse to be used for normal mode analysis test

type 4294 was used to calibrate the accelerometer. In order to approximate free condition, lower suspension arm was placed on a soft Styrofoam. The uni-axial accelerometer was attached first alongside x direction then y and z -direction. In the single input experiment, the lower suspension arm was impacted with one hammer along the x , y , then z -axis separately. It was single input-multiple output system.

Three equipment functions should be considered in the process of experimental modal testing (Cantley, 2003): Excitation method, response measurement method, Data acquisition, and analysis software.

Modal damping was measured automatically by the analyzer PULSE at each resonance through identifying the half power (-3 db) points of the magnitude of the frequency response function. For a particular mode, damping ratio ζ_r is calculated by

$$\zeta_r = \frac{\Delta f}{2f_r} \quad (8)$$

where Δf is the frequency band width between the two half power points and f_r is the resonance frequency. PULSE type 3560 contains a built-in standard cursor reading, which calculates the modal damping. The accuracy of this method is dependent on the frequency resolution (1 Hz for this measurement) used for the measurement because this determines how accurately on the computer screen the peak magnitude can be measured.

The weight of the accelerometer was 7.8 g. The weight of the lower suspension arm was 2.4 kg, which was made of SAE1045 steel, and despite the size, it was much heavier than the accelerometer. The total weight of the accelerometers was 0.3% of the lower suspension arm and had negligible effects on the measurement.

4.3.2 Analytical

In numerical method, a FE model of the component was created by MSc.Patran and sent to MSc.Nastran for analysis. The output transferred back to MSc.Patran for visualization of the results. Damping was measured during the experimental part and updated into the numerical analysis. These values only have meaning around resonance frequencies; mass and stiffness components neutralized each other and damping could be calculated. Lumped mass characteristic was used for modelling the structure to save memory and time needed for analysis. The Lanczos method was utilized to extract eigenvalues for all the modes of such a medium model in the frequency span of 5 kHz. It substantially increases computational speed and reduces disk space. The main advantages of finite element models are: 4 models used for design development and no prototypes are necessary, while the disadvantages are: modelling assumptions, joint design difficult to model, component interactions are difficult to predict and damping generally ignored.

4.4 Loads and boundary conditions

Three main parts in the lower suspension arm has been considered in the FE boundary conditions, i.e. ball joint, bushing_1 and bushing_2. Fig. 7 shows the FE model with related boundary conditions applied at specific location.

In the analysis, a distributed load has been applied on the inner surface of bushing_1. Bushing_2 considers as a rigid section with a rotation around x -axis from the side of the vehicle body. In the same time, the rigid condition has been considered on the ball joint with

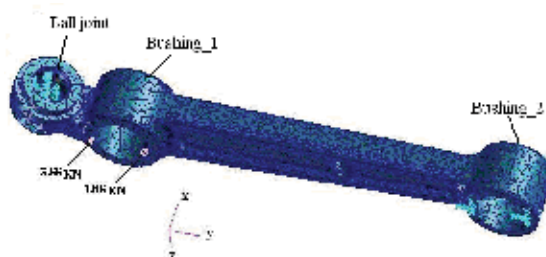


Fig. 7. Finite element model of the lower suspension arm

translations in x and y direction while the rotation around x , y , and z -axis is used to represent the braking and cornering loads. There are no acceleration loads as inputs for the analysis, due to collecting data during driving of the car at constant speed.

4.5 Static analysis

An initial static FEA has been performed to obtain the strain distribution along the lower suspension arm, in order to classify the critical areas for choosing the position of fixing the strain gauges during the strain data collection, which explained in next section. After that, the measured values of strain were used later for validation purposes of the applied load values and boundary conditions in the static and frequency FEA through the measured strain values and experimental identification for the higher stress or strain area of the component as damage criteria.

4.6 Road data collection

A distribution load has been applied on the inner surface of bushing_1 with a value of 3.88 kN with a slope of 60° as a result for load calculation which effected on the lower arm due to vehicle and passengers weight. To ensure the reliability and for validation purposes, a load history was obtained from the real automotive lower suspension arm of this study, which was driven over a country road. The frequency sample, f_s , for this case was 500 Hz. This f_s value was chosen in order to improve the accuracy of the data (Stephens et al., 1997; Oh, 2001). The data was measured using a data acquisition system at an automobile speed of 25 km/h, and recorded as strain time histories. The data acquisition set-up is shown in Fig. 8.



Fig. 8. The set up of data acquisition used for data collection

The strain gauge could not be physically fixed at the most critical point due to its design. Four strain gauges were fixed at different locations, as shown in Fig. 9. After collecting the data for four strain gauges for the country road type at different locations (Fig. 10) and for the confirmation purposes of the current FEA reliability, the damage was determined for all the collected load histories (Table 2) by using a software as explained in the schematic diagram in Fig. 11.

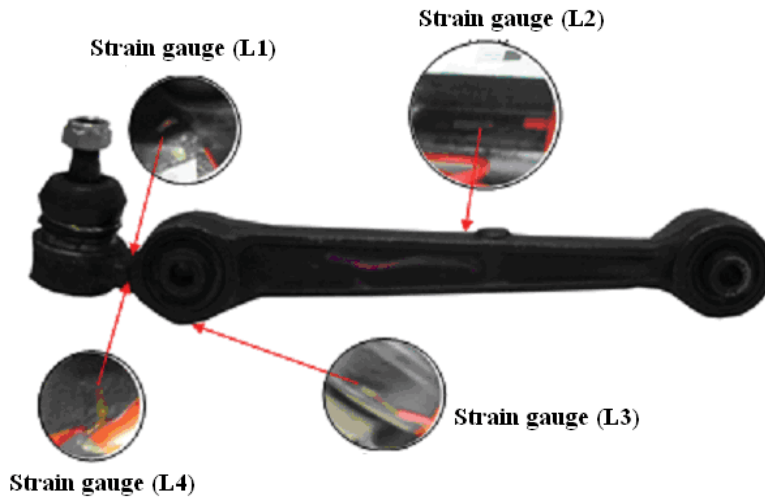


Fig. 9. The strain gauge positions on the lower suspension arm

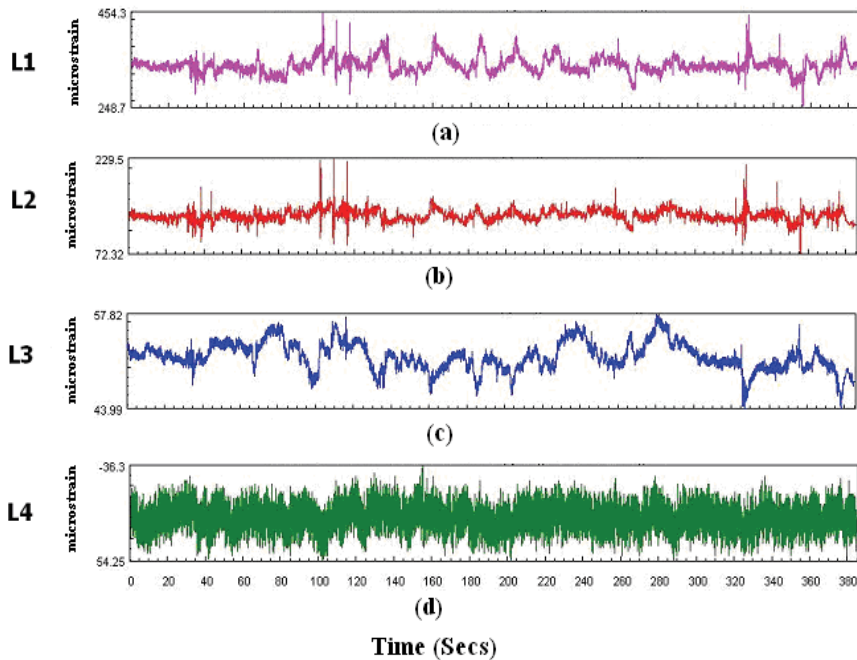


Fig. 10. Strain time history plot for different strain gauge positions: (a) L1, (b) L2, (c) L3, (d) L4

Strain gauge signal	Damage
L1	0.734
L2	0.0888
L3	0.0033
L4	4.8E-6

Table 2. The fatigue damage values for different strain loadings

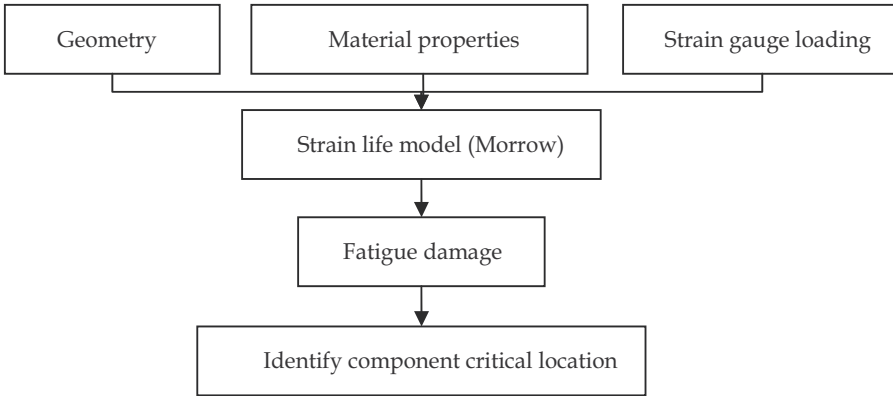


Fig. 11. Schematic diagram of calculating fatigue damage values for the collected loadings

The life has been calculated using Morrow strain life model. Based on the model developed by Morrow (1968), the relationship of the total strain amplitude (ϵ_a) and the fatigue life in reversals to failure ($2N_f$) can be expressed as

$$\epsilon_a = \frac{\sigma'_f}{E} \left(1 - \frac{\sigma_m}{\sigma'_f} \right) (2N_f)^b + \epsilon'_f (2N_f)^c \tag{9}$$

where E is the material modulus of elasticity, ϵ_a is the true strain amplitude, $2N_f$ is the number of reversals to failure, σ'_f is the fatigue strength coefficient, b is the fatigue strength exponent, ϵ'_f is the fatigue ductility coefficient and c is the fatigue ductility exponent, σ_m is the mean stress.

The damage fraction, D, is defined as the fraction of life used up by an event or a series of events. Awareness of these individual cycles' lives, however, still does not immediately indicate the predicted life and reliability for an actual variable amplitude history. To obtain the life of a whole loading history block, a damage summation model will attempt to combine the individual life found for each defined cycle into the predicted reliability for the whole history. With respect to the relationship between damage and cycle, the damage for one cycle, D_i , can be calculated as

$$D_i = 1 / N_{fi} \tag{10}$$

where N_{fi} is the number of constant amplitude cycles to failure. To calculate the fatigue damage for a block of VA loading, a linear cumulative damage approach has been defined by Palmgren (1924) and Miner (1945). The technique, known as the Palmgren-Miner (PM) linear damage rule, is defined as

$$D = \sum_{i=1}^n \frac{N_i}{N_{fi}} = 1 \quad (11)$$

where n is the number of loading blocks, N_i is the number of applied cycles and N_{fi} is the number of constant amplitude cycles to failure. The failure will occur when the summation of individual damage values caused by each cycle reaches a value of one. After the fatigue damage for a representative segment or block of load history has been determined, the fatigue life for each block is calculated by taking the reciprocal.

4.7 Modal frequency response analysis

Frequency based FEA can be a powerful qualitative as well as quantitative tool for reliability assessment of certain components. One of the main capabilities for the fatigue analysis of dynamic system is a vibration fatigue analysis, which requires input PSDs, and cross PSDs, and the structure transfer functions computed by FE model. Once these transfer functions are available, any number of duty cycles can be accommodated with some computational effort. The frequency response analyses were performed using the procedure explained in Fig. 2. The 3.88 KN load applied with arrange of frequency between 500 Hz and 5000 Hz which can give changing in load value during the analysis. Frequency response analysis with damping was implemented. The extracted damping ratio from experimental modal test had been used in modal frequency response analysis. It is the ratio of the actual damping in the system to the critical damping. Most of the experimental modal reported that the modal damping in terms of non-dimensional critical damping ratio expressed as a percentage (Formenti, 1999; Gade et al., 2002). In fact, most structures have critical damping values in the range of 0 to 10%. Zero damping ratio indicates that the mode is undamped. Damping ratio of one represents the critically damped mode.

5. Results and discussions

The modal analysis is usually used to determine the natural frequency, damping and mode shape parameters of a component. The dynamic characteristics such as natural frequency and mode shape can be obtained experimentally and predicted analytically while the damping ratio can be measured only experimentally. It can be used as the starting point for the frequency response, the transient and random vibration analyses. The extracted number of modes was useful to understand the dynamic behaviour of the component such as the natural frequency span and the extracted damping ratio from the experimental which used in the numerical analysis. The frequency response analysis (FRF) output can be considered as the most important input for the future vibration fatigue analysis.

A sampling rate of 5000 Hz was used in order to capture the whole vibration characteristics (Aykan & Celik, 2009). Based on the obtained data from the modal analysis simulation (Table 3), frequency up to 5000 Hz, can give six modes starting from 1172 and end in 4578 Hz. This is true since the modes or resonances are inherent properties of the structure (Bujang et al., 2008). In theory, resonance is determined by the material properties and the boundary conditions of the component (Alfano et al., 2008). Therefore, if the material properties of the component change, the modes will change. The mode shape results with their frequencies for the first three modes of an automobile lower suspension arm are shown in Fig. 12 as the mode shape deflection pattern is clearly shown. These results can be useful for designers to understand the dynamic characteristics of the component in order to take a decision to build their design depending on the mode number, which can provide higher

stress to represents the most critical mode. According to the boundary conditions and material properties, the deflection of the component can be noticed in the y-z plane. Mode 1 is bending in y-z, mode 2 is twisting in y-z, and mode 3 is sine shape in y-z.

Mode no.	Natural Frequency (Hz)
1	1172
2	1560
3	2809
4	3159
5	4175
6	4578

Table 3. The natural frequency results obtained from modal analysis

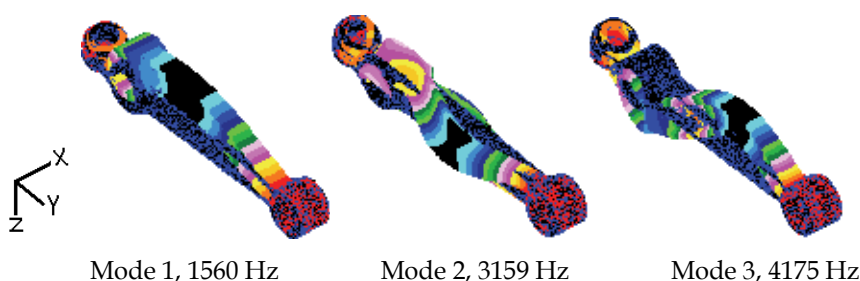


Fig. 12. Simulated modal frequencies and mode shapes from FEA

The frequency response analysis was performed experimentally and analytically using the particular FEA code. It used the damping ratio that extracted from the experimental modal test. The output result file for this type of analysis represented by the stress values for the most damaging mode were used as one of the main input for vibration fatigue analysis. Four natural frequencies were detected from the modal test in 537, 1738, 3394, and 4360 Hz as shown in Fig.13.

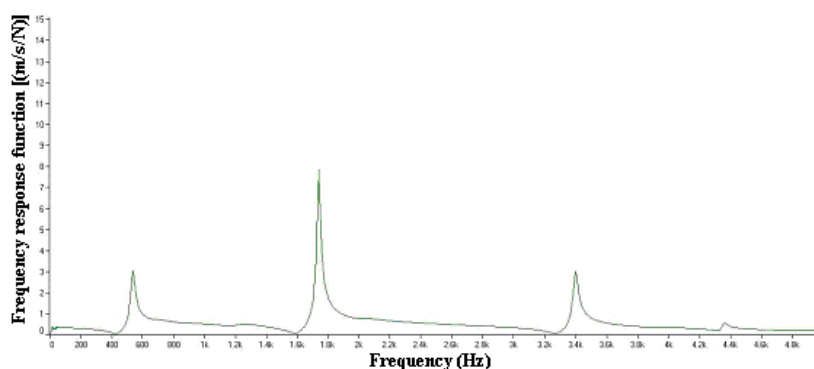


Fig. 13. Automobile lower suspension arm FRF plotted against frequency (0-5000 Hz)

The experimental results represented by the natural frequency with its damping ratio are shown in Table 4. The damping ratio is the ratio of the actual damping in the system to the critical damping. In fact, most structures have critical damping values in the range of 0 to

10%, with values of 1 to 5% as the typical range (Dynamic analysis user's manual, 2005). A zero damping ratio indicates the mode is undamped.

No.	Experimental Natural Frequency (Hz)	Experimental damping ratio (%)
1	537	2.19
2	1738	0.89
3	3394	0.47
4	4360	0.9

Table 4. The experimental natural frequency and damping ratio

The extracted damping ratio from the experimental modal test has been feed back to the numerical modal analysis to increase the analysis accuracy. There are some differences in the resonance or natural frequency between the numerical and the experimental. This is due to consider the standard material properties for the SAE 1330H steel in the modal analysis, which did not represent the lower suspension arm fabricated SAE 1330H steel properties. The material properties of the fabricated lower suspension arm are different from the standard (ASM Specialty Handbook, 1996). This is due to the elements addition by the manufactured company to improve the component performance. Only one kind of experiment has been performed to specify one of the fabricated material properties represented by the density measurement, which has the value of 7.75 g/cm³. The density has been measured using Electronic Densitometer (MD-200S) and used as input for the FEA. The first and third experiment natural frequencies (Fig.13) could not be detected by FEA while second and fourth were detected. The first natural frequency from the FEA represents the most important stress result due to consider it as the most critical frequency in the experimental and analytical work and its FEA stress results was used later in vibration fatiue analysis. These differences were due to manipulation error as a possible source of error (Robert et al., 2002) which is introduced as equations are processed; for example, results of multiplication are truncated or rounded. Manipulation error may be minor if global equations $[k]\{D\}=\{R\}$ are solved once, as in time-independent analysis. In some dynamic and nonlinear problems, where each step builds on the step before and a calculation sequence must be executed repeatedly, manipulation error may accumulate. Another source may be due to not using the exact material properties as mentioned before. The result of the frequency response analysis with zero Hz is presented in Fig.14 for AISI 1330H_steel. It can be noticed that the maximum principal stress is 271 MPa at zero Hz. The variation of the maximum principal stresses with the frequency range 0-5000 Hz is shown in Fig.15. It is observed that the maximum principal stress occurs at a frequency of 1560 Hz for the first mode with value of 865 MPa. This value of stress is for the most critical case in the frequency response analysis and it is also shown as contour graph in Fig.16. This value is less than the tensile yield stress value of 1034 MPa for the AISI 1330H steel. It also can be noticed that the maximum principal stresses varies with the frequencies. This variation is due to the dynamic influences of the first mode shape.

From the results and analysis obtained in this research, it is noticed that modal and frequency response analysis is an efficient tools to understand the dynamic behaviour of the component. This type of analysis can provide information about the modal parameters and

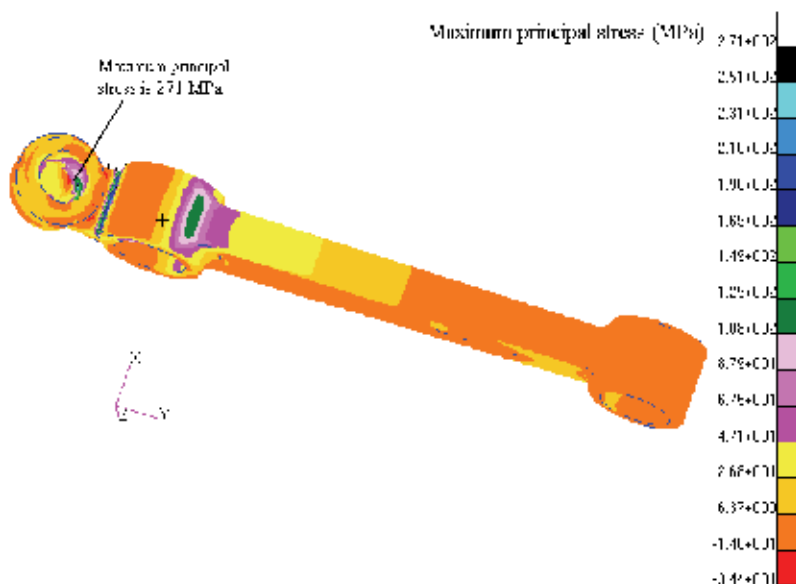


Fig. 14. The Maximum principal stress distribution for the frequency response analysis with zero Hz for AISI 1330H_steel

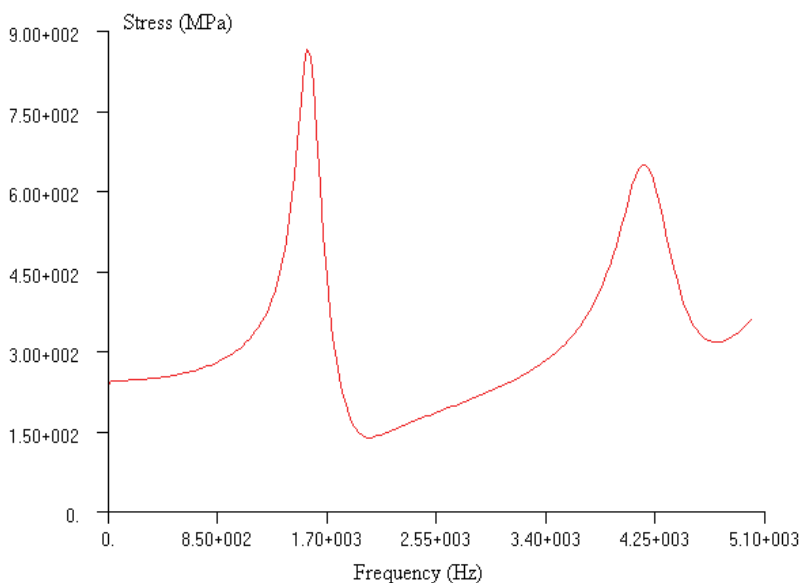


Fig. 15. Automobile lower suspension arm stress plotted against frequency (0-5000 Hz)

the stress distribution to be used to predict fatigue life in vibration analysis. For further validation purposes, static analysis has been performed and its result has been compared with the road strain data. Finally, it is suggested to perform the vibration fatigue analysis depending on the frequency response analysis result in automotive durability research for the purpose of component life estimation under random loading.

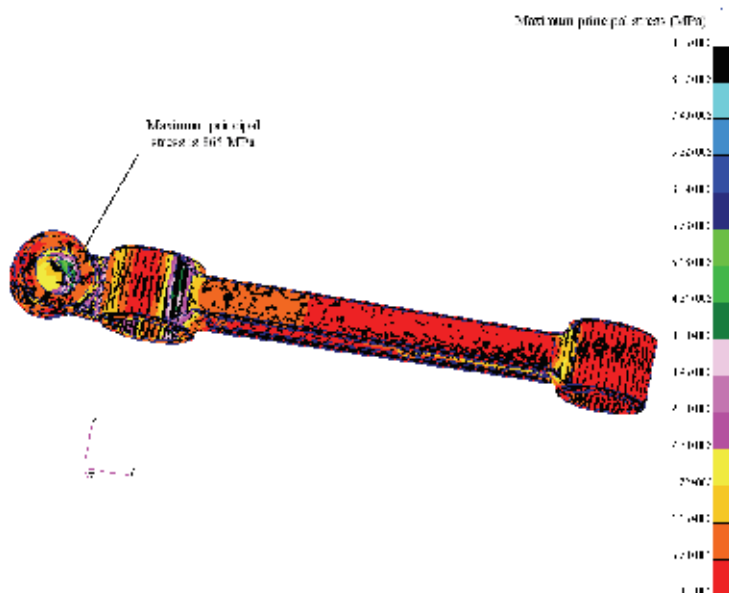


Fig. 16. The maximum principal stress contour for the frequency response analysis at 1560 Hz

6. Conclusion

The research was carried out to investigate the dynamic characteristic of the automotive lower suspension arm, experimentally and numerically. FEA part as a numerical technique has been validated. Another validation has been performed through a comparison of the static FEA predicted strain data and experimentally collected road strain data. One of the most important parts of a vibration fatigue analysis is the calculation of transfer functions. With NASTRAN this is called a frequency response analysis, so this kind of analysis has been performed for future vibration fatigue analysis.

One of the results expected to show higher stress effects on the component in a certain frequency. In another words, it was to extract the FRF of the component in most critical vibration mode in order to use it as a specific resonance in vibration fatigue analysis, which can be examined, then solved for the purpose of component life estimation. The mode 1 of 1172 Hz has been found as the most critical mode. Both of the maximum principal strain contours plots are identical for static and frequency response analysis at zero Hz. This result is a proof that strain distribution of the lower suspension arm has been reliably predicted using the finite element model. This study has highlighted the need for experimental work to validate FEA modelling and to allow its advantages be maximised. Work is currently under progress to exploit this research results to investigate the lower suspension arm vibration fatigue life and to perform optimization studies to assess how to overcome various dynamic problems.

7. Acknowledgment

The authors would like to express their gratitude to University Kebangsaan Malaysia and Ministry of Science, Technology and Innovation, through the fund of 03-01-02-SF0052, for supporting these research activities.

8. References

- Agneni, A. & Coppotelli, G. (2004). Modal parameter prediction for structures with resistive loaded piezoelectric devices. *Experimental Mechanics*, Vol. 44, No.1, 2004, pp. 97-100, ISSN. 10.1007/BF02427983.
- Alfano, M., Pagnotta, L., Stigliano, G. (2008). Elastic properties of cold rolled aluminium plates with irregular shape by dynamic testing. *International conference on engineering optimization*, pp. 01 - 05, Rio de Janeiro, June 2008, Brazil
- ASM Specialty Handbook. (1996). *Carbon and Alloy Steels*, edited by J. R. Davis & Associates, ASM International, Metals Park, OH, Metals Handbook, Vol. 1 - properties and Selection: irons, Steels, and High-Performance Alloys, ASM International 10th Ed.1990)
- Aykan, M.& Celik, M. (2009). Vibration fatigue analysis and multi-axial effect in testing of aerospace structures. *Mechanical Systems and Signal Processing*, Vol. 23, pp. 897-907, 0888-3270
- Bujang, I. Z., Kamaruddin, K. A. & Nordin, M. T. (2008). Identification of Structural Defects Using Modal Technology. *International conference on constucyion and building technology*. Malaysia
- Cantley, C. (2003). Modal testing facility for advanced LIGO, University of Glasgow, *Advanced LIGO SUS Workshop*, LIGO-G030534-00-K
- Choi, F. C.; Li J. & Samali B. (2007). Application of modal-based damage-detection method to locate and evaluate damage in timber beams, *J. Wood Science* 53(5) 394-400.
- Crandell, S.H. & Mark W.D. (1973). *Random vibration in mechanical systems*, Academic Press, 0121967506, New York
- Damir, A.N.; Elkhatib A. & Nassef G. (2007). Prediction of fatigue life using modal analysis for grey and ductile cast iron, *International J. Fatigue*, Vol. 29, pp. 499-507, 0142-1123
- Formenti, D. (1999). The relationship between % of critical and actual damping in a structure, *J. Sound & Vibrations*, Vol. 33, No. 4, pp. 14-18, 0022-460X
- Gade, S; Herlufsen, H. & Konstantin-Hansen H. (2002). How to determine the modal parameters of simple structures. *J. Sound & Vibrations*, Vol. 36, No. 1, pp. 72-73, 0022-460X
- Gibson, M.E. (2003). Correlation of modal results from a MSC.Patran/MSC.Nastran finite element model to modal test, Presented at the *Virtual Product Development Conference*, pp. 1-22, Dearborn, April 2003, Michigan.
- Guan, D.; Fan C. & Xie X. (2005). A dynamic tyre model of vertical performance rolling over cleats, *J. Vehicle System Dynamics*, Vol. 43, No. 1, 2005, pp. 209-222, 10.1080/00423110500109398
- Hosseini, M.; Mohd M.; Ariffin A. & Abdullah S. (2009). Inverse combustion force estimation based on response measurements outside the combustion chamber and signal processing, *Mech. System and Signal Processing*, Vol. 23, pp. 2519-2537
- Hosseini, M.; Mohd, M.; Ariffin, A. & Abdullah, S. (2007). Mobility analysis of vehicle crankshaft, in Proc. *Conference on Advances in Noise, Vibration and Comfort*, pp. 167-175, Selangor, Malaysia, November 2007, Putrajaya.
- Jun, K. J., Park T.W., Lee S. H., Jung S.P. & Yoon J.W. (2008). Prediction of fatigue life and estimation of its reliability on the parts of an air suspension system, *International J. Automotive Technology*, Vol. 9, No. 6, pp. 741-747, 1976-3832
- Jung, H.; Park, T. W.; Seo, J. H.; Jun, K. J.; Yim, H. J.; Kim, H. & Park, J. K. (2005). A study on the fatigue life prediction of OHT vehicle structures using the modal stress recovery method. *Proc. IDETC/CIE, DETC 2005-84319*.

- Kadhim, N.A.; Abdullah, S.; Ariffin, A.K. & Beden, S.M. (2010). Fatigue behaviour of automotive lower suspension arm, 8th International conference on fracture and strength of solids (FEOFS 2010), pp. 1-6, Istana hotel, June 2010, Kuala Lumpur
- Kim, H.S.; Yim, H.J. & Kim, C.M. (2002). Computational durability prediction of body structure in prototypes vehicles. *International J. Automotive Technology*, Vol. 3, No. 4, pp 129-136, 1976-3832
- Kuo, E.Y. & Kelkar S.G. (1995). Body structure durability analysis, *Automotive Eng.* Vol. 103, No. 7, pp. 73-77, 0098-2571
- Lanczos, C. (1950). An iteration method for the solution of the eigenvalue problem of linear differential and integral operators, *J. Research of the National Bureau of Standards* Vol. 45, No. 4, pp. 255-282, 0091-0635, OCLC: 4723507
- Leclere, Q.; Pezerat C.; Laulagnet B. & Polac L. (2005). Indirect measurement of main bearing loads in an operating diesel engine. *J. Sound and Vibration*, Vol. 286, No. 1-2, August 2005, pp. 341-361, 0022-460X
- Lee, S. B.; Park, T. W. & Yim, H. J. (2000). A study on computational method for fatigue life prediction of vehicle structure, *J. KSNVE*, Vol. 10, No. 4, pp. 686-691, 0963-8695
- Miner, M. A. (1945). Cumulative damage in fatigue, *J. Appl. Mech.*, Vol. 67, pp. A159-A164, 0021-8936
- Morrow, J. (1968). *Fatigue Design Handbook*, Advances in Eng., Society of Automotive Engineers, Warrendale, Pa., Vol. 4, pp. 3-36, 978-1-56091-917-9
- MSC. NASTRAN. (2005). *MSC. NASTRAN dynamic analysis user's manual*. Los Angeles, USA: MSC Software Corporation
- MSC. Patran users guide* (2002). Vol.1. Los Angeles, MSC. Software Corporation. USA
- Newland, D.E. (1993). *An introduction to random vibrations, spectral and wavelet analysis*, (Essex, Longman Scientific and Technical)
- Oh, C.S. (2001). Application of wavelet transform in fatigue history editing, *International J. Fatigue*, Vol. 23, No. 3, pp. 241-250, 0142-1123
- Palmgren. (1924). Die Lebensdauer von Kugellagern, *Verfahrenstechnik*, Berlin, Vol. 68, pp. 339-341
- Robert, D.; David S.; Michael E. & Robert J. (2002). *Concepts and applications of finite element analysis*. USA, John Wiley and Sons
- Sanders, J.R. & D. (1978). Tesar, The analytical and experimental evaluation of vibration oscillations in realistically proportioned mechanisms. *ASME Paper* No. 78-DE-1
- Sitton, G. (1997). *MSC/NASTRAN Basic dynamic analysis-user's guide*, Vol. 1, The MacNeal-Schwendler Corporation, USA.
- Stephens, R.I.; Dindinger P.M. & Gungler J.E. (1997). Fatigue damage editing for accelerated durability testing using strain range and SWT parameter criteria, *International J. Fatigue*, Vol. 19, No. 8-9, pp. 599-606, 0142-1123
- Wamsler, M. & Rose, T. (1998). Advanced mode shape identification method for automotive application via modal kinetic energy plots assisted by numerous printed outputs. Presented at the *MSC Americas Users' Conference*, pp. 1-17, Sheraton Universal Hotel, Universal City, October 1998, California.
- Wirsching, P.H.; Paez, T.L. & Oritz, K. (1995). *Random vibration: theory and practice*, John Wiley and Sons, Inc., 0-471-58579-3, New York
- Yim, H.J. & Lee, S.B. (1996). An integrated CAE system for dynamic stress and fatigue life prediction of mechanical systems, *KSME International J.*, Vol. 10, No. 2, pp. 158-168, 1226-4865

Increased Cooling Power with Nucleate Boiling Flow in Automotive Engine Applications

Helfried Steiner¹, Günter Brenn¹,
Franz Ramstorfer² and Bernd Breitschädel²

¹*Graz University of Technology*

²*Competence Center "The Virtual Vehicle" (vif) Graz
Austria*

1. Introduction

In modern automotive design, the increasing output of power delivered by ever more compact, i.e., less space consuming, engines requires a highly efficient liquid cooling system to keep the wall temperatures of the individual components on acceptable levels. A maximum possible cooling power is particularly needed on surfaces exposed to high thermal loads typically located in the periphery of the exhaust gas outlets in the cylinder head. Searching for a most intense transfer of heat across very confined surface areas, the modern layout of liquid cooling systems must make ever more use of the potential of the nucleate boiling regime to provide significantly enhanced heat transfer rates at acceptable wall superheats. It has been long known in the community of engine developers that nucleate boiling locally occurs in cooling jackets near the exhaust valves, especially when the engine is run under thermally critical operating conditions. These are typically reached when the vehicle is brought to a halt after operation at maximum engine load, so that a considerable amount of heat has to be removed with the help of the fan cooling on the air side only. Nonetheless, the traditional design concepts are essentially based on purely convective single-phase cooling, although under real maximum load conditions the peak temperatures would markedly exceed the allowed limits, if boiling did not occur. In view of this fact it appears very reasonable to make a more deliberate use of the boiling phenomenon for further optimization of the cooling system. The prominent goal of this novel concept is to provide a controlled transition from single-phase convection to the so called subcooled boiling flow regime, as soon as the local heat loads reach a certain level. The targeted regime of subcooled boiling flow offers the attractive feature that vapour is present only in a thin superheated near-wall layer, while the outer bulk flow region, where the bubbles collapse due to the subcooling, contains only liquid phase. Hence, there is basically no net production of vapour, and the cooling system practically remains in the single-phase regime. Going otherwise further beyond into the saturated boiling regime, associated with non-zero net production of vapour, the advection of a significant amount of vapour with the bulk flow, or a possible agglomeration of vapour in stagnant regions could be hazardous to a safe and stable operation of the liquid cooling system.

Relying on the incipience of nucleate boiling in the thermal layout requires appropriate wall heat flux models which cover the range from single-phase convection to the two-phase

boiling flow with acceptable accuracy. A realistic, physically sound model description of nucleate boiling flow is still challenged by very fundamental difficulties, as this highly complex phenomenon involves many sub-processes which are not fully understood yet. In particular, considering flow boiling on real life technical surfaces, it is basically impossible to describe mathematically the sub-process of bubble nucleation in a deterministic way. The complexity of the underlying contact physics between the gaseous, liquid and solid phases has thus far impeded any generally applicable parameterization of this sub-process. Hence, today's available model correlations bear a good deal of uncertainty due to a basically incomplete parameterization of the problem. As a result, the existing model approaches involve many tuning coefficients, which have to be appropriately adjusted from case to case. A survey of the basic model concepts proposed for subcooled boiling flow will be presented in this chapter.

To a great extent, the development of enhanced heat transfer concepts based on flow boiling was strongly driven by the need of compact high efficiency heat exchangers for use in spacecraft devices as well as in the field of chip cooling. Concerning the former application, much research work was focused on the effect of gravity, as buoyancy forces play an important role in the dynamics of the bubbles (Klausner et al., 2003; Kim et al., 2005; Bower & Klausner, 2006). The latter application has been mostly investigated in the context of "boiling in microchannels" (Kew & Cornwell 1997; Kandlikar, 2002; Thome, 2004; Cheng et al., 2007). This distinction has been made due to the small dimensions of the electronic devices, and the occurrence of the confined boiling regime, where the bubble diameters are of the size as the channel height, leading in general to higher heat transfer rates in comparison to the unconfined case.

Concerning the automotive engine application, several studies have been carried out investigating the convective boiling of typical engine coolants (Campbell et al., 1995; Kandlikar, 1998a; Kobor, 2003). Besides demonstrating the possible gain in cooling power, these investigations were strongly focused on the development, evaluation and further improvement of model correlations for the highly complex flow boiling heat transfer. In comparison to single-phase forced convection, the nucleate boiling heat transfer depends on many more parameters, which are often hard to determine, or whose relevance is not clear. Facing this fundamental difficulty, a safe and reliable thermal layout requires a most comprehensive knowledge on how specific operating conditions and system parameters typically found in engine cooling jackets can affect the subcooled boiling heat transfer. In particular, the actual state of the heated surface, be it characterized by a micro-scale surface topology, roughness or contamination, or by a macroscopic property like the orientation of the surface relative to the gravitational force, may have a significant influence on the boiling behaviour. Since automotive coolants are always multi-component mixtures, the effect of the composition of the working liquid has to be considered as well. Operating modes and operation time may also be important for the number of available active bubble nucleation sites (mostly surface imperfections like cavities or fissures). A selection of all these automotive engine relevant conditions and their potential relevance for the heat flux modelling shall be addressed and discussed in this chapter.

During the last decade, considerable boiling research was devoted to the development and investigation of so-called enhanced surfaces. Applying special, mostly porous, surface coatings can notably reduce the wall superheat required for the onset of nucleate boiling, and, beyond this point, it may intensify the process of bubble nucleation resulting in markedly enhanced boiling heat transfer rates. The prospective additional gain in total wall

heat flux makes this concept certainly attractive for a future application in automotive cooling as well. Some recent investigations on this specific approach will be addressed in this chapter as well.

2. Fundamental aspects of boiling flow heat transfer

Boiling flow represents one of the most challenging two-phase flow problems which to date could not be rigorously described based on physical principles. It involves many sub-processes associated with the nucleation, growth, detachment, coalescence, and collapse of vapour bubbles. These individual sub-processes can act on very different scales in time and space, and many of them are inaccessible to detailed experiments. Some basic mechanisms contributing to the total heat transfer can be still distinguished, which, despite their often unknown quantitative relevance, constitute at least a reasonable qualitative description of the whole phenomenon.

2.1 Basic mechanisms

The heat flux of boiling flow depends on numerous thermo-physical interactions between the liquid, the vapour phase, and the solid heater, as schematically shown in Fig. 1. The interaction between the liquid bulk flow and the non-boiling part of the heated surface, denoted by 1, represents basically the convective single-phase heat transfer, generally termed macroconvection. The interaction between the bulk flow and the vapor bubbles, denoted by 2, comprises the hydrodynamic forces of the flow acting on the bubbles and vice versa. These flow induced forces can strongly influence the bubble growth, the bubble detachment from the nucleation sites, as well as the paths of the rising bubbles. Moreover, a densely populated heated surface may change the near-wall flow conditions significantly. The bubble-liquid phase interaction, denoted by 3, is often subsumed as the so-called microconvection. It includes the entrainment of liquid into the wake of a rising bubble immediately after detachment, which mixes portions of cool liquid from the - mostly subcooled - outer flow region into the superheated wall layer. This bubble lift-off induced transport of cool bulk liquid towards the heated surface increases instantaneously the local convective heat transfer. At the same time, it cools down the area around the nucleation sites below the critical temperature for nucleation. This cooling down of the nucleation sites immediately after bubble lift-off is generally termed "surface quenching". A quenched nucleation site needs some time to be re-heated beyond a critical temperature, where bubble nucleation is initiated again. The required heat is supplied by the solid heater via conductive heat transfer, denoted by 4.

Aside from the hydrodynamical effect of the bubble motion on the liquid, the bubble-liquid interaction also includes the thermal effect of condensation at the vapour-liquid interface. This process occurs at the top of the bubbles, once the interface reaches a zone where the local temperature is below the saturation level. The evaporative counterpart of this mechanism of latent heat transport is realized by the interaction between the bubble foot and the heated surface, denoted by 5. While the bubble is growing on its nucleation site, the latent heat needed for evaporation is continuously removed from the solid heater material, which causes a local drop of the temperature on the heated surface. The local cooling due to the removal of heat of evaporation during bubble growth, as well as the local cooling associated with the surface quenching after bubble detachment, are the main reasons why the surface temperature is highly non-uniform in time and space. This non-uniformity of the

surface temperature also leads to considerable thermal interactions (conductive heat exchange) between the individual nucleation sites inside the solid heater, denoted by 6. It is noted that most of the boiling models used today do not account for these spatial and temporal fluctuations in the surface temperature, assuming in general a stationary and uniform wall temperature. For denser bubble populations occurring at higher wall superheats, the bubble-bubble interactions, denoted by 7, such as coalescence or formation of columns, can play an important role. It is conceivable that this type of interaction makes simple single bubble considerations, on which many boiling models are based, highly questionable. The complexity shown in Fig. 1 does still not give the complete picture. Contact surface related aspects associated with surface tension, wettability, surface roughness, and porosity are known to have an important influence on the number of active nucleation sites needed for the formation of vapour bubbles. The so-called surface aging, which can be caused by chemical depositions on the heater surface leading to a long term deactivation of nucleation sites, also falls into this group. It is especially these surface related properties which impede a rigorous parameterization. Despite the numerous and physically complex effects which can be relevant in nucleate boiling, it is generally agreed that the marked increase in the heat transfer rate relative to the single-phase convection essentially results from two basic mechanisms:

- the microconvection induced by the motion of the bubbles, and
- the latent heat transport to and from the bubbles.

However, in many cases no consensus has been reached on the quantitative contribution of each mechanism to the total heat flux.

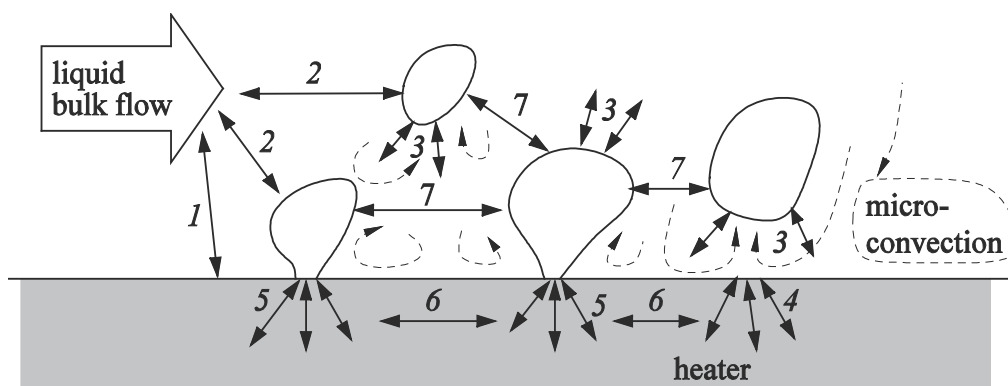


Fig. 1. Interactions between liquid phase, the vapour bubbles and the solid heater.

2.2 Onset of nucleate boiling and the subcooled boiling flow regime

A typical subcooled boiling flow configuration is schematically shown in Fig. 2a. The regime is basically characterized by a superheated wall with $T_w > T_s$, and a bulk temperature, which is lower than the saturation temperature, $T_b < T_s$. The formation of vapour bubbles starts, once the heated wall has reached the onset of nucleate boiling (ONB) temperature, $T_w = T_{ONB}$ at point B. Fig. 2b shows three boiling curves depicting the wall heat fluxes q_w versus the wall temperatures T_w for three different bulk velocities, with zero velocity - representing the pool boiling case - being the lowest. Two subranges can be distinguished in the subcooled boiling region: in the partially developed boiling (PDB) regime at lower wall superheats, the

bulk flow rate affects the heat transfer significantly. So the onset of nucleate boiling is shifted to higher wall superheats for higher flow rates ($B \rightarrow B'$), as shown in Fig. 2b. In the fully developed boiling (FDB) regime at higher wall superheats, the boiling curves converge towards the pool boiling curve, which indicates that the flow becomes insignificant, once the wall superheat is sufficiently high. A further increase of the wall heat flux can heat up the bulk liquid to finally reach the saturation temperature, such that $T_b = T_s$. This denotes the transition from the subcooled to saturated flow boiling, where the bulk flow contains a significant fraction of vapour, as there is no subcooled region, where the bubbles could collapse.

The onset of nucleate boiling is a crucial point for the heat transfer characteristics, as it denotes the incipience of the formation of vapour bubbles initiating the desired substantial increase in the heat transfer rate. In the considered case of surface boiling, the ONB is associated with the activation of nucleation sites on the heated wall. Potential nucleation sites are mostly surface imperfections like cavities, fissures, or impurities.

Hsu (1962) was the first to develop an analytical condition for the onset of nucleate boiling at a given cavity. Hsu considered strongly idealized conditions shown in Fig. 3, assuming a cone-shaped cavity with an exact circular mouth of radius r_c , a quiescent liquid, whose temperature T_l decreases linearly with the normal distance to the wall y , and a bubble of spherical shape. Applying such simplifications, Hsu determined the temperature at ONB

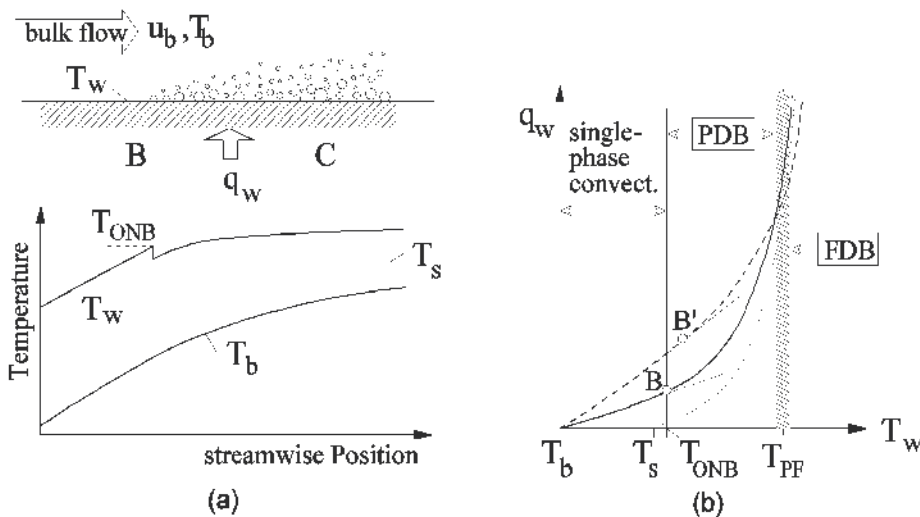


Fig. 2. Subcooled boiling flow: (a) variation of bulk and wall temperatures with the streamwise position; (b) boiling curves for different velocities of the bulk liquid; the dashed line, ---, denotes the highest velocity case, the dotted line,, denotes the pool boiling case.

from the minimum wall superheat $\Delta T_{sat,min}$ required for the activation of a cavity of a given mouth radius r_c . This superheat at ONB is obtained as

$$T_{ONB} - T_s = \Delta T_{sat,min} = \frac{4 T_s \sigma \sin \beta}{\rho_g h_{lg} r_c}, \tag{1}$$

and the corresponding heat flux reads

$$q_{ONB} = \frac{\lambda_l \rho_g h_{lg} (T_{ONB} - T_s)^2}{8 T_s \sigma (1 + \cos \beta)} \quad (2)$$

with λ_l being the thermal conductivity of the liquid, ρ_g the vapour density, h_{lg} the latent heat of evaporation, σ the surface tension, and β the liquid/vapour contact angle.

Hsu's concept, which is strongly idealized concerning the geometry of the cavity and the conditions of the liquid, remained the baseline also of later advancements in the modelling of the ONB, although it ignores completely the flooding of cavities. This occurs especially with well wetting liquids, where Hsu's criterion (1) significantly underpredicts the minimum superheat required for ONB. Basu (2002) accounted for the wettability of the surface by reducing r_c to an *effectively* available cavity size $r_{c,eff} = r_c \Phi$. The correction factor Φ is computed as an empirical function of the contact angle β . Φ decreases from unity to zero for increasing wettability associated with $\beta \rightarrow 0$.

Following Hsu's strongly simplifying analytical approach to model the bubble nucleation is basically not feasible for real technical surfaces, where it appears impossible to consider all relevant, mostly microscale effects like the microscopic surface topology, dynamics at the contact line between liquid, solid and vapour phase, corrosive abrasion or deposition, the instantaneous variation of the temperature inside the solid heater, or the content of dissolved gases. Many of these effects are to date not accessible by detailed experimental or numerical investigations. Therefore, in most approaches the ONB is not modelled explicitly, as this does not notably improve the overall accuracy of the predictions.

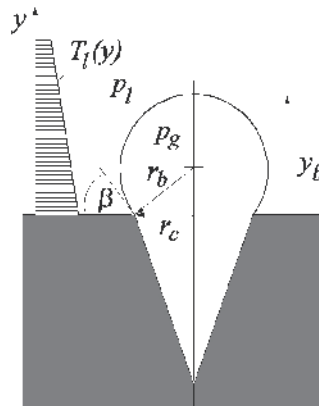


Fig. 3. Bubble nucleus at the onset of nucleate boiling (ONB) on an idealized cavity.

2.3 Models for the wall heat flux

In pace with the increasing computational resources it has become possible to simulate the conditions inside the very thin liquid microlayer at the wall, on which the growing bubble basically resides (Dhir et al., 2005). However, due to the high computational costs such detailed simulations are still restricted to configurations with very few bubbles on ideal surfaces. Therefore, the basically model-free direct simulation is way off the flow boiling on real technical surfaces (Mei et al., 1995a,b; Shin et al., 2005).

Some researchers even abandon the deterministic approach of mechanistic modelling. They consider boiling rather as a chaotic process (Shoji, 2004). This approach was proven as useful

to describe the chaotic fluctuations of the surface temperature associated with the non-linear interaction of bubble nucleation on neighbouring sites (Mosdorf & Shoji, 2004). As such the concept of boiling chaos gave important insight into individual sub-processes, but it did not yet deliver a full predictive wall heat flux model.

A great variety of wall heat flux models has been developed for use in engineering applications, and basically all of them adhere to the deterministic approach. The proposed models can be broadly grouped into two categories:

- *General empirical correlations*, which describe the wall heat transfer rates mostly as general power functions of non-dimensional groups.
- *Mechanistic models*, which attempt to capture the basic relevant mechanisms for the total heat flux, i.e., the hydrodynamic convective transport and the thermal heat transport associated with evaporation.

While the first concept relies completely on experimental data in deriving the non-dimensional model correlations, the latter is more analytical in that it accounts explicitly for the different physical mechanisms contributing to the total heat flux. Therefore, the mechanistic models in general perform better in transition regimes, where the relative contribution of the individual mechanisms may change substantially. Despite their more physical basis, the mechanistic models still involve a good deal of empiricism in the sub-models for the individual mechanisms.

2.3.1 General empirical correlations

In the FDB region, most empirical correlations model the total heat flux as a power function of the wall superheat generally written as

$$q_w = K(T_w - T_s)^m = K\Delta T_{sat}^m \quad (3)$$

where K and m are empirically determined model parameters. McAdams (1949) proposed this ansatz for water with $K=4.77$ and $m=3.86$. The so called Boiling number based model of Shah (1977)

$$q_w = \alpha_{fc} 230 Bo^{0.5} \Delta T_{sat} \quad (4)$$

falls also into this group. It basically models the total heat flux as a forced single-phase convective transport associated with the heat transfer coefficient α_{fc} , which is enhanced by boiling. The enhancement is represented by the Boiling number

$$Bo = \frac{q_w / \rho_l h_{lg}}{u_b} \quad (5)$$

which relates the “boiling velocity” given in the nominator to the velocity of the bulk flow. Kandlikar (1998b) modified Shah’s correlation to

$$q_w = \alpha_{fc} 1058 F_{fl} Bo^{0.7} \Delta T_{sat} \quad (6)$$

introducing a fluid-surface parameter F_{fl} representing the surface fraction covered by the liquid phase. The Boiling number based models are basically designed for the FDB regime, where they perform fairly well. On the other hand, they are quite inaccurate in the PDB

regime close to the ONB, where, according to Eqs. (4) and (6), the total wall heat flux vanishes as the superheat goes to zero.

2.3.2 Mechanistic models

The basic strategy of mechanistic models is to identify and to model the essential physical mechanisms which contribute significantly to the total wall heat flux. They mostly assume the heat flux to be composed of three components, namely, the single-phase convection q_{fc} , the evaporation heat flux needed for the phase change q_{ev} , and the sensible heating of the portion of liquid which fills the volume vacated by a departing or collapsing bubble q_{qu} . The total wall heat flux can then be written as

$$q_w = q_{fc} + q_{ev} + q_{qu}. \quad (7)$$

The forced convection component is commonly obtained using simply the classical textbook correlation by Dittus-Boelter, or more sophisticated correlations (Gnielinski, 1976).

The modeling of the evaporation heat flux q_{ev} faces the problem that it requires the number density of active nucleation sites, whose determination brings in again a great deal of empiricism. The same applies to the quenching component q_{qu} , regarding the determination of the quenching period, which depends on the time needed for the transient heat-up of the liquid filling the void of a departed bubble. Due to these difficulties in the modeling of the individual components associated with the phase change, most mechanistic models do not account for these fluxes separately. They rather combine them to one single "pool boiling", or "nucleate boiling" term, q_{nb} , such that Eq. (7) becomes

$$q_w = q_{fc} + q_{nb}. \quad (8)$$

A large number of models of this category have been proposed. In contrast to the Boiling number based methods discussed above, the explicit distinction between a convective and a nucleate boiling contribution brings about much freedom in selecting an appropriate model for each component. It also provides by definition the right asymptotic behaviour when approaching the limits of single-phase convection, where the nucleate boiling composition becomes zero, $q_{nb} \rightarrow 0$, as well as the limit of pool boiling, where the forced convection contribution goes to zero, $q_{fc} \rightarrow 0$. The latter limit is particularly troublesome for the Boiling number based empirical correlations, because, as seen from its definition in (5), the Boiling number goes to infinity for vanishing bulk velocity $u_b \rightarrow 0$, which makes this type of models incapable to provide a smooth transition between the flow boiling and the pool boiling regimes.

A pioneering superposition model, whose underlying concept is still widely used, was proposed by Chen (1966). Chen defined the total heat transfer coefficient as composed of a "macroconvection" coefficient of the two-phase flow and a "microconvection" coefficient associated with nucleate boiling, written as

$$\alpha = \alpha_{mac} + \alpha_{mic} = F \alpha_{fc} + S \alpha_{nb} \quad (9)$$

The heat transfer coefficient for the macroconvection is obtained from the Dittus-Boelter correlation using an increased two-phase flow Reynolds number Re_{2ph} incorporated through the factor F . As such, the factor $F = (Re_{2ph}/Re_{1ph})^{0.8}$ accounts for the enhanced convective heat

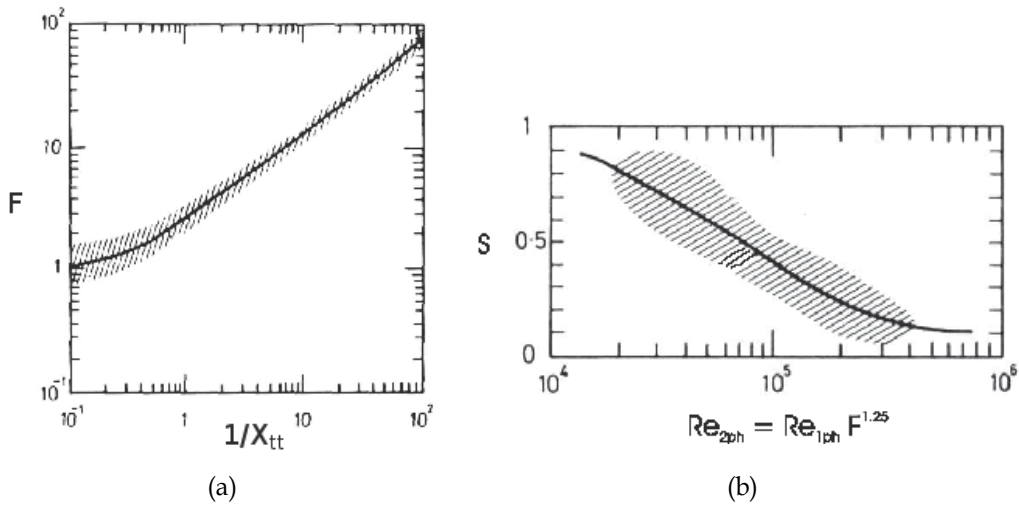


Fig. 4. Best fit curves for correction factors in Chen model: (a) convection enhancement factor; (b) boiling suppression factor. The shaded regions denote the ranges of experimental data (reprinted from Chen (1966) with permission of ACS).

transport caused by the vapour bubble agitation. It was graphically obtained by Chen as dependent on the Martinelli parameter

$$X_{tt} = \left(\frac{1-x}{x} \right)^{0.9} \left(\frac{\rho_g}{\rho_l} \right)^{0.5} \left(\frac{\eta_l}{\eta_g} \right)^{0.1} \quad (10)$$

based on a best fit to experimental data as shown in Fig. 4a. Aside from the liquid-vapour phase density and viscosity ratios, X_{tt} essentially depends on the vapour mass fraction x . For small vapour fractions x associated with $1/X_{tt} \leq 0.1$, the factor F is assumed to be unity.

The microconvection coefficient is obtained from the pool boiling correlation by Forster and Zuber (1955). Chen further modified this contribution introducing a suppression factor S in order to reflect the generally observed decrease in the nucleate boiling activity with increasing flow velocity. Chen graphically correlated the flow induced suppression factor S as a best-fit curve to experimental data dependent on the two-phase flow Reynolds number Re_{2ph} , as shown in Fig. 4b. In a later work, Butterworth (1979) provided an analytical best-fitting dependence for the parameter S written as

$$S = \frac{1}{1 + 2.53 \cdot 10^{-6} Re_{2ph}^{1.17}} \quad (11)$$

Chen's concept, which was originally proposed for saturated boiling flow of water, has become a well established, very popular approach. It has been modified and developed further by many other authors (Gungor and Winterton, 1986; Campbell et al., 1995; Kobor, 2003; Steiner et al. 2005). These generally termed Chen-type models mainly differ in the sub-model for the nucleate boiling component and in the determination of the boiling suppression factor S .

Chen's linear superposition concept was also generalized to a non-linear combination

$$\alpha = \left[(\alpha_{fc} F)^n + (\alpha_{nb} S)^n \right]^{1/n} \quad (12)$$

as suggested by Kutateladze (1963), Liu & Winterton (1991) with $n=2$, and by Steiner & Taborek (1992) with a general exponent n . For increasing values of n , the power-additive formulation inherently gives more weight to the nucleate boiling, where $\alpha_{nb} \gg \alpha_{fc}$, which nicely reflects the vanishing influence of the liquid flow on the total heat flux in the FDB regime. At low superheats, the formulation pronounces the convective heat transfer, where $\alpha_{fc} \gg \alpha_{nb}$, which basically has the effect of a flow induced suppression. Therefore, Steiner & Taborek (1992) model the factor S as independent of the flow rate. The degree of the flow induced suppression is inherently determined by the magnitude of the exponent n .

Campbell et al. (1995) were the first group who considered subcooled boiling flow in automotive cooling systems. They carried out experiments with a typical engine coolant composed of 50Vol% ethylene-glycol and 50Vol% water, and they adopted Chen's ansatz for the heat flux modelling. Due to the subcooling they ignored the enhancement of the macroconvection caused by the agitation of the bubbles assuming $F = 1$, which implies $Re_{2ph} = Re_{1ph}$. Based on their experimental results they proposed the following correlations for the flow induced suppression factor:

$$S = \begin{cases} 1.0, & Re_{1ph} < 10^4 \\ -0.6 \log_{10} Re_{1ph} + 3.4, & 10^4 \leq Re_{1ph} \leq 4 \cdot 10^5 \\ 0.04, & Re_{1ph} > 4 \cdot 10^5. \end{cases} \quad (13)$$

The model of Campbell et al. (1995) is, like most of the proposed superposition models, not well suited for application in the CFD of coolant flows in engineering devices, because the model correlation for the suppression factor depends on the bulk flow Reynolds number as a non-local parameter. On the other hand, suppression is basically a local effect, and it should therefore be modelled dependent of local flow quantities, which may be readily provided by the CFD solution. Moreover, dealing with CFD of geometrically complex flow configurations like those in coolant jackets, it is practically not possible to define a Reynolds number based on bulk flow conditions in a meaningful way. To circumvent these obvious shortcomings, Kobor (2003) developed a Chen-type approach, termed Boiling Departure Lift-off (BDL) model, which accounts for the dynamic effect of the near-wall flow field on the bubble detachment from the heated surface. In the BDL model the suppression factor is modelled as dependent on the ratio of two characteristic bubble diameters, the departure and the lift-off diameters, such that

$$S \propto \frac{d_D}{d_L}. \quad (14)$$

The diameters d_D and d_L are computed from local force balances at the instants of bubble departure from the nucleation site and bubble lift-off from the surface, respectively, relying on a concept of Zeng et al. (1993). The BDL model was introduced into the CFD software FIRE, where it performed very well in simulations of automotive coolant jackets. Steiner et al. (2005) extended the BDL model to the boiling of pure water, where they introduced an

additional suppression factor for the nucleate pool boiling component to capture explicitly the influence of the subcooling. The BDL model predicted the flow induced suppression fairly well, as exemplarily shown in Fig. 5 by a comparison against experiments and predictions from other models.

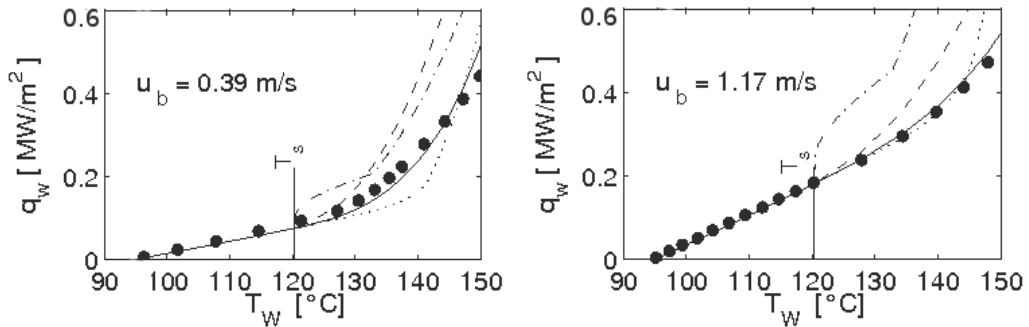


Fig. 5. Predicted flow boiling curves for water at $p=2\text{bar}$ and two different bulk flow velocities: solid line '—', BDL, dashed line '- - -', Chen (1966), dash-dotted line '----', Shah (1977), dotted line '....', Kandlikar (1998b); (reprinted from Steiner et al. (2005) with permission of Elsevier).

The neglect of the influence of the bubble agitation on the convective heat transfer generally assumed in subcooled boiling flow loses its justification as the void fractions become higher near the wall, which is especially the case at high wall superheats combined with low liquid velocities (Maurus, 2003; Ramstorfer et al., 2008a). In order to account for the dynamic effects of the bubbles, while still remaining within the framework of a single-fluid formulation, Ramstorfer et al. (2008a) proposed to introduce a bubble-equivalent wall roughness. The increased wall roughness leads to a higher turbulence intensity in the near-wall region, yielding the enhanced convective heat transfer which is in reality due to the agitation of the bubbles.

3. Subcooled boiling flow under automotive engine conditions

In general, the models proposed for the wall heat flux in nucleate boiling flow are calibrated and validated for very specific conditions concerning working fluid, material and surface quality of the heater, as well as flow configuration. As such, the models, be they empirical or mechanistic, involve correlations and parameter settings, which are typically based on laboratory experiments using purified, degassed liquids, clean homogeneous surfaces with a specified finish and a defined, uniformly heated area. The experimental set-ups are mostly designed to ensure well defined stationary flow conditions in the test-sections. Experimental findings obtained with such particular set-ups may therefore not apply straightforwardly to real-life conditions in technical applications.

It has therefore become best practice to still apply the available well-established standard approaches to real engineering problems, however, using specially adapted model coefficients and/or introducing additional parameters to capture effects of particular importance for the actually considered case. Several of these effects with relevance for automotive cooling systems shall be discussed in the following.

3.1 Composition of the liquid

The boiling of multi-component mixtures can be strongly affected by diffusion as well as differing volatilities of the individual components. The latter leads to an enrichment of the vapour/liquid interface with the less volatile component, so that the local mixture at the interface has an effectively higher saturation temperature, $T_{s,int} > T_s$, and the evaporation rate decreases. This non-azeotropic behaviour of the mixture is in principle due to the finite speed of diffusion, which impedes a prompt balancing of the deficit of the more volatile component at the interface. Accordingly, its effect on the boiling activity is typically accounted for by incorporating a diffusion-induced suppression factor F_D into the model correlations which are basically derived for pure liquids (Wenzel & Müller-Steinhagen, 1995; Kandlikar 1998a). The suppression factor $F_D \leq 1$ reduces the nucleate boiling component, analogous to the factor S in Eqs. (9) or (12), and it essentially depends on the effective increase in the saturation temperature, $T_{s,int} - T_s$.

The working liquid in automotive cooling systems generally consists of two main components, water and the antifreeze component ethylene-glycol. The volumetric mixing ratio is mostly 50/50Vol%. Figs. 6a und b show two sets of flow boiling curves experimentally measured for three different mixtures at the Reynolds numbers $Re_b = 5500$ and 22000 (Breitschädel, 2008). The bulk velocities corresponding to the two Reynolds numbers are about $u_b = 0.1$ and 0.4 m/s, respectively. It becomes obvious that in both cases the 60/40Vol% mixture, i.e., the liquid with the smallest fraction of the more volatile component (water), exhibits the lowest total wall heat fluxes at a given wall superheat $\Delta T_{sat} > 0$ in the nucleate boiling regime. The boiling curves obtained with the BDL model (Kobor, 2003) are also shown in Figs. 6a,b to demonstrate the predictive capability of a typical Chen-type model which does not account explicitly for non-azeotropic effects of the mixture. The predictions also reflect the experimentally observed tendency for the considered mixtures. It appears to be sufficient to model the effect of the varying water/ethylene-glycol ratio in terms of a corresponding variation of the material properties of the mixture. This basically means that the binary system can be treated as an azeotropic mixture, and a diffusion induced suppression needs not to be introduced.

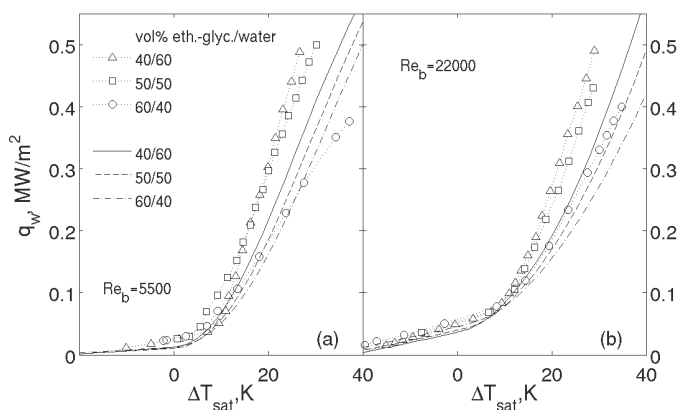


Fig. 6. Flow boiling curves for varying coolant compositions: (a) $Re_b = 5500$; (b) $Re_b = 22000$; experimental data denoted by symbols, BDL model predictions by lines; pressure: $p = 1.5$ bar (from Steiner et al., 2008).

3.2 Microgeometry of the heated surface

The microgeometry of technical surfaces is generally described in terms of the surface roughness, which is mostly expressed as an average roughness height R_a given in μm . Being a rather crude measure, R_a certainly does not represent the effectively boiling relevant microgeometry, which may be constituted by many different types of geometry elements, such as plateaus, peaks, valleys, cavities, etc. . It is generally accepted that only those surface elements can act as stable bubble generating centres (active nucleation sites), which are not completely filled with liquid after bubble departure. Therefore, an increase in the average surface roughness may lead to an increase in the boiling heat transfer only if the higher roughness is associated with additional active and stable nucleation sites. Numerous - mostly pool boiling - experiments have investigated this effect (see, e.g., Jakob & Fritz, 1931; Corty & Foust, 1955; Kuhihara & Myers, 1960). They showed that the heat transfer rate in general rises as the surface roughness is increased. The quantitative extent, however, strongly depends on the considered surface quality. The variation of surface roughness affects the nucleate boiling heat transfer most pronouncedly when considering high quality finished surfaces, where the average roughness is of the order of $R_a \approx 1 \mu\text{m}$ and lower, as it was recently confirmed in pool boiling experiments of Jones et al. (2009) (see Fig. 7). In contrast, typical surface roughness in automotive cooling systems is markedly higher, where the mostly applied iron or Aluminium as cast surfaces have an average roughness height $R_a \approx 40 \mu\text{m}$ and higher. Breitschädle (2008) carried out experiments for automotive cooling conditions, varying the roughness of the aluminium surface between $R_a=2 \mu\text{m}$ ("smooth"), $R_a=45.7 \mu\text{m}$ ("standard"), and $R_a=130 \mu\text{m}$ ("rough").

As seen from the boiling curves in Fig. 8, which were measured after different operation times, both the smooth and the rough surfaces exhibit almost the same heat transfer conditions at a primary stage, because the earliest measured boiling curves of both surfaces almost coincide. The considerable concentration of large cavities on the very rough surface does evidently not provide additional active nucleation centres compared to the smooth,

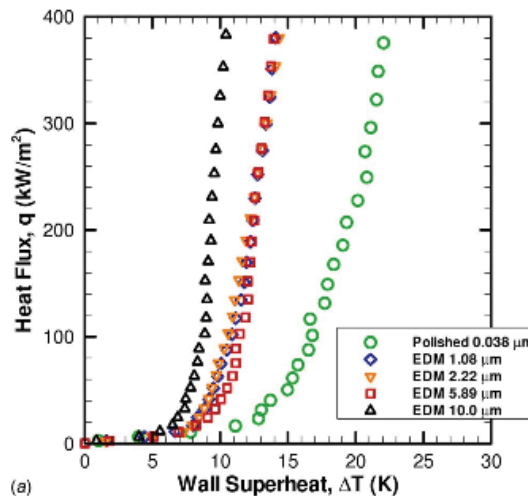


Fig. 7. Pool boiling curves for water on Electrical Discharge Machined (EDM) surfaces with different roughness R_a (reprinted from Jones et al. (2009) with permission of ASME).

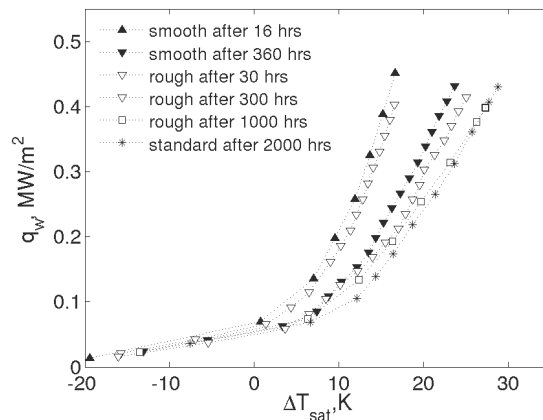


Fig. 8. Flow boiling curves for varying surface roughness after different operation times; bulk liquid velocity $u_b = 0.476 \text{ m/s}$; mixture 50/50Vol% ethylene-glycol/water; pressure $p = 1.5 \text{ bar}$ (from Breitschädel, 2008).

polished surface. With increasing operation time, both types of surfaces exhibit a notable degradation of the heat transfer rate, as seen from the shift of the boiling branches towards higher wall superheats. This tendency points to a successive deactivation of initially active nucleation sites, so that they finally approach the boiling curve of a long-term measurement using the standard surface. The shown trends illustrate again the dominant role of the microgeometry, which finally levels out any potential primary surface roughness effect on the boiling heat transfer during long-term operation. For the considered surface types, the effect of the macroscopic surface roughness needs not to be explicitly considered in the modelling of the wall heat flux.

The potential increase in the boiling heat flux attainable with special superficial layers of the heater has become an important research topic investigating the boiling behaviour on so-called *enhanced surfaces*. Depending on their fabrication, these specially designed surfaces may be structured (Memory et al., 1995; Kim & Choi, 2001), e.g., with microfins, with pores connected by subsurface gaps, or unstructured such as porous coatings (Afgan et al., 1985; Kim et al., 2002; Rainey et al., 2001, 2003).

Using enhanced surfaces provides in general a higher number of active nucleation sites, which leads to lower minimum wall superheats required for the onset of nucleate boiling (ONB). Beyond the ONB, mostly higher boiling heat transfer rates are observed as compared to the unmodified smooth surfaces. The intensified boiling activity is commonly explained by the hypothesis that, on enhanced surfaces, the bubble nucleation occurs predominantly in subsurface, hence higher superheated, microchannel-like dendritic cavities, which are also more likely to entrap a gaseous rest after bubble departure than the superficial cavities on the unmodified surfaces. The potential of this concept to enhance the boiling activity for use in automotive cooling was investigated by Ramstorfer et al. (2008b). They experimentally examined flow boiling of an automotive coolant composed of 60 and 40Vol% water and ethylene-glycol, respectively, using heated surfaces with two different types of coatings. The first type of coating ("coating S1") was produced by spraying molten mild steel on the ground cast-iron surface. The second type of coating ("coating S2") was fabricated by sintering a highly porous layer of iron particles on the cast-iron ground body (see Fig. 9).

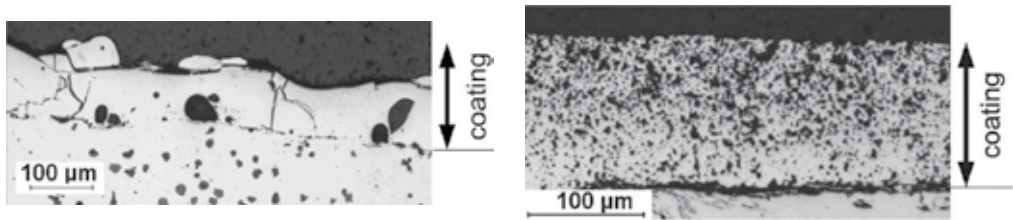


Fig. 9. Cross-sectional photomicrographs of the superficial layers of the heaters: left subfigure coating S1, right subfigure coating S2 (reprinted from Ramstorfer et al. (2008b) with permission of ASME).

The comparison of individual flow boiling curves shown in Fig. 10 reveals significantly higher boiling heat transfer rates for the coated surfaces, which can be clearly observed from the markedly reduced wall superheats ranging up to 15 K. It is interesting to note that coating S1 performs best, although its porosity is much lower than that of coating S2. This can be attributed to the particular microstructure of the coating S1. The coating S1 is not a typical granular-porous, nor a channel-porous layer, as it consists for the most part of a solid metallic base matrix, which is penetrated by a few, but comparatively deep cavities. These deep cavities are evidently most capable to entrap vapor, hence, to act as bubble nucleation centres, as it was also observed by Qi et al. (2004).

Ramstorfer et al. (2008b) also demonstrated that the superposition ansatz generally defined in Eq. (8) can be well extended to boiling on enhanced surfaces. Considering a vertical heated surface, they modelled the convective component q_{fc} following an ansatz of Churchill (1972) proposed for mixed (natural + forced) convection. For the nucleate boiling component q_{nb} they used the classical pool boiling correlation of Rohsenow (1952) with experimentally fitted model parameters. The predicted wall heat fluxes on the coated surfaces agree very well with the experiments over a wide range of bulk velocities, as seen from Fig. 11.

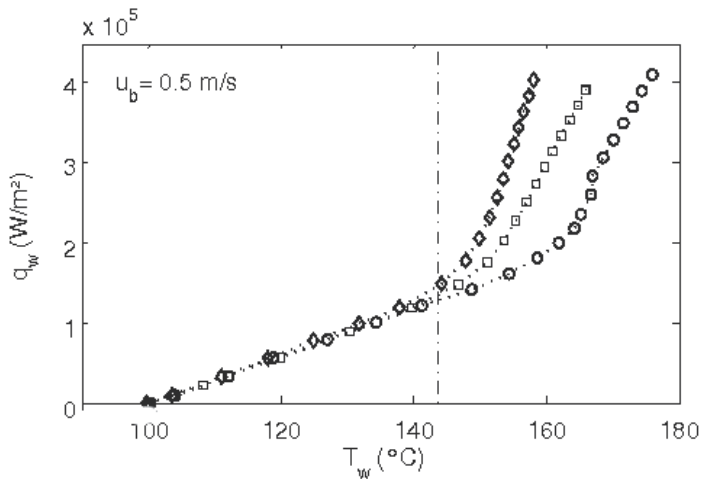


Fig. 10. Flow boiling curves of a 60/40Vol% water/ethylene-glycol mixture on different surfaces: \circ plain cast iron; \diamond coating S1; \square coating S2; saturation temperature $T_s = 143$ °C (dash-dotted line) ; subcooling $\Delta T_{sub} = T_s - T_b = 43$ K (reprinted from Ramstorfer et al. (2008b) with permission of ASME).

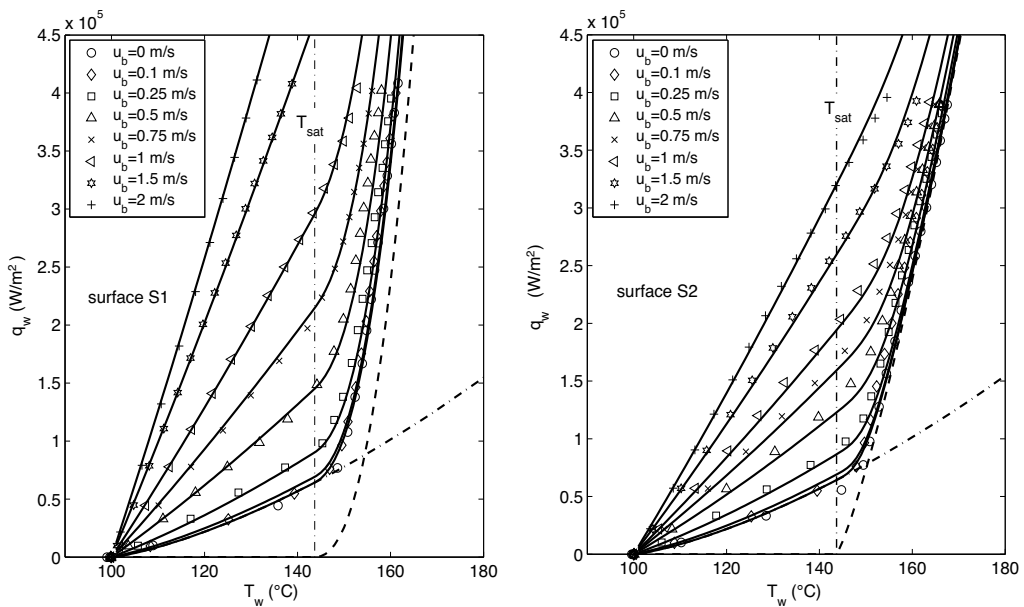


Fig. 11. Predicted flow boiling curves for the porous surfaces S1 and S2 at different velocities of the bulk flow: full line, “—”, model prediction; dash-dotted line, “- · - ·”, natural convection; dashed line, “- - -”, pool boiling curve; the symbols denote the measurements reprinted from Ramstorfer et al. (2008b) with permission of ASME).

Based on these findings, it can be noted that the use of enhanced surfaces represents a promising concept to increase the efficiency of automotive cooling systems. However, before its technical realization, several open questions need to be answered. Critical issues related to the manufacturing of the surface, the long term stability of the coating, or the effect on the mechanical resilience of the base structure, call for further detailed investigations. The modelling for the wall heat flux can rely on standard approaches using an appropriate parameter setting for the considered surface. These model parameters may vary considerably for different combinations of coatings and working liquids.

3.3 Orientation of the heated surface

Since nucleate boiling by nature involves the motion of a low-density vapour phase in a high-density liquid carrier phase, the dynamics in the thermal boundary layer may be strongly influenced by the buoyancy forces, especially at low flow rates of the bulk liquid. In such a case the orientation of the superheated surface relative to the direction of gravitational acceleration is of major importance. This aspect is mostly ignored by the nucleate boiling models though. Klausner et al. (2003) investigated the influence of buoyancy on the detachment process of the bubbles in much detail, computationally as well as experimentally. They carried out experiments with the perfluorocarbon liquid FC-87 for varying streamwise inclination angle of the heated surface from 0° to 360° . They found the influence of the surface orientation to be mainly dependent on wall superheat, liquid/vapour density ratio, and the flow velocity. Furthermore, they observed that the critical heat flux, where film boiling sets in, was reduced by almost an order of magnitude for a certain inclination at low flow rates. Roughly the same extent of reduction in the

critical heat flux was measured by Kim et al. (2005) for saturated pool boiling with water comparing upward against downward facing surfaces.

The potential effect of surface orientation was also investigated for automotive cooling conditions (Steiner et al., 2007). Fig. 12 shows the experimental results obtained for the subcooled boiling of a 50/50Vol% mixture of water and ethylene-glycol on a downward facing heated surface. The boiling curve in the lower left subfigure displays the measurements at three distinct positions, A, B, and C, as schematically shown in the subfigure above. The full line denotes the arithmetic mean of the three positions. Beyond a certain heat flux, marked by the transition point TP, the boiling curves at position B, and more pronouncedly at position C, deviate significantly towards higher wall superheats as compared to the almost straight boiling branch at A. The obvious streamwise decrease of the local heat transfer coefficient can be attributed to a transition from nucleate boiling to partial film boiling. This can be seen from the photographs in the right column of Fig. 12, displaying three distinct conditions corresponding to the points I, II, and III on the averaged boiling curve. Beyond the transition point (at conditions II and III), the vapour phase evidently tends to form ever larger film-like agglomerates, which cover a substantial part of the surface at the downstream end of the heater.

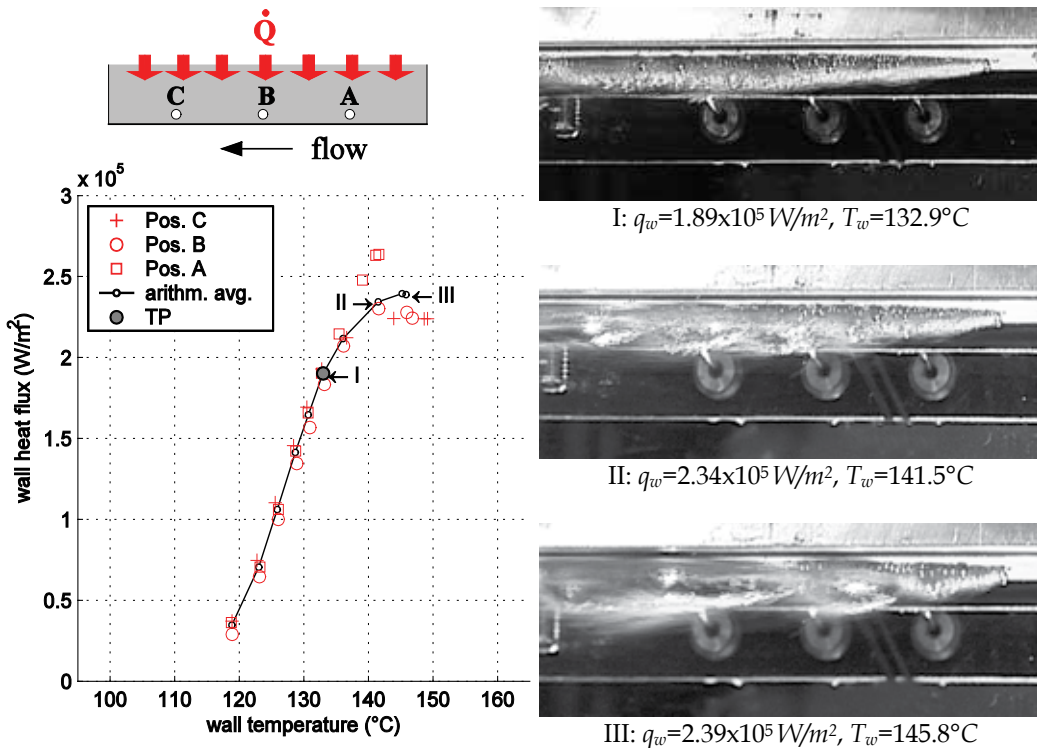


Fig. 12. Left column: wall heat flux q_w vs. wall temperature T_w measured at three positions for the bulk velocity $u_b = 0.2 \text{ m/s}$ and subcooling $T_s - T_b = 18^\circ\text{C}$; right column: photographs of the two-phase region at the three distinct conditions I, II and III as specified in the boiling curves in the left column. The direction of flow is right to left (from Steiner et al., 2007).

Based on a dimensional analysis, a criterion for the observed transition from nucleate to partial film boiling was derived in terms of a non-dimensional correlation for a transitional Boiling number

$$Bo_{trans} = C Re_L Ec_{sub}^{-n} \quad (15)$$

dependent on the Reynolds number $Re = u_b \rho_l L / \eta_l$ with the length scale $L = [\sigma / g(\rho_l - \rho_g)]^{0.5}$, and the Eckert number $Ec_{sub} = u_b^2 / c_{p,l}(T_s - T_b)$ representing the effect of subcooling. $C = 8.5 \cdot 10^{-11}$ and $n = 0.63$ are empirically determined model parameters. As such, correlation (15) provides via the Boiling number Bo_{trans} an important estimate for the transitional wall heat flux $q_{w,trans}$, beyond which a transition to partial film boiling has to be expected, which may eventually lead to a hazardous increase of the wall temperature.

Aside from the issue of ensuring acceptable wall superheats, the transitional wall heat flux $q_{w,trans}$ also represents an upper limit for the applicability of standard wall heat flux models generally used in subcooled boiling flow. The boiling contributions in these approaches are mostly correlated and calibrated assuming fully developed nucleate boiling on upward or sideward facing surfaces, so that they expectedly reach their limit, once partial film boiling sets in. This limitation is illustrated in Fig. 13, comparing experimental data measured for a downward facing surface with the predictions of the BDL model using a parameter setting proposed for automotive engine coolants (Kobor, 2003). The model predictions agree in general fairly well with the experiments below the transitional heat flux $q_{w,trans}$ computed from (15), while they exhibit considerable deviations above.

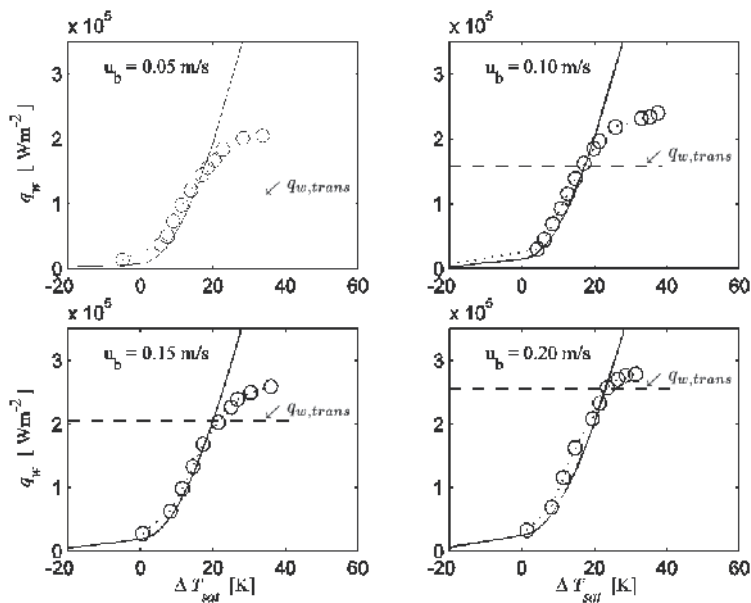


Fig. 13. Flow boiling curves of a 50/50Vol% mixture of water and ethylene-glycol on a downward facing heated surface at different velocities of the bulk flow u_b . The open circles, \circ , denote the experiments, the solid lines, '—', denote the predictions of the BDL model, the dashed lines, '- -', denote the transitional wall heat flux $q_{w,trans}$ computed from Eq. (15). The subcooling $\Delta T_{sub} = T_s - T_b = 25\text{K}$ is constant; (from Steiner et al., 2007).

The horizontal dashed lines in Fig. 13 also illustrate the strong flow rate dependence of the transitional limit $q_{w,trans}$. Accordingly, at the lower bulk velocities, $q_{w,trans}$ drops down to a level which is an order of magnitude lower than the critical heat flux in the corresponding pool boiling case on an upward facing surface. The quantitative extent of this reduction is well in line with the findings of Klausner et al. (2003) and Kim et al. (2005) mentioned above.

3.4 Aging

Aging is a phenomenon which may strongly affect the long-term activity of the nucleation sites on the heated surface. It therefore represents a great challenge and persistent source of inaccuracy for all boiling models. Due to its potential influence on the liquid-vapour-solid interfacial interactions at the nucleation sites, it may be highly relevant for the entire boiling process, starting from the onset of nucleate boiling (ONB). Aging subsumes the gradual, mostly slow changes of the working fluid, as well as those of the heated surface, which in general lead to less favourable conditions for the incipience of nucleate boiling. As such, aging is a process acting over long time scales, which is manifested in a steady decrease of the boiling heat transfer rate observed during long periods of operation time (weeks or months). Especially under technical flow conditions it is often impossible to clearly identify and eventually eliminate all relevant causes for aging. It can have many – single or multiple – causes, such as a continuous flooding of cavities, depositions on the surface, corrosion and/or mechanical erosion of the surface material, chemical reactions in the liquid phase, etc.. The quantitative impact of aging on subcooled boiling can be exemplarily seen from Fig. 14, showing experimental data obtained for one given liquid/surface combination, a mixture of ethylene-glycol and water on an as-cast aluminium surface, which is typically met in cooling jackets of modern internal combustion engines. The shown curves were measured over a period of two weeks. The temperature, pressure and velocity of the bulk liquid were always kept the same. Within the considered range of wall heat fluxes, the first

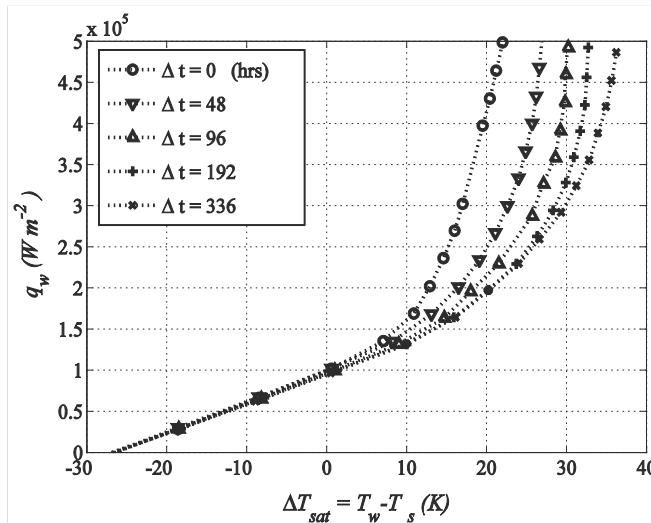


Fig. 14. Boiling curves of a 50/50Vol% mixture water and ethylene-glycol; the subcooling and the velocity of the bulk liquid are $\Delta T_{sub} = T_s - T_b = 25$ K and $u_b = 1$ m/s, respectively (from Kobor, 2003).

and the last curves differ up to 15 K in wall superheat $\Delta T_{sat} = T_w - T_s$. It could be shown that the aging effect observed here is partly caused by a continuous flooding of the cavities on the surface, which reduces the number of active nucleation sites. The other part could be attributed to depositions on the heated surface originating from the employed coolant liquid. The observed significant shift in the boiling curves strongly suggests that the aging conditions of the heated surface and the working fluid must not be overlooked in the interpretation of boiling flow measurements and in the specification of the model parameters based on such data. This caveat is particularly relevant for boiling of aqueous liquids on real technical surfaces.

7. Conclusions

The enhancement of heat transfer rates based on a controlled transition from pure single-phase convection to subcooled boiling flow appears to be a promising approach for application in automotive cooling systems. A reliable and save thermal management requires a most comprehensive knowledge of how certain operation and system conditions may affect the boiling behaviour. Therefore, we put our focus on a selection of engine relevant conditions and their possible impact on the modelling of the wall heat flux. This led us to the following resume.

As for the influence of the mixing ratio of the two main components of the coolant, water and ethylene-glycol, the heat transfer rates in the boiling regime tend to decrease when the fraction of the more volatile water component is smaller. The tested wall heat flux model, which basically assumes the coolant as an azeotropic mixture, reflected the observed tendency very well. The effect of the mixing ratio can be evidently captured with sufficient accuracy in terms of the material properties of the mixture. For the considered range of engine relevant mixing ratios and subcooled boiling flow conditions, non-azeotropic effects, such as the increase of the effective saturation temperature due to the depletion of the more volatile component at the liquid/gas interfaces, appeared to be of minor importance.

The effect of the macroscopic surface roughness turned out to be very limited in time. Long-term experiments confirm the dominant role of the microstructure of the surface, which finally leads to approximately the same boiling behaviour of all considered surface finishes. Based on this observation it may be concluded that the effect of the surface finish in terms of a roughness height may be disregarded in the wall heat flux model.

The use of porously coated, "enhanced", surfaces appears also attractive for application in automotive cooling. The scope of most studies on this subject is, however, in general strongly limited to the particularly considered type of coating and working liquid. Making use of this concept requires therefore further detailed investigations especially devoted to porous superficial layers, which can be technically realized in engine cooling systems. The standard wall heat flux models can be well extended to enhanced surfaces, when an appropriately adapted parameter setting is used.

Concerning the effect of the surface orientation, the case of a downward facing surface heated from above is expectedly the most critical one. Since the buoyancy force counteracts the bubble lift-off from the surface, a transition from nucleate boiling to partial film boiling can occur well below the critical heat flux associated with an upward facing surface. The observed strong dependence of this transitional heat flux on the velocity and subcooling of the bulk liquid could be cast into a non-dimensional criterion for the corresponding transitional Boiling number. Applying exemplarily the BDL model for predicting the wall

heat fluxes, it could be further shown that this standard Chen-type superposition approach is capable to produce acceptably accurate predictions up to the transitional heat flux without any special modifications accounting for the effect of orientation.

Aging is probably one of the most critical phenomena, especially when using aqueous working liquids typically found in automotive cooling systems. The phenomenon may be sustained by many complex chemical/physical sub-processes, which are hard or even impossible to control under real technical conditions. The boiling curves obtained after different operation times, or operations modes, may be shifted by 15 K and even more in the wall superheats. It therefore often requires long-term experiments to obtain reliable results, which exhibit no notable change in time, so that they can be used for model evaluation and calibration.

8. Acknowledgements

The financial support of the presented research work from the Austrian Forschungsförderungsgesellschaft (FFG) and the K plus Competence Center Program, initiated by the Austrian Federal Ministry of Transport, Innovation, and Technology (BMVIT), is gratefully acknowledged.

9. References

- Afgan, N.H.; Jovic, L.A.; Kovalev, S.A. & Lenykov, V.A. (1985). Boiling heat transfer from surfaces with porous layers, *International Journal of Heat and Mass Transfer*, 28, 415-422.
- Bower, J.S. & Klausner J.F. (2006). Gravity independent subcooled flow boiling heat transfer regime, *Experimental Thermal and Fluid Science*, 31, 141-149.
- Breitschädel, B. (2008). Analyse des Wärmeübergangs beim unterkühlten Strömungssieden an metallischen Oberflächen, *Doctoral thesis*, Graz University of Technology.
- Butterworth, D. (1979). The correlation of cross flow pressure drop data by means of a permeability concept, UKAEA Report AERE-R9435, 1979.
- Campbell, N.A.F.; Charlton, S.J. & Wong, L. (1995). Designing toward nucleate boiling in combustion engines, *Proceedings of the Institute of Mechanical Engineers* 1995, C496/092, 587-594.
- Chen, J.C. (1966). Correlation for Boiling Heat Transfer to Saturated Fluids in Convective Flow, *Industrial and Engineering Chemistry Process Design and Development*, 5, 322-329.
- Cheng, P.; Wu, H. & Hong, F.J. (2007). Phase-change heat transfer in microsystems, *ASME Journal of Heat Transfer*, 129, 101-107.
- Churchill, S.W. (1972). Comprehensive correlating equations for heat, mass and momentum transfer in fully developed flow in smooth tube. *Industrial and Engineering Chemistry Fundamentals*, 15, 789-900.
- Corty, C. & Foust, A.S. (1955). Surface variables in nucleate boiling, *Chemical Engineering Progress, Symposium Series*, 51, 1-12.
- Dhir, V.K.; Abarjith, H.S. & Warriar, G.R. (2005). From nano to micro to macro scales in boiling. In: *Microscale heat transfer: fundamentals and application*, Kakaç, S. (Ed.), 197-216, Springer.

- Forster, H.K. & Zuber, N. (1955). Dynamics of vapor bubbles and boiling heat transfer, *American Institute of Chemical Engineering Journal*, 1, 531-535.
- Gnielinski, V. (1976). New equations for heat and mass transfer in turbulent pipe and channel flow, *International Chemical Engineering*, 16, 359-368.
- Gungor, K.E. & Winterton, R.H.S. (1986). A general correlation for flow boiling in tubes and annuli, *International Journal of Heat and Mass Transfer*, 29, 351-358.
- Hsu, Y.Y. (1962). On the size range of active nucleation cavities on a heating surface, *ASME Journal of Heat Transfer*, 84, 207-216.
- Jakob, M.; & Fritz, W. (1931). Versuche über den Verdampfungsvorgang, *Forschung auf dem Gebiete Ingenieurwesens*, 2, 435-447.
- Jones, B.J.; McHale, J.P. & Garimella, S.V. (2009). The influence of surface roughness on nucleate pool boiling heat transfer, *ASME Journal of Heat Transfer*, 131, 121009-1–121009-14.
- Kandlikar, S.G. (1998a). Boiling heat transfer in binary systems: Part II – flow boiling, *ASME Journal of Heat Transfer*, 120, 388-394.
- Kandlikar, S.G. (1998b). Heat transfer characteristics in partial boiling, fully developed boiling, and significant void flow regions of subcooled flow boiling, *ASME Journal of Heat Transfer*, 120, 395-401.
- Kandlikar, S.G. (2002). Fundamental issues related to flow boiling in minichannels and microchannels, *Experimental Thermal and Fluid Science*, 26, 389-407.
- Kew, P.A. & Cornwell, K. (1997). Correlations for the prediction of boiling heat transfer in small-diameter channels, *Applied Thermal Engineering*, 17, 707-715.
- Kim, Y.H.; Kim, S.J.; Kim, J.J.; Noh, S.W.; Suh, K.Y., Rempe, J.L., Cheung, F.B. & Kim, S.B. (2005). Visualization of boiling phenomena in inclined rectangular gap, *International Journal of Multiphase Flow*, 31, 618-642.
- Kim, N.H. & Choi, K.K. (2001). Nucleate pool boiling on structured enhanced tubes having pores with connecting gaps, *International Journal of Heat and Mass Transfer*, 44, 17-28.
- Kim, J.H.; Rainey, K.N.; You, S.M. & Pak, J. Y. (2002). Mechanism of nucleate boiling heat transfer from microporous surfaces in saturated FC-72, *ASME Journal of Heat Transfer*, 124, 500-506.
- Klausner, J.F.; Bower J.S. & Sathyanarayan, S. (2003). Development of advanced gravity-independent high heat flux phase-change heat exchanger technology and design, Final Report Grant No. NAG3-2593.
- Kobor, A. (2003). Entwicklung eines Siedemodells für die Simulation des kühlmitteleitigen Wärmeübergangs bei Verbrennungskraftmaschinen, *Doctoral thesis*, Graz University of Technology.
- Kuhihara, H.M. & Myers, J.E. (1960). The effects of superheat and surface roughness on boiling coefficients, *American Institute of Chemical Engineering Journal*, 6, 83-91.
- Kutateladze, S.S. (1963). *Fundamentals of heat transfer*, Edward Arnold, London.
- Liu, Z. & Winterton, R.H.S. (1991). A general correlation for saturated and subcooled flow boiling in tubes and annuli based on a nucleate boiling equation, *International Journal of Heat Mass Transfer*, 34, 2759-2766.
- Maurus, R. (2003). Bestimmung des Blasenverhaltens beim unterkühlten Strömungssieden mit der digitalen Bildfolgenanalyse, *Doctoral Thesis*, Technical University Munich.

- McAdams, W.H.; Kennel, W.E.; Minden, C.S.; Carl, R.; Picornell, P.M. & Dew, J.E. (1949). Heat transfer at high rates to water with surface boiling, *Industrial and Engineering Chemistry*, 41, 1945-1953.
- Mei, R.; Chen, W. & Klausner, J.F. (1995a). Vapour bubble growth in heterogeneous boiling. I. Formulation, *International Journal of Heat and Mass Transfer*, 38, 909-919.
- Mei, R.; Chen, W. & Klausner, J.F. (1995b). Vapour bubble growth in heterogeneous boiling. II. Growth rate and thermal fields, *International Journal of Heat and Mass Transfer*, 38, 921-934.
- Memory, S.B.; Sugiyama, D. C. & Marto, P.J. (1995). Nucleate pool boiling of R-114 and R-114-oil mixtures from smooth and enhanced surfaces - I. Single tubes, *International Journal of Heat and Mass Transfer*, 38, 1347-1361.
- Mosdorf, R. & Shoji, M. (2004). Chaos in nucleate boiling - nonlinear analysis and modelling, *International Journal of Heat and Fluid Flow*, 47, 1515-1524.
- Qi, Y.; Klausner, J.F. & Mei, R. (2004). Role of surface structure in heterogeneous nucleation, *International Journal of Heat and Mass Transfer*, 47, 3097-3107.
- Ramstorfer, F.; Steiner, H. & Brenn, G. (2008a). Modeling of the microconvective contribution to wall heat transfer in subcooled boiling flow, *International Journal of Heat and Mass Transfer*, 51, 4069-4082.
- Ramstorfer, F.; Steiner, H.; Brenn, G.; Kormann, C. & Rammer, F. (2008b). Subcooled boiling flow heat transfer from plain and enhanced surfaces in automotive applications, *ASME Journal of Heat Transfer*, 130, 011501-1--011501-9.
- Rainey, K.N.; Li, G. & You, S.M. (2001). Flow boiling heat transfer from plain and microporous coated surfaces in subcooled FC-72, *ASME Journal of Heat Transfer*, 123, 918-925.
- Rainey, K.N., You, S.M. & Li, G. (2003). Effect of pressure, subcooling and dissolved gas on pool boiling heat transfer from microporous surfaces in FC-72, *ASME Journal of Heat Transfer*, 125, 75-83.
- Rohsenow, W. M. (1952). A method of correlating heat transfer data for surface boiling of liquids, *ASME Journal of Heat Transfer*, 74, 969-975.
- Shah, M.M. (1977). A general correlation for heat transfer during subcooled boiling in pipes and annuli, *ASHRAE Transactions*, 83, Part I, 205-217.
- Shin, S; Abdel-Khalik, S.I. & Juric, D. (2005). Direct three-dimensional numerical simulation of nucleate boiling using the level contour reconstruction method, *International Journal of Multiphase Flow*, 31, 1231-1242.
- Shoji, M. (2004). Studies of boiling chaos: a review, *International Journal of Heat and Fluid Flow*, 47, 1105-1128.
- Steiner, D. & Taborek, J. (1992). Flow boiling heat transfer in vertical tubes correlated by an asymptotic model, *Heat Transfer Engineering*, 13, 43-69.
- Steiner, H.; Kobor, A. & Gebhard, L. (2005). A wall heat transfer model for subcooled boiling flow, *International Journal of Heat and Mass Transfer*, 48, 4161-4173.
- Steiner, H.; Brenn, G. & Breitschädel, B. (2007). Onset of partial film boiling on a downward facing heated surface, *Proceedings of the 6th International Conference on Multiphase Flow (ICMF 2007)*, Paper S5_Tue_B_17, Leipzig, Germany, July 2007.
- Steiner, H.; Breitschädel, B.; Brenn, G.; Petutschnig, H. & Samhaber, C. (2008). Nucleate boiling flow - experimental investigations and wall heat flux modelling for auto-

- motive engine applications. In: *Advanced Computational Methods and Experiments in Heat Transfer 10*, Sunden, B. & Brebbia, C.A. (Eds.), 169-178, WIT Press.
- Thome, J.R. (2004). Boiling in microchannels: a review of experiment and theory, *International Journal of Heat and Fluid Flow*, 25, 128-139.
- Wenzel, U. & Müller-Steinhagen, H. (1994). Heat transfer to mixtures of acetone, isopropanol and water under subcooled flow boiling conditions - I. Experimental Results, *International Journal of Heat and Mass Transfer*, 37, 175-184.
- Zeng, L.Z.; Klausner, J.F.; Bernhard, D.M. & Mei, R.(1993). A unified model for the prediction of bubble detachment diameters in boiling systems - II. Flow boiling, *International Journal of Heat and Mass Transfer*, 36, 2271-2279.

The “Equivalent Cable Bundle Method”: an Efficient Multiconductor Reduction Technique to Model Automotive Cable Networks

Guillaume Andrieu¹, Xavier Bunlon², Lamine Koné³,
Jean-Philippe Parmantier⁴, Bernard Démoulin³ and Alain Reineix¹

¹*Xlim Laboratory, University of Limoges,*

²*Renault Technocenter, Guyancourt,*

³*IEMN Laboratory, University of Lille,*

⁴*Onera, Toulouse,*

France

1. Introduction

In automotive electromagnetic (EM) compatibility (EMC), the cable bundle network study is of great importance. Indeed, a cable network links all the electronic equipment interfaces included the critical ones and consequently can be assimilated both to a reception antenna and to an emission antenna at the same time. On the one end, as far as immunity problem is concerned, where an EM perturbation illuminates the car, the cable network acts as a receiving antenna able to induce and propagate interference currents until the electronic equipment interfaces and potentially induce dysfunction or in the worst case destruction of the equipment. At low frequency, the interference signal propagating on the cable network is generally considered as more significant than the direct coupling between the incident field and the equipment. On the other end, as far as emission problem is concerned, the EM field emitted by the cable network may disturb itself the electronic equipments by direct coupling.

To avoid these problems, automotive manufacturers have to perform normative tests before selling vehicles. These tests are applied on electronic equipments outside and inside the car first to verify that the equipments are not disturbed by an EM perturbation of given magnitude and second to ensure that the EM emission of each equipment does not exceed a limit value at a given distance. Obviously, these tests are not exhaustive and fully representative of real conditions. For example, in immunity tests, two polarizations (vertical and horizontal polarizations) of the EM perturbation are generally tested in free space conditions. In reality, the EM perturbation due for example to a mobile phone outside the car could happen from any direction of space and be reflected by all the scattering objects located in the close environment of the vehicle (ground, other vehicles, buildings,...).

Consequently, the contribution of EM modelling is a great tool for automotive manufacturers in order to proceed to numerical normative, additional and also parametric tests at early stages of the car development on numerical models and for a reasonable cost. Moreover, numerical modelling will reduce the number of prototypes built during the

development of a vehicle which is actually a strong trend in the automotive industry due to the cost of prototypes.

A 2-step approach is generally used (Paletta et al., 2002) for immunity problem. First, electric fields tangent to the cable bundle paths are computed with a 3-dimensional (3D) computer code solving Maxwell's equations such as Finite Difference Time Domain (FDTD) (Taflove & Hagness, 2005) or method of moments (MoM) (Harrington, 1993). Second, a multiconductor transmission line (MTL) (Paul, 2008) technique assuming transverse EM (TEM) mode propagation is used to calculate currents and voltages induced at the input of the electronic equipment devices by the excitation fields calculated in the previous steps (Agrawal et al., 1980). Unfortunately, this method presents two important drawbacks. Indeed, the MTL formalism is frequency limited by the appearance of transverse electric (TE) or magnetic (TM) modes and due to the fact that the EM emission of cables are not taken into account. Moreover, the huge complexity of a real automotive cable network seems to be unreasonable to model considering the required computer resources. Thus, the use of 3D computer codes at high frequency should be a suitable solution to overcome the limits of the MTL formalism but with a large increase of computation times required.

Consequently, this chapter presents the so-called « equivalent cable bundle method » (Andrieu et al., 2008), derived from previous work (Poudroux et al., 1995) developed to model a "reduced" cable bundle containing a limited number of conductors called "equivalent conductors" instead of the initial cable bundle. The huge reduction of the cable network complexity highly reduces the computer resources required to model a real automotive cable network. As an example, Fig. 1 presents the cross-section geometry of an initial cable bundle containing 10 conductors and the corresponding reduced cable bundle containing 3 equivalent conductors.

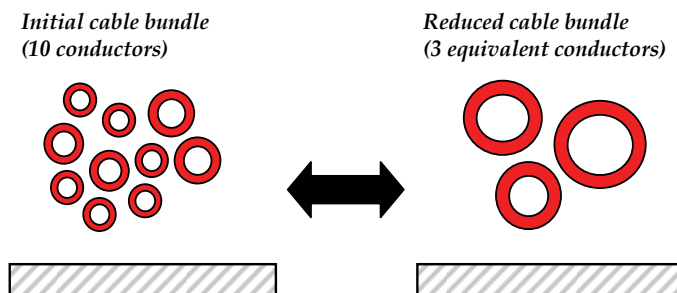


Fig. 1. Principle of the « equivalent cable bundle method »: definition of reduced cable bundle containing a limited number of equivalent conductors

Each equivalent conductor of the reduced cable bundle represents the effect of a group of conductors of the initial cable bundle.

The objective of the method is to be able to calculate the common mode current (algebraic sum of the currents in all the conductors of a cable bundle) induced at the extremities of the reduced cable bundle. The method does not compute the current on each conductor of the cable. For EM immunity problems, the common mode current nevertheless remains the most significant and robust observable.

The method can be used for a large frequency range which constitutes an important advantage provided that the simulation method is able to take into account the cross-coupling between conductors.

After an exhaustive presentation of the method for immunity problems (Andrieu et al., 2008) as well as an application to a concrete example, the adjustments required on the method for emission problems (Andrieu et al., 2009) are detailed with an other example. Finally, the results of a measurement campaign performed on a simplified half scale car body structure are presented in order to show the capability of the method when applied on representative automotive cases.

2. The “Equivalent Cable Bundle Method” for immunity problems

The determination of the electric and geometric characteristics of a reduced cable bundle for an immunity problem (Andrieu et al., 2008) requires a four step procedure detailed in this section. It is important to make precise that the method is applied on a point-to-point cable link. To model a cable bundle network as a real automotive one, the procedure has to be repeated on each path of conductors of the network.

2.1 Constitution of group of conductors

The aim of the first step of the method is to sort out all the conductors of the initial cable bundle in different groups according to the termination loads connected at their ends. Indeed, each termination load, linking the end of a wire conductor to the ground reference, is compared to the common mode characteristic impedance Z_{mc} of a whole cable bundle section, themselves sorted out in one of the four groups defined in Table 1.

	Group 1	Group 2	Group 3	Group 4
Common mode load at end 1	$R_{1i} < R_{mc}$	$R_{1i} < R_{mc}$	$R_{1i} > R_{mc}$	$R_{1i} > R_{mc}$
Common mode load at end 2	$R_{2i} < R_{mc}$	$R_{2i} > R_{mc}$	$R_{2i} < R_{mc}$	$R_{2i} > R_{mc}$

Table 1. Definition of the method used to sort each conductor in one of the four groups of conductors

All the impedance loads R_{ij} are considered in this work as resistances, therefore with no variation with the frequency; it is compared to the real part of Z_{mc} called R_{mc} . The index i corresponds to the label of the extremity (1 or 2) and the label j is the number of the conductor.

The determination of Z_{mc} requires the use of the modal theory in order to obtain the characteristics of all the modes propagating along the cable. The diagonalization of the product of the per-unit-length matrices of the MTL theory provides the modal basis. For example, the diagonalization of the product $[L].[C]^{-1}$ of a cable bundle of N conductors gives the $[Z_c^2]$ matrix containing the square of the characteristic impedances (Z_1, Z_2, \dots, Z_N) of all the modes:

$$[Z_c^2] = [T_x]^{-1} \cdot [L] \cdot [C]^{-1} \cdot [T_x] = [T_y]^{-1} \cdot [C]^{-1} \cdot [L] \cdot [T_y] = \begin{bmatrix} Z_1^2 & 0 & \dots & 0 \\ 0 & Z_2^2 & \dots & 0 \\ \vdots & \vdots & \ddots & \vdots \\ 0 & 0 & \dots & Z_N^2 \end{bmatrix} \quad (1)$$

$$[\Gamma^2] = [T_v]^{-1} \cdot [L] \cdot [C] \cdot [T_v] = [T_i]^{-1} \cdot [C] \cdot [L] \cdot [T_i] = \begin{bmatrix} 1/v_1^2 & 0 & \dots & 0 \\ 0 & 1/v_2^2 & \dots & 0 \\ \vdots & \vdots & \ddots & \vdots \\ 0 & 0 & \dots & 1/v_N^2 \end{bmatrix} \quad (2)$$

In the same way, the square of modal propagation matrix $[\Gamma^2]$ containing the propagation velocity v of all the modes is obtained with the diagonalization of the $[L] \cdot [C]$ product.

$[T_x]$, $[T_y]$, $[T_v]$, $[T_i]$ are the eigenvector matrices allowing to link real and modal basis.

The authors make precise that the transmission lines are considered in the method as lossless. In order to consider lossy ones, the following impedance $[Z]$ and admittance $[Y]$ matrices (containing respectively the resistance $[R]$ and the conductance $[G]$ matrices) should be used:

$$[Z] = [R] + j\omega[L] \quad (3)$$

$$[Y] = [G] + j\omega[C] \quad (4)$$

Z_{mc} is determined from the common mode characteristic impedance of each conductor z_i of a cable which is determined thanks to the analysis of the eigenvector matrices $[T_x]$ or $[T_y]$. For example, a $[T_x]$ matrix of a 3-conductors cable bundle is presented in equation (5):

$$[T_x] = \begin{bmatrix} 0.57 & 0.81 & -0.1 \\ 0.56 & -0.48 & -0.67 \\ 0.6 & -0.32 & 0.74 \end{bmatrix} \quad (5)$$

Each column of the matrix contains an eigenvector associated to a propagation mode. The eigenvector associated to the common mode can be distinguished from the others. Indeed, all its terms have the same sign and all the coefficients of the eigenvector have close values. Consequently, in the example of equation (5), the eigenvector linked to the common mode is contained in the first column.

The last step to determine Z_{mc} consists in finding the characteristic impedance of the $[Z_c^2]$ modal matrix linked to the common mode.

In equation (6), where $[T_x]$ has been replaced by its value, the characteristic impedance z_i linked to the common mode eigenvector is Z_1 . Indeed, Z_1 depends of the term of the first column of $[T_x]$ matrix, the eigenvector of the common mode.

$$[Z_c^2] = [T_x]^{-1} \cdot [L] \cdot [C]^{-1} = \begin{bmatrix} 0.57 & 0.81 & -0.1 \\ 0.56 & -0.48 & -0.67 \\ 0.6 & -0.32 & 0.74 \end{bmatrix} = \begin{bmatrix} Z_1^2 & 0 & 0 \\ 0 & Z_2^2 & 0 \\ 0 & 0 & Z_3^2 \end{bmatrix} \quad (6)$$

z_i also corresponds to the ratio of the common mode voltage V_{mc} and current I_{mc} in the modal basis as it is presented in Fig. 2.

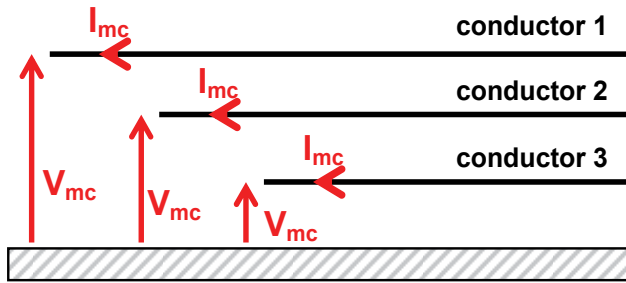


Fig. 2. Representation of the common mode currents and voltages in the modal basis for a 3-conductor cable bundle

z_i being determined, it is easy to determine Z_{mc} . The common mode voltage V_{mc} is assumed to be identical on all the conductors of the cable bundle and Z_{mc} equals the common mode impedance of the cable bundle when all the conductors are short-circuited as it is shown in Fig. 3.

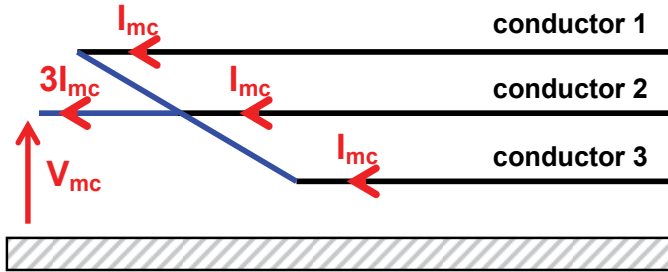


Fig. 3. Physical representation of the common mode characteristic impedance of a cable bundle

On the example in Fig. 3, Z_{mc} can be written:

$$Z_{mc} = \frac{V_{mc}}{3I_{mc}} = \frac{z_i}{3} \quad (7)$$

In the general case of a N-conductor cable bundle, equation (8) provides Z_{mc} from z_i :

$$Z_{mc} = \frac{z_i}{N} \quad (8)$$

Each group of conductors made in this step corresponds to one equivalent conductor of the reduced cable bundle. Thus, each multiconductor cable bundle can be modelled by a reduced cable bundle containing between one to four equivalent conductors according to the terminal load configurations at the end of all the conductors of the initial cable bundle. From a physical point of view, this operation consists in grouping together conductors having a similar distribution of current which is strongly dependent of terminal loads.

2.2 Determination of the per-unit-length matrices of the reduced cable bundle

Group current and group voltage: The second step of the method consists in determining the inductance [$L_{reduced}$] and capacitance [$C_{reduced}$] matrices of the reduced cable bundle by

making a simple assumption which considers a short-circuit between all the conductors of a group. This assumption first allows defining a group current I_{EC} and a group voltage V_{EC} for each group of conductors. As an example, the group current and the group voltage of a group containing N conductors can be written:

$$I_{EC} = I_1 + I_2 + \dots + I_N \tag{9}$$

$$V_{EC} = V_1 = V_2 = \dots = V_N \tag{10}$$

From this point, in order to clearly present the demonstration allowing to obtain the inductance matrix of a reduced cable bundle containing 4 equivalent conductors from an initial cable bundle containing N conductors, the authors prefer to change the index of the conductors belonging to the same group. Thus:

- the N_1 conductors of the first group have the index 1 to α ;
- the N_2 conductors of the second group have the index $\alpha+1$ to β ;
- the N_3 conductors of the third group have the index $\beta+1$ to γ ;
- the N_4 conductors of the fourth group have the index $\gamma+1$ to N .

Determination of the inductance matrix of the reduced cable bundle: In the MTL formalism, the inductance matrix links the currents and the voltages on each conductor on an infinitesimal segment of length dz :

$$\frac{\partial}{\partial z} \begin{bmatrix} V_1 \\ V_2 \\ \vdots \\ V_N \end{bmatrix} = -j \cdot \omega \cdot \begin{bmatrix} L_{11} & L_{12} & \dots & L_{1N} \\ L_{21} & L_{22} & \dots & L_{2N} \\ \vdots & \vdots & \ddots & \vdots \\ L_{N1} & L_{N2} & \dots & L_{NN} \end{bmatrix} \cdot \begin{bmatrix} I_1 \\ I_2 \\ \vdots \\ I_N \end{bmatrix} \tag{11}$$

The determination of the $[L_{reduced}]$ matrix requires two additional assumptions. To present and clearly justify these new assumptions, the currents flowing along all the N conductors of a cable bundle are decomposed in Fig.4 in common mode currents I_{c_i} and differential current $I_{d_{ij}}$.

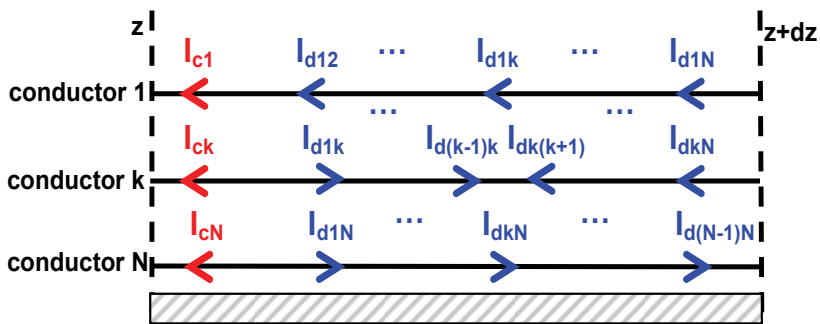


Fig. 4. Decomposition of the common and differential mode currents on a cable bundle containing N conductors

Thus, the currents I_1 , I_k and I_N on conductors 1, k and N can be expressed according to the decomposition in common and differential mode currents:

$$I_1 = I_{c1} + \sum_{i=2}^N I_{d1i} \quad (12)$$

$$I_k = I_{ck} - \sum_{i=1}^{k-1} I_{dik} + \sum_{i=k+1}^N I_{dki} \quad (13)$$

$$I_N = I_{cN} - \sum_{i=1}^{N-1} I_{diN} \quad (14)$$

In eq. (11), currents I_i can be replaced by general expressions reported in equations (12), (13), (14). When developing the system, the k^{th} line of the system can be written in this form:

$$\frac{\partial V_k}{\partial x} = -j \cdot \omega \left[\sum_{i=1}^N (L_{ki} \cdot I_{ci}) + \sum_{i=1}^{N-1} \sum_{j=i+1}^N (I_{dij} \cdot (L_{ki} - L_{kj})) \right] \quad (15)$$

Consequently the per-unit-length voltage $\frac{\partial V_k}{\partial x}$ on a infinitesimal segment of length dx equals the sum of a term depending of the common mode currents I_{ci} and a term depending of differential mode currents I_{dij} between conductor k and all the other conductors. The assumption made in the method consists in considering that the second term can be neglected compared to the first term depending on the common mode currents. Indeed, in an EM immunity problem, the common mode current induced on a multiconductor cable bundle may be considered as larger than differential currents. This assumption can be generalized with the following equation:

$$L_{ki} \cdot I_{ci} \gg \sum_{i=1}^{N-1} \sum_{j=i+1}^N (I_{dij} \cdot (L_{ki} - L_{kj})) \quad (16)$$

The following matrix system linking the voltages on each conductor V_i to the common mode current on each conductor I_{ci} can then be written:

$$\frac{\partial}{\partial z} \begin{bmatrix} V_1 \\ V_2 \\ \vdots \\ V_N \end{bmatrix} = -j \cdot \omega \cdot \begin{bmatrix} L_{11} & L_{12} & \cdots & L_{1N} \\ L_{21} & L_{22} & \cdots & L_{2N} \\ \vdots & \vdots & \ddots & \vdots \\ L_{N1} & L_{N2} & \cdots & L_{NN} \end{bmatrix} \cdot \begin{bmatrix} I_{c1} \\ I_{c2} \\ \vdots \\ I_{cN} \end{bmatrix} \quad (17)$$

The second assumption consists in considering that the common mode current on all the conductors of a group is identical on each conductor. This assumption can be written in this form for a group of N conductors:

$$I_{ck} = \frac{I_{EC}}{N} \quad (18)$$

where I_{EC} is the group current and I_{ck} is the common mode current on a conductor of index k in the group. This second assumption allows writing the matrix system in this form:

$$\begin{aligned}
 \frac{\partial V_1}{\partial x} &= -j.\omega. \left[\frac{\sum_{j=1}^{\alpha} L_{1j}}{N_1} .I_{EC1} + \frac{\sum_{j=\alpha+1}^{\beta} L_{1j}}{N_2} .I_{EC2} + \frac{\sum_{j=\beta+1}^{\gamma} L_{1j}}{N_3} .I_{EC3} + \frac{\sum_{j=\gamma+1}^N L_{1j}}{N_4} .I_{EC4} \right] \\
 &\vdots \\
 \frac{\partial V_k}{\partial x} &= -j.\omega. \left[\frac{\sum_{j=1}^{\alpha} L_{kj}}{N_1} .I_{EC1} + \frac{\sum_{j=\alpha+1}^{\beta} L_{kj}}{N_2} .I_{EC2} + \frac{\sum_{j=\beta+1}^{\gamma} L_{kj}}{N_3} .I_{EC3} + \frac{\sum_{j=\gamma+1}^N L_{kj}}{N_4} .I_{EC4} \right] \\
 &\vdots \\
 \frac{\partial V_\delta}{\partial x} &= -j.\omega. \left[\frac{\sum_{j=1}^{\alpha} L_{Nj}}{N_1} .I_{EC1} + \frac{\sum_{j=\alpha+1}^{\beta} L_{Nj}}{N_2} .I_{EC2} + \frac{\sum_{j=\beta+1}^{\gamma} L_{Nj}}{N_3} .I_{EC3} + \frac{\sum_{j=\gamma+1}^N L_{Nj}}{N_4} .I_{EC4} \right]
 \end{aligned} \tag{19}$$

where I_{EC1} , I_{EC2} , I_{EC3} and I_{EC4} are the group current of all the equivalent conductors.

It is reminded that the voltages on each conductor belonging to a same group are considered as equal. Consequently, the $N*N$ matrix system of equation (19) can be reduced to a simplified $4*4$ matrix system relating the group currents and the groups voltages on the four groups of conductors as follows:

$$\begin{aligned}
 \frac{\partial V_{EC1}}{\partial x} &= -j.\omega. \left[\frac{\sum_{i=1}^{\alpha} \sum_{j=1}^{\alpha} L_{ij}}{N_1^2} .I_{EC1} + \frac{\sum_{i=1}^{\alpha} \sum_{j=\alpha+1}^{\beta} L_{ij}}{N_1.N_2} .I_{EC2} + \frac{\sum_{i=1}^{\alpha} \sum_{j=\beta+1}^{\gamma} L_{ij}}{N_1.N_3} .I_{EC3} + \frac{\sum_{i=1}^{\alpha} \sum_{j=\gamma+1}^N L_{ij}}{N_1.N_4} .I_{EC4} \right] \\
 \frac{\partial V_{EC2}}{\partial x} &= -j.\omega. \left[\frac{\sum_{i=\alpha+1}^{\beta} \sum_{j=1}^{\alpha} L_{ij}}{N_1.N_2} .I_{EC1} + \frac{\sum_{i=\alpha+1}^{\beta} \sum_{j=\alpha+1}^{\beta} L_{ij}}{N_2^2} .I_{EC2} + \frac{\sum_{i=\alpha+1}^{\beta} \sum_{j=\beta+1}^{\gamma} L_{ij}}{N_2.N_3} .I_{EC3} + \frac{\sum_{i=\alpha+1}^{\beta} \sum_{j=\gamma+1}^N L_{ij}}{N_2.N_4} .I_{EC4} \right] \\
 \frac{\partial V_{EC3}}{\partial x} &= -j.\omega. \left[\frac{\sum_{i=\beta+1}^{\gamma} \sum_{j=1}^{\alpha} L_{ij}}{N_1.N_3} .I_{EC1} + \frac{\sum_{i=\beta+1}^{\gamma} \sum_{j=\alpha+1}^{\beta} L_{ij}}{N_2.N_3} .I_{EC2} + \frac{\sum_{i=\beta+1}^{\gamma} \sum_{j=\beta+1}^{\gamma} L_{ij}}{N_3^2} .I_{EC3} + \frac{\sum_{i=\beta+1}^{\gamma} \sum_{j=\gamma+1}^N L_{ij}}{N_3.N_4} .I_{EC4} \right] \\
 \frac{\partial V_{EC4}}{\partial x} &= -j.\omega. \left[\frac{\sum_{i=\gamma+1}^N \sum_{j=1}^{\alpha} L_{ij}}{N_1.N_4} .I_{EC1} + \frac{\sum_{i=\gamma+1}^N \sum_{j=\alpha+1}^{\beta} L_{ij}}{N_2.N_4} .I_{EC2} + \frac{\sum_{i=\gamma+1}^N \sum_{j=\beta+1}^{\gamma} L_{ij}}{N_3.N_4} .I_{EC3} + \frac{\sum_{i=\gamma+1}^N \sum_{j=\gamma+1}^N L_{ij}}{N_4^2} .I_{EC4} \right]
 \end{aligned} \tag{20}$$

where V_{EC1} , V_{EC2} , V_{EC3} and V_{EC4} are the group voltages of the 4 equivalent conductors. Finally, with the assumptions made, a 4*4 reduced matrix system corresponding to the reduced cable bundle is obtained and the $[L_{reduced}]$ matrix appears:

$$\frac{\partial}{\partial x} \begin{bmatrix} V_{EC1} \\ V_{EC2} \\ V_{EC3} \\ V_{EC4} \end{bmatrix} = -j \cdot \omega \cdot [L_{reduced}] \cdot \begin{bmatrix} I_{EC1} \\ I_{EC2} \\ I_{EC3} \\ I_{EC4} \end{bmatrix} \quad (21)$$

Each diagonal term of $[L_{reduced}]$ corresponds to the MTL inductance of an equivalent conductor of the reduced cable bundle with respect to the ground reference. It is equal to the sum of each diagonal and off-diagonal inductance terms of the initial $[L]$ matrix between all the conductors of the group divided by the square of the number of conductors of the group.

Off-diagonal terms of $[L_{reduced}]$ represent the mutual inductance between both groups of conductors and equal the sum of the mutual inductances between all the conductors belonging to two different groups divided by the number of conductors of both groups.

As an example, the following 7-conductors cable bundle has been studied.

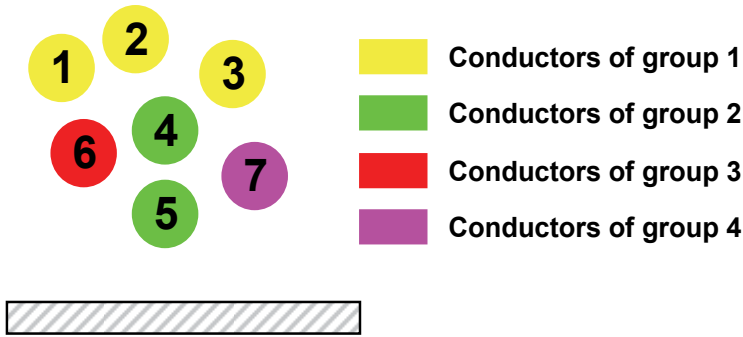


Fig. 5. Example of groups of conductors of a 7-conductor cable bundle

The reduced inductance matrix of the reduced cable bundle containing 4 equivalent conductors equals:

$$[L_{reduced}] = \begin{bmatrix} \frac{L_{11} + L_{22} + L_{33} + 2.L_{12} + 2.L_{13} + 2.L_{23}}{9} & \dots & \dots & \dots \\ \frac{L_{14} + L_{15} + L_{24} + L_{25} + L_{34} + L_{35}}{6} & \frac{L_{44} + L_{55} + 2.L_{45}}{3} & \dots & \dots \\ \frac{L_{16} + L_{26} + L_{36}}{3} & \frac{L_{46} + L_{56}}{2} & L_{66} & \dots \\ \frac{L_{17} + L_{27} + L_{37}}{3} & \frac{L_{47} + L_{57}}{2} & L_{67} & L_{77} \end{bmatrix} \quad (22)$$

Determination of the capacitance matrix of the reduced cable bundle: In the MTL formalism, the the capacitance matrix links the currents and the voltages on each conductor on an infinitesimal segment of length dx :

$$\frac{\partial}{\partial z} \begin{bmatrix} I_1 \\ I_2 \\ \vdots \\ I_N \end{bmatrix} = -j \cdot \omega \cdot \begin{bmatrix} C_{11} & C_{12} & \cdots & C_{1N} \\ C_{21} & C_{22} & \cdots & C_{2N} \\ \vdots & \vdots & \ddots & \vdots \\ C_{N1} & C_{N2} & \cdots & C_{NN} \end{bmatrix} \cdot \begin{bmatrix} V_1 \\ V_2 \\ \vdots \\ V_N \end{bmatrix} \quad (23)$$

The determination of the capacitance matrix depends of the medium surrounding all the conductors and the ground reference of the cable bundle.

In a homogeneous medium (generally air), all the modes have the same propagation velocity v depending of the light velocity in the vacuum ($C=3.10^8\text{m.s}^{-1}$) and the relative dielectric permittivity ϵ_r of the medium:

$$v = \frac{C}{\sqrt{\epsilon_r}} \quad (24)$$

The capacitance matrix of the reduced cable bundle $[C_{\text{reduced}}]$ is then directly obtained with this simple formula:

$$[C_{\text{reduced}}] = \frac{1}{v^2} \cdot [L_{\text{reduced}}]^{-1} \quad (25)$$

In a inhomogeneous medium where all the conductors are surrounded by a non uniform dielectric medium as for example various insulating dielectric coatings, equation (25) cannot be used to derive the $[C_{\text{reduced}}]$ matrix.

Replacing voltages V_i on each conductor by the group voltage V_{CEi} of each group of index i and developing the matrix system, equation (23) can be written:

$$\begin{aligned} \frac{\partial I_1}{\partial x} &= j \cdot \omega \cdot \left[\sum_{j=1}^{\alpha} C_{1j} \cdot V_{EC1} + \sum_{j=\alpha+1}^{\beta} C_{1j} \cdot V_{EC2} + \sum_{j=\beta+1}^{\gamma} C_{1j} \cdot V_{EC3} + \sum_{j=\gamma+1}^N C_{1j} \cdot V_{EC4} \right] \\ &\vdots \\ \frac{\partial I_k}{\partial x} &= j \cdot \omega \cdot \left[\sum_{j=1}^{\alpha} C_{kj} \cdot V_{EC1} + \sum_{j=\alpha+1}^{\beta} C_{kj} \cdot V_{EC2} + \sum_{j=\beta+1}^{\gamma} C_{kj} \cdot V_{EC3} + \sum_{j=\gamma+1}^N C_{kj} \cdot V_{EC4} \right] \\ &\vdots \\ \frac{\partial I_\delta}{\partial x} &= j \cdot \omega \cdot \left[\sum_{j=1}^{\alpha} C_{Nj} \cdot V_{EC1} + \sum_{j=\alpha+1}^{\beta} C_{Nj} \cdot V_{EC2} + \sum_{j=\beta+1}^{\gamma} C_{Nj} \cdot V_{EC3} + \sum_{j=\gamma+1}^N C_{Nj} \cdot V_{EC4} \right] \end{aligned} \quad (26)$$

Then, the common mode current of each group of conductors can be calculated by adding all the lines corresponding to the current I_i if i is a conductor of the group. Thus, a 4×4 matrix system is obtained from the $N \times N$ matrix system linked to the initial cable bundle.

This reduced matrix system, a 4×4 matrix system the $[C_{\text{reduced}}]$ matrix having a dimension equal to the number of groups of conductors made in the first step of the method.

Applying the simple assumptions described in this section, the reduced matrix system of the MTL obtained has a dimension equal to the number of groups of conductors made in the first step of the procedure.

$$\begin{aligned}
 \frac{\partial I_{EC1}}{\partial x} &= j.\omega. \left[\sum_{i=1}^{\alpha} \sum_{j=1}^{\alpha} C_{ij}.V_{EC1} + \sum_{i=1}^{\alpha} \sum_{j=\alpha+1}^{\beta} C_{ij}.V_{EC2} + \sum_{i=1}^{\alpha} \sum_{j=\beta+1}^{\gamma} C_{ij}.V_{EC3} + \sum_{i=1}^{\alpha} \sum_{j=\gamma+1}^N C_{ij}.V_{EC4} \right] \\
 \frac{\partial I_{EC2}}{\partial x} &= j.\omega. \left[\sum_{i=\alpha+1}^{\beta} \sum_{j=1}^{\alpha} C_{ij}.V_{EC1} + \sum_{i=\alpha+1}^{\beta} \sum_{j=\alpha+1}^{\beta} C_{ij}.V_{EC2} + \sum_{i=\alpha+1}^{\beta} \sum_{j=\beta+1}^{\gamma} C_{ij}.V_{EC3} + \sum_{i=\alpha+1}^{\beta} \sum_{j=\gamma+1}^N C_{ij}.V_{EC4} \right] \\
 \frac{\partial I_{EC3}}{\partial x} &= j.\omega. \left[\sum_{i=\beta+1}^{\gamma} \sum_{j=1}^{\alpha} C_{ij}.V_{EC1} + \sum_{i=\beta+1}^{\gamma} \sum_{j=\alpha+1}^{\beta} C_{ij}.V_{EC2} + \sum_{i=\beta+1}^{\gamma} \sum_{j=\beta+1}^{\gamma} C_{ij}.V_{EC3} + \sum_{i=\beta+1}^{\gamma} \sum_{j=\gamma+1}^N C_{ij}.V_{EC4} \right] \\
 \frac{\partial I_{EC4}}{\partial x} &= j.\omega. \left[\sum_{i=\gamma+1}^N \sum_{j=1}^{\alpha} C_{ij}.V_{EC1} + \sum_{i=\gamma+1}^N \sum_{j=\alpha+1}^{\beta} C_{ij}.V_{EC2} + \sum_{i=\gamma+1}^N \sum_{j=\beta+1}^{\gamma} C_{ij}.V_{EC3} + \sum_{i=\gamma+1}^N \sum_{j=\gamma+1}^N C_{ij}.V_{EC4} \right]
 \end{aligned} \tag{27}$$

Equation(28) presents the reduced matrix system obtained in a condensed form.

$$\frac{\partial}{\partial x} \begin{bmatrix} I_{EC1} \\ I_{EC2} \\ I_{EC3} \\ I_{EC4} \end{bmatrix} = j.\omega. [C_{reduced}] \cdot \begin{bmatrix} V_{EC1} \\ V_{EC2} \\ V_{EC3} \\ V_{EC4} \end{bmatrix} \tag{28}$$

The $[C_{reduced}]$ capacitance matrix corresponding to the cable bundle presented in Fig. 5 can be written:

$$[C_{reduced}] = \begin{bmatrix} C_{11} + C_{22} + C_{33} + 2.C_{12} + 2.C_{13} + 2.C_{23} & \dots & \dots & \dots \\ C_{14} + C_{15} + C_{24} + C_{25} + C_{34} + C_{35} & C_{44} + C_{55} + 2.C_{45} & \dots & \dots \\ C_{16} + C_{26} + C_{36} & C_{46} + C_{56} & C_{66} & \dots \\ C_{17} + C_{27} + C_{37} & C_{47} + C_{57} & C_{67} & C_{77} \end{bmatrix} \tag{29}$$

Diagonal terms of the reduced capacitance matrix $[C_{reduced}]$ equal the sum of the physical capacitances between each conductor of the group and the ground reference minus all the physical capacitances between two conductors belonging to the group. As an example, the $C_{22_reduced}$ term of the Fig.5 $[C_{reduced}]$ matrix can be expressed in this following form according to the physical capacitances:

$$C_{22_reduced} = \sum_{i=1}^N C_{4i}^p + \sum_{i=1}^N C_{5i}^p - 2.C_{45}^p \tag{30}$$

Off-diagonal terms of the $[C_{reduced}]$ matrix represents either the mutual capacitances between two equivalent conductors or between both corresponding groups of conductors.

In this example, the $C_{12_reduced}$ term corresponds to the mutual capacitances between equivalent conductors 1 and 2. The value of $C_{12_reduced}$ can be expressed with respect to the physical capacitances existing between the various conductors of group 1 and group 2 in the initial cable bundle.

$$C_{12_reduced}^p = C_{14}^p + C_{15}^p + C_{24}^p + C_{25}^p + C_{34}^p + C_{35}^p \tag{31}$$

Thus, the physical capacitances existing between two equivalent conductors equals the sum of all the physical capacitances existing between 2 conductors belonging to these two different groups.

2.3 Procedure used to obtain the cross-section geometry of a reduced cable bundle

The aim of the third step of the method is to create the cross-section geometry of the reduced cable bundle. This operation is not mandatory and is only required in case of a 3D modeling. Indeed, for a MTL simulation, the reduced inductance and capacitance matrices obtained in the previous step are sufficient and can be directly introduced in the MTL models.

The procedure developed in this method requires 6 phases detailed in the following. It makes the assumption that the ground reference is a plane.

In the first phase, the height h_i of each equivalent conductor with respect to the ground reference is chosen by the user to be coherent with the geometry of the initial cable bundle. For example, the height of an equivalent conductor can be the mean of the height of all the conductors belonging to the corresponding group.

In the second phase, the radius r_i of each equivalent conductor is calculated with the well-known approximated analytical formula giving the inductance L_{ii} of a wire upon a ground plane.

$$r_i = \frac{2 \cdot h_i}{e^{\frac{L_{ii}}{\mu_0}}} \quad (32)$$

where h_i and r_i are respectively the height of the conductor over the ground reference and its radius.

In the third phase, distances d_{ij} between equivalent conductors of index i and j are calculated with the analytical formula giving the mutual inductances L_{ij} between two conductors above a ground plane:

$$d_{ij} = \sqrt{\frac{4 \cdot h_i \cdot h_j}{e^{\frac{L_{ij}}{\mu_0}} - 1}} \quad (33)$$

where h_i and h_j are the height of equivalent conductors i and j with respect to the ground reference.

After the first three phases, a first cross-section of the reduced cable bundle is obtained; the geometry is only an approached one. Indeed, the analytical formulas used are approximated. The use of an electrostatic code allows to obtain a cross-section geometry which perfectly matches the inductance and capacitance matrix of the reduced cable bundle obtained in the previous step could help but would not give a fully optimized solution. Indeed, this process is necessarily iterative and may not give a unique solution.

By using an electrostatic code, the objective is to optimized the radius and the distances between all the equivalent conductors to get a good convergence with the $[L_{\text{reduced}}]$ matrix.

In the case where all the conductors of the initial cable bundle are not surrounded by a dielectric coating (not a realistic situation for electrical wiring in systems), the building of the cross-section geometry is completed. Otherwise, two additional phases are required.

In the fifth phase, the thickness of all the dielectric coating ϵ_r surrounding each equivalent conductor is fixed to avoid overlapping.

In the sixth and last phase, on optimization is made on the relative permittivity of the dielectric coating surrounding all the equivalent conductors. The objective of the optimization process is to calculate ϵ_r in order to comply the C_{ii} terms surrounding all the equivalent conductors in order to respect the C_{ii} term of the $[C_{\text{reduced}}]$ matrix obtained at step 2. This process is also an

iterative process which requires the use of an electrostatic two dimensional (2D) code solving Laplace's equation.

The six-phase procedure used to determine the cross-section geometry of the reduced cable bundle is illustrated in Fig. 6 for a 3 equivalent conductor:

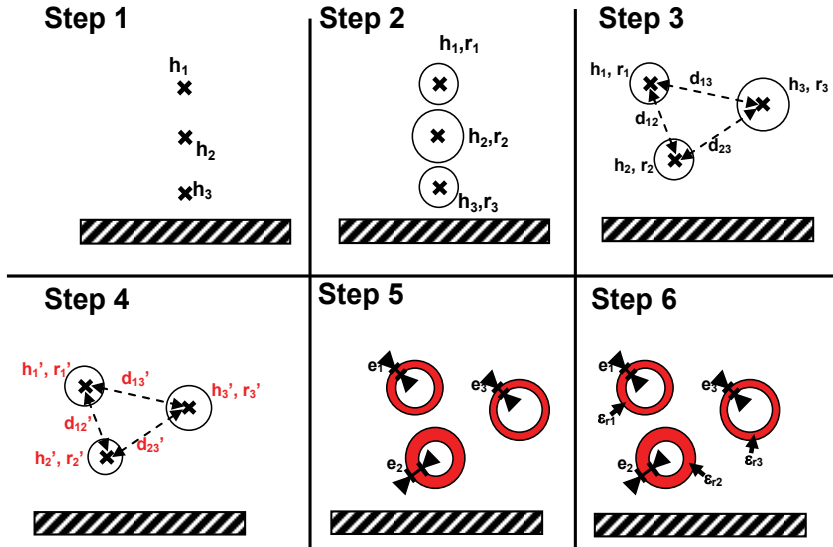


Fig. 6. Illustration on 3 equivalent conductors of the 6-phases procedure used to build the cross-section geometry of a reduced cable bundle

2.4 Equivalent termination loads of the reduced cable bundle

In the fourth and last step of the procedure, the objective is to determine the equivalent termination loads to be connected at each end of the equivalent conductors of the reduced cable bundle. Two kinds of loads have to be distinguished: termination loads connecting the end of a conductor to the ground reference which are called common-mode loads and termination loads connecting the ends of two conductors called differential loads.

Common-mode loads: Conductors of the same group are considered as short-circuited together as it is shown on the left of Fig. 7.

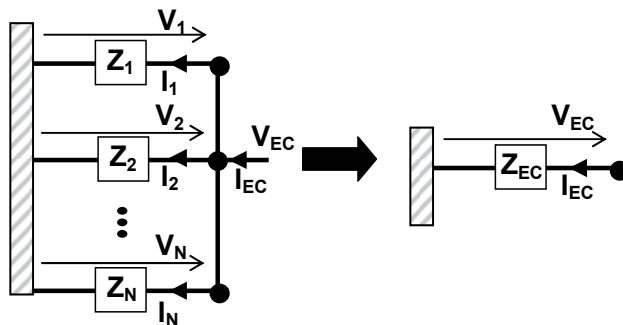


Fig. 7. Terminal impedance network of a group of conductors and equivalent load at the end of the corresponding equivalent conductor

Consequently, the group current I_{EC} can be expressed with respect to this straightforward equation according to the group voltage V_{EC} :

$$I_{EC} = I_1 + I_2 + \dots + I_N = V_{EC} \cdot \left(\frac{1}{Z_1} + \frac{1}{Z_2} + \dots + \frac{1}{Z_N} \right) \tag{34}$$

Thus, the termination load Z_{EC} at one end of an equivalent conductor equals all the termination loads of all the conductors of the corresponding group at the same end set in parallel.

$$Z_{EC} = \frac{1}{\left(\frac{1}{Z_1} + \frac{1}{Z_2} + \dots + \frac{1}{Z_N} \right)} = Z_1 // Z_2 // \dots // Z_N \tag{35}$$

Differential loads: Two kind of differential loads have to be considered depending if the load connects two conductors belonging to the same group or not.

The case of differential loads connecting two conductors belonging to the same group is illustrated in Fig. 8 on a group of 3 conductors having three differential loads Z_{12} , Z_{13} and Z_{23} .

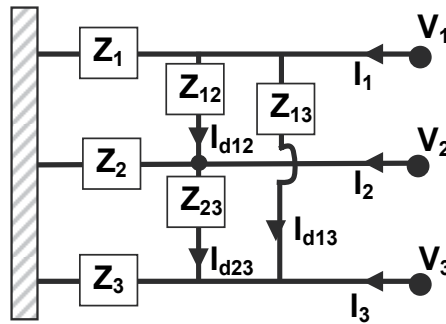


Fig. 8. Terminal impedance network of a 3-conductor group having 3 differential loads: Z_{12} , Z_{13} and Z_{23}

The admittance matrix of this termination load network is:

$$\begin{bmatrix} I_1 \\ I_2 \\ I_3 \end{bmatrix} = \begin{bmatrix} \frac{1}{Z_1} + \frac{1}{Z_{12}} + \frac{1}{Z_{13}} & -\frac{1}{Z_{12}} & -\frac{1}{Z_{13}} \\ -\frac{1}{Z_{12}} & \frac{1}{Z_2} + \frac{1}{Z_{12}} + \frac{1}{Z_{13}} & -\frac{1}{Z_{23}} \\ -\frac{1}{Z_{13}} & -\frac{1}{Z_{23}} & \frac{1}{Z_3} + \frac{1}{Z_{12}} + \frac{1}{Z_{13}} \end{bmatrix} \begin{bmatrix} V_1 \\ V_2 \\ V_3 \end{bmatrix} \tag{36}$$

For this group of conductors, the hypothesis of the method is applied:

$$I_{EC} = I_1 + I_2 + I_3 \tag{37}$$

$$V_{EC} = V_1 = V_2 = V_3 \tag{38}$$

Consequently, the I_{EC} group current can be expressed in this simple form:

$$I_{cm} = I_1 + I_2 + I_3 = \frac{V_1}{Z_1} + \frac{V_2}{Z_2} + \frac{V_3}{Z_3} \quad (39)$$

Equation(39) clearly shows that the group current does not depend of differential loads connecting two conductors of the same group hypothesis. Consequently, in the method, this type of differential loads is neglected.

The case of differential loads connecting two conductors belonging to two different groups (conductors 1 and 2 in group 1, conductors 3 and 4 in group 2) is illustrated in Fig. 9 with the loads Z_{13} and Z_{24} .

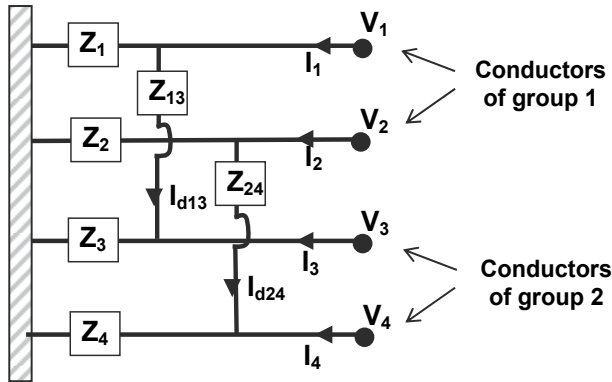


Fig. 9. Terminal impedance network of two groups of 2 conductors having 2 differential loads : Z_{13} and Z_{24}

The admittance matrix of this terminal load network can be written:

$$\begin{bmatrix} I_1 \\ I_2 \\ I_3 \\ I_4 \end{bmatrix} = \begin{bmatrix} \frac{1}{Z_1} + \frac{1}{Z_{13}} & 0 & -\frac{1}{Z_{13}} & 0 \\ 0 & \frac{1}{Z_2} + \frac{1}{Z_{24}} & 0 & -\frac{1}{Z_{24}} \\ -\frac{1}{Z_{13}} & 0 & \frac{1}{Z_1} + \frac{1}{Z_{13}} & 0 \\ 0 & -\frac{1}{Z_{24}} & 0 & \frac{1}{Z_2} + \frac{1}{Z_{24}} \end{bmatrix} \cdot \begin{bmatrix} V_1 \\ V_2 \\ V_3 \\ V_4 \end{bmatrix} \quad (40)$$

For this example, the hypothesis of the method are the following ones :

$$I_{EC1} = I_1 + I_2 \quad (41)$$

$$I_{EC2} = I_3 + I_4 \quad (42)$$

$$V_{EC1} = V_1 = V_2 \quad (43)$$

$$V_{EC2} = V_3 = V_4 \quad (44)$$

Thanks to the admittance matrix of the terminal load network and the hypothesis of the method, group currents I_{EC1} and I_{EC2} can be written:

$$I_{EC1} = I_1 + I_2 = \frac{V_1}{Z_1} + \frac{V_2}{Z_2} + (V_{EC1} - V_{EC2}) \cdot \left(\frac{1}{Z_{13}} + \frac{1}{Z_{24}} \right) \quad (45)$$

$$I_{EC2} = I_3 + I_4 = \frac{V_3}{Z_3} + \frac{V_4}{Z_4} + (V_{EC2} - V_{EC1}) \cdot \left(\frac{1}{Z_{13}} + \frac{1}{Z_{24}} \right) \quad (46)$$

Both equations lead to the conclusion that the common mode current of a group of conductors depends of the common mode loads (Z_1 , Z_2 , Z_3 and Z_4 in this example) and of the differential loads connected to conductors belonging to the other groups (Z_{13} and Z_{24} in this example).

Thus, the group current I_{EC1} depends of the differential voltage between the first and the second group of conductors ($V_{CE1} - V_{CE2}$) multiplied by the differential loads placed between the conductors belonging to different groups Z_{13} and Z_{24} set in parallel.

Thus, the terminal load network to be placed in this example at the end of both equivalent conductors is presented in Fig. 10.

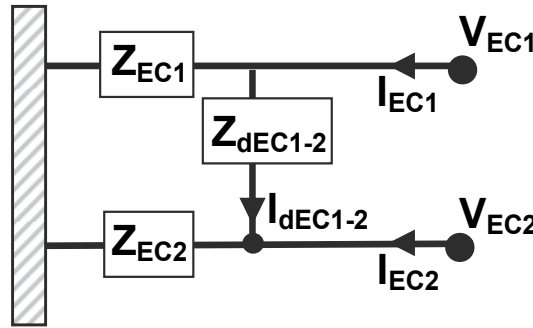


Fig. 10. Terminal load network at the extremity of both equivalent conductors

The terminal load values of this network have the following expressions:

$$Z_{EC1} = \frac{1}{\frac{1}{Z_1} + \frac{1}{Z_2}} = Z_1 // Z_2 \quad (47)$$

$$Z_{EC2} = \frac{1}{\frac{1}{Z_3} + \frac{1}{Z_4}} = Z_3 // Z_4 \quad (48)$$

$$Z_{dEC1-2} = \frac{1}{\frac{1}{Z_{13}} + \frac{1}{Z_{24}}} = Z_{13} // Z_{24} \quad (49)$$

In the general case, the equivalent terminal loads between two equivalent conductors equal all the differential loads connecting conductors of the two groups in parallel.

Consequently, the method is able to take into account all the types of terminal load networks made of resistive loads.

2.5 Example of application

To present a concrete example of use of the method in immunity, a 4-conductor cable bundle of 1m length and located at a distance of 2 cm from a perfect electric ground has been studied.

The following table presents the terminal loads of all the conductors having a 1 mm radius at both extremities:

	Conductor 1	Conductor 2	Conductor 3	Conductor 4
End 1	24 Ω	10 Ω	59 Ω	63 Ω
End 2	50 Ω	22 Ω	38 Ω	16 Ω

Table 2. - Values of the common mode loads connected at the ends of each conductor of the cable bundle

Considering the terminal load values and the common mode characteristic impedance of the initial cable bundle ($Z_{mc} = 161 \Omega$), the reduced cable bundle only requires one equivalent conductor connected at both ends by loads of respective values 5.7 and 6.5 Ω.

Fig. 11. presents the cross-section geometry of the initial cable bundle and of the corresponding reduced cable bundle containing one equivalent conductor.

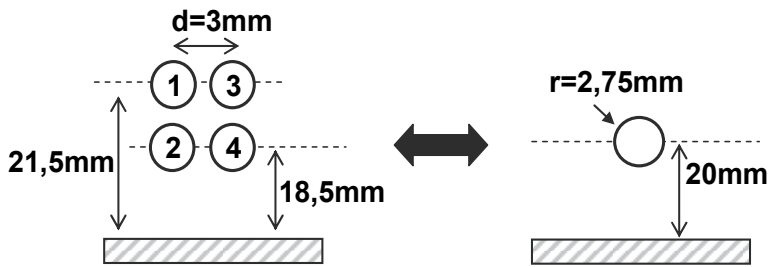


Fig. 11. Cross-section geometry of the initial cable bundle and of the corresponding equivalent conductor

The per-unit-length inductance and capacitance matrices of the initial cable bundle are given in the following (the matrices are symmetric and lower off-diagonal terms have not been written):

$$[L] = \begin{bmatrix} 694.3 & 501.6 & 511.6 & 455.5 \\ & 674.2 & 455.5 & 491.6 \\ & & 694.3 & 501.6 \\ & & & 674.2 \end{bmatrix} nH / m \quad (50)$$

$$[C] = \begin{bmatrix} 45.8 & -19.1 & -19.3 & -2.7 \\ & 46.2 & -2.7 & -18.8 \\ & & 45.8 & -19.1 \\ & & & 46.2 \end{bmatrix} pF / m \quad (51)$$

The per-unit-length inductance and capacitance of the equivalent conductor are respectively $L=536 \text{ nH/m}$ and $C=20.8 \text{ pF/m}$.

Both cable bundles are supposed to be illuminated by a plane wave of 3 V/m amplitude propagating in the direction of the cables. The electric field component is oriented vertically compared to the ground reference.

Fig. 12. presents the comparison between the common mode current (in dBA) induced at the first end of the initial cable bundle and the current on the corresponding equivalent conductor at the same end. The calculations have been performed with the FEKO software using the method of moments (MoM) to solve Maxwell's equations.

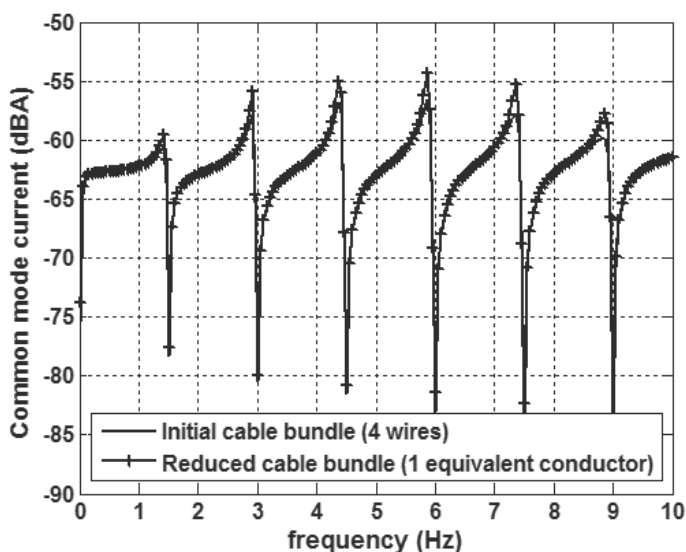


Fig. 12. Comparison of common mode current induced at the first end of both cable bundles (initial and reduced) by a 3V/m plane wave

The excellent agreement between both curves shows the high accuracy of the method. Moreover, the total computation times required to compute the $[Z]$ impedance matrix in MoM has been divided by a factor higher than 10 for this simple modelling.

3. The “Equivalent Cable Bundle Method” for emission problems

3.1 Specificity of the EM emission problem

In EM immunity problems, all the conductors are excited by the same EM incident field whereas in EM emission problems, each conductor of a cable bundle can be excited by sources of different amplitudes and internal impedances in different frequency ranges (or for different time domain spectrums). Consequently, the application of the method requires specific adjustments to be applied for EM emission problems.

In the following sub-section, the procedure required to define the electric and geometric characteristics of a reduced cable bundle for an emission problem (Andrieu et al., 2009) is presented. As in the previous section, the method is described on a point-to-point cable link. To be applied on a tree-like cable network, the procedure has to be repeated on each path of conductors inside the network.

The authors make precise that the whole problem is considered in the frequency domain and the excitation sources are restricted to voltage sources localized at conductor ends.

3.2 Presentation of the modified procedure

For EM emission problems, the procedure required to constitute the groups of conductors is decomposed in two phases to take into account the second degree of freedom due to the fact that each conductor of the cable bundle can be excited by its own source.

After a first classification of all the conductors of the initial cable bundle in four groups as it is made for an EM immunity problem, a second phase is made inside the groups according to the magnitude of the voltage source applied on each conductor belonging to the same group. The objective is to avoid that two conductors belonging to the same group are excited by sources having significant amplitude difference. Indeed, this configuration could lead to important differential currents between both conductors of a same group not taken into account by only one equivalent conductor. As it has been explained in section 2, the method assumes that the EM emissions of a cable bundle mainly come from the common mode current. Thus, the differential mode currents are neglected. The ratio of the voltage source magnitude applied on two conductors belonging to the same group must not be higher than a factor 3, 5 or 10 according to the accuracy aimed in the calculation.

Then, the three steps presented in sub-sections 2.2, 2.3 and 2.4 are performed identically.

Finally, a fifth additional step is required to determine the equivalent voltage sources used to excite each equivalent conductor. Fig. 13. presents an example of a N-conductor group where each conductor is lumped by a resistance Z_i and excited by a voltage source V_i . The equivalent voltage source V_{EC} and terminal load Z_{EC} to connect at the end of the corresponding equivalent conductor are also presented in the figure.

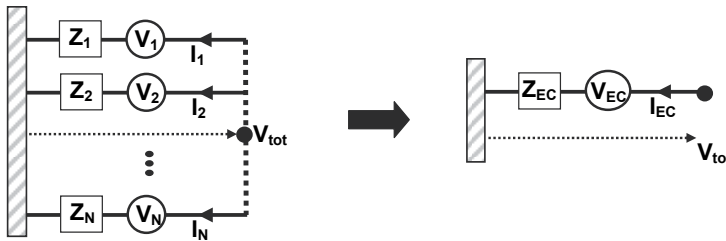


Fig. 13. Equivalent voltage source and impedance of an equivalent conductor corresponding to a 4-conductor group

According to Fig. 13, the current I_i flowing along conductor i belonging to the group of 4 conductors and the current I_{EC} on the corresponding equivalent conductor can be written:

$$I_i = \frac{V_{tot} - V_i}{Z_i} \quad (52)$$

$$I_{EC} = \frac{V_{tot} - V_{EC}}{Z_{EC}} \quad (53)$$

With (52), the common mode current I_{EC} of the 4-conductor group can be expressed in this simple form:

$$I_{EC} = \frac{V_{tot}}{Z_{EC}} - \left(\frac{V_1}{Z_1} + \frac{V_2}{Z_2} + \dots + \frac{V_N}{Z_N} \right) \quad (54)$$

Thus, the equivalent source voltage V_{EC} to be inserted on the equivalent conductor model is:

$$V_{EC} = (Z_{EC}) \cdot \left(\frac{V_1}{Z_1} + \frac{V_2}{Z_2} + \dots + \frac{V_N}{Z_N} \right) \quad (55)$$

where Z_{EC} equals all the termination loads of each group of conductors set in parallel:

$$Z_{EC} = Z_1 // Z_2 // \dots // Z_N \quad (56)$$

3.3 Example of application

To present a concrete application of the method for an EM emission problem, the initial cable bundle presented in section 2.5 has been studied. In this case, each conductor of the cable bundle has been excited at the first end by a voltage source respectively equals to 1 V for wire 1, 2 V for wire 2, 3 V for wire 3 and 4 V for wire 4. As for the immunity problem, the reduced cable bundle contains one equivalent conductor according to the terminal load and voltage source configurations.

The equivalent voltage source located at the first end of the equivalent conductor and corresponding to this configuration equals 2.04 V as it is demonstrated with the following equation:

$$V_{eq} = 5,73 \cdot \left(\frac{1}{24} + \frac{2}{10} + \frac{3}{59} + \frac{4}{63} \right) = 2,04V \quad (57)$$

The total radiated power by both initial and reduced cable bundles has been calculated by the FEKO 3D MoM software on the half-superior sphere (above the infinite ground plane). The total radiated power is obtained by making the integration of the Poynting vector on numerous points of the half superior sphere after the calculation of the electric and magnetic fields emitted at these points. Fig. 14 presents the comparison of the total radiated power (in dBW) of both cable bundle models:

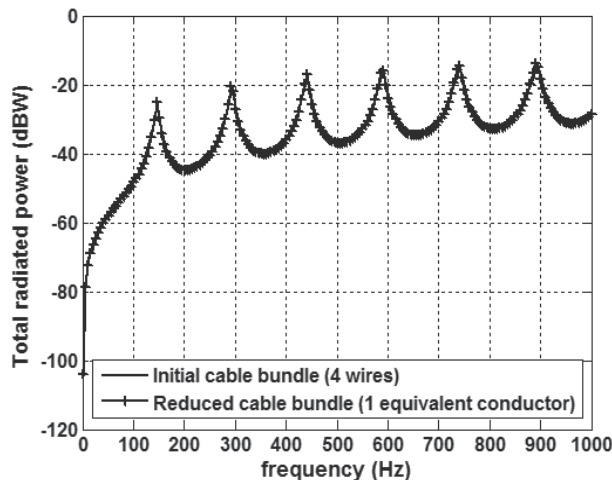


Fig. 14. Comparison of the total radiated power (in dBW) of both cable bundle models when introduced in a 3D MoM simulation

As for the EM immunity problem, the results show on this example the high accuracy of the method for EM emission problem. From the computation time point of view, the use of the reduced cable bundle has been reduced by a factor 14 the time necessary to compute all the terms of the $[Z]$ impedance matrix with the MoM technique.

4. Example of application on a representative automotive case

This section presents some results of a measurement campaign performed on a realistic automotive structure which is a half scale simplified car model, 180cm long, 80cm large and 70cm high presented in Fig. 15.



Fig. 15. Picture of the simplified car structure

The experiment has been performed in an anechoic chamber to ensure free space conditions. The measurement setup is presented in Fig. 16.

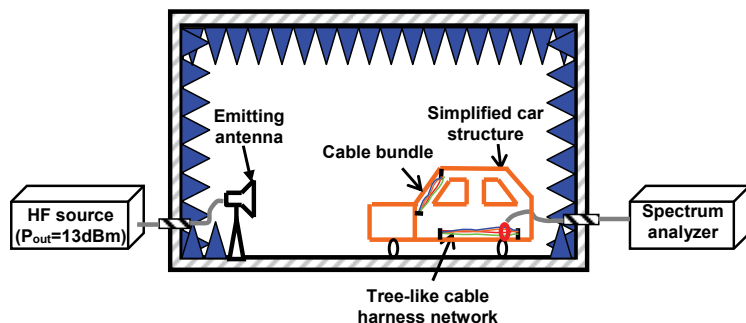


Fig. 16. Schematic description of the measurement setup

An emitting antenna illuminates with a vertical polarized electric field the front of the simplified car structure located approximately at 3m. In order to cover a large frequency range, two types of emitting antennas have been considered: a log periodic antenna up to 1 GHz and a double ridge horn antenna from 1 to 2 GHz. One cable bundle containing 5 conductors of 48 cm length plus one tree-like network having 4 extremities and a total of 16 conductors have been placed in the simplified structure. SMT (Surface Mount Technology) termination loads have been connected to each extremity of all the conductors to a metallic bracket fixed on the walls of the car which are considered as the ground reference. A current probe measured the common mode current induced at the ends of the cables by the EM incident field applied by the antennas.

The corresponding 3D model has been built thanks to the FEKO software. The MoM model of the simplified car structure containing the reduced cable bundle and the reduced tree-like cable network are presented in Fig. 17.

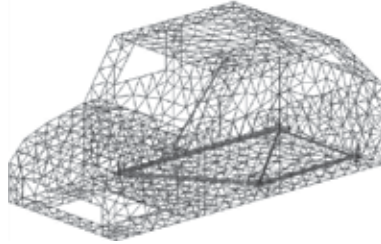


Fig. 17. MoM modelling of the test structure

The first result presented in Fig. 18 corresponds to the comparison of the common mode current at an extremity of the cable measured and calculated in MoM with a reduced cable bundle containing one equivalent conductor. Indeed, all the termination loads connected at both ends of all the conductors are small compared to the common mode characteristic impedance Z_{mc} .

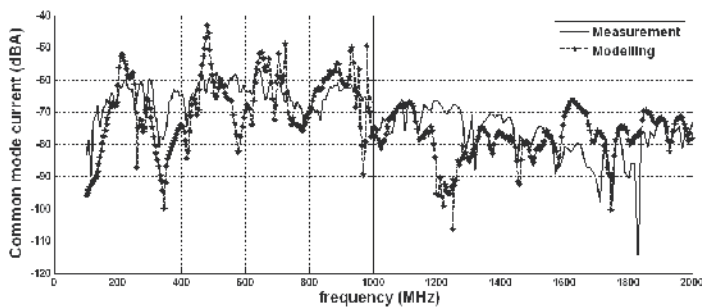


Fig. 18. Comparison of the common mode current measured and calculated at one extremity of the cable bundle

The second result presented in Fig. 19 concerns the comparison of the current measured and calculated at one extremity of the tree-like cable bundle network placed on the floor of the simplified car structure.

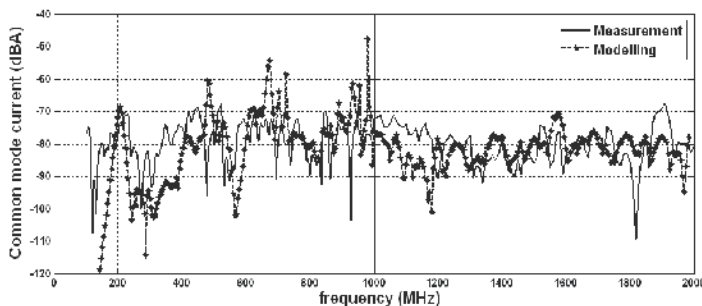


Fig. 19. Comparison of the common mode current measured and calculated at one extremity of the tree-like cable bundle network

Both figures present two very satisfying comparisons between measurements and modelling results on a large frequency range (100 MHz – 2 GHz). The average level is very close and the fundamental resonances of the bundles are quite well reproduced by the calculation. These results are very encouraging due to the fact that the tested structure is very oversized according to the wavelength.

To conclude, thanks to the use of the Fast Multipole Method (FMM) (Engheta et al., 1992), our method provides reasonable computation times compatible with an industrial application. For example, at the frequency of 1 GHz and on a 2.66 GHz processor with a memory of 1.5 Go, only 4 minutes are required to solve the MoM problem which contains more than 15 000 unknowns.

Applying the four-step procedure, our method has decreased the complexity of the reduced cable bundle and network by a 50 % factor.

5. Conclusion

This chapter has presented the so-called "equivalent cable bundle method" allowing to highly reduce the complexity of a real automotive cable bundle network. Consequently, the modelling of the simplified cable bundle network can be made with a strong reduction of involved computation times both for immunity and emission problems for any simulation method able to take into account the couplings between coupled conductors and for a large frequency range.

This work presents a lot of interesting future axis of work. The first one is to compute the current on each conductor of the initial cable bundle after the use of the reduced cable bundle. Another important one is to take into account real passive loads as inductive and capacitive ones to represent with a more important accuracy real loads encountered at the input of automotive electronic equipments.

6. References

- Agrawal, A.K.; Price, H.J. & Gurbaxani, S.H. (1980), Transient response of multiconductor transmission lines excited by a nonuniform electromagnetic field, *IEEE Trans. on EMC*, Vol. 22, No., (may 1980), (pp 119-129), ISSN 0018-9375
- Andrieu, G.; Koné, L.; Bocquet, F.; Démoulin, B. & Parmantier, J.P. (2008), Multiconductor reduction technique for modelling common mode currents on cable bundles at high frequency for automotive applications, *IEEE Trans. on EMC*, Vol. 50, No. 1, (february 2008), (pp 175-184), ISSN 0018-9375
- Andrieu, G.; Reineix, A.; Bunlon, X; Parmantier, J.P.; Koné, L. & Démoulin, B. (2009), Extension of the "equivalent cable bundle method" for modeling electromagnetic emissions of complex cable bundles, *IEEE Trans. on EMC*, Vol. 51, No. 1, (february 2008), (pp 108-118), ISSN 0018-9375
- Engheta, N.; Murphy, W.D.; Rohklin, V & Vassiliou, M.S. (1992), The fast multipole method (FMM) for electromagnetic scattering problems, *IEEE Trans. on AP*, Vol. 40, No. 6, (june 1992), (pp 634-641), ISSN 0018-926X
- Harrington, R.F. (1993). *Field computation by moment methods (reprinted edition)*, John Wiley and Sons, ISBN 978-0-470-13154-1, New York
- Paletta, L.; Parmantier J.P.; Issac F.; Dumas, P. & Alliot, J.C. (2002), Susceptibility analysis of wiring in a complex system combining a 3-D solver and a transmission-line

network simulation, *IEEE Trans. on EMC*, Vol. 44, No. 2, (may 2002), (pp 309-317), ISSN

Paul, C.R. (2008). *Analysis of Multiconductor Transmission Lines (second edition)*, John Wiley and Sons, ISBN 978-0-470-13154-1, Hoboken, New Jersey

Poudroux, C.; Rifi, M. & Démoulin, B. (1995), A simplified approach to determine the amplitude of the transient voltage induced on a cable bundle, *IEEE Trans. on EMC*, Vol. 37, No. 4, (november 1995), (pp 497-504), ISSN 0018-9375

Taflove, A. & Hagness S.C. (2005). *Computational Electrodynamics: The Finite-Difference Time-Domain Method (3rd revised edition)*, Artech house, ISBN 978-1580538329, Norwood

Fatigue Characteristic of Automotive Jounce Bumper

Aidy Ali, R.S. Sidhu and M.S.A. Samad
*Department of Mechanical and Manufacturing Engineering
Faculty of Engineering, Universiti Putra Malaysia
43400 Serdang, Selangor,
Malaysia*

1. Introduction

Most rubber components in the automotive industry are subjected to static and dynamic loading. Research on fatigue analysis and ways to enhance fatigue life is constantly done as it is directly related to the safety and reliability of a product. Fatigue life determination carried out experimentally has the best accuracy however these methods are not feasible when the components are constantly being renewed. In this study, experimental fatigue test and simulation via Abaqus were carried out to determine the fatigue life of the jounce bumper and pinpoint the failure location. Scanning electron microscopy (SEM) embedded with Energy Dispersive Spectroscopy (EDS) was used to determine the characteristic of crack propagation in the rubber jounce bumper. Results indicate crack propagation has a tendency to initiate and propagate from flaws that pre-exist in materials.

2. Background

Rubber components deteriorate much faster under fatigue loading compared to static loading. This is due to the fact that repetitive fatigue loading accumulates more damage and causes components to fail at a faster rate. This study was undertaken on a rubber jounce bumper which is a part of the McPherson strut assembly in chassis suspension system. It acts as a damper making the suspension progressive by allowing a smooth transition to full compression (Harza & Nallasamy, 2007). Figure 1 shows a typical jounce bumper use in light vehicles. There are two approaches commonly used to predict the fatigue life of rubber, the crack nucleation approach and the crack growth approach. Crack nucleation approach defines the failure as the number of cycles needed to cause a noticeable crack of a new component. Crack growth approach monitors the growth of a pre-existing crack (Mars & Fatemi, 2002; Saintier et al., 2006). Other than appearance of crack, load drop is used to acknowledge the existence of fatigue. Stiffness base approach is defined as the failure of a specimen at the point where the load drops at a significant amount usually 15 - 20 %. Researchers including Harbour and Kim use the load drop method as a failure criterion to acknowledge fatigue failure (Kim et al., 2004; Kim & Jeong, 2005; Harbour et al., 2008). Investigations on the cause of failure due to fatigue can be further explored using Scanning Electron Microscopy (SEM) embedded with Energy Dispersive X-ray Spectroscopy (EDS).

Previous researchers (Mathew & De, 1983; Kurian et al., 1989; Wang et al., 2002; Saintier et al., 2006) pointed out failures in components using SEM. Nucleation and growth of initial defects such as inclusions, microvoids, decohesions and cavitations are examples of fatigue damage found in fatigue rubber specimens (Wang et al., 2002). Traces of inclusions can be detected using EDS. Inclusions are foreign material trapped inside components during formation.

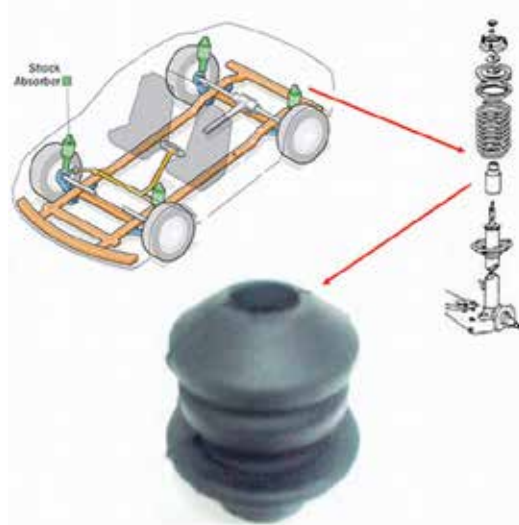


Fig. 1. Jounce Bumper in light automotive vehicles

3. Objective of study

The objectives of this study are to determine the maximum load that the jounce bumper can withstand, fatigue life under displacement control and characterization of the jounce bumper before and after fatigue. By achieving the objectives, we can improve the quality and design of the jounce bumper hence prolonging its durability. The jounce bumpers used for this study are the product of a Malaysian car, the Proton Saga (P2-11A) which consists of Natural rubber (90%) and Butadiene rubber (10%). It has a hardness of 60 IRHD (International Rubber Hardness Degrees). Table 1 shows the composition of the jounce bumper.

No	Test Parameter	Value
1	Polymer Type	Natural Rubber 90 % Butadiene Rubber 10 %
2	Polymer Content (%)	39.4
3	Calcium Carbonate (%)	39.8
4	Carbon Black (%)	Nil
5	Ash (%)	5.7
6	Acetone extract (%)	15.1
7	MBT (%)	0.8
8	Zinc Oxide (%)	1.7
9	Total Sulphur	2.1

Table 1. Jounce Bumper composition

A jig made out of mild steel is design to accommodate the loading condition by allowing the air to flow out while the jounce bumper is compressed. It also mimics the shock rod where it keeps the jounce bumper in line and prevents slips. The jig is shown in Figure 2.



Fig. 2. Jig

4. Experiment

The monotonic compression test was conducted using the Instron 3382 Floor Model Universal Testing System as shown in Figure 3. The test was done at a rate of 10mm/min to determine the maximum force of the jounce bumper and to obtain the Load versus Deflection response (L-D). For the fatigue compression test, twelve samples with different displacements were tested in an ambient temperature of 20 °C. The tests were carried out using the Instron 8871 table top model fatigue systems (Figure 4) with a sine waveform at frequency of 2 Hz at a load ratio of 0.

The jounce bumpers were cycled for 30 rounds to eliminate the Mullins effect before the number of cycles to failure is taken into consideration. Mullins Effects can be described as an initial softening that occurs at the start of the fatigue test (Diani et al., 2009). The determination of fatigue failure is based on the 15 % load drop. For the SEM and EDS testing, the samples were cut from the failure surface (after fatigue) and also a controlled surface (before fatigue) and placed onto specimen stub with carbon double-sided tape. Then the specimens were coated by evaporative coating with ultra-thin layers of Platinum under high vacuum. This process creates a conducting layer that permits SEM examination to take place. The JEOL FE-SEM JSM-6701F as shown in Figure 5, was operated at 20 kV with 15 mm working distance. For elemental analysis, Energy dispersive x-ray (EDS) was used.



Fig. 3. Instron 3382 Floor Model Universal Testing System



Fig. 4. Instron 8871 table top model fatigue systems



Fig. 5. JEOL FE-SEM JSM-6701F

5. Results and discussion

A load versus deflection curve was plotted from the compression test and shown in Figure 6. The test recorded a maximum force of 7 kN at 60 mm deflection. This shows that the jounce bumper is able to withstand a maximum load of 7 kN. Even though the jounce bumper is capable of handling high loads, it's unlikely for it to experience such loads in normal driving conditions. The optimum load experience by the jounce bumper is in the range of 0.5 - 2 kN (Harza & Nallasamy, 2007) as highlighted in Figure 6.

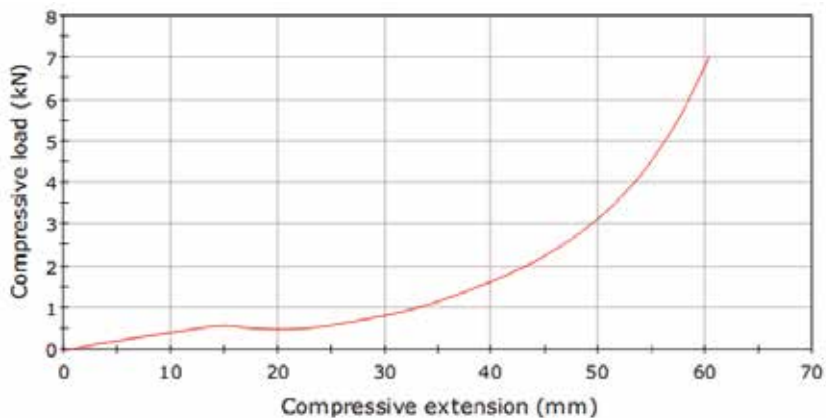


Fig. 6. Compression result

Figure 7 shows the strain versus fatigue life curve. The fatigue curve can be categorized into three zones. Zone one has the highest strain range between 0.88 - 1.14 mm/mm. Strains in this zone should be avoided at all cost as it yields very low fatigue life. Jounce bumper undergoing strains in zone two (0.53 - 0.79 mm/mm) will have a much longer fatigue life. However a regular replacement is necessary since it would not last for more than a 100000 cycles. Zone three is the safest zone with strains below 0.43 mm/mm. Strain values in this zone have fatigue life ranging from 675000 cycles and goes above 1.5 million cycles. Tests conducted on strains above 0.8 reveals significant fracture in the jounce bumper. The cracks originate from the lower part of the jounce bumper as highlighted in Figure 8.

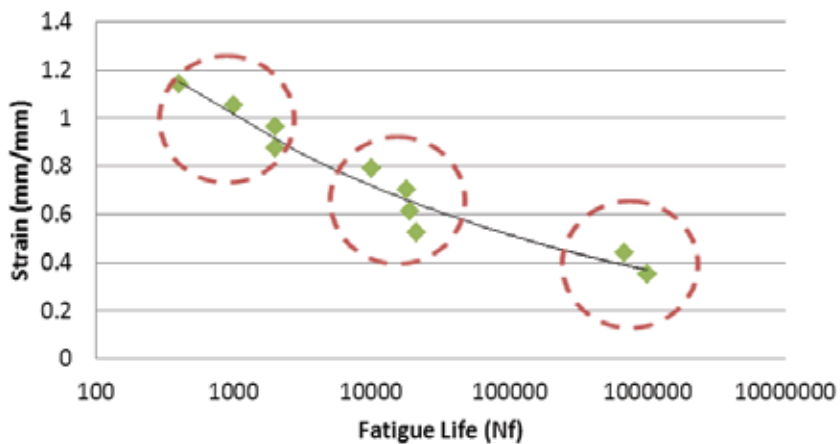


Fig. 7. Strain - Life (ϵ -N)



Fig. 8. Cracked jounce bumper

To pin point the exact location of the crack initiation, simulation was done using Abaqus. Reverse engineering method was used to obtain the jounce bumper's dimensions. The process involves the use of Coordinate Measuring Machine (CMM) and a 3D Scanner. The Neo-Hookean hyperelasticity model was chosen as the constitutive model for this analysis and constant was based on the experiment. Figure 9 shows the results of the simulation.

The simulation predicted the exact point of failure as the experimental results. The SEM micrographs are shown in Figures 10. Figure 10 (a) and (b) shows the control specimens at the crack location at x 150 and x 400 respectively while Figure 10(c) and (d) shows the failed specimen at the same location and magnification. The result from the elemental analysis using Energy dispersive x-ray (EDS) is shown in Table 2.

sample/element	C	O	S	Ci	Ca	Al	Zn
Area 1	60.36	37.49	-	-	1.42	0.59	0.14
Area 2	57.05	39.28	0.38	-	2.54	0.63	0.12
Area 3	61.81	35.76	-	-	1.66	0.51	0.27

Table 2. Elements of Sample

Figure 10 a) and b) indicates the presence of decohesion in the virgin specimen. Crack tends to initiate from pre-existing flaws. In this case inclusions in the material, causes decohesion (Saintier et al., 2006; Oshima et al., 2007). Decohesion causes crack to propagate much faster and speeds up the crack growth under fatigue loading. Decohesion is predominant in SiO₂ and CaCo₃ based materials. Since the rubber jounce bumper is made out of 39.8 % CaCo₃ and there were traces of aluminium found in the EDS analysis, it explains the formation of decohesions which results poor build in quality of the jounce bumper. Figure 10 c) and d) indicates that the fatigue failure occurred at high strains. This is due to the fact that major cracks throughout and area restrains the formation of microvoids and microcracks in that same area (Wang et al., 2002).

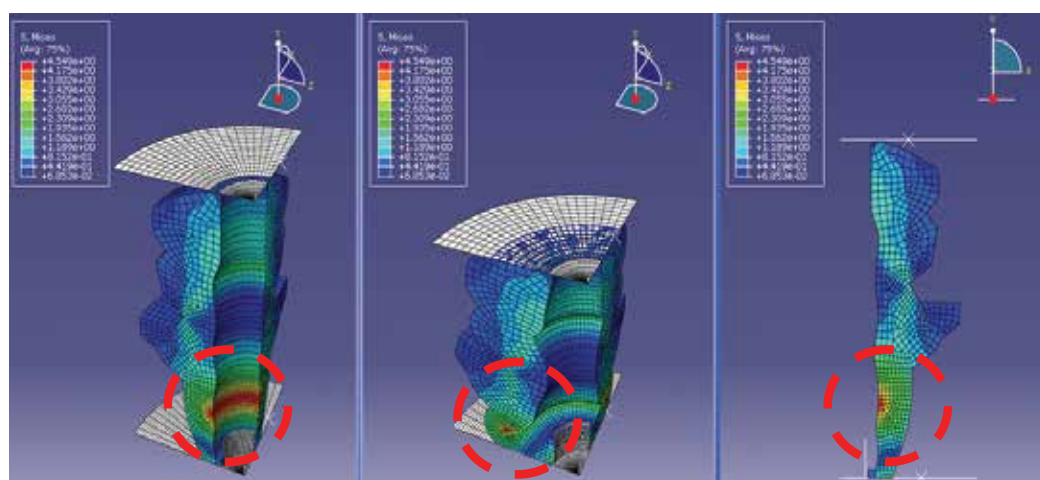


Fig. 9. Simulation of jounce bumper

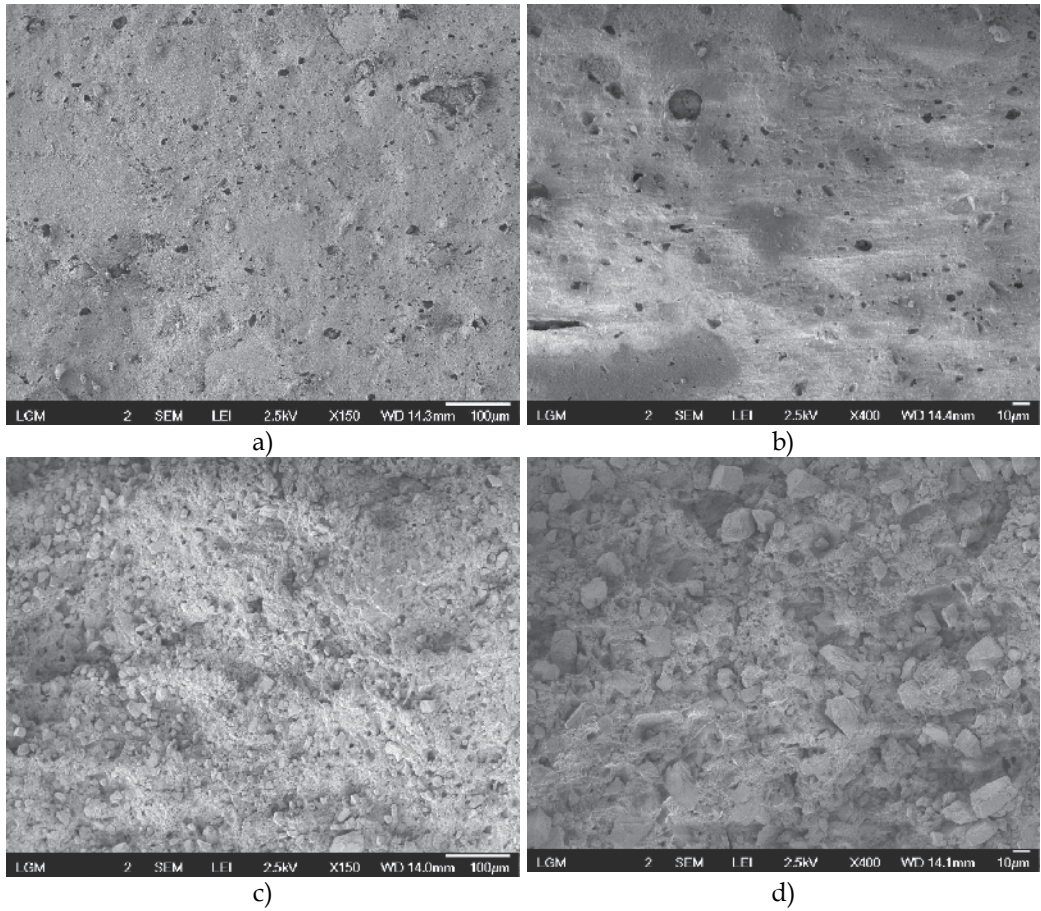


Fig. 10. Control Specimen a) x 150 & b) x 400. Failed Specimen c) x 150 & d) x 400

6. Conclusion

The fatigue characterization of the automotive jounce bumper was successfully determined. The compression test reveals that the jounce bumper is able to withstand a maximum force of 7 KN. From the fatigue test conducted, we were able to characterize the jounce bumper depending on the strain acted upon it. Three zones were established to separate the safe zone from the potential danger zone. FEA simulation using Abaqus successfully predicted the point of failure which matches the experimental results. Pre-existing flaws accelerates the initiation of cracks under fatigue loading. The SEM result proves that the virgin jounce bumper have decohesions. Type of material used to fabricate rubber components as well as the process of producing the component plays an important role in determining the quality of a product. In this case, the use of CaCO_3 and the mysterious existence of Aluminium compound reflect the poor quality of the rubber jounce bumper.

7. References

- Diani, J., Fayolle, B., and Gilormini, P. (2009). A review on the Mullins effect. *European Polymer Journal* 45, 601-612.
- Harbour, R. J., Fatemi, A., and Mars, W. (2008). Fatigue life analysis and prediction for NR and SBR under variable amplitude and multi-axial loading conditions. *International Journal of Fatigue* 1231-1247.
- Harza, S., and Nallasamy (2007). Jounce Bumper Optimization - FE Approach. *Abaqus India Regional User's Meet*, 1-10.
- Kim, J. H., and Jeong, H.-Y. (2005). A study on the material properties and fatigue life of natural rubber with different carbon blacks. *International Journal of Fatigue* 27, 263-272.
- Kim, W. D., Lee, H. J., and Kim, J. Y. (2004). Fatigue life estimation of an engine rubber mount. *International Journal of Fatigue* 26, 553-560.
- Kurian, J., Chaki, T. K., and Nando, G. B. (1989). Scanning electron microscope studies on tension fatigue failure of high density polyethylene filled natural rubber vulcanizate. *International Journal of Fatigue* 11, 129-133.
- Mars, W. V., and Fatemi, A. (2002). A literature survey on fatigue analysis approaches for rubber. *International Journal of Fatigue* 24, 949-961.
- Mathew, N. M., and De, S. K. (1983). Scanning electron microscopy studies on flexing and tension fatigue failure of rubber. *International Journal of Fatigue* 5, 23-28.
- Oshima, H., Aono, Y., Noguchi, H., and Shibata, S. (2007). Fatigue characteristics of vulcanized natural rubber for automotive engine mounting (characteristics of composition and mechanical properties). *Memoirs of the Faculty of Engineering, Kyushu University* 67, 75-83.
- Saintier, N., Cailletaud, G., and Piques, R. (2006a). Multiaxial fatigue life prediction for natural rubber. *International Journal of Fatigue* 28, 530-539.
- Saintier, N., Cailletaud, G., and Piques, R. (2006b). Crack initiation and propagation under multi-axial fatigue in natural rubber. *International Journal of Fatigue* 28, 61-72.

Wang, B., Lu, H., and Kim, G.-h. (2002). A damage model for the fatigue life of elastomeric materials. *Mechanics of Materials* 34, 475-478.

Part 4

Control Systems and Algorithms

On the Control of Automotive Traction PEM Fuel Cell Systems

Ahmed Al-Durra¹, Stephen Yurkovich² and Yann Guezennec²

¹*Department of Electrical Engineering, The Petroleum Institute, Abu Dhabi*

²*Center for Automotive Research, The Ohio State University*

930 Kinnear Road, Columbus, OH 43212

¹*United Arab Emirates*

²*USA*

1. Introduction

A fuel cell (FC) is an electro-chemical device that converts chemical energy to electrical energy by combining a gaseous fuel and oxidizer. Lately, new advances in membrane material, reduced usage of noble metal catalysts, and efficient power electronics have put the fuel cell system under the spotlight as a direct generator for electricity (Pukrushpan, Stefanopoulou & Peng, 2004a). Because they can reach efficiencies of above 60% (Brinkman, 2002),(Davis et al., 2003) at normal operating conditions, Proton Exchange Membrane (PEM) fuel cells may represent a valid choice for automotive applications in the near future (Thijssen & Teagan, 2002), (Bernay et al., 2002).

Compared to internal combustion engines (ICEs) or batteries, fuel cells (FCs) have several advantages. The main advantages are efficiency, low emissions, and dual use technology. FCs are more efficient than ICEs, since they directly convert fuel energy to electrical energy, whereas ICEs need to convert the fuel energy to thermal energy first, then to mechanical energy. Due to the thermal energy involved, the ICE conversion of energy is limited by the Carnot Cycle, not the case with FCs (Thomas & Zalowitz, 2000). Fuel cells are considered zero emission power generators if pure hydrogen is used as fuel.

The PEM fuel cell consists of two electrodes, an anode and a cathode, separated by a polymeric electrolyte membrane. The ionomeric membrane has exclusive proton permeability and it is thus used to strip electrons from hydrogen atoms on the anode side. The protons flow through the membrane and react with oxygen to generate water on the cathode side, producing a voltage between the electrodes (Larminie & Dicks, 2003). When the gases are pressurized, the fuel cell efficiency is increased, and favorable conditions result for smooth fluid flow through the flow channels (Yi et al., 2004). Pressurized operation also allows for better power density, a key metric for automotive applications. Furthermore, the membrane must be humidified to operate properly, and this is generally achieved through humidification of supplied air flow (Chen & Peng, 2004). Modern automotive fuel cell stacks operate around 80° C for optimal performance (EG&G-Technical-Services, 2002),(Larminie & Dicks, 2003).

For such efficient operation, a compressor must supply pressurized air, a humidification system is required for the air stream, possibly a heat exchanger is needed to feed pressurized hot air at a temperature compatible with the stack, and a back pressure valve is required to control system pressure. A similar setup is required to regulate flow and pressure on

the hydrogen side. Since the power from the fuel cell is utilized to drive these systems, the overall system efficiency drops. From a control point of view, the required net power must be met with the best possible dynamic response while maximizing system efficiency and avoiding oxygen starvation. Therefore, the system must track trajectories of best net system efficiency, avoid oxygen starvation (track a particular excess air ratio), whereas the membrane has to be suitably humidified while avoiding flooding. This can only be achieved through a coordinated control of the various available actuators, namely compressor, anode and cathode back pressure valves and external humidification for the reactants.

Because the inherently coupled dynamics of the subsystems mentioned above create a highly nonlinear behavior, control is typically accomplished through static off-line optimization, appropriate design of feed-forward commands and a feedback control system. These tasks require a high-fidelity model and a control-oriented model. Thus, the first part of this chapter focuses on the nonlinear model development in order to obtain an appropriate structure for control design.

After the modeling section, the remainder of this chapter focuses on control aspects. Obtaining the desired power response requires air flow, pressure regulation, heat, and water management to be maintained at certain optimal values according to each operating condition. Moreover, the fuel cell control system has to maintain optimal temperature, membrane hydration, and partial pressure of the reactants across the membrane in order to avoid harmful degradation of the FC voltage, which reduces efficiency (Pukrushpan, Stefanopoulou & Peng, 2004a). While stack pressurization is beneficial in terms of both fuel cell voltage (stack efficiency) and of power density, the stack pressurization (and hence air pressurization) must be done by external means, i.e., an air compressor. This component creates large parasitic power demands at the system level, with 10 – 20% of the stack power being required to power the compressor under some operating conditions which can considerably reduce the system efficiency. Hence, it is critical to pressurize the stack optimally to achieve best system efficiency under all operating conditions. In addition, oxygen starvation may result in a rapid decrease in cell voltage, leading to a large decrease in power output, and “torque holes” when used in vehicle traction applications (Pukrushpan, Stefanopoulou & Peng, 2004b).

To avoid these phenomena, regulating the oxygen excess ratio in the FC is a fundamental goal of the FC control system. Hence, the fuel cell system has to be capable of simultaneously changing the air flow rate (to achieve the desired excess air beyond the stoichiometric demand), the stack pressurization (for optimal system efficiency), as well as the membrane humidity (for durability and stack efficiency) and stack temperature. All variables are tightly linked physically, as the realizable actuators (compressor motor, back-pressure valve and spray injector or membrane humidifier) are located at different locations in the systems and affect all variables simultaneously. Accordingly, three major control subsystems in the fuel cell system regulate the air/fuel supply, the water management, and the heat management. The focus of this paper will be solely on the first of these three subsystems in tracking an optimum variable pressurization and air flow for maximum system efficiency during load transients for future automotive traction applications.

There have been several excellent studies on the application of modern control to fuel cell systems for automotive applications; see, for example, (Pukrushpan, Stefanopoulou & Peng, 2004a), (Pukrushpan, Stefanopoulou & Peng, 2004b), (Domenico et al., 2006), (Pukrushpan, Stefanopoulou & Peng, 2002), (Al-Durra et al., 2007), (Al-Durra et al., 2010), and (Yu et al., 2006). In this work, several nonlinear control ideas are applied to a multi-input,

A_{fc}	Cell active area [cm^2]
F	Faraday constant [$\frac{C}{mol}$]
i	Cell current density [$\frac{A}{cm^2}$]
I	Cell current [A]
M	Molecular weight [$\frac{kg}{mol}$]
n	Angular speed [rpm]
n_e	Number of electrons [-]
N	Number of cells [-]
p	Pressure in the volumes [bar]
R	Gas constant [$\frac{bar \cdot m^3}{kgK}$]
\bar{R}	Universal gas constant [$\frac{bar \cdot m^3}{molK}$]
T	Temperature [K]
V	Volume [m^3]
ω	Specific humidity [-]
W	Mass flow rate [$\frac{kg}{s}$]
μ	Fuel utilization coefficient

Table 1. Model nomenclature

multi-output (MIMO) PEM FC system model, to achieve good tracking responses over a wide range of operation. Working from a reduced order, control-oriented model, the first technique uses an observer-based linear optimum control which combines a feed-forward approach based on the steady state plant inverse response, coupled to a multi-variable LQR feedback control. Following this, a nonlinear gain-scheduled control is described, with enhancements to overcome the fast variations in the scheduling variable. Finally, a rule-based, output feedback control design is coupled with a nonlinear feed-forward approach. These designs are compared in simulation studies to investigate robustness to disturbance, time delay, and actuators limitations. Previous work (see, for example, (Pukrushpan, Stefanopoulou & Peng, 2004a), (Domenico et al., 2006), (Pukrushpan, Stefanopoulou & Peng, 2002) and references therein) has seen results for single-input examples, using direct feedback control, where linearization around certain operating conditions led to acceptable local responses. The contributions of this work, therefore, are threefold: Control-oriented modeling of a realistic fuel cell system, extending the range of operation of the system through gain-scheduled control and rule-based control, and comparative studies under closed loop control for realistic disturbances and uncertainties in typical operation.

2. PEM fuel cell system model

Having a control-oriented model for the PEM-FC is a crucial first step in understanding the system behavior and the subsequent design and analysis of a model-based control system. In this section the model used throughout the chapter is developed and summarized, whereas the interested reader is referred to (Domenico et al., 2006) and (Miotti et al., 2006) for further details. Throughout, certain nomenclature and notation (for variable subscripts) will be adopted, summarized in Tables 1 and 2.

A high fidelity model must consist of a structure with an air compressor, humidification chambers, heat exchangers, supply and return manifolds and a cooling system. Differential equations representing the dynamics are supported by linear/nonlinear algebraic equations

<i>an</i>	Anode
<i>ca</i>	Cathode
<i>cmp</i>	Compressor
<i>D</i>	Derivative
<i>da</i>	Dry air
<i>fc</i>	Fuel cell
H_2	Hydrogen
<i>in</i>	Inlet conditions
<i>I</i>	Integrative
<i>mem</i>	Membrane
N_2	Nitrogen
<i>out</i>	Outlet conditions
O_2	Oxygen
<i>P</i>	Proportional
<i>rm</i>	Return manifold
<i>sm</i>	Supply manifold
<i>vap</i>	Vapor

Table 2. Subscript notation

(Kueh et al., 1998). For control design, however, only the primary critical dynamics are considered; that is, the slowest and fastest dynamics of the system, i. e. the thermal dynamics associated with cold start and electrochemical reactions, respectively, are neglected. Consequently, the model developed for this study is based on the following assumptions: i) spatial variations of variables are neglected¹, leading to a lumped-parameter model; ii) all cells are considered to be lumped into one equivalent cell; iii) output flow properties from a volume are equal to the internal properties; iv) the fastest dynamics are not considered and are taken into account as static empirical equations; v) all the volumes are isothermal.

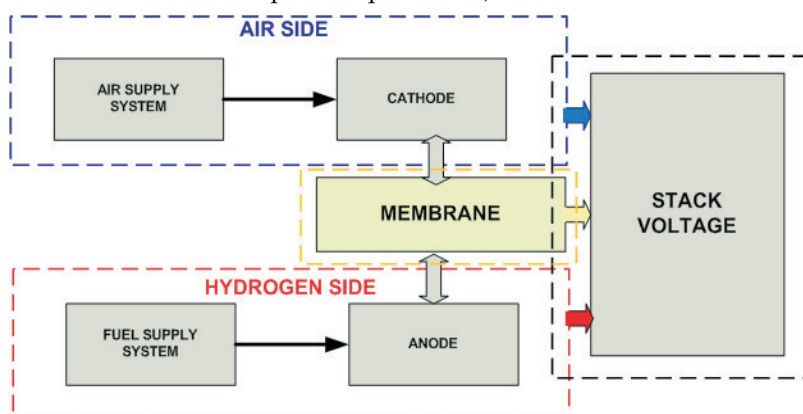


Fig. 1. Fuel cell system schematic.

An equivalent scheme of the fuel cell system model is shown in Figure 1, where four primary blocks are evident: the air supply, the fuel delivery, the membrane behavior and the stack

¹Note: spatial variations are explicitly accounted for in finding maps used by this model obtained from an extensive 1+1D model (see Section 2.3)

voltage performance. In what follows, the primary blocks are described in more detail. The state variables of the overall control-oriented model are chosen to be the physical quantities listed in Table 3.

2.1 Air supply system

The air side includes the compressor, the supply and return manifolds, the cathode volume, the nozzles between manifolds and cathode and the exhaust valve. Since pressurized reactants increase fuel cell stack efficiency, a screw compressor has been used to pressurize air into the fuel cell stack (Guzzella, 1999). The screw type compressor provides high pressure at low air flow rate. The compressor and the related motor have been taken into account as a single, comprehensive unit in order to describe the lumped dynamics of the system to a reference speed input. The approach followed for the motor-compressor model differs from the published literature on this topic. Commonly, thermodynamics and heat transfer lead to the description of the compressor behavior, while standard mathematical models define the DC or AC motors inertial and rotational dynamics. The compressor/motor assembly has been defined by means of an experimental test bench of the compressor-motor pair including a screw type compressor, coupled to a brushless DC motor through a belt and a pulley mechanism. Using the system Identification toolbox in MatlabTM, an optimization routine to maintain stability and minimum phaseness, different time based techniques have been investigated to closely match the modeled and the experimental responses. This was accomplished with an optimization routine that explored different pole-zero combinations in a chosen range. Finally, a two-pole, two-zero Auto Regressive Moving Average eXtended (ARMAX) model was identified, described by

$$\frac{n_{cp}}{n_{cmd}} = \frac{-3.96 \cdot 10^{-5}s^2 + 0.528s + 567.5}{s^2 + 9.624s + 567.8} \quad (1)$$

where n_{cp} is the speed of the compressor and n_{cmd} is the speed commanded. Moreover, the motor compressor assembly model simulates and computes the mass flow rate from the compressor via a static map depending on pressure and compressor speed.

For the air side, a supply and a return manifold was represented with mass balance and pressure calculation equations (Pukrushpan, 2003). Dry air and vapor pressure in the supply

State Variables
1. Pressure of O_2 in the cathode
2. Pressure of H_2 in the anode
3. Pressure of N_2 in the cathode
4. Pressure of cathode vapor
5. Pressure of anode vapor
6. Pressure of supply manifold vapor in the cathode
7. Pressure of supply manifold dry air in the cathode
8. Pressure of cathode return manifold
9. Pressure of anode return manifold
10. Pressure of anode supply manifold
11. Water injected in the cathode supply manifold
12. Angular acceleration of the compressor
13. Angular velocity of the compressor

Table 3. State variables for the control-oriented model.

manifold can be described as follows ((Kueh et al., 1998) (Pukrushpan, Stefanopoulou & Peng, 2002)):

$$\begin{aligned}\frac{dp_{da}}{dt} &= \frac{R_{da}T_{sm,ca}}{V_{sm,ca}}(W_{da,in} - W_{da,out}) \\ \frac{dp_{vap}}{dt} &= \frac{R_{vap}T_{sm,ca}}{V_{sm,ca}}(W_{vap,in} + W_{vap,inj} - W_{vap,out})\end{aligned}\quad (2)$$

The inlet flows denoted by subscript *in* represent the mass flow rates coming from the compressor. Outlet mass flow rates are determined by using the nonlinear nozzle equation for compressible fluids (Heywood, 1998):

$$W_{out} = \begin{cases} \frac{C_d A_t p_{up}}{\sqrt{RT_{up}}} \left(\frac{p_{dw}}{p_{up}}\right)^{1/\gamma} \sqrt{\frac{2\gamma}{\gamma-1} \left(1 - \left(\frac{p_{dw}}{p_{up}}\right)^{\frac{\gamma-1}{\gamma}}\right)} & \text{if } \frac{p_{dw}}{p_{up}} > \left(\frac{2}{\gamma+1}\right)^{\frac{\gamma}{\gamma-1}} \\ \frac{C_d A_t p_{up}}{\sqrt{RT_{up}}} \sqrt{\gamma} \left(\frac{2}{\gamma+1}\right)^{\frac{\gamma+1}{2(\gamma-1)}} & \text{if } \frac{p_{dw}}{p_{up}} \leq \left(\frac{2}{\gamma+1}\right)^{\frac{\gamma}{\gamma-1}} \end{cases}\quad (3)$$

where p_{dw} and p_{up} are the downstream and upstream pressure, respectively, and R is the gas constant related to the gases crossing the nozzle.

Many humidification technologies are possible for humidifying the air (and possibly) hydrogen streams ranging from direct water injection through misting nozzles to membrane humidifier; their detailed modeling is beyond the scope of this work and very technology-dependent. Hence, a highly simplified humidifier model is considered here, where the quantity of water injected corresponds to the required humidification level for a given air flow rate (at steady state), followed by a net first order response to mimic the net evaporation dynamics. Similar models have been used for approximating fuel injection dynamics in engines where the evaporation time constant is an experimentally identified variable which depends on air flow rate and temperature. For this work, the evaporation time constant is kept constant at $\tau = 1$ s. The humidifier model can be summarized by the following equations:

$$\begin{aligned}W_{inj,com} &= W_{da,in}(\omega_{out} - \omega_{in}) \\ \dot{W}_{inj} &= W_{inj,com} - W_{inj}\end{aligned}\quad (4)$$

where $W_{inj,com}$ is the commanded water injection, ω is the specific humidity, $W_{da,in}$ is the dry air and W_{inj} is the water injection.

The mass flow rate leaving the supply manifold enters the cathode volume, where a mass balance for each species (water vapor, oxygen, nitrogen) has been considered (Pukrushpan, Stefanopoulou & Peng, 2004):

$$\begin{aligned}\frac{dp_{vap}}{dt} &= \frac{R_{vap}T_{ca}}{V_{ca}}(W_{vap,in} - W_{vap,out} + W_{vap,mem} + W_{vap,gen}) \\ \frac{dp_{O_2}}{dt} &= \frac{R_{O_2}T_{ca}}{V_{ca}}(W_{O_2,in} - W_{O_2,out} - W_{O_2,reacted}) \\ \frac{dp_{N_2}}{dt} &= \frac{R_{N_2}T_{ca}}{V_{ca}}(W_{N_2,in} - W_{N_2,out})\end{aligned}\quad (5)$$

In the equations above, $W_{vap,mem}$ indicates the vapor mass flow rate leaving or entering the cathode through the membrane, whereas $W_{vap,gen}$ and $W_{O_2,reacted}$ are related to the electrochemical reaction representing the vapor generated and the oxygen reacted, respectively. Moreover, p is the partial pressure of each element and thus the cathode pressure is given by

$$p_{ca} = p_{vap} + p_{O_2} + p_{N_2} \quad (6)$$

The gases leaving the cathode volume are collected inside the return manifold which has been modeled using an overall mass balance for the moist air:

$$\frac{dp_{rm}}{dt} = \frac{R_{da}T_{rm,ca}}{V_{rm,ca}} (W_{air,in} - W_{air,out}) \quad (7)$$

In order to control the pressure in the air side volumes, an exhaust valve has been applied following the same approach of Equation (3) where the cross sectional area may be varied accordingly to a control command.

2.2 Fuel side

As seen for the air side, three volumes have been taken into account: anode, supply and return manifolds. Indeed, no humidification system has been applied to the fuel side, thus leading to hydrogen inlet relative humidity equal to zero. Due to the lack of incoming vapor into the hydrogen flow, the supply manifold equation is given by (Arsie et al., 2005)

$$\frac{dp_{H_2}}{dt} = \frac{R_{H_2}T_{sm,an}}{V_{sm,an}} (W_{H_2,in} - W_{H_2,out}) \quad (8)$$

where $W_{H_2,in}$ is the hydrogen inlet flow supplied by a fuel tank which is assumed to have an infinite capacity and an ideal control capable of supplying the required current density. The delivered fuel depends on the stoichiometric hydrogen and is related to the utilization coefficient in the anode (u_{H_2}) according to

$$W_{H_2,in} = A_{fc} N \frac{i \cdot M_{H_2}}{n_e F} \mu_{H_2} \quad (9)$$

In Equation (9), A_{fc} is the fuel cell active area and N is the number of cells in the stack; the fuel utilization coefficient μ_{H_2} is kept constant and indicates the amount of reacted hydrogen. The outlet flow from the supply manifold, $W_{H_2,out}$, is determined through the nozzle Equation (3). As previously done for the cathode, the mass balance equation is implemented for the anode:

$$\begin{aligned} \frac{dp_{vap}}{dt} &= \frac{R_{vap}T_{an}}{V_{an}} (W_{vap,in} - W_{vap,mem} - W_{vap,out}) \\ \frac{dp_{H_2}}{dt} &= \frac{R_{H_2}T_{an}}{V_{an}} (W_{H_2,in} - W_{H_2,out} - W_{H_2,reacted}) \end{aligned} \quad (10)$$

where $W_{vap,in}$ is the inlet vapor flow set to zero by assumption, $W_{vap,mem}$ is the vapor flow crossing the membrane and $W_{vap,out}$ represents the vapor flow collecting in the return manifold through the nozzle (Equation 3). For the return manifold, the same approach of Equation (7) is followed.

2.3 Embedded membrane and stack voltage model

Because the polymeric membrane regulates and allows mass water transport toward the electrodes, it is one of the most critical elements of the fuel. Proper membrane hydration

and control present challenges to be solved in order to push fuel cell systems toward mass commercialization in automotive applications.

Gas and water properties are influenced by the relative position along both the electrodes and the membrane thickness. Although a suitable representation would use partial differential equations, the requirement for fast computation times presents a significant issue to consider. Considering also the difficulties related to the identification of relevant parameters in representing the membrane mass transport and the electrochemical phenomena, static maps are preferred to the physical model.

Nevertheless, in order to preserve the accuracy of a dimensional approach, a static map is utilized with a 1+1-dimensional, isothermal model of a single cell with 112 Nafion membrane. The 1+1D model describes system properties as a function of the electrodes length, accounting for an integrated one dimensional map, built as a function of the spatial variations of the properties across the membrane. The reader is referred to (Ambühl et al., 2005) and (Mazunder, 2003) for further details.

For the model described here, two 4-dimensional maps have been introduced: one describing the membrane behavior, the other one performing the stack voltage. The most critical variables affecting system operation and its performance have been taken into account as inputs for the multi-dimensional maps:

- current density;
- cathode pressure;
- anode pressure;
- cathode inlet humidity.

A complete operating range of the variables above has been supplied to the 1+1-dimensional model, in order to investigate the electrolyte and cell operating conditions and to obtain the corresponding water flow and the single cell voltage, respectively, starting from each set of inputs. Thus, the membrane map outputs the net water flow crossing the electrolyte towards the anode or toward the cathode and it points out membrane dehydration or flooding during cell operation. Figure 2 shows the membrane water flow behavior as a function of the current density and the pressure difference between the electrodes, fixing cathode pressure and relative humidity.

On the other side, the stack performance map determines the single cell voltage and efficiency, thus also modeling the electrochemical reactions. As previously done, the cell voltage behavior may be investigated, keeping constant two variables and observing the dependency on the others (Figure 3).

2.4 Model parameters

A 60 kW fuel system model is the subject of this work, with parameters and geometrical data obtained from the literature (Rodatz, 2003),(Pukrushpan, 2003) and listed in Table 4.

2.5 Open loop response

The fuel cell model of this study is driven by the estimated current rendered from demanded power. Based on the current profile, different outputs will result from the membrane and stack voltage maps. However, to see the overall effect of the current, a profile must be specified for the compressor and manifold valves on both sides. In order to test the model developed, simple current step commands are applied to the actuators, which are the return manifolds

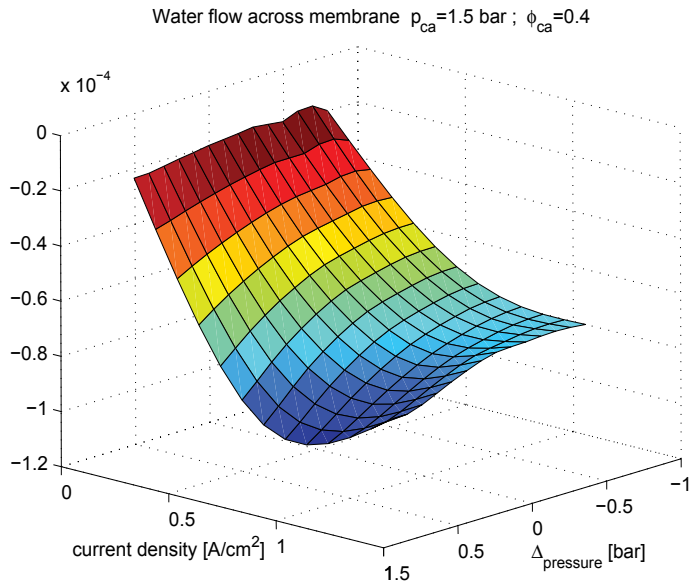


Fig. 2. Membrane water flux as a function of current density and pressure difference at constant cathode pressure and relative humidity.

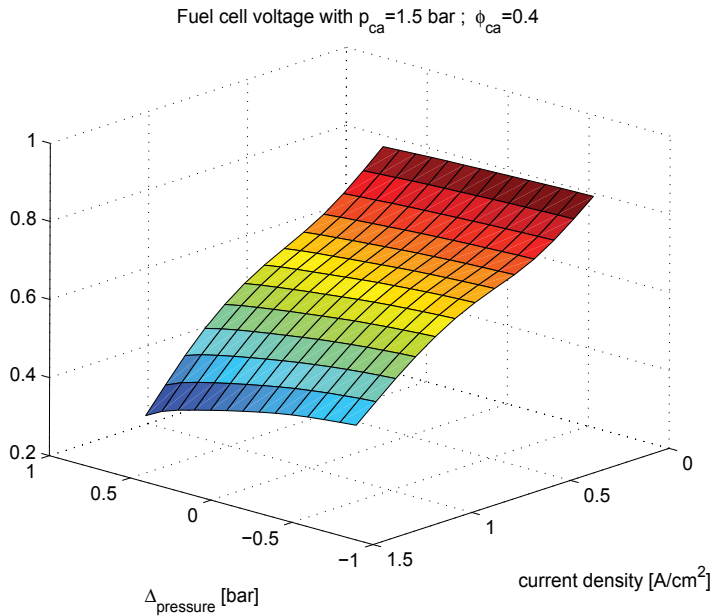


Fig. 3. Cell voltage as a function of current density and pressure difference at constant cathode pressure and relative humidity.

Variables	Values
Active cell area [cm^2]	312
Membrane thickness [μm]	51
Number of cells	385
Desired cathode relative humidity	0.6
Inlet anode relative humidity	0
Max current demand	230
Fuel cell temperature [K]	353
Fuel utilization	0.9
Excess of air	2

Table 4. Fuel cell parameters.

valves on both sides and the compressor command. Figure 4 shows open-loop results under three different loads (see Figure 4(a)).

From the open-loop results, it is worth noting that both electrode pressures increase when the current demand approaches higher value, thus ensuring a higher mass flow rate as expected. In particular, note that oxygen mass guarantees the electrochemical reaction for each value of current demand chosen, avoiding stack starvation. Moreover, because the compressor increases its speed, a fast second order dynamic results in the air mass flow rate delivered, whereas a slower first order dynamic corresponds to the electrodes pressures. These results indicate that the model captures the critical dynamics, producing results as expected.

2.6 Control strategy and reference inputs

Because the fuel cell system must satisfy the power demand, oxygen starvation is an issue and must be avoided. In fact, the air mass flow rate decreases for each load change and the control system must avoid fast cell starvation during the transient. Thus, increasing power requirements lead to higher mass flow rates fed by the compressor and higher pressures in the volumes. Moreover, Figure 5 indicates that as long as pressurized gases are supplied, the fuel cell improves its performance, providing higher voltage at high current density, without reaching the region of high concentration losses.

Pressurized gases increase cell efficiency, but since the stack experiences a nontrivial energy consumption to drive the motor of the compressor, the overall system efficiency drops, described by

$$\eta_{sys} = \frac{P_{st} - P_{cmp}}{W_{in,H_2} LHV_{H_2}} \quad (11)$$

where P_{st} is the electrical power generated by the stack, P_{cmp} is the power absorbed by the compressor, W_{in,H_2} is the amount of hydrogen provided and LHV_{H_2} is lower heating value for the fuel. In order to achieve the best system efficiency, the entire operating range in terms of requested power and air pressure is investigated. Using a simple optimization tool, for each value of current demand a unique value of optimal pressure can be derived, maximizing the system efficiency. Thus, the map showed in Figure 6 interpolates the results of the optimization and plots the optimal pressures as functions of the desired current. Furthermore, since the membrane should not experience a significant pressure difference between the electrodes, the pressure set points related to the anode side have been chosen to have values of 0.1 bar lower than the optimal cathode pressure.

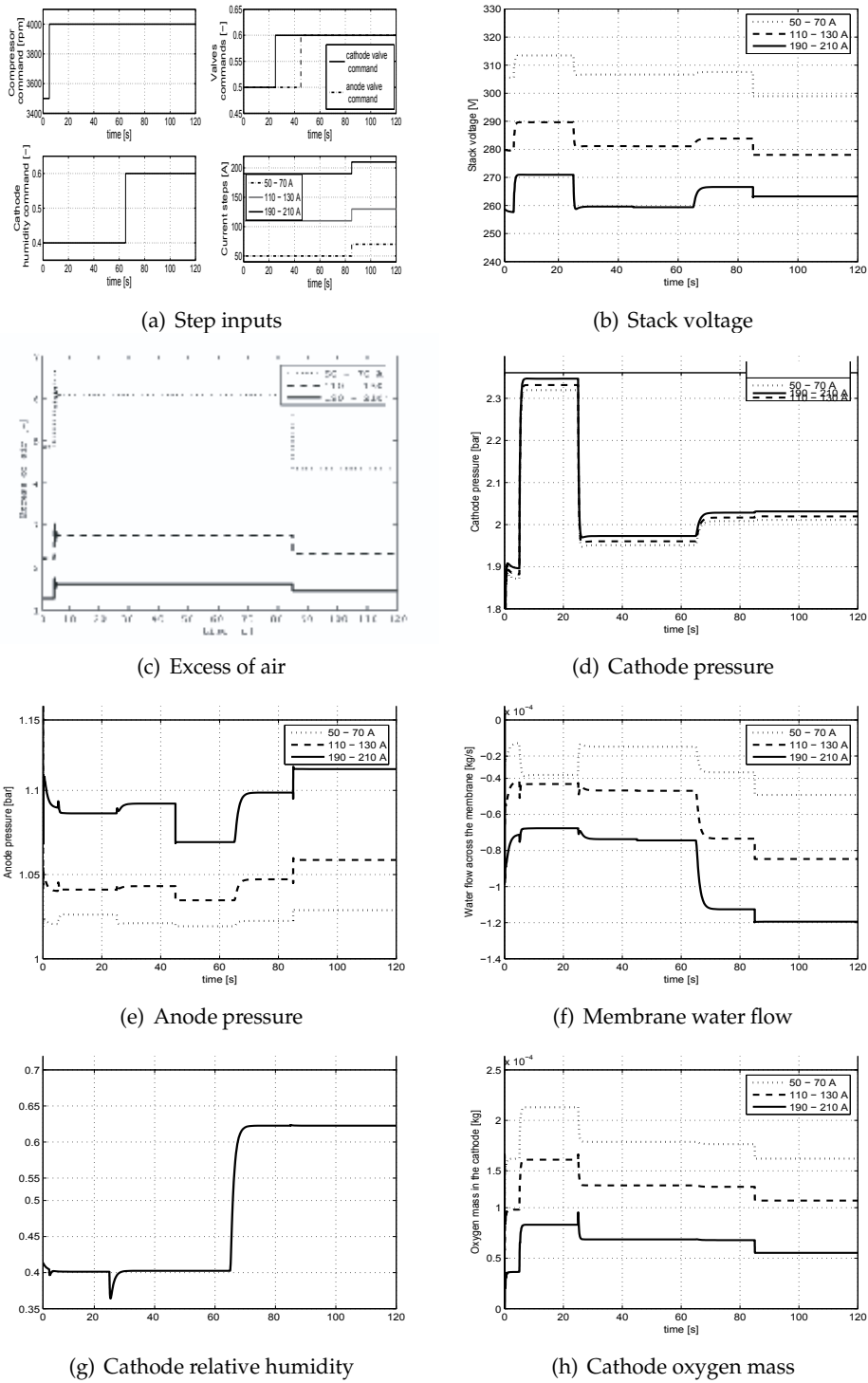


Fig. 4. Results for the open loop model.

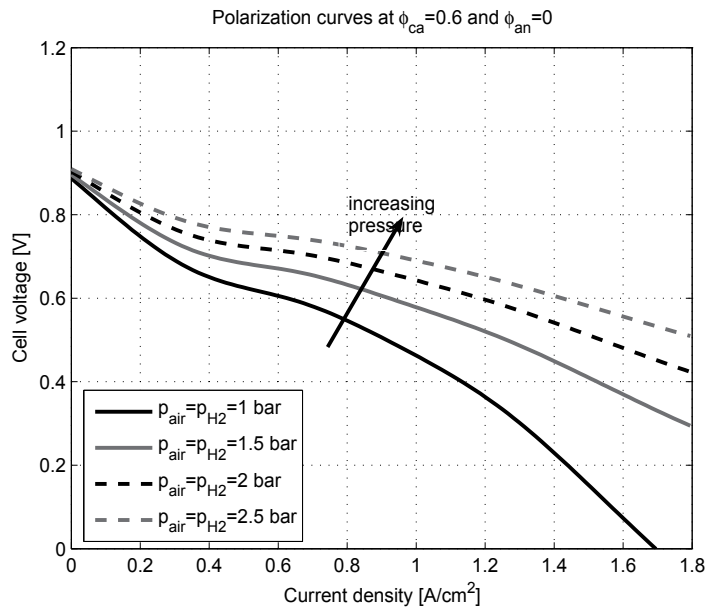


Fig. 5. Fuel cell polarization curves for different pressures.

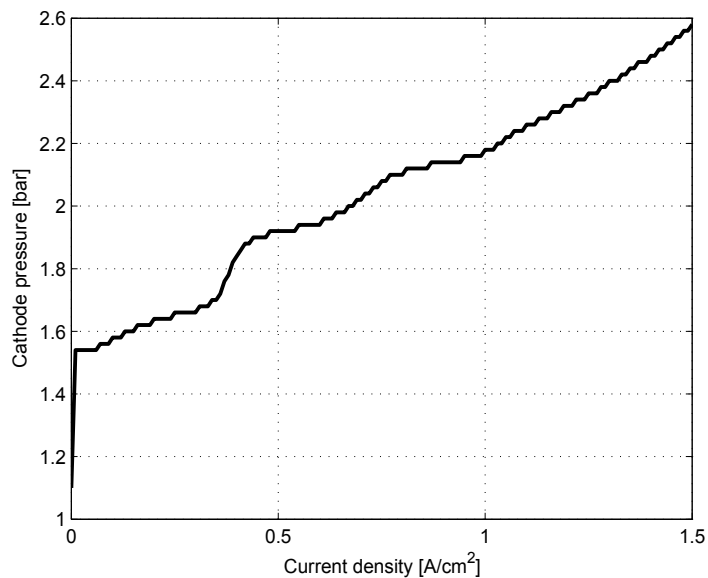


Fig. 6. Cathode optimal pressure as function of the current demand.

The current demand translates into a requested air mass flow rate, choosing the excess air equal to 2, i.e. air flow twice the required by stoichiometry (Bansal et al., 2004):

$$W_{cp,req} = \frac{I_{st} M_{O_2} \lambda_{des} N}{4F0.233} \quad (12)$$

where λ_{des} is the excess of air ratio. The low level control showed must operate the fuel cell stack at his best efficiency point while meeting the demanded current.

2.7 Feed-forward component

The main advantage of using a feed-forward control component is to obtain an immediate effect on the system response. Since there are three different actuators in this system, three static maps have been built. A 2-D map was built for the compressor speed based on the air flow and the cathode pressure. The anode and cathode back-pressure valves have been adjusted by two different static maps based on the optimal pressure for each volume.

Figure 7 shows that simple feed-forward control *alone* is not adequate to achieve a fast and accurate response; the plots are for various quantities of interest for the feed-forward control *alone* applied to the full nonlinear truth model. Being essentially an open-loop action, the feed-forward control is certainly not robust during transient operation, because it is obtained based on steady state responses of the available model. Consequently, there is a need for a more complicated system control that can produce a faster response with less steady state error, and one that is robust to modeling uncertainties, sensor noise, and variations.

3. Linear control

3.1 Model reduction and linearization

Linearization of the complex nonlinear truth model requires specification of an operating point, obtained here as open loop steady-state response with the nominal values given in Table 5. This nominal operating point represents a reasonable region of operation where all parameters are physically realizable.

Since the compressor airflow and pressure in the cathode return manifold affect the power produced, they are chosen to be the system outputs. Moreover, these variables are available and easy to measure in an actual application. Their values, corresponding to the operating condition in Table 5, are 0.023 kg/sec and 1.7 bar for the compressor air flow and return manifold cathode pressure, respectively.

For the purpose of specifying the control inputs, the inlet humidity level is considered constant at 0.6. From the physical fuel cell system configuration, the anode control valve is virtually decoupled from the cathode side of the fuel cell system, and the same static feedforward map used in the feedforward scheme is used here to control the anode control valve (Domenico et al., 2006). Therefore, the two control inputs are chosen to be the compressor speed command and the cathode return manifold valve command. The linearization therefore produces a control-oriented model with two inputs and two outputs.

Variable	Operating point
Current	80 A
Compressor speed command	2800 RPM
Cathode valve opening	38%
Anode valve opening	48%
Humidity	60%

Table 5. Operating values for linearization.

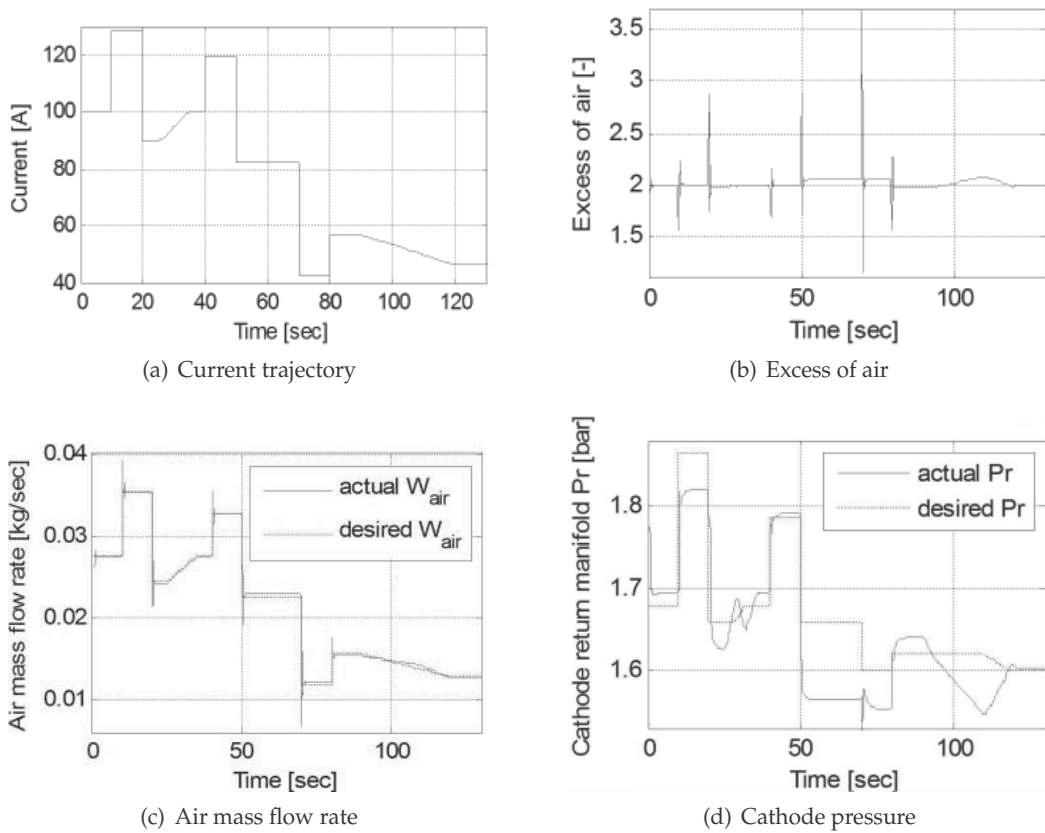


Fig. 7. Response for feed-forward control, applied to nonlinear truth model.

The time-based linearization block in Simulink is used to linearize the model using the LINMOD command over a specific simulation time interval (Domenico et al., 2006). The resulting continuous-time linearized model is given in standard state-variable form as

$$\begin{aligned} \dot{x} &= Ax + Bu \\ y &= Cx + Du \end{aligned} \quad (13)$$

where x is the state vector, y is the system output, u is the system input, and A , B , C , and D are matrices of appropriate dimension.

The 13-state linear system obtained in this way is highly ill-conditioned. To mitigate this problem, a reduced-order 5-state model is derived by returning to the nonlinear simulation and reducing the order of the nonlinear model. Based on the frequency range most important to and most prominently affected by the system controller, namely, for the compressor and the back pressure valve, some states are targeted for removal in model-order reduction. That is, the states associated with the cathode and anode (states 1-5 and 9-11 in Table 3) possess much faster dynamics relative to the other five states. Therefore, static relationships to describe those states are represented in the form of simple algebraic equations. This results in a 5-state reduced order model that preserves the main structural modes that we wish to control (Domenico et al., 2006). The remaining states for the 5th order model are: i) Vapor pressure cathode SM; ii) Dry air pressure cathode SM; iii) Air pressure cathode RM; iv) Compressor

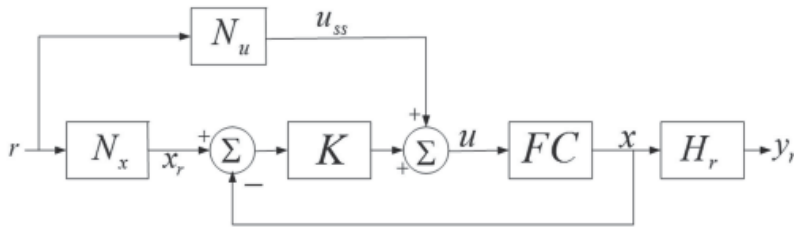


Fig. 8. State command structure.

acceleration; v) Compressor speed, where SM refers to supply manifold and RM refers to return manifold.

The analysis of the full nonlinear model, and subsequent linearization (with validation) for this system were reported in (Domenico et al., 2006). Analysis of the resulting linear models reveals that the 13-state model is stable and controllable, but not completely observable; however, the unobservable state is asymptotically stable. The reduced-order 5-state model is stable, controllable and observable.

3.2 Control design

3.2.1 The state-command structure

The linear control scheme chosen for this application is full state feedback for tracking control with a feed-forward steady-state correction term. For the feed-forward part, a state command structure is used to produce the desired reference states from the reference input tracking command. A steady-state correction term, also a function of the reference, augments the control input computed from the state feedback (Franklin et al., 1990). The controlled-system configuration is depicted as the block diagram in Figure 8.

The control scheme consists of two main parts: the feed-forward and the state feedback control. For the feedback part, a state command matrix N_x is used to calculate the desired values of the states x_r . N_x should take the reference input r and produce reference states x_r . We want the desired output y_r to be at the desired reference value, where H_r determines the quantities we wish to track. Also, the proportionality constant N_u is used to incorporate the steady state, feedforward portion of the control input (u_{ss}). Calculation of N_x and N_u is a straightforward exercise; the task remaining is to specify the matrix K , which is the subject of the next section.

For our structure, the controller objective is to track the optimum compressor supply air flow (r_1) and the optimum cathode return manifold pressure (r_2). We will assume that the compressor supply air flow and the cathode return manifold pressure are measured and are outputs of the system (y_r). The plant input vector consists of the compressor speed and the cathode return manifold valve opening (u). Clearly, the system will be a multi-input, multi-output system (MIMO).

3.2.2 LQR design

Because there are many feasible configurations for the state feedback gain matrix, the method we will use herein is the Linear Quadratic Regulator (LQR) control method which aims at realizing desirable plant response while using minimal control effort. The well-known objective of the LQR method is to find a control law of the form that minimizes a performance index of the general form

$$J = \int_0^{\infty} (x^T Q x + u^T R u) dt \quad (14)$$

For ease in design, we choose diagonal structures for the Q and R matrices in (14), with elements based on simple rules of thumb: (i) the bandwidth of the system increases as the values of the Q elements increases (Franklin et al., 1990); (ii) some system modes can be made faster by increasing the corresponding elements in the Q matrix; (iii) input weights in the R matrix can be used to force the inputs to stay within limits of control authority. In addition to these rules, intuition about the system is needed to be able to specify the Q and R matrices. In our model, we know from the eigenvalues that the second and third states are the slowest, so we can put high penalty on the corresponding Q elements in order to force the state to converge to zero faster. Also, for design of the R matrix, it is important to maintain the valve input to be within $[0 - 1]$. That is, the corresponding element in R should be chosen so as to force the input to stay within this range. Otherwise, if for example the control signal were truncated, saturation incorporated into the nonlinear system model would truncate the control signal provided by the valve input, which could ultimately result in instability.

3.2.3 Simulation results

The full nonlinear truth model is used in all control result simulations to follow. The LQR controller described above is implemented based on the structure depicted in Figure 8, assuming full state feedback. Figure 9 shows the various responses obtained from application to the full nonlinear simulation, for a trajectory current input consisting of a sequence of steps and ramps emulating a typical user demand in the vehicle.

The response is adequate, especially in a neighborhood of the nominal point (current demand $I = 80A$). However, if the input demand goes over $130A$, assumptions of linearity are violated, and the responses diverge. Thus, to illustrate these results we use a trajectory which keeps the system in a reasonable operating range.

For these results, the air excess ratio is almost at the desired value of 2 when the system stays close to the nominal point. But that value increases rapidly if the demand goes higher, which will lower the efficiency of the system (supplying more air than the FC needs). For the air mass flow rate and the cathode return manifold pressure responses, we obtain a good response in the vicinity of the linearization region (0.023 kg/sec and 1.697 bar for the compressor air flow rate and the cathode return manifold pressure, respectively). Even though these results are adequate for operation within the neighborhood of the nominal point of linearization, we have assumed that all states are available for feedback. In reality, we would not have sensors to measure all five states. Therefore, we move to schemes wherein the control uses feedback from measurable outputs.

3.3 Observer-Based Linear Control Design

The control law designed in section 3.2 assumed that all needed states are available for feedback. However, it is typically the case that in practice, the various pressures within the fuel cell system are not all measured. Therefore, state estimation is necessary to reconstruct the missing states using only the available measurements.

For the system of this study, an observer is designed for the reduced-order (5-state) model, where the available measurements are taken to be the system outputs: compressor airflow rate and cathode return manifold pressure. The observer is designed to produce the estimated state, \hat{x} , according to

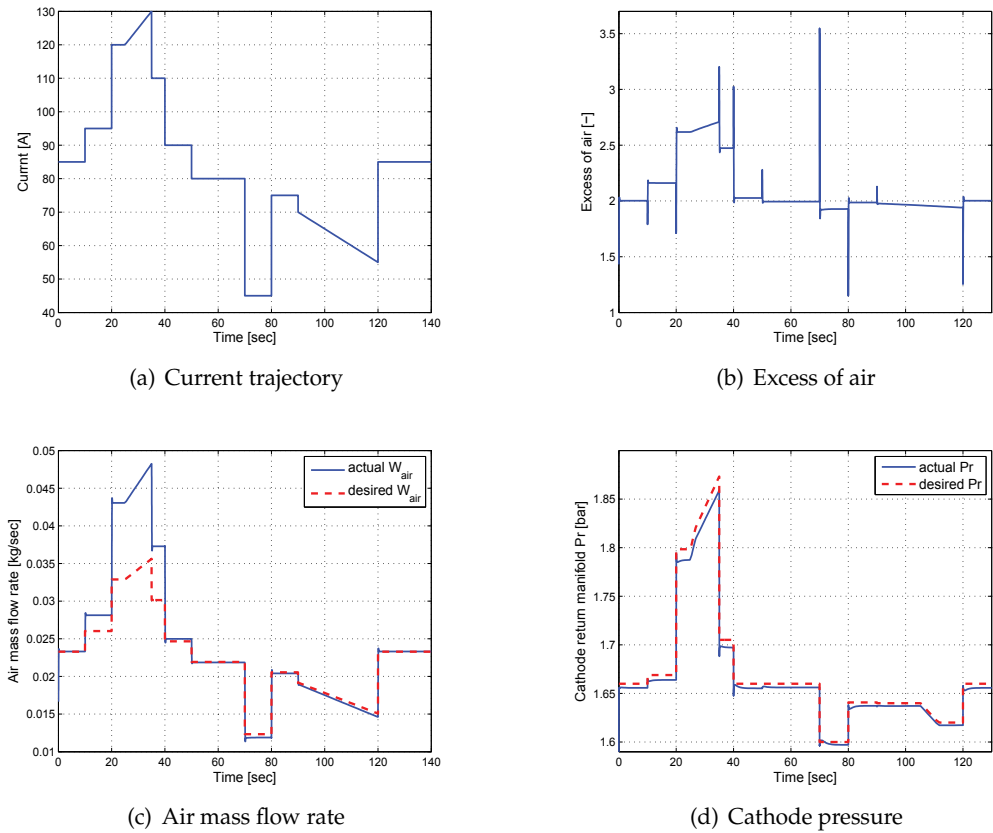


Fig. 9. Response using full-state feedback, applied to nonlinear truth model.

$$\begin{aligned} \dot{\hat{x}} &= A\hat{x} + Bu + L(y - \hat{y}) \\ \hat{y} &= C\hat{x} + Du \end{aligned} \tag{15}$$

where, L is the observer gain matrix, and \hat{x} and \hat{y} represent the estimated state and output, respectively. The observer-based control design structure is depicted by the block diagram in Figure 10. In this design, the observer poles are placed so as to achieve a response which is three times faster than the closed-loop response (determined by the control poles), guaranteeing that the estimated states converge sufficiently fast (to their true values) for this application.

Almost the same current input demand used for the responses in Figure 9(a) is used in this simulation, except that we shortened the range of operation because of unstable behavior outside this range. Figure 11 shows that the air mass flow rate and the cathode return manifold pressure responses are very good except when we deviate from the nominal point of linearization (very clear from the peak at $t = 35$ sec). Nonetheless, their responses are very quick and accurate in a small neighborhood of the nominal point. The air excess ratio is almost at the desired value of 2, except during the transients.

Compared to the feedforward response alone, these results are an improvement when the system operates close to the nominal point at which we linearized the system. The more the

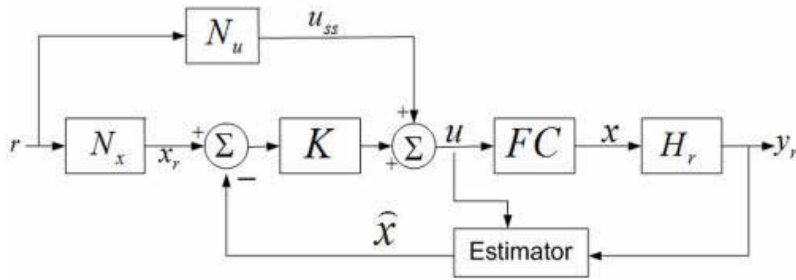
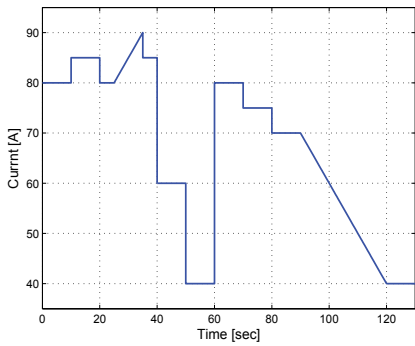
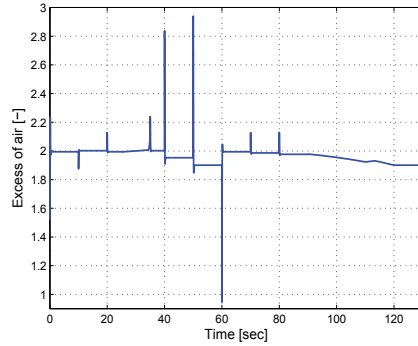


Fig. 10. Control structure with observer.

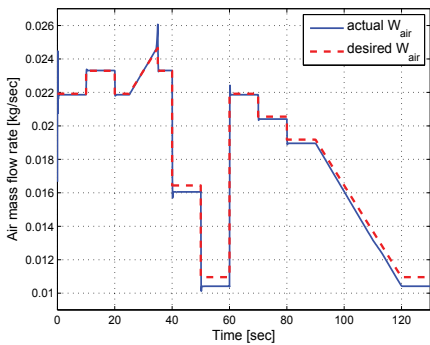
system deviated from this point, the worse the response was. In fact, if we demanded more than 95A, the response diverged. To overcome this problem, we move to the next phase of this study, which is to investigate a more sophisticated control technique that will allow a wider range of operation.



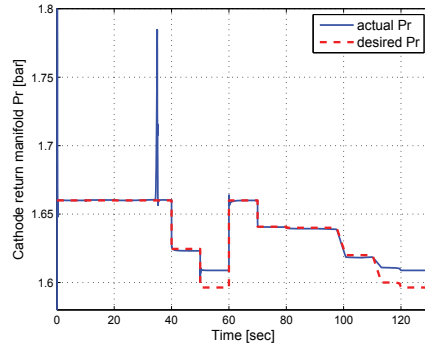
(a) Current trajectory



(b) Excess of air



(c) Air mass flow rate



(d) Cathode pressure

Fig. 11. Response to observer-based feedback, applied to nonlinear truth model.

4. Gain scheduled control

In this section we investigate a nonlinear control approach, referred to as gain scheduling. The basic idea behind gain-scheduled control is to choose various desired operating points, model the system at these points, and apply an appropriate controller (in this case, linear) for each of these ranges.

Gain scheduling is a common engineering practice used to control nonlinear systems in many engineering applications, such as flight control and process control (Shamma & Athans, 1992). The main idea is that one algorithm from several different control designs is chosen based on some operating conditions. The control algorithms are designed off-line with *a priori* information, so the main job of gain scheduling is to identify the proper control algorithm to be used. Herein, the design is broken into exclusive regions of operation. In each region, a fixed control design is applied about a nominal point that is included in that region. Then, a global nonlinear control is obtained by scheduling the gains of the local operating point designs. The controller parameter that determines selection of the appropriate operating region is called the *scheduling variable*.

Despite the popularity of gain scheduling techniques, they are sometimes considered in a class of *ad hoc* methodologies, since the robustness, performance, or even stability properties of the overall design are not explicitly addressed (Shamma & Athans, 1992). However, we can infer these properties via extensive simulations. Many heuristic rules-of-thumb have emerged in guiding successful gain scheduled design; however, the most important guideline is to ensure “slow” variation in the scheduling variable. In (Shamma & Athans, 1992), “slow” is defined for situations wherein the scheduling variable changes slower than the slowest time constant of the closed loop system.

4.1 Scheduling regions

The electrical current demand is chosen to be the scheduling variable that determines the instantaneous operating region. With each different current demand level, the desired reference inputs are picked from the feedforward open-loop system given earlier. To cover the region from $I = 0A$ to $I = 150A$, the domain is divided into six exclusive regions as shown in Table 6.

The criteria for choosing these regions is *ad hoc* in nature, and based on the results obtained in the last section. We noticed from the linear control results that the low current demand (below 50 A) has less-pronounced nonlinear behavior, so the first region covers the larger domain (see Table 6). The rationale for making the range of the other domains of length 20A is the rapidly unstable behavior noticed when the demand exceeded 90A, while the nominal point was 80A. To proceed with the gain scheduled implementation, the 5-state nonlinear fuel cell model is linearized at each of the operating points specified in Table 6. Thus, we obtain six different state matrices, one for each operating point. Then, six linear controllers are designed offline,

Region	I	II	III	IV	V	VI
Range of current demanded [A]	[0, 50)	[50, 70)	[70, 90)	[90, 110)	[110, 130)	[130, 150]
Nominal current [A]	40	60	80	100	120	140
Compressor airflow rate [g/s]	11.4	16.2	22.9	27.3	32.9	38.4
Cathode return manifold pressure [bar]	1.53	1.67	1.70	1.77	1.80	1.89

Table 6. Operating regions based on the current demand level.

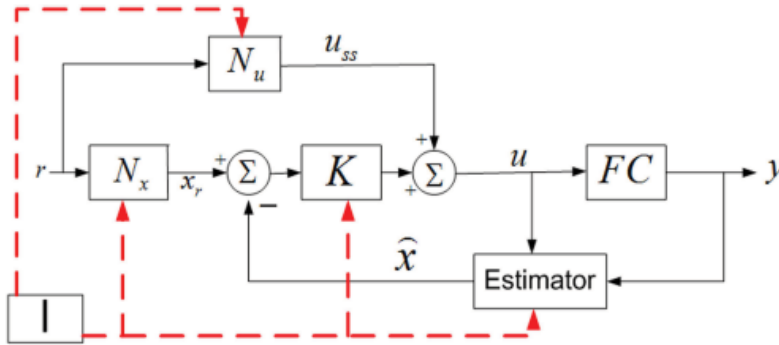
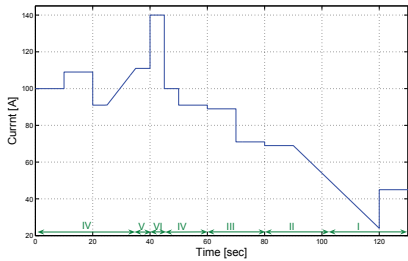


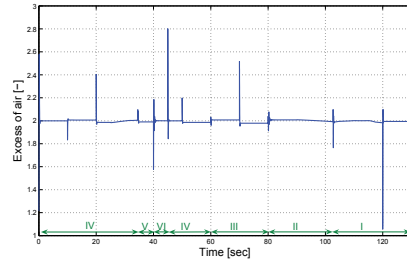
Fig. 12. Gain scheduling scheme.

based on each linearized model. Consequently, we obtain six matrices for each control matrix (N_x , N_u , and K) as well as six observer gain matrices (L). The diagram in Figure 12 is similar to that of Figure 10, but is adapted to the gain scheduling scheme.

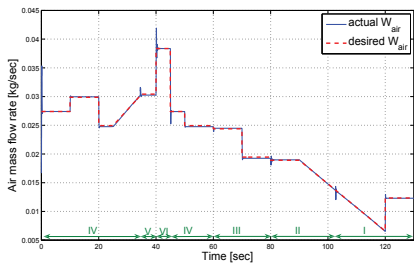
Figure 13 gives the response of the gain-scheduled control with a current demand input similar to that in Section 3, but with wider range. The air mass flow rate and the cathode return manifold pressure responses are very good, except for a few jumps and very small steady state errors (under 1% in either case). However, the overshoot of the cathode return manifold pressure at $t = 35$ seconds almost reaches 10%, which in theory is undesirable (but in practice may not actually be realized). The air excess ratio is very near the desired value of 2, except for the drop at $t = 120$ seconds, which is due to operation away from the nominal value of region-I.



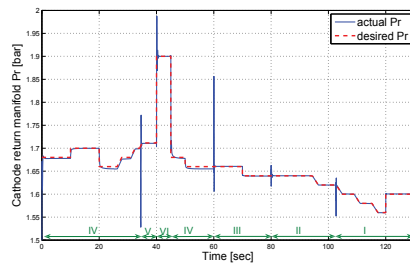
(a) Current trajectory



(b) Excess of air



(c) Air mass flow rate



(d) Cathode pressure

Fig. 13. Response for Gain-Scheduled Control, Applied to Nonlinear Truth Model.

4.2 Controller refinement

The results of the gain scheduling controller are quite good, except during the transients; this behavior is characteristic of this type of control scheme. That is, the most important design constraint for gain scheduling is the requirement for slow variation of the scheduling variable. The input current trajectory that we are using has very fast frequency components because of the nature of the steps (in actual implementation, however, such harsh steps can often be avoided by appropriate input shaping). This fast switching causes a rapid change in the controller as well as the observer gains, which results in the spike behavior. This is true even for some steps of smaller amplitude, such as in the cases for $t = 60$ seconds or $t = 80$ seconds; in those cases, the system “quickly” switches across regions. To mitigate the effects of fast switching in the gains, we will introduce a technique combining two components: (i) interpolation of the gain matrices, and (ii) shaping the current input trajectory.

4.2.1 Interpolating the gain matrices

In this method, some of the gain matrices are interpolated with respect to the gain scheduling variable. Interpolation of state feedback and observer gains is used to obtain a smooth transition from one region to another (Rugh & Shamma, 2000). There are many different methods of interpolation; however, the simplest method is linear interpolation.

Recall that we have six matrices (one for each region) of each type of the gain matrices (K , N_x , N_u , and L) resulting from the observer-based control design that can be interpolated as depicted in Figure 14 to render the six sets of matrices into one set for the overall range. The elements of each of the resulting matrices, for example \bar{K} , are a function of the scheduling variable (current demand). As the current demand trajectory changes, the gain matrices change more smoothly, as compared to fast switching used in the previous subsection. An interpolation of K , N_x , and L , but not N_u , provided the best results (Al-Durra et al., 2007), and are used in conjunction with the second component, input shaping.

4.2.2 Input shaping

The idea of input shaping has shown an advantage in reducing vibration and subsequent excitations caused by rapid changes in reference command (Fortgang & Singhose, 2002), (Tzes & Yurkovich, 1993). As mentioned earlier, to have an effective gain scheduled controller, the scheduling variable should not change faster than the slowest dynamic in the system. This restriction was violated in the control results given to this point, since the scheduling variable (current input trajectory) is characterized by step functions. We now investigate the concept of shaping the current trajectory by passing it through a low pass filter. However, since we still want to see the response to fast transients, we design the corner frequency of the filter to be at 10 Hz; this choice is relatively fast by drivability standards, and would not noticeably change vehicle responsiveness.

Figure 15 shows the results achieved by refining the gain-scheduled control using input shaping with the interpolated gain concept of the last section. Comparing the results of Figure 13 and Figure 15 and using the same current input as in 13(a), we see improvement in the excess of air ratio, now between 1.75 and 2.2, compared to 1.5 and 2.8 without the refinement. Overall, we notice fewer variations, but the response still suffers from the transients (spikes).

5. Rule-based control

Controlling a nonlinear system using a sophisticated nonlinear control technique, such as feedback linearization or sliding mode control, requires knowledge of the nonlinear

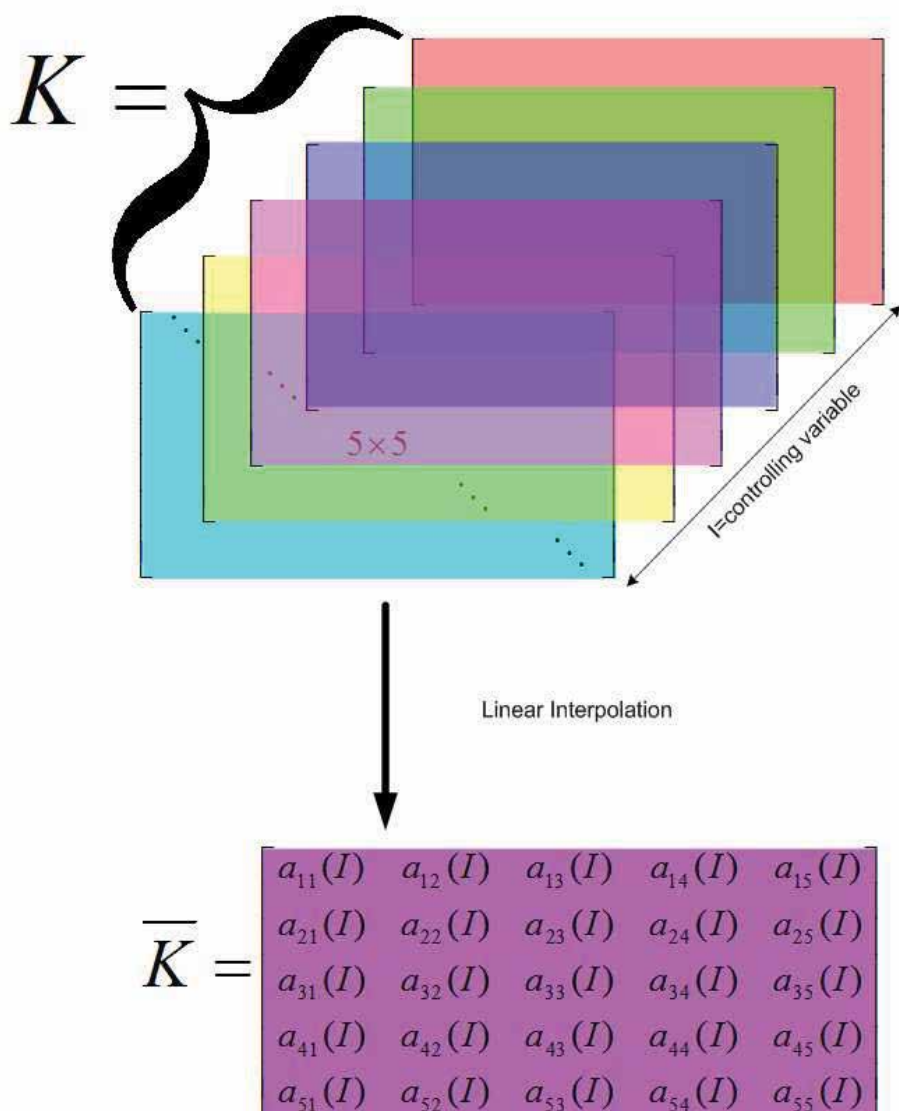


Fig. 14. Linear interpolation.

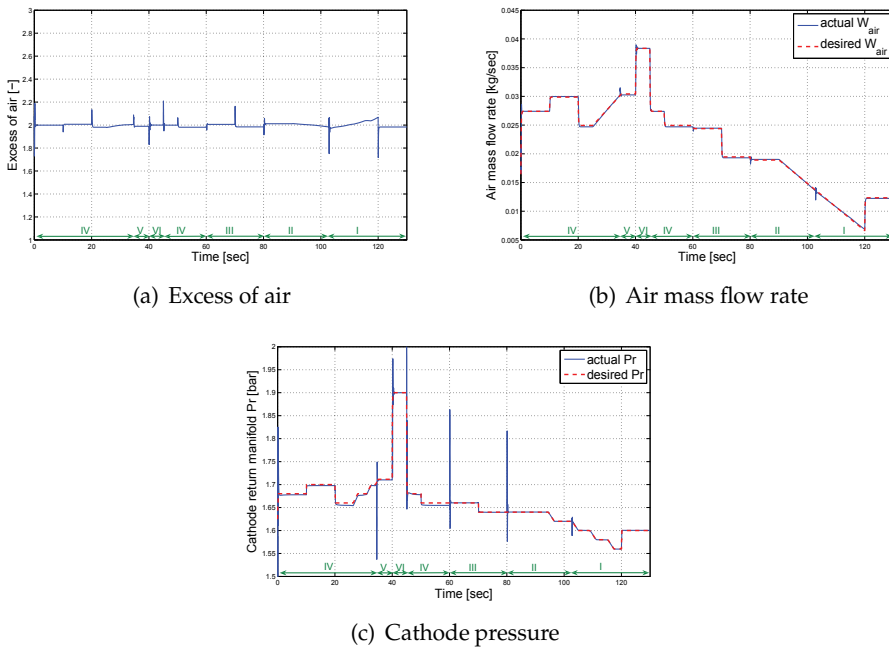


Fig. 15. Gain scheduling using interpolation and input shaping, applied to nonlinear truth model.

differential equations describing the system. Our PEM fuel cell model contains several maps and lookup tables which limit our ability to use such model-based nonlinear control. Linearization of the system and application of linear control gave an adequate response only in the vicinity of the point of linearization. Expansion to a gain-scheduled control widened the range of operation, but the response still suffered somewhat from transient spikes when switching from one operating region to another. In this section, another nonlinear control technique is explored, rule-based control, which does not require full knowledge of the dynamical equations of the system. The results and experience gained in the control schemes of the preceding sections are used here for synthesis of the controller.

5.1 Rule-based control implementation on the PEM-FC model

A rule-based controller can be characterized as an expert system which employs experience and knowledge to arrive at heuristic decisions. Most often, the design process is a result of experience with system operation (Passino & Yurkovich, 1998).

5.1.1 Choosing the rule-based controller inputs and outputs

The input to the controller should be rich enough to lead to decisions that produce the system input (output of the controller); those decisions are based on the knowledge base made up of cause and effect rules. In order to ascertain which signals are relevant as controller inputs, we study the coupling between the inputs and the outputs of the PEM-FC model, and control results from the previous sections. From the linearized models obtained in various regions, frequency response information (Bode plots) can be utilized. For example, this characterization for region-III shows that the gain from input-1 to output-2 is at most -70dB ,

indicating mild coupling. The same results appeared for the correlation between input-2 and output-1 where the gain is at most -125dB . From this we conclude that we can regulate the system inputs using a single-input, single-output approach for two separate subsystems (air and pressure), neglecting the mild coupling.

5.1.2 Rule-based controller characteristics

In this design, a typical fuzzy control scheme (Passino & Yurkovich, 1998) is used. The number of triangular membership functions for each controller input and output is nine; a higher number could lead to greater precision, but at the expense of increased computations. The shape of each membership function is chosen to be triangular, since this will reduce the computations needed (compared to, for example, Gaussian-shaped membership functions). A typical process in design is to shift the centers of these functions, to be closer to or further away from the origin on the input scale, in order to result in a certain effect. For example, if shifted closer to the origin, the intent is to stress the effect of that particular membership function for smaller values of the input, and vice versa. It should also be noted that separations between the membership functions were tuned empirically, based on prior experience in such designs. However, the general trend for the separation is linear; that is, the positions are closer for the memberships close to the origin and the separation is wider for those away from the origin. Another important characteristic in the design of rule-based controllers is the domains (universes of discourse) of each controller input and output. For this problem, these are chosen based on the experiences reaped from the gain-scheduled control design described earlier, indicating the range of values for the controller input and output shown in Table 7. For the inference operation, the *min* function (truncation) is chosen it requires fewer calculations when compared to the *prod* (scaling) function; the *max* operation is used for aggregation. Finally, to produce a crisp controller output (the defuzzification step), the centroid method is used.

5.2 Control design and simulation

Because there are few systematic design methods for constructing a rule-based control system, several control schemes were investigated in this work. Two schemes are compared in this section.

5.2.1 Baseline design

The controller inputs (v_i) for each separate controller (air and pressure) are the error between the reference inputs (r_i) and the system outputs (y_i). However, to avoid transient spikes in the control inputs to the system, a concept of “memory” in the control will be needed to remember the previous error received. Therefore, integrators are added, limited to avoid exceeding each controller authority; the resulting lag introduced into the system response can be mitigated by adding a gain to the output of the rule-based controller. Figure 16(a) shows the Baseline control scheme with integrators and gains; by increasing the gains (g_i), the system response time can be decreased in a tradeoff with other characteristics (such as overshoot and settling

Input (v) / Output (u)	Universe of Discourse
v_1	$[-0.03, 0.03]$
u_1	$[-3000, 3000]$
v_2	$[-4, 4]$
u_2	$[-1, 1]$

Table 7. Domains for controller inputs and outputs.

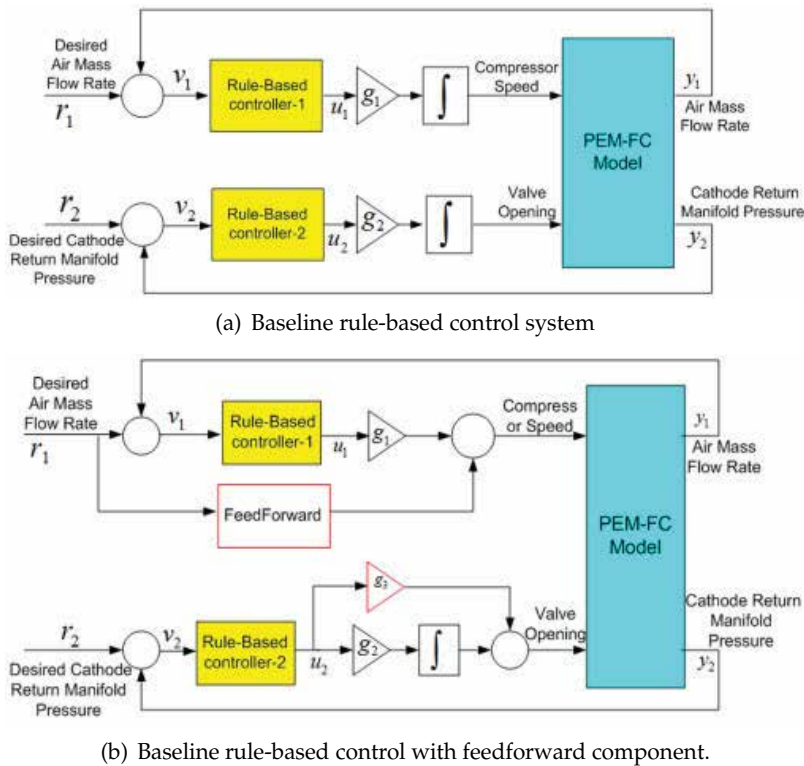


Fig. 16. Rule-based schemes.

time). The fuzzy surfaces that characterize each of the two controllers (controller input-output maps) behave similarly to an inverse tangent curve, designed in order to diminish the effect of rapid changes in the errors (v_i) to avoid the transient spike effects seen with the gain scheduled controller.

The response of this Baseline scheme, for the same current trajectory (Figure 13(a)), is shown in Figure 17 (a,b, and c). Compared to the results of the gain scheduled control, the air mass flow rate has improved (less transient effect with less steady state errors). However, lag is noticeable in the response due to the integrator; note, for example, in the transient at $t = 40$ seconds, more than a half second is needed to reach a 5% settling time. The cathode return manifold pressure responses improve, but still suffer from transient spikes. The air excess ratio is now almost at 2 most of the time; however, spikes are still noticeable, particularly at $t = 120$ seconds, which could damage the fuel cell.

5.2.2 Addition of feedforward component

The two deficiencies of the Baseline design can be remedied with simple feedforward components. The first deficiency is the slow response of the compressor air mass flow rate. This can be improved by adding a nonlinear feedforward term that is based on the steady state plant inverse response. In so doing, we remove the first integrator to further increase the speed of the response. The second deficiency of the Baseline controller is presence of transient spikes in the cathode return manifold pressure. Decreasing the gain of the integrator has a positive effect, but a proportional gain is needed to obtain a faster response. Figure 16(b)

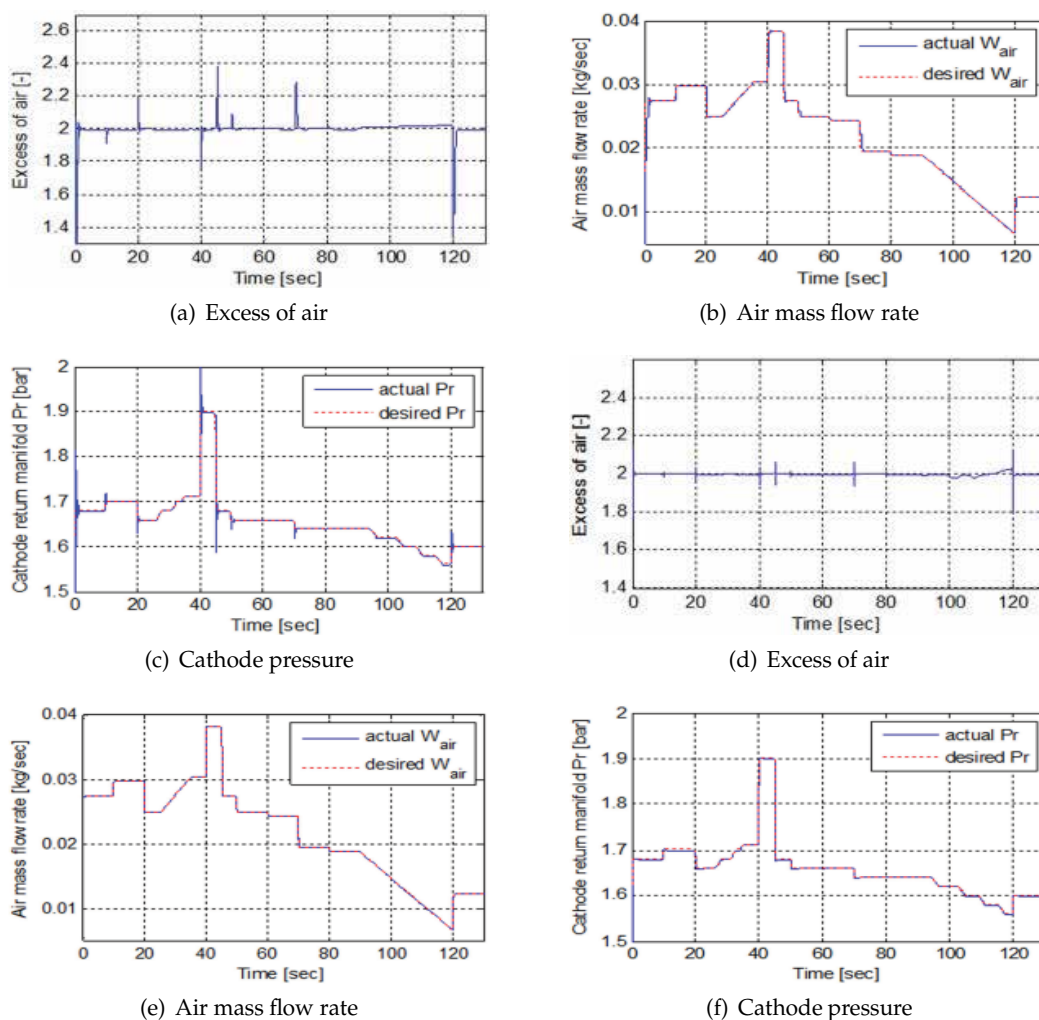


Fig. 17. Response of Baseline rule-based controller (a, b, and c) and Baseline with feedforward component (d, e, and f).

shows a schematic for the addition of feedforward component, with proportional gain. Figure 17 (d, e, and f) shows the results obtained using this final control architecture. Compared to the Baseline scheme, the air mass flow rate response is now faster, since it takes 0.1 seconds for 5% settling time. Also, the transient spikes in the cathode return manifold pressure response have been successfully eliminated; this was a particularly difficult issue for all of the techniques used in this study. The air excess ratio response for this scheme is particularly good, essentially achieving a value of 2 throughout, with a maximum excursion of 0.2 at $t = 120$ seconds.

In addition to the desirable performance on the nonlinear truth model, one of the major advantages of using the rule-based controller is the fact that an observer (to estimate system states) is not needed. On the other hand, a drawback is that more calculations are needed in computing the implied fuzzy sets and the final control input value (Passino & Yurkovich,

1998); this effect is evident if we compare the time needed for these simulations compared to the simulations of the gain scheduled controller (roughly a factor of three different). Another disadvantage is the add-hoc nature of this technique, requiring the designer to be familiar with the system in order to efficiently tune the membership functions to achieve the best performance. However, experience gained in the linear and gain-scheduled control designs is useful here.

6. Performance comparison

Although the controllers developed heretofore performed well in simulation on the nonlinear truth model, which contains a variety of nonlinearities and maps, an important consideration is the capability of the controllers to perform adequately in the presence of realistic disturbances and uncertainties that may be experienced in typical operation. In this section, we consider three types of uncertainties that are typically not predicted by a model: disturbances, unmodeled dynamics (time delay), actuator limits, and input noise. In the analysis of this section, we compare the final (observer-based) gain-scheduled-interpolated controller with the final rule-based controller. Although there are several quantities of interest in the fuel cell system as a whole, these comparative studies will focus on the response of the compressor air mass flow, the cathode return manifold pressure, and the excess of air, because these are the most important variables in this PEM-FC model.

6.1 Disturbances

It is well known that the ionic conductivity of the membrane in a PEM-FC system is dependent upon its water content (McKay et al., 2005). Recall that for the model of this study, the inlet humidity level was considered constant at 0.6. Thus, a critical disturbance to consider for this model and the subsequent control design is uncertainty (disturbance) in the inlet humidity level, which directly affects the plant input. The response to significantly increased (or decreased) humidity levels, from the value assumed in the model-based control design, would be expected to degrade somewhat; the degree of degradation for each control scheme developed is of concern in this section.

First for the gain-scheduled control scheme developed earlier, we investigate the effect of changing the humidity inlet input to the FC-Model response by examining two values, 0.4 and 0.8, representing a 33% decrease and increase, respectively. Figure 18 (a, b, and c) shows the response of the system with 0.4 and 0.8 inlet humidity input (in separate traces on the same sizes). Clearly, the air mass flow rate was not affected by changing the inlet humidity because the compressor air mass flow rate is measured before the humidification process. However, an effect is evident on the cathode return manifold pressure. When the relative humidity is less than the value for which the control was designed (0.4 versus 0.6), a pressure lower than the desired response results; the effect is opposite for the higher humidification case. This is expected, since the cathode return manifold pressure mainly depends on the cathode pressure, which is affected by the inlet humidity level. The effect is manifested in steady state errors that reach 1.5%, as well as in a pronounced increase in transient spikes. Furthermore, the overshoot in the return manifold pressure reaches 11.3% in some transients. The excess air ratio is not affected since it depends on the response of the air mass flow rate. The same arguments apply when the inlet humidity level is increased to 0.8, except that the steady state errors are smaller, but higher overshoot occurs in both the return manifold pressure and the excess of air response.

The rule-based control copes with an inlet humidity level disturbance much better than the

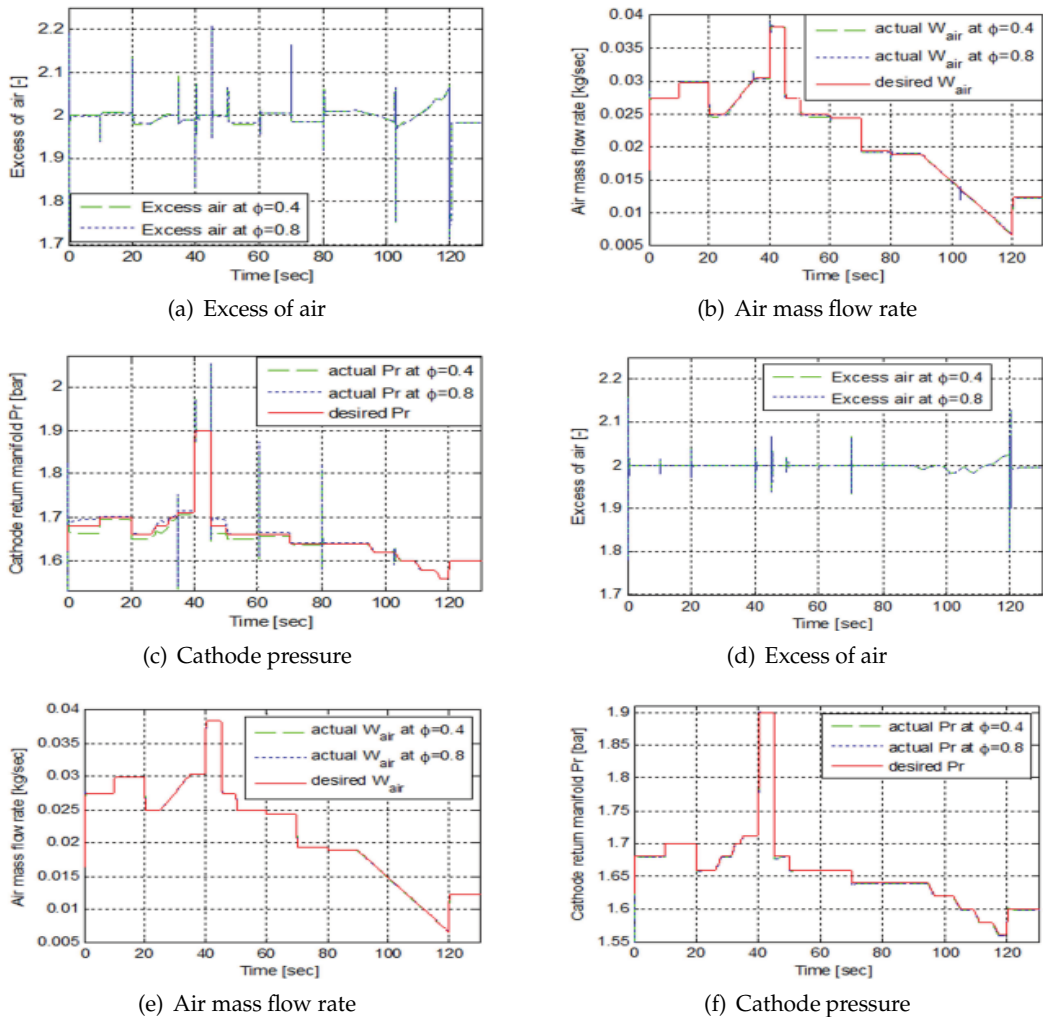


Fig. 18. Response of gain-scheduled control (a, b, and c) and rule-based control (d, e, and f) with disturbance

gain scheduled control. Figure 18 (d, e, and f) shows the response for both cases, 0.4 and 0.8 inlet humidity levels. The increased performance of this scheme is evident in terms of the cathode return manifold pressure response. The steady state error is less than 0.1% and the overshoot is less than 3%, which is very good considering the size of the disturbance. The excess air ratio was not affected, since it depends on the response of the air mass flow rate.

6.2 Unmodeled dynamics (time delay)

Unmodeled dynamics represented by a time delay due in the sensor dynamics will now be introduced and simulated. In this implementation, the time delay has been added to both outputs (compressor air flow rate and cathode return manifold pressure) before being fed to the observer (in the case of the gain scheduling scheme) and before being fed to the control decision blocks (in the case of the rule-based control scheme).

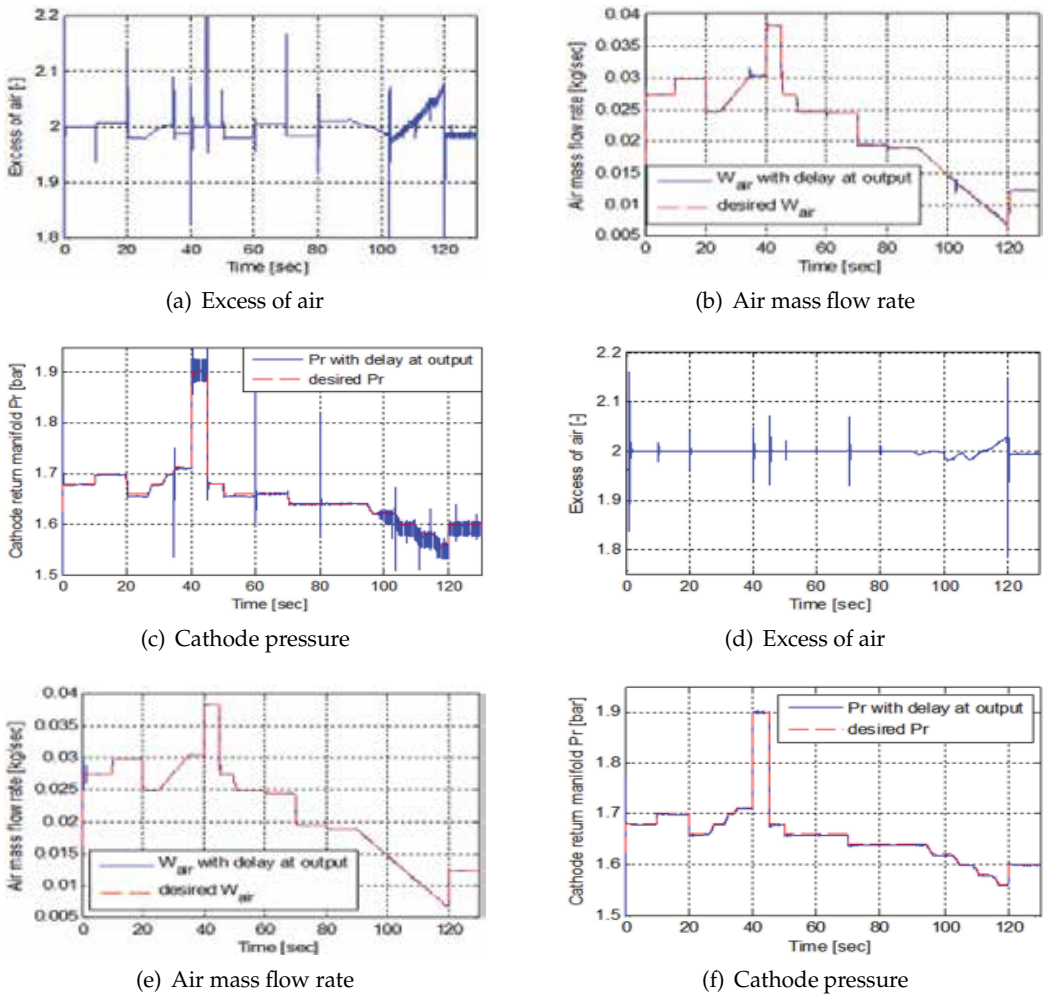


Fig. 19. Response of gain-scheduled control (a, b, and c) and rule-based control (d, e, and f) with sensor time delay.

The delay is gradually increased until the gain schedule controller scheme started to exhibit unstable behavior. The maximum sensor delay reached, while still exhibiting a reasonable response, is 10 milliseconds. The controller is sluggish, and noticeable transient spikes can be observed in Figure 19 (a, b, and c). On the other hand, for the rule-based controller, the same time delay applied to the sensors once again results in comparatively good behavior in the presence of this uncertainty. Figure 19 (d, e, and f) shows the response, where only small fluctuations in the pressure response are evident, which does not exceed 1% of the steady state value.

6.3 Actuator limits

The final robustness test in this study investigates controller performance when the actuators undergo some limitation in authority. Two experiments are performed; the first assumes that

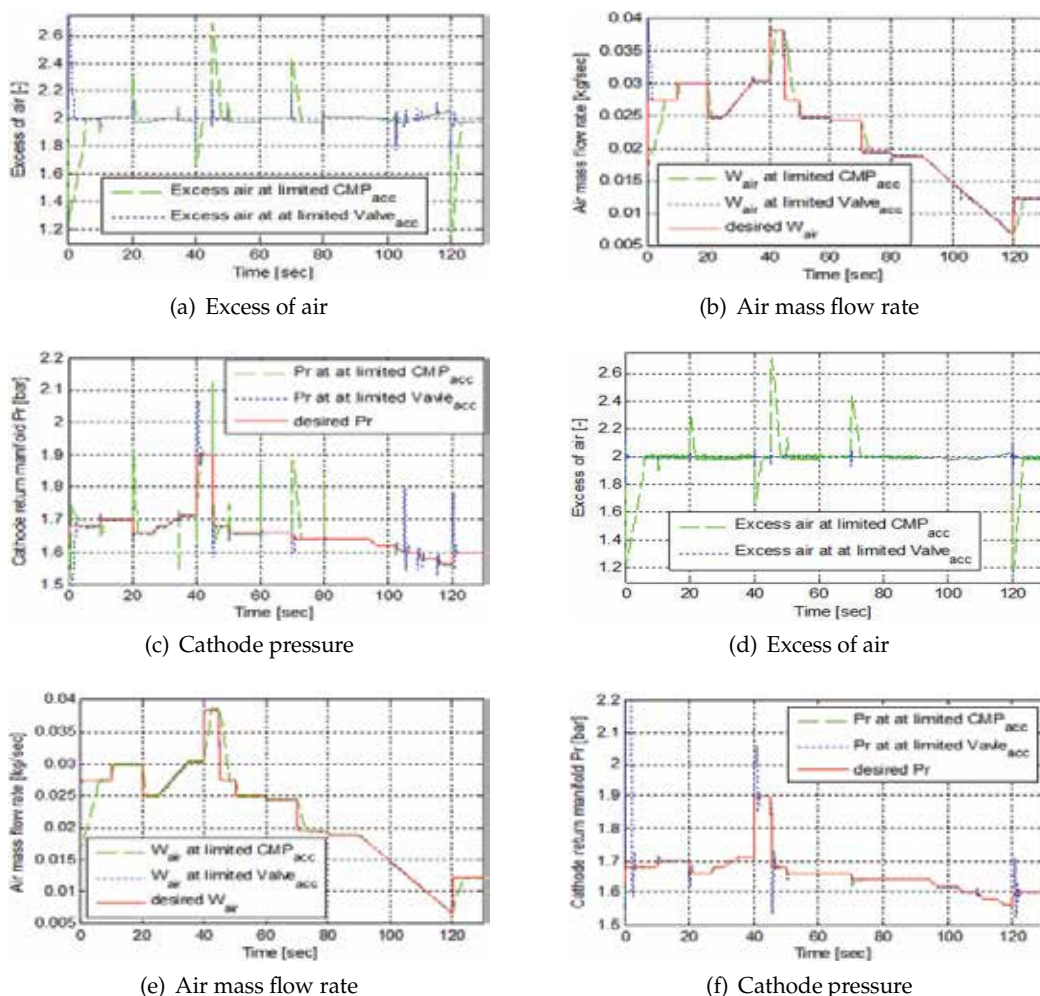


Fig. 20. Response of gain-scheduled control (a, b, and c) and rule-based control (d, e, and f) with actuator limits.

the compressor response is slower than the modeled speed-driven screw compressor, where the acceleration of the compressor was limited to 200 RPM/s. The second experiment assumes that the valve opening rate is limited to 25% per second.

Consider first the observer based gain-scheduled controller. Figure 20 (a, b, and c) are reasonable, where two traces (one for limited compressor response, CMP, and the other for valve opening rate). As we mentioned earlier, the compressor air flow and the cathode return manifold pressure both have a mild coupling. Therefore, we notice that when we limited the compressor acceleration, the air mass flow rate was affected much more than the return manifold pressure. Limiting the valve opening acceleration affected the compressor air flow rate, but only slightly. Nevertheless, it did clearly affect the return manifold pressure, especially at the transients where we see spikes that did not exist before. Notice also the spikes observed in the excess air ratio response; the compressor is not able to provide the air needed

as fast as the FC desires, and effect which could harm the stack and reduce the durability of the FC.

Applying the same two parametric uncertainty experiments to the system controlled by a rule-based controller results in the traces shown in Figure 20 (d, e, and f). When limiting the compressor acceleration, a slow response in the air flow results as in the case of gain-scheduled control system. However, limiting the valve opening acceleration results in fewer transient spikes compared to the gain-scheduled controller. The excess air ratio behavior is reasonable under this uncertainty, although we should point out that limiting the compressor acceleration will affect the air flow rate and therefore the excess air ratio. In fact, neither controller completely overcame this uncertainty.

6.4 Input noise

The last robustness test is to check the effect of the noise. To achieve this, random number generators are added to the FC system input signals. The parameters of the noise generated are chosen to be zero mean with the variance equal to 3% of input steady state values at I=80A. This time, the responses for both control techniques are plotted on the same axes to make the comparison easier. From Figure 21, it is clear that the rule-based controller is more robust to input noise than the gain-scheduling controller. This is clear in all of the responses, especially the cathode return manifold pressure and the excess air. For the rule-based response, we do not see large spikes and the variance of the response from the desired trajectory is not large compared to the response of the gain-scheduled controller.

7. Conclusion

Beginning with a highly nonlinear model, a simplified, reduced-order control-oriented model was obtained by linearizing about a nominal operating point. We then investigated linear

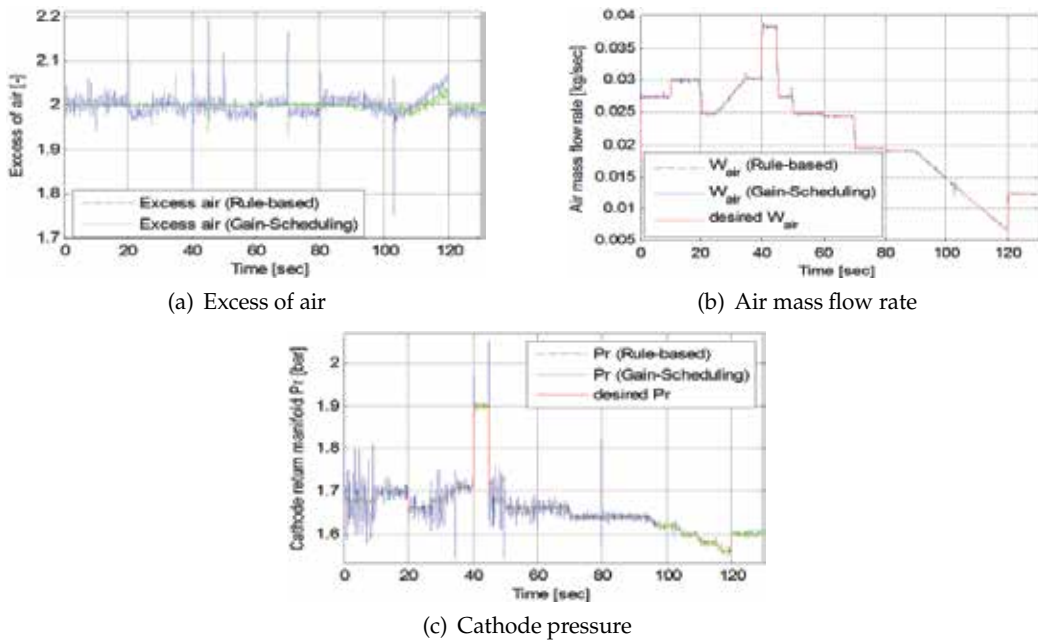


Fig. 21. The response of both controllers with input noise.

quadratic regulator control, with observer, for the reduced-order model, where shortcomings due to the limited range of the linearization were evident. This led to the concept of gain scheduling control, introduced for this architecture to allow operation in a wider range. Simulation results showed that this technique does, indeed, allow a wider range of operation; however, as expected, transient spikes appeared due to the fast switching in the region of operation. Two methods were used to reduce these spikes: interpolating the controller gains, and reshaping the input trajectory. The two techniques reduce the undesirable behavior considerably, but the response still has overshoot during the transients because of the fast switching between regions of operation. A rule-based, output feedback control, was implemented with fuzzy logic and coupled with a nonlinear feed-forward approach. The resulting control system was examined under the same conditions applied to the first two techniques. The rule-based controller achieved the best results in terms of the speed of response and overall performance during the transients. Robustness of the gain-scheduled control and the rule-based control to disturbance, time delay, actuators limits, and input noise was investigated. Overall, the rule-based controller performed very well when the system was subjected to these effects.

The contributions of this study include a high fidelity nonlinear model of a typical fuel cell system (intended for automotive applications), formulation of a reduced order, control-oriented mode suitable for modern control design, nonlinear control designs offered in comparison, and a performance study for a range of uncertainties expected in typical system operation. The control design methodologies chosen for comparison are straightforward and effective, in keeping with the overriding intent of the work to maintain designs which would be readily applied to an actual system.

8. References

- Al-Durra, A., Yurkovich, S. & Guezennec, Y. (2007). Gain-Scheduled Control for an Automotive Traction PEM Fuel Cell System, *Proceedings of the 2007 ASME International Mechanical Engineering Congress and Exposition*.
- Al-Durra, A., Yurkovich, S. & Guezennec, Y. (2010). Study of Nonlinear Control Schemes for an Automotive Traction PEM Fuel Cell System, *International Journal of Hydrogen Energy* (doi:10.1016/j.ijhydene.2010.07.046).
- Ambühl, D., Anguiano, N., Sorrentino, M., Y. Guezennec, S. M. & Rizzoni, G. (2005). 1&1D Isothermal Steady State Model of a Single PEM Fuel Cell, *Proceedings of 2005 IMECE, Orlando, FL, U.S.A.*
- Arsie, I., Di-Domenico, A., Pianese, C. & M.Sorrentino (2005). Transient Analysis of PEM Fuel Cell for Hybrid Vehicle Application, *Proceedings of 2005 ASME 3rd Int. Conference on Fuel Cell Science, Ypsilanti, MI*.
- Bansal, D., Rajagopalan, S., Choi, T., Guezennec, Y. & Yurkovich, S. (2004). Pressure and Air Fuel Ratio Control of PEM Fuel Cell System for Automotive Traction, *IEEE - VPP conference*.
- Bernay, C., Marchanda, M. & Cassir, M. (2002). Prospects of Different Fuel Cell Technologies for Vehicle Applications, *Journal of Power Sources* 108 pp. 139–152.
- Brinkman, N. (2002). Well to Wheel Energy Use and Greenhouse Gas Emission of Advanced Fuel/Vehicle System - North American Analysis, *General Motors Executive Summary Report, available at the <http://www.epa.gov>* pp. 139–152.
- Chen, D. & Peng, H. (2004). Modeling and Simulation of a PEM Fuel Cell Humidification System, *Proceeding of the 2004 American Control Conference*.

- Davis, C., Edelstein, B., Evenson, B. & Brecher, A. (2003). Hydrogen Fuel Cell Vehicle Study, *American Physical Society Report available at the <http://www.aps.org>* .
- Domenico, A., Miotti, A., Alhetairshi, M., Guezennec, Y., Rajagopalan, S. & Yurkovich, S. (2006). Multi-Variable Control for Automotive Traction PEM Fuel Cell System, *IEEE American Control Conference* .
- EG&G-Technical-Services (2002). *Fuel Cell Handbook-Sixth edition*, U.S. Department of Energy - National Energy Technology Laboratory Strategic Center for Natural Gas.
- Fortgang, J. & Singhose, W. (2002). Concurrent Design of Input Shaping and Vibration Absorbers, *Proceeding of American Control Conference* pp. 1491–1496.
- Franklin, G., Powell, J. & Workman, M. (1990). *Digital Control of Dynamic Systems*, Addison-Wesley.
- Guzzella, L. (1999). Control Oriented Modeling of Fuel Cell Based Vehicles, *NSF Workshop on the Integration of Modeling and Control for Automotive System* .
- Heywood, J. (1998). *Internal Combustion Engine Fundamentals*, McGraw Hill.
- Kueh, T., Ramsey, J. & Threlkeld, J. (1998). *Thermal Environmental Engineering*, McGraw Hill.
- Larminie, J. & Dicks, A. (2003). *Fuel Cell System Explained*, Wiley.
- Mazunder, S. (2003). A Generalized Phenomenological Model and Database for the Transport of Water and Current in Polymer Electrolyte Membranes, *Journal of Electrochemical Society* .
- McKay, D., Ott, W. & Stefanopoulou, A. (2005). Modeling, Parameter Identification, and Validation of Reactant and Water Dynamics for a Fuel Cell Stack, *Proc. of IMECE* .
- Miotti, A., Domenico, A., Esposito, A. & Y. Guezennec, Y. (2006). Transient Analysis and Modeling of Automotive PEM Fuel Cell System Accounting for Water Transport Dynamics, *Proc. of ASME 2006 4th International Conference on Fuel Cell Science, Engineering and Technology* .
- Passino, K. & Yurkovich, S. (1998). *Fuzzy Control*, Addison-Wesley.
- Pukrushpan, J. (2003). *Modeling and Control of Fuel Cell System and Fuel Processor*, PhD thesis, The University of Michigan, Ann Arbor, U.S.A.
- Pukrushpan, J., Stefanopoulou, A. & Peng, H. (2002). Modeling and Control for PEM Fuel Cell Stack System, *Proceeding of American Control Conference* pp. 3117–3122.
- Pukrushpan, J., Stefanopoulou, A. & Peng, H. (2004a). Control of Fuel Cell Breathing, *IEEE Control Systems Magazine* .
- Pukrushpan, J., Stefanopoulou, A. & Peng, H. (2004b). Control of Fuel Cell Breathing: Initial Results on the Oxygen Starvation Problem, *IEEE Control Systems Magazine* 24: 30–46.
- Pukrushpan, J., Stefanopoulou, A. & Peng, H. (2002). Modeling and Control for PEM Fuel Cell Stack System, *Proceeding of American Control Conference* pp. 3117–3122. Anchorage, AK.
- Pukrushpan, J., Stefanopoulou, A. & Peng, H. (2004). Simulation and Analysis of Transient Fuel Cell System Performance Based on Dynamic Reactant Flow Model, *Proceedings of 2002 ASME International Mechanical Engineering Conference and Exposition*.
- Rodatz, P. (2003). *Dynamics of the Polymer Electrolyte Fuel Cell: Experiments and Model-Based Analysis*, PhD thesis, Swiss Federal Institute of Technology, Zurich, Swiss.
- Rugh, W. & Shamma, J. (2000). Survey Paper: Research on Gain Scheduling, *Automatica* 36: 1401–1425.
- Shamma, J. & Athans, M. (1992). Gain Scheduling: Potential Hazards and Possible Remedies, *IEEE Control Systems Magazine* .

- Thijssen, J. & Teagan, W. (2002). Long-Term Prospects for PEMFC and SOFC in Vehicle Applications, *SAE paper 2002-01-0414* .
- Thomas, S. & Zalowitz, M. (2000). Fuel Cells Green Power, *Los Alamos National Laboratory* .
- Tzes, A. & Yurkovich, S. (1993). An Adaptive Input Shaping Control Scheme for Vibration Suppression in Slewing Flexible Structures, *IEEE Transactions on Control Systems Technology* 1: 114–121.
- Yi, J., Yang, J. D. & King, C. (2004). Water Management Along the Flow Channels of PEM Fuel Cells, *AIChE Journal* .
- Yu, Q., Srivastava, A., Choe, S. & Gao, W. (2006). Improved Modeling and Control of a PEM Fuel Cell Power System for Vehicles, *Proceedings of the IEEE SoutheastCon* .

An Adaptive Two-Stage Observer in the Control of a New Electromagnetic Valve Actuator for Camless Internal Combustion Engines

Paolo Mercorelli

*Ostfalia University of Applied Sciences, Faculty of Automotive Engineering
Robert Koch Platz 12, D-38440 Wolfsburg
Germany*

1. Introduction

In this paper, the experimental results for the design and operation of a special linear electromagnetic motor as a variable engine valve actuator are presented. A detailed description is given on the design procedure aimed at meeting the requirements of a high dynamic range and low power consumption, including determinations of the actuator's topology and parameters, the force and the dynamic and power loss calculations. Moreover, based on a nonlinear model, an adaptive two-stage observer is presented to tackle unobservable points and achieve sensorless control. Further, this paper presents feasible real-time self-tuning of an approximated velocity estimator based on measurements of current and input voltage. The robustness of the velocity tracking is addressed using a minimum variance approach. The effect of the noise is minimised, and the position can be achieved through a two-stage structure between this particular velocity estimator and an observer based on the electromechanical system. This approach avoids a more complex structure for the observer and yields an acceptable performance and the elimination of bulky position-sensor systems. A control strategy is presented and discussed as well. Computer simulations of the sensorless control structure are presented in which the positive effects of the observer with optimised velocity are visible in the closed-loop control.

2. Background and state of the art

With the recent rapid progress in permanent-magnet technology, especially through the use of high-energy-density rare-earth materials, very compact and high-performance electromagnetic linear actuators are now available. They open new possibilities for high-force motion control in mechatronic applications, for which great flexibility, highly controlled dynamics and precise positioning are required at the same time. In the last years, variable engine valve control has attracted a lot of attention because of its ability to reduce pumping losses (work required to draw air into the cylinder under part-load operation) and to increase torque performance over a wider range than conventional spark-ignition engines. Variable valve timing also allows the control of internal exhaust gas recirculation, thereby improving fuel economy and reducing NO_x emissions. Besides mechanical and hydraulic variable valvetrain options, electromagnetic valve actuators have been reported in the past, see Refs.

(Ahmed & Theobald (1999)) and (Schlechter & Levin (1996)). Recent works mark technical progress in this area, in particular, Refs. (Tai & Tsao (2003)), (Hoffmann & Stefanopoulou (2001)) and (Peterson (2005)). Theoretically, electromagnetic valve actuators offer the highest potential to improve fuel economy due to their control flexibility. In real applications, however, the electromechanical valve actuators developed so far mostly suffer from high power consumption and other control problems. Therefore, innovative concepts are required to reduce the losses while keeping the actuator dynamic. In the first part of this paper, the theoretical and experimental results for the design of a novel permanent-magnet linear valve actuator are presented, allowing short-stroke high-dynamic operations combined with low power losses. In the second part of the paper, a sensorless control is shown. In such applications, sensorless control has always been a challenging problem when trying to avoid bulky position-sensor systems. To realise this goal, it is necessary to create an observer structure. The paper presents a two-stage observer. In particular, an approximated velocity observer is proposed. The parameters of this velocity observer are optimised using a technique similar to that presented in Ref. (Mercorelli (2009)). A second observer is considered, through measurement of the current and the velocity estimated by the first observer, to estimate the position of the valve. The paper is organised as follows. In Section 3, a new actuator design is shown. Section 4 is devoted to the analysis of the model. Next, an observability analysis is performed in Section 5. Section 6 shows the approximated velocity observer (first-stage) and its optimisation. Section 7 shows the design position observer (second-stage). In Section 8, a control strategy is presented and discussed. Section 9 presents computer simulations of the sensorless control structure, in which the positive effects of the optimised velocity observer are visible in the closed-loop control. The conclusions and future work close the paper.

3. Design specifications and actuator design

A sketch of an electromagnetic valve shaft is shown in the left part of Fig. 1 and its typical valve movement required by engine operation is shown in the right part of Fig. 1. The variable stroke needed is between 0 and 8 mm and is to be realised within a time interval of about 4 ms. Thus, high accelerations up to $4,000 \text{ m/s}^2$ have to be achieved, even in the case of large disturbances due to a strong cylinder pressure acting against the exhaust valve opening. For this reason, high forces coupled with a low moving mass are essential for actuator design. Furthermore, copper loss and the physical size of the actuator are also very important parameters to be considered.

Most electromechanical valve actuators reported so far are based on the principle of electromagnets see Refs. (Furlani (2001) & Butzmann et al. (2000)), utilising Maxwell attracting forces at both ends of the motion range. This operation principle is simple to implement, difficult to control and specifically lacks the ability to influence the valve motion in the middle range. Thus, variable opening strokes, which have recently been proven to be efficient for engine operation, are rarely possible. For this reason, we considered linear motors as valve actuators to allow for the ability to control the motion in the total range, including positioning the valve at every specified stroke. Due to the limited mounting space in the focused application, we chose perpendicularly formed linear motors. The actuator width was restricted to around 36 mm. As the main design goal was to have a high acceleration and low power loss at the same time, we used the following quality function Q as the design criterion to be minimised:

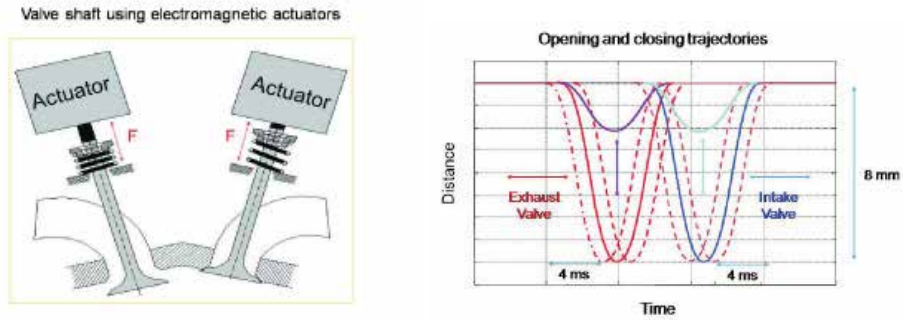


Fig. 1. Left: Electromagnetic actuators. Right: Opening and closing loop for valve operation

$$Q = \frac{P_v}{a} = \frac{P_v m}{F}, \quad (1)$$

where P_v is the copper loss, a is the possible acceleration, m is the mass (moving part of the actuator and the valve), and F is the actuator force. Different permanent-magnet actuator topologies using NdFeB magnets were considered for the design. In this paper, we present a design study based on the following moving-magnet reluctance DC-actuator, whose basic element is shown in the left part of Fig. 2. One of the shortages of conventional linear motors in this application is the linear dependence between the desired force and the required current density (the Maxwell attracting force is quadratic to the current and inversely quadratic to the distance between the valve armature and the electromagnets). Thus, one needs high currents to generate high forces. Therefore, to reduce maximally the electrical power loss during normal valve operation, we use a spring oscillator supporting the periodic motion. The initial considerations for our actuator design are therefore based on a spring-mass system. The start and end positions of the system have high spring forces to give the moving part high accelerations. On the other hand, in conventional electromechanical valve actuators, it is usually necessary to have a constant hold current generating an electromagnetic force against the spring force at the end positions to keep the valve unmoved during the closed and opened phases (most of the time). This causes additional non-negligible power loss. In our design, we combine the linear motor with a reluctance armature using permanent magnets, such that the actuator can be kept at the end positions without a holding current. Furthermore, the reluctance force can be influenced by a coil current in such a way that a very high acceleration is possible. The principle topology of the novel-reluctance linear motor is depicted in the left part of Fig. 2. The stator of the actuator consists of a laminated iron core divided into two parts with a copper coil embedded in it. The armature sitting between the stator packages is built of thin permanent-magnet plates mechanically connected to each other. To produce a small moving mass, NdFeB magnets with a high energy density are used. Our basic idea is to utilise the position-dependent reluctance force to generate forces of different signs. In the case where the permanent magnets are in the position shown in the left part of Fig. 2 (valve closed), a magnetic flux is generated in the iron poles. This flux leads to a negative (i.e., valve opening) reluctance force in the y -direction without a current flowing in the coil. When the magnets are in the position at the opposite end, the same functional mechanism enables a reluctance force with a positive sign (valve opened). With an actively controlled current with different directions in the coils, it is possible to increase, reduce or reverse the

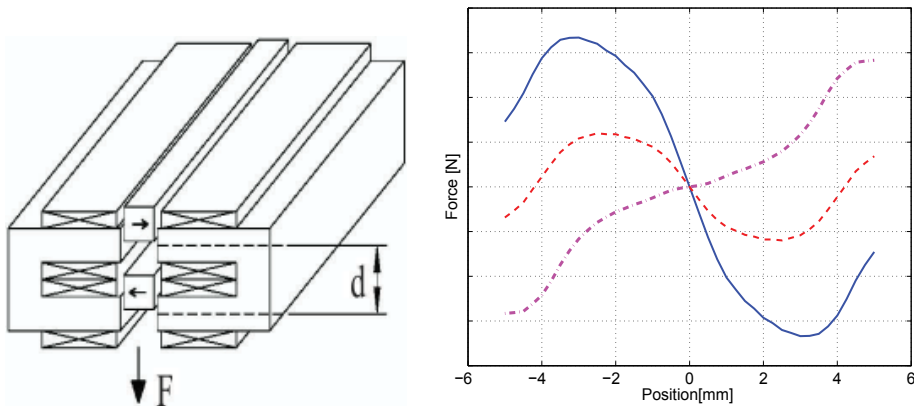


Fig. 2. Left: Basic element of the linear reluctance motor. Right: Calculated force depending of position and current (bl - neg. current, rd - no current, viol. - pos. current)

force. Obviously, this effect is determined by the geometry of the permanent magnets and iron poles with respect to each other and by the electrical current used. One important design criterion is the following. In the totally closed or opened valve position, the electromagnetic force (holding force) must be of the opposite sign and slightly stronger than the spring force to achieve low power consumption. In the right part of Fig. 2, the calculated position-dependent characteristics of the force generation using different current densities are presented. The calculation was

done using the finite-element tool ANSYS. It can be easily seen that if we put the holding position at -5 mm, there will be a reasonable negative holding force available. On the other hand, in the range of about -4 to -3 mm, a large acceleration force can be generated. Thus, by applying some suitable strategy, it is possible to combine both properties for an optimal motion. For this particular purpose, we designed a special system with separated hold and start positions for the valve. There are two different springs within the system: one valve spring connected with the valve shaft and one motor spring connected with the motor armature. They are identically built but have opposite unstressed points. In total, they act as a resulting spring in the motion range between 4 and -4 mm. After having seated the valve at 4 mm: however, the permanent-magnet armature with the motor spring continues to move to the hold position at 5 mm controlled by electronics. To open the valve, one must apply a proper current to release the motor from the hold position, travel to the top end of the valve shaft and make the valve move by generating the maximum reluctance force. In this way, the motor-spring system can be used at a very high efficiency, and an overall reduced power consumption can be achieved. Of course, a smooth motion is only possible using a sophisticated control strategy. The base element shown in the left part of Fig. 2 can be connected in series to obtain higher forces. Generally, due to the weight of the valve shaft, it is theoretically better to have more poles, enabling a higher acceleration. However, there are also tight limits for both the actuator volume and the material costs. We determined during our design process that some optimum can be reached using a four-pole or a six-pole topology. The left part of Fig. 3 shows such an actuator arrangement with its calculated force in position and current dependence depicted in the right part of Fig. 3. Clearly, combined with the spring, acceleration forces of 600 N or even larger values are possible. Such high forces are needed to open the exhaust valve against the gas pressure coming from the combustion chamber.

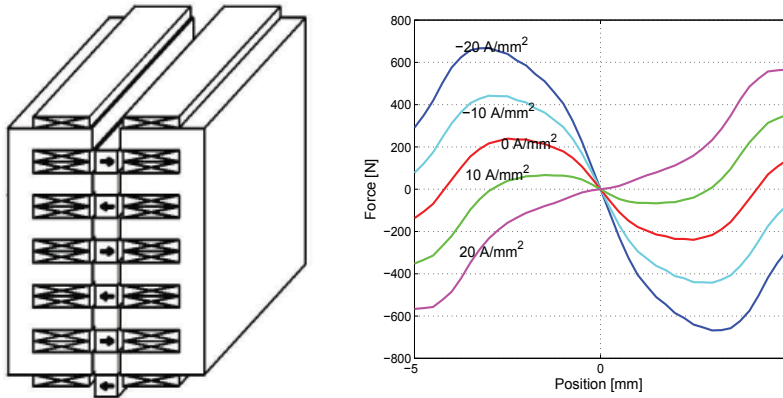


Fig. 3. Left: Actuator with 6 poles (valve position at -4 mm, i.e. in the opened position). Right: Reluctance force depending on position and current densities in a 6-pole motor (negative force - moving down).

Having determined the proper topology, we extensively used finite-element calculation to optimise the dimensions of the actuator. The actuator's outer width, height and depth are limited by the available mounting space and are very restrictive. The maximum width allowed is about 36 mm. Thus, subtracting the air gap of 0.5 mm on both sides of the armature, the remaining width is available for the stator and armature magnet systems. The operating point of the iron parts is defined to have a slight saturation, resulting in an effective use of the dimensions and good performance. Based on these considerations, adjustments of the dimensions were made to ensure optimal operating points of the magnets and iron parts. While the actuator geometry parameters in the width direction are important for the reachable magnetic flux density in the air gaps, the parameters in the height are also essential for the form of the force curves (position dependence). One of the design goals is to have distinctive high forces using a negative current at the beginning of the valve opening phase (position $4 - 2$ mm) and, on the other hand, to obtain a reasonable holding force without current. This is because if there is a high gas pressure (some hundred Newtons) acting against the valve opening, it will decrease very rapidly after the opening phase has begun. Therefore, the higher the available reluctance force at the beginning, the faster the reduction of the gas pressure that will follow, leading to a better motion dynamic and reduced copper loss. That is, we did not look for an as-constant-as-possible motor but for a nonlinear force curve adapted to the motion conditions. This is one of the special design aspects for the presented actuator. After having fixed some basic design parameters, the forces were calculated by finite-element calculation, and the quality function Q was evaluated to assess the performance. Subsequently, iterative calculations based on an optimisation strategy were carried out to optimise the design step-by-step, also taking into account the nonlinear saturation and leakage effects. As above mentioned, this optimisation procedure started using the finite-element tool ANSYS. In the left part of Fig. 4, a diagram used inside this optimization procedure excerpted from ANSYS program is shown. The iteration was also supported by dynamic simulations to determine the overall power loss during a total engine operation cycle at different speeds. For this purpose, a complex dynamic simulation model including the actuator, power electronics and simple control loops was developed and coupled with the FEM calculations. At the end of this process, a novel linear reluctance

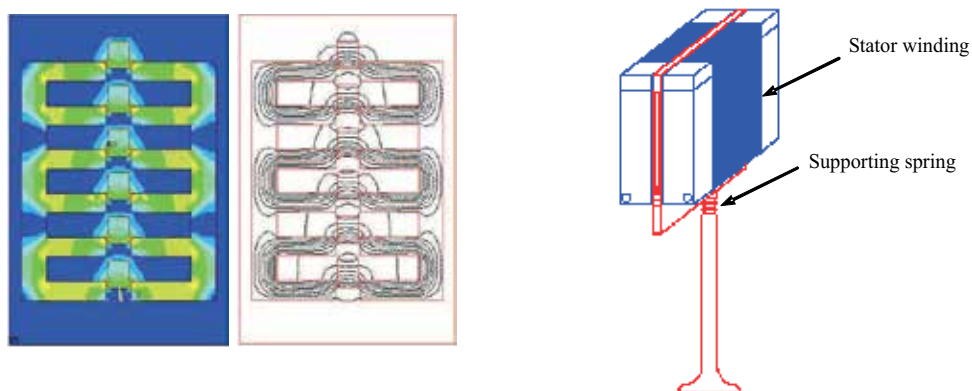


Fig. 4. Left: Flux density and magnetic field distribution (position 3mm, current density -15 A/mm^2). Right: Mechanical structure with valve coupling.

actuator with excellent dynamic parameters and low power losses was derived. The right part of Fig. 4 shows the mechanical structure of the actuator connected with the engine valve. In Table 1, some of the most interesting parameters of the developed actuator are given. It is easy to recognise that the specified technical characteristics were fully reached.

4. Description of the model

The electromagnetic actuator depicted in the left part of Fig. 3 can be modelled mathematically in the following way:

$$\frac{di_{\text{Coil}}(t)}{dt} = -\frac{R_{\text{Coil}}}{L_{\text{Coil}}}i_{\text{Coil}}(t) + \frac{u_{\text{in}}(t) - u_q(t)}{L_{\text{Coil}}}, \quad (2)$$

$$\frac{dy(t)}{dt} = v(t), \quad (3)$$

Moving mass: (including an 50 g valve)	157 g
maximum opening force (for -20 A/mm^2)	625 N
maximum acceleration loss per acceleration quality function $Q \text{ W s}^2/\text{m}$	3981 m/s^2 0.015
Dimensions: W * H * D mm	36 * 61.5 * 100
volume:	222 mm^3
magnet mass:	60 g
copper wire:	48 m (ca. 0.4 kg)
stator iron package:	490 g

Table 1. Parameters of the actuator (6 poles)

$$\frac{dv(t)}{dt} = \frac{f(i_{Coil}(t), y(t))}{m} i_{Coil}(t) + \frac{-k_d v(t) - k_f y(t) + F_0(t)}{m}, \quad (4)$$

where

$$f(i_{Coil}(t), y(t)) = F_{lin}(y(t), i_{Coil}(t)) + F_{sin}(y(t), i_{Coil}(t)), \quad (5)$$

$$u_q(t) = k_1(y(t) + \text{sign}(y(t))k_2)v(t), \quad (6)$$

$$\text{and } f(i_{Coil}(t), y(t)) = i_{Coil}(t)k_1(y(t) + \text{sign}(y(t))k_2) + F_{sin}(y(t), i_{Coil}(t)), \quad (7)$$

where k_1 and k_2 are physical constants. The non-linear electromagnetic force generation can be separated into two parallel blocks, $F_{sin}(y(t))$ and $F_{lin}(y(t), i_{Coil}(t))$, corresponding to the reluctance effect and the Lorentz force, respectively:

$$f(y(t), i_{Coil}(t)) = F_{sin}(y(t)) + F_{lin}(y(t), i_{Coil}(t)) \quad (8)$$

with the following approximation equations

$$F_{sin}(y(t)) = F_{0,max} \sin(2\pi y(t)/d) \quad (9)$$

$$\text{and } F_{lin}(y(t), i_{Coil}(t)) = k_1(y(t) + \text{sign}(y(t))k_2)i_{Coil}(t). \quad (10)$$

R_{Coil} and L_{Coil} are the resistance and the inductance, respectively, of the coil windings, $u_{in}(t)$ is the input voltage and $u_q(t)$ is the induced emf. $i_{Coil}(t)$, $y(t)$, $v(t)$ and m are the coil current, position, velocity and mass of the actuator respectively, while $k_d v(t)$, $k_f y(t)$ and $F_0(t)$ represent the viscous friction, the total spring force and the disturbance force acting on the valve, respectively.

5. Observability analysis

Definition 1 Given the following nonlinear system:

$$\dot{\mathbf{x}}(t) = \mathbf{f}(\mathbf{x}(t)) + \mathbf{g}(\mathbf{x}(t))\mathbf{u}(t) \quad (11)$$

$$\mathbf{y}(t) = \mathbf{h}(\mathbf{x}(t)), \quad (12)$$

where $\mathbf{x}(t) \in \mathbb{R}^n$, $\mathbf{u}(t) \in \mathbb{R}^m$, and $\mathbf{y} \in \mathbb{R}^p$, a system in the form of Eqs. (11) and (12) is said to be locally observable at a point \mathbf{x}_0 if all states $\mathbf{x}(t)$ can be instantaneously distinguished by a judicious choice of input $\mathbf{u}(t)$ in a neighbourhood \mathbf{U} of \mathbf{x}_0 (Hermann & Krener (1997)), (Kwatny & Chang (2005)). \square

Definition 2 For a vector $\mathbf{x} \in \mathbb{R}^n$, a real-valued function $\mathbf{h}(\mathbf{x}(t))$, which is the derivative of $h(\mathbf{x}(t))$ along \mathbf{f} according to Ref. (Slotine (1991)) is denoted by

$$L_{\mathbf{f}}\mathbf{h}(\mathbf{x}(t)) = \sum_{i=1}^n \frac{d\mathbf{h}(\mathbf{x}(t))}{d\mathbf{x}_i(t)} \mathbf{f}_i(\mathbf{x}(t)) = \frac{d\mathbf{h}(\mathbf{x}(t))}{d\mathbf{x}(t)} \mathbf{f}(\mathbf{x}(t)).$$

Function $L_f \mathbf{h}(\mathbf{x}(t))$ represents the derivative of \mathbf{h} first along a vector field $\mathbf{f}(\mathbf{x}(t))$. Function $L_f^i \mathbf{h}(\mathbf{x}(t))$ satisfies the recursion relation

$$dL_f^i \mathbf{h}(\mathbf{x}(t)) = \frac{dL_f^{i-1} \mathbf{h}(\mathbf{x}(t))}{d\mathbf{x}(t)} \mathbf{f}(\mathbf{x}(t)) \quad (13)$$

with $L_f^0 \mathbf{h}(\mathbf{x}(t)) = \mathbf{h}(\mathbf{x}(t))$. □

Test criteria can be derived according to the local observability definitions (Hermann & Krener (1997)), (Kwatny & Chang (2005)). In particular, if $\mathbf{u}(t) = 0$ the system is called "zero input observable," which is also important for this application because if a system is zero input observable, then it is also locally observable (Xia & Zeitz (1997)). In fact, the author in Ref. Fabbrini et al. (2008) showed how an optimal trajectory, derived from a minimum power consumption criterion, is achieved by an input voltage that is zero or very close to zero for some finite time intervals.

Rank Condition 1 The system described in Eqs. (11) and (12) is autonomous if $\mathbf{u}(t) = 0$. The following rank condition (Hermann & Krener (1997)), (Kwatny & Chang (2005)) is used to determine the local observability for the nonlinear system stated in Eq. (11). The system is locally observable if and only if

$$\dim(O(\mathbf{x}_0)) = \left. \frac{dl(\mathbf{x}(t))}{d\mathbf{x}(t)} \right|_{\mathbf{x}_0} = n, \text{ where } l(\mathbf{x}(t)) = \begin{bmatrix} L_f^0(\mathbf{h}(\mathbf{x}(t))) \\ L_f^1(\mathbf{h}(\mathbf{x}(t))) \\ L_f^2(\mathbf{h}(\mathbf{x}(t))) \end{bmatrix}. \quad \square$$

Applying the above criterion with $\mathbf{x}(t) = \begin{bmatrix} i_{Coil}(t) \\ y(t) \\ v(t) \end{bmatrix}$ and $\mathbf{h}(\mathbf{x}(t)) = i_{Coil}(t)$, then

$$dL_f^0 \mathbf{h}(\mathbf{x}(t)) = \frac{d\mathbf{h}}{d\mathbf{x}(t)} = (1 \quad 0 \quad 0), \quad (14)$$

$$L_f \mathbf{h}(\mathbf{x}(t)) = -\frac{R_{Coil}}{L_{Coil}} I_{Coil}(t) - \frac{u_q(t)}{L_{Coil}}, \quad (15)$$

$$dL_f \mathbf{h}(\mathbf{x}(t)) = \frac{1}{L_{Coil}} \left[-R_C \quad -\frac{du_q(t)}{dy(t)} \quad -\frac{du_q(t)}{dv(t)} \right], \quad (16)$$

where

$$\frac{du_q(t)}{dy(t)} = k_1 v(t)$$

and

$$\frac{du_q(t)}{dv(t)} = k_1 (y(t) + \text{sign}(y(t))k_2).$$

According to the definition in Eq. (2), then

$$L_f^2 \mathbf{h}(\mathbf{x}(t)) = \frac{dL_f \mathbf{h}(\mathbf{x}(t))}{d\mathbf{x}(t)} \mathbf{f}(\mathbf{x}(t)),$$

$$\frac{dL_f \mathbf{h}(\mathbf{x}(t))}{d\mathbf{x}(t)} \mathbf{f}(\mathbf{x}(t)) = -\frac{1}{L_{Coil}} \left(R_{Coil} \left(-\frac{R_{Coil}}{L_{Coil}} I_{Coil}(t) - \frac{u_q(t)}{L_{Coil}} \right) + \frac{du_q(t)}{dy(t)} v(t) + \frac{du_q(t)}{dv(t)} \frac{dv(t)}{dt} \right). \quad (17)$$

For the sake of notation,

$$dL_f^2 \mathbf{h}(\mathbf{x}(t)) = [M_1(t) \quad M_2(t) \quad M_3(t)],$$

where $M_1(t)$, $M_2(t)$ and $M_3(t)$ are functions of the variables $i_{Coil}(t)$, $y(t)$ and $v(t)$. In particular, it is useful to note that the term

$$M_2(t) = \frac{R_{Coil}}{L_{Coil}^2} \frac{du_q(t)}{dy(t)} - \frac{1}{L_{Coil}} \left(\frac{d^2 u_q(t)}{dy(t)^2} v(t) + \frac{du_q(t)}{dy(t)} v(t) + \frac{d}{dy(t)} \left(\frac{du_q(t)}{dv(t)} \right) \frac{dv(t)}{dt} + \frac{du_q(t)}{dv(t)} \frac{d}{dy(t)} \left(\frac{dv(t)}{dt} \right) \right) \quad (18)$$

and

$$M_3(t) = \frac{R_{Coil}}{L_{Coil}^2} \frac{du_q(t)}{dv(t)} + \frac{2}{L_{Coil}^2} \frac{F_{0,max} \pi}{d} \cos\left(\frac{\pi y(t)}{d}\right) v(t) + \frac{du_q(t)}{dv(t)} \frac{d}{dv(t)} \left(\frac{dv(t)}{dt} \right). \quad (19)$$

Matrix $O(\mathbf{x}_0)$ becomes

$$O(\mathbf{x}_0) = \begin{bmatrix} 1 & 0 & 0 \\ -R_C & -\frac{du_q(t)}{dy(t)} & -\frac{du_q(t)}{dv(t)} \\ M_1(t) & M_2(t) & M_3(t) \end{bmatrix}. \quad (20)$$

If set $\mathbf{x}_0 = \{v(t) = 0, y(t) = 0\}$ is considered, then matrix (20) has not full rank. In fact, being $\frac{du_q(t)}{dv(t)} = k_1(y(t) + \text{sign}(y(t))k_2)$, then $\frac{du_q(t)}{dv(t)}|_{\mathbf{x}_0} = 0$; considering Eq. (19) calculated in \mathbf{x}_0 , it follows that $M_3(t) = 0$. So it is shown that the third column of matrix (20) is equal to zero, thus matrix (20) has not full rank.

If set $\mathbf{x}_1 = \{v(t) = 0\}$ is considered, then matrix (20) has not full rank. In fact, being $\frac{du_q(t)}{dy(t)} = k_1 v(t)$, then $\frac{du_q(t)}{dy(t)}|_{\mathbf{x}_1} = 0$; if $y(t) \neq 0$, then also $\frac{dv(t)}{dt} = 0$ and considering Eq. (18) calculated in \mathbf{x}_1 , it follows that $M_2(t)|_{\mathbf{x}_1} = 0$. So it is shown that the three rows of matrix (20) are linearly dependent, and thus matrix (20) has not full rank.

Rank Condition 2 The system described in (11) and (12) is not autonomous if $\mathbf{u}(t) \neq 0$. The following condition (Hermann & Krener (1997)), (Kwatny & Chang (2005)) is used to determine the local observability for the nonlinear system stated in (11). The system is locally observable if and only if

$$\dim(O(\mathbf{x}_0)) = \left. \frac{dl(\mathbf{x}(t))}{d\mathbf{x}(t)} \right|_{\mathbf{x}_0} = n, \text{ where } l(\mathbf{x}(t)) = \begin{bmatrix} L_f^0(\mathbf{h}(\mathbf{x}(t))) \\ L_f(\mathbf{h}(\mathbf{x}(t))) \\ L_f^2(\mathbf{h}(\mathbf{x}(t))) \\ L_g L_f(\mathbf{h}(\mathbf{x}(t))) \end{bmatrix}. \quad \square$$

It is to note that $L_g L_f(\mathbf{h}(\mathbf{x}(t))) = -\frac{R_{Coil}}{L_{Coil}^2}$ and that $dL_g L_f(\mathbf{h}(\mathbf{x}(t))) = [0 \ 0 \ 0]$. This means that, even for a *judicious choice* of input $\mathbf{u}(t)$, no contribution to the observability set is given if compared with the autonomous case provided above. The rank criteria provide sufficient and necessary conditions for the observability of a nonlinear system. Moreover, for applications it is useful to detect those sets where the *observability level* of the state variables decreases; thus, a measurement of the observability is sometimes needed. A heuristic criterion for testing the level of unobservability of such a system is to check where the *signal connection* between the mechanical and electrical system decreases or goes to zero. Although this criterion does not guarantee any conclusions about observability, it could be useful in an initial analysis of the system. In fact, it is well-known that the observability is an analytic concept connected with the concept of distinguishability. In the present case, the following two terms,

$$u_q(t) = k_1(y(t) + \text{sign}(y(t))k_2)v(t) \quad \text{and} \quad \mathbf{f}(i_{Coil}(t), y(t))$$

are responsible for the feedback mentioned above. If the term $u_q(t) \rightarrow 0$, and $\mathbf{f}(i_{Coil}(t), y(t)) \neq 0$ when $v(t) \rightarrow 0$, then the above tests result in unobservability. In fact, as Eq. (4) for $v(t) \rightarrow 0$ is satisfied by more than one point position $y(t)$, this yields the indistinguishability of the states and thus the unobservability. If $y(t) \rightarrow 0$, it is noticed that both terms $u_q(t) \rightarrow 0$ and $\mathbf{f}(i_{Coil}(t), y(t)) \rightarrow 0$; nevertheless, Eq. (4) is unequivocally satisfied and this yields observability. However, the "level of observability," if an observability function is defined and calculated, decreases. In fact, if the observability is calculated as a function at this point, it assumes a minimum.

The *unobservable sets* should be avoided in the observer design; thus, a thorough analysis of the observability is important. Sensorless operations tend to perform poorly in low-speed environments, as nonlinear observer-based algorithms work only if the rotor speed is high enough. In low-speed regions, an open loop control strategy must be considered. One of the first attempts to develop an open loop observer for a permanent motor drive is described in Ref. (Wu & Slemon (1991)). In a more recent work (Zhu et al (2001)), the authors proposed a nonlinear-state observer for the sensorless control of a permanent-magnet AC machine, based to a great extent on the work described in Refs. (Rajamani (1998)) and (Thau (1973)). The approach presented in Refs. (Rajamani (1998)) and (Thau (1973)) consists of an observable linear system and a Lipschitz nonlinear part. The observer is basically a Luenenberger observer, in which the gain is calculated through a Lyapunov approach. In Ref. (Zhu et al (2001)), the authors used a change of variables to obtain a nonlinear system consisting of an observable linear part and a Lipschitz nonlinear part. In the work presented here, our system does not satisfy the condition in Ref. (Thau (1973)); thus, a Luenenberger observer is not feasible.

6. First-stage of the state observer design: open loop velocity observer

As discussed above, the proposed technique avoids a more complex non-linear observer, as proposed in Refs. (Dagci et al. (2002)) and (Beghi et al. (2006)). A two-stage structure is used for the estimation. An approximated open loop velocity observer is built from equation 2; then, a second observer is considered which, through the measurement of the current and the velocity estimated by the first observer, estimates the position of the valve. This technique avoids the need for a complete observer. If the electrical part of the system is considered, then

$$\frac{di_{Coil}(t)}{dt} = -\frac{R_{Coil}}{L_{Coil}}i_{Coil}(t) + \frac{u_{in}(t) - C\phi(i_{Coil}(t), y(t))v(t)}{L_{Coil}}; \quad (21)$$

considering that $C\phi(y(t)) = k_1(y(t) + \text{sign}(y(t))k_2)$, and that if $y(t) = 0 \rightarrow \text{sign}(y(t)) = +1$, then $\forall y(t) C\phi(y(t)) = k_1(y(t) + \text{sign}(y(t))k_2) \neq 0$, it is possible to write that

$$v(t) = -\frac{L_{Coil}\frac{di_{Coil}(t)}{dt} + R_{Coil}i_{Coil}(t) - u_{in}(t)}{C\phi(y(t))}. \quad (22)$$

Consider the following dynamic system

$$\frac{d\hat{v}(t)}{dt} = -\mathcal{K}\hat{v}(t) - \mathcal{K}\frac{k_{di}L_{Coil}\frac{di_{Coil}(t)}{dt} + k_{pi}R_{Coil}i_{Coil}(t) - k_{pu}u_{in}(t)}{C\phi(y(t))}, \quad (23)$$

where \mathcal{K} , k_{di} , k_{pi} and k_{pu} are functions to be calculated. If the error on the velocity is defined as the difference between the true and the observed velocity, then:

$$e_v(t) = v(t) - \hat{v}(t) \quad (24)$$

and

$$\frac{de_v(t)}{dt} = \frac{dv(t)}{dt} - \frac{d\hat{v}(t)}{dt}. \quad (25)$$

If the following assumption is given:

$$\left\| \frac{dv(t)}{dt} \right\| \ll \left\| \frac{d\hat{v}(t)}{dt} \right\|, \quad (26)$$

then in Eq. (25), the term $\frac{dv(t)}{dt}$ is negligible. Using equation (23), Eq. (25) becomes

$$\frac{de_v(t)}{dt} = \mathcal{K}\hat{v}(t) + \mathcal{K}\frac{k_{di}L_{Coil}\frac{di_{Coil}(t)}{dt} + k_{pi}R_{Coil}i_{Coil}(t) - k_{pu}u_{in}(t)}{C\phi(y(t))}. \quad (27)$$

Remark 1 Assumption (26) states that the dynamics of the approximating observer should be faster than the dynamics of the physical system. This assumption is typical for the design of observers. \square

Because of Eq. (22), (27) can be written as follows:

$$\frac{de_v(t)}{dt} = \mathcal{K}\hat{v}(t) - \mathcal{K}v(t)$$

and considering (24), then

$$\frac{de_v(t)}{dt} + \mathcal{K}e_v(t) = 0 \quad (28)$$

\mathcal{K} can be chosen to make Eq. (28) exponentially stable. To guarantee exponential stability, \mathcal{K} must be

$$\mathcal{K} > 0.$$

To guarantee $\|\frac{dv(t)}{dt}\| \ll \|\frac{d\hat{v}(t)}{dt}\|$, then $\mathcal{K} \gg 0$. The observer defined in (23) suffers from the presence of the derivative of the measured current. In fact, if measurement noise is present in the measured current, then undesirable spikes are generated by the differentiation. The proposed algorithm needs to cancel the contribution from the measured current derivative. This is possible by correcting the observed velocity with a function of the measured current, using a supplementary variable defined as

$$\eta(t) = \hat{v}(t) + \mathcal{N}(i_{\text{Coil}}(t)), \quad (29)$$

where $\mathcal{N}(i_{\text{Coil}}(t))$ is the function to be designed.

Consider

$$\frac{d\eta(t)}{dt} = \frac{d\hat{v}(t)}{dt} + \frac{d\mathcal{N}(i_{\text{Coil}}(t))}{dt} \quad (30)$$

and let

$$\frac{d\mathcal{N}(i_{\text{Coil}}(t))}{dt} = \frac{d\mathcal{N}(i_{\text{Coil}}(t))}{di_{\text{Coil}}(t)} \frac{di_{\text{Coil}}(t)}{dt} = \mathcal{K} \frac{k_{di}L_{\text{Coil}}}{C\phi(y(t))} \frac{di_{\text{Coil}}(t)}{dt}. \quad (31)$$

The purpose of (31) is to cancel the differential contribution from (23). In fact, (29) and (30) yield, respectively,

$$\hat{v}(t) = \eta(t) - \mathcal{N}(i_{\text{Coil}}(t)) \quad \text{and} \quad (32)$$

$$\frac{d\hat{v}(t)}{dt} = \frac{d\eta(t)}{dt} - \frac{d\mathcal{N}(i_{\text{Coil}}(t))}{dt}. \quad (33)$$

Substituting (31) in (33) results in

$$\frac{d\hat{v}(t)}{dt} = \frac{d\eta(t)}{dt} - \mathcal{K} \frac{k_{di}L_{\text{Coil}}}{C\phi(y(t))} \frac{di_{\text{Coil}}(t)}{dt}. \quad (34)$$

Inserting Eq. (34) into Eq. (23) the following expression is obtained¹:

$$\begin{aligned} \frac{d\eta(t)}{dt} - \mathcal{K} \frac{k_{di}L_{\text{Coil}}}{C\phi(y(t))} \frac{di_{\text{Coil}}(t)}{dt} = & -\mathcal{K}\hat{v}(t) - \\ & \mathcal{K} \frac{k_{di}L_{\text{Coil}} \frac{di_{\text{Coil}}(t)}{dt} + k_{pi}R_{\text{Coil}}i_{\text{Coil}}(t) - k_{pu}u_{in}(t)}{C\phi(y(t))}; \end{aligned} \quad (35)$$

then

$$\frac{d\eta(t)}{dt} = -\mathcal{K}\hat{v}(t) - \mathcal{K} \frac{k_{pi}R_{\text{Coil}}i_{\text{Coil}}(t) - k_{pu}u_{in}(t)}{C\phi(y(t))}. \quad (36)$$

Letting $\mathcal{N}(i_{\text{Coil}}(t)) = k_{app}i_{\text{Coil}}(t)$, where with k_{app} a parameter has been indicated, then, from (31) $\Rightarrow \mathcal{K} = \frac{k_{app}}{k_{di}L_{\text{Coil}}}C\phi(y(t))$, Eq. (32) becomes

$$\hat{v}(t) = \eta(t) - k_{app}i_{\text{Coil}}(t). \quad (37)$$

¹Expression (23) works under the assumption (26): fast observer dynamics.

Finally, substituting (37) into (36) results in the following equation

$$\frac{d\eta(t)}{dt} = -\frac{k_{app}}{k_{di}L_{Coil}}C\phi(y(t))(\eta(t) - k_{app}i_{Coil}(t)) + \frac{k_{app}C\phi(y(t))}{k_{di}L_{Coil}}(k_{pu}u_{in}(t) - k_{pi}R_{Coil}i_{Coil}(t)) \quad (38)$$

$$\hat{v}(t) = \eta(t) - k_{app}i_{Coil}(t). \quad (39)$$

Remark 2 If $y(t) > 0$, then $C\phi(y(t)) > 0$, condition $\lim_{t \rightarrow \infty} e_v(t) = v(t) - \hat{v}(t) = 0$ is always guaranteed for $k_{app} > 0$. In fact, under condition (26), the system described in (39) satisfies condition (28) by construction. If $y(t) \leq 0$, then $C\phi(y(t)) < 0$, $\lim_{t \rightarrow \infty} e_v(t) = v(t) - \hat{v}(t) = 0$ is always guaranteed for $k_{app} < 0$. \square

Using the implicit Euler method, then the following velocity observer structure is obtained:

$$\eta(k) = \frac{\eta(k-1)}{1 + t_s \frac{k_{app}C\phi(y(k))}{k_{di}L_{Coil}}} + \frac{t_s \frac{k_{app}^2 C\phi(y(k))}{k_{di}L_{Coil}} - \frac{t_s k_{pi} R_{Coil} k_{app} C\phi(y(k))}{k_{di}L_{Coil}}}{1 + t_s \frac{k_{app}C\phi(y(k))}{k_{di}L_{Coil}}} i_{Coil}(k) + \frac{t_s \frac{k_{app}C\phi(y(k))}{k_{di}L_{Coil}} k_{pu}}{1 + t_s \frac{k_{app}C\phi(y(k))}{k_{di}L_{Coil}}} u_{in}(k) \quad (40)$$

$$\hat{v}(k) = \eta(k) - k_{app}i_{Coil}(k), \quad (41)$$

where t_s is the sampling period. The digital asymptotic convergence that can be expressed by $\lim_{k \rightarrow \infty} e_v(k) = v(k) - \hat{v}(k) = 0$ is guaranteed for $k_{app} > 0$.

Remark 3 A more useful case for the presented application is where the asymptotic convergence is oscillatory. If the transfer function of (41) is considered, to realize an oscillatory asymptotic convergence, it is necessary that the denominator in (41) must be

$$(1 + t_s \frac{k_{app}}{k_{di}L_{Coil}}) < -1,$$

as in Ref. (Franklin et al. (1997)). In fact, the denominator in (41) must be < -1 . Then,

$$k_{app} < -2 \frac{k_{di}L_{Coil}}{t_s}. \quad (42)$$

Condition (42) is important in the structure of the presented approach. In fact, the proposed observer originates through the assumption

$$\| \frac{dv(t)}{dt} \| \ll \| \frac{d\hat{v}(t)}{dt} \|. \quad (43)$$

To achieve this condition, it is helpful to combine oscillations of $\hat{v}(t)$ with the high speed dynamics of the observer. High speed dynamics is obtained with a relative large value of the parameter $\|k_{app}\|$. \square

State variable $y(k)$ has a slow dynamics if it is compared with the other state ones. For that, $y(k)$ can be considered as a parameter. Transforming the velocity observer represented in (40) and (41) with the Z-transform, then the following equations are obtained:

$$\hat{V}(z) = \frac{t_s \frac{k_{app} C\phi(y(k))}{k_{di} L_{Coil}} (-k_{pi} R_{Coil} + k_{app})}{1 + t_s \frac{k_{app}}{k_{di} L_{Coil}} C\phi(y(k)) - z^{-1}} I_{Coil}(z) + \frac{t_s \frac{k_{app} C\phi(y(k))}{k_{di} L_{Coil}} k_{pu}}{1 + t_s \frac{k_{app}}{k_{di} L_{Coil}} C\phi(y(k)) - z^{-1}} U_{in}(z) - k_{app} I_{Coil}(z), \quad (44)$$

and

$$\hat{V}(z) = \frac{-k_{app} + k_{app} z^{-1} - t_s \frac{k_{app} C\phi(y(k))}{k_{di} L_{Coil}} k_{pi} R_{Coil}}{1 + t_s \frac{k_{app}}{k_{di} L_{Coil}} C\phi(y(k)) - z^{-1}} I_{Coil}(z) + \frac{t_s \frac{k_{app} C\phi(y(k))}{k_{di} L_{Coil}} k_{pu}}{1 + t_s \frac{k_{app}}{k_{di} L_{Coil}} C\phi(y(k)) - z^{-1}} U_{in}(z). \quad (45)$$

6.1 Optimal choice of the observer parameters: real-time self-tuning

Parameters k_{app} , k_{pi} , k_{di} and k_{pu} are now optimised using an algorithm similar to that presented in Ref. (Mercorelli (2009)). As described earlier, the objective of the minimum variance control is to minimise the variation in the system output with respect to a desired output signal, in the presence of noise. This is an optimisation algorithm, i.e., the discrete $\hat{v}(k)$ is chosen to minimise

$$J = E\{e_v^2(k+d)\},$$

where $e_v = v(k) - \hat{v}(k)$ is the estimation velocity error, d is the delay time, and E is the expected value. It should be noted that the velocity observer described in Eq. (45) has a relative degree equal to zero, and that the plant can be approximated with a two-order system. In fact, the electrical dynamics is much faster than the mechanical dynamics. Considering

$$\hat{V}_i(z) = \frac{-k_{app} + k_{app} z^{-1} - t_s \frac{k_{app} C\phi(y(k))}{k_{di} L_{Coil}} k_{pi} R_{Coil}}{1 + t_s \frac{k_{app}}{k_{di} L_{Coil}} C\phi(y(k)) - z^{-1}} I_{Coil}(z) \quad (46)$$

and

$$\hat{V}_u(z) = \frac{t_s \frac{k_{app} C\phi(y(k))}{k_{di} L_{Coil}} k_{pu}}{1 + t_s \frac{k_{app}}{k_{di} L_{Coil}} C\phi(y(k)) - z^{-1}} U_{in}(z), \quad (47)$$

it is obtained that:

$$\hat{V}(z) = \hat{V}_i(z) + \hat{V}_u(z). \quad (48)$$

Considering the estimated velocity signal $\hat{v}_i(t)$ due to the current input and with $u_{in}(t) = 0$, then it is possible to assume an ARMAX model as follows:

$$v_i(k) = \hat{v}_i(k) + a_{1i}\hat{v}_i(k-1) + a_{2i}\hat{v}_i(k-2) + b_{1i}i_{Coil}(k-1) + b_{2i}i_{Coil}(k-2) + n(k) + c_{1i}n(k-1) + c_{2i}n(k-2), \quad (49)$$

letting $e_{v_i}(k)$ be the estimation velocity error defined as follows:

$$e_{v_i}(k) = v_i(k) - \hat{v}_i(k), \quad (50)$$

it follows that:

$$e_{v_i}(k) = a_{1i}\hat{v}_i(k-1) + a_{2i}\hat{v}_i(k-2) + b_{1i}i_{Coil}(k-1) + b_{2i}i_{Coil}(k-2) + n(k) + c_{1i}n(k-1) + c_{2i}n(k-2), \quad (51)$$

where $\hat{v}_i(k) = \mathcal{Z}^{-1}(\hat{V}_i(z))$, $v_i(k)$ is the real velocity due to the current, coefficients a_{1i} , a_{2i} , b_{1i} , b_{2i} and c_{1i} , c_{2i} are to be estimated, $n(k)$ is assumed to be the white noise. The next sample is:

$$e_{v_i}(k+1) = a_{1i}\hat{v}_i(k) + a_{2i}\hat{v}_i(k-1) + b_{1i}i_{Coil}(k) + b_{2i}i_{Coil}(k-1) + n(k+1) + c_{1i}n(k) + c_{2i}n(k-1). \quad (52)$$

The prediction at time "k" is:

$$\hat{e}_{v_i}(k+1/k) = a_{1i}\hat{v}_i(k) + a_{2i}\hat{v}_i(k-1) + b_{1i}i_{Coil}(k) + b_{2i}i_{Coil}(k-1) + c_{1i}n(k) + c_{2i}n(k-1). \quad (53)$$

Considering that:

$$J = E\{e_{v_i}^2(k+1/k)\} = E\{[\hat{e}_{v_i}(k+1/k) + n(k+1)]^2\},$$

and assuming that the noise is not correlated to the signal $\hat{e}_{v_i}(k+1/k)$, it follows:

$$E\{[\hat{e}_{v_i}(k+1/k) + n(k+1)]^2\} = E\{[\hat{e}_{v_i}(k+1/k)]^2\} + E\{[n(k+1)]^2\} = E\{[\hat{e}_{v_i}(k+1/k)]^2\} + \sigma_n^2, \quad (54)$$

where σ_n is defined as the variance of the white noise. The goal is to find $\hat{v}_i(k)$ such that:

$$\hat{e}_{v_i}(k+1/k) = 0. \quad (55)$$

It is possible to write (51) as

$$n(k) = e_{v_i}(k) - a_{1i}\hat{v}_i(k-1) - a_{2i}\hat{v}_i(k-2) - b_{1i}i_{Coil}(k-1) - b_{2i}i_{Coil}(k-2) - c_{1i}n(k-1) - c_{2i}n(k-2). \quad (56)$$

Considering the effect of the noise on the system as follows

$$c_{1i}n(k-1) + c_{2i}n(k-2) \approx c_{1i}n(k-1), \quad (57)$$

and using the Z-transform, then:

$$N(z) = \hat{V}_i(z) - a_{1i}z^{-1}\hat{V}_i(z) - a_{2i}z^{-2}\hat{V}_i(z) - b_{1i}z^{-1}I_{Coil}(z) - b_{2i}z^{-2}I_{Coil}(z) - c_{1i}z^{-1}N(z) \quad (58)$$

and

$$N(z) = \frac{(1 - a_{1i}z^{-1} - a_{2i}z^{-2})}{1 + c_{1i}z^{-1}} \hat{V}_i(z) - \frac{(b_{1i}z^{-1} + b_{2i}z^{-2})}{1 + c_{1i}z^{-1}} I_{Coil}(z). \quad (59)$$

The approximation in Eq. (57) is equivalent to consider $\|c_{2i}\| \ll \|c_{1i}\|$. In other words this position means that a noise model of the first order is assumed. An indirect validation of this assumption is given by the results. In fact, the final measurements show in general good results with the proposed method. Inserting Eq. (59) into Eq. (53) after its Z-transform, and considering positions (57) and (55), the following expression is obtained:

$$\hat{V}_i(z) = -\frac{(a_{1i} + c_{1i} + b_{1i}z^{-1})}{b_{1i}(1 + c_{1i}z^{-1}) + b_{2i}(1 + c_{1i}z^{-1})} I_{Coil}(z). \quad (60)$$

Comparing (60) with (46), it is left with a straightforward diophantine equation to solve. The diophantine equation gives the relationship between the parameters $Y_i = [a_{1i}, b_{1i}, b_{2i}, c_{1i}]$, the parameter k_{app} and the parameters of the system (R_{Coil} , L_{Coil}) as follows:

$$-b_{1i} = k_{app} \quad (61)$$

$$a_{1i} + c_{1i} = k_{app} + t_s \frac{k_{app} C \phi(y(k))}{k_{di} L_{Coil}} k_{pi} R_{Coil} \quad (62)$$

$$b_{1i} + b_{2i} = 1 + t_s \frac{k_{app}}{k_{di} L_{Coil}} C \phi(y(k)) \quad (63)$$

$$b_{1i}c_{1i} + b_{2i}c_{1i} = -1. \quad (64)$$

Considering the estimated velocity signal $\hat{v}_u(t)$ due to the voltage input and with $i_{Coil}(t) = 0$, then it is possible to assume an ARMAX model as follows:

$$v_u(k) = \hat{v}_u(k) + a_{1u}\hat{v}_u(k-1) + a_{2u}\hat{v}_u(k-2) + b_{1u}u_{in}(k-1) + b_{2u}u_{in}(k-2) + n(k) + c_{1u}n(k-1) + c_{2u}n(k-2), \quad (65)$$

letting $e_{v_u}(k)$ be the estimation velocity error defined as follows:

$$e_{v_u}(k) = v_u(k) - \hat{v}_u(k), \quad (66)$$

it follows that:

$$e_{v_u}(k) = a_{1u}\hat{v}_u(k-1) + a_{2u}\hat{v}_u(k-2) + b_{1u}u_{in}(k-1) + b_{2u}u_{in}(k-2) + n(k) + c_{1u}n(k-1) + c_{2u}n(k-2), \quad (67)$$

where $\hat{v}_u(k) = \mathcal{Z}^{-1}(\hat{V}_u(z))$, $v_u(k)$ is the real velocity due to the input voltage, coefficients a_{1u} , a_{2u} , b_{1u} , b_{2u} and c_{1u} , c_{2u} are to be estimated, $n(k)$ is assumed to be the white noise. The next sample is:

$$e_{v_u}(k+1) = a_{1u}\hat{v}_u(k) + a_{2u}\hat{v}_u(k-1) + b_{1u}u_{in}(k) + b_{2u}u_{in}(k-1) + n(k+1) + c_{1u}n(k) + c_{2u}n(k-1). \quad (68)$$

The prediction at time "k" is:

$$\hat{e}_{v_u}(k+1/k) = a_{1u}\hat{v}_u(k) + a_{2u}\hat{v}_u(k-1) + b_{1u}u_{in}(k) + b_{2u}u_{in}(k-1) + c_{1u}n(k) + c_{2u}n(k-1). \quad (69)$$

Considering that:

$$J = E\{e_{v_u}^2(k+1/k)\} = E\{[\hat{e}_{v_u}(k+1/k) + n(k+1)]^2\},$$

and assuming that the noise is not correlated to the signal $\hat{e}_{v_u}(k+1/k)$, it follows:

$$E\{[\hat{e}_{v_u}(k+1/k) + n(k+1)]^2\} = E\{[\hat{e}_{v_u}(k+1/k)]^2\} + E\{[n(k+1)]^2\} = E\{[\hat{e}_{v_u}(k+1/k)]^2\} + \sigma_n^2, \quad (70)$$

where σ_n is defined as the variance of the white noise. The goal is to find $\hat{v}_u(k)$ such that:

$$\hat{e}_{v_u}(k+1/k) = 0. \quad (71)$$

It is possible to write (67) as

$$n(k) = e_{v_u}(k) - a_{1u}\hat{v}_u(k-1) - a_{2u}\hat{v}_u(k-2) - b_{1u}u_{in}(k-1) - b_{2u}u_{in}(k-2) - c_{1u}n(k-1) - c_{2u}n(k-2). \quad (72)$$

Considering the effect of the noise on the system as follows

$$c_{1u}n(k-1) + c_{2u}n(k-2) \approx c_{1u}n(k-1), \quad (73)$$

and using the Z-transform, then:

$$N(z) = \hat{V}_u(z) - a_{1u}z^{-1}\hat{V}_u(z) - a_{2u}z^{-2}\hat{V}_u(z) - b_{1u}z^{-1}U_{in}(z) - b_{2u}z^{-2}U_{in}(z) - c_{1u}z^{-1}N(z) \quad (74)$$

and

$$N(z) = \frac{(1 - a_{1u}z^{-1} - a_{2u}z^{-2})}{1 + c_{1u}z^{-1}}\hat{V}_u(z) - \frac{(b_{1u}z^{-1} + b_{2u}z^{-2})}{1 + c_{1u}z^{-1}}U_{in}(z). \quad (75)$$

The approximation in Eq. (73) is equivalent to consider $\|c_{2u}\| \ll \|c_{1u}\|$. In other words this position means that a noise model of the first order is assumed. An indirect validation of this assumption is given by the results. In fact, the final measurements show in general good results with the proposed method. Inserting Eq. (75) into Eq. (69) after its Z-transform, and considering positions (73) and (71), the following expression is obtained:

$$\hat{V}_u(z) = -\frac{(a_{1u} + c_{1u} + b_{1u}z^{-1})}{b_{1u}(1 + c_{1u}z^{-1}) + b_{2u}(1 + c_{1u}z^{-1})}U_{in}(z). \quad (76)$$

Comparing (76) with (47), it is left with a straightforward diophantine equation to solve. The diophantine equation gives the relationship between the parameters $Y_u = [a_{1u}, b_{1u}, b_{2u}, c_{1u}]$, the parameters k_{app}, k_{pu} and the parameters of the system (R_{Coil}, L_{Coil}) as follows:

$$-b_{1u} = 0 \quad (77)$$

$$a_{1u} + c_{1u} = t_s \frac{k_{app} C \phi(y(k))}{k_{di} L_{Coil}} k_{pu} \quad (78)$$

$$b_{1u} + b_{2u} = 1 + t_s \frac{k_{app}}{k_{di} L_{Coil}} C \phi(y(k)) \quad (79)$$

$$b_{1u} c_{1u} + b_{2u} c_{1u} = -1. \quad (80)$$

Procedure:

Heuristic value for parameters $k_{app}, k_{di}, k_{pi}, k_{pu}$ are calculated in order to estimate the state variable according to the desired dynamic performance. This yields initial values for the parameters $Y_i = [a_{1i}, b_{1i}, b_{2i}, c_{1i}]$ and $Y_u = [a_{1u}, b_{1u}, b_{2u}, c_{1u}]$. New values for the vector Y_i and Y_u are calculated using the recursive least squares method with the constraints $b_{1i}c_{1i} + b_{2i}c_{1i} = -1$ and $b_{1u}c_{1u} + b_{2u}c_{1u} = -1$. The technique is described in the following steps:

- **Step 0** Set heuristic values for k_{app}, k_{di} , and k_p . k_{app} is a big enough value to guarantee the asymptotic approximation of the velocity signal.
- **Step 1:** Calculate the new Y_i, Y_u and parameters of the ARMAX model using the recursive least squares method with the constraints $b_{1i}c_{1i} + b_{2i}c_{1i} = -1$ and $b_{1u}c_{1u} + b_{2u}c_{1u} = -1$.
- **Step 2:** Calculate a new k_{app}, k_{di}, k_{pi} , and k_{pu} from the parameterization of the velocity observer.
- **Step 3:** Calculate the new signals.
- **Step 4:** Update the regressor, $i_{Coil}(k) \rightarrow i_{Coil}(k-1)$, $\hat{v}_i(k-1) \rightarrow \hat{v}_i(k-2)$, $\hat{v}_u(k-1) \rightarrow \hat{v}_u(k-2), \dots$

Steps 1-4 are repeated for each sampling period.

7. Second-stage of the state observer design: open loop position observer

If the magneto-mechanical part of the system is considered, then

$$\dot{y}(t) = v(t) \quad (81)$$

$$\dot{v}(t) = \frac{f(y(t), i_{Coil}(t))}{m} - \frac{k_v v(t)}{m} - \frac{k_f y(t)}{m}, \quad (82)$$

where $f(y(t), i(t)) = F_{0,max} \sin(2\pi y(t)/d) + k_1(y(t) + \text{sign}(y(t))k_2)i(t)$ as above defined. If the system is written in the following form

$$\begin{bmatrix} \dot{y}(t) \\ \dot{v}(t) \end{bmatrix} = \begin{bmatrix} 0 & 1 \\ -\frac{k_f}{m} & -\frac{k_v}{m} \end{bmatrix} \begin{bmatrix} y(t) \\ v(t) \end{bmatrix} + \begin{bmatrix} 0 \\ \frac{f(y(t), i_{Coil}(t))}{m} \end{bmatrix}, \quad (83)$$

and if $h(x) = v(t)$, then the observability matrix is the following:

$$(O(x_0, u^*)) = \begin{bmatrix} 0 & 1 \\ \frac{F_{0,max}2\pi/d}{m} \cos(2\pi y(t)/d) - \frac{k_f}{m} & -\frac{k_v}{m} \end{bmatrix}. \quad (84)$$

Matrix (84) indicates a local uniform observability of the considered system except at the point in which $\cos(2\pi y(t)/d) = \frac{dk_f}{F_{0,max}2\pi}$. This means that, if the velocity is known, then the outputs of the systems are uniformly ($\forall u(t)$) distinguishable except for two isolated points. In fact, according to the data of the developed actuator it results that $dk_f < F_{0,max}2\pi$. Equation (85) is written in the following way:

$$\begin{bmatrix} \dot{y}(t) \\ \dot{v}(t) \end{bmatrix} = \mathbf{A} \begin{bmatrix} y(t) \\ v(t) \end{bmatrix} + \begin{bmatrix} 0 \\ \frac{f(y(t), i_{Coil}(t))}{m} \end{bmatrix}, \quad (85)$$

while the output equation

$$v(t) = \begin{bmatrix} 0 & 1 \end{bmatrix} \begin{bmatrix} y(t) \\ v(t) \end{bmatrix} = \mathbf{C} \begin{bmatrix} y(t) \\ v(t) \end{bmatrix}. \quad (86)$$

It can be clearly seen that (\mathbf{A}, \mathbf{C}) is an observable pair, then, according to (Thau (1973)), the observer can be designed as

$$\begin{bmatrix} \dot{\hat{y}}(t) \\ \dot{\hat{v}}_L(t) \end{bmatrix} = \mathbf{A} \begin{bmatrix} \hat{y}(t) \\ \hat{v}_L(t) \end{bmatrix} + \begin{bmatrix} 0 \\ \frac{f(\hat{y}(t), i_{Coil}(t))}{m} \end{bmatrix} + \begin{bmatrix} K_y \\ K_v \end{bmatrix} (\hat{v}(t) - \hat{v}_L(t)), \quad (87)$$

where $\hat{v}(t) = \mathcal{Z}^{-1}\hat{V}(z)$ calculated above. The corresponding estimation error dynamics are given by

$$\dot{e}(t) = (\mathbf{A} - \mathbf{K}\mathbf{C})e(t) + \Delta f(t) = \mathbf{A}_0 e(t) + \Delta f(t), \quad (88)$$

where

$$e(t) = \begin{bmatrix} e_y(t) \\ e_v(t) \end{bmatrix} = \begin{bmatrix} y(t) - \hat{y}(t) \\ v(t) - \hat{v}(t) \end{bmatrix}, \quad (89)$$

with

$$\begin{aligned} \mathbf{A}_0 &= \mathbf{A} - \mathbf{K}_0 \mathbf{C}, \\ \mathbf{K}_0 &= \begin{bmatrix} K_y \\ K_v \end{bmatrix}, \end{aligned}$$

and

$$\Delta f(t) = \begin{bmatrix} 0 \\ \frac{f(y(t), i_{Coil}(t))}{m} - \frac{f(\hat{y}(t), i_{Coil}(t))}{m} \end{bmatrix}.$$

Because of (\mathbf{A}, \mathbf{C}) is an observable pair, matrix \mathbf{A}_0 for a suitable choice of the observer gain \mathbf{K}_0 is a Hurwitz matrix. This yields that there exist symmetric and positive matrices \mathbf{P}_0 and \mathbf{Q}_0 which satisfy the so called *Lyapunov equation*

$$\mathbf{A}_0^T \mathbf{P}_0 + \mathbf{P}_0 \mathbf{A}_0 = -\mathbf{Q}_0. \quad (90)$$

In order to show the asymptotic stability of (88), the following Lyapunov function is introduced:

$$V(e(t)) = e^T(t) \mathbf{P}_0 e(t). \quad (91)$$

The time derivative is given by

$$\frac{dV(e(t))}{dt} = \dot{e}^T(t) \mathbf{P}_0 e(t) + e^T(t) \mathbf{P}_0 \dot{e}(t) \quad \text{and} \quad (92)$$

from (88) it follows that

$$\frac{dV(e(t))}{dt} = (\mathbf{A}_0 e(t) + \Delta f(t))^T \mathbf{P}_0 e(t) + e^T(t) \mathbf{P}_0 \dot{e}(t) + e^T(t) \mathbf{P}_0 e(t) + e^T(t) \mathbf{P}_0 (\mathbf{A}_0 e(t) + \Delta f(t)). \quad (93)$$

This yields the following equation:

$$\frac{dV(e(t))}{dt} = (e^T(t) \mathbf{A}_0^T + (\Delta f(t))^T) \mathbf{P}_0 e(t) + e^T(t) \mathbf{P}_0 \dot{e}(t) + e^T(t) \mathbf{P}_0 e(t) + e^T(t) \mathbf{P}_0 (\mathbf{A}_0 e(t) + \Delta f(t)). \quad (94)$$

At the end, considering Eq. (90) it follows that

$$\frac{dV(e(t))}{dt} = (2e^T(t) \mathbf{Q}_0 e(t) + (\Delta f(t))^T \mathbf{P}_0 e(t) + e^T(t) \mathbf{P}_0 (\Delta f)). \quad (95)$$

Being $\Delta f(t)$ a Lipschitz function, then exists a positive constant L such that, for all points x_1 and x_2 in the domain of the function $\Delta f(t)$

$$\Delta f(x_1, x_2) \leq L \|x_1 - x_2\|.$$

If $\lambda_{Q_{0m}}$ is the small eigenvalue of matrix \mathbf{Q}_0 and $\lambda_{P_{0M}}$ the biggest eigenvalue of matrix \mathbf{P}_0 , if

$$\lambda_{Q_{0m}} > \lambda_{P_{0M}}, \quad (96)$$

then

$$\frac{dV(e(t))}{dt} = -2 \|\lambda_{Q_{0m}} - L \lambda_{P_{0M}}\| e^2(t). \quad (97)$$

The last equation says that $e(t) = 0$ is an asymptotically stable equilibrium point. The presented demonstration is constrictive in order to build an observer. In other words, it is enough to choice matrices \mathbf{K}_0 and \mathbf{Q}_0 such that, through Eq. (90), condition (96) is satisfied.

8. Actuator control

Figure 5 shows the control structure applied to the actuator. The actuator consists of three parts from the control point of view: an electrical system (motor coil), an electromagnetic system (generation reluctance force) and a mechanical system (mass-spring-damper), with the back emf as an internal voltage feedback for the electrical system. Under normal operating conditions, the electrical subsystem is linear and can be represented by the transfer function

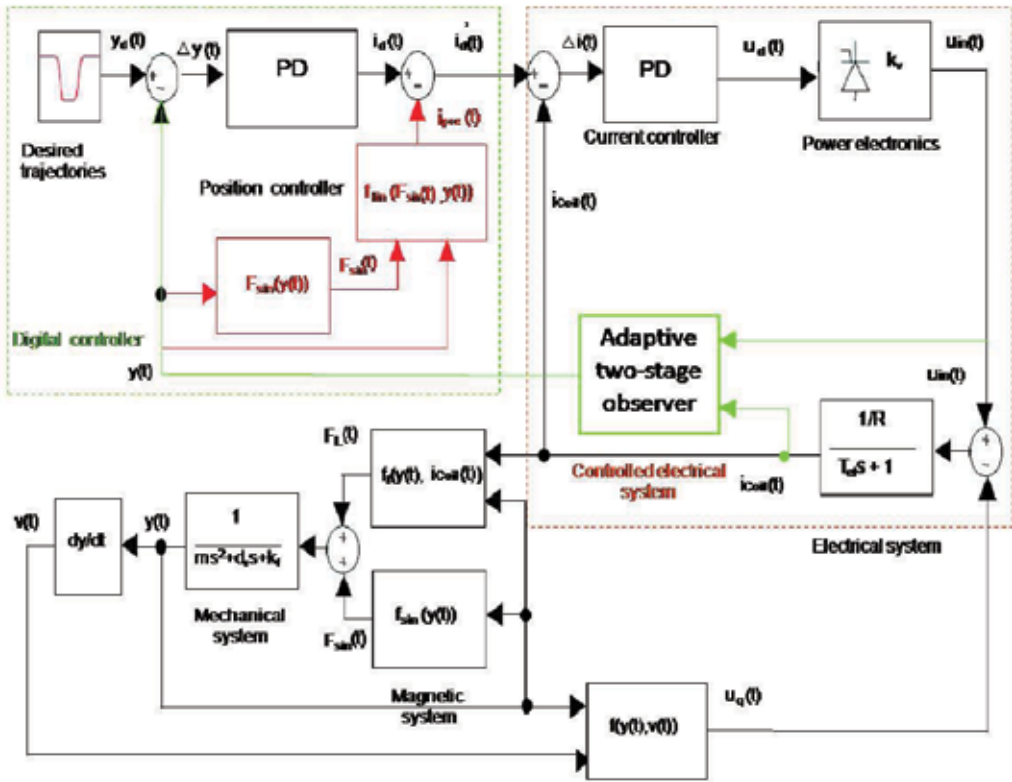


Fig. 5. Control structure

$$G_{el} = \frac{1/R}{T_s + 1} \quad (98)$$

where R is the resistance, and T is the time-constant of the coil. The non-linear electromagnetic force generation can be separated into two parallel blocks, $F_{sin}(y(t))$ and $F_{lin}(y(t), i_{Coil}(t))$ corresponding to the reluctance effect and the Lorentz force, respectively:

$$F(y(t), i_{Coil}(t)) = F_{sin}(y(t)) + F_{lin}(y(t), i_{Coil}(t)), \quad (99)$$

with the following approximative equations

$$F_{sin}(y(t)) = F_{0,max} \sin(2\pi y(t)/d) \quad \text{and} \quad (100)$$

$$F_{lin}(y(t), i_{Coil}(t)) = k_1(y(t) + \text{sign}(y(t))k_2)i_{Coil}(t), \quad (101)$$

where k_1 and k_2 are physical constants. Finally, the mechanical subsystem is characterized by

$$G_m(s) = \frac{Y(s)}{F(s)} = \frac{1}{ms^2 + d_r s + k_f}, \quad (102)$$

with the moving mass m , the viscose damping factor d_r and the spring constant k_f . $Y(s)$ and $F(s)$ are the Laplace transformations of the position $y(t)$ and of the force defined by

Eq. (99) respectively. Because the system damping is very weak, it is obviously up to the control to enable a well-damped overall system. The control structure basically consists of two PD controllers organised in a cascade scheme. PD regulators are often utilised in control problems where a high dynamic range is required. The internal loop is devoted to the current control and provides a compensation of the electrical system, which is the fastest time constant of the physical system. This current controller has an inner loop for back-emf compensation. As the back-emf is difficult to sense, a nonlinear estimator is used for on-line observation. Due to the very high dynamic range required by the valve actuation, the current control loop was realised in an analogue technique, while the trajectory generation and the position control were implemented on a DSP. A common problem of PD-type controllers is the existence of steady-state error. As shown in Fig. 5, a nonlinear feed-forward block, containing the inverse reluctance characteristics, was used to compensate for the nonlinear effects of the actuator and to ensure the stationary accuracy. In fact, having compensated for the nonlinearities, the overall system behaviour can be approximated by a linear third-order system. In particular, the nonlinear compensation is performed while generating the desired current from the inversion of the linear part of the motor characteristic, as described in the following:

$$i_{pre}(t) = \frac{F_{lin}(t)}{k_1(y_d(t) + \text{sign}(y_d(t))k_2)}. \quad (103)$$

The inversion of the force-position characteristic of the motor leads to the total actuator force, from which its non-linear part is then subtracted:

$$F_{lin}(t) = ky_d(t) + d\dot{y}_d(t) + m\ddot{y}_d(t) - F_{0,max}\sin(2\pi y_d(t)/d) \quad (104)$$

Finally the following equation is obtained:

$$i_{pre}(t) = \frac{k_f y_d(t) + d_r \dot{y}_d(t) + m \ddot{y}_d(t) - F_{0,max} \sin(2\pi y_d(t)/d)}{k_1(y_d(t) + \text{sign}(y_d(t))k_2)}. \quad (105)$$

Based on the desired position signal coming out of the trajectory generator and the measured valve position, a PD-type position controller (lead compensator) is applied. Contrary to the conventional position control in drive systems, where PI-type controllers are mostly used, in this special case we need to increase substantially the exiting phase margin to achieve the desired system damping.

9. Experimental measurements and simulations

The actuator was realised and tested (see the left part of Fig. 6) in our laboratory. Further investigations under real engine conditions were planned. In the right part of Fig. 6, measured reluctance forces for different current densities and armature positions are depicted. Again, the current density was chosen to be -20 , -10 , 0 , 10 or 20 A/mm², respectively. Compared to the calculated values the measurements show deviations up to $\sim 8\%$ except for that for the current density of -20 A/mm² (here around 13%). The deviation is due to iron saturation, which could not be modelled exactly in the FEM calculation because the material characteristics contained missing data for this region. In other cases, the agreement is obviously better. Here, some typical simulation results using the control structure described above are presented in Fig. 5. The positive effects of the optimised velocity observer are visible in the closed loop control. For the opening phase, a strong but rapidly decreasing gas

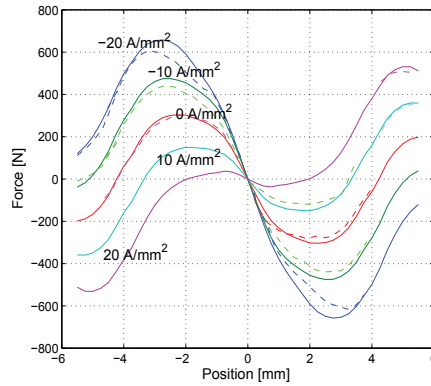
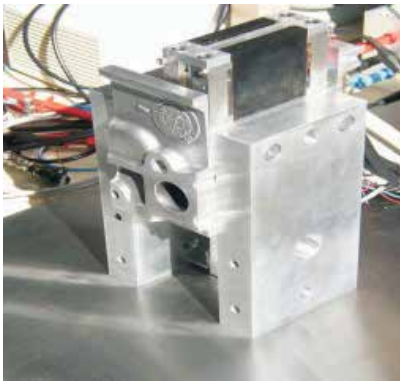


Fig. 6. Left: Actuator experimental set-up. Right: Comparison of calculated and measured characteristic of the motor.

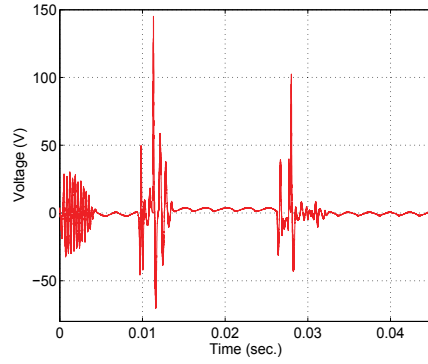
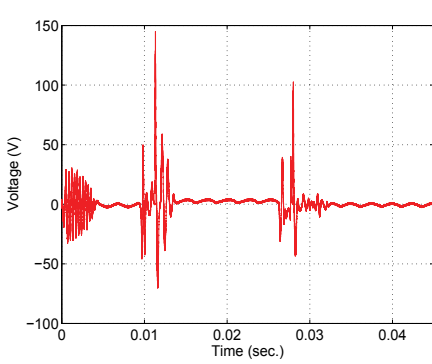


Fig. 7. Left: Closed loop input voltage without optimized observer. Right: Input voltage with optimized observer.

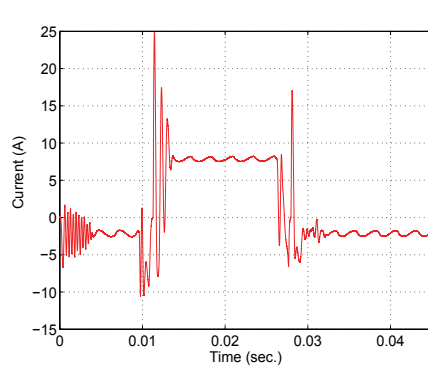
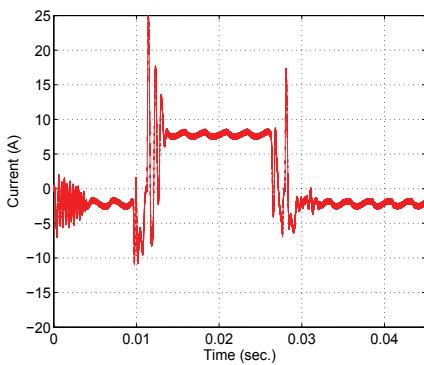


Fig. 8. Left: Closed loop coil current without optimized observer. Right: Coil current with optimized observer.

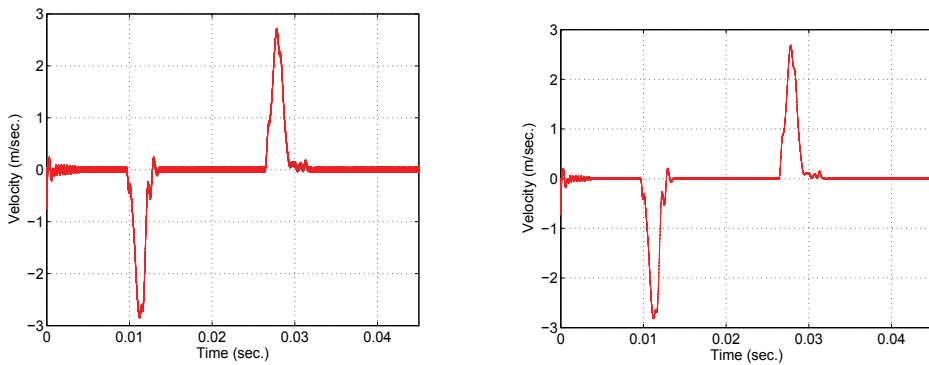


Fig. 9. Left: Closed loop velocity without optimized observer. Right: Velocity with optimized observer.

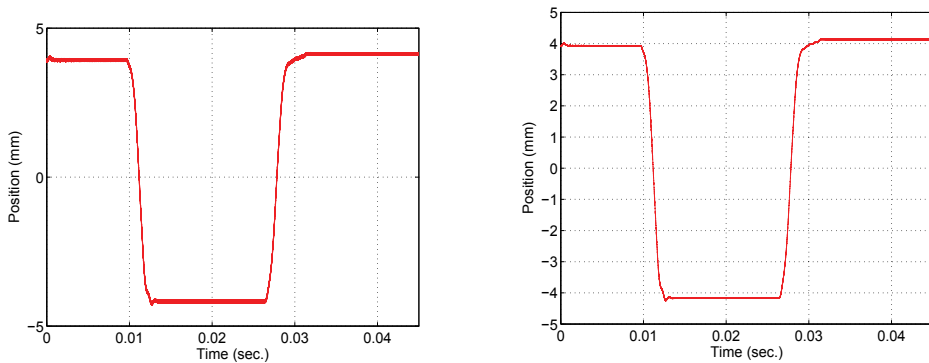


Fig. 10. Left: Closed loop position without optimized observer. Right: Position with optimized observer.

pressure is assumed to be present and is simulated as an unknown disturbance. Even though the presented control strategy does not consider this disturbance condition, the system shows excellent control behaviour. In the simulation, a realistic white noise in the measurement of the current is considered. The typical control behaviour is demonstrated in Fig. 10, where a full-range operation cycle at an engine speed of 3,000 rpm (rounds per minute) is shown. Here, high tracking accuracy is demonstrated, and a reduction of the noise effect is visible. Figure 9 shows also the improvement in the velocity control in the closed loop. The positive effects on the velocity and position control in the closed loop can be justified by the de-noised current and input voltage (see Figs. 8 and 7). Theoretically and in computer simulations, control precision can be further improved by increasing the gain of the controllers. However, measurement noises can cause serious oscillations, which may lead to local stability problems in practical situations.

10. Conclusions and Future Works

The design of a novel linear reluctance motor using permanent-magnet technology is presented. The developed actuator is specifically intended to be used as an electromagnetic engine valve drive. Besides a design analysis, the structure and properties of the applied

control strategy are also discussed. Dynamic simulation results of a sensorless control strategy are presented and show good performance. In particular, based on a nonlinear model, an adaptive two-stage observer is presented that addresses unobservable points and achieves sensorless control. This paper presents feasible real-time self-tuning of an approximated velocity estimator based on measurements of current and input voltage. The robustness of the velocity tracking is addressed using a minimum variance approach. The effect of the noise is minimised, and the position can be achieved through a two-stage structure between this particular velocity estimator and an observer based on the electromechanical system. A control strategy is presented and discussed as well. Computer simulations of the sensorless control structure are presented, in which the positive effects of the optimised velocity observer are visible in the closed-loop control.

10.1 Future Works

Future works could be oriented towards analysis of the stability of the whole closed-loop structure (plant-observer-controller). This analysis could provide useful indications in the determination of the parameters of the PD controller and also in the parameters of the two proposed observers. Future work should also include investigations of further improvements of dynamic range and accuracy using more sophisticated control methods (e.g., sliding-mode control) and experimental measurements under real engine conditions.

11. Acknowledgement

This work was supported by IAI institut für Automatisierung und Informatik (GmbH) Wernigerode (Germany) and Volkswagen Research Center Wolfsburg (Germany). Thanks to them this work was accomplished.

12. References

- Ahmed, T. & Theobald, M.A. (1989). A survey of variable valve actuation technology, In: *SAE Paper (SAE1989)*, SAE, (Ed.), paper number 891674.
- Beghi, A., Nardo, L. & Stevanato, M. (2006). Observer-based discrete-time sliding mode throttle control for drive-by-wire operation of a racing motorcycle engine. *Journal Control Systems Technology, IEEE Transactions*, Vol. 14, No. 4, July -2006, pp. 767-775.
- Butzmann, S., Melbert, J. & Koch, A. (1989). Sensorless control of electromagnetic actuators for variable valve train, *Proceeding of SAE 2000 World Congress*, paper number 2000-01-1225, Michigan (USA), SAE, (Ed.), Detroit.
- Dagci, O.H., Pan, Y. & Ozguner, U. (2002). Sliding mode control of electronic throttle valve, *Proceedings of the 2002 American Control Conference*, pp. 1996-2001, ISBN: 0743-1619, Alaska, 8-10 May 2002, IEEE, Anchorage.
- Furlani, E.P. (2001). *Permanent Magnet and Electromechanical Devices*, Academic Press, USA.
- Fabbrini, A., Doretto, D., Braune, S., Garulli, A. & Mercorelli, P. (2008). Optimal trajectory generation for camless internal combustion engine valve control, *Proceedings of of IECON 2008, the 34th Annual Conference of the IEEE Industrial Electronics Society*, pp. 303-308, Florida, 10-13 November 2008, IEEE, Orlando.
- Franklin, G.F., Powell, J.D. & Workman, L.M. (1997). *Digital Control of Dynamic Systems*, Prentice Hall, ISBN-10: 0201820544, USA.
- Hermann, R. & Krener, A.J. (1977). Nonlinear controllability and observability, *IEEE Transactions on Automatic Control*, Vol. 22, No. 5, October-1977, pp. 728-740.

- Hoffmann, W. & Stefanopoulou, A.G. (2001). Iterative learning control of electromechanical camless valve actuator, *Proceedings of the 2001 American Control Conference*, pp. 2860-2866, ISBN: 0-7803-6495-3, VA (USA), 25-27 June 2001, IEEE, Arlington.
- Kwatny, H.G. & Chang, B.C. (2005). Symbolic computing of nonlinear observable and observer forms, *Applied Mathematics and Computation Elsevier Science Publishing*, Vol. 171, pp. 1058-1080.
- Peterson, K.S. (2005). *Control Methodologies for Fast & Low Impact Electromagnetic Actuators for Engine Valves*, PhD Thesis, University of Michigan.
- Mercorelli, P. (2009). Robust feedback linearization using an adaptive PD regulator for a sensorless control of a throttle valve, *Mechatronics a journal of IFAC. Elsevier publishing*, Vol. 19, No. 8, November-2009, pp. 1334-1345.
- Schlechter, M.M. & Levin, M.B. (1996). Camless engine, In: *SAE Papers (SAE1996)*, SAE, (Ed.), paper number 960581.
- Rajamani, R. (1998). Observers for lipschitz nonlinear systems, *IEEE Transactions on Automatic Control*, Vol. 43, No. 3, pp. 397-401.
- Slotine, J.J. (1991). *Applied Nonlinear Control*, Ed. Prentice-Hall, ISBN: 0-13-040890-5, Englewood Cliffs, New Jersey (USA).
- Tai, C. & Tsao, T. (2003). Control of an electromechanical actuator for camless engines, *Proceedings of the 2001 American Control Conference*, pp. 3113-3118, ISBN: 0-7803-7896-2, Colorado (USA), 4-6 June 2003, IEEE, Denver.
- Thau, F.E. (1973). Observing the state of nonlinear dynamic systems, *International Journal of Control*, Vol. 17, No. 3, pp. 471-479.
- Wu, R. & Slemon, G.R. (1991). A permanent magnet motor drive without a shaft sensor, *IEEE Transactions on Industrial Applications*, Vol. 27, No. 5, pp. 1005-1011, ISSN: 0093-9994.
- Xia, X. & Zeitz, M. (1997). On nonlinear continuous observers, *International Journal of Control*, Vol. 66, No. 6, pp. 943-954.
- Zhu, G., Kaddouri, A., Dessaint, L.A. & Akhrif, O. (2001). A nonlinear state observer for the sensorless control of a permanent-magnet AC machine, *IEEE Transactions on Industrial Electronics*, Vol. 48, No. 6, pp. 1098-1108, ISSN: 0278-0046.

Integrated Controller Design for Automotive Semi-Active Suspension Considering Vehicle Behavior with Steering Input

Masaki Takahashi, Takashi Kumamaru and Kazuo Yoshida
*Keio University,
Japan*

1. Introduction

Semi active suspension control systems have recently been utilized to improve ride comfort of vehicles and their effectiveness has also been demonstrated (Ohsaku et al., 2000). However, it is not easy to improve simultaneously both ride comfort and steering stability when steering. To achieve it, several control methods have been proposed (Hrovat, 1993)-(Yoshida et al., 2006). In addition, because both ride comfort and steering stability greatly depend on the sensitivity of the human body to vibration, vehicle design that takes this and visual sensitivity into consideration is expected to be introduced. Furthermore, it has been reported that the phase difference in motion by pitching and rolling has an influence on steering stability and passenger ride comfort (Sakai et al., 2006)-(Kawagoe et al., 1997).

To improve both ride comfort and steering stability, this study proposes a controller design method for semi-active suspension system taking into consideration the most sensitive frequency range of the human body and vehicle behavior when steering. A method that can improve both the ride comfort and the vehicle stability is proposed by separating the control range in terms of the frequency domain, where the frequency weighting in controlled variables is used. Furthermore, the controller is scheduled in the time domain to attain a positive pitch angle during slaloms. The dynamics of road disturbance is assumed and is accommodated into the controller to make control more effective. In order to verify the effectiveness of the proposed method, a full-vehicle model that has variable stiffness and a damping semi-active suspension system is constructed and the numerical simulations are carried out. From the simulation results, it is demonstrated that the proposed method can improve ride comfort in the frequency domain that humans feel uncomfortable, reduce vehicle motion, and synchronize the roll and pitch angles caused by steering.

2. Modeling

A full-vehicle model which has variable stiffness and a damping semi-active suspension system is shown in Fig.1. The equations of motion are as follows:

$$\begin{aligned}
M_b \ddot{z}_g(t) &= \sum_{i=1}^4 f_{si}(t) \\
M_{ii} \ddot{z}_{ui}(t) &= -f_{si}(t) - K_{ii} z_{ii}(t) \quad (i = 1, \dots, 4) \\
I_p \ddot{\theta}_p(t) &= -L_f (f_{s1}(t) + f_{s2}(t)) + L_r (f_{s3}(t) + f_{s4}(t)) + M_b g H_p \theta_p(t) - M_b H_p \ddot{x}_g(t) \\
I_r \ddot{\phi}_r(t) &= \frac{T_f}{2} (f_{s1}(t) - f_{s2}(t)) + \frac{T_r}{2} (f_{s3}(t) - f_{s4}(t)) + M_b g H_r \phi_r(t) + M_b H_r \ddot{y}_g(t) \\
I_y \ddot{\psi}_y(t) &= L_f \left(\sum_{i=1}^2 f_{xi}(t) \sin \delta_f(t) + \sum_{i=1}^2 f_{yi}(t) \cos \delta_f(t) \right) - L_r (f_{y3}(t) + f_{y4}(t)) \\
M \ddot{x}_g(t) &= \sum_{i=1}^2 f_{xi}(t) \cos \delta_f(t) - \sum_{i=1}^2 f_{yi}(t) \sin \delta_f(t) + \sum_{i=3}^4 f_{xi}(t) - M_b H_p \ddot{\theta}_p(t) \\
M \ddot{y}_g(t) &= \sum_{i=1}^2 f_{xi}(t) \sin \delta_f(t) + \sum_{i=1}^2 f_{yi}(t) \cos \delta_f(t) + \sum_{i=3}^4 f_{yi}(t) + M_b H_r \ddot{\phi}_r(t)
\end{aligned} \tag{1}$$

where H_p and H_r show the distance from the pitch rotation axis to the ground and the distance from the body center of gravity to the roll center respectively. f_{si} is the force that acts on the suspension of each wheel and is shown the following equation including the variable stiffness k_{si} and the variable damping c_{si} . f_{ai} is an output of the semi-active suspension system.

$$\begin{aligned}
f_{si}(t) &= -K_f(t) z_{si}(t) - C_f(t) \dot{z}_{si}(t) + f_{ai}(t) \quad (i = 1, 2) \\
f_{si}(t) &= -K_r(t) z_{si}(t) - C_r(t) \dot{z}_{si}(t) + f_{ai}(t) \quad (i = 3, 4) \\
f_{ai}(t) &= -k_{si}(t) z_{si}(t) - c_{si}(t) \dot{z}_{si}(t) \quad (i = 1, \dots, 4)
\end{aligned} \tag{2}$$

where $z_{si}(t)$ is the suspension stroke.

$$\begin{aligned}
z_{s1}(t) &= z_g(t) - L_f(t) \theta_p(t) + T_f/2 \phi_r(t) - z_{u1}(t) \\
z_{s2}(t) &= z_g(t) - L_f(t) \theta_p(t) - T_f/2 \phi_r(t) - z_{u2}(t) \\
z_{s3}(t) &= z_g(t) + L_r(t) \theta_p(t) + T_r/2 \phi_r(t) - z_{u3}(t) \\
z_{s4}(t) &= z_g(t) + L_r(t) \theta_p(t) - T_r/2 \phi_r(t) - z_{u4}(t)
\end{aligned} \tag{3}$$

f_{xi} and f_{yi} show the longitudinal and lateral forces that act on the tire respectively and are derived from a nonlinear tire model of magic formula (Bakker et al., 1987), (Bakker et al., 1989). From the motion of equation in Eq. (1), the following bilinear system of 7 degree of freedom model for controller design is derived.

$$\dot{\mathbf{x}}(t) = \mathbf{A}\mathbf{x}(t) + \mathbf{B}\mathbf{X}^*(t)\mathbf{u}(t) + \mathbf{E}_r\mathbf{w}(t) + \mathbf{E}_s\mathbf{f}_d(t) \tag{4}$$

where

$$\begin{aligned}
\mathbf{x}(t) &= [z_g \ \theta_p \ \phi_r \ z_{u1} \ z_{u2} \ z_{u3} \ z_{u4} \ \dot{z}_g \ \dot{\theta}_p \ \dot{\phi}_r \ \dot{z}_{u1} \ \dot{z}_{u2} \ \dot{z}_{u3} \ \dot{z}_{u4}]^T \\
\mathbf{X}^*(t) &= \text{diag}(z_{s1} \ z_{s2} \ z_{s3} \ z_{s4} \ \dot{z}_{s1} \ \dot{z}_{s2} \ \dot{z}_{s3} \ \dot{z}_{s4}) \\
\mathbf{u}(t) &= [k_{s1} \ k_{s2} \ k_{s3} \ k_{s4} \ c_{s1} \ c_{s2} \ c_{s3} \ c_{s4}]^T \\
\mathbf{w}(t) &= [w_1 \ w_2 \ w_3 \ w_4]^T \\
\mathbf{f}_d(t) &= [f_{dp} \ f_{dr}]^T
\end{aligned}$$

symbol	parameter	value
M	total mass	1598 kg
M_b	mass of body	1424 kg
M_{t1}, M_{t2}	mass of front tire	45 kg
M_{t3}, M_{t4}	mass of rear tire	42 kg
I_p	pitch moment of inertia	3500 kgm ²
I_r	roll moment of inertia	1019 kgm ²
I_y	yaw moment of inertia	3270 kgm ²
K_{t1}, K_{t2}	stiffness coefficient of front tire	190000 N/m
K_{t3}, K_{t4}	stiffness coefficient of rear tire	190000 N/m
K_f	stiffness coefficient (front, passive)	27000 N/m
K_r	stiffness coefficient (rear, passive)	28000 N/m
C_{t1}, C_{t2}	damping coefficient of front tire	0 Ns/m
C_{t3}, C_{t4}	damping coefficient of rear tire	0 Ns/m
C_f	damping coefficient (front, passive)	1500 Ns/m
C_r	damping coefficient (rear, passive)	1750 Ns/m
L_f	length from C.G. to axle (front)	1.22 m
L_r	length from C.G. to axle (rear)	1.46 m
T_f, T_r	length of track	1.52 m
H_p	pitch height	0.715 m
H_r	roll height	0.620 m
K_{fmin}	minimum value of variable stiffness coefficient (front)	11000 N/m
K_{fmax}	maximum value of variable stiffness coefficient (front)	100000 N/m
K_{rmin}	maximum value of variable stiffness coefficient (rear)	11000 N/m
K_{rmax}	maximum value of variable stiffness coefficient (rear)	102000 N/m
C_{fmin}	maximum value of variable damping coefficient (front)	100 Ns/m
C_{fmax}	maximum value of variable damping coefficient (front)	8000 Ns/m
C_{rmin}	maximum value of variable damping coefficient (rear)	450 Ns/m
C_{rmax}	maximum value of variable damping coefficient (rear)	8250 Ns/m

Table 1. Model Specification

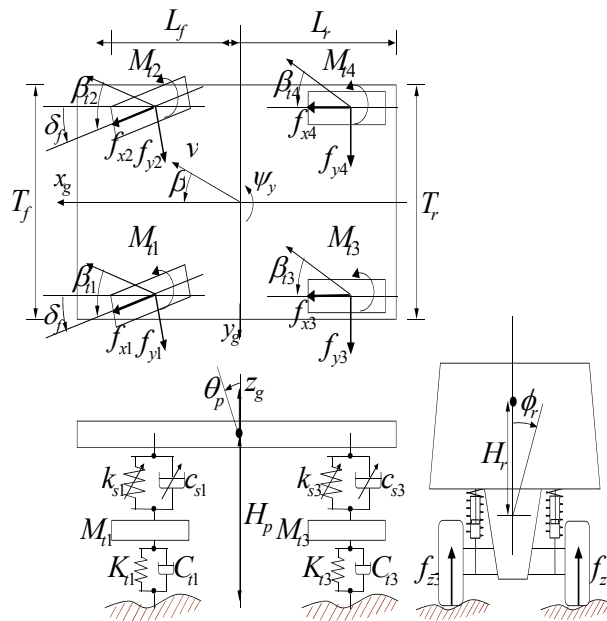


Fig. 1. Full Vehicle Model

In Eq. (4), the second term is the force which semi active suspension generates, the third term is the road surface disturbance, and f_{dp} and f_{dr} of the fourth term show the inertia force and the centrifugal force. Table 1 shows the parameter which are used for the numerical simulation (Hrovat, 1997), (Takahashi, 2003).

3. Controller design

Figure 2 shows the control system. The robustness of the system is guaranteed in the frequency domain in which it is assumed that the impact of road disturbance is small utilizing an H_∞ controller. Furthermore, it is possible to change the frequency weight according to the circumstance the vehicle is traveling under by designing gain scheduling control. In this chapter, the concrete control design method is shown.

3.1 Disturbance-accommodation control

It is known that typical irregularities on road surface are inversely proportional to the square of frequency in the low-frequency domain and they have the kind of power spectral density that is inversely proportional to four powers or more in the high-frequency domain. The effectiveness of designing control that can be merged with the feedforward control of the disturbance has been demonstrated (Nishimura et al., 1989). Techniques of control that accommodate disturbances in which power spectral density flattens in the limited frequency domain have been used to deal with various disturbances. The road disturbance model in this study has been assumed to be colored disturbances and input from four tires. The augmented system of the disturbance model and the controlled system model is as follows:

$$\begin{aligned} \dot{\mathbf{x}}_{wi}(t) &= \mathbf{A}_{wi} \mathbf{x}_{wi}(t) + \mathbf{B}_{wi} \mathbf{v}(t) \\ w_i(t) &= \mathbf{C}_{wi} \mathbf{x}_{wi}(t) \quad (i = 1, \dots, 4) \end{aligned} \tag{5}$$

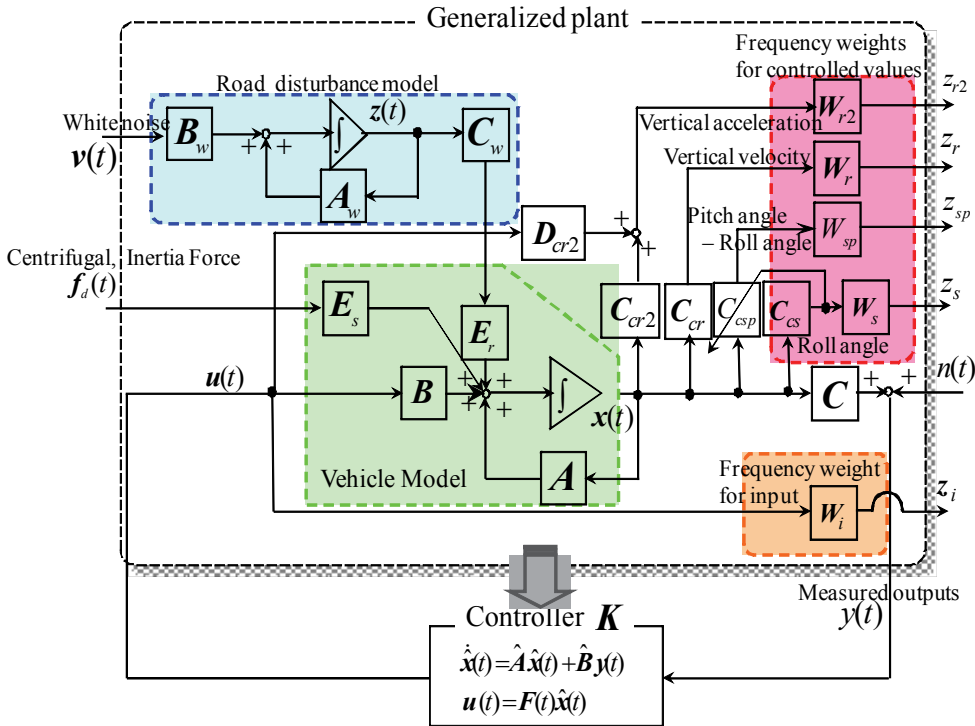


Fig. 2. Generalized plant

where $\mathbf{v}(t)$ is white noise. In this study, dynamics of the disturbance is represented as the low-pass characteristics.

$$\mathbf{A}_{wi} = \begin{bmatrix} -1 & 1 & 0 \\ 0 & 0 & 1 \\ 0 & -\omega_d^2 & -2\zeta_d\omega_d \end{bmatrix}, \mathbf{B}_{wi} = \begin{bmatrix} 0 \\ 0 \\ \omega_d^2 \end{bmatrix} \quad (6)$$

$$\mathbf{C}_{wi} = [1 \ 0 \ 0] \quad (i = 1, \dots, 4)$$

From Eqs. (4) and (5), the augmented system is derived.

$$\begin{bmatrix} \dot{\mathbf{x}}(t) \\ \dot{\mathbf{x}}_{wi}(t) \end{bmatrix} = \begin{bmatrix} \mathbf{A} & \mathbf{E}_r \mathbf{C}_{wi} \\ \mathbf{0} & \mathbf{A}_{wi} \end{bmatrix} \begin{bmatrix} \mathbf{x}(t) \\ \mathbf{x}_{wi}(t) \end{bmatrix} + \begin{bmatrix} \mathbf{B} \\ \mathbf{0} \end{bmatrix} \mathbf{X}^*(t) \mathbf{u}(t) + \begin{bmatrix} \mathbf{0} \\ \mathbf{B}_{wi} \end{bmatrix} \mathbf{v}(t) + \begin{bmatrix} \mathbf{E}_s \\ \mathbf{0} \end{bmatrix} \mathbf{f}_d(t) \quad (7)$$

$$\mathbf{y}(t) = \begin{bmatrix} \mathbf{C} & \mathbf{0} \end{bmatrix} \begin{bmatrix} \mathbf{x}(t) \\ \mathbf{x}_{wi}(t) \end{bmatrix}$$

The cutoff frequency of the low-pass filter is $\omega_d = 50 \times 2\pi \text{ rad/s}$ and the damping ratio is $\zeta_d = 1/\sqrt{2}$. An optimal control input in the augmented system is

$$\mathbf{u}^o(t) = -\mathbf{R}^{-1} \mathbf{B}^T \mathbf{P}_{11} \mathbf{x}(t) - \mathbf{R}^{-1} \mathbf{B}^T \mathbf{P}_{12} \mathbf{x}_{wi}(t) \quad (8)$$

\mathbf{P}_{11} and \mathbf{P}_{12} are unique positive definite solution of the following Riccati equation.

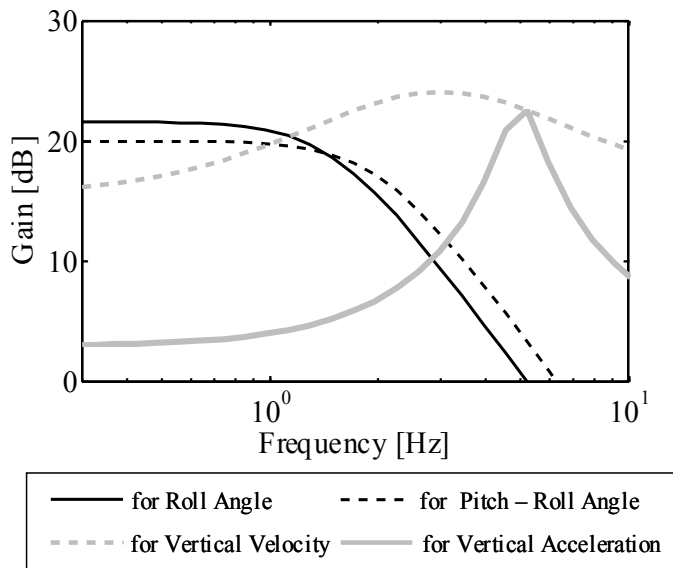


Fig. 3. Frequency Weights for Controlled Values

$$\mathbf{P}_{11}\mathbf{A} + \mathbf{A}^T\mathbf{P}_{11} - \mathbf{P}_{11}\mathbf{B}\mathbf{R}^{-1}\mathbf{B}^T\mathbf{P}_{11} + \mathbf{Q} = \mathbf{0} \quad (9)$$

$$\mathbf{P}_{11}\mathbf{E}_r\mathbf{C}_{wi} + \mathbf{P}_{12}\mathbf{A}_{wi} + \mathbf{A}^T\mathbf{P}_{12} - \mathbf{P}_{11}\mathbf{B}\mathbf{R}^{-1}\mathbf{B}^T\mathbf{P}_{12} = \mathbf{0} \quad (10)$$

From Eq.(8), it is confirmed that the feedback gain is decided unrelated to the quality of the disturbance and the feedforward gain is decided according to the quality of the disturbance.

3.2 Bilinear disturbance-accommodation H_∞ control

It has been pointed out that the response level deteriorates in the frequency domain in which the estimated disturbance level is small when an unexpected disturbance is input (Nishimura et al., 1989). Improved robustness in the frequency domain is regarded as uncertainty in an augmented system (Kang et al., 1992).

In addition, to separate the control range in terms of the frequency domain, the frequency weighting in controlled variables is used. The frequency weightings \mathbf{W}_r and \mathbf{W}_{r2} are shown in Fig. 3. To improve ride comfort, these frequency weightings which have peaks near the body resonance frequency and near the frequency domain of 4 - 8 Hz, which make humans feel uncomfortable, are designed (Janeway, 1948).

Changes in body attitude should be decreased to improve steering stability. The controlled variable is the roll angle. The frequency weight \mathbf{W}_s for the roll angle is designed in the low-frequency domain. Furthermore, the controlled variable is the relative angle of pitch and roll, and the pitch and roll angles caused by steering need to be synchronized to reduce the feeling of rolling. For both controlled variables, the frequency weight \mathbf{W}_{sp} is designed in the low-frequency domain. In this study, H_∞ control theory (Umehara, 2005) and the disturbance accommodation control theory which are expanded to the bilinear system are applied to control of the semi-active suspension. To design of the generalized plant, the frequency weights for the controlled variable and control input are designed.

$$\begin{aligned}
 Q_c \begin{cases} \dot{\mathbf{x}}_c(t) = \mathbf{A}_c \mathbf{x}_c(t) + \mathbf{B}_c \mathbf{x}_z(t) \\ \mathbf{z}_c(t) = \mathbf{C}_c \mathbf{x}_c(t) + \mathbf{D}_c \mathbf{x}_z(t) \end{cases} \\
 Q_i \begin{cases} \dot{\mathbf{x}}_i(t) = \mathbf{A}_i \mathbf{x}_i(t) + \mathbf{B}_i \mathbf{X}(t)^* \mathbf{u}(t) \\ \mathbf{z}_i(t) = \mathbf{C}_i \mathbf{x}_i(t) + \mathbf{D}_i \mathbf{X}(t)^* \mathbf{u}(t) \end{cases}
 \end{aligned} \quad (11)$$

where \mathbf{x}_z represents the variable of the augmented system. \mathbf{z}_c is the controlled variable and \mathbf{z}_i is the output of the frequency weight for control input. The controlled model, the disturbance model, and the frequency weight are merged and the state-space representation of the generalized plant is as follows:

$$\begin{aligned}
 \dot{\mathbf{x}}_g(t) &= \mathbf{A}_g \mathbf{x}_g(t) + \mathbf{B}_1 \mathbf{w}_g(t) + \mathbf{B}_2 \mathbf{X}^*(t) \mathbf{u}(t) \\
 \mathbf{z}(t) &= \mathbf{C}_1 \mathbf{x}_g(t) + \mathbf{D}_{12} \mathbf{X}^*(t) \mathbf{u}(t) \\
 \mathbf{y}(t) &= \mathbf{C}_2 \mathbf{x}_g(t) + \mathbf{D}_{21} \mathbf{w}_g(t)
 \end{aligned} \quad (12)$$

where $\dot{\mathbf{x}}_g(t) = [\dot{\mathbf{x}} \ \dot{\mathbf{x}}_{wi} \ \dot{\mathbf{x}}_c \ \dot{\mathbf{x}}_i]^T$, $\mathbf{z}_g(t) = \text{diag}(\mathbf{z}_c, \mathbf{z}_i)$ and $\mathbf{w}_g(t) = [\mathbf{v} \ \mathbf{f}_d \ \mathbf{w}_n]^T$. \mathbf{w}_g represents the vector which includes road disturbances, the inertial forces, the centrifugal force vectors and measurement noise. The output vector \mathbf{y} is the sprung mass velocity of each suspension. The H_∞ norm of transfer function G_{zw} from disturbance \mathbf{w}_g of the generalized plant to evaluation output \mathbf{z} is expressed making use of the L_2 gain of the time domain.

$$\min_u \|G_{zw}\|_\infty = \min_u \sup_w \frac{\|\mathbf{z}\|_2}{\|\mathbf{w}_g\|_2} =: \gamma^* \quad (13)$$

where γ is the minimum H_∞ norm. The performance function is expressed by arbitrary γ .

$$\begin{aligned}
 J(\mathbf{u}, \mathbf{w}_g) &:= \int_0^\infty [\mathbf{z}(t) \mathbf{z}(t) - \gamma^2 \mathbf{w}_g^T(t) \mathbf{w}_g(t)] dt \\
 &= \int_0^\infty [\mathbf{x}_g(t)^T \mathbf{Q} \mathbf{x}_g(t) + 2 \mathbf{x}_g(t)^T \mathbf{S} \mathbf{x}_g^*(t) \mathbf{X}(t) \mathbf{u}(t) + \mathbf{u}(t)^T \mathbf{X}^*(t)^T \mathbf{R} \mathbf{X}^*(t) \mathbf{u}(t) - \gamma^2 \mathbf{w}_g(t)^T \mathbf{w}_g(t)] dt
 \end{aligned} \quad (14)$$

The problem in Eq. (13) can be replaced with that in Eq. (14).

$$J(\mathbf{u}^0, \mathbf{w}^0) := \min_u \max_w J(\mathbf{u}, \mathbf{w}_g) \quad (15)$$

where \mathbf{w}^0 is the worst disturbance. \mathbf{u}^0 represents the optimal control input.

$$\mathbf{u}^0(t) = -(\mathbf{D}_{12}^T \mathbf{D}_{12} \mathbf{X}^*(t))^{-1} (\mathbf{B}_2^T \mathbf{X}_u + \mathbf{S}^T) \mathbf{x}_g(t) \quad (16)$$

The problem in Eq. (13) becomes that of calculating the saddle point solution, $J(\mathbf{u}^0, \mathbf{w}^0)$, which is acquired by actualizing optimal control input \mathbf{u}^0 under the worst disturbance, \mathbf{w}^0 . Next, the following compensator is designed as an output feedback control problem.

$$\hat{\mathbf{x}}(t) = \hat{\mathbf{A}} \hat{\mathbf{x}}(t) + \hat{\mathbf{B}} \mathbf{y}(t) \quad (17)$$

$$\hat{\mathbf{u}}(t) = \mathbf{F}(t)\hat{\mathbf{x}}(t) \quad (18)$$

The solution to this compensator is the center solution to a robust stabilization compensator for a bilinear system using solution \mathbf{Y} of the Riccati algebraic equation. The details of each matrix are as follows:

$$\begin{aligned} \hat{\mathbf{A}} &= \mathbf{A}_g + (\mathbf{B}_2 + \hat{\mathbf{B}}\mathbf{D}_{22})\mathbf{X}^*(t) + \gamma^{-2}\mathbf{B}_1\mathbf{B}_1^T\mathbf{X} - \hat{\mathbf{B}}(\mathbf{C}_2 + \gamma^{-2}\mathbf{D}_{21}\mathbf{B}_1^T\mathbf{X}) \\ \hat{\mathbf{B}} &= -(\mathbf{I} - \gamma^2\mathbf{Y}\mathbf{X})^{-1}(\mathbf{Y}\mathbf{C}_2^T + \mathbf{B}_1\mathbf{D}_{21}^T)(\mathbf{D}_{21}\mathbf{D}_{21}^T)^{-1} \\ \mathbf{F}(t) &= -(\mathbf{R}\mathbf{X}^*(t))^{-1}(\mathbf{B}_2^T\mathbf{X} + \mathbf{S}^T) \end{aligned} \quad (19)$$

3.3 Gain scheduling control

It has been reported that the feel of rolling reduces when the pitch angle always takes a positive value (Kawagoe et al., 1997). From the viewpoint of feeling by humans, we need to find a nonlinear relationship between roll and pitch angles (Sakai et al., 2006), (Yamamoto, 2006). The controller is scheduled in the time domain to achieve a positive pitch angle during slaloms. A gain scheduling controller that adapts the frequency weight, $a_p(t)$, of the frequency-shaped filter according to the variable parameter, $p(t)$, is introduced.

$$p(t) = a_p(t) \quad (p_{\min} \leq p(t) \leq p_{\max}) \quad (20)$$

The generalized plant which includes variable parameter, $p(t)$, is as follows:

$$\begin{aligned} \dot{\mathbf{x}}_g(t) &= \mathbf{A}_g(p(t))\mathbf{x}_g(t) + \mathbf{B}_1\mathbf{w}_g(t) + \mathbf{B}_2\mathbf{X}^*(t)\mathbf{u}(t) \\ \mathbf{z}(t) &= \mathbf{C}_1(p(t))\mathbf{x}_g(t) + \mathbf{D}_{12}\mathbf{X}^*(t)\mathbf{u}(t) \\ \mathbf{y}(t) &= \mathbf{C}_2\mathbf{x}_g(t) + \mathbf{D}_{21}\mathbf{w}_g(t) \end{aligned} \quad (21)$$

The parameter variable system which includes variable parameter, $p(t)$, in Eq. (21) is

$$\begin{bmatrix} \mathbf{A}_n(p(t)) & \mathbf{B}_n \\ \mathbf{C}_n & \mathbf{D}_n \end{bmatrix} = \sum_{i=1}^2 \alpha_i \begin{bmatrix} \mathbf{A}_{ni} & \mathbf{B}_{ni} \\ \mathbf{C}_{ni} & \mathbf{D}_{ni} \end{bmatrix} \quad (22)$$

where

$$\begin{aligned} \begin{bmatrix} \mathbf{A}_{n1} & \mathbf{B}_{n1} \\ \mathbf{C}_{n1} & \mathbf{D}_{n1} \end{bmatrix} &= \begin{bmatrix} \mathbf{A}_n(p_{\min}) & \mathbf{B}_n \\ \mathbf{C}_n(p_{\min}) & \mathbf{D}_n \end{bmatrix} \\ \begin{bmatrix} \mathbf{A}_{n2} & \mathbf{B}_{n2} \\ \mathbf{C}_{n2} & \mathbf{D}_{n2} \end{bmatrix} &= \begin{bmatrix} \mathbf{A}_n(p_{\max}) & \mathbf{B}_n \\ \mathbf{C}_n(p_{\max}) & \mathbf{D}_n \end{bmatrix} \end{aligned} \quad (23)$$

At the top of the parameter box, \mathbf{A}_{ni} , \mathbf{B}_{ni} , \mathbf{C}_{ni} , \mathbf{D}_{ni} are given

$$\begin{aligned} a_1(p(t)) &= \frac{p_{\max} - p(t)}{p_{\max} - p_{\min}} \\ a_2(p(t)) &= \frac{p(t) - p_{\min}}{p_{\max} - p_{\min}} \end{aligned} \quad (24)$$

$$\begin{aligned} \mathbf{F}_1(t) &= \mathbf{F}(t, p_{\min}) \\ \mathbf{F}_2(t) &= \mathbf{F}(t, p_{\max}) \end{aligned} \quad (25)$$

The gain scheduling controller, $\mathbf{F}(t, p)$, is as follows:

$$\mathbf{F}(t, p) = \sum_{i=1}^2 \alpha_i(p) \mathbf{F}_i(t) \quad (26)$$

More concretely, the third power of the roll angle is used as variable parameter $p(t)$, to achieve nonlinearity and positive value conversion of the pitch.

$$p(t) = 1000\phi_r^3(t) + 2.2 \quad (27)$$

To achieve a nonlinear relationship between the roll and pitch angles, relative angle of the roll to the pitch is scheduled by using the matrix C_{csp} shown in Fig. 2.

$$\begin{aligned} C_{sp \min} &= \begin{bmatrix} 0 & -40 & -1 & 0 & 0 & 0 & \dots \end{bmatrix} \\ C_{sp \max} &= \begin{bmatrix} 0 & 40 & -1 & 0 & 0 & 0 & \dots \end{bmatrix} \end{aligned} \quad (28)$$

The control input is calculated based on bilinear disturbance-accommodation H_∞ control and gain scheduling control.

4. Simulation result

In order to verify the effectiveness of the proposed method, the numerical simulations were carried out. Figure 4 has the results of numerical simulation for the slalom. The road width in the simulation was about 3 m, and the velocity of the vehicle was 15 m/s (=54 km/h) and a road disturbance of ISO standard C level was used.

The time history of the scheduling parameter in case 1 is shown in Fig. 5. It was confirmed that the scheduling parameter is changed according to the roll angle caused by steering. The time histories of the body roll and pitch angles are shown in Figs. 6 and 7 respectively. From the results, it was confirmed that the roll angle is reduced by comparison with passive control.

Figure 8 shows the relationship between the roll and pitch angles. The results confirmed that the proposed method achieves the nonlinear relationship between the pitch and roll angles.

Figure 9 shows the PSD of vertical acceleration. The result confirmed that the vertical acceleration near the body resonance frequency and in the frequency domain of 4 - 8 Hz, which make humans feel uncomfortable, can be reduced. In addition, ride comfort that takes into consideration human sensitivity to vibrations in the slalom can be improved.

Figure 10 shows the maximum reduction ratio of RMS. The results confirmed that the proposed method can reduce the body vertical acceleration as well as skyhook control and the soft fixed model. In addition, the body roll angle, which cannot be decreased with these controls, can be reduced as well as the hard fixed model.

Figure 11 shows the simulation course in case 2. The simulation results in case 2 are shown in Figs. 12 to 17. All results verified control could be accomplished that was equal to case 1. The results in Fig.16 especially confirmed that the body attitude, which changes more drastically in the slalom, can be reduced. In addition, the nonlinear relationship between the pitch and roll angles can be achieved.

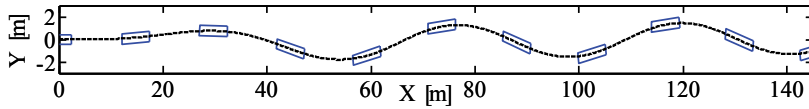


Fig. 4. Simulation Course (Case 1)

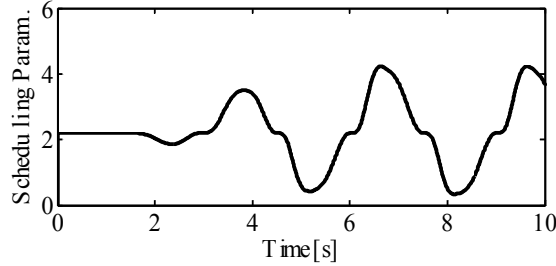


Fig. 5. Scheduling Parameter (Case 1)

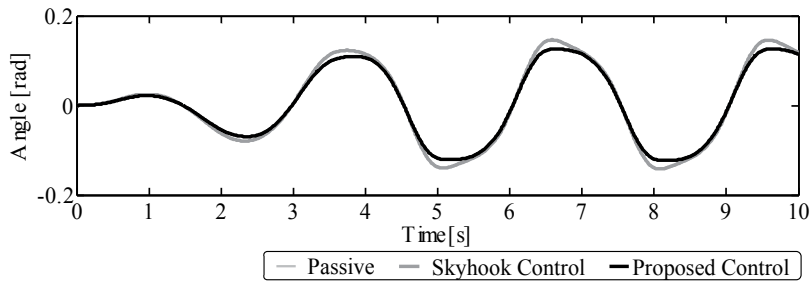


Fig. 6. Roll Angle (Case 1)

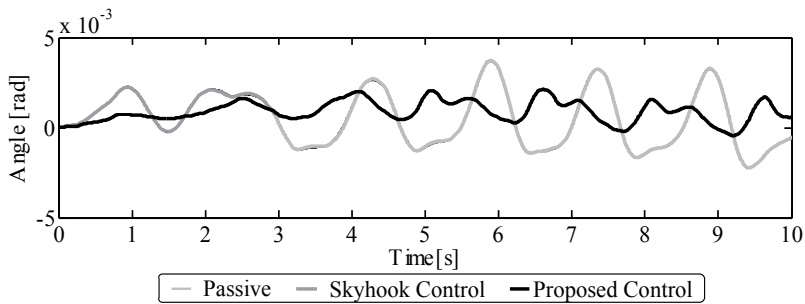


Fig. 7. Pitch Angle (Case 1)

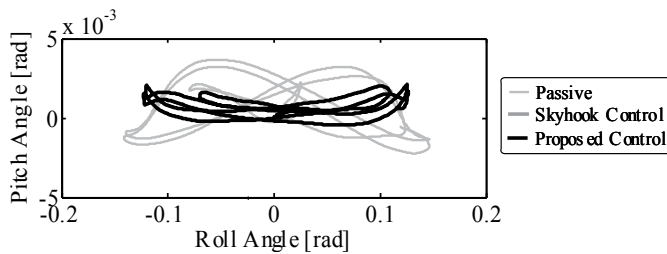


Fig. 8. Relationship between Roll Angle and Pitch Angles (Case 1)

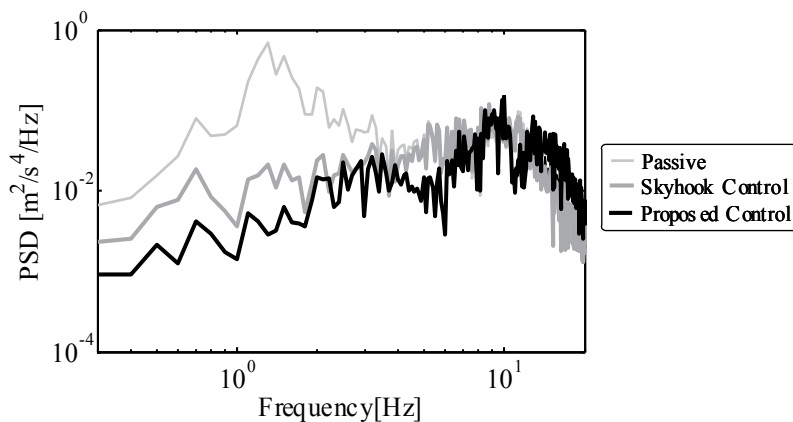


Fig. 9. PSD of Vertical Acceleration (Case 1)

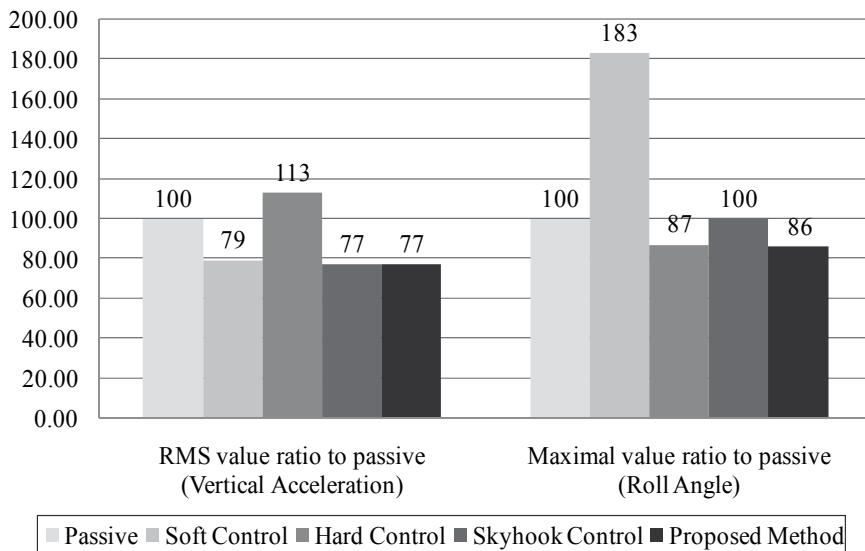


Fig. 10. RMS Values and Peak Values for Each Method (Case 1)

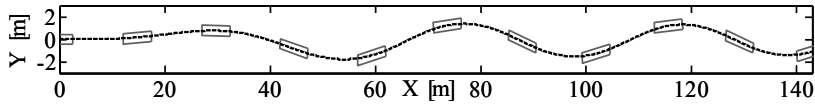


Fig. 11. Simulation Course (Case 2)

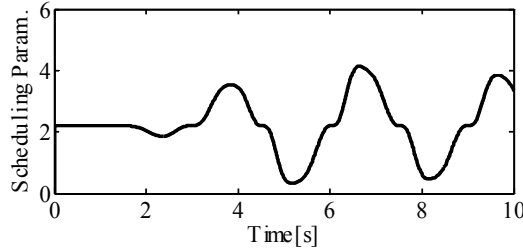


Fig. 12. Scheduling Parameter (Case 2)

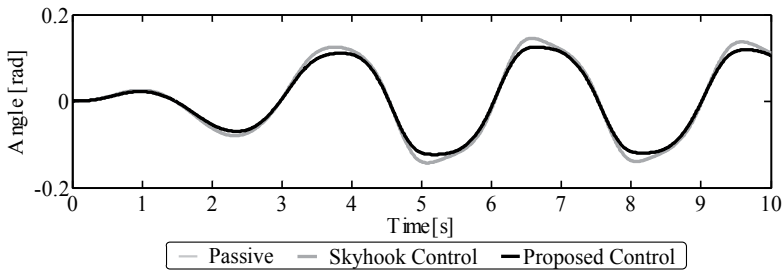


Fig. 13. Roll Angle (Case 2)

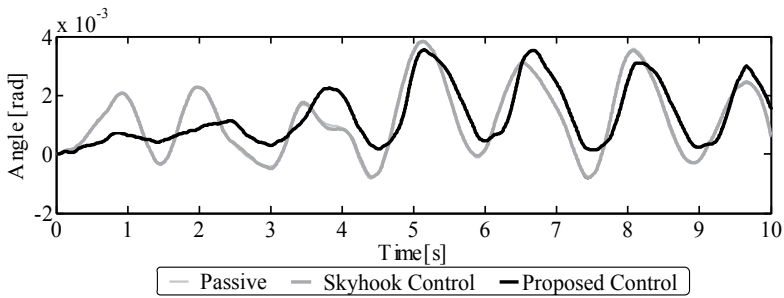


Fig. 14. Pitch Angle (Case 2)

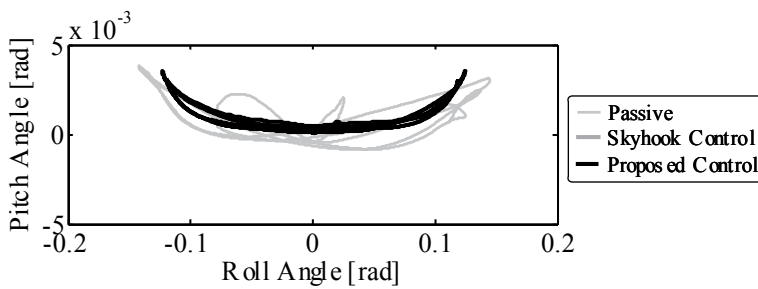


Fig. 15. Relationship between Roll Angle and Pitch Angles (Case 2)

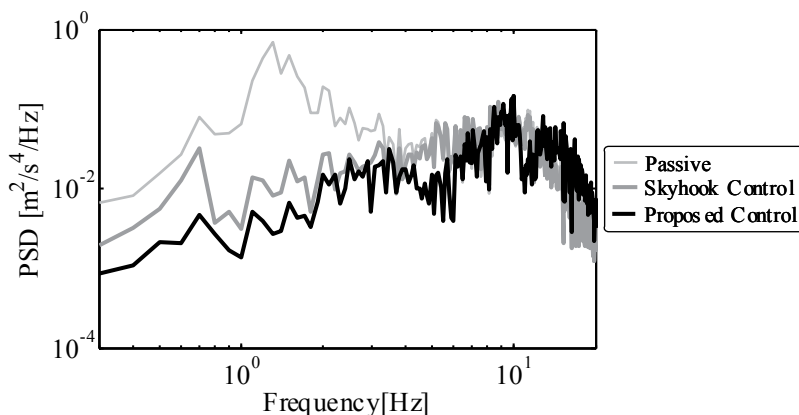


Fig. 16. PSD of Vertical Acceleration (Case 2)

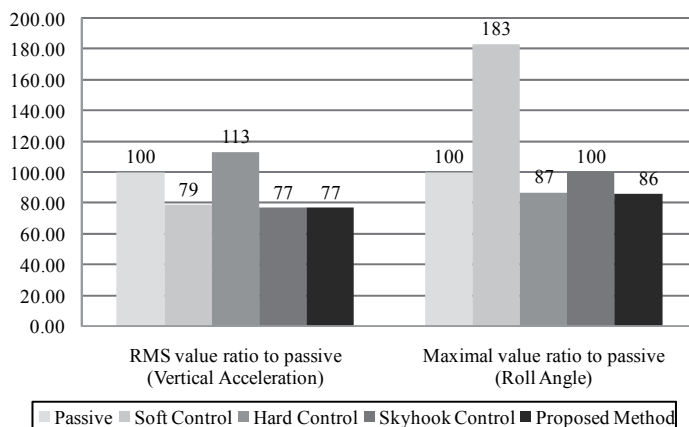


Fig. 17. RMS Values and Peak Values for Each Method (Case 2)

5. Conclusion

Controller design to achieve variable stiffness and a variable damping semi-active suspension system was attained by applying disturbance accommodation control theory, bilinear H^∞ control theory, and gain scheduling control theory to improve the efficiency of ride comfort and vehicle behavior during steering. Several numerical simulations confirmed that ride comfort in the frequency domain, in which humans feel uncomfortable, can be improved without deteriorating passenger ride comfort in comparison with skyhook control. The change in body attitude when steering can also be reduced and vehicle behavior with synchronized phase difference between roll and pitch can be acquired. The results confirmed that both ride comfort and steering stability can be improved in a balanced manner.

6. References

Ohsaku, S., Sampei, M., Shimizu, E. and Tomida, K. (2000), Nonlinear Control for Semi-Active Controlled Suspension, *Journal of the Society of Instrument and Control Engineers*, Vol.39, No.2, pp.126-129.

- Hrovat, D. (1993), Application of optimal control to advanced automotive suspension design, Transaction on ASME: Journal of Dynamic Systems, Measurement, and Control, pp.328-342.
- Hrovat, D. (1997), Survey of advanced suspension developments and related optimal control applications, *Automatica*, Vol.33, No.10, pp.1781-1816.
- Abdel-Hardy, M.B.A. and Crolla, D.A. (1989), Theoretical analysis of active suspension performance using a four-wheel model, *Proceedings of the Institution of Mechanical Engineers*, No.203(D), pp.125-135.
- Abdel-Hardy, M.B.A. and Crolla, D.A. (1992), Active suspension control algorithms for a fourwheel vehicle model, *International Journal of Vehicle Design*, Vol.13, No.2, pp.144-158.
- Hanamura, Y., Fujita, K., Araki, Y., Oya, M., and Harada, H. (1999), Control of Vehicle Maneuverability and Stability of 4 Wheeled Vehicle by Active Suspension Control with Additional Vertical Load Control, *Transactions of the Japan Society of Mechanical Engineers, Series C*, Vol.65, No.629, pp.236-243.
- Doi, S., Yamaguchi, H., Iwama, N., Hayashi, Y. (1992), Study of Semiactive Control by Optimum Damping Adjustment (Suspension Control Using Frequency-Shaped Functionals), *Transactions of the Japan Society of Mechanical Engineers, Series C*, Vol.58, No.549, pp.3297-3304.
- Yoshida, K., Kumamaru, T. and Nagata, S. (2006), Frequency-Shaped Gain-Scheduling Control for Automotive Semi-Active Suspension, *Proceedings of The 8th International Conference on Motion and Vibration Control*.
- Janeway, R.N. (1948), *SAE Journal*, pp.48.
- Sakai, H., Ono, E., Yamamoto, Y., Fukui, K., Oki, M. and Yasuda, E. (2006), Improvement of Roll Feeling Based on Visual Sensitivity, *Toyota Technical Review*, Vol.55, No.1, pp.20-25.
- Yamamoto, M. (2006), History and Future of Vehicle Dynamics, *Toyota Technical Review* · Vol.55, No.1, pp.6-13.
- Kawagoe, K. (1997), A Study of Vehicle Roll Behavior, *Journal of Society of Automotive Engineers of Japan*, Vol.51, No.11, pp.20-24.
- Bakker, E., Nyborg, L., and Pacejka, H. B. (1987), Tyre Modelling for Use in Vehicle Dynamics Studies, *SAE paper*, 870421.
- Bakker, E., Pacejka, H. B. and Nyborg, L. (1989), A New Tire Model with an Application in Vehicle Dynamics Studies, *SAE paper*, 890087.
- Takahashi, T. (2003), Modeling, Analysis and Control Methods for Improving Vehicle Dynamic Behavior (Overview), *R&D Review of Toyota CRDL*, Vol.38, No.4, pp.1-9.
- Nishimura, H., Yoshida, K. and Shimogo, T. (1989), Optimal Active Dynamic Vibration Absorber for Multi-Degree-of-Freedom Systems: Feedback and Feedforward Control Using a Kalman Filter, *Transactions of the Japan Society of Mechanical Engineers, Series C*, Vol.55 · No.517, pp.2321-2329.
- Kang, S., and Yoshida, K. (1992), Vibration Isolation Control with Feedforward Link using H_∞ Control Theory, *Transactions of the Japan Society of Mechanical Engineers, Series C*, Vol.58, No.556, pp.3627-3633.
- Umehara, R., Otsuki, M., and Yoshida, K., (2005) Bilinear Robust Control Method and Its Application to Semi-Active Suspension for Railway Vehicle, *Transactions of the Japan Society of Mechanical Engineers, Series C*, Vol.71, No.701, pp129-136.

Design of an Embedded Controller for Some Applications of an Automotives

Dr. Preeti Bajaj and Dinesh Padole
*G.H. Raisonni College of Engineering, Nagpur
India*

1. Introduction

Developments in Automotive Engineering describes the applications of modern electronics, communications, and control technologies to guide and control of vehicle's operation. Since the last two decades there has been a phenomenal increase in the use of electronic components in automotive systems, resulting in the replacement of purely mechanical or hydraulic-implementations of much functionality. The main motivation behind this is because of fast response, lower cost, reduced weight, new and innovative functionalities, most user-friendly and faster design cycles.

The work presented in the chapter, deals with the design of an Embedded Controller for some applications of an Automotives.

Embedded controller is a special-purpose controller that is embedded in an electronic system. Embedded controllers has major role in modern automobile. There is ever increasing demand being placed on the functionality, complexity and reliability in intelligent transportation systems related to body electronics, vehicle diagnostics, remote access, security, emergency aid, GPS and navigation, infotainment, drive-by services, and fleet management system, torque control, vehicle stability and traction control, electronic control of windows and driver-seat setting, in vehicle communication, entertainment etc.

There are two basic approaches for controlling vehicle functions as shown in figure 1.

Distributed Control

Distributed control, grouped the parameter according to their location & functionality. Each group has their controller and all are communicating with each other accordingly.

Central Body Control

In this approach the main controller managing rage of different functions & can be referred as Central Body Controller. Using this controlling, there is improvement in the sharing of information between different functions to allow better control of body space. Also there are fewer opportunities for overlapping functionality. Such type of architecture provides simplicity, may be effective solution. But this will increases the number of wires with functionality in vehicle.

Multi Core Processor

A multi-core processor is a processing system composed of two or more independent cores. It can be described as an integrated circuit to which two or more individual processors

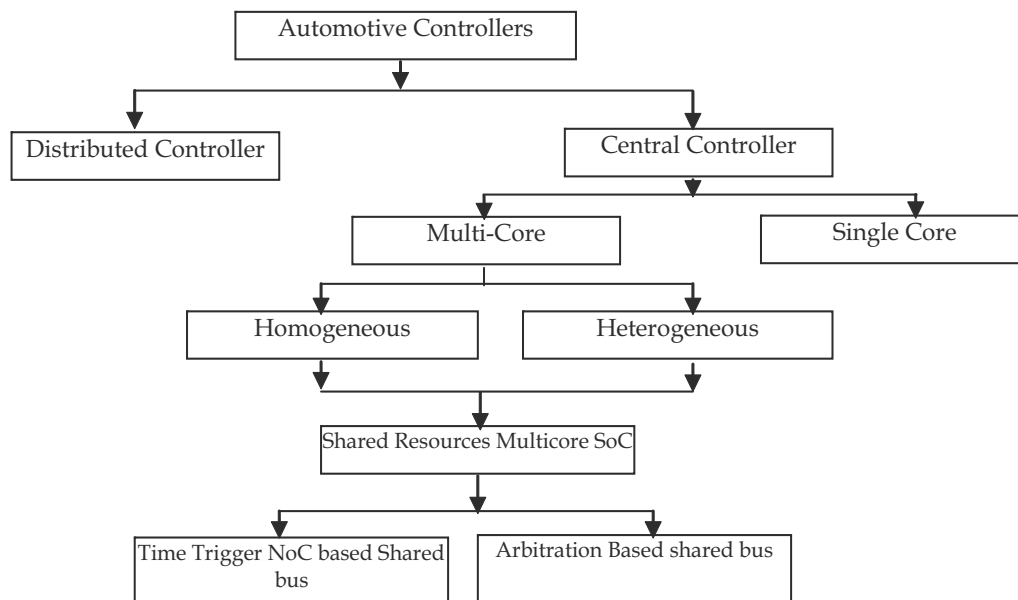


Fig. 1. Various approaches for designing the embedded controller for automotive

(called cores) have been attached. The cores are typically integrated onto a single integrated circuit die (known as a chip multiprocessor or CMP), or they may be integrated onto multiple dies in a single chip package. Cores in a multi-core device may be coupled together tightly or loosely. For example, cores may or may not share caches, and they may implement message passing or shared memory inter-core communication methods. Common network topologies to interconnect cores include bus, ring, 2-dimensional mesh, and crossbar. All cores are identical in homogeneous multi-core systems and they are not identical in heterogeneous multi-core systems. Multi-core processors are widely used across many application domains including general-purpose, embedded, network, digital signal processing (DSP), graphics, etc. study shows that Multicore chips perform better than single core systems. The performance of multicore/ multiprocessor systems depends more on efficient communication among processors and on the balanced distribution of computation among them, rather than on pure speed of processor. Although there are many possible communication architectures, shared bus is very popular in small number of processors system for its simplicity and area efficiency in sharing resource architecture the resources like common buses. Peripheral and memory are shared and utilize by any processor according to need.

Optimum design for an embedded controller can be proposed based on followings design parameters.

- Best arbiter design in term of latency, Master request acceptance rate, Average Waiting Time for master & Average Bandwidth Utilization shared bus.
- Utility of Shared bus.
- Optimum power consumption by embedded controller.

2. Automotive embedded controller.

Controlling In-vehicle gadget with an embedded controller is a very challenging task in Intelligent Transportation system (ITS). Leading electronics manufacturer like Freescale

semiconductor & Intel have established their research wing for automotive controller design.

Proposed Automotive Embedded Controller consists of four master cores. The master cores are Leon processor programmed for Whether Data processing, Digital Image Processing, Battery Controlling and Dashboard Controlling applications. Wiper controller and Air controller core are slave core and don't have processing power. All core are connected with arbiter based AMBA shared bus. Memory is use for the data storage on shared basic to all cores.

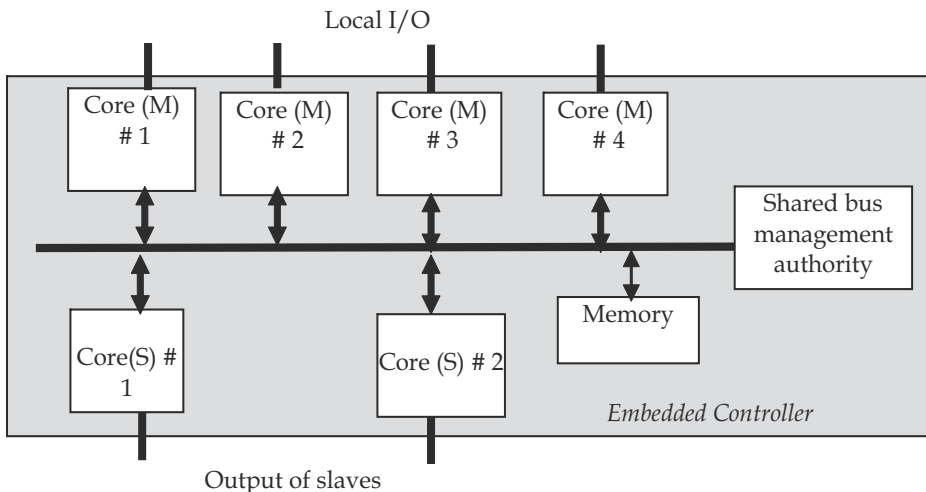


Fig. 2. Shared bus Integrated Multicore Embedded Controller

The integrated Multicore Embedded Controller has following Features

- An Embedded Controller consists of multiple cores with sharing common Bus.
- Cores can be master or slave including memory
- More than one master core.
- Each core are self-sufficient processor with it's Local I/O buses.
- Core may be homogeneous or heterogeneous in nature or architecture
- Core may have different clock speed according to nature of their applications.
- There may be dedicated slave cores for inter-vehicular/ intra-vehicular communication standards communications (eg. CAN, LIN, TTP, FlexRay), User communication standers (Eg. RS232, USB), RF communication (Eg. Bluetooth), standard peripherals (Timers, PPI, Data handling) etc.
- All cores are connected with a common shared bus. Shared bus will consist of Data, Address and Control buses.
- Allocation of bus will be taken care by shared bus management authority.

In figure 2 Core (M) denoted for master core or processor core which can be a self-contained computer with CPU, memory, and I/O interfaces. Alternatively, a core could be an FPGA fabric. Each core is an island of synchronicity, i.e., different cores can operate at different frequencies, which can be changed at run-time in order to effect dynamic power management. Master core are design for different jobs and applications job are rightly assigned to the master core by software. Core (S) denotes for slave core which can be peripheral core. These cores may be of category like programmable peripheral core eg.

Timer, Interrupt controller, Direct Memory Access etc, peripheral device control core eg. Stepper motor control, DC or may be outside communication standard core like LIN, CAN, FlexRay etc.

Out of the available options LEON processor is chosen for designing Multicore Embedded Controller system because it is highly configurable, fully synthesizable over a variety of platforms, VHDL code freely available under suitable license reasonably good amount of documentation and active online help is available.

Leon Processor:

LEON is a 32-bit CPU microprocessor core, based on the SPARC-V8 RISC architecture and instruction set. It was originally designed by the European Space Research and Technology Centre, part of the European Space Agency (ESA), and after that by Gaisler Research. It is design for embedded applications and are described in synthesizable VHDL. The core is configurable through VHDL generics, and is used in system-on-a-chip (SOC) designs both in research and commercial settings. The architecture consists of AMBA AHB/APB shared bus. New modules can easily be added due to facility of shared bus architecture.

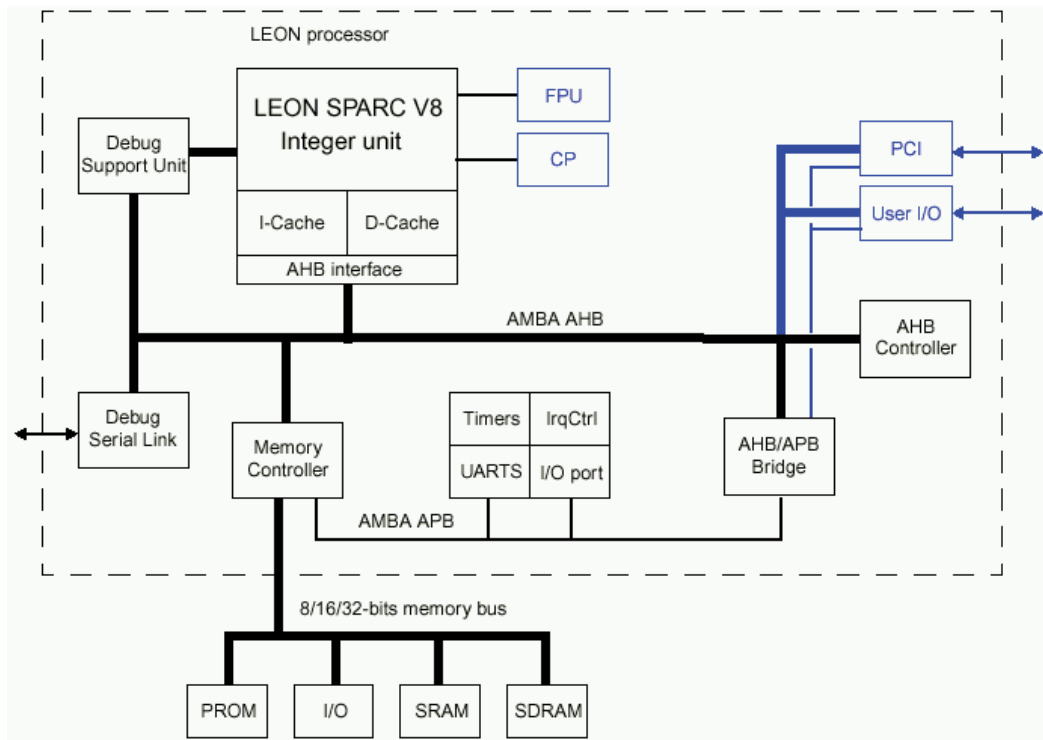


Fig. 3. Block Diagram of LEON2 processor

AMBA Bus:

The Advanced Microcontroller Bus Architecture (AMBA) was introduced by ARM Ltd in 1996 and is widely used as the on-chip bus in System-on-a-chip (SoC) designs. It consist of following three buses.

- The Advanced High-performance Bus (AHB)
- The Advanced System Bus (ASB)
- The Advanced Peripheral Bus (APB).

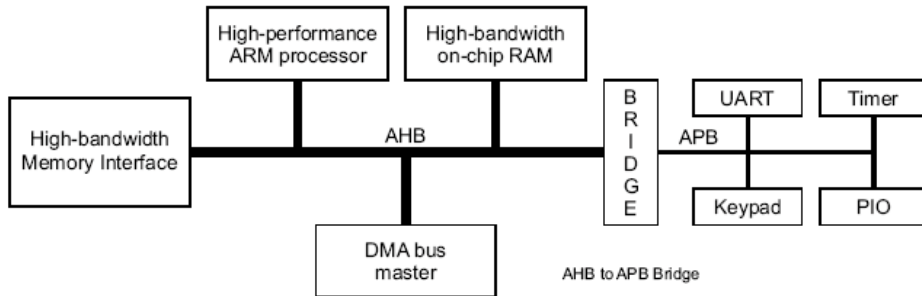


Fig. 4. Block Diagram of AMBA Bus

Design of Proposed Automotive Embedded Controller

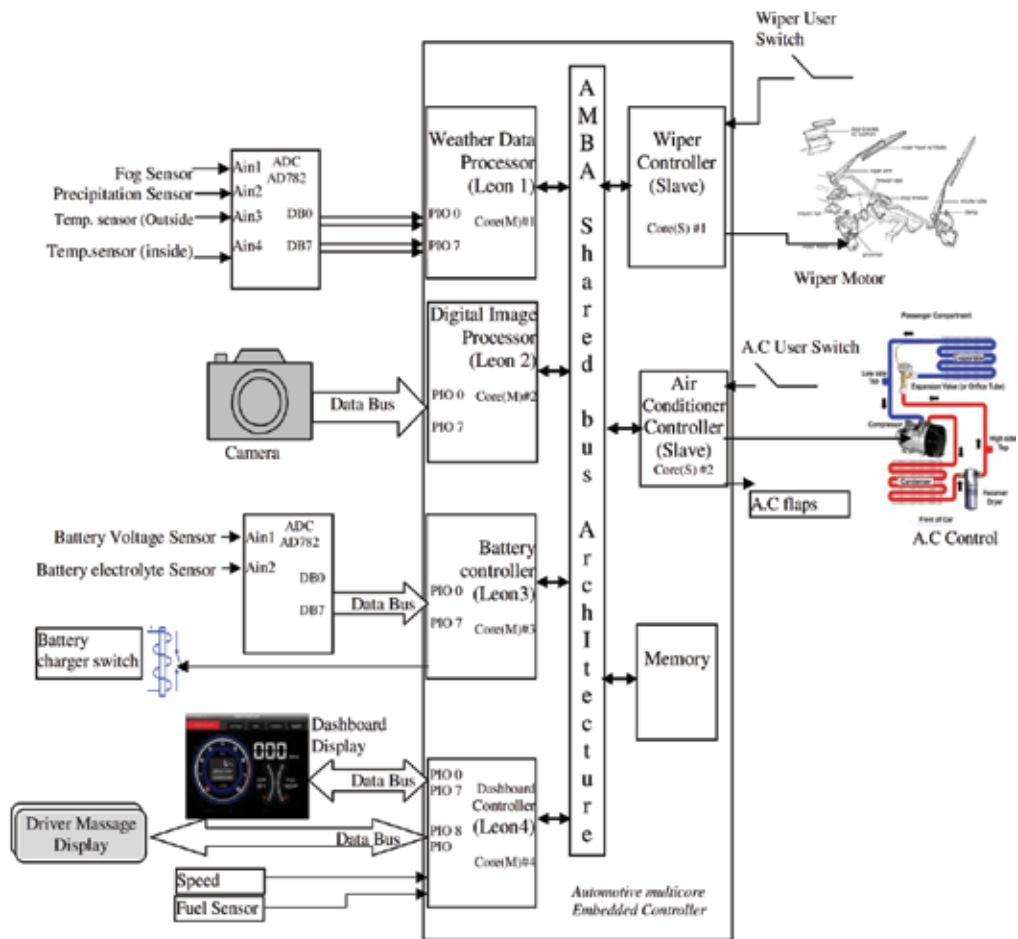


Fig. 4. Automotive Embedded Controller

An embedded controller prototype proposed here utilizing same sensor data for multiple processor cores and optimizing the design by reducing number of individual microcontrollers. This will lead to optimize the resources, cost & power in controlling of in-vehicle gadgets. An Automotive Embedded Controller for multi-application and controlling multiple gadgets is shown in figure 4.

3. Some applications of multicore automotive embedded controller

The above explained system can be effectively utilized for the controlling of vehicular applications. Some of the applications are discussed as below.

3.1 Wiper controlling

Wiper motor controlling is a basic application in case of vehicular controlling. Figure 5 shows weather data processor and Digital image processor as master processor and wiper controller as a peripheral controller. The internal core (master and peripherals) are connected with AMBA shared bus.

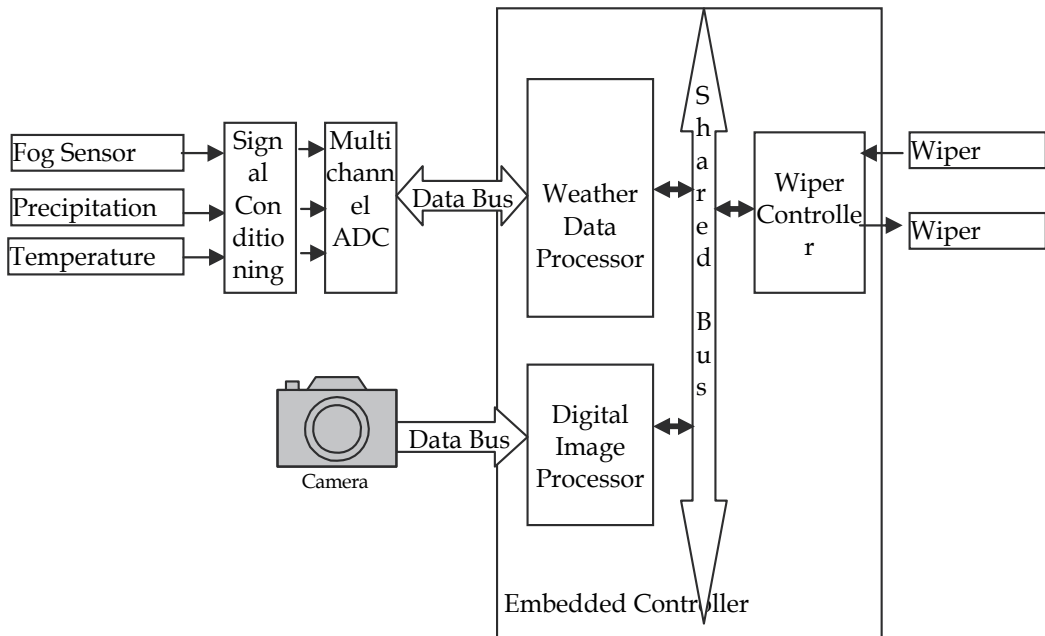


Fig. 5. Block diagram of Multicore Embedded controller for wiper control.

Weather Data Processor: It is a processor processing the data coming from the different sensors regarding weather condition outside and inside the vehicle. For this application three sensors are utilized, precipitation sensor will sense the rain fall outside of vehicle.

According to the data coming to weather sensor, weather data processor will decide the weather condition and inform to other respective core (masters or peripherals) regarding the same for necessary action. In case this processor justifies that there is a raining condition, it will send data or command to wiper controller. This can be explained from flow diagram 6

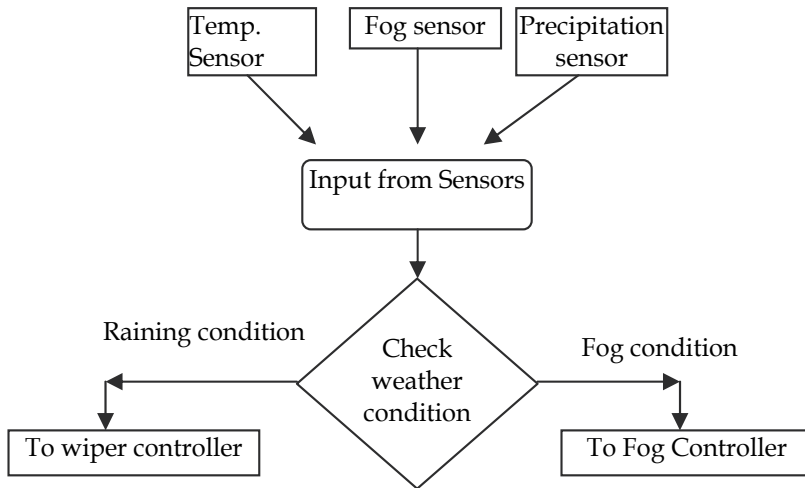


Fig. 6. Flow diagram of functioning of weather data processor

Digital Image Processor: This processor processes the digital images captured by video camera placed aside of driver seat. If this processor identifies dust on front window glass, it will communicate with wiper controller to switch on the wiper for short duration to clear the dust. This action can be understood by flow diagram shown in figure 7.

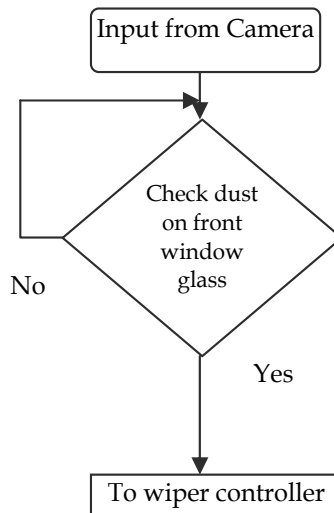


Fig. 7. Flow diagram of Digital Image processor

Wiper controller: This is a peripheral core, allotted the task of wiper motor controlling. This receives data from multiple masters, as shown in figure and accordingly control the wiper motor. Wiper motor will switch on in three different conditions.

- By switching on the user wiper switch
- As per communicated by Digital Image Processor (if there is dust on front window glass). In this wiper motor will switch on for short duration.
- As per communicated by weather data processor. (if raining condition is identified)

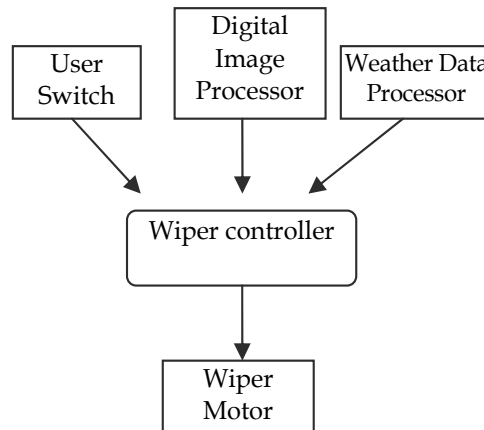


Fig. 8. Flow diagram of wiper controlling application.

3.2 Air conditioning system

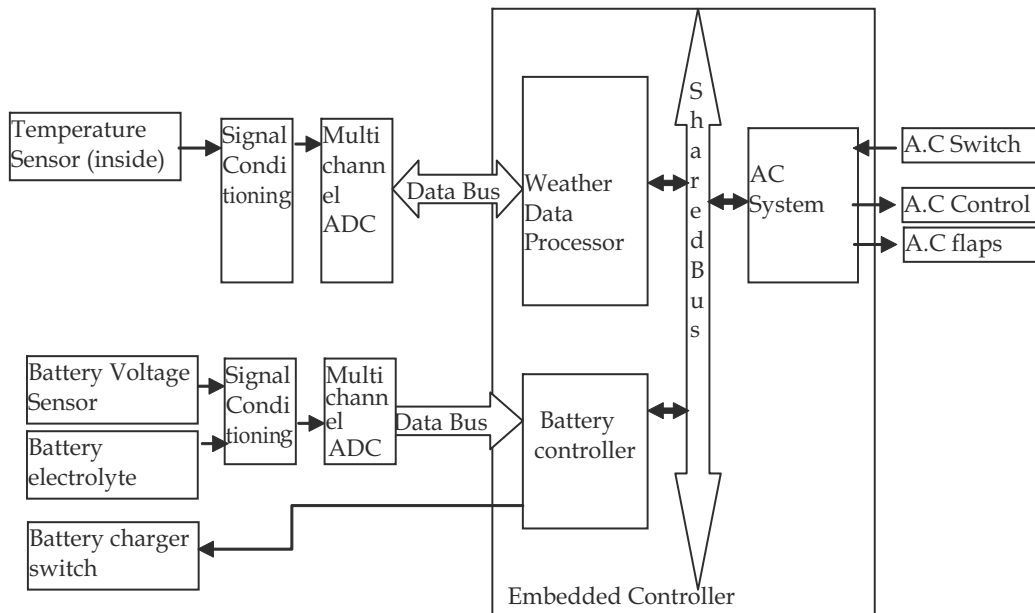


Fig. 9. An Embedded controller block diagram for Air conditioning system

Air Conditioning systems deliver air to the vehicle interior to provide comfort to passengers. These controller typically have control several motors (for blower and flaps), based on different inputs (e.g., temperature). Figure 9 shows block diagram of an embedded controller. This controller consists of weather data processor and battery controller as master and Air conditioning system as slave.

Weather Data Processor: It is a processor processing the data coming from the different sensors regarding temperature condition inside the vehicle. According to the data this processor will decides the hot condition in the vehicle and communicated to AC system (peripheral) for necessary action.

Battery Controller: This processor monitor the battery condition of vehicle and responsible to take necessary action. It will monitor the charging of battery, if battery get overcharge, it will stop charging and vice versa. It also monitors the lever of electrolyte in the battery and warns the driver accordingly by communicating to other inbuilt core related to driver monitor display.

In case of low battery, this processor will communicate with air conditioning module to tern it off to save the battery. Figure 10 shows working flow of this processor.

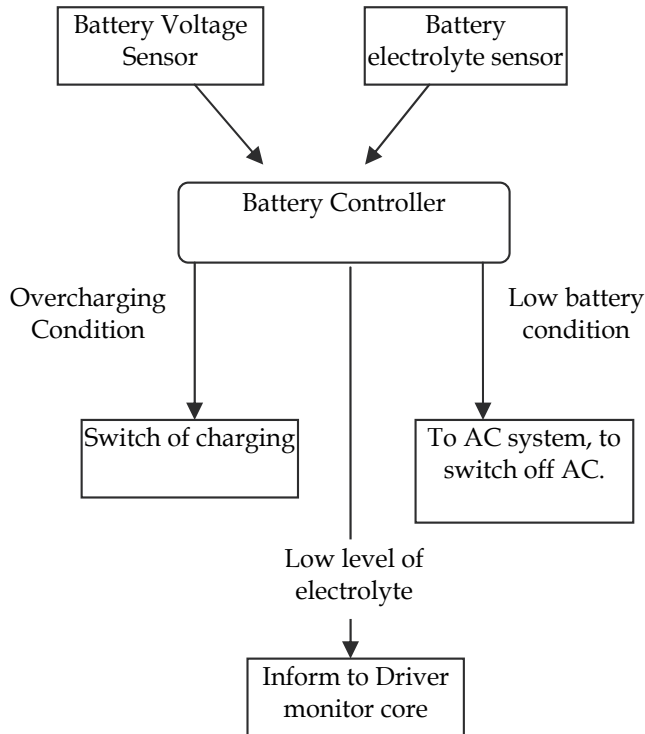


Fig. 10. Flow diagram of working of battery controller

Air conditioning system: It is a peripheral core responsible to control all function of vehicle AC. It receives user switch input as well as other command from weather data processor and battery controller regarding the operating of AC.

3.3 Driver alert message display

In modern era, passenger safety and safe drive is one of the most hot issue in automotives. Safe driving also depends on the driver alertness regarding the surrounding conditions. For example if there is raining or fog condition, driver should get alert readings, and suggestion to reduce driving speed if speed extending the defined value. The system for this can be implemented as shown in figure 12. This consists of weather data processor & Dashboard display controller. Both core are having processing power are master core interfaced with AMBA shared bus architecture.

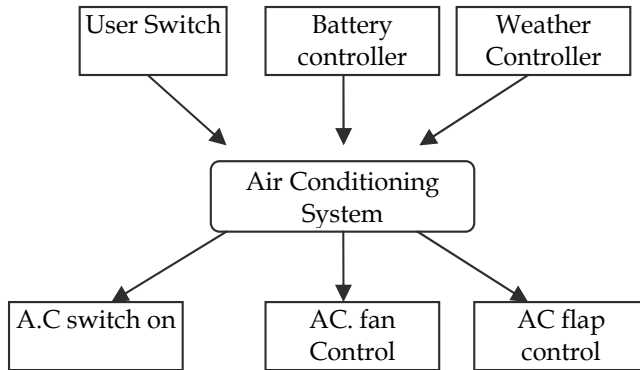


Fig. 11. Working of AC control system

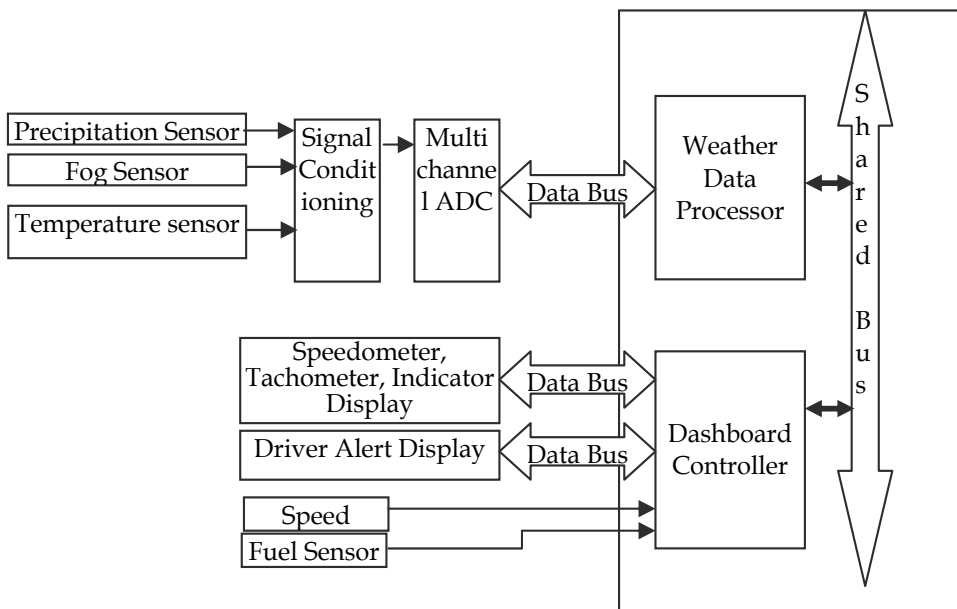


Fig. 12. Embedded controller for driver alert message display

Weather Data processor is sensing the weather condition as explain in previous section. It is sharing the weather condition with dashboard controller.

Dashboard controller: It is a processor processing data related to dashboard display. Mainly it is handling two displays.

Dashboard display- This digital LCD displays speed, distance in Km, fuel level, indicator condition etc.

Driver alert display- This display is use to display certain information to driver related to car. Example information of weather, car engine over temperature, any linkage in car, security issue in car, emergency messages propagated by road side base stations, messages of inter vehicular communication or particular sign detection by in-vehicular camera. This display will be placed just side to dash board display and easily seen by driver.

In this application weather data processor will process the sensor data and decides the environment condition like raining condition or fog condition. The information will be communicated to dashboard controller to display on alert display. Also dashboard will see the speed of vehicle, if it found more speed it will display message regarding lower down the speed of vehicle.

4. Conclusion

The embedded system for an automotive control system can be effectively design by extracting the benefit of multicore SoC technology. An integrated automotive controller can be design by using homogeneous or heterogeneous multiple cores (processors) connected with the shared bus like AMBA. The architecture will give better result with efficient resource sharing like peripheral device and memory.

5. References

- AMBA Specifications (Rev 2.0), ARM Limited 1999.
- Andy Birnie,(2006). "Centre Body Control: A Finely Balanced Systems", *Freescale semiconductor Forum, Peris,*
- Andy Birnie (Oct. 2006, "Meeting the Low Power Challenge in Body Systems at Each Performance Level- from 8 to 32 bit", *Freescale semiconductor Forum, Peris.*
- ARM controller user's manual
- David Geer(May 2005). "Chip maker turn to multicore Processor", *IEEE Conf.*
- David Lopez (Oct.2006). "Intelligent Distributed Control (IDC) Small and Cost Efficient Local Intelligence Solutions", *Freescale semiconductor Forum, Peris.*
- Dimitris Nikolopoulos (2006), "Facing the Challenges of Multicore Processor Technologies using Autonomic System Software", *Proceedings of 20th IEEE International Parallel & Distributed Processing Symposium,*
- P.Peti, R. Obermaisser (2005), "An Integrated Architecture for Future Car Generations", *Proceedings of the Eighth IEEE International Symposium on Object-Oriented Real-Time Distributed Computing (ISORC'2005)*
- Roman Obermaisser et. al, (July 2009). "From a Federated to an Integrated Automotive Architecture", *IEEE Transaction on Computer-Aided Design Of Integrated Circuits And Systems, Vol. 28, No. 7.*
- The LEON Processor User's Manual

- Thomas Beck (2001). " Current trends in the design of automotive electronic systems", *Proceeding of Design, Automation, and Test in Europe Conference pp.0038*,
- Y. Tanurhan, et. Al (1996), "A Rapid Prototyping Approach for Specification and Design of Distributed Automotive Control Systems", *IEEE Proceedings of EURWRTS*.

Arbitration Schemes for Multiprocessor Shared Bus

Dr. Preeti Bajaj and Dinesh Padole
*G.H. Rasoni College of Engineering,
Nagpur
India*

1. Introduction

Performance of Multicore Shared bus Embedded Controller depends on how effectively the sharing resources can be utilized. Common bus in System on Chip is one of the sharing resources, shared by the multiple master cores and also acting as a channel between master core and slave core (peripherals) or Memories. Arbiter is an authority to use the shared resource (Shared bus) effectively, so performance also depends on arbitration techniques.

The arbitration mechanism is used to ensure that only one master has access to the bus at any one time. The arbiter performs this function by observing a number of different requests to use the bus. Master may request to bus master (arbiter) to use the bus during any cycle. The arbiter will sample the request on the rising of the clock and then use predefined algorithm to decide which master will be the next to gain access to the bus. On-chip communication architecture plays an important role in determining the overall performance of the System-on-Chip (SoC) design. In the recourse sharing mechanism of SoC, the communication architecture should be flexible to offer high performance over a wide range of data traffic.

2. Arbitration techniques.

There are several arbitration techniques has been developed mention as below.

2.1 Static fixed priority algorithm

Static fixed priority is a common scheduling mechanism on most common buses. In a static fixed priority scheduling policy, each master is assigned a fixed priority value. When several masters request simultaneously, the master with the highest priority will be granted. The advantage of this arbitration is its simple implement and small area cost. The static priority based architecture does not provide a means for controlling the fraction of communication bandwidth assigned to a component. If masters with high priority requests frequently, it will lead to the starvation of the ones with low priority.

Advantages: It is simple in implement & Small area cost

Disadvantages: In Heavy communication traffic, master that has low priority value can not get a grant signal.

2.2 TDM/Round-Robin algorithm

Time division multiplexed (TDM) scheduling divides execution time on the bus into time slots and allocates the time slots to adapters requesting use of the bus. Each time slot can span several physical transactions on the bus. A request for use of the bus might require multiple slot times to perform all required transfers. However, in this architecture, the components are provided access to the communication channel in an interleaved manner, using a two level arbitration protocol.

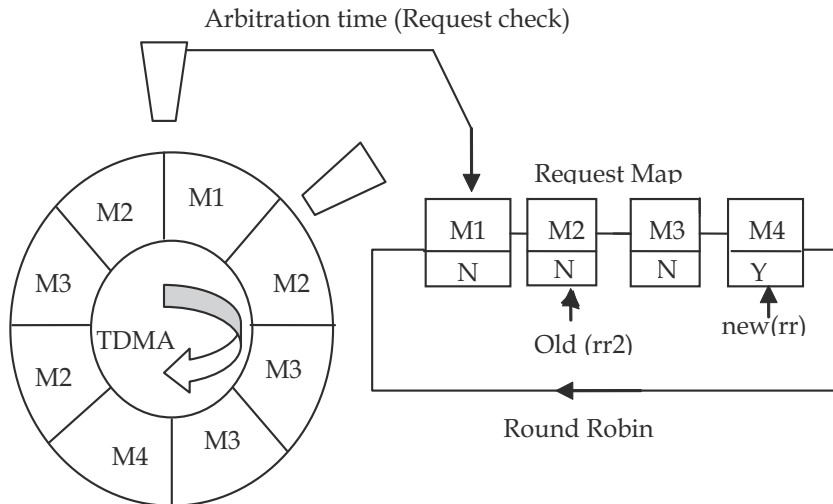


Fig. 1. Round Robin based arbiter communication architecture

The first level of arbitration uses a timing wheel where each slot is statically reserved for a unique master. In a single rotation of the wheel, a master that has reserved more than one slot is potentially granted access to the channel multiple times. If the master interface associated with the current slot has an outstanding request, a single word transfer is granted, and the timing wheel is rotated by one slot. To alleviate the problem of wasted slots, a second level of arbitration is supported. The policy is to keep track of the last master interface to be granted access via the second level of arbitration, and issue a grant to the next requesting master in a round-robin fashion, at figure 1, the current slot is reserved for M1, but it has no data to communicate. The second level increments a round-robin pointer $rr2$ from its current position at M2 to the next outstanding request at M4.

Advantages: Easy to implement

Disadvantages: Leads to the mistake of data transfer

However, these techniques are often inadequate. In the former, low priority components may suffer from starvation, while high priority components may have large latency. Low system performance because of bus distribution latency in a bus cycle time. Hence there is need to design some more efficient arbitration scheme. The chapter presents four arbitration schemes for system on chip communication as below.

- Static Lottery Bus architecture
- Dynamic lottery bus architecture
- ATM switch architecture
- Fuzzy Logic based arbiter

2.3 Static Lottery Bus architecture

The core of the LOTTERYBUS architecture is a probabilistic arbitration algorithm implemented in a centralized “lottery manager” for each bus in the communication architecture. The architecture does not presume any fixed communication topology. Hence, various SoC components may be interconnected by an arbitrary network of shared channels or a flat system wide bus as shown in figure 2.

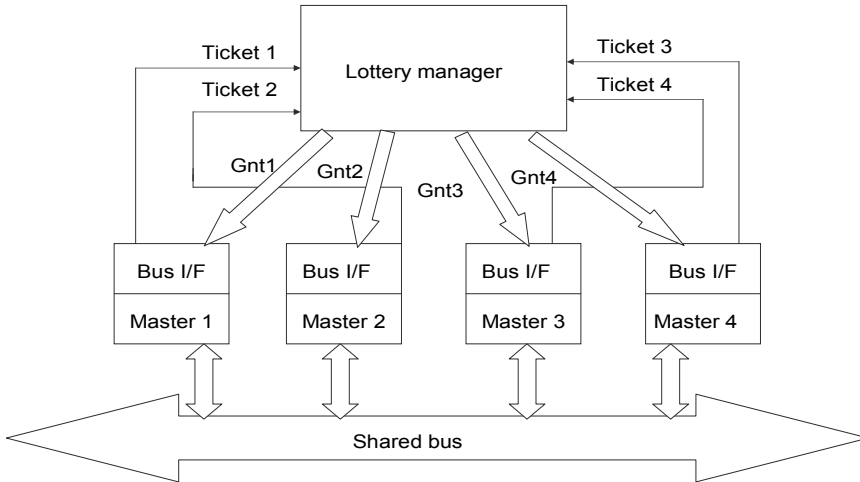


Fig. 2. Lottery manager for a bus in a Lottery bus based communication architecture

The lottery manager accumulates requests for ownership of the bus from one or more masters, each of which is (statically) assigned a number of “lottery tickets,” as shown in figure 3. The manager pseudo-randomly chooses one of the contending masters to be the winner of the lottery, favoring masters that have a larger number of tickets, and grants access to the chosen master for a certain number of bus cycles. Multiple word requests may be allowed to complete without incurring the overhead of a lottery drawing for each bus word. However, to prevent a master from monopolizing the bus, a maximum transfer size is used to limit the number of bus cycles for which the granted master can utilize the bus. Also, the architecture pipelines lottery manager operations with actual data transfers, to minimize idle bus cycles. The inputs to the lottery manager are a set of requests (one per master) and the number of tickets held by each master. The output is a set of grant lines (again one per master) that indicate the number of words that the currently chosen master is allowed to transfer across the bus. The arbitration decision is based on a lottery. The lottery manager periodically (typically, once every bus cycle) polls the incoming request lines to see if there are any pending requests. If there is only one request, a trivial lottery results in granting the bus to the requesting master. If there are two or more pending requests, then the master to be granted access is chosen using the approach described next.

2.3.1 Lottery-based arbitration algorithm

Let the set of bus masters be C_1, C_2, C_3, C_4 & Let the number of tickets held by each master are t_1, t_2, t_3, t_4 . At any bus cycle, let the set of pending bus access requests be represented by a set of Boolean variables r_i ($i=1, 2, \dots, n$) where $r_i=1$ if component C_i has a pending request, and $r_i=0$ otherwise. The master to be granted is chosen in a pseudo-random way, favoring components with larger numbers of tickets. The probability of granting component C_i is given by

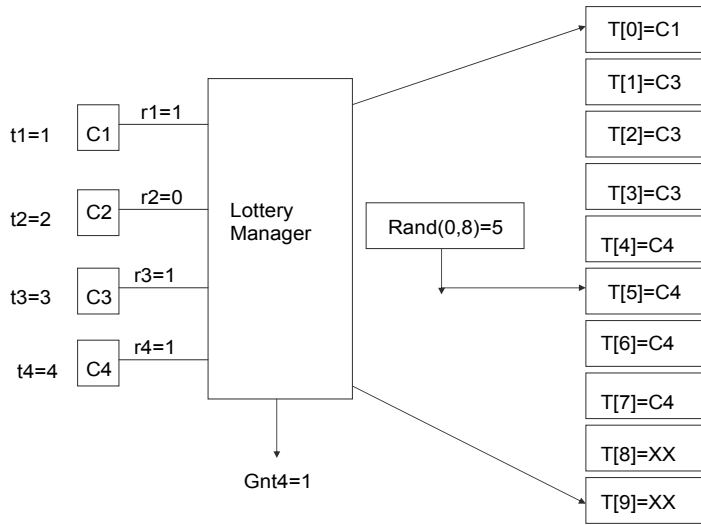


Fig. 3. Illustration of a lottery that determines which master should be awarded ownership of the bus.

$$P(C_i) = \frac{r_i * t_i}{\sum_{j=1}^n r_j * t_j}$$

Figure 3 shows an example where three out of four bus masters have contending requests, with tickets in the ratio 1:3:4. For this request map and ticket holding combination, the lottery-based approach should result in $P(C1)=0.12$, $P(C2)=0$, $P(C3)=0.37$, $P(C4)=0.5$. To make an arbitration decision, the lottery manager examines the number of “active” tickets, or the number of tickets in possession of the set of components that have pending requests. This is given by

$$\sum_{j=1}^n r_j * t_j$$

It then generates a pseudo-random number (or picks a winning “ticket”) from the range $\left[0, \sum_{j=1}^n r_j * t_j\right]$ to determine which component to grant the bus. If the number falls in the range $[0, r1*t1]$ the bus is granted to component C1, if it falls in the range $[r1*t1, r1*t1+r2*t2]$ it is granted to component C2. and so on. In general, if it lies in the range $\left[\sum_{k=1}^i r_k * t_k, \sum_{k=1}^{i+1} r_k * t_k\right]$ it is granted to component C_{i+1} . The component with the largest number of tickets occupies the largest fraction of the total range, and is consequently the most likely candidate to receive the grant, provided the random numbers are uniformly distributed over the interval $\left[0, \sum_{j=1}^n r_j * t_j\right]$. For example, in Figure 3, components C1, C2, C3 and C4 are

assigned 1, 2, 3, and 4 tickets, respectively. However, at the instant shown, only C1,C3,C4 have pending requests hence the number of current tickets is

$$\sum_{j=1}^n r_j * t_j = 1 + 3 + 4 = 8$$

Therefore, a random number is generated uniformly in the range (0, 8) In the example, the generated random number is 5, and lies between $r_0*t_0+r_1*t_1+r_2*t_2=4$ and $r_0*t_0+r_1*t_1+r_2*t_2+r_3*t_3=8$. Therefore, it indexes to a ticket owned by component C4. According to the rule described above, and as illustrated in Figure 3. Therefore, the bus is granted to component C4 win the very first lottery.

Figure 4 shows block diagram of Lottery Bus architecture. It contains three basic blocks. (1)Lottery manager:-In this block r_1, r_2, r_3, r_4 are the requests signal of the master and t_1, t_2, t_3 and t_4 are the tickets of the master respectively. That will generate the ticket values that are $r_1t_1, r_1t_1+r_2t_2, r_1t_1+r_2t_2+r_3t_3, r_1t_1+r_2t_2+r_3t_3+r_4t_4$. (2)Random number generator:-Random number generator is working on the principle of pseudo random binary sequence generator .That will generate the number randomly. (3) Comparison and grant generation hardware:- The random number is compared in parallel against all four partial sums. Each comparator outputs a "1" if the random number is less than the partial sum at the other input. Since for the same number, multiple comparators may output a "1" (e.g., if $r_1=1$ and the generated random number is smaller than, all the comparators will emit "1"), it is necessary to choose the first one, starting with the first comparator. For example, for the request map 1011 if the generated random number is 5, only's C4 associated comparator will output a "1." However, if the generated random number is "1," then all the comparators will output a "1," but the winner is C1. The architecture is model using VHDL for three masters. Ticket values are keeping fixed. Figure 4 shows the simulation results for the discussed architecture. Here t_0, t_1, t_2 & t_3 are tickets values and gnt_0, gnt_1, gnt_2 & gnt_3 are grant signals of the master processor. Signal n_1 is random number generated signal and signal h_0, h_1, h_2 & h_3 are calculated value for the master or processor according to it's ticket value and request signal r .

As shown in figure 4 the signal $r(0), r(1), r(2)$ and $r(3)$ are the request of master 0, master 1, master 2 and master 3 respectively the signal t_0, t_1, t_2 and t_3 are the ticket values of master 0, master 1, master 2 and master 3 respectively. The signal s_0, s_1, s_2 and s_3 are the total ticket values of master 0, master 1, master 2 and master 3 respectively. The signal n_1 represents the number generated by pseudo random number binary sequence generator (figure 4). The signal gnt_0, gnt_1, gnt_2 and gnt_3 are the grant signal of master 0, master 1, master 2 and master 3 respectively. Figure 4 shows the simulation results for static lottery bus as per the algorithm. The numbers in the simulation results indicate the number of master getting the grant of shared bus utilization.

2.4 Dynamic lottery bus architecture

In this architecture (figure 5), the inputs to the lottery manager consist of a set of request lines ($r_0r_1r_2r_3$), and the number of tickets currently possessed by each corresponding master that are generated by ticket generated by ticket generator. Therefore, under this architecture, not only Range of current tickets varies dynamically but it can take on any arbitrary value (unlike the static case, where it was fixed). Therefore at each lottery, the lottery manager

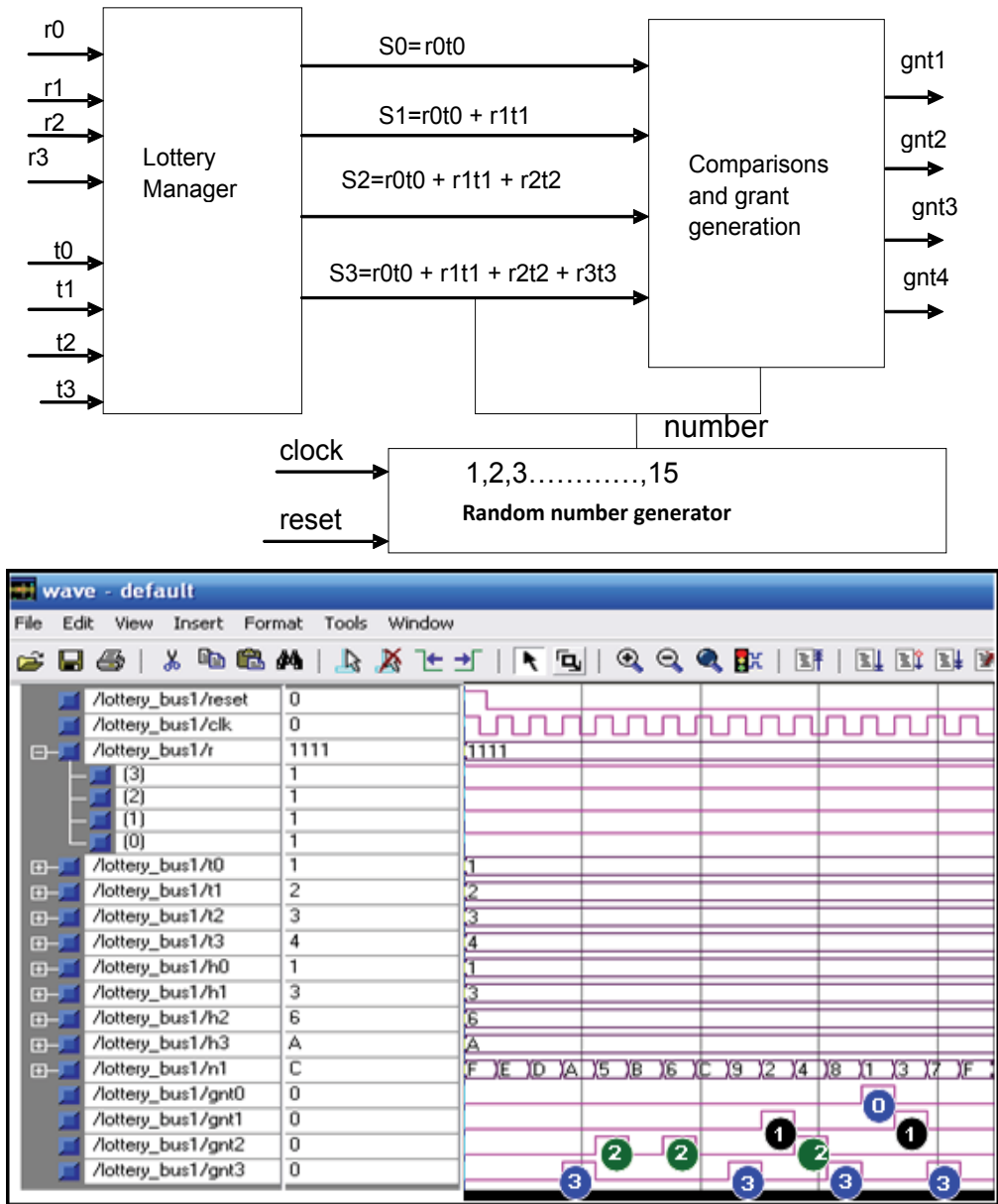


Fig. 4. Structure and simulation results of Static Lottery Based arbiter

needs to calculate for each component C_i , the partial sum $\sum_{j=1}^n r_j * t_j$. This is implemented using a bit wise AND operation and tree of adder, as shown in figure 5. The final result, $T=r_0t_0+r_1t_1+r_2t_2+r_3t_3$, defines the range in which the random number must lie. A limitation of this implementation is that distribution of the resulting random number is not uniform. The rest of the architecture consists of comparison and grant hardware, and follows directly from the design of the static lottery manager.

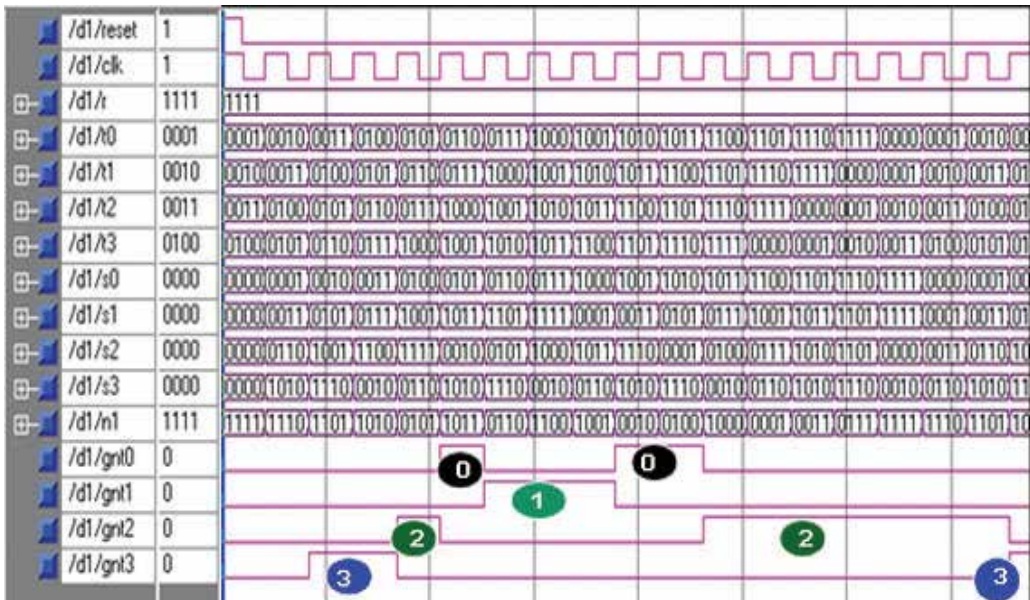
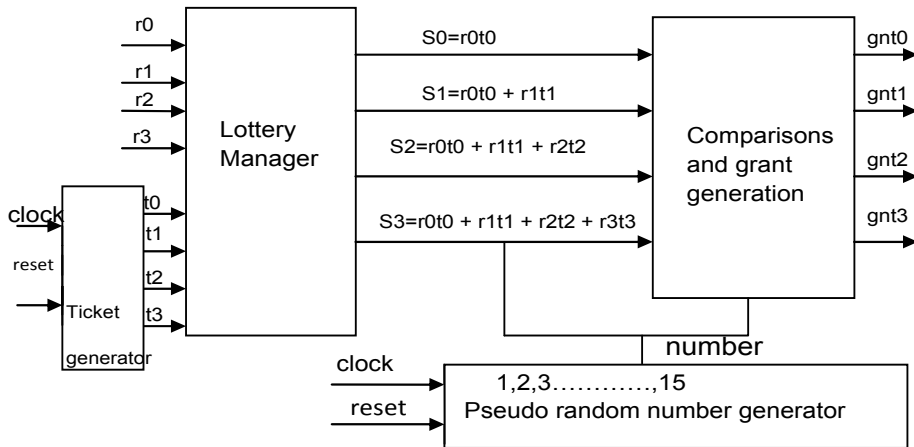


Fig. 5. Structure & simulation Results of Dynamic Lottery bus

The architecture is modeled using VHDL. Ticket values are keeping varying. Figure 5 shows the waveforms for the discussed architecture. Here t_0, t_1, t_2 & t_3 are tickets values and gnt_0, gnt_1, gnt_2 and gnt_3 are grant signals of the master processor. Signal n_1 is random number generated signal and signal s_0, s_1, s_2 and s_3 are calculated value for the master or processor according to its ticket value and request signal r .

Advantages: All the masters that are requesting gain the control of bus.

Disadvantages: If the pseudo random number is greater than total ticket value then none of the masters will get the grant signal.

2.5 ATM switch architecture

In this arbitration algorithm, it accepts three parameters (Requests, Tickets, Adaptive signal) for the input of arbiter. Request and Ticket are the input for the static bus distribution.

Adaptive signal value is used as an additional input to improve the probability of the bus grant. This adaptive signal value is transmitted from the master that requires the bus grant more than another master because of the stressful traffic. Since we do not know which IP is used for the shared bus in advance of the SOC design, the adaptive signal can be fixed by the specific parameter. The master counts the buffer position storing the ATM cell and if the data approaches to the limited amount, the adaptive signal is generated to improve the drawing probability.

$$P(C_i) = \frac{r_i(t_i + a_i)}{\sum_{j=1}^n r_j * (t_j + a_j)}$$

Above equation shows the shared bus probability for each master. The current pending request and ticket value is used to obtain the shared probability of each C_i . In order to improve the probability of the master, a_i values are obtained from the look up table and two of the master requests accomplish the bit-wise AND operation by the values i . 'a' is the additional ticket value to solve the problem that if the total ticket value is lower than the pseudo random value, the bus is assigned to the master of the low priority by the priority inversion.

If the pseudo random value is bigger than $\sum_{j=1}^n r_j * t_j = 4$, the control signal of MUX generates

the enable signal by the OR operation of the request bit from the master. The partial summation value of each master is obtained by the bit-wise AND operation between the request values and the ticket value. If the pseudo random value from LFSR and the total ticket value generate modulo $\left(R, \sum_{j=1}^n r_j * t_j \right) = 5$. C4 is assigned to be use because the pending request value is 0001.

In figure 6 (in simulation results) signal r represents for the masters request signal. For the testing all masters accept master 2, are requesting for bus. Signal gnt0 to gnt3 are the grant signal. The master grant signals are indicated by numbers.

Advantages: The adaptive signal is used to solve the problem that the characteristics of LFSR are disappeared if the pseudo random number is bigger than total ticket value.

2.6 Fuzzy logic arbiter

Fuzzy logic has already proved to be an innovative and successful design methodology in certain key areas of embedded control where its attributes of simplicity, sensitivity, robustness and easy optimization are tremendously advantageous. Fuzzy logic has been applied widely across the consumer market, where superior product performance has been achieved whilst reducing development time. Typical "fuzzy goods" that have been particularly successful include control systems in washing machines, air conditioners, cameras and camcorders incorporating an auto focusing mechanism, video cassette recorders and audio systems.

The basic concept of fuzzy sets is a generalization of the classical or crisp set. The crisp set is defined in such a way as to dichotomize the individuals in some given universe of discourse into two groups: members (those that certainly belong in the set) and nonmembers (those that certainly do not). A sharp, unambiguous distinction exists between the members and

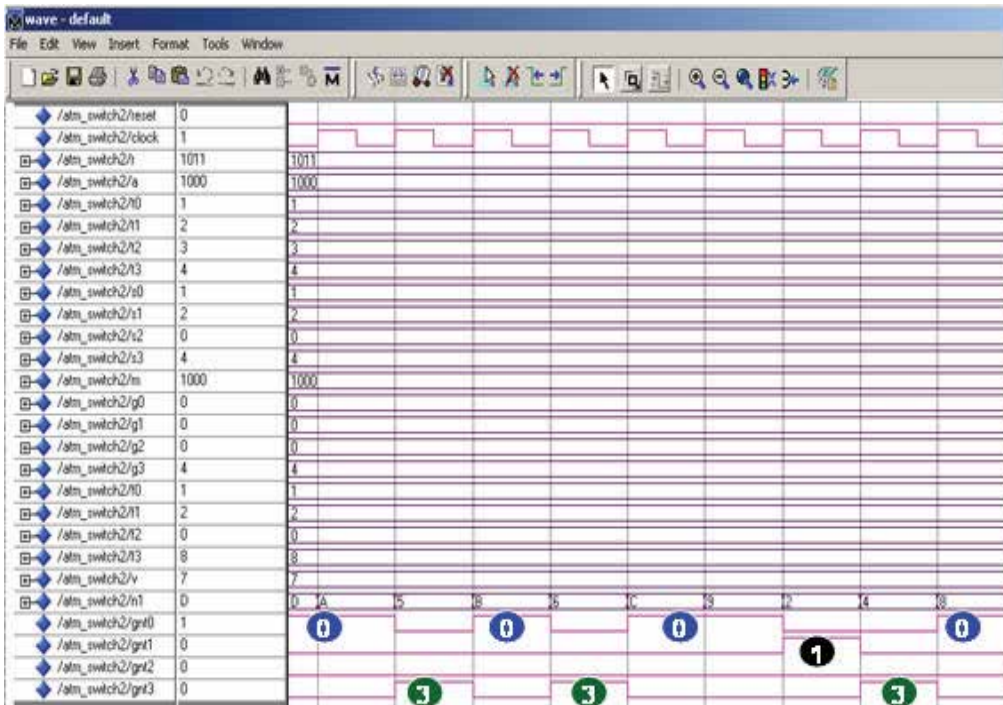
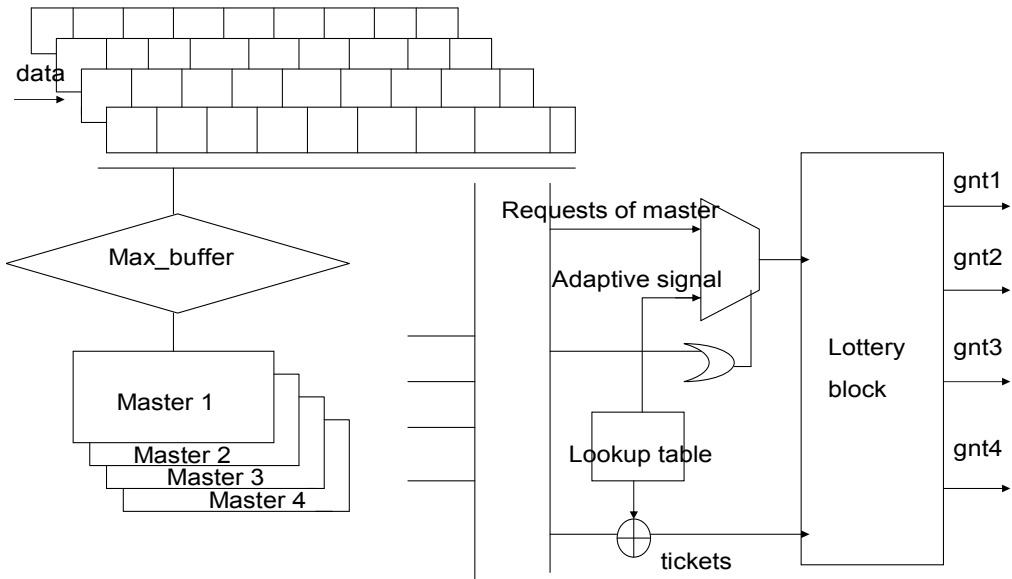


Fig 6. Structure & Simulation Results of ATM Switch arbiter

nonmembers of the class or category represented by the crisp set. Fuzzy sets boundaries are vague, and the transition from member to nonmember appears gradual rather than abrupt. A fuzzy set can be defined mathematically by assigning to each possible individual in the universe of discourse a value representing its grade of membership in the fuzzy set. This

grade corresponds to the degree to which that individual is similar or compatible with the concept represented by the fuzzy set.

The fuzzy arbiters are modeled using appropriate membership function and rules in such a way as to maximize the acceptance probability of the processors and distribute it evenly. In such systems, arbiters are used to resolve conflicts between processor requests shared bus. Typically, these conflicts are resolved by using two-stage arbitration schemes that employ policies such as random choice, daisy chaining, round-robin, etc. A new way of implementing these arbiters is the use of fuzzy logic to resolve resource request conflicts based on the system state and performance variables.

2.6.1 Working principal

The entire membership function can be divided into three segments: 0, 1 and 2 as shown in Figure 7. The Y-axis shows the degree of membership (μ) as a value between 0 and 1. The X-axis shows the universe of discourse and is divided into three segments. Figure 3.8 shows how triangular input membership functions are formed in the fuzzification process. The calculation of the degree of membership (μ) can be categorized into three different segments: (a) In segment 0: $\mu = 0$, (b) In segment 1: slope is upward from left to right, therefore: $\mu = (\text{Input value} - \text{point 1}) * \text{slope1}$, μ is limited to max value of 1, (c) In segment 2: slope is downward from left to right, therefore: $\mu = 1 - (\text{Input value} - \text{point 2}) * \text{slope 2}$ where μ is limited to a minimum value of 0.

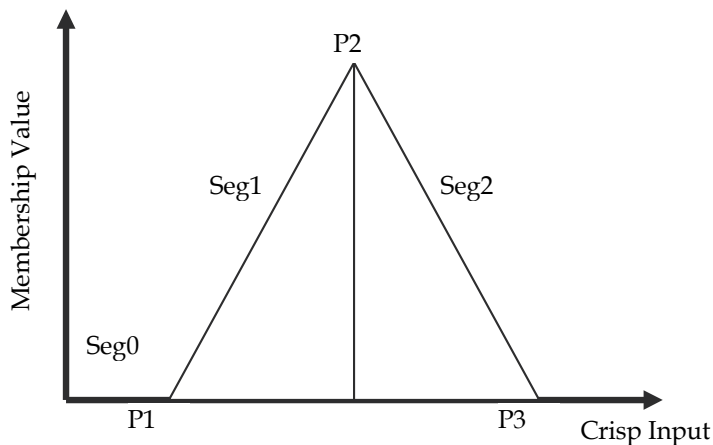


Fig. 7. Membership Functions

2.6.2 Design of fuzzy logic arbiter

Specifications: The arbiter has been designed for following specification.

- To improve Acceptance rate of each processor
- Using two level of arbitration first rule based and second priority based
- Designed for Three Masters.

Acceptance Rate calculation

Acceptance rate for each processor can be calculated as the ratio of master request granted with the master requested. If AAR_i is acceptance rate for i th processor, $P_i.\text{accept}$ is number of request granted by FLA and $P_i.\text{nreq}$ is total master request to FLA. Then Acceptance rate can be calculated as follows.

$$AAR_i = \frac{P_i.accept}{P_i.nreq} \times 100$$

For implementation, it will have two inputs as request and grant, output as Acceptance rate which is 8-bit crisp value.

Fuzzification of inputs

In this step the degree of input is being determined by appropriate fuzzy sets via membership functions.

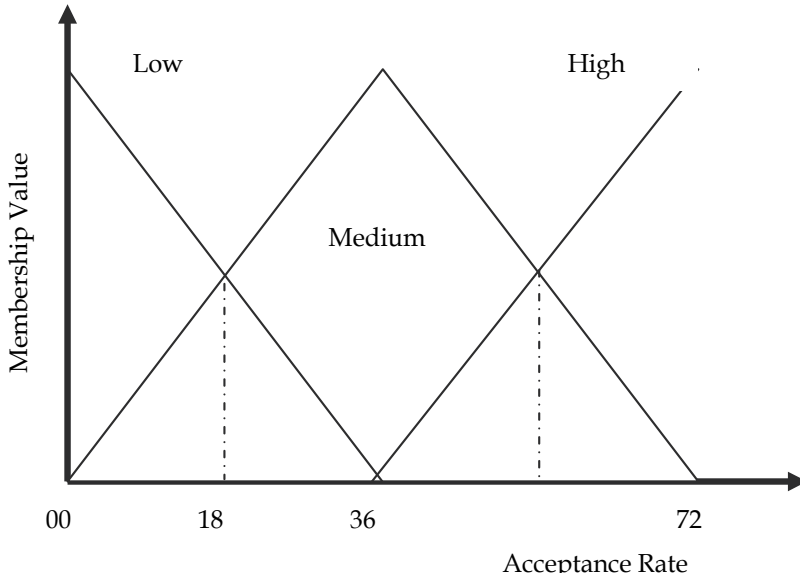


Fig. 8. Membership Functions for each processor

A membership function is a curve that defines how each point in the input space is mapped to a membership value (or degree). The inputs in this case are chosen to be the current acceptance rate of each processor. The input is a crisp numerical value limited to the universe of discourse which is in this case. Three membership functions are defined for each input; low, medium, and high, see in figure 8.

Rule Base Design

Once the inputs have been fuzzified, we know the degree to which each part of the antecedent has been satisfied for each rule. A set of rules have been defined for a fuzzy arbiter. The listing of the rules for a three-input system is given bellow, where AP1, AP2 & AP2 are the current acceptance rates of input processor1 to processor3 respectively. The output is the processor selected (I1, I2 & I3). The rules have been chosen in such a way as to increase the acceptance rate of all processors, by selecting the lowest acceptance rate processor. In case of conflict i.e two processors acceptance rate are having in same category then problem will be solve by priority method. In such case processor 1 has highest priority and master 3 has lowest priority. Eg. In the table 1 fuzzy rule no 3, processor 1 and processor 2 has acceptance rate in low category but then processor 1 is selected due to high priority. Figure 12 shows block diagram of the rulebase module. Table 1 gives rule list.

Fuzzy rule	Ap1	Ap2	Ap3	Processor Selected
1	Low	Low	Low	I1
2	Low	Low	Medium	I1
3	Low	Low	High	I1
4	Low	Medium	Low	I1
5	Low	Medium	Medium	I1
6	Low	Medium	High	I1
7	Low	High	Low	I1
8	Low	High	Medium	I1
9	Low	High	High	I1
10	Medium	Low	Low	I2
11	Medium	Low	Medium	I2
12	Medium	Low	High	I2
13	Medium	Medium	Low	I3
14	Medium	Medium	Medium	I1
15	Medium	Medium	High	I1
16	Medium	High	Low	I3
17	Medium	High	Medium	I1
18	Medium	High	High	I1
19	High	Low	Low	I2
20	High	Low	Medium	I2
21	High	Low	High	I2
22	High	Medium	Low	I3
23	High	Medium	Medium	I2
24	High	Medium	High	I2
25	High	High	Low	I3
26	High	High	Medium	I3
27	High	High	High	I1

Table 1. Fuzzy Rule set for three processors

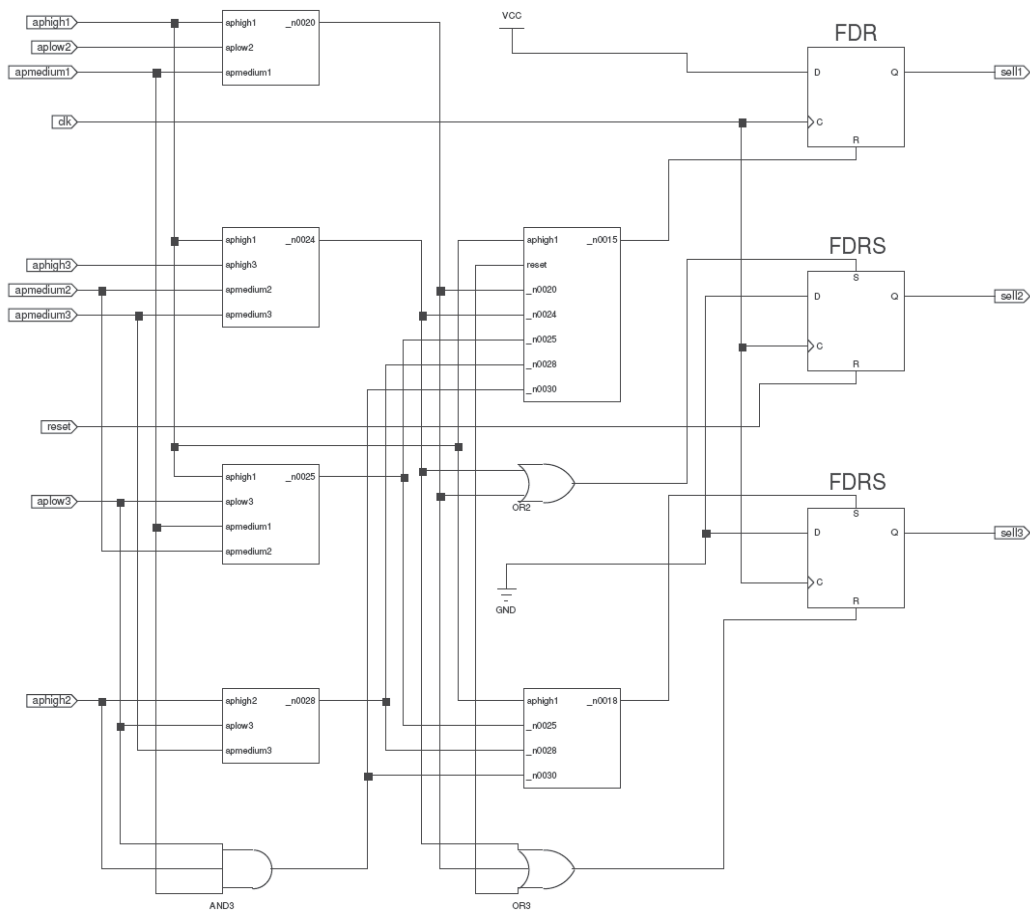


Fig. 9. Structure of Rule based Module

Fuzzy Arbiter for Three Processor

The figure 10 shows total structure for fuzzy logic arbiter for three processors. This structure has input as request signal Ireq1, Ireq2 & Ireq3 from respective three masters and output as grant signal I1grant, I2grant & I3grant to the masters. The structure is divided into three basic part from input side acceptance rate calculation, Middle part as fuzzification and output side as rule based module.

Fuzzy logic arbiter is complex to implement. The complexity increases exponentially with the increase in the number of processor. As the arbiter requires so many calculations to do, it will be slow for responding. Also it will hard to implement in FPGA because architecture consist of so many number of byte multiplier and divider that took huge hardware to implement.

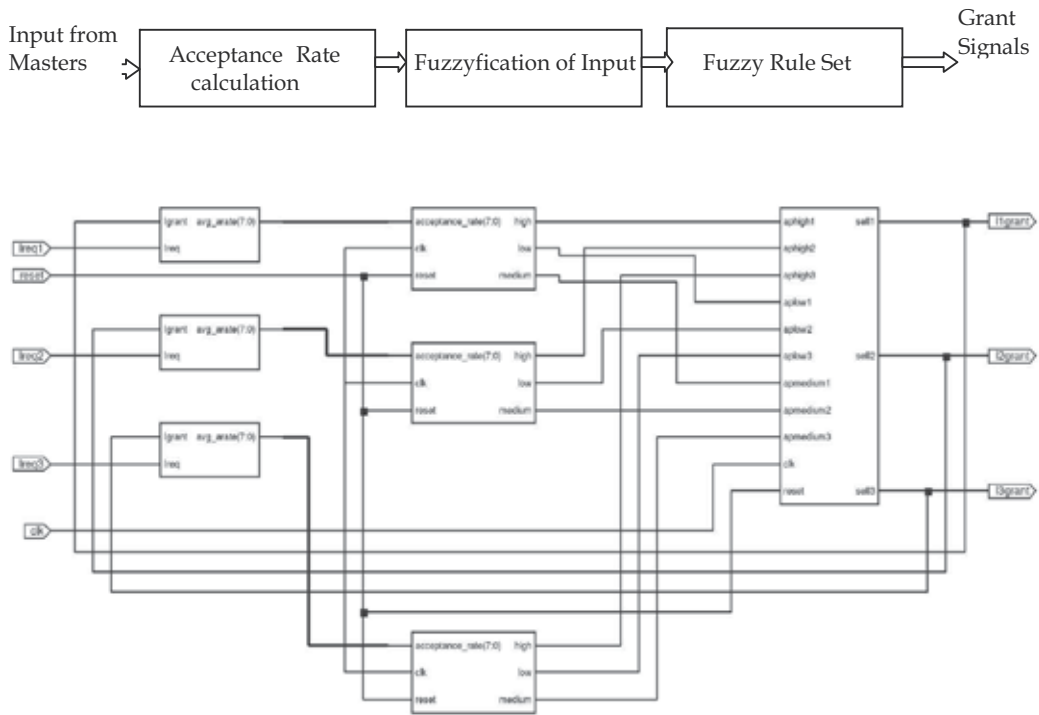


Fig. 10. Structure for fuzzy logic arbiter

3. Performance comparison of arbiters

Performance of the designed arbitration schemes has compared based on the parameter like Latency, Acceptance rate of Masters, Average Waiting time of masters & Shared bus bandwidth utilization by individual masters.

Average Latency (Cycles/word): It is a time delay between the moment something is initiated, and the moment one of its effects begins or becomes detectable. Ideally this should be zero or as minimum as possible.

Acceptance Rate: Acceptance rate is defined as percentage of how many times masters request for shared bus among how many times it request is granted and bus is allotted. Theoretically acceptance rate of every processor should be as high as possible.

Average Waiting Time: It is the average time for particular master in between request and grant of the shared bus. Average waiting time for every processor should be as low as possible.

Average Bandwidth Utilization: It is measure of shared utilized by different masters. The bus should be ideally equally utilized by all masters.

Figure 11 indicate that the ATM switch based arbiter gives optimum performance based on the monitoring parameters.

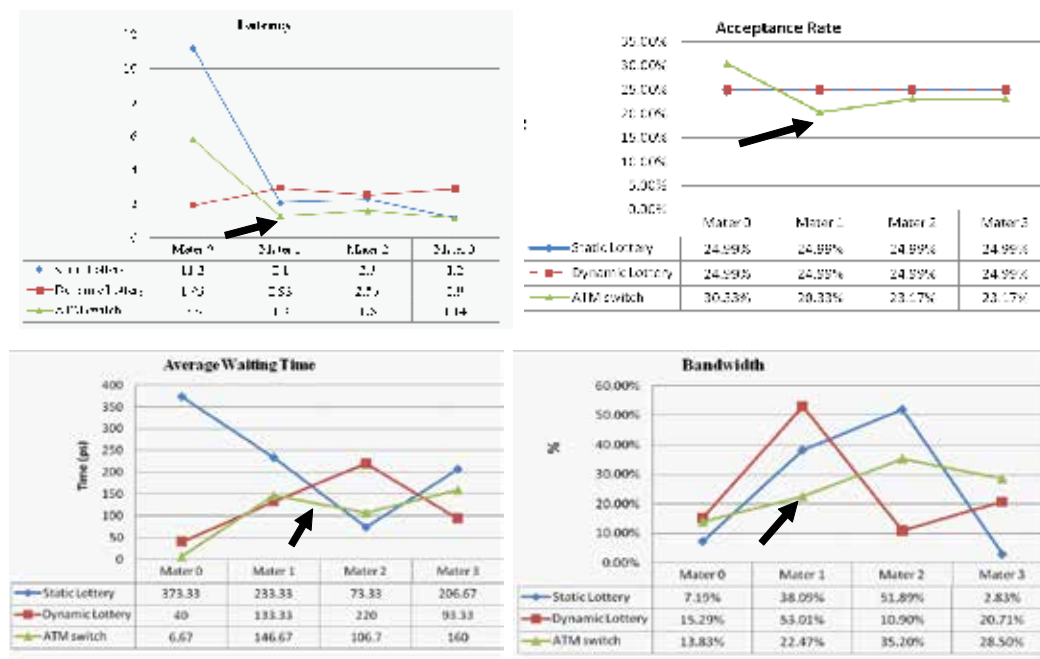


Fig. 11. Performance comparison of arbitration Techniques.

4. References

A.Y.Deshmukh, Dr.P.R.Bajaj, Dr.A.G.Keskar (2006). "Hardware implémentation of fuzzy logic controllers-Approach & Constraints", *KES 2006, Brighton 2006*.

Chang Hee Pyoun, et. al. (2003). "The Efficient Bus Arbitration Scheme In SoC Environment", *IEEE International Workshop on System-on-chip*.

Dent,D.J. (2000). "System -on-Chip research leads to hardware/ software co-design degree", *Frontiers in Educationa Conference, 2000. FIE 2000. 30th Annual Volume:2*.

G. Klir and T. Folger(1988). *Fuzzy Sets Uncertainty and Information*. New York: Prentice-Hall,

H. Diab,(2004). "Fuzzy logic arbiter for multiple-bus multiprocessor systems", *IEEE Trans. On Systems, Man, And Cybernetics*,

Jun Xiao et. al.(2004). "Fuzzy controller for wall climbing microrobots", *IEEE transactions on fuzzy systems, vol 12, no.4*,

K. Lahiri, A. Raghunathan (2006). "The Lotterybus on-chip communication architecture", *IEEE Trans. On VLSI system*.

K. Lahiri, A. Raghunathan, and S. Dey (2000) "Performance Analysis of Systems with Multi-Channel Communication Architectures", *International Conference on VLSI design, pp,530-537*

K. Lahiri, A. Raghunathan, and S. Dey, (2001)"System Level Performance analysis for designing on-chip communication architecture", *IEEE Trans. Computer- Aided Des. Integr. Circuits Syst. Vol. 20*.

K. Lahiri, A. Raghunathan, G, Lakshminaray,(2001) "Lotterybus : A new high-performance communication architecture for system-on-chip designs" *Proc. Design Automation Conf. pp 15-20*

- K. Lahiri, A. Raghunathan, G. Lakshminaray,(2001) "LOTTERYBUS : A new high-performance communication architecture for system-on-chip designs" *Proc. Design Automation Conf.* pp 15-20
- K.A Kettler, et.al (1995) "Modeling Bus Scheduling Policies for Real Time Systems", *16th IEEE Real Time Systems Symposium.*
- Pawel Gepner et.al, (2006) "Multi-Core Processors: New Way to Achieve High System Performance", *IEEE Parallel Computing in Electrical Engineering (PARELEC'06)*
- Sameep Singh, Kuldip Rattan (2003), "Implementation of a Fuzzy Logic Controller on an FPGA using VHDL", *IEEE*
- Thomas D. Richardson, et. Al (2006) "A Hybrid SoC Interconnect with Dynamic TDMA-Based Transaction-Less Buses and On-Chip Networks", *IEEE 19th International Conference on VLSI Design (VLSID'06)*
- Yi Xu , Li Li, Ming-lun Gao, Bing Zhang, Zhao-yu Jiang, Gaoming Du, Wei Zhang (2006)" An Adaptive Dynamic Arbiter for Multi- Processor SoC" *2006 IEEE*
- Youngwoo Kim et.al (2003), "AMBA Based Multiprocessor System", *IEEE International Symposium on System-on-Chip.*

Towards Automotive Embedded Systems with Self-X Properties

Gereon Weiss, Marc Zeller and Dirk Eilers
*Fraunhofer Institute for Communication Systems ESK
Germany*

1. Introduction

Since the first pieces of software have been introduced into automobiles in 1976, the complexity of automotive software systems is growing rapidly. Today automotive software is widely installed for diverse applications ranging from the infotainment domain (e.g. entertainment, navigation, etc.) with typically no real-time requirements to safety-critical control software (e.g. engine control, safety functionalities, etc.) with hard real-time requirements. In addition, many comfort functionalities of automobiles are realized by software nowadays (e.g. the control of the air condition system, electronic window regulator, etc.). Up to 90% of today's innovations in the automotive industry are realized by hard- and software (Pretschner et al., 2007). This results in up to 2,500 "atomic" functions realized in software on up to 67 electronic control units (ECUs) in modern high-end cars (Fürst, 2010).

For the future development of automobile electronics, there are two major trends: A growing number of functionalities and through this a growing importance of software in the car (Hardung et al., 2004). Future generations of cars will be equipped with many new, complex *features* (Czarnecki & Eisenecker, 2000). For example, functionalities to support active driving safety (e.g. driver assistance systems), features which enable new innovative driving concepts (e.g. engine control for hybrid vehicles), or new functionalities in the comfort domain (e.g. new infotainment features). Most of these functionalities will be realized in software, which increases the amount and importance of software within the automotive domain necessarily. But these new features will also increase the complexity of future vehicular system architectures. For instance, driver assistance systems increase the complexity because they interact with several in-vehicle domains, e.g. the power-train and infotainment domain. In future, the trend of establishing more and more interactions between software components will continue, e.g. through x-by-wire features, where mechanical transmission is replaced by electrical signals. This results in a growing interdependency of separated software domains and in an increased need for interconnection. Another important aspect is the continuously growing number of functional variants caused by customer-specific equipment options or country-specific regulations. At the same time, the demand on the software quality within the automotive domain is very high at all times. These requirements must be satisfied in the future, despite the increasing complexity of automotive software architectures. Even today it is a great challenge to manage these systems from the outside.

In recent years, a lot of research has been done, trying to explore new methods for the management of general complex software systems. Within the research area of *Self-adaptation* (McKinley et al., 2004) and *Self-organization* (Serugendo et al., 2004) new paradigms for the management of complex systems have been introduced. Both approaches utilize control-loops for feedback-based control of the system. Self-adaptive systems realize the adaptation of the system in a top-down manner by setting global goals which are enforced hierarchically. On the contrary, self-organizing systems follow a bottom-up approach in which the local interaction of elements results in the intended global behavior. These paradigms for the development of general systems which are capable of adaptation also constitute a promising solution to master the complexity within automotive embedded systems (Weiss et al., 2009). Thereby, vehicular software systems can be enhanced with self-management capabilities. These so-called *self-x properties* (like self-configuration, self-healing, self-optimization or self-protection (Kephart & Chess, 2003)) improve the scalability, robustness and flexibility of the system.

In 2001 IBM introduced the *Autonomic Computing (AC)* paradigm (Horn, 2001). The main idea is the adaptation of the behavior of the central nervous system which interacts autonomously. As basic principle the management of *autonomic elements* is realized by a reconfiguration-cycle where each autonomic element monitors and analyzes the environment, plans its next steps and executes the resulting actions. Originally, the focus lies on the management of large-scale computer networks. With *Organic Computing (OC)* (Schmeck, 2005) a novel principle for self-organizing systems is given by imitating adaptive, life-like behavior in the nature. Self-organization is realized on different abstraction levels with observer/controller models utilizing control-loops. No particular field of application is addressed and interdisciplinary research is covered. With the *Self-adaptive Software Program* (Robertson et al., 2001) a very ambitious research field is addressed where software evaluates and changes its own behavior at runtime. Therefore descriptions of intentions and alternative behavior need to be added in the deployed software.

In the automotive sector several initiatives have already focused on evaluating self-x techniques for vehicles. A high-demanding goal for the future of transportation are autonomous cars which can adapt even in high complex scenarios as in urban traffic (Urmson & Whittaker, 2008). As promising as early results are, many - not only technical - problems are not solved yet and thus the practical appliance of autonomous driving is still not foreseeable yet.

For the in-vehicle information and entertainment functionalities the *Media Oriented Systems Transport (MOST)* bus (MOST Cooperation, 2008) is a widespread established standard. It facilitates functional composition with a powerful API and already features very limited self-x properties with its configuration management. The *Automotive Open System Architecture (AUTOSAR)* (AUTOSAR Consortium, 2010) initiative is a consortium with the goal of an open standard for the automotive software architecture. Through a component-based architecture the reuse and scalability of future automotive software is pursued. By a virtual integration of software components (*Virtual Function Bus*) the allocation of functions to ECUs can be assembled at design time. Even though this approach facilitates a more liberal way of the allocation, it does not support any dynamic allocation at runtime. Hence, self-adaptation techniques that rely on reallocation of functions cannot be applied. In (Trumler et al., 2007) self-healing and self-configuration is evaluated in a component-based automotive architecture which indicates the potentials arising with these techniques. Dinkel (Dinkel, 2008) focuses on the development and simulation of a completely new IT-

architecture for future cars with self-x capabilities. It utilizes Java and OSGi for simulation purposes and is not applied in the field. The DySCAS project (Anthony et al., 2006) focuses on developing a middleware enabling dynamic self-configuration in today's cars. For the reconfiguration of the system a policy-based mechanism is utilized. Another approach was proposed by DaimlerChrysler (Hofmann & Leboch, 2005). The *EvoArch* project tries to put more value on the autonomy of the different parts of the automobile enhancing the automobile with self-x properties. Within the research project ReCoNets (Teich et al., 2006) fault-tolerance is addressed by bringing Hardware/Software- Reconfiguration into the automobile. Although, reallocation of both hardware and software is a consequent progression of the currently advancing adaptivity and decomposability, it is not aligned with present automotive development method (e.g. FPGA reconfiguration).

As briefly described before, different approaches are in progress enabling self-x properties in future cars with various degrees of a possible adaptation. Many open challenges need to be researched for meeting the domain-specific requirements of automotive electronic systems (e.g. the verification of adaptation). But no project focuses on the embedding of techniques in present automotive electronic systems allowing a transition to self-adaptive systems.

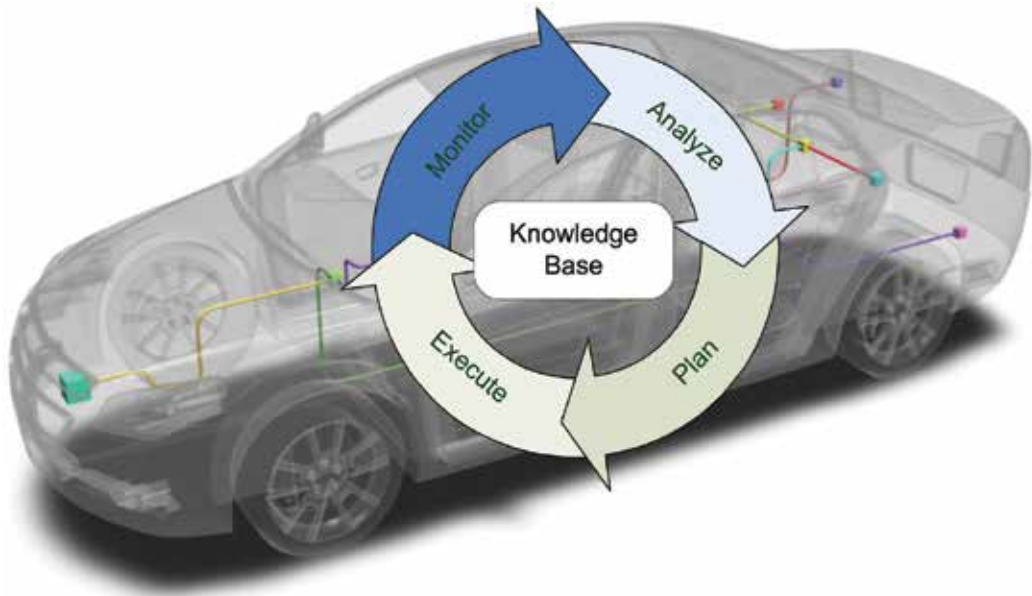


Fig. 1. Self-adaptation in the context of automotive embedded systems

The characteristics of *self-adaptive* or *self-organized systems* might provide a solution for the growing complexity in the automotive domain. Within this chapter we present an approach for enhancing automotive embedded software systems with self-x properties which increases the scalability, robustness and flexibility of vehicular software systems (cp. Figure 1). The structure of this paper is organized as follows: In Section 3 we present the challenges in the realization of self-x properties in automotive embedded systems. Afterwards, we illustrate the advantages of self-adapting automotive software systems by presenting concrete use cases. Our model-based approach to design self-adaptive automotive software systems is outlined in Section 5. In Section 6 we introduce an approach to realize self-x capabilities during runtime. Finally, we conclude the chapter in Section 7.

2. Self-adaptation in the context of automotive embedded systems

Under the umbrella term self-adaptation a set of terms is defined, e.g. self-x properties. In this section we will explain relevant terms in the domain-specific context of automotive embedded systems.

Self-adaptive software systems must be able to adapt the behavior (*Behavioral Adaptation*) or/and the structure (*Structural Adaptation*) of the system to changes in the environment or within the system itself (Zadeh, 1963)(McKinley et al., 2004). To adapt itself autonomously, the system must be able to detect and to evaluate its own context. Therefore, a model of the system and its feasible states is needed. The comparison of the currently detected context and the reference situation of the system model enables the evaluation of the current system state. This so-called *Self-Awareness* is the basis for the adaptation of the system or a sub-system.

During runtime self-awareness is enabled by the *Self-Description* of each component within the system. The language and the scope of this description must be as small as possible to fulfill their purpose. Furthermore, the description must be processable by an embedded system with limited resources.

Today, there are already examples for adaptive behavior in modern automobiles. For example, the engine control adapts the fuel injection according to the current road behavior. But this kind of adaptivity is limited to control applications and allows adaptation only in predetermined variants. To fully exploit the potentials of adaptivity, it is not practical to limit the variability by calculating all possible system configurations in advance (during design time). Due to the enormous amount of possible variability in today's and future automotive software systems, it is necessary to adapt the system dynamically at runtime (*Dynamic Reconfiguration*) (Geihs, 2008).

With respect to (Hofmeister, 1993) three different kinds of dynamic reconfiguration can be differentiated:

1. The implementation of a component is replaced by another one (Behavioral Adaptation).
2. The relation between components of the system is modified. New components and features can be added or removed (Behavioral Adaptation).
3. The allocation of the software components is changed without the modification of the logical structure. Therefore, components are migrated from one hardware platform to another (Structural Adaptation).

In the context of automotive embedded systems behavioral adaptation is achieved by the dynamic activation or deactivation of specific software-based features during runtime. Structural adaptation is realized by the dynamic reallocation of software components onto the available control units during runtime.

To apply dynamic reconfiguration successfully in the context of automotive embedded systems, we have to deal with so-called *emergent behavior*. Emergence is defined as a property of a total system which cannot be derived from the simple summation of properties of its constituent sub-systems (Müller-Schloer, 2004). It is a result of self-adaptive or self-organizing processes and leads to a system behavior which is not explicitly defined (Wolf & Holvoet, 2004). This may lead to unwanted or uncontrolled behavior - so-called *emergent misbehavior* (Mogul, 2005). Because automotive embedded systems provide safety-relevant applications (e.g. airbag), it is very important that the predefined requirements and constraints of the system are preserved during runtime. Therefore, emergent behavior is not tolerated in adaptive automotive software systems.

Instead, the aim of self-adaptation in the context of vehicles is to improve to the system with different self-x properties:

Self-Management: The system must be able to manage its own functionalities without actions from outside the system. The complexity of the system management task can be decreased by increasing the management capability of single components. For example, by adding a self-description to each element within the system the current status of self-aware elements does not need to be supervised continuously. Thereby, a divide-and-conquer strategy is applied. The more complex the management of individual elements is, the less complex is the management of the overall system. In the context of automotive embedded systems, a trade-off is needed between the self-management of the overall system and the management of individual parts of the system.

Self-Configuration: Today, the configuration of complex systems (e.g. vehicular software systems) is performed by experts. By enhancing a system with self-configuration capabilities, it is possible to find a feasible configuration in a distributed and autonomous way. Thus, the manual and error-prone configuration process can be omitted. Furthermore, self-configuration enables the dynamic integration of new components and features during the runtime of the system. For example, in today's cars the autonomous configuration is already supported by the infotainment system MOST in which a central instance - the so-called *NetworkMaster* - enables the configuration of features (*MOST FBlocks*) independent from their position.

Self-Healing: The autonomous diagnosis of the current system state enables the detection of invalid system states. Afterwards, a valid system state is restored by means of self-healing. The self-healing process is supported by the self-configuration capabilities of the system. To achieve the complete "healing" of the system a certain degree of redundancy is assumed. The ability to heal itself is growing with the size of the overall system. Thus, self-healing is especially interesting in the field of infotainment and telematics applications. Delays due to the process of self-healing must be considered additionally during system design.

Self-Protection: Self-protection of specific elements is necessary if the system is operating in a dynamic environment. For automobiles which are divided into different separated domains of automotive software, self-protection is an additional overhead which is not justifiable in the context of present automotive embedded systems. But the protection against critical system states and the prediction of problematic conditions is an option to prevent the system from failures and to satisfy the safety requirements within the automotive domain. Furthermore, by opening the in-vehicle communication to the outside world (e.g. car-2-x communication (CAR 2 CAR Communication Consortium, 2010)), the importance of self-protection will increase.

Self-Optimization: The proactive search of a specific element for new opportunities to optimize its own behavior helps to reach the optimal system state. But to achieve such an optimization, resources are continuously needed. In the context of automobiles, it is necessary to evaluate carefully if this effort for self-optimization is justifiable. Context-based self-optimization in terms of different predefined scenarios may be a potential trade-off for automobiles.

To use the full potential of the previously described self-x properties in automotive embedded systems, certain challenges must be met. In the next Section we will describe these challenges in detail.

3. Challenges in realizing self-x properties in automotive embedded systems

For realizing self-adaptive software systems for automobiles which enhance the system with self-x properties, several challenges have to be addressed which we describe in the following. Today, the software-based features of modern vehicles are statically assigned to specific ECUs. Since the number of control units cannot be expanded arbitrarily for the integration of new features, new concepts for the dynamic allocation of features to ECUs are needed. The Automotive Open System Architecture (AUTOSAR) (AUTOSAR Consortium, 2010) initiative aims to establish a standardized software architecture for cars since 2002. By using a component-based approach, the reusability and the scalability of automotive software is increased. The so-called *Virtual Function Bus (VFB)* enables the virtual integration of software components by allocating these components to ECUs during design time. Thereby, the flexibility of designing automotive embedded systems is increased. However, with a more modular approach like AUTOSAR there is the need to decompose features into services and services into atomic functions. This approach enables the reuse of functionalities and reduces the overhead by eliminating redundant implementations within the software system. Furthermore, more freedom for the runtime adaptation is achieved by a more fine-granular decomposition of features.

Modern runtime environments for automotive software, like *Offene Systeme und deren Schnittstellen für die Elektronik in Kraftfahrzeugen (OSEK)* (OSEK VDX Portal, n.d.) or AUTOSAR, are only configured statically during design time. Within statically designed systems most of the available resources are assigned permanently. Dynamic changes of this configuration (e.g. creating a new task) during runtime are not allowed. As runtime adaptation is needed to control the growing complexity, a runtime resource and conflict management is inevitable for the dynamic reconfiguration of the system (e.g. instead of a statically resolved virtual function bus with fixed port assignments in AUTOSAR, a real communication bus with a dynamic scheduling is needed). Therefore, the resources of each ECU - like CPU, memory, etc. - must be managed dynamically.

Although sensors and actuators are separated from the computation, there is still the necessity for locality of the software functions to access the sensor/actuator data in today's automotive embedded systems. Caused by the growing cross-linking of different functionalities - even inter-domain (e.g. caused by driver assistance features) - sensor and actuator data must be accessible by all features. Techniques like publish/subscribe and distributed data access might ease this problem. By the complete separation of sensors or actuators from the computation (control unit), their data can be accessed throughout the whole in-vehicle network. In case of an ECU breakdown the data of sensors or actuators will still be available. Thus, a more flexible distribution of software components is enabled which is mandatory to tap the full optimization potential of self-adaptation.

Another challenge for the realization of self-x properties poses the heterogeneity of today's vehicle electrical system architecture where diverse technologies are incorporated. The various hardware platforms and the different interconnection systems make it difficult to reallocate software components to different ECUs during runtime. For the migration to a different ECU, software components must be recompiled which increases the latency to adapt the system enormously or the program code of each component must be pre-compiled for the corresponding hardware platform and stored within the in-vehicle network. But for the various hardware platforms in today's automobiles the memory capacity must be increased significantly which is not cost-effective. Only an abstraction from the underlying

technology (e.g. via a runtime environment or middleware) will allow the interaction of the components and thus the efficient self-adaptation of the overall system.

In the automotive domain several applications with divergent safety and real-time requirements (specified as *Safety Integrity Level, SIL* (International Electrotechnical Commission (IEC), 1998)) are composed to one system. Presently, the requirements are met by a separation into domains (infotainment, power-train, comfort and chassis). Thus, a major challenge is to guarantee and meet the safety requirements of automotive systems even in adaptive systems (for example the ability to satisfy hard timing constraints). This results in an implied limitation of possible configurations of the system. The mandatory system constraints must be extracted during the design process and enforced during runtime. Thereby, the reconfiguration process of the system must not influence the behavior of safety-critical features. For this reason, the constraints and the effects of the adaptation must be considered in safety-relevant systems - like automobiles.

To realize self-adaptive or self-organizing (technical) systems a control instance is needed which collects information about the system, analyses these information and decides how to adapt the system to reach the predefined objectives (Mühl et al., 2007). Such a control instance must ensure that the system is in a correct state at any time. Present automotive systems have no capabilities to describe their properties and requirements at runtime so that a controller instance could not obtain enough information about the current systems state, only deduced information. Accordingly, a description of the components has to be made available at runtime. For component-based approaches a self-description (for hardware and software components) generated out of the design seems promising. But a trade-off between the expressiveness with more potential for self-adaptation and the overhead of a higher complexity for analysis algorithms has to be done.

To address these challenges in realizing self-adaptive automotive embedded systems with self-x properties, a design process is necessary which allows the modeling and the verification of adaptivity while considering the domain-specific requirements. Furthermore, we need a runtime environment which monitors the requirements and constraints specified during design and which enables the dynamic reconfiguration of the system. Before we introduce these concepts in Section 5 and 6, use cases which exploit self-x properties of automobiles are presented in the next section.

4. Use cases for the application of self-x properties in automobiles

By enhancing the automotive software system with the self-x properties as described in Section 2, significant improvements beyond today's state of the art may be realized.

4.1 Resource optimization

A car operates in a continuously changing environment. On the freeway, features like the cruise control system, the lane departure warning system or the adaptive driving speed control are used. While driving in the city, other or modified driver assistance features are needed (e.g. the parking assistant system). The night view assistant, adaptive headlights or the high-beam assistant are only used by night or in cases of restricted view. To reach the optimal utilization of the available resources, individual features have to be used situation-based. Thereby, the required hardware resources are reduced by mutually exclusive features. The situation-based deactivation of unnecessary but simultaneously possible features saves resources (e.g. energy, computing time, etc.) during runtime.

4.2 Fault tolerance

Due to reasons of cost and efficiency, there is almost no redundancy in today's automobiles. The failure of software-based functionalities must be repaired normally by a specialized car repair. In some cases, the failure of an electronic component may lead to the total breakdown of the car. These failures within the car's electric/electronic are very negative experiences for the customers and in worst case may possibly threaten the life of the driver. By enhancing automotive embedded systems with self-healing capabilities, the fault tolerance and the availability of the systems is increased by software without costs for additional hardware resources. For example, the failure of a control unit can be compensated by the dynamic adaptation of the system's structure. Thus, a temporary *emergency operation* of the automotive embedded system is enabled by equipping the system with self-x properties. Life-threatening situations for the driver can be avoided and the satisfaction of the customers can be increased.

4.3 Third party consumer device integration

Today, the replacement of vehicle components, the upgrade of new components (after-market products) within the car repair or the update of the vehicular software may lead to problems because the software versions of specific components may not be compatible with the shipped vehicle software. Furthermore, the user demand for integrating modern consumer devices (e.g. mobile phones, smart phones, PDAs, etc.) into the vehicle is very high. The short lifecycles (especially in comparison to the life-cycles of automobiles) and the diversity of these devices have led to proprietary solutions for connecting consumer devices to the vehicle infotainment system. Enhancing the automotive embedded system by self-configuration enables the seamless, flexible and scalable integration of new software-based features, new hardware components and consumer devices. Thereby, failures due to software versions which are incompatible are eliminated. Based on the autonomous allocation of software components to ECUs, self-configuration reduces the complexity for the system integrator and the effort during the production of the automobile. The error-prone manual assignment of features to hardware platforms and the time-consuming flashing (software deployment) of the ECUs during the end-of-line production can be omitted.

4.4 Partial in-vehicle network operation

Another use case which can be enabled by self-adaptive automotive systems with self-x properties is the partial in-vehicle network operation. In this use case certain parts of the in-vehicle network or single ECUs can be shut down to save resources (e.g. energy) during runtime. This can be done in certain contexts (situations) when all features located in a distinct area of the network are not required or can be substituted by functions running on other platforms. These functions might be started dynamically or for simplicity run as shadow tasks in the background all the time. The potential benefits of a partial in-vehicle network operation of course strongly depend on the mapping of software components to the ECUs. For an optimal allocation, with respect to the partial in-vehicle network operation, the distribution should cluster functionality which is and is not used in the same context. Self-x properties may improve the partial in-vehicle network operation by dynamically reallocating software components to shut down even more parts of the network.

5. Designing automotive embedded systems with self-x properties

Nowadays software development in the automobile area has been dominated by its traditional development of mechanical components, as it has been practiced for the last decades. With the growing number of automobile features realized mainly in software, the design process is becoming more and more challenging. For managing the complexity of distributed embedded systems like automotive electronic systems a specialized software development process is necessary which allows the abstraction and realization of single system components and the whole system. Therefore, the description and the description language are a critical factor how well - in terms of how close to the reality - the system can be modeled on different layers of abstraction. In a distributed adaptive system with self-x properties - beneath the static description - the dynamic description in particular is of great importance.

An architecture of a software system is generally described by an *Architecture Description Language*. In the automobile domain several efforts for the system modeling are undertaken. EAST-ADL (Electronics Architecture and Software Technology - Architecture Description Language) (Cuenot et al., 2008) as a domain-specific architecture description language is a promising standard for the seamless automotive architecture design. On the Implementation Level it also targets the component-based architecture AUTOSAR (AUTOSAR Consortium, 2010) allowing an integration with this standard. In our approach we foresee to utilize EAST-ADL as basis for describing an automotive electronic system enhanced with self-x properties. EAST-ADL allows the design of static automotive systems based on UML (EAST-ADL2, 2010), but for adaptive systems with self-x properties it has to be enhanced, e.g. by considering dynamic behavior at runtime. Additionally defined attributes are modeled to specify the runtime variability of the EAST-ADL system components. Thereby, for example self-configuration and self-healing can be supported by annotating components to be reconfigurable at runtime. Thus, they can be instantiated in a self-configuration or self-healing process.

The design space of runtime adaptive systems with self-x properties increases exponentially in terms of possible runtime configurations. Thus, special emphasis has to be placed on the *validation of the dynamic behavior* in early design phases. This allows an iterative validation of the system and its adaptation behavior leading to find faults early in the development process. By this, the development costs can be decreased as late design changes typically result in drastically increased costs. The designed and validated system has to be executed by a tailored runtime environment as outlined in Section 6. The allowed degree of variability has to be defined in the design to comply with requirements on the system safety. An uncontrolled self-organization is not feasible in safety-related systems as certain requirements need to be met at any time. Especially, the abstraction of the definition of the adaptation is crucial. For the validation of the system and its behavior this should be defined on a rather high level of abstraction. Thereby, the allowed nominal behavior - including the adaptation behavior - can be constrained. On a high level of abstraction so-called features can be modeled representing user-visual functionality. Additional to static features which are present in a product, dynamic features can be defined. These represent adaptive functionality on an abstract level. They contain interdependencies and distinct selection criteria which define their selection at runtime. Derived contexts can be used to select a set of dynamic features with respect to the actual driving situation. Car manufacturers may specify distinct scenarios (e.g. driving situations) in which defined functions of the automobile are necessary.

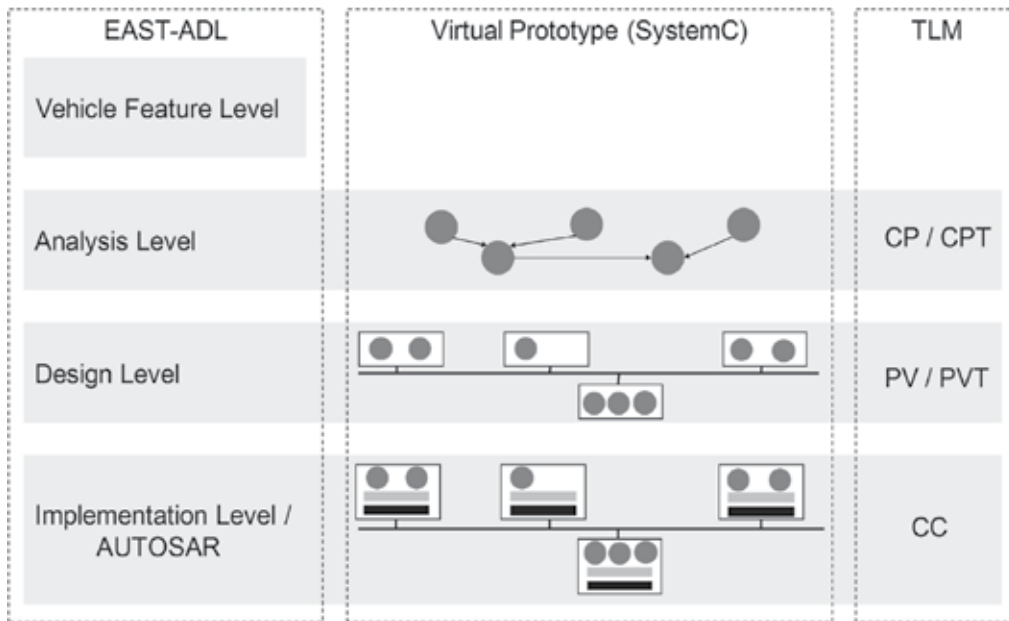


Fig. 2. Integration of SystemC validation on EAST-ADL layers of abstraction

For the iterative validation of the design we use SystemC simulations. SystemC is a standardized system modeling and simulation language which supports Hardware/Software-Co-Design and Co-Simulation. It is specified and promoted by the *Open SystemC Initiative (OSCI)* (Open SystemC Initiative (OSCI), 2010) and has been approved by the IEEE Standards Association as IEEE 1666-2005 (IEEE, 2005). Based on the wide-spread programming language C++, SystemC provides artifacts to simulate concurrent processes and an event-driven simulation kernel. It incorporates semantic constructs of hardware description languages (like VHDL and Verilog) and can be used to model the holistic system using plain C++. A stepwise refinement in a top-down design process is realized with the SystemC *Transaction-Level Modeling (TLM)* (Cai & Gajski, 2003) methodology. TLM is a methodology used for modeling digital systems which separates the details of communication among computational components from the details of the computational components. Details of communication or computation can be hidden in early stages of the design and added later. Since the application of SystemC for a simulation-based validation of automotive electronic systems is a promising approach for the design exploration and hardware sizing, it is integrated within our approach for adaptive automotive systems with self-x properties. Therefore, we adopt SystemC in the development process with architecture descriptions based on EAST-ADL. An automatic transformation on the layers of abstraction of EAST-ADL to the SystemC TLM levels is performed (see Figure 2) which enables a simulation-based validation. Thereby, architecture models can be iteratively refined and improved in the development process. Through this, adaptive automobile systems can be seamlessly developed and described. The design of such a system including the defined adaptivity has to be realized and enforced at runtime in the end, which is described in Section 6. In the next section we present an automotive example which has been designed with the above methodology and validated by a SystemC simulation.

5.1 Automotive example for validation

As outlined before, in the design of automotive systems with self-x properties the validation of such systems is increasingly challenging. Therefore, we transform EAST-ADL models to executable SystemC models in a prototypical tool-chain. For evaluation purposes an automotive case study (Hardung et al., 2004) has been modeled in EAST-ADL and transformed to SystemC simulations on different levels of abstraction.

The use case is located within the so-called body domain of an automobile and consists of the four features *exterior light*, *direction indication*, *central door locking* and *keyless door entry*. The exterior light feature allows controlling the front and rear lights of the vehicle. The lights can be switched on/off manually or automatically through darkness or rain detected by the rain/light sensor. These inputs are interpreted by the function exterior light control which controls the light units (front and rear). For the direction indication a direction indication switch can be used to signal the turning direction. With the hazard light switch, risky driving situations can be signaled to other road users. Therefore, the direction indication master control informs the direction indication front and rear controls about the designated status of the direction indication lights. These turn the direction indication lights on or off in the front and rear light units. Central door locking allows locking and unlocking all doors simultaneously by using the key in the lock or by radio transmission. A radio receiver signals the information to the central door locking control. This function flashes the direction indication lights for a feedback to the driver and controls the four door locks of the car. An additional feature to the un-/locking of an automobile is the keyless entry. A driver can approach his car with the key in his pocket and the doors will unlock automatically. It can be locked by simply pressing a button on the door handle. Antenna components detect the key in the surrounding and inform the central door locking function which in turn unlocks the doors. With respect to the interaction with exterior light (which gives feedback via the direction indication lights), it does not make any difference whether the doors have been unlocked in a standard way or via the keyless entry. At Analysis Level this use case is modelled in EAST-ADL by so-called *FunctionalDevices* components: *KeylessEntryController*, *CentralDoorLockingController*, *DirectionIndicationMasterController*, *DirectionIndicationFrontController*, *DirectionIndicationRearController* and *ExteriorLightController* as is depicted in Figure 3. The behavior of these functionalities is described as UML opaque behavior of the components (C++ source code). Additionally, behavior can also be modeled with UML Statecharts as a UML based behavior specification. Communication is designed as data flow between the components represented by *FunctionFlowPorts* and *FunctionConnectors*. A SystemC simulation generated from this level includes modules interconnected for each of the above mentioned *FunctionalDevices*. They implement the respective behavior of these modeled components in a thread of the module. A simulation based on the abstract EAST-ADL Analysis Level of the use case was realized. Thus, the interaction of the abstract modeled functionalities can be validated with a simulation-based analysis.

At Design Level the use case is modeled in a Functional Design Architecture (FDA) representing the software parts and a Hardware Design Architecture (HDA) representing the hardware parts of the use case realization. The FDA includes *DesignFunctionTypes* for the software functionalities of the use case and *LocalDeviceManagers* representing the software access to the modeled sensors and actuators. Latter are designed in the HDA together with the hardware platforms (*Nodes*) and the interconnecting *LocalBus*. Components in the FDA are interconnected with *FunctionConnectors* and in the HDA

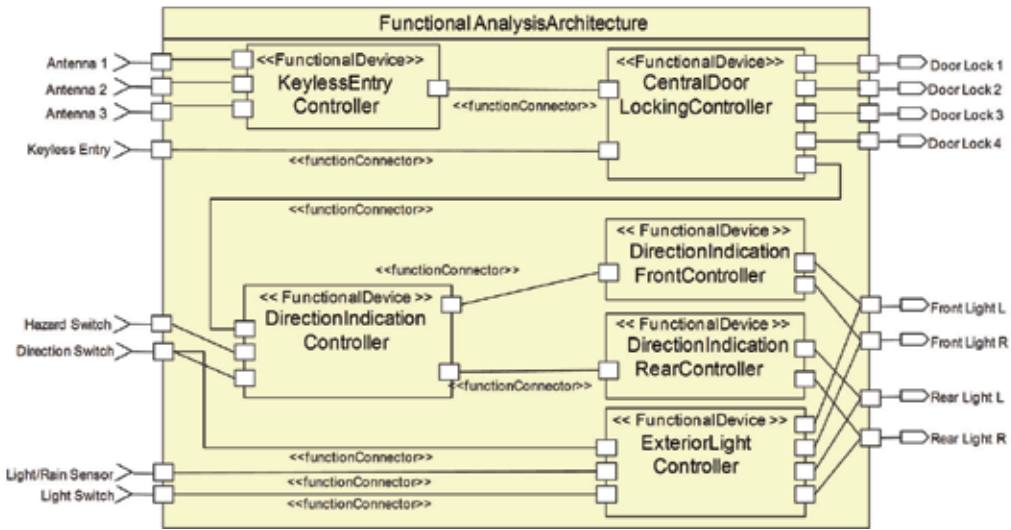


Fig. 3. Composite diagram of the use case at Analysis Level

with HardwareConnectors. Additionally, LocalDeviceManagers exist for each depicted Sensor and Actuator in the Functional Design Architecture which are not explicitly displayed in this figure. The generated SystemC implementation of the use case at Design Level - which models software and hardware explicitly - is depicted in Figure 4. It includes the use of a framework for automotive-specific modules. For example, ECUs and software functions can be included out of a library as specific *sc_module* implementations. As can be derived from Figure 4 the EAST-ADL Design Level components are generated as *sc_modules* representing software functions. These modules are included in another SystemC module which realizes a hardware platform with attached sensors and actuators in form of *sc_modules*. These hardware platforms are interconnected by a module implementation of the

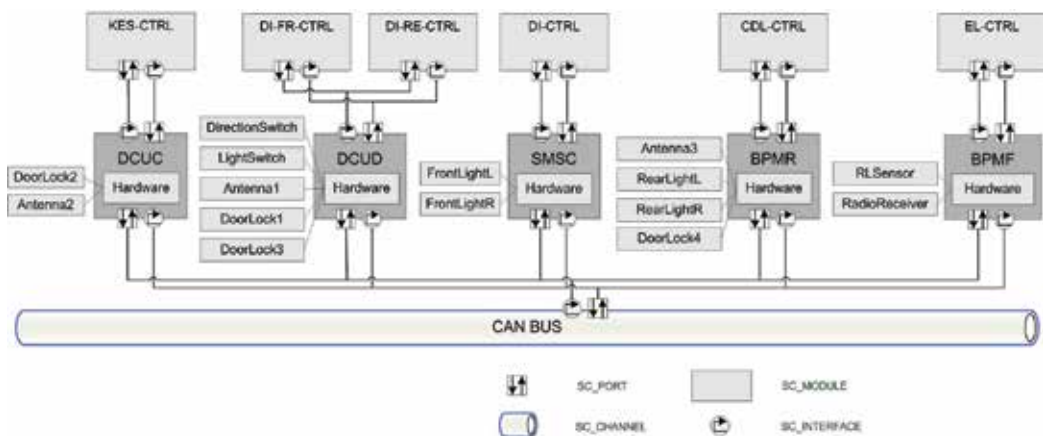


Fig. 4. Overview of the generated SystemC simulation at the Design Level

defined *LocalBus*. SystemC interfaces and channels realize the concrete interconnections of the modules. For example, a specialized type of *sc_interface* (*EcuSw_Iif*) realizes the communication between software functions and ECU modules.

The introduced transformation is realized in a prototypical *toolchain* which integrates into the Eclipse environment as a plug-in. By this, it can easily be used with EAST-ADL models based on UML in Eclipse (e.g. with the Papyrus UML modeling tool which supports EAST-ADL). The transformations itself are implemented as templates of the *Xpand* model-to-text transformation language. They use EAST-ADL models as input and generate the single SystemC files according to the mapping of the languages. Currently, simulations can be generated from the Analysis Level or Design Level. Simple checks allow to examine the conformity for a simulation. Because a generation of incomplete models in early design stages should be possible, the checks are only as strict as needed for generating correct SystemC simulations. This supports the iterative simulation of ADL models in the design process. For the simulation at Design Level we utilize a self-developed framework called *DynaSim* which allows the modeling of an automotive in-vehicle network in SystemC. The generated files refer to SystemC models in the DynaSim library (e.g. ECUs or software functions). By this, a simulation can be performed considering the automotive-specific system environment. We have briefly introduced our approach for the validation of self-x properties in adaptive automotive systems at different design stages on the basis of a case study. Since the designed properties of the models have to be ensured at runtime, the next section focuses on the runtime mechanisms.

6. Enforcing self-x properties during runtime

To enforce self-x properties in automotive embedded systems during runtime, an adopted runtime environment is needed. This must provide mechanisms to manage system resources dynamically and must enable the structural and behavioral adaptation of the automotive software system. Furthermore, it is essential to satisfy all mandatory requirements and constraints which are defined during the design process (see Section 5). Thereby, the correct system behavior can be guaranteed during runtime and unwanted or uncontrolled behavior can be avoided. In our approach this is realized by using a control loop based mechanism according to the AC paradigm. The automotive embedded system is monitored continuously, changes are analyzed and adaptations of the system are planned and executed.

Especially for automotive systems with various requirements and constraints, enabling self-x properties and building such a control loop is a difficult task. Not only functional but also non-functional requirements (e.g. timing, safety) have to be met during runtime. Generally, automotive software features are divided into so-called *Safety Integrity Level (SIL)* according to their safety relevance. Each SIL has different requirements which must be considered by the control loop accordingly. For example, a safety-critical feature (e.g. the airbag control) may not be affected at any time - even during reconfiguration. However, a feature from the infotainment domain (e.g. the hands-free kit) can be deactivated during reconfiguration without life-threatening consequences. The control architecture of the automotive embedded systems must take these requirements into account.

Furthermore, the control architecture of a self-adaptive system which provides safety-relevant applications has to be highly dependable and needs to provide the necessary degree of flexibility to react on changing conditions in an appropriate way. Therefore, managing the whole system by one single control loop is complex and results in a single-point-of-failure.

In order to cope with these requirements, a divide-and-conquer strategy can be applied which is partitioning the system into smaller entities - so-called *clusters*. A cluster is defined as a logic group of software components as well as a sub-set of requirements and system objectives which have to be met by all of software components within the cluster.

The partitioning of the system into different clusters can be based on different criteria:

- Functional dependencies
- Non-functional dependencies
- Physical location of the functions
- Requirements and system objectives

These criteria can be combined in any way in order to provide an optimal segmentation of the automotive software system. In this context, an optimal segmentation means that decisions can be made in a single cluster from a local point of view without interfering other clusters.

Repeated partitioning of the system leads to a hierarchy of clusters, representing the entire automotive software system. Each cluster within this hierarchy is controlled by its own control loop resulting in a hierarchical multi-layered control architecture (cp. Figure 5). This control loop is an external component which is not included in the cluster itself. It is monitoring and controlling the current state of a cluster continuously, so that all requirements and system objectives are satisfied. If one of the defined requirements or system objectives is not met anymore, the affected cluster must be adapted in order to meet all requirements and system objectives again. This is either done by the reassignment of software components to different ECUs (structural adaptation) or by the activation/deactivation of specific software-based features (behavioral adaptation).

The clusters on the lower layers have a local scope with only a few requirements to be satisfied and software components to be controlled. Thereby, an individual implementation of the control loop and a fast reaction on changes is possible. Many clusters have only one system objective, so tailored methods and algorithms can be applied for the observation and control of the cluster. Due to different implementations of the control cycle, the control architecture can be customized individually for the different needs of the automotive software domains. As a drawback, the clusters on the lower layers have a restricted scope and may not be capable of finding a new valid assignment of software components to ECUs.

On higher layers, the number of software components managed by a cluster is increasing, as the number of requirements and system objectives, which have to be met. Thus, on the one hand the chance of finding a new allocation which satisfies all requirements is increased; on the other hand, it is more complex to find one at all.

The *Root Cluster* on the top layer represents the top element in the hierarchy and manages the entire automotive embedded system. But it is only involved in the self-adaptation process as a last instance. The Root Cluster is not aware of the decisions made on the lower clusters.

Within an n -layered control architecture up to n control loops are involved in the process of self-adaptation. In worst case, calculations of the control cycle are performed n times until a new valid allocation is found, resulting in a long response time to changes and a certain overhead. To reduce this overhead, partial solutions of calculations are passed to the next higher layer and will be reused there. But nevertheless, a trade-off is needed between the overhead provided by each new layer added to the control architecture and the advantages gained by it.

Each control loop within the hierarchical multi-layered control architecture consists of four stages, according to the AC paradigm:

Monitoring: Certain parameters of the system must be monitored continuously to detect changes quickly and dependably within the system's environment or within the system itself. To enhance the system with self-healing capabilities, malfunctions must be discovered autonomously. Traditionally, monitoring and fault detection recognize the malfunction of individual components. Thereby, the expected behavior is compared to the actual behavior of the component. If the actual behavior deviates from the expected behavior, a failure is likely. The representation of the expected behavior or the measurement of the actual behavior is very specific and tailored for a certain component. With growing complexity, interdependencies and distribution of the vehicles software features the following problems need to be solved:

- Monitoring the complete system behavior: Although each individual component is working correctly, the overall system exhibits incorrect behavior.
- Monitoring the dynamic system behavior: Adaptive systems may operate in different system configurations. Thus, it is difficult to predict all possible configurations (State Explosion) and to monitor the system with static monitoring techniques.
- Detection of unknown failures: Today's monitoring techniques have limited abilities to discover unknown failures during runtime. This is due to the use of error patterns to identify specific errors in most monitoring mechanisms. Errors which do not match the predefined patterns are not detected.

Analysis: During the analysis stage the present, the desired and the future state of the system must be detected and predicted. Thereby, the analysis stage is closely linked to the monitoring stage, because the observations from the monitoring of the system are directly passed to the analysis. In contrary to the monitoring stage, the analysis of the system uses additional information (e.g. current environmental conditions, predefined system objectives, etc.) for the evaluation of the actual system state. The so-called *Livingstone Model* (Cimatti et al., 2003) may be used for this purpose. It describes a model-based diagnostic mechanism for autonomous spacecrafts with self-configuration capabilities. Therefore, it compares the predicted behavior with the actual behavior and makes statements concerning the needed actions based on the model of the system. In diagnosis, information about which features are needed for the further operation of the system beyond the detection of error causes are made depending on the current environmental conditions of the system and the system's objective (Williams et al., 1996). With these information about the available resources and the features needed in future which are gained from the analysis stage, the next stage (planning) may find a new allocation of software components to ECUs.

Planning: The planning stage creates or composes a set of actions to modify the managed elements of the system. In the context of automotive embedded systems the planning stage determines a new set of features and a new allocation of software components and control units which fulfills all predefined requirements. This allocation problem can be either expressed as *Generalized Assignment Problem (GAP)* (Cattrysse & VanWassenhove, 1990) or as *Constraint Satisfaction Problem (CSP)* (Dinkel & Baumgarten, 2007). Since the allocation problem is a \mathcal{NP} -hard optimization problem, a heuristic approach is needed to solve this problem during runtime. The challenge of the planning stage is to find a trade-off between the computation time and the quality of the solution in order to satisfy the requirements of the automotive domain.

Execution: The execution stage of the control cycle provides mechanisms to execute the plan determined by the planning stage in order to adapt the system. Within the vehicular software system these changes refer to the activation or deactivation of features as well as the migration of software components to different ECUs. In the context of safety-relevant applications, it is important that the normal system behavior is not disturbed during the reconfiguration of the system. The migration of software components can be chosen whether the context of the software component (variables, program stack, etc.), the program code (binary or source code) or both is transferred to another ECU. Thus, for example, a safety-relevant feature may exist on several ECUs. In case of a migration only the current context of this feature must be transferred to another ECU. Other features may be recompiled for the target hardware platform in case of a migration and transmitted as binary code. According to the predefined requirements of a feature, specific techniques for the migration of software components may be used.

As pointed out before, a multi-layered control architecture provides the necessary performance and degree of flexibility to react on changes within the system's environment or within the system itself in an adequate way. Thus, it is possible to supervise these requirements predefined during the design and to adapt the system if one of the requirements is not satisfied anymore. Small clusters with individually tailored control loops can react quickly, while clusters on higher layers have a wider scope and more information to find the optimal configuration of the automotive embedded system. Thus, the chance of finding a new valid allocation of software components to ECUs is better on upper layers. Furthermore, a software component is always supervised by more than one control loop. This avoids single-point-of-failures and increases the dependability of the control architecture. In comparison to other control architectures the hierarchical multi-layered approach reduces the complexity of the self-adaptation process within automotive embedded systems (Zeller et al., 2009). Thus, the hierarchical multi-layered control architecture enables the extension of automotive embedded systems by self-x properties like self-configuration, self-healing and self-optimization.

6.1 Example control architecture for today's automotive embedded systems

Managing today's vehicle software systems, means managing about 270 features, running on nearly 70 different ECUs (Pretschner et al., 2007). These ECUs and various sensors and actuators are interconnected through different network buses.

Nowadays there are three major vehicle network systems (cp. Figure 6): The most common network technology used in vehicles is the *Controller Area Network (CAN)* bus (Robert Bosch GmbH, 1991). CAN is a multi-master broadcast bus for connecting ECUs without central control, providing real-time capable data transmission. FlexRay (FlexRay Consortium, 2005) is a fast, deterministic and fault-tolerant automotive network technology. It is designed to be faster and more reliable than CAN. Therefore, it is used in the field of safety-critical applications (e.g. active and passive safety systems). The *Media Oriented Systems Transport (MOST)* (MOST Cooperation, 2008) bus is used for interconnecting multimedia and infotainment components proving high data rates and synchronous channels for the transmission of audio and video data.

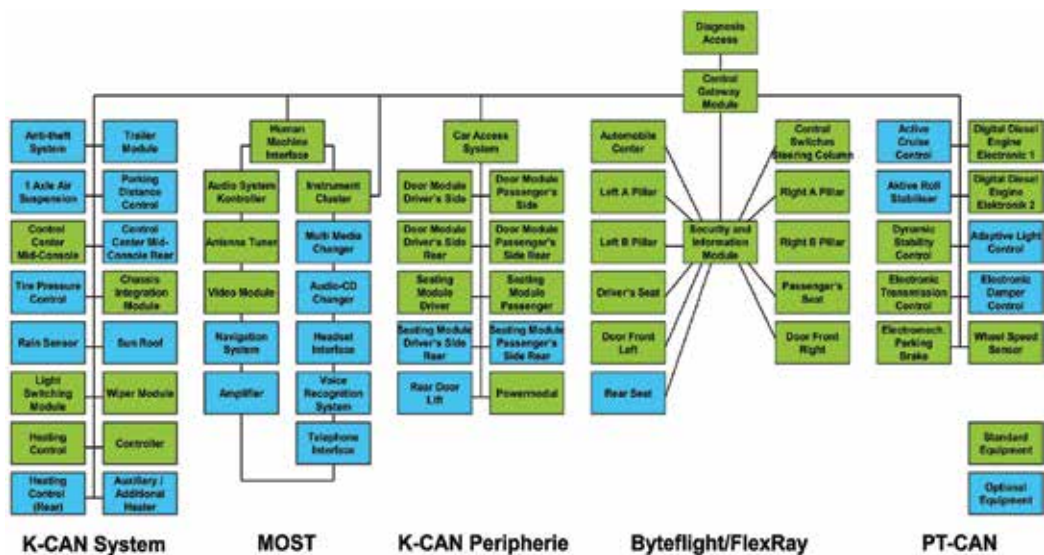


Fig. 6. In-vehicle network topology of a BMW 7-series (Source: BMW AG, 2005)

The vehicle features reach from infotainment functionalities without real-time requirements over features with soft real-time requirements in the comfort domain up to safety-critical features with hard real-time requirements in the chassis or power train domain. Therefore, various requirements and very diverse system objectives have to be satisfied during runtime.

By using a multi-layered control architecture it is possible to manage the complexity and heterogeneity of modern vehicle electronics and to enable adaptivity and self-x properties. To achieve a high degree of dependability and a quick reaction to changes, we use different criteria for partitioning the automotive embedded system into clusters (see Figure 7):

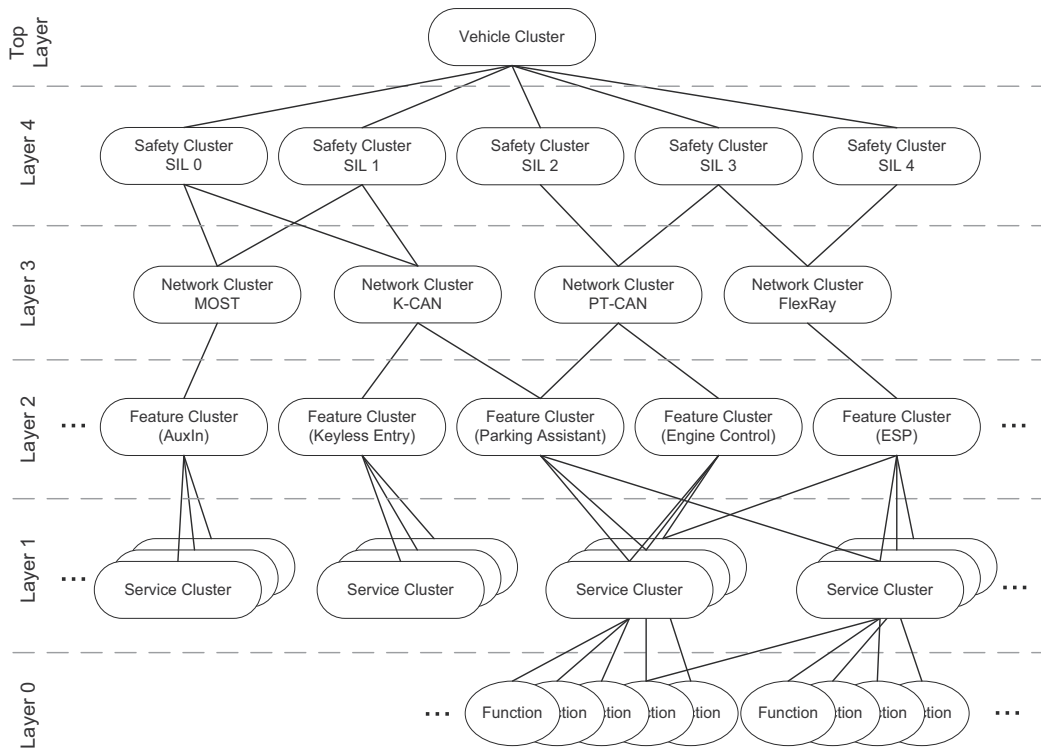


Fig. 7. Example of a hierarchical multi-layered architecture for today's automotive embedded systems

In a first step, the whole system (*Vehicle Cluster* on the top layer) is divided into the five *Safety Integrity Levels (SIL 0-4)* (International Electrotechnical Commission (IEC), 1998), because features with the same requirements on functional safety can be managed using the same algorithms and reconfiguration mechanisms. Nowadays, this classification is more appropriate than the traditional division into different automotive software domains because most new driver-assistance features do not fit into this domain-separated classification anymore.

In a second partitioning, the system is divided into the physical location of the vehicle's features according to the network bus the feature is designed for. This layer is added, so that all features with the same or similar communication requirements (e.g. required bandwidth) and real-time requirements can be controlled in the same way.

On the next layer, each *Network Cluster* is divided into the different features which are communicating using this vehicle network bus. Hence, each feature is controlled by its own control loop, managing its individual requirements and system objectives.

Most features within the automotive domain are composed of several software components as well as sensors and actuators. One example is the Adaptive Cruise Control (ACC) feature which can automatically adjust the car's speed to maintain a safe distance to the vehicle in front. This is achieved through a radar headway sensor to detect the position and the speed of the leading vehicle, a digital signal processor and a longitudinal controller for calculating

the car's deceleration. If the leading vehicle slows down or if another object is detected by the radar sensor, the system sends a signal to the braking system (the actuators) to decelerate. When the road is clear, the system will re-accelerate the vehicle back to the set speed of the cruise control.

On the bottom layer, each feature is decomposed into one or more *services* by which the feature is composed of. For example, the *ACC Feature Cluster* can be decomposed into the radar sensor service, the digital signal processing service, the longitudinal controller service and the engine and braking system services to decelerate. Each sensor, actuator and computation or controlling algorithm is a software-based function represented by a service. Each *Service Cluster* consists of either one or several software components (so-called *functions*) and represents the lowest control layer in our approach. Because services are often used by more than one feature, a service may be part of more than one Feature Cluster.

This hierarchical multi-layered control architecture provides a suitable mechanism for realizing adaptive automotive embedded systems. The requirements specified during design (see Section 5) can be enforced during runtime and self-x properties like self-healing, self-optimization or self-configuration are enabled by a control loop based approach.

7. Conclusion

The growing complexity of automotive software systems is getting more and more unmanageable. Enhancing these systems with self-x properties (e.g. self-healing or self-configuration) by self-adaptation or self-organization may overcome these problem. This increases the flexibility and efficiency of complex software systems at the same time. In this chapter, we described the domain-specific challenges in realizing self-adaptive automotive embedded systems which provide self-x capabilities. To cope with the safety and the real-time requirements of vehicular software systems, the degree of variability must be defined and uncontrolled behavior must be prevented.

This is pursued by an integrated development process which enables the verification and validation of the dynamic system behavior in iterative steps during the design. We presented our approach which incorporates the automotive domain-specific architecture description language EAST-ADL. The focus of the presented work is on enabling the validation through simulation. By this, the system and adaptation behavior realizing self-x properties can be validated. Since the designed requirements have to be met and the constraints have to be enforced at runtime, we introduced a cluster-based methodology for the runtime. For the reduction of the variability and to guarantee the predefined system behavior at runtime the satisfaction of the predefined requirements and constraints is supported by a hierarchical multi-layered control architecture. If any system requirement is not met anymore, the system is adapted to meet the constraints again. Thus, we have shown in this work the challenges of automotive embedded systems with self-x properties and presented our approach for the design and runtime.

8. References

- Anthony, R., Ekelin, C., Chen, D., Törngren, M., de Boer, G., Jahnich, I. et al. (2006). A future dynamically reconfigurable automotive software system, *Proceedings of the "Elektronik im Kraftfahrzeug"*.
- AUTOSAR Consortium (2010). AUtomotive Open Sytem ARchitecture (AUTOSAR).

- <https://www.autosar.org>.
- Cai, L. & Gajski, D. (2003). Transaction level modeling: an overview, *Proceedings of the 1st IEEE/ACM/IFIP international conference on Hardware/software Codesign and system synthesis (CODES+ISSS '03)*, pp. 19–24.
- CAR 2 CAR Communication Consortium (2010).
<http://www.car-to-car.org>.
- Cattrysse, D. & Van Wassenhove, L. (1990). *A survey of algorithms for the generalized assignment problem*, Erasmus University, Econometric Institute.
- Cimatti, A., Pecheur, C. & Cavada, R. (2003). Formal verification of diagnosability via symbolic model checking, *In Proceedings of the 18th International Joint Conference on Artificial Intelligence IJCAI03*, pp. 363–369.
- Cuenot, P., Frey, P., Johansson, R., Lönn, H., Reiser, M., Servat, D., Koligari, R. & Chen, D. (2008). Developing Automotive Products Using the EASTADL2, an AUTOSAR Compliant Architecture Description Language, *Embedded Real-Time Software Conference, Toulouse, France*.
- Czarnecki, K. & Eisenecker, U. (2000). *Generative programming: methods, tools, and applications*, Addison-Wesley.
- Dinkel, M. (2008). *A Novel IT-Architecture for Self-Management in Distributed Embedded Systems*, PhD thesis, TU Munich.
- Dinkel, M. & Baumgarten, U. (2007). Self-configuration of vehicle systems - algorithms and simulation, *WIT '07: Proceedings of the 4th International Workshop on Intelligent Transportation*, pp. 85–91.
- EAST-ADL2 (2010). Profile Specification 2.1 RC3,
http://www.atesst.org/home/liblocal/docs/ATESST2_D4.1.1_EAST-ADL2-Specification_2010-06-02.pdf.
- FlexRay Consortium (2005). The FlexRay Communications System Specifications Version 2.1. <http://www.flexray.com/>.
- Fürst, S. (2010). Challenges in the design of automotive software, *Proceedings of Design, Automation, and Test in Europe (DATE 2010)*.
- Geihs, K. (2008). Selbst-adaptive Software, *Informatik Spektrum* 31(2): 133–145.
- Hardung, B., Kölzow, T. & Krüger, A. (2004). Reuse of software in distributed embedded automotive systems, *Proceedings of the 4th ACM international conference on Embedded software* pp. 203 – 210.
- Hofmann, P. & Leboch, S. (2005). Evolutionäre Elektronikarchitektur für Kraftfahrzeuge (Evolutionary Electronic Systems for Automobiles), *it-Information Technology* 47(4/2005): 212–219.
- Hofmeister, C. (1993). *Dynamic reconfiguration of distributed applications*, PhD thesis, University of Maryland, Computer Science Department.
- Horn, P. (2001). Autonomic computing: IBM's perspective on the state of information technology, *IBM Corporation* 15.
- IEEE (2005). *IEEE Standard 1666-2005 - System C Language Reference Manual*.
- International Electrotechnical Commission (IEC) (1998). *IEC 61508: Functional safety of Electrical/Electronic/Programmable Electronic (E/E/PE) safety related systems*.

- Kephart, J. O. & Chess, D. M. (2003). The vision of autonomic computing, *Computer* 36(1): 41–50.
- McKinley, P. K., Sadjadi, S. M., Kasten, E. P. & Cheng, B. H. (2004). Composing adaptive software, *IEEE Computer* 37(7): 56–64.
- Mogul, J. (2005). Emergent (Mis)behavior vs. Complex Software Systems, *Technical report*, HP Laboratories Palo Alto.
- MOST Cooperation (2008). MOST Specification Rev. 3.0.
<http://www.mostcooperation.com/>.
- Mühl, G., Werner, M., Jaeger, M., Herrmann, K. & Parzyjegl, H. (2007). On the definitions of self-managing and self-organizing systems, *KiVS 2007 Workshop: Selbstorganisierende, Adaptive, Kontextsensitive verteilte Systeme (SAKS 2007)*.
- Müller-Schloer, C. (2004). Organic computing: on the feasibility of controlled emergence, *CODES+ISSS '04: Proceedings of the 2nd IEEE/ACM/IFIP international conference on Hardware/software codesign and system synthesis*, ACM, pp. 2–5.
- Open SystemC Initiative (OSCI) (2010). SystemC,
<http://www.systemc.org>.
- OSEK VDX Portal (n.d.). <http://www.osek-vdx.org>.
- Pretschner, A., Broy, M., Kruger, I. & Stauner, T. (2007). Software engineering for automotive systems: A roadmap, *Future of Software Engineering (FOSE '07)* pp. 55–71.
- Robert Bosch GmbH (1991). CAN Specification Version 2.0.
<http://www.semiconductors.bosch.de/pdf/can2spec.pdf>.
- Robertson, P., Laddaga, R. & Shrobe, H. (2001). Self-adaptive software, *Proceedings of the 1st international workshop on self-adaptive software*, Springer, pp. 1–10.
- Schmeck, H. (2005). Organic computing - a new vision for distributed embedded systems, *ISORC '05: Proceedings of the Eighth IEEE International Symposium on Object-Oriented Real-Time Distributed Computing*, IEEE Computer Society, pp. 201–203.
- Serugendo, G., Foukia, N., Hassas, S., Karageorgos, A., Mostéfaoui, S., Rana, O., Ulieru, M., Valckenaers, P. & Aart, C. (2004). Self-organisation: Paradigms and Applications, *Engineering Self-Organising Systems* pp. 1–19.
- Teich, J., Haubelt, C., Koch, D. & Streichert, T. (2006). Concepts for self-adaptive automotive control architectures, *Friday Workshop Future Trends in Automotive Electronics and Tool Integration (DATE'06)*.
- Trumler, W., Helbig, M., Pietzowski, A., Satzger, B. & Ungerer, T. (2007). Self-configuration and self-healing in autosar, *14th Asia Pacific Automotive Engineering Conference (APAC-14)*.
- Urmson, C. & Whittaker, W. R. (2008). Self-driving cars and the urban challenge, *IEEE Intelligent Systems* 23: 66–68.
- Weiss, G., Zeller, M., Eilers, D. & Knorr, R. (2009). Towards self-organization in automotive embedded systems, *ATC '09: Proceedings of the 6th International Conference on Autonomic and Trusted Computing*, Springer-Verlag, Berlin, Heidelberg, pp. 32–46.
- Williams, B. C., Nayak, P. P. & Nayak, U. (1996). A model-based approach to reactive self-configuring systems, *In Proceedings of AAAI-96*, pp. 971–978.
- Wolf, T. D. & Holvoet, T. (2004). Emergence and self-organisation: a statement of similarities and differences, *Lecture Notes in Artificial Intelligence*, Springer, pp. 96–110.

Zadeh, L. (1963). On the definition of adaptivity, *Proceedings of the IEEE* 51(3): 469–470.

Zeller, M., Weiss, G., Eilers, D. & Knorr, R. (2009). A multi-layered control architecture for self-management in adaptive automotive systems, *ICAIS '09: Proceedings of the 2009 International Conference on Adaptive and Intelligent Systems*, IEEE Computer Society, Washington, DC, USA, pp. 63–68.

4D Ground Plane Estimation Algorithm for Advanced Driver Assistance Systems

Faisal Mufti¹, Robert Mahony¹ and Jochen Heinzmann²

¹*Australian National University*

²*Seeing Machines Ltd.*

Australia

1. Introduction

Over the last two decades there has been a significant improvement in automotive design, technology and comfort standards along with safety regulations and requirements. At the same time, growth in population and a steady increase in the number of road users has resulted in a rise in the number of accidents involving both automotive users as well as pedestrians. According to World Health Organization, road traffic accidents, including auto accidents and personal injury collisions account for the deaths of an estimated 1.2 million people worldwide each year, with 50 million or more suffering injuries (Organization, 2009). These figures are expected to grow by 20% within the next 20 years (Peden et al., 2004). In the European Union alone the imperative need for Advanced Driver Assistance Systems (ADAS) sensors can be gauged from the fact that every day the total number of people killed on Europe's roads are almost the same as the number of people killed in a single medium-haul plane crash (Commission, 2001) with 3rd party road users (pedestrian, cyclist, etc) comprising the bulk of these fatalities (see Figure 1 for proportion of road injuries) (Sethi, 2008). This transforms into a direct and indirect cost on society, including physical and psychological damage to families and victims, with an economic cost of 160 billion euros annually (Commission, 2008). These statistics provide a strong motivation to improve the ADAS ability of automobiles for the safety of both passengers and pedestrians.

The techniques to develop vision based ADAS depend heavily on the imaging device technology that provides continuous updates of the surroundings of the vehicle and aid

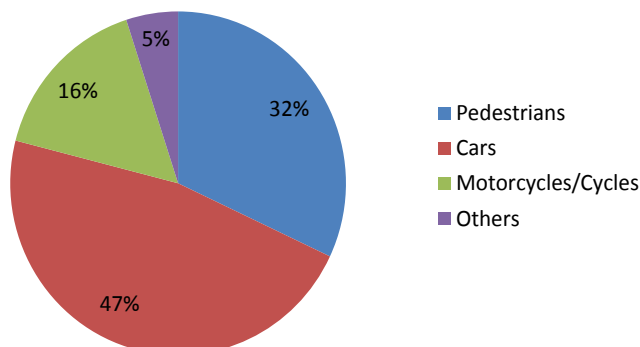


Fig. 1. Proportion of road traffic injury deaths in Europe (2002-2004).

drivers in safe driving. In general these sensors are either spatial devices like monocular CCD cameras, stereo cameras or other sensor devices such as infrared, laser and time-of-flight sensors. The fusion of multiple sensor modalities has also been actively pursued in the automotive domain (Gern et al., 2000). A recent autonomous vehicle navigation competition DARPA (US Defense Advanced Research Projects Agency) URBAN Challenge (Baker & Dolan, 2008) has demonstrated a significant surge in efforts by major automotive companies and research centres in their ability to produce ADAS that are capable of driving autonomously in an urban terrain.

Range image devices based on the principle of time-of-flight (TOF) (Xu et al., 1998) are robust against shadow, brightness and poor visibility making them ideal for use in automotive applications. Unlike laser scanners (such as LIDAR or LADAR) that traditionally require multiple scans, 3D TOF cameras are suitable for video data gathering and processing systems especially in automotive that often require 3D data at video frame rate. 3D TOF cameras are becoming popular for automotive applications such as parking assistance (Scheunert et al., 2007), collision avoidance (Vacek et al., 2007), obstacle detection (Bostelman et al., 2005) as well as the key task of ground plane estimation for on-road obstacle and obstruction avoidance algorithms (Meier & Ade, 1998; Fardi et al., 2006).

The task of obstacle avoidance has normally been approached as by either (a) directly detecting obstacles (or vehicles) and pedestrian or (b) estimating ground plane and locating obstacles from the road geometry. Ground plane estimation has been tackled using methods such as least squares (Meier & Ade, 1998), partial weighted eigen methods (Wang et al., 2001), Hough Transforms (Kim & Medioni, 2007), and Expectation Maximization (Liu et al., 2001), amongst others. Computationally expensive semantic or scene constraint approaches (Cantzler et al., 2002; Nüchter et al., 2003) have also been used for segmenting planar features. However, these methods work well for dense 3D point clouds and are appropriate for laser range data. A statistical framework of RANdom SAMple Consensus (RANSAC) for segmentation and robust model fitting using range data is also discussed in literature (Bolles & Fischler, 1981). Existing work in applying RANSAC to 3D data for plane fitting uses single frame of data (Bartoli, 2001; Hongsheng & Negahdaripour, 2004) or tracking of data points (Yang et al., 2006), and does not exploit the temporal aspect of 3D video data.

In this work, we have formulated a spatio-temporal RANSAC algorithm for ground plane estimation using 3D video data. The TOF camera/sensor provides 3D spatial data at video frame rate and is recorded as a video stream. We model a planar 3D feature comprising two spatial directions and one temporal direction in 4D. We consider a linear motion model for the camera. In order that the resulting feature is planar in the full spatio-temporal representation, we require that the camera rotation lies in the normal to the ground plane, an assumption that is naturally satisfied for the automotive application considered. A minimal set of data consisting of four points is chosen randomly amongst the spatio-temporal data points. From these points, three independent vector directions, lying in the spatio-temporal planar feature are computed. A model for the 3D planar feature is obtained by computing the 4D cross product of the vector directions. The resulting model is scored in the standard manner of RANSAC algorithm and the best model is used to identify inlier and outlier points. The final planar model is obtained as a Maximum likelihood (ML) estimation derived from inlier data where the noise is assumed to be Gaussian. By utilizing data from a sequence of temporally separated image frames, the algorithm robustly identifies the ground plane even when the ground plane is mostly obscured by passing pedestrians or cars and in the presence of walls (hazardous planar surfaces) and other obstructions. The fast segmentation of the obstacles

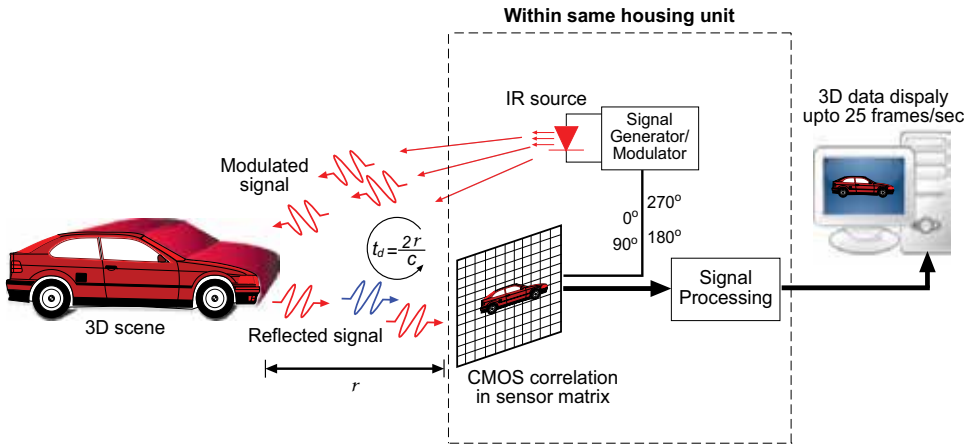


Fig. 2. Basic principle of TOF 3D imaging system.

is achieved using the statistical distribution of the feature and then employing a statistical threshold. The proposed algorithm is simple as no spatio-temporal tracking of data points is required. It is computationally inexpensive without the need of image/feature selection, calibration or scene constraint and is easy to implement in fewest possible steps.

This chapter is organized as follows: Section 2 describes the time-of-flight camera/sensor technology, Section 3 presents the structure and motion model constraints for planar feature, Section 4 describes formulation of spatio-temporal RANSAC algorithm, Section 5 describes application of the framework and Section 6 presents experimental results and discussion, followed by conclusion in Section 7.

2. Time-of-flight camera

Time-of-Flight (TOF) sensors estimate distance to a target using the time of flight of a modulated infrared (IR) wave between the sender and the receiver (see Fig. 2). The sensor illuminates the scene with a modulated infrared waveform that is reflected back by the objects and a CMOS (Complementary metal-oxide- semiconductor) based lock in CCD (charge-coupled device) sensor samples four times per period. With the precise knowledge of speed of light c , each of these (64×48) smart pixels, known as Photonic Mixer Devices (PMD) (Xu et al., 1998), measure four samples a_0, a_1, a_2, a_3 at quarter wavelength intervals. The phase φ of the reflected wave is computed by (Spirig et al., 1995)

$$\varphi = \arctan \frac{a_0 - a_2}{a_1 - a_3}.$$

The amplitude A (of reflected IR light) and the intensity B representing the gray scale image returned by the sensor are respectively given by

$$A = \frac{\sqrt{(a_0 - a_2)^2 + (a_1 - a_3)^2}}{2}, \quad B = \frac{a_0 + a_1 + a_2 + a_3}{4}.$$

With measured phase φ , known modulation frequency f_{mod} and precise knowledge of speed of light c it is possible to measure the un-ambiguous distance r from the camera,

$$r = \frac{c \cdot \varphi}{4\pi f_{\text{mod}}}. \quad (1)$$

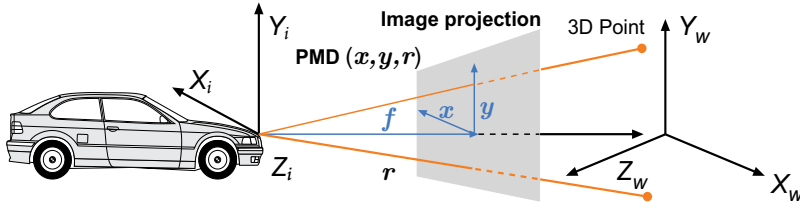


Fig. 3. Time-of-Flight sensor geometry

With a modulation wavelength of λ_{mod} , this leads to a maximum possible unambiguous range of $(\lambda_{\text{mod}}/2)$. For a typical camera such as PMD 3k-S (PMD, 2002), $f_{\text{mod}}=20\text{MHz}$ and with a speed of light c given by 3×10^8 m/s, the non-ambiguous range r_{max} of the TOF camera is given as

$$r_{\text{max}} = \frac{c}{2f_{\text{mod}}} = \frac{3 \times 10^8}{2 \cdot 20 \times 10^6} = 7.5\text{meters.}$$

The sensor returns a range r value for each pixel as a function of pixel coordinates (x, y) as shown in Fig. 3.

The range values are used to compute 3D position $\mathbf{X}(X, Y, Z)$ of the point

$$Z = r(x, y) \cdot \frac{f}{\sqrt{f^2 + x^2 + y^2}}; \quad X = Z \frac{x}{f}; \quad Y = Z \frac{y}{f}, \quad (2)$$

where f is the focal length of the camera.

3. Structure and motion constraints

In the following section we will discuss the motion model and the planar feature parameters essential to derive the spatio-temporal RANSAC formulation for a planar feature.

3.1 Motion model

Consider a TOF camera moving in space. Let $\{i\}$ denote the frame of reference at time stamp i , $1 \leq i \leq n$, attached to the camera. Let $\{W\}$ denote the fixed world reference frame. The rigid body transformation

$${}^W_i\mathcal{M} : \mathbb{R}^3 \rightarrow \mathbb{R}^3; \quad \mathbf{X}_i \mapsto \mathbf{X}_W := {}^W_iR\mathbf{X}_i + {}^WT_i \quad (3)$$

is defined as the coordinate mapping from frame $\{i\}$ to world frame $\{W\}$ with rotation $({}^W_iR)$ and translation $({}^WT_i)$ respectively. Let $\bar{\mathbf{X}} \in \mathbb{R}^4$ denote the homogenous coordinates of $\mathbf{X} \in \mathbb{R}^3$, then the transformation (3) in matrix form is given by

$${}^W_i\bar{\mathcal{M}} : \mathbb{R}^4 \rightarrow \mathbb{R}^4; \quad (4)$$

$$\bar{\mathbf{X}}_W = \begin{bmatrix} \mathbf{X}_W \\ 1 \end{bmatrix} = \begin{bmatrix} {}^W_iR & {}^WT_i \\ 0 & 1 \end{bmatrix} \begin{bmatrix} \mathbf{X}_i \\ 1 \end{bmatrix} = {}^W_i\bar{\mathcal{M}}\bar{\mathbf{X}}_i. \quad (5)$$

Let ${}^i_j\bar{\mathcal{M}}$ be the rigid body mapping from frame $\{j\}$ to frame $\{i\}$ then,

$${}^i_j\bar{\mathcal{M}} = {}^i_W\bar{\mathcal{M}} {}^W_j\bar{\mathcal{M}} = ({}^i_W\bar{\mathcal{M}})^{-1} {}^W_j\bar{\mathcal{M}}.$$

Hence

$${}^i_j\bar{\mathcal{M}} = \begin{bmatrix} ({}^i_WR^\top)({}^W_jR) & ({}^i_WR^\top)({}^W_jT_j - {}^WT_i) \\ 0 & 1 \end{bmatrix}. \quad (6)$$

3.2 Equation of planar feature with linear motion

Let P be a 2D planar feature that is stationary during the video sequence considered. Let $\eta_i \in \{i\}$ be the normal vector to P in frame $\{i\}$, then η_i is a direction that transforms between frames of reference as

$$\eta_i = {}^jR^T \eta_j = {}^iR \eta_j. \quad (7)$$

The homogenous coordinates of a direction (free vector) such as η_i are given by

$$\bar{\eta}_i = \begin{bmatrix} \eta_i \\ 0 \end{bmatrix} \in \mathbb{R}^4, \quad {}^j\mathcal{M}\bar{\eta}_i = {}^i\mathcal{M} \begin{bmatrix} \eta_i \\ 0 \end{bmatrix} = \begin{bmatrix} {}^jR\eta_i \\ 0 \end{bmatrix} = \bar{\eta}_j. \quad (8)$$

Let $\mathbf{X}_i, \mathbf{X}_j \in P$ be different elements of the planar feature P observed in different frames $\{i\}$ and $\{j\}$. Note that $\mathbf{X}_i \neq {}^j\mathcal{M}\mathbf{X}_j$ in general as the points do not correspond to the same physical point in the plane, however, $(\mathbf{X}_i, {}^i\mathcal{M}\mathbf{X}_j)$ must both lie in P in $\{i\}$. Since η_i is a normal to P in $\{i\}$, one has

$$\langle (\bar{\mathbf{X}}_i - {}^i\mathcal{M}\bar{\mathbf{X}}_j), \bar{\eta}_i \rangle = 0. \quad (9)$$

Thus

$$\begin{aligned} & \left\langle \begin{bmatrix} \mathbf{X}_i \\ 1 \end{bmatrix} - \begin{bmatrix} ({}^WR^T)({}^jR)\mathbf{X}_j + ({}^WR^T)({}^WT_j - {}^WT_i) \\ 1 \end{bmatrix}, \begin{bmatrix} \eta_i \\ 0 \end{bmatrix} \right\rangle = 0 \\ & \langle \mathbf{X}_i - ({}^WR^T)({}^jR)\mathbf{X}_j - ({}^WR^T)({}^WT_j - {}^WT_i), \eta_i \rangle = 0 \\ & \langle \mathbf{X}_i - ({}^WR^T)({}^jR)\mathbf{X}_j, \eta_i \rangle - \langle ({}^WR^T)({}^WT_j - {}^WT_i), \eta_i \rangle = 0 \\ & \langle \mathbf{X}_i - \mathbf{X}_j, ({}^jR)({}^iR^T)\eta_i \rangle - \langle ({}^WT_j - {}^WT_i), ({}^iR)\eta_i \rangle = 0. \end{aligned} \quad (10)$$

Let $V \in \{W\}$ denote the linear velocity then the rigid body dynamics for a moving body (an automotive) is modelled by

$$\begin{aligned} \dot{T} &= V; \quad T(0) = T_1 \\ \dot{R} &= \hat{\omega}R; \quad R(0) = R_1, \end{aligned} \quad (11)$$

where $\omega \in \{W\}$ is the angular velocity and $\hat{\omega} \in \mathbb{R}^{3 \times 3}$ denote the skew symmetric matrix that corresponds to vector cross product operation in 3D.

Assumption: We assume that the angular velocity ω of the camera is parallel to $\eta \in \{W\}$, the normal to the ground plane at all times and the translation velocity V in the direction normal to the ground plane is constant such that

$$\eta \times \omega = 0 \quad \text{and} \quad \langle V, \eta \rangle = \text{constant}, \quad (12)$$

where \times represents a cross product between two vectors. For normal motion of a vehicle, roll and pitch rotations are negligible compared to yaw motion associated with angular velocity of the turning vehicle Gracia et al. (2006) and corresponds to common ground-plane constraint (GPC) Sullivan (1994) (see Figure 4).

In real environments for motion captured at nearly video frame rate, the piecewise linear velocity along the normal direction can be assumed constant as evident from the experiments

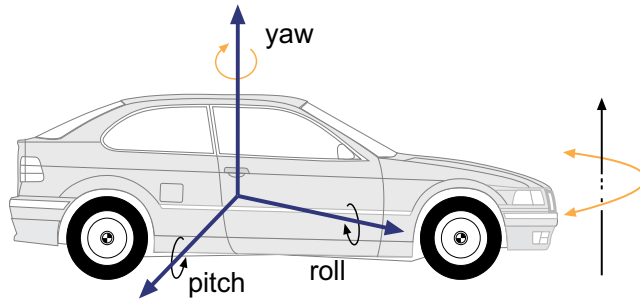


Fig. 4. Vehicle with roll, pitch and dominant yaw motion

in Section 4. This is to be expected in the case where the camera is attached to a vehicle that moves on a plane P , precisely the case for the automotive example considered. In practice, this degree of motion is important to model situations where the car suspension is active and is also used to identify non-ground features that the vehicle may be approaching with constant velocity.

As a consequence of (12)

$$\omega = s(t)\eta \in \{W\}; s : \mathbb{R} \rightarrow \mathbb{R} \text{ in time } t. \quad (13)$$

Following (13) one can re-write (11) as

$$\dot{R} = s(t)\hat{\eta}R; R(0) = R_1.$$

Therefore the continuous rotation motion $R(t) : \mathbb{R} \rightarrow SO(3)$ for the automobile trajectory is expressed as

$$R(t) = \exp(\theta(t_i)\hat{\eta})R_1; \theta(t_i) = \int_0^{t_i} s(\tau)d\tau \quad (14)$$

where t_i time is at frame $\{i\}$ and

$${}_i^W R = R(t_i).$$

By definition ${}_i^W R\eta_i = \eta$ and hence,

$$\begin{aligned} \eta_i &= {}_i^W R^\top \eta \\ &= R_1^\top \exp(\theta(t_i)\hat{\eta})^\top \eta \\ &= R_1^\top \eta = \eta_1 \end{aligned} \quad (15)$$

Using (15), we can re-write (10) as

$$\langle \mathbf{X}_i - \mathbf{X}_j, \eta_1 \rangle - \langle {}^W T_j - {}^W T_i, \eta_1 \rangle = 0. \quad (16)$$

We assume the frames are taken at constant time interval δt and hence $t_i = \delta t(i-1) + t_1$. Since $\langle V, \eta \rangle$ is constant and $t_1 = 0$, the linear translation motion ${}^W T_i$ satisfies

$$\langle {}^W T_i, \eta_i \rangle = \langle V, \eta \rangle \delta t(i-1) + \langle T_1, \eta_1 \rangle. \quad (17)$$

Using assumption (12), define $\alpha \in \mathbb{R}$ to be

$$\alpha = \langle V, \eta \rangle \delta t = \text{constant}. \quad (18)$$

Thus, from (16) and (17), the structure and motion constraint that $\mathbf{X}_i, \mathbf{X}_j$ lie in the plane P can be expressed as

$$\langle \mathbf{X}_i - \mathbf{X}_j, \eta_1 \rangle - \alpha(j - i) = 0. \quad (19)$$

This is an equation for a plane P parameterized by $\eta_1 \in S^2$ ($\|\eta_1\| = 1$) and motion parameter $\alpha \in \mathbb{R}$. An additional parameter, the distance $h \in \mathbb{R}$ of the plane P from the origin in frame $\{1\}$ in the direction η_1 , completes the structure and motion constraints of planar feature. Note that α is the component of translational camera velocity in the direction normal to the planar feature P . The component α will be the defining parameter for the temporal component of the 3D planar feature that is identified in the RANSAC algorithm (see Section 4).

Let $\bar{\mathbf{X}}_i$ be a 4D spatio-temporal coordinate that incorporates both spatial coordinates \mathbf{X}_i and a reference to the frame index or time coordinates i

$$\bar{\mathbf{X}}_i = \begin{bmatrix} \mathbf{X}_i \\ i \end{bmatrix}. \quad (20)$$

Associated with this we define a normal vector that incorporates the spatial normal direction η_1 and the motion parameter α

$$\bar{\eta} = \begin{bmatrix} \eta_1 \\ \alpha \end{bmatrix}. \quad (21)$$

Using these definitions (19) may be re-written as

$$\langle \bar{\mathbf{X}}_i - \bar{\mathbf{X}}_j, \bar{\eta} \rangle = 0. \quad (22)$$

4. Spatio-temporal RANSAC algorithm

In this section we present the spatio-temporal RANSAC algorithm and compute a 3D spatio-temporal planar hypothesis based on the structure and motion model derived in Section 3.2 and a minimal data set.

4.1 Computing a spatio-temporal planar hypothesis

Equation (19) provides a constraint that $(\bar{\mathbf{X}}_i - \bar{\mathbf{X}}_j) \in \mathbb{R}^4$ lies in the 3D spatio-temporal planar feature P in \mathbb{R}^4 with parameters $\eta_1 \in S^2$, $\alpha \in \mathbb{R}$ and $h \in \mathbb{R}$. Given a sample of four points $\{\bar{\mathbf{X}}_{i_1}, \bar{\mathbf{X}}_{i_2}, \bar{\mathbf{X}}_{i_3}, \bar{\mathbf{X}}_{i_4}\}$, one can construct a normal vector $\bar{\eta}$ to P by taking the 4D cross product (see Appendix A)

$$\bar{\eta}_o = \mathbf{cross}_4(\bar{\mathbf{X}}_{i_1} - \bar{\mathbf{X}}_{i_2}, \bar{\mathbf{X}}_{i_1} - \bar{\mathbf{X}}_{i_3}, \bar{\mathbf{X}}_{i_1} - \bar{\mathbf{X}}_{i_4}) \in \mathbb{R}^4, \quad (23)$$

where $\bar{\mathbf{X}}_i \in \{\{1\}, \dots, \{n\}\}$. To apply the constraint $\eta_1 \in S^2$ we normalize $\bar{\eta}_o = (\bar{\eta}_o^x, \bar{\eta}_o^y, \bar{\eta}_o^z, \bar{\eta}_o^t)$ by

$$\bar{\eta} = \frac{1}{\beta} \bar{\eta}_o; \quad \beta = \sqrt{(\bar{\eta}_o^x)^2 + (\bar{\eta}_o^y)^2 + (\bar{\eta}_o^z)^2}. \quad (24)$$

The resulting estimate $\bar{\eta} = (\eta_1, \alpha)$ is an estimate of the normal $\eta_1 \in S^2$ and α , the normal vector component of translation velocity (18).

Note that the depth parameter h can be determined by

$$h_1 = \langle \mathbf{X}_i, \eta_1 \rangle - \alpha(i - 1). \quad (25)$$

However, the parameter h is not required for the robust estimation phase of the RANSAC algorithm and is evaluated in the second phase where a refined model is estimated.

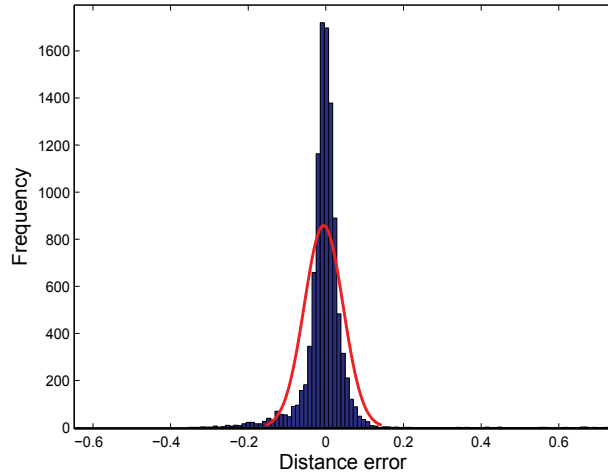


Fig. 5. Statistical distribution of planar feature data points derived from experimental data documented in Section 6.

4.2 Statistical distribution of 4D data points

The spatio-temporal data points that have a probability p of lying in the planar feature are defined as inliers. Due to Gaussian noise in range measurements of TOF camera, the distance of these inliers from the model (planar feature) have a Gaussian distribution with $\mathcal{N}(0, \sigma)$ as shown in Fig. 5.

As a consequence, the point square distance a_{\perp}^2 ,

$$a_{\perp}^2 = \langle (\bar{\mathbf{X}} - \bar{\mathbf{X}}_{i_1}), \bar{\mathbf{n}} \rangle^2; \quad \bar{\mathbf{X}} \in \text{all spatio-temporal data points,}$$

of the inliers (Hartley & Zisserman, 2003) from the planar feature associated with the data point $\bar{\mathbf{X}}_i$, have a chi-squared distribution χ^2 . Since we consider a spatio-temporal planar feature, there are three degrees of freedom in the chi-squared distribution. Let $F_{\chi_3^2}$ denote the cumulative frequency of three degree of freedom of chi-squared distribution χ_3^2 then one can define the threshold coefficient q^2 by

$$q^2 = F_{\chi_3^2}^{-1}(p)\sigma^2. \quad (26)$$

Thus, the statistical test for inliers is defined by

$$\begin{cases} \text{inliers} & a_{\perp}^2 < q^2 \\ \text{outliers} & a_{\perp}^2 \geq q^2. \end{cases} \quad (27)$$

In the experiments documented in Section 6, we use a value of $p = 0.95$. In this case the threshold is $q^2 = 7.81\sigma^2$ where σ is determined empirically. Spatial ground plane estimation algorithms using single 3D images (Cantzler et al., 2002; Bartoli, 2001; Hongsheng & Negahdaripour, 2004) are associated with two degree of chi-squared distribution since they lack temporal dimension. As a result the same analysis leads to a threshold of $q^2 = 5.99\sigma^2$ (for $p = 0.95$). The additional threshold margin for the proposed spatio-temporal algorithm quantifies the added robustness that comes from incorporating the temporal dimension along with the data available by incorporating multiple images from the

video stream. This leads to significant improvement in robustness and performance of the proposed algorithm over single image techniques. The resulting spatio-temporal RANSAC algorithm is outlined in Algorithm 1.

5. Application

The planar feature estimation algorithm in 4D is an approach that can be utilized in multiple scenarios with reference to automotive domain. Since the dominating planar feature for an automotive is a road, we have presented an application of the proposed algorithm for robust ground plane estimation and detection.

A constant normal velocity component α (18) helps to detect ground plane due to the fact that piecewise linear velocity in the normal direction of the automotive motion is small and constant over the number of frames recorded at frame rate. Detection of ground plane in spatio-temporal domain provides an added advantage for cases where there is occlusion and single frame detection is not possible. Section 6 presents number of examples for ground plane.

Algorithm 1: Pseudo code Spatio-temporal RANSAC algorithm

Initialization: Choose a probability p of inliers. Initialize a sample count $m = 0$ and the trial process $N = \infty$.

repeat

- a. Select at random, 4 spatio-temporal points $(\bar{\mathbf{X}}_{i_1}, \bar{\mathbf{X}}_{i_2}, \bar{\mathbf{X}}_{i_3}, \bar{\mathbf{X}}_{i_4})$.
- b. Compute the temporal normal vector $\bar{\eta}$ according to (23) and (24).
- c. Evaluate the spatio-temporal constraint (22) to develop a consensus set C_m consisting of all data points classified as inliers according to (27).
- d. Update N to estimate the number of trials required to have a probability p so that the selected random sample of 4 points is free from outliers as (Fischler & Bolles, 1981),

$$N = \log(1 - p) / \log \left(1 - \frac{\text{number of inliers}}{\text{number of points}} \right)^4.$$

until at least N trials are complete

Select the consensus set C_m^* that has the most inliers.

Optimize the solution by re-estimating from all spatio-temporal data points in C_m^* by maximizing the likelihood of the function ϕ

$$\phi(\bar{\eta}, h) = \sum_{\bar{\mathbf{X}} \in C_m^*} (\langle \bar{\eta}, \bar{\mathbf{X}} \rangle - h)^2 \quad (28)$$

$$\mathcal{L}(\phi) = \prod_{\bar{\mathbf{X}} \in C_m^*} \phi(\bar{\mathbf{X}} | \bar{\eta}, h); \quad (\hat{\bar{\eta}}, \hat{h}) = \arg \max_{\bar{\eta}, h} (\mathcal{L}),$$

where we assume a normal distribution in observed depth.

An obstacle detection algorithm can be applied once a robust estimation of planar ground surface is available. In the proposed framework, the algorithm evaluates each spatio-temporal data point and categorizes traversable and non-traversable objects or obstacles. Traversable objects are the points that can be comfortably driven over in a vehicle. We are inspired by a similar method proposed in (Fornland, 1995). The estimated Euclidean distance \hat{d} to the plane for an arbitrary data point $\bar{\mathbf{X}}$ is defined as

$$\hat{d} = \langle \bar{\mathbf{X}}, \hat{\mathbf{n}} \rangle - \hat{h}. \quad (29)$$

Objects (in each frame) are segmented from the ground plane by a threshold τ as

$$\bar{\mathbf{X}} = \begin{cases} \text{Obstacle} & |\hat{d}| \geq \tau_o \\ \text{Traversable object} & |\hat{d}| < \tau_o, \end{cases} \quad (30)$$

where τ_o is set by the user for the application under consideration. This threshold segmentation helps in reliable segregation of potential obstacles. The allowance of larger threshold in inliers for plane estimation makes obstacle detection phase robust for various applications especially for on road obstacle detection.

6. Experimental results and discussions

Experiments were performed using real video data recorded from PMD 3k-S TOF camera mounted on a vehicle with an angle varying between 2° to 20° to the ground. The camera records at approx 20 fps and provides both gray scale and range images in real time. The sensor has a field of view of $33.4^\circ \times 43.6^\circ$. The video sequences depict scenarios in an under cover car park. In particular, we consider cases with pedestrians, close by vehicles, obstacles, curbs/footpaths and walls etc. Five experimental scenarios have been presented to evaluate the robustness of the algorithm against real objects and also compared with standard 3D RANSAC algorithm. The gray scale images shown represent the first and the last frame of video data. It is not possible to have a 4D visualization environment, therefore a 3D multi-frame representation (each data frame represented in different color) provides a spatio-temporal video range data. The estimated spatio-temporal planar feature is represented in frame $\{1\}$. The final solution is rotated for better visualisation.

In the first set of experiments shown in Fig. 6 and Table. 1(sequence 1-4), four different scenarios are presented. The first scenario shows multiple walls at varying level of depth and a ground plane. The algorithm correctly picks the ground plane rejecting other planar features. In the next scenario, a truck in close vicinity is obstructing the clear view but the ground plane has been identified by exploiting the full video sequence of the data. A number of obstacles including cars, wall and a person are visible while the car is manoeuvring a turn in the third scenario. The algorithm clearly estimates actual ground plane. In the fourth scenario the result is not perturbed by passing pedestrians and the algorithm robustly identifies the ground plane. In a typical sequence a 8-10 frame data is enough to resolve a ground plane even in the presence of some kind of occlusion.

In another experiment shown in Fig. 7a (sequence 5 with single frame data), the standard RANSAC algorithm is applied using a single frame data for comparison.

The obvious failure of a standard RANSAC algorithm is due to the bias of planar data points towards the wall. On the other hand, the proposed algorithm has correctly identified the ground surface in Fig. 7b by simply incorporating more frames (10 frames and $|\alpha| = 0.0018$) due to the availability of temporal data without imposing any scene constraint.

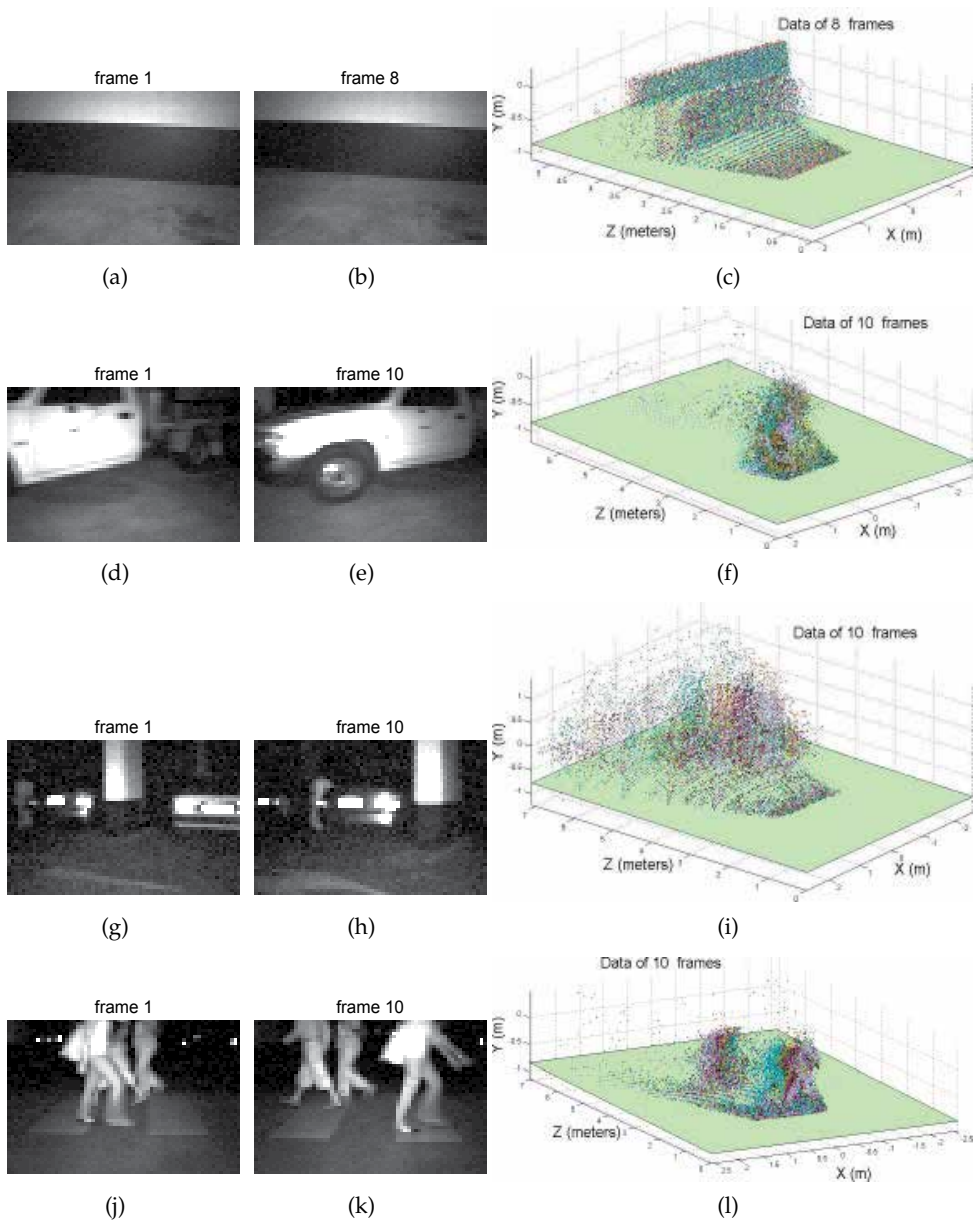


Fig. 6. Experimental data shown in a three column format. First two columns show gray scale image of first and last video frame and third column shows spatio-temporal fit on 4D data. Each frame of 3D data is represented by a different color. (a-b) Gray scale images of a double wall and ground plane at turning (c) Spatio-temporal ground plane fitting of 8 frames at $t=1$. (d-e) A truck in close vicinity (f) Corresponding spatio-temporal ground plane fit of 10 frames. (g-h) Cars, wall and a person as obstacles at turning. (i) Corresponding spatio-temporal ground plane fit. (j-k) Pedestrians. (l) Ground plane fit.

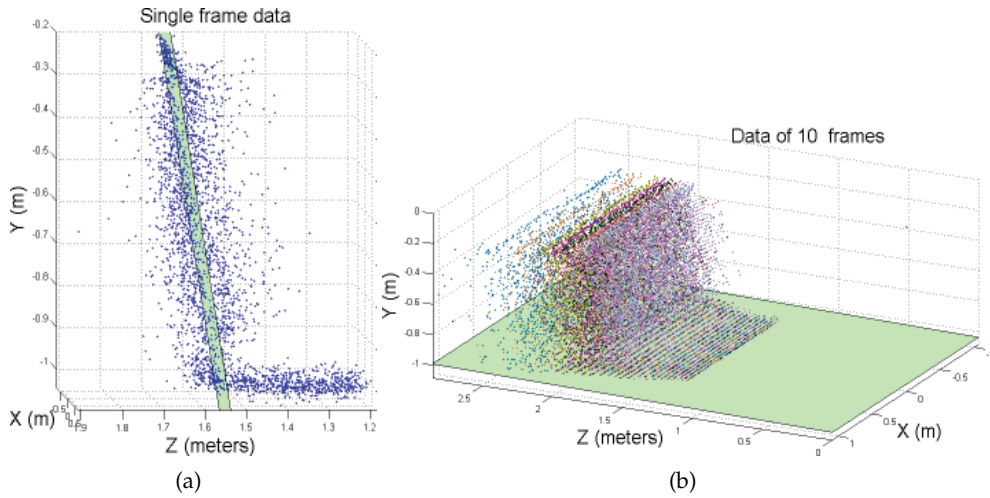


Fig. 7. Using data from sequence 5, (a) Standard RANSAC plane fitting algorithm picks the wall with a single frame data. (b) Spatio-temporal RANSAC algorithm picks the correct ground plane (10 frames).

Obstacle detection algorithm is effectively applied after robust estimation of ground plane. In the experiment shown in Fig. 8, pedestrians are segmented with $\tau_o = 0.1$ by the obstacle detection algorithm after correct identification of ground plane. This threshold implies that objects with a height greater than 10 cm (shown in red color) are considered as obstacle where data points close to ground plane are ignored (traversable objects) with this threshold.

The experimental results are straightforward and show excellent performance. The proposed 4D spatio-temporal RANSAC algorithm's computation cost is associated with picking the normal vector to the 3D planar feature by random sampling (please note that this is the only computation cost associated with 4D spatio-temporal RANSAC algorithm). This eliminates any computation cost associated with pre-processing images unlike conventional algorithms. The experiments were performed on a PC machine with Intel Core 2 Duo 3GHz processor and 2 GB RAM. The algorithm is implemented in MATLAB. The computation cost varies with the number of inliers and the planar surface occlusion in the range data as shown in Fig. 9.

7. Conclusion

Many vision based applications use some kind of segmentation and planar surface detection as a preliminary step. In this paper we have presented a robust spatio-temporal RANSAC framework for ground plane detection for use in ADAS of automotive industry. Experimental

Sequence no	Sequence	No of frames used	$ \alpha $ (m/frame)
1	Double Wall	8	0.0016
2	Moving truck	10	0.0017
3	Multiple objects	10	0.0021
4	Pedestrian	10	0.0020
5	Front wall	10	0.0018

Table 1. Experimental data for ground plane estimation

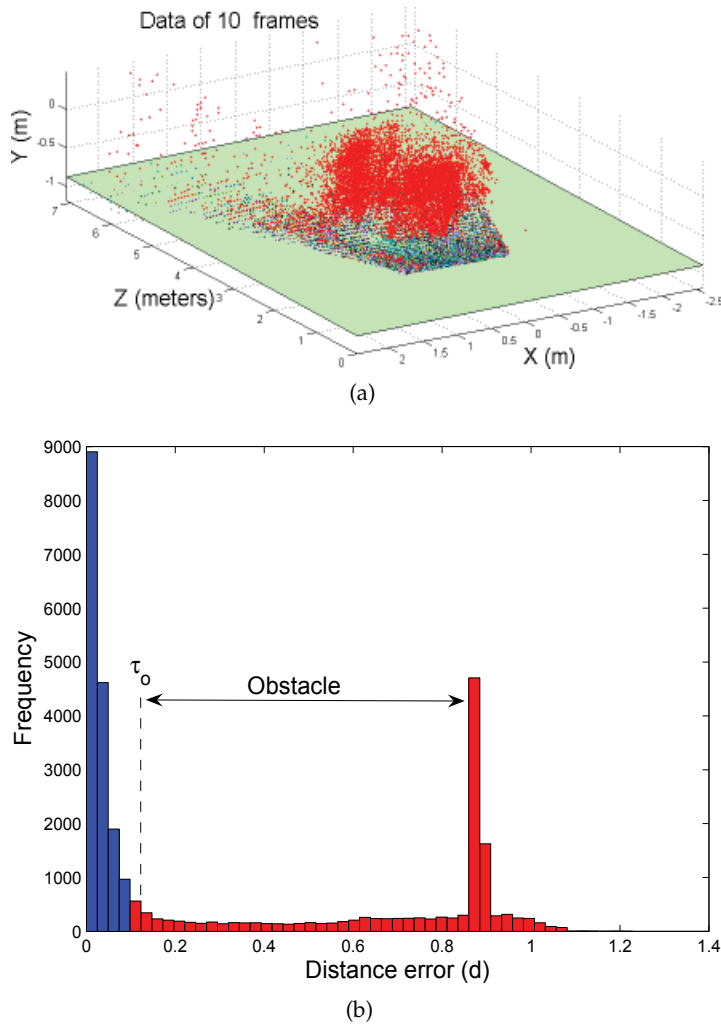


Fig. 8. (a) Potential obstacles and Pedestrians are shown in red color. (b) Histogram of ground plane and obstacles.

results validate the structure and motion model of a 3D spatio-temporal planar feature in 4D. Since the algorithm does not involve any tracking or feature selection, it is highly robust, simple and practical to implement. The algorithm is suitable not only for automotive industry but also in general computer vision applications that satisfy the particular motion constraint ($\eta \times \omega = 0$). This constraint ensures that a spatial planar feature generates a planar feature in spatio-temporal domain. The spatio-temporal constraints increases reliability in planar surface estimation that is otherwise susceptible to noisy data in any algorithm developing a single frame data. Further improvement in computation cost can be achieved through dedicated hardware implementation.

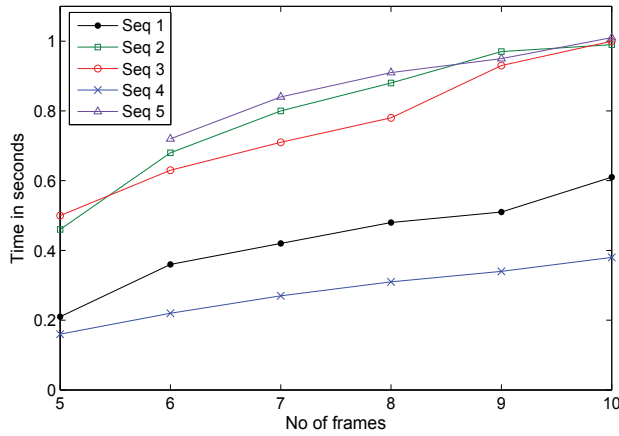


Fig. 9. Performance plots for Spatio-temporal RANSAC for all the sequences.

8. Appendix A

Given an orthonormal basis $\{\mathbf{e}_1, \dots, \mathbf{e}_n\} \in \mathbb{R}^n$ the 'Levi-Civita' (ε) antisymmetric tensor is defined as (Shaw, 1987)

$$\varepsilon_{i,j,\dots,n} = \begin{cases} +1 & \text{if } (i, j, \dots, n) \text{ an even permutation of } (1, 2, \dots, n) \\ -1 & \text{if } (i, j, \dots, n) \text{ an odd permutation of } (1, 2, \dots, n) \\ 0 & \text{if } (i, j, \dots, n) \text{ not a permutation of } (1, 2, \dots, n) \end{cases}$$

The cross product of three vectors $\mathbf{a}, \mathbf{b}, \mathbf{c} \in \mathbb{R}^4$ is defined as

$$\mathbf{cross}_4(\mathbf{a}, \mathbf{b}, \mathbf{c}) = (\mathbf{a} \times \mathbf{b} \times \mathbf{c}) = \sum_{i,j,k,l=1}^{n=4} \varepsilon_{ijkl} a_j b_k c_l \mathbf{e}_i \quad (31)$$

The vector cross product of the three vectors in \mathbb{R}^4 has the following properties (amongst others).

1. *Trilinearity*: For $\alpha, \beta, \gamma \in \mathbb{R}$, $\alpha \mathbf{a} \times \beta \mathbf{b} \times \gamma \mathbf{c} = \alpha \beta \gamma (\mathbf{a} \times \mathbf{b} \times \mathbf{c})$.
2. *Linear dependence*: $\mathbf{cross}_4(\mathbf{a}, \mathbf{b}, \mathbf{c}) = 0$ iff $\langle \mathbf{a}, \mathbf{b}, \mathbf{c} \rangle$ are linearly dependent.
3. *Orthogonality*: Let $\mathbf{d} = \mathbf{a} \times \mathbf{b} \times \mathbf{c} \Rightarrow \langle \mathbf{d}, \mathbf{a} \rangle = \langle \mathbf{d}, \mathbf{b} \rangle = \langle \mathbf{d}, \mathbf{c} \rangle = 0$

9. References

- Baker, C. & Dolan, J. (2008). Traffic interaction in the urban challenge: Putting boss on its best behavior, *Proc. International Conference on Intelligent Robots and Systems (IROS 2008)*, pp. 1752–1758.
- Bartoli, A. (2001). Piecewise planar segmentation for automatic scene modeling, *Proc. IEEE Int. Conf. Computer Vision and Pattern Recognition (CVPR '01)*.
- Bolles, R. C. & Fischler, M. A. (1981). A RANSAC-based approach to model fitting and its application to finding cylinders in range data, *Proc. Seventh Int. Joint Conf. Artificial Intelligence*, pp. 637–643.

- Bostelman, R., Hong, T. & Madhavan, R. (2005). Towards AGV safety and navigation advancement obstacle detection using a TOF range camera, *Proc. 12th Int. Conf. Advanced Robotics (ICAR '05)*.
- Cantzler, H., Fisher, R. B. & Devy, M. (2002). Improving architectural 3D reconstruction by plane and edge constraining, *Proc. British Machine Vision Conf. (BMVC '02)*, pp. 43–52.
- Commission, E. (2001). European transport policy for 2010: time to decide (white paper), *Technical Report COM(2001) 370 final*, Commission of the European Communities, Brussels.
- Commission, E. (2008). CARS 21 mid-term review high level conference conclusions and report, *Technical report*, European Commission, Enterprise and Industry.
- Fardi, B., Dousa, J., Wanielik, G., Elias, B. & Barke, A. (2006). Obstacle detection and pedestrian recognition using a 3D PMD camera, *Proc. IEEE Intell. Vehicles Symp.*, pp. 225–230.
- Fischler, M. A. & Bolles, R. C. (1981). Random sample consensus: A paradigm for model fitting with applications to image analysis and automated cartography, *Communications of the ACM* 24, Issue 6 June 1981: 381–395.
- Fornland, P. (1995). Direct obstacle detection and motion from spatio-temporal derivatives, *Proc. 6th Intl. Conf. Comp. Anal. of Images and Patterns*, pp. 874–879.
- Gern, A., Franke, U. & Levi, P. (2000). Advanced lane recognition-fusing vision and radar, *Proc. IEEE Intelligent Vehicles Symposium IV 2000*, pp. 45–51.
- Gracia, G. A., Jimenez, F., Paez, J. & Narvaez, A. (2006). Theoretical and experimental analysis to determine the influence of the ageing process of the shock-absorber on safety, *Int. J. Vehicle Design* 40(1/2/3): 15–35.
- Hartley, R. & Zisserman, A. (2003). *Multiple View Geometry in Computer Vision*, Cambridge University Press, chapter Estimation-2D Projective Transformation. pp. 118.
- Hongsheng, Z. & Negahdaripour, S. (2004). Improved temporal correspondences in stereo-vision by RANSAC, *Proc. 17th Int. Conf. Pattern Recognition (ICPR '04)*, Vol. 4, pp. 52–55.
- Kim, E. & Medioni, G. Lee, S. (2007). Planar patch based 3D environment modeling with stereo camera, *Proc. 16th IEEE Int. Symp. Robot and Human Interactive Communication*, Jeju island, Korea.
- Liu, Y., R., E., Charabarti, D., Burgard, W. & Thrun, S. (2001). Using EM to learn 3D models of indoor environments with mobile robots, *Proc. 18th Int. Conf. Machine Learning*, pp. 329–336.
- Meier, E. B. & Ade, F. (1998). Object detection and tracking in range image sequences by separation of image features, *Proc. IEEE Int. Conf. Intelligent Vehicles*.
- Nüchter, A., Surmann, H. & Hertzberg, J. (2003). Automatic model refinement for 3D reconstruction with mobile robots, *Proc. Fourth Int. Conf. 3-D Digital Imaging and Modeling (3DIM '03)*, pp. 394–401.
- Organization, W. H. (2009). Global status report on road safety: Time for action, *Technical report*, World Health Organization.
- Peden, M., Scurfield, R., Sleet, D., Mohan, D., Hyder, A. A., Jarawan, E. & Mathers, C. (2004). *World Report on Road Traffic Injury Prevention*, World Health Organization(WHO).
- PMD (2002). PMD tech., <http://www.pmdtec.com>.
URL: <http://www.pmdtec.com>
- Scheunert, U., Fardi, B., Mattern, N., Wanielik, G. & Keppeler, N. (2007). Free space determination for parking slots using a 3D PMD sensor, *Proc. IEEE Intelligent Vehicles Symposium*, pp. 154–159.

- Sethi, D. (2008). Road traffic injuries among vulnerable road users.
- Shaw, R. (1987). Vector cross products in n dimensions, *Int. J. Math. Educ. Sci. Technol.* 18(6): 803–816.
- Spirig, T., Seitz, P., Vietze, O. & Heitger, F. (1995). The lock-in CCD-two dimensional synchronous detection of light, *IEEE J. Quantum Electron.* 31: 1705–1708.
- Sullivan, G. D. (1994). *Real-time Computer Vision*, Cambridge University Press, Cambridge, chapter Model-based vision for traffic scenes using the ground plane constraint, pp. 93–115.
- Vacek, S., Schamm, T., Schroder, J. & Dillmann, R. (2007). Collision avoidance for cognitive automobiles using a 3D PMD camera, *Proc. 6th IFAC Symp. on Intell. Autonomous Vehicles Symp.*
- Wang, C., Tanahashi, H., Hirayu, H., Niwa, Y. & Yamamoto, K. (2001). Comparison of local plane fitting methods for range data, *Proc. IEEE Conf. Computer Vision and Pattern Recognition (CVPR '01)*.
- Xu, Z., Schwarte, R., Heinol, H., Buxbaum, B. & Ringbeck, T. (1998). Smart pixel - photonic mixer device (PMD), new system concept of a 3D-imaging camera-on-a-chip, *5th Int. Conf. Mechatronics and Machine Vision in Practice*, Nanjing, pp. 259–264.
- Yang, A., Rao, S. & Ma, Y. (2006). Robust statistical estimation and segmentation of multiple subspaces, *Proc. Conference on Computer Vision and Pattern Recognition Workshop CVPRW '06*, pp. 99–99.

Part 5

Infotainment and Navigation Systems

The Car Entertainment System

Niels Koch
*Altran GmbH & Co. KG, Munich
Germany*

1. Introduction

In recent years, we spent more and more time in our cars. So it became obvious to implement *Car Entertainment Systems* into the car for comfort and driver information. We can differ between driver information devices and passenger entertainment devices.

Car entertainment began with AM-reception. FM-tuners followed soon, with stereo sound, cassette players and CD-players to entertain passengers. Today we know a number of different analog- and digital broadcasting systems, such as DAB, DMB, DRM, DVB and player standards like MP3, MP4, DVD, BlueRay and many more, which are integrated into the car console. With the variety of different entertainment sources in the car, each passenger in the vehicle may wish for their own program. For this, rear-seat entertainment systems are implemented.

For driver information, modern navigation systems not only help to find the most efficient route, but also give an overview of traffic situation. New concepts of user interaction shall provide comfort and intuitive usage of the devices. So the man-machine-interface is an important marketing feature, on which car manufacture philosophy is mirrored. Touch-screens provide an intuitive operation as information and buttons merge to one device.

This Chapter is structured into different subsections, explaining the tool chain of vehicular entertainment systems from reception of radio waves, demodulation and distribution of signal to the audio and visual end.

We begin with a brief historical overview of car entertainment and show modern installations in contrast. In order to understand the evolution better, we give a list of existing broadcasting standards and explain tuner concepts and diversity reception to combat fading effects for analog and digital broadcasting systems.

When the signal is demodulated it needs to be distributed to the audio subsystem.

The audio system consists of amplifier, equalizer and loudspeakers. We unveil the secrets of high quality sound.

As passengers wish to get their own entertainment source, the distribution of these sources in a rear-seat entertainment system is described.

For driver information, navigation systems offer intelligent route guidance, road status and helpful information on and along the way. In the recent years the development of navigation systems is advancing. So the pro- and contra for portable navigators in contrast to integrated systems are discussed.

2. History of vehicular entertainment

From year 1920 onwards, broadcasting systems became popular. At these days, they were large devices with tube amplifiers, utilizing medium wave and short wave bands. It was common to integrate the radios into the furniture, e.g. sideboards.

Car manufacturers began very soon to install smaller, compact shortwave radios into their vehicles, e.g. Ford, Chevrolet, Daimler [Klawitter, 2005].

In the beginning of the car radio, tube amplified devices were used. These required high voltages and currents to operate. Their exhaust heat was very high. In harsh vehicular environment the robustness of the tubes were low, so the tuner device was installed on rubber bands and was cushioned. With the use of transistors the car radio devices became smaller and more rugged. From year 1950 onwards, technology provided printed circuit boards where modules could be manufactured in high volumes. The invention of small transistors as well as integrated circuits helped that sound broadcasting tuners could emerge rapidly.

A number of companies specialized in vehicular radio systems, some of them still exist. While first car tuners could only receive shortwave (SW) and medium wave bands (MW), the transistorized tuners could also receive ultra-shortwaves (VHF) with frequency modulation. With the utilization of the VHF-band using frequency modulated signals (FM) instead of amplitude modulation (AM), the car radio market began to rise exponentially from 1960 for about 30 years. In the 80th stereo sound entered the broadcasting world and some years after that virtual 3D sound. Due to the fact, that car manufactures began to integrate the radio into a complete car entertainment system, replaceable single devices nearly disappeared from the market by today.

With digital information, digital broadcasting systems were introduced into the market in the late 1990th. Digital Audio Broadcasting (DAB) and Digital Video Broadcasting (DVB) replace analog broadcasting systems steadily all over the world.

With the advent of digital satellite communication, a number of broadcasters started with large coverage broadcasting programs. One of the successors is Sirius, an US satellite broadcaster using low orbit satellites, covering the whole USA with a sheer vast number of programs for all tastes and genres. In Europe, all efforts failed, mainly to the fact that VHF-broadcasting stations are closely clustered providing an exceptionally good coverage. In addition, the number of different countries with different languages makes it difficult to provide a common program in Europe. Nowadays, Ondas Media S.A. is launching the first satellite based multilingual broadcasting system for Europe, currently running tests in Italy, Spain and France.

Mid of the 1990th car manufacturers began to focus on family suitable vehicles, known as Mini-Van for a larger group of people. As kids are quickly bored while driving, the need for more entertainment inside the car was required.

The beginning of rear-seat entertainment was comparably simple. Headphone jacks provided sound entertainment from the CD-player, while the driver could listen to sound broadcasting and use the navigation system independently. With the advent of DVDs, screens were needed to watch movies.

Very soon the request for a more divert entertainment program lead to separate screens in each backseat. Today we find an IP-based media-center connected to touch-screens and consoles, where each passenger can select its program individually or can play games against each other.

3. System overview

The entertainment system of a modern car can be described as a number of entertainment sources organized and embedded into the car interior infrastructure. One group of sources is broadcasted via radio frequency, e.g. sound broadcasting, TV, mobile phone signals. The other group of sources is found inside the vehicle, such as Compact Disc (CD), Digital Video Disc (DVD), MP3-player and more. Sound and video information are decoded and amplified and made audible on a loudspeaker system and made visible on displays.

The most popular entertainment source is the broadcasting sound radio. It offers a number of advantageous features in contrast to video sources. While driving, listening to a sound broadcasting program can be done in parallel, however watching DVD video is unlawful. Separate tuners with antennas attached cover different broadcasting standards and frequency ranges.

The processed sound and video information is then split to the speaker system and to the displays. For better sound sensation an equalization and amplification of the signal can be added before loudspeakers provide the sound.

For CD- or DVD players, a big portion of the existing architecture can be reused. A switch between broadcasting tuners and in-vehicle audio sources offers an efficient way, when only one entertainment source can be attended.

For rear-seat entertainment, where a variety of sources can be accessed individually by each rear-seat passenger, a number of switches must be added. A more clever way is to provide a media center. The handling of the whole entertainment system is done by a number of buttons and switches. A man-to-machine interface (MMI) interacts between devices and human, where a number of settings and selections can be made. In modern cars a sophisticated man-machine-interface provides information and settings. The MMI differs from car manufacturer to another widely, as there are no common rules and a lack of harmonization. Instead, the MMI appearance and handling became a marketing tool to distinguish between car manufacturers and brands.

With the advent of touch-screen displays, information and buttons merge to one device which helps to control functions more intuitively.

Figure 1 displays the architectural overview of a modern entertainment system.

A number of antennas feed the tuners, either for analog or digital broadcasting systems. A switch lets the user select between broadcasting systems and in-vehicle sources. All in common, these sources are demodulated to sound- and video information and made audible on loudspeakers and visible on displays.

4. Entertainment bus-architecture

Modern vehicles comprise various bus systems. The engine- and wheel controls require a very speedy bus to connect all control units to share information. Chassis controller, e.g. doors & windows, are networking with each other on another independent bus. On top of this, the entertainment system is organized in an individual bus. The interconnection of information from one bus-ring to another can be organized by gateways. These gateways filter the required information from one bus, re-code messages - if required - and transmit them to the other bus ring.

A typical bus architectures can be classified in 3 main groups and a variety of mixtures between these.

These main groups are:

- Star Network Architecture
- Ring Network Architecture
- Cascaded Network Architecture

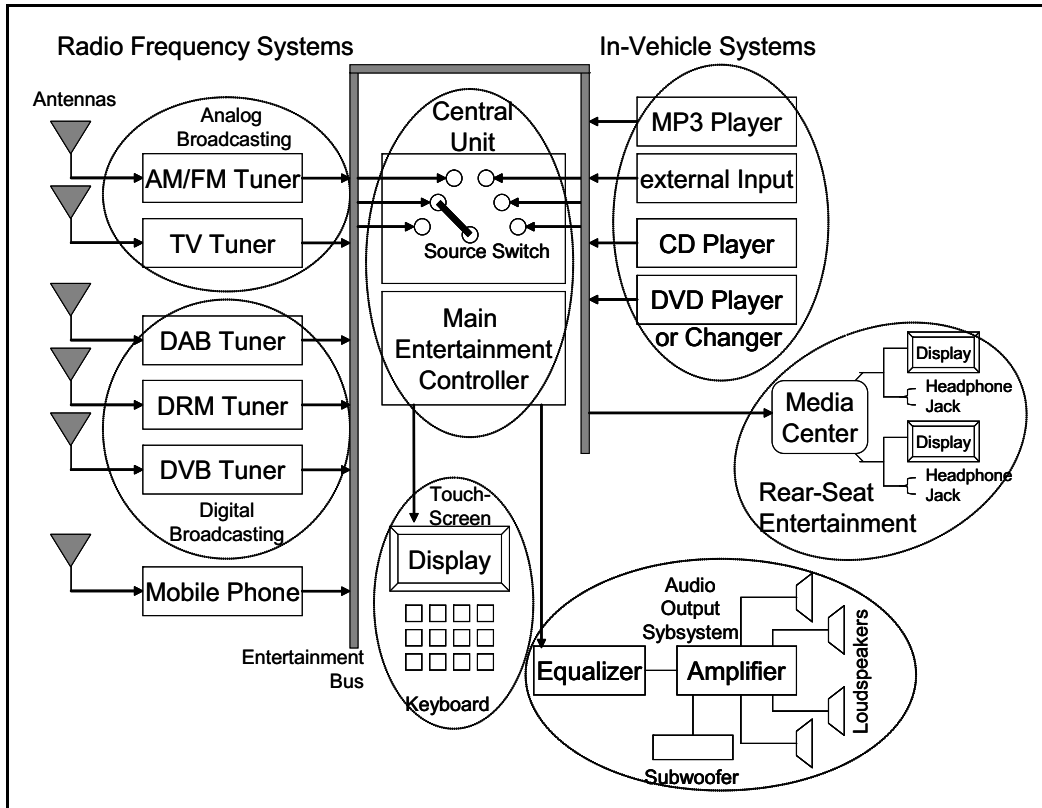


Fig. 1. Architectural overview of modern entertainment system

4.1 Star-network

In a star-network, there is one master controller unit, to which slave controllers are directly connected. Each slave operates on an individual connection to the master. The advantage of this is to provide an independent, dedicated connection. Especially when interference critical messages need to be transmitted, a dedicated connection provides security. In addition, star networks are used when high data rates are required. With the advent of separate dedicated connections full capacity can be used. Furthermore, star networks are used for parallel interactions, where time delays are critical.

The disadvantage is the high number of connections, which may lead to cabling problems in the harness and long routing lengths. With rising length of the cabling, the signal quality decreases due to electric losses, crosstalk and EMC-disturbances. Figure 2 shows an example of star network topology.

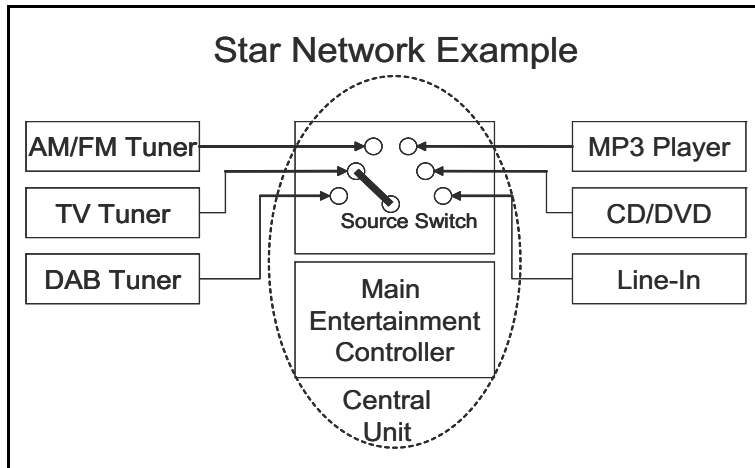


Fig. 2. Entertainment system organized in a star network architecture

4.2 Ring-network

In a ring network, all control units are connected with each other by its neighbouring device. The messages are read and pushed forward to the next device in the ring. All devices in the ring listen to all messages on the bus but react only when their specific address or keyword is recognized. This leads to a certain time delay from the sender to the receiver, depending on the individual processing time inside the control units and the number of devices between sender and receiver address.

When a device recognizes its address and keyword it begins to operate. The processing results are then re-broadcasted into the bus. The organization of the messages inside the bus can be very critical. The bus capacity can only be exploited to a limit of 50%. Beyond this capacity limit the ring bus becomes increasingly instable.

During the development cycle of a car, requirements may change. Often new features must be added. While the ring-bus system runs well and stable with the old configuration, it is an often realized phenomenon that the new setup does not, although only one more function were added. Analyzing the problem in detail reveals timing problems.

To cope with this timing problem, the straight forward countermeasure is to re-sort the bus organization, so that more time is provided between specific messages. However, when capacity is becoming critical, time gaps cannot be added.

Next step would be to reduce the number broadcast messages. This gives capacity but other timing problems occur, as controllers wait for messages or frames to broadcast. A pile of unsent messages inside the controllers may lead to crashes and unwanted effects when FIFO-registers overflow.

Beside the advantage of ring networks where each controller has access to all messages, the inefficient capacity exploration and complicated message organization are the main reason against controller chains in ring structure. Figure 3 shows a ring network topology.

4.3 Cascaded network

Cascaded networks originally can be derived from star networks. Each branch is split and subdivided into arms. In a next tier, each arm can further subdivide into more arms. The

advantage is that each branch with its arms can be organized to a logical group, handled in parallel as well as sequential processing. Cascaded networks are hierarchical organizations in relation to function and competences of devices. Figure 4 shows a cascaded network topology.

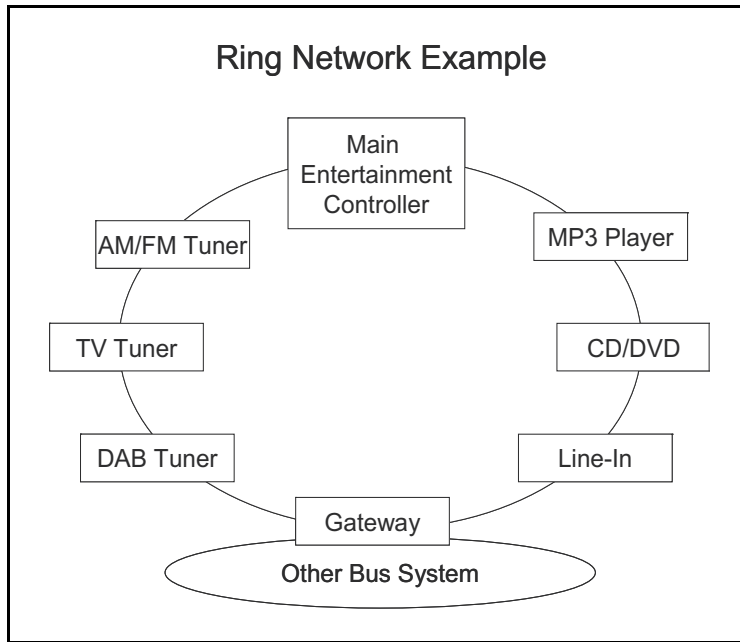


Fig. 3. Entertainment system organized in ring architecture

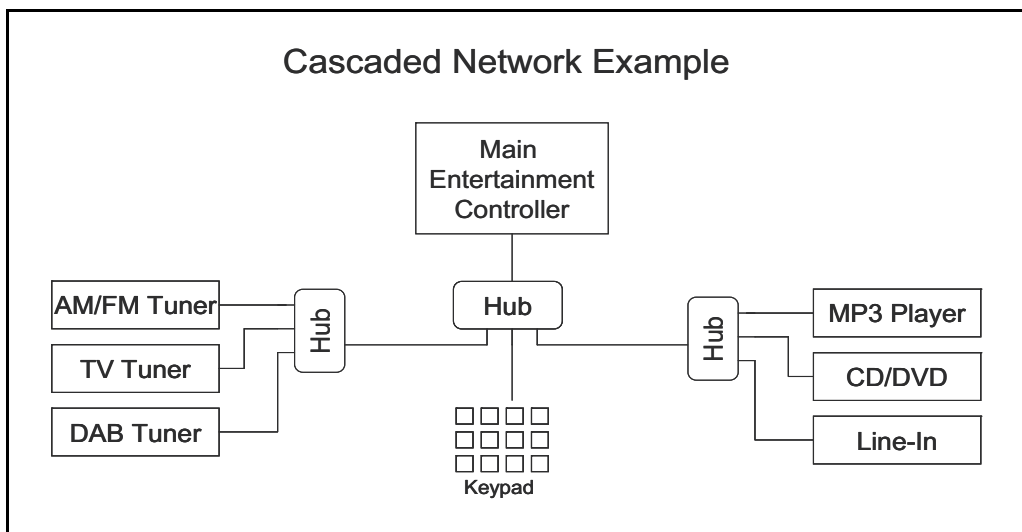


Fig. 4. Entertainment system organized in cascaded network architecture.

4.4 Mixed network topology

Analyzing existing car structures, a mix of network topologies can be found. Beside a master unit with branches (star network), a number of sub-branches can be found forming a logical group (branched network). In addition, some branches are connected to a ring of components (ring network). Figure 6 shows a possible mixed network.

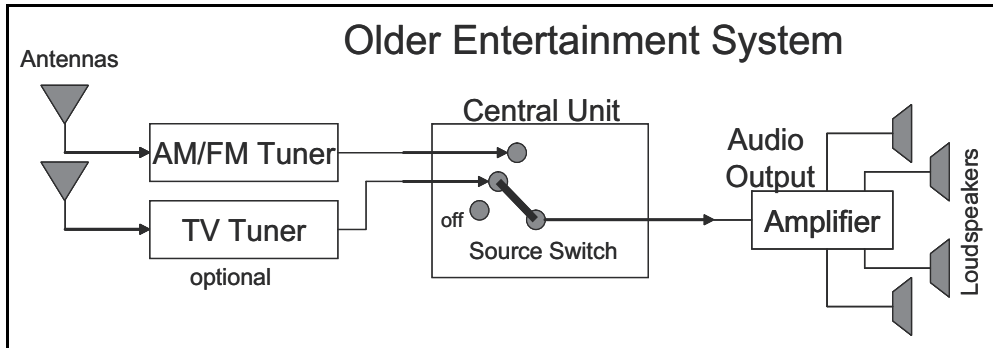


Fig. 5. Typical entertainment system for more than 30 years in the car industry

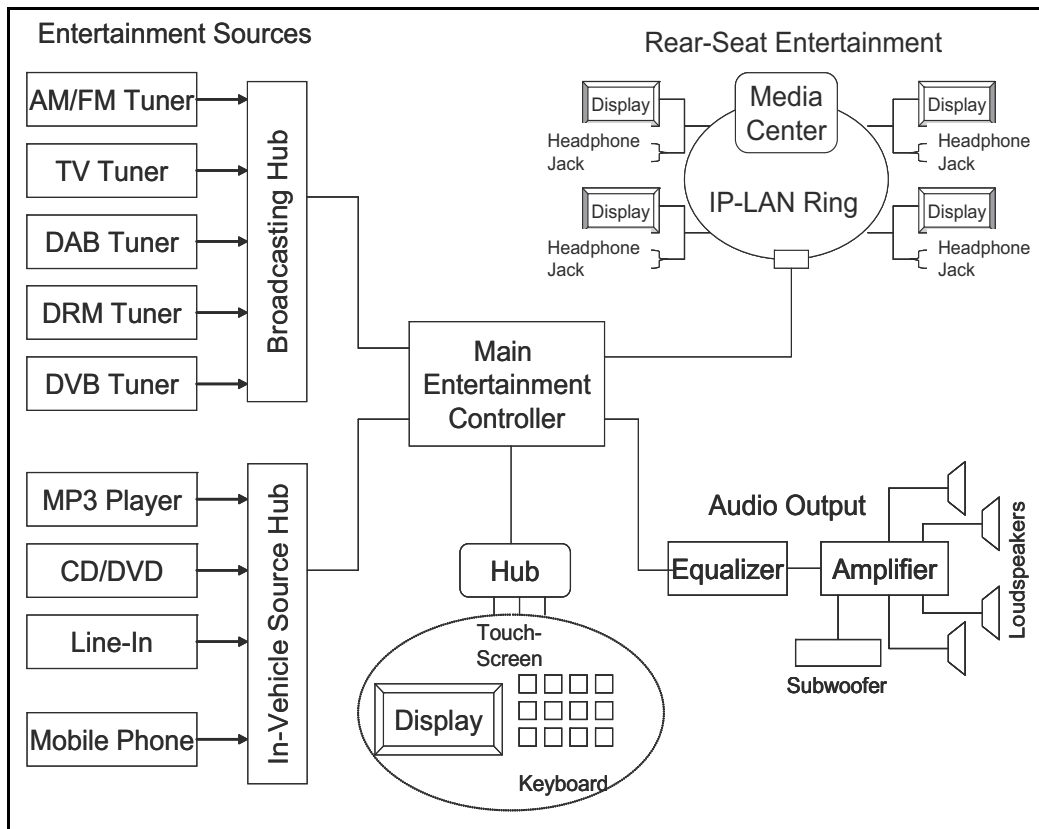


Fig. 6. A modern entertainment system organized around a main entertainment controller, usually installed into the central console of the car.

4.5 Older entertainment systems

For many years, the radio unit was the master, to which loudspeakers were directly connected. We had a classical star network. With the implementation of additional sound amplifiers and multi-way speaker systems, a branched cascaded topology can be seen.

With the introduction of CD/DVD-players or CD-changers as an additional master device, the topology became mixed up. With the number of different receiving systems for analog and digital broadcasting as well as the rising number of entertainment sources, the entertainment system became more and more confusing.

4.6 Modern entertainment system

Desired backward compability and required flexibility for customized options lead to a car-specific entertainment architecture in modern entertainment systems. For this, entertainment devices were organized to logical groups. However, technological development moved on, a higher integration of devices provided compact all-in-one devices, e.g. double tuners with CD-player. It became difficult to identify hierarchy structures, so devices were organized in ring bus structures.

The MOST-bus is a prominent entertainment ring bus with the use of lightwave cables. During the development of this bus system, capacity limits were not an issue. Some years later however, DVD-video signal transmission on the MOST-bus revealed that capacity is insufficient.

Furthermore, flexible additions to other entertainment sources with other standards led to problems. All devices in the chain needed software updates for new addresses and keywords. Testing effort explodes with a rising number of new devices and configurations.

Requirements for flexibility and scalability in addition to rising data rates offered only one way, back to branched star networks. The trend is using USB 2.0 connectivity in a cascaded star connection. As USB 2.0 offers up to 480 Mbit/s data capacity, is easily scalable. USB interconnection can attach a vast number of devices, so it fulfils all requirements. It is future safe for the next decade of years.

Figure 6 displays a modern car entertainment architecture based on USB 2.0 connectivity.

Entertainment sources, such as over-the-air broadcasting systems as well as in-vehicle sources, provide demodulated digital information on one USB-branch to the main entertainment controller.

Depending on the preference and selection of the user, these data can be streamed via the IP-based rear-seat entertainment ring or made audible on the vehicular loudspeaker system for all passengers inside the car.

As USB-connectivity is derived from the computer industry, user interactions by keypads, displays and touch-screens is straight forward and easy to implement.

With the USB-connection it is comparably easy installing external devices, such as mobile phones, mass storage devices and navigation systems.

5. Broadcasting systems

Broadcasting systems reign a long history so backward compability is a major requirement for modern cars. Although the number of mobile shortwave listeners is very limited, each car entertainment system offers shortwave-reception.

Table 1 summarizes the existing broadcasting systems.

System Name	Abbreviation	Frequency Band	Modulation
Long-Short-Medium Wave	LW/MW/SW	172 kHz - 30 MHz	Amplitude Modulation AM
Ultra short Wave	VHF	76 MHz - 109 MHz	Frequency Modulation FM
In-Band On-Channel	IBOC	76 MHz - 109 MHz	Quadratur Phase Shift Keying, QPSK
Digital Broadcasting System	DAB	174 MHz - 210 MHz	Orthogonal Frequency Division Multiplex, OFDM
Digital Broadcasting System with enhanced codec	DAB+	174 MHz - 210 MHz	Orthogonal Frequency Division Multiplex, OFDM
Digital Multimedia Broadcasting	DMB	174 MHz - 210 MHz	Orthogonal Frequency Division Multiplex, OFDM
terrestrial Digital Video Broadcasting	DVB-T	480 MHz - 860 MHz	Orthogonal Frequency Division Multiplex, OFDM
terrestrial Digital Video Broadcasting with enhanced codec	DVB-T2	480 MHz - 860 MHz	Orthogonal Frequency Division Multiplex, OFDM
Satellite Digital Audio Radio System	SDARS	2,30 GHz - 2,33 GHz	Orthogonal Frequency Division Multiplex, OFDM

Table 1. Overview of broadcasting systems

5.1 Short and medium wave bands

Short wave (SW) and medium wave (MW) band provide a worldwide coverage due to ground wave propagation and wave reflection at ionosphere layers in the atmosphere. As these layers are approximately 80 km to 300 km high, a large distance can be bridged. For large-area countries such as Australia, Brazil or Canada just to name a few, a nation-wide broadcasting coverage can easily be done on MW-bands. From history we adopted AM-modulated signals with relatively poor sound quality, compared to today's quality expectations.

5.2 Digital radio mondiale (DRM)

In order to overcome poor sound problems in SW/MW-bands, transmission became digital. Digital Radio Mondiale (DRM) decodes sound information to a digital data stream which is modulated with OFDM and broadcasted on SW/MW-bands. The receiver can decode this data stream and correct transmission errors. The sound quality is intuitively better than analog broadcasting but coverage is found to be reduced. That is mainly due to the fact that digital wireless systems have an abrupt go-nogo border, while analog systems degrade gradually until signals disappear in noise [Koch, 2008].

5.3 VHF-band and UHF-band

Around 1950, VHF-frequency spectrum was utilized in Europe. Radio propagation in 100-MHz-band can reach approximately 30% beyond the optical horizon, so called radio horizon. This leads to a limited coverage of sound or TV broadcasting stations. Depending on transmitter location and radiated transmit power the typical coverage area is about 100 km². For a nation wide broadcasting network, a high number of transmitters must be installed. Especially in hilly terrain uncovered areas occur due to radio shadows. When reception is needed there, filling transmitters are needed. On VHF-band (76-109 MHz) sound broadcasting is transmitted while on UHF-band (400-800 MHz) TV-broadcasting is located. Typically, a dual layer broadcasting network is rolled out in VHF- and UHF-bands. The first layer consists of transmitters with high power on prominent locations, covering a large area. The second layer fills coverage gaps with low-power transmitters.

As each transmitter requires a separate frequency in order not to interfere with each other, the dedicated frequency spectrum is quickly used up. Clever frequency allocation and frequency reuse is needed.

During a journey car passengers want to listen to the same broadcasting station, however receiving frequency changes from time to time according to coverage of transmitters. In year 1988, Radio Data System (RDS) was introduced to solve the problem that car drivers need to search for a new frequency in order to stay tuned to their broadcasting program, when leaving the coverage area of one transmitter to another.

RDS combined a number of functions. The most advantageous and intensely used function is the alternative frequency list (AF). Here a broadcasting station lists their alternative frequency where their program is also transmitted simultaneously. When reception becomes disturbed the tuner scans the alternative frequency list to find an undisturbed reception of the same program.

Other important functions are traffic announcements (TA) and traffic program (TP) to inform about traffic jams and road problems. Beside a number of other functions, text information can be displayed on the radio display, known as radio text, such as broadcasting station name, music title, interpret and many more. Especially Italian broadcasters explored capabilities of radio text functions and began to use it as advertising channel. Today it is quite common using radio text for a variety of information for the listener, e.g. stock exchange prices, weather forecasts or breaking news.

5.4 Digital broadcasting systems

In 1987 development of digital broadcasting systems began and a number of digital transmission standards derived since then. Digital Audio Broadcasting (DAB), former Eureka-147 Project, was the start into digital data processing and digital broadcasting transmission. DAB decodes sound information to a digital data stream which is modulated with 4-PSK-OFDM and broadcasted on VHF-band. The receiver can decode this data stream and correct transmission errors. The sound quality is intuitively better than analog broadcasting. Similar to all other digital wireless systems, DAB reception is experienced having an abrupt go-nogo border, which is often misunderstood that coverage is smaller than analog systems.

One of the benefits of digital broadcasting system is that more programs can be transmitted with one frequency allocation. While in analog broadcasting one radio station used one

frequency, now up to 64 radio stations can be received on one single frequency. This offered new broadcasting capacity for more divert channels covering more genres and clientele. Another benefit of digital transmission is the higher sound quality.

With better coding capabilities using MP3 and MP4 codecs a more efficient transmission could be implemented. Digital Multimedia Broadcasting (DMB) is using MP4 AAC+ codec in contrast to DAB, where MUSICAM codec is implemented. For video transmission, Digital Video Broadcasting (DVB) is used. DVB is similar to DAB and DMB, except that video signal compression H.264 is added to sound compression algorithms and higher intrinsic modulation schemes are used, often 16QAM-OFDM. DVB is successively replacing analog TV-transmitters in Europe.

5.5 IBOC system

In USA, another method of digitalisation is used. Beside the analog modulated signal, an additional digital modulated signal with same content is transmitted, so called in-band on channel (IBOC) signal. Figure 7 displays the spectrum of such an IBOC signal.

Having good reception, the tuner decodes the digital information and provides high-quality sound. Reaching the go-nogo-border of digital transmission, the tuner switches to traditional analog broadcast. The listener may observe a small degradation in sound quality but is still able to follow the program.

In Europe, IBOC was tested in Switzerland in a range limited test environment [Ruoss, 2008]. It is unlikely that IBOC will be introduced in Europe, as VHF-band channel raster of 200 kHz interferes with US-IBOC channel bandwidth requirements of 400 kHz. To fit into the existing channel raster, one of the redundant digital sidebands can be removed. This method is known as FMeXtra and is currently under test in a testbed [Henk,Hamelink, 2008].

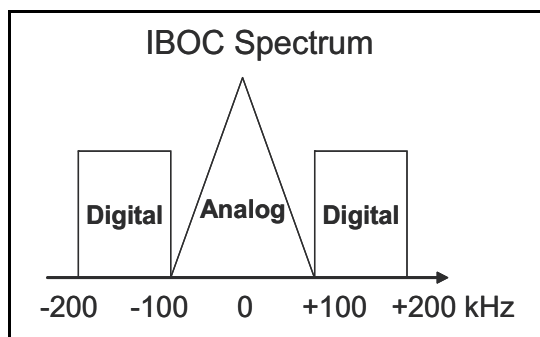


Fig. 7. Spectrum of IBOC system with analog and digital modulation containing identical information

5.6 Satellite Digital Audio Radio System (SDARS)

For large area countries such as Australia, Brazil, Canada, Russia or USA, just to name a few, traditional nationwide terrestrial broadcasting systems are very expensive to install. Using low orbit satellites offers an efficient nationwide coverage. In USA, Satellite Digital Audio Radio Systems (SDARS) in 2.3-GHz-band was implemented and succeeded with a sheer overwhelming number of different programs for all sorts of listeners. Even a monthly fee could not stop listeners to attend SDARS in USA.

6. Tuner concepts

With the invention of transistors small tuners could be made. A transistorized tuner was able to receive LW, MW, SW and VHF bands. Figure 8 shows a block diagram of such a tuner [Klawitter, 2005].

The radio signal from the antenna is bandpass (BP) filtered and amplified before it is mixed to an intermediate frequency (IF) of about 10 MHz. A switch selects between frequency bands and its receiving antennas. In most car radios this switch is identified as AM/FM button. The demodulator transforms the modulated signal to the baseband, where it is lowpass filtered (LP), amplified and the sound given on a loudspeaker.

This principal layout is found in all car tuners with minor modifications.

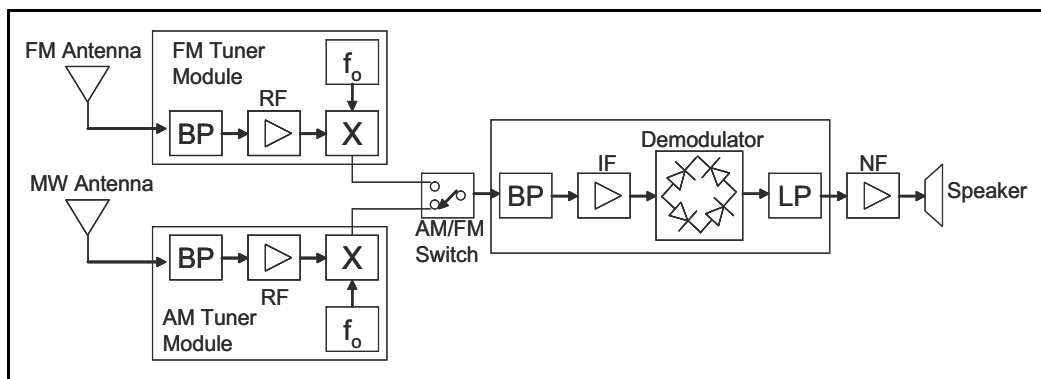


Fig. 8. Block diagram of a single tuner concept for VHF (FM) and MW (AM) reception

6.1 Double tuner concept

When the coverage area of a nationwide VHF-broadcasting station reaches its limit, another frequency must be searched by the listener in order not to change the program. By using two receivers at the same time (double tuner concept), it is possible to receive one program and scan for an alternative frequency, where the same program is distributed at the same time. RDS was used to transmit a list of alternative frequencies (AF) on which the secondary tuner was tuned to. When the signal of the main tuner became out of range, the output was switched to the second tuner which is already tuned to the alternative frequency by then. Now the other tuner searches the AF-list. By this method, continuous listening to a program was established.

Figure 9 shows a block diagram of a double-tuner concept utilizing RDS with alternative frequency selection.

Beside the RDS-Decoder for the AF-list which controls the frequency selection of the tuner modules, a portion of the demodulated signal is split and fed into another branch.

The feedback loop consists of a highpass (HP) filter with threshold-trigger. The HP-filter selects the noise in the audio signal. When a certain limit of noise intensity is reached the tuner selection switch is triggered to the alternative frequency of the other tuner. By this an seamless switching is applied.

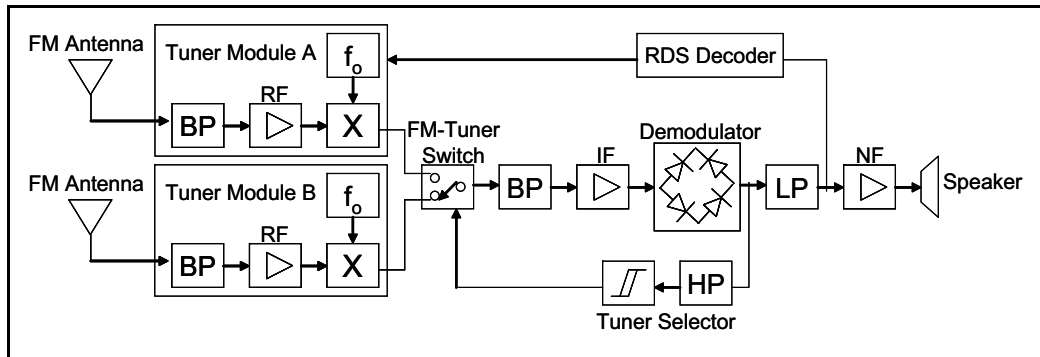


Fig. 9. Block diagram of double tuner concept for VHF (FM) reception utilizing RDS AF

6.2 Diversity - combating fading

In vehicular receiving environments fading of signals occur due to multipath reception. When a radio signal is transmitted, it reaches the receiver on a direct path as well as on reflected paths from buildings, landscape and obstructions, see Figure 10. The reflected paths reach the receiver at different times than the direct path. This leads to superposition of multiple signals of the same content. Signals can add or subtract each other at the receiving zone, leading to a varying loudness impression in amplitude modulated signals and signal dropouts in frequency modulated signal. In digital systems, bit errors can occur.

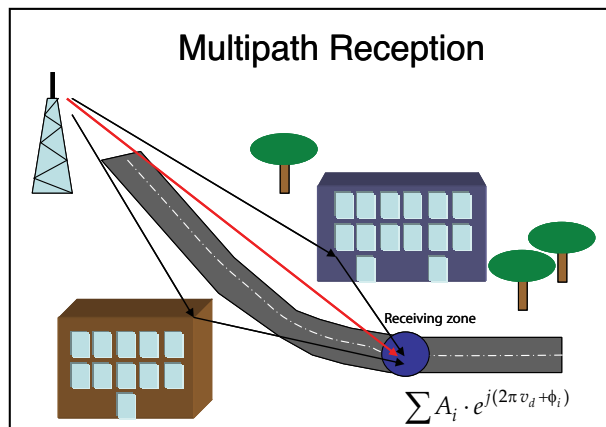


Fig. 10. Principle of multipath environment where transmitter signal is reflected, diffracted and attenuated by environment. At the receiving zone signal paths are summed.

A number of methods were invented to reduce the audible effect of multipath fading. One method is to apply a number of receiving antennas on different positions of the car. Different antennas at different locations are assumed to receive different signal components. This effect is known as spatial diversity. A switch selects the best receiving antenna according to the signal strength and noise level. Figure 11 shows the principle of switching diversity for VHF-FM reception. Another method is to use both tuners in a dual-tuner concept which are connected to individual antennas. Due to the different location of the antennas phase differences occur which are corrected by phase shifters. Then, both phase

corrected receiving signals can be added in-phase and can prevent fading dropouts. This method is known as phase diversity.

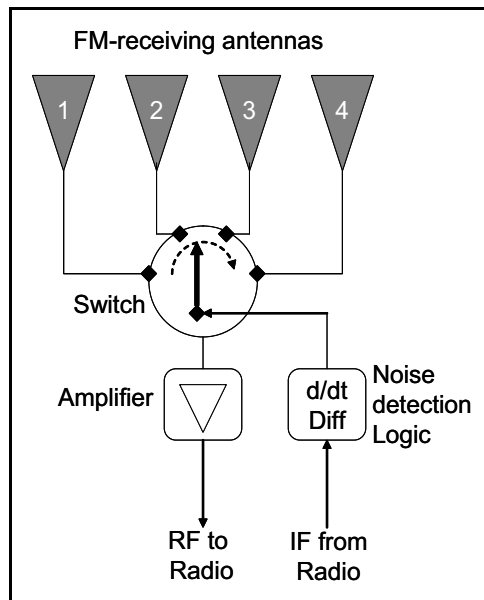


Fig. 11. Principle of switched diversity in modern tuners [Koch, 2008]

In digital broadcasting systems, bit streams can be combined to correct transmission errors. Here, two receivers operate individually but synchronized by internal clocks. The digital data streams are compared with each other and bit errors corrected when necessary. The combined data stream provides a more consistent data rate which results in a better quality of service for the listener. Figure 12 shows a principle bit stream diversity for DAB.

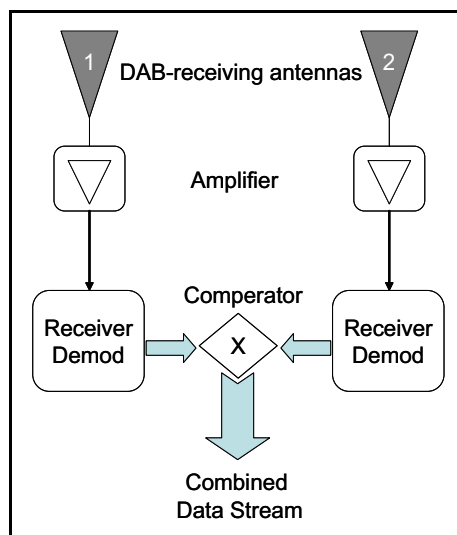


Fig. 12. Principle of bit stream combining method for digital broadcasting systems [Koch, 2008]

6.3 Triple tuner

However, when both tuners are used to receive the actual program in phase diversity configuration, a seamless switch to an alternative frequency is not possible when the coverage border is reached. Beside a number of switching algorithms, where one tuner is temporarily used to scan the AF-list, a more simple method was widely applied.

Adding a third tuner became easy when tuner modules were available as integrated circuits. Two tuners received the broadcasting signal on different antennas and utilizing diversity, while a third tuner scanned in the background for alternative frequencies.

At the end of a product lifecycle, cost reductions are the main focus of the industry. In order to reduce costs, the diversity reception was transferred to the antenna amplifier, where a switch could select the best receiving signal between up to 4 antennas. By this, only one tuner module was needed as main receiver. Each manufacturer followed a different concept, so that a general best-practice is not given.

For background scan of the AF-list a simple secondary tuner was applied by some manufacturers and connected to one of the diversity receiving antennas. As 5-inch or 7-inch color LCD-displays became cheap, all receivable stations could be shown at the same time to the user. So the station list needs to be updated periodically, which is done by an additional tuner. This triple tuner concept was also applied in TV broadcasting receivers.

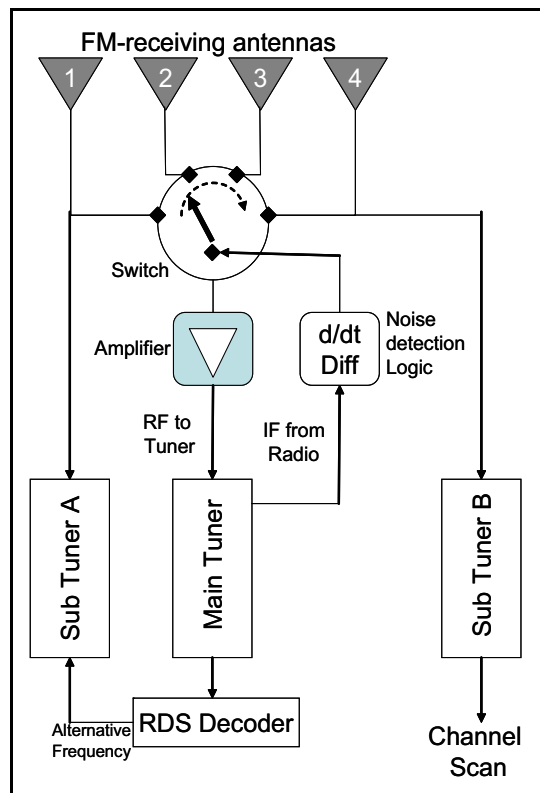


Fig. 13. Principle of switched diversity in modern tuners

6.4 Software defined radio

With the digitalization of the broadcasting world more and more fast working microcontrollers replaced discrete electronic elements and a number of modules were reduced to a single integrated circuit.

Following this trend, it seemed obvious that processing the signal is made in software. Nowadays, Software Defined Radios (SDR) are the big playground of the car electronic manufacturers.

In contrast to traditional tuner concepts, the SDR concept digitizes a frequency band and extracts and demodulates the wanted signals by digital filters and signal processors. With SDR it is possible to create a multi-standard receiver for all existing and upcoming broadcasting standards, analog or digital. It is also possible to exploit multipath reception by applying MIMO concepts.

7. Sound amplifier, equalizer and speakers

One of the important parts in the whole entertainment tool chain is the audio output. Often it is seen that expensive CD/DVD-player equipment is installed but the audio output end is culpable neglected. Figure 14 shows a block diagram of a modern sound system.

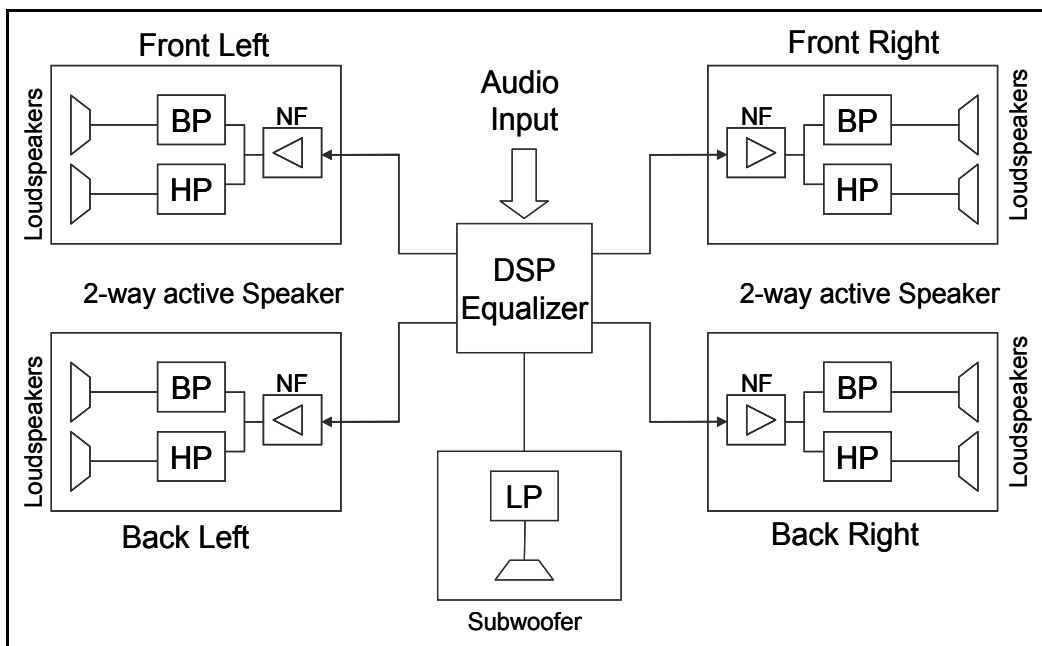


Fig. 14. Block diagram of modern sound system

The audio signal is fed to a digital signal processor (DSP) which acts as equalizer and delay line. In addition, virtual 3D-sound can be calculated in the DSP. The audio signal is then split into 4 branches for stereo sound into a left and right sided branch, as well as covering front passengers and rear-seat passengers. It is also possible to connect all four speakers to provide surround sound. Active 2-way speakers are very common.

The principles of a good sound output are comparably easy and similar for digital and analog sources. Three key-issues need to be respected:

1. frequency response of speakers matching the human perception response
2. maximally flat phase response leading to a low group delay
3. echo reduced environment

The loudspeaker itself has a frequency response, meaning that the loudspeaker is resonant for some audio frequencies, depending on the construction and type of speaker. They can be classified to bass speakers, where only very low end frequencies are audible, mid range speakers and high tone speakers, where only the highest tones are transmitted. Beside these band-limited speakers many vendors offer broadband loudspeakers, which try to transmit a broad range of the audible spectrum. Either the speaker is shifted downwards to the lower end spectrum, neglecting the upper part or wise versa. Due to the mechanical limits in construction of broadband speakers, the frequency response is rippled and not flat, meaning some frequencies are exposed while others are reduced. Figure 15 shows typical 2-way loudspeakers covering the midrange and high tones, while the bass is covered by a single bass speaker, known as subwoofer. The source of very low frequencies cannot be detected by the human ear, therefore only a single bass speaker is sufficient and its position is uncritical.

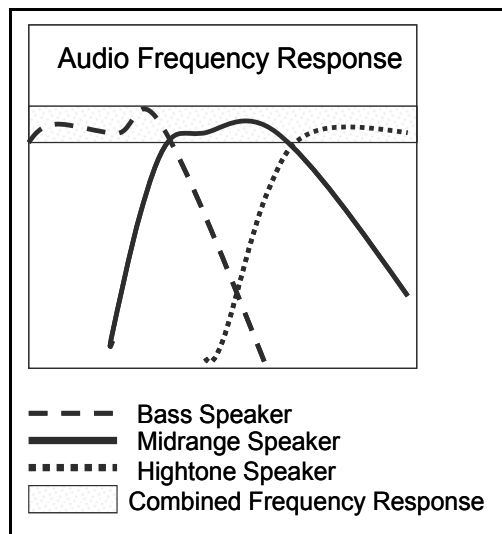


Fig. 15. Typical frequency responses for a 2-way speaker with bass-reflex booster and 3-way speaker systems

The environment in which the speaker operates influences the frequency response of the individual speaker. When the environment is comparably rigid the frequency response shifts to lower frequency band, similar a spring-mass-system where the mass is raised. The volume of the surrounding offers resonances which disturb the frequency responses of the speakers. A good sound system offers a matched frequency response similar the human perception. In order to compensate the deficiency of the speakers and the surroundings, an equalizer corrects this. Equalizing the interior of a vehicle is time consuming and most often a compromise.

Another key factor is that frequencies reach the ear at about the same time. This part is often neglected. For a natural sound impression it is obvious that not only the sound representation shall be matched but also the phase representation, known as group delay response.

When loudspeakers transmit from a different distance to the listener, transmission delays occur. These delays can be compensated by delay lines in the equalizer. The speaker close to the listener will be delayed, so that sounds from all speakers reach the ear at approximately the same time. When sounds are reflected inside the car more delay is seen. The human hearing system can compensate a certain sound delay, beyond that it becomes recognized as echoes. Echoes are annoying.

Taking the interior of a car into account, speakers must be placed cleverly. On the one hand it is necessary that sound reaches the human head directly. On the other hand, echoes must be reduced. Which is quite simple for one person inside the car, the job becomes difficult for all passengers. As this is mostly a compromise between frequency response, group delay response and echoes, some car manufacturers tune the sound to certain positions. For self-driving cars, the focus is the driver and the front passenger, for high-class limousines with backseat passengers, the focus is on rear seats. Some manufacturers offer to change these settings.

While regular sound systems provide single broadband speakers, higher class sound systems offer at least dual-way - or better - triple-way speaker systems.

Here, a lowpass filter, a bandpass and a highpass filter separates the audio spectrum according to their speaker frequency responses. Adding all frequency responses shall provide a maximally flat response.

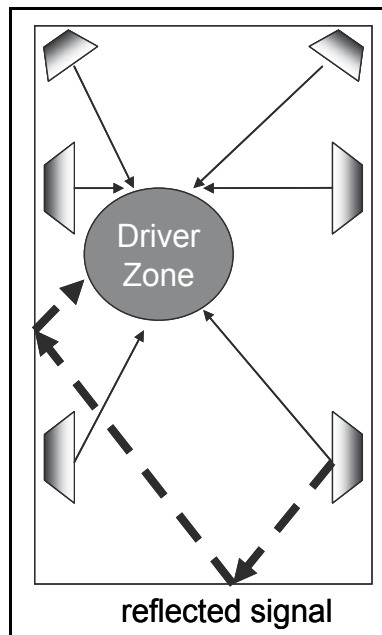


Fig. 16. Typical audio loudspeaker distribution inside the car, exhibit direct signals and reflected signals

8. Rear-Seat entertainment

Figure 17 displays a modern layout of a rear-seat entertainment system.

The media center consists of a computer with a harddrive, on which sound MP3, video MP4 and computer games, e.g. chess, are stored. The console is connected to the media center by USB 2.0 interface and interacts similar a monitor, keyboard and mouse. Today we find touch-screens to combine controls and monitor in a space-efficient manner.

The advantage of USB-interface is its scalability for a number of passenger consoles with individual entertainment program. In a basic configuration, up to 4 consoles can be connected simultaneously. For more, cascades of USB-hubs are needed. As each USB-interface has its own addressing, the limit of parallel streams is just given by the computer power. Each USB 2.0 connection can handle a datastream up to 480 Mbit/s. The length of the cable is limited to 10 meters.

The disadvantage of cascaded star-connected entertainment systems is a rising number of cables in the vehicle, especially at the media center, where all connections are concentrated. Crosstalk and EMC problems are very common then. Therefore it is advisable to use shielded cables with ground connection.

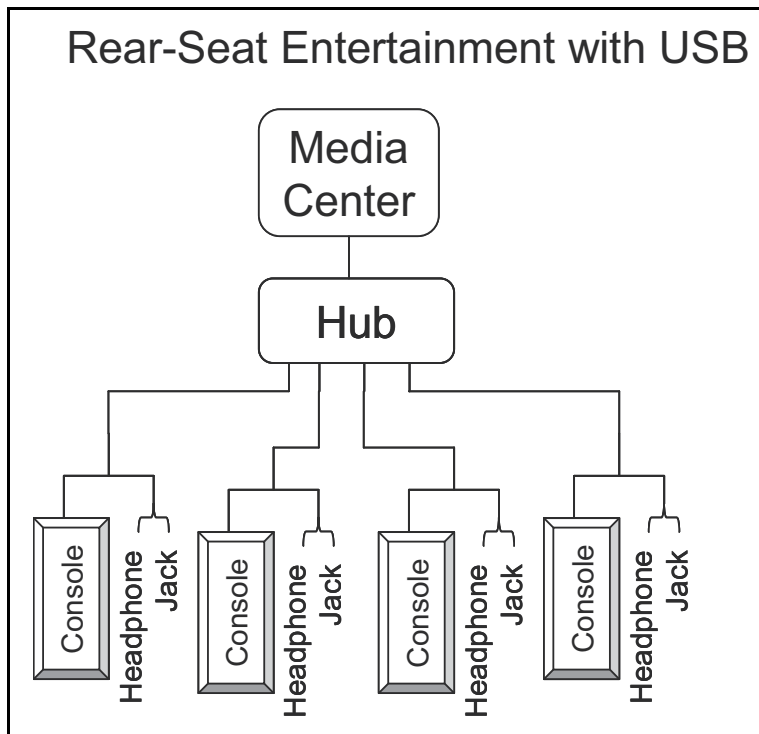


Fig. 17. Block diagram of a modern rear-seat entertainment system based on USB 2.0

Alternatively, a ring-bus structure can be applied, where each console is connected to the media center in a loop, see Figure 6. Although the IP-based ring structure reduces the cabling effort, the bottleneck is the bandwidth limit. While USB 2.0 can handle up to 480 Mbit/s per connection, the regular IP-LAN handles 100 Mbit/s for all connected consoles. Gigabit-LANs may solve the bandwidth limitations for a short time. With rising data rates

and consoles, the bandwidth is quickly exhausted. In addition, cabling distance for GBit-LANs is also limited. Inside a vehicle, a cabling length of 50 meters or more is not unusual for ring-networks. When the entertainment ring is opened at any point, the whole entertainment program is interrupted.

9. Navigation system

It was a long dream of mankind to navigate effortlessly to any destination. Since end of 1990th, we have adapted a satellite position determination free of charge from the US military, called Global Positioning System (GPS). Since then, the navigation market raised rapidly. Today we know navigator mobile phones, portable car-retrofit devices and sophisticated in-vehicle map navigation. The Russian GLONASS satellite system has been offered as alternative to the US-system but never reached the awareness limit. In addition, European countries joined to setup their own navigation system GALILEO in opposition to GPS. At the time of this book is written, Galileo satellite system is still years away to come. Hence, we concentrate on GPS in this chapter.

For GPS, low orbit satellites fly around the earth in such a way and number that at any point on the surface, minimum 3 satellites are in communication range to the receiver. Each satellite transmits a unique pseudo-noise data stream which is synchronized with an atomic clock. Inside the data stream satellite orbital information are implemented as well as timestamps. The receiver can synchronize to the data streams and calculates the position by time-differences between timestamps and orbital data. With 3 or more such time differences and orbital information, the position on earth can be determined.

With the position information and a destination coordinate, a route can be calculated. Today we know a number of vectorized digital maps. Some of them are free of charge, some require a license agreement.

The car industry offers a specific roadmap for their fleet. Beside the vector map, a number of additional layers are offered, e.g. petrol stations, fleet repair stations, museums, hotels, restaurants, car parks, etc. known as Point of Interest (POI). These map information are regularly updated.

As the vector map base is mostly identical, car manufacturers differ between the qualities of POIs, which becomes a unique selling point. Furthermore, the algorithm to calculate the best route from actual position to destination is one of the important features to distinguish between good and better systems. There are not only shortest route and fastest route available, but in future more in concern becomes the most economic route with a number of parameters, such as fuel consumption for regular engine cars, electric power consumption for electric vehicles and hybrid cars as well as CO₂-footprint, just to address the most popular.

Today we find a number of portable external navigation systems by vendors beyond the car industry. These gadgets are comparably easy to operate and often battery powered. Mobile phones or so called smartphones offer all capabilities needed for guidance by map and voice commands. For these external devices, cabling effort is very limited to DC-power only. An external GPS-antenna is not necessarily required as the reception through regular windscreen glass is sufficient in most of the cases. When sun protective metalized windows are installed in the car, GPS-reception may be disturbed. In this exception an external GPS-antenna is needed.

Comparing performance for vehicle installed navigation systems with portable external devices the cost difference is hard to explain to customers as both work equally well. However, the internal system can compensate navigation errors with wheel speed and steering angle even when GPS-reception is not available for some distance, e.g. in tunnels. The upcoming trend in the car industry is to provide interfaces for mobile phones. That means for instance that a smartphone can connect by Bluetooth or USB 2.0 to the vehicular internal GPS-positioning data, which is backed up by wheel speed and steering angles. This enables the phone to be used as hands-free telephone as well as a portable navigation system, having excellent GPS-reception and precise position. The costs and effort for a navigation computer, user interface and map updates are reduced. On top of this, it gives customers the flexibility using any phone model and is future safe.

10. Outlook and future trends

From the performance point of view, a lot can be optimized in the entertainment system in the future. Especially broadcasting reception is deemed to be improved. Historically, the tuner was installed in the center console, while the receiving antenna was on the fender. The cable length was comparably short. Modern cars however offer a number of receiving antennas for diversity reception in the rear-window, side-window, bumper and fender for instance. Long cabling ways attenuate RF signals.

The wide range of broadcasting standards requires multiple tuners buried in the car. Integration and size reduction is a major playground in R&D departments. Transceivers of modern mobile phones are approximately 30x30 mm² or less and 3 mm thick, offering multi-frequency and multi-standard operation already. With SDR-tuners it will become possible in near future to provide compact multi-standard broadcasting receivers exploiting diversity gain by MIMO concepts. This allows integrating such receivers into - or at least close to - the antennas. Reception performance will improve drastically unless EMC problems occur.

Another mega trend of this decade is a permanent internet connection. With UMTS and WLAN it is already possible to connect laptops and mobile phones to the internet while riding in car. In near future, the vehicle itself gets connected to the internet. Upcoming mobile phone standard Long-Term Evolution (LTE) will support this trend. The merge of internet services and vehicular entertainment functionality will provide efficiency and convenience to the passengers. The sheer endless list of new service ideas for the drivers and passengers is overwhelming and becoming unique selling points for car manufactures. They will offer new services to drivers, from intelligent traffic routing, parking aid to firmware updates inside the car. Passengers will be able to stream music and videos as well as communicate while surfing the internet.

11. References

- Henk, C.M, Hamelink, S.G (2008). FMeXtra – the Principle and its Application, *9th Workshop Digital Broadcasting*, Fraunhofer Institute IIS Erlangen, Germany
- Klawitter, G. (2005). Autoradios, Siebel Verlag, ISBN 3-88180-644-x, Verlag für Technik und Handwerk, Baden-Baden, Germany

- Koch, N. (2008). Diversity for DAB - Worth the Effort?, *9th Workshop Digital Broadcasting*, Fraunhofer Institute IIS Erlangen, Germany
- Ruoss, M. (2008). The Digitalization of the FM-Band in Europe, *9th Workshop Digital Broadcasting*, Fraunhofer Institute IIS Erlangen, Germany

Information and Communication Support for Automotive Testing and Validation

Mathias Johanson
Alkit Communications AB
Sweden

1. Introduction

The need for automotive testing and validation is growing due to the increasing complexity of electronic control systems in modern vehicles. Since testing and validation is expensive in terms of prototypes and personnel, simply increasing the volume of the testing can be prohibitively costly. Moreover, since product development cycles must be shortened in order to reduce the time-to-market for new products, there is less time available for testing and validation. Consequently, more testing and validation work will have to be performed in less time in future automotive development projects. To some extent this challenge can be met through virtual product development techniques and simulation, but there will still be an increasing need for testing and validation of physical prototypes. This can only be accomplished by improving the efficiency of automotive testing and validation procedures, and the key to realizing this, we will argue in this chapter, is by introducing novel information and communication support tools that fundamentally transform the way automotive testing and validation is conducted.

With the explosive proliferation of wireless communication technology over the last few years, new opportunities have emerged for accessing data from vehicles remotely, without requiring physical access to the vehicles. Special purpose wireless communication equipment can be installed in designated test vehicles, acting as gateways to the internal communication buses and to on-board test equipment such as flight recorders. With a fleet of test vehicles thus configured, sophisticated telematics services can be implemented that enable communication of virtually any kind of data to and from any vehicle, providing the bandwidth of the wireless connection is sufficient. This has an enormous potential of making automotive testing and validation more efficient, since much of a test engineer's time is spent finding the right data to analyse.

By eliminating the need for the engineer to have physical access to the test vehicle, scarce vehicle prototypes can be made available for multiple simultaneous tests, reducing the overall need for physical prototypes. Moreover, the test vehicles can be accessed by the engineers irrespective of their geographical location, which makes a much broader range of test objects available for tests and frees up time for the engineers in scheduling a prototype for a test. The data resulting from the test can be uploaded from the vehicles to a server from where it can be accessed by any number of interested (and duly authorized) engineers. By having measurement data automatically collected into a central database, as opposed to being stored on the hard drive of each engineer's computer, the opportunities for reuse of data is greatly

improved. One can also imagine (semi-)automated analysis mechanisms being executed on the data being uploaded to a server, assisting the engineer in interpreting the data.

A specific kind of data of paramount importance in automotive testing and validation is diagnostic data generated by designated diagnostic functions built into the vehicle's Electronic Control Units (ECU). By collecting and analysing Diagnostic Trouble Codes (DTC) for test vehicles, faults can be detected and corrected before the vehicle goes into production. Statistical analysis of DTCs is also important in order to find correlations between faults and to prioritise different development efforts. With the advent of wireless telematics services, diagnostic data can be collected more systematically in different development phases. This means that there will be fewer faults in production vehicles, preventing costly recalls.

Since many faults that are detected in the testing and validation phases of automotive development are software related, having wireless access to fleets of test vehicles means that the software in the ECUs can be remotely updated with a bug-fixed software release over the wireless connection. Reprogramming an ECU in the traditional way is a time consuming procedure that requires test equipment to be connected physically to each vehicle. Through remote software download, many vehicles can be updated simultaneously without requiring physical access.

Automotive testing facilities are commonly located in remote rural areas, due to the need for extreme climate conditions and privacy. A side-effect of this is that a significant part of the budget for automotive testing expeditions is the travel costs for the engineers. By utilizing tools to remotely access data, complemented with tools for distributed collaborative work between the test site and the automotive company's development sites, engineers can take part in testing expeditions remotely, without having to travel.

The tremendous impact on automotive testing and validation processes that will result from large scale introduction of the technology and concepts described here has the potential of affecting the whole automotive development process. Referring to the established V-model of product development that is often used to elucidate automotive development processes, the testing and validation phases are at the same level as the design and simulation phases (see Fig. 1). This captures the fact that there is a considerable interplay of creative and

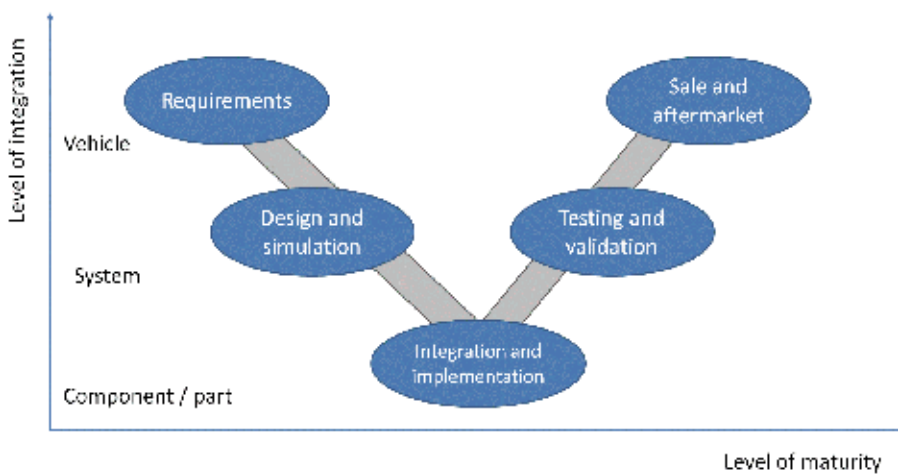


Fig. 1. V-model of automotive product development

analytical processes between these stages of the automotive development (Weber, 2009). Hence, it is easy to see that when the testing and validation phases are changed, this will heavily influence the design and simulation stages. Specifically, with an improved testing and validation process, whereby performance measurements and diagnostic data can be efficiently collected, analysed and fed back into the design process, the opportunities for component and system re-design is greatly facilitated. Moreover, validation of simulation models by measurement data improves the possibilities of more extensive simulations and virtual prototyping.

Since the innovations in automotive engineering made possible by telematics services and related information and communication systems go way beyond the testing and validation stages, automotive management processes will have to be adapted to maximize the benefits. From an innovation management standpoint, Lenfle and Midler (2003) argue that the introduction of telematics services constitutes a definitive turning point for the automotive industry, which will require the adoption of management tools specifically adapted to the collective learning process involved in this field of innovation.

In the remainder of this chapter we will explore the opportunities of improving automotive testing and validation by means of sophisticated information and communication support tools. Specifically, the following classes of applications will be studied:

- automotive metrology and data collection,
- remote vehicle diagnostics,
- remote software download,
- distributed collaborative automotive engineering.

The focus is primarily on consumer grade vehicle development (i.e. passenger cars), although most of the technology and applications are equally relevant (and in some cases even more relevant) for trucks, buses, construction equipment, and other special purpose vehicles. Furthermore, the focus is on the later stages of the automotive development process, where testing and validation of physical prototypes and pre-series vehicles is of vital importance.

The rest of this chapter is organized as follows: Section 2 gives a short introduction to automotive testing and validation; section 3 contains an overview of vehicular communication infrastructure; section 4 discusses information and communication support for automotive metrology and data collection; section 5 deals with automotive diagnostics and prognostics applications, in particular concerning telematics services and statistical analysis of diagnostic data; section 6 treats telematics services for remote ECU software updates; section 7 discusses distributed collaborative automotive engineering, and section 8 provides conclusions and a future outlook.

2. Automotive testing and validation

The development of complex products in the exceedingly competitive automotive industry is a demanding undertaking that requires a very sophisticated quality assurance process. Quality assurance in the automotive industry is complicated by the high level of integration of components from many different suppliers and the fact that many of the subsystems are safety-critical. Specifically, for the embedded electronic systems that constitute a substantial part of the total development cost, the design process is based on a close cooperation

between car manufacturers and suppliers, whereby the carmakers provide the specifications of the subsystems to the suppliers, who design and deliver the systems. The resulting components are integrated into the vehicle platform by the carmaker, which performs the necessary testing and validation (Navet & Simonot-Lion, 2009).

The automotive testing and validation processes have undergone dramatic developments following the exponential increase in the number and complexity of electronic control systems in vehicles. With as much as 23 percent of the total manufacturing cost of a high-end vehicle being related to electronics, and an estimate that more than 80 percent of all automotive innovation stem from electronics (Leen & Heffernan, 2002), the importance of testing and validation methods for electronic components, including software, becomes evident. This situation has spurred the development of on-board diagnostics functions being designed in parallel with the electronics components. Increasingly sophisticated external test equipment connected to the vehicles' internal communication buses has also been developed and the ability to measure physical properties through built-in sensors has been greatly improved. This has led to the current situation where automotive testing and validation is largely a practice of data capture (metrology), communication and processing. Sophisticated data analysis software has been developed to meet the need for high volume data processing, which includes filtering, transformations, visualization and various statistical methods.

2.1 Validation and verification

In many situations a distinction is made between verification and validation. Verification refers to a process to determine whether a system or service complies with its specification, whereas validation is a quality assurance process for determining if a system or service fulfils its requirements and lives up to customer expectations. In this chapter we will use the term validation informally in both meanings, leaving to the reader to discern the subtle distinction from the context.

3. Vehicular communication infrastructure

The tremendous development of digital communication technologies over the last few decades has fundamentally transformed automotive testing and validation, making it possible to access and distribute vehicle data efficiently and reliably. We will briefly outline the state of the art in communication infrastructure for automotive applications.

3.1 In-vehicle communication networks

Modern automobiles typically contain between 20 and 50 ECUs, controlling different subsystems of the vehicle. The ECUs are interconnected by an in-vehicle communication bus. In many cases there is more than one such bus, interconnecting different subsets of ECUs. The original motivation for in-vehicle networks was to reduce weight by replacing discrete wiring, but the additional benefit of improved means of communication between electronic subsystems can now be seen as one of the major facilitators of technological innovation in automotive engineering.

The most common in-vehicle bus technology currently in use is the Controller Area Network (CAN) developed by Bosch in the mid 1980s. CAN is a broadcast serial bus

technology with a prioritization scheme based on arbitration. More recently the FlexRay bus technology which is based on time-division multiplexing for multiple access has been developed. FlexRay provides higher data rates than CAN, while being a deterministic protocol suitable for time critical applications. For in-vehicle applications requiring very high data rates, such as infotainment services, the fiber-optic-based Media-Oriented Systems Transport (MOST) has been introduced. MOST is a bus technology usually based on a ring topology with a Timing Master controlling access to the bus. Although not originally designed for automotive applications, the prolific Ethernet technology is now also making its way into vehicle architectures. Due to its unquestionable success as the foremost Local Area Network (LAN) technology, it will be increasingly important also as an in-vehicle network technology complementing FlexRay and MOST.

In emerging vehicle architectures, CAN, FlexRay, MOST and Ethernet are combined to form a network topology with a backbone bus (typically based on FlexRay) interconnecting multiple subnetworks based on CAN and MOST. Other network technologies such as LIN (Local Interconnect Network, a time-triggered master-slave protocol) can also be interconnected. With this evolution, automobiles become distributed systems of ECUs interconnected in sophisticated network topologies. The next natural step is to interconnect the in-vehicle networks to the outside world using telematics systems.

3.2 Automotive telematics

Grymek et al. (2002) define automotive telematics as the convergence of telecommunications and information processing for automation in vehicles. This encompasses systems to enhance the experience of the end-users of a vehicle, such as navigation aids based on GPS positioning and various infotainment services, but what mainly interests us here is the capability of such systems to communicate data between in-vehicle networks and the outside world for use in the testing and validation phases of automotive development. However, the opportunity of leveraging the technology investments in telematics systems designed for aftermarket services for development benefits is particularly compelling. By implementing remote diagnostics and remote software download functions into telematics units that are installed in production vehicles the need for dedicated systems for testing and validation, installed in test vehicles only, is reduced. It must be noted though, that testing and validation will most likely always require some amount of external equipment connected to test vehicles.

3.3 Wireless networking for automotive applications

The explosive proliferation of digital mobile telephony and wireless data communication networks is one of the foremost catalysts of automotive telematics. The almost ubiquitous wireless communication infrastructure provided by cellular networks, together with the availability of inexpensive microelectronic communication devices make it possible to design powerful automotive telematics systems for many different applications. A differentiating feature of telematics services for automotive testing and development, compared to many other mobile communication services, is that the data upload capacity is usually more interesting than the download capacity. Somewhat unfortunately, many of the wireless communication technologies targeting mobile computing are by design asymmetrical, with higher downstream capacities. Nevertheless, the evolution of wireless

communication technology with higher bandwidths and better coverage will continue to benefit the automotive telematics industry.

One of the most important wireless communication technologies for automotive telematics is the General Packet Radio Service (GPRS), which is a packet-switched data service available in second generation (2G) cellular telephony systems. GPRS provides data rates of 56-114 kilobits per second, which is good enough for many automotive applications. By using multiple time slots of the underlying GSM network, Enhanced GPRS (EGPRS), also known as EDGE (Enhanced Data Rates for GSM Evolution), up to four times the bandwidth of a traditional GPRS connection can be achieved.

Third and fourth generation (3G, 4G) mobile telecommunication technologies based on UMTS (Universal Mobile Telecommunications System) and HSPA (High Speed Packet Access) are now gaining momentum in automotive telematics. The higher bandwidths, up to several megabits per second in ideal situations, will enable improved services and novel applications.

In addition to mobile telephony technologies, automotive telematics systems frequently also utilize wireless LAN technologies, mainly based on the IEEE 802.11 standards, and short range personal area radio networks such as Bluetooth or ZigBee. Special versions of short range wireless communication technologies customized for vehicular communication are sometimes labelled Dedicated Short-Range Communication (DSRC) technologies. The main target for DSRC is vehicle to roadside equipment communication for Intelligent Transportation Systems (ITS), to improve safety and reduce traffic congestion.

Multiple short range wireless communication devices can be organized into a self-configuring network known as a Mobile Ad hoc Network (MANET). For vehicular applications, Vehicular Ad hoc Networks (VANET) have attracted a lot of research interest lately. An overview of VANET technology is given by Jakubiak and Koucheryavy (2008).

3.4 Secure vehicular communication

Due to the safety-critical nature of many applications of vehicular communication, the need for security and privacy mechanisms to protect sensitive data and prevent malicious behaviour is well understood (Papadimitratos et al., 2008, Schaub et al., 2009). When interconnecting in-vehicle networks with public network infrastructures through telematics services for remote diagnostics and remote software download, the safety of the users of the vehicles may be compromised. Although this difficulty is somewhat lesser for automotive development applications (i.e. testing and validation vehicles), compared to aftermarket applications, appropriate security mechanisms nevertheless need to be carefully designed.

Traditionally, the automotive industry is very security minded and secretive about its engineering and design data. As expected, this also applies to data communication in testing and validation and hence security measures to protect all kinds of data from illicit eavesdropping are necessary. Fortunately, this is a mature field of information technology and a multitude of data encryption techniques and products are readily available.

4. Automotive metrology and data collection

Metrology, the science of measurement, can be defined as the application of one or more well-defined measurement methods in an effort to obtain quantifiable information about an

object or phenomena (Bucher, 2004). In the automotive industry, the process of measuring various physical properties of a vehicle in operation, and collecting the measurement data for analysis of the behaviour of components or subsystems, is a crucial part of the testing and validation stages of development. Automotive metrology encompasses a vast array of different measurement techniques, measurement systems, data formats and analysis software for different applications.

A specific application of metrology that is of fundamental importance in automotive engineering is diagnostics. Because of its significance, we will devote section 5 entirely to diagnostic data management and confine this section to the study of collection and analysis of measurement data not specifically for diagnostics. This involves collection of a broad range of data resulting from various sensors built into in the vehicle and from specialized measurement systems installed in dedicated test vehicles. The data collected is typically used for troubleshooting faults appearing during testing or to collect performance data on different subsystems for validation.

One of the most common kinds of data collection is the recording of signals from sensors connected to ECUs and communicated over the in-vehicle network (e.g. the CAN bus). In modern automobiles, a large number of such signals (several thousand), are available for monitoring and recording on special purpose devices known as *flight recorders*¹. A flight recorder is a versatile piece of equipment that can be configured to monitor and record a number of signals that later can be analysed using a plethora of analysis tools. The conditions for when to start and stop recording the signals is typically controlled using some sort of triggering method, which can be for instance a change of the vehicle's power mode, the push of a button, or the appearance of a certain CAN frame on the CAN bus. Usually, there is a configurable time period before and after the event during which the signals will be recorded (known as pre-trigger and post-trigger times). The specification of which signals to record, along with capture parameters such as the trigger conditions, sample rates and precision for each signal, is typically defined in a configuration file on the flight recorder. We will call this configuration file a *measurement assignment*. The measurement assignment is created by the test engineer using a dedicated software tool, and compiled into a format readable by the flight recorder. The assignment is then downloaded to the flight recorders in the test vehicles designated for the specific tests. As the test vehicles are operated, measurement data is generated, which can subsequently be offloaded from the flight recorders for analysis. Based on the results of the analysis, the measurement assignment may need to be re-designed and the process reiterated to capture additional data. In this fashion, specific malfunctions or operational anomalies can be provoked during testing and the relevant sensor data for fault tracing can be captured and analysed. The process is illustrated in Fig. 2, highlighting the cyclical nature of the work.

¹ The name reflects the origin of the technology in the aerospace industry. For automotive applications, the terms 'data recorder' or 'data logger' are sometimes used synonymously.

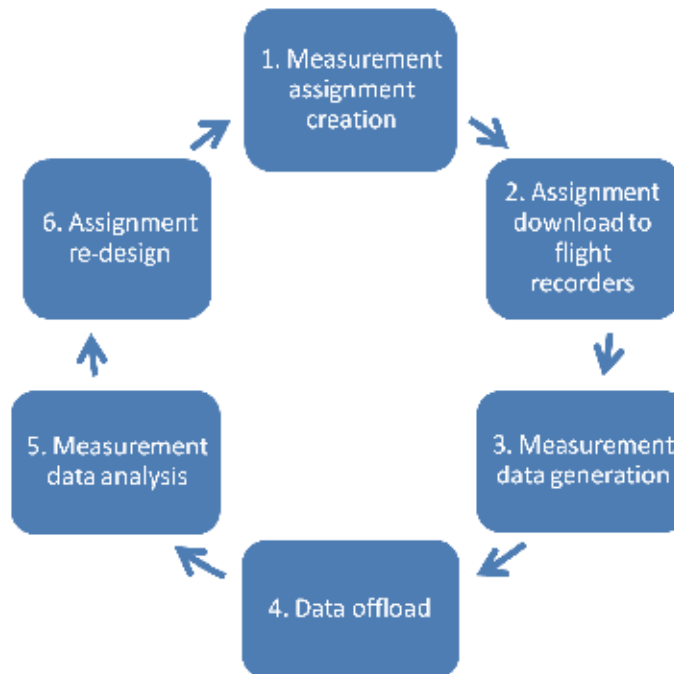


Fig. 2. Measurement data capture and analysis cycle

4.1 Wireless communication in automotive metrology

To improve the efficiency of fault tracing in automotive development, a key concern is to reduce the time of the data capture and analysis cycle, shown in Fig. 2. With the advent of more or less ubiquitous wireless data communication networks, as discussed in section 3.3, the measurement assignment download and the measurement data upload can be realized over a wireless connection using a telematics service. This means that the engineer does not need physical access to the test vehicle to reconfigure the flight recorder or to access the measurement data for analysis. Since prototype vehicles are often physically inaccessible to the engineers for extended periods of time while away on testing expeditions this is a significant benefit.

A telematics service for remote metrology and data collection is generally based on an architecture with a web server acting as a gateway between the wirelessly accessible flight recorders and the users. Measurement assignments are uploaded to the server by the users, and the identities of the test vehicles that the assignment is intended for are specified. The assignment is then automatically downloaded to the flight recorders of the specified vehicles, by means of the telematics service. Once the flight recorders are configured by the assignment, measurement data can be generated and continually uploaded to the server, where it is stored in a database. The user can then download the data from the server and perform the desired analysis.

4.2 Measurement data storage and management

Telematics based metrology systems not only increase the availability of prototype vehicles for tests and reduce the time needed for the data collection; they also open up many new

opportunities to further improve the automotive testing process. For instance, the aggregation of data into a centralized database with a common (web-based) interface improves the possibilities of reuse of data compared to the situation where the engineers manage their or own data. Hitherto, the typical situation has been that the measurement data generated by a particular test is offloaded from the flight recorder onto the hard drive of the responsible engineer's computer, and once the analysis is finished the data is discarded. With proper metadata tagging, appropriate database schemas and a consistent signal naming scheme (e.g. as standardized by ASAM, the Association for Standardisation of Automation and Measuring Systems), measurement data can instead be stored in a central repository, and be made available for search, retrieval and reuse for other purposes than what it was originally intended for. Preservation and reuse of data throughout the product lifecycle is an increasingly important factor for competitiveness, not only in the automotive industry but in design and engineering in general (Wilkes et al., 2009). With the advent of telematics based metrology systems that automatically upload measurement data to a centralized database, a more systematic preservation and reuse of data can be achieved as an additional benefit.

4.3 Automated analysis of measurement data

Another possibility arising with the introduction of telematics based automotive data collection systems is that certain processing of the data can be performed automatically when the data is uploaded to the server. The data collected by the flight recorder is typically stored on a solid state drive, in some well-known measurement data file format (such as MDF developed by Vector and Bosch), before being uploaded to the server. The upload is typically triggered by some event such as the ignition going off, indicating that a measurement session is complete. At the arrival of the measurement data files at the server, a software component is launched that extracts the measurement data and applies some preconfigured processing, storing the results into a database. Ideally, different kinds of processing can be applied as defined by the user, from simple preprocessing operations (such as filtering out invalid or uninteresting data) to sophisticated signal processing algorithms. An automated data analysis system of this kind is described by Isernhagen et al. (2007), although no telematics service is included in their concept. The system supports user-defined data analysis through a descriptive language and parametrisation files and includes many different signal processing modules for different analyses. As an alternative to temporary storage of data on the flight recorder, the data can be transmitted in real time as a measurement data stream. The processing of the data stream at the server can then be performed by a Data Stream Management System (DSMS). Such an approach for online analysis of streaming CAN data is outlined by Johanson et al. (2009).

4.4 Geographical positioning of data

Since telematics systems are commonly equipped with GPS receivers, measurement data that is collected through a telematics service can easily be tagged with metadata about the geographical location of the measurement. This provides provenance of the data, which is important for preservation and reuse. Knowing where a measurement was conducted can also be valuable contextual information in the analysis of the data.

5. Remote vehicle diagnostics and prognostics

Collection and analysis of diagnostic data from electronic control units in vehicles is of vital importance in the automotive industry, both from a life cycle support perspective and during product development, providing performance data and statistics as input to decision making. Moreover, through vehicle diagnostics services, prognostics to anticipate vehicle failures and improve operational availability can be realized, lowering support costs through anticipatory maintenance. For pre-series test vehicles, access to diagnostic data is crucial in order to be able to track problems as early as possible in the development process, preventing serious faults to pass undetected into production vehicles. However, systematic collection of diagnostic data from test vehicles is complicated by the fact that pre-series vehicles are frequently unavailable for diagnostic read-outs, while away on testing expeditions in remote rural areas or being otherwise inaccessible. In response, a multitude of systems and services for wireless read-out of diagnostic data have been suggested (Campos et al., 2002, Johanson & Karlsson, 2007, Vilela & Valenzuela, 2005, Zhang et al., 2008).

5.1 Integrated vehicle diagnostics

In the automotive industry, the need for verification of the functionality and quality of products does not end when the product is sold; on the contrary, this is an important part of the service and maintenance agreement. For this purpose, diagnostic functions are built into the electronic control units, making it possible to access diagnostic data when vehicles are brought in for service. The diagnostic data can be uploaded to the car manufacturer's database over the Internet or using dial-up connections. Statistical analysis of collected diagnostic trouble codes is important in order to monitor the quality of components and subsystems, to prioritise in which order problems should be addressed, and to find correlations between different faults, or correlations between faults and the operating environment. To track problems earlier in the development phase of a new car model, it has been suggested that collection of diagnostic data from test vehicles and pre-series vehicles, in different stages of the development cycle, can be utilized in a more systematic way (Johanson & Karlsson, 2007). However, as previously mentioned, systematic diagnostic read-outs from test vehicles are cumbersome to administer, since the vehicles are often inaccessible. By making test vehicles available for remote wireless diagnostic read-outs, faults can be detected and corrected before the vehicle goes into production and is sold. This prevents costly recalls and warranty obligations. Wireless remote diagnostic read-outs from production vehicles in the aftermarket can also be envisioned; indeed for special purpose vehicles like construction equipment and trucks, such systems are already in commercial use. Commercial services are also emerging for premium cars (Hiraoka, 2009).

Since diagnostics systems are important both for aftermarket services and during product development, an integrated framework for collection, analysis and management of diagnostic data is highly desirable. Campos et al. (2002) argue that previous generations of diagnostics systems have not been well integrated, resulting in unnecessary duplication of effort in developing different diagnostics applications, each with its own infrastructure and software components. This leads to inefficient use of resources and high costs for developing and maintaining the diagnostics applications. Luo et al. (2007) further stress the

need for integrated diagnostics and propose a new model-based diagnostic development process for automotive engine control systems, which seamlessly employs a graph-based dependency model and mathematical models for both online and offline diagnosis. Johanson and Karlsson (2007) present an integrated diagnostics system, that can accommodate both aftermarket and product development needs. With this approach, the infrastructure and workflow for diagnostics and prognostics can be streamlined and optimized for high productivity.

5.2 Information and communication support systems for diagnostics

The main information and communication support components of a diagnostics system can be categorized as follows:

- diagnostic read-out systems,
- diagnostic databases,
- diagnostic analysis toolsets,
- diagnostic authoring tools.

Below we will discuss each of these classes of tools and systems and explore the interdependencies between them.

5.2.1 Diagnostic read-out (DRO)

A diagnostic read-out system connects to the in-vehicle communication network, typically through the OBD-II connector, and queries the ECUs for diagnostic data. This is generally performed using a collection of standardised protocols for automotive diagnostics (ISO 14229, ISO 15765) transported over the Controller Area Network (CAN) communication bus, which interconnects the vehicle's ECUs.

As discussed above, diagnostic read-out system can be implemented as telematics services, which precludes the need for physical access to the vehicles. For such systems, sometimes referred to as remote or wireless DRO services, there are two main modes of operation: synchronous (online) read-out or asynchronous (offline) read-out. In a synchronous remote DRO application, the diagnostics tool establishes a direct network connection to a gateway unit in a vehicle, which relays diagnostic queries and answers between the DRO tool and the ECUs on the in-vehicle network. This can be realized using a tunnelling protocol, such as the CAN-over-IP protocol described by Johanson et al. (2009), or using a dedicated online diagnostics protocol such as the emerging ISO standard Diagnostics-over-IP (DoIP, ISO 13400). In an asynchronous remote DRO application, the diagnostic queries are assembled into a diagnostic script file, which is downloaded to the telematics unit for execution at a suitable time. The actual read-out of diagnostic data is performed by the telematics unit (or some other on-board equipment), and the resultant diagnostic data is encoded in a suitable representation (typically an XML file) and uploaded to the server infrastructure supporting the asynchronous read-out service.

The distinction between the two modes of operation reflects two different kinds of diagnostic applications. The synchronous case is preferable for applications like remote troubleshooting of specific (test) vehicles, whereas the asynchronous case is more appropriate for automated diagnostic read-outs from fleets of vehicles for state-of-health or prognostics applications. The distinction is not clear-cut however.

5.2.2 Diagnostic databases

The diagnostic database is a crucial component wherein all diagnostic data of all vehicles produced by a specific manufacturer is stored. This requires a substantial amount of storage capacity, typically realized using data warehousing solutions, for managing the large volume of data accumulated over the lifetime of the vehicles. The database must be easily searchable and data must be efficiently retrievable. Moreover, to support provenance of diagnostic data, the data must be tagged with metadata describing the origin and capture parameters of the data. This includes vehicle identification data, read-out time, geographical position of read-out (if available), various troubleshooting data and other metadata.

5.2.3 Diagnostic analysis toolsets

The diagnostic analysis toolset is a collection of software tools for performing various kinds of processing and analysis of the diagnostic data. This includes tools for data visualization, case-based reasoning, data mining, statistical analysis and various prognostics tools. A variety of generic data processing systems such as Microsoft Excel and MATLAB are heavily used for realizing the specific analysis tools.

A simple form of diagnostic data analysis is the troubleshooting assistance support built into diagnostics tools used at authorized repair shops. These tools are based on a knowledge database mapping specific fault conditions, indexed by DTC, into suggested troubleshooting and repair actions. A more sophisticated data analysis takes place at the automotive company after the DTCs have been uploaded to the diagnostic database, either from aftermarket (i.e. production) vehicles or from test vehicles during product development. This processing, consisting primarily of data mining and statistical analysis, will be described in more detail in section 5.3.

5.2.4 Diagnostic authoring tools

Diagnostic authoring tools are used by diagnostics engineers to develop new diagnostic functions in the ECUs, in the DRO tools, and in the analysis toolsets. Based on requirements from the product development, and novel needs identified in the analysis phase, new diagnostics functions are developed in tandem with new analysis tools in a constantly ongoing development process. A diagnosis script editor is typically used to design new read-out functions in DRO systems, based on new or updated diagnostic functions in the ECUs. Preprocessing and interpretation of the results of the new DRO functions then need to be implemented, before the data can be stored in the diagnostic database. The analysis tools may also need to be updated for processing the new diagnostic data.

The information flow between the different stages of the automotive diagnostics process is illustrated in Fig. 3.

5.3 Statistical analysis of DTCs

A DTC is a compact representation (typically five digits encoded in two bytes) of specific component malfunctions. A number of DTCs are standardised through the OBD-II (on-board diagnostics) initiative (SAE J2012/ISO 15031-6), but each vehicle manufacturer typically also defines a large number of additional codes. The conversion from the compactly encoded form into a humanly legible text format is performed through a table

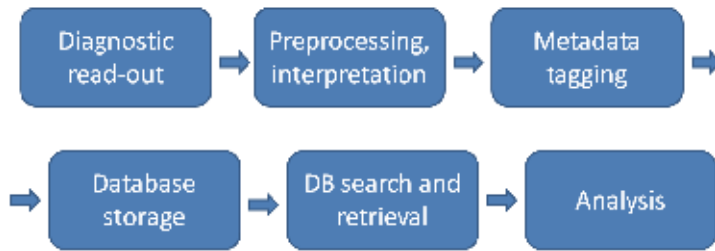


Fig. 3. Typical information flow in automotive diagnostics

look-up by the diagnostics tool. After a DTC has been read out from an ECU, it is generally erased from the ECU's memory bank. To enable statistical analysis, the DTCs must be uploaded to the diagnostics database for persistent storage.

Let's consider an illuminating example of how statistical analysis of DTCs can be performed. When a large number of DTCs have been collected, we can query the database for a specific DTC set during a specified time interval in a fleet of vehicles defined by a number of characteristics such as car model, engine type, transmission type, etc. The frequency of DTCs over time can be plotted in a histogram (see Fig. 4). Here, mileage is used instead of time as independent variable, as is common practice in automotive reliability engineering.

In order to perform statistical analysis, we can design a function $f(t)$ that approximates the histogram. Such a function is called a probability density function (PDF). The probability of a failure (resulting in a DTC) in a time interval $[t_1, t_2]$ is then the area under the curve $f(t)$ between $t=t_1$ and $t=t_2$, i.e.

$$P(t_1 \leq t \leq t_2) = \int_{t_1}^{t_2} f(t) dt. \quad (1)$$

The probability of failure before a given time t_1 , $F(t_1) = P(t \leq t_1)$, is called the cumulative distribution function (CDF). Conversely, the probability of survival beyond a given time t_2 is given by the reliability function $R(t_2) = P(t > t_2) = 1 - F(t_2)$.

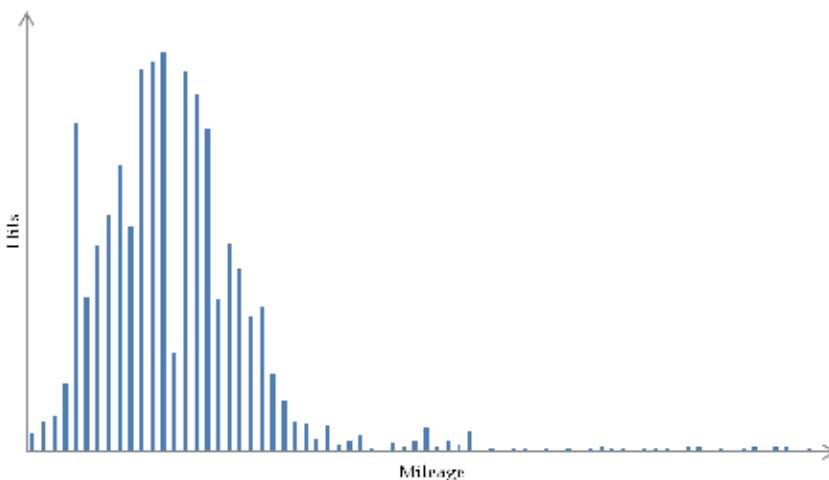


Fig. 4. Histogram showing the frequency of failures in discrete intervals of mileage

The hazard function $h(t)$ gives the probability of instant failure in the next small time interval Δt , given survival until time t . The hazard function is better known as the failure rate, and is simply the number of failures at time t divided by the numbers at risk at t , i.e.

$$h(t) = f(t) / R(t). \quad (2)$$

To visualize a trend of failures, we can study the integral of the hazard function, called the cumulative hazard, which is calculated as

$$H(t) = \int_0^t h(t) dt = \int_0^t \frac{f(t)}{R(t)} dt = \int_0^t \frac{f(t)}{1-F(t)} dt = -\ln(1-F(t)) \quad (3)$$

The cumulative hazard can be interpreted as the probability of failure at time t given survival until time t .

Now, to be able to calculate all of the abovementioned useful statistics of a collected data set, we need to find a PDF that approximates the histogram of collected DTCs in a good way. One very well known PDF that has proven highly useful for statistical modelling in reliability engineering and failure analysis is the Weibull distribution, given by

$$f(t; k, \lambda) = \frac{k}{\lambda} \left(\frac{t}{\lambda} \right)^{k-1} e^{-(t/\lambda)^k}, \quad (4)$$

where $k > 0$ is the shape parameter and $\lambda > 0$ is the scale parameter of the distribution.

Using regression analysis, the parameters k and λ can be easily calculated from the histogram data. For instance, looking at our histogram in Fig. 4 we can calculate the values $k=3.1$ and $\lambda=1.5$ from the histogram data by a simple curve-fitting algorithm. This gives the Weibull density function for our hypothetic DTC shown in Fig. 5.

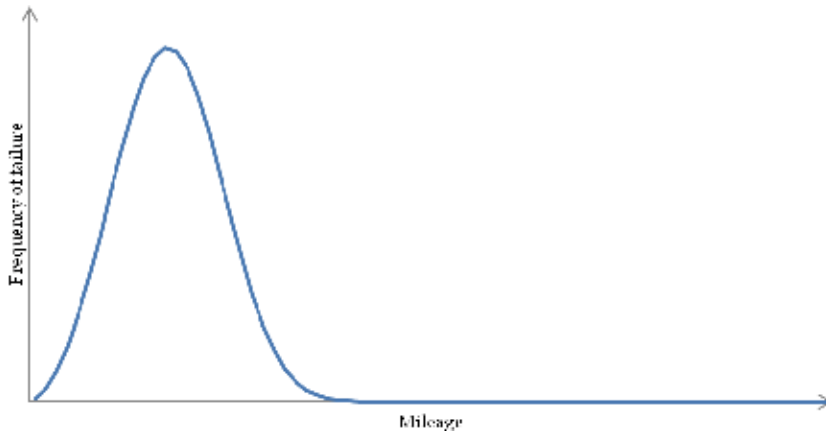


Fig. 5. Weibull density function

From the Weibull function we can now calculate the hazard function using formula (2) and the cumulative hazard, shown in Fig. 6, using formula (3). This gives a good visualization of the trend of failures of the component or subsystem from which the DTC originates, and can be used for instance to optimise service intervals or as input to the development of the next generation of the component or subsystem.

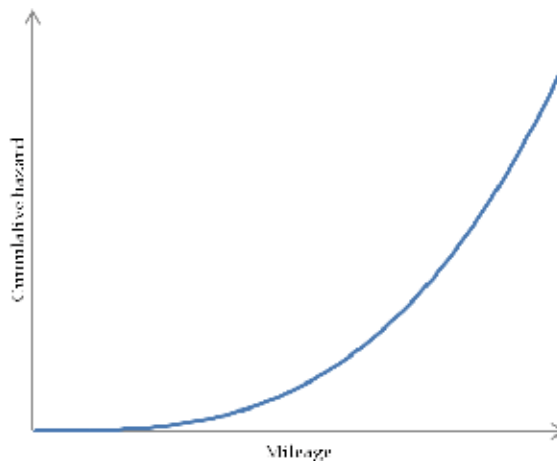


Fig. 6. Cumulative hazard function

The statistical analysis shown above is just one example out of a wide variety of computational methods for diagnostics and prognostics. When the volume of the diagnostic data collected grows due to improved means of collecting data through telematics services, it will be increasingly important to have sophisticated computer-based tools for processing the data.

6. Remote software download

With the explosive growth of software in vehicles, development and maintenance of ECU software (firmware) are increasingly important tasks in automotive engineering. From a testing and validation perspective, tracking down and documenting ECU software bugs have become major issues. When a software bug has been found and fixed, the new version of the software needs to be installed, followed by new testing to verify that the problem is solved and that no new problems have been introduced. The cycle of finding software related problems, upgrading the software and repeating the tests can quickly become very time-consuming and needs to be streamlined as much as possible to optimise efficiency. In this context it is of great value to be able to upgrade ECU software as quickly and effortlessly as possible. Unfortunately, ECU reprogramming is typically a rather tricky and time-consuming procedure, often requiring the vehicle to be taken to a workshop. With test vehicles frequently being inaccessible, as previously discussed, software updates are commonly delayed. Once again, telematics services seem to be the answer. With the ability to remotely update the ECU software over a wireless network connection, test vehicles can get the latest software versions installed with little or no manual intervention. Moreover, with version management systems keeping track of all vehicles' software status, the burden of keeping track of which software version is currently installed on a particular test vehicle is lifted from the engineer.

Remote software download has also been suggested as an aftermarket service, giving the customers the opportunity to get the latest ECU software versions installed without having to take the car to an authorized repair shop.

6.1 Telematics services for remote software download

A telematics service for remote software download can be developed by implementing an ECU upgrade component in the telematics unit and making new ECU software releases available on a server for download over a wireless network connection. A revision control system keeps a centralized record of the versions of all ECUs in all vehicles managed by the system. When the telematics service detects a new version of the software for one or more of its ECUs, it downloads the software packages, sets the vehicle in programming mode, and replaces the software in the ECUs via the in-vehicle network (e.g. the CAN bus).

Automated software update mechanisms are well-known in the computer and telecommunications industry. For upgrades of mobile phone firmware over a wireless network, the term FOTA (Firmware update Over the Air) is commonly used. It has been suggested that the principles of FOTA in the telecommunications industry can be applicable also in the automotive industry (Shavit et al., 2007).

A generic mechanism for remote ECU software update is presented by de Boer et al. (2005). Their approach is based on a generic OSGi (Open Service Gateway initiative) service platform installed on a telematics unit and a remote administration server, which keeps a repository of ECU flash-bundles. A key feature of their solution is that the ECU reprogramming controller is downloaded from the server together with the flash-bundles, which alleviates problems with different reprogramming procedures for different ECUs.

Although the prospects of remote ECU software upgrades seem very promising, many practical obstacles related to safety and security need to be overcome before large-scale deployment of telematics based services can be realized. Specifically, remote access to vehicles must be restricted based on authorization mechanisms and the integrity of ECU software updates must be guaranteed. To this end, Nilsson and Larson (2008) suggest a protocol for secure remote ECU software updates based on symmetric key encryption and digital signatures. In a similar vein, Mahmud et al. (2005) present an architecture for secure ECU software updates through a combination of one-time authentication keys and symmetric key encryption.

7. Distributed collaborative automotive engineering

Automotive proving grounds are commonly located in remote rural areas, due to the need for extreme climate conditions and privacy. As a consequence, test engineers must travel to remote locations for extended periods of time, which is time consuming and expensive. By making heavy use of broadband communication infrastructure and by developing new work procedures based on distributed collaborative work, automotive testing can be performed with less need to send highly qualified personnel to remote regions. The specialists on a subsystem of a car can stay at the car manufacturer's development site, where they can be more productive in their work, while still having immediate access to the measurement data of the tests being performed elsewhere. Less qualified test engineers can be hired for conducting the tests, with data being analysed and the tests being coordinated from a remote location. Furthermore, the opportunity of conveying test results in real time over a network to the development site means that people traditionally not involved in testing until a much later stage can be engaged earlier, shortening development cycles.

To realize such a distributed collaborative work environment requires a number of sophisticated software tools for remote interactions and data sharing between the engineers.

Traditionally, tools for collaborative engineering and design have focused on supporting distributed group meetings using synchronous communication tools, like videoconferencing and application sharing. Sophisticated collaboration studios have been built for the purpose of group-to-group communication. Although useful, these collaboration studios do not explore the full potential of distributed collaborative work, and in particular they fail to support the day-to-day communication between engineers. Arranging a distributed meeting using a collaboration studio is of course less troublesome compared to travelling to face-to-face meetings, but it still requires the involved engineers to get out of their ordinary workplaces, book a studio, and so on. Instead, software tools supporting distributed collaborative work directly from the engineers' workstations are needed. This way synchronous collaboration sessions can be initiated effortlessly, supporting impromptu interactions and a much tighter collaboration between the members of a distributed team.

A technological framework supporting distributed collaborative automotive testing is presented by Johanson and Karlsson (2007), along with a pilot study demonstrating the use in distributed winter testing of climate control systems. This system supports audiovisual communication, synchronous sharing of measurement data and shared visualization of data. Validation of climate control systems is an interesting application, since it involves a considerable amount of subjective testing, complementing the measurement data collection and analysis. In this context it was found useful to have direct voice (and even video) communication with the engineers riding in the test vehicles, to communicate subjective impressions.

Nybacka et al. (2006) describe a system for feeding real time measurement data from a car into a simulator, for computation of dynamical properties that cannot be measured directly. With this system, measurement data about a car's current position, velocity and acceleration can be used as input to a simulation model, to calculate the normal forces acting on the tires of the car. The result is visualized collaboratively in real time using a 3D model of the car, giving the distributed engineers an improved understanding of the behaviour of the car during handling tests. This kind of hardware-in-the-loop simulations, combining real time measurement data acquisition, simulation techniques and collaborative visualization has a strong potential of improving automotive multi-body dynamics testing and validation in the future.

8. Conclusions and future outlook

In this chapter we have explored the information and communication needs of the testing and validation stages of automotive development. As we have seen, the growing complexity of electronic control systems in modern vehicles increases the need for testing and validation. The challenge of achieving this extended testing in less time, due to shortened development cycles, must be met with improved testing and validation processes based on sophisticated information and communication systems for data capture and processing.

The interconnection of in-vehicle communication networks with wireless internetworks through telematics services enables communication of measurement data, diagnostics data and other vehicle data almost ubiquitously. This has a tremendous impact on the way automotive testing and validation is conducted. Instead of devoting much of their time to hunting down prototype vehicles for the purpose of reading out diagnostic data or

reconfiguring flight recorders, the engineers can focus on designing test procedures and analyzing the data made available through telematics services. When software-related problems are found through remote metrology and diagnostics services, the ECUs can be remotely updated with new versions of the software. With computer-based tools for distributed collaborative work, engineers at remote test sites can seamlessly collaborate with colleagues at the automotive company's development sites, without need for excessive travel.

When fleets of test vehicles are interconnected with server-side infrastructure through sophisticated telematics services they are in a sense being transformed into a giant distributed system of data producing units. Probing into the future, we can envision a situation when all vehicles (not just test vehicles) are constantly online, monitored by sophisticated management systems operated by the automotive manufacturers or third party service providers. This poses many challenges of scalability, maintainability, safety and security, but at the same time promises great opportunities for meeting the challenge of delivering superior products to future customers in the automotive sector.

9. References

- de Boer, G.; Engel, P. & Praefcke, W. (2005). Generic Remote Software Update for Vehicle ECUs Using a Telematics Device as a Gateway, In: *Advanced Microsystems for Automotive Applications*, Valldorf, J. & Gessner, W., (Ed.), pp. 371-380, Springer, ISBN 3-540-24410-7, Berlin
- Bucher, J.L. (2004). *The Metrology Handbook*, ASQ Quality Press, ISBN 0-87389-620-3, Milwaukee
- Campos, F.T.; Mills, W.N. & Graves, M.L. (2002). A reference architecture for remote diagnostics and prognostics applications, *Proceedings of Autotestcon*, pp. 842-853, ISBN 0-7803-7441-X, Huntsville, USA, October 2002, IEEE Xplore
- Grymek, L.; Singh, S. & Pattipati, K. (2007). Vehicular Dependence Adds to Telematics' Allure, *IEEE Potentials*, Vol. 26, No. 2, pp. 12-16, March 2007, ISSN 0278-6648
- Hiraoka, C. (2009). *Technology Acceptance of Connected Services in the Automotive Industry*, Gabler, ISBN 978-3-8349-1870-3, Wiesbaden
- Isernhagen, H.; Neemann, H.; Kühn, S. & Gühmann, C. (2007). Intelligent Signal Processing in an Automated Measurement Data Analysis System, *Proceedings of IEEE Symposium on Computational Intelligence in Image and Signal Processing*, pp. 83-87, ISBN 1-4244-0707-9, Honolulu, USA, April 2007, IEEE Xplore
- Jakubiak, J. & Koucheryavy, Y. (2008). State of the Art and Research Challenges for VANETs, *Proceedings of the 5th IEEE Consumer Communications and Networking Conference*, pp. 912-916, ISBN 978-1-4244-1456-7, Las Vegas, USA, January 2008, IEEE Xplore
- Johanson, M.; Karlsson, L. & Risch, T. (2009). Relaying Controller Area Network Frames over Wireless Internetworks for Automotive Testing Applications, *Proceedings of the 4th International Conference on Systems and Network Communications*, pp. 1-5, ISBN 978-1-4244-4772-5, Porto, Portugal, September 2009, IEEE Xplore
- Johanson, M. & Karlsson, L. (2007). Improving Vehicle Diagnostics through Wireless Data Collection and Statistical Analysis, *Proceedings of the 66th IEEE Vehicular Technology*

- Conference, pp. 2184-2188, ISBN 978-1-4244-0263-2, Baltimore, USA, September 2007, IEEE Xplore
- Johanson, M. & Karlsson, L. (2006). A Framework for Distributed Collaborative Automotive Testing, *Proceedings of the 4th Workshop on Challenges in Collaborative Engineering*, ISBN 91-975604-3-X, Prague, Czech Republic, April 2006
- Leen, G. & Heffernan, D. (2002). Expanding Automotive Electronic Systems. *Computer*, Vol. 35, Issue 1, pp. 88-93, ISSN 0018-9162
- Lenfle, S. & Midler, C. (2003). Innovation in automotive telematics services: characteristics of the field and management principles. *International Journal of Automotive Technology and Management*, Vol. 3, No. 1-2, pp. 144-159, ISSN 1470-9511
- Luo, J.; Pattipati, K.R.; Qiao, L. & Chigusa, S. (2007). An Integrated Diagnostic Development Process for Automotive Engine Control Systems, *IEEE Transactions on Systems, Man, and Cybernetics, Part C: Applications and Reviews*, Vol. 37, No. 6, pp. 1163-1173, ISSN 1094-6977
- Mahmud, S.M.; Shanker, S. & Hossain, I. (2005). Secure software upload in an intelligent vehicle via wireless communication links, *Proceedings of IEEE Intelligent Vehicles Symposium*, pp. 588-593, ISBN 0-7803-8961-1, Detroit, USA, June 2005, IEEE Xplore
- Navet, N. & Simonot-Lion, F. (2009). *Automotive Embedded Systems Handbook*, CRC Press, ISBN 978-0-8493-8026-6, Boca Raton
- Nilsson, D. & Larson, U. (2008). Secure Firmware Updates over the Air in Intelligent Vehicles, *Proceedings of the First IEEE Vehicular Networks and Applications Workshop (Vehi-Mobi)*, pp. 380-384, ISBN 978-1-4244-2052-0, Beijing, People's Republic of China, May 2008, IEEE Xplore
- Nybacka, M.; Larsson, T.; Johanson, M. & Törlind, P. (2006). Distributed Real-Time Vehicle Validation, *Proceedings of IDETC/CIE 2006, ASME 2006 International Design Engineering Technical Conferences & Computers and Information in Engineering Conference*, pp. 805-812, ISBN 0-7918-4257-8, Philadelphia, USA, September 2006, ASME
- Papadimitratos, P.; Buttyan, L.; Holczer, T.; Schoch, E.; Freudiger, J.; Raya, M.; Ma, Z.; Kargl, F.; Kung, A. & Hubaux, J.P. (2008). Secure vehicular communication systems: design and architecture, *IEEE Communications Magazine*, Vol. 46, No. 11, November 2008, pp. 100-109, ISSN 0163-6804
- Schaub, F.; Ma, Z. & Kargl, F. (2009). Privacy Requirements in Vehicular Communication Systems, *Proceedings of the International Conference on Computational Science and Engineering*, pp. 139-145, ISBN 978-1-4244-5334-4, Vancouver, Canada, August 2009, IEEE Xplore
- Shavit, M.; Gryc, A. & Miucic, R. (2007). Firmware Update Over The Air (FOTA) for Automotive Industry, *Proceedings of Asia Pacific Automotive Engineering Conference*, Los Angeles, USA, August 2007, SAE International
- Vilela, J.P.T. & Valenzuela, J.C.M. (2005). Design and implementation of a wireless remote data acquisition system for mobile applications, *Proceedings of 5th International Workshop on Design of Reliable Communication Networks*, pp. 8, ISBN 0-7803-9439-9, Naples, Italy, October 2005, IEEE Xplore

- Weber, J. (2009). *Automotive Development Processes: Processes for Successful Customer Oriented Vehicle Development*, Springer Verlag, ISBN 978-3-642-01252-5, Heidelberg
- Wilkes, W.; Brunsmann, J.; Heutelbeck, D.; Hundsdörfer, A.; Hemmje, M. & Heidbrink, H.U. (2009). Towards Support for Long-Term Digital Preservation in Product Life Cycle Management, *Proceedings of the Sixth International Conference on Preservation of Digital Objects*, San Francisco, USA, October 2009, California Digital Library
- Zhang, Y.; Gantt, G.; Rychlinski, M.; Edwards, R.; Correia, J. & Wolf, C. (2008). Vehicle Design Validation via Remote Vehicle Diagnosis: A feasibility study on battery management system, *Proceedings of the International Conference on Prognostics and Health Management*, pp. 1-6, ISBN 978-1-4244-1935-7, Denver, USA, December 2008, IEEE Xplore

Trends towards Automotive Electronic Vision Systems for Mitigation of Accidents in Safety Critical Situations

Ciarán Hughes¹, Ronan O'Malley², Diarmaid O'Cualain²,
Martin Glavin² and Edward Jones²

¹*Vision Technology and Expertise Group, Valeo Vision Systems*

²*Connaught Automotive Research Group, National University of Ireland, Galway
Ireland*

1. Introduction

When discussing vehicular safety, there are two key concepts: The first is the concept of *Primary Safety*, which can be defined as 'the vehicle engineering aspects which as far as possible reduce the risk of an accident occurring' (DfT (UK), 2008a); in contrast, *Secondary Safety* can be defined as 'all structural and design features that reduce the consequences of accidents as far as possible' (DfT (UK), 2008b).

It is important to note that these two aspects of safety sometimes interact in conflicting ways. For example, to improve secondary safety in vehicles, manufacturers often strengthen and increase the size of a vehicle's A-pillar (the vertical or near vertical shaft of material that supports the vehicle roof on either side of the wind-shield). However, this can decrease the visibility of the vehicle's immediate environment to a driver (i.e. increase the vehicle's blind-zones¹), which has a negative impact on the primary safety of the vehicle.

In this chapter, we will discuss the role of automotive vision systems in improving the primary safety of vehicles. The development of electronic vision systems for the automotive market is a strongly growing area of development, driven in particular by consumer demand for increased safety in vehicles, both for drivers and for other road users, including Vulnerable Road Users (VRUs), such as pedestrians, cyclists or motorcyclists. Consumer demand is matched by legislative developments in a number of key automotive markets; for example Europe, Japan and the US have either introduced or are in the process of introducing legislation with the intention of reducing the number of VRU fatalities, with some emphasis on the use of vision systems.

There are several areas in which electronic vision systems can be utilised. These can be broadly divided into two applications: visual display applications for passive human

¹ A vehicles blind-zones are the areas around the vehicle that cannot be seen directly by the driver by looking forward or by using any of the vehicles standard rear-view mirrors (internal and external) from the normal sitting position. The term "blind-zone" is used in preference over the other commonly used term "blind-spot", as this is the term used in some of the jurisdictions described in this section, and more accurately describes the (often sizeable) areas that cannot be seen by a driver of a vehicle.

actualisation, and scene processing for active machine vision-based safety assessment. Visual display applications require the display of the vehicle's environment in such a manner that is both intuitive and useful to the driver of the vehicle. Scene processing applications require a video stream that is suitable for automated processing of the scene.

For display-based applications, typically, the aim is to display a vehicle's blind-zones to the driver. With this in mind, we discuss some of the factors that motivate the use of wide-angle and fish-eye camera technologies in vehicles. With scene processing applications, typically the aim is to process the scene captured by the cameras to intelligently provide or enhance information delivered to the vehicle driver. This information would then be used to provide active warning to the driver in safety critical situations such as detecting the presence of a VRU, a lane departure warning or lane-merge situation. Another application might be to prepare the vehicle for an imminent impact in pre-crash situations. Additionally, some non-safety critical situations (or driver assist situations) include vehicle detection and distancing for adaptive cruise control, auto headlamp dimming and road-sign recognition.

Low-light situations are of critical importance to the overall safety of all road users. Proportionally, there is a far higher accident-per-trip ratio during night-time compared to daytime. Due to advances in technology, the sensitivity of image sensor has improved in recent years, and continues to improve, which allows continually improved low-light performance of camera systems. However, in the absence of a minimum of environmental lighting, visual cameras will fail to return useful information. Therefore, we also discuss the use of passive far-infrared imaging devices for both display and scene-processing applications.

The remainder of this chapter is broken down as follows: in Section 2, we will discuss the general global trend towards the use of electronic vision systems on vehicles, including a detailed examination of statistics, legislation and standards, and with a particular emphasis on safety of pedestrians and other VRUs. In Section 3, we will describe some of the basic technologies that exist and some of the issues with particular applications. Finally, in Section 4, we draw some conclusions about the future roles of automotive camera devices.

2. Global trends

The World Health Organisation states that traffic accidents are one of the leading causes of death globally, accounting for 1.2 million fatalities and 50 million injuries annually (Peden et al., 2004), with pedestrians accounting for 65% of the fatalities; 35% of these being children. Therefore, safety both within and in the presence of vehicles is a growing concern globally. Traditionally, specific emphasis has been placed on the secondary safety of vehicles. For example, the European New Car Assessment Program (Euro-NCAP, 1997), which was established in 1997, provides objective information on the safety of drivers and passengers in cars in crash situations. In a study commissioned by the Euro-NCAP, 94% of respondents list safety in vehicles as a major concern (Hobbs, 1996). There are similar organisations in Japan (J-NCAP, 2010), the United States (US-NCAP, 2010), Australia and New Zealand (A-NCAP, 2010), China (C-NCAP, 2010) and Korea (K-NCAP, 2010). However, more recently, interest in the protection of VRUs, e.g. pedestrians and cyclists, has increased. The OECD define VRUs as "those unprotected by an outside shield, namely pedestrians and two-wheelers" (OECD, 1998). This section discusses the global trend towards increased VRU safety, with specific emphasis on how automotive vision systems can be utilised to meet these demands.

2.1 Statistics

2.1.1 European Union

In Europe, official statistics for VRU deaths due to the victims not being visible to the driver of a vehicle are not readily available, as there is no single repository for such information. However, the European Commission's CARE Road Accident Database claims that there were 3,961 VRU pedestrian fatalities within urban areas in 2005 (CARE, 2010). It is reasonable to assume that a significant number of these deaths were caused by the driver of the vehicle being unaware of the presence of a VRU. This assumption is supported by several statistics. The European Commission Directorate-General for Energy and Transport estimates that the lack of visibility in the blind-zone towards the rear of a vehicle directly causes 500 deaths a year in the EU (ECDGET, 2004). Furthermore, the Commission of the European Communities estimates that every year, approximately 400 European road users lose their lives in collisions with Large Goods Vehicles (LGVs)², because the driver did not see them when turning to the blind side of their vehicle (i.e., turning to the left in the UK and Ireland, to the right in other EU countries) (CEC, 2009).

2.1.2 North America

Statistics for the United States are equally disjointed, with no official statistics directly available for VRU injuries due to vehicle blind-zones. However, there are several sources that strongly suggest that blind-zones are a cause of injuries and fatalities: The Kids and Cars Organisation in the United States claims that 941 children were killed in non-traffic collisions³ in the United States between 2002 and 2006. They further claim that 49.5% of the fatalities (or 466 children) were due to the vehicle reversing while children were present in a vehicle's rearward blind-zone (KCO, n.d.). The National Highway Traffic Safety Administration claims that 221 people were killed and 14,000 people were injured in 2007 by vehicles that were completing a reversing manoeuvre. 99 of the deaths and 2,000 of the injuries involved children under the age of 14 (NHTSA, 2007).

In a study between July 2000 and June 2001, the Centers for Disease Control and Prevention (CDC) (McLoughlin et al., 2002) reported that there were an estimated 9,160 non-fatal injuries to children in non-traffic automotive collisions, with approximately 20% (or 1,832 children) of these injuries caused by the vehicle moving backwards. Between 2001 and 2003, the CDC reported that an estimated 7,475 children (2,492 per year) were treated for moving vehicle backover injuries (Patel et al., 2005). In Canada, it has been shown that the age distribution for children struck by a vehicle reversing is lower than children struck by a vehicle moving forward (Nhan et al., 2009), with over 50% being below the age of five. Again, while the blind-zone is not directly implicated in these injuries, it is reasonable to assume that a significant proportion of these injuries were due to the children being present in the vehicle's rearward blind-zone. Wang & Knipling (1994) estimated that lane change/merge crashes in 1991 accounted for approximately 244,000 police-reported crashes with 224 associated fatalities. Furthermore, the authors reported that the principal causal factor in such crashes is that the driver "did not see other vehicle".

² The term 'LGV' is used in this paper, instead of the term 'heavy goods vehicle (HGV)', as this is the terminology used in most European Union documentation because of the fact that the word "heavy" does not have a direct translation in all European languages.

³ Non-traffic collisions are collisions involving vehicles while they are not in a traffic situation (for example, while on private residential property)

2.1.3 Asia

Gandhi & Trivedi (2007) give a good overview of statistics in developing countries in their introduction. During 2001, there were 80,000 fatalities on Indian roads, which grew in the last decade by 5% per year (Singh, 2005), with 60%–80% of the road fatalities being VRUs (Mohan, 2002). In China, in 1994 pedestrians and cyclists accounted for 27% and 23% of the fatalities respectively, compared to 13% and 2% in the United States (Mohan, 2002). In Japan, 25% of all fatal car accidents involve pedestrians (Takeuchi & Ikari, 2007).

2.1.4 Night-time

Vehicle collision statistics confirm that night conditions are an important area of focus for road safety and collision prevention. In the EU (EU-15) there were more than 43,000 fatal road accidents in 2006 (CARE, 2010). Almost one third of these road fatalities (32.3%) occurred during the hours of darkness (ERSO, 2008). In 2005, 45.5% of pedestrian fatalities in the EU were in darkness (ERSO, 2007). A similar pattern is prevalent in statistics from the USA, with 47.2% of fatal accidents occurring in darkness (FARS, 2010) and 70% of pedestrian fatalities occurring at night (6pm–6am) in 2008 (NHTSA, 2008). In Japan, 55% of all road fatalities occur during night-time (Oya et al., 2002). These statistics confirm that the hours of darkness account for a disproportionate amount of road collisions and fatalities, as there is a substantially reduced traffic volume during night hours. It has been estimated that per vehicle mile, the road fatality rate is 3–4 times higher in darkness than in daylight (Fors & Lundkvist, 2009).

A review by VTI, the Swedish National Road and Transport Research Institute (Fors & Lundkvist, 2009), provides an in-depth analysis of the numerous factors that contribute to the imbalance between day-time and night-time road accident rates. They determine that human vision is not well adapted to night conditions. Visual acuity, contrast sensitivity, spatial resolution, distance perception and reaction time all deteriorate as overall light levels decrease. VTI state that numerous factors contribute to driver performance at night including low luminance (Plainis et al., 2006), tiredness (Akerstedt et al., 2001), alcohol (Akerstedt et al., 2001), and glare from oncoming headlamps (Andre, 1996).

2.2 Legislation and standards

2.2.1 European Union

To match the consumer desire for increased safety in vehicles, the European Union has introduced legislation that requires LGVs to have large portions of their blind-zones made visible to the driver. Legislation in the form of Directive 2003/97/EC (EPC, 2003) was introduced in 2003. Although the initial requirements of this directive aimed to reduce collisions caused by the blind-zones of LGVs and improve road safety for new vehicles circulating from 2006/2007 onwards, the legislation does not cover the existing fleet of LGVs in the EU. However, since it has been estimated that existing fleets will not be fully replaced until 2023, Directive 2007/38/EC (EPC, 2007) was introduced in 2007. This legislation required the retrofitting of the required indirect vision systems to all existing fleets within 24 months of enactment of the bill (i.e. by July 2009). Directives 2003/97/EC and 2007/38/EC were introduced in response to the UNECE World Forum for Harmonization of Vehicle Regulations Agreement E/ECE/324 Regulation No. 46 (UNECE, 2009).

The shaded areas in Figure 1 show the areas of a left-hand drive LGV's environment that must be visible to the driver via the use of "Indirect Vision Systems" (IVS), as required by these directives. The United Kingdom have suggested increasing the size of the visible regions for objects 1m off the ground UNECE (2010). Examples of IVS's include additional

mirrors to the standard rear-view mirrors (internal and external), as well as camera-monitor devices. However, practical problems arise with the use of additional mirrors as the extra mirrors can themselves introduce additional blind-zones, by obstructing direct forward vision, as well as having additional cost and styling implications.

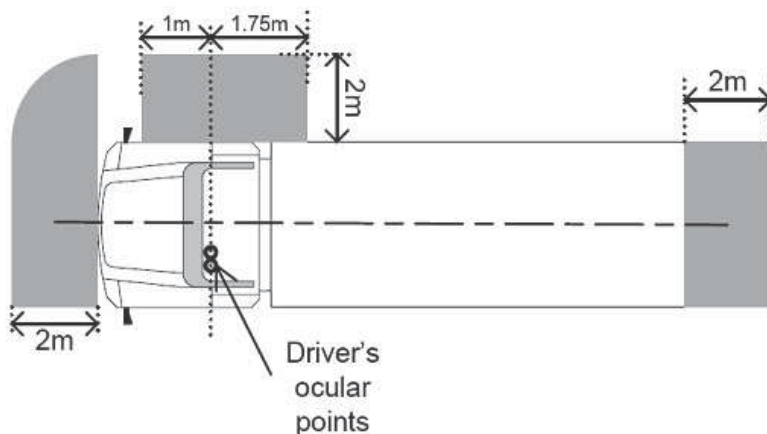


Fig. 1. Area required by Directive 2003/97/EC to be visible to drivers of (left-hand drive) LGVs via the use of IVSs (not including areas covered by the standard and wide-angle wing-mirrors).

As early as 1994, camera devices were identified as a means of reducing accident rates on roads in Europe: “A camera fitted at the rear of the vehicle with a screen on the dashboard to enable the driver to see directly what is happening behind the vehicle, particularly when backing up, is often claimed to be a facility that should be introduced more generally, but so far no country has made it compulsory” (ECMT, 1994). Now, there is a clear provision in Directive 2003/97/EC for the use of camera-monitor devices for the coverage of vehicle blind-zones in this directive. In fact, the use of camera-monitor devices over mirrors is often not only desirable, but necessary in certain situations. For example, it is practically impossible to cover the area at the rear of an LGV with mirrors alone, so camera-monitor systems are the only practical solution.

More recently, EU regulations place the onus on automotive manufacturers to protect VRUs by introducing new passive secondary standards (EC, 2009) on a staggered basis from 2011-2019. However, a vehicle will be granted immunity from a large section of the requirements if it is equipped with a collision avoidance system. This is based on a European Commission study (Lawrence et al., 2006) that found that VRU protection can be significantly improved by a combination of primary and secondary safety measures, particularly adoption of active brake assistance systems. While secondary safety systems aim to reduce injury on impact, primary safety measures aim to avoid an impact or mitigate the conditions under which it takes place.

2.2.2 United States

In the United States, legislation in the form of H.R.1216 (The Cameron Gulbransen Transportation Safety Act of 2007) (HR1216, 2007) is designed to protect against children being injured or killed in non-traffic vehicle related incidents, such as when a vehicle is reversing. Relating to the potential use of cameras, the H.R.1216 Act requires a “field-of-

view to enable the driver of a motor vehicle to detect areas behind the motor vehicle to reduce death and injury resulting from backing incidents, particularly incidents involving small children and disabled persons" and that the expanded field-of-view "may be met by the provision of additional mirrors, sensors, cameras, or other technology to expand the driver's field of view". H.R.1216 also requires the National Highway Traffic Safety Administration (NHTSA) to "maintain a database of injuries and deaths in non-traffic, non-crash events involving motor vehicles". (HR1216, 2007).

Additionally, H.R.1216 also requires the NHTSA to initiate rulemaking to amend the Federal Motor Vehicle Safety Standard (FMVSS) No. 111: Rearview Mirrors (FMVSS, 1971) to improve a driver's ability to see areas to the rear of a motor vehicle in order to mitigate fatalities and injuries associated with backover incidents (FMVSS, 2009). This rulemaking was initiated in March 2009, with final rulemaking due in February 2011. Several major automotive manufacturer's have made submissions on this review that explicitly propose camera-monitor devices for inclusion in the standard (GM, 2009; Nissan, 2009; Magna, 2009; Gentex, 2009; IIHS, 2009), with at least one stating that "it is clear that rearview video systems can provide the widest range of coverage" (Magna, 2009), and another "urges [the NHTSA] to establish a no-blind-spot requirement" and that they "expect that rearview video systems will be a popular means of meeting such a requirement" (IIHS, 2009).

In addition to vision based applications, the NHTSA have committed to continue to review technologies that provide object detection capabilities (FMVSS, 2009). Indeed, in their documentation, the NHTSA have explicitly acknowledged that, in future, video-based and infrared-based obstacle detection may be employed in meeting the requirements of the proposed standard.

2.2.3 Japan

In Japan, legislation has also been proposed (again in response to UNECE Regulation No. 46 (UNECE, 2009)) that would require medium and large vehicles to be equipped with devices that allow drivers to detect objects in the vehicles blind-zones, either directly or indirectly using mirrors or camera-monitor devices (see Figure 2) (UNECE, 2005). For the purpose of the proposed legislation, a cylinder one metre high with a diameter of 0.3 metres placed anywhere within the coverage areas must be at least partially visible to the driver of the

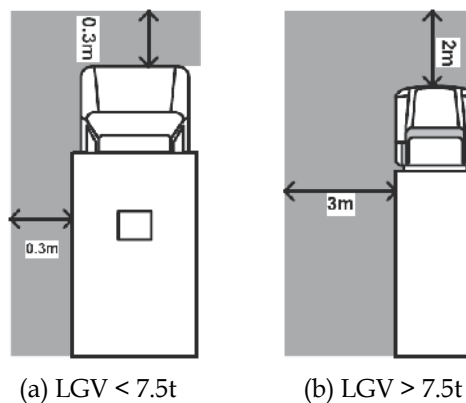


Fig. 2. Proposed Japanese legislation: area in which a cylinder (1m high, 0.3m diameter) must be at least partially visible to the driver of the (right-hand drive) LGV (UNECE, 2005).

LGV directly, by mirror or by camera. However, in this legislation, it is proposed that objects within blind-zones caused by A-pillars and external mirrors need not be visible to the driver of the vehicle (UNECE, 2002).

In both the EU and the Japanese requirements, the focus has been on LGVs, as these pose the greatest risk to other road users, including pedestrians (Desapriya et al., 2010).

3. Technologies

The general opinion of within the automotive industry is that camera-based technologies will provide the best means to prevent road fatalities. For example, the Insurance Institute for Highway Safety recently stated that "NHTSA has presented evidence suggesting that current non-visual technologies (e.g., radar and sonar sensors) do not represent an effective solution to the problem of backover crashes. Both the unreliability of current sensors to detect people and drivers slow responses to audible warnings suggest that requiring or even allowing such systems in lieu of vision-based systems is not advisable at this time" (IIHS, 2009). The NHTSA themselves have said that "camera based systems may have the greatest potential to provide drivers with reliable assistance in identifying people in the path of the vehicle when backing" (NHTSA, 2006).

The camera-monitor combination can be thought of as a passive device - it displays information to the user, but provides no active warning in the presence of, for example, pedestrians or other objects. While the visual display of information is perhaps the most important aspect for driver/VRU safety, the NHTSA have said that a "driver must look at the display and have the capability to identify an object or person in the path when backing up, and to react and brake quickly enough to prevent the incident" (NHTSA, 2006). This reaction time can potentially be reduced significantly if a warning can be issued to the driver of the vehicle. One automotive manufacturer has stated in a research paper that "sensing the surroundings of the vehicle is the key technology for such [driving assistance and warning systems]. Machine vision technology, especially, is expected to detect surrounding objects with high space resolution as well as lane markings painted on the road surface" (Takahashi et al., 2003).

Thus, in this section, we discuss some of the camera-based technologies that can be utilised to provide visual information and active warnings to drivers of vehicles.

3.1 Visual systems

The aim of a visual camera systems is typically to display a vehicle's blind-zones to the driver. The sizes of blind-zones are determined by the size and design of the vehicle and mirrors, and will vary significantly according to vehicle model and manufacturer.

Consumers' Union (2010) have examined the rearward blind-zone of many non-commercial light-duty passenger vehicles (from small passenger cars to large sports utility vehicles). The zone was measured by determining how far behind the vehicle a 28-inch (0.71 metre) traffic cone needed to be before a person, seated in the drivers seat, could see its top while looking directly through the rear window, i.e. not using mirrors. For a 5-foot 8-inch (1.73 metres) tall driver, the distance measured was up to 44 feet (13.4 metres) for a commercially available four-wheel drive vehicle registered in 2006. In the same vehicle, the blind-zone distance for a 5-foot 1-inch (1.55 metres) driver extends to 69 feet (21 metres).

The blind-zone for LGVs is naturally much larger than that of light-duty vehicles. Ehlgen & Paidla (2007) calculated the forward blind-zones of a given LGV as shown in Figure 3.

Furthermore, the rearward blind-zones of LGVs tend to be very large; it has been calculated that several LGVs have a rearward blind-zone that can extend up to 65 metres on the ground plane behind the vehicle.

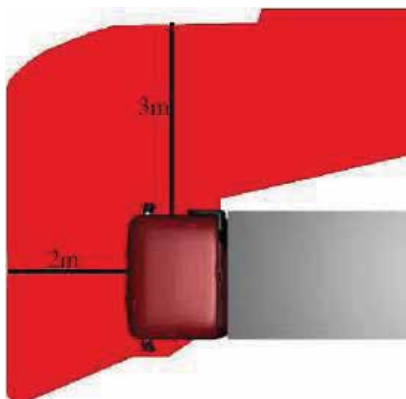


Fig. 3. Measured blind-zones around the front of a given (left-hand drive) LGV (Ehlgén & Paidla, 2007).

While rear-facing cameras can be used to cover some blind zones, the use of standard lenses has limitations. As shown in Figure 4(a), standard lens camera systems (e.g. 45° Field-Of-View (FOV) lenses) are unable to fully cover the blind-zone of some SUVs. A standard lens camera with FOV of 45° can only cover perhaps 1m of the SUV rearward blind-zone. Figure 4(b) illustrates how the use of a wide-angle lens camera system (e.g. > 100° FOV lenses) enables the entire SUV rearward blind-zone to be covered.

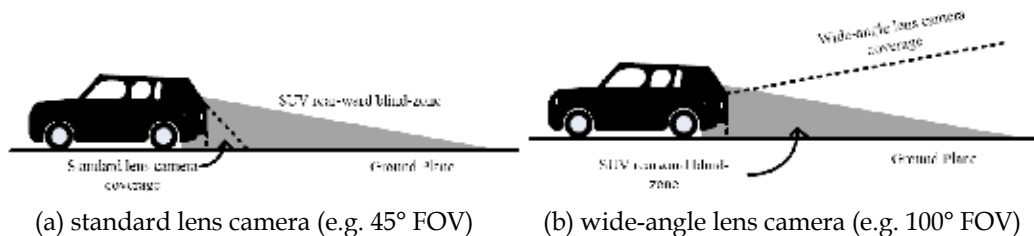


Fig. 4. Coverage for standard and wide-angle lens cameras mounted on the rear of a typical SUV.

Figure 5(a) shows a sample placement of two wide-angle cameras mounted on an LGV. Camera 1 is a 170° FOV fish-eye camera, located approximately half-way down the length of the LGV, and 3m off the ground plane. The optical axis of camera 1 is tilted at 15° from the side of the LGV trailer. Camera 2 is a 135° wide-angle camera, located in the middle of the front cabin at about 2m off the ground plane. The optical axis of camera 2 is tilted at 20° from the front face of the cabin. The angles and locations of the cameras are chosen to maximise the usable field-of-view of the cameras, and minimise the amount of the body of the vehicle captured by the cameras. With both cameras corrected for distortion, Figure 5(b) shows the areas in the vicinity of the vehicle that can be displayed to the driver. Such a camera system would cover all the blind zones of the LGV shown in Figure 3, and would meet the requirements of both the EU Directive 2003/97/EC (Figure 1), and the proposed Japanese legislation (Figure 2).

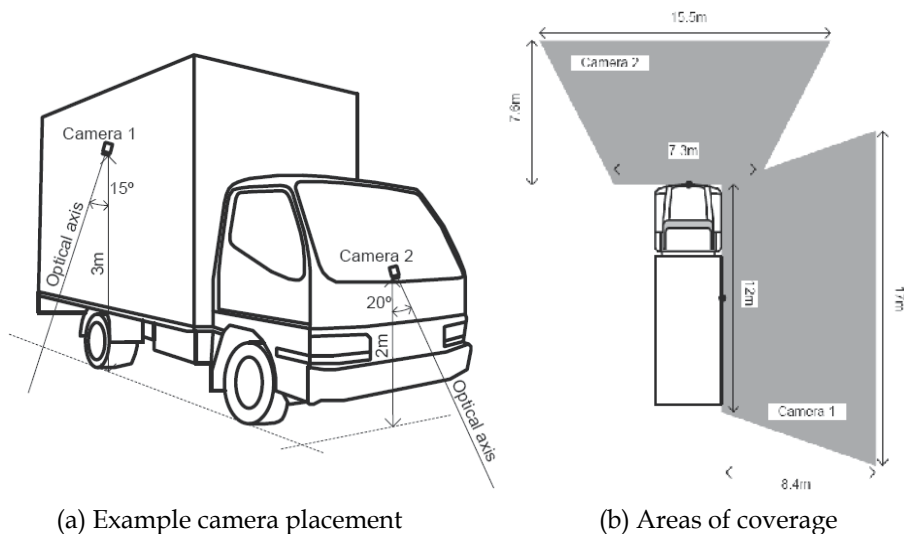


Fig. 5. Example of a potential wide-angle camera placement on an LGV that would meet the requirements of the EU Directive 2003/97/EC and the proposed Japanese legislation.

While wide-angle lenses greatly increase the area in blind zones that can be covered, problems arise due to the deviation of wide-angle lens cameras from the rectilinear pin-hole camera model, due to geometric distortion effects caused by lens elements. Fish-eye cameras deviate substantially from the pin-hole model, introducing high levels of geometric nonlinear distortion. Figure 6 shows an example of an image captured from an automotive fisheye camera. Because of this distorted representation of the real world scene on-screen, there is the potential for the driver to not recognise obstacles and VRUs. Additionally, the distortion may cause the driver to misjudge distance to objects, due to the nonlinearity of the view presented. Thus, camera calibration and fish-eye compensation are important tasks for automotive camera applications. Not only do they make images captured by the camera more visually intuitive to the human observer, they are often also necessary for computer vision tasks that require the extraction of geometric information from a given scene. Hughes et al. (2009) describe in detail how the geometric fish-eye effects of can be compensated, and Friel et al. (2010) describe a method demonstrating how calibration can be performed automatically using typical automotive video sequences.



Fig. 6. Automotive fish-eye example illustrating the effects of fisheye distortion.

3.2 Advanced Driver Assistance Systems (ADAS)

Driver inattention is one of the most common causes of traffic collisions (Ledesma et al., 2010), and as such, there is a desire for technologies that actively draw the attention of a driver in a danger situation. Thus, the demand for Advanced Driver Assistance Systems (ADAS) is expected to increase as consumers grow increasingly safety conscious, and insurance companies and regulators begin to recognise the positive impact such systems can have on accident rates. Concurrently, vision systems are becoming increasingly common in road vehicles due to advances in technology, as discussed in the previous section. Some vehicles currently come equipped with vision systems for displaying blind zone and as parking and reversing aids. However, supplemental functionality can be extracted from these cameras by using them to detect other road vehicles and VRUs. The detection of other road vehicles is a core component of many ADASs such as Automatic Cruise Control (ACC) (Hofmann et al., 2003), Advanced Collision Warning (ACW) (Dagan et al., 2004), overtaking vehicle monitoring (Hegeman et al., 2005), automatic headlamp dimming (Alcantarilla et al., 2008) and automatic blind zone monitoring (Kiefer & Hankey, 2008). It is beneficial to use standard colour cameras for these functions as they are low-cost, readily available, and may already be present on the vehicle. The colour video produced can be simultaneously used for other ADAS utilising colour data and for full colour display purposes. Additionally, standards exist that outline the performance of manoeuvring aids with distance ranging (BS ISO, 2004; 2009). Further information on vehicle detection techniques can be found in the comprehensive review by Sun et al. (2006).

Quite apart from vehicle detection algorithms, there are a several other topics of interest in the area of ADAS.

3.2.1 Lane Departure Warning (LDW)

The NHTSA has recognised that Single-Vehicle Road Departure (SVRD) crashes lead to more fatalities than any other crash type (Wang & Knipling, 1994), and as such, lane departure warning was a key technology identified by the NHTSA Intelligent Vehicle Highway System (IVHS) program that could potentially reduce the number of fatalities and injuries associated with SVRD (Mironer & Hendricks, 1994). However, at present, there are no EC directives, US directives, standards or regulations that cover LDW systems. The main forum for the creation of Standards for LDW systems is the International Organisation for Standardisation (ISO). However, while ISO standards are voluntary, there have been several instances where existing ISO standards have formed the basis for proposals to amend European Legislation (Visvikis et al., 2008).

Two standards documents are identified that are relevant for LDW systems. These are the ISO 17361:2007 Lane Departure Systems (ISO, 2007) and the American Federal Motor Carrier Safety Administration Concept of Operations and Voluntary Operational Requirements for Lane Departure Warning Systems (FMCSA-MCRR-05-005) (FMCSA, 2005). These define LDW systems as in-vehicle systems that warn the driver when an unintentional lane departure has occurred.

A previous study of the area can be found in (McCall & Trivedi, 2006). Typically, LDW algorithms segment the road markings, followed by localisation of the lane borders before lane departure can be determined. There have been several proposals for the segmentation of road markings from images, including, for example, tangent-vectors (Furusho et al., 2002), colour information in various colour spaces (Chiu & Lin, 2005; Tsung-Ying et al.,

2006)⁴, or width and colour intensity using top-hat or Gaussian filters (Takahashi et al., 2003; Baldassano et al., 2009). The localisation of lane markings can also be achieved in several ways, for example, lane-deformable models (Park et al., 2003; Wang et al., 2004) or indeed simple linear models (e.g. Hough transform), which are within the technical specification of ISO 17361:2007 and FMCSA-MCRR-05-005.

Once the lane markings are localised, the time at which lane departure occurs needs to be predicted to provide warning to the driver. Reviews of the literature have revealed that there are two main methods for lane departure prediction (Gonzalez-Mendoza et al., 2004; Taylor et al., 1999). One is lateral offset (Taylor et al., 1999), which monitors the relative distance between the lane-boundary and the vehicle, and gives a warning when the vehicle approaches to or remains near the vicinity of the lane edge. In essence, this can be thought of as a “virtual rumble strip”. The second is Time to Lane Crossing (TLC), which is the calculation of the time remaining until the vehicle crosses over the lane edge, assuming that the vehicle speed and steering angle do not change. Typically, both are reliable warning criteria (Sukhan et al., 1999). In general, TLC provides more warning time, because warnings are issued when the system predicts that the vehicle is likely to be in danger. However, as it does not take into account the drivers’ reactions, the rate of false positives is generally higher than the lateral offset method (Gonzalez-Mendoza et al., 2004). Also, the lateral offset method is generally simpler to implement, as specialised hardware is not needed to measure the host vehicles steering angle or speed. Both ISO 17361:2007 and FMCSA-MCRR-05-005 describe the concept of lane departure warning in terms of lines across which a warning is issued by the system, which is similar to the lateral offset method. Figure 7 shows an example of lane boundary detection for an LDW system.



(a) Automotive image (b) Segmented roadmarkings (c) Detected lane boundaries

Fig. 7. Example of lane boundary detection for a lane departure warning system

3.3 Night-time

3.3.1 Infrared for pedestrian detection

Visible spectrum cameras are severely limited when it comes to the task of detecting pedestrians in low-light conditions, as they can only observe what is illuminated by vehicle lamps or street lamps. While removing the near-infrared blocking filter from a regular camera can extend its low-light pedestrian detection capabilities, it has been found that far-infrared thermal night vision technology yields substantially better range for detecting

⁴ Though an issue with this is the lack of international standards in the area: lane marking colours can vary from country to country

pedestrians than these near-infrared systems (Tsimhoni et al., 2004). Far-Infrared technology is greatly suited to the task of night-time automotive pedestrian detection as thermal radiation from humans peaks in the 8-14 μ m spectral band, and no illumination is required. As pedestrians are generally warmer than the background environment, especially at night, they appear with higher intensity in far-IR imagery, greatly aiding automatic segmentation. Figure 8 shows an example of the difference between a pedestrian viewed using a visible spectrum camera and an infrared camera at night.

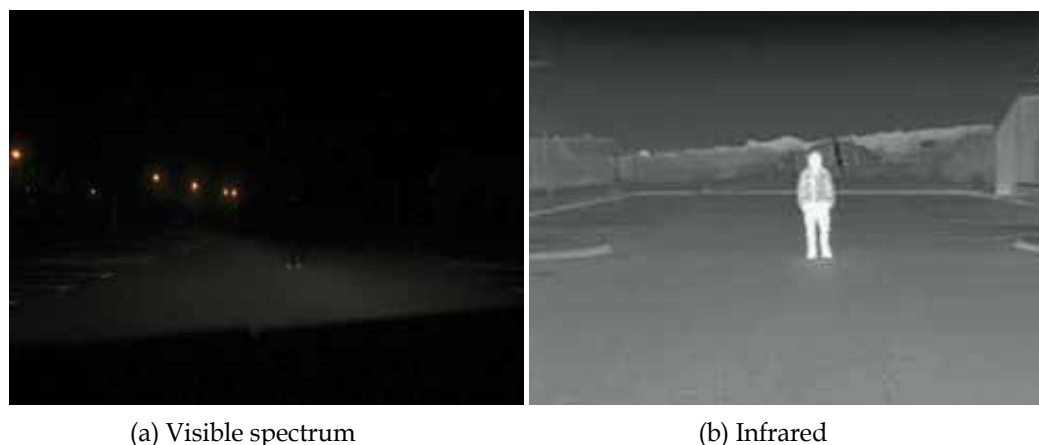


Fig. 8. Example automotive images of a pedestrian at 35m with dipped headlights

The structure of most pedestrian detection systems consists of a Region of Interest (ROI) generation stage, typically via thresholding of some form, for example, Bayes Classification (Nanda & Davis, 2002), region-growing (Bertozzi et al., 2005; Chen et al., 2008), or defining a threshold based on maximum/minimum intensity values in the infrared image (Fang et al., 2004; Xu et al., 2005). This is generally followed by a process that classifies these regions as pedestrian or non-pedestrian. Objects can be filtered according to, for example, aspect-ratio (since pedestrians are generally expected to be taller than they are wide) (Xu et al., 2005), inertial parameters (total rotational momentum of a candidate with respect to its centre) (Fang et al., 2004), horizontal and vertical grey-level intensity profiles (Fang et al., 2004), or, as humans display bilateral symmetry, grey-level symmetry and edge symmetry of pedestrians can also be used to segment regions of interest (Bertozzi et al., 2004). Edge density can also be analysed as pedestrians in far-IR images are usually much brighter than the background, and there can be a sharp change in image intensity at their edges (Bertozzi et al., 2004). The gradient operator can also be used to aid detection (Meis et al., 2003; Suard et al., 2006).

3.3.2 Vehicle detection at night

As already noted, the techniques commonly employed for vehicle detection in daylight conditions have been comprehensively reviewed by Sun et al. (2006). However, most of the features employed for daylight vehicle detection have limited use in dark conditions and night-time. Vehicle shadows, horizontal and vertical edges and corners are difficult or impossible to detect in darkness, and the most significant preceding vehicle features in dark environments are rear-facing lamps. Vehicular rear lamps appear as some of the brightest

regions in a frame of night time automotive video, so it is common in image processing techniques for lamp detection to begin with some form of thresholding. Grayscale or brightness thresholding is a common starting point (Alt et al., 2008; Alcantarilla et al., 2008), though typically further filtering is required as there are many potential light sources that are not rear vehicle lamps, such as street lamps, headlamps of oncoming vehicles and reflections from signs. Employing a red color filter has been shown to be an effective way to remove non-vehicle light-sources, using a variety of colour spaces (Chen, 2009; Wang et al., 2005; Cabani et al., 2005; O'Malley et al., 2010a).

Current commercial systems use non-standard camera hardware with custom hardware filters – i.e. non-Bayer colour filter arrays with combinations of red and clear filters have proven effective in detection of red lamps and differentiating between tail lamps and other light sources (Stein et al., 2009; López et al., 2008). Another system utilises two coated lenses (one blocking red light, one allowing only red light to pass) to focus incoming light onto different parts of a single image sensor (Schadel & Falb, 2007; Beschtel et al., 2008). While custom hardware can have performance advantages, these cameras cannot produce color images so cannot be reused for other ADAS that use color image processing. Thus, they have very limited use in terms of displaying video to the driver, and can also add cost and complexity to automotive systems.

In addition to tail lamp detection, headlamp detection (O'Malley et al., 2010b) is an important application for systems such as automatic headlamp dimming, or rearward vehicle detection for applications such as collision warning, blind-spot monitoring and overtaking vehicle detection. Headlamps have been detected by utilising, for example, top-hat filters (Alcantarilla et al., 2008) or optical flow (Ohta & Nijijima, 2005).

Once tail lamp or headlamp candidates have been detected in a video frame, to improve robustness, a system can be put in place to pair the detected tail-lamps, to associate detected lamps with a target vehicle (Chen, 2009; O'Malley et al., 2010a;b). Figure 9 shows an example of the detection of tail lamps and headlamps.

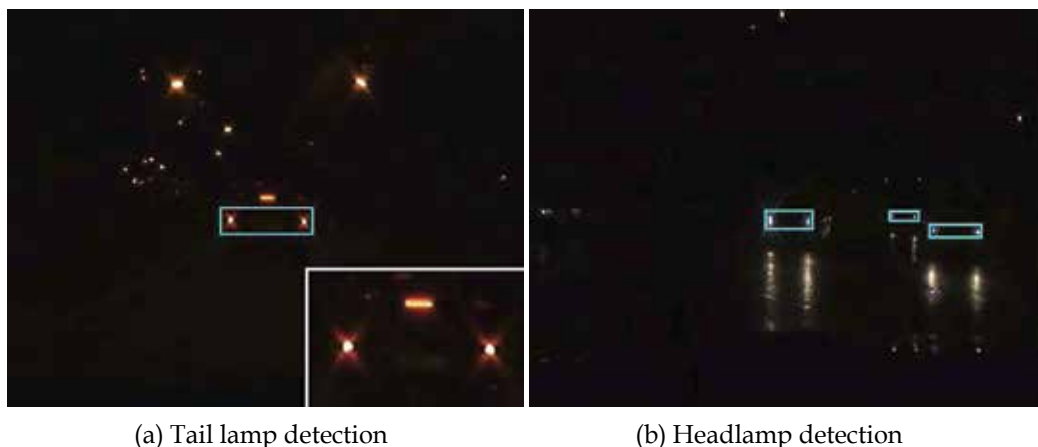


Fig. 9. Examples of vehicle detection at night (O'Malley et al., 2010a;b).

3.4 Other

There are other applications of vehicular vision systems that are, perhaps, less safety critical than those discussed in previous sections. For example, road-sign recognition is becoming a

popular application (Lopez & Fuentes, 2007). Poor weather conditions can also be detected (Kurihata et al., 2005). Cameras that are already installed on vehicles could also be used for recording in accident situations, with benefits such as decreasing management and legal costs, be a tool for education and emphasis of safety to drivers and, in general, discourage poor driving practices (Sul & Cho, 2009).

4. Conclusions

In this chapter, the rationale for the on-vehicle use of camera systems has been discussed. With increasing numbers of vehicles on the world's roads, statistics show that a significant percentage of traffic fatalities are caused by drivers who are not aware of VRUs and other road users. While customer demand for products that give information about a vehicle's blind-zones to the driver is already high, pending and existing legislation is, de facto, making the installation of such cameras on vehicles a necessity, particularly for large SUVs and LGVs. However, while small vehicles are exempt from current European and Japanese legislation, US legislation specifically targets the smaller private vehicles.

Ultimately, camera systems will be necessary equipment for improved visibility around vehicles, particularly SUVs and LGVs, where the blind-zones are substantial. Wide-angle/fish-eye camera systems are currently the best candidates, because of their ability to display even the largest blind-zones of a vehicle.

Given that camera systems will be used extensively in the future for visual systems, the versatility of vision systems means that it makes economic sense that these systems should be reused for automotive machine vision tasks. Several safety-critical ADAS applications have been discussed in this chapter, though these are only the more popular applications. There are, undoubtedly, a multitude of other applications that can be applied to an automotive camera system, for safety or assistance situations.

Camera systems will soon be as commonplace on vehicles as climate control systems or antilock braking systems.

5. References

- A-NCAP (2010). Australasian New Car Assessment Program (A-NCAP) website. <http://www.ancap.com.au>, accessed May 2010.
- Akerstedt, T., Kecklund, G. & Hörte, L.-G. (2001). Night driving, season, and the risk of highway accidents, *Sleep* 24(4): 401–406.
- Alcantarilla, P., Bergasa, L., Jimenez, P., Sotelo, M., Parra, I., Fernandez, D. & Mayoral, S. (2008). Night time vehicle detection for driving assistance lightbeam controller, *Proceedings of the IEEE Intelligent Vehicles Symposium*, Eindhoven, The Netherlands, pp. 291–296.
- Alt, N., Claus, C. & Stechele, W. (2008). Hardware/software architecture of an algorithm for vision-based real-time vehicle detection in dark environments, *Proceedings of Design, Automation and Test in Europe*, Munich, Germany, pp. 176–181.
- Andre, J. (1996). Visual functioning in challenging conditions: Effects of alcohol consumption, luminance, stimulus motion, and glare on contrast sensitivity, *Journal of Experimental Psychology: Applied* 2(3): 250–269.
- Baldassano, C., Franken, G., Mayer, J., Saxe, A. & Yu., D. (2009). Kratos: Princeton university's entry in the 2008 intelligent ground vehicle competition, *Proceedings of*

- the IS&T/SPIE Conference on Intelligent Robots and Computer Vision XXVI : Algorithms and Techniques*, Vol. 7252, San Jose, California, USA.
- Bertozzi, M., Broggi, A., Fascioli, A., Graf, T. & Meinecke, M.-M. (2004). Pedestrian detection for driver assistance using multiresolution infrared vision, *IEEE Transactions on Vehicular Technology* 53(6): 1666–1678.
- Bertozzi, M., Broggi, A., Lasagni, A. & Rose, M. (2005). Infrared stereo vision based pedestrian detection, *Proceedings IEEE Intelligent Vehicles Symposium*, Las Vegas, Nevada, USA, pp. 24–29.
- Beschtel, J. H., Stam, J. S. & Roberts, J. K. (2008). Vehicle vision based systems having improved light source distinguishing features, U.S. Patent US 7,408,136 B2.
- BS ISO (2004). BS ISO 17386:2004: Transport information and control systems – Manoeuvring Aids for Low Speed Operation (MALSO) – Performance requirements and test procedures.
- BS ISO (2009). Draft BS ISO 22840: Intelligent transport systems – Devices to aid reverse manoeuvres – Extended range backing aid systems (ERBA).
- C-NCAP (2010). Chinese New Car Assessment Program (C-NCAP) website. <http://www.c-ncap.org/> (Chinese Language), accessed May 2010.
- Cabani, I., Toulminet, G. & Bensrhair, A. (2005). Color-based detection of vehicle lights, *Proceedings of the IEEE Intelligent Vehicles Symposium*, Las Vegas, Nevada, USA, pp. 278–283.
- CARE (2010). European Road Accident Database: Trends. http://ec.europa.eu/transport/road_safety/observatory/statistics/care_en.htm, accessed May 2010.
- CEC (2009). Commission of the European Communities, Commission Staff Working Document: Accompanying document to the proposal for a directive of the European Parliament and of the Council on the retrofitting of mirrors to heavy goods vehicles registered in the Community Full Impact Assessment COM(2006)570. [http://www.europarl.europa.eu/registre/docs_autres_institutions/commission_europeenne/sec/2006/1238/COM_SEC\(2006\)_1238_EN.pdf](http://www.europarl.europa.eu/registre/docs_autres_institutions/commission_europeenne/sec/2006/1238/COM_SEC(2006)_1238_EN.pdf), accessed May 2010.
- Chen, Y.-L. (2009). Nighttime vehicle light detection on a moving vehicle using image segmentation and analysis techniques, *WSEAS Transactions on Computers* 8(3): 506–515.
- Chen, Y.-L., Liu, X. & Huang, Q. (2008). Real-time detection of rapid moving infrared target on variation background, *Infrared Physics & Technology* 51(3): 146–151.
- Chiu, K. & Lin, S. (2005). Lane detection using color-based segmentation, *Proceedings of the IEEE Intelligent Vehicle Symposium*, Las Vegas, USA, pp. 706–711.
- Consumers' Union (2010). Consumer reports: Blind-zone measurements. <http://www.consumerreports.org/cro/cars/car-safety/car-safety-reviews/mind-that-blind-spot-1005/overview/index.htm>, accessed May 2010.
- Dagan, E., Mano, O., Stein, G. & Shashua, A. (2004). Forward collision warning with a single camera, *Proceedings of the IEEE Intelligent Vehicles Symposium*, Parma, Italy, pp. 37–42.
- Desapriya, E., Subzwari, S., Sages, D., Basic, A., Alidina, A., Turcotte, K. & Pike, I. (2010). Do light truck vehicles (LTV) impose greater risk of pedestrian injury than passenger cars? a meta-analysis and systematic review, *Traffic Injury Prevention* 11(1): 48–56.
- DfT (UK) (2008a). Department for Transport (UK) Research Database: 'Primary and Electronic Safety'. <http://www.dft.gov.uk/rmd/subprogramme.asp?intProgrammeID=74&intSubProgrammeID=134>, accessed May 2010.

- DfT (UK) (2008b). Department for Transport (UK) Research Database: 'Secondary Safety'. <http://www.dft.gov.uk/rmd/subprogramme.asp?intProgrammeID=74&intSubProgrammeID=132>, accessed May 2010.
- EC (2009). Official Journal of the European Union, REGULATION (EC) No 78/2009 on the type-approval of motor vehicles with regard to the protection of pedestrians and other vulnerable road users.
- ECDGET (2004). European Commission Directorate-General for Energy and Transport, Halving the number of road accident victims in the EU by 2010: A shared responsibility. http://ec.europa.eu/transport/roadsafety_library/rsap/memorsap_en.pdf, accessed May 2010.
- ECMT (1994). Principal actions of ECMT in the field of road safety, *Technical report*, European Conference of Ministers of Transport.
- Ehlgen, T. & Paidla, T. (2007). Maneuvering aid for large vehicle using omnidirectional cameras, *Proceedings of the IEEE Workshop on Applications of Computer Vision*, Austin, Texas, USA, p. 17.
- EPC (2003). European Parliament and Council, Directive 2003/97/EC of 10 November 2003 on the approximation of the laws of the Member States relating to the type-approval of devices for indirect vision and of vehicles equipped with these devices, amending Directive 70/156/EEC and repealing Directive 71/127/EEC. <http://eur-lex.europa.eu/LexUriServ/LexUriServ.do?uri=CELEX:32003L0097:EN:NOT>, accessed May 2010.
- EPC (2007). European Parliament and Council, Directive 2007/38/EC of 11 July 2007 on the retrofitting of mirrors to heavy goods vehicles registered in the Community. <http://www.europarl.europa.eu/meetdocs/0042009/documents/dt/647/647885/647885en.pdf>, accessed May 2010.
- ERSO (2007). Traffic Safety Basic Facts 2007 - Pedestrians, *Technical report*, European Road Safety Observatory.
- ERSO (2008). Traffic Safety Basic Facts 2008 - Motorways, *Technical report*, European Road Safety Observatory. Report No. D.1.21.
- Euro-NCAP (1997). European New Car Assessment Program (Euro NCAP) website. <http://www.euroncap.com>, accessed May 2010.
- Fang, Y., Yamada, K., Ninomiya, Y., Horn, B. & Masaki, I. (2004). A shape independent method for pedestrian detection with far-infrared images, *IEEE Transactions on Vehicular Technology* 53(6): 1679-1697.
- FARS (2010). Fatality Analysis Reporting System: Fatal Crashes by Weather Condition and Light Condition, USA, 2008. <http://www-fars.nhtsa.dot.gov/Crashes/CrashesTime.aspx>, accessed May 2010.
- FMCSA (2005). FMCSA-MCRR-05-005: Lane departure warning systems - Concept of operations and voluntary operational requirements for lane departure warning systems on-board commercial motor vehicles.
- FMVSS (1971). National Highway Traffic Safety Administration - Federal Motor Vehicle Safety Standard No. 111 (49 CFR 571.111): Rearview Mirrors.
- FMVSS (2009). National Highway Traffic Safety Administration - Federal Motor Vehicle Safety Standard: Rearview Mirrors - Proposed Rule (Docket Number NHTSA-2009-0041) - Advanced notice of proposed rulemaking (ANPRM).
- Fors, C. & Lundkvist, S.-O. (2009). Night-time traffic in urban areas - a literature review on road user aspects, *Technical report*, V.T.I. Rapport 650Av.

- Friel, M., Hughes, C., Denny, P., Jones, E. & Glavin, M. (2010). Automatic calibration of fisheye cameras from automotive video sequences, *IET Intelligent Transport Systems*. To be published (accepted).
- Furusho, H., Shirato, R. & Shimakage, M. (2002). A lane recognition method using the tangent vectors of white lane markers, *Proceedings of the International Symposium on Advanced Vehicle Control*, Hiroshima, Japan, pp. 9–12.
- Gandhi, T. & Trivedi, M. (2007). Pedestrian Protection Systems: Issues, Survey, and Challenges, *IEEE Transactions on Intelligent Transportation Systems* 8(3): 413–430.
- Gentex (2009). Submission regarding docket NHTSA 2009-0041 - FMVSS 111 ANPRM: Rearview mirrors.
- GM (2009). General Motors North America, submission regarding docket NHTSA 2009-0041 - FMVSS 111 ANPRM: Rearview mirrors.
- Gonzalez-Mendoza, M., Jammes, B., Hernandez-Gress, N., Titli, A. & Esteve, D. (2004). A comparison of road departure warning systems on real driving conditions, *Proceedings of the IEEE Conference on Intelligent Transportation Systems*, Washington, District of Columbia, USA, pp. 349–354.
- Hegeman, G., Brookhuis, K. & Hoogendoorn, S. (2005). Opportunities of advanced driver assistance systems towards overtaking, *European Journal of Transport and Infrastructure Research* 5(4): 281–296.
- Hobbs, A. (1996). Euro ncap/mori survey on consumer buying interests (speech and presentation), *Proceedings of the Euro NCAP Conference: Creating a Market for Safety - 10 years of Euro NCAP*, Brussels, Belgium.
- Hofmann, U., Rieder, A. & Dickmanns, E. (2003). Radar and vision data fusion for hybrid adaptive cruise control on highways, *Machine Vision and Applications* 14(1): 42–49.
- HR1216 (2007). HR 1216: Cameron Gulbransen Transportation Safety Act. <http://www.govtrack.us/congress/bill.xpd?bill=h110-1216>, accessed May 2010.
- Hughes, C., Glavin, M., Jones, E. & Denny, P. (2009). Wide-angle camera technology for automotive applications: a review, *IET Intelligent Transport Systems* 3(1): 19–31.
- IIHS (2009). Insurance institute for highway safety, submission regarding docket NHTSA 2009-0041 - FMVSS 111 ANPRM: Rearview mirrors.
- ISO (2007). ISO 17361:2007: Intelligent transport systems - Lane departure warning systems - Performance requirements and test procedures.
- J-NCAP (2010). Japanese New Car Assessment Program (J-NCAP) website. <http://www.nasva.go.jp/mamoru/indexe.html>, accessed May 2010.
- K-NCAP (2010). Korean New Car Assessment Program (KNCAP) website. <http://www.car.go.kr/> (Korean Language), accessed May 2010.
- KCO (n.d.). Kids and Cars Organisation website. <http://kidsandcars.org/>, accessed May 2010.
- Kiefer, R. & Hankey, J. (2008). Lane change behavior with a side blind zone alert system, *Accident Analysis and Prevention* 40(2): 683–690.
- Kurihata, H., Takahashi, T., Ide, I., Mekada, Y., Murase, H., Tamatsu, Y. & Miyahara, T. (2005). Rainy weather recognition from in-vehicle camera images for driver assistance, *Proceedings of the IEEE Intelligent Vehicles Symposium*, Las Vegas, Nevada, USA, pp. 205–210.
- Lawrence, G., Hardy, B., Carroll, J., Donaldson, W., Visvikis, C. & Peel, D. (2006). A study on the feasibility of measures relating to the protection of pedestrians and other vulnerable road users, *Technical Report UPR/VE/045/06*, Transport Research Laboratory Ltd.

- Ledesma, R., Montes, S., Poó, F. & López-Ramón, M. (2010). Individual differences in driver inattention: The attention-related driving errors scale, *Traffic Injury Prevention* 11(2): 142-150.
- López, A., Hilgenstock, J., Busse, A., Baldrich, R., Lumbreras, F. & Serrat, J. (2008). Nighttime vehicle detection for intelligent headlight control, *Proceedings of the International Conference on Advanced Concepts for Intelligent Vision Systems*, Juan-les-Pins, France, pp. 113-124.
- Lopez, L. & Fuentes, O. (2007). Color-based road sign detection and tracking, *Proceedings of the International Conference on Image Analysis and Recognition*, Montreal, Canada, pp. 1138-1147.
- Magna (2009). Submission regarding docket NHTSA 2009-0041 - FMVSS 111 ANPRM: Rearview mirrors.
- McCall, J. & Trivedi, M. (2006). Video-based lane estimation and tracking for driver assistance: survey, system, and evaluation, *IEEE Transactions on Intelligent Transportation Systems* 7(1): 20-37.
- McLoughlin, E., Middlebrooks, J., Anest, J., Holmgreen, P. & Dellinger, A. (2002). Injuries and deaths among children left unattended in or around motor vehicles - United States, July 2000-June 2001, *Centers for Disease Control and Prevention (United States Department of Health and Human Services) Morbidity and Mortality Weekly Report* 51(26): 570- 572.
- Meis, U., Ritter, W. & Neumann, H. (2003). Detection and classification of obstacles in night vision traffic scenes based on infrared imagery, *Proceedings IEEE Intelligent Transportation Systems Conference*, Vol. 2, Shanghai, China, pp. 1140-1144.
- Mironer, M. & Hendricks, D. (1994). Examination of single vehicle roadway departure crashes and potential IVHS countermeasures, *Technical report*, Department Of Transport (US). Report no. HS 808 144.
- Mohan, D. (2002). Traffic safety and health in indian cities, *Journal of Transport and Infrastructure* 9(1): 79-94.
- Nanda, H. & Davis, L. (2002). Probabilistic template based pedestrian detection in infrared videos, *Proceedings of the IEEE Intelligent Vehicle Symposium*, Versailles, France , pp. 15- 20.
- Nhan, C., Rothman, L., Slater, M. & Howard, A. (2009). Back-over collisions in child pedestrians from the Canadian hospitals injury reporting and prevention program, *Traffic Injury Prevention* 10(4): 350-353.
- NHTSA (2006). Vehicle backover avoidance technology study - report to congress, *Technical report*, National Highway Traffic Safety Administration.
- NHTSA (2007). National Highway Traffic Safety Administration (United States), Not-in-Traffic Surveillance 2007 - Highlights.
<http://www-nrd.nhtsa.dot.gov/Pubs/811085.PDF>, accessed May 2010.
- NHTSA (2008). Traffic Safety Facts: 2008 Data: Pedestrians, *Technical report*, National Highway Traffic Safety Administration. Report No. DOT HS 811 163.
- Nissan (2009). Submission regarding docket NHTSA 2009-0041 - FMVSS 111 ANPRM: Rearview mirrors.
- OECD (1998). Programme of Co-operation in the Field of Research on Road Transport and Intermodal Linkages, Safety of Vulnerable Road Users, *Technical report*, Scientific Expert Group on the Safety of Vulnerable Road Users, Organisation for Economic Co-operation and Development (OECD). Report No. DSTI/DOT/RTR/RS7(98)1/FINAL.

- Ohta, N. & Nijjima, K. (2005). Detection of approaching cars via artificial insect vision, *Electronics and Communications in Japan (Part III: Fundamental Electronic Science)* 88(10): 57–65.
- O'Malley, R., Jones, E. & Glavin, M. (2010a). Rear-lamp vehicle detection and tracking in low exposure color video for night conditions, *IEEE Transactions on Intelligent Transportation Systems* 11(2).
- O'Malley, R., Jones, E. & Glavin, M. (2010b). Vision based detection and tracking of vehicles to the rear with perspective correction in low-light conditions, *IET Intelligent Transport Systems*. To be published (accepted).
- Oya, H., Ando, K. & Kanoshima, H. (2002). A Research on Interrelation between Illuminance at Intersections and Reduction in Traffic Accidents, *Journal of Light and Visual Environment* 26(1): 29–34.
- Park, J., Lee, J. & Jhang, K. (2003). A lane-curve detection based on an LCF, *Pattern Recognition Letters* 24(14): 2301–2313.
- Patel, R., Dellinger, A. & Anest, J. (2005). Nonfatal motor-vehiclerelated backover injuries among children – United States, 2001–2003, *Centers for Disease Control and Prevention (United States Department of Health and Human Services) Morbidity and Mortality Weekly Report* 54(6): 144–146.
- Peden, M., Scurfield, R., Sleet, D., Mohan, D., Hyder, A., Jarawan, E. & Mathers, C. (2004). *World Report on Road Traffic Injury Prevention*, World Health Organization.
- Plainis, S., Murray, I. & Pallikaris, I. (2006). Road traffic casualties: understanding the nighttime death toll, *Injury Prevention* 12(2): 125–128.
- Schadel, C. & Falb, D. (2007). Smartbeam – a high-beam assist, *Proceedings of the International Symposium on Automotive Lighting*, Darmstadt, Germany, pp. 774–782.
- Singh, S. (2005). Review of urban transportation in India, *Journal of Public Transportation* 8(1): 79–97.
- Stein, G. P., Hadassi, O., Haim, N. B. & Wolfvovitz, U. (2009). Headlight, taillight and streetlight detection, U.S. Patent US 7,566,851 B2.
- Suard, F., Rakotomamonjy, A., Bensrhair, A. & Broggi, A. (2006). Pedestrian detection using infrared images and histograms of oriented gradients, *Proceedings IEEE Intelligent Vehicles Symposium*, Tokyo, Japan, pp. 206–212.
- Sukhan, L., Woong, K. & Jae-Won, L. (1999). A vision based lane departure warning system, *Proceedings of the IEEE/RSJ International Conference on Intelligent Robots and Systems*, Kyongju, South Korea, pp. 160–165.
- Sul, J. & Cho, S. (2009). Obtaining and applying of traffic accident data using automatic accident recording system in korea, *Proceedings of the International Road Traffic and Accident Database Conference*, Seoul, South Korea, pp. 394–395.
- Sun, Z., Bebis, G. & Miller, R. (2006). On-road vehicle detection: A review, *IEEE Transactions on Pattern Analysis and Machine Intelligence* 28(5): 694–711.
- Takahashi, A., Ninomiya, Y., Ohta, M., Nishida, M. & Yoshikawa, N. (2003). Research report – image processing technology for rear view camera (1): Development of lane detection system, *R&D Review of Toyota Central Research and Development Labs* 38(2): 31–36.
- Takeuchi, K. & Ikari, T. (2007). The correlation between JNCAP pedestrian head protection performance test and real-world accidents, *Proceedings of the 20th Enhanced Safety of Vehicles Conference: Innovations for Safety: Opportunities and Challenges*, Lyon, France.
- Taylor, C., Kosecká, J., Kosecká, C., Blasi, R. & Malik, J. (1999). A comparative study of vision-based lateral control strategies for autonomous highway driving, *International Journal of Robotics Research* 18(5): 442–453.

- Tsimhoni, O., Bärghman, J., Minoda, T. & Flannagan, M. (2004). Pedestrian Detection with Near and Far Infrared Night Vision Enhancement, *Technical report*, The University of Michigan, Transportation Research Institute 48109-2150. Report No. UMTRI-2004-38.
- Tsung-Ying, S., Shang-Jeng, T. & Chan, V. (2006). Hsi color model based lane-marking detection, *Proceedings of the IEEE Intelligent Transportation Systems Conference*, Toronto, Canada, pp. 1168-1172.
- UNECE (2002). The United Nations Economic Commission for Europe (UNECE) Working Party on General Safety Provisions (GRSG), GRSG- 83-Inf15e: Outline of Draft Amendment to ECE Regulation No.46 (Draft Requirements for Driver's Field of Vision of Immediate Frontward and Sideward). <http://www.unece.org/trans/doc/2002/wp29grsg/TRANS-WP29-GRSG-83-inf15e.doc>, accessed May 2010.
- UNECE (2005). The United Nations Economic Commission for Europe (UNECE) Working Party on General Safety Provisions (GRSG), GRSG-89-26: Proposal for Step-2 revision of Regulation No. 46. <http://www.unece.org/trans/doc/2005/wp29grsg/TRANS-WP29-GRSG-89-inf26e.pdf>, accessed May 2010.
- UNECE (2009). The United Nations Economic Commission for Europe (UNECE) World Forum for Harmonization of Vehicle Regulations Agreement concerning the adoption of uniform technical prescriptions for wheeled vehicles, equipment and parts which can be fitted and/or used on wheeled vehicles and the conditions for reciprocal recognition of approvals granted on the basis of these prescriptions: Addendum 45: Regulation No. 46: Revision 3: Uniform provisions concerning the approval of devices for indirect vision and of motor vehicles with regard to the installation of these devices. E/ECE/324 E/ECE/TRANS/505 Rev.1/Add.45/Rev.3. <http://www.unece.org/trans/main/wp29/wp29regs/r046r3e.pdf>, accessed May 2010.
- UNECE (2010). The United Nations Economic Commission for Europe (UNECE) Working Party on General Safety Provisions (GRSG), ECE/TRANS/WP.29/GRSG/2010/9: Proposal for amendments to Regulation No. 46. <http://www.unece.org/trans/doc/2010/wp29grsg/ECE-TRANS-WP29-GRSG-2010-09.pdf>, accessed May 2010.
- US-NCAP (2010). US National Highway Traffic Safety Administration (US-NCAP) website. <http://www.safercar.gov/>, accessed May 2010.
- Visvikis, C., Pitcher, T. & Smith, R. (2008). Review of Technical Standards, in T. Smith (Ed.): Study on lane departure warning and lane change assistant systems (Transport Research Laboratory).
- Wang, C.-C., Huang, S.-S. & Fu, L.-C. (2005). Driver assistance system for lane detection and vehicle recognition with night vision, *Proceedings of the IEEE/RSJ International Conference Intelligent Robots and Systems*, Edmonton, Alberta, Canada, pp. 3530-3535.
- Wang, J. & Knipling, R. (1994). Lane change/merge crashes: problem size assessment and statistical description, *Technical report*, United States Department of Transportation Publication. Report No. DOT HS 808-075.
- Wang, Y., Teoh, E. & Shen, D. (2004). Lane detection and tracking using B-Snake, *Image and Vision Computing* 22(4): 269-280.
- Xu, F., Liu, X. & Fujimura, K. (2005). Pedestrian detection and tracking with night vision, *IEEE Transactions on Intelligent Transportation Systems* 6(1): 63-71.

Advancements in Automotive Antennas

Brendan D. Pell, Edin Sulic, Wayne S. T. Rowe,
Kamran Ghorbani and Sabu John
*RMIT University
Australia*

1. Introduction

Today's production vehicles are fitted with a multitude of antennas to facilitate communication and enable a moving vehicle to connect with the outside world. Recent years have seen the introduction of new electronic devices to the automotive environment. These devices are usually designed to aid the driver, increase safety, or enhance the driving experience, and many of them rely on wireless communication to perform their task. Antennas are a necessary part of any wireless communication system, enabling transmission and reception of signals in free-space.

At the same time, automobile manufacturers have been seeking to create cost effective, fuel efficient vehicles with attractive styling. This leads to a focus on sleek, lightweight vehicles with reduced aerodynamic drag and improved styling - an emphasis that would naturally conflict with fitment of traditional antennas. These market preferences, along with the technological factors, have combined in the past few years to drive significant innovation in the world of vehicular antennas.

In this chapter, we review the basics of antennas and radiation and examine the frequencies and services which are commonly used in the automotive environment. We will briefly discuss the antennas traditionally used on vehicles, and then detail the recent developments and trends in automotive antenna research.

2. Antenna fundamentals

Antennas are necessary components of any wireless communications device or system. An antenna is a device designed to send or receive radio waves. The antenna takes a guided wave, usually bound to a transmission line of some type such as a coaxial line, waveguide or microstrip transmission line and allows that same energy to propagate through free space. Antennas are passive devices, meaning that they do not require an external power source. They are also linear, meaning that their function is preserved regardless of the applied power level, and reciprocal, which implies that they behave in an equivalent manner in either transmit or receive modes.

Electrically conductive materials are commonly used to create antennas. Most antennas are made from metals, although they can be constructed from dielectric materials.

2.1 Key properties of antennas

Specialised terminology is used to describe antenna performance. This language allows engineers to express antenna behaviour, specify requirements, and compare various design options. Some of the most commonly used terms are included below. Text which appears in quotation marks is from the IEEE Standard Definitions of Terms for Antennas (IEEE Std 145-1993).

Bandwidth

The *bandwidth* of an antenna refers to “the range of frequencies within which the performance of the antenna, with respect to some characteristic, conforms to a specified standard”. The most common usage of bandwidth is in the sense of *impedance bandwidth*, which refers to those frequencies over which an antenna may operate. This is often defined with the aid of the Voltage Standing Wave Ratio (VSWR) or return loss values from measurements.

Other bandwidths which may be referred to are *gain bandwidth*, which defines the range of frequencies over which the gain is above a certain value, and *axial ratio bandwidth* which may be used in the case of a circularly polarised antenna.

Radiation Pattern

The *radiation pattern* represents the energy radiated from the antenna in each direction, often pictorially. The IEEE Definition states that it is “the spatial distribution of a quantity that characterizes the electromagnetic field generated by an antenna”. Most often this is the radiation intensity or power radiated in a given direction.

Gain

In many wireless systems an antenna is designed to enhance radiation in one direction while minimising radiation in other directions. This is achieved by increasing the *directivity* of the antenna which leads to *gain* in a particular direction. The *gain* is thus “the ratio of the radiation intensity, in a given direction, to the radiation intensity that would be obtained if the power accepted by the antenna were radiated isotropically” (that is, equally in all directions). In the case of a receiving antenna, an increase in gain produces increased sensitivity to signals coming from one direction with the corollary of a degree of rejection to signals coming from other directions. Antenna gain is often related to the gain of an isotropic radiator, resulting in units *dBi*. An alternative is to relate the gain of any given antenna to the gain of a dipole thus producing the units *dBd*. (0 dBd = 2.15 dBi). Antenna gain may be viewed with the aid of a *radiation pattern*.

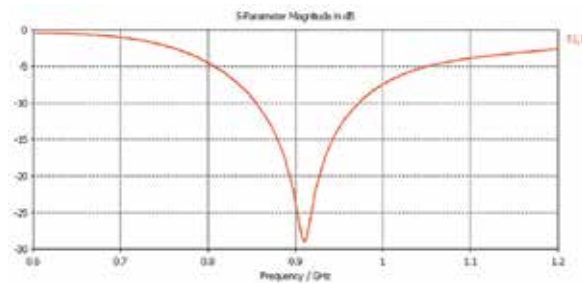
Polarisation

Polarisation of the wave radiated from an antenna describes the behaviour of the electric and magnetic field vectors as they propagate through free space. Polarisation is typically approximately *linear*. When linear the polarisation may be further described as either *vertical* or *horizontal* based on the orientation of the electric field with respect to earth. In the automotive environment, the polarisation of signals depends on the service in question. Many satellite services (such as GPS) use *circularly polarised* signals. For best performance the polarisation of the receive antenna should match the polarisation of the transmitted signal.

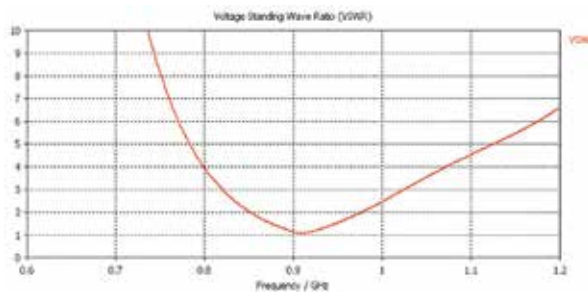
2.2 Impedance matching conventions

In low frequency electronic circuits ordinary wires are used to connect components together to form a circuit. When the frequency in the circuit is high, or the circuit dimensions approach that of a wavelength, a transmission line (a special configuration of wires or flat conductors) must be used to connect these components and avoid reflections. This transmission line has a defined impedance, and allows the high frequency energy to propagate down the line. Impedance discontinuities in this transmission line will cause a reflection and stop effective transmission down the line. For this reason the input impedance of an antenna is critical to achieving proper matching to the transmitting device to which it is attached. Most transmission lines have an impedance of 50Ω , while the impedance of an antenna changes with frequency. At some frequencies a given antenna will not be matched to the transmission line, and will not accept or radiate power, while at those frequencies where the antenna is designed to operate, the impedance of the antenna will allow the electromagnetic energy to pass into the structure and radiate into the surrounding space. These frequencies would be deemed to be inside the antenna's *impedance bandwidth*.

Two measures of stating the impedance matching are commonly used, both of which are based on the reflection coefficient, which is a measure of how much energy is reflected back into the source from the antenna's terminals. The first measure shows the reflection coefficient on a logarithmic scale as $|S_{11}|$. Common definitions require that $|S_{11}|$ be below the -10 dB line to declare an acceptable impedance match. The second measure is similar, but on a linear scale and is referred to as VSWR (Voltage Standing Wave Ratio). In this terminology an antenna is deemed to be well matched to the line where VSWR is less than 2:1. This corresponds to a value of -9.54 dB in the logarithmic scheme, meaning the measures are approximately equivalent. Fig. 1 shows plots of $|S_{11}|$ and VSWR for a dipole



(a) $|S_{11}|$ of a dipole Antenna



(b) VSWR of same dipole antenna

Fig. 1. (a) $|S_{11}|$ and (b) VSWR of a dipole antenna

antenna which is resonant near 900 MHz. Although the shape of the curves is different due to the use of either log or linear scaling, both plots reveal that the antenna presents a good impedance match to frequencies in the range from approximately 850 MHz to 970 MHz. Although a 10 dB return loss is typically required in the majority of antenna applications, there are some exceptions. While some high performance systems may specify more precise matching, a notable exception is the cellular phone industry which permits more relaxed specifications. Most modern cellular phone antennas meet an $|S_{11}|$ requirement of -6 dB (Waterhouse, 2008) which is equivalent to a VSWR of 3:1. Recent years of handset design have led to a trade off which sacrifices antenna performance in order to obtain an attractive small sized handset. The signal strengths used in cellular networks combined with advances in receiver technology and modulation schemes compensate for handset antennas having low radiation efficiency and poor electrical performance, resulting in adequate performance of the overall system.

2.3 Radiation pattern essentials

Gain and Radiation Pattern were introduced in Section 2.1. This section describes some common radiation patterns and identifies radiation pattern features. Three dimensional radiation patterns are shown in Fig. 2, while a 2D radiation pattern on a polar plot is shown in Fig. 3.

Isotropic

According to IEEE Standard 145-1993 an *Isotropic* radiator is “a hypothetical, lossless antenna having equal radiation intensity in all directions” (Fig. 2(a)). Such an antenna does not exist, nor can one be created. Nevertheless, an isotropic radiator is a useful concept as a truly omni-directional source and as a reference for gain comparison purposes. When gains are specified in *dBi* the gain of the antenna under test is being described relative to this theoretical standard.

Omni-directional

When an antenna is described as *omni-directional* this is understood to mean that the antenna radiates an “essentially non-directional pattern in a given plane of the antenna and a directional pattern in any orthogonal plane”. A pattern of this type is shown in Fig. 2(b). In this figure it may be observed that the magnitude of the radiation is non-directional in the azimuth (around the sides) but not in elevation (sweeping from high to low). A pattern of this type is produced by dipole antennas and monopoles on an infinite ground plane. It represents an ideal standard for many services in the automotive environment where coverage is required on all angles around the vehicle but not required in the upward direction towards the sky.

Directional

A *directional* radiation pattern is shown in Fig. 2(c). This type of pattern can boost the signal strength due to its higher gain if aimed in the required direction. This comes at the expense of reduced effectiveness in other directions which may be desirable in certain applications. Highly directional antennas are desirable for point-to-point links and have application in automotive radar systems where a narrow beam may be scanned to detect nearby targets.

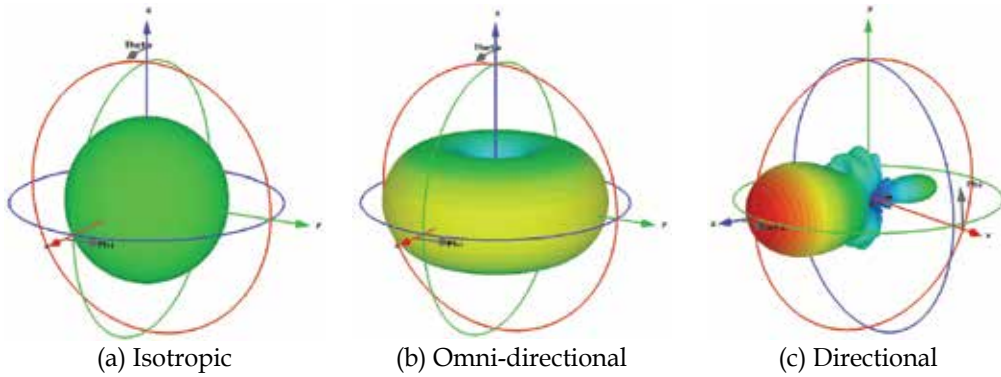


Fig. 2. Three dimensional radiation patterns

A two-dimensional representation highlighting common features

Radiation patterns are often plotted in two-dimensional form. Fig. 3 shows a 2D cut through the y-z plane of the 3D radiation pattern shown in Fig. 2(c). Careful examination of both figures will reveal the equivalence of the radiation information presented.

Distinct parts of a radiation pattern are referred to as lobes. These lobes and other characteristic features of radiation patterns are highlighted in Fig. 3.

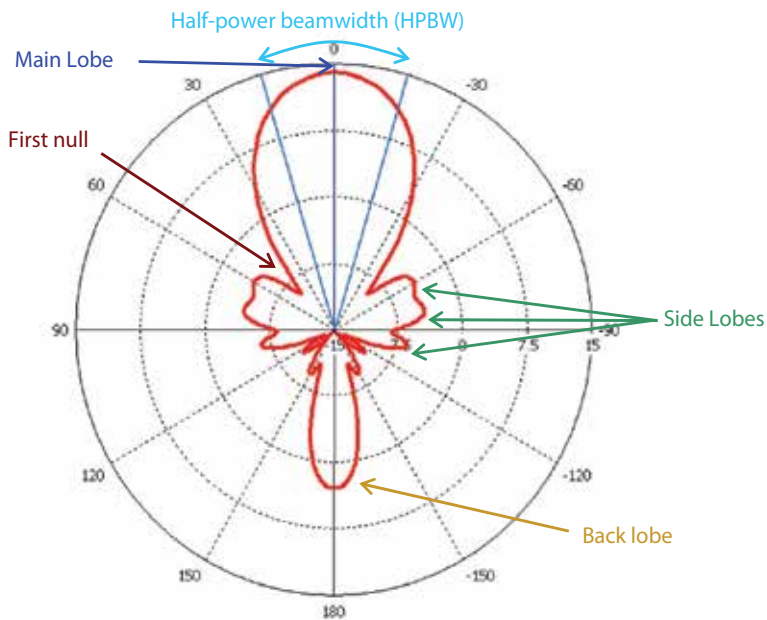


Fig. 3. A sample two dimensional radiation pattern

2.4 Near-field and far-field regions

The space surrounding an antenna may be divided into three approximate regions based on the behaviour of the electromagnetic fields in each of these regions. The first two regions are the *reactive near-field* and *radiating near-field* regions. The properties and configuration of

surrounding material in these regions may alter antenna performance, and the field at any angle is dependent on the distance to the antenna. In the third region known as the *far-field* region however it can be assumed that the antenna is a point source. The far-field region is normally regarded as beginning when the distance to the antenna is equal to $2D^2/\lambda$, where D is the maximum overall dimension of the antenna and continues on to infinity. Once in the far-field region, the radiation pattern and gain may be measured.

2.5 System considerations

Antennas are necessary components of all wireless systems, but are not of themselves sufficient for signal reception. Antennas do not operate in isolation. Here we briefly examine other important factors related to vehicular antenna systems.

Diversity Reception

Some automotive services use *diversity* to enhance the quality of the received signal. In non-line-of-site propagation environments such as the urban environment, reflections and shadows cast by buildings and other structures can cause fading in the signal strength in particular spatial locations or in given directions. In a diversity scheme two or more antennas are mounted in different locations or with different orientations on the vehicle. This provides two independent propagation paths for the signal. On an elementary level the diversity receiver switches between antennas to choose the one with the stronger signal. This provides a higher quality signal with fewer dropouts. Diversity is most commonly employed for FM radio reception purposes. Given that cars fitted with multiple antennas are regarded as being less visually appealing, vehicle manufacturers tend to combine an external mast antenna with a glass mounted antenna to give two distinct antennas for diversity purposes. This approach often achieves spatial and polarisation diversity, along with diversity in radiation direction.

Noise, Sensitivity and the Receiver

Any communications system receives the desired signal plus an unwanted signal which we may call *noise*. Noise comes from a variety of sources, ranging from the random movement of electrons inside any conductor (at a temperature above absolute zero) to Electromagnetic Interference (EMI) coupled in with the signal from nearby devices. In the automotive environment the vehicle's ignition system can be a source of significant EMI, meaning that antennas mounted near the front of the vehicle may receive more noise than an equivalent antenna mounted towards the rear.

Receiving systems have a specified *sensitivity*, which relates the minimum signal strength at the input required to achieve an acceptable Signal-to-Noise ratio (SNR). The sensitivity of commercial automotive receiving systems will have a large impact on the overall quality of the received service, particularly in areas of low signal strength.

In car radio systems the *receiver* may be called a *tuner* since it tunes its internal oscillators to demodulate the required station. The input impedance of the tuner, along with other fundamental properties are important in ensuring proper system operation.

3. Automotive frequencies and wireless services

In previous decades the use of antennas in vehicles was primarily limited to those employed for AM and FM radio. In contrast, today's vehicles are often fitted with many antennas for

additional purposes such as remote keyless entry, satellite navigation, and others. In the future it is likely that vehicles will require still more antennas for such things as mobile internet and mobile video, collision avoidance radar, and vehicle-to-vehicle or vehicle-to-infrastructure communication. A list of present and soon to be realised services is provided in Table 1. Each of these wireless services necessitates the incorporation of a suitable antenna into the vehicular platform to receive signals at the appropriate frequency.

Service	Typical Frequency	Tx*	Rx#	Direction of Radiation
AM Radio	Approximately 1 MHz		Yes	Horizontal
FM Radio	88 MHz to 108 MHz		Yes	Horizontal
In-vehicle TV	50 MHz to 400 MHz		Yes	Horizontal
Digital Audio Broadcasting (DAB)	100 MHz to 400 MHz		Yes	Horizontal
Remote Keyless Entry (RKE)	315 MHz/413 MHz/ 434 MHz		Yes	Horizontal
Tyre Pressure Monitoring System (TPMS)	315 MHz/413 MHz/ 434 MHz	Yes	Yes	Intra-vehicular
Cellular Phone (provision of Internet via HSPA)	850 MHz 900 MHz 1800 MHz 1900 MHz 2100 MHz	Yes	Yes	Horizontal
Satellite Navigation (GPS)	1.575 GHz		Yes	Satellite
Satellite Digital Audio Radio Service (SDARS)	2.3 GHz		Yes	Satellite
IEEE 802.11 b/g/n (Wi-Fi)	2.4 GHz	Yes	Yes	Horizontal
Bluetooth	2.4 GHz	Yes	Yes	Intra-vehicular
WiMAX	2.3 GHz/2.5 GHz/3.5 GHz	Yes	Yes	Horizontal
Electronic Toll Collection (ETC)	5.8 GHz (or 900 MHz)	Yes	Yes	Overhead
V2V* and VII*	5.9 GHz	Yes	Yes	Horizontal
Collision Avoidance Radar	24 GHz and 77 GHz	Yes	Yes	Forward

* Transmit # Receive * These terms are acronyms for Vehicle-to-Vehicle communication and Vehicle-Infrastructure-Integration using IEEE 802.11p

Table 1. Summary of signals used on modern and next generation vehicles

The lowest frequencies used in vehicles are often for *AM* and *FM radio*. The history of radios in cars is vague but dates back to the 1920's. During this time period the installation of such devices was deemed unsafe and illegal in at least one US state (Rowan & Altgelt, 1985). Significant policy change obviously occurred over the years given that AM and FM Radio are installed in nearly all modern day passenger vehicles and are used to provide entertainment for the driver and passengers.

The third entry in the list of services in Table 1 describes *in-vehicle television* for which the necessary hardware is available including diversity receivers to minimise dropouts. In-vehicle television is rarely installed by the factory in present day vehicles, although DVD and multimedia entertainments systems are finding increased uptake in high-end luxury vehicles. *Digital Audio Broadcasting* is a more modern format for broadcasting entertainment radio. DAB uses digital rather than analogue modulation schemes, providing higher spectral efficiency and better quality audio in certain circumstances.

Many present day vehicles are able to be locked and unlocked by pressing a button on a radio transmitter integrated into the car's key or key ring. These services are known as *Remote Keyless Entry*, and typically operate in one of the low power bands shown in the table. These bands are often shared with *Tyre Pressure Monitoring Systems* which are finding increased acceptance in the passenger vehicle market and are available as third-party accessories. A typical TPMS has an air pressure sensor and wireless transmitter fitted to each wheel with a receiver unit mounted in or on the dash. The system can alert the driver to low tyre pressure before a flat tyre becomes a safety hazard.

Many frequency bands are used globally for *cellular telephone* (a.k.a. mobile telephone). Blocks of new spectrum are occasionally released by the authorities and purchased by telecommunications companies to cater for increased demand. The most commonly used frequencies are provided in the table. Inclusion of these frequency bands into a vehicle could allow for voice calls and additionally a full suite of services based on high speed access to the internet provided by HSPA (High Speed Packet Access). This has the potential to bring about a realisation of useful Location Based Services, XML based traffic updates and internet connectivity almost anywhere in urban and rural environments.

Guidance and navigation facilities are becoming more cost effective and seeing large uptake in the modern market. These navigation systems usually rely on the constellation of approximately thirty *Global Positioning System* (GPS) satellites to determine the location of the vehicle before plotting it on a map. The GPS L1 band is received in a narrow 20 MHz channel centred at 1.575 GHz.

The *Satellite Digital Audio Radio Service* is also described in the table. This service delivers hundreds of additional radio stations and is implemented by using circularly polarised signals from satellites arranged in an orbit which dwells over the North American continent. In urban environments where buildings can cause multipath and shadowing of the satellites, terrestrial based transmitters are also used.

The 2.4 GHz ISM band has seen enormous growth in the past decade due to the ubiquitous application and implementation of *Wi-Fi* and *Bluetooth* which occupy part of this band. Bluetooth is incorporated into many present day vehicles to allow hands free calling and operation of an equipped mobile through the vehicle's multimedia system. Future vehicles may be fitted with Wi-Fi to enable passengers to access the internet while on a journey.

An emerging technology that will need to compete with LTE and HSPA technologies is *WiMAX*. In a manner similar to the 3G and 4G cellular wireless standards, WiMAX could be used to provide a high speed wireless internet connection to a moving vehicle many kilometres from a base station.

Many *Electronic Toll Collection* systems are implemented at 5.8 GHz, often achieved by windscreen mounted removable wireless tags operating in an active-RFID system.

Vehicle-to-Vehicle communication systems are currently being developed and trialled to enable safer and more efficient road transport. A portion of spectrum at 5.9 GHz has been reserved in many countries for this purpose, where vehicles and road side objects would form networks and share safety information as part of an Intelligent Transportation System (ITS). As an example a system such as this would alert the driver to sudden braking in traffic ahead, and of upcoming lane closures or unexpected obstructions. Emergency vehicles could broadcast warnings to drivers up to 1km away, signalling their presence and intentions. Many phrases have been coined to describe this technology including *Dedicated Short Range Communications* (DSRC), *Vehicle2Vehicle* (V2V), and *Vehicle-Infrastructure-*

Integration (VII). The relevant IEEE standard upon which the wireless connection is based is IEEE 802.11p. The US Department of Transport is developing these technologies in the IntellidriveSM program.

Collision Avoidance Radar is a technology which integrates with the Adaptive Cruise Control (ACC) system of a vehicle to prevent accidents, or in the case where a collision is unavoidable, reduce the severity of the impact. In normal use the system uses RADAR (or optionally LIDAR) to scan the road ahead and will reduce the throttle and apply brakes to automatically maintain a safe buffer distance to the car in front. Some systems will also detect pedestrians or other objects. In the event that the system detects an imminent collision, it may apply emergency braking and other precautionary measures to increase vehicle safety. Collision Avoidance Radar uses very high frequencies for numerous reasons including spectrum availability, the small size of antenna elements enabling integration of necessary phased array radar antennas, and the fact that a higher frequency helps to increase the Radar Cross Section, and therefore, the detection range of targets of interest, such as pedestrians and other vehicles.

4. Traditional AM/FM antennas

4.1 Mast antennas

The low frequency and relatively high signal strengths encountered in AM and FM car radio systems have allowed the use of uncomplicated antenna systems in the past. The most common antenna traditionally used for these bands is the mast antenna. A conductive rod is used to form a monopole antenna, approximately one quarter wavelength ($\lambda/4$) in length, which equates to approximately 75 cm in the middle of the FM band. Locating such an antenna in the centre of the roof gives the best radiation performance, with the antenna elevated above obstructions and surrounded by a conducting ground plane of approximately equal extent in all directions. Despite this, the front or rear fender is usually preferred for aesthetic reasons. Retractable and non-retractable versions are commercially available.

Antennas for receiving FM radio in vehicles should receive signals equally well from all directions around the horizon, due to the movement and rotation of the vehicle with respect to the transmitting source. This quarter wavelength monopole antenna would provide an ideal radiation pattern in the azimuth if it was mounted above an infinite ground plane. Typical fender mounting provides a very non-ideal ground plane however, leading to radiation patterns that are less omni-directional (ie. the radiation becomes directional). Hence, designing such antennas for vehicles has traditionally been an iterative process involving several stages of prototyping and measurement on completed vehicle bodies.

Retractable mast antennas (Fig. 4) allow the antenna to be retracted, hidden and protected when not in use. Such antennas consist of a long rod divided into numerous segments. The segments are appropriately dimensioned to slide inside one another when retracted, leading to a tapering profile when extended. Most modern retractable antennas are raised and lowered by an electric motor leading to increased cost and expense. Such power retractable antennas are often mounted on the passenger side of the vehicle, whilst manually operated retractable antennas tend to be installed on the driver side so the driver can raise or lower the mast without having to walk to the other side of the vehicle.



(a) Manually retractable mast antenna

(b) Power retractable mast antenna

Fig. 4. Technical drawings of typical mast antennas

4.2 Glass mounted AM/FM Antennas

A second kind of AM and FM antenna is the glass mounted antenna. AM and FM antennas using this technique have become very common in the last decade, as pre-amplifiers have helped to compensate for poor radiation performance. On modern vehicles, these antennas are similar in appearance to the demister elements commonly embedded in the rear windscreen.

Many glass mounted antennas installed in present day vehicles are based on wire geometry although the antenna may or may not be an actual wire. It can be formed by using wire of a very thin diameter or a silk screened film which is laminated between layers of glass in the vehicle windows (Jensen, 1971). Glass mounted antennas provide no additional aerodynamic drag and create no wind noise which is a significant advantage over mast type designs. They also require no holes to be created in the vehicle body, which may lead to cheaper tooling for the metal work. Despite this, on glass antennas tend to be more directional than mast antennas, which can lead to nulls in the reception on certain angles around the vehicle.

On-glass antennas were first located in the rear windscreen, and this remains a common position on sedans made today. Many SUV's or station wagons use the rear quarter window in preference to the rear window. A variety of different shapes are used for the antennas, often forming grid or meandering geometries, with a shape that works well on one vehicle not necessarily performing well on other vehicles (Gottwald, 1998). No universal glass mounted antenna has yet been discovered. This is due to the effect of the vehicle body on the antenna's impedance and radiation, which is significant for on-glass antennas. Antenna oriented vertically may provide better reception of vertically polarised signals.

Fig. 5 shows a typical active rear window antenna. Early designs adopted the defogger elements themselves and connected through a DC blocking capacitor to the radio tuner. Newer designs often separate these two functions, having a defogger element which occupies most of the glass, with a smaller area set aside for antenna lines.

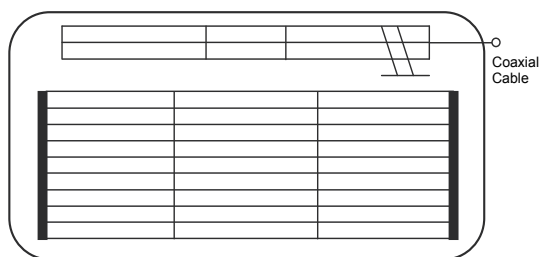


Fig. 5. Schematic of a typical rear windscreen glass antenna.

5. New developments and research outcomes

Examination of production vehicles produced over the past ten to fifteen years reveals a shift away from the traditional quarter wavelength mast antenna towards more aesthetically pleasing antennas. This section provides a review of new findings and innovative solutions to vehicular antenna problems along with the advantages and disadvantages of each type.

5.1 Bee-sting antennas

The bee-sting antenna is a wire antenna similar to the mast antenna used for many decades, but consists of a shortened element installed in a raked back attitude (Fig. 6). An amplifier is used to boost the signal level to compensate for the poor performance obtained by the shorter antenna length (Cerretelli & Biffi Gentili, 2007). Some antennas also include a separate feed for a Cellular phone or DAB system.



Fig. 6. Bee sting antenna © IEEE with permission (Cerretelli & Biffi Gentili, 2007)

5.2 Blade or Shark-fin antennas

Many varieties of shark-fin antennas exist, having been popularised primarily by the European marques near the turn of the 21st century. Shark-fin antennas are commonly a collection of several antennas. Most designs consist of multiple narrowband antennas all located together under a single radome or housing. This housing is typically shaped like a blade or dorsal fin, and is usually located on the roof towards the rear of the vehicle. Two examples of shark-fin designs are shown in Fig. 7.



Fig. 7. Shark-fin Antennas

Fig. 8 shows an early shark-fin antenna design in detail. This design was fitted to the BMW 3-Series (E46) and provides for cellular phone frequencies. The antenna consists of a cast steel base and a fin-shaped cover made from an ABS and Polycarbonate polymer. Radiating elements are on both sides of an FR-4 circuit board which stands erect in the middle of the device. Rubber gaskets are used to seal the inner components from the environment. The design achieves an impedance match (shown in Fig. 9) at the required frequencies by incorporating inline filters which allow the radiators to be a quarter wavelength long at high

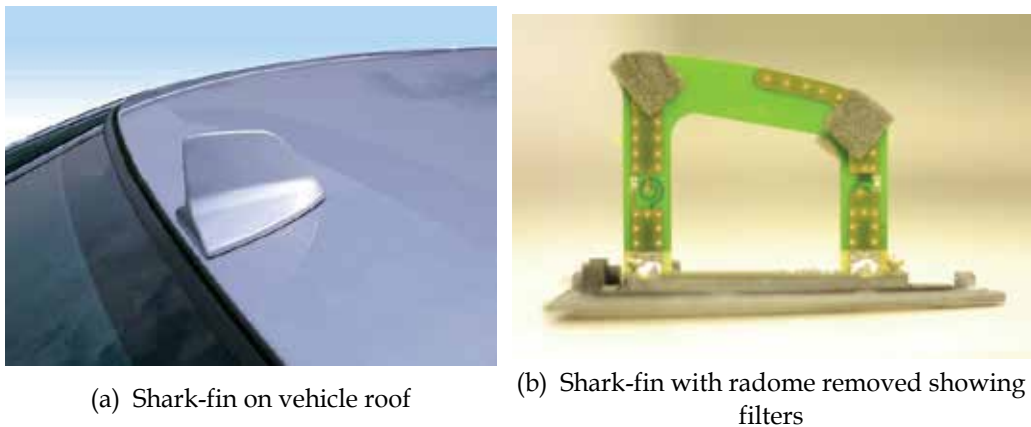


Fig. 8. BMW 3-Series E46 Sharkfin Antenna

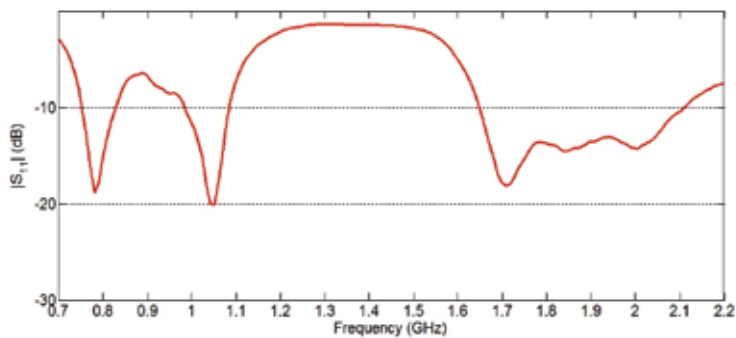


Fig. 9. Measured reflection coefficient of BMW 3-series E46 Shark-fin Antenna

and low frequencies simultaneously. A surface mount resistor is used in conjunction with a printed inductor on the reverse side of the board to form a filter. This filter has the effect of connecting the upper radiating elements at lower frequencies by creating an electrical short circuit. At higher frequencies the filter creates an open circuit, leaving only the short elements connected to the feed line.

Fig. 10 shows a shark-fin style antenna which was published in the literature for use in US automobiles (J.F. Hopf et al., 2007). With the cover removed, it is clear that this antenna demonstrates the case where multiple individual antennas are located together under a single radome.

The leftmost antenna in the figure is a GPS antenna, constructed using a probe fed patch design on a high dielectric constant substrate. This provides a hemispherical radiation pattern covering the sky which is appropriate for receiving satellite signals. Circular polarisation may be induced in patch antennas such as these by truncating diagonally opposite corners of the patch, or by feeding the antenna off centre.

The white antenna to the right of centre in the figure is a crossed frame antenna for SDARS reception.

The two posts present in the design provide for cellular telephone reception. The elements are based on quarter wavelength monopoles with top loading elements to increase the effective electrical length at the low end of the band. The presence of these posts is typical of shark-fin antennas, however these particular posts contain filters which have been optimized to have minimal effect on the nearby SDARS antenna.



Fig. 10. Internals of a modern shark-fin antenna © IEEE with permission (J.F. Hopf et al., 2007)

5.3 TV antennas on glass

Research has continued into traditional AM and FM antennas mounted on glass even today (Bogdanov et al., 2010), particularly in the area of effective simulation techniques. At the same time, antenna configurations for other services have also been investigated. An early paper describes the system shown in Fig. 11 of a diversity reception system for analogue TV. The antennas are printed on the rear quarter glass and have four branches. The antennas are arranged symmetrically on the left and right sides of the vehicle. The design includes some meandering elements which give a long electrical length in a small space. Other branches of the design include slanted and short horizontal elements. The authors claim the system provides improved performance over a rod antenna, and is capable of operating in the range from 90 MHz to 770 MHz (Toriyama et al., 1987).

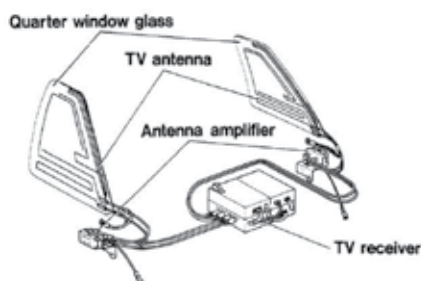


Fig. 11. Analogue TV Antenna system in rear quarter glass
© IEEE with permission (Toriyama et al., 1987)

A glass mounted antenna designed for the newer Digital Terrestrial TV reception is shown in Fig. 12. The H-shaped elements allow both long and short current paths to be formed, providing a wideband impedance match (Iizuka et al., 2005). The long path occurs when current flows diagonally from top left to bottom right in Fig. 12(a), while the shorter path runs diagonally from bottom left to top right. The impedance matching of this design results in a VSWR of less than 3:1 from 470 MHz to 710 MHz when connected to a 110 Ω line. The antenna is formed on a low cost FR-4 substrate, and is integrated with an RF circuit which provides a balun, some filtering, and a Low Noise Amplifier (LNA) to boost the signal before it is sent down the transmission line to the tuner. Four of these antennas were installed in the test vehicle shown in Fig. 12(b), being located in the upper portion of both the front and rear windscreen on both driver and passenger sides. The gain and radiation pattern of the system was measured at 530 MHz, and it was found that the radiation pattern was nearly omni-directional at this frequency when all four antennas were excited.

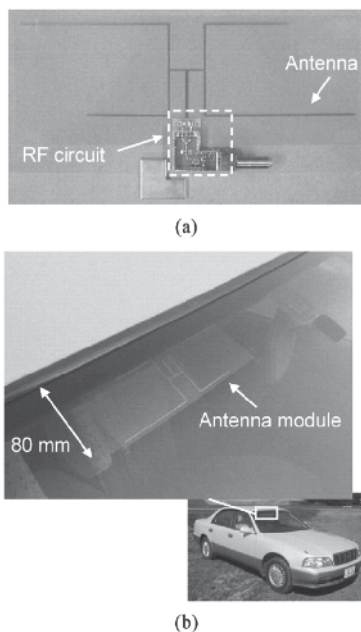


Fig. 12. Digital TV Antenna attached to vehicle glass
© IEEE with permission (Iizuka et al., 2005)

5.4 Circular microstrip patch antenna on glass

Microstrip Patch antennas have many advantages in communication systems including being thin, cheap to produce, and easy to integrate into devices. The application of this kind of antenna to automotive glass has been investigated by several researchers. One paper suggested two methods of patch antenna integration (Economou & Langley, 1998). The first is a patch antenna formed on a traditional microwave substrate such as Rogers RT Duroid® which is then attached to the inside of a vehicle windscreen (Fig. 13(a)). The second describes a more integrated concept which uses a layer of glass itself as the antenna substrate, and excites the patch with a proximity coupled feed line (Fig. 13(b)).

Patch antennas using the first method of integration were designed to resonate near 2 GHz and 6 GHz respectively, and were adhered to a vehicle windscreen for testing. A useful increase in impedance bandwidth from less than 2% to about 7% was observed due to the addition of a thick dielectric superstrate. Presence of the glass also generates surface waves which create undesirable ripples in the far-field radiation pattern.

The second method using glass as the antenna substrate poses fabrication complexities, and would lead to a high windscreen replacement cost in the event of cracking or breakage, so was only investigated by simulation. Simulation results showed that this geometry would also result in lower radiation efficiency due to increased surface wave losses.

The electrical properties of the layers in the windscreen were $\epsilon_{r1} = 6.75$, $\tan \delta = 0.03$ for the glass and $\epsilon_{r2} = 2.9$, $\tan \delta = 0.05$ for the middle plastic layer.

The thickness of automotive glass may vary by up to 15% in the standard manufacturing process. This causes no problems or distortions for driver vision, but could present a problem for patch antennas attached to glass. The centre frequency of the antenna may be shifted by up to 3% and could be coupled with an additional but slight change in the impedance bandwidth.

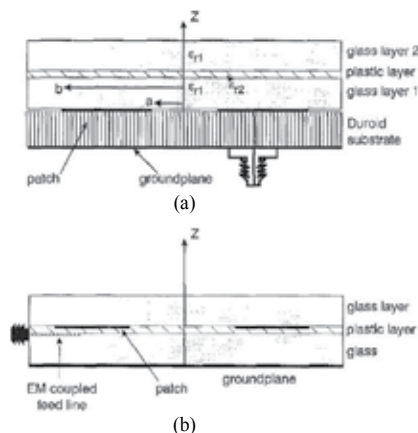


Fig. 13. Patch Antennas on glass © IEEE with permission (Economou & Langley, 1998)

5.5 Rear spoiler with built-in antenna

In the late 1990's a team of Japanese engineers working with Toyota and Aisin Seiki developed a rear spoiler to be mounted up high on the rear of a compact SUV. This spoiler was the first to be fitted with an invisible antenna (Fig. 14). The paper describes a blow molded part made from a polymeric material (Koike et al., 1999). The spoiler is located high

on the vehicle, minimizing shadowing from passing traffic. The antenna is similar to a dipole which would normally require a balanced feed. In order to connect a dipole antenna to a coaxial line, a balun is usually required. The geometry of the spoiler and processing temperature during manufacture would make integration of such a balun difficult. In order to overcome this, an innovative antenna design is used. The shorter element in Fig. 14(a) is approximately $\lambda/4$ long, while the longer element is approximately $\lambda/2$. Parametric investigations found that a tab at the end of the longer radiating element improved antenna performance by coupling to the vehicle's metallic roof. Although the directivity is less than perfect (Fig. 14(b)), it is adequate for the intended application.

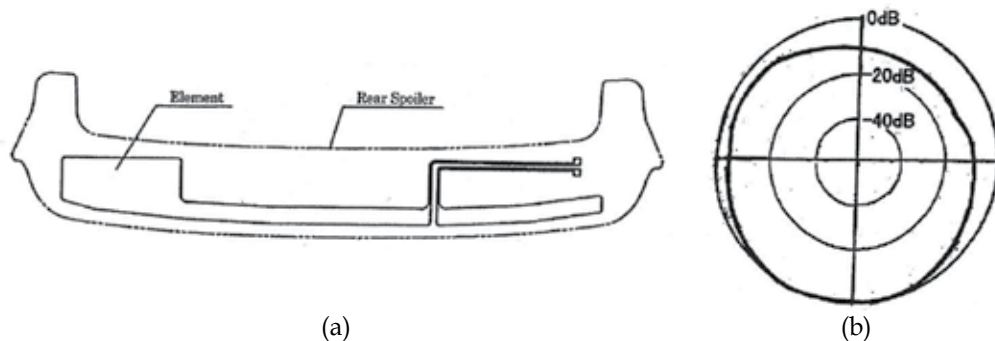


Fig. 14. Integrated antenna in spoiler
© SAE International with permission (Koike et al., 1999)

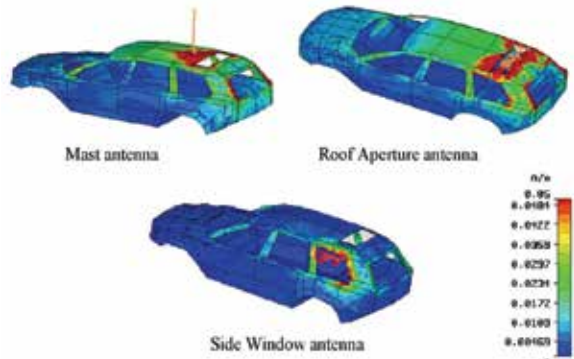
5.6 Volvo XC90 aperture antenna

Swedish manufacturer Volvo fitted a unique antenna to their XC90 SUV, launched in 2003. The system provides an alternative to glass mounted wire antennas which may be adversely affected by heated windscreen elements and window tinting films containing conductive metallic layers. The XC90 is fitted with a traditional metallic skinned "turret top" roof, but an aperture is created at the rear of the vehicle. This opening is covered with a polymeric panel, and forms an ideal location for some hidden antennas (Low et al., 2006). Fig. 15(a) shows the XC90 from above and Fig. 15(b) shows some simulation results of the vehicle's metallic structure for different antenna configurations. The aperture in the vehicle body is clearly shown. The portion of roof which contains the antennas is the black unpainted section at the rear of the vehicle in Fig. 15(a) which at first glance may look like a sunroof.

Seven antenna components (Fig. 16) are formed by printing wire shapes onto a large polyester film using conductive ink. The antennas act as monopole probes, exciting the aperture in which they are placed. For some services, multiple antennas are used in different locations to achieve radiation and polarisation differences between elements allowing diversity reception. The film bearing the printed antennas is attached to a plastic carrier which contains the necessary amplifiers, and the whole unit is located in the aperture and covered with a black polymeric composite material. Examination of Fig. 16 reveals that these antennas are for low frequency services, with Table 1 revealing each service is centred well below 1 GHz. This low frequency implies a long wavelength which requires physically long antenna elements. Note that the services targeted in this design are different from those commonly used in the smaller shark-fin style antennas.



(a) Completed XC90 vehicle



(b) Simulations of surface currents for various antennas

© IEEE with permission (Low et al., 2006)

Fig. 15. Volvo XC90

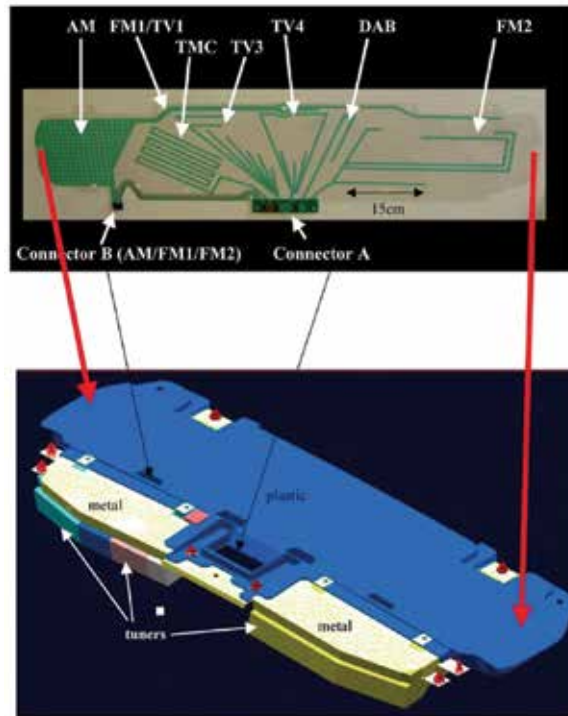


Fig. 16. XC90 antenna configuration. The film from the top image attaches to the carrier in the lower image as shown. © IEEE with permission (Low et al., 2006)

Performance of the roof aperture antenna for the FM band was compared in both simulation and measurement against a roof mounted monopole with a length of 80 cm and a side window antenna as used in an estate car Fig. 15(b). Unsurprisingly, the authors report that the roof mounted monopole provided exceptional performance for vertically polarised signals, but performed poorly for horizontally polarised signals. On average, the roof

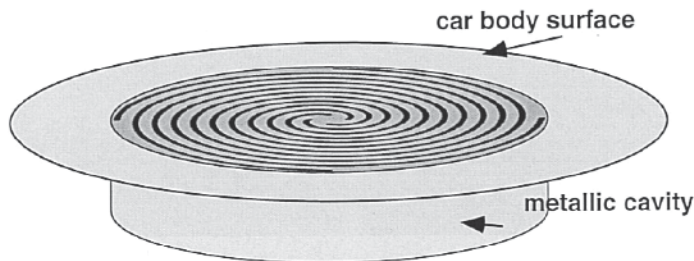
mounted aperture antenna performed approximately 2 dB better than the side window antenna, but was unable to trump the roof mounted monopole for vertical polarisation gain.

5.7 Body integrated spiral antenna

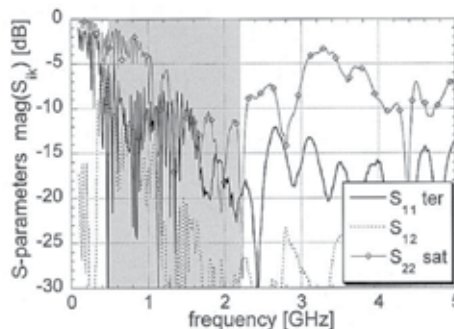
Researchers in Germany investigated the possibility of mounting a cavity-backed spiral antenna in the trunk lid of a car (Gschwendtner & Wiesbeck, 2003). The four arm spiral antenna produced is approximately 40cm in diameter and is backed by a metallic cavity (Fig. 17(a)). The spiral supports two modes of radiation depending on how the signal is fed into the structure. The first mode is a coplanar waveguide (CPW) mode which creates a null at zenith (ie. directly above the antenna) with omni-directional radiation around the sides of the device. This mode generates a radiation pattern that is suitable for terrestrial services.

The second mode, known as the coupled slot line (CSL) mode feeds only two of the four arms, creating a circularly polarised radiator with a maximum at zenith (directly overhead). This mode of radiation is ideal for satellite services.

A metallic cavity with a height of 4 cm was placed below the spiral to stop back-radiation into the vehicle body. Measured S-parameters of the antenna with the cavity present are shown in Fig. 17(b). The curve is below -10 dB from 670 MHz to beyond 5 GHz for the terrestrial mode ($|S_{11}|$), with the exception of some peaks as high as -8 dB in the frequencies below 1.4 GHz. These peaks are due to the presence of the metallic cavity. The satellite mode ($|S_{22}|$) meets the -10 dB requirement from 1.3 GHz to 2.2 GHz, providing broadband circularly polarized satellite reception. The $|S_{12}|$ curve illustrates the coupling between the two ports.



(a) Antenna design showing metallic cavity



(b) Measured S-parameters of spiral antenna with cavity

Fig. 17. Four arm spiral antenna © IEEE with permission (Gschwendtner & Wiesbeck, 2003)

Fig. 18 shows the finished antenna installed in the intended location on a vehicle. The top surface is mounted flush with the exterior trunk-lid panel. No measurements of the antenna installed in the vehicle were provided. The antenna provides for more multiple services due to its wideband impedance match and results in an elegant solution, given that the structure does not protrude from the vehicle body, eliminating additional drag.

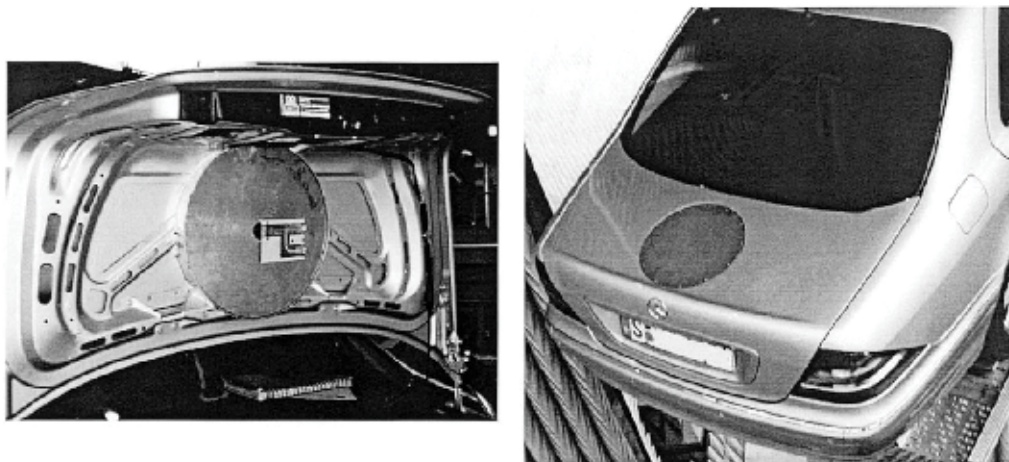


Fig. 18. Spiral antenna integrated into the trunk lid of a Mercedes Sedan
© IEEE with permission (Gschwendtner & Wiesbeck, 2003)

5.8 Planar Inverted Cone Antenna (PICA)

The PICA is a low profile antenna (Fig. 19) with a very wideband impedance match (Pell et al., 2009). In its intended application in a vehicle it would be encapsulated in or mounted under a polymeric panel in a manner similar to the Volvo XC90 antenna. This may be achieved if the electrical properties of the material are known (Sulic et al., 2007). However, rather than leaving the polymeric panel black, the covering panel could be painted to match the colour of the vehicle so that the assembled structure becomes a colour co-ordinated component which is indistinguishable from a section of bonnet, roof or trunk.



Fig. 19. Planar Inverted Cone Antenna

The use of a wideband antenna is similar in concept to that used by Gschwendtner and Wiesbeck in the previously examined spiral antenna. Due to its wide impedance bandwidth, a single antenna can cover more than one service if appropriate interfacing hardware is provided. In contrast to the cavity-backed spiral antenna, the PICA provides a wider impedance bandwidth and is fabricated on industry standard circuit board material (FR-4), making series production affordable. It requires no cavity, giving a thinner overall structure, and may be attached to the underside of surfaces which feature a gentle curve, making it a truly conformal solution.

Being fabricated on a square 20 cm x 20 cm substrate, the enlarged uniplanar CPW-fed PICA provides a suitable antenna for many of the services in Table 1. It presents a good impedance match to a 50 ohm line over a wide range of frequencies extending from 730 MHz to beyond 10 GHz (Fig. 20).

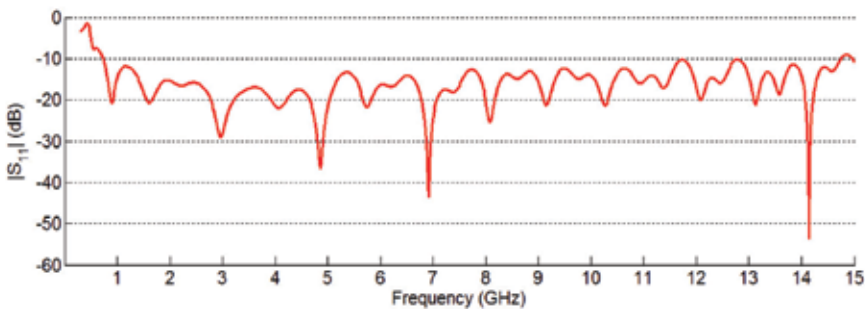


Fig. 20. Simulated impedance response of the Large PICA antenna

In the case where an antenna such as the PICA may be encapsulated in the middle of a dielectric material, it may experience deformation due to the pressure and flow of material during the moulding process. This requires a thorough understanding of the rheology of the material to be used (Sulic et al., 2010). An understanding of the properties of the polymer may influence the temperature at which the material is cured during manufacturing, and will impact on the way the charge is loaded into the tool in preparation for moulding.

The radiation pattern of the antenna in free space changes across the frequency band in a manner convenient for the application. At each frequency the level of gain in the required direction is suitable for vehicular use when mounted in a horizontal attitude, as would be the case in a bonnet, roof or trunk lid. Fig. 21 shows the simulated radiation pattern of the antenna at key frequencies in the band. Where possible, these frequencies were selected to align with an automotive service.

At cellular phone frequencies (Fig. 21(a)) the pattern is wide with low directivity. The peak gain occurs at broadside to the antenna substrate, yet in the plane of the substrate (x-y plane) the gain averages about 0 dBi with a null in the y direction. Given that cellular phone towers are terrestrially based, it is this horizontal part of the radiation pattern which is critical, and the gain is adequate.

Fig. 21(b) shows the radiation pattern at the frequency used for GPS. The radiation pattern has become slightly more directed, with a realised gain of 5.7 dBi. Despite the lack of circular polarisation, the radiation performance of the PICA should provide a satisfactory signal to a modern receiver unit like the SiRFStarIII™ to enable accurate positioning. Verification of this assumption is a matter of present investigation.

At 5.9 GHz (Fig. 21(d)) the radiation pattern of the PICA is dominated by the currents formed along the tapered slot between the two PICA shapes. This leads to high gain y -directed lobes encroaching upon endfire. This is suitable for vehicle-to-vehicle applications where signals should be directed close to the horizon to communicate with nearby automobiles and roadside infrastructure.

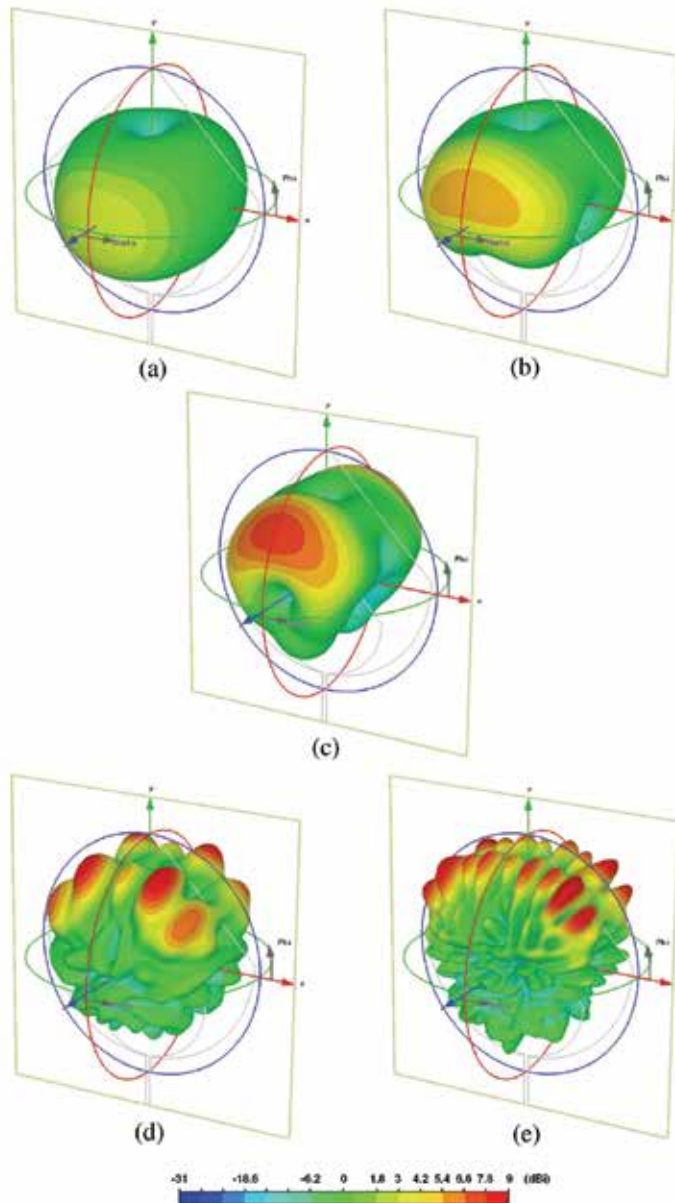


Fig. 21. Simulated 3D radiation patterns of the enlarged uniplanar CPW fed PICA. (a) 850 MHz, Max gain is 3.9 dBi (b) 1.575 GHz, Max gain is 5.7 dBi (c) 2.4 GHz, Max gain is 8.1 dBi (d) 5.9 GHz, Max gain is 9.6 dBi (e) 9.5 GHz, Max gain is 11 dBi

5.9 Antennas integrated into Plastic Trunk Lid

Heinz Lindenmeier and his team at the University of the Bundeswehr Munich have made an outstanding contribution to vehicular antennas over many decades, particularly with regards to amplifiers and diversity systems. Lindenmeier and his team presented an antenna concept for application in cars with plastic trunk lids (Lindenmeier et al., 2006) as is common in some cabriolets and convertibles. In such vehicles a traditional fixed glass rear window is not normally available, so integration into the plastic trunk lid is an ideal substitute.

In order to create an antenna a copper ring is created around the perimeter of the plastic trunk lid near the metallic supporting structure (Fig. 22). Two switches are inserted into this ring, and act to control the impedance of the network. Both ends of the ring are connected to an amplifier unit which is used to obtain both FM-diversity and TV reception.

A separate AM radio feed is connected to a wire antenna geometry which is located inside the previously mentioned ring. A ground plane is also included in the middle of the ring. The intention is that a cellular phone antenna, or GPS patch antenna may be installed to this location under the polymeric trunk lid. This would provide an ideal spot to locate antennas for higher frequency services and would not disrupt the operation of the lower frequency services.

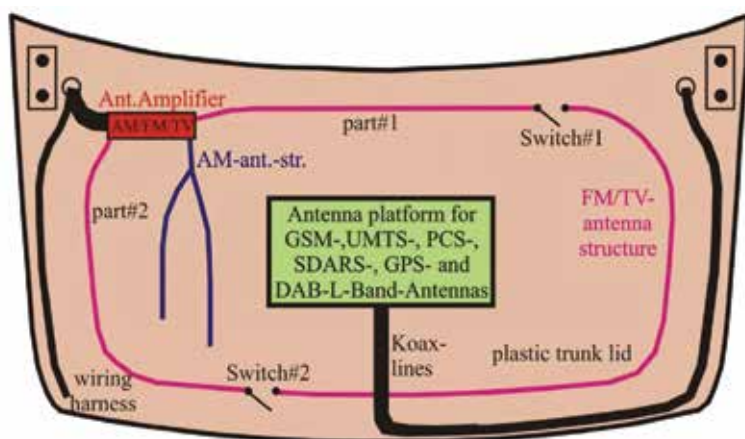


Fig. 22. Active antennas integrated into Plastic Trunk Lid
© SAE International with permission (Lindenmeier et al., 2006)

5.10 Other automotive antenna configurations

Satellite Antennas

Several designs exist for reception of Ku-band satellite signals on either moving or stationary vehicles. High gains of 30 dBi or higher are required, leading to the use of reflector antennas (Eom et al., 2007) or array antennas (Mousavi et al., 2008). Reflector antennas are often mechanically steered and housed in a radome which results in a high profile device approaching half a meter in depth (Fig. 23(a)). Array antennas use a collection of many patch antennas and typically result in roof mounted components with a lower profile, thinner than even 10 cm (Fig. 23(b)). These systems may be steered mechanically with motors, or electronically by changing the phase between elements.



Fig. 23. (b) Satellite reflector system © IEEE with permission (Eom et al., 2007), (c) Satellite phased array system © IEEE with permission (Mousavi et al., 2008)

Collision Avoidance Radar

Antennas designed to work as part of a collision avoidance radar system are very small because of the high frequencies of operation (typically 24 GHz or 77 GHz) which leads to a correspondingly short wavelength, and small antenna size. 77 GHz is preferred for *Long Range Radar* detection, up to 150 m in front of the vehicle, while 24 GHz systems are used for *Short Range Radar* where the distance is less than 30 m. Many requirements need to be satisfied in designing such antennas (Hoare & Hill, 2000). Fig. 24 shows some recently presented antennas for these purposes. Fig. 24(a) and (c) show antennas for 77 GHz radar systems published in the literature, while Fig. 24(b) shows a commercial system used by Mercedes.

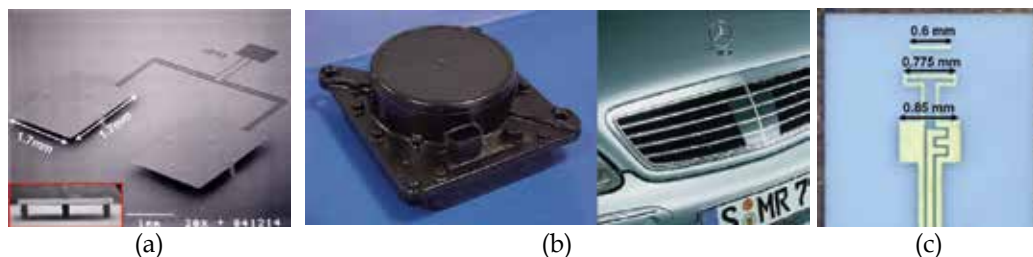


Fig. 24. Automotive Radar antenna configurations (a) a fabricated 2x1 77 GHz Patch array © IEEE with permission (Lee et al., 2005) (b) the Mercedes Long Range Radar System © IEEE with permission (Wenger, 2005) (c) a 77 GHz Yagi-Uda antenna used to feed a reflector © IEEE with permission (Beer et al., 2009)

6. The effect of automotive paints on vehicular antennas

The effect of automotive paints on vehicular antennas was recently studied in depth (Pell et al., n.d.). Two different paint families were investigated including a traditional polyurethane chemistry and the modern water-based paints which are gaining increased use because of their environmental benefits. Both metallic and non-metallic varieties of the paints were investigated.

Metallic paints present an interesting scenario for antenna applications. Such paints create a shimmering visual effect by the inclusion of thousands of small flakes of aluminium in the paint (Fig. 25), yet these flakes are inherently conductive. It seems reasonable that the presence of these conductive flakes in the near-field of an antenna may potentially cause severe disruption to proper antenna operation.

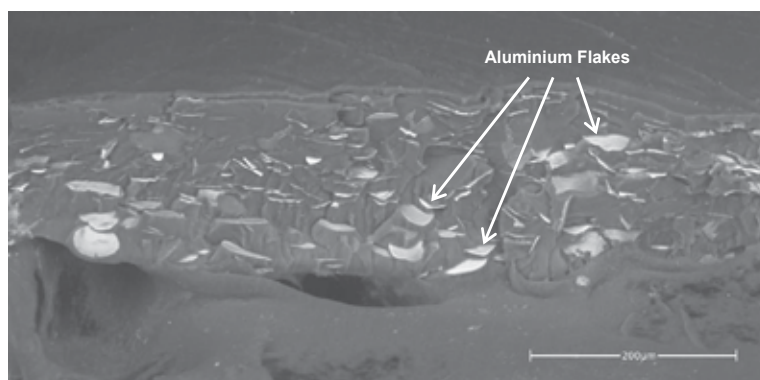


Fig. 25. Scanning Electron Microscope image of the edge of a section of paint

The authors report that the presence of automotive paints has potential to bring about a shift in the resonant frequency of an antenna due to the addition of dielectric material. This effect is more pronounced on narrowband antennas.

Metallic particles in the paint are very small compared to a wavelength at the frequencies of interest. The free electrons in the aluminium flakes are not truly free to move since they are isolated in the paint binder. This prevents a true shielding effect as in the case of a continuous conductor. A slight gain reduction may be observed when paints containing metallic particles are applied to antennas.

Electrostatic primers were also investigated in this work. Such coatings are intended to provide a level of DC conductivity to enable electrostatic painting of polymeric parts, which results in a high yield with less overspray, and hence a more efficient painting process with lower levels of paint wastage. It was found that these coatings were lossy at microwave frequencies (due to their DC conductivity), bringing about a gain reduction of approximately 1.5 dB on a narrowband patch antenna. This implies that for any polymeric panels containing antennas, the structure should be painted offline, or in a manner not requiring application of an electrostatic primer.

7. Conclusion

Automotive antennas have seen significant advancements in recent years. No longer is a large protruding fender mounted mast antenna the norm for production vehicles. As seen from the antenna configurations mentioned here, a good impedance match can be obtained for a wide frequency range. Also, depending on the frequency range being targeted, it is possible to achieve acceptable gains and directivities. These developments augur well for the deployment of a new range and type of integrated vehicular antennas. Future developments will likely focus on two key areas: further integration of the antenna components with the vehicle structure, and new antenna configurations for radar and vehicle-to-vehicle communication services. With the developments in antenna design mentioned in this chapter, further integration of antennas within vehicular components will be expected, particularly with the present inexorable drive from within the automotive industry, to shift more automotive components from metallic to polymeric materials.

8. Acknowledgement

The authors wish to acknowledge other members of the research group, Kefei Zhang and Rahul Gupta. Brendan D. Pell thanks Hao V. Nguyen for sharing his knowledge and experience.

9. References

- Beer, S., Adamiuk, G. & Zwick, T. (2009) Novel Antenna Concept for Compact Millimeter-Wave Automotive Radar Sensors. *Antennas and Wireless Propagation Letters, IEEE*, 8, pp.771-774.
- Bogdanov, F., Karkashadze, D., Jobava, R., Gheonjian, A., Yavolovskaya, E., Bondarenko, N. & Ullrich, C. (2010) Validation of Hybrid MoM Scheme With Included Equivalent Glass Antenna Model for Handling Automotive EMC Problems. *IEEE Transactions on Electromagnetic Compatibility*, 52 (1), pp.164-172.
- Cerretelli, M. & Biffi Gentili, G. (2007) Progress in Compact Multifunction Automotive Antennas. In: *International Conference on Electromagnetics in Advanced Applications*. pp.93-96.
- Economou, L. & Langley, J. (1998) Circular microstrip patch antennas on glass for vehicle applications. *IEE Proceedings Microwaves, Antennas and Propagation*, 145 (5), pp.416-420.
- Eom, S.Y., Son, S.H., Jung, Y.B., Jeon, S.I., Ganin, S., Shubov, A., Tobolev, A. & Shishlov, A. (2007) Design and Test of a Mobile Antenna System With Tri-Band Operation for Broadband Satellite Communications and DBS Reception. *IEEE Transactions on Antennas and Propagation*, 55 (11), pp.3123-3133.
- Gottwald, G. (1998) Numerical Analysis of Integrated Glass Antenna Systems. In: *SAE Technical Paper Series*. Paper ID 982386, Society of Automotive Engineers.
- Gschwendtner, E. & Wiesbeck, W. (2003) Ultra-broadband car antennas for communications and navigation applications. *IEEE Transactions on Antennas and Propagation*, 51 (8), pp.2020-2027.
- Hoare, E. & Hill, R. (2000) System requirements for automotive radar antennas. In: *IEE Colloquium on Antennas for Automotives*. pp.1/1-111.
- Hopf, J., Reiter, L. & Lindenmeier, S. (2007) Compact multi-antenna system for cars with electrically invisible phone antennas for SDARS frequencies. In: *2nd International ITG Conference on Antennas, 2007. INICA '07*. pp.171-175.
- IEEE Std 145-1993 (1993) IEEE Standard Definitions of Terms for Antennas. [Internet]. Available from: <10.1109/IEEESTD.1993.119664>.
- Iizuka, H., Watanabe, T., Sato, K. & Nishikawa, K. (2005) Modified H-Shaped Antenna for Automotive Digital Terrestrial Reception. *IEEE Transactions on Antennas and Propagation*, 53 (8), pp.2542-2548.
- Jensen, W.K. (1971) Concealed Windshield Broadband Antenna, U.S. Pat. 3,576,576.
- Koike, T., Hase, N., Koide, E., Murakami, Y., Izawa, S., Ohira, T., Nagasaka, O., Tanaka, Y. & Suzuki, T. (1999) Development of a Rear Spoiler with Built-in Antenna. In: *SAE Technical Paper Series*. Paper ID 1999-01-0807, Society of Automotive Engineers.
- Lee, H.S., Jeong-Geun Kim, Songcheol Hong & Jun-Bo Yoon (2005) Micromachined CPW-fed suspended patch antenna for 77 GHz automotive radar applications. In: *The*

- European Conference on Wireless Technology, 2005.* pp.249-252. Available from: <10.1109/ECWT.2005.1617704>.
- Lindenmeier, H., Reiter, L., Ramadan, A., Hopf, J. & Lindenmeier, S. (2006) A New Design Principle of Active Receiving Antennas Applied with a High Impedance Amplifier-Diversity-Module in a Compact Multi-Band-Antenna-System on a Plastic Trunk Lid. In: *SAE Technical Paper Series*. Paper ID 2006-01-0480, Society of Automotive Engineers.
- Low, L., Langley, R., Breden, R. & Callaghan, P. (2006) Hidden Automotive Antenna Performance and Simulation. *IEEE Transactions on Antennas and Propagation*, 54 (12), pp.3707-3712.
- Mousavi, P., Fakharzadeh, M., Jamali, S., Narimani, K., Hossu, M., Bolandhemmat, H., Rafi, G. & Safavi-Naeini, S. (2008) A Low-Cost Ultra Low Profile Phased Array System for Mobile Satellite Reception Using Zero-Knowledge Beamforming Algorithm. *IEEE Transactions on Antennas and Propagation*, 56 (12), pp.3667-3679.
- Okada, Y., Tanaka, H. & Yamane, K. (2007) Electromagnetic Field Analysis for Smart Key Antenna. In: *SAE Technical Paper Series*. Paper ID 2007-01-0943, Society of Automotive Engineers.
- Pell, B.D., Sulic, E., Rowe, W.S.T. & Ghorbani, K. (2009) Custom-directional wideband PICA for multi-service vehicular applications. In: *APMC 2009. Asia Pacific Microwave Conference, 2009.* pp.1863-1866.
- Pell, B.D., Sulic, E., Rowe, W.S.T., Ghorbani, K. & John, S. Experimental Study of the Effect of Modern Automotive Paints on Vehicular Antennas. *Accepted (August 2010) for publication in IEEE Transactions on Antennas and Propagation.*
- Rowan, C.W. & Altgelt, C.A. (1985) When car radios were illegal: A history of early American and European car radios. In: *SAE Technical Paper Series*. Paper ID 850019, Society of Automotive Engineers.
- Sulic, E., Pell, B., John, S., Gupta, R., Rowe, W., Ghorbani, K., Zhang, K. & Lewis, M. (2007) Parametric Evaluation of Communication Devices in Smart Composite Structures. In: *Proceedings of the 5th Australasian Congress on Applied Mechanics (ACAM)*. Brisbane, Australia, Engineers Australia, pp.477-482.
- Sulic, E., Pell, B., John, S., Gupta, R., Rowe, W., Ghorbani, K. & Zhang, K. (2010) Deformation Evaluation of Embedded Antennas in Vehicular Components. In: *Proceedings of the World Congress of Engineering 2010*. London, UK, pp.2389-2394.
- Toriyama, H., Ohe, J., Kondo, H. & Yotsuya, H. (1987) Development of printed-on glass TV antenna system for car. In: *37th IEEE Vehicular Technology Conference, 1987.* pp.334-342.
- Waterhouse, R. (2008) *Printed Antennas for Wireless Communications*. Wiley. p30.
- Wenger, J. (2005) Automotive radar - status and perspectives. In: *IEEE Compound Semiconductor Integrated Circuit Symposium, 2005.* CSIC '05. p.4 pp. Available from: <10.1109/CSICS.2005.1531741>.

Part 6

Development Tools

Automotive VHDL-AMS Electro-mechanics Simulations

Mariagrazia Graziano and Massimo Ruo Roch
Politecnico di Torino
Italy

1. Introduction

Automotive sub-systems, from security and energy, to comfort and entertainment, include several examples of entanglement between electronics and mechanics (H. Casier & Appeltans, 1998). Their correct modeling is of key importance during the design cycle, and, from conception to test, real critical conditions due to mechanic, thermal and electromagnetic stress sources must be taken into account. Typical design and test methodologies are both electronic and electro-thermo-mechanical, but they focus on a single fault source at a time. Moreover in most of the cases they are applied late in the design cycle. Accurately emulating a multi-disciplinary system during both design and test phases is of great importance when reliability is the first concern as in the automotive scenario case. The methodology tackled in this chapter, based on the VHDL-AMS language, can be applied both during design and performance or fault analysis and allows to focus on electronic devices internal parameters at a detailed level, and, meanwhile, to evaluate the influence of other electronics devices in the car system, the electro-mechanics of the vehicle and the static and dynamic usage conditions. One of the language/simulator used by system engineers in this field is Matlab/Simulink (Friedman, 2005) which allows modeling both electronic and mechanical systems at a very high hierarchical level, thus allowing to understand relations between the two fields from a system perspective. Problems arise when designers need to accurately model both electronic and mechanical devices.

VHDL-AMS (1076.1, 1999) is a superset of VHDL, thus not only digital constructs are supported but electrical quantities, differential equations and algebraic constraints can be modeled as well. The effect is the possibility to describe mixed-technology systems, ranging from mechanics to optics, from thermodynamics to chemistry without the need to change simulation tool. Its suitability for automotive electro-mechanical systems modeling results in the effectiveness in capturing the impacts of electronic blocks at the system level, and, on the other hand, in achieving a good understanding of impact mechanics on electronic design choices as well.

Multi-resolution is a further relevant VHDL-AMS characteristic: It allows to describe different blocks in the system using different levels of abstraction, depending on the focus needed for different devices. In the automotive context this is a great improvement as it implies, for example, that critical electronic blocks can be accurately described, while the thermo-mechanical car environment can be only approximately represented. This favours a lightweight simulation in terms of required CPU time. A further important achievement consists in the possibility to capture the effects of electronic details at the system level, and, on

the other hand, in obtaining a good understanding of mechanics impact on electronics design choices.

As a case of study on the subject, in this chapter we describe the behaviour of CD players for vehicle dashboard when realistic shocks through the vehicle suspension system due to the variable roadway profile are considered as environment conditions. A VHDL-AMS analysis environment is modeled based on the CD player electro-mechanical structure, on its connections to the vehicle dashboard, body, and suspension system, and on the relationships to roadway irregular profile. A real audio waveform is included in the simulation, modulated and transformed in the optical binary informations stored in the CD. Afterwards it is used as a real input.

This methodology is compared to traditional ones which imply real mechanical shocks transmitted to a CD player to emulate roadway profiles and audio quality detection.

We show that this multi-disciplinary and multi-resolution methodology, a new approach in fault-related literature, is feasible. We show that it allows to reproduce traditional shock tests as well. We thus demonstrate how faults conditions could be anticipated before the production phase. A simulation framework as the one described in this chapter gives the possibility to analyze the impact of electronics sub-systems parameters and of vehicle characteristics on system performance. This "integrated method" allows then to understand the failure sources connected to a real application environment and their possible solutions. This detailed information are not usually derived from traditional simulations and tests. In several points of the chapter, thus, evidences are given of how such a multi-disciplinary and multi-resolution methodology pinpoints that critical conditions could be anticipated before the production phase. On the author knowledge, often in the industrial field specific design values are not defined on a rigorous basis, but, on the contrary, chosen using a trial and error methodology. This is clearly expensive, especially in the car electro-mechanical system industry.

The chapter is organized as follows: in section 2 the principle of CD player electrical, mechanical and optical operations are given together with the vehicle suspension system organization, while in section 3 traditional test structures for autovehicle and dashboard CD player are described. In section 4 previous works based on VHDL-AMS are briefly reviewed and few hints on VHDL-AMS are reported. In section 5 the detailed model of the whole system is described giving VHDL-AMS examples, while in section 6 simulation results are presented and discussed. Final remarks and conclusions are in section 7.

2 The CD player in a car dashboard: electronic, optical and mechanical system

In this section the basic operations of the CD player (for details see Mansuripur (1994)) and the car system will be given without the aim of being exhaustive, as this is not the focus of the work.

Audio data, sampled at 44.1kHz, are not directly stored in the Compact Disk, but are partially modified to decrease error rates during music play back. Error codes insertion and interleaving are used during data packets creation. Furthermore, data are encoded using Eight Fourteen Modulation (EFM): Each 8 bits packet is encoded in a 14 bits one, in such a way that the number of '1's is as small as possible, and the distance between two '1's is as high as possible. Such encoded numbers are not directly stored on the CD support in the EFM form as each '1' is interpreted as a variation between a stored '0' (called *land*) and a stored '1' (called *pit*) or vice-versa. Thanks to EFM encoding, then, the physical distance between two transitions is higher than a given threshold. This is important as the reading system has an intrinsic

inertia and a limited accuracy in detecting the 0/1 or 1/0 variations. In figure 1 an example of data stored on the physical disk surface in terms of *pits* and *lands* and their correspondence to the EFM encoded data is shown. By means of a laser diode and a complex optical system

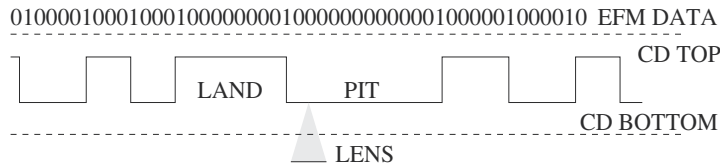


Fig. 1. CD pits and lands stored data.

a light signal with $\lambda \approx 500\text{ nm}$ is focused on the bottom side of the CD. The light is reflected back by *pits* and *lands* with a phase difference. The *land* and *pit* vertical height is accurately sized so that the signal reflected by the land has a phase difference of 180° with respect to the incoming wave. Thus a destructive interference occurs and no light signal is noticed back at the detecting system – i.e. a *land* corresponds to a '0'. On the other hand, the *pit* fully reflects the signal, and thus it corresponds to a '1'. These informations are read back by the audio data reconstruction system. The pit/land sequence is stored in a spiral on the CD support. Each sequence is separated from its neighbour one by a *land* track, as detailed in figure 2. The

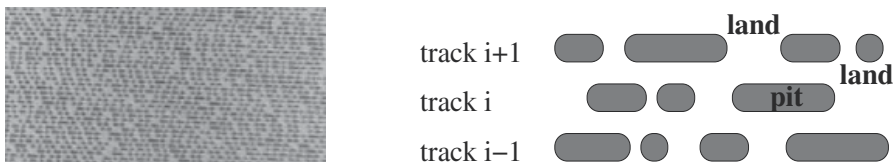


Fig. 2. CD data tracks. Left: photograph (Mansuripur, 1994). Right: detail of three tracks organized in pits and lands.

optical system, called *pick-up*, follows the track thanks to the rotation of the CD support due to a spindle motor and to a radial movement of the lens support. For a correct *pit/land* reading three important errors must be controlled. First, the optical system must be in focus; second, the laser should follow almost exactly the track spiral; third, the disk must be aligned to its ideal rotational axis. In the first case, shown in figure 3, if the lens is not at the right distance from the rotating disk, the focus point might not correspond to the *pit/land* surface, and the 0/1 data is incorrectly detected. The error is of vertical type and depends on external shaking, positioning tolerances or not planar CD surface. The tracking error, shown in the right sketch of figure 3, is of radial type, depends on bad disk centering and must be accurately checked as in a CD radius of about 3 cm the spiral may count up to 20000 adjacent tracks. Again, if this error is larger than a given threshold the 0/1 data is incorrectly detected. Last, due to the CD positioning system intrinsic errors, the disk may not be aligned to its ideal rotational axis: In this case both a vertical (focus) and a horizontal (tracking) error will be present. The CD player has an automatic system to control both focus and tracking errors. The signal reflected by the *pit/land* surface is elaborated by the lens system and deflected towards a photo-diode array. Whether the focus point is correct, then the deflection is uniform on all the photo-diodes; on the contrary, if the focus point is ahead of or behind the *pit/land* surface, each couple of photo-diodes senses a different deflected light. Uniform or different electrical signals will be then transmitted by the photo-diodes to an electronic system combining its inputs into a single amplified output correspondent to the detected focusing error. This signal will be used to drive a coil, which will generate the force needed to correct the optical system vertical

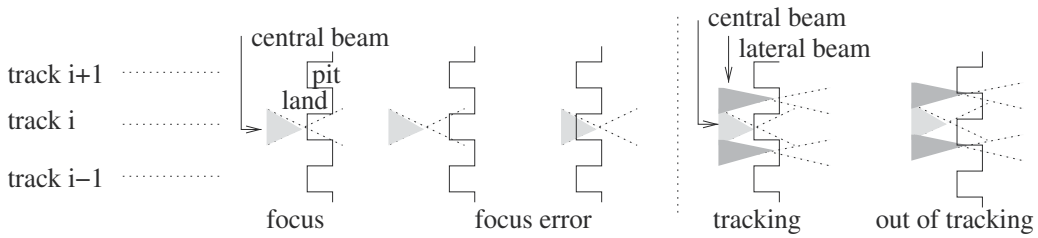


Fig. 3. Neighbour tracks stored in spirals as shown in figure 2. Focus and tracking errors.

position with respect to the disk. Theoretically, this feedback system will reach a balance point when the error is zeroed. In a real case, a given tolerance is the reached target. The tracking system is based on a similar principle and acts on the signal of other two photo-diodes. They receive, when on track, almost zeroed light back by the land spirals which are on the right and left of the main track spiral. These lands are lighted by two lateral components of the main laser diode emitted beam (details in figure 3 on the right). In case the radial motion of the lens system is not correctly following the track spiral, then the lateral components would reflect part of a pit of another track, and then the lateral diodes will receive a higher light signal. Consequent electrical signals at the two photo-diodes output are then combined to force a current on the coil responsible of the lens radial motion adjustment.

Both tracking and focus correction systems are influenced by external shaking, in particular in an auto-vehicle which is constantly moving on a not uniform surface. The most relevant accelerations are not the longitudinal or transversal ones, which are usually negligible with respect to track system readings, but the vertical one, strongly influencing focus regulation. Road irregularities are directly applied to car tyres, which transmit them to wheel axis, and to the moving part of the suspension system. The set built up by these three components is usually called *not suspended mass*, to underline its direct connection to the road, even if a little degree of displacement filtering is anyway guaranteed by tyres elasticity. The suspension system links the not suspended mass to the car body (called *suspended mass*), reducing the extent of vertical movement, thanks to the combined effect of its spring and shock absorber. The car body is then supposed to be connected to the dashboard, and to the CD player enclosure, with a structure of infinite stiffness, while the pick-up mass is linked to the CD player structure through a suitable damping system.

In section 5 details on the models used to describe the essential electrical, mechanical and optical systems are reported together with model approximations adopted in this work.

3. The traditional test equipment

Whenever dashboard CD player was tested by a specialized industry, a shaker system is adopted similar to the one used by our industrial partner (Magneti Marelli S.p.A.). In figure 4, a block diagram of a typical test configuration is shown. In the lower part a detailed view of the shaker actuator is visible, which propagates vibrations to the object fixed upon it according to a given vibrational profile. It is composed by three main blocks: an external fixed structure, an inductor, which is connected to it by means of a damper, and the vibrating plate upon which the object to be tested is fixed. The inductor is immersed in a static magnetic field, and, thanks to an appropriate current which flows through it, generates a force transmitted to the vibrating plate. The current is controlled by an external instrument connected to a PC and amplified before being injected in the inductor. Feedback through a control system is

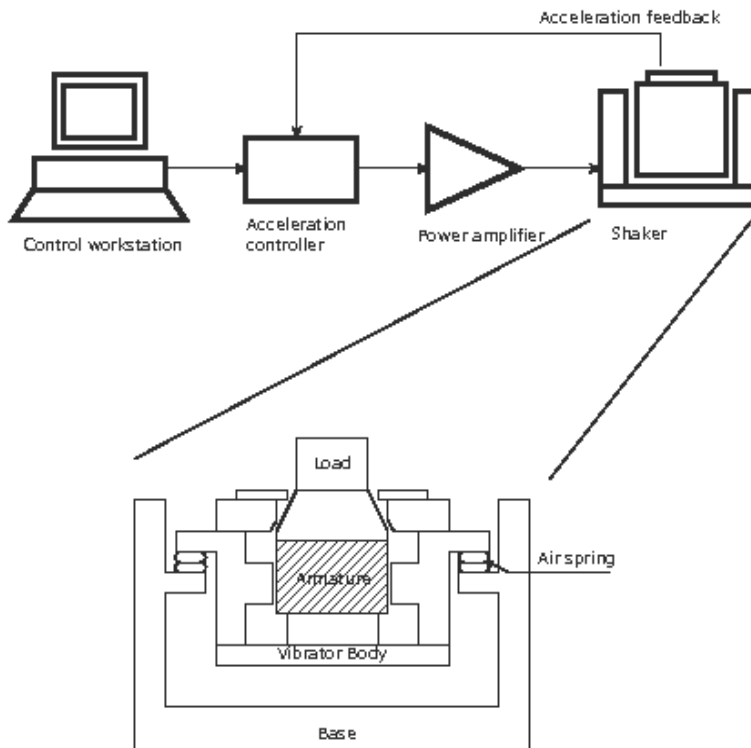


Fig. 4. Block diagram of CD player test configuration.

needed, to guarantee desired acceleration of the device under test. Input of the control system is the shaking profile defined by the user through the PC. This vibrating shape, in most of the cases, is directly provided by the CD player producer and should correspond to the maximum shocks tolerated by the device. The most frequently used profiles are of *sine* and *bump* type. In the former case, frequencies are automatically swept within a range chosen by the user. The aim is to analyze the response when a continuous vibration is present, as, for example, in the case of an auto-vehicle driving on a constantly irregular road profile. In the latter wave, a single but more violent vibration is used to test the CD player functionality (often, a sine semi-period is used as a profile) emulating a unique road irregularity.

The problems with this kind of tests are threefold. First, the vibrational profiles should be as similar as possible to the dashboard ones, but, on one hand, they are extremely dependent on the vehicle characteristics, and, on the other hand, the shaker system, even if carefully controlled, may introduce differences with respect to a real car system. Second, CD player performance are revealed by listening to the audio track and simply defining if, and how much frequently, an interruption occurred. Even if near to what the car user perceives, this is only a superficial error detection, it is subject to the user who is executing the test, and, most important, is an on-off test, as it does not reveal the error entity nor the location of the cause. Third, these are performed very late in the production cycle, as they are post-production tests or, in many cases, executed once the car producer has already installed the player and verified a systematic failure in the car plus CD player ensemble. From the point of view of CD player

or car manufacturers the information available after the execution of this kind of tests are far from being useful. In fact the need is to understand how and in which point modifications suitable to problem recovery can be performed. Moreover, the kind of vehicle must be taken in account as well. Even if this traditional system can still be useful, new, more sophisticated methods should be adopted to avoid long and expensive trial-and-error iterations.

4. VHDL-AMS: a multidisciplinary language for multi-resolution simulations

The VHDL language is thought for discrete systems modeling, like digital signals in digital circuits, but nowadays designs often needs the description of continuous characteristics. For example this happens in digital systems when sub-micron effects must be taken into account, or in analog and mixed-signal electrical design, or even in mixed electrical/not-electrical systems. VHDL-AMS supports discrete features but allows the adoption of continuous models based on differential algebraic equations, thanks to a dedicated analog solver. A few works document the use of VHDL-AMS as an effective simulation language for efficient design of complex mixed-signal electronics systems (Christen & Bakalar, 1999), especially in the telecommunication field. In (R. Ahola & Sida, 2003) a Bluetooth transceiver was first modeled using a simple behavioral description. Later, few blocks were refined and described so as to match the transistor level model. Basic functionality tests using an abstract VHDL-AMS behavioural description were used in (J. Oudinot & Le-clerc, 2003) showing the feasibility of a full transceiver circuit simulation. In (E. Normark & Nikitin, n.d.) RF blocks of a DQPSK transceiver and a channel model were implemented adding white Gaussian noise and achieving results very close to theoretical models. A methodology for the design of RF circuits in VHDL-AMS starting from flexible specifications and assuring an accurate description of noise and nonlinear effects was proposed in (W. Yang & Yan, 2005). In (Godambe & Shi, 1998) the real behavior of a PLL was modeled using VHDL-AMS adding jitter: the phase noise simulated spectrum was in good agreement with measured results. A top-down design methodology, validated by measurements, was proposed in (V. Nguyen & Naviner, 2005) for the design of a delta-sigma modulator. After a coarse description of components, various error sources like jitter, thermal noise, and capacitor mismatch were added to models. The modulator was finally designed in a CMOS process and measurements confirmed both model accuracy and top-down methodology effectiveness. In (L.A. Barragan & Burdío, 2008) authors use both VHDL and VHDL-AMS to model digital and mixed-signal circuits thought to reduce conducted electromagnetic interference (EMI) caused by resonant inverters in induction heating home appliances. A methodology for the design, the simulation and the fault analysis of a Controller Area Network (CAN) bus is presented in (W. Prodanov & Buzas, 2009). In (Santarini, 2006) VHDL-AMS is suggested to model complex electronic systems interacting inside the automotive environment, with varying hierarchical depth. An interesting application to automotive systems is in (M. Gursoy & Pelz, 2008) where a methodology is presented to investigate and predict the effects of the interaction between CAN transceivers and twisted pair transmission line connecting them in terms of electromagnetic emission. The language ability to solve differential algebraic equations allows modeling of not-electronic systems. In (F. Pecheux & A. Vachoux, 2005) several disciplines are involved in the modeling of an airbag system. Electrical, thermal, optical, mechanical and chemical knowledges are synthesized in the resulting model. A further up-to-date example is in F. Gao & Moudni (2010), where a multidomain dynamic proton-exchange-membrane fuel-cell stack model is described and simulated using VHDL-AMS. In (H. Boussetta & Soudani, 2010) a physical model of a microelectromechanical system piezoelectric microgenerator and its controlling

circuit is presented and their interaction analyzed. This capability is in fact particularly suitable to accurately represent automotive electro-mechanic components. Actually, the design of automotive systems requires a multitude of single components and sub-blocks, while, at the same time, complete system analyses are needed as well. In (Moser & Mittwollen, 1998) the first results of a joint project between automotive industry partners and tool makers are presented in the modeling of a brake system with ABS including hydraulics, mechanics and control aspects. In (D. Metzner & Schafer, 2002) a methodology for VHDL-AMS based specification, design and verification of an automotive Smart Power IC is presented. In (Wang & Kazmierski, 2005a) the same language is used for modeling, simulating and optimizing a fuzzy logic controller for an active suspension system. In (Wang & Kazmierski, 2005b) mixed mode simulation is the basis to model an active vibration isolation system in automotive environment. As previously pointed out, the VHDL-AMS language has another key characteristic: it allows to describe systems with different levels of abstraction. This makes a top-down design methodology viable, in which a preliminary behavioural description of components allows a coarse functionality test of the system, while progressive refinements define real circuit performance. This feature is particularly enhanced by ADMS (MentorGraphics, 2004) which allows to co-simulate both high level VHDL-AMS architectures and Spice-level netlists using ELDO in the same simulation environment, as shown in (M. R. Casu & Zamboni, 2007)(M.R. Casu & Graziano, 2008). In case an automotive device was to be modeled, this multi-resolution capability implies that critical electronic blocks can be roughly described at first. Later they are accurately refined, thus exploiting the native VHDL-AMS strength in modeling digital and analog devices, if needed, down to transistor level. On the other hand, the thermo-mechanical car environment can be coarsely represented, if less important, thus allowing a lightweight simulation from the point of view of CPU time. It is then of great interest the possibility to capture the effects of electronic details at system automotive level, and, conversely, the crucial capability of deriving electronic device design constraints from car system bound required performance. The design of the electronic system will be thus effectively optimized taking into account a real mechanical environment, so that reliability and fault test cases are reduced. In this work, starting from (Bisoffi, 2006) even if we do not go into details of the electronic system, we show how it is possible to create, early in the production phase, a fault analysis exploiting VHDL-AMS capabilities. It means co-simulating electronic and mechanical devices to point out their entangled operations, and, most important, analyzing how the performance of such a system is influenced by its real application environment.

5. Modeling dashboard CD player using VHDL-AMS

In section 5.1 we will describe the entire car and CD player macro-blocks and their principal interactions, while in the successive sections we will focus on the most important sub-blocks.

5.1 The system

The block diagram described using VHDL-AMS is shown in figure 5, in which the three mechanical, electrical and optical systems are depicted, together with their relationships.

The *mechanical* block includes the car tyres and suspensions system, the dashboard, the CD external structure, the pick-up and the track control sections. Inputs of this part are:

- Anterior and posterior roadway profiles to the tyres **Z-road-ant** and **Z-road-post**.
- **Vertical shift** and **radial shift** of the disk due to an error in its positioning system.

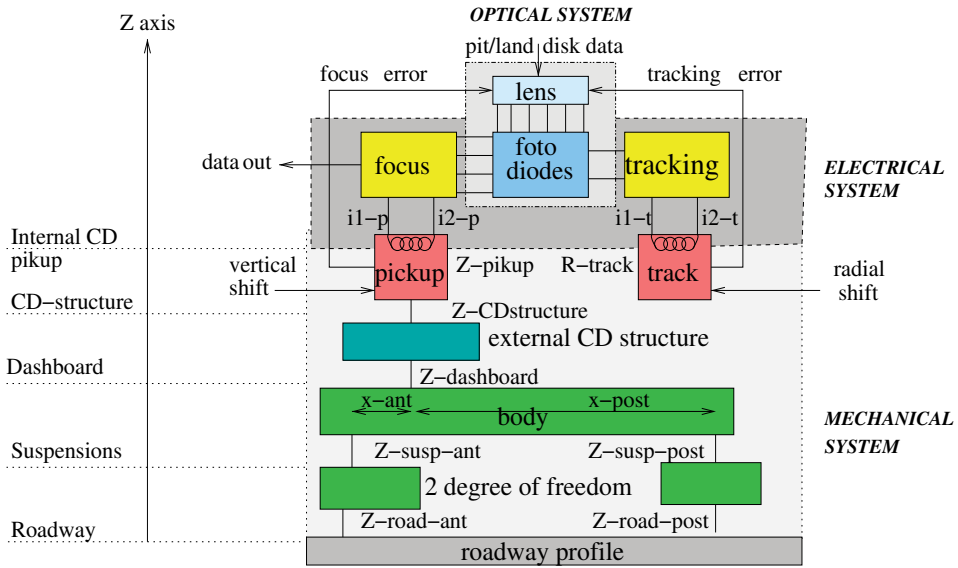


Fig. 5. Block diagram of the car and CD player mechanical (dotted box), electrical (dashed box) and optical (dash-dotted box) systems.

- Inductors currents of the pick-up $i1-p$, $i2-p$ and radial tracking $i1-t$, $i2-t$, driven by the electrical system.

The pick-up and track block positions **Z-pickup** (vertical) and **R-track** (radial) are the physical outputs, used in the model to generate the **focus** and **tracking** error, used as inputs of the optical system model.

State variables are the vertical positions of the suspensions, the dashboard and the CD structure. Parameters are the auto-vehicle and CD player mechanical characteristics.

The *electrical* block includes the focus and tracking control devices and the audio data reconstruction system. Photo-diodes output signals **a**, **b**, **c**, **d**, **e**, **f** are the inputs, while the currents for the pick-up and tracking coils ($i1-p$, $i2-p$, $i1-t$, $i2-t$) and the binary **data out** correspondent to *pit* and *land* variations are the computed outputs. The electrical characteristics of electronic control devices are the parameters of this system.

The *optical* block is composed of lens and photo-diodes. It receives as inputs **pit/land** physical track data and **focus** and **tracking** errors from the mechanical system. Last, it generates as outputs the photo-diodes signals. The latter devices characteristics are parameters for this system, together with the factors we used to model optical lenses.

5.2 The car model

We simplified the model assuming the vehicle was symmetrical with respect to the longitudinal axis. Moreover, the suspension system is simplified, as already explained in section 2 using a two degrees of freedom (2dof) De Carbon model of type mass-spring-damper, representing one quarter of the vehicle and sketched in figure 6. The model consists of two masses, the suspended (M_s) and the not-suspended (M_{ns}) ones. The former includes vehicle structure and half of the spring-damper-suspension mass. The latter includes wheel and its connection structure, brake and the other half of above-mentioned mass. Both suspension and tyre are modeled with their rigidity and damping factors K_s , C_s , K_t , C_t .

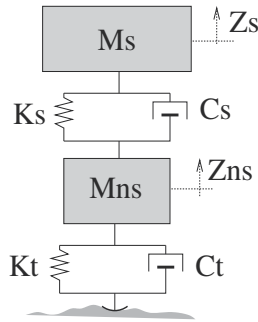


Fig. 6. Mechanical model of two degrees of freedom car suspension. The depicted model leads to the following differential equations pair:

$$\frac{d^2 Z_s}{dt^2} = \frac{K_s(Z_{ns} - Z_s) + C_s\left(\frac{dZ_{ns}}{dt} - \frac{dZ_s}{dt}\right)}{M_s}$$

$$\frac{d^2 Z_{ns}}{dt^2} = \frac{K_t(h - Z_{ns}) + C_t\left(\frac{dh}{dt} - \frac{dZ_{ns}}{dt}\right) - M_s \frac{d^2 Z_{ns}}{dt^2}}{M_{ns}}$$

According to them, the resulting VHDL-AMS description of the two degrees of freedom system can be written in the following way:

```
entity twodof is
  generic (constant Kt :REAL := 0.0;
           constant Ct :REAL := 0.0;
           constant Ks :REAL := 0.0;
           constant Cs :REAL := 0.0;
           constant Mns :REAL := 0.0;
           constant Ms :REAL := 0.0);
  port (terminal t_h,t_zns,t_zs: translational);
end entity twodof;

architecture Level0 of twodof is
  quantity h across t_h to translational_ref;
  quantity zns across zns2 through t_zns
           to translational_ref;
  quantity zs across zs2 through t_zs
           to translational_ref;
begin
  zs'dot'dot == (Ks*(zns-zs) +
                + Cs*(zns'dot-zs'dot))/Ms;
  zns'dot'dot == (Kt*(h-zns) +
                 + Ct*(h'dot-zns'dot) +
                 - Ms*zs'dot'dot)/Mns;
end architecture Level0;
```

The structure is composed, as in standard VHDL, by an **entity**, *twodof*. Rigidity and damping parameters are passed as **generics**, which values are set when this block will be instantiated within the higher hierarchical levels of the architecture. The **ports**, instead, represent the available connections to other blocks.

They are of *translational* type, an addition in the VHDL-AMS syntax with respect to traditional VHDL. They represent as *translational_ref* the position (t_h , that is, the road), the not-suspended mass position (t_{zns}) and, the suspended mass position (t_{zs}), respectively.

The model is described in the **architecture** part, in which two differential equations allow to find the position of the two masses with respect to the road profile. For describing the equations system VHDL-AMS uses the variable called **quantity**, which can be of the needed physical type, in this case *translational*. Each quantity is based on **through** and **across** variables that can be assimilated to a current and a voltage in an electrical system. An example is in figure 7, where through and across variables are shown for an electrical, a mechanical and a thermal system.

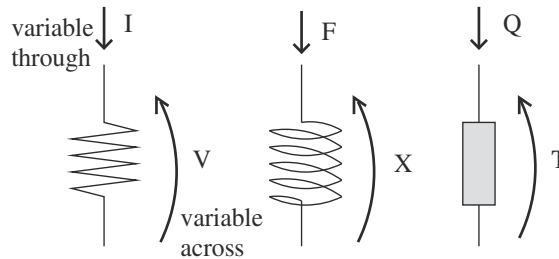


Fig. 7. Electrical, mechanical and thermal VHDL-AMS through and across variables.

A reference model, based on Matlab-Simulink blocks, and shown in figure 8, has been realized as well, to compare description complexity and results reliability with respect to more standard modeling techniques. As can be easily seen, VHDL-AMS allows to use a simpler description, leading to easier model understanding and maintenance.

Simulations have been performed, then, to compare system behaviour with the two modeling techniques, excited by manifold road profiles. As an example of the obtained results, in figure 9 the suspension position (Z_s) caused by a typical bump on the road is reported for the two models. The profiles are almost superposed, thus showing a good reliability of the VHDL-AMS description. The input is exactly one half period of sine wave with 10 cm amplitude and 10 Hz frequency.

The vehicle described in our model is composed of two *2dof* blocks connected to the front and back axles, as sketched in figure 5. They are used to reckon the dashboard vertical position using the vehicle body model and the distances between the dashboard and the two suspensions (x_{ant} and x_{post}). For simplicity, in our model, car body is supposed to be rigid, and dashboard position is computed as

$$Z_{dashboard} = \frac{Z_{susp-ant}x_{ant} + Z_{susp-post}x_{post}}{x_{ant} + x_{post}}$$

This complexity reduction leads to four degrees of freedom compared to eight ones and will collapse the influence of the road irregularity on the vertical error. We will not take into account radial error effects due to different road profiles coupled to two tyres on the same axle. This does not influence essential results of our work, but will be implemented in its future development to improve results accuracy. Suspension parameter values used in our simulations are for two kind of vehicles: a comfort one and a handling one, representing two different kind of performance required by suspension systems. Their values are reported in table 1.

The car system *vehicle* is described using VHDL-AMS stepping up to a higher hierarchical level, which includes the body model and the suspension block as components, as reported in the preceding code. Before the real architecture description begins, four terminals are declared for supporting the connections among the blocks. The architecture is described using one instance of the body (*vehicle-instance*) and two instances (front and back) of the *2dof* blocks (*anterior-susp-instance* and *posterior-susp-instance*).

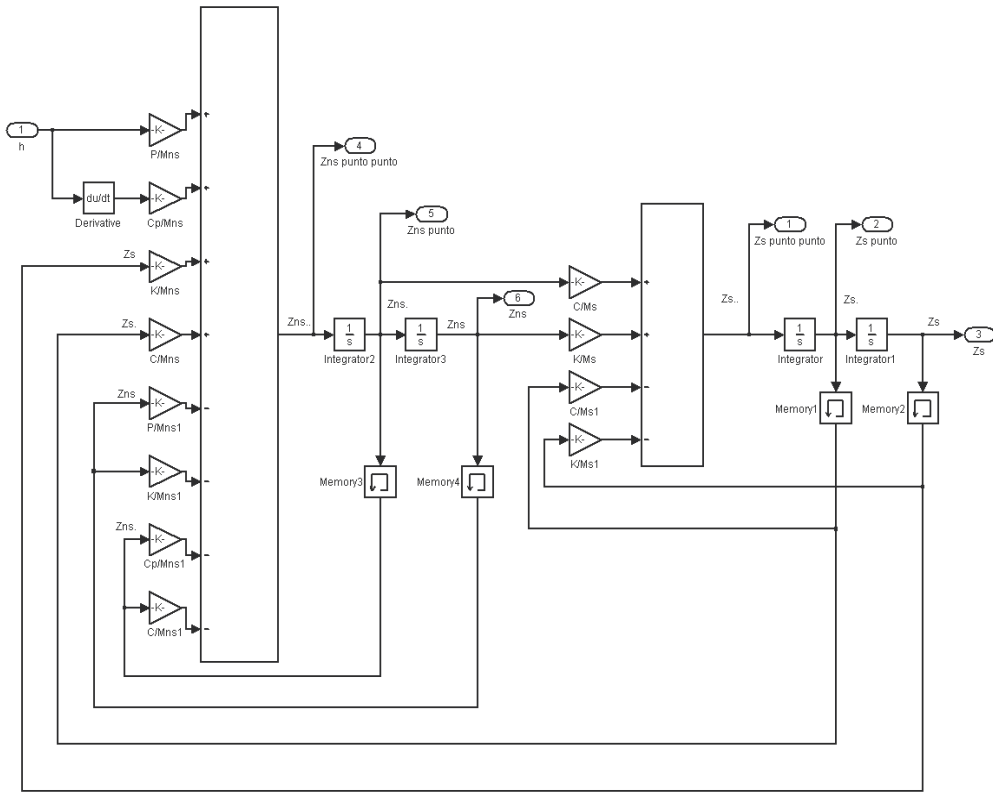


Fig. 8. Matlab-Simulink model of two degrees of freedom car suspension..

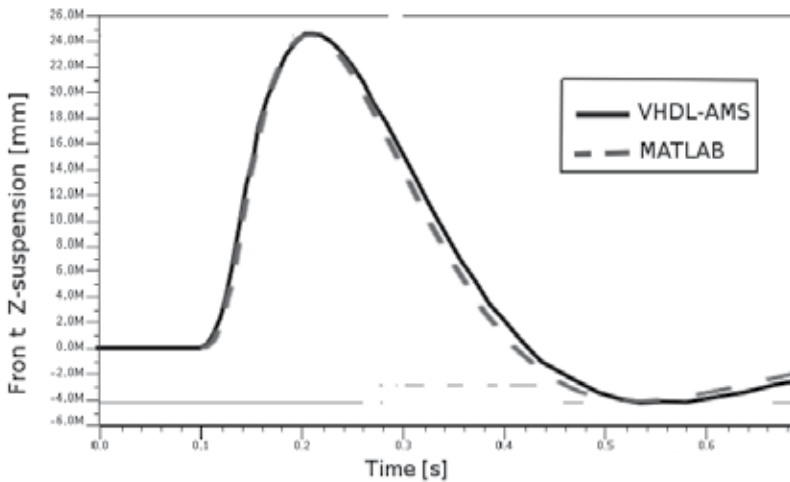


Fig. 9. Suspension displacement (Z_s) for a roadway bump profile. Matlab and VHDL-AMS simulation results.

	Comfort		Handling	
	front axle	back axle	front axle	back axle
m_s	756.7 Kg	596.3 Kg	756.7 Kg	596.3 Kg
m_{ms}	85 Kg	80 Kg	85 Kg	80 Kg
K_s	33333.3 N/m	21428.6 N/m	46666.6 N/m	30000.04 N/m
C_s	8667 N/(m/s)	6667 N/(m/s)	12133 N/(m/s)	9333 N/(m/s)
K_t	17000 N/m	17000 N/m	+40 23800 N/m	23800 N/m
C_t	1000 N/(m/s)	1000 N/(m/s)	1400 N/(m/s)	1400 N/(m/s)

Table 1. Rigidity and damping factors for comfort and handling vehicle models.

```

entity vehicle is
  port (terminal t-road-ant, t-road-post,
        t_dashboard: translational);
end veicolo;

architecture Level1 of vehicle is
  component twodof
    generic ( constant Kt :REAL := 0.0;
              constant Ct :REAL := 0.0;
              constant Ks :REAL := 0.0;
              constant Cs :REAL := 0.0;
              constant Mns :REAL := 0.0;
              constant Ms :REAL := 0.0);
    port (terminal t_h, t_zns,
          t_zs: translational);
  end component;
  component bodymodel
    generic (constant x-ant :REAL := 0.0;
              constant x-post :REAL := 0.0);
    port (terminal t_zsant, t_zspost,
          t_zdash: translational);
  end component;

  terminal zns_ant, zns_post,
           zs_ant, zs_post: translational;
begin
  vehicle-instance : bodymodel
  generic map (x-ant => 0.82, x-post => 1.88)
  port map ( t_zsant => zs_ant, t_zspost =>
            zs_post, t_zdash => t_zdashboard);

  anterior-susp-instance : twodof
  generic map ( Kt => 1.7e5, Ct =>1.0e3,
              Ks => 33333.3, Cs => 8666.6,
              Mns => 85.0, Ms => 756.7)
  port map ( t_h => t-road-ant, t_zns =>
            zns_ant, t_zs => zs_ant);

  posterior-susp-instance : twodof
  generic map (Kt => 1.7e5, Ct =>1.0e3,
              Ks => 21428.6, Cs => 6666.6,
              Mns => 80.0, Ms => 596.3)
  port map ( t_h => t-road-post, t_zns =>
            zns_post, t_zs => zs_post);
end Level1;

```

Their terminals are properly connected by a **port map** and **generics** are set to values correspondent to the vehicle model (see table 1). The top level block is connected to the road profile. This is described, by means of mathematical expressions, as a vertical translation of the two terminals describing the *Z-road-ant* and *Z-road-post* positions. Three different profiles have been adopted: a *sine* wave, a *bump* (a sine semi-period) and a *step*, in all cases with parametric amplitudes and frequencies.

5.3 The CD mechanical structure

The block connected to the car body/dashboard is the CD external structure. It has the *Z-cdstructure* vertical position. We suppose a rigid connection between the two masses as usually no suspension system is used by automotive or CD player manufacturers. The optical body, which position is *Z-cd*, is linked to the CD external structure, thanks to a suspension system which limits vibrations transmission from the dashboard to the pick-up. Rigidity and damping factors which model such suspension are shown in figure 10. The CD pick-up must be kept at right distance from the CD surface, so that tracks are correctly beamed. To accomplish this, a coil corrects the pick-up position (*Z-pickup*) thanks to a current signal *i* imposed by the focus block through terminals *i1-p*, *i2-p*. The block diagram shows the force generated by the coil, the inertia opposed by the pick-up mass, and the rigidity and damping factors of the spring connecting the two components.

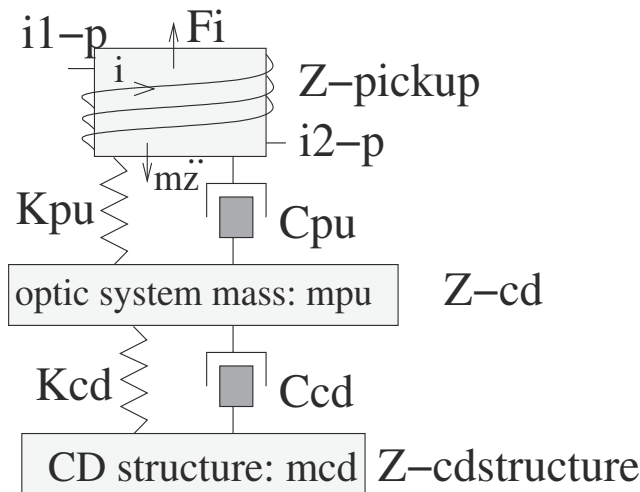


Fig. 10. Mechanical model of the CD structure.

The CD pick-up VHDL-AMS code is reported in the following. Two mechanical and electrical descriptions can be easily recognized. The rigidity and dumping parameters, together with the K_i constant in the permanent magnet law, are extremely important for CD behaviour and performance. The values adopted are reported in table 2. They have been obtained from CD player specifications, when available, and through a parametric study of the CD behaviour compared with traditional test results.

```
entity pickup is
  generic (constant Ki : REAL := 0.0;
           constant Cpu : REAL := 0.0;
           constant Kpu : REAL := 0.0;
           constant mpu: REAL := 0.0;
```

```

    ind : inductance := 0.0;
    i_ic : real := real'low);
port (terminal t_zstrcd, t_zpu: translational;
      terminal i1-p, i2-p: electrical);
end entity pickup;

architecture Level0 of pickup is
  quantity h across t_zstrcd to translational_ref;
  quantity z across z2 through t_zpu
           to translational_ref;
  quantity v across i through i2-p to i1-p;
  quantity Fi: force;
begin
  if domain = quiescent_domain and
    i_ic /= real'low use i == i_ic;
  else v == ind * i'dot; end use;
  z'dot'dot == (Kpu*(h-z) +
               + Cpu*(h'dot-z'dot)-Fi)/mpu;
  Fi == Ki*i*(z+1.0-h)**2;
end architecture Level0;

```

The tracking system is similar to the focus one, but simpler. It has no connection to the dashboard: only a system similar to the pick-up one reported in the previous VHDL-AMS code. As described above, CD position may be subject to variation with respect to the ideal one: This corresponds to vertical and radial shifts. These errors are here modeled as displacements forced by the external world. Both the focus and tracking mechanical sub-blocks, thus, have been modified by adding as inputs the **vertical shifts** and **radial shifts** respectively. Again, the updated model is not included for sake of brevity.

Kcd $3.0e^4 N/m$	Ccd $3.0e^4 N/(m/s)$	Cpu $10 N/(m/s)$
Kpu $100 N/m$	Ki $35 N/Am^2$	mcd / mpu $0.5Kg/0.02Kg$

Table 2. Values adopted for the CD pick-up model.

5.4 The focus and tracking electrical subsystems

The focus block elaborates photo-diodes currents to accomplish the following tasks:

- First, it decides if a '0' or a '1' is present in the CD track.
- Second, it generates an error signal to correct the pick-up position if the four signals from the photo-diodes **a**, **b**, **c**, **d** are different, i.e., the CD surface is out of focus.

Focusing block architecture is reported in figure 11. Four amplifiers buffer impedances of the photo-diodes output to the cascaded block. A differential amplifier generates then the signal

$$Vd = \frac{R}{R_{abcs}}(b + d) - (a + c)$$

(if $R_a = R_b = R_c = R_d = R_{abcs}$) related to the photo-diodes physical position and the optical deflection system. As reported in above boxes in figure 11, when the pick-up is in the right position all photo-diodes receive the same signal, thus $Vd = 0$. Otherwise, depending on the focus point position, ahead of the track line or behind, the photodiodes receive vertically or horizontally unbalanced light signals respectively. The differential signal Vd will be thus negative or positive. An example of the VHDL-AMS code used to behaviourally model the operational amplifier is in the following.

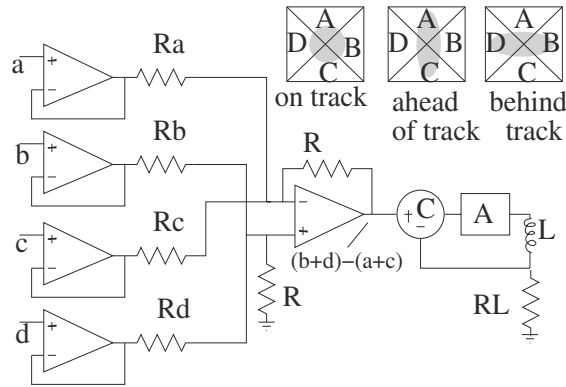


Fig. 11. Focus electrical subsystem.

```

entity opamp is
  generic (alim_plus : REAL := 12.0;
          alim_min : REAL := -12.0;
          gain : REAL := 1.0e5);
  port (terminal in_plus, in_min,
        out_op: electrical);
end opamp;

architecture Level0 of opamp is
  quantity vd across in_plus to in_min;
  quantity vout across i_out through out_op
    to electrical_ref;

  quantity q : REAL;
begin
  q == vd*gain;
  if q > (alim_plus-0.5) use
    vout == alim_plus-0.5;
  elsif q < (alim_min+0.5) use
    vout == alim_min+0.5;
  else
    vout == q;
  end use;
end architecture Level0;

```

In this work we did not model any amplifier offset error as they are considered not meaningful with respect to the impact of mechanical induced vibrations on system performance. On the other hand, we model saturation effects in our description, as such distortion could affect focusing block effectiveness. Anyway, it will be interesting to include in future developments of this work second order effects of electronic devices as well, in order to assess their impact on focusing error. The V_d signal should be able to drive the coil which generates the force needed to correct the pick-up position, as described in section 5.3. This is realized by a system with feedback that generates a bipolar current needed to drive the linear motor coil L . VHDL-AMS code of this circuit is not reported for space reasons. The tracking block has a similar structure and acts on two other photo-diode outputs (e and f) generating a zero signal when the system is on track: If a lateral shift occurs on the laser direction with respect to the track, the light received by the two photo-diodes is unbalanced. The correction occurs again forcing a current with proper direction and amplitude on the tracking block coil.

5.5 The optical subsystem

The optical block includes a photo-diodes array and the lens part. The VHDL-AMS behavioral model of one of the photo-diodes is reported below. The light intensity is defined as an *electrical* quantity for simplicity.

```
entity photodiode is
  port (terminal A, C, E: Electrical);
end photodiode;

architecture Level0 of photodiode is
  quantity v across i through A to C;
  quantity lum across E to electrical_ref;
begin
  i == -8.2e-6*lum;
end Level0;
```

The light terminal is connected to the lens block, which code is reported in the following. This has been modeled in a simple way, as it is normally a closed-box which, in its internal composition, is not influenced by the errors we are considering. The emitted light focus point is influenced by the position of the optical block. For this reason, outputs for this entity are the emitted light signal of the six diodes **Eea, Ee, Eec, Eed, Eee, Eef**. Inputs of this entity are **sign_foc** and **sign_track**, that is the *pit/land* nominal input transition sequence and the track-ok land signal respectively. In much detail, it must be underlined that the real light signal reflected back by the track is not an abrupt one, but, still modulated, has a shape similar to the one reported in figure 12. We generated it (for details see Mansuripur (1994)) starting from the digital EFM data as described in section 6

```
entity lens is
  generic (constant toll_foc :REAL := 0.0;
          constant toll_track :REAL := 0.0;
          constant K_foc :REAL := 0.0;
          constant K_track: REAL := 0.0);
  port (terminal in_err_foc,in_err_track: translational;
        terminal Eea,Eeb,Eec,Eed,Eee,Eef: electrical;
        terminal sign_foc, sign_track: electrical);
end entity lens;

architecture Level0 of lens is
  quantity err_foc across in_err_foc
    to translational_ref;
  quantity err_track across in_err_track
    to translational_ref;
  quantity sig across sign_foc to electrical_ref;
  quantity land across sign_track to electrical_ref;
  quantity Qeea across iea through Eea to electrical_ref;
  quantity Qeeb across ieb through Eeb to electrical_ref;
  quantity Qeec across iec through Eec to electrical_ref;
  quantity Qeed across ied through Eed to electrical_ref;
  quantity Qeee across iee through Eee to electrical_ref;
  quantity Qeef across ief through Eef to electrical_ref;
  quantity verify_foc: voltage;
  quantity verify_tracking: voltage;
begin
  if err_foc'ABOVE(toll_foc) use
    Qeea == sig ; Qeec == sig ;
  if sig'ABOVE(K_foc*(err_foc-toll_foc)) use
```

```

    Qeeb == sig-K_foc*(err_foc-toll_foc);
    Qeed == sig-K_foc*(err_foc-toll_foc);
  else
    Qeeb == 0.0;    Qeed == 0.0;
  end use;
  elsif err_foc'ABOVE(-toll_foc) use
    Qeea == sig;    Qeeb == sig;
    Qeec == sig;    Qeed == sig;
  else
    Qeeb == sig ;   Qeed == sig ;
    if sig'ABOVE(-K_foc*(err_foc+toll_foc)) use
      Qeea == sig+K_foc*(err_foc+toll_foc);
      Qeec == sig+K_foc*(err_foc+toll_foc);
    else
      Qeea == 0.0;   Qeec == 0.0;
    end use;
  end use;
  verify_foc == Qeea+Qeec-Qeeb-Qeed;

  if err_track'ABOVE(toll_track) use
    Qeef == land;
  if land'ABOVE(+K_track*(err_track-toll_track)) use
    Qeee == land-K_track*(err_track-toll_track);
  else
    Qeee == 0.0;
  end use;
  elsif err_track'ABOVE(-toll_track) use
    Qeee == land;   Qeef == land;
  else
    Qeee == land;
    if land'ABOVE(-K_track*(err_track+toll_track)) use
      Qeef == land+K_track*(err_track+toll_track);
    else
      Qeef == 0.0;
    end use;
  end use;
  verify_tracking == Qeef-Qeee;
end architecture Level0;

```

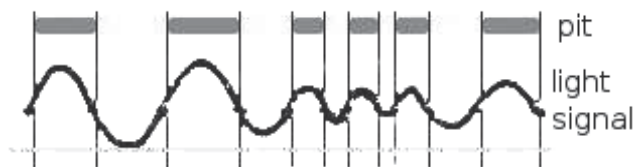


Fig. 12. Example of the EFM modulated light signal received by the photo-diodes when the track reflects back the laser light.

Further inputs of this block are position errors generated by the focusing and tracking systems described in section 5.3: **in_err_foc** and **in_err_track**. In absence of focusing error, light signals are identical to the **sign_foc** input. If a focusing error is occurring, light waves are unbalanced towards the correspondent diodes, as described in section 5.4, depending on error sign and on the value of a proper constant **K_foc**. In the same way the **Eee**, **Eef** signals depend on tracking error and the constant **K_track**. Tolerance factors are defined for both focus and tracking errors.

6. Simulation results

Every single block has been separately simulated and its behavior compared, when feasible, to the one found in the laboratory in collaboration with our industrial partner. System simulations consist in forcing irregular road profiles, of bump type or of sine type, in analyzing the focusing and tracking errors, when a digital data is forced at the CD input, and in comparing digital input and output. These data have been generated starting from a “wav” file, transformed in a EFM modulated input, and then digitized so that a ‘1’ corresponds to a ‘pit’ in the CD track and a ‘0’ corresponds to a ‘land’. Afterwards these *pit/land* data are transformed in a light signal as in figure 12 and used as input to the *lens* block described in section 5.5. Road profile inputs reproduce the ones used in the traditional test described in section 3 (e.g. sin, bump, step). Several simulations have been accomplished varying available stimulus parameters. The main values used are wave shape (bump and sine are reported here), wave maximum amplitude (10cm and 20cm are reported herein), bump duration and stimulus frequency. Moreover, presence or absence of a CD rotational axis displacement and, finally, the vehicle type (comfort and handling) have been varied. Digital output generated by the pick-up system is compared with the input: When different, the fault simulation engine points out a logical error, as sketched in the simulation output in figure 13. In all illustrations of this section, N and M letters on axis are scaling factors, representing 10^{-9} and 10^{-3} , respectively.

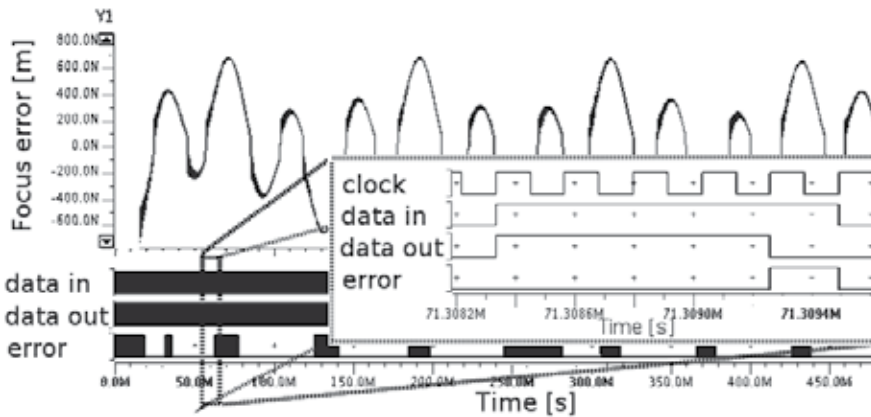


Fig. 13. Digital input, focus error, digital output and digital error.

Traditional test results are available only as presence or absence of audible audio errors. Our comparisons demonstrates that the detection of an error in the simulation is a needed but not sufficient condition to have an audible error in the real system. This behaviour can be ascribed to the following factors:

- a) Error detection in the real system is accomplished through human ear, thus allowing to skip subtle glitches.
- b) Our model does not take in account the ECC performed by electronic circuitry down the reproduction chain.

From this point of view, our test is more reliable as it is deterministic and does not depend on subjective characteristics. Anyway, as our simulation environment allows to go deep inside data error sources, we prefer to analyze and report in the following focusing error behaviour dependency on the parameters. We will concentrate only on focusing error and neglect the

tracking one, as less dependent on the car system in our simple four degrees of freedom model. A focusing error greater than $0.5 \mu\text{m}$ is considered a critical one as, for sure, it causes a 0/1 evaluation error. A near to $0.5 \mu\text{m}$ error is still critical, but may not generate a digital error: This depends on the optical and electrical device parameters. We will then analyze the cases in which this error approaches the critical range. In figure 14 the case of a bump wave (10cm maximum amplitude) is reported, with a disk perfectly aligned to its rotational axis

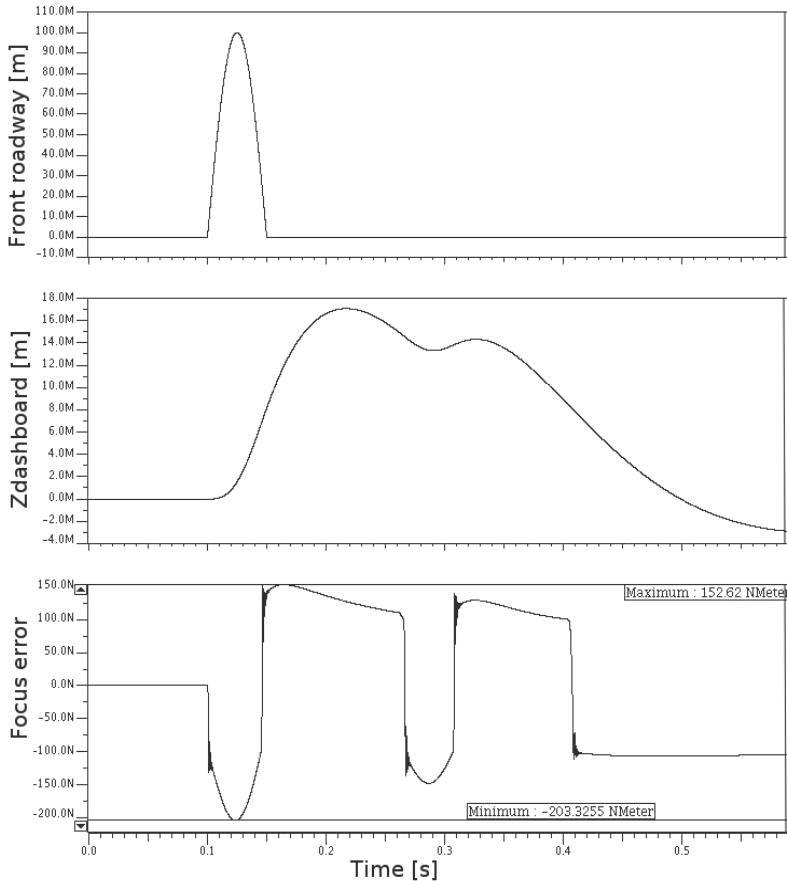


Fig. 14. Dashboard displacement and focus error in case of a bump road profile for a comfort vehicle suspension. No disk radial or vertical shift are used.

(radial and vertical shifts are zero, that is, an unrealistic state). The dashboard displacement is sketched as well, showing the superposed effects of the front and back axles. The focus error approaches a maximum of 200nm, which, at least in our simple model, is not expected to cause a digital error. In figure 15 the same signals are reported in case of a sine wave. The error is clearly dependent on the sine frequency and reaches higher values: The continuous roadway irregularity impacts on the focus correction system which is less capable to react to perturbations.

Figure 16 shows again a bump waveform as roadway profile, but a CD vertical shift is present as well, modeled as a sine wave of 1mm peak and 8Hz frequency. Both the suspension and the dashboard displacements are presented: Two different waves are superimposed for the

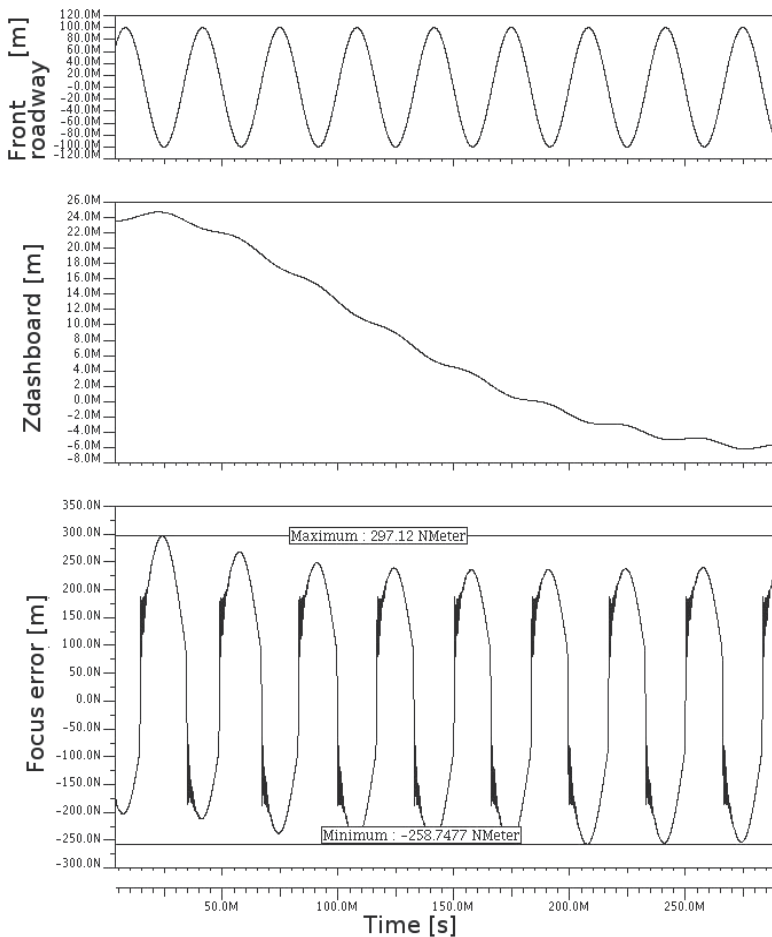


Fig. 15. Dashboard displacement and focus error in case of a sine road profile for a comfort vehicle suspension. No disk radial or vertical shift are used.

suspension parameters of a comfort and a handling vehicle respectively. The comfort model exhibits an almost doubled focus error if compared to the absence of the disk irregular rotation axis. The handling vehicle shows a 40% displacement increase with respect to the comfort one, with a 10% focus error increase. It is interesting to analyze the focus error data in table 3 in which the bump profile results are summarized. The bump peaks used were 0.1m and 0.2m long, and three bump durations are considered – correspondent to three different road irregularity lengths (ΔT).

A double bump amplitude has, of course, a higher impact on focus error when the CD is ideally rotating, while, the more realistic case of a periodical vertical shift causes only a 12% focus error worsening.

In figure 17 a simulation is reported in case of a sine road profile (0.1m peak, 25Hz) with a CD vertical shift for both a comfort and a handling vehicle. In this case the focus error increases up to 487nm for the comfort case, and to 574 for the handling one: In both cases the error will cause a digital error. We summarized sine test results in figures 18 and 19: The focus error

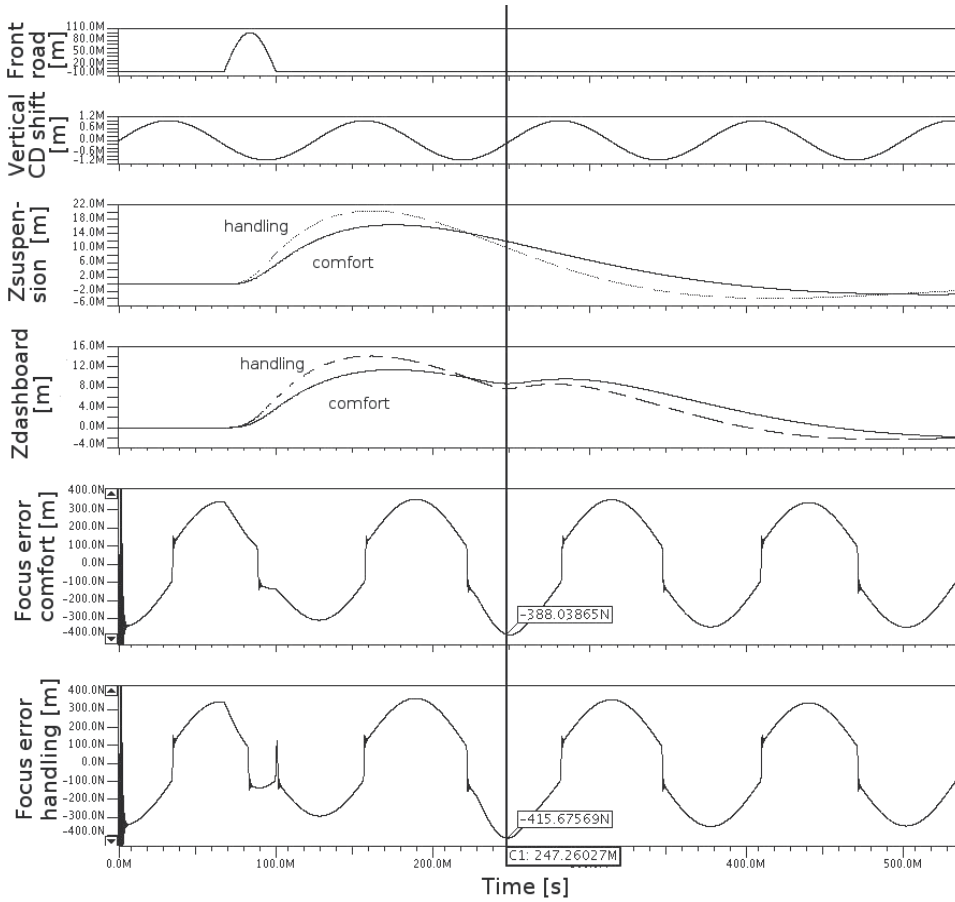


Fig. 16. Dashboard displacement and focus error in case of a bump road profile for a comfort and an handling vehicle suspension parameters. Disk vertical shift of 1mm peak and 8Hz frequency.

Test type	Bump ampl.	ΔT 33ms	ΔT 25ms	ΔT 20ms
Comfort vehicle model				
No CD misalign.	0.1m	207nm	207nm	206nm
	0.2m	314nm	313nm	213nm
CD misalign.	0.1m	390nm	351nm	356nm
	0.2m	439nm	358nm	370nm
Handling vehicle model				
CD mis.	0.1m	416nm	351nm	380nm

Table 3. Focus error caused by a bump road profile. CD misalignment has 1mm, 8Hz parameters.

is shown as a function of road profile frequency, which is swept within the values for which the two degrees of freedom model is valid for a 20cm and 10cm sine amplitude respectively. In figure 18 only a few tests (20Hz, 25Hz and 30Hz) reach the critical error range in case the

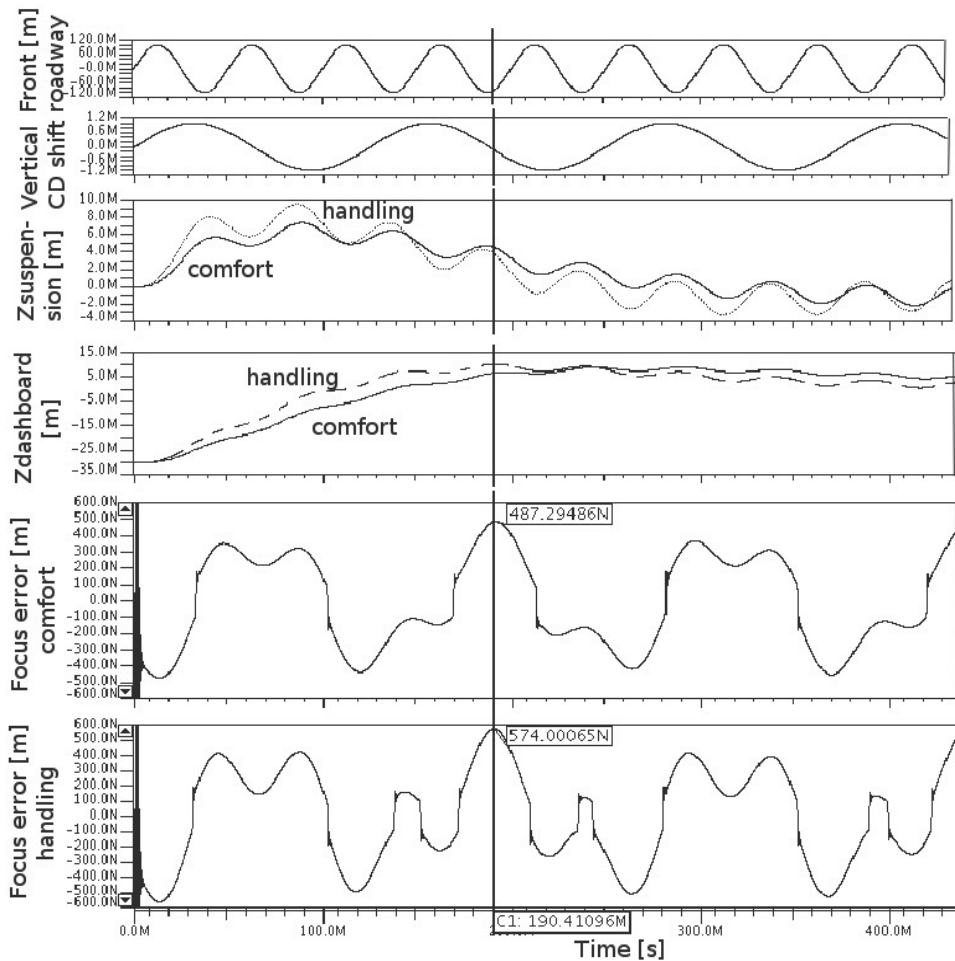


Fig. 17. CD player focus error for suspension parameters in the case of a comfort and a handling vehicle. The roadway profile is changing in a sinusoidal way in both the front and the back of the vehicle. Sine roadway profile (front and back): 0.1m peak, 25Hz. CD vertical shift max 1mm.

CD displacement is zero. On the other hand, the presence of the CD vertical shift causes an intolerable focusing error for almost every frequencies.

When a lower road irregularity peak is used (figure 19) then error is not critical when the disk has an ideal position. CD misalignment, instead, even in the comfort car model, produces an error around the limit range. The same tests conducted on a handling car bring the error above the limit, so that an audio mistake should be expected. This result supports the focus point of this work: The CD player manufacturer required the test to our partner as the car manufacturer received claims by customers of handling vehicles mounting those CD players on board. When tested by our partner by means of the traditional test equipment, they showed a worst behavior in the sine test as in our case. This has especially been verified when the CD players on the shaker plate was subject to vertical accelerations coherent with the dashboard of a handling vehicle. In every case reported in figure 18 and 19 a correlation

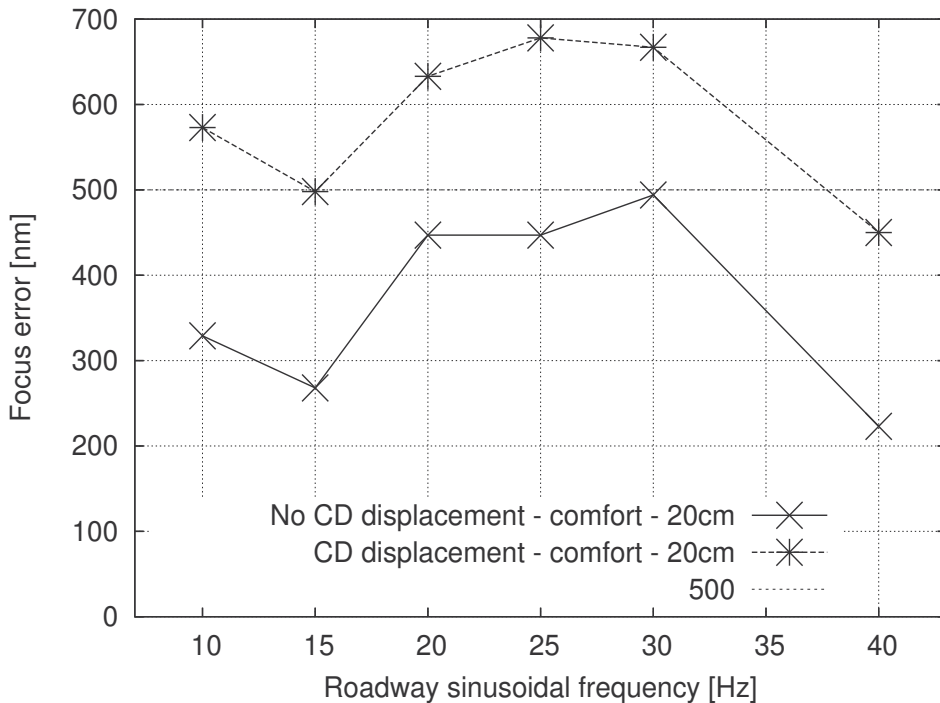


Fig. 18. Maximum focus error found with a sinusoidal roadway profile (0.2m peak) for different frequencies. No CD displacement effect, comfort vehicle parameters.

between road profile frequency and the mechanical car and CD player parameters can be observed, as only the values in the central range clearly show the worst behavior. It would be interesting to sweep such model parameters within proper ranges, once precisely provided by the manufacturers, as values adopted here are the only reliable ones we found. This way, a clean dependency between faults and electro-mechanical design choices could be pinpointed (e.g. CD mechanical structure rigidity and dumping parameters, coil properties, CD structure connection to the dashboard, amplification factors in the focusing differential amplifier and in the following power block,...), so that critical fault cases as the one we were involved in could be avoided. Anyway, the results achieved in this work show how this methodology may help both during fault and design analysis. The CD mechanical structure and pick-up electrical parameters, when chosen, are to be strictly related to the whole environment, especially to vehicle parameters and to real application conditions. Traditional test methodologies clearly do not take in consideration these aspects, if not in a late phase, as in the case of our industrial partners.

7. Conclusions

In this chapter we show how a VHDL-AMS multidisciplinary model can be used with success for setting up a new fault simulation methodology involving the automotive electro-mechanical system. We simulated a CD player electrical, optical and mechanical structure, its reaction to a vehicle dashboard-suspension-tyre shaking due to an irregular road profile. Results show good agreements with tests performed in laboratory. Furthermore,

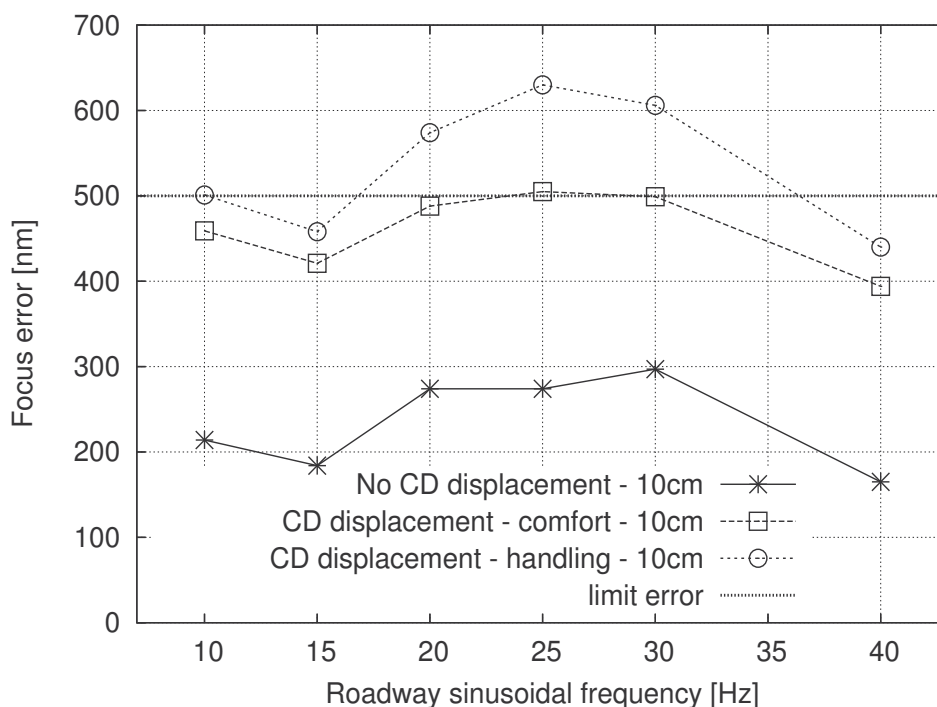


Fig. 19. Maximum focus error for a sinusoidal roadway profile (0.1m peak) for different frequencies. CD displacement effect, comfort and handling car parameters.

we demonstrate how fault cases could have been anticipated by both CD player and vehicle manufacturers still in the pre-production phase. This methodology allows thus to understand critical points of the system and to find possible solutions. For instance, pick-up electrical and mechanical parameters may be varied to more efficiently reaching the lens focus point on the CD audio track.

8. References

- 1076.1, I. S. (1999). *VHDL Analog and Mixed-Signal Extensions*, IEEE Std. 1076.1.
- Bisoffi, A. (2006). *VHDL-AMS Modeling of a Vehicle CD-ROM system*, Politecnico di Torino, Thesis.
- Christen, E. & Bakalar, K. (1999). Vhdl-ams—a hardware description language for analog and mixed-signal applications, *IEEE Transactions on Circuits and Systems—Part II: Analog and Digital Signal Processing* Vol. 46(No. 10): 1263–1272.
- D. Metzner, G. P. & Schafer, J. (2002). Architecture development of mixed signal ics for automotive application with vhdl-ams, *Proceedings of IEEE International Behavioral Modeling and Simulation Conference (BMAS'02)*, San José, California.
- E. Normark, L. Yang, C. W. & Nikitin, P. (n.d.). *Proceedings of IEEE International Behavioral Modeling and Simulation Conference (BMAS'04)*.
- F. Gao, B. Blunier, A. M. & Moudni, A. E. (2010). A multiphysic dynamic 1-d model of a proton-exchange-membrane fuel-cell stack for real-time simulation, *IEEE TRANSACTIONS ON INDUSTRIAL ELECTRONICS* Vol.57(No. 6): 1853–1864.

- F. Pecheux, C. L. & A. Vachoux (2005). Vhdl-ams and verilog-ams as alternative hardware description languages for efficient modeling of multidiscipline systems, *IEEE Transactions on Computer-Aided Design of Integrated Circuits and Systems* Vol. 24(No.2): 204–225.
- Friedman, J. (2005). Matlab/simulink for automotive system design, *Proceedings of Design and Test Conference (DATE'05)*, Munich, Germany.
- Godambe, N. J. & Shi, C.-J. R. (1998). Behavioral level noise modeling and jitter simulation of phase-locked loops with faults using vhdl-ams, *Journal of Electronic Testing Theory and Applications* Vol. 13(No. 1).
- H. Boussetta, M. Marzencki, S. B. & Soudani, A. (2010). Efficient physical modeling of mems energy harvesting devices with vhdl-ams, *IEEE SENSORS JOURNAL* Vol. 10(No. 9): 1427 – 1437.
- H. Casier, P. M. & Appeltans, K. (1998). Technology considerations for automotive, *Proceedings of IEEE International Design and Test Conference (DATE'98)*, Paris, France.
- J. Oudinot, S. Scotti, J. R. & Le-clerc, A. (2003). Full transceiver circuit simulation using vhdl-ams, *Journal of Microwave Engineering* pp. 29–33.
- L.A. Barragan, D. Navarro, I. U. & Burdio, J. (2008). Fpga implementation of a switching frequency modulation circuit for emi reduction in resonant inverters for induction heating appliances, *IEEE TRANSACTIONS ON INDUSTRIAL ELECTRONICS* Vol. 55(No. 1): 11–20.
- M. Gursoy, S. Jahn, B. D. & Pelz, G. (2008). Methodology to predict eme effects in can bus systems using vhdl-ams, *IEEE TRANSACTIONS ON ELECTROMAGNETIC COMPATIBILITY* Vol. 50(No. 4): 993–1002.
- M. R. Casu, M. Graziano, M. C. & Zamboni, M. (2007). An effective ams top-down methodology applied to the design of a mixed-signal uwb system-on-chip, *Proceedings of IEEE Design Automation and Test Conference*, Nice, France.
- Mansuripur, M. (1994). Principles of optical disk data storage, *Handbook of Optics* Vol. 1, Chapter 13.
- MentorGraphics (2004). *ADVance MS (ADMS) Reference Manual*, Mentor Graphics.
- Moser, E. & Mittwollen, N. (1998). Vhdl-ams: The missing link in system design - experiments with unified modelling in automotive engineering, *Proceedings of IEEE International Design and Test Conference (DATE'98)*, Paris, France.
- M.R. Casu, M. C. & Graziano, M. (2008). A vhdl-ams simulation environment for an uwb impulse radio transceiver, *IEEE TRANSACTIONS ON CIRCUITS AND SYSTEMS: REGULAR PAPERS*, Vol.55(No. 5): 1368 – 1381.
- R. Ahola, D. W. & Sida, M. (2003). Bluetooth transceiver design with vhdl-ams.
- Santarini, M. (2006). Design challenges steer automotive electronics, *EDN Magazine*.
- V. Nguyen, P. L. & Naviner, J.-F. (2005). Vhdl-ams behavioral modelling and simulation of high-pass delta-sigma modulator, *Proceedings of IEEE International Behavioral Modeling and Simulation Conference (BMAS'05)*, San José, California.
- W. Prodanov, M. V. & Buzas, R. (2009). A controller area network bus transceiver behavioral model for network design and simulation, *IEEE TRANSACTIONS ON INDUSTRIAL ELECTRONICS* Vol. 56(No. 9): 3762 – 3771.
- W. Yang, H. C. & Yan, J. (2005). A high level vhdl-ams model design methodology for analog rf lna and mixer, *Proceedings of Int. Beh. Modeling and Simul. Conf. (BMAS'04)*, San José, California.
- Wang, L. & Kazmierski, T. (2005a). Vhdl-ams based genetic optimization of a fuzzy

logic controller for automotive suspension system, *Proceedings of IEEE International Behavioral Modeling and Simulation Conference (BMAS'05)*, San José, California.

Wang, L. & Kazmierski, T. J. (2005b). Vhdl-ams modeling of an automotive vibration isolation seating system, *Proceedings of IASTED international conference on Signals and Systems (CSS 2005)*, Marina Del Rey, USA.

Potential and Drawbacks of Raman (Micro)Spectrometry for the Understanding of Iron and Steel Corrosion

Philippe Colomban

*LADIR, CNRS – Université Pierre-et-Marie-Curie
France*

1. Introduction

Raman scattering theory and first observation date back to the first decades of the 20th Century but the technique did not generalise until the 70s, with the development of lasers technology. Two major breakthroughs occurred in the 80s with the replacement of monochannel PM detectors by multichannel CCDs (Delhaye et al., 1996) and in the 90s with the rejection of Rayleigh elastic scattering by photonic crystals (Notch filter) or multilayer coatings (Edge filter) rather than monochromator(s). These latter technological changes improved the sensitivity by many orders of magnitude, which allowed either cutting the counting time (allowing mapping or real time monitoring) or reducing the illumination power (thus allowing for the analysis of black compounds). The latest developments concern the miniaturization of solid laser sources and the replacement of electronic boxes controlling the CCD detector by softwares uploaded on a common laptop, leading to portable Raman instruments. All these developments and the increase of the Raman instrument production lowered the price and made the technique more and more available, even for in-line/at-line/on-line control.

Among the many interactions of light with matter, Raman scattering is particularly well suited to the multiscale analysis of ill-organized heterogeneous solids as the corrosion films (Gouadec & Colomban, 2007a; *ibidem*, 2007b). The Raman probe being for interatomic bonds themselves, the technique offers a “bottom-up” approach to study nanomaterials and amorphous compounds which best works in the case of imperfect crystals with strong covalent bonds (Fig. 1) such as those typically produced by metal corrosion.

Raman signal results from the interaction of a monochromatic coherent light (laser beam) with electronic and vibrational levels of atomic bonds (Long, 1977; Lewis & Edwards, 2001; Gouadec & Colomban, 2007 for a more complete theoretical description). The interaction with the electronic levels is often described as virtual; this is true for non-coloured samples or non-absorbent for the excitation laser line, but wrong for absorbent materials, leading to (pre)resonance Raman features. Consequently, peak intensity will depend on the exciting wavelength and 2nd order Raman features could be present (harmonics, combinations). Theory predicts both elastic (so called Rayleigh scattering) and inelastic (namely Raman) contributions in the scattered electric field. The latter occurs only if vibrations change bond polarizability, which is a second rank tensor containing the crystal symmetry. Raman scattering is

complementary to infrared absorption with the advantage of much narrower peaks: the Raman peak shape is thus very informative because the Raman probe is very local. On the other hand, the IR spectroscopy probes, the instantaneous dipole moments which are subjects of much longer distance interactions. Consequently, IR bands are often very broad.

Raman spectroscopists in general refer the vibrational modes, the phonons, by i) their wavenumber $\bar{\nu} = \nu_{\text{vib}}/c$ (c the light speed, $\bar{\nu}$ in cm^{-1} unit, here after and usually noted ν) and expressed it in cm^{-1} , however energy (meV), wavelength (nm) are frequency (THz) units can also be used and ii) their symmetry (total symmetric modes are the strongest ones).

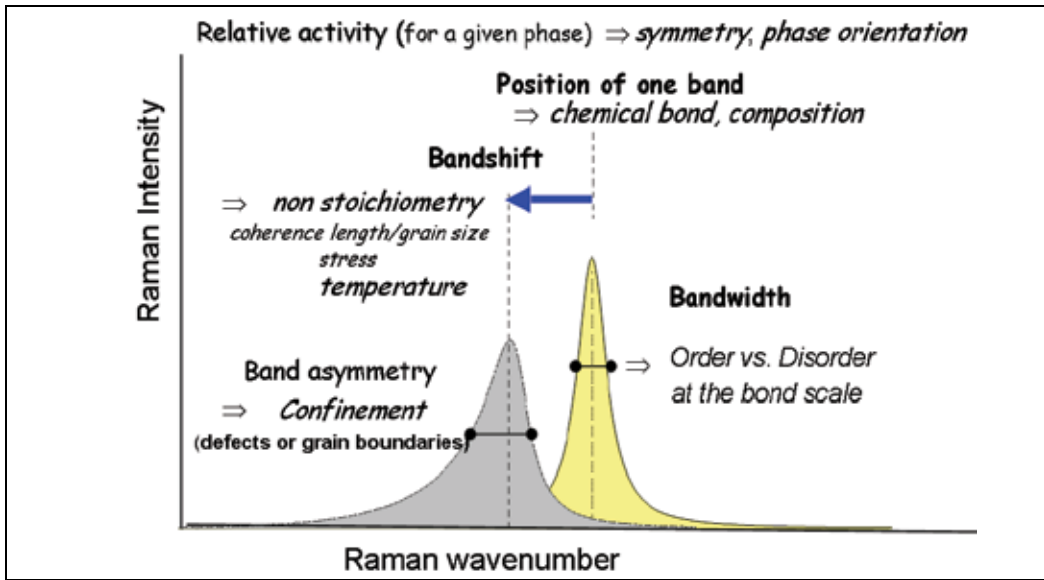


Fig. 1. The basics of the information to be extracted from a Raman spectrum (after Gouadec et al., 2010).

The polarization of a sample illuminated with light (electric field \vec{E}_0 ; frequency ν_l) has the following form:

$$\vec{P} = \bar{\alpha} \times \vec{E}_0 \cos(2\pi\nu_l t) \quad (1)$$

In Eq. (1), $\bar{\alpha}$ represents the polarizability tensor, which depends on matter vibrations (the oscillations of atoms and molecules around their equilibrium positions). The polarization can be expressed as a function of the atomic displacement (normal coordinates) using a Taylor approximation, thus predicting elastic scattering ($\nu = \nu_l$, the exciting laser wavenumber) and inelastic ($\nu = \nu_l \pm \nu_{\text{vib}}$) scattering by atomic vibrations. The former is called Rayleigh scattering and the latter, which occurs only if vibrations change polarizability ($\partial\alpha_{ij}/\partial Q \neq 0$), is Raman scattering. Other terms correspond to Hyper and higher orders Raman scattering (Long, 1977; Gouadec & Colombari, 2007a).

The signal intensity is predicted with the following formula:

$$I_{\text{Raman}} \propto I_{\text{laser}} \bar{\nu}_{\text{laser}}^4 \left| e_0 \bar{\alpha} e_s \right|^2 d\Omega \quad (2)$$

In Eq. (2), e_o and e_s are unit vectors indicating the laser polarization and direction of observation, respectively, whereas $d\Omega$ represents the solid angle of light collection, at a maximum when high magnification, high aperture number microscope objectives are used. Classical electromagnetic theory predicts Raman peaks should have a Lorentzian shape (Long, 1977; Lewis & Edwards, 2001; Gouadec & Colombar, 2007a). Isotropic disorder leads to a distribution of Lorentzian usually described by a Gaussian shape. Actually more complex shapes (e.g. asymmetric ones in the case of anisotropic disorder, Fig. 1) occur and complex laws should be used (Havel et al., 2004; Gouadec & Colombar, 2007a; Havel et al., 2007) to describe the Raman signature of some nanophased materials or when defects break the phonon propagation (Havel et al., 2007; Chi et al., 2011).

The scattering intensity varies by orders of magnitude depending on the bond polarisability (the more covalent the bonds, the higher the number of electrons involved and the higher the Raman peak intensity), the crystal symmetry and the exciting wavelength. As polarizability ($\bar{\alpha}$ second rank tensor) changes drastically from one bond to another, Raman intensity may not be used to measure the relative amounts of different phases without preliminary calibration. Consequently, minor phases or even traces could have a stronger Raman signature than some major phases. The preferential orientation of certain phases, common for surface grown phases enhances some peaks and calibration cannot be efficient. The absorption of the laser light by coloured phases can be very high and thus the penetration depth can be less than a few tenths of nm (Gouadec & Colombar, 2001; Havel & Colombar, 2006). Furthermore light absorption may involve strong local heating and thus phase transformation towards more stable ones, crystallization of amorphous ones or oxidation (de Faria et al., 1997; de Faria & Lopez, 2007; Cvejic et al., 2006). Raman analysis appears very sensitive to answer some questions on a given material whereas can be nether useless to study some others. Mapping (see further) and quantitative analysis should be then performed with caution.

Since Raman instruments were made available in the 70s, attempts to characterize the corrosion products of iron-based artefacts were performed. Most of studies concerned pure iron or low carbon content alloys but reference spectra are now available for large majority of the most common corrosion products: haematite, (Beattie & Gilson, 1970), magnetite (Morke et al., 1980), lepidocrocite (Thibeau et al. 1978). First series of corrosion studies flourish during the 80's (Farrow, 1980; Farrow & Nagelberg, 1980; Keiser et al., 1982; Hugot-Le Goff & Pallotta, 1985; Naouer et al. 1985; Ohtsuka et al., 1986; Boucherit et al. 1989, Dünwald & Otto, 1989). Then, high sensitivity instruments made it possible to study black and low crystallinity/amorphous films that were easily transformed into the stable ones by laser heating (Gouadec et al. 2001; Mazetti & Thistlethwaite, 2002; Cvejic et al., 2006; Gouadec & Colombar, 2007; Gouadec et al., 2010). More recently, mapping allowed getting a semi-quantitative global view (Neff et al., 2005; Neff et al., 2006; Monnier et al., 2010). A great effort was made to obtain reference phases and their signature, especially by controlled electrochemically synthesis (Savoy et al., 2001; Sinard et al., 2001; Joinet et al., 2002; Legrand et al. 2003, Refait et al. 2003, Poupard et al. 2006, Pineau et al. 2008; Dubois et al. 2008).

In this chapter we address the advantages of Raman spectroscopy and mapping, with particular attention to the intrinsic experimental and conceptual drawbacks of the methods as well as possible ways to overcome them.

2. Phases issued from metal corrosion and their Raman signature

2.1 Phase and structure relationship

The corrosion of metal results from the reaction with anions and the formation of new bonds at the surface. The simplest case is the oxidation (formation of Fe^{II/III}-O bonds) but hydroxylation (Fe^{II/III}-OH), carbonation (Fe-CO₃), phosphatation (Fe-PO₄), and sulfatation (Fe-SO₄), etc... can occur by uncontrolled or controlled reactions with the moieties present in the vicinity of the metal surface. Ionic diffusion is driven by chemical and electrochemical gradients, which depends on the material structure. The ionic (mostly protonic) (Colomban, 1992) and electronic conductivity as well as the presence of liquid electrolytes such as water are prominent parameters. We will discuss the Raman signature of iron-based compounds but all the phases (oxides, hydroxides, carbonates, sulphates, etc.) of any element used in the alloy must be considered because corrosion may promote their formation and trace phases may have a signature sufficiently strong to be detected.

The densest phase is wustite because of its high Fe/O ratio (Fe^{II}O, space group Fm3m, density: ~6, black). Two other dense phases are built with two available ways of oxygen atom packing: magnetite (Fe^{III/II}₃O₄, spinel structure with space group Fd-3m, cubic ABCABC packing, density 5.18, black) and haematite (Fe^{III}₂O₃, corundum structure with space group R-3c, hexagonal ABAB packing, density 5.23, dark red, Froment et al., 2008). When oxygen vacancies are formed - that decreases the density - the oxygen layer packing is preserved but some protonation may occur: i) maghemite (γ Fe₂O₃, space group P4₃32 preserves the cubic spinel structure but its density lowers to 4.87, brown), ii) goethite (α FeOOH, space group 2/m2/m2/m, density : 4.3 to 3.3, ochre to black) and lepidocrocite (γ FeOOH, Cmc, density : ~4, dark red) ; these phases retain the initial framework made of oxygen atom layers but the structure becomes more open due to oxygen defects. Furthermore, some oxygen atoms may be replaced by Cl ones (akaganite β FeOOH, density : 3.8 to 3.6, orange), especially at the phase surface. Other disordered phases are observed : ferroxhyte (δ Fe^{III}OOH, density : 4.2, yellow), ferrihydrites (Fe^{III}₅HO₈, 9H₂O, ABACA or mixed ABA ACA packing, density : 3.8, brown), hydroxylchlorides, β Fe^{II}₂(OH)₃Cl or the so-called "green rust" (Fe^{II}_(1-x)Fe^{III}_x (OH)₂ Cl_x (SO₄)_z, nH₂O, AABBC packing, a variant of the ABC cubic packing, green). White rust consists in the iron lamellar hydroxides (main phase: β Fe^{II}(OH)₂, P-3m1, ABAB compact packing, white). Carbonates (siderite, Fe^{III}CO₃, density ~3.9; Fe₂(CO₃)(OH)₂, and some other mixed frameworks) may also form. Sulfates (Fe^{II}SO₄) result from sulphuric acid treatment in the finishing of steel before coating or plating.

Galvanized steel sheets received ZnFe or more complex (ZnNiMn, etc...) coatings that enlarge the variety of phases to be formed (Bernard et al., 1993; Marchebois et al., 2002a; ibidem, 2002b; Tomandl et al., 2004; Yadav et al., 2004; Hernandez et al., 2006; Refait et al., 2007; Colomban et al., 2008; Dubois et al., 2008) : smithsonite ZnCO₃, Zn(OH)₂ and complex phases like hydrozincite Zn₅(OH)₆(CO₃)₂ ("white corrosion"), ZnCl₂(OH)₄ SO₄, 5 H₂O, phosphates like Zn₃(PO₄)₂, H₂O, ZnS ("black corrosion").

In the same way, water and/or high temperature resistant steels such as Ni and Cr-rich and the corresponding oxides/hydroxides are formed : α CrOOH, Cr₂O₃, NiO, spinels, ... (Beatie & Gilson, 1970; Bernard et al., 1993; Zuo et al., 1996; Delichère et al., 1997; Colomban et al., 1999; Maslar et al., 2001). Reference spectra of common phases can be also found in review books (see e.g. Karr Jr, 1975; Nakamoto, 1997) and the data on parent compounds are very useful for the identification of solid solutions and ill-crystallized compounds (Delichère et al., 1988; Desilvestro et al., 1988; Colomban et al., 1999). Table 1 lists the most frequent corrosion products and their characteristic Raman fingerprints.

Compound	Formula/structure	Characteristic Wavenumber ⁺	Remarks
Wustite	FeO	655	
Haematite	Fe ₂ O ₃ / Corundum	~1320, 290, 220	
Magnetite	Fe ₃ O ₄ / spinel	670	Easily transforms into haematite under laser beam
Maghemite	γFe ₂ O ₃ xH ₂ O / spinel	670-720, ~1400	idem
Ferrihydrite	Fe ₅ HO ₈ ,9H ₂ O	710, ~1380	
Goethite	α FeOOH	390	
Lepidocrocite	γ FeOOH	250, 1300	
Akaganeite	β FeOOH (Cl)	310, 390, 720	
Ferroxhyte	δ FeOH	680, ~1350	idem
Hydroxychloride	β Fe ₂ (OH) ₃ Cl	160, 423	
Green rust		430-510	
Iron chloride	FeCl ₂	610	
Zinc chloride	ZnCl ₂	80, 248	
Zinc oxide	ZnO	100, 540-580	
Zinc hydroxide	Zn(OH) ₂	470	
Zinc carbonates	ZnCO ₃	1095, 370	
White rust	3Zn(OH) ₂ 2ZnCO ₃	1050, 385	
"	4Zn(OH) ₂ ZnCl ₂ (OH) ₄ H ₂ O	910, 3455-3486	
"	Zn(OH) ₄ Cl ₂ SO ₄ 5H ₂ O	955, 208, 292	
"	ZnSO ₄ 3 Zn(OH) ₂ 3H ₂ O	961, 1007, 463	
Zinc phosphate	ZnPO ₄	996	
"	Zn ₃ (PO ₄) ₂ H ₂ O	1055, 1150	
Manganese oxide	MnO ₂	~600	
Nickel oxide	NiO	~510	
Chromium oxide	Cr ₂ O ₃	351, 551,609	
Chromium hydroxide	CrOOH (Cr ₂ O ₃ , nH ₂ O)	485	
Mackinawite	FeS	~280-300	
Greigite	Fe ₃ S ₄	~350-360	

Table 1. Raman fingerprint of main corrosion products.

2.2 Understanding Raman signature

If the analytic approach is useful (identification and quantification of the phases formed by corrosion), a more comprehensive understanding of the phase structures and relationship is necessary for a comprehension of the reaction scheme and the prospect of regulating them. The recording of the Raman signatures will depend on the phase colour - i.e. their electronic band structure - that determines the light penetration and the intensity of the scattered

signal as well as on the phase structure : the higher the symmetry, the lower number of Raman peaks (Lewis & Edwards, 2001; Gouadec & Colombar, 2007a).

Fig. 2 shows the Raman signature of the main phases encountered in the corrosion layers. Typical intensity ratios in comparable recording conditions are:

Lepidocrocite (1) > wustite, haematite, goethite, hydroxychloride, ferrihydrites, ferroxihite ($\sim 1/3$) > akaganeite ($\sim 1/4$) >> magnetite, maghemite ($\sim 1/10$).

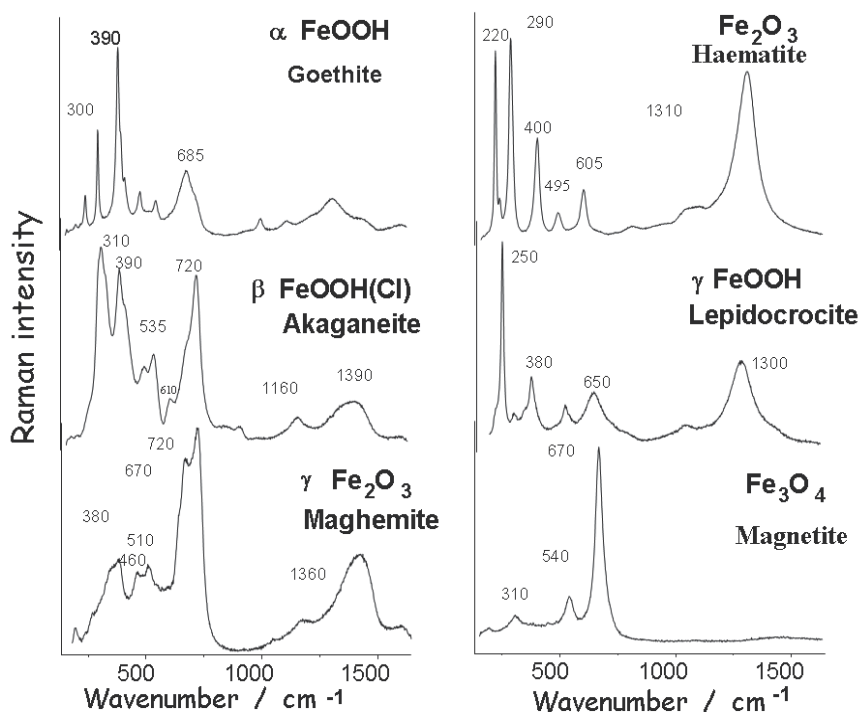


Fig. 2. Raman signature of the main (crystalline) iron oxi(hydroxy)des observed in corrosion films (after Colombar et al., 2008).

It is thus clear that the analysis of a mixture will strongly lower the contribution of the latter phases.

The Raman signature of any compound that structure is built with one or many strong covalent-bonded vibrational units, can be separated in four groups (Gouadec & Colombar, 2007a):

- (symmetric) stretching modes, for instance $\text{Fe}^{\text{II}}\text{-O}$ and/or $\text{Fe}^{\text{III}}\text{-O}$ modes peaking in the 400-700 cm^{-1} region for oxides, 300-600 cm^{-1} for chlorides, 200-400 cm^{-1} for sulphides. In symmetric modes, the strongest ones, only oxygen atoms move and thus the peak wavenumber mainly depends on the Fe-O distance (Vucinic-Vasic et al., 2006). These modes are very sensitive to oxygen vacancies that broaden the peaks.
- bending modes peak at lower energy, namely 400-500 cm^{-1} range for oxides or less for chlorides, sulphides,... They are very sensitive to the short range disorder in the first neighbouring shell (1-5 nm around the chemical bond) and their broadness can be very informative on the short-range (dis)order. Because the mean symmetry often brokes the symmetry of the vibrational units, many components are frequently observed.

- iii. librational (orientational oscillations, 150-400 cm^{-1} range) and lattice modes ($<200 \text{ cm}^{-1}$). Librational modes are very sensitive to the short range disorder of the vibrational entities (e.g. FeO_4 tetradron); lattice modes reflect the long range crystalline order, like X-ray diffraction, and strongly depend on atom mass (\sqrt{M}).
- iv. additional features (combination, harmonics,...) consisting bands between 1000 and 1500 cm^{-1} : their origin lies in the interaction between electronic (and magnetic, see e.g. (Morke et al., 1980)) levels and the light because the laser beam wavelength interacts with the electronic levels. The high intensity of these bands facilitates the phase identification. On the other hand the high light-matter coupling leads to a strong heating under the laser spot: temperatures close to 500°C can be easily achieved. The temperature does not depend on the laser power and objective magnification only but also on the heat dissipation (Gouadec et al., 2001): the dissipation is often better for small aggregates but matrix effects are important. Measurements at low temperature (liquid N_2) or in water should be preferred .

Taking into account the above rules it is obvious that the narrow low wavenumber peaks of lepidocrocite, hematite, goethite and some hydrochlorides are characteristic of crystalline phases. The strong intensity of their lattice modes is typical for layered materials. Replacing atoms by heavier ones (O/Cl for instance in hydrochlorides) shifts the lattice modes toward lower wavenumbers and broadens the different components. The relationships between haematite, lepidocrocite, goethite and akaganeite on one side (both phases having AB derived packing, Fig. 2), and on the other hand magnetite, maghemite, ferrihydrites (ABC packing) are obvious (Colomban et al., 2008). Partial substitution modifies the bandwidth (Cvejic et al., 2006).

Detection of "pure" hydroxides (white rust), carbonates and sulphates (black rust) is very easy because of the narrowness of their stretching mode (1020-1100 cm^{-1} range) and because reference spectra are well documented (Karr Jr, 1975; Nakamoto, 1997)). Furthermore, high power of illumination can be used for non-coloured phases. Actually, in most of the practical cases, corrosion films are made of complex intergrowths at the nanoscale, giving rise to mixed oxyhydroxycarbonates/sulfates/etc. with complex Raman signatures because of the solid solutions formation, intimate mixtures of ill-crystallised phase with a very small grain size. Synthesis and characterisation of reference compounds are complex (handling in CO_2 - and/or water-free media, redox control...). Fig. 4 shows spectra recorded on galvanized steel sheets corroded in real conditions. In most of the cases fluorescence, a phenomenon in competition with Raman scattering but more efficient, gives rise to a strong background for real samples (galvanised steel coupons have been cut from vehicles that have been in circulation for years in severe weather conditions). The fluorescence often due to microbiological activity can be eliminated by H_2O_2 or $\sim 500^\circ\text{C}$ thermal treatment (furnace heating or laser cleaning). On the other hand, spectra free of fluorescence background are easier recorded on coupons accelerated corroded at the laboratory. Indeed, reagents are simpler and cleaner. However, the most stringent point is that formed phases are often different. It is clear that many improvements on the procedure to conduct accelerated tests, more representative for real corrosion have to be made.

For specific applications special coatings like Cr(Al)N , NiCrAlY (Colomban et al., 1999) or polyaniline films (Delichère et al., 2007; Bernard et al., 2002; Nguyen et al., 2004) are used. This requires special database.

Note that Raman analysis is possible through a layer, inorganic (enamel, ceramic matrix (Wu et al, (1997); Gouadec et al.(1998)) or organic one (paint, e.g. Colomban et al., 2008). Typically, good Raman signatures are obtained up to 20 to 40 μm below the surface.

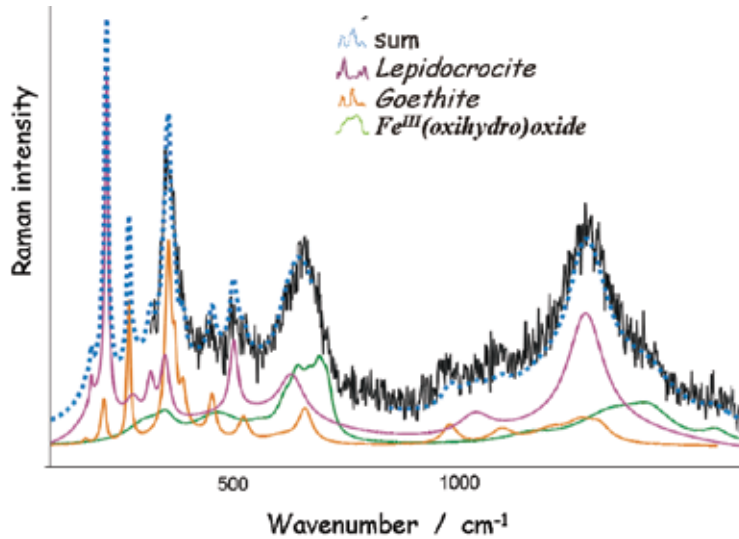


Fig. 3. Example of the decomposition of the Raman spectrum of a corroded film using the 3 signatures of pure reference phases. The appropriate program was then ran to adjust the data in all the mapped area with these combination spectra and to image the protective ability index in all the studied area (adapted from Gouadec et al., 2010). Note the very narrow 250 cm^{-1} peak characteristic of Lepidocrocite layer structure and the strong 2nd order features at $\sim 1350\text{-}1400\text{ cm}^{-1}$ of spinel derived ill crystallized phases.

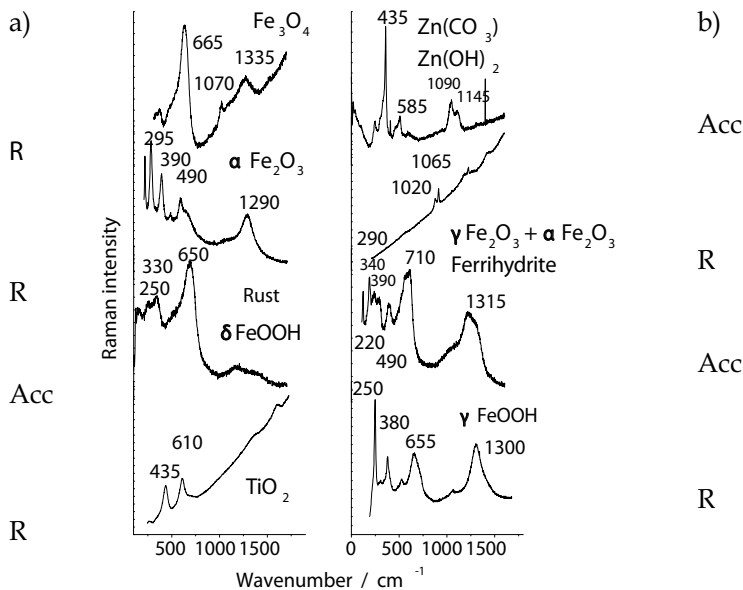


Fig. 4. Example of Raman signatures recorded in different spots of a corroded galvanized steel sheet with the sequences a) steel/Zn-based coating/phosphate coating/epoxy-TiO₂ paint and b) steel/ZnFe coating/ZnNiMn coating/ epoxy-TiO₂ paint; accelerated (Acc) or real (R) corrosion conditions (after Colomban et al., 2008).

2.3 Semiquantitative analysis and phase mapping

Raman mapping is most valuable to point out subtle composition and structure modifications taking place from one place of a sample to another. The images are obtained by extracting pertinent parameters from the hyperspectral map, which is a collection of individual Raman spectra, each being associated with a given point on the sample surface (Turrell, 1996; Colomban, 2003).

The great advantage of the automatic mapping procedure is the achievement of a more representative view of the present phases. However, the visual selection of the spot to be analysed is very subjective and leads to neglect places where the optical focus view through the microscope objective looks poor (low contrast, roughness,...).

Using the parameter(s) extracted from each spectrum (peak intensity, wavenumber shift but also grain size, defect concentration, etc.), it is possible to build a map of the investigated area the so-called *smart* image (Colomban, 2003). The following requirements are mandatory to record and exploit Raman mapping (Gouadec et al., 2010):

- i. the analysed area must be horizontal and the roughness smaller than the vertical height of the laser spot (typically, $\sim 10 \mu\text{m}$ for $\times 100$, $\sim 50 \mu\text{m}$ for $\times 50$ magnification objective,...)
- ii. the horizontal resolution, i.e. the laser spot diameter (less than $\sim 1 \mu\text{m}$ for $\times 200$, $\sim 5 \mu\text{m}$ for $\times 100$, $\sim 10 \mu\text{m}$ for $\times 50$ magnification objectives) combined to the stage step ($\sim 0.1 \mu\text{m}$ or more) must be compatible with the material/phase/grain size.
- iii. the analyzed area must be chosen in order to be representative of the different topological features but limiting the number of spectrum to be collected and processed to build smart images (Colomban, 2003; Havel et al., 2004; Havel & Colomban, 2006; Gouadec et al., 2010).

The image resolution will thus depend on the optical parts (objective and spectrometer), the laser beam quality (alignment, fundamental mode), the sample (parasite refractions at interfaces, roughness), Raman signature contrast, light absorption and penetration in the sample as well as the stage motion step, usually up to $0.1 \mu\text{m}$

The mapping has been used to understand the long term atmospheric and in soil corrosion taking advantage of the big thickness and large grain size of corrosion films (tenths of microns) present in heritage buildings (cathedrals, churches,...) and archaeological artefacts (Neff et al., 2005; ibidem, 2006; Monnier et al., 2010). Archaeological and Cultural Heritage artefacts are however considered as good analogues for the understanding and prediction of iron alloys corrosion behaviour in soil and in atmosphere, and hence to determinethe lifetime of over-containers used to protect the vitrified nuclear waste.

The Raman technique has also been used to compare the thinner ($\sim 1\text{-}3 \mu\text{m}$ thick) corrosion films obtained on automotive galvanized steels in accelerated corrosion tests, at the laboratory, and in real use (intense corrosion for used cars in severe mountain weathering conditions (temperature, water, salt (Colomban et al., 2008)). Raman analysis in the bottom of the pits formed by the corrosion is possible using long focus, large aperture high quality objectives.

3. New challenges

The current challenges are i) the development of data bases of complex mixed and nanosized phases, ii) the improvement of procedures/data treatment for two dimensional (2D) and three dimensional (3D) Raman mapping and iii) a better understanding of the 2nd order Raman signature of coloured phases in order to obtained smart imaging of pertinent

parameters, for instance to image the phase amount ratio that has been proposed to establish if the corrosion is passive or active (Kashima et al., 2000).

3.1 Mixed oxides and oxyhydroxycarbonates

Although the reference signatures of pure iron oxides are well established, those of the mixed compounds like spinels associating Fe, Mn, Cr, Ni... atoms or of oxyhydroxycarbonates, hydrated or not, are very poorly documented (Colomban et al., 1999; Colomban et al. 2008; Cvejic et al., 2006). These phases may be unstable under the laser spot and may transform into more stable ones having different structure. Furthermore, for many films it is not established if the matter consists in a mixture, a phase or nanoparticles with another phase covering the grain surface. In many cases, because of the sample colour and its absorption of the laser light by electronic level, the interaction with electronic levels is anymore virtual and Raman (pre)resonance phenomenon is observed: the Raman intensity concentrates in some modes, a (small) wavenumber shift is observed and harmonic/combination second order peaks become visible. Note that in situ measurements under controlled electrochemical condition allow to record nice vibrational signature. However the representativity of these signatures is not straightforward because the real conditions are more complex what can promote the formation of other minor phases with stronger Raman cross section.

3.2 Controlling the analysed area

Most of the phases formed on the metal surface are coloured and hence absorb the light. Consequently the penetration depth of the light depends on the absorption coefficient. For dark phase the depth can be very limited and the information obtained from a mapping is perturbed: the analysed thickness will vary from spot to spot and correction is not possible. From a practical point of view, microscope objectives are usually characterized by the numerical aperture NA:

$$NA = n \sin(\theta_{\text{back}}) \quad (3)$$

In Eq (3), θ_{back} is the maximum collection angle for the backscattered light and n is the refractive index in the medium between the sample and the microscope lens (Fig. 5). The numerical aperture is a key parameter because it sets the resolution R of the microscope, defined as the shortest spacing for two points on a sample surface to be resolved with λ wavelength observation (see references in Gouadec & Colomban, 2007a; Gouadec et al., 2010):

$$R = 0.6 \lambda / NA \quad (4)$$

Since the optics of ultraviolet light devices are expensive and not very efficient, the lasers offering violet (~450 to ~400nm) or deep violet (~365 nm) excitations are preferred to obtain the best resolution. Actual laser beams are not perfectly parallel (this has been exaggerated in Fig. 5) and their focusing through a microscope lens gives an elongated volume called the focal domain or focal cylinder. The diameter $\phi(z)$ of the focal domain at z axial coordinate must be defined arbitrarily as the electric field obviously does not drop to zero for a definite r distance away from the optical axis. The radial decrease of the electric field in a laser beam actually obeys a Gaussian law. Similarly to the lateral resolution, the in depth Δz or axial ($\sim \phi(z)$) resolution of Raman spectroscopy can not be defined unambiguously. Indeed, the laser intensity does not drop to zero for a given z value and one has to choose an arbitrary

threshold (the Raman efficiency shows order of magnitude variation that makes the choice very difficult !). Δz also depends on the generally unknown refractive index of the studied compound.

In confocal Raman microscopy set up, pinholes are placed in the microscope at intermediate image planes, resulting in a better in-depth discrimination power but a great increase of the counting times, 10 times and even more ! In that case, the integrated intensity coming from a given plane perpendicular to the optical axis is no longer a constant but, rather, decreases by 50% between the focal plane ($z=0$) and $\Delta z_{\text{confocal}}$ (the half width of the so-called point spread function). The use of confocal pinholes goes with a lateral resolution improvement of about one third but confocal microscopy interest mainly consists in the possibility to select sample layers axially. However, even with the best dry ($n=n_{\text{air}}=1$, $NA=0.95$) or oil immersion ($n=1.51$, $NA=1.4$) objectives, and in the most favourable case of a violet excitation (e.g. $\lambda \sim 407$ nm), ϕ_{spot} will remain above 275 nm (Eq. (4)). The use of high quality (expensive) objectives is often more efficient than the confocal setting. Note bias polishing enlarges the topological resolution and micronic films can be easily analysed by the Raman technique (Gouadec et al., 2001).

Consequently the spatial repartition and relative proportion deduced from a Raman mapping may be interpreted with caution. The information can be however very useful to characterise the evolution of the corrosion film as a function of time, temperature, external parameters, etc.

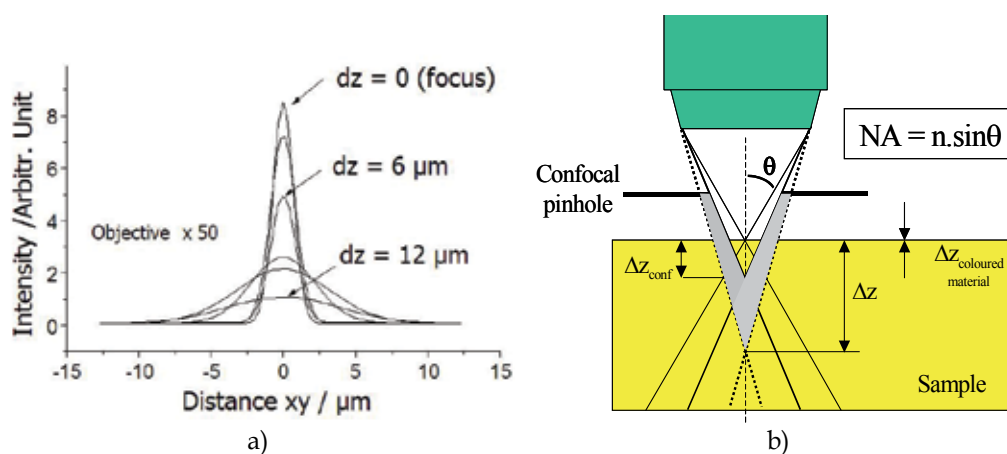


Fig. 5. a) Intensity distribution of the illuminating laser spot as a function of the de-focus (after Colombar, 2003) ; b) schematic comparison of the focus in a non-absorbing medium with and without the use of a confocal pinhole in the optical system. Note the very limited penetration for coloured material (after Gouadec & Colombar, 2007a).

3.3 Understanding at the nanostructure scale

The decrease of the grain size (D , see Fig. 6) makes that atoms at the particle surface or atoms having their chemical bonding perturbed by the vicinity of the surface (t : distance where the surface perturbs the structure and chemical bonds) become more important than the bulk atoms when the particle size drops below 30 to 5nm as a function of elements and chemical bonding. Vacancy concentration is maximal close to the surface and adsorbed species can be present: hydroxylation, water, etc.

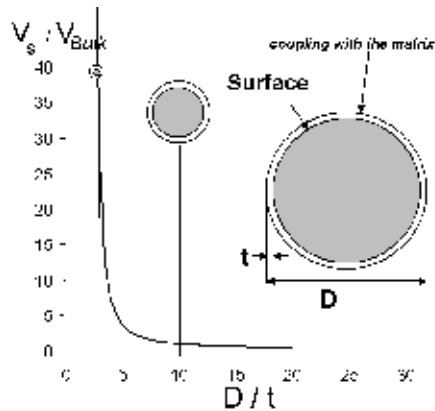


Fig. 6. Schematic of the relative contribution of skin/bulk matter for a particle as a function of its size: for a nanosized grain less than 1-10 nm in diameter the contribution of the surface atoms is very dominant (after Colombari, 2003).

The disorder modifies the Raman signature: symmetry exclusion can disappear leading to the activity of new components. The most prominent effect is the modification of the Raman peaks shapes. A reliable analysis of the Raman spectra requires the use of appropriate modelling to describe the band shape of the different spectral components (Gouadec & Colombari, 2007a, Chi et al. 2010).

The use of simple Gaussian and Lorentzian band profiles is often preferred than the Voigt profile; many fitting modules misleadingly name Voigt profile the simple sum of one Lorentzian and one Gaussian, as both depend on three parameters rather than four. The exact position, intensity, width and lineshape of each band depend on many different parameters such as the actual chemistry (neighbouring inclusions, substitutions or vacancies), crystallinity, domain size, phase orientation and corresponding polarization effects or thermomechanical stress (anharmonic effects). In grains much larger than the wavelength, phonons propagate almost in the same way as in perfect "infinite" crystals. When the grain size falls below a few tens of nanometers, the Phonon Confinement Model (PCM) accounts for the phonons coherence length limitation by a weighed exploration of longitudinal optical dispersion curves (see Gouadec & Colombari, 2007a and 2007b and references herein). Below a certain size, the very notion of collective vibrations disappears and the Elastic Sphere Model (ESM) takes over, using first principle description of low wavenumber vibrations in a "free-standing", homogeneous (constant density) and elastic sphere (Fig. 7). In this scheme, the wavenumbers of the two most intense modes are inversely proportional to the grain size (Fig. 6).

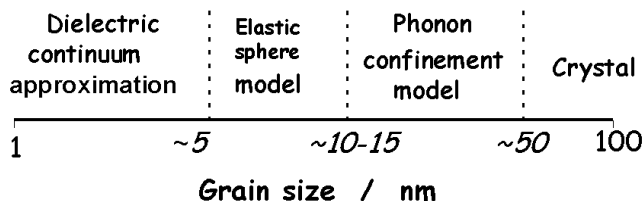


Fig. 7. Modelling spherical nanocrystals vibrations as a function of the grain size (after Gouadec & Colombari, 2007)

3.4. Understanding the corrosion mechanisms and anticipating the evolution

Although the phenomenological description of corrosion has received attention since long time from the electrochemical and thermodynamical points of view, the understanding of the mechanisms from the solid state chemistry point of view remains very limited. For instance, many phases contain protons in different forms and data on proton conductivity are very scarce (Colomban, 1992). Vibrational spectroscopy can be very useful to document the structural changes associated to ion diffusion.

The action of micro-organisms was poorly documented from the spectroscopic point of view. Microbiologically influenced corrosion is used since millennia to improve the plasticity of kaolin and clays by chemical modifications of silicates. This results from both, the direct action of microorganisms and the indirect one via the species generated by their metabolic activity. For iron-based materials, the phenomenon is induced in anoxic environments by sulphate-reducing bacteria (SRB), microorganisms that produced sulphide species. Thus, in media where sulphides are not naturally present, the observation of Fe^{II} sulphides (all sulphides have their stronger peak at ~250-350 cm⁻¹) inside the rust layer may be a clear indication that SRB were active and play a role in the corrosion process. The heterogeneity of the biofilm that covers the metal surface can lead to a galvanic interaction between regions of microbial activity and the surface. This leads to locally accelerated corrosion pits (Videla & Characklis, 1992; Marchal, 1999; Beech & Sunner, 2004; Little & Lee, 2007). When metal is associated with organic materials (some paints, films used for "conservation" treatments of archaeological artefacts, ...), consequence of microbiologically induced corrosion can be severe when contact with air: cracks occur due to the volume increase associated to iron oxidation and simultaneously sulphuric acid is produced. Raman study confirms that FeS (mackinawite) is very reactive towards oxygen (Remazeilles et al., 2010).

4. Conclusion

During decades Raman spectroscopy remains a useful technique for solid state physics and chemistry, giving valuable information about the structure and the reactivity of colourless single crystals. Then, clean polycrystalline, ill-crystallized samples can be analyzed. The high sensitivity of the modern instruments makes it possible to study any kind of samples if a palette of exciting laser wavelength is available to avoid detrimental pollution of the Raman information by strong fluorescence phenomenon. Very recently the potential of algorithmic methods to extract pertinent information from the spectra dominated by the fluorescence has been demonstrated (Widjaja et al., 2010) and the application of the Band-Target Entropy Minimization (BTEM) or similar techniques to the "poor" Raman signature of certain corrosion films appears very interesting.

5. References

- Beattie, I.R. & Gilson, T.R. (1970). The single-crystal Raman spectra of nearly opaque materials; Iron (III) oxide and chromium (III) oxide, *J. Chemical Soc. A*, 980-986.
- Beech, I.B. & Sunner, J. (2004). Biocorrosion: towards understanding interactions between biofilms and metals, *Current Opinion Biotechnology*, 15, [3], 181-186.

- Belo, M.D.; Walls, M.; Hakiki, N.E.; Corset, J.; Picquenard, E.; Sagon, G. & Noel, D. (1998). Composition, structure and properties of the oxide films formed on the stainless steel 316L in a primary type PWR environment, *Corrosion Science*, 40, [2-3], 447-463.
- Bernard, M.C.; Abourazzouk, D. & Hugot-le-Goff, A. (1993a). The corrosion of Ni-Cr dental alloys studied by in-situ Raman spectroscopy – Role of Beryllium, *Corrosion Science*, 35, [1-4], 809-815.
- Bernard, M.C., Hugot-Le Goff, A., Thierry, D.; Massinon, D. & Philipps N. (1993b). Underpaint corrosion of Zinc-coated steel sheet studied by in-situ Raman spectroscopy, *Corrosion Science*, 35, [5-8], 1339-1345.
- Bernard, M.C.; Duval, S.; Joiret, S.; Keddou, M.; Ropital, F. & Takenouti, H. (2002). Analysis of corrosion products beneath an epoxy-amine varnish film, *Progress Org. Coat.*, 45, [4], 399-404.
- Boucherit, N.; Hugot-Le-Goff, A. & Joiret, S. (1991). Raman studies of corrosion films grown on Fe and Fe-Mo in pitting conditions, *Corrosion Sci.*, 32, [5-6], 497-507.
- Boucherit, N., Hugot-Le-Goff A. & Joiret S. (1992). Influence of Ni, Mo and Cr on pitting corrosion of steels studied by Raman scattering, *Corrosion*, 48, [7], 569-579.
- Bourdoiseau, J.-A.; Jeannin, M.; Remazeilles, C.; Sabot, R. & Refait, Ph. (2010). The transformation of mackinawite into greigite studied by Raman spectroscopy, *J. Raman spectroscopy* DOI: 10.1002/jrs.2729.
- Chi, T.T.K.; Gouadec, G.; Colomban, Ph.; Wang, G.; Mazerolles, L.; Thanh, D.X. & Liem, N.Q. (2010). Off Resonance Raman Spectroscopy of Stacking Disorder and Phase Transitions in Wurtzite Crystals Grown to Nanometric Dimensions: the Example of CdS, *J. Raman Spectroscopy* in press DOI:10.1002/jrs.2793.
- Colomban Ph (1992), New Edition (2009) Proton Conductors, Cambridge University Press, Cambridge.
- Colomban Ph (2003) Raman Analyses and "Smart Imaging" of Nanophases and Nanosized Materials, *Spectroscopy Europe* 15, 8-16.
- Colomban, Ph.; Jullian, S.; Parlier, M. & Monge-Cadet, P. (1999). Identification of the high-temperature impact/friction of aeroengine blades and cases by micro-Raman spectroscopy, *Aerospace Science and Technology*, 3, [7], 447-459.
- Colomban, Ph.; Cherifi, S. & Dexpert, G. (2008). Raman identification of corrosion products on automotive galvanized steel sheets, *J. Raman Spectroscopy*, 39, [7], 881-886.
- Cook, D.C. (2005). Spectroscopic identification of protective and non-protective corrosion coatings on steel structures in marine environments, *Corrosion Science*, 47, [10], 2550-2570.
- Cvejić Z.; Rakic S.; Kremenovic A.; Antic B.; Jovalekic C. & Colomban Ph. (2006). Nanosize ferrites obtained by ball milling. Crystal structure, cation distribution, size-strain analysis and Raman investigations, *Solid State Science*, 8, [8], 908-915.
- Delhaye, M.; Barbillat, J.; Aubard, J. et al. (1996) Chap 3: Instrumentation. in: Turrell G and Corset J (eds) Raman Microscopy. Developments and Applications. Academic Press, London.
- Delichère, P.; Hugot-le-Goff, A.; Pallotta, C.; Thierry, D. & Yu N. (1987). Raman spectroscopy for the study of passive and transpassive film on Ni/Mo and Fe/Cr alloys, *Proc. Eurocorr'87*, Karlsruhe, Germany, 6-10 April 1987.

- Delichère, P.; Hugot-le-Goff, A. & Joiret, S. (1988). Study of thin corrosion films by in situ Raman spectroscopy combined with direct observation of nuclear reactions, *Surface and Interface Analysis*, 12, [1-12], 419-423.
- Delichère, P.; Joiret, S. & Hugot-le-Goff, A. (1988). Electrochromism in nickel oxide film, *SPIE Vol 1016 Optical Material Technology for Energy Efficiency and Solar Energy Conversion VII*, 165-169.
- Desilvestro, J.; Corrigan, D.A. & Weaver, M.J. (1988). Characterization of redox state of Nickel hydroxide film electrodes by in situ Surface Raman spectroscopy, *J. Electrochemical Society*, 135, [4], 885-892.
- Dubois, F.; Mendibide, C. & Pagnier, T. (2008). Raman mapping of corrosion products formed onto spring steels during salt spray experiments. A correlation between the scale composition and the corrosion resistance, *Corrosion Science*, 50, [12], 3401-3409.
- Dünnwald, J. & Otto, A. (1989). An investigation of phase transitions in rust layers using Raman Spectroscopy, *Corrosion Science*, 29, [9], 1167-1176.
- Farrow, R.L. & Nagelberg A.S. (1980). Raman spectroscopy of surface oxides at high temperature, *Applied Physics Letters*, 36, [12], 945-947.
- Farrow, R.L.; Benner R.E.; Nagelberg A.S. & Mattern P.L. (1980). Characterization of surface oxides by Raman spectroscopy, *Thin Solid Films*; 73, [2], 353-358.
- de Faria, D.L.A.; Venâncio Silva, S. & de Oliveira, M.T. (1997). Raman microspectroscopy of some iron oxides and oxyhydroxides, *J. Raman Spectroscopy* 28, [11], 873-878.
- de Faria, D.L.A. & Lopes F.N. (2007). Heated goethite and natural hematite: Can Raman - spectroscopy be used to differentiate them?, *Vibrational Spectroscopy* 45, [2], 117-121.
- Froment, F. ; Tournié, A. & Colomban Ph. (2008). Raman identification of natural red to yellow pigments: ochre and iron-containing ores, *J. Raman Spectroscopy* 39, [5], 560-568.
- Gouadec, G.; Karlin, S. & Colomban, Ph. (1998). Raman extensometry study of NLM202 and Hi-Nicalon[®] SiC fibres, *Composites, Part B* 29, [3], 251-261
- Gouadec, G.; Ph. Colomban, Ph. & Bansal, N.P. (2001). Raman Study of Hi-Nicalon Fiber Reinforced Celsian Composites. Part I : Distribution and Nanostructure of Different Phases, *J. Amer. Ceram. Soc.* 84, [5], 1129-1135. Part II: Residual Stress In The Fibers, *J. American Ceramic Society* 84, [5], 1136-42.
- Gouadec, G. & Colomban, Ph. (2007a). Raman study of Nanomaterials : How spectra relate to disorder, particle size and mechanical properties, *Progr. Cryst. Growth & Charact. Mater.*, 53, [1], 1-56.
- Gouadec, G & Colomban Ph (2007b) Raman Spectroscopy of Nanostructures and Nanosized Materials. *J. Raman Spectrosc.* 38, [6], 598-603.
- Gouadec, G.; Bellot-Gurlet, L.; Baron, D. & Colomban, Ph. (2010). *Raman mapping for the investigation of nanophased materials*, ch. 4, *Raman Imaging* , A. Zoubir Ed., Springer
- Havel M, Baron D and Colomban Ph (2004) Smart Raman/Rayleigh Imaging of Nanosized SiC Materials Using the Spatial Correlation Model. *J. Material Science* 39, [20], 6183-6190.
- Havel, M. & Colomban, Ph. (2006). Smart Raman and Rayleigh Spectroscopy for the Analysis of Nanomaterials, *Microscopy and Analysis*, 20, [3], 11-14.
- Havel, M., Baron, D., Mazerolles L. & Colomban Ph. (2007). Phonon confinement in SiC nanocrystal. Comparison of the size determination using TEM and Raman spectroscopy, *Applied Spectroscopy* 61 [8] 855-859.

- Hernandez, M., Genesca, J., Uruchurtu, J., Galliano, F. & Landolt, D. (2006). Effect of an inhibitive pigment zinc-aluminum-phosphate (ZAP) on the corrosion mechanisms of steel in waterborne coatings, *Progr. Organic Coatings*, 56, [2-3], 199-206.
- Hugot-le-Goff, A. & Pallotta C. (1985). In situ Raman spectroscopy for the study of iron passivity in relation to solution composition, *J. Electrochemical Soc.*, 132, [11], 2805-2806.
- Joiret, S.; Keddad, M.; Novoa, X.R.; Perez, M.C.; Rangel, C. & Takenouti, H. (2002). Use of EIS, ring-disk electrode, EQCM and Raman spectroscopy to study the film of oxides formed on iron in 1 M NaOH, *Cement & Concrete Composites*, 24, [1], 7-15.
- Karr C. Jr, Ed. *Infrared and Raman Spectroscopy of Lunar and Terrestrial Minerals*, (Academic Press, New York, 1975).
- Kashima, K.; Hara, S.; Kishikawa, H. & Miyuki, H. (2000). Evaluation of protective ability of rust layers on weathering steels by potential measurements, *Corrosion Engineering*, 49, 25-37.
- Hara, S.; Kashima, K.; Kishikawa, H. & Miyuki, H. (2001). Evaluation on the protective ability by the potential of steel with rust layer related to the composition of the rust formed on the weathered steel bridge using ternary diagrams, *Tetsu to Hagane - J. Iron & Steel Institute of Japan*, 87, [1], 43-48.
- Keiser, J.T.; Brown C.W. & Heidersbach R.H. (1982). Use of Raman spectroscopy in iron corrosion studies, *American Laboratory*, 14, [4], 17-18.
- Kihira, H.; Misawa, T.; Kusunoki, T.; Tanabe, K. & Saito, T. (1999). How to use the composition ratio index obtained by internal standard quantitative x-ray diffraction to evaluate the state of rust on weathering steel, *Corrosion Engineering*, 48, 979-987.
- Lewis, I.R. & Edwards, H.G.M. (2001). *Handbook of Raman Spectroscopy, From the Research Laboratory to the Process Line*, Practical Spectroscopy Series, Marcel Dekker Inc., New-York.
- Little, B.J. & Lee, J.S. (2007). *Microbiologically influenced corrosion*, John Wiley & Sons Inc., Hoboken.
- Long, D.A., (1977). *Raman Spectroscopy*. McGraw-Hill, New York.
- Lopez, D.A.; Schreiner, W.H.; de Sanchez, S.R. & Simison, S.N. (2003). The influence of carbon steel microstructure on corrosion layers - An XPS and SEM characterization, *Appl. Surface Science*, 207, [1-4], 69-85.
- Marchebois, H.; Joiret, S.; Savall, C.; Bernard, J. & Touzain, S. (2002a). Characterization of zinc-rich powder coatings by EIS and Raman spectroscopy, *Surface & Coatings Technology*, 157, [2-3], 151-161.
- Marchebois, H., Touzain, S., Joiret, S., Bernard, J. & Savall, C. (2002b). Zinc-rich powder coatings in sea water: influence of conductive pigments, *Progr. Organic Coatings*, 45, [4], 415-421.
- Maslar, J. E.; Hurst, W.S.; Bowers Jr., W.J.; Hendricks, J.H.; Aquino, M.I. & Levin I. (2001). In situ Raman spectroscopic investigation of chromium surfaces under hydrothermal conditions, *Applied Surface Science* 180, [1-2], 102-118.
- Maslar, J. E.; Hurst, W.S.; Bowers Jr., W.J. & Hendricks, J.H. (2002). In situ Raman spectroscopic investigation of stainless steel hydrothermal corrosion, *Corrosion* 58, [9], 739-747.
- Mazzetti, L. & Thistlethwaite, P.J. (2002). Raman spectra and thermal transformations of ferrihydrite and schwertmannite, *J. Raman Spectroscopy*, 33, [2], 104-111.

- Monnier, J.; Bellot-Gurlet, L.; Baron, D.; Neff, D.; Guillot, I. & Dillmann P. (2010). *A methodology for Raman structural quantification imaging and its application to iron indoor atmospheric corrosion products*, *J. Raman Spectroscopy* to be published.
- Morke, I.; Stasch A. & P Wachter (1980). Magnons in Raman scattering of magnetite, *Helvetica Physica Acta* 53, [4], 582-582.
- Nakamoto, K., *Infrared & Raman Spectra of Inorganic and Coordination Compounds: Theory and Application in Inorganic Chemistry*, J. Wiley & Sons, 1997.
- Neff, D.; Bellot-Gurlet, L.; Dillmann, P.; Reguer, S. & Legrand, L. (2006). Raman imaging of ancient rust scales on archaeological iron artefacts for long-term atmospheric corrosion mechanisms study, *J. Raman spectroscopy*, 37, [10], 1228-1237.
- Neff, D.; Dillmann, P.; Bellot-Gurlet, L. & Beranger, G. (2005). Corrosion of iron archaeological artefacts in soil: characterisation of the corrosion system, *Corrosion Science*, 47, [2], 515-535.
- Nguyen, T.D., Nguyen, T.A., Pham, M.C., Piro, B., Normand, B. & Takenouti, H. (2004). Mechanism for protection of iron corrosion by an intrinsically electronic conducting polymer, *J. Electroanalytical Chemistry*, 572, [2], 225-234.
- Ohtsuka, T.; Kubo, K. & Sato N. (1986). Raman spectroscopy in thin corrosion films on iron at 100 to 150°C in air, *Corrosion-NACE (National Association of Corrosion Engineers)*, 42, [8], 476-481.
- Pineau, S.; Sabot, R.; Quillet, L.; Jeannin, M.; Caplat, C.; Dupont-Moral, I. & Refait, P. (2008) : Formation of the Fe(II-III) hydroxysulphate green rust during marine corrosion of steel associated to molecular detection of dissimilatory sulphite-reductase, *Corrosion Science*, 50, [4], 1099-1111.
- Poupard, O.; L'Hostis, V.; Catinaud, S. & Petre-Lazard I. (2006). Corrosion damage diagnosis of a reinforced concrete beam after 40 years natural exposure in marine environment, *Cement and Concrete Research*, 36, [3], 504-520.
- Refait, Ph.; Memet, J.B.; Bon, C.; Sabot, R. & Génin J.-M.R. (2003). Formation of the Fe(II)-Fe(III) hydroxysulphate green rust during marine corrosion of steel, *Corrosion Science*, 45, [4], 833-845.
- Refait, Ph.; Reffass, M.; Landoulsi, J.; Sabot, R. & Jeannin, J. (2007). Role of phosphate species during the formation and transformation of the Fe(II-III) hydroxycarbonate green rust, *Colloids and Surfaces A: Physicochem. & Eng. Aspects*, 299, [1-3], 29-37.
- Remazeilles, C.; Saheb, M.; Neff, D.; Guilminot, E.; Tran, K.; Bourdoiseau, J.-A.; Sabot, R.; Jeannin, M.; Matthiesen, H.; Dillman, Ph. & Refait, Ph. (2010). Microbiologically influenced corrosion of archaeological artefacts : characterization of iron (II) sulfides by Raman spectroscopy, *J. Raman Spectroscopy*, DOI: 10.1002/jrs.2717.
- Saheb, M.; Neff, D.; Dillmann, P.; Matthiesen, H. & Foy, E. (2009). Long-term corrosion behaviour of low-carbon steel in anoxic environments - Characterisation of archaeological artefacts, *J. Nuclear Materials*, 379, [1-3], 118-123.
- Savoie, S.; Legrand, L.; Sagon, G.; Lecomte, S.; Chausse, A.; Messina, R. & Toulhoat, P. (2001). Experimental investigations on iron corrosion products formed in bicarbonate/carbonate-containing solutions at 90°C, *Corrosion Science*, 43, [11], 2049-2064.
- Simard, S.; Odziemkowski, M.; Irish, D.E.; Brossard, L. & Ménard, H (2001). In situ micro-Raman spectroscopy to investigate pitting corrosion product of 1024 mild steel in

- phosphate and bicarbonate solutions containing chloride and sulphate ions? *J. Appl. Electrochemistry*, 31, [8], 913-920.
- Thibeau, R.J.; Brown, C.W. & Heidersbach, R.H. (1978). Raman spectra of possible corrosion products of iron, *Appl. Spectroscopy* 32, [6], 532-535.
- Tomandl, A.; Wolpers, M. & Ogle, K. (2004). The alkaline stability of phosphate coatings II: in situ Raman spectroscopy, *Corrosion Science*, 46, [4], 997-1011.
- Turrell, G. (1996). Chap 4: Raman Imaging. in: Turrell G and Corset J (eds) Raman Microscopy. Developments and Applications. Academic Press, London.
- Yadav, A.P.; Nishikata, A. & Tsuru, T. (2004). Degradation mechanism of galvanized steel in wet-dry cyclic environment containing chloride ions, *Corrosion Science*, 46, [2], 361-376.
- Videla, H.A. & Characklis, W.G. (1992). Biofouling and microbially influenced corrosion, *Int. Biodeterioration Biodegradation*, 29, [3-4], 195-212.
- Vucinic-Vasic, M.; Antic, B.; Kremenovic, A.; Nikolic A.; Stoiljkovic, M.; Bibic N.; Spasojevic, V. & Colombari Ph. (2006). Zn,Ni ferrite/NiO nanocomposite powder obtained from acetylacetonato complexes, *Nanotechnology* 17, [19], 4877-4884.
- Widjaja, E.; Lim, C.H.; Lim, Q.; Mashadi, A.B. & Garland M. (2010). Pure component Raman spectral reconstruction for glazed and unglazed Yuan, Ming and Qing shards: a combined Raman microscopy and BTEM study, *J. Raman Spectrosc.* DOI: 10.1002/jrs.2721.
- Wu, J. & Colombari Ph. (1997). Raman spectroscopy study on the stress distribution in the continuous fibre reinforced ceramic matrix composites. *J. Raman Spectrosc.* 28 523-529.
- Yamashita, M.; Miyuki H.; Matsuda Y.; Nagano H. & Misawa T. (1994). The long-term growth of the protective rust layer formed on weathering steel by atmospheric corrosion during a quarter of century, *Corrosion Science* 36, [2], 283-299.
- Zuo, J.; Xu, C.; Hou, B.; Wang, C.; Xie, Y. & Quian Y. (1996). Raman spectra of Nanophase Cr₂O₃, *J. Raman Spectroscopy*, 27, 921-923.

Computational Techniques for Automotive Antenna Simulations

Faik Bogdanov^{1,2}, Roman Jobava^{1,3}, David Karkashadze^{1,3},
Paata Tsereteli¹, Anna Gheonjian¹, Ekaterina Yavolovskaya¹,
Detlef Schleicher⁴, Christoph Ullrich⁵ and Hicham Tazi^{5,6}

¹*EM Consulting and Software, EMCoS Ltd., Tbilisi*

²*Georgian Technical University, Tbilisi*

³*Iv. Javakhisvili Tbilisi State University, Tbilisi*

⁴*VW AG, Wolfsburg*

⁵*AUDI AG, Ingolstadt*

⁶*Technische Universität München*

^{1,2,3}*Georgia*

^{4,5,6}*Germany*

1. Introduction

Automotive antenna design is a sophisticated process, related to both specific features of antennas itself, and their installation and operation in the complex electromagnetic (EM) environment of an automobile. Modern automobiles include a number of antenna solutions (AM/FM radio, remote control systems, satellite services, etc.), operating simultaneously in the presence of car body, harness and electronic equipment. Design of them becomes even more complicated, when conformal and hidden antenna solutions are applied. These solutions encompass integrated glass antennas or active antennas, in combination with amplifiers, radio/TV receivers and other network devices. Moreover, parametric tuning is required at all stages of development, making the complete chain of antenna design rather laborious and complex. These problems can be overcome using computer simulations with numerical analysis. However, accurate modelling of complicated models requires a combined usage of both traditional and special methods and techniques, including adaptive and hybrid ones, and special means for a fast and optimized numerical solution.

Though different computational methods are used, the Method of Moments (MoM) (Harrington, 1968) is the most popular method in automotive antenna design. This chapter describes the recent enhancements (Bogdanov & Jobava, 2003; Bogdanov et al. 2004a, Bogdanov et al., 2004b; Jobava et al., 2005; Bogdanov et al., 2009; Bogdanov et al., 2010a; Bogdanov et al., 2010b) of the traditional MoM, offering a set of up-to-date methods and techniques, whose application provides an accurate and effective solution of EM problems related to modern automotive antenna simulations. After description of methods or techniques, application examples are presented. These examples include comparisons to other methods and experimental data. All the calculations are performed using the MoM-based code "TriD" (Bogdanov et al., 2010c) being a core of the program packages "EMC Studio" (EMCoS, 2010a) and "EMCoS Antenna VirtualLab" (EMCoS, 2010b).

2. Traditional MoM

First, consider the traditional MoM applied to the boundary-value problem on geometry G (Harrington, 1993):

$$L(\vec{J}) = \vec{g} \quad (1)$$

where L is an integrodifferential operator, \vec{g} is an excitation, and \vec{J} is unknown current density on a given geometry G . Further, we discretize G to consider the following expansion for the unknown current:

$$\vec{J}(\vec{r}') = \sum_{n=1}^N I_n \vec{f}_n(\vec{r}') \quad (2)$$

where $\{\vec{f}_n(\vec{r}')\}_{n=1}^N$ are the expansion (basis) functions, I_n are unknown current coefficients, and N is the total number of unknowns dependent on the quality of discretization. Next, we substitute (2) into (1) and apply the testing procedure with weighting functions $\vec{w}_1(\vec{r}), \dots, \vec{w}_m(\vec{r}), \dots$ defined in the range of L to reduce (1) to a linear set of equations written as:

$$\mathbf{Z}^{MoM} \mathbf{I} = \mathbf{V} \quad (3)$$

where \mathbf{Z}^{MoM} and \mathbf{V} are, respectively, the MoM impedance matrix and voltage matrix-vector with elements $Z_{mn}^{MoM} = \langle \vec{w}_m, L\vec{f}_n \rangle$ and $V_m = \langle \vec{w}_m, \vec{g} \rangle$, and \mathbf{I} is a vector of unknown coefficients I_n in the current expansion (2). Equation (3) defines the traditional MoM solution to the stated problem:

$$\mathbf{I} = (\mathbf{Z}^{MoM})^{-1} \mathbf{V} \quad (4)$$

3. Iterative MoM scheme for adaptive meshing

Analysis of (4) for the different discretizations of geometry G shows, that a uniformly fine mesh is not optimal enough to obtain a reasonably accurate solution. This section describes an iterative MoM scheme for generation of more optimal computational model. The scheme is based on analysis of an appropriate error metric for the solution. In each iteration step, the geometry is automatically re-discretized in a non-uniform way, until the best solution with a minimum number of unknowns is found.

Recent investigations (Bogdanov & Jobava, 2003; Bogdanov et al. 2004a, Bogdanov et al., 2004b; Jobava et al., 2005) show, that the accuracy of the MoM calculations can be controlled by estimation of the boundary conditions performance (BCP) on the scatterer surface S . Thus, a pair of BCP errors:

$$\varepsilon_E[\%] = 100 \frac{\int_S |\vec{n} \times (\vec{E}^{sc} + \vec{E}^{inc})| dS}{\int_S |\vec{n} \times \vec{E}^{inc}| dS}, \quad \varepsilon_H[\%] \equiv 100 \frac{\int_S |\vec{n} \cdot (\vec{H}^{sc} + \vec{H}^{inc})| dS}{\int_S |\vec{n} \times \vec{H}^{inc}| dS} \quad (5)$$

calculated for the total electric (\vec{E}) and magnetic (\vec{H}) fields, is sufficient enough to completely characterize the accuracy of the obtained MoM solution. Here, \vec{n} is a normal to the scatterer

surface, and superscripts *inc* and *sc* denote the incident and scattered fields. Note, that the BCP error metric (4) is applicable to both closed and open surfaces providing the finite values of surface integrals and the proper normalization of error expressions. Besides, (4) directly indicates, how well the obtained solution satisfies the formulated problem. Also, the partial BCP errors may be considered to find the contribution of each geometry element to the total BCP error on the surface. Thus, the BCP error metric is the most convenient measure to estimate the accuracy of MoM solutions and build the adaptive iterative MoM scheme.

Fig. 1 shows a task flow for the iterative MoM scheme based on the analysis of the total and partial BCP errors on scatterer surface. This algorithm is working in hierarchical way.

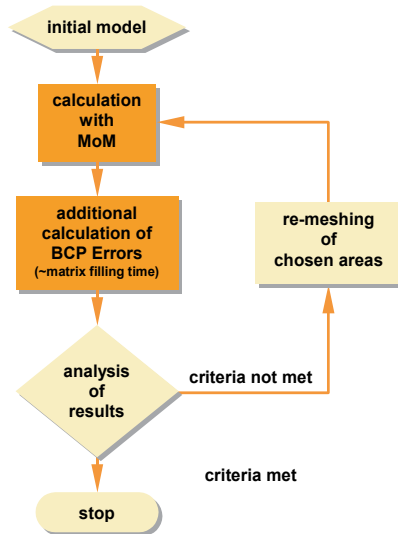


Fig. 1. Task flow for the BCP based adaptive iterative MoM scheme

First, MoM calculation for the initial “coarse” mesh is performed. Next, the BCP errors are calculated to estimate the solution accuracy and pick the geometry elements, which have contributed most strongly to the total BCP errors on the structure. After analysis of the BCP errors, further calculations are either stopped, or continued for the refined mesh, obtained after re-discretization of the chosen elements. The iterations are performed, till total BCP errors fall within a reasonable range.

The adaptive iterative scheme can be enhanced using the so-called *LSDM* (*Level-Surface-Difference-Minimum*) criteria (Jobava et al., 2005). After performing the initial calculation, the partial BCP errors are analyzed, so that all triangles with partial BCP errors higher than a prescribed value L (L -criterion) are considered as those for re-meshing. However, if the total area of triangles chosen for re-meshing is larger than a certain value $S\%$, in percentage to the total surface area (S -criterion), L -criterion is automatically enlarged, until the S -criterion is met. Further, a difference between the triangle areas chosen on the current and previous iterations is checked to be larger than a prescribed value $D\%$ (D -criterion). Finally, area of the chosen triangles is checked to be more than a prescribed value $M\%$, measured in percentage to the total surface area (M -criterion). If the previous criteria do not stop the iterations, re-meshing of the chosen areas and the further calculations are performed.

The adaptive iterative scheme has been verified on both closed and open geometries. Fig. 2 shows the total BCP errors on uniformly triangulated and adaptively meshed sphere

geometry. A sphere of radius $R = 0.5$ m is excited at a frequency $f=300$ MHz by a vertical electric dipole located at $h = 0.02$ m above the sphere surface to create a highly inhomogeneous incident near field. Fig. 2 illustrates a large advantage of the obtained adaptive meshes compared to the uniform mesh. Starting with a uniform mesh of 1,620 triangles and BCP errors of $\varepsilon_E=55.4\%$ and $\varepsilon_H=21.8\%$, at the 2nd iteration we obtain a mesh with 1,910 triangles and BCP errors of $\varepsilon_E=17.40\%$ and $\varepsilon_H=11.1\%$. The same accuracy may be provided by a uniform mesh with 20,170 triangles (for BCP-E) and 20,720 triangles (for BCP-H). Compared to these uniform meshes, the calculation time for matrix inversion is lower by a factor of $G_E=1,178$, and $G_H=1,277$.

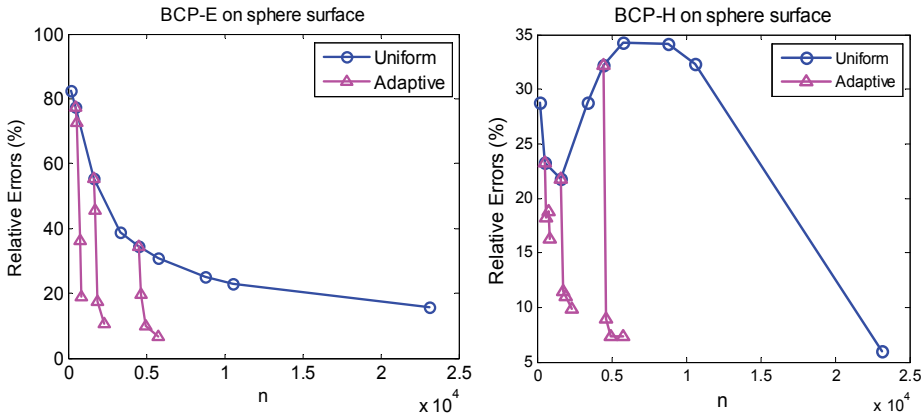


Fig. 2. Total BCP errors on a sphere surface for the uniform and adaptive meshes

Fig. 3 shows the adaptive meshes obtained for both closed (sphere) and open (square plate) geometries. The adaptive sphere mesh obtained at the 3rd iteration consists of 2,342 triangles and is characterized by BCP errors $\varepsilon_E=10.7\%$ and $\varepsilon_H=9.8\%$. Such accuracy cannot be achieved by any uniform mesh with less than 25,000 triangles. For the open geometry, 1-m plate is excited by a normally incident plane wave at frequency $f = 300$ MHz. The adaptive plate mesh obtained at the 2nd iteration from an initial uniform mesh of 1,800 triangles, consists of 3,385 triangles and is characterized by the BCP errors $\varepsilon_E=8.0\%$ and $\varepsilon_H=7.4\%$. Such accuracy cannot be achieved by a uniform mesh with less than 10,000 triangles.

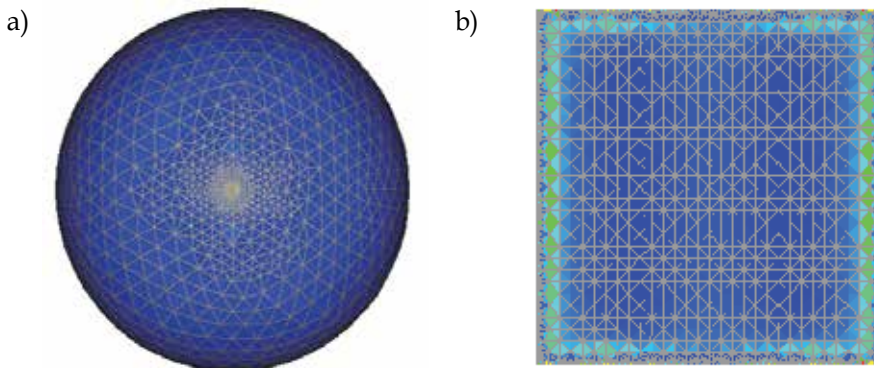


Fig. 3. The adaptive meshes: a) sphere geometry, b) plate geometry

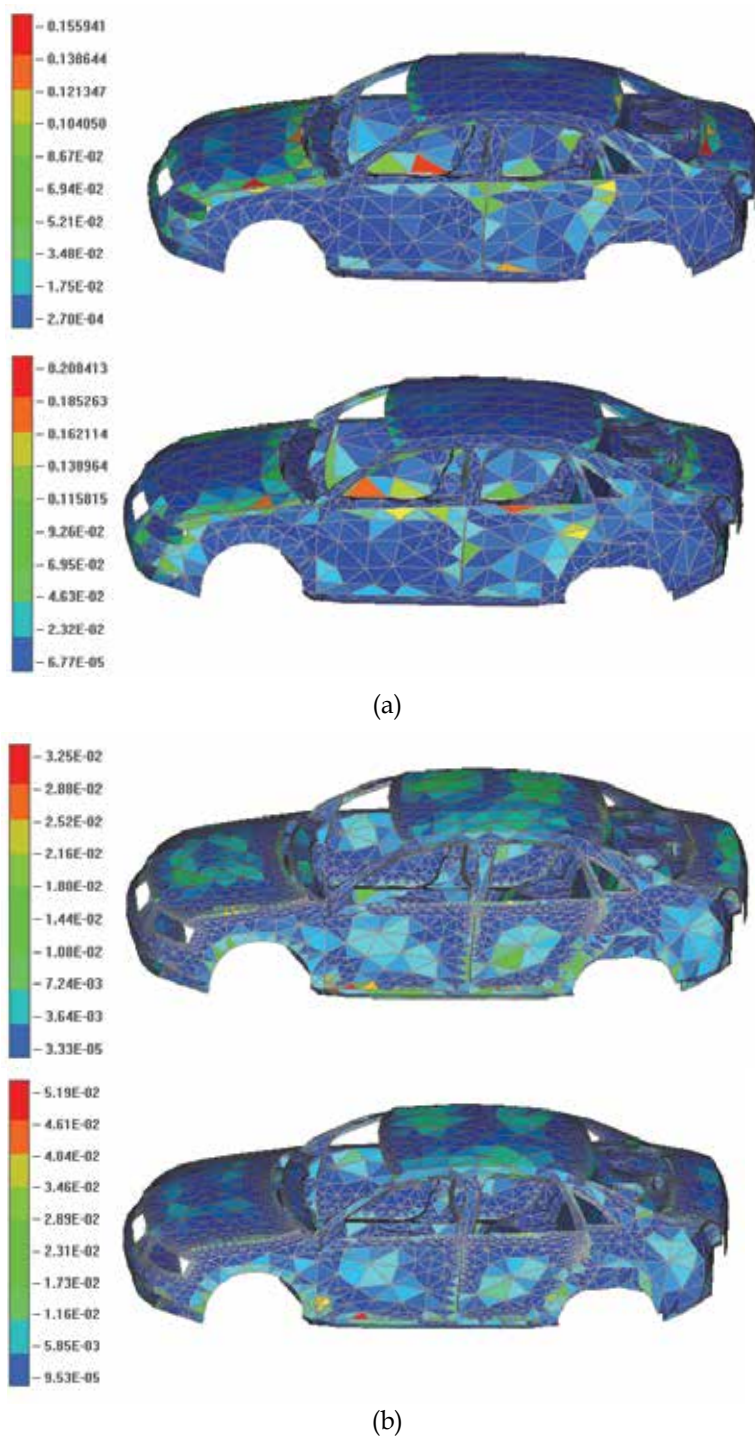


Fig. 4. BCP-E (top) and BCP-H (bottom) partial error distributions on: (a) initial car surface (4,449 triangles), (b) surface at iteration 2 (9,012 triangles)

Figs. 4 a) and b) present the distribution of partial BCP errors on initial and refined car model surfaces. It can be seen, that application of the suggested scheme leads to decrease of maximum partial errors. This results in more uniform distribution of partial BCP errors on the car surface.

So, at the 2nd iteration, the maximum partial BCP errors on the car surface are decreased by 5 and 3.5 times for BCP-E and BCP-H errors, respectively. Such accuracy can be obtained by a uniform mesh with 13,340 triangles for BCP-E error and 14,550 triangles for BCP-H error.

4. Hybridization of MoM with multiport networks

4.1 Incorporation of network equations in the MoM

Modern automotive antennas frequently involve a number of network devices (“black boxes”), detailed analysis of which in the frame of MoM is either impossible, or unnecessary because of excessive computational intensity. This section describes a hybridization of the MoM with general multiport networks specified through their network parameters, such as open-circuit impedances (Z-matrices), short-circuit admittances (Y-matrices), scattering parameters (S-matrices), transmission lines (TL), etc.

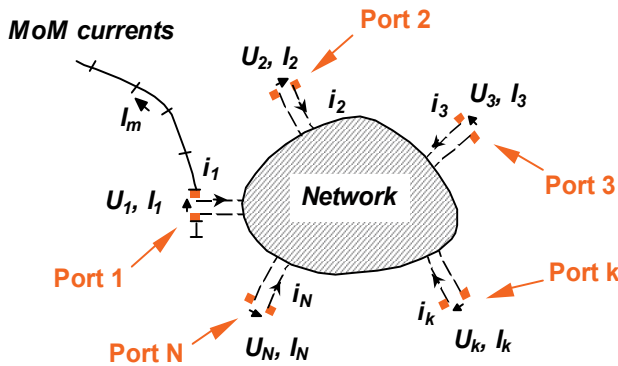


Fig. 5. N-port network directly connected to the MoM geometry

Fig. 5 shows a general N-port network connected to the wire segments, or ports of the MoM geometry. A network connection to the ports 1,2,...,N forces the currents i_1, i_2, \dots, i_N through and voltages U_1, U_2, \dots, U_N over the ports, according to the network parameters of the considered network.

Network parameters can be introduced via different forms of network equations:

$$\mathbf{U} = \mathbf{Z}^{Net} \mathbf{i} \quad (6a)$$

$$\mathbf{i} = \mathbf{Y}^{Net} \mathbf{U} \quad (6b)$$

$$\mathbf{a}^- = \mathbf{S}^{Net} \mathbf{a}^+ \quad (6c)$$

where $\mathbf{i} = [i_1, i_2, \dots, i_N]$ and $\mathbf{U} = [U_1, U_2, \dots, U_N]$ are the network port current and voltage matrix-vectors, \mathbf{Z}^{Net} , \mathbf{Y}^{Net} and \mathbf{S}^{Net} are the network Z-, Y- and S-matrices with network parameters Z_{mn}^{Net} , Y_{mn}^{Net} and S_{mn}^{Net} ; $\mathbf{a}^\pm = \frac{1}{2}(\bar{\mathbf{U}} \pm \bar{\mathbf{I}})$ are normalized incident (+) and reflected

(-) port voltage vectors, $\bar{\mathbf{U}} = \mathbf{Z}_L^{-1/2} \mathbf{U}$ and $\bar{\mathbf{i}} = \mathbf{Z}_L^{1/2} \mathbf{i}$ are, respectively, normalized network voltage and current vectors, and \mathbf{Z}_L is a diagonal matrix of characteristic impedances $Z_{L_1}, Z_{L_2}, \dots, Z_{L_N}$ of transmission lines, connected to each port (reference impedances). To incorporate the network equations (6a) to (6c) into the MoM system (3), it is necessary to relate the elements of matrix-vectors \mathbf{V} and \mathbf{I} in (3) to the network port voltage and current matrix-vectors \mathbf{U} and \mathbf{i} . Let us choose the expansion and testing functions $\bar{f}_n(\bar{r}')$ and $\bar{w}_m(\bar{r}')$ in (2) and (3) so as to interpret V_m and I_n in (3) as segment currents and voltages. Then the segment voltages $\mathbf{V} = [V_1, \dots, V_m, \dots]$ can be shared between those caused by external sources $\mathbf{V}^S = [V_1^s, \dots, V_m^s, \dots]$ and those by network voltages $\mathbf{U} = [U_1, U_2, \dots, U_N]$:

$$\mathbf{V} = \mathbf{V}^S + \mathbf{U} \quad (7)$$

For a free-port network (with controlled voltages), the port currents $\mathbf{i} = [i_1, i_2, \dots, i_N]$ are easily related to the segment currents $\mathbf{I} = [I_1, I_2, \dots, I_N]$:

$$\mathbf{i} = -\mathbf{I} \quad (8)$$

Therefore, inserting (8) in (6a) and then in (7) yields:

$$\mathbf{V} = \mathbf{V}^S - \mathbf{Z}^{Net} \mathbf{I} \quad (9)$$

Now introducing (9) in (3) and regrouping components with the currents \mathbf{I} yields the following hybridized MoM and network algebraic system:

$$(\mathbf{Z}^{MoM} + \mathbf{Z}^{Net}) \mathbf{I} = \mathbf{V}^S \quad (10)$$

For the mixed (free and forcing ports), the network equation (10) is generalized to:

$$(\mathbf{Z}^{MoM} + \mathbf{Z}^{Net}) \mathbf{I} = \mathbf{V}^S + \mathbf{V}^{add} \quad (11)$$

where $\mathbf{Z}^{Net} = (\mathbf{Y}^{Net})^{-1}$ is the free-port generalized impedance matrix of N-port network,

$$\mathbf{V}^{add} = -\mathbf{Z}^{Net} \mathbf{Y}^{mNet} \mathbf{U}^S \quad (12)$$

is an additional voltage matrix-vector on free ports induced due to the connection to forcing ports, and \mathbf{Y}^{Net} , \mathbf{Y}^{mNet} are the free-port and mixed-port generalized network admittance matrices. The latter are mixed matrices with row index for the free port, and column index for the forcing port.

The matrix equations (11) represent the general hybridization of the MoM with multiport networks. Here, the total impedance matrix is composed of the MoM matrix and a reduced general network matrix for free ports, while the voltage column is composed of the MoM voltages and impressed network voltages, induced by the connection to the forcing ports. Specifically, for free-port network, (11) reduces to (10), while for the forcing-port network to (3), with $\mathbf{V} = \mathbf{V}^S$. In the latter case, the MoM system remains unchanged.

4.2 Validation of the hybrid MoM and network scheme

The derived hybrid MoM scheme is validated on a simple PSPICE model shown in Fig. 6. It consists of a 2-port linear amplifier network (outlined by the dashed line) connected to a 1-V voltage generator with internal resistance 50 Ω and loaded with a 1-m transmission line (TL)

with characteristic impedance 150Ω and termination resistance R . The hybrid MoM simulation model is constructed of 4 wire segments to model the network ports (of S- and TL- types), 8 wire segments to model the excitation, connections and loads, and a frequency dependent S-matrix supplied by the PSPICE.

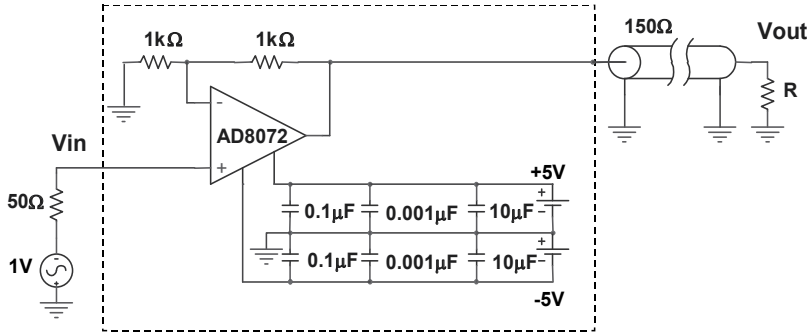


Fig. 6. Amplifier model with a transmission line

Fig. 7 shows a comparison of the transfer function calculated by hybrid MoM (TriD) and PSPICE (Su at al., 2008)

$$TF_V = V_{out} / V_{in} \tag{13}$$

where V_{out} is voltage on a transmission line termination, V_{in} is voltage at an amplifier input.

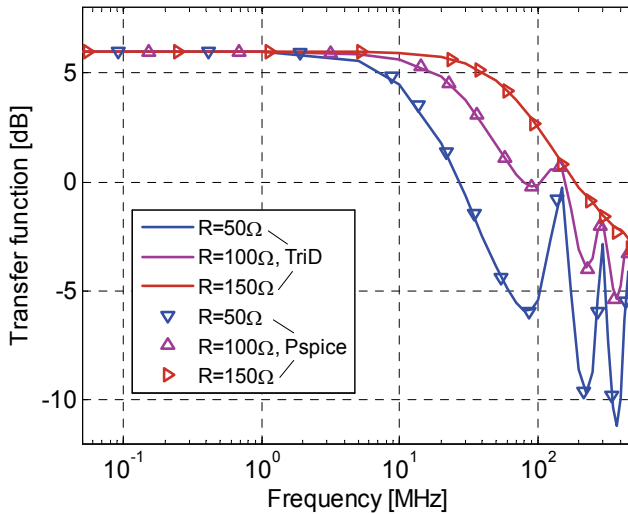


Fig. 7. Comparison of transfer functions calculated by the hybrid MoM (TriD) and PSPICE

The comparison of the TriD results with those calculated by PSPICE demonstrates a perfect agreement between them in a wide frequency range up to 500 MHz, including a flatness range up to 10 MHz, a smooth range for the matched termination resistance $R = 150 \Omega$, and a high frequency oscillation range for the unmatched termination resistances $R = 50 \Omega$ and 100Ω . These results validate the derived hybrid MoM and network scheme.

5. Hybridization of MoM with a special Green's function

5.1 Problem formulation

Modern automotive design tends towards conformal and hidden antenna applications, such as glass antennas integrated in vehicle windowpanes, as depicted in Fig. 8. An accurate MoM analysis of such antennas requires the discretization of the dielectric substrate of the glass, which results in an excessively large amount of unknowns (a several hundred of thousands). The usage of rigorous Green's functions of infinite layered geometries, represented by Sommerfeld integrals (Sommerfeld, 1949), is unfortunately too time-consuming and inflexible, whereas a frequently used approximate sheet impedance approximation (Harrington. & Mautz, 1975) fails for the complex glass antenna geometries (Bogdanov at al., 2010a). This section describes an equivalent glass antenna model of layered antenna structures and derives the hybrid MoM scheme, which incorporates the approximate Green's function of such a model.

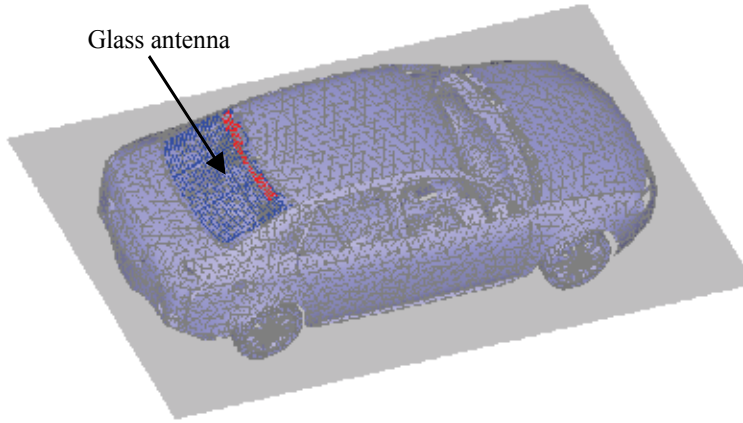


Fig. 8. Vehicle computational model with a glass antenna in the rear window

Let the total MoM geometry G of the considered problem be divided into basis (car) geometry B , glass antenna elements A and dielectric substrate D . The hybrid MoM formulation, excluding the dielectric geometry D from the consideration, can be written, instead of (1), as:

$$L(\vec{J}^B) + L_G(\vec{J}^A) = \vec{g}^B + \vec{g}_G^A \text{ on } S^B \quad (14a)$$

$$L_G(\vec{J}^B) + L_G(\vec{J}^A) = \vec{g}_G^B + \vec{g}_G^A \text{ on } S^A \quad (14b)$$

where the superscripts B and A stand for the basis and glass antenna elements, and L_G and \vec{g}_G are the boundary operator and excitation modified so as to include the dielectric effect and automatically satisfy boundary conditions on the dielectric. To derive the hybrid MoM scheme and define the operators L_G and \vec{g}_G , consider an equivalent glass antenna model, allowing construction of approximate Green's function for the layered antenna structures.

5.2 Equivalent glass antenna model

Fig. 9 a) shows an original structure of the metallic strip (glass antenna element) A with current \vec{J} placed above, inside or under the dielectric layer (regions $i=1,2,3$, respectively).

The layer of thickness l and material parameters ϵ_0, μ_0 (region $i=2$) is placed in vacuum with parameters ϵ_0, μ_0 ($i=1,3$). In a multilayer case, effective material parameters are considered.

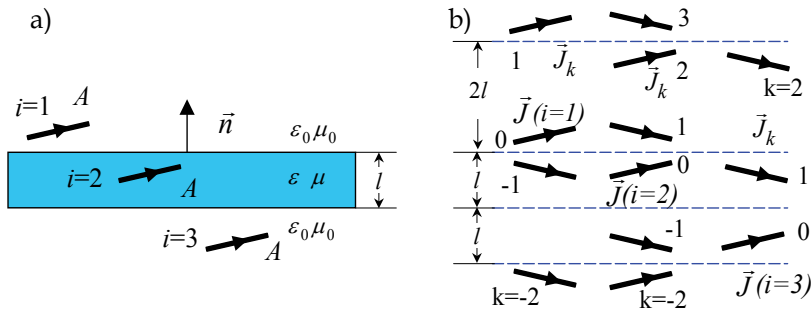


Fig. 9. a) Original and b) equivalent glass antenna model

Fig. 9 b) shows an equivalent model of microstrip structure in Fig. 2 a) consisting of the source current \vec{J} on element A and its mirror images \vec{J}_k ($k = 0, \pm 1, \pm 2, \dots$) in top and bottom dielectric layer interfaces. For the source current \vec{J} in the region i , an electromagnetic field in the observation region $j=1,2,3$ is composed of the field of the original current \vec{J} (if only $j=i$) and that produced by its images \vec{J}_k taken with amplitudes A_{kv}^{ji} and A_{kh}^{ji} for the vertical and horizontal components of the vector potentials, and A_{kq}^{ji} for the scalar potentials. Hereinafter, the 1st superscript indicates the observation region, and the 2nd the source region.

Note, that both the source and image currents, radiate in medium with material properties of the observation region j , and only images, which are not placed in the observation region, radiate into this region. The image amplitudes A_{kt}^{ji} , $t = v, h, q$ can be approximately found by recursive application of the mirror image method to relate these amplitudes with those (a_t^{ji}) obtained for the approximate solution of the boundary-value problem on a separate dielectric interface.

5.3 Derivation of image amplitudes

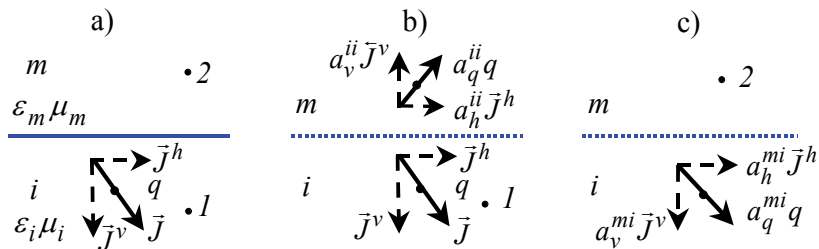


Fig. 10. Sources and images in the presence of dielectric interface: a) original problem, b) equivalent problem for the source region i , c) equivalent problem for the mirror region m

In order to find the image amplitudes a_t^{ji} , let's place the current \vec{J} and the associated charge $q = \mp \frac{1}{i\omega} \text{div } \vec{J} dV$ from one side (for instance, in medium i) of the interface between the two dielectric media m and i , as depicted in Fig. 10 a). Following the modified image theory (MIT) (Miller et al., 1972a; Ala & Di Silvestre, 2002), an electromagnetic response from the imperfect interface is approximately described by inserting the mirror image source

radiating to the source region i , and the space-like image source radiating to the mirror region m , see Figs. 10 b) to c). The original current \vec{J} is decomposed into its vertical \vec{J}^v and horizontal \vec{J}^h components, and $\vec{J}^v = -\vec{J}^v$. Unlike the canonical mirror image method, image amplitudes a_i^{ji} are modified so as to approximately satisfy the boundary conditions.

Unlike other MIT applications, we reconsider the derivation of image amplitudes a_i^{ji} , imposing boundary conditions on both electric and magnetic fields and applying the quasi-static approximation $(kR)^2 \ll 1$, where k is a wavenumber, and R is a distance between the image and observation points. Besides, we assign the different amplitudes a_v^{ji} , a_h^{ji} and a_q^{ji} for the current and charge images, in view of nonuniqueness of vector and scalar potentials in the presence of a dielectric boundary (Erteza & Park, 1969). This results in the following approximate solution to Sommerfeld problem in Figs. 10 b) and c) (Bogdanov et al., 2010b):

$$a_q^{ii} = a_v^{ii} = \frac{\varepsilon_i - \varepsilon_m}{\varepsilon_i + \varepsilon_m}, \quad a_q^{mi} = a_v^{mi} = \frac{2\varepsilon_m}{\varepsilon_i + \varepsilon_m} \quad (15a)$$

$$a_h^{ii} = \frac{\mu_m - \mu_i}{\mu_i + \mu_m}, \quad a_h^{mi} = \frac{2\mu_i}{\mu_i + \mu_m} \quad (15b)$$

Once the image amplitudes a_i^{ji} of the equivalent interface problem are found, we develop a recursive procedure (Bogdanov et al., 2010b) to derive the image amplitudes A_{kt}^{ji} of the equivalent glass antenna problem in Fig. 9 b). Let us derive it for the source current \vec{J} situated in the region $i=1$ (above the layer). To satisfy boundary conditions on the upper dielectric interface, we introduce, along with source current \vec{J} radiating in the source region 1, two image currents located on equal distances d from the interface: mirror current \vec{J}_{-1} with amplitude $A_{-1t}^{11} = a_t^{11}$, again radiating in region 1, and space-like image \vec{J}_0 with amplitude $A_{0t}^{21} = a_t^{21}$ radiating in region 2. The same procedure for the image current \vec{J}_0 radiating in region 2 in the presence of the bottom interface, requires a pair of additional image currents located at equal distances $l+d$ from this interface: \vec{J}_{-2} with amplitude $A_{-2t}^{21} = a_t^{21} a_t^{22}$ radiating in region 2, and \vec{J}_0 with amplitude $A_{0t}^{31} = a_t^{21} a_t^{12}$ radiating in region 3. Next, we should adjust the boundary conditions on the upper interface, which are unbalanced due to the radiation of image current \vec{J}_{-2} with amplitude $a_t^{21} a_t^{22}$ in region 2 in the presence of the upper interface. Recursively continuing this procedure results in:

$$A_{-1t}^{11} = a_t^{11}; \quad A_{-kt}^{11} = a_t^{21} a_t^{12} (a_t^{22})^{2k-3}, \quad A_{-kt}^{21} = a_t^{21} (a_t^{22})^{2k-3}, \quad k = 2, 3, \dots \quad (16a)$$

$$A_{kt}^{21} = a_t^{21} (a_t^{22})^{2k}, \quad A_{kt}^{31} = a_t^{21} a_t^{12} (a_t^{22})^{2k}, \quad k = 0, 1, 2, \dots \quad (16b)$$

5.4 MoM Solution to the equivalent glass antenna model

The equivalent glass antenna model in Fig. 9 b) allows to introduce the equivalent current and charge associated with antenna element A into any observation region $j=1,2,3$:

$$\vec{J}' = \vec{J} \delta_{ij} + \sum_k [A_{kv}^{ji} \vec{J}_k^v + A_{kh}^{ji} \vec{J}_k^h] \quad (17)$$

$$i / \omega \nabla \vec{J}' = i / \omega (\nabla \vec{J} \delta_{ij} + \sum_k A_{kq}^{ji} \nabla \vec{J}_k) \quad (17a)$$

where \vec{J} is the original current in the i -th region, δ_{ij} is the Kronecker delta, $\vec{J}_k = \mathfrak{R}_k \vec{J}$ is the current on the k -th image, \mathfrak{R}_k is the imaging operator, $\vec{J}_k^v = (\vec{J}_k \hat{n}) \hat{n}$ and $\vec{J}_k^h = \vec{J}_k - \vec{J}_k^v$ are the vertical and horizontal components of the k -th image currents, and \hat{n} is a unit normal vector to the dielectric interface. Since (17) can be considered as $\vec{J}' = \mathfrak{Z}(\vec{J})$, where \mathfrak{Z} is a transforming operator, and modifying the excitation $\vec{g}' = \mathfrak{Z}(\vec{g})$, after substitution in (1), we arrive at the following equivalent boundary-value problem on antenna element geometry A:

$$L_G(\vec{J}) = \vec{g}_G \quad (18)$$

where:

$$L_G = L\mathfrak{Z}, \quad \vec{g}_G = \mathfrak{Z}\vec{g} \quad (19)$$

are the modified boundary operator and excitation in the glass area including the dielectric effect. Equation (18) allows to obtain the MoM solution to the glass antenna problem, applying the traditional MoM scheme of Section 2 to the equivalent model in Fig. 9 b) with expansion functions taken on both original and image geometries, and testing only on the original geometry.

5.5 Hybrid MoM scheme with incorporated equivalent glass antenna model

Expression (19) allows to reduce the hybrid MoM formulation (14) to a linear set of algebraic equations. Applying the traditional MoM scheme of Section 2 with expansion functions $\{\vec{f}_n(\vec{r}')\}_{n=1}^N$ and weighting functions $\{\vec{w}_m(\vec{r})\}_{m=1}^N$ results in the following matrix equations:

$$\begin{bmatrix} [Z_{mn}^{BB}] & [Z_{mn}^{BA}] \\ [Z_{mn}^{AB}] & [Z_{mn}^{AA}] \end{bmatrix} \begin{bmatrix} [I_n^B] \\ [I_n^A] \end{bmatrix} = \begin{bmatrix} [V_m^{BB}] + [V_m^{BA}] \\ [V_m^{AB}] + [V_m^{AA}] \end{bmatrix} \quad (20)$$

where $Z_{mn}^{BB} = \langle \vec{w}_m^B, L \vec{f}_n^B \rangle$, $Z_{mn}^{\beta\alpha} = \langle \vec{w}_m^\beta, L_G \vec{f}_n^\alpha \rangle$ are the MoM impedance matrix elements, $V_m^{BB} = \langle \vec{w}_m^B, \vec{g}^B \rangle$, $V_m^{\beta\alpha} = \langle \vec{w}_m^\beta, \vec{g}_G^\alpha \rangle$ the excitation elements, and $\alpha, \beta = \{A, B\}$. The linear set (20) incorporates the equivalent glass antenna model into the full MoM geometry.

Note, that although equivalent glass antenna model is derived for infinite dielectric layers, it also can approximately be applied to finitely sized and even slightly curved glass antenna geometries. For this purpose, a finite-size dielectric substrate is subdivided into separate flat areas, and each antenna element is associated with the closest glass area. The antenna elements near this area are considered to radiate as located in the presence of infinite dielectric substrate being the extension of this smaller glass area.

5.6 Application of hybrid MoM scheme with incorporated equivalent glass antenna

The derived hybrid MoM scheme has been applied to simulate reflection coefficient of rear window glass antenna in full car model. Results were compared with measurements.

A simulation model of the measurement setup with glass antenna and its AM/FM1/TV1 port is shown in Fig. 11. This model consists of 19,052 metal triangles to model the car bodyshell, 67 wire segments to model the antenna to body connections, and 2,477 triangles to model the glass antenna elements, giving a total of $N = 31,028$ unknowns. The curved glass surface is represented by 5,210 triangles. The dielectric substrate is of thickness $l = 3.14$ mm, relative permittivity $\epsilon_r = 7.5$, and dielectric loss tangent $\tan(\delta) = 0.02$. The metallic elements are assumed to be perfectly conducting. To accurately represent measurement

setup, BNC connectors attached to the antenna terminals. The connectors are modelled as non-radiating TL elements of 64-mm length and 50-Ohm characteristic impedance.

Fig. 12 shows measured and simulated results for the reflection coefficient $|S_{11}|$ at the FM1 port of the glass antenna. Comparison between these results shows that simulated results are in a close agreement with measurement data at all frequencies in the range from 30 to 300 MHz.

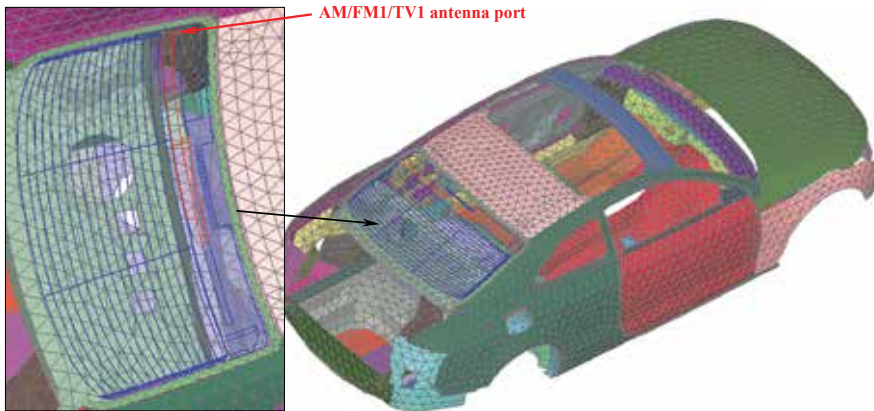


Fig. 11. A simulation model of the measurement setup with the glass antenna with FM port

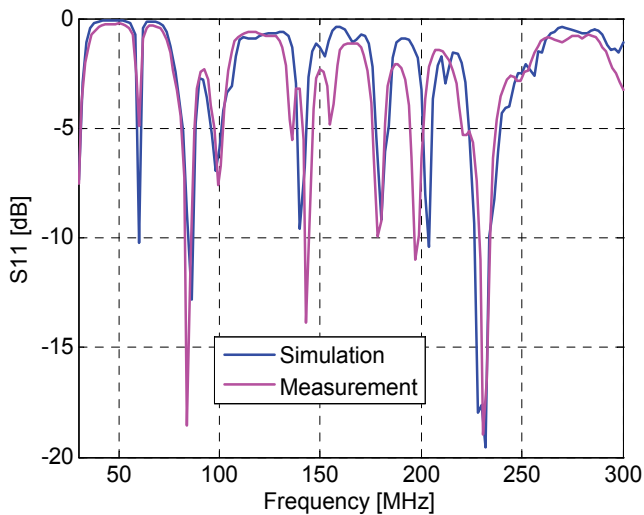


Fig. 12. Comparison of measurement and simulation results for a full car model

6. Multi-partitioned and multi-excitation MoM scheme

6.1 Problem formulation

In the optimization of automotive antenna, a considerable part of the vehicle geometry remains the same in different calculations. For instance, this happens when one compares characteristics of different antennas mounted in a windowpane of the same car model. This

also happens when optimizing the shape, dimensions, position and material parameters of certain antenna installed in the vehicle. Besides, an optimization of the calculation procedure for different sets of excitations is required. This section describes a multi-partitioned and multi-excitation MoM scheme to effectively handle such geometries and excitations.

Let G be a series of geometries G_1, G_2, \dots, G_K with a predominant common (basis) part

$G^b = \bigcap_{k=1}^K G_k$ being an intersection of the geometries G_k . The analysis of the geometries G_k ,

$k = 1, 2, \dots, K$ using the traditional MoM scheme of section 2 requires CPU time that K times exceeds that needed to handle a single geometry. Our intention is to enhance the MoM scheme in such a way as to essentially minimize the total CPU time needed to handle a series of geometries under different sets of excitations.

6.2 Partitioned MoM scheme

Let geometry G_k be partitioned on the basis G^b and additional G^a parts, so that $G_k = G^b + G^a$. Reconsidering the boundary-value problem (1) with applying the partitioned sets of expansion and testing functions for the basis G^b and additional G^a geometries, we reduce (1) to the matrix equations with the following block structure:

$$\begin{bmatrix} Z^{bb} & Z^{ba} \\ Z^{ab} & Z^{aa} \end{bmatrix} \begin{bmatrix} I^b \\ I^a \end{bmatrix} = \begin{bmatrix} V^b \\ V^a \end{bmatrix} \quad (21)$$

where the first superscript is associated with the testing procedure, and the second one with the expansion procedure, so that the total number of unknowns is $N = N^b + N^a$.

Considering now the LU decomposition of the partitioned impedance matrix:

$$\begin{bmatrix} Z^{bb} & Z^{ba} \\ Z^{ab} & Z^{aa} \end{bmatrix} = \begin{bmatrix} L^{bb} & 0 \\ L^{ab} & L^{aa} \end{bmatrix} \begin{bmatrix} U^{bb} & U^{ba} \\ 0 & U^{aa} \end{bmatrix} \quad (22)$$

one can see that the decomposition of the basis block matrix $Z^{bb} = L^{bb}U^{bb}$ is the same as the one which would be obtained for the basis geometry G^b . Therefore, considering first the boundary-value problem on the basis geometry G^b and storing the inverted matrices $\tilde{L}^{bb} = (L^{bb})^{-1}$ and $\tilde{U}^{bb} = (U^{bb})^{-1}$ for this geometry, one then only needs to calculate the additional blocks of the partitioned impedance matrix in (21) to determine the additional blocks in the LU decomposition (22). Then, the solution of the initial boundary-value problem on the total geometry G_k is found to be:

$$\begin{bmatrix} I^b \\ I^a \end{bmatrix} = \begin{bmatrix} U^{bb} & U^{ba} \\ 0 & U^{aa} \end{bmatrix}^{-1} \begin{bmatrix} L^{bb} & 0 \\ L^{ab} & L^{aa} \end{bmatrix}^{-1} \begin{bmatrix} V^b \\ V^a \end{bmatrix} \quad (23)$$

or, after inversion of block matrices

$$\begin{bmatrix} I^b \\ I^a \end{bmatrix} = \begin{bmatrix} \tilde{U}^{bb} & \tilde{U}^{ba} \\ 0 & \tilde{U}^{aa} \end{bmatrix} \begin{bmatrix} \tilde{L}^{bb} & 0 \\ \tilde{L}^{ab} & \tilde{L}^{aa} \end{bmatrix} \begin{bmatrix} V^b \\ V^a \end{bmatrix} \quad (24)$$

where $\tilde{U}^{ba} = -(\tilde{U}^{bb} U^{ba}) \tilde{U}^{aa}$, $\tilde{L}^{ab} = -(\tilde{L}^{aa} L^{ba}) \tilde{L}^{bb}$. In (24), a predominant part of the calculations is associated with determining the inverse block matrices \tilde{L}^{bb} and \tilde{U}^{bb} for the basis geometry G^b to be stored at the first stage of calculations. If the additional part G^a of the total geometry G_k is much less than the basis part G^b , the calculation of additional blocks needs far fewer operations than those required for the total geometry. This allows performing the additional calculations to obtain the sought solution without considerable usage of CPU time. The structure of multi-partitioned and multi-excitation calculations is illustrated in Fig. 13.

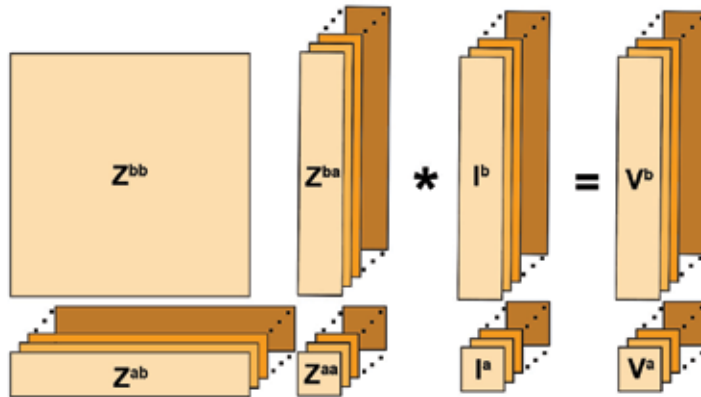


Fig. 13. Structure of multi-partitioned and multi-excitation calculations

A theoretical gain in solving time obtained when applying the partitioned MoM scheme (if using the stored LU matrices for the basis geometry) may be evaluated as:

$$G = \frac{1}{(1 - \beta) / K + \beta} \tag{25}$$

where $K = 1 / [1 - (1 - \alpha)^3]$ is a theoretical gain of LU decomposition, $\alpha = N^a / (N^b + N^a)$ is a share of additional unknowns in a total number of unknowns, and β is a share of the additional time in a direct task time, which is necessary for the calculation processing (this is characterized by the computational system). This time includes the needed data preparation, loops and threads organization, memory access, etc. For in-core calculations, this time may be ignored, while for out-of-core calculations it should include HDD read/write time, and for the cluster (distributed memory) calculations it should include the data exchange time (the latter time may be rather significant to appreciably reduce the estimation gain).

Tables 1 and 2 compare the solving times and gains for the sequential/multithreaded and cluster calculations. These tasks have been run on 2CPU Intel Xeon 3.00 GHz computers (totally 4 cores); and the cluster consists of the 9 computers (altogether 36 processes).

N^b	N^a	α	$G \equiv K$	1 thread used		4 threads used	
				Direct [s]	Partition [s]	Direct [s]	Partition [s]
28093	2935	0.095	3.87	8063	2116	2233	750
28093	118	0.004	80.03	6052	91	1696	38

Table 1. Solving times and gains for sequential calculations for $\beta = 0$.

N^b	N^a	α	K	Direct [s]		β	G	Partition [s]
				Solve	Exchange			Solve
28093	2935	0.095	3.87	474	200	0.42	1.75	332
28093	118	0.004	80.03	383	170	0.44	2.22	211

Table 2. Solving times and gains for cluster calculations.

The presented data shows the sufficient advantage of using the partitioned MoM scheme when applied to a series of partitioned geometries with a predominant basis part (small values of α). However, this scheme is less effective in the case of distributed memory (parallel) calculations, because of a large amount of data exchange (even theoretically, it cannot be more than $1/\beta$). Optimizing the data exchange in the multi-partitioned regime, one can significantly decrease the average β , which results in increase of the gain.

6.3 Application of the multi-partitioned MoM scheme

The derived multi-partitioned MoM scheme has been applied to optimize glass antenna structure in a full car model. Fig. 14 shows a computational model of AUDI A5 with a heating structure and antenna pattern printed on the rear windscreen. A part of the antenna structure used for AM, FM and TV services, is to be optimised (this part is electrically separated from the heating structure and therefore may be easily changed during the antenna design).

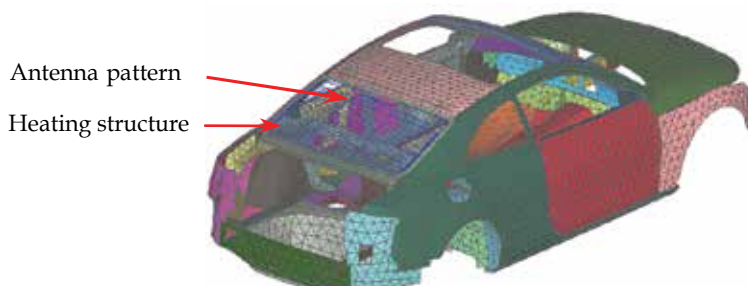


Fig. 14. AUDI A5 car body with heating structure printed on rear windscreen

In using the multi-partitioned scheme, we consider the car bodyshell and the heating structure as a basis part of geometry (altogether 20,573 metallic elements), and the antenna structure as additional (partition) part. Figs. 15 a) to c) show different variants of the antenna structure with a corresponding pigtail wire, which are considered as partitions. Fig. 15 d) compares the reflection coefficients of the full car models with the above antenna variants, calculated in the frequency range from 30 MHz to 300 MHz. The obtained results show that modification of the antenna structure do not change the reflection coefficient in the FM frequency range, but significantly shifts and change the level of resonances in the TV range (150-175 MHz and 210-225 MHz).

Table 3 compares the computational times needed for calculation of 3 variants of the antenna structure using the direct MoM respectively the multi-partitioned approach. Comparison of CPU times shows 1.5 gain in calculation time for 3 partitions that demonstrates advantage of the multi-partitioned scheme to solve optimization problems on full car models. It should also be mentioned that the benefit of the multi-partitioned

approach increases if more variants are to be compared. This is quite often the case in early stages of development when many different antenna positions and layouts are still viable.

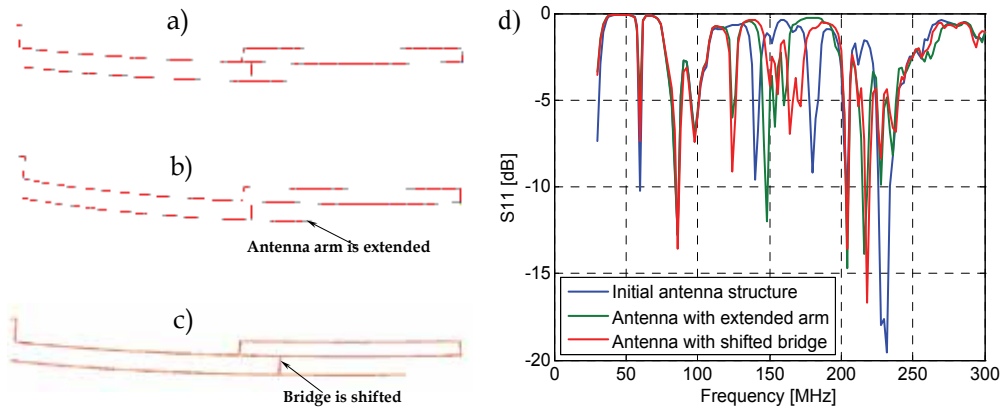


Fig. 15. Different variants of the antenna structure: a) initial structure, 102 metallic elements, b) structure with extended arm, 117 metallic elements, c) structure with shifted bridge, 117 metallic elements, d) reflection coefficient of above antennas as a function of frequency

Solution type	CPU time for one frequency point
Direct solution (3 tasks)	3.7 hours (1.23 hours per task)
Matrix partitioned approach (3 partitions)	2.55 hours (1.9 hours for basis + 0.65 hours for 3 partitions; 13 minutes for each partition)

Table 3. Summary of computational times

7. Application of computational techniques to automotive EM problems

7.1 Simulations of vehicle antenna validation tests

The developed techniques have been applied to simulate various EM and EMC (Electromagnetic Compatibility) problems on automotive antennas.

First, a vehicle antenna validation test (usually, it precedes a chamber vehicle emission test) is modelled. A schematic representation of this test is shown in Fig. 16.

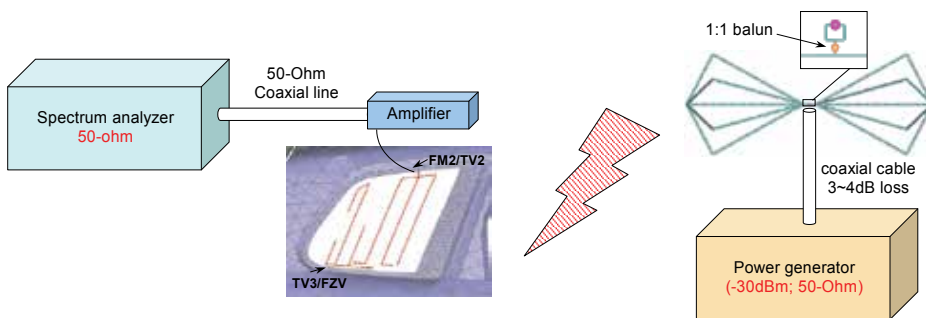


Fig. 16. Schematic representation of antenna validation test

A measurement setup consists of active vehicle antenna (with amplifier) exposed by a test antenna with defined feeding, and a spectrum analyzer to measure the coupled voltage. The obtained voltage level is compared to the standard acceptable reception level, known for each type of vehicle antenna. The computer simulations are aimed to predict the total antenna system performance in order to detect possible problems, especially if a real car prototype is not yet available for measurements. Fig. 17 shows used mutual location of the car and test antennas in an anechoic chamber.

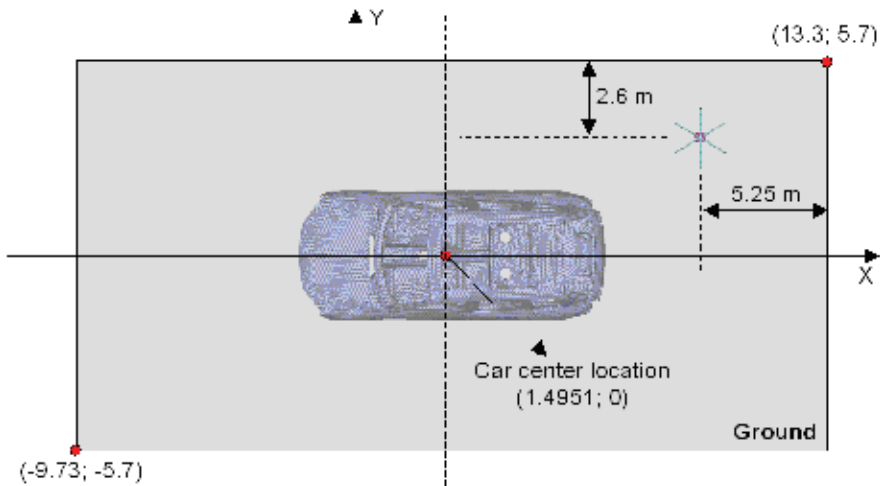


Fig. 17. Mutual location of the car and test antenna in anechoic chamber

In a current example, a vertically polarized biconical SCHWARZBECK BBA9106 test antenna with 1:1 balun is used. The antenna located at 1.0 m above the ground is fed by a -30dBm generator with 50-Ohm internal resistance, connected to the antenna by a lossy coaxial cable. The dimensions and antenna factor of the test antenna are presented in Figs. 18 and 19.

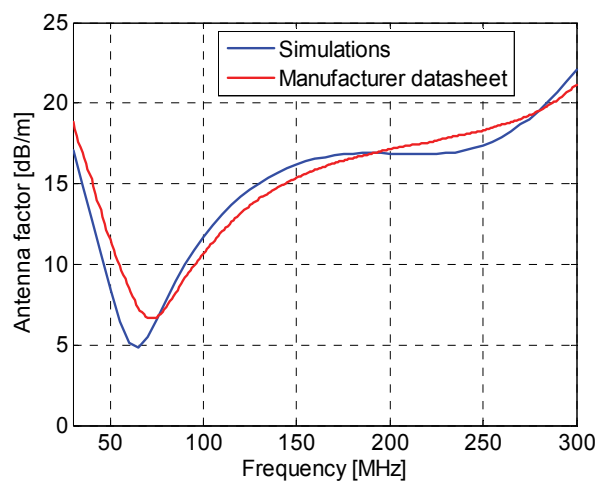


Fig. 18. Antenna factor

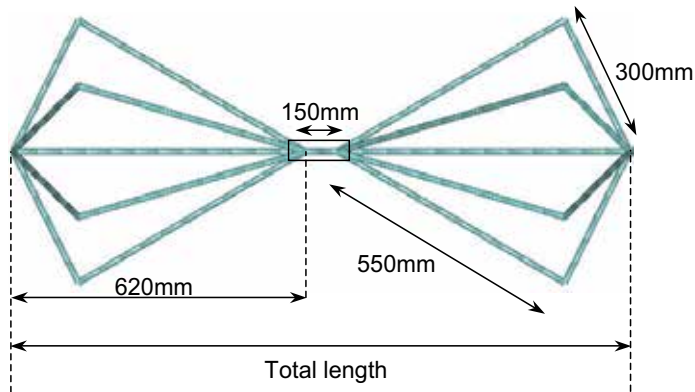


Fig. 19. Test antenna dimensions

A simulation model of the side window TV2 antenna in a VW car is shown in Fig. 20. It consists of 31,045 triangles to model the car bodyshell, and 535 triangles and 19 wire segments to model the antenna pattern. The antenna pattern is printed on the right rear window glass of thickness $l=3$ mm, permittivity $\epsilon_r=7$, loss tangent $\tan(\delta)=0.02$, and is adjacent to the TV3/FZV antenna.

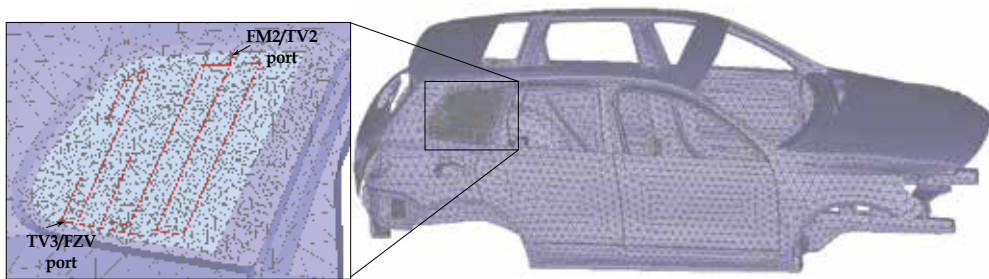


Fig. 20. VW car model with glass antenna in right window

To properly model the validation test, the antenna amplifiers are also included in the simulation model as non-radiating networks. The scattering parameters of the TV2 and TV3 antenna amplifiers are depicted in Figs. 21 a) and b). It is assumed, that a backward transmission of the signal from radio to antenna pattern is negligibly small, and that the amplifier output is perfectly matched with a 50-Ohm coaxial cable connected to radio. Thus, a complete simulation model consists of the biconical test antenna, car bodyshell model and side window glass antenna with amplifiers. The analysis of such a model requires the following modelling techniques: power normalization of the biconical antenna source, hybridization of the MoM with special Green's function to model the glass antenna, and hybridization of the MoM with multiport networks to model the amplifiers and lossy coaxial cables.

Fig. 22 shows the comparison of the simulated voltage at TV2 amplifier output port with measurement results obtained in Volkswagen AG. Two separate frequency ranges are considered: 40 MHz - 110 MHz (Bands I and II), and 170 MHz - 230 MHz (Band III).

Comparison of the simulated results with measurements shows a rather good agreement between them in both TV1 and TV2 frequency ranges. The maximum difference between coupled voltages does not exceed 6 dB.

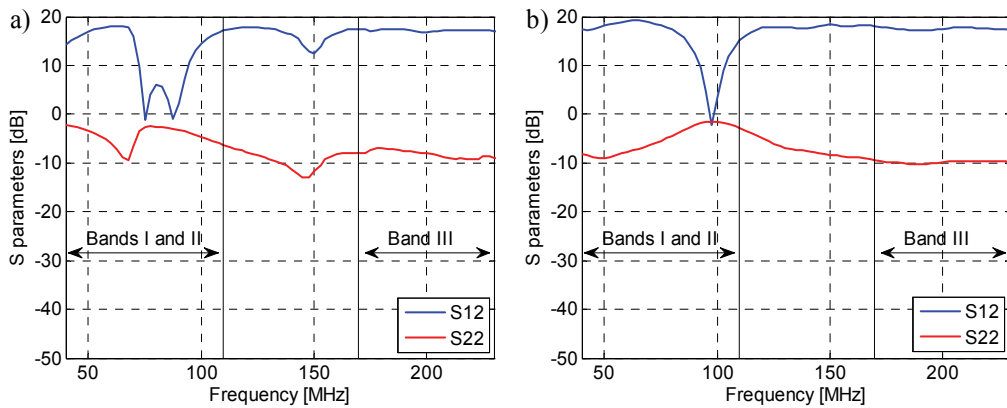


Fig. 21. S-parameters of: a) TV2 amplifier, b) TV3 amplifier

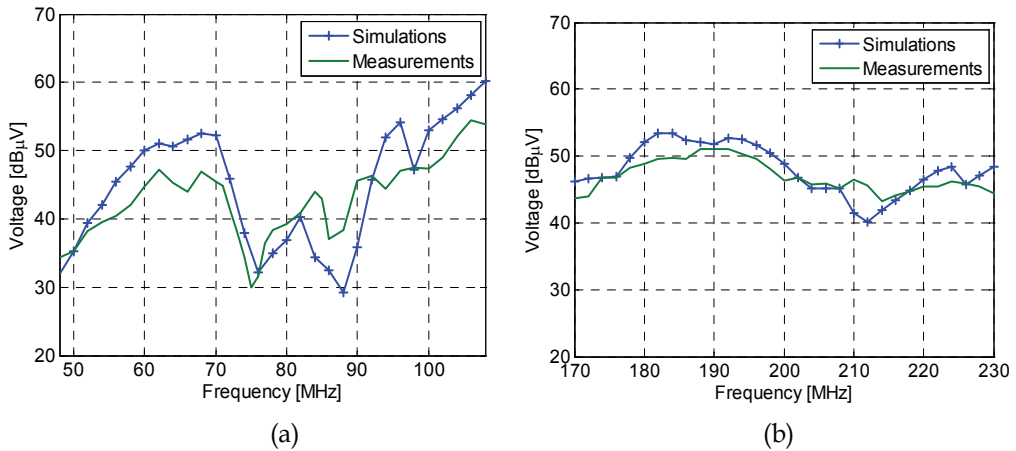


Fig. 22. Voltage received by TV2 antenna in: a) Band I and II, b) Band III

7.2 Testing of vehicle antenna reception in an open-area far-field test setup

Next, a vehicle antenna reception in an open-area far-field test setup is modelled. Examination of vehicle antenna reception is one of the stages in system development and certification. A single-axis rotational technique is used to measure the antenna reception pattern. This technique involves placing the equipment under test on a rotational positioner and rotating about the azimuth to measure a two-dimensional polar pattern. It is important to be able to measure two perpendicular (vertical and horizontal) components of pattern. This measurement is usually accomplished by using a dual-polarized horn, log-periodic dipole array, or dipole antenna as the transmitting antenna and requires two transmitters or the ability to automatically switch the polarization of a single transmitter. A typical polar-pattern test setup is shown in Fig. 23.

The vehicle with antenna under test (AUT) is placed on a rotating turntable; transmitting antenna is placed at a certain level above ground and at fixed distance away from the AUT. The turntable is rotated over 360°, and the response between the antennas is measured as a function of angle. A distance between the transmitting antenna and AUT is taken to be large enough to satisfy far-field condition.

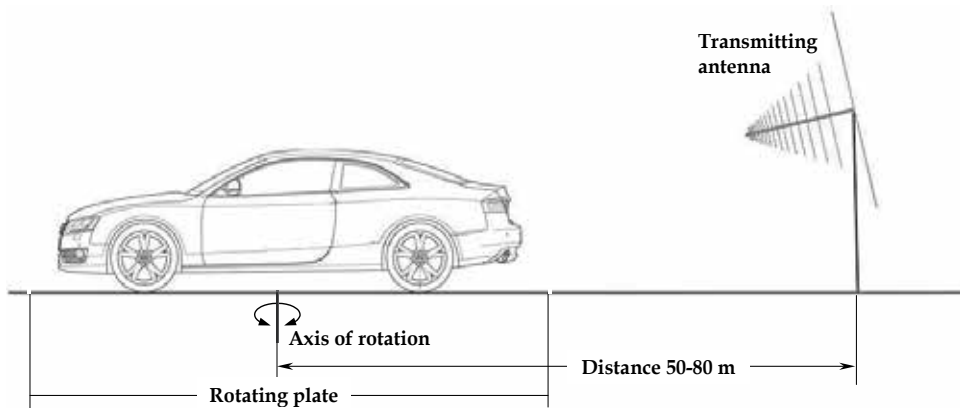


Fig. 23. Test setup for antenna pattern measurements

In the current example, reception of the glass antenna placed in a rear window of an AUDI A5 model is examined. An aim of the testing is to analyze the influence of different antenna amplifiers on the level of the received signal. First, a passive antenna is analyzed, and then five different amplifiers, one after another, are connected to the antenna to compare the received voltages. The simulations are done at selected frequencies in FM and DAB/TV (band III) ranges. To obtain vertical and horizontal components of the far-field antenna patterns, excitation of the transmitting antenna is replaced by vertically and horizontally polarized plane waves with equivalent magnitudes. The elevation angle of the incident plane wave corresponds to the location of the transmitting antenna (Fig. 23) and is $\theta = 85^\circ$. Instead of rotating the car, in simulation model it is possible to vary the azimuth angle ϕ from 0° to 360° to obtain the received signal as a function of azimuth angle. In a given example, angle ϕ varies from 0° to 350° with a step of 10° (Fig. 24). One set of vertically polarized waves and one with horizontal polarization gives a total of 72 incident plane waves. A multi-excitation technique is used to effectively perform these simulations.

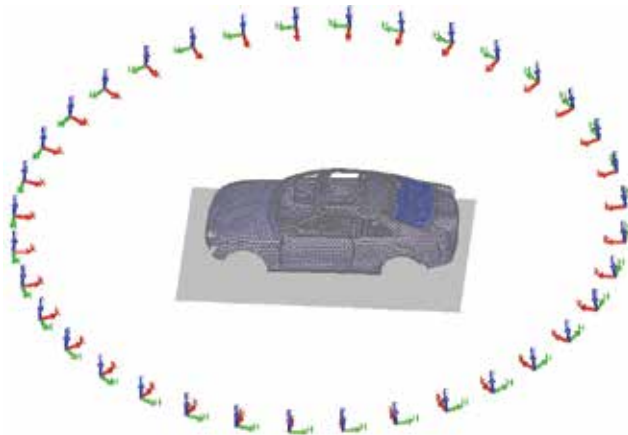


Fig. 24. A Car body exposed by plane waves incident from different angles

To consider different amplifiers, a multi-partitioned technique is also used. Amplifiers are included in a simulation model as 2-port networks with measured S-parameters, see Fig. 25 a) to e), and applied to the pigtail wire connected to the antenna structure. In multi-

partitioned calculations, the car body and the complete glass antenna (Fig. 26), except of the pigtail wire connected to the antenna, are defined as the basis part. While 6 copies of the pigtail wire are defined as additional parts: 5 for active antenna with different amplifiers (Fig. 27), 1 with non-radiating 3-cm TL element with 50-Ohm resistance for passive antenna.

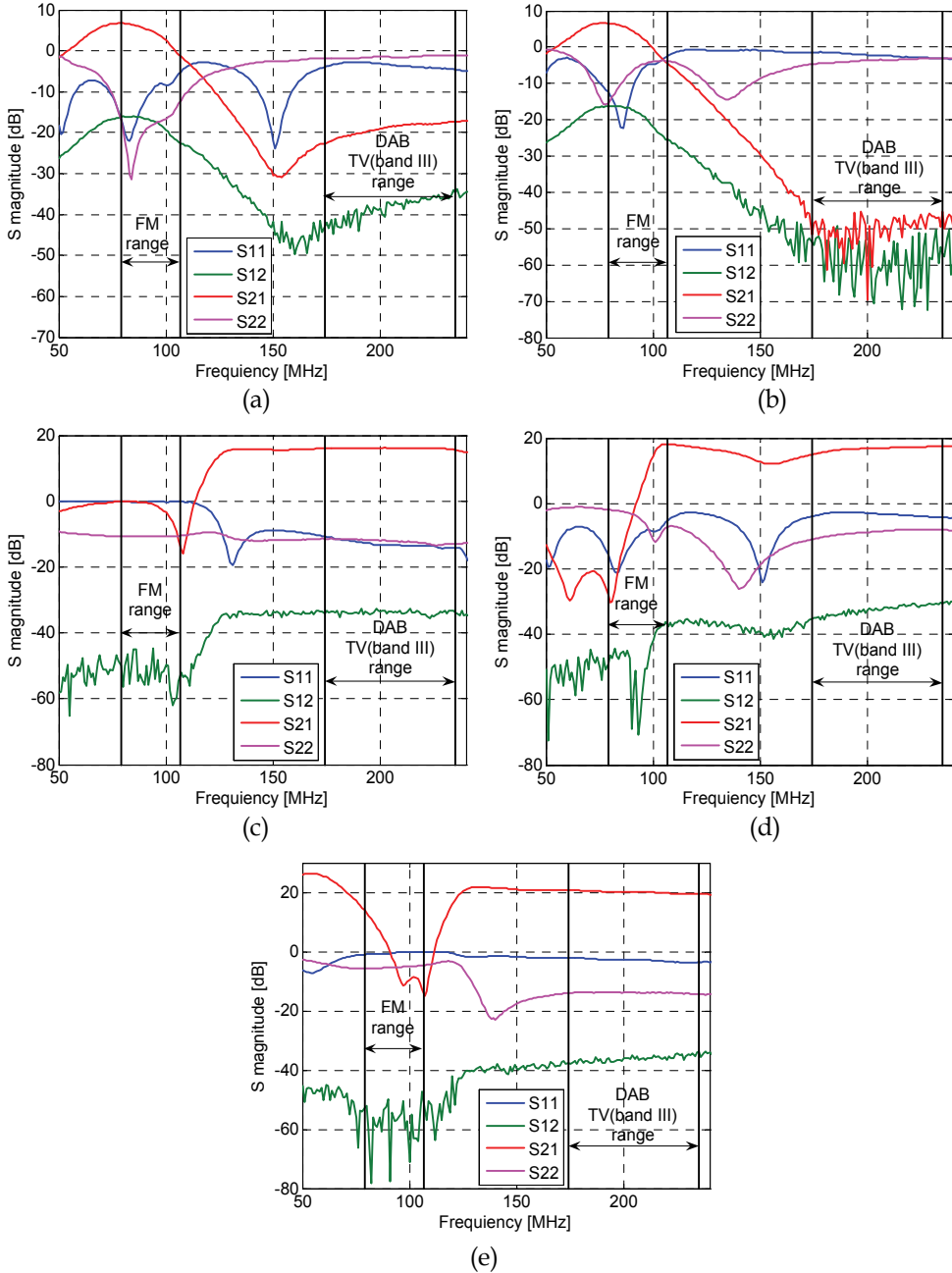


Fig. 25. Measured S-parameters of RF amplifiers as a function of frequency: a) AM/FM1 amplifier, b) FM2 amplifier, c) DAB amplifier, d) TV1 amplifier, e) TV3 amplifier

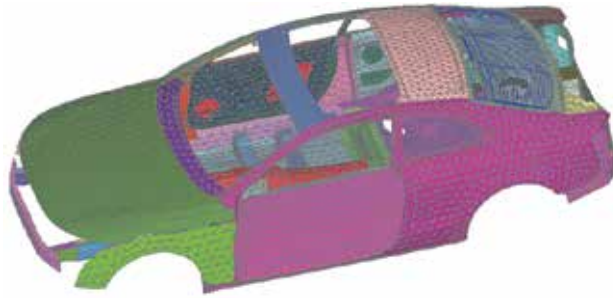
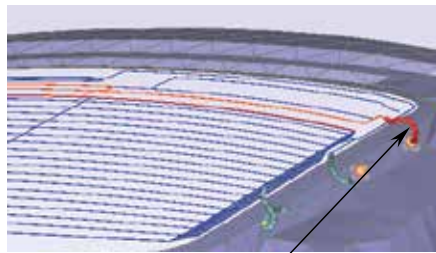


Fig. 26. A car model with a complete antenna pattern considered as a basis part



Pigtail wire with amplifier model

Fig. 27. Pigtail wire copies with different amplifiers (partitions)

Fig. 28 shows calculated voltages received by the antenna with different amplifiers at a certain frequency $f = 174$ MHz as a function of azimuth angle ϕ of incident plane wave for vertical and horizontal polarizations. A received voltage for the passive antenna is considered as a reference to show the effect of the amplifier. Besides, Figs. 29 and 30 show the frequency dependencies of the averaged received voltages (over ϕ angle) for the different frequency ranges and polarizations of incident plane wave.

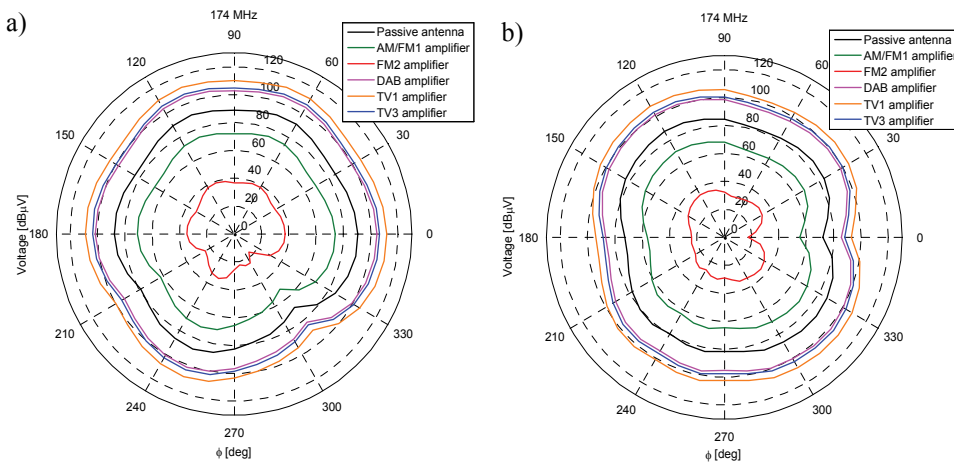


Fig. 28. Voltage received by antenna with different amplifiers as a function of azimuth angle of plane wave at a frequency 174 MHz: a) vertical polarization, b) horizontal polarization

The presented results clearly show the effect of amplifiers. In the FM frequency range AM/FM1 and FM2 amplifiers give a gain of 5-6 dB for both components, except of frequencies 100 MHz and 106.6 MHz, where the amplifier gain goes down. DAB, TV1 and TV3 amplifiers give a quite stable amplification of 15-20 dB in a complete DAB/TV (band III) range. While this may seem to be a rather trivial result, it is quite important to be able to assess the actual gain of the amplifier in the complex environment of a complete vehicle, where the many installed antennas and amplifiers are strongly coupled.

Comparison of CPU times for the direct and multi-partitioned approach, both using the multi-excitation regime (Table 4), shows the 3.5 gain in calculation time for 6 partitions. This demonstrates the efficiency of the multi-partitioned scheme for vehicle antenna problems.

Solution type	CPU time for a one frequency point
Direct solution with multi-excitation (6 tasks; 72 excitation sources)	9.84 hours (1.64 hours per task)
Matrix Partitioning with multi-excitation (6 partitions; 72 excitation sources)	2.85 hours (2 hours for basis + 0.85 hours for 6 partitions; 8.5 minutes for each partition)

Table 4. Summary of computational times

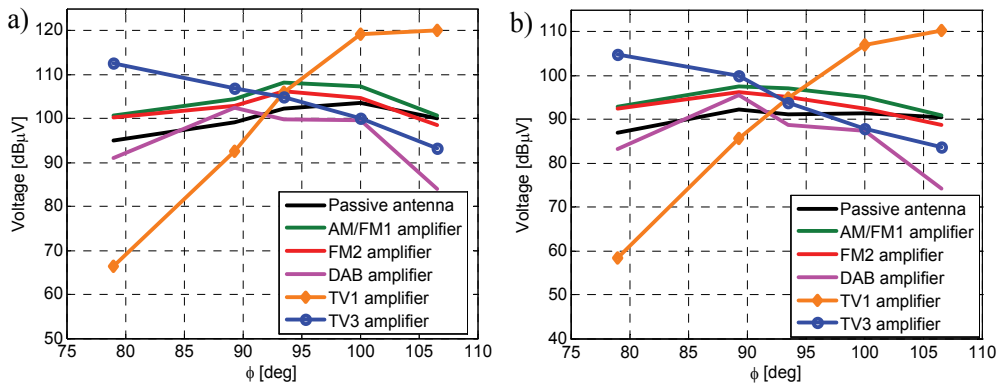


Fig. 29. Averaged received voltage in FM frequency range:

a) vertical component, b) horizontal component

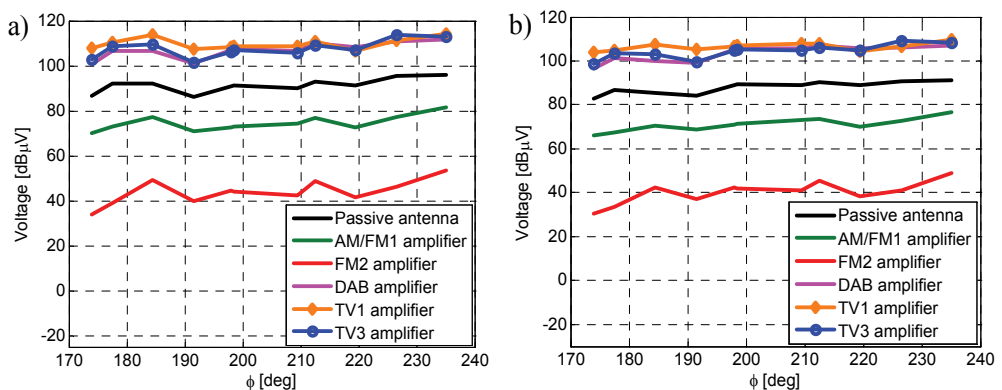


Fig. 30. Averaged received voltage in DAB/TV (band III) frequency range:

a) vertical component, b) horizontal component

8. Conclusion

Modern automotive antenna simulations represent a sophisticated process that requires development of the new computational methods and techniques. When these methods are applied, the overall design process can be speed up considerably. In this chapter, a number of recent developments in this area have been described, which are based on the enhancements of the traditional MoM scheme. A special attention has been devoted to the adaptive and hybrid methods, special Green's functions for conformal glass antennas, and optimization techniques. Validation and application examples have been considered along with supplied experimental data. The benefits of the described new computational methods and techniques have been illustrated. It has been shown that the combined usage of traditional and special methods and techniques described in this chapter facilitates obtaining the accurate and optimal solution of complicated automotive antenna problems.

9. References

- Ala, G. & Di Silvestre, M.L. (2002). A simulation model for electromagnetic transients in lightning protection systems. *IEEE Transactions on Electromagnetic Compatibility*, Vol. 44, No. 4, November 2002, pp. 539-554.
- Bogdanov, F.G. & Jobava, R.G. (2003). Examination of boundary conditions performance for estimating accuracy of MoM solutions on square plate benchmark geometry using triangle doublet basis functions. *Microwave and Optical Technology Letters*, Vol. 39, No. 3, November 2003, pp. 193-196.
- Bogdanov, F.G.; Jobava, R.G. & Frei, S. (2004a). Scheme of improving accuracy of MoM solutions based on analysing boundary conditions performance, *Proceedings of the 2004 East-West Workshop, Advance Techniques in Electrodynamics*, pp. 217-224, Warszawa, Poland May 2004.
- Bogdanov, F.G.; Jobava, R.G. & Frei, S. (2004b). Estimating accuracy of MOM solutions on arbitrary triangulated 3-D geometries based on examination of boundary conditions performance and accurate derivation of scattered fields. *Journal of Electromagnetic Waves and Applications*, Vol. 18, No. 7, 2004, pp. 879-897.
- Bogdanov, F.G.; Jobava, R.G.; Gheonjian, A.L.; Yavolovskaya, E.A.; Bondarenko, N.G. & Injgia T.N. (2009). Development and application of an enhanced MoM scheme with integrated generalized N-Port networks. *PIERM 07*, pp. 135-148.
- Bogdanov, F.G.; Karkashadze, D.D.; Jobava, R.G.; Gheonjian, A.L.; Yavolovskaya, E.A. & Bondarenko, N.G. (2010a). Advantage of a hybrid MoM scheme with approximate Green function to model integrated glass antennas, *Microwave and Optical Technology Letters*, Vol. 52, No. 2, February 2010, pp. 351-354.
- Bogdanov, F.G.; Karkashadze, D.D.; Jobava, R.G.; Gheonjian, A.L.; Yavolovskaya, E.A.; Bondarenko, N.G. & Ullrich, C. (2010b). Validation of hybrid MoM scheme with included equivalent glass antenna model for handling automotive EMC problems. *IEEE Transactions on Electromagnetic Compatibility*, Vol. 52, No. 1, 2010, pp. 164-172.
- Bogdanov, F.G.; Jobava, R.G. & Tsereteli, P. (2010c). TriD: Tri-Dimensional code for electromagnetic modeling of arbitrary surface and wire configurations. User's Manual. Version 5.08, EMCoS, Tbilisi.
- EMCoS (2010a): EMC Studio, <http://www.emcos.com>
- EMCoS (2010b): EMCoS Antenna VirtualLab, <http://www.emcos.com>

- Erteza, A. & Park, B.K. (1969). Nonuniqueness of resolution of Hertz vector in presence of a boundary, and a horizontal dipole problem. *IEEE Transactions on Antennas and Propagation*, Vol. AP-17, May 1969, pp. 376-378.
- Jobava, R.; Bogdanov F.G.; Gheonjian, A. & Frei, S. (2005). Application of adaptive scheme for the method of moments in EMC automotive problems, *Proceedings of the 16th International Zurich Symposium on Electromagnetic Compatibility*, pp. 131-136, Zurich, Switzerland, February 2005.
- Harrington, R.F. (1968). *Field Computation by Moment Methods*, Macmillan Publishing Company, New York.
- Harrington, R.F. & Mautz, J.R. (1975). An impedance sheet approximation for thin dielectric shells. *IEEE Trans. Antennas and Propagation*, Vol. 23, No. 4, July 1975, pp. 531-534.
- Miller, E.K.; Poggio, A.J.; Burke, G.J. & Selden, E.S. (1972a). Analysis of wire antennas in the presence of a conducting half-space: Part I. The vertical antenna in free space. *Canadian Journal of Physics*, Vol. 50, 1972, pp. 879-888.
- Sommerfeld, A. (1949). *Partial Differential Equations in Physics*. New York: Academic Press.
- Su, D.Y.; Fu, D.-M. & Chen, Z.-H. (2008). Numerical modeling of active devices characterized by measured S-parameters in FDTD, *Progress in Electromagnetics Research*, PIER 80, 2008, pp. 381-392.

Voltage Stability Analysis of Automotive Power Nets Based on Modeling and Experimental Results

Tom P. Kohler¹, Rainer Gehring², Joachim Froeschl²,
Dominik Buecherl¹ and Hans-Georg Herzog¹

¹*Technische Universitaet Muenchen*

²*BMW Group
Germany*

1. Introduction

In recent years, there has been a trend toward increasing electrification in automotive engineering. On the one hand, the quantity of electronic control units (ECUs) as well as installed functions has increased. With the goal of reduced fuel consumption, engine-start-stop systems were being introduced, and more and more components which were previously mechanically driven are now electrically operated. In today's luxury class vehicles there are up to 80 ECUs (Polenov et al., 2007; Hillenbrand & Muller-Glaser, 2009) servicing a wider range of customer needs in the areas of comfort, driving dynamics, and safety. On the other hand, the demands for electrical power as well as the power dynamics have permanently been increasing, as well. Loads like electrical power steering, chassis control systems, and engine cooling fans with more than 1 kW peak power are installed in the 12 V power net. Fig. 1 presents the increase of both installed alternator power and the total nominal current of the fuses in the latest decades.

As the electric power demand increases, automotive power nets must operate close to their limits and it has become increasingly difficult to guarantee voltage stability within the 12 V system (Surewaard & Thele, 2005; Gerke & Petsch, 2006; Polenov et al., 2007). In the example of a luxury class vehicle, the continuous power of heating in winter, air conditioning in summer, ECUs, sensors, and consumer electronics can be more than 600 W. If this load is augmented by electric chassis control systems, voltage drops will be inevitable. Voltages below a certain level across the terminals of electrical components can lead to non specified behaviour. This can be manifested in a flicker of lights or changes in noise of the blower fans (Surewaard & Thele, 2005), a malfunction of the navigation system or even an ECU reset. Therefore, such complex problems are not only noticeable to passengers, but are also a safety relevant issue.

To guarantee the proper functioning of all electrical components, a stable voltage supply must be realized during the development and design of the electrical power net. For this reason, a thorough understanding of the electrical phenomena in distributed power nets is necessary.

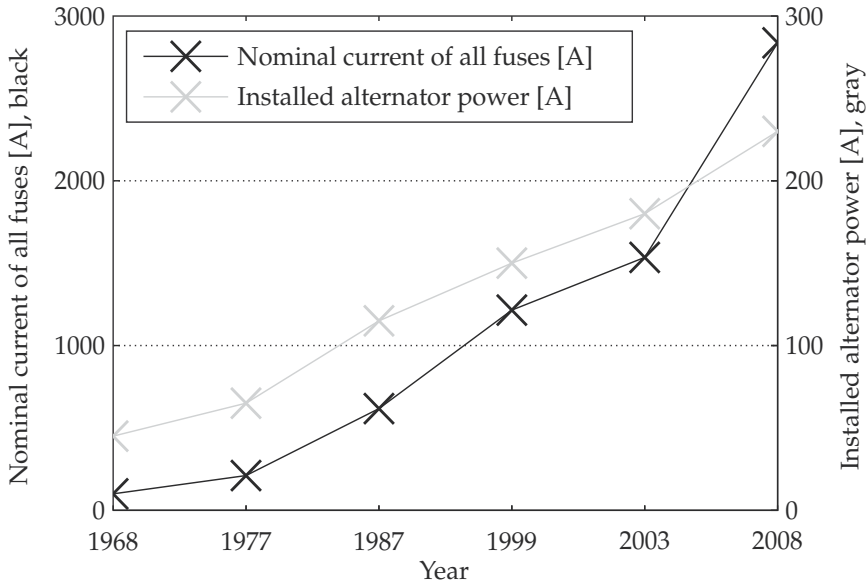


Fig. 1. Increase of the total nominal current of the fuses (left scale) and the installed alternator power (right scale) in the latest decades.

2 Goals and approach

This paper describes the modeling of a distributed automotive power net with emphasis on the wiring harness and the chassis ground. All relevant physical effects and electrical phenomena should be taken into account to enable sustainable statements on voltage stability. With this knowledge, a modeling environment will be developed that enables simulations and analysis of the voltage characteristics within the entire wiring harness. So critical situations can be detected, an optimization of both power demand and topology of power nets must be feasible.

First of all, the electric power net and its components are described to give a system understanding. Likewise, a power net test bench is presented, to serve as a platform to verify and evaluate the simulation results. In the next step, the primary components necessary for power net analysis are examined. Besides the alternator, battery, load, and fuses, the focus is on the modeling of the chassis ground as well as the wiring harness.

After deducing characteristic equations of the electrical field, voltage drop, DC resistance, and AC resistance from physical laws, the respective models are compared with measurements of the real components in the power net test bench which was previously introduced.

In the analysis of the chassis ground, a method for calculating the resistance between two grounding bolts is shown. Important technical aspects of the car body are also discussed, such as the thickness of the sheet steel or the influence of the weld seam at the grounding bolts. As part of the development of the wiring harness model, the derivation of the per length parameters R' , L' , and C' is discussed, and the influence of the existing frequencies is considered. Furthermore, guidelines that show appropriate models for different frequencies are derived. Next, the entire distributed network of the electrical power net of a luxury class vehicle is investigated, and conclusions concerning voltage stability are drawn. Finally, we present an outlook on further research.

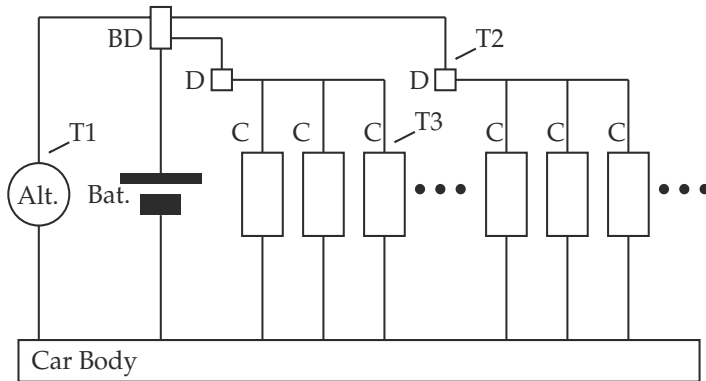


Fig. 2. Schematic of the automotive 12 V power net. The alternator (Alt.) is connected to the battery (Bat.) via the battery distribution unit (BD). The electrical components (C) are supplied via further distribution boxes (D). These are connected to the car body to close the circuits to the alternator and the battery. T1, T2, and T3 are test points of the measurement in Fig. 4.

3. The electric power net

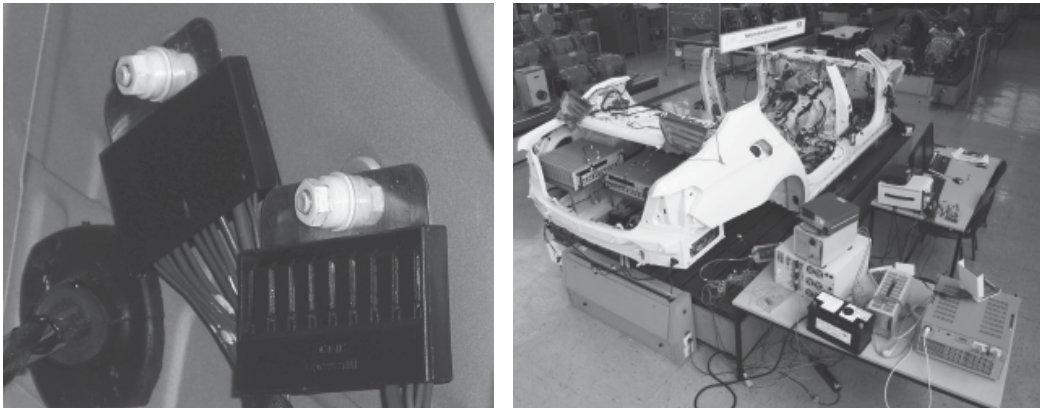
The automotive power net serves the electric and electronic components in the vehicle with electric power. In this article, the wiring of the communication systems such as bus lines or sensor and signal wires are not perceived as a part of the electric power net.

3.1 Single level power nets

At first, to begin with a basic example, only power nets with one single voltage level are considered. A schematic topology of a 12 V power net is shown in Fig. 2. The alternator (Alt. in Fig. 2), which is coupled via a belt drive to the combustion engine, is used as an energy source. It delivers electrical energy to charge the battery (Bat.) and to supply the electrical components (C).

The alternator is able to supply all power demands and forces the maximum voltage to its setpoint of about 14 V in normal operation. Both at the start-up of the combustion engine and when the power demand of all loads exceeds the alternator's supply, the battery must provide the power difference. In this case, the power net voltage decreases to the battery's terminal voltage of 12.7 V and below (Kiehne, 2003). Due to the internal resistance of the battery, the terminal voltage depends on the battery load, and further voltage reductions occur in case of high current demands. Therefore, the resulting voltage at the battery's terminals can be significantly lower than 12 V. Since the alternator's dynamics are limited in order to avoid fluctuations of the combustion engine speed and reduction of customer's driving comfort (Reif, 2009) these voltage drops occur especially when a significant current draw with a short rising time occurs.

Starting from the battery distribution box (BD), all electrical components (C) are connected to the power net via further distribution boxes (D) and wires that are assembled to a wiring harness. The negative terminals of the components are connected via wires to grounding bolts that are welded to the car body (Fig 3a). The negative terminal of the battery is also connected to a nearby grounding bolt. This means that the car body is used as a return conductor to close the circuits to the battery. Additionally, there are further voltage reductions in the distributed system of the wiring harness, in power distribution units, and in fuse boxes.



(a) The negative terminals of the components are connected to bus bars. Here, two bus bars are screwed to two grounding bolts that are welded to the car body.

(b) Installation of the power net test bench using an entire power net consisting of an original car body and wiring harness of a luxury class vehicle as well as source, storage and loads.

Fig. 3. Power net test bench.

Therefore, the installation point of a component is an important factor in determining its resulting voltage. Thus, the electric power net can be modelled as a tree with the root node at the positive terminal of the alternator or battery and all end-nodes connected to the car body return conductor.

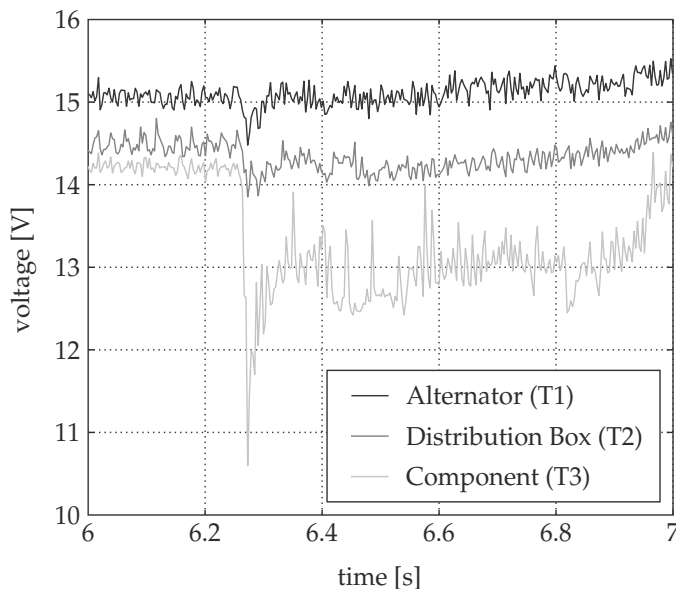


Fig. 4. Voltage curves measured across test points at the alternator (T1), a distribution box (T2), and at the terminals of a chassis control system (T3), see Fig. 2. The different voltage levels and voltage drops show that the voltage at each component depends on its connection to the power net.

The measured voltage curves at a high power demand during the start-up of an electrical chassis control system are exemplified in Fig. 4. The peak current of the chassis control system is 50 A. The current peak of 50 A causes a voltage drop of 3.5 V at the terminals of the chassis control system (test point T3 in Fig. 2). At the distribution box, a drop of 0.7 V can be detected (T2); at the alternator, the voltage drop is 0.6 V (T1).

Thus, it can be affirmed that there is not one single voltage in the power net, but a range from the maximum voltage at the alternator or battery, to a minimum at the farthest electrical components. The different voltage levels and voltage drops at the test points show that the voltage across the terminals of a component depends on the connection to the power net. As a consequence, it is necessary to consider the influence of the wiring harness and the chassis ground for voltage stability analysis.

3.2 Multi level power nets

For many years, the introduction of multi-voltage systems has been discussed, as this would bring many benefits (Kassakian et al., 1996). The advantages of higher voltage power nets, e.g. the proposed 42 V system, were clearly shown in (Miller et al., 1999; Miller & Nicastrì, 1998; Lukic & Emadi, 2002), but the automotive industry mainly stuck to the conventional reliable 12 V power net.

From the view of voltage stability analysis, multi level power nets are only two separated single level power nets coupled by an energy converter like a DC chopper converter. Therefore, without loss of generality, only a single voltage level is analyzed in this article. However, the components are analyzed for a wide range of voltages, so as to enable an eventual simulation of different types of power nets including multivoltage nets.

3.3 Power net test bench

To verify both the single components and the the whole system, a power net test bench has been built (Fig. 3b). This reference power net implements the schematic topology presented in Fig. 2. The primary goal of this power net is to achieve accurate measurement results. A further goal was to make the power net easily configurable, so that both real scenarios and synthetic test cases can easily be tested. In the following, the components necessary to emulate a realistic behavior of the power net in the test bench are described.

Storage/Battery: Although a battery simulation system has the advantage that the measurements and tests are easily repeatable and configurable (Schweighofer et al., 2003; Thanheiser et al., 2009), real batteries are used. Since the electrochemical processes in batteries are very complex, it is not easy to model, especially the transient processes, with the required accuracy. Several commercial battery sizes can be employed, ranging from compact to luxury class car's batteries ($C_{\text{bat}} = 60\text{...}90\text{Ah}$) in this test bench. The state of charge (SOC) can be precisely adjusted at a dedicated battery conditioning test bench in order to provide equal conditions in the experimental procedure.

Source/Alternator: The alternator is emulated by a physical model executed on a real time system. Input parameters are the battery's voltage, the engine speed and the alternator's start temperature. The real time system controls a regulated 300 A power supply unit.

Wiring harness and chassis ground: For a realistic analysis of the power net's behavior, the distributed structure must be reproduced as accurately as possible. In particular, the exact location of power distribution units, fuse boxes, and clamp control is important. Therefore, a real wiring harness of a luxury class vehicle is used.

The car body, which serves as return conductor, is also part of the power distribution network.

Especially if several loads are using the same grounding bolt, interactions may be caused. Here, a car body of the BMW 7 series is applied (Fig. 3b).

Electric loads: The structure of up to 80 loads is very complex in reality. Therefore, it is sufficient to consider only a representative selection to analyze voltage stability. While placing the electric loads, it is necessary to regard the power system's structure. This includes the choice of power distribution and fuse boxes, the wire's lengths and cross sections, as well as the number and location of grounding bolts. With an accurate placement, it is possible to analyze all real kinds of requests on the power net with considerably fewer loads. The ECUs in itself are not built in, but substituted by regulated electronic loads having high dynamics, which can demand arbitrary power profiles and emulate the behavior of the ECUs. In this way, the experimental studies are more flexible. For example, worst cases can easily be conducted, where multiple ECUs make power demands simultaneously.

Control and measurement: Both synthetic test cycles and measured power curves of the electric loads can be applied by the control software via analog control signals. A grid of about fifty voltage and current measurement points reports the state of the power net.

4. Modeling of the power net's components

To simulate the voltage, it is necessary to have stability models of the power net's components. The main components of the power net are the alternator, the battery, and the electrical loads. The wires of the wiring harness connect these components with each other. Furthermore, as presented in Fig. 2 the car body is part of the power distribution network. It is shown how these components can be modeled, with a particular focus on the wiring harness and the chassis ground modeling.

4.1 Alternator

The alternator delivers the electrical energy that is needed to supply the loads and to charge the battery. Usually, a claw-pole or Lundell alternator is employed in automotive power nets. The Lundell alternator itself is an electrically excited synchronous machine with a rectifier bridge. Via belt drive, the alternator is coupled to the combustion engine. As a consequence, the electrical energy output, and especially the current output I_{alt} , depends on the speed of the combustion engine. A voltage regulator modulates the excitation current I_{exc} to obtain a voltage level V_{alt} up to 15.5 V. Modern voltage regulators are equipped with diagnosis functions and are connected to one of the car's communication networks, e.g. the Local Interconnect Network (LIN). Fig. 5 shows a schematic of an alternator.

A suitable way to model the alternator for the voltage stability analysis is by means of electrical equivalent circuits. Examples of how such models can be derived are presented in (Bai et al., 2002; Lange et al., 2008).

4.2 Battery

For battery modeling, different approaches are possible. The most common are electrochemical models, mathematical models, and electrical models (Chen & Rincon-Mora, 2006). Depending on the purpose of the simulation, an adequate approach must be chosen. Because the I-V-characteristics are the most relevant physical phenomena to describe the battery in a voltage stability analysis of the automotive power net, an electrical model is the most suitable. These electrical models are equivalent circuits, consisting of voltage sources, resistors, and capacitors. (Ceraolo, 2000; Barsali & Ceraolo, 2002; Chen & Rincon-Mora, 2006) present detailed information on electrical battery models.

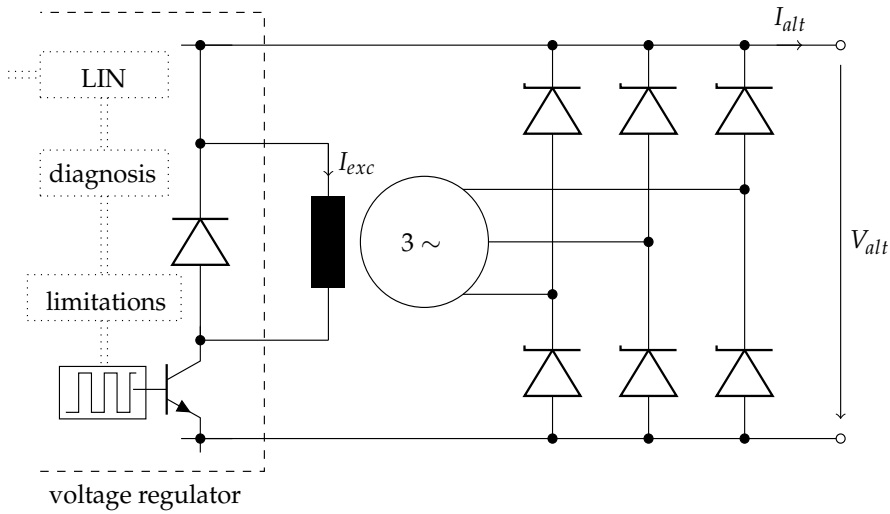


Fig. 5. Schematic of an automotive alternator. A voltage regulator controls the excitation of the electrical machine. The rectifier bridge converts the output of the electrical machine to DC.

A possible way to derive the parameters of such models is the method of impedance spectroscopy (Mauracher & Karden, 1997). Another method is to measure the voltage during discharge pulses and to fit the parameters based on the current and voltage curves (Bohlen, 2008).

4.3 Wiring harness

A common way to model transmission lines is by means of lumped circuit models (Paul, 1994). An example of a lumped- π model of two wires above a ground plane is shown in Fig. 6. The derivation of the parameters of this model is presented.

To obtain simple but accurate models, it is discussed how the model can be simplified. To calculate the parameters, information on the geometrical arrangement of the single wires is needed. Fig. 7 shows an example of an arrangement of two wires above a ground plane.

The DC resistance of a wire with constant cross section A and length l can be calculated by

$$R_{dc} = \rho \frac{l}{A}, \tag{1}$$

where ρ is the specific resistance of the conductor material. Additionally, it is common to use the per length resistance R' in Ω/m .

$$R'_{dc} = \frac{\rho}{A} \tag{2}$$

Furthermore, the specific resistance ρ is a function of the temperature and can be approximated by a Taylor series. For the temperature range that is relevant for the voltage analysis, this series can be stopped after the linear term:

$$\rho(\vartheta) = \rho_{\vartheta_{20}} (1 + \alpha_{\vartheta_{20}} (\vartheta - \vartheta_{20})) \tag{3}$$

In (3) a reference temperature of 20°C was chosen. For copper $\alpha_{\vartheta_{20}}$ is $3.9 \cdot 10^{-3} \text{ 1/K}$ and $\rho_{\vartheta_{20}}$ is $0.0178 \text{ }\Omega\text{mm}^2/\text{m}$. This means a temperature rise of 25.8 K results in an increase in resistance of 10%.

The frequency f must also be considered. Because of the skin effect, the AC resistance increases with frequency. The following formulas apply to solid, cylindrical conductors with circular cross section. The skin depth δ is the depth below the surface of the conductor at which the current density decays to $\frac{1}{e}$. The skin depth δ is given by

$$\delta = \frac{1}{\sqrt{\pi\mu\sigma f}} \tag{4}$$

μ is the permeability and σ is the conductivity of the conductor material.

Usually, the AC resistance is calculated with the assumption that the current is uniformly distributed over an annulus at the wire surface of thickness equal to δ according to:

$$R'_{ac} = \frac{r^2}{2r\delta - \delta^2} R'_{dc} \approx \frac{r}{2\delta} R'_{dc} \text{ for } \delta \ll r \tag{5}$$

This approximation is suitable for high frequencies (Paul, 1994). To get an estimation of when the influence of the skin effect has to be considered, a more accurate calculation is based on a power series expansion for the Bessel functions (Simonyi, 1963). If the skin depth is more than 50% of the radius, the AC resistance can be approximated by

$$R'_{ac} = \left(1 + \frac{1}{3} \left(\frac{r}{2\delta}\right)^4\right) R'_{dc} \text{ for } \delta > \frac{r}{2}. \tag{6}$$

A method to calculate the skin effect in stranded wires is presented in (Gaba & Abou-Dakka, 1998), where a_{geo} is the geometrical mean distance of the strands.

$$R'_{ac} = \sqrt{2 \left(\frac{1 + (0,86\zeta)^4}{2 + (0,86\zeta)^4} \right)} \cdot R'_{dc} \text{ with } \zeta = \frac{a_{geo}}{\sqrt{2}\delta} \tag{7}$$

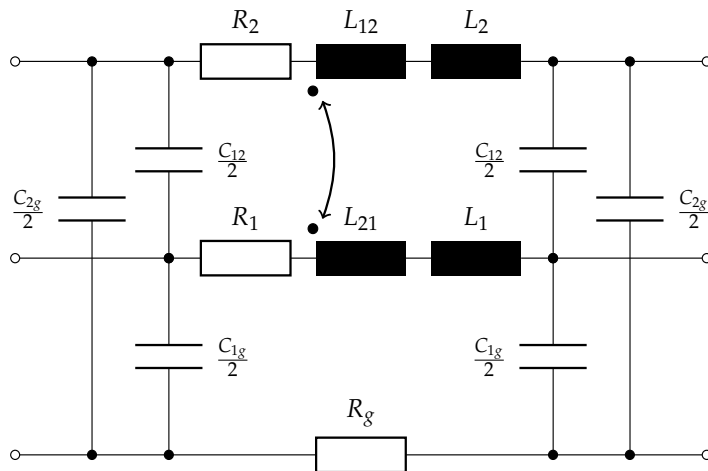


Fig. 6. Lumped- π model for two wires above a ground plane (Smith et al., 1994). The model consists of 13 concentrated circuit elements.

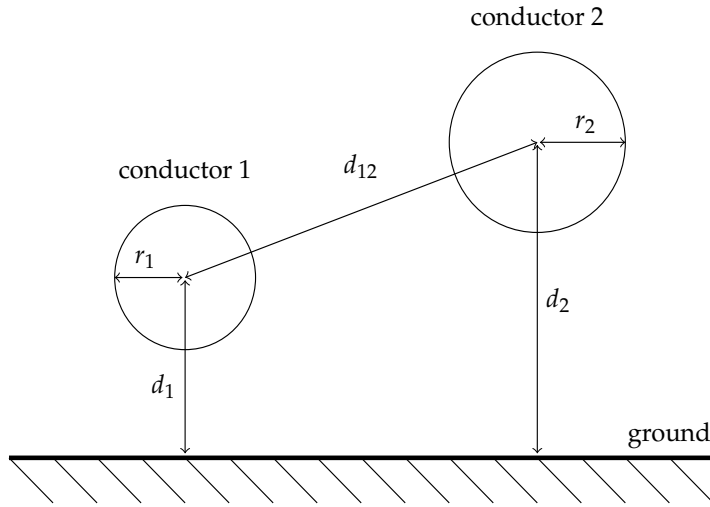


Fig. 7. Two conductors above a ground plane. Information on the geometrical dimensions of the arrangement is necessary to calculate the parameters of the lumped- π model.

The per length self inductances L'_1 and L'_2 can be calculated according to:

$$L'_1 = \frac{\mu}{2\pi} \ln\left(\frac{2d_1}{r_1}\right) \quad L'_2 = \frac{\mu}{2\pi} \ln\left(\frac{2d_2}{r_2}\right). \quad (8)$$

The per length mutual inductance L'_{12} is:

$$L'_{12} = L'_{21} = \frac{\mu}{2\pi} \ln\left(\frac{D_{12}}{d_{12}}\right) \quad \text{with} \quad D_{12} = \sqrt{d_2^2 + 4d_1d_2} \quad (9)$$

The per length capacitances can be derived by:

$$C'_{1g} = 2\pi\epsilon \frac{\ln\left(\frac{2d_2d_{12}}{r_2D_{12}}\right)}{\ln\left(\frac{2d_1}{r_1}\right) \ln\left(\frac{2d_2}{r_2}\right) - \ln^2\left(\frac{D_{12}}{d_{12}}\right)} \quad (10)$$

$$C'_{2g} = 2\pi\epsilon \frac{\ln\left(\frac{2d_1d_{12}}{r_1D_{12}}\right)}{\ln\left(\frac{2d_1}{r_1}\right) \ln\left(\frac{2d_2}{r_2}\right) - \ln^2\left(\frac{D_{12}}{d_{12}}\right)} \quad (11)$$

$$C'_{12} = 4\pi\epsilon \frac{\ln\left(\frac{D_{12}}{d_{12}}\right)}{\ln\left(\frac{2d_1}{r_1}\right) \ln\left(\frac{2d_2}{r_2}\right) - \ln^2\left(\frac{D_{12}}{d_{12}}\right)} \quad (12)$$

ϵ is the permittivity of the material surrounding the conductors.

Such calculations can be used to determine values of the parameters for typical wiring harness arrangements in automotive applications. Based on these guidelines, the influence of resistance, inductance, and capacitance on the voltage stability is evaluated in (Gehring et al., 2009) and modeling guidelines are derived.

The relevant frequency range for the voltage stability analysis is up to 10 kHz. In this range, the capacitance of the wires can be neglected. The per length capacitance is in the range of

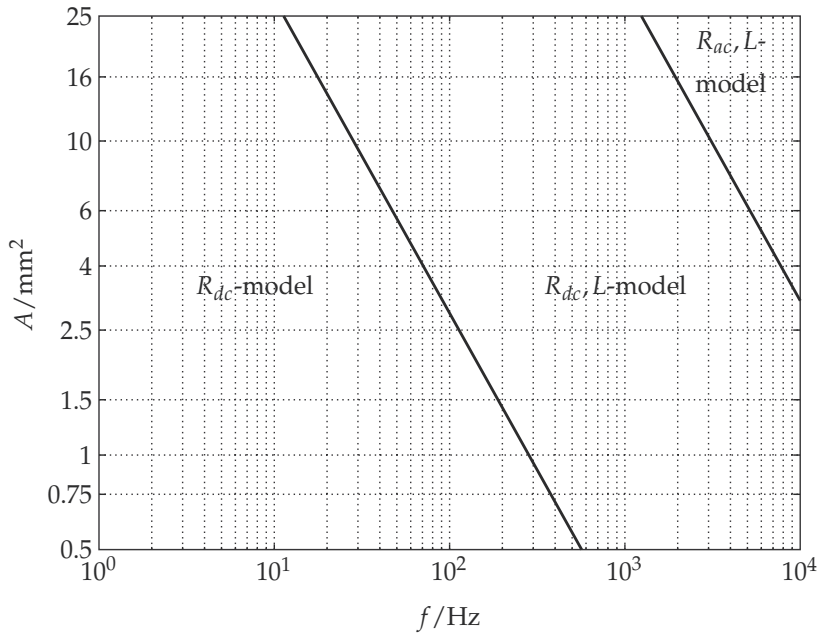


Fig. 8. Modeling guidelines: Based on the relevant frequency and the cross section of the wire, an adequate model can be selected.

picofarad. This means that for a frequency up to 10 kHz, $\frac{1}{\omega C}$ is in the range of megohm. Compared to the per length resistance, which is in the range of milliohm, the influence of the capacitance is not relevant.

In contrast to this, the influence of the inductance must be considered (Gehring et al., 2009). The per length inductance is in the range of microhenry. This means that for a frequency up to 10 kHz $\omega L'$ is in the range of milliohm and comparable to the per length resistance.

In addition, the influence of the skin effect can become relevant even in the range of a few kilohertz.

Based on typical arrangements of automotive wiring harnesses, parameter values can be derived and used to define modeling guidelines. Fig. 8 shows these modeling guidelines.

Depending on the cross section and the frequency, a suitable model can be selected. For a cross section of 25 mm^2 , a simple model with R_{dc} can be used up to 10 Hz. For a cross section of 2.5 mm^2 , the R_{dc} model is appropriate up to a frequency of 100 Hz. If the cross section is 0.5 mm^2 , the R_{dc} model can be used up to a frequency of 560 Hz. The validation of these modeling guidelines can be found in (Gehring et al., 2009).

4.4 Fuses

Fuses protect the wires of the power net against overcurrent. The most common fuses in automotive power nets are blade fuses or bolt-on fuses with diffusion pill. Fig. 9 shows a schematic of these two different kinds of fuses.

Blade fuses usually have a rated current below 100 A. For higher currents, bolt-on fuses are used.

For the voltage stability analysis, the voltage drop across the fuses must be considered. Datasheets of fuse manufacturers offer resistance values that can be used to model fuses using electrical resistors. The behavior of fuses during opening is not part of the voltage stability

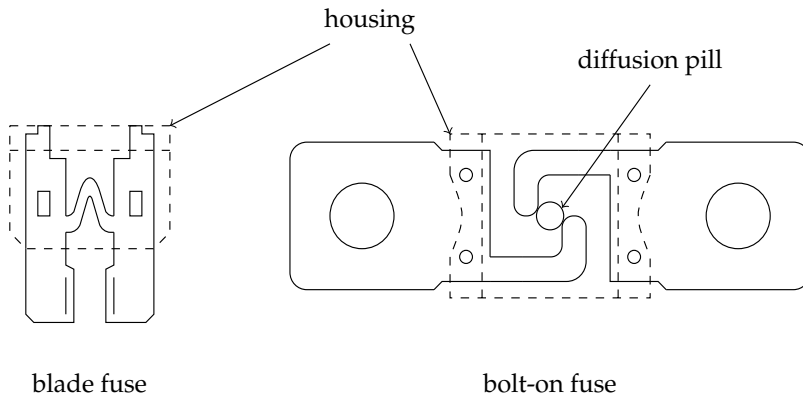


Fig. 9. For circuit protection, different kinds of fuses can be used. In the automotive wiring harness, the most common fuses are blade fuses or bolt-on fuses.

analysis presented in this article. For further information on this aspect see (Batchelor & Smith, 1999; 2001).

4.5 Chassis ground

As shown in Fig. 2, the car body is part of the power distribution network. As a consequence, it is necessary to analyze the voltage drop across the car body. Fig. 3a shows how the wires of the wiring harness are connected to the car body. The single wires are mounted to a bus bar. A screw nut connects the bus bar to a threaded bolt. The bolt itself is welded to the car body. Based on considerations known in the field of high voltage engineering (Velazquez & Mukhedkar, 1984), a method to calculate the resistance between two grounding bolts is presented. Furthermore, the calculation results are compared with measurements from a real car body.

As the car body is a complex structure, the following assumptions simplify the theoretical approach to calculate the resistance.

- the considerations are based on a stationary electric flow field
- the electric field close to the grounding bolts is radially symmetric
- the car body is regarded to be a plane sheet of steel with constant thickness and constant electrical conductivity

Fig. 10 shows the simplified system. Two grounding bolts, each with a radius of r_1 , are welded to a flat sheet of steel. The steel thickness is d , the distance between the bolts is r_2 .

Firstly, the field of one grounding bolt is regarded. The electric field \vec{E} is related to the electric current density \vec{J} through the conductivity σ :

$$\vec{J} = \sigma \vec{E} \tag{13}$$

The current I is defined by the integral over a control surface S over the current density \vec{J} .

$$I = \int_S \vec{J} d\vec{S} \tag{14}$$

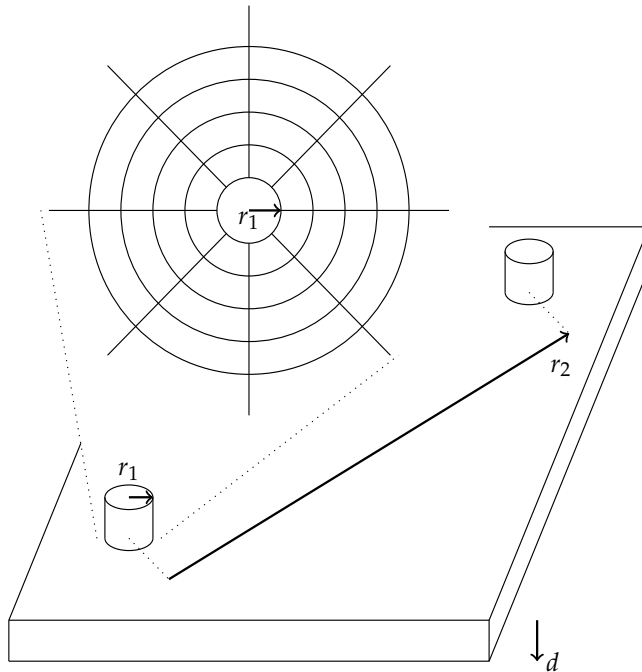


Fig. 10. The car body is regarded as a plane sheet of steel and it is assumed that the field close to the grounding bolts is radially symmetric.

In case of a grounding bolt, S is the jacket of a cylinder with radius r_1 , the radius of the grounding bolt, and the height d , the thickness of the sheet of steel. With (13) and (14) the electric field for $r > r_1$ becomes

$$\vec{E} = \frac{I}{2\pi\sigma r d} \vec{e}_r. \quad (15)$$

Because of the radially symmetric field, \vec{E} only has a component in r -direction. By superposition of two fields, as described in (15), the voltage and resistance between two grounding bolts, respectively, can be calculated. The voltage between the two bolts is

$$V = \int_{r_1}^{r_2-r_1} \vec{E} dr. \quad (16)$$

For the system of two grounding bolts as shown in Fig. 10, it follows that:

$$V = \frac{I}{2\pi\sigma d} \int_{r_1}^{r_2-r_1} \frac{1}{r} + \frac{1}{r_2-r} dr \quad (17)$$

With $V = RI$, the resistance between the two grounding bolts is:

$$R = \frac{1}{\pi\sigma d} \ln \frac{r_2-r_1}{r_1} \quad (18)$$

As the bolts are welded to the car body, an offset $R_{welding}$ is added, to account for the influence of the welding quality. This offset is the sum of the resistances caused by the weld seam at each of the two grounding bolts. Hence, to calculate the resistance between two grounding

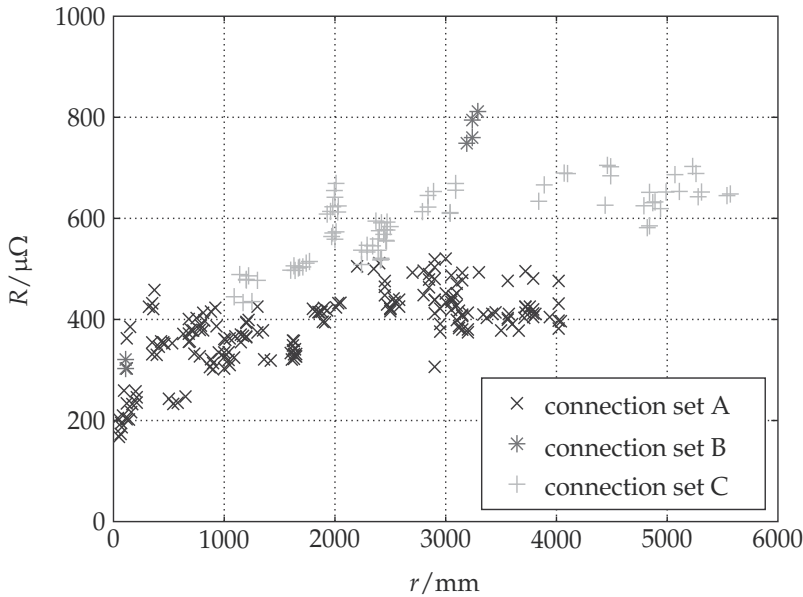


Fig. 11. Measured resistance between two grounding bolts. The resistance values are grouped according to the location of the grounding bolts.

bolts with radius r_1 set at a distance r_2 apart, the bolts being welded to a plane sheet of steel with thickness d and conductivity σ , the following equation can be used:

$$R = R_{welding} + \frac{1}{\pi\sigma d} \ln \frac{r_2 - r_1}{r_1} \tag{19}$$

This theoretical approach was based on the assumption of a radially symmetric and stationary electric flow field. Furthermore, the car body was regarded as a plane sheet of steel with constant thickness. However, the car body is a complex structure of many metallic parts like girders and sheets of steel. Therefore, (19) has been compared with measurements on a real car body containing 23 grounding bolts. These 23 grounding bolts form a network with 253 possible connections. For each connection, a resistance value was measured by a four point measurement technique with a micro-ohm-meter. Fig. 11 shows the results.

The measured resistance values between two grounding bolts are grouped according to their location on the car body. One group represents connections of grounding bolts that are located in the passenger compartment or the trunk. These resistance values are marked as connection set A in Fig. 11. Another group represents the connections of grounding bolts that are located in the engine compartment. This is marked as connection set B in Fig. 11. The connection set C marks the connections with one grounding bolt located in the engine compartment and the other one in the passenger compartment or the trunk.

The measured resistance values can be used to parameterize the model derived in (19). This parameterization is shown in (Gehring et al., 2009). The influence of the weld seam $R_{welding}$ is between 85 and 160 $\mu\Omega$. If the grounding bolts are located close to each other on the same sheet of steel, than the parameter d is the thickness of this sheet of steel.

Equation (19) is based on the assumption of a plane sheet of steel with constant thickness. The car body, however, is a complex structure of girders and many different sheets of steel that are welded together. As a consequence, an equivalent thickness d' must be used for distant

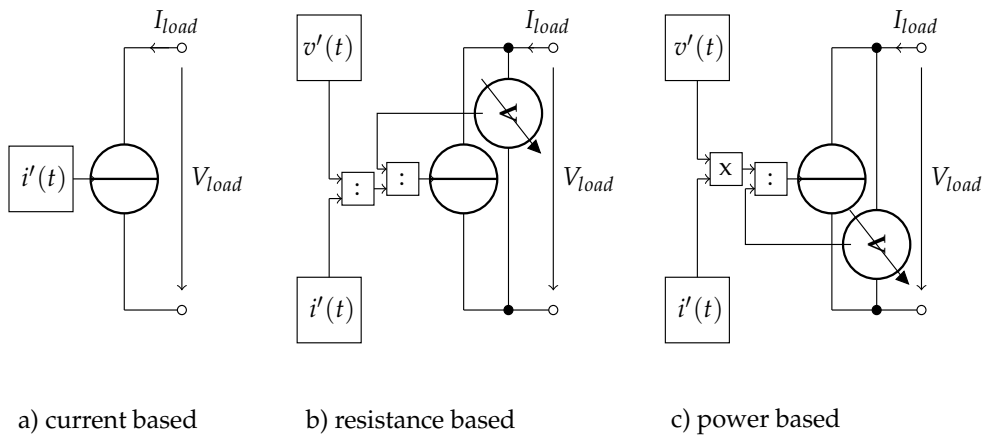


Fig. 12. Structure of the loads' models. Loads are modeled by current-, voltage- or power-based sinks.

connections. The grouping in the connection sets A, B, and C results in three different values for d' .

An overview of these parameters is shown in Tab. 1. As the considerations are based on a stationary flow field, the proposed model can be used for the low frequencies that are relevant for the voltage stability analysis. For investigations of higher frequencies, for example considerations in the field of EMC, other approaches are more appropriate. An example can be found in (Smith et al., 1994).

4.6 Loads

Loads can be modeled as controlled current sinks. Input information for these sinks are data derived by measurements of the voltage and the current of each load. Depending on the characteristics of each load, the structure of the sinks is current-, resistance- or power-based. Fig. 12 shows the structure of the loads' models.

If, according to the modeling guidelines shown in Fig. 8, the inductance of the wires needs to be modeled, then loads should be modeled as controlled resistors. Furthermore, the input impedance of each load, caused by the capacitors and inductors of the EMI filters, should be accounted for the controlled resistor.

Distance	Variable	Value
close connections	$R_{welding}$	85 $\mu\Omega$... 160 $\mu\Omega$
	d	1.0 mm
distant connections	$R_{welding}$	85 $\mu\Omega$... 160 $\mu\Omega$
	d' , passenger compartment & trunk (set A)	0.60 mm ... 0.86 mm
	d' , engine compartment (set B)	0.34 mm
	d' , mixed (set C)	0.45 mm ... 0.61 mm

Table 1. parameters of the grounding model according to (19)

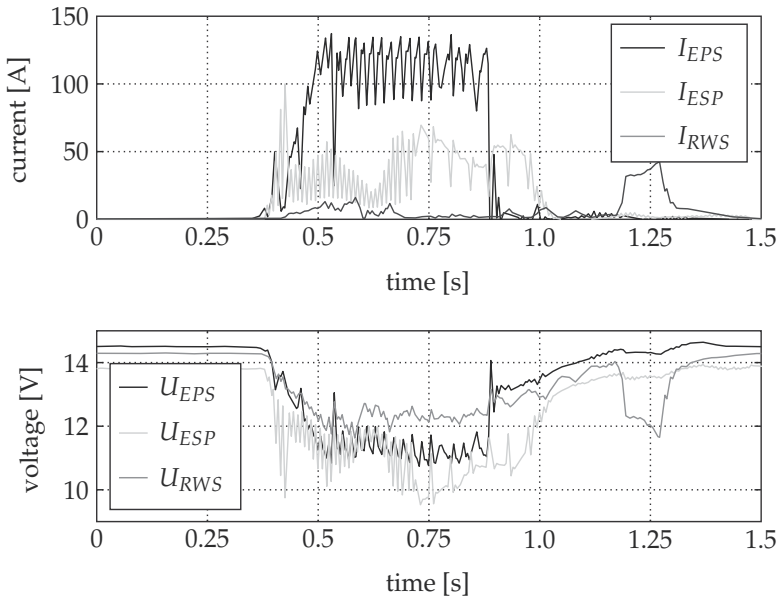


Fig. 13. Simulation example. During this driving scenario, different chassis control systems are active.

5. Simulation of the entire system

The models of the components form the basis for the simulation of the entire power net. With the simulation, different power net configurations with various loads and topologies can be put together and be evaluated in terms of voltage stability.

Fig. 13 shows a simulation example. The results of the simulation are compared with experimental results at the power net test bench. The first scenario which was investigated is based on measurements from a real car. In this scenario, the driver is driving at low speed and suddenly brakes to avoid hitting a pedestrian. The current and voltage curves of different loads were measured in the real car and used as inputs for the simulation and the test bench. Fig. 13 shows the current curves of three chassis control systems that are active during the driving scenario, and the resulting voltage curves at the terminals of these systems. The electrical power steering (EPS) reaches a maximum current of about 150 A, the rear wheel steering (RWS) a maximum current of 45 A. The electronic stability program (ESP) causes a current peak with a maximum of 90 A.

A comparison between the simulation results and the experimental results of the voltage curves of two of the three chassis control systems is shown in Fig. 14. U_{EPS} sim. is the simulated voltage, U_{EPS} me. is the measured voltage at the terminals of the electrical power steering. Analogously, U_{ESP} sim. and U_{ESP} me. are the simulated and measured voltages at the terminals, as produced by the electronic stability program. The deviations between the simulation and the experimental results are below 300 mV. Even at high current peaks, the accuracy of the simulated voltage compared to the measured voltage is in the range of 300 mV.

This means that the simulation can be used to investigate the voltage stability within the automotive power net. The derived simulation results represent the voltage behavior in an accurate manner.

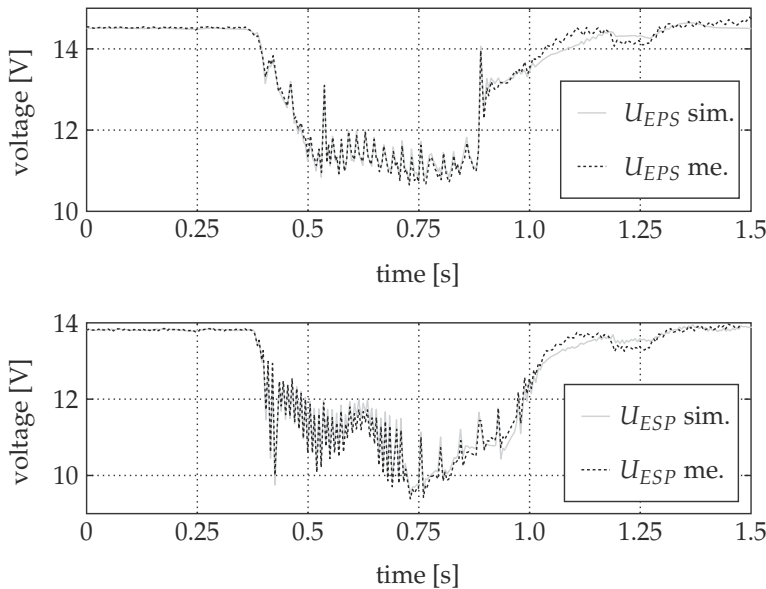


Fig. 14. Accuracy of the simulation at high voltage drops. The deviations are below 300 mV.

The advantage of using the simulation is that many different topologies of the power net can be evaluated virtually.

It must be considered, however, that the test bench is an additional and necessary tool to validate the simulation results.

6. Conclusion

Using the simulation models of section 4 and 5 or the power net test bench of section 3.3, it is possible to draw some conclusions about voltage stability issues and inherent risk for the electric components:

6.1 Critical situations

All investigations clearly show that there are mainly two critical cases:

- The electric power demand as a whole is high, so that the alternator is not able to completely supply the power net. Every additional load can generate critical (local) voltage drops.
- The activation of today's driver assistance systems causes extreme power rise times. More than 100 A in under 5 ms are a common scenario. The alternator cannot ramp up its power supply in the same period because its dynamics are limited to avoid feedback, which would potentially decrease the driving comfort.

To counteract these voltage drops, a dimensioning of the power net with thick wires and a big battery or more than one battery could be a solution. Another possibility is to develop an active and predictive power distribution management system that detects critical situations in advance. Then, suitable measures can be taken to pre-condition the electric power net. Some possible stabilizing measures are mentioned in (Kohler, Wagner, Gehring, Froeschl, Thanheiser, Bertram, Buecherl & Herzog, 2010).

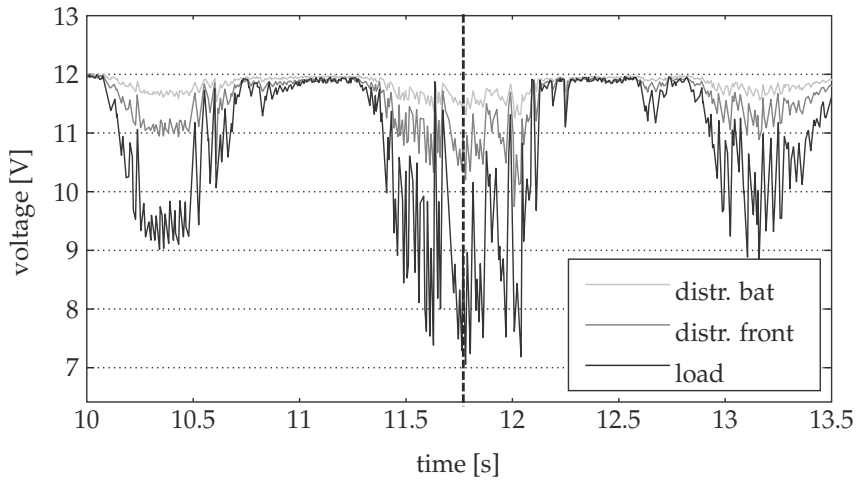


Fig. 15. Cut-off of a slalom driving maneuver with measurements at different places in the power net (distribution box at the battery and in the front and at the load) at the test bench. The vertical dashed line marks the time at which the analysis shown in Fig. 16 takes place.

6.2 Voltage drops in the wiring harness and car body

Besides the obvious voltage drops over the wiring harness at high currents, there are further drops at the distribution and fuse boxes. Likewise, there are significant losses on the return conductor, which have to be taken into account.

Fig. 15 presents the voltages, measured in a slalom driving maneuver at the power net test bench. In this case, as a result of the fast steering interventions, a few systems showing high peak power like electric power steering or dynamic stability control are simultaneously activated, and therefore particularly high power peaks occur in the whole system. The vertical dashed line in Fig. 15 marks the global load peak. Fig. 16 presents an analysis of the different voltages within the power distribution net at the moment in which the peak takes place.

Comparing the battery's and the load's terminals, it can be seen that the voltage decreased from 12.5 V to 7.1 V, which is a decline of above 40%. The main part of this decrease—4.4 V or 81%—is caused by the wiring harness, but a non-negligible part of 1.0 V or 19% is due to the return conductor.

6.3 Voltage stabilization

All the losses mentioned above depend on the installation location of the respective electric loads. Therefore, a power distribution management system should comprise both local and global levels. Today's systems that use a simple priority table and drop the less prioritized loads can be ineffective. The cut-off of a 40 A-load increases the voltage at the same distribution box by about 0.4 V. The influence on other places in the power net is only 0.2 V, or even less. For this reason, an optimized power distribution management system should account for the location of the power net's components and their interactions, specified in section 4 and 5.

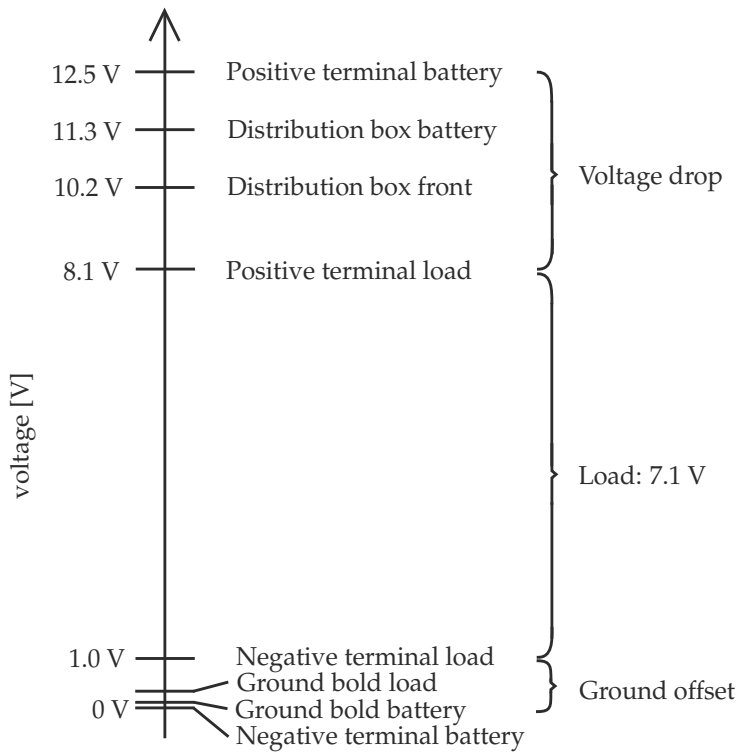


Fig. 16. Voltage at different measurement points at $t = 11.8$ s of the slalom driving maneuver in Fig. 15. The resulting voltage at the terminals of the load is only 7.1 V.

7. Outlook

The analysis of voltage stability in various automotive power nets by simulation still requires further research, so as to gain a more detailed and profound understanding of various aspects of simulating voltage stability. As a contribution to the ongoing research, in this paper several aspects have been explored and understood, as reviewed below.

Firstly, with the method given in this paper, the wires can optimally be dimensioned. Further, one can inspect whether one wire is able to supply more than one component without having adverse reciprocal effects. For this reason, it will be possible to reduce both the weight and cost of the wiring harness.

Secondly, an optimization of the wiring harness' topology itself can be conducted. Conceptually, today's topologies are the same as they were in the 1960s; they have merely expanded with the increasing number of electric equipment components. Therefore, with the simulation methods outlined in this paper, alternative power net topologies should be tested: for example, alternative nets may include a collecting power bus, or a concept using distributed energy storage units. Furthermore, the influence of the packaging on the voltage stability becomes calculable. For instance, the assets and drawbacks of assembling the battery in the back of the vehicle can be investigated from a voltage stability point of view.

In spite of all topological improvements, voltage variation and drop can always occur. Therefore, all possible active measures should be taken to ensure safety and functionality, even

if a voltage drop should occur. For this purpose—finally—a power distribution management system should be developed, as was recommended in Kohler, Froeschl, Bertram, Buecherl & Herzog (2010). This system should detect critical situations in advance, and initiate stabilizing countermeasures. Using the knowledge of voltage stability analysis, measures can be tailored to the location of the voltage problem so as to guarantee maximum effectiveness.

8. References

- Bai, H., Pekarek, S., Tichenor, J., Eversman, W., Buening, D., Holbrook, G., Hull, M., Krefta, R. & Shields, S. (2002). Analytical derivation of a coupled-circuit model of a claw-pole alternator with concentrated stator windings, *IEEE Transactions on Energy Conversion* Vol. 17(No. 1): 32 – 38.
- Barsali, S. & Ceraolo, M. (2002). Dynamical models of lead-acid batteries: Implementation issues, *IEEE Transactions on Energy Conversion* Vol. 17(No. 1): 16 – 23.
- Batchelor, A. & Smith, J. (1999). Time-current characteristic of miniature zinc-element electric fuses for automotive applications, *IEE Proceedings - Science, Measurement and Technology* Vol. 146(No. 4): 210–216.
- Batchelor, A. & Smith, J. (2001). Extreme overcurrent analysis for the protection of automotive circuit components, *IEE Proceedings - Science, Measurement and Technology* Vol. 148(No. 2): 55–61.
- Bohlen, O. (2008). *Impedance-based battery monitoring*, PhD thesis, Institute for Power Electronics and Electrical Drives - RWTH Aachen University.
- Ceraolo, M. (2000). New dynamical models of leadacid batteries, *IEEE Transactions on Power Systems* Vol. 15(No. 4): 1184 – 1190.
- Chen, M. & Rincon-Mora, G. (2006). Accurate electrical battery model capable of predicting runtime and i-v performance, *IEEE Transactions on Energy Conversion* Vol. 21(No. 2): 504 – 511.
- Gaba, G. & Abou-Dakka, M. (1998). A simplified and accurate calculation of frequency dependence conductor impedance, *Proceedings of the 8th Interantional Conference on Harmonics and Quality of Power*, IEEE, Athens, Greece, pp. 939 – 945.
- Gehring, R., Froeschl, J., Kohler, T. & Herzog, H.-G. (2009). Modeling of the automotive 14 v power net for voltage stability analysis, *Proceedings of the Vehicle Power and Propulsion Conference, VPPC '09, IEEE, Dearborn, USA*, pp. 71– 77.
- Gerke, T. & Petsch, C. (2006). Analysis of vehicle power supply systems using system simulation, *SAE 2006 World Congress & Exhibition, Detroit, MI, USA*.
- Hillenbrand, M. & Muller-Glaser, K. (2009). An approach to supply simulations of the functional environment of ecus for hardware-in-the-loop test systems based on ee-architectures conform to autosar, *Rapid System Prototyping, 2009. RSP '09. IEEE/IFIP International Symposium on*, pp. 188 –195.
- Kassakian, J., Wolf, H.-C., Miller, J. & Hurton, C. (1996). Automotive electrical systems circa 2005, *Spectrum, IEEE* 33(8): 22 –27.
- Kiehne, H. A. H. (ed.) (2003). *Battery technology handbook*, Electrical and computer engineering ; 118, 2nd ed. edn, Dekker, New York. Includes bibliographical references and index.
- Kohler, T., Froeschl, J., Bertram, C., Buecherl, D. & Herzog, H.-G. (2010). System approach of a predictive, cybernetic power distribution management, *The World Electric Vehicle Symposium and Exposition (EVS), Shenzhen, 2010*.
- Kohler, T., Wagner, T., Gehring, R., Froeschl, J., Thanheiser, A., Bertram, C., Buecherl, D. & Herzog, H.-G. (2010). Experimental investigation on voltage stability in

- vehicle power nets for power distribution management, *Vehicle Power and Propulsion Conference, 2010. VPPC '10. IEEE*.
- Lange, E., van der Giet, M., Henrotte, F. & Hameyer, K. (2008). Circuit coupled simulation of a clawpole alternator by a temporary linearization of the 3dfe model, *Proceedings of the Interantional Conference on Electrical Machines, IEEE, Vilamoura , Portugal*, pp. 1 – 6.
- Lukic, S. & Emadi, A. (2002). Performance analysis of automotive power systems: effects of power electronic intensive loads and electrically-assisted propulsion systems, *Vehicular Technology Conference, 2002. Proceedings. VTC 2002-Fall. 2002 IEEE 56th*, Vol. 3, pp. 1835 – 1839 vol.3.
- Mauracher, P. & Karden, E. (1997). Dynamic modelling of lead /acid batteries using impedance spectroscopy for parameter identification, *Journal of Power Sources* Vol. 67(No. 1-2): 69 – 84.
- Miller, J., Emadi, A., Rajarathnam, A. & Ehsani, M. (1999). Current status and future trends in more electric car power systems, *Vehicular Technology Conference, 1999 IEEE 49th*, Vol. 2, pp. 1380 –1384 vol.2.
- Miller, J. & Nicastrri, P. (1998). The next generation automotive electrical power system architecture: issues and challenges, *Digital Avionics Systems Conference, 1998. Proceedings., 17th DASC. The AIAA/IEEE/SAE*, Vol. 2, pp. I15/1 –I15/8 vol.2.
- Paul, C. (1994). *Analysis of Multiconductor Transmission Lines*, John Wiley & Sons.
- Polenov, D., Proebstle, H., Brosse, A., Domorazek, G. & Lutz, J. (2007). Integration of supercapacitors as transient energy buffer in automotive power nets, *Power Electronics and Applications, 2007 European Conference on*, pp. 1 –10.
- Reif, K. (ed.) (2009). *Automobilelektronik: Eine Einfuehrung fuer Ingenieure*, Vieweg+Teubner Verlag / GWV Fachverlage GmbH, Wiesbaden, Wiesbaden. In: Springer-Online.
- Schweighofer, B., Raab, K. & Brasseur, G. (2003). Modeling of high power automotive batteries by the use of an automated test system, *Instrumentation and Measurement, IEEE Transactions on* 52(4): 1087 – 1091.
- Simonyi, K. (1963). *Foundations of Electrical Engineering*, Macmillan.
- Smith, W., Paul, C., Savage, J., Das, S., Coopriider, A. & Frazier, R. (1994). Crosstalk modeling for automotive harnesses, *Proceedings of the IEEE Interantional Symposiumon Electromagnetic Compatibility, IEEE, Chicago, USA*, pp. 447 – 452.
- Surewaard, E. & Thele, M. (2005). Modelica in automotive simulations – powernet voltage control during engine idle, *4th International Modelica Conference, 2005*, pp. 309 –318.
- Thanheiser, A., Meyer, W., Buecherl, D. & Herzog, H.-G. (2009). Design and investigation of a modular battery simulator system, *Vehicle Power and Propulsion Conference, 2009. VPPC '09. IEEE*, pp. 1525 –1528.
- Velazquez, R. & Mukhedkar, D. (1984). Analytical modelling of grounding electrodes transient behaviour, *IEEE Transactions on Power Apparatus and Systems* Vol. 103(No. 6): 1314–1322.

Part 7

Vehicle Design

Urban and Extra Urban Vehicles: Re-Thinking the Vehicle Design

Andrea Festini¹, Andrea Tonoli² and Enrico Zenerino¹

¹*Mechatronics Laboratory - Politecnico di Torino*

²*Mechanics Department, Mechatronics Laboratory - Politecnico di Torino*
Italy

1. Introduction

The problems related to transport are reaching unacceptable levels due to congestion, number of accidents with related casualties, pollution, and availability of energy sources. Some small commuter vehicles are already of widespread use, and the steady growth of the number of motorcycles and scooters in the urban areas demonstrates the validity of the lean vehicle approach to solve the problem.

Regardless of their advantages, scooters and motorcycles are affected by several drawbacks, the main disadvantage is related to the safety in dynamic conditions and during crash. Moreover two wheeled vehicles do not have an enclosed cockpit to provide protection from the environment, as cold wind, dust and rain.

For these reasons the demand of personal mobility vehicles must be satisfied by re-thinking the vehicle itself from the beginning, and basing its design on clearly defined basic general needs.

Aim of the present work is to propose a vehicle capable of covering all the different missions typical of a mid size car, including highway and city to city transportation, not confining (limiting) it to the small range usage. The proposed vehicle design starts from the general needs definition.

The mobility in urban environment has to deal mainly with the emissions reduction and the parking problems, the first one can be achieved locally by using a powertrain capable of a zero emission mode, and the second by reducing the vehicle size. Moreover the design of a lightweight vehicle allows the pollution reduction also when using an internal combustion engine. Cities are furthermore characterized by uneven or slippery road and high risk of crashes, therefore the vehicle must provide static and dynamic stability, together with crash protection.

Sub-urban and extra-urban mobility, intended as the working commuting, are characterized by needs that are different from those of the urban environment. Outside the cities the vehicle must be capable of covering a long distance, with reasonable energy consumption, and of travelling at highway speeds, with a high level of active safety, for this purpose an all wheel drive system can increase the levels of safety.

The need of having a closed cockpit to ensure safety and protection, requires a stable position during stops, this leads to the adoption of at least three wheels. To avoid rollover during cornering the vehicle must be able to bank (tilt).

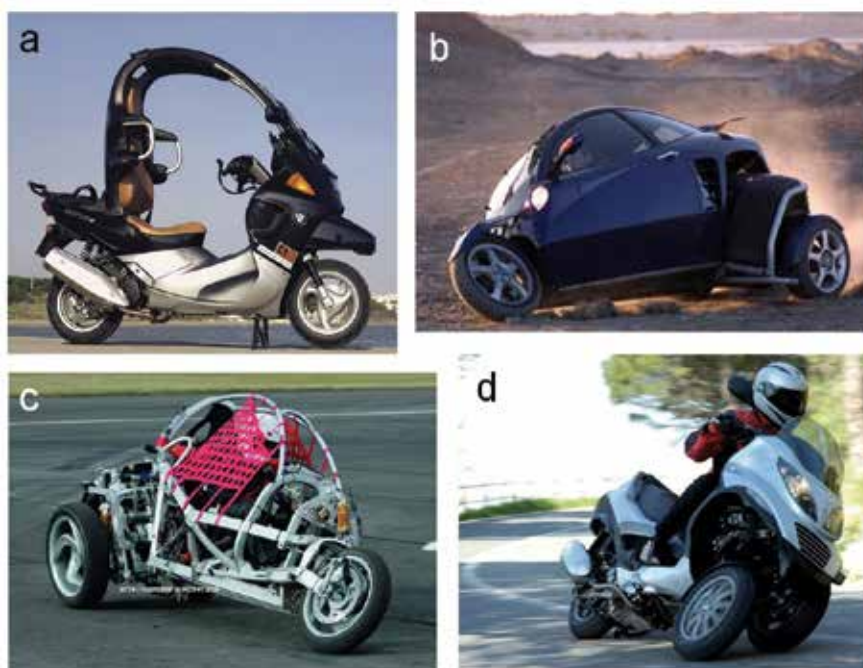


Fig. 1. a) BMW C1, a two wheeled scooter with roll bar, restraint system and front crash box. b) Carver, in production, automatic leaning control. c) Clever, an European project, automatic leaning control. d) Piaggio mp3, actually in production, no roll control.

From the safety point of view the state of the art shows little experience apart from few examples. BMW C1 (Figure 1 a)) is an example of a scooter provided with a closed frame and crash box in order to have structural protection. This kind of solution presents some critical points: vehicle sides are opened, to allow the use of feet during stops, then the height of the mass centre limits the vehicle's agility, and generates some problems in the learning of driving skills.

Since the beginning of the '90s for about twenty years several lean vehicles with more than two wheels were developed (Hibbard and Karnopp, 1996; Riley, 2003). Their failure mainly related to the lack of an available technology.

In last decade, the congestion of urban traffic, the pollution problem, the increment of energy costs and the technology progress motivated a renewed interest in small and narrow vehicles for individual mobility. New concepts were proposed and new configurations were designed (Gohl et al., 2006), a number of solutions have been proposed at prototype or at production level. Most important 1990's prototypes of three wheeled tilting vehicles were the GM Lean machine and the Mercedes F300. In 2002 the Vanderbrink "Carver" was the first tilting narrow vehicle to become a commercial product (Figure 1 b) and the Clever project (Figure 1 c) of University of Bath and BMW applied the same concept to urban mobility. In 2003 the Prodrive concept "Naro" showed the application of tilting to four wheeled vehicles. Since 2006 Piaggio "MP3" is the first three wheels scooter in production (Figure 1 d).

On the powertrain side, electric scooters have been developed to reduce emissions and consumptions. Nevertheless limited autonomy and high cost limit their diffusion. At the

same time the increasing diffusion of alternative fuels, such as ethanol, has demonstrated as a viable way to reduce emissions.

Honda Civic, Insight and CRz, Lexus RX400h, Toyota Prius, are examples of cost-effective solutions with large sales volumes. The application of the full hybrid technology to lean vehicles is promising to further reduce their consumption and emissions.

The design of a hybrid lean vehicle requires the development of a novel design methodology. As a matter of fact this type of vehicle is very different from a car, and even from a motorbike. From this point of view the literature that deals with the design methodology and global optimisation for such kind of vehicle is very rare.

The dynamics of three wheels tilting vehicles can be assimilated to the one of a motorcycle when the wheels camber angle is equal to the vehicle's roll angle. Under this assumption, a reference for the study of narrow commuter vehicles is the literature on motorbike's dynamics. The studies on motorcycle dynamics mainly deals with stability (Cossalter, 1999): in particular weave and wobble oscillations (Sharp, 1992; Sharp & Limebeer, 2004) have been investigated using multi-body models (Sharp & Alstead, 1980; Sharp, 1999; Sharp & Limebeer, 2001; Cossalter et al., 1999; Cossalter & Lot, 2002; Cossalter et al., 2003; Sharp, Evangelou & Limebeer, 2005; Cheli et al., 2006) in order to analyse the motorcycle stability as a function of chassis flexibility (Sharp and Alstead, 1980; Spierings, 1981). On the other hand literature on commuter dynamics is very poor: only analytical first approximation models are available to illustrate specific control issues (Snell, 1998; Karnopp and So, 1997). In particular Karnopp's analysis are devoted to study the DTC (Direct Tilt Control) and STC (Steer Tilt Control) strategies using inverse pendulum models (Karnopp and So, 1997). The most evolved model deals with simplified vehicle's analytical models which neglect relevant effects of the vehicle dynamics (i.e. chassis compliance, dynamic behaviour of the tires, suspension's kinematics) (Gohl et al., 2004).

Objectives of the present work are: 1) define the specifications to be used as reference for designing the vehicle; 2) describe the main design steps and iterations; 3) illustrate the solutions adopted for its main subsystems (frame, suspension system, steering, powertrain, sensors & ECU); 4) validate the design by means of calculations and experiments.

2. Functional analysis and target settings

The following section will describe the basic functional needs starting from the previously described mobility environment, trying to obtain some implications which will be then used to define the configuration of each subsystem.

In the urban environment the main request comes from parking problems and traffic, this leads to the need of a small footprint, a dimensions reduction that means the shortening of the vehicle or reducing its width or, possibly, both at the same time.

Reducing the vehicle's width, together with the need of having acceptable cornering performances, suggests to design a vehicle capable of leaning into corners as a motorbike to avoid rollover (Pacejka, 2002; Genta, 2003; Karnopp, 2004). The need of ensuring stability on uneven road and at standstill without the use of a foot on the other hand leads to a vehicle architecture with at least three non aligned wheels. This suspension architecture must comply with the need of banking into corners, and leads to the definition of an important subsystem, the tilting suspension, that, on the vehicle, has to be applied to every axle with more than one wheel.

For the front axle two tilting suspension strategies were considered: passive (free) and active tilting. In the first case, to allow the leaning of the vehicle, a free tilting suspension provides

the roll degree of freedom, as in a two wheels bike. The driver then controls the roll angle by acting on the steering system. In active tilting, the vehicle roll is controlled by connecting an actuator to the suspension. The active control system sets the vehicle roll angle basing its commands on sensors and a suitable control strategy.

Crash and weather protection requirements can only be satisfied by designing a crash proof frame, together with a full fairing enclosed cockpit, the vehicle layout and design of the frame must deal with this specification.

One of the main targets together with traffic and safety is the pollution and fuel consumption reduction. Local emission reduction can be obtained by a hybrid powertrain, for its simplicity and the capability of running at zero emission the most suitable layout seems to be the parallel hybrid, using electric motors and an internal combustion engine. A parallel hybrid electric vehicle may be used as a dual mode commuter. A Zero Emission Vehicle (ZEV) when using only the electric motor (with or without a grid plug in to recharge batteries), or a low pollution vehicle when travelling in Hybrid Electric Vehicle (HEV) mode using both powertrains.

Considering the Extra-Urban environment, some specifications have to be added. To satisfy the need of having a large autonomy together with a maximum speed compatible with extra urban environment and highways the Internal Combustion Engine (ICE) must be sized to reach a high cruise speed without the usage of electric motors, for this reason, together with the higher complexity and costs a series hybrid layout has to be excluded.

An increase of active safety can be obtained by a vehicle dynamics control system, here called Intelligent Vehicle Dynamics (IVD), and an all wheel drive system, together with an active system for the tilt control.

The capability of controlling the current in the electric motors allows to implement independent traction control for the front wheels, avoiding slip during acceleration and cornering. Moreover the parallel hybrid powertrain, when integral traction is active, can work as a set of differentials, providing the correct torque on each wheel, allowing the vehicle to corner properly, and even interact with the vehicle dynamics.

In accordance with the definition of the needs for the vehicle, it is possible to list the main technical characteristics:

- small and lean,
- three wheels,
- active tilting,
- parallel hybrid powertrain capable of behaving as a HEV or a ZEV,
- IVD with anti slip and differentials,
- all wheel drive,
- crash proof structural frame,
- enclosed cockpit.

3. Vehicle layout description

The designed prototype vehicle is a compact commuter, weights less than 300 [kg] without the driver, and is able to carry two people. It has three wheels, and all of them are able to tilt together with the frame. The vehicle uses motorcycle tires in order to be able of large roll angles. The chosen layout (Figure 2 and Figure 3) is with two in line seats with the rear passenger's knees surrounding the driver's hips (as in motorbikes), this layout allows to reduce the vehicle cross section ($S \approx 1$ [m²]) and therefore the aerodynamic resistance if

compared to conventional small urban vehicles. A motorcycle handlebar has been chosen to control the steering, as it allows to control also throttle, brakes, and clutch.

According to state of the art studies in vehicle dynamics, due to the acceleration during braking, which is the highest longitudinal vehicle acceleration, a three wheels vehicle should have a single wheel rear axis (Riley, 2003). So the chosen layout is a three wheels vehicle with the front axle having two wheels, this feature requires the design of a front tilting and steering suspension system, but allows the adoption of a motorbike rear end design. This solution helps the design of a lightweight vehicle, and a simple rear transmission layout, avoiding the need of a mechanical differential for the ICE.

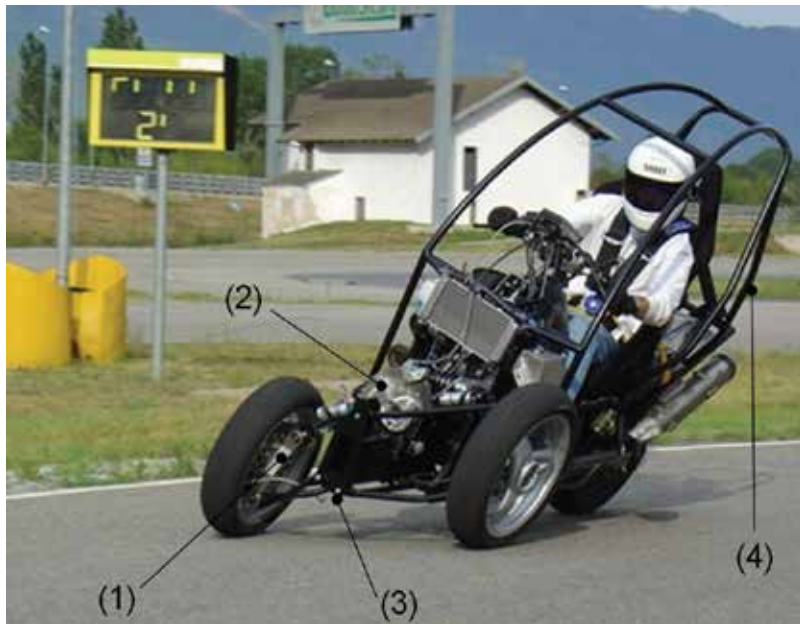


Fig. 2. The vehicle during track tests, front (3) and main (4) frames are visible, the tilt actuator/brake (2) and the hubs (1) are shown.

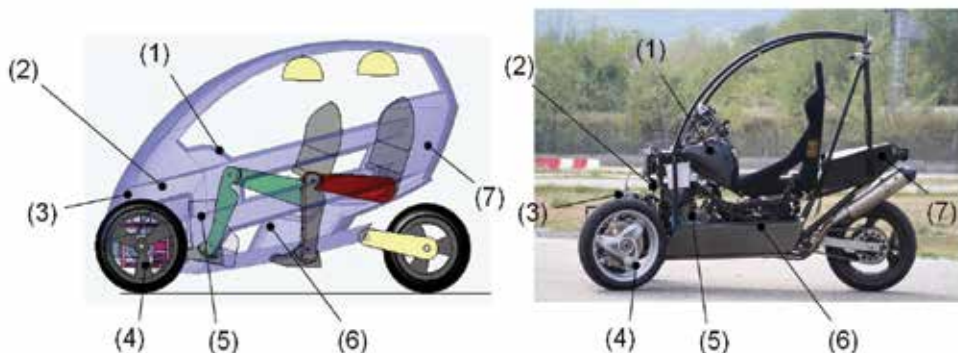


Fig. 3. Vehicle layout showing control handlebars (1), tilt/steer sensors (2), tilt actuator (3), wheels and hubs (4), internal combustion engine (5), room for batteries (6) and passenger/luggage/acquisition system (7).

Vehicle mass	With driver	300	[Kg]
Front track		1.16	[m]
Wheelbase		1.75	[m]
Dimensions	width x length x height	1.2 x 2.35 x 1.6	[m]
Suspensions	Front	Double wishbones	-
	Rear	Swing arm	-
	Max tilt angle vs vertical	45	[°]
Brakes	Front	Double disc 318 mm 2 cylinder floating calipers	-
	Rear	Single disc 245 mm with a single cylinder floating caliper	-
Wheels	Front	Motorcycle 150/60 R17"	-
	Rear	Motorcycle 170/60 R17"	-
ICE	Type	Single cylinder 4 stroke 4 valves water cooled Minarelli Yamaha - Euro2	-
	Displacement	660	[cc]
	Power	35.3 @ 6.000 rpm	[kW]
	Torque	58.4 @ 5.250 rpm	[Nm]
	Transmission	Chain	-
Batteries	Positioned under seat	NiMh	-

Table 1. Prototype characteristics

The design started with the layout described in Figure 3, and has been carried on with the development and integration of a series of subsystems, according to the previously defined technical characteristics, these subsystems can be listed as:

- frame with enclosed cockpit,
- tilting suspension with steering system & tilting actuator,
- powertrain with in wheel motors, internal combustion engine and energy storage unit,
- electronic control units & power electronics.

All the subsystems have been developed starting from a trade off between feasible solutions, then a design and modelling phase together with a test rig validation has defined the final subsystems configurations. A series of track tests has then been performed on the prototype to validate the models and verify its dynamic behaviour. Table 1 shows the overall characteristics of the vehicle.

The subsystem development and prototype configuration is described in the following sections together with a description of the main characteristics.

4. Frame subsystem description

The need of having compact dimensions has led to the adoption of ergonomics similar to the one of a scooter, with the passengers seating one behind the other. To provide passengers support the main vehicle frame structure has been designed basing on a main structural tunnel placed under the seats and supporting the roll bars, the entire prototype frame is a space frame structure based on square and circular section tubes with diameter and side of 30 [mm], and thickness of 1.5mm. The material is 25CrMo4 (25NCd4) TIG welded. Figure 4 shows the frame layout (Renna, 2005).

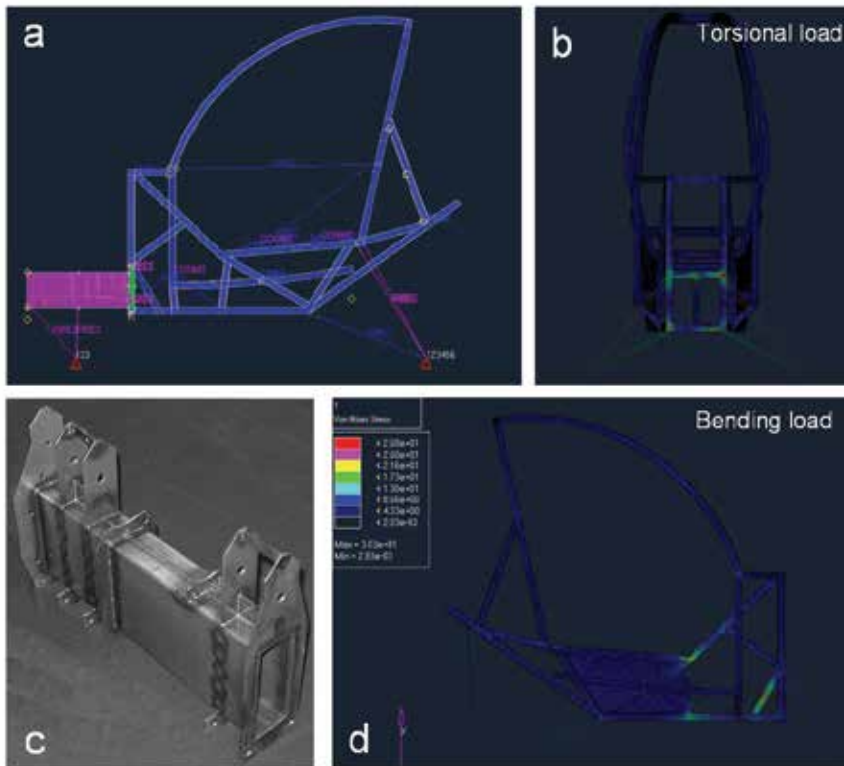


Fig. 4. Prototype enclosed frame a) model side view, b) torsional load FEM front view c) front frame d) bending load FEM side view

The structural support for the front suspension has been realized with a separate front beam carrying also the steering and the tilting mechanism, this structure can be completely disassembled from the main frame to allow the testing of different suspensions configurations. As a three wheels vehicle, the prototype is characterized by stiffness requirements that have been determined by vehicle dynamics issues such as weave and wobble modes. FEM calculations on the frame models have provided a bending stiffness value larger than 500 [kN/m] and a torsional stiffness of 150 [kNm/rad] with an overall frame weight of about 50 [kg]. The stress maximum values have been evaluated too, as it is shown in Figure 4b and Figure 4d.

5. Tilting suspension and actuator description

The capability to lean into corners actively is the main dynamic characteristic of the vehicle, this feature needs the design and implementation of a tilting suspension system, and a tilting actuator together with its control system and power electronics.

The rear suspension is a motorcycle swing arm equipped with a motorcycle mono-shock absorber with a progressive link. The designed suspension is a double wishbone suspension with tuneable castor angle and castor trail, the steering axis has a non null kingpin angle:

- castor trail: 10 to 40 [mm],
- steer ratio: 0.9,
- kingpin: 10°.

The two wheels are connected to two independent motorcycle mono-shock absorbers that are completely tuneable, in springs preload, compression and rebound damping.

The designed suspension keeps the wheel mid plane always parallel to the frame, this means that the camber angle of all the three wheels is the same angle of inclination of the vehicle. The vertical ground stiffness is almost constant with suspension travel (Figure 5), the suspension double wishbone architecture shows the typical track variation (Figure 6) and allows the positioning of the maximum track value by means of preload adjustment.

With reference to Figure 7, the steering mechanism is based on a lever (1) connected to the steering column (2), the steering rods (3) are linked to this lever and the uprights. To allow the decoupling of the tilting movement from the steering these two joints have been placed one behind the other, aligned with the upper wishbones link to the frame. The steering ratio is almost unity, as in motorbikes. Some Ackermann effect is introduced in the system by the inclination of the lever rotation axis, which gives the inner wheel a "toe out" rotation when steering. Figure 8 shows the obtained behaviour.

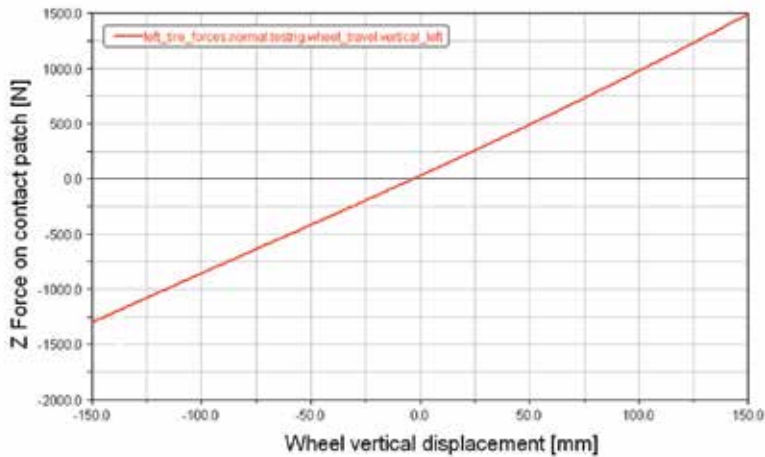


Fig. 5. Front suspension vertical force versus displacement.

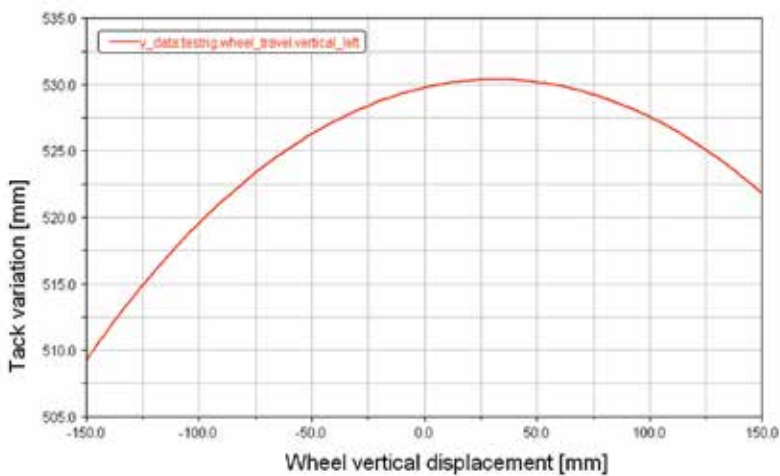


Fig. 6. Track variation versus wheel vertical displacement.

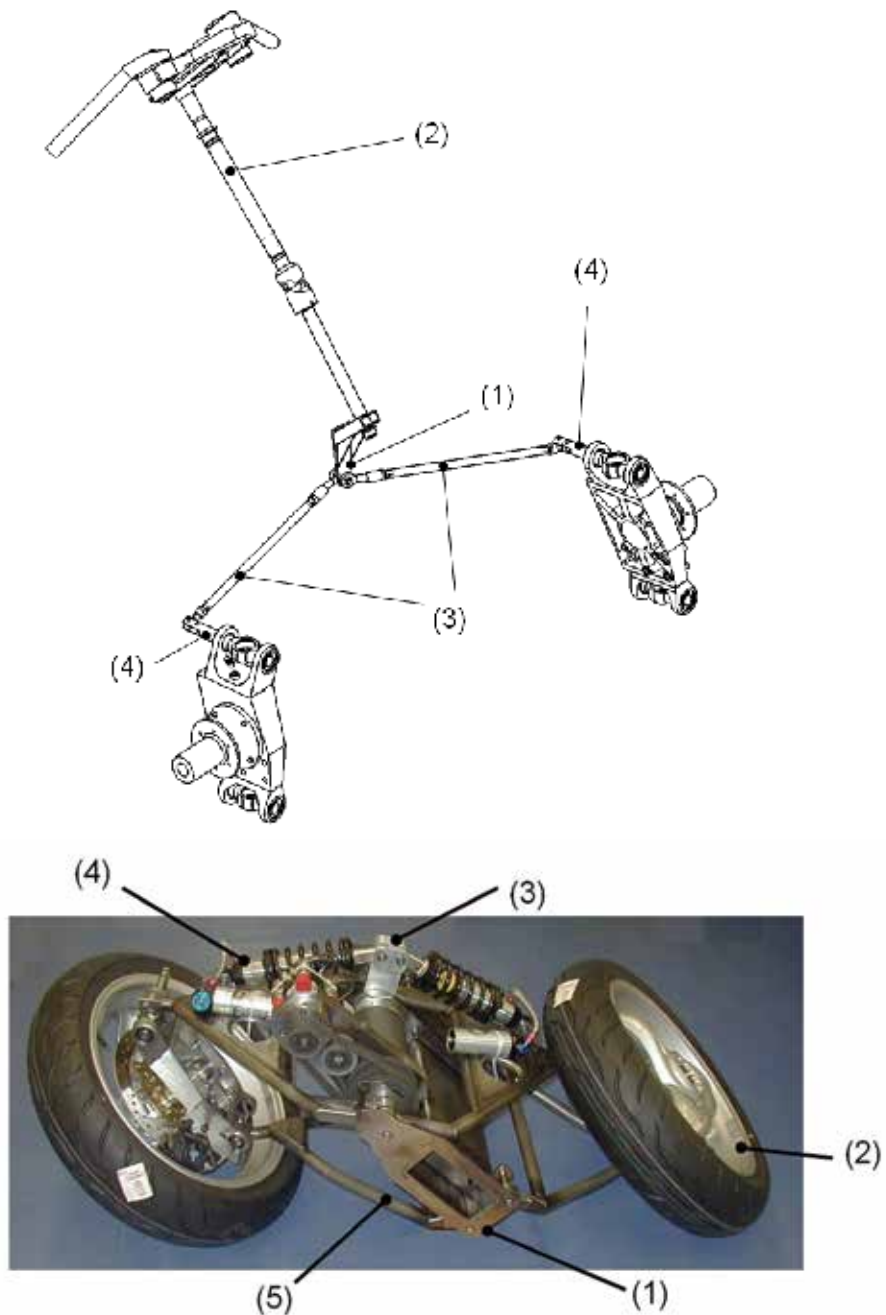


Fig. 7. a) Steering subsystem (1) lever, (2) steering column, (3) steering rods, (4) steering arm. b) Front frame (1) with tilting suspension assembled (2) Front wheels, (3) Tilt crank, (4) Tuneable dampers (5) Wishbones

The steering arm (4) can rotate relative to the upright about a longitudinal axis. This allows large roll angles without influencing the steering mechanism.

A special effort was dedicated during the design of the TTW vehicle to the tilting system design i.e. the device that allows the driver to control the roll angle.

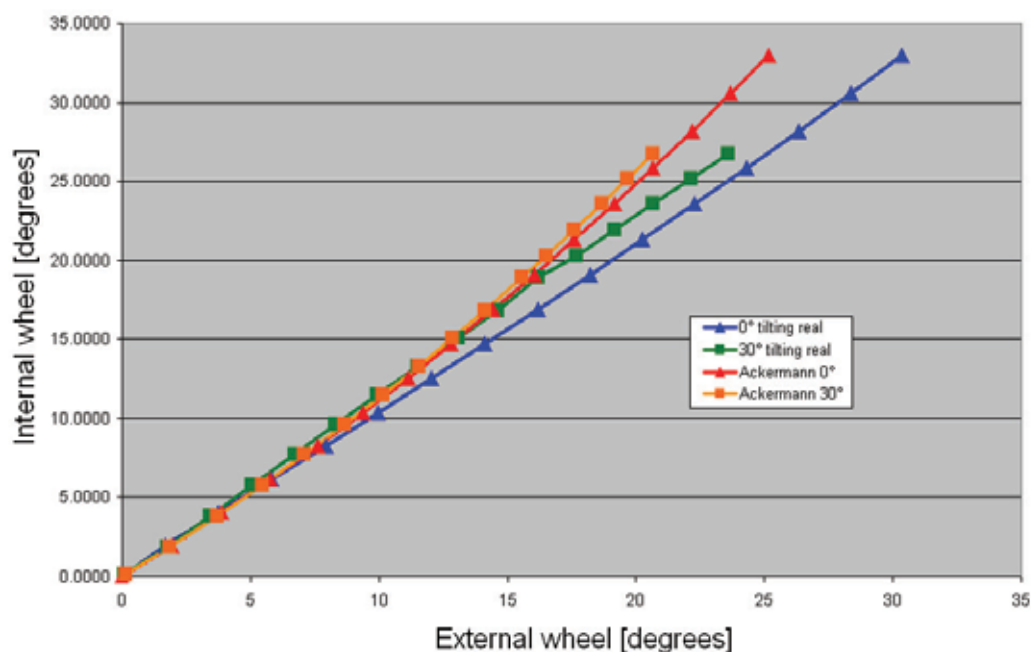


Fig. 8. Steering angle internal wheel versus external wheel at 0° and 30° tilting angles, red and orange reference curves are calculated according to Ackermann's kinematics.

To control the tilt degree of freedom the shock absorbers are connected to a pivotable support (called tilt crank, as seen in (3) in Figure 7b) whose rotation can be left free or controlled by a tilt actuator. Because the upper wishbones and the tilt crank are rotating about the same axis, there is no coupling between tilting and suspension motion.

Two types of strategies were pursued for tilting: passive and active tilting. In the passive tilting mode no tilting actuator is present. The tilting lever is free to rotate about its hinge axis. The tilting degree of freedom is therefore free. The driver controls the roll angle by acting on the steering system, this is the same as in the case of a motorbike. A mechanical brake allows stable stopping. This configuration has been mainly used for testing and vehicle dynamics model validation.

In the active tilting mode the angle between the tilting crank and the frame is controlled by an electromechanical actuator. In this case the driver acts on the steer as on a car and an active control system imposes the vehicle roll angle during bends.

The tilting actuator design has been based upon the estimation of the two worst working conditions. In the first design load case the tilting actuator must be able to resist the torque corresponding to the maximum centrifugal force without vehicle rollover:

- max lateral acceleration allowed by the three wheels layout: 0.54 [g],
- max lateral force = 1600 [N],
- necessary tilt torque = 870 [Nm].

In the second load case the actuator must be able to raise the vehicle from the maximum allowed parking inclination (32°) without rollover:

- necessary tilt torque = 850 [Nm].

The electromechanical tilting actuator has then been prototyped with two brushless motors (for redundancy purpose), connected by means of a belt transmission to a planetary gearbox providing the torque to the tilt crank with an overall ratio of 112/1. The actuator overall mass added to the vehicle is 20 [kg]. The torque required on each motor is then 3.25 [Nm].

Two motors with a maximum continuous torque of 4.76 [Nm] were then chosen. The tilt actuator has been built and tested on a test rig, it is now under track testing.

6. Powertrain description

The powertrain is a parallel hybrid three wheel drive. This hybrid powertrain technology has been chosen to give a further reduction of emissions and consumptions in both urban and extra-urban traffic. The need of a hybrid powertrain together with that of having an all wheel drive vehicle, suggest to adopt two powertrains working in parallel (Figure 10), one with an internal combustion engine and one completely electric, driving different wheels independently. Moreover the elimination of a mechanical power split device helps to reduce the vehicle mechanical complexity and weight.

The solution is based on the development of an in wheel electric motor, here called "power wheel". The integration inside the front wheels allows reaching of high vehicle roll angles (up to 45°). Different alternatives have been evaluated in terms of type and power, transmission and architecture, the chosen layout is direct drive technology.

The electric motors have been integrated in the wheel hubs to guarantee high tilting angles. The drawback to pay is an increase of the unsprung mass.

The most promising solution in terms of weight and complexity adopts a brushless direct drive motor and a perimeter disc brake in each front wheel.

The power electric wheel based on the use of a direct drive has been completely designed on purpose. Figure 9 shows a 3D view and a section for the right wheel, the space for the electric motor has been obtained by adopting a perimetral brake. In Figure 9b the electric motor is shown together with the bearing, shared with the hub. Table 2 shows the overall direct drive hub characteristics.

Designed brushless electric motor		
Max power	13	[kW]
Max torque at the wheel	130	[Nm]
Unsprung mass	22	[kg]
Added unsprung mass respect idle	3.2	[kg]

Table 2. Direct drive electric motor characteristics.

The parallel hybrid layout requires also the choosing of a suitable internal combustion engine, in terms of type, layout, power and torque, together with its impact on ergonomics and vehicle layout. The internal combustion engine (ICE) together with its own powertrain is here considered as a separate subsystem to be developed and tested. The choice has been

for an off the shelf motorcycle gasoline powered engine, which has been placed immediately behind the front wheels.

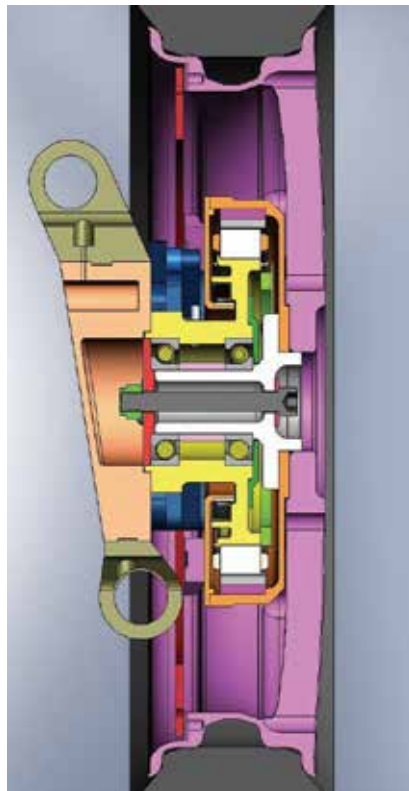
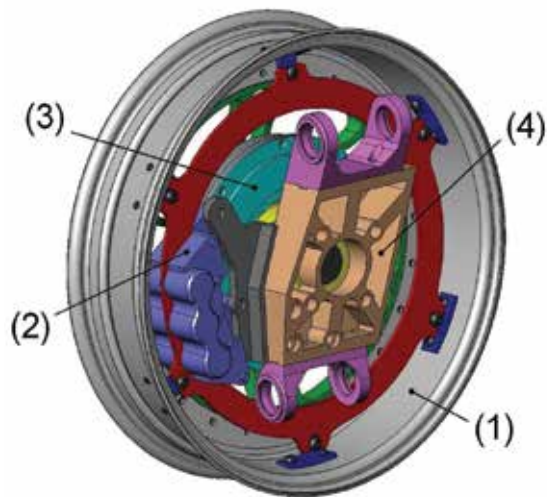


Fig. 9. a) Direct drive power wheel (Right) 1 Rim; 2 Perimeter brake and caliper; 3 direct drive brushless motor; 4 Upright. b) Direct drive power wheel (Right)

Due to its simplicity and weight the adopted solution for the internal combustion engine is a single cylinder, 660 cc gasoline engine, alternative fuels such as ethanol or natural gas are also promising alternatives to be evaluated.

The hybrid powertrain layout is shown in Figure 10, its management is realized by an Electronic Power Control Unit (ECU). The power source for the ICE is a gasoline tank and an Electronic Storage Unit (ESU) (Figure 11) feeds the electric traction. Two power electronics modules are used for the front electric motors.

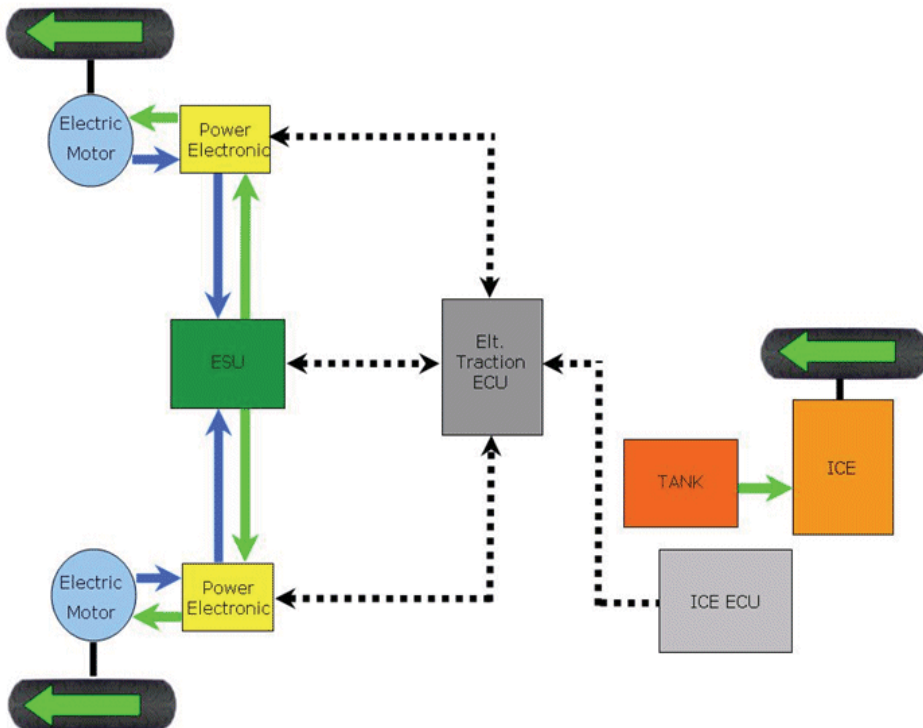


Fig. 10. Hybrid powertrain layout.

To let the driver control both powertrains, electric motors are chosen to behave as “slaves” of the ICE, driver commands and signals from ICE ECU are used to drive electric motors. The driver’s controls (throttle, brake) are used to drive the ICE, and then, to adapt the torque on front wheels to the behaviour of the ICE, the electric traction ECU is able to read the ICE ECU states.

The Electronic Storage Unit (ESU, shown in Figure 11) is necessary for the electric powertrain and can be considered as another subsystem to be developed, the opportunity to use different kinds of batteries, together with super capacitors has been evaluated. The ESU prototype configuration is based on NiMh batteries, the cells are 84×1.2 V, with a capacity of 3.2 [Ah]. These batteries have been chosen because of the availability of a high discharge current, important for the electric boost feature implementation. For this prototype the autonomy is limited to 12 km at a constant speed of 50 km/h using only the electric motors (ZEV).

At the moment the hybrid powertrain is performing bench tests for the evaluation of performances, reliability and consumptions, the project is being continued by a small company in Turin in cooperation with the Mechatronics Lab, and has participated to the 2010 Progressive Insurance Automotive X Prize.

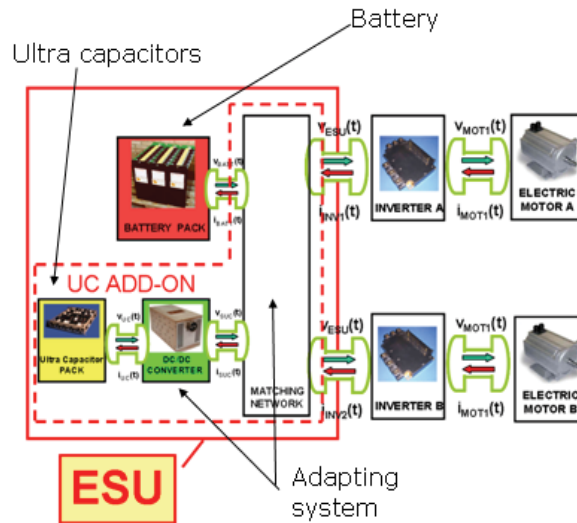


Fig. 11. Electric powertrain layout with Electronic Storage Unit (ESU).

7. Conclusions

The present paper describes the main decisions at the base of the design of a hybrid vehicle for urban and extra urban mobility.

The design methodology starts from a functional analysis that sets the main characteristics for the vehicle. The main vehicle subsystems are then described in terms of configuration and design procedure. A series of analytical simulations, FEM analysis, test bench tests and track tests has then been performed to write and validate the models, allowing to verify the static and dynamic subsystems behaviour.

The designed and built vehicle has a mass of 300 [kg] and a trackwidth of 1.16 m, and is capable of transporting two people in a closed cockpit, satisfying the most common car usage with 1/3 of the mass. This means that, from the performance point of view, the power to weight ratio is the same of a 150 kW car. Moreover, if performances are not mandatory, by downsizing the powertrains the mass and consumption can be further reduced, still having higher performance than an usual city car.

Although preliminary the track tests demonstrate that such a vehicle is feasible with available technology and design methodologies.

8. References

Cheli, F.; Boccione, M.; Pezzola, M. & Leo, E. (2006). Numerical and experimental approaches to investigate the stability of a motorcycle vehicle, *Proceedings of ASME*

- 8th Biennial Conference on Engineering Systems Design and Analysis, pp. 105-114, Italy, 2006, Torino.
- Cossalter, V. (1999). *Cinematica e dinamica della motocicletta*, Casa Editrice Progetto, Padova.
- Cossalter, V.; Doria, A. & Lot, R. (1999). Steady turning of two-wheeled vehicles, *Vehicle system dynamics*, 31, pp 157-181.
- Cossalter, V.; Da Lio, M.; Lot, R. & Fabbri, L. (1999). A general method for the evaluation of vehicle manoeuvrability with special emphasis on motorcycles *Vehicle system dynamics*, 31, pp 113-135.
- Cossalter, V. & Lot, R. (2002). A motorcycle multi-body model for real time simulations based on the natural coordinates approach, *Vehicle system dynamics* 37, pp 423-447.
- Cossalter, V.; Doria A.; Lot R.; Ruffo N. & Salvador M. (2003). Dynamic properties of motorcycle and scooter tires: measurement and comparison, *Vehicle system dynamics* 39, pp 329-352.
- Genta, G. (2003). *Motor vehicle dynamics*, World Scientific, ISBN, Singapore
- Gohl, J.; Rajamani, R.; Alexander, L. & Starr, P. (2004). Active roll mode control implementation on a narrow tilting vehicle, *Vehicle system dynamics*, 42, pp 347-372.
- Gohl, J.; Rajamani, R.; Starr, P. & Alexander, L. (2006). Development of a novel tilt-controlled narrow commuter vehicle, *Report no. CTS 06-05, Center for transportation studies*.
- Hibbard, R. & Karnopp, D. (1996). Twenty first century transportation system solutions – a new type of small, relatively tall and narrow active tilting commuter vehicle, *Vehicle system dynamics* 25, pp 321-347.
- Karnopp, D. & So, S. (1997). Active dual mode tilting control for narrow ground vehicles *Vehicle system dynamics*, 27, pp 19-36.
- Karnopp, D. (2004). *Vehicle stability*, Marcel Dekker, NY.
- Pacejka, H. B. (2006). *Tire and Vehicle Dynamics*, SAE International.
- Renna, A. (2005). Analisi e progetto di telaio per veicolo leggero. *Master thesis*. Politecnico di Torino, Turin, Italy.
- Riley, R.Q., (2003). *Alternative cars in the 21st century*, SAE.
- Sharp, R. & Alstead, C. (1980). The influence of structural flexibilities on the straight-running stability of motorcycles, *Vehicle system dynamics*, 9, pp 327-357.
- Sharp R. (1992). Wobble and weave of motorcycles with reference to police usage, *Automotive Engineer*, 17, pp. 25–27.
- Sharp, R. (1999). Stability, control and steering responses of motorcycles, *Vehicle system dynamics*, 35, pp 291-318.
- Sharp, R. & Limebeer, J. (2001). A motorcycle model for stability and control analysis, *Multibody system dynamics*, 6, pp 123-142.
- Sharp R. & Limebeer J. (2004). On steering wobble oscillations of motorcycles, *P I MECH ENG C-J MEC Vol.(218) No.(12)*, C12, pp. 1449-1456.
- Sharp, R.; Evangelou, S. & Limebeer, J. (2004). Advances in the modelling of motorcycle dynamics, *Multibody system dynamics*, 12, pp 251-283.

Sharp R.; Evangelou S. & Limebeer J. (2005). Multibody aspects of motorcycle modelling with special reference to Autosim, In: *Advances in Computational Multibody Systems*, Jorge A. C. Ambrosio, Springer, Netherlands.

Snell, A. (1998). An active roll moment control strategy for narrow tilting commuter vehicles, *Vehicle system dynamics*, 29, pp 277-307.

Spierings, P.T.J. (1981). The effects of lateral front fork flexibility on the vibrational modes of straight running single track vehicles, *Vehicle System Dynamics*, 10 (1), pp 37-38.

http://www.maxmatic.com/ttw_moto.htm

<http://www.carver-worldwide.com/Home/Index.asp?nc=1>

<http://www.clever-project.net>

<http://www.naro.co.uk/>

http://www.mp3.piaggio.com/index_ita.html

<http://www.vectrixusa.com/>

Analysis Approach of How University Automotive Competitions Help Students to Accelerate Their Automotive Engineer Profile

Francisco J. Sánchez-Alejo, Miguel A. Álvarez,
Francisco Aparicio and José M. López
*University Institute for Automobile Research, INSIA, Polytechnic University of Madrid
Spain*

1. Introduction

Today, the world's leading universities in the world not only are concerned about the importance of enhancing student's personal and professional skills, but most of them are modifying their study's programs to adapt them to these new requirements (Aparicio et al., 2005), (Bowen et al., 2005) and (Chadha & Nicholls, 2006).

Even though different definition can be found, skills are "a combination of knowledge, abilities and attitudes that are suited to particular circumstances" (European Parliament, 2006). On the other hand, skills can be understood as "the set of knowledge, abilities, behaviour and attitudes that favour work being done properly and which the organisation is interested in developing or recognising in its co-workers when it comes to achieving the company's strategic goals" (De Miguel et al., 2006).

Many years before the major of these universities became fully aware of the importance of promoting personal and professional skills among their students, companies in different sectors recognised the gap existing between university and business, and on some occasions proposed activities to try to narrow it.

For instance, in 1982 engineers from Ford, DaimlerChrysler and General Motors, grouped together in the SAE (Society of Automotive Engineers), in the United States, being aware of how little newly graduated engineers were adapted to automotive companies, designed a competition for universities throughout the world, which involved conceiving, designing, manufacturing and competing with a single seat formula-type vehicle under some strict rules. This competition was called Formula SAE.

These pioneers were of the opinion that this challenge would serve to accelerate engineering students' professional profiles, forcing them to work as part of a team, with high levels of communication, responsibility and motivation, forcing them to use in their work a large part of the knowledge acquired in their degree. Today, more than 200 universities of five continents compete at some of the tests that Formula SAE has round the world.

Since then, some other automotive competitions for engineering universities have come up, each of them with their specific objectives and rules. Shell Eco-marathon consists on the development of a vehicle able to cover the maximum distance with a litre of petrol. At Baja SAE, engineering students are tasked to design and build an off-road vehicle that must

survive on rough terrain. The World Solar Challenge is a solar-powered car race that covers more than 3.000 km in Australia. Due to the high expenses these competitions used to involve, that prevent lots of universities to take part on them, the latest competition created was called Formula Low-cost, which main objectives is the designing, manufacturing and competing with a go-kart build with less than 2.000 €.

The mentioned competitions and some others, with their own peculiarities, constitute an educational experience that provides the students with a real-life exercise in design, manufacture and the business elements of automotive engineering. They teach them all about team working under schedule and cost pressure, with the illusion and challenge of competing against themselves and others. They demand total commitment, important personal effort, and involve many frustrations and challenges along the way, but the net result is the development of highly talented young engineers. It has been demonstrated that these challenges allow the participant to highly improve personal and professional skills as important as creativity, responsibility, solving conflicts, leadership, teamwork, etc.

These principles are in the scope of what political and educational authorities in major developed countries are proposing to modernize university studies and to meet the needs of companies in the automotive industry today and tomorrow (De Miguel et al., 2006), (Davies et al., 1999), (González & Wagenaar, 2003), (Bologna Declaration, 1999).

Although the needs of this sector are not very different from the others, the dynamic character, competitiveness and technological challenges of the automotive industry make that the most demanded skills in new graduates are leadership and team motivation, responsibility at work and teamwork. Also highly rated are the capacity to innovate, and communication and negotiating skills (Sánchez et al., 2009).

2. Description of six of the most representative automotive university competitions for engineers

As it was mentioned before, today there are several automotive competitions oriented to undergraduate students in which the multidisciplinary groups of each university have to build a vehicle. Each competition has different educational objectives, as teamwork, leadership, innovation or problem solving, among others. The most important, for their educational goals, are shown on Table 1.

Although there are many differences between these competitions, all of them have in common the way the students do the work (with technical, schedule and budget requirements and constraints) and assume their responsibilities.

It should be noticed that the responsibility given to each student is real: each one is aware that a mistake by one of them is a mistake for the whole team. Equivalent responsibility would only be found in any company after some years of work. The students themselves even take it upon themselves to raise part of the financial resources needed, and it is they, under the supervision of the teachers, who manage these resources.

In the course of the educational experience carried out by taking part in these projects, planned with different teaching methods, the student must face up to specifically designed situations that will challenge them and promote their personal and professional skills. Some studies (Sánchez et al., 2009) have shown the different learning situations through which the students must pass, and the skills each experience helps to reinforce.

Competition	Evaluation	Main Event	Main Features
Formula SAE	<ul style="list-style-type: none"> • Design • Cost • Sales • Vehicle Performance 	22km track	<ul style="list-style-type: none"> • Engine limited to 600cc • All air must pass through a 20mm restriction • Restriction on vehicle overall dimension
Mini Baja SAE	<ul style="list-style-type: none"> • Design • Cost • Sales • Vehicle Performance 	Maximum distance performed in 4 hour	<ul style="list-style-type: none"> • Engine provide by organization • Not to modify engine • Restriction on vehicle overall dimension
Eco-Shell	<ul style="list-style-type: none"> • Vehicle Performance 	22km to 25km set track	<ul style="list-style-type: none"> • Several fuel possibilities supported • Restriction on overall dimensions
Supermileage SAE	<ul style="list-style-type: none"> • Design • Vehicle Performance 	15 km oval test track	<ul style="list-style-type: none"> • Engine provide by organization • Restriction to modify engine • Travel a specified distant with minimum fuel consumption
World Solar Challenge	<ul style="list-style-type: none"> • Vehicle Performance 	3.000km distance	<ul style="list-style-type: none"> • Only solar vehicles • Restriction on overall dimensions
Formula Low Cost	<ul style="list-style-type: none"> • Design • Cost • Innovations • Vehicle Performance 	60 laps on set course	<ul style="list-style-type: none"> • Engine limited to 12kw • Maximum budget of 2000€ • Event to evaluate innovations

Table 1. Main characteristics of six competitions.

2.1 The formula SAE competition

Formula SAE is probably the automotive competition that poses the greatest challenge for students and, therefore, today is the largest university event round the world. (<http://students.sae.org/competitions/formulaseries/>).

To ensure uniformity and equal opportunities in the competition, the SAE sets strict standards as to the design and manufacture of the different vehicle parts, in addition to severe safety standards. In spite of this, the participants enjoy a wide autonomy and capacity to innovate, as can be seen in the differences between the prototypes developed by each university.

Teams must present a project as if it involved a company that manufactured 1000 vehicles per year for an amateur public competing at weekends, and with a cost of less than 25,000\$.

The most important condition refers to vehicle power, restricted by engine cylinder capacity (maximum 600 cm³) and by a restricted air intake. Therefore, most machines use motorbike



Fig. 1. Formula SAE car at competition.

engines which are standard engines of around 110 HP, but by restricting the air intake their capacity is reduced to around 70 HP after appropriately designing of the intake and exhaust with fluid dynamics programs and after electronically changing the engine torque and power curves.

There are other restrictions, that are referred to vehicle size (minimum 1,520 mm wheelbase, and minimum 9 m slalom track pass), which means that the vehicles are around 2,700 to 3,000 mm long. There is also an exhaustive verification of the materials making up the chassis, and close attention is paid to safety and driving seat ergonomics.

The competition score cards are divided into two kinds: static and dynamic. Also, there are some preliminary tests that do not score, but need to be overcome in order to compete. Table 2 shows the tests together with a brief description of each one.

It is, therefore, an authentic engineering competition where in addition to vehicle speed and performance at track, the project and the product achieved are also appreciated. In this competition the students have a totally leading role. They have to organise themselves, find the resources needed, administer project time, costs, etc, and all this under the supervision and guidance of the teachers and the Faculty Advisor. They have to design and build the parts by hand (the fewer purchased the better), and four of them must finally drive the car.

What is new about this project, apart from it being a new, innovative educational methodology where the vehicle is simply the means to get the best possible training, is the challenge posed to the students by having to take on and participate in an entire vehicle development life cycle. This can only be achieved by forming a strong working team, promoting active participation, the assumption of responsibilities, decision making and involvement in reaching a common objective. In exchange the student gets the satisfaction of being able to take the vehicle built by their own effort to an actual competition.

In 2009, more than 200 universities throughout the world took part in the Formula SAE. For this it has been necessary to extend the competitions to other countries, like England, where it is called Formula Student, Australia, etc, as well as the original in Michigan.

2.2 The Baja SAE competition

Baja SAE is a university competition whose aim is to improve the preparation and education of young engineers through an event that simulates a real engineering project where students have to design, manufacture, test, and compete with an off-road vehicle. (<http://students.sae.org/competitions/bajasae/>).

Events	Points	Description
Preliminary tests	0	Pre-competition safety tests.
Technical inspection	-	General check of car by judges.
Tilt	-	Car inclination up to 60° checking its stability and that no type of liquid is leaking.
Brakes	-	Simultaneous blocking of all four wheels after a brief acceleration.
Noise	-	Check to ensure vehicle emits less than 110 dB under certain acceleration conditions.
Static	325 in total	Presentations and oral defence in front of the judges of technical solutions adopted.
Design	150	Technical defence of vehicle design and solutions proposed.
Presentation	75	Marketing presentation, convincing the judges to choose their car compared to the others.
Costs	100	Written report detailing cost of each part and component of the unit built.
Dynamic	675 in total	Different on-track trials with the single-seater.
Acceleration	75	Cover 75 m on a straight run in the shortest possible time
Manoeuvrability (Skidpad)	50	Manoeuvrability to run a 9 metre circle in both directions.
Sprint	150	Quick lap of the circuit.
Endurance	350	Overall vehicle performance and reliability in 22 laps of a circuit.
Fuel	50	Minimum consumption in endurance trial
Total	1000	

Table 2. Description of Formula SAE competition trials.

Teams have to assume that they have been hired by a manufacture firm to build an off-road vehicle capable of competing in any field. The restrictions are on the design of chassis, and the engine modifications are forbidden, as the engine is the same for all teams. Unlike Formula SAE standards these restrictions limit the design and innovation in these areas, leaving the engineer's imagination for other areas of the vehicle. This, in turn, results in a reduction in costs and activities compared with Formula SAE. The target for selling the prototype is the non-professional weekend racer, as well as the Formula SAE, and the teams must develop a product that has high performance in acceleration, traction, with common parts and easy maintenance. It is a competition that also simulates a case study of the life cycle of a vehicle, where students also have to get organized sponsorship for their project. All the teams have the same 10HP engine, and it is not allowed to make any changes or modifications. The overall dimension of the vehicle is recommended to be around 2750 mm,

and the track is restricted to a maximum of 1900 mm. The cage in the chassis is very limited in terms of innovation to ensure the safety at all situations, as in the event of rollover or impacting with another vehicle.



Fig. 2. Baja SAE vehicles have to overcome all kind of fields.

Judges positively value the manufacturing capacity with conventional tools that are available to anyone. Teams will be evaluated on design, and marketing costs (not all of Baja competitions own this event). In the dynamic performance, the students must demonstrate their ability to accelerate, steer, and drive the vehicle to finally be evaluated in endurance where they is allowed to repair the vehicle in the race if necessary. Table II shows the events with a brief description of each one.

Baja SAE competition began in 1976, and currently has 6 competitions in the USA, Brazil, South Africa and South Korea, and more than 250 universities are involved with more than 4000 students participating.

2.3 Eco-Shell Marathon

Eco-Shell Marathon is a university and college competition that has the goal to compete with more efficient vehicle for a given distance. There are two categories, one corresponding to futuristic vehicles where reducing drag and maximizing efficiency is the major premise and the second category corresponding to four-wheeled vehicle using conventional or alternative fuels. (<http://www.shell.com/home/content/ecomarathon/>)

The rules limit the size in wheelbase, track and height of vehicles, chassis design (to ensure safety), the type of propulsion (it can be used combustion, fuel cell or solar) and fuel tank is limited to 30 cm³ to 250 cm³, limiting the engines size to use. The following list outlines the types of fuel that can be used:

- Shell Unleaded 95 (Europe & Asia) / Shell Regular 87 (U.S.)
- Shell Diesel]
- Liquefied Petroleum Gas (LPG)
- Shell Gas to Liquid (GTL 100%)
- Fatty Acid Methyl Ester (100% FAME)
- Ethanol E100 (100% Ethanol)
- Hydrogen

Event	Points	Description
Static Events -	300 in total	Presentations and oral defence in front of the judges
Design Report & Evaluation	150	Technical defence of vehicle design and solutions proposed
Cost Report & Cost Production	100	Writing report dealing cost of each part and component of the unit built
Presentation	50	Marketing presentation, convincing the judges to choose their car.
Dynamic Events -	700 points	Different on-track trials with the off-road vehicle
Acceleration/Speed	85	Cover 30m o 45m on a straight run in the shortest possible time
Traction/Hill Climb	75	The traction event will be either hill climb or pulling an object
Manoeuvrability	75	Manoeuvrability including tight turns, pylon manoeuvres, ruts and bumps, drop-offs, sand, rocks, gullies, logs, and inclines.
Specialty Rock Crawl	75	A special event to test the vehicle on unique off-road conditions
Endurance	400	Maximum distance performed in 4 hours
Total Points	1000	

Table 3. Description of Formula Baja competition trials.



Fig. 3. Aerodynamics is an important goal at Ecoshell Marathon.

Depending on the category in which they participate, vehicles must meet travel between 22 km or 25 km. The assessment of efficiency is done in accordance with a table of equivalence developed by the competition.

The objective of the competition is to simulate a real art project where teams work for a year designing and building a vehicle. The event organizers also want students to integrate, design and develop a product that is sustainable, that controls the energy used and that is concern about environmental protection. This target causes that the greatest number of team efforts are focused in engines, transmissions and aerodynamics.

2.4 Supermileage

Supermileage's objective goes in the same line as the previous competition, that is, developing a single person, extremely high mileage vehicle that complies with the organization rules. The competition intention passes through encourage the fuel economy. (<http://students.sae.org/competitions/supermileage/>).



Fig. 4. Supermileage vehicle at competition.

Team's vehicles must be conceived, designed and manufactured by the team members without direct involvement from faculty and technical staff in the college/school or professionals in the motorsports community.

All the innovation and creativity of the teams is focused on consumption and weight reduction. The rules set restrictions on engine type, fuel used, chassis construction, and minimum driver mass allowed. Although in this competition there are no rules for vehicle dimension boundaries, which represents a plus to creativity, one of the technical inspections test, call manoeuvrability, has specific and defined turn radius and fix cone slalom distant, which are considered as rule restrictions.

The competition is divided into the design event and the performance run, as the other SAE competition series. At the design event the teams have to elaborate a report to describe their design decisions, and the students have to defend it in front a jury. The performance run consist on a race of 15Km in which the car is weighted before and after the completion of the track, calculating then the kilometres per litter of fuel, weighing them with the elapsed time.

2.5 World solar challenge

First promoted in 1987 by the adventurer Hans Tholstrup, World Solar Challenge began in Australia, and consists on building a solar vehicle with certain rules described in the technical regulations. The aim is to stimulate research into sustainable transportation. (<http://www.globalgreenchallenge.com.au/>).



Fig. 5. WSC cars have large areas to place solar panels.

From an academic point of view, the goal is to encourage the students to put their efforts on developing a sustainable vehicle that is able to travel a distance of 3.000km in the shortest time using only sunlight as fuel. The competition take place in Australia and it is sponsored by Australian administrations. It usually takes three days to complete the distance, and there are not other events to evaluate the design concepts, sales or management skills.

Teams are restricted by the overall vehicle dimensions, the solar array area, and the minimum driver's weigh. There are also some other rules about chassis design focused on ensuring the driver safety.

The competition has actually 32 participants in the university category, and most of them also participate in the eco-shell Marathon held in Europe.

2.6 Formula Low Cost

Formula Low Cost was created by the Institute of Automotive and Transport Engineering (ISAT) in Nevers (France) in 2008 with the aim of extend these kind of competitions to universities all around the world, regardless their economic possibilities, Low Cost Formula is a competition aimed at extending university engineering education through the construction of a kart type vehicle. The main difference with Formula SAE is the budget, which cannot exceed 2.000€ for its build, based on fixed prices of components. (<http://www.kartlowcost.com/Presentation.html>)

Teams have to assume they have been contracted to manufacture a vehicle whose main feature is that it has not suspension. The rules establish that they must design the chassis to ensure safety, and the materials are limited to steel and/or aluminum. The engine cannot exceed 12KW and are well worth the innovations that can be made. Although the size of vehicle is complete free, the possibilities with the 2,000€ budget restriction are limited.

As well as the other engineering competitions, teams valuation is done through a set of tests, both static (where it is evaluated the technical and cost features) and dynamic (where it is evaluated the track vehicle performance). The statics events have the aim to assess the designs, innovations and cost of the prototype. The dynamic events are composed of three: a classification, a sprint race (15 laps) and resistance (60 laps).



Fig. 6. Karting competition at Formula Low Cost s.

Formula Low Cost also provides an opportunity for students to participate throughout the life cycle of a real project, in order to prepare engineers to manage projects, budgets and learn to work as a part of a team. Table III shows the events with a brief description of each one.

Event	Points	Description
Static Events -	478 in total	Presentations and oral defence in front of the judges
Cost Report	183	Writing report detailing cost of each part and component of the unit built
Innovations	183	Technical evaluation of innovations
Design	112	Technical defence of vehicle design and solutions proposed
Dynamic Events -	441 points	Different on-track trials with the off-road vehicle
Acceleration/Speed	75	Cover a straight run in the shortest possible time
Sprint	183	A event to classified the vehicle for the main event
Endurance	183	60 laps to a circuit
Total Points	919 points	

Table 3. Description of Formula Low Cost competition trials

In a general view, Table 1 lists the main characteristics of these competitions. Some of them are focused on evaluating the engineering, product cost and sales skills, as are the SAE Series Events; some others are focused on developing an specific vehicle based on fuel

efficiency using conventional or alternative fuels; and the newest competition, the Formula Low Cost, makes the costs the main restriction, and it is the only one with an specific event evaluating innovations.

Each competition present differences in team member's size, depending on the universities and work philosophy. Formula SAE and Mini Baja teams tend to be more numerous than the others, surely because of fewer restrictions and greater design possibilities.

The principal common characteristic or these competitions, and some other round the world, is that they represent a challenge for the students to overcome themselves and exchange experiences with students from five continents.

3. An example of the activities performed at one of these competitions: the participation of the UPM on Formula SAE.

UPMracing is the first Spanish Formula SAE competition team, and was founded on 2003 at the Madrid Polytechnic University, UPM. At that moment, a group of teachers and professors of the School of Industrial Engineering, ETSII-UPM, and researchers of the University Institute for Automobile Research, INSIA-UPM, selected this competition as the most complete. The team consisted of about 35 students from the final courses or ETSII and the Master's course in Automotive Engineering (Figure 7). In the years that followed, several students from other university schools joined in, like the Aeronautic Techniques and Industrial Techniques schools, what lead to important improvements in the performance (Figure 7).



Fig. 7. The first team with the UPM-01 at INSIA-UPM.

When writing this article, UPMracing has accumulated seven years of experience with the same number of single-seaters built that have taken part in the 2004 - 2010 editions of the Formula Student in England and Germany.

From the beginning, the team has had four principles that are a statement of the teaching method used:

- Learn by applying
- Learn by doing
- Learn in a team
- Learn by competing

The members of the team have been organized in several departments according to the main systems of the vehicle, with the aim of reproduce similar conditions to the work carried out in real companies. These divisions are supervised by a small team of teachers, but the students have a great level of autonomy both on technical and organizational field.

Learning situations Skills	1. Initial training in all knowledge areas	2. Supplementary material and in-process tutorial sessions	3. Division into sub-groups according to work areas	4. Assigning duties, objectives and responsibilities.	5. Organisation and planning according to general costs and schedules	6. Every student is responsible for their work and collaborates with the others	7. Wide personal autonomy and possibilities for innovation	8. Periodic presentation and update meetings	9. Resources searches and usage management	10. All take part in vehicle manufacture	11. Former students coordinate activities of newcomers	12. Participation in a real experience	13. Putting acquired knowledge into practice	14. Competing against the world's best universities	15. Presenting and defending work done in front of a panel	16. Need to disseminate the experience and the results
1. Ability to work as part of a team			X	X	X	X		X	X	X	X	X		X	X	X
2. Leadership qualities			X	X	X	X		X	X	X	X	X		X	X	X
3. Ability to motivate			X	X	X	X		X		X	X	X		X	X	X
4. Capacity for responsibility and commitment		X	X	X	X	X	X	X	X	X	X	X		X	X	X
5. Capacity for innovation				X		X	X			X		X	X	X		
6. Negotiating skills			X	X	X	X	X	X	X	X	X	X		X	X	X
7. Capacity for self-motivation	X	X	X	X		X	X		X					X	X	
8. Analytical skills	X	X	X	X	X	X	X	X	X				X	X		
9. Ability to summarise				X	X	X	X			X		X	X	X	X	X
10. Capacity for criticism and self-criticism		X	X	X	X	X	X	X		X	X	X	X	X	X	X
11. Ability for self-learning	X	X	X	X			X					X	X			
12. Organisational and planning skills		X	X	X	X	X	X	X	X	X	X	X	X	X	X	X
13. Ability to identify problems			X	X	X	X	X	X	X	X	X	X	X	X	X	X
14. Ability to resolve conflicts				X	X	X		X	X	X	X	X	X		X	X
15. Ability to generate new ideas (creativity)				X		X	X	X	X			X	X	X	X	X
16. Ability to take up new initiatives				X	X	X	X		X	X		X	X	X		X
17. Ability to adapt to changing circumstances	X		X	X	X	X			X	X	X	X	X	X	X	X
18. Ability to work on one's own	X	X		X	X	X	X						X			
19. Ability to make decisions				X	X	X	X	X	X	X	X	X	X	X	X	X
20. Interpersonal skills			X	X	X	X		X	X	X	X	X		X	X	X
21. Ability to assimilate and apply knowledge	X	X		X		X	X			X	X	X	X		X	
22. Capacity for dynamism				X	X	X	X		X	X	X	X		X	X	X
23. Capacity for discipline and self-control	X	X	X	X	X	X	X	X	X	X	X	X	X	X	X	X
24. Oral and written communication in english	X	X							X			X		X	X	X

Table 7. Promotion of personal and professional skills according to different activities and learning situations.



Fig. 8. Students and Faculty Advisors with the UPM'06.

To sum up, the educational experience provided by taking part in the project and the teaching methods used mean that the student must face up to specifically designed situations that will challenge them and promote their personal and professional skills. Table 7 shows 16 learning situations related to different moments or activities of the project, cross-referenced with 24 skills, which in the light of the literature consulted and the studies and surveys presented, are deemed to be the most sought after in an engineer getting ready to work in the automotive sector.

3.1 Assessing the experience

From the first steps of the project the faculty advisors have been interested to know the opinion of the students taking part, what needs to be kept as it is, what needs improving, and obviously, to what extent the project's goals have been achieved. And among these goals is the distinguishing improvement in students' personal and professional skills compared to traditional activities.

Every year, all the students are given a survey with the 24 most important skills for an engineer in the automotive sector in order to get to know their opinion of the importance of these skills when working in their profession, as well as the level of their success in the subjects taken as part of their degree, and likewise during the SAE Formula training process. Several conclusions can be drawn from the general results of the survey that are shown in Table 8:

- The most important skills for the participants are the capacity for responsibility and commitment, teamwork, decision making, creativity, solving conflicts and communication in English. This classification is in total harmony with the opinion of companies, which shows that the training experience suitably orients students towards the labour market, especially if we compare the results with those shown in Table 1.
- The students give an average score of 4.2 points out of 5 to the list of 24 skills. Their average level of success during their degree is 2.3 points, while achievement during the SAE Formula project is 3.6 points.
- Focusing on the 7 most appreciated skills, the average score of importance given is 4.7 points out of 5, with a score during their degree of 1.9 points and practically double, 3.7 points for the SAE Formula project.

Skills	Level of importance for students	Degree of success in ETSII	Degree of success in F SAE
1. Ability to work as part of a team	4.9	2.0	4.1
2. Leadership qualities	4.2	1.1	3.6
3. Ability to motivate	4.4	1.3	3.8
4. Capacity for responsibility and commitment	5.0	3.2	3.8
5. Ability to innovate	4.2	1.3	3.6
6. Negotiating skills	3.6	1.2	2.8
7. Capacity for self-motivation	4.0	2.2	3.2
8. Analytical skills	4.4	2.8	3.4
9. Ability to summarise	4.0	3.1	3.3
10. Capacity for criticism and self-criticism	4.0	2.1	3.6
11. Ability for self-learning	4.2	3.9	4.3
12. Organisational and planning skills	4.0	3.2	3.2
13. Ability to identify problems	4.8	2,6	4.0
14. Ability to resolve conflicts	4.4	1.9	3.3
15. Ability to generate new ideas (creativity)	4.4	1.3	3.6
16. Ability to take up new initiatives	3.7	1.3	3.3
17. Ability to adapt to changing circumstances	4.1	2.7	3.9
18. Ability to work on one's own	3.4	3.8	3.2
19. Ability to make decisions	4.9	2.0	4.0
20. Interpersonal skills	3.8	2.7	4.3
21. Ability to assimilate and apply knowledge	4.1	3.0	4.0
22. Capacity for dynamism	3.8	2.0	3.7
23. Capacity for discipline and self-control	3.8	3.0	3.3
24. Oral and written communication in English	4.4	1.6	3.1
Mean value	4,2	2,3	3,6

Table 8. Scores from 0 to 5 points of the importance given by students to the 24 most important personal and professional skills for an engineer in the automotive sector, as well as the extent of success during their degree at the School of Industrial Engineers (ETSII-UPM) and during their time on the project (F SAE).

As can be seen, the students find their way through the competition has contributed to the promotion of their personal and professional skills more than the rest of the activities carried out during his career in engineering. This assessment is certainly influenced, year after year, for the interest they awakened this activity, but it has been shown in both the UPM and in other participating universities, the great importance that these competitions have in the integral formation of engineering students before they enter the job market. And this importance is even greater if the sector that leads the student is the automotive.

4. Conclusions

In this paper it has been described the growing importance given by leading universities to improving the skills of their students, beyond mere theoretical – practical knowledge.

In this way, different automotive competitions for engineering universities round the world are presented, analyzing their objectives, work to be performed by the students, tests, etc.

A growing number of these leading technical universities consider them very useful activities for the improvement of those desired skills.

The paper presents as well, the way the first university in Spain (ETSII-UPM) that competed in the most complete of these competition (Formula SAE) manage their students on it, how the competition is integrated into their own academic programs, and the assessment of their experience in terms of personal and professional skills' improvement among their students.

Surveys of student conducted each year show that they consider that taking part on one of this competition has more contributed to the improvement of their personal and professional abilities and skills than the rest of the activities done during the whole career of five years.

Students, teachers and company employers around the world agree that this competitions promote careers and excellence in engineering as it encompasses all aspects of the automotive industry including research, design, manufacturing, testing, developing, marketing, management and finances. They take students out of the classroom and allow them to apply textbook theories to real work experiences.

5. References

- Aparicio, F., González, R.M., Sobrevila, M.A. (2005). *Formación de Ingenieros. Objetivos, métodos y estrategias*, Instituto de Ciencias de la Educación, UPM.
- Bolívar, C., *Más allá de la formación: el desarrollo de competencias*. (2001). <http://www.arearh.com/formación/masallaformacion.htm>.
- Bologna Declaration. (1999). Joint declaration of the European Ministers of Education, 19th June.
- Bowen, E., Lloyd, S. and Thomas, S. (2005). *Embedding Personal Development Planning into the Curriculum Via a Key Skills Assignment*, Int. J. Engineering Education. Vol. 21, No. 6, pp. 1159±1167.
- Chadha, D. and Nicholls, G. (2006). *Teaching Transferable Skills to Undergraduate Engineering Students: Recognising the Value of Embedded and Bolt-on Approaches*, Int. J. Engng Ed. Vol. 22, No. 1, pp. 116±122.
- Davies, H. A., Csete, J. and Poon, L. K. (1999). *Employer's Expectations of the Performance of Construction Graduates*, Int. J. Engineering Education. Vol. 15, No. 3, pp. 191-198,
- De Miguel, M., Alfaro, I.J., Apocada, P.M., Arias, J.M., García, E., Lobato, C. and Pérez, A. (2006). *Metodologías de enseñanza y aprendizaje para el desarrollo de competencias*. Madrid: Alianza Editorial.
- European Parliament. (2006). Recommendation 2006/962/EC of the European Parliament and of the Council on key competences for lifelong learning: OJ L 394, 30.12.2006; Bull. 12
- González, J., Wagenaar, R. (2003). *Tuning Educational Structures in Europe*. Universidad de Deusto,.

Sánchez, F.J., Aparicio, F., Álvarez, M.A. and Jiménez, F. (2009). *SAE Formula Project for Developing Personal and Professional Skills in Automotive Engineers*, Int. J. Engineering Education. Vol. 25, No. 3, pp. 585-594.

<http://students.sae.org/competitions/bajasae/>

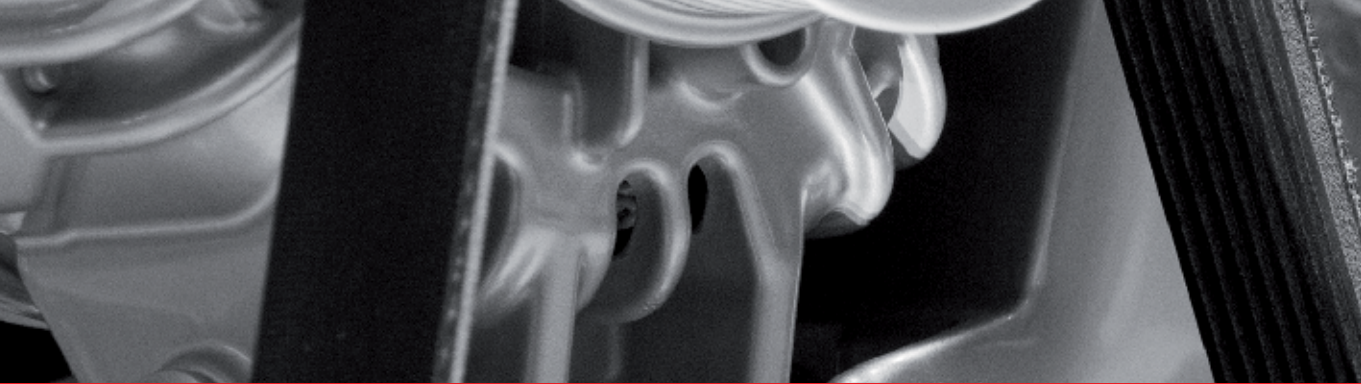
<http://students.sae.org/competitions/formulaseries/>

<http://students.sae.org/competitions/supermileage/>

<http://www.globalgreenchallenge.com.au/>

<http://www.kartflowcost.com/Presentation.html>

<http://www.shell.com/home/content/ecomarathon/>



Edited by Marcello Chiaberge

In the last few years the automobile design process is required to become more responsible and responsibly related to environmental needs. Basing the automotive design not only on the appearance, the visual appearance of the vehicle needs to be thought together and deeply integrated with the “power” developed by the engine.

The purpose of this book is to try to present the new technologies development scenario, and not to give any indication about the direction that should be given to the research in this complex and multi-disciplinary challenging field.

Photo by VanderWolf / iStock

IntechOpen

